H. CHOI
H. G. CHOI
J. Y. YOO (EDS.)

Computational Fluid Dynamics 2008

Springer

Computational Fluid Dynamics 2008

“This page left intentionally blank.”

Haecheon Choi · Hyoung Gwon Choi
Jung Yul Yoo (Eds.)

Computational Fluid Dynamics 2008

Springer

Prof. Haecheon Choi
School of Mechanical and Aerospace Engineering
Seoul National University
San 56-1, Shinlim-dong, Kwanak-gu,
Seoul 151-742, Republic of Korea
E-mail: choi@snu.ac.kr

Prof. Hyoung Gwon Choi
Department of Mechanical Engineering
Seoul National University of Technology
172 Gongreung-2-dong, Nowon-gu,
Seoul 139-743, Republic of Korea
E-mail: hgchoi@snut.ac.kr

Prof. Jung Yul Yoo
School of Mechanical and Aerospace Engineering
Seoul National University
San 56-1, Shinlim-dong, Kwanak-gu,
Seoul 151-742, Republic of Korea
E-mail: jyyoo@snu.ac.kr

ISBN 978-3-642-01272-3 e-ISBN 978-3-642-01273-0

DOI 10.1007/978-3-642-01273-0

Library of Congress Control Number: Applied for

Typesetting: Scientific Publishing Services Pvt. Ltd., Chennai, India.
Cover Design: WMX Design GmbH, Heidelberg.

Printed in acid-free paper

9 8 7 6 5 4 3 2 1

springer.com

Preface

We are delighted to present this book which contains the Proceedings of the Fifth International Conference on Computational Fluid Dynamics (ICCFD5), held in Seoul, Korea from July 7 through 11, 2008. The ICCFD series has established itself as the leading international conference series for scientists, mathematicians, and engineers specialized in the computation of fluid flow. In ICCFD5, 5 Invited Lectures and 3 Keynote Lectures were delivered by renowned researchers in the areas of innovative modeling of flow physics, innovative algorithm development for flow simulation, optimization and control, and advanced multidisciplinary applications.

There were a total of 198 contributed abstracts submitted from 25 countries. The executive committee consisting of C. H. Bruneau (France), J. J. Chattot (USA), D. Kwak (USA), N. Satofuka (Japan), and myself, was responsible for selection of papers. Each of the members had a separate subcommittee to carry out the evaluation. As a result of this careful peer review process, 138 papers were accepted for oral presentation and 28 for poster presentation. Among them, 5 (3 oral and 2 poster presentation) papers were withdrawn and 10 (4 oral and 6 poster presentation) papers were not presented. The conference was attended by 201 delegates from 23 countries. The technical aspects of the conference were highly beneficial and informative, while the non-technical aspects were fully enjoyable and memorable.

In this book, 3 invited lectures and 1 keynote lecture appear first. Then 99 contributed papers are grouped under 21 subject titles which are in alphabetical order. Lastly, 12 poster presentation papers appear as Technical Notes.

Thanks are due to our sponsors, NASA Ames Research Center, Seoul National University (SNU), The Korean Society of Mechanical Engineers, and a number of other domestic and international organizations. In particular, the continued support of NASA is essential for the success of this conference series. I would also like to express my deepest gratitude to my fellow Local Organizing Committee members, in particular, to Prof. Haecheon Choi, the Secretary General, who displayed his utmost intelligence and resourceful dedication throughout the entire process of ICCFD5. Further, I would like to thank my staffs in the Institute of Advanced Machinery and Design, and the graduate students in the School of Mechanical and Aerospace Engineering, SNU, for their tremendous efforts in making this conference a success.

Seoul, Korea
January 2009

Jung Yul Yoo
Chairman

“This page left intentionally blank.”

Contents

Part 16: Compressible Flow 2

Part 17: Error Estimation and Control

Part 18: Flow Control/Instability

Part 1
Plenary Lectures

“*This page left intentionally blank.*”

Lattice Boltzmann Methods for Viscous Fluid Flows and Two-Phase Fluid Flows

Takaji Inamuro

Department of Aeronautics and Astronautics, and
Advanced Research Institute of Fluid Science and Engineering,
Graduate School of Engineering, Kyoto University, Kyoto 606-8501, Japan
inamuro@kuaero.kyoto-u.ac.jp

Abstract. Lattice Boltzmann methods (LBMs) for viscous fluid flows and for two-phase fluid flows are presented. First, the LBMs for incompressible viscous fluid flows and for temperature fields are described. Then, a numerical example of unsteady flows in a three-dimensional porous structure is illustrated. Second, the LBM for two-phase fluid flows is presented. The method can simulate flows with the density ratio up to 1000. Numerical examples of binary droplet collision and two-phase flows in a branch channel are illustrated. Finally, the method for simulating solid-fluid mixture flows by the LBM for multicomponent immiscible fluids with the same density is explained, and a numerical example of the behavior of a biconcave discoid particle in a square pipe flow is illustrated.

1 Introduction

Recently, the lattice Boltzmann method (LBM) has been developed into an alternative and promising numerical scheme for simulating viscous fluid flows and multi-phase fluid flows (e.g., see [1, 2, 3, 4, 5]). The LBM is based on a discrete particle kinetics, where the kinetic-type equation for the particle velocity distribution function is solved. Macroscopic quantities such as mass density and momentum density are obtained by evaluating the hydrodynamic moments of the distribution function. The advantages of the LBM are the simplicity of the algorithm, the accuracy of the mass and momentum conservations, and the suitability for parallel computing.

On the other hand, the kinetic-equation approaches of fluid-dynamic equations called the kinetic schemes have been proposed for obtaining numerical solutions of the Euler or Navier–Stokes equations (e.g., see [6, 7]). Junk and Rao [8] have proposed a new discrete velocity method for Navier–Stokes equations based on kinetic schemes and have investigated the relation between the lattice Boltzmann method and the kinetic scheme. Also, Sone [9] has presented a simple way to construct a kinetic system of equations and initial conditions from a set of partial differential equations in a conservative form

(e.g., the Euler and Navier–Stokes sets) in such a way that some moments of the solution of the kinetic system satisfy a set of partial differential equations exactly.

From the above-mentioned point of view, the LBM is considered as one of the kinetic schemes for incompressible viscous fluid flows. Namely, both the LBMs and the kinetic schemes originate from the kinetic-type equations with the simple linear form of the differential term. Thus with these methods we can avoid some difficulties in numerical calculations of the Navier-Stokes equations (e.g., the pressure term in the incompressible Navier–Stokes set). In this sense, the LBM is a heuristic scheme for a set of partial differential equations in a conservative form.

In the present paper, the LBM is considered as a heuristic kinetic scheme of the Navier-Stokes equations for viscous fluid flows and for two-phase fluid flows. The formal relation between the LBM and the Navier-Stokes equations has been derived by Inamuro et al. [10]. We do not consider the direct connection between the LBM and the kinetic theory.

2 Lattice Boltzmann Method

2.1 Lattice Gas Model and Evolution Equation

Hereafter, we use non-dimensional variables as shown in Appendix of Ref. [5]. In LBM, a modeled fluid composed of identical particles whose velocities are restricted to a finite set of N vectors $\boldsymbol{c}_i$ $(i = 1, 2, \cdots, N)$ is considered. The fifteen-velocity model ($N = 15$) is used in the present paper. The velocity vectors in this model are given by

$$[\boldsymbol{c}_1, \boldsymbol{c}_2, \boldsymbol{c}_3, \boldsymbol{c}_4, \boldsymbol{c}_5, \boldsymbol{c}_6, \boldsymbol{c}_7, \boldsymbol{c}_8, \boldsymbol{c}_9, \boldsymbol{c}_{10}, \boldsymbol{c}_{11}, \boldsymbol{c}_{12}, \boldsymbol{c}_{13}, \boldsymbol{c}_{14}, \boldsymbol{c}_{15}] = \begin{bmatrix} 0 & 1 & 0 & 0 & -1 & 0 & 0 & 1 & -1 & 1 & 1 & -1 & 1 & -1 & -1 \\ 0 & 0 & 1 & 0 & 0 & -1 & 0 & 1 & 1 & -1 & 1 & -1 & -1 & 1 & -1 \\ 0 & 0 & 0 & 1 & 0 & 0 & -1 & 1 & 1 & 1 & -1 & -1 & -1 & -1 & 1 \end{bmatrix}. \quad (1)$$

The physical space is divided into a cubic lattice, and the evolution of particle population at each lattice site is computed by using the particle distribution function. The evolution of the particle distribution function $f_i(\boldsymbol{x}, t)$ with velocity $\boldsymbol{c}_i$ at the lattice point $\boldsymbol{x}$ and at time t is computed by the following equation [11, 12]:

$$f_i(\boldsymbol{x} + \boldsymbol{c}_i \Delta x, t + \Delta t) = f_i(\boldsymbol{x}, t) - \frac{1}{\tau_f} \left[f_i(\boldsymbol{x}, t) - f_i^{\mathrm{eq}}(\boldsymbol{x}, t) \right], \quad (2)$$

where Δx is a spacing of the cubic lattice, Δt is a time step during which the particles travel the lattice spacing, τ_f is a dimensionless single relaxation time of $O(1)$, and f_i^{eq} is an equilibrium distribution function defined below. Note that BGK model with a single relaxation time is used for the collision term in Eq. (2).

A suitable equilibrium distribution function for incompressible viscous flows is given by [12]

$$f_i^{\mathrm{eq}} = E_i \rho \left[1 + 3\boldsymbol{c}_i \cdot \boldsymbol{u} + \frac{9}{2}(\boldsymbol{c}_i \cdot \boldsymbol{u})^2 - \frac{3}{2}\boldsymbol{u} \cdot \boldsymbol{u} \right], \tag{3}$$

where $E_1 = 2/9$, $E_2 = E_3 = \cdots = E_7 = 1/9$, $E_8 = E_9 = \cdots = E_{15} = 1/72$, and ρ and $\boldsymbol{u}$ are fluid density and fluid velocity, respectively, which are calculated in terms of the particle velocity distribution functions as

$$\rho = \sum_{i=1}^{15} f_i, \tag{4}$$

$$\boldsymbol{u} = \frac{1}{\rho} \sum_{i=1}^{15} \boldsymbol{c}_i f_i. \tag{5}$$

Eq. (3) is derived so that macroscopic variables satisfy the Navier-Stokes equations as shown in Sec. 2.4 and has a similar form to an expansion of the Maxwell distribution up to $|\boldsymbol{u}|^2$ on the assumption of $|\boldsymbol{u}| \ll c$ (incompressible condition).

The pressure p is related to the density by

$$p = \frac{1}{3}\rho \ . \tag{6}$$

2.2 Lattice Boltzmann Method for Temperature Field

The above LBM is an athermal model (in which no temperature effect is included) for incompressible viscous fluid flows. We can construct an LBM for fluid temperature T as a passive scalar by using a new particle distribution function g_i as follows [13]:

$$g_i(\boldsymbol{x} + \boldsymbol{c}_i \Delta x, t + \Delta t) = g_i(\boldsymbol{x}, t) - \frac{1}{\tau_g} \left[g_i(\boldsymbol{x}, t) - g_i^{\mathrm{eq}}(\boldsymbol{x}, t) \right], \tag{7}$$

where

$$g_i^{\mathrm{eq}} = E_i T \left(1 + 3\boldsymbol{c}_i \cdot \boldsymbol{u} \right). \tag{8}$$

In the above equation, $\boldsymbol{u}$ is obtained by Eq. (5), and the temperature T is calculated by

$$T = \sum_{i=1}^{15} g_i. \tag{9}$$

Eq. (8) is derived so that the temperature T satisfies the convection–diffusion equation as shown in Sec. 2.4.

2.3 Boundary Condition

Boundary conditions in LBMs are different from usual computational fluid dynamics (CFD) methods. In the LBM, the distribution functions of the particles pointing to the fluid region needs to be specified on the boundary. The bounce-back boundary condition, in which the distribution function of the particle pointing to the fluid is set equal to that of the particle in the opposite direction, has been usually used to model stationary walls. The details of the boundary conditions for the LBM are reviewed in the paper by Yu et al. [14].

2.4 Governing Equations for Macroscopic Variables

Applying the asymptotic theory [9, 10] to Eqs. (2), (3), (7), and (8) with appropriate initial and boundary conditions, we find that the asymptotic expansions of the macroscopic variables with respect to Δx can be expressed by $u_\alpha = (\Delta x)u_\alpha^{(1)} + (\Delta x)^3 u_\alpha^{(3)} + \cdots$, $p = 1/3 + (\Delta x)^2 p^{(2)} + (\Delta x)^4 p^{(4)} + \cdots$, and $T = T^{(0)} + (\Delta x)^2 T^{(2)} + \cdots$, and that $u_\alpha^{(1)}$, $p^{(2)}$, and $T^{(0)}$ satisfy

$$\frac{\partial u_\alpha^{(1)}}{\partial x_\alpha} = 0, \tag{10}$$

$$\frac{\partial u_\alpha^{(1)}}{\partial t} + u_\beta^{(1)} \frac{\partial u_\alpha^{(1)}}{\partial x_\beta} = -\frac{\partial p^{(2)}}{\partial x_\alpha} + \frac{1}{3}\left(\tau_f - \frac{1}{2}\right) \frac{\partial^2 u_\alpha^{(1)}}{\partial x_\beta^2}, \tag{11}$$

$$\frac{\partial T^{(0)}}{\partial t} + u_\alpha^{(1)} \frac{\partial T^{(0)}}{\partial x_\alpha} = \frac{1}{3}\left(\tau_g - \frac{1}{2}\right) \frac{\partial^2 T^{(0)}}{\partial x_\alpha^2}, \tag{12}$$

where $\alpha, \beta = x, y, z$ (subscripts α and β represent Cartesian coordinates and the summation convention is used). Eqs. (10), (11), and (12) are the continuity equation, the Navier–Stokes equations, and the convection–diffusion equation for the fluid temperature, respectively, in which the kinematic viscosity ν and the thermal diffusivity α_T of the fluid are given by

$$\nu = \frac{1}{3}\left(\tau_f - \frac{1}{2}\right) \Delta x, \tag{13}$$

$$\alpha_T = \frac{1}{3}\left(\tau_g - \frac{1}{2}\right) \Delta x. \tag{14}$$

Therefore, it is found that the solutions of the lattice Boltzmann method give the macroscopic flow velocities, the pressure gradient, and the fluid temperature for incompressible fluid with relative errors of $O[(\Delta x)^2]$ [10, 13]. It is noted that the relative errors of $O[(\Delta x)^2]$ are caused by the compressibility effect.

Finally, it can be shown that the heat flux $\boldsymbol{q} = (\Delta x)\boldsymbol{q}^{(1)} + (\Delta x)^3 \boldsymbol{q}^{(3)} + \cdots$ is related to $\boldsymbol{u}_T = (\Delta x)\boldsymbol{u}_T^{(1)} + (\Delta x)^3 \boldsymbol{u}_T^{(3)} + \cdots$ as

$$\boldsymbol{q}^{(1)} = -\frac{1}{3}\tau_g \nabla T^{(0)} = T^{(0)}(\boldsymbol{u}_T^{(1)} - \boldsymbol{u}^{(1)}), \tag{15}$$

where the thermal conductivity λ is given by

$$\lambda = \frac{1}{3}\tau_g \Delta x, \tag{16}$$

and

$$\boldsymbol{u}_T = \frac{1}{T}\sum_{i=1}^{15} \boldsymbol{c}_i g_i. \tag{17}$$

2.5 Numerical Examples

Unsteady flows in a three-dimensional porous structure shown in Fig. 1 are illustrated. There exist nine identical spherical bodies in a rectangular domain. The domain is divided into $73 \times 69 \times 69$ cubic lattice in the x-, y- and z-directions. The spherical body is made up of a lattice block; the body does not have a smooth surface. The diameter of the circumscribed sphere of the body is $28.4\Delta x$. The no-slip boundary condition [15] is used on the body, and the slip boundary condition is used on the side walls. The periodic boundary condition with a pressure difference fixed in time [16] is used at the inlet and the outlet. Figure 2 shows velocity vectors on the planes of (a) $y/H = 0.62$, (b) $z/W = 0.09$, and $x/L = 0.45$ at $Re = \overline{u}_{\rm in} D_{\rm p}/\nu = 127$ where $\overline{u}_{\rm in}$ is the time- and space-averaged velocity at the inlet, and $D_{\rm p} = 29.4\Delta x$ is the equivalent diameter of the body made up of a lattice block. In the figure, the lattice block bodies are depicted by spheres with the equivalent diameter $D_{\rm p}$. It is seen that the three-dimensional vortices appear behind the bodies, and the flow field is very complicated. The calculated pressure drops are in good agreement with well-known empirical equations based on experimental data [17].

The LBM has been applied to heat and mass transfer problems in the three-dimensional porous structure [18, 19], Rayleigh-Bénard convection [13, 20, 21], the simulation of moving particles in fluid [16, 22], and so on.

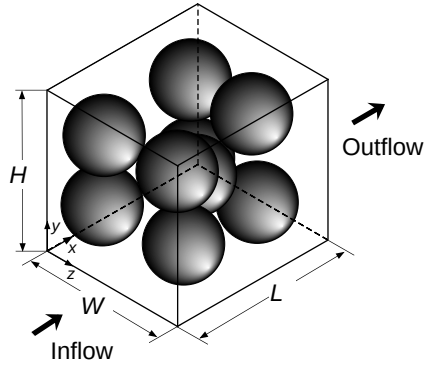

Fig. 1. Three-dimensional porous structure

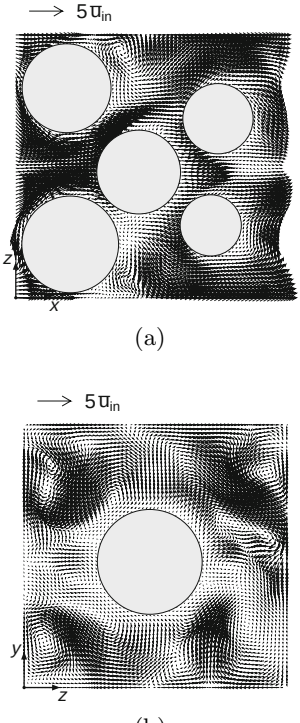

Fig. 2. Velocity vectors on the plane of (a) $y/H = 0.62$ and (b) $x/L = 0.45$ at $Re = 127$

3 Lattice Boltzmann Method for Two-Phase Fluids

In this section, a heuristic LBM for two-phase fluids with large density differences is presented [23]. The difficulty in the treatment of large density differences is resolved by using the projection method [24]. In the projection method the continuity equation in the interfacial region is satisfied at every time step. Two particle velocity distribution functions are used. One is used for the calculation of an order parameter which distinguishes two phases, and the other is used for the calculation of a predicted velocity of the two-phase fluid without a pressure gradient. The current velocity satisfying the continuity equation can be obtained by using the relation between the velocity and the pressure correction which is determined by solving the Poisson equation.

3.1 Formulation

Two particle velocity distribution functions, f_i and g_i, are used. The function f_i is used for the calculation of an order parameter which represents two

phases, and the function g_i is used for the calculation of a predicted velocity of the two-phase fluid without a pressure gradient. The evolution of the particle distribution functions $f_i(\boldsymbol{x}, t)$ and $g_i(\boldsymbol{x}, t)$ with velocity $\boldsymbol{c}_i$ at the lattice point $\boldsymbol{x}$ and at time t is computed by

$$f_i(\boldsymbol{x} + \boldsymbol{c}_i \Delta x, t + \Delta t) = f_i^{\mathrm{c}}(\boldsymbol{x}, t), \tag{18}$$

$$g_i(\boldsymbol{x} + \boldsymbol{c}_i \Delta x, t + \Delta t) = g_i^{\mathrm{c}}(\boldsymbol{x}, t), \tag{19}$$

where f_i^{c} and g_i^{c} are functions of Chapman–Enskog type in which variables $\boldsymbol{x}$ and t enter only through macroscopic variables and/or their derivatives,

The order parameter ϕ distinguishing the two phases and the predicted velocity $\boldsymbol{u}^*$ of the multicomponent fluids are defined in terms of the two particle velocity distribution functions

$$\phi = \sum_{i=1}^{15} f_i, \tag{20}$$

$$\boldsymbol{u}^* = \sum_{i=1}^{15} g_i \boldsymbol{c}_i. \tag{21}$$

The functions f_i^{c} and g_i^{c} in Eqs. (18) and (19) are given by

$$\begin{aligned} f_i^{\mathrm{c}} = {} & H_i \phi + F_i \left[p_0 - \kappa_f \phi \nabla^2 \phi - \frac{\kappa_f}{6} |\nabla \phi|^2 \right] \\ & + 3 E_i \phi c_{i\alpha} u_\alpha + E_i \kappa_f G_{\alpha\beta}(\phi) c_{i\alpha} c_{i\beta}, \end{aligned} \tag{22}$$

$$\begin{aligned} g_i^{\mathrm{c}} = {} & E_i \left[1 + 3 c_{i\alpha} u_\alpha - \frac{3}{2} u_\alpha u_\alpha + \frac{9}{2} c_{i\alpha} c_{i\beta} u_\alpha u_\beta \right. \\ & \left. + \frac{3}{4} \Delta x \left(\frac{\partial u_\beta}{\partial x_\alpha} + \frac{\partial u_\alpha}{\partial x_\beta} \right) c_{i\alpha} c_{i\beta} + 3 c_{i\alpha} \frac{1}{\rho} \frac{\partial}{\partial x_\beta} \left\{ \mu \left(\frac{\partial u_\beta}{\partial x_\alpha} + \frac{\partial u_\alpha}{\partial x_\beta} \right) \right\} \Delta x \right] \\ & + E_i \frac{\kappa_g}{\rho} G_{\alpha\beta}(\rho) c_{i\alpha} c_{i\beta} - \frac{2}{3} F_i \frac{\kappa_g}{\rho} |\nabla \rho|^2, \end{aligned} \tag{23}$$

where

$$\begin{aligned} & H_1 = 1, H_2 = H_3 = \cdots = H_{15} = 0, \\ & F_1 = -7/3, F_i = 3E_i \, (i = 2, 3, \cdots, 15), \end{aligned} \tag{24}$$

and

$$G_{\alpha\beta}(\phi) = \frac{9}{2} \frac{\partial \phi}{\partial x_\alpha} \frac{\partial \phi}{\partial x_\beta} - \frac{3}{2} \frac{\partial \phi}{\partial x_\gamma} \frac{\partial \phi}{\partial x_\gamma} \delta_{\alpha\beta}, \tag{25}$$

with $\alpha, \beta, \gamma = x, y, z$. In the above equations, $\delta_{\alpha\beta}$ is the Kronecker delta, κ_f is a constant parameter determining the width of the interface, κ_g is a constant parameter determining the strength of the surface tension, and the

other variables, ρ, $\rho_{\rm L}$, μ, and $\boldsymbol{u}$ are defined below. Note that $\kappa_g G_{\alpha\beta}$ and $\kappa_g|\nabla\rho|^2$ are of $O[(\Delta x)^2]$. In Eq. (22), p_0 is given by

$$p_0 = \phi T_\phi \frac{1}{1-b\phi} - a\phi^2, \tag{26}$$

where a, b, and T_ϕ are free parameters determining the maximum and minimum values of ϕ. It is noted that $f_i^{\rm c}$ is the same as that of the model proposed by Swift et al. [25]. For the calculation of the derivatives in Eqs. (22), (23), and (25), Eq. (25) is used for the first derivative, and the following finite-difference approximation is used for the second derivative:

$$\frac{\partial\psi}{\partial x_\alpha} \approx \frac{1}{10\Delta x}\sum_{i=1}^{15} c_{i\alpha}\psi(\boldsymbol{x}+\boldsymbol{c}_i\Delta x), \tag{27}$$

$$\nabla^2\psi \approx \frac{1}{5(\Delta x)^2}\left[\sum_{i=2}^{15}\psi(\boldsymbol{x}+\boldsymbol{c}_i\Delta x) - 14\psi(\boldsymbol{x})\right]. \tag{28}$$

The density in the interface is obtained by using the cut-off values of the order parameter, $\phi_{\rm L}^*$ and $\phi_{\rm G}^*$, for the liquid and gas phases with the following relation:

$$\rho = \begin{cases} \rho_{\rm G}, & \phi < \phi_{\rm G}^*, \\ \dfrac{\Delta\rho}{2}\left[\sin\left(\dfrac{\phi-\overline{\phi^*}}{\Delta\phi^*}\pi\right)+1\right]+\rho_{\rm G}, & \phi_{\rm G}^* \le \phi \le \phi_{\rm L}^*, \\ \rho_{\rm L}, & \phi > \phi_{\rm L}^*, \end{cases} \tag{29}$$

where $\rho_{\rm G}$ and $\rho_{\rm L}$ are the density of gas and liquid phase, respectively, $\Delta\rho = \rho_{\rm L} - \rho_{\rm G}$, $\Delta\phi^* = \phi_{\rm L}^* - \phi_{\rm G}^*$, and $\overline{\phi^*} = (\phi_{\rm L}^* + \phi_{\rm G}^*)/2$. The viscosity μ in the interface is obtained by

$$\mu = \frac{\rho-\rho_{\rm G}}{\rho_{\rm L}-\rho_{\rm G}}(\mu_{\rm L}-\mu_{\rm G}) + \mu_{\rm G}, \tag{30}$$

where $\mu_{\rm G}$ and $\mu_{\rm L}$ are the viscosity of gas and liquid phase, respectively, and both are of $O(\Delta x)$. The interfacial tension σ is given by

$$\sigma = \kappa_g \int_{-\infty}^{\infty}\left(\frac{\partial\rho}{\partial\xi}\right)^2 {\rm d}\xi, \tag{31}$$

with ξ being the coordinate normal to the interface [26, 27].

Since $\boldsymbol{u}^*$ is not divergence free ($\nabla\cdot\boldsymbol{u}^* \neq 0$) in general, a correction of $\boldsymbol{u}^*$ is required. The current velocity $\boldsymbol{u}$ which satisfies the continuity equation ($\nabla\cdot\boldsymbol{u} = 0$) can be obtained by using

$${\rm Sh}\frac{\boldsymbol{u}-\boldsymbol{u}^*}{\Delta t} = -\frac{\nabla p}{\rho}, \tag{32}$$

$$\nabla \cdot \left(\frac{\nabla p}{\rho} \right) = \mathrm{Sh} \frac{\nabla \cdot \boldsymbol{u}^*}{\Delta t}, \tag{33}$$

where $\mathrm{Sh} = U/c$ is the Strouhal number and p is the pressure. The Poisson equation (33) can be solved by various methods. In the present paper, we solve it in the framework of LBM. Namely, the following evolution equation of the velocity distribution function h_i is used for the calculation of the pressure p:

$$h_i^{n+1}(\boldsymbol{x} + \boldsymbol{c}_i \Delta x) = h_i^n(\boldsymbol{x}) - \frac{1}{\tau_h} \left[h_i^n(\boldsymbol{x}) - E_i p^n(\boldsymbol{x}) \right] - \frac{1}{3} E_i \frac{\partial u_\alpha^*}{\partial x_\alpha} \Delta x, \tag{34}$$

where n is the number of iterations and the relaxation time τ_h is given by

$$\tau_h = \frac{1}{\rho} + \frac{1}{2}. \tag{35}$$

The pressure is obtained by

$$p = \sum_{i=1}^{15} h_i. \tag{36}$$

The iteration of Eq. (34) is repeated until $|p^{n+1} - p^n|/\rho < \varepsilon$ (e.g., $\varepsilon = 10^{-6}$) is satisfied in the whole domain.

3.2 Algorithm of Computation

We now summarize the algorithm of computation.

Step 1. Using Eqs. (18) and (19), compute $f_i(\boldsymbol{x}, t + \Delta t)$ and $g_i(\boldsymbol{x}, t + \Delta t)$, and then compute $\phi(\boldsymbol{x}, t + \Delta t)$ and $\boldsymbol{u}^*(\boldsymbol{x}, t + \Delta t)$ with Eqs. (20) and (21). Also, $\rho(\boldsymbol{x}, t + \Delta t)$ is calculated with Eq. (29).

Step 2. Using Eqs. (34)–(36), compute $p(\boldsymbol{x}, t + \Delta t)$. The iteration is repeated until $|p^{n+1} - p^n|/\rho < \varepsilon$ is satisfied in the whole domain.

Step 3. Compute $\boldsymbol{u}(\boldsymbol{x}, t + \Delta t)$ using Eq. (32).

Step 4. Advance one time step and return to Step 1.

It is found in preliminary calculations that using the present method we can simulate multiphase flows with the density ratio up to 1000.

3.3 Governing Equations for Macroscopic Variables

Applying the asymptotic theory, one can obtain the governing equations for macroscopic variables (see [23]).

3.4 Numerical Examples

Binary Droplet Collision

The method has been applied to the simulations of binary droplet collisions for various Weber numbers and for impact parameters [28, 29] as shown in Fig. 3. The dimensionless parameters of the problem are the diameter ratio $\lambda = D_s/D_l$ where D_s and D_l are the diameters of smaller and larger droplets, respectively, the Weber number $We = \rho_L D_s V^2/\sigma$ in which V is the relative speed of two droplets, the Reynolds number $Re = \rho_L D_l V/\mu_L$, and the impact number $B = 2X/(D_l + D_s)$ in which X is the distance from the center of one droplet to the relative velocity vector placed on the center of the other droplet. The density ratio of the liquid to the gas is fixed at 50 which is nearly the ratio of injected fuel to compressed oxidizer in diesel engines. The calculated results are classified into coalescence collision and two different types of separating collisions, namely reflexive and stretching separations, and the boundaries of three types of collisions are compared with available theoretical predictions in good agreement. Figure 3 shows calculated results for $\lambda = 0.5$, $We = 61.5$, $Re = 4300$, and $B = 0.6$. The results correspond to the stretching separation. The mixing processes during separating collisions are also simulated for various parameters at by tracing different-colored fluid particles in the two droplets.

Rising Bubbles

The method was applied to the simulation of a single rising bubble in liquid, and the terminal shapes and the terminal Reynolds numbers of the bubble for various Morton and Eötvös numbers were in good agreement with available experimental data [30]. The behavior of many bubbles (234 bubbles) in a long duct was calculated by using the parallel computing with 6 CPUs in the paper by Inamuro and Ogata [31]. In the calculation, the density ratio was $\rho_L/\rho_G = 1000$, and an $80 \times 80 \times 780$ cubic lattice was used.

Two-Phase Flows in a Branch Channel

We also applied the method to the simulation of two-phase flows in a branch channel (Fig. 4). The branch has one inlet at the bottom and two outlets at the top. The computational conditions are $\rho_L/\rho_G = 45.1$, $\mu_L/\mu_G = 16.1$, and $Re = \rho_G V L/\mu_G = 2.1 \times 10^4$ where V is the averaged gas velocity and L is the hight of the branch. The conditions correspond to a coolant in air-conditioners. As shown in Fig. 4, Complicated behaviors of two-phase flows in the branch channel at a high Reynolds number can be computed by the present method.

t^*=1.41

t^*=2.55

t^*=4.13

t^*=7.07

t^*=9.19

t^*=13.4

Fig. 3. Time evolution of droplet shape for $\lambda = 0.5$, $We = 61.5$, $Re = 4300$, and $B = 0.6$ $[t^* = 2tV/(D_l + D_s)]$. Figure taken from Ref. [29].

$t^* = 4.38$ $t^* = 13.8$

Fig. 4. Unseady two-phase flows in a branch channel; the interface of two-phase is shown. ($t^* = tV/L$).

Solid-Liquid Mixture Flows

Finally, a solid-fluid mixture flow simulated by the LBM for multicomponent immiscible fluids with the same density [32] is presented. In the calculation, a particle is modeled by a hard droplet with large viscosity and strong surface tension, and consequently there is no need to track the moving solid-liquid boundary explicitly [33]. In addition, nonspherical particles are made by applying artificial forces to the droplet. we get a discoid particle by applying a centrifugal force, and also by applying a compression force to the discoid particle, we can make a biconcave discoid particle by applying a compression force to the discoid particle. Figure 5 shows the calculated result for a biconcave discoid particle in a square pipe flow at $Re = 107$. It is found that the biconcave discoid particle moves along a periodic helical path around the center of the pipe with changing its attitude, and the radius of the helical path and the polar angle of the minor axis of the particle increase as the hollow of the concave becomes large.

4 Concluding Remarks

The LBMs for viscous fluid flows and for temperature fields are presented. The advantages of the LBM are the simplicity of the algorithm, the accuracy of mass and momentum conservations, and the suitability for parallel computing. In addition, the LBM for two-phase fluid flows is presented. The method can simulate two-phase flows with the density ratio up to 1000. The accuracy of the method would depend on the interface width related to

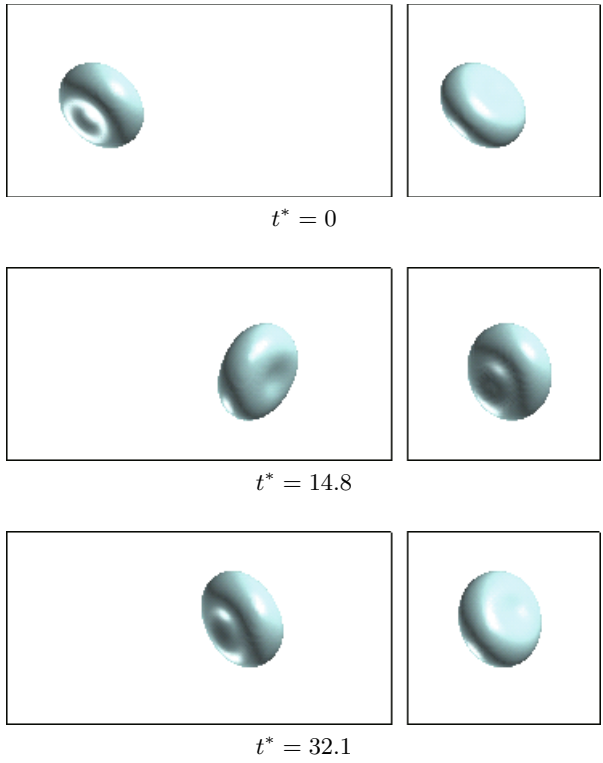

Fig. 5. The motion of a biconcave discoid particle in a square pipe flow; side view (left) and front view (right). $t^* = Vt/L_x$ (V: the averaged velocity, L_x: the length of the square pipe.)

the parameter κ_f, the mobility of the order parameter, and the lattice spacing Δx. The study of the accuracy concerning these parameters is required in future work. Also, the development of methods without solving the Poisson equation for pressure field is desired.

Finally, we expect that the present LBMs will become promising numerical schemes for simulating viscous fluid flows and two-phase fluid flows, and that the schemes will be used in many new areas of applications. For example, the author applies the two-phase LBM to the calculations of two-phase fluid flows in micro channels and in porous media where the capillary force plays an important role for determining the flow characteristics. Moreover, the LBMs have been successfully applied to complex fluids such as colloidal flows. Those topics are found in the books by Rothman & Zaleski [1] and Succi [4].

This work was supported by the Grant-in-Aid for Scientific Research (No. 18360089) from JSPS and by the COE program (the Center of Excellence for Research and Education on Complex Functional Mechanical Systems) of the Ministry of Education, Culture, Sports, Science and Technology, Japan.

References

[1] Rothman, D.H., Zaleski, S.: Lattice-Gas Cellular Automata. Cambridge University Press, Cambridge (1997)
[2] Chen, S., Doolen, G.D.: Lattice Boltzmann method for fluid flows. Annu. Rev. Fluid Mech. 30, 329–364 (1998)
[3] Wolf-Gladrow, D.A.: Lattice-Gas Cellular Automata and Lattice Boltzmann Models. Springer, Berlin (2000)
[4] Succi, S.: The Lattice Boltzmann Equation for Fluid Dynamics and Beyond. Oxford University Press, Oxford (2001)
[5] Inamuro, T.: Lattice Boltzmann methods for viscous fluid flows and for two-phase fluid flows. Fluid Dynamics Research 38, 641–659 (2006)
[6] Xu, K., Prendergast, K.H.: Numerical Navier-Stokes solutions from gas kinetic theory. J. Comput. Phys. 114, 9–17 (1994)
[7] Chou, S.Y., Baganoff, D.: Kinetic flux-vector splitting for the Navier-Stokes equations. J. Comput. Phys. 130, 217–230 (1997)
[8] Junk, M., Rao, S.V.: A new discrete velocity method for Navier-Stokes equations. J. Comput. Phys. 151, 178–198 (1999)
[9] Sone, Y.: Kinetic Theory and Fluid Dynamics. Birkhäuser, Basel (2000)
[10] Inamuro, T., Yoshino, M., Ogino, F.: Accuracy of the lattice Boltzmann method for small Knudsen number with finite Reynolds number. Phys. Fluids 9, 3535–3542 (1997)
[11] Chen, S., Chen, H., Martinez, D., Mattaeus, W.H.: Lattice Boltzmann model for simulation of magnetohydrodynamics. Phy. Rev. Lett. 67, 3776–3779 (1991)
[12] Qian, Y., d'Humiéres, D., Lallemand, P.: Lattice BGK models for the Navier-Stokes equation. Europhys. Lett. 17, 479–484 (1992)
[13] Inamuro, T., Yoshino, M., Inoue, H., Mizuno, R., Ogino, F.: A lattice Boltzmann method for a binary miscible fluid mixture and its application to a heat transfer problem. J. Comput. Phys. 179, 201–215 (2002)
[14] Yu, D., Mei, R., Luo, L.-S., Shyy, W.: Viscous flow computation with the method of lattice Boltzmann equation. Progress in Aerospace Sciences 39, 329–367 (2003)
[15] Inamuro, T., Yoshino, M., Ogino, F.: A non-slip boundary condition for lattice Boltzmann simulations. Phys. Fluids 7, 2928–2930 (1995) (Erratum: 8, 1124 (1996))
[16] Inamuro, T., Maeba, K., Ogino, F.: Flow between parallel walls containing the lines of neutrally buoyant circular cylinders. Int. J. Multiphase Flow 26, 1981–2004 (2000)
[17] Inamuro, T., Yoshino, M., Ogino, F.: Lattice Boltzmann simulation of flows in a three-dimensional porous structure. Int. J. Numer. Meth. Fluids 29, 737–748 (1999)
[18] Lattice Boltzmann simulation of flow and heat- and mass-transfer with a chemical reaction in a porous structure. In: Taine, J. (ed.) Proceedings of the 12th International Heat Transfer Conference, pp. 519–524. Elsevier SAS, Amsterdam (2002)
[19] Yoshino, M., Inamuro, T.: Lattice Boltzmann simulations for flow and heat/mass transfer problems in a three-dimensional porous structure. Int. J. Numer. Meth. Fluids 43, 183–198 (2003)
[20] Shan, X.: Simulation of Rayleigh-Bénard convection using a lattice Boltzmann method. Phys. Rev. E 55, 2780–2788 (1997)

[21] He, X., Chen, S., Doolen, G.D.: A novel thermal model for the lattice Boltzmann method in incompressible limit. J. Comput. Phys. 146, 282–300 (1998)
[22] Ladd, A.J.C.: Sedimentation of homogeneous suspensions of non-Brownian spheres. Phys. Fluids 9, 491–499 (1997)
[23] Inamuro, T., Ogata, T., Tajima, S., Konishi, N.: A lattice Boltzmann method for incompressible two-phase flows with large density differences. J. Comput. Phys. 69, 628–644 (2004)
[24] Chorin, A.J.: Numerical solution of the Navier-Stokes equations. Math. Comput. 22, 745–762 (1968)
[25] Swift, M.R., Osborn, W.R., Yeomans, J.M.: Lattice Boltzmann simulation of nonideal fluids. Phys. Rev. Lett. 75, 830–833 (1995)
[26] Rowlinson, D.H., Widom, B.: Molecular Theory of Capillarity, pp. 50–60. Clarendon, Oxford (1989)
[27] Inamuro, T., Konishi, N., Ogino, F.: A Galilean invariant model of the lattice Boltzmann method for multiphase fluid flows using free-energy approach. Comput. Phys. Commun. 129, 32–45 (2000)
[28] Inamuro, T., Tajima, S., Ogino, F.: Lattice Boltzmann simulation of droplet collision dynamics. Int. J. Heat Mass Transfer 47, 4649–4657 (2004)
[29] Sakakibara, B., Inamuro, T.: Lattice Boltzmann simulation of collision dynamics of two unequal-size droplets. Int. J. Heat Mass Transfer 51, 3207–3216 (2008)
[30] Inamuro, T., Ogata, T., Ogino, F.: Numerical simulation of bubble flows by the lattice Boltzmann method. Future Generation Computer Systems 20, 959–964 (2004)
[31] Inamuro, T., Ogata, T.: A lattice kinetic scheme for bubble flows. Phil. Trans. R. Soc. Lond. A 362, 1735–1743 (2004)
[32] Inamuro, T., Tomita, R., Ogino, F.: Lattice Boltzmann simulations of drop deformation and breakup in shear flows. Int. J. Modern Phys. B 17, 21–26 (2003)
[33] Inamuro, T., Ii, T.: Lattice Boltzmann simulation of the dispersion of aggregated particles under shear flows. Mathematics and Computers in Simulation 72, 141–146 (2006)

“*This page left intentionally blank.*”

Coping with Uncertainty in Turbulent Flow Simulations

Pierre Sagaut

Institut Jean Le Rond d'Alembert, Université Pierre et Marie Curie - Paris 6,
4 place Jussieu -case 162, F-75252 Paris cedex 5, France
pierre.sagaut@upmc.fr

1 Introduction

Real-life CFD applications involve a large number of choices that are to be made in order to setup the computational configurations of the problem. These choices include the physical models and related arbitrary constants, boundary conditions, initial conditions as well as tuning parameters in the numerical methods. In many cases, all physical and geometrical parameters are not *exactly* known and in some instances are not known at all. This lack of information raises the issue of taking into account uncertainties in the CFD process, modeling it and measuring the dependency/sensitivity of the results with respect to these uncertainties. Consequently, this approach implies that instead of seeking a single deterministic solution, we are now interested in recovering a continuous description of the space of possible solutions spanned by uncertain parameters.

This article aims at providing a survey of recent progress made in the field of uncertainty and error quantification and propagation in CFD, the emphasis being put on Large-Eddy Simulation (LES) of turbulent flows. All issues addressed below are also relevant to Reynolds-Averaged Numerical Simulations (RANS) and hybrid RANS/LES methods. Section 2 illustrates why, even in a simple academic turbulent flow, arbitrary parameters that appear in turbulence models must be considered as uncertain parameters, since their values are flow-dependent. The concept of robust model, i.e. whose sensitivity to the tuning of arbitrary parameters is minimal, is then presented in Section 3. The issue of representing the space of solutions spanned by possible variations of the computational setup parameters is then addressed. Section 4 first illustrates the use of the generalized Polynomial Chaos (gPC) [Xiu and Karniadakis (2002), Xiu and Karniadakis (2003)] method on an academic case and then exemplifies the use of the Kriging method [Krige (1951)] on an engineering problem.

2 Inertial Range Consistent Subgrid/Turbulence Models

In simulations, subgrid-scale models do not always yield their theoretically expected solution, and this is often experienced in the significant discrepancy between a priori tests and a posteriori results. This is caused by simplifications and assumptions related to the shape of the LES filter, the type of turbulence at the filter cut-off, etc., in combination with the non-linear nature of the NavierStokes equations. We illustrate here this problem by considering the value of the adaptable model constant parameter C in the Smagorinsky subgrid viscosity model for large-eddy simulation. The well-known Lilly analysis [Lilly (1967)], which leads to $C = C_\infty = 0.17 - 0.18$, was carried out in a simplified asymptotic framework, which is not relevant in most flows of interest, since it does not account for Reynolds effects, large-scale dynamics, shear ... Usual tuning methodology for arbitrary parameters in turbulence/subgrid models relies on simple test case solutions: the model parameters are adjusted so that a satisfactory solution is recovered. A very popular test case is Decaying Homogeneous Isotropic Turbulence (DHIT), which is characterized at the global level by the turbulent kinetic energy decay rate. The recovery of the observed decay rate via LES or VLES method is still a challenging issue. One of the main reasons for this is that the decay rate is not universal, since it depends on several fine spectral features of the solution, among which: the Reynolds number, the spectrum shape at very large scales and very small scales, cutoff effects originating in the finite size of the wind tunnel/computational domain. Therefore, no universal value for C can be expected, even in the DHIT case. The exact value of the C constant was derived by [Meyers and Sagaut (2006)] using Pope's formulation for the turbulent kinetic energy spectrum $E(k)$:

$$C(L/\Delta, Re_L) = \frac{C_\infty}{\gamma}\Phi^{-3/4}\sqrt{1 - \left(\frac{\gamma\eta}{C_\infty\Delta}\right)^{4/3}\phi}, \tag{1}$$

where the spectrum shape is defined as

$$E(k) = K_0\varepsilon^{2/3}k^{-5/3}f_L(kL)f_\eta(k\eta), \tag{2}$$

and the auxiliary function is defined as

$$\phi(L/\Delta, Re_L) = \frac{4}{3}\frac{1}{(\gamma\pi L/\Delta)^{4/3}}\int_0^{+\infty} x^{1/3}G^2(x/L)f_L(x)f_\eta(xRe_L^{-3/4})dx, \tag{3}$$

where G is the LES filter kernel, L the integral lengthscale, η the Kolmogorov scale, Δ the LES cutoff scale and C_∞= 0.17-0.18 the usual value. The filter-dependent parameter γ is computed as

$$\gamma = \frac{\pi}{\Delta}\left(\frac{4}{3}\int_0^{+\infty} x^{1/3}G^2(x)dx\right)^{3/4}. \tag{4}$$

Since this is an exact formulation of the Smagorinsky constant, it is seen that this parameter is flow-dependent and filter-dependent. Therefore, it must be considered as an uncertain parameter in practical LES, since most of these parameters remain unknown. It is worth noting that the usual value is recovered as an asymptotic limit (see Fig.1). The definition given above is very complex, and does not satisfy the basic constraint of numerical viability. Meyers and Sagaut proposed an efficient approach to recover inertial-range consistency, which makes it possible to mimic the exact behaviour using the asymptotic value of the Smagorinsky model by remapping the total effective viscosity (defined as the sum of molecular and subgrid-induced dissipative effects) as follows:

$$\nu_{eff} = \sqrt{\nu_{Lilly}^2 + \nu^2} \tag{5}$$

This analysis and remapping approach was also applied to Variational Multiscale variants of the Smagorinsky model. Other models including additional transport equations (DES, SAS,) remain to be analysed from the inertial range consistency viewpoint. Let us also notice that the usual one-test-filter dynamic procedure fails in recovering the correct behaviour, as shown by Porté-Agel and co-workers [Porté-Agel et al. (2000)].

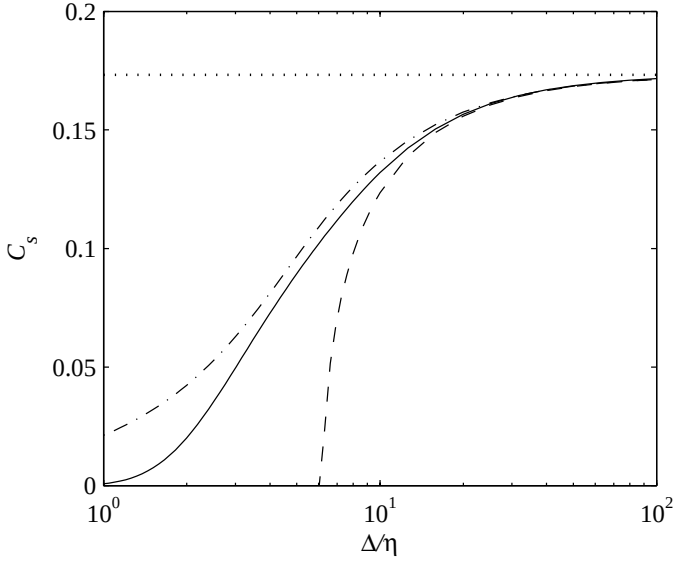

Fig. 1. Smagorinsky constant as a function of the ratio between cutoff length and Kolmogorov scale. Solid line: exact value; dotted line: asymptotic value; dashed line: linear and quadratic remapping.

3 The Concept of Robust Modelling

The existence of intrinsic uncertainties in LES/VLES modelling automatically raises the question of model robustness, i.e. of the sensitivity of the results to the tuning of the free parameters in the model. A robust model will naturally be preferred for practical purposes, even if it does not yield the best possible results, since it will provide users with results of constant level of accuracy. More sensitive models will be disgarded in practice. In this section, we will propose some quality indicator, and show that robust models exist and can be derived in simple ways [Meyers et al. (2006)]. The quantification of the sensitivity will be addressed in the next section.

An error measure must first be introduced in order to quantify the committed error. Following Meyers and coworkers, let us consider the following error indicator

$$\epsilon_p(N,C) = \sqrt{\frac{\int_0^T \left(\int_0^{k_c} k^p (E_{LES}(k,t) - G^2(k) E_{DNS}(k,t)) dk\right)^2 dt}{\int_0^T \left(\int_0^{k_c} k^p G^2(k) E_{DNS}(k,t)) dk\right)^2 dt}}. \quad (6)$$

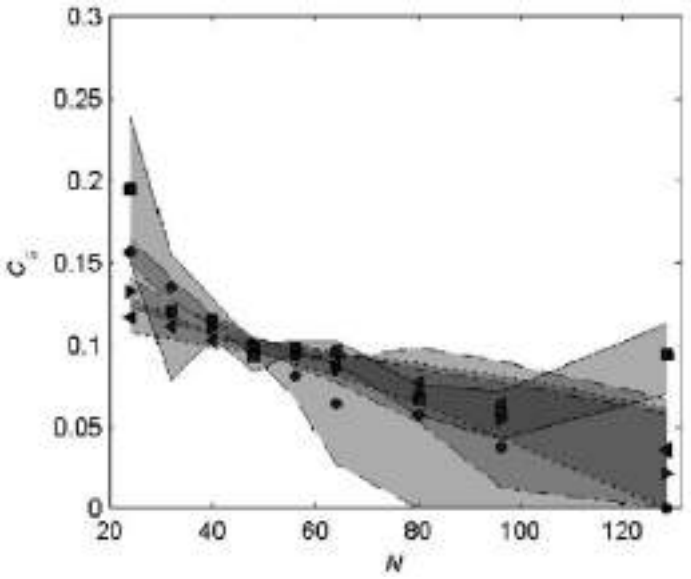

Fig. 2. Error for the Smagorinsky model as a function of the number of grid points N and the value of the Smagorinsky constant. Shadded regions denote optimality regions for the mode constant, in which the committed error is within 20 percents of the minimum possible error on the same grid. Symbols: square: p= -1; circle: p=0; right-pointing triangle: p=1; left-pointing triangle: p=2.

Choosing p=-1,0 or 2, one can put the emphasis on the error committed on the integral lengthscale, the resolved kinetic energy and the resolved enstrophy, respectively. Since in practical applications one can be interested in predicting several parameters at the same time with satisfactory accuracy, it is convenient to introduce the following multiobjective error measure

$$\tilde{\epsilon}(N,C) = \frac{\sum_{p=-1,0,1,2}\left(\epsilon_p(N,C)/\epsilon_p(N,\hat{C}(p,N)\right)}{\sum_{p=-1,0,1,2}\left(1/\epsilon_p(N,\hat{C}(p,N)\right)}, \tag{7}$$

which is expressed as an explicit function of the number of grid points N and the subgrid model constant C. Here, $\hat{C}(p,N)$ denotes the value of he constant which yields the lowest error on $\epsilon_p(N,C)$ at fixed N. A model will be referred to as a robust model if, keeping the same value of C, a constant level of accuracy is recovered when varying N. Results obtained in DHIT with the usual Smagorinsky model are presented in Fig. 2, while those obtained using the inertial-range consistant model based on a quadratic remapping introduced above are displayed in Fig. 3. It is seen that the former is not robust, while the latter is. This analysis can be extended to VLES, DES and SAS-type methods in a straightforward manner.

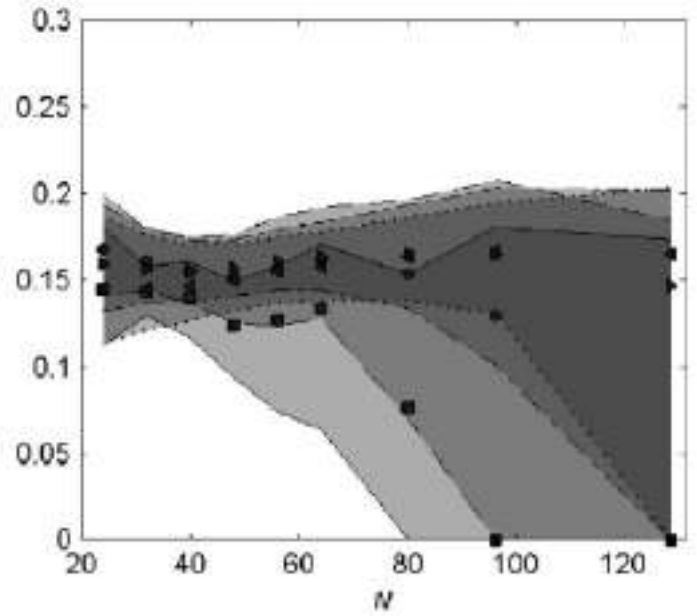

Fig. 3. Error map for the quadratically approximated inertial-range consistent Smagorinsky model. Same caption as in Fig. 2.

4 Copping with Uncertainties: Response Surface

Several mathematical tools are available to compute the sensitivity of the solution with respect to a parameter of the simulation. Local gradient of the solution can be computed in several ways, including complex differentiation [Lu and Sagaut (2007)]. A limitation of this approach is that the local gradient does not give access to the full space of spanned solutions, and that it is a linearized analysis. The response surface approach is becoming more and more popular to parameterize a full subspace, without relying on linearization. One example is the Kriging approach that is becoming increasingly acknowledged (e.g. [Jouhaud et al. (2006)]). The present paper will focus on results obtained with a stochastic spectral method referred to as the generalized Polynomial Chaos (gPC) approximation [Lucor et al. (2007)]. The gPC approach consists of discretizing the space spanned by the uncertain parameters using a pseudo-spectral method. This is a means of representing second-order random fields parametrically through a finite set of random variables. The basis functions, which are orthogonal polynomials, should be chosen in accordance with the probability density function of the uncertain solution of the problem to ensure an optimal convergence of the representation. When this density is not known, one choice is to use basis functions

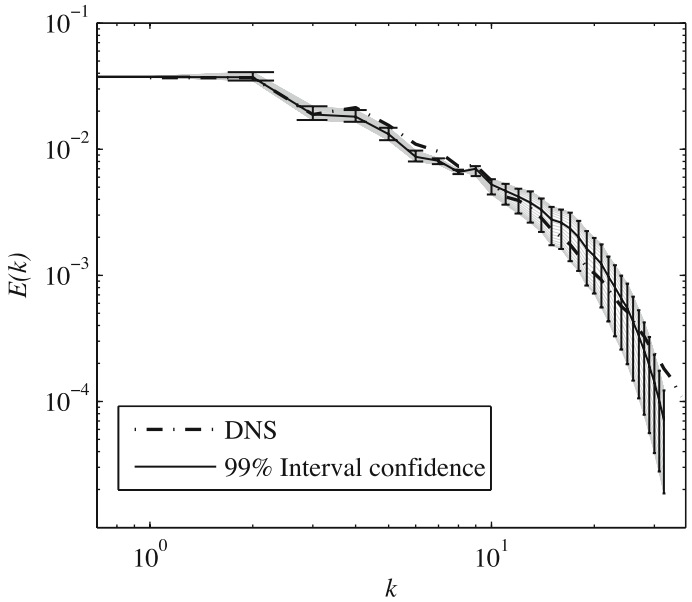

Fig. 4. Uncertainty error bars on the 64^3 grid resolved turbulent kinetic energy spectrum computed using a Smagorinsky model with uncertain constant: envelope of possible solutions

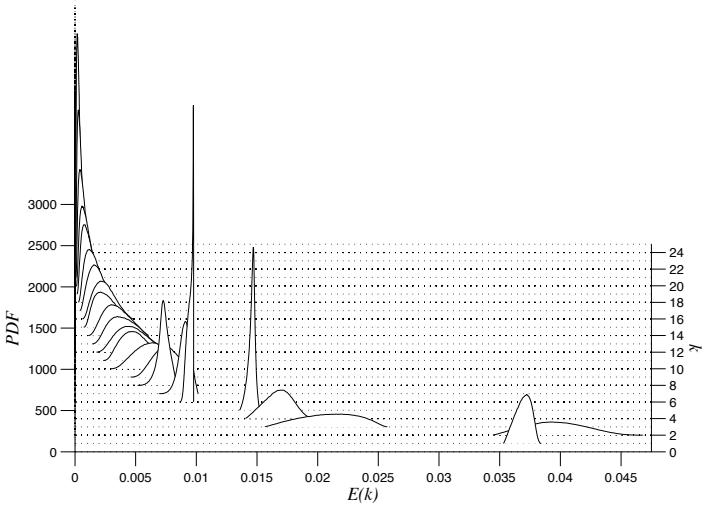

Fig. 5. pdf of the turbulent kinetic energy E(k) in DHIT with uncertain Smagorinsky constant following a *beta* distribution

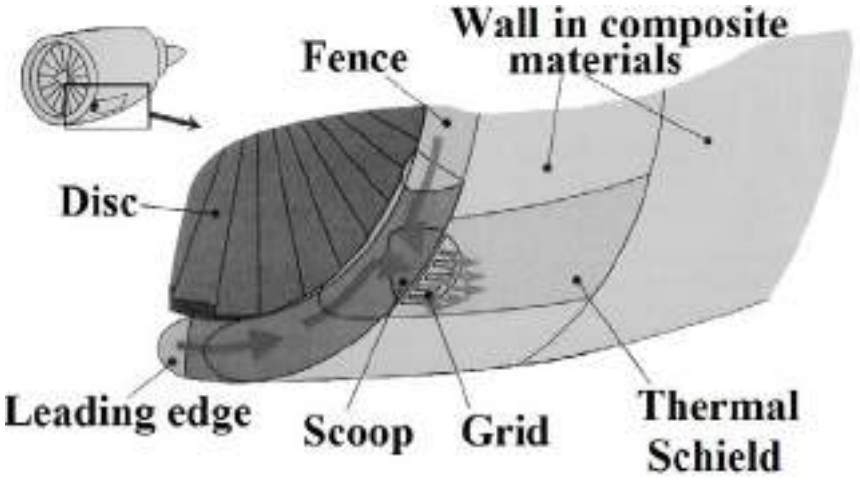

Fig. 6. Flow configuration for the hot jet exhaust of an aeronautical engine cooling system

that are optimal for the representation of the random inputs to the problem. Using this approach, a continuous reconstruction of the space of possible solutions is obtained using a restricted set of usual LES realizations. The analysis of decaying turbulence with an uncertain Smagorinsky model has been performed. We thus treat the Smagorinsky constant as an uncertain input to the stochastic problem, and its probability distribution is assumed. In order to

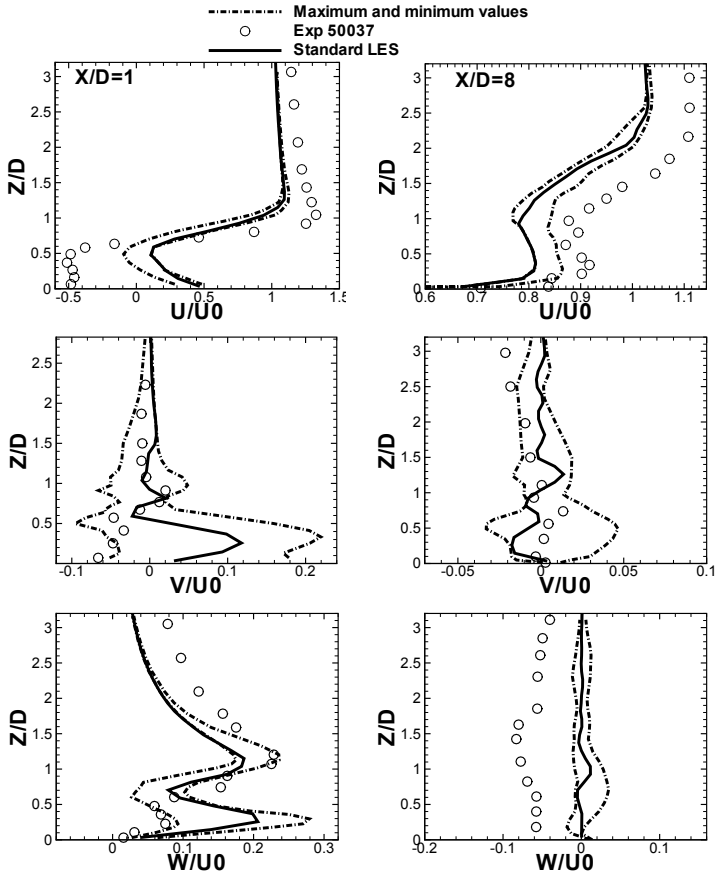

Fig. 7. Mean velocity response based on the Kriging approach

simplify the system, we make the additional assumption than Cs is a random variable, which means that its statistical properties do not depend on spatial or temporal dimensions. The induced uncertainty on the computed energy spectrum is illustrated in Fig. 4. Here, the distribution of the Smagorinsky constant is *uniform* and the LES computational domain is discretized with a 64^3 grid.

Looking at the results, it is observed that all scales do not respond to the uncertainty in the same way, i.e. the level of sensitivity is scale-dependent. Another striking feature is the existence of a mode which is almost insensitive to variations in the Smagorinsky model constant. This feature was observed for smaller grid sizes as well. The scale-by-scale sensitivity is better illustrated in Fig. 5, which displays the pdf of the value of $E(k)$ for all k. Here, the distribution of the Smagorinsky constant is a $beta(4,4)$ distribution and the LES computational domain is discretized with a 48^3 grid. It is seen that both the amplitude and the shape of the pdf distribution are scale-dependent

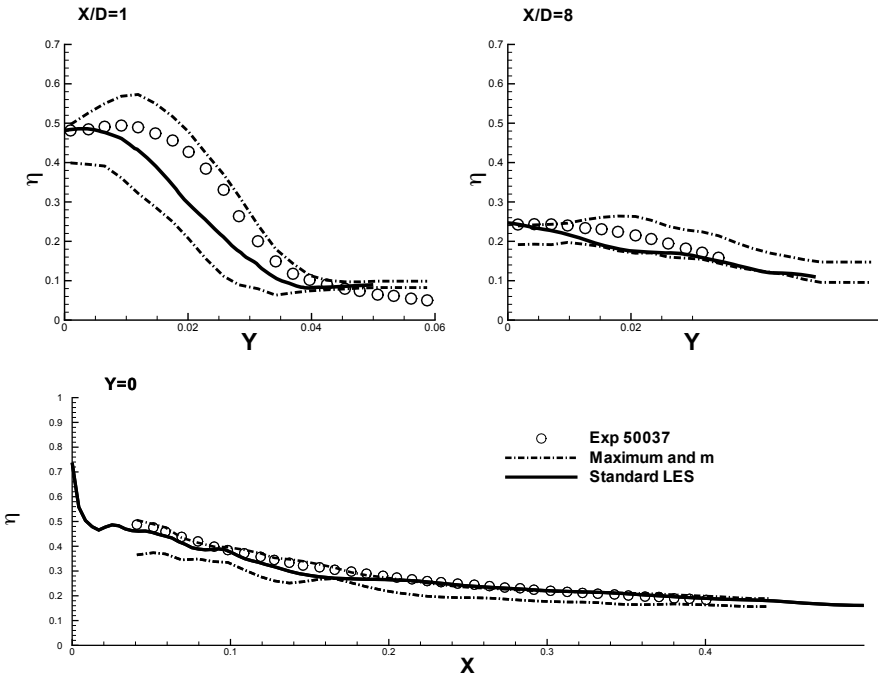

Fig. 8. Cooling effectiveness response based on the Kriging approach

functions, showing the great complexity of the LES solution response to random variability in the Smagorinsky constant.

We now illustrate the use of the response surface approach on a practical engineering problem, namely the separated flow at the exhaust of the cooling system in a aeronautical engine (see figure 6). Most numerical methods used for practical engineering purposes involve artificial dissipation. However, it is known that numerical dissipation and subgrid/turbulence model induced dissipation are in competition. They must be tuned in an ad hoc manner to adapt to the case in order to recover the best possible results (e.g. [Garnier et al.(2001), Ciardi et al. (2005)]). In the following example [Jouhaud et al. (2008)], it is chosen to retain both the Smagorinsky constant C_S and the artificial fourth-order dissipation parameter $smu4$ which appears in Jameson's scheme as uncertain optimization parameters. A variability range of $\pm 30\%$ around the standard values $C_s = 0.18$ and $smu4 = 0.01$ is considered. The sensitivity of the mean flow with respect to these two parameters is illustrated in Figs. 7 and 8, which compare the standard LES solution (i.e. the LES solution computed using the standard parameters), experimental data, and the extreme values retrieved from the response surface built for the mean flow solution at every grid point. The sensitivity of the solution is directly related to the differences between the two

extrema profiles. It is observed that the robustness of the solution depends on both the spatial location and the physical variable under consideration.

The figures reveal the existence of two cases. In the first case, the experimental data lie within the two extrema, meaning that it might be possible to tune up the parameters to match the experimental results. This will obviously lead to a very accurate LES solution at the considered location. In the second case, the experimental data are outside the response surface: the exact solution does not belong to the space of solutions spanned by the LES method on the considered grid.

5 Concluding Remarks

The present paper aimed at presenting recent results dealing with unresolved scale modelling for unsteady simulation of turbulent flows. The emphasis was put on LES, but proposed analysis tools can be extended to hybrid RANS-LES method in a straightforward manner. In a first step, the concept of inertial range consistency was introduced. Let us notice that this non-trivial issue is of direct interest for practical application, since it was shown that the usual value of the Smagorinsky constant can be used if and only if $L/\Delta > 20 - 30$ and that $\Delta/\eta > 100$, i.e. for coarse grids in flows such that $L/\eta > 2000 - 3000$. Since similar criteria may be defined for hybrid approaches, one may wonder if model tuning on test cases with nearly-infinite Reynolds number is of practical interest for VLES models which involve several tuning parameters.

A second step is to design robust models, i.e. models which will lead to very good results even if some parameters of the simulation (grid resolution,) are changed. Using the error map approach and the concept of inertial-range consistency, it will be shown that robust, nearly-optimal subgrid models can be designed, which satisfy the three basic modelling constraints: 1/ physical constistency 2/ robustness 3/ numerical viability [Meyers and Sagaut (2006), Meyers et al. (2006)]. In a third step, a deeper insight in the solution sensitivity was gained using the gPC approach. One may wonder if DHIT is a relevant test case for model validation, since it is a very simple turbulent flow. Let us first remark that theoretical analysis needs relevant, unambiguous test cases. A last point is therefore the reliability of some famous test cases for LES-like model validation, such as the plane channel flow. It was recently shown that the error associated with coarse-grid plane channel DNS exhibits a complex non-linear behavior, which can lead to misleading interpretations of the results in [Meyers and Sagaut (2007)]. These authors show that coarse-grid DNS may, in some cases, lead to exact prediction of usual test parameters such as skin friction, mean centreline velocity and peak of streamwise turbulence intensity.

The last point dealt with the representation of the uncertainty in the solution which originates in the lack of knowledge of complex flows. The response surface approach is observed to be an efficient tool for that purpose. Response surfaces can be used toinvestigate the sensitivity of the solution, but also to draw error maps at lowcost is some reference data are available.

Acknowledgements. The author would like to warmly acknowledge the fruitful and enlightning collaborations which lead to the results presented here. The error map approach and the robust modelling theory were developped in close collaboration with Dr. Johann Meyers. The Kriging-based results were obatined with Dr. Jean-Christophe Jouhaud. Dr. Didier Lucor was the main contributor to the development of the gPC-based researches presented here.

References

[Ciardi et al. (2005)] Ciardi, M., Sagaut, P., Klein, M., Dawes, W.N.: A dynamic finite-volume scheme for large-eddy simulation on unstructured grids. Journal of Computational Physics 210, 632–655 (2005)

[Garnier et al.(2001)] Garnier, E., Sagaut, P., Deville, M.: A class of explicit ENO filters with application to unsteady flows. Journal of Computational Physics 170, 184–204 (2001)

[Jouhaud et al. (2006)] Jouhaud, J.C., Sagaut, P., Labeyrie, B.: A Kriging approach for CFD/wind tunnel data comparison. Journal of Fluids Engineering 128(4), 847–855 (2006)

[Jouhaud et al. (2008)] Jouhaud, J.C., Sagaut, P., Eneaux, C., Laurenceau, J.: Sensitivity analysis and multi-objective optimization for LES numerical parameters. Journal of Fluids Engineering 130, 021401 (2008)

[Krige (1951)] Krige, D.G.: A statistical approach to some basic mine valuations problems on the Witwatersrand. Journal of Chemical, Metallurgy and Mining Society of South Africa 52, 119–139 (1951)

[Lilly (1967)] Lilly, D.K.: The representation of small-scale turbulence in numerical simulation experiments. In: Proceedings of the IBM Scientific Computing Symposium on Environmental Sciences, Yorktown Heights, USA (1967)

[Lu and Sagaut (2007)] Lu, S.Y., Sagaut, P.: Direct sensitivity analysis for smooth unsteady compressible flows using complex differentiation. International Journal for Numerical Methods in Fluids 53(12), 1863–1886 (2007)

[Lucor et al. (2007)] Lucor, D., Meyers, J., Sagaut, P.: Sensitivity analysis of LES to subgrid-scale-model parametric uncertainty using polynomial chaos. Journal of Fluid Mechanics 585, 255–279 (2007)

[Meyers and Sagaut (2006)] Meyers, J., Sagaut, P.: On the model coefficient for the standard and the variational multiscale Smagorinsky model. Journal of Fluid Mechanics 569, 287–319 (2006)

[Meyers et al. (2006)] Meyers, J., Sagaut, P., Geurts, B.J.: Optimal model parameters for multi-objective large-eddy simulations. Physics of Fluids 18, 095103 (2006)

[Meyers and Sagaut (2007)] Meyers, J., Sagaut, P.: Is plane channel flow a friendly test-case for the testing of LES subgrid scale models? Physics of Fluids 19, 048105 (2007)

[Porté-Agel et al. (2000)] Porté-Agel, F., Meneveau, C., Parlange, M.: A scale-dependent dynamic model for large-eddy simulation: application to a neutral atmospheric boundary layer. Journal of Fluid Mechanics 415, 261–284 (2000)

[Xiu and Karniadakis (2002)] Xiu, D., Karniadakis, G.E.: The Wiener-Askey Polynomial Chaos for stochastic differential equations. SIAM Journal of Scienitifc Computing 24, 137–167 (2002)

[Xiu and Karniadakis (2003)] Xiu, D., Karniadakis, G.E.: Modeling uncertainty in flow simulations vi generalized Polynomial Chaos. Journal of Computational Physics 187, 137–167 (2003)

Adaptive Finite Element Discretization of Flow Problems for Goal-Oriented Model Reduction

Rolf Rannacher

Institute of Applied Mathematics
University of Heidelberg,
INF 293/294, D-69120 Heidelberg, Germany
rannacher@iwr.uni-heidelberg.de

Summary. This article surveys recent developments of duality-based methods for "goal-oriented" mesh adaptivity and error control in the numerical solution of flow problems. The emphasis is on laminar viscous incompressible flows governed by the Navier-Stokes equations. But also inviscid transonic flows and heat-driven low-Mach number flows are considered. The Galerkin finite element method and a functional analytic setting provide the basis for a unified approach, the "Dual Weighted Residual (DWR) Method", to a posteriori error control and model reduction by successive mesh adaptation.

1 Introduction

We present a general approach to a posteriori error control and mesh adaptation for solving flow problems by the Galerkin finite element (FE) method. A large part of the existing work on a posteriori error analysis deals with error estimation in global norms such as the "energy norm" involving usually unknown stability constants. However, in most CFD applications, the error in a global norm does not provide useful bounds for the errors in the quantities of real physical interest. Such "goal-oriented" error bounds can be derived by duality arguments borrowed from optimal control theory. These a posteriori error estimates provide the basis of a feedback process for successively constructing economical meshes and corresponding error bounds tailored to the particular goal of the computation. This approach, called the "Dual Weighted Residual (DWR) Method" (see [BR03]), is developed within an abstract functional analytic setting, thus providing the general guideline for application to various kinds of flow models including also aspects of flow control and hydrodynamic stability. Several examples are discussed in order to illustrate the main features of the DWR method. For more details the reader may consult the references [BR00], [GS02], [BHR02], [BR03], and the literature cited therein.

2 Goal-Oriented Adaptivity: Concept and Examples

Suppose that the goal of the simulation is the computation of a quantity $J(u)$ involving the solution of a continuous model $\mathcal{A}(u) = 0$, say a partial differential equation, from an approximate discrete model $\mathcal{A}_h(u_h) = 0$, corresponding to a computational mesh $\mathbb{T}_h$. Then, "goal-oriented adaptivity" means the optimization of the mesh $\mathbb{T}_h$ and possibly also the discrete model $\mathcal{A}_h(u_h) = 0$ on the basis of an a posteriori error representation of the form

$$J(u)-J(u_h) \;\approx\; \eta(u_h) := \sum_{K\in\mathbb{T}_h} \rho_K(u_h)\omega_K, \tag{1}$$

where $\rho_K(u_h)$ are certain cell-oriented residuals and ω_K local weights. Depending on the size of the local "error indicators" $\eta_K := \rho_K(u_h)\omega_K$ the mesh adaptation is organized according to

$$\eta_K \gg \delta \;\Rightarrow\; \text{refine } K, \quad \eta_K \approx \delta \;\Rightarrow\; \text{keep } K, \quad \eta_K \ll \delta \;\Rightarrow\; \text{coarsen } K.$$

The complex local and global error interaction has to be detected by computation, i.e. by solving an associated "adjoint" or "dual" problem, which gives information about

- error propagation in space (global error pollution),
- interaction of physical error sources (local model sensitivities).

The use of this concept results in a feed-back process for achieving economical computation tailored to the goal of the simulation, the DWR method.

2.1 Example 1. Drag Computation in 2-d Viscous Flow

As an illustrative example for the use of the DWR method (from [BR03]), we consider drag computation in a laminar viscous fluid modeled by the stationary Navier-Stokes equations for velocity v and pressure p together with suitable conditions at the boundary $\partial\Omega = \Gamma_{\rm rigid} \cup \Gamma_{\rm in} \cup \Gamma_{\rm out}$:

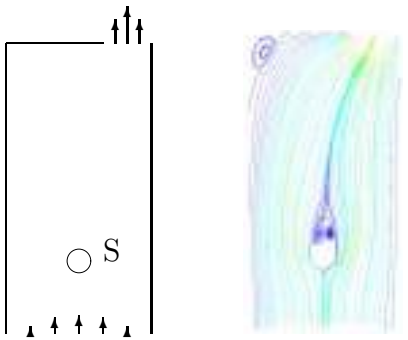

$$c_{\rm drag} := c \int_S n\cdot\sigma\cdot d\,{\rm ds}$$
$$\sigma := \tfrac{1}{2}\nu(\nabla v + \nabla v^T) - pI$$
$$d := (0,1)^T \text{ flow direction}$$

Fig. 1. Configuration and streamline plot for computation of drag coefficient $c_{\rm drag}$

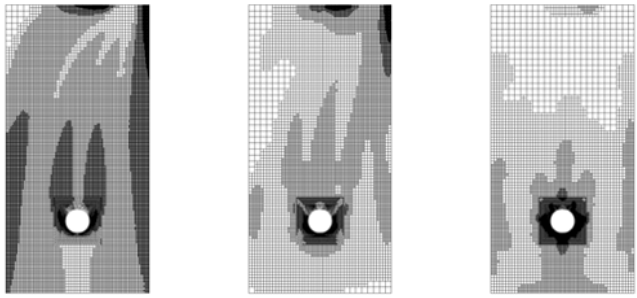

Fig. 2. Adapted meshes with 5,000 cells obtained by the vorticity indicator (left), the residual indicator (middle), and the weighted indicator (right)

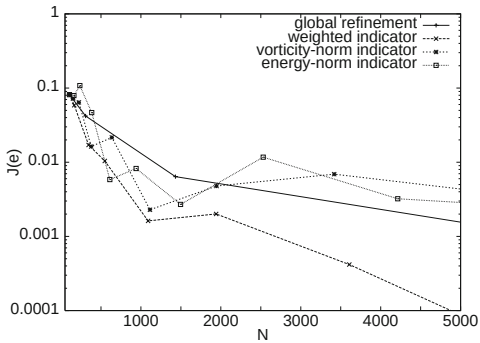

Fig. 3. Drag error $J(e)$ versus number of cells N

$$
\begin{aligned}
&-\nu\Delta v + v\cdot\nabla v + \nabla p = f, \quad \nabla\cdot v = 0,\\
&v|_{\Gamma_{\rm rigid}} = 0, \quad v|_{\Gamma_{\rm in}} = v^{\rm in}, \quad \nu\partial_n v - np|_{\Gamma_{\rm out}} = 0.
\end{aligned}
\tag{2}
$$

This problem in its natural variational formulation is well-posed and for moderate Reynolds number $\mathrm{Re} = 50$, has a stable solution. The configuration considered is shown in Figure 1

The discretization is by a standard FE method of 2nd-order accuracy (cell-wise bilinear velocity and pressure with least-squares stabilization). For mesh adaptation one may use one or more of the following local refinement indicators defined for each mesh cells K:

- *Vorticity*: $\eta_K := h_K\|\nabla\times v_h\|_K$.
- *Pressure gradient*: $\eta_K := h_K\|\nabla p_h\|_K$.
- *Velocity gradient*: $\eta_K := h_K\|\nabla_h^2 v_h\|_K$.
- *Residual indicator*: $\eta_K = \rho_K(v_h, p_h)$,

$$\rho_K(v_h,p_h) := h_K\|R_h\|_K + h_K^{1/2}\|r_h\|_{\partial K\setminus\partial\Omega} + h_K\|\nabla\cdot v_h\|_K$$
$$R_{h|K} := f+\nu\Delta v_h - v_h\cdot\nabla v_h - \nabla p_h,$$
$$r_{h|\Gamma} := \tfrac{1}{2}[\nu\partial_n v_h - np_h], \quad \text{if } \Gamma\not\subset\partial\Omega.$$

- "Weighted" indicator: $\eta_K := \rho_K(v_h,p_h)\,\omega_K$,
  sensitivity factors ω_K computed from an associated "dual" problem.

The resulting meshes and the corresponding solution efficiencies are shown in Figures 2 and 3. This clearly demonstrates the principle superiority of sensitivity-based mesh adaptation over purely feature- or smoothness-based refinement in computing local properties of the solution.

2.2 Example 2. Drag Computation in 3-d Viscous Flow ([BR06])

The second example concerns the accurate computation of drag in a real 3-d configuration, namely channel flow around a cylinder with a square cross section, as shown in Figure 4. The model is chosen analogously to that in Example 1. For the discretization three different Stokes elements are considered:

a) Q_2/Q_1-element - with uniform refinement,
b) Q_1/Q_1-element - with local refinement driven by "smoothness" indicator,
c) Q_1/Q_1-element - with local refinement driven by "weighted" indicator.

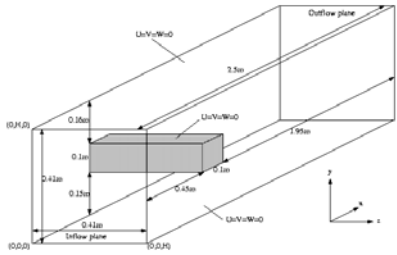

Fig. 4. Configuration of the 3-d cylinder flow benchmark

Table 1. Results of 3-d drag computation (error level of $\approx 1\%$ in boldface)

a) N_{uniform}	c_d	b) $N_{\text{smoothness}}$	c_d	c) N_{weighted}	c_d
15 960	8.2559	3,696	12.7888	3 696	12.7888
117 360	7.9766	21 512	8.7117	8 456	9.8262
899 040	7.8644	80 864	7.9505	15 768	8.1147
7 035 840	7.8193	182 352	7.9142	30 224	8.1848
55 666 560	7.7959	473 000	7.8635	**84 832**	7.8282
–	–	**1 052 000**	7.7971	162 680	7.7788
–	–	–	–	367 040	7.7784
∞	7.7730	∞	7.7730	∞	7.7730

Fig. 5. Refined Mesh and zoom generated by the "weighted indicator"

The corresponding results and adapted meshes are shown in Table 1 and in Figure 5. This example demonstrates the enormous potential of "model reduction" by sensitivity-driven mesh adaptation for achieving high accuracy at moderate cost.

2.3 Example 3. Inviscid 2-d Euler Equations ([Har02])

The third example deals with the stationary inviscid 2-d Euler equations:

$$\begin{aligned} \partial_t \rho + \nabla \cdot (\rho v) &= 0, \\ \partial_t (\rho v) + \nabla \cdot (\rho v \otimes v) + \nabla p &= \rho g, \\ c_p \partial_t (\rho e) + c_p \nabla \cdot (\rho e v + p v) &= h, \end{aligned} \tag{3}$$

supplemented with appropriate boundary conditions. We consider the case of supersonic flow around a BAC3-11 airfoil (see AGARD Report 1994) with inflow velocity at $\mathrm{Ma} = 1.2$ and angle of attack $\alpha = 5°$. In this case the (stationary) solution develops two shocks (see Figure 6). The quantity of interest is the pressure point value

$$J(\rho, v, e) := p(a) = (\gamma - 1)(e(a) - \tfrac{1}{2}\rho v(a)^2),$$

at the (subsonic) leading edge of the airfoil.

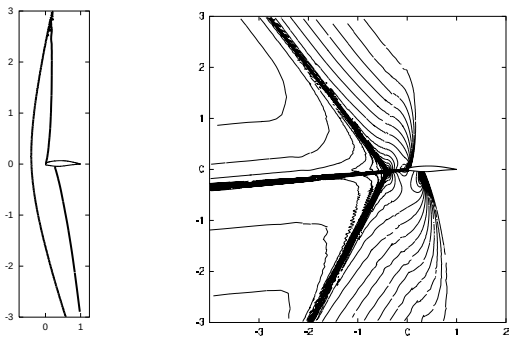

Fig. 6. Left: Ma = 1 isolines of primal solution, right: isolines of z_ρ component of dual solution

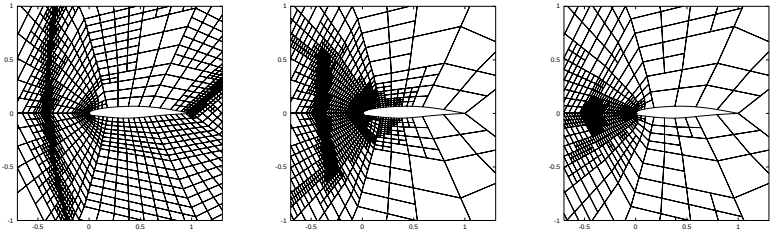

Fig. 7. Adapted meshes (for 1% solution accuracy) generated by the "smoothness" indicator with $N = 13,719$ (left), by constrained "smoothness" indicator with $N = 9,516$ (middle), and by the weighted indicator with $N = 1,803$ (right)

The discretization is by a "discontinuous" Galerkin method using bilinear finite elements. For comparison the mesh adaptation is driven by a residual-based indicator $\eta_K^{\rm res}$ and its artificially localized version, $\tilde\eta_K^{\rm res}$,

$$\eta_K^{\rm res} := h_K\|R_h\|_K + h_K^{1/2}\|r_h\|_{\partial K}$$
$$\tilde\eta_K^{\rm res} := \begin{cases}\eta_K^{\rm res}, & \text{if } K\cap C\neq\emptyset, \quad C = 90^\circ-\text{cone}\\ 0, & \text{otherwise.}\end{cases}$$

The resulting meshes shown in Figure 7 correspond to a solution accuracy of about 1%. This example demonstrates that duality-based mesh adaptation may even work well in cases where the sensitivity information has to pass through solution discontinuities such as shocks.

2.4 Example 4. A 2-d Heat-Driven Cavity Benchmark ([BR00])

The fourth example presents a problem with two different physical processes: a square flow cavity driven by a large temperature difference $\theta_h - \theta_c = 720\,K$

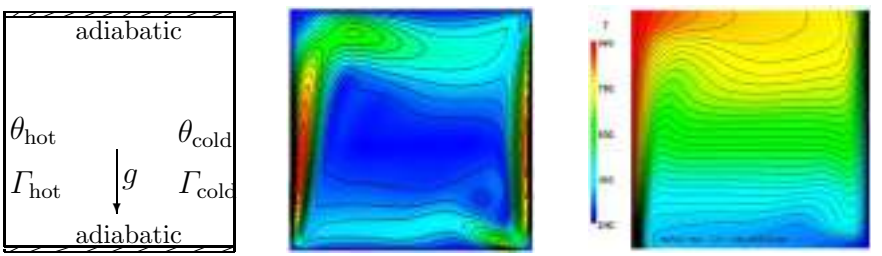

Fig. 8. Configuration (left), velocity norm (middle) and temperature (right) isolines

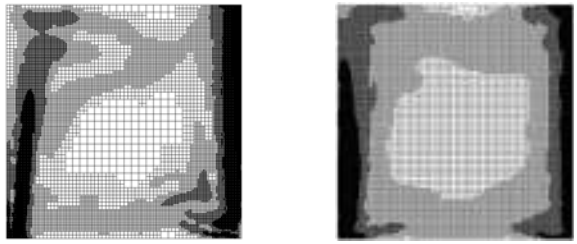

Fig. 9. Adapted meshes with about 58,000 cells for a 1% error generated by the smoothness-based indicator (left) and by the weighted indicator (right)

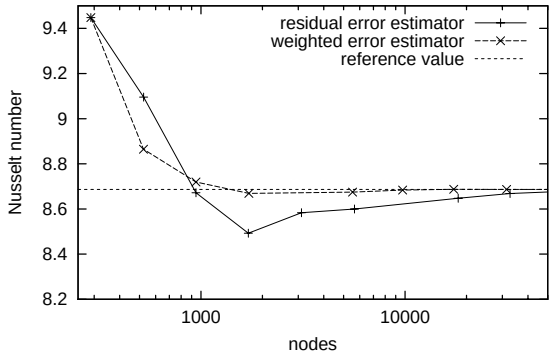

Fig. 10. Computed Nusselt number versus the number of cells

and gravity g, corresponding to a Rayleigh number $Ra \sim 10^6$. The quantity of interest is the Nusselt number (mean heat flux) along the cold wall:

$$J(u) = \langle \mathrm{Nu} \rangle_c := \frac{\mathrm{Pr}}{0.3\mu_0\theta_0} \int_{\Gamma_{cold}} \kappa \partial_n \theta \, ds$$

The configuration of this problem and computed velocity as well as temperature isolines can be seen in Figure 8. Figure 9 shows the corresponding adapted meshes and Figure 10 the achieved accuracy on adapted meshes. It can be seen that the smoothness-oriented indicator emphasizes mesh refinement in the steep layer of the velocity while the weighted indicator prefers refinement in the temperature boundary layer, which according to the achieved accuracy is more appropriate in this coupled problem. This result demonstrates the superiority of sensitivity-driven over purely smoothness-based adaptivity.

3 The Theoretical Framework

We begin the development of the DWR method within an abstract functional analytic setting in order to provide a guideline for its application to a

sufficiently large class of problems such as general nonlinear equations, eigenvalue problems, and optimization problems.

In a Hilbert function space X consider the approximative computation of a stationary point $x \in X$ of a differentiable functional $L(\cdot)$,

$$L'(x)(y) = 0 \qquad \forall y \in X, \tag{4}$$

by a Galerkin scheme in finite dimensional subspace $X_h \subset X$:

$$L'(x_h)(y_h) = 0 \qquad \forall\, y_h \in X_h. \tag{5}$$

Proposition 1. *([BR03]) There holds the error representation*

$$L(x) - L(x_h) = \tfrac{1}{2} \underbrace{L'(x_h)(x-y_h)}_{\textit{weighted residual}} + \ \mathcal{R}_h^{(3)}, \quad y_h \in X_h, \tag{6}$$

where the remainder $\mathcal{R}_h^{(3)}$ *is cubic in* $x-x_h$.

Proof. By elementary calculus, the use of the trapezoidal rule and Galerkin orthogonality for the error $e = x-x_h$, we conclude

$$\begin{aligned} L(x) - L(x_h) &= \int_0^1 L'(x_h+se)(e)\,\mathrm{ds} \\ &= \underbrace{\tfrac{1}{2}\big\{L'(x)(e) + L'(x_h)(e)\big\}}_{\text{trapezoidal rule}} + \underbrace{\tfrac{1}{2}\int_0^1 L'''(x_h+se)(e,e,e)\,\sigma(s)\,\mathrm{ds}}_{\text{remainder}} \\ &= \underbrace{\tfrac{1}{2}L'(x_h)(x-y_h)}_{\text{by Galerkin orthogonality}} \ + \ \mathcal{R}_h^{(3)}, \quad y_h \in X_h \end{aligned}$$

3.1 Application in Flow Simulation

We apply the general result of Proposition 1 to the situation of a general nonlinear variational problem in a Hilbert space V of the form

$$a(u)(\psi) = 0 \quad \forall \psi \in V, \qquad \text{target quantity } J(u). \tag{7}$$

The Galerkin approximation in finite dimensional subspaces $V_h \subset V$ reads

$$a(u_h)(\psi_h) = 0 \quad \forall \psi_h \in V_h, \qquad \text{error } J(u)-J(u_h). \tag{8}$$

In order to embed this situation into the general framework layed above, we view the determination of the functional value $J(u)$ from the solution of the variational equation as a trivial constrained optimization problem and use the Euler-Lagrange approach for its solution. Hence, the minima $u \in V$ are

determined by the stationary points $\{u,z\} \in V \times V$ of the Lagrangian functional $\mathcal{L}(u,z) := J(u) - a(u)(z)$ with the "dual" variable z, i.e., $\mathcal{L}'(u,z) = 0$. This is equivalent to the set of equations

$$\left\{ \begin{array}{l} J'(u)(\varphi) - a'(u)(\varphi, z) \\ -a(u)(\psi) \end{array} \right\} = 0 \quad \forall \{\varphi, \psi\}. \tag{9}$$

Its Galerkin approximation seeks $\{u_h, z_h\} \in V_h \times V_h$ satisfying

$$\left\{ \begin{array}{l} J'(u_h)(\varphi_h) - a'(u_h)(\varphi_h, z_h) \\ -a(u_h)(\psi_h) \end{array} \right\} = 0 \quad \forall \{\varphi_h, \psi_h\}. \tag{10}$$

The corresponding "primal" and "dual" residuals are defined by

$$\rho(u_h)(\cdot) := -a(u_h)(\cdot), \quad \rho^*(z_h)(\cdot) := J'(u_h)(\cdot) - a'(u_h)(\cdot, z_h).$$

For embedding this situation into the abstract framework, we introduce the product spaces $X := V \times V$ and $X_h := V_h \times V_h$ with elements $x := \{u,z\} \in X$ and $x_h := \{u_h, z_h\} \in X_h$, respectively. Then, setting $L(x) := \mathcal{L}(u,z) = J(u) - a(u)(z)$, at stationary points there holds

$$L(x) - L(x_h) = J(u) - a(u)(z) - J(u_h) + a(u_h)(z_h) = J(u) - J(u_h),$$

and the general Proposition 1 yields the following result.

Proposition 2. *([BR03]) There hold the error representations*

$$J(u) - J(u_h) \;=\; \rho(u_h)(z - \psi_h) \;+\; \mathcal{R}_h^{(2)}, \tag{11}$$

$$J(u) - J(u_h) \;=\; \tfrac{1}{2}\rho(u_h)(z - \psi_h) \;+\; \tfrac{1}{2}\rho^*(z_h)(u - \varphi_h) \;+\; \mathcal{R}_h^{(3)}, \tag{12}$$

for arbitrary $\varphi_h, \psi_h \in V_h$, with remainders $\mathcal{R}_h^{(2)}$ and $\mathcal{R}_h^{(3)}$, which are quadratic and cubic, respectively, in the errors $u - u_h$ and $z - z_h$.

3.2 Practical Aspects

The practical evaluation of the error representations (11) or (12) within the DWR method consists in the following steps:

1. Solution of discrete linear dual problem:

$$a'(u_h)(\varphi_h, z_h) = J'(u_h)(\varphi_h) \quad \forall \varphi_h \in V_h.$$

2. Linearization by neglecting the higher-order remainder term.
3. Approximation of weights by patch-wise higher-order interpolation,

$$(z - z_h)_{|K} \;\approx\; (\tilde{I}_{2h}^{(2)} z_h - z_h)_{|K},$$

where $\tilde{I}_{2h}^{(2)} z_h$ denotes the d-quadratic nodal interpolation of the computed d-linear approximation z_h on certain cell patches of the current mesh $\mathbb{T}_h$.

4. Mesh adaptation on the basis of cell-wise error indicators η_K by successive "error balancing", $\eta_K \approx TOL/N$, or by a "fixed fraction" strategy, e.g., refining a certain fraction $(20-30\%)$ of cells with the largest η_K.

For more details on the practical realization of the DWR method, we refer to [BR03] and the literature cited therein.

4 Applications

4.1 Drag Minimization by Boundary Control ([Bec01])

We consider the configuration shown in Figure 11, i.e. flow through a channel around a fixed cylinder with circular cross section and surface S. The mathematical model are the stationary Navier-Stokes equations (2) complemented by Neumann-type boundary conditions at the two openings Γ_Q,

$$\nu\partial_n v - np|_{\Gamma_Q} = P, \tag{13}$$

where P represents mean pressure. The diameter of the cylinder, the viscosity and the mean inflow velocity are chosen such that for $P = 0$ the Reynolds number is moderate, $\mathrm{Re} \sim 40$, corresponding to stable stationary flow.
The goal is to minimize the drag coefficient $J(v,p) := c_{\mathrm{drag}}$ by varying the mean pressure P. For given P the corresponding state $\{v,p\} \in H^1(\Omega) \times L^2(\Omega)$ is determined by the variational equation

$$\nu(\nabla v, \nabla\psi) + (v\cdot\nabla v, \psi) - (p, \nabla\cdot\psi) - (\chi, \nabla\cdot v) = (P, n\cdot\psi)_{\Gamma_Q}, \tag{14}$$

for all admissible test pairs $\{\psi,\chi\}$, and the appropriate boundary conditions at $\Gamma_{\mathrm{in}} \cup \Gamma_{\mathrm{rigid}}$.

The discretization of this optimization problem is by a standard 2nd-order FE method using equal-order bilinear elements for velocity and pressure with least-squares pressure stabilization (see [Ran00] and [Ran05]). Applying the DWR approach to this situation yields the following "primal" residual:

$$\rho(u_h)(z-z_h) := \sum_{K\in\mathbb{T}_h} \big\{(R(u_h), z^v - z_h^v)_K + (r(u_h), z^v - z_h^v)_{\partial K\setminus(\Gamma_{\mathrm{in}}\cup\Gamma_{\mathrm{rigid}})} + (z^p - z_h^p, \nabla\cdot v_h)_K - (v^{\mathrm{in}} - v_h, \partial_n z^v)_{\partial K\cap\Gamma_{\mathrm{in}}}\big\},$$

Fig. 11. Configuration of the drag minimization problem

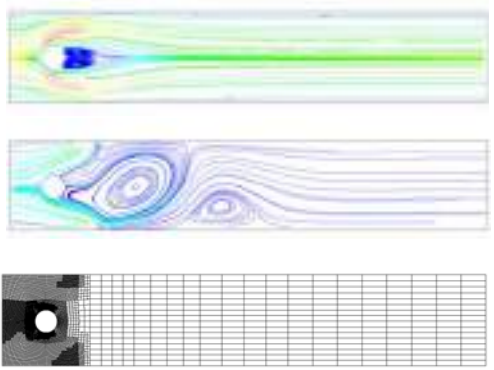

Fig. 12. Streamlines of uncontrolled flow ($P = 0$), controlled flow ($P = P_{\text{opt}}$), and adapted mesh

Table 2. Uniform versus adaptive refinement

Uniform refinement		Adaptive refinement	
N	J_{drag}	N	J_{drag}
10,512	3.31321	1,572	3.28625
41,504	3.21096	4,264	3.16723
164,928	3.11800	11,146	3.11972

with the cellwise equation and normal-jump residuals

$$R(u_h)_{|K} := f + \nu\Delta v_h - v_h \cdot \nabla v_h - \nabla p_h$$

$$r(u_h)_{|\Gamma} := \begin{cases} -\frac{1}{2}\nu n \cdot [\nabla v_h - p_h I], & \Gamma \not\subset \partial\Omega, \\ -\nu n \cdot (\nabla v_h - p_h I), & \Gamma \subset \Gamma_{\text{out}}, \\ P - \nu n \cdot (\nabla v_h - p_h I), & \Gamma \subset \Gamma_Q. \end{cases}$$

The "dual" residual $\rho^*(z_h)(u - u_h)$ has an analogous form. The results obtained by the DWR method for this optimization problem are shown in Figure 12 and Table 2. The drag minimization on an adapted mesh with only about 11,000 cells is as accurate as that on a uniformly refined mesh with about 164,000 cells. This demonstrates the enormous potential of the DWR method particularly in solving optimal control problems.

The rough pattern of the optimal state shown in Figure 12 races the question of its stability. This has to be investigated by an accompanying stability analysis (see [HR06]).

4.2 Fluid-Structure Interaction ([DR06]), [Dun07], [BDR08])

The use of systematic mesh adaptation in solving complex (viscous) fluid - (elastic) structure interaction (FSI) problems has begun only recently. For

the application of the DWR concept this coupled problem has to be written in a "monolithic" variational form either in Lagrangian/Eulerian coordinates, as used in the traditional ALE approach ("Arbitrary Lagrangian Eulerian"), or in an unconventional purely Eulerian/Eulerian setting. The consistent discretization of these models by the Galerkin finite element method then results in fully coupled discrete models the main difference being in the types of meshes used (body fitted moving mesh or fixed background mesh) and the corresponding handling of the fluid-structure interface (either by "shock-fitting" or by "shock-capturing"). Both approaches yield very much comparable results but have possible week points in its range of applicability. The ALE method suffers from ill-conditioning in case of large structure deformation and structure-structure touching while the Eulerian/Eulerian formulation can deal with this situation but generally involves higher computational cost. However, both frameworks are principally suitable for the use of the DWR method. This is demonstrated for a simple 2-d FSI benchmark problem, the "Vibrating Thin Plate" as shown in Figure 13 (for more details see [HT06]). Here, the fluid is assumed as incompressible and Newtonian and for the structure a compressible St. Venant-Kirchhoff model is used.

Starting from the monolithic variational formulations of the problem the numerics uses a global FE discretization with equal-order (bilinear) elements for all variables with stabilization. The mesh adaptation is either hand-made

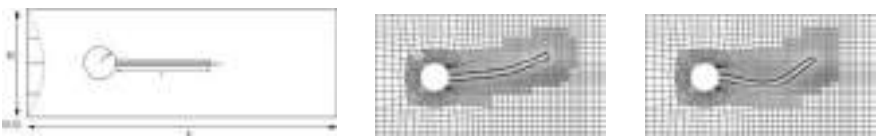

Fig. 13. FSI benchmark "Vibrating Thin Plate": configuration and snapshot computed by the ALE approach (middle) and by the fully Eulerian approach (right)

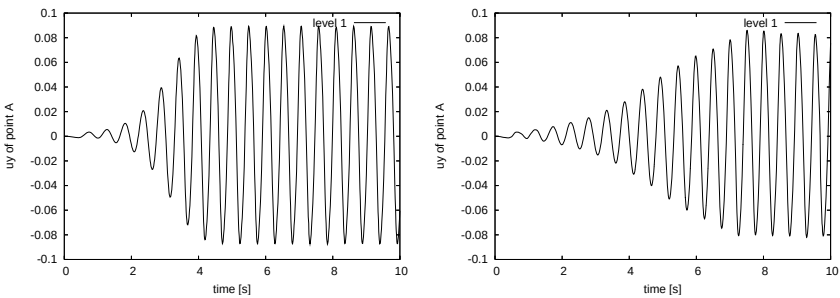

Fig. 14. Position of the plate's tip computed by the ALE (left); max $= 0.0882m$, $\nu = 1.95\, s^{-1}$, and the Eulerian approach (right): max $= 0.0822m$, $\nu = 1.92\, s^{-1}$

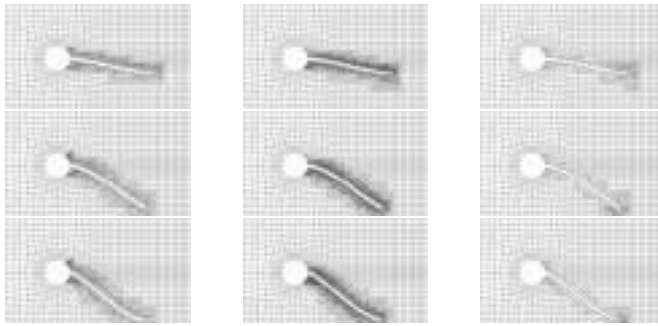

Fig. 15. Snapshots of the plate obtained by zonal refinement with $N \sim 3,000$ (left) and $N \sim 12,000$ (middle) compared against sensitivity-driven refinement with $N \sim 1,900$ (right)

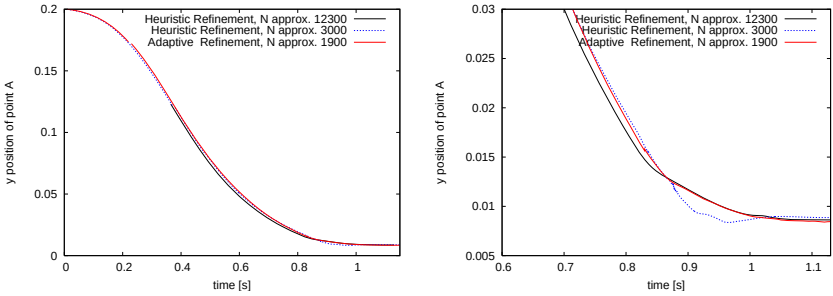

Fig. 16. Position of the plate's tip as function of time (left) and a zoom (right)

zonal or by the DWR method. The resulting nonlinear algebraic equations are solved by a Newton-type iteration and the linear subproblems by GMRES with multigrid preconditioning. One of the quantities of interest used for measuring the discretization accuracy is the vertical displacement of the plate's tip. For this test both approaches, ALI and fully Eulerian, yield comparable results on hand-adapted (almost uniform) meshes; see Figure 14.

A harder test involves the touching of the plate's tip with the lower wall under the action of gravity for zero inflow. This yet simple case cannot be handled by the standard ALE method, while the fully Eulerian method has no problems as can be seen in Figure 15. The quality of the different meshes is shown in Figure 16. The same accuracy was achieved on the zonal mesh with about $30h$ CPU time while that on the locally refined mesh required only $4h$.

5 Summary and Outlook

The DWR method provides a universal approach to a posteriori error estimation and model reduction by recursive mesh adaptation for Galerkin FE

schemes. In principle it can be applied to any flow model posed in a variational form. For surveys of extensions and open problems see [BR00], [GS02], and [BR03]. Applications include so far:

- Inviscid and viscous flows ([Ran00], [Har05]),
- Viscous fluid - rigid/elastic structure interaction ([DR06], [BDR08]),
- Thermally driven and reactive flows ([BR98], [BB06]),
- Flow control ([Bec01], [BMRV06], [Ran08]),
- Stability eigenvalue problems ([HR06]),

Applications outside fluid mechanics are among many others:

- Elasticity and elasto-plasticity ([RS02]),
- Astrophysical radiative transport ([MKRW06]),
- Acoustic wave propagation ([BR99]),
- Parameter identification and model calibration ([BMRV06]).

References

[BR99] Bangerth, W., Rannacher, R.: Finite element approximation of the acoustic wave equation: Error control and mesh adaptivity. East-West J. Numer. Math. 7, 263–282 (1999)

[BR03] Bangerth, W., Rannacher, R.: Adaptive Finite Element Methods for Differential Equations. Birkhäuser, Basel (2003)

[Bec00] Becker, R.: An optimal-control approach to a posteriori error estimation for finite element discretizations of the Navier-Stokes equations. East-West J. Numer. Math. 9, 257–274 (2000)

[Bec01] Becker, R.: Mesh adaptation for stationary flow control. J. Math. Fluid Mech. 3, 317–341 (2001)

[BHR02] Becker, R., Heuveline, V., Rannacher, R.: An optimal control approach to adaptivity in computational fluid mechanics. Int. J. Numer. Meth. Fluids 40, 105–120 (2001)

[BMRV06] Becker, R., Meidner, D., Rannacher, R., Vexler, B.: Adaptive finite element methods for PDE-constrained optimal control problems. In: Jäger, W., et al. (eds.) Reactive Flow, Diffusion and Transport. Springer, Heidelberg (2006)

[BR00] Becker, R., Rannacher, R.: An optimal control approach to error estimation and mesh adaptation in finite element methods. In: Iserles, A. (ed.) Acta Numerica 2000, pp. 1–102. Cambridge University Press, Cambridge (2001)

[BB06] Becker, R., Braack, M., Rannacher, R., Richter, T.: Mesh and model adaptivity for flow problems. In: Jäger, W., et al. (eds.) Reactive Flows, Diffusion and Transport. Springer, Heidelberg (2006)

[BDR08] Bönisch, S., Dunne, T., Rannacher, R.: Lecture on numerical simulation of liquid-structure interaction. In: Galdi, G.P., et al. (eds.) Hemodynamical Flows: Aspects of Modeling, Analysis and Simulation. Birkhäuser, Basel (2008)

[BR98] Braack, M., Rannacher, R.: Adaptive finite element methods for low-Mach-number flows with chemical reactions. In: 30th Computational Fluid Dynamics. Lecture Series, vol. 1999-03. von Karman Institute of Fluid Dynamics, Brussels (1999)

[BR06] Braack, M., Richter, T.: Solutions of 3D Navier-Stokes benchmark problems with adaptive finite elements. Comp. and Fluids 35, 372–392 (2006)

[Dun07] Dunne, T.: Adaptive Finite Element Simulation of Fluid Structure Interaction Based on an Eulerian Formulation. Doctoral thesis, Institute of Applied Mathematics, University of Heidelberg (2007)

[DR06] Dunne, T., Rannacher, R.: Adaptive finite element approximation of fluid-structure interaction based on an Eulerian variational formulation. In: Bungartz, H.-J., Schäfer, M. (eds.) Fluid-Structure Interaction: Modelling, Simulation, Optimisation. Springer, Heidelberg (2006)

[GS02] Giles, M.B., Süli, E.: Adjoint methods for PDEs: a posteriori error analysis and postprocessing by duality. In: Iserles, A. (ed.) Acta Numerica 2002, pp. 145–236. Cambridge University Press, Cambridge (2002)

[Har02] Hartmann, R.: Adaptive Finite Element Methods for the Compressible Euler Equations, Doctoral Thesis, University of Heidelberg (2002)

[Har05] Hartmann, R.: Discontinuous Galerkin methods for compressible flows: higher order accuracy, error estimation and adaptivity. In: Deconinck, H., Ricchiuto, M. (eds.) CFD - Higher Order Discretization Methods. VKI LS 2006-01. von Karman Institute of Fluid Dynamics, Brussels (2005)

[HR06] Heuveline, V., Rannacher, R.: Adaptive FE eigenvalue approximation with application to hydrodynamic stability analysis. In: Fitzgibbon, W., et al. (eds.) Advances in Numerical Mathematics. Institute of Numerical Mathematics RAS, Moscow (2006)

[MKRW06] Meinköhn, E., Kanschat, G., Rannacher, R., Wehrse, R.: Numerical methods for multidimensional radiative transfer. In: Jäger, W., et al. (eds.) Reactive Flow, Diffusion and Transport. Springer, Heidelberg (2006)

[HT06] Hron, J., Turek, S.: Proposal for numerical benchmarking of fluid-structure interaction between an elastic object and laminar incompressible flow. In: Bungartz, H.-J., Schäfer, M. (eds.) Fluid-Structure Interaction: Modelling, Simulation, Optimisation. Springer, Heidelberg (2006)

[Ran00] Rannacher, R.: Finite element methods for the incompressible Navier-Stokes equations. In: Galdi, G.P., et al. (eds.) Fundamental Directions in Mathematical Fluid Mechanics. Birkhäuser, Basel (2000)

[Ran05] Rannacher, R.: On the discretization of PDE-constrained optimization problems by adaptive finite element methods. In: Fernandez, L.M., et al. (eds.) PDE Constrained Optimization. Springer, Heidelberg (to appear)

[Ran08] Rannacher, R.: Lectures on numerical flow simulation: Finite element discretization, numerical boundary conditions and automatic mesh adaptation. In: Galdi, G.P., et al. (eds.) Hemodynamical Flows: Aspects of Modeling, Analysis and Simulation. Birkhäuser, Zürich (2008)

[RS02] Rannacher, R., Suttmeier, F.-T.: Error estimation and adaptive mesh design for FE models in elasto-plasticity. In: Stein, E. (ed.) Error-Controlled Adaptive FEMs in Solid Mechanics. John Wiley, Chichster (2002)

“*This page left intentionally blank.*”

Part 2
Keynote Lectures

“*This page left intentionally blank.*”

Progress in Computational Magneto-Fluid-Dynamics for Flow Control

J.S. Shang, P.G. Huang, and D.B. Paul*

Wright State University
Dayton Ohio, USA
Wright-Patterson Air Force Base*
Ohio, USA

1 Introduction

In the late 1990's a promising and innovative concept of the Magnetohydrodynamic (MHD)-bypass scramjet engine rejuvenated interest in magneto-aerodynamic research worldwide [1]. Many interdisciplinary ideas were put forth in the areas of plasma actuator for flow control, MHD propulsion, remote energy deposition for drag reduction, radiation driven hypersonic wind tunnel, sonic boom meditation, and enhanced plasma ignition and combustion stability [2,3]. Extensive and in-depth research however has revealed that additional and refined fidelity of physics for modeling and analyzing are required to reach a conclusive assessment for the MHD-bypass scramjet engine [4]. From this lesson learned; most recent research activities tend to refocus on more basic and simpler aerodynamic-electromagnetic interaction phenomena.

The mostly widely used plasma generating processes for flow control are either the direct current discharge (DCD) or dielectric barrier discharge (DBD). These gas discharges are based on the electron collision process in which the Townsend's mechanism controls the multiple primary avalanches, secondary emission and ultimately maintains the plasma. At atmospheric pressure some highly luminous and concentrated streamers (micro discharges) from the electrodes have also been observed [5]. The charged particle number density is generally limited to the order of magnitude of 10^{12} per cubic centimeter. The generated plasma consists of electrons in a highly excited state but the heavy ions retain the thermodynamic condition of its surrounding environment. Therefore, the weakly ionized gas is far from thermodynamic equilibrium. Meanwhile the drift motion and diffusion of charged particles, including the ambipolar diffusion, profoundly modifies the transport properties of the ionized medium.

The electromagnetic effects generated by DCD and DBD can be summarized as the Lorentz acceleration, electrostatic/electrodynamic force, plasma and electrode heating all of which have limited magnitude [6,7]. The Lorentz acceleration is significant only in the presence of an externally applied magnetic field and due to the relatively low current density the magnitude of electrodynamic force is just a few kN/m^3. On the other hand the electrostatic force is significant only in the cathode layer where the space charge separation occurs; its magnitude is around

one kN/m^3 [8]. DBD operates at atmospheric pressure and is sustained by alternative electrical potential at 5-20 kV and in the frequency range up to 10 kilo Hertz. Again, the driving force is derived from charges separation over an exposed and encapsulated electrode and the discharging field is dominated by a series of multiple micro discharges. Although a complete understanding of this multiple scale phenomenon is still beyond our reach, it is incontrovertible that a net momentum transfer between charged and neutral results in a wall jet with a magnitude of few meters per second moving from the exposed electrode toward the dielectric barrier [3,8,9]. Corke has sustained a series of investigation in using DBD for flow modification at fluid bifurcation such as the flow separation and dynamic stall of lifting surfaces. In short, the electromagnetic forces by a plasma actuator are in general two to three order-of-magnitudes lower than the aerodynamic inertia of a typical high-speed flow. Therefore the electromagnetic perturbation must either be amplified by viscous-inviscid interaction or applied at fluid dynamic bifurcation to be effective as flow control mechanism [7,8].

The thermal effects of the DCD to fluid medium include plasma and electrode heating. The former consists of mainly Joule heating and stochastic heating. The latter however is nearly negligible in the absence of oscillating plasma sheath. The Joule heating also concentrates within the cathode layer and becomes a rather small but effective spatial heat source to the surrounding air stream. In the electron collision process for plasma generation, the electrode heating is an unavoidable consequence. This heat flux enters the flow field by the conductive process and has a magnitude around 10 W/m^2. In a laboratory environment, these two heat fluxes have a comparable order of magnitude but are still very much smaller in comparison to the energy content of the hypersonic flow. And yet experimental and computational investigations have repeatedly shown perceptible effect for flow control [6,7,10].

Hypersonic flow modification by plasma can be understood only in the light of the subsequent viscous-inviscid interaction which is a unique feature of hypersonic flow [11]. In essence, the flow displacement by a thin boundary layer is no longer negligible under the high-speed flow condition. The near-surface DCD becomes a triggering mechanism to produce a suddenly increased displacement thickness through heat sources in the shear layer and from solid surface. The injected thermal flux heats the surrounding air stream and lowers the density within the shear layer and leads to a sudden increase in the displacement thickness. This event initiates the pressure interaction for which the induced pressure has been successfully formulated and verified by experiments with a single interaction parameter, $\chi = M^3(C/Rey)^{1/2}$ [21]. This interaction actually forms a close feed-back loop between the growth rate of the displacement thickness and the induced streamwise pressure rise. Most importantly the magnitude of the induced pressure increases according to the cubic power of the free-stream Mach number to become a viable hypersonic flow control mechanism.

The present study summarizes the computational simulations of magneto-fluid-dynamic interactions using the surface DCD and DBD by a drift-diffusion weakly ionized gas model [12]. The periodic electrodynamic force of DBD will first be delineated to reveal the unique self-limiting future of the DBD plasma actuator

from arcing. However, the major portion of the present analysis will be focused on a glow discharge over the sharp leading edge of immobile surface and constant cross-section rectangular and cylindrical inlets. The verified computational results of virtual leading edge strake and virtual variable geometric inlet cowls will be presented.

2 Governing Equations

The combined Navier-Stokes and the reduced Maxwell equations govern all plasma-based flow control phenomena. In the traditional MHD formulation, only the Faraday's law is included but the Ampere's law is replaced by the generalized Ohm's law. In addition, the two Gauss' laws for magnetic and electric field are not explicitly integrated into the formulation [13]. The system of governing equations is;

$$\frac{\partial \rho}{\partial t} + \nabla \cdot (\rho \vec{u}) = 0, \tag{1-1}$$

$$\frac{\partial \vec{B}}{\partial t} + \nabla \cdot (\vec{u}\vec{B} - \vec{B}\vec{u}) = -\vec{u}\nabla \cdot \vec{B}, \tag{1-2}$$

$$\frac{\partial (\rho \vec{u})}{\partial t} + \nabla \cdot (\rho \vec{u}\vec{u} + p\vec{\vec{I}} - \vec{\vec{\tau}}) = \vec{J} \times \vec{B}, \tag{1-3}$$

$$\frac{\partial (\rho e)}{\partial t} + \nabla \cdot (\rho e\vec{u} - \vec{q} - \vec{u} \cdot \vec{\vec{\tau}}) = \vec{E} \cdot \vec{J}. \tag{1-4}$$

By omitting the viscous dissipation and conductive heat transfer, the resultant classic ideal MHD equations constitute a non-strictly hyperbolic system and are also nonconvex [14]. In addition, the ideal MHD equations in divergence form are not symmetrizable because the Jacobian of the coefficient matrix has a zero eigenvalue [15]. Its physical reason is also clear; for ideal MHD equation the induction law reduces to;

$$\frac{\partial \vec{B}}{\partial t} - \nabla \times (\vec{u} \times \vec{B}) = 0. \tag{1-5}$$

It is observed that the temporal variation of $\vec{B}$ depends only on the spatial variation perpendicular to the component in consideration. Nevertheless by including an added evolution equation, the Gauss's law for magnetic flux density $\nabla \cdot \vec{B} = 0$; the symmetrizable system of MHD equation can be recovered and the system of equations also become Gallilean invariant [15,16].

For plasma flow control, when the interaction is lower than the microwave frequency range the inducted magnetic field is negligible [13]. Under this circumstance and if the magnetic Reynolds $uL/(\mu_m \sigma)^{-1}$ is much less than unity, equations (1-1), (1-3), and (1-4) become the only required components of the low magnetic

Reynolds approximation. These equations are essentially the compressible Navier-Stokes equation with source terms but offer more challenge for numerical analysis because of the great disparity in wave speeds of light and sound. However viable numerical procedures have been highly developed by the CFD discipline either the form of flux splitting or flux difference splitting, thus will not be elaborated in here [17,18]

3 Model of Weakly Ionized Gas

In plasma-based flow control applications, additional complexities arise from the ionization-recombination process, the drifting velocities of charged particle, and diffusion [19]. The eigenvalues of the equations system span a wide range and seriously degrade the computational stability of numerical simulations. As a consequence, the progress of gaining a better understanding of plasma actuation is seriously impeded [2,3,4]. Until recently the interrelationship of electrical current $\vec{J}$, electric field intensity $\vec{E}$, the magnetic flux $\vec{B}$, and electric conductivity σ was described by the simplified Ohm's law; $\vec{J} = \sigma(\vec{E} + \vec{u} \times \vec{B})$ [13]. In this formulation, the electric conductivity of plasma is the required transport property of the flow medium. A wide range of assumptions have been imposed for this tensorial variable and has led to considerable uncertainties in physical fidelity of numerical simulation.

A viable alternative to alleviate this uncertainty is to introduce a physics-based model for the partially ionized gas. The physics of ionization by electron collision is very complex and involves interaction of gas and solid at atomic level. However, the microscopic plasma generation via electron collision at macroscopic scale has been accurately described by the Townsend's formula [5,19]. Two fundamental mechanisms of charged particle dynamics are the drift velocity and the diffusion [5,12]. This behavior is independent of how the gas discharge is generated. Therefore a rational model for the direct current discharge only needs to concentrate on the dynamics of the charged particles motion for these basic mechanisms [18].

In self-sustain plasma, the net rate of change for the charged particle number density in a control volume must be balanced by generation through ionization and depletion by recombination. The species continuity equations for electrons and ions are given by the drift-diffusion model [12,19].

$$\frac{\partial n_e}{\partial t} + \nabla \cdot \vec{\Gamma}_e = \alpha\left(\left|\vec{E}\right|, p\right)\left|\vec{\Gamma}_e\right| - \beta n_e n_+ \tag{2-1}$$

$$\frac{\partial n_+}{\partial t} + \nabla \cdot \vec{\Gamma}_+ = \alpha\left(\left|\vec{E}\right|, p\right)\left|\vec{\Gamma}_e\right| - \beta n_e n_+ \tag{2-2}$$

where $\Gamma_e = -D_e \nabla n_e - n_e \mu_e \left(\vec{E} + \vec{u}_e \times \vec{B}\right)$ and

$\Gamma_+ = -D_+ \nabla n_+ + n_+ \mu_+ \left(\vec{E} + \vec{u}_+ \times \vec{B}\right)$ are the flux vectors of the charged particle

number density. In fact, the externally applied magnetic field generated an effective electric field intensity which can be described by the Hall parameters for electron and ion, β_e and β_+ respectively [6,12]. In the above charged particle density flux functions, α and β are the first Townsend ionization and recombination coefficient. It needs to be pointed out that the Townsend ionization coefficient α is an exponential function of the electric field intensity and ambient pressure, $\alpha(E,P)=C_1P\ \exp[-C_2/(|E|/P)]$ [12]. The parameters μ_e and μ_+ are the electron and ion mobility, and D_e and D_+ are the electron and ion diffusion coefficients. In fact these transport properties of charged particles are coupled by the Einstein relationship [5,12].

A unique feature of the present plasma model equation is that it satisfied fully the electric current conservation equation. This constitution equation can be derived by taking the divergence of the Ampere's law and inserting Gauss's law for electric displacement. In application, it is often adopted as an internal consistent checking procedure like the reinforcement of Gauss's law for magnetic field, $\nabla\cdot B = 0$, for classic MHD computations.

$$\frac{\partial \rho_e}{\partial t} + \nabla \cdot \vec{J} = 0 \tag{2-3}$$

The electric field intensity in globally neutral plasma can be introduced by an electrical potential function $\vec{E} = -\nabla\phi$. The electrical field potential is then the solution of the well-known Poisson equation of plasmadynamics associated with the net space charge density, ρ_e.

$$\nabla^2\phi = -\frac{\rho_e}{\varepsilon} \tag{2-4}$$

The electric current density appearing in equations (1-3) and (1-4) is given by the difference of the charged particle density flux $\vec{J} = e(\vec{\Gamma}_+ - \vec{\Gamma}_e)$. This term is the sole linkage between the low magnetic Reynolds MHD and the plasma model equations (2-1) and (2-2).

4 Solving Scheme

The MFD equations (1-1), (1-3), and (1-4) together with the drift-diffusion plasma model equations (2-1), (2-2), and (2-4) can be cast into a flux vector form [5,6,8],

$$\frac{\partial \vec{U}}{\partial t} + \nabla \cdot \bar{\bar{F}} = \vec{S} \tag{3-1}$$

A wide range of numerical methods have been applied to solving this system of equations from the penta-diagonal implicit [12], Sharfetter-Gummel [20], and compact differencing [21] to diagonal dominant alternating direction (DDADI) schemes [18,22]. However, an element of the well-known flux splitting or flux

vector difference splitting approximation is frequently included to solve the steep gradient domains associated with edges of discharging electrodes [12,14,16-18,21].

A high-resolution, diagonally dominant alternative direction implicit scheme has been specially developed to solve the stiff partially differential system for the plasma model equations [22]. In essence, the convective components of the source term on the RHS of the equation are obtained by a high-order upwind Lagrange interpolation from the values at the nodal point to the interface of the control volume. The diffusive component is evaluated by the explicit central differencing scheme. Because of the large disparity in speeds of light and sound, multiple internal iterations of the plasma model equations through a cascading sequence can be applied before the resultant electric current density is transmitted to the MHD equations. For the rapidly varying discharging phenomenon in short duration, the distinguishing of temporal accuracy and iterative convergence is less critical. The discretized equations can be given as;

$$\frac{\delta U^n}{\delta t} + \frac{\delta(\Delta F_x)^*}{\delta x} = -\frac{\delta F^n{}_x}{\delta x} - \frac{\delta F^n{}_y}{\delta y} - \frac{\delta F^n{}_z}{\delta z} + S^n \tag{3-2}$$

$$\frac{\delta U^{**}}{\delta t} + \frac{\delta(\Delta F_y)^{**}}{\delta y} = -\frac{\delta U^*}{\delta t} \tag{3-3}$$

$$\frac{\delta U^{n+1}}{\delta t} + \frac{\delta(\Delta F_z)^{n+1}}{\delta z} = -\frac{\delta U^{**}}{\delta t} \tag{3-4}$$

However, there is an important distinction of the present DDADI formulation from the conventional delta formulation in that all diagonal elements of the discretized dependent variables are resided on the LHS of the formulas. Since the source terms are computed accurately, any modification to the LHS to maintain positive and definitive for unconditional stable should not affect the final interactive result as long as numerical convergence can be reached. By the approach, the resultant numerical procedure meets the axiom of achieving the high physical fidelity on the RHS terms but also maintaining best possible computational stability.

The LHS is solved implicitly by a first-order upwind differencing scheme to ensure numerical stability and the increment of the flux component is approximated as

$$\Delta F_{i+\frac{1}{2},j,k} = \frac{1}{2} A_{i+\frac{1}{2},j,k} (\Delta U_{i+\frac{1}{2},j,k} + \Delta U_{i,j,k}) - \frac{1}{2} |A_{i+\frac{1}{2},j,k}| (\Delta U_{i+\frac{1}{2},j,k} - \Delta U_{i,j,k}) \tag{3-5}$$

where $A_i = \dfrac{\partial F_x}{\partial U} = \Lambda[0, -\mu_e E_x, \mu_+ E_x]$,

$$A_j = \frac{\partial F_y}{\partial U} = \Lambda[0, -\mu_e E_y, \mu_+ E_y],$$

and $A_k = \dfrac{\partial F_z}{\partial U} = \Lambda[0, -\mu_e E_z, \mu_+ E_z]$.

The initial values and boundary conditions are straight forward for this differential system. At the far field of the computational domain the vanishing gradient condition is uniformly applied to all dependent variables. On the cathode, the secondary emission condition requires the electron number density flux is only a fractional value of the positively charged ion; $\Gamma_e = -\gamma\Gamma_+$ and γ is the so-called coefficient of the secondary emission [5]. On the anode, all the positively charged particles must be repelled and the electric potential φ will be determined by the external circuit equation [12].

Most importantly, the appropriate boundary condition at the media interface across the dielectric barrier and plasma is imposed by the discontinuous normal component of the electric displacement, $\vec{D}$ ($\vec{D} = -\varepsilon\nabla\varphi$). This condition is intermediately associated with Maxwell equations that require the jump across the interface to be balanced by the surface charge which has not been rigorously enforced by almost all previous investigations. In terms of the electrical potential, this critical condition can be given as;

$$\varepsilon_p \frac{\partial \varphi_p}{\partial n} - \varepsilon_d \frac{\partial \varphi_d}{\partial n} = \rho_{e,s} \tag{3-6}$$

where ε_p and ε_d are the electric permittivity of plasma and dielectric. In the present investigation the surface desorption is not taken into the consideration for computing the surface discharge, $\rho_{e,s}$. Nevertheless, this boundary condition has been overlooked by most earlier numerical simulations but is the key to reveal the self-limiting feature of DBD from arcing [8].

5 Results of Numerical Simulation

A high resolution diagonally dominant alternative direction implicit (DDADI) procedure has been shown to be effective with the enhanced computational stability. This improvement also significantly reduced the numerical artifact by eliminating the numerical smoothing. The present predicted discharge between infinite parallel electrodes agrees very well with the classic theory and previous numerical results [22]. The computational simulations have correctly duplicated the dependence of discharging pattern to the ratio ambient pressure and electric field intensity, p/E. The bistable bifurcation of discharge column between parallel electrodes of finite dimension is also convincingly demonstrated for the first time.

The numerical resolution in the extremely high gradient regions that at the edge of electrodes abridges the perfect electrically conducting and the dielectric surface by DDADI is depicted in Figure 1. Two numerical simulations are performed for the side-by-side, 2-D electrode arrangement; the cathode on the left has a separation distance of 1.0 cm from the anode. Both electrodes have the width of 0.5 cm and subjects to an EMF of 2.0 kV and under an ambient pressure of 5 Torr. The computed normal components of the electric field intensity from the coarse and fine mesh systems (163×124) and (81×62) are essentially duplicated each other,

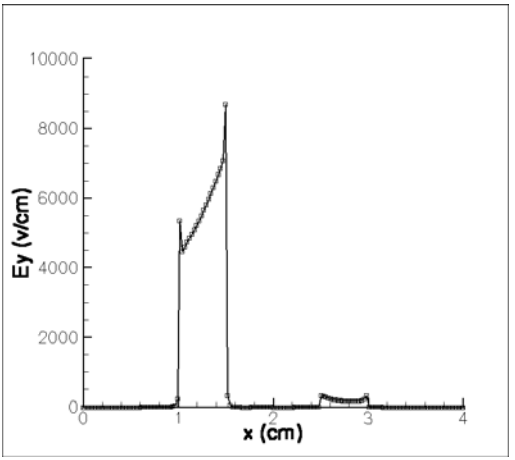

Fig. 1. Numerical resolution at edges of electrode by two grid system of (163×124) and (81×62)

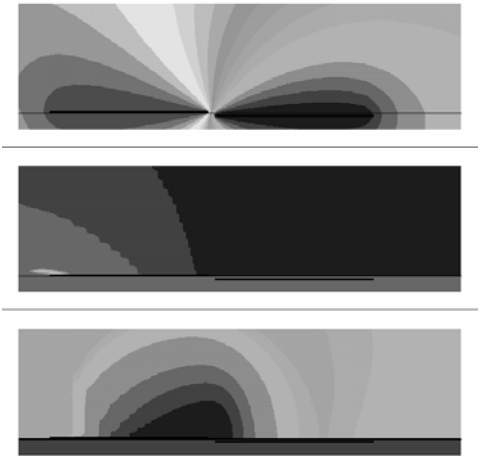

Fig. 2. Electric potential, electron, and ion number density contours of DBD, EMF=5.0 kV, ϖ=10 kHz

except the peak values at the edges of cathode which attaining a value of 24,000 V/cm. Otherwise, the numerical oscillations near the piecewise discontinuity are conspicuously absent and the numerical results by the two grid system are nearly identical. The discrepancy between two numerical results over the electrodes is less than 0.1%.

A typical instantaneous numerical simulation of dielectric barrier discharge in alternating current (AC) field with the electric potential of 5.0 kV and a frequency of 10 kHz is depicted in Figure 2. The contours of computed electric potential, electron, and ion number density are presented in a top-to-bottom panel sequence.

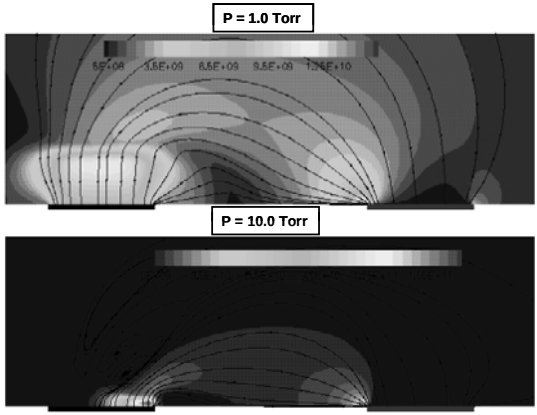

Fig. 3. Diffusive and constrictive discharge over side-by-side electrodes, p=1.0 & 10.0 Torr, EMF=2.0 kV

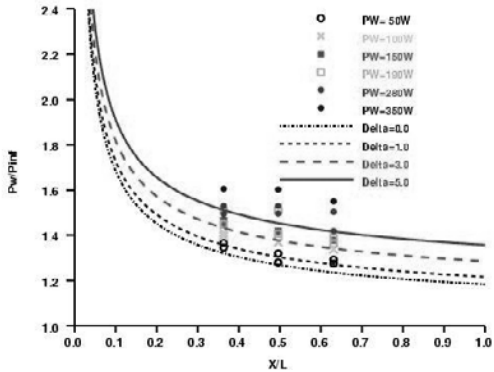

Fig. 4. Plasma generation power scaling law for virtual hypersonic leading-edge strake, M_∞=5.15, Rey=2.57×10^5

The outstanding feature of the electric potential distribution is that the free-space charge has significantly modified the externally applied electric field over the symmetric electrodes configuration. As a consequence, the symmetric electric field is loss. In the middle panel, the electrons are generated by the avalanche growth of secondary emission from the encapsulated electrode (on the left) and propagate toward the exposed electrode. Meanwhile, the ion is repulsed from the exposed electrode and accumulated on the dielectric barrier. The momentum coupling of the heavy ion and neutral particle leads to the well-known electric wind of DBD for flow control [8,9].

As an illustration, the distinction between a diffusive and constrictive discharge on the side-by-side electrode arrangement is shown in Figure 3. Two numerical simulations at the ambient pressure of one and ten Torr are depicted together. At an ambient pressure of 1 Torr, the diffusive discharge is clearly displayed by the

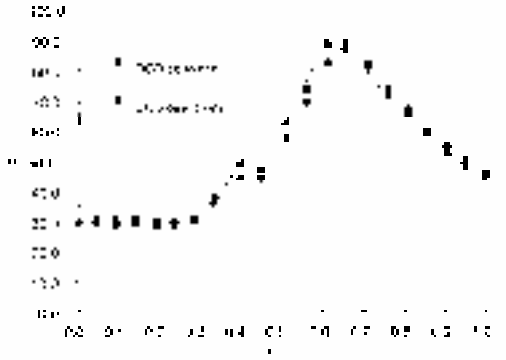

Fig. 5. Comparison of magneto-fluid-dynamic Compression for hypersonic rectangular inlet

uniform outward normal electric current in the cathode layer and the maximum electric potential of 650.27 V is required to sustain a current of 4.50 mA. On the other hand, the discharge is highly constricted under the same condition except at a higher ambient pressure of ten Torr, where the discharge takes place less than a half of the electrode width. Under these conditions, the total voltage drops to 539.5 V and the electric current yields a value of 4.87 mA. For the constrictive discharge, multiple eddy current loops are also observed over the cathode and away from the anode.

The numerical simulations are compared with measurements at the Mach number of 5.15 and Reynolds number of 2.57×10^5 by different plasma generation power input. The increased surface pressure distribution over the immobile wedge with an activated DCD acts as if the surface had executed a pitching motion – the performance identical to a movable leading edge strake. In Figure 4, a series of calculations with the discharge current from 50 to 350 mA yield the equivalent angles of attack from one to exceeded five degrees for the deployed virtual strake. Most important, the DCD induces a bona fide electro-aerodynamic interaction that is not possible with electrode heating alone [2,7]. It was found that a scaling of power required for the plasma actuator per electrode area is about 9.17 watts/cm^2 per degree.

Figure 5 presents the comparison of experimental and computed Pitot pressures along the centerline of the rectangular inlet when the DCD is either activated or deactivated. Both results generated at a stagnation pressure of 580 Torr have captured the interacting oblique shocks within the inlet [23]. When the DCD is actuated, the induced oblique shock becomes steeper and moves the interception of the shock waves upstream. The ensured expansion follows the strengthened shock and produces a slightly lower Pitot pressure along the centerline downstream. The actuated DCD leads to a higher peak Pitot pressure and an upstream movement in contrast to its deactivated counterpart. The computed results have good agreement with the experimental data. The computations underpredict the peak Pitot pressure by 2% and overpredict the uniform entrance condition by 1.2%. Using the small amount energy of 69 watts for plasma generation, the magneto-fluid-dynamic compression produces 11.7% static pressure gain over the unperturbed flow counterpart at the inlet exit.

6 Summary

A viable application of plasma actuators for flow control in the high-speed regime has been demonstrated by computational analysis using the magneto-fluid-dynamic equation in the low magnetic Reynolds number limit with a plasma model. The physics-based weakly ionized gas model has demonstrated its viability in describing the dynamics of charged particles for both direct current and dielectric barrier discharges.

A high resolution diagonally dominant alternative direction implicit (DDADI) procedure has been shown to be effective with the enhanced computational stability. This improvement also significantly reduced the numerical artifact by eliminating the numerical smoothing. Additional numerical resolution improvement is still urgently needed to accelerate the iterative convergence of the nonlinear, stiff nonlinear partial differential equations system.

The dielectric barrier discharge at atmospheric pressure has been applied for alleviating dynamic stall of lifting surface and flow separation on trailing edge of low-pressure turbine blade. The self-limiting arcing feature is now understood from the charge accumulation on the dielectric barrier by the appropriately imposed boundary conditions. The flow control using direct current discharge in hypersonic flow is derived from a chain-of-event from a small electromagnetic perturbation and subsequent viscous-inviscid interactions. The control effectiveness has been demonstrated for the virtual hypersonic leading edge strake and hypersonic virtual inlet cowl.

Acknowledgment

The support by Dr. F. Fahroo and Dr. J.D. Schmisseur of AFOSR is deeply appreciated. Authors are thankful for the fruitful exchange and earnest support by Dr. D. Gaitonde, Dr. R. Kimmel, and Mr. J Hayes of Air Force Research Laboratory, as well as, my colleague at Wright State University Dr. J. Menart, but not the least; we value highly our collaboration with Prof. S. Surzhikov of the Russian Academy of Science, Moscow.

References

1. Gurijanov, E.P., Harsha, P.T.: Ajax: New Directions in Hypersonic Technology, AIAA 1996-4609 (November 1996)
2. Shang, J.S.: Recent Research in Magneto-Aerodynamics. Progress in Aerospace Science 37(1), 1–20 (2001)
3. Bletzinger, P., Ganguly, B.N., Van Wie, D., Garscadden, A.: Plasma in High-Speed Aerodynamics. J. of Physics D: Applied Physics 38, R33–R57 (2005)
4. Park, C., Bagdanoff, D.W., Mehta, U.B.: Theoretical Performance of a Magnetohydrodynamic-Bypass Scramjet Engine with Nonequilibrium ionization. J. Propulsion and Power 19(4), 529–537 (2004)
5. Raizer, Y.P.: Gas Discharge Physics. Springer, Berlin (1991)

6. Shang, J.S., Surzhikov, S.T.: Magnetoaerodynamic Actuator for Hypersonic Flow Control. AIAA Journal 43(8), 1633–1643 (2005)
7. Shang, J.S., Surzhikov, S.T., Kimmel, R., Gaitonde, D.V., Hayes, J.R., Menart, J.: Mechanisms of Plasma Actuators for Hypersonic Flow Control. Progress in Aerospace Sciences 41(8), 642–668 (2005)
8. Post, M.L., Corke, T.C.: Separation Control on High Angle of Attack Airfoil Using Plasma Actuator. AIAA J. 42(2), 2177–2184 (2004)
9. Moreau, E.: Air Flow Control by Non-thermal Plasma Actuators. J. Physics D: Appl. Physics 40, 605–635 (2007)
10. Kimmel, R.L., Hayes, J.L., Menart, J.A., Shang, J.: Effect of Magnetic Fields on Surface Plasma Discharges at Mach 5. J. Spacecraft & Rockets 42(6), 1340–1346 (2006)
11. Hayes, W.D., Probstein, R.F.: Hypersonic Flow theory. Academic Press, London (1959)
12. Surzhikov, S.T., Shang, J.S.: Two-Component Plasma Model for Two-Dimensional Glow Discharge in Magnetic Field. J. Computational Physics 199, 437–464 (2004)
13. Sutton, G.W., Sherman, A.: Engineering Magnetohydrodynamics, p. 300. McGraw-Hill, New York (1965)
14. Brio, M., Wu, C.C.: An upwind Differencing Scheme for the Equations of Ideal Magnetohydrodynamics. J. Comp. Physics 75, 400–422 (1988)
15. Godunov, S.K.: Symmetric form of the equations of magnetohydrodynamics. Numerical Methods for Mechanics of Continuum Medium 1, 26 (1972)
16. Powell, K.G., Roe, P.L., Linde, T.J., Gombosi, T.I., De Zeeuw, D.L.: A Solution-Adaptive Upwind Scheme for Ideal MHD. J. Comp. Physics 154, 284–309 (1999)
17. Roe, P.L.: Approximate Riemann Solvers, Parameter Vectors and Difference Schemes. J. Comp. Phys. 43, 357–372 (1981)
18. Shang, J.S.: Solving Schemes for Computational Magneto-Fluid-Dynamics. Journal of Scientific Computing 25(1), 289–306 (2005)
19. Von Engel, A., Steenbeck, M.: Elektrische Gasenladungen, vol. II. Springer, Berlin (1932)
20. Boeuf, J.-P.: Numerical Model of RF Glow Discharges. Physical Review E 36(6), 2782–2792 (1987)
21. Gaitonde, D.V.: High-Order Solving Procedure for Three-Dimensional Nonideal Magneto-hydrodynamics. AIAA J. 39(11), 2111–2120 (2001)
22. Shang, J.S., Huang, P.G., Yan, H., Surzhikov, S.T.: Electrodynamics of Direct Current Discharge, AIAA 2008-1101, Reno NV (2008)

Part 3
Aeroacoustics 1

“*This page left intentionally blank.*”

Computation of Noise Radiated from a Turbulent Flow over a Cavity with Discontinuous Galerkin Method

Sungwoo Kang[1] and Jung Yul Yoo[1,2]

[1] Institute of Advanced Machinery and Design, Seoul National University, San 56-1, Sillim-dong, Kwanak-gu, Seoul 151-742, Korea
swkang1207@gmail.com
[2] School of Mechanical and Aerospace Engineering, Seoul National University, San 56-1, Sillim-dong, Kwanak-gu, Seoul 151-742, Korea
jyyoo@snu.ac.kr

1 Introduction

Noise generated from cavity flows has been the subject of many studies due to its frequent encounters in engineering applications. Cavity noises are affected by various parameters such as boundary layer thickness, length-to-depth ratio, Mach and Reynolds numbers, which can be categorized into two modes, i.e., shear-layer and wake modes [RCB02]. In shear-layer mode, noises are generated from oscillations of mixing layer which are sustained by acoustic feedback. On the other hand, they are generated from vortex shedding in wake mode. For shorter cavities and for low Mach numbers, shear-layer mode is likely to occur. When the Reynolds number increases or boundary-layer thickness is reduced, the chance of occurrence of wake mode increases. While possible frequencies can be predicted analytically, it is difficult to predict the dominant ones and their amplitudes by an analytical method due to various parameters.

Computational methods for aeroacoustics can be categorized into two groups, i.e., hybrid and direct methods. Hybrid methods [Lig52][Cur55] uncouple flow and acoustics, and solve flow by computational fluid dynamics and acoustics by analogies. On the other hand, direct methods [CLM97][IH02] [GBJ03] solve compressible Navier-Stokes equations for both flow and acoustics and are capable of solving resonance problems such as that in cavity flows. Since small acoustic fluctuations must be resolved, the method is computationally expensive.

In the present study, noises from cavity flows are predicted by directly solving unsteady compressible Navier-Stokes equations. To resolve small acoustic fluctuations that are weak compared to near-field fluctuations and propagate long distance without being dissipated, equations have to be solved with a high-order-accurate method. For this purpose, we adopt discontinuous Galerkin (DG) method that can apply high-order-accurate spatial

discretizations on unstructured meshes in complex geometries. In conjunction with this method, a finite element method is adopted, which allows discontinuities at inter-element boundaries. Thus, the present numerical method can easily incorporate different types of elements, change order of polynomial basis in an element without affecting adjacent ones and implement boundary conditions without loss of accuracy. The equations discretized by DG are integrated in time explicitly and k-ω model [Wil98] is adopted for representing the turbulence. Buffer zone [Fre97] is set up at boundaries to prevent wave reflections. Unsteady turbulent flows over a cavity are solved to show that the computed frequencies and amplitudes of noise are in good agreement with those measured experimentally.

2 Numerical Formulations

In DG discretization of the governing equations for unsteady compressible flow, each variable is double-valued at element interfaces. To treat such discontinuities, approximate Riemann solvers of finite volume methods are used for convection terms and various formulations [BR97][BO99] have been proposed for diffusion terms. Recently, these formulations have been applied to Reynolds-Averaged Navier-Stokes (RANS) equations for turbulence problems [BCRS05][NPP07]. In this study, we use mixed formulation that define derivatives as variables for diffusion terms [BCRS05] and Roe flux [Roe97] for convection terms. As a result, the compressible flow equations can be transformed into the following system of equations:

$$\begin{aligned} &\mathbf{Z} = \nabla Q, \\ &\frac{\partial Q}{\partial t} + \nabla \cdot \mathbf{F_c}(Q) + \nabla \cdot \mathbf{F_\nu}(Q, \mathbf{Z}) = S(Q, \mathbf{Z}). \end{aligned} \tag{1}$$

Final weak formulation of (1) is in surface and volume integral forms as follows:

$$\begin{aligned} &\int_{\Omega_e} \mathbf{g} \cdot (\mathbf{Z^\sigma} - \nabla Q) d\Omega = -\int_\sigma \frac{\mathbf{g^+} + \mathbf{g^-}}{2} \cdot (Q^+ \mathbf{n^+} + Q^- \mathbf{n^-}) d\sigma, \\ &\int_{\Omega_e} \mathbf{g} \cdot (\mathbf{Z} - \nabla Q) d\Omega = -\sum_{\sigma \in \partial\Omega_e} \int_\sigma \frac{\mathbf{g^+} + \mathbf{g^-}}{2} \cdot (Q^+ \mathbf{n^+} + Q^- \mathbf{n^-}) d\sigma, \\ &\int_{\Omega_e} \phi \frac{\partial Q}{\partial t} d\Omega - \int_{\Omega_e} \nabla\phi \cdot (\mathbf{F_c}(Q) + \mathbf{A_\nu Z}) d\Omega \\ &+ \int_{\partial\Omega_e} \phi \mathbf{n} \cdot (\widehat{\mathbf{F_c}}(Q) + \widehat{\mathbf{A_\nu Z^\sigma}}) d\sigma = \int_{\Omega_e} \phi S(Q, \mathbf{Z}) d\Omega, \end{aligned} \tag{2}$$

where superscript + and - stand for the two values of variables and hat for numerical flux at element interfaces. Functions g and ϕ are polynomial basis functions [SK95] so that high-order accuracy can be obtained by increasing order of these polynomial functions in an element.

3 Results and Discussions

To validate the accuracy of cavity noise predicted, we solve the flow over a cavity at a condition similar to previous experiment [CLG04]. Noise generated from the cavity of L/D = 1 is solved at Re = 3×10^6. Inflow and outflow boundaries are placed at 20L upstream and downstream of the cavity to reduce the effects of boundary conditions. Two computational domains with and without upper wall are used to compare the effects of reflection and are shown in Fig. 1. All detailed flow conditions are stated in Table 1.

Under the present conditions, no vortices are shed in the mixing layer as shown in Fig. 2(a) so that the noises are due to oscillation of the mixing layer. Fig. 2(b) shows the sound pressure level (SPL) at the downstream corner of the cavity for all cases. For case II which is similar to the experimental condition, the largest SPL is 128.4 dB at St = 1.81, close to the experimental result of 130 dB at St = 1.85.

To find the source of the noise, we performed discrete Fourier transform (DFT) at each dominant frequency. Amplitudes of DFT coefficients in cases I and II are compared in Fig. 3 to find the effect of wall on cavity noise. In Figs. 3(a) and 3(b), amplitudes are large at the bottom of the cavity for both cases as shear layer disturbances excite normal mode of cavity oscillations at St = 1.81. However, it is much larger for case II due to the reflection from the upper wall. In Figs. 3(c) and 3(d) at St = 5.42, amplitudes are large at the upstream and downstream walls of the cavity as shear layer disturbances excite longitudinal mode of cavity oscillations. Compared to the two figures

Table 1. Flow conditions of cavity flow

Case	Ma	δ/L	Wall
I	0.1	0.033	X
II	0.1	0.033	O
III	0.1	0.132	O
IV	0.2	0.033	X

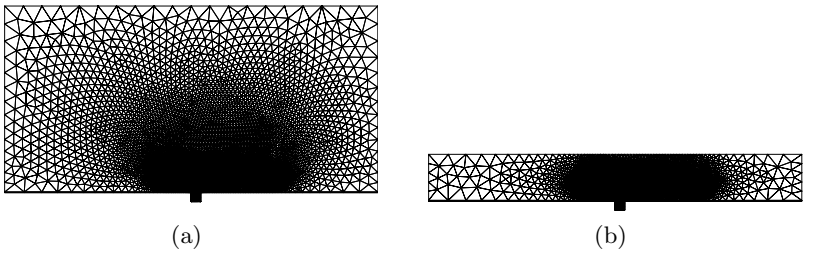

(a) (b)

Fig. 1. Computational domains for predicting the noise from the cavity flow: (**a**) without wall; (**b**) with wall

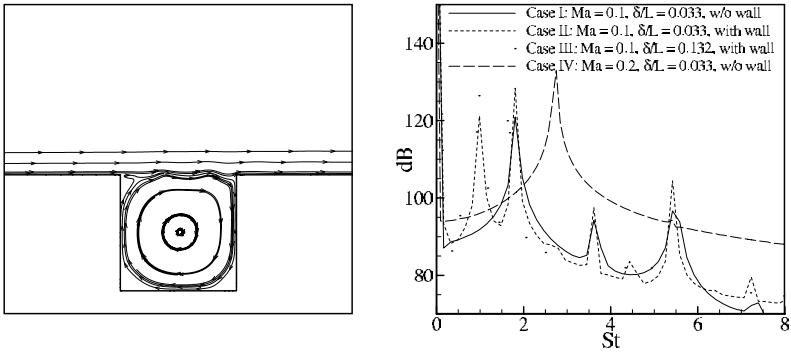

Fig. 2. (**a**) Streamlines and (**b**) SPL of the cavity flow

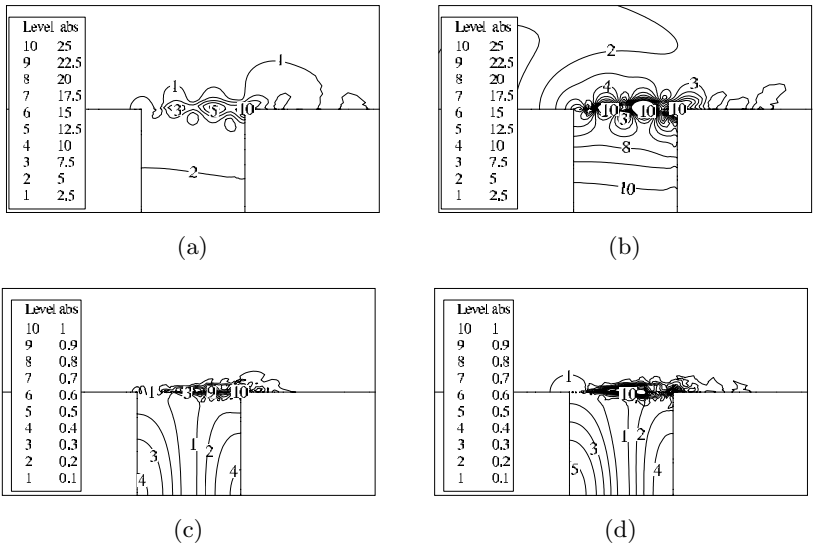

Fig. 3. Amplitudes of DFT: (**a**) St = 1.81 in case I; (**b**) St = 1.81 in case II; (**c**) St = 5.42 in case I; (**d**) St = 5.42 in case II

at St = 1.81, differences at St = 5.42 are small showing that the effect of the wall on the longitudinal mode of cavity oscillations is small in comparison to that on normal mode.

To find the effects of different parameters in cavity flows, imaginary parts of DFT coefficients corresponding to phase variation are compared in Fig. 4. When boundary layer thickness changes, noises can be generated at different frequencies. In case III, one of the dominant frequencies has changed from

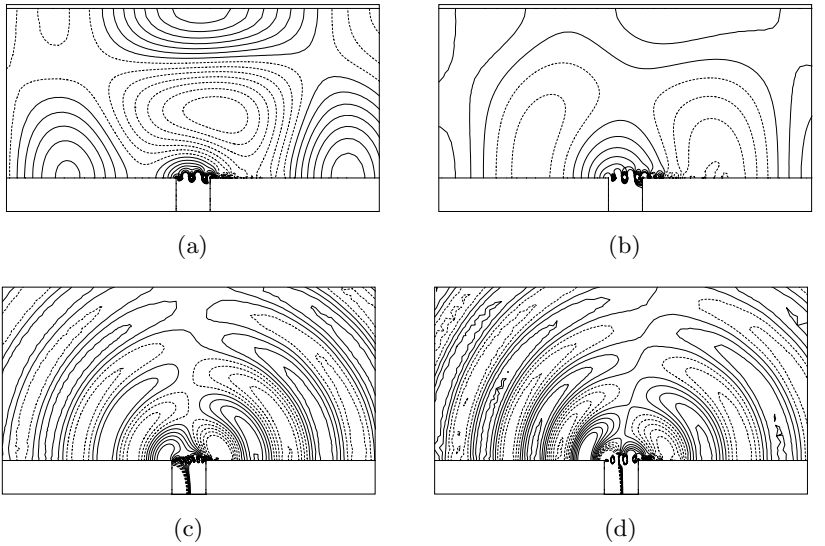

Fig. 4. Imaginary parts of DFT: (**a**) St = 1.81 in case II; (**b**) St = 1.64 in case III; (**c**) St = 5.42 in case I; (**d**) St = 2.66 in case IV

St = 1.81 to 1.64 due to thickened boundary layer. Imaginary parts of these two cases are shown in Figs. 4(a) and 4(b). At St = 1.64 in case III, the disturbances in mixing layer does not excite acoustic modes while normal modes are excited at St = 1.81 in case II. As normal modes are not excited in case III, reflections due to the wall are small and noise propagates in the upstream and downstream directions from the cavity.

Frequencies can be also changed when the Mach number is increased. As shown in Fig. 2(b), SPL in case IV are largely increased compared to that in case I, where the noises are generated at St = 2.66. Phase variations at St = 2.66 in case IV is similar to that at St = 5.42 in case I, which can be confirmed through Figs. 4(c) and 4(d). It seems that disturbances in the mixing layer excite the same longitudinal mode of cavity oscillations and both cases exhibit similar propagation patterns.

4 Conclusions

Discontinuous Galerkin method with mixed formulation is used to implement RANS equations. Noises are predicted directly by solving unsteady RANS equations so that the predicted results are in good agreement with previous experiments. The effects of upper wall, boundary layer thickness and the Mach number on noises have been compared. SPL with upper wall, thinner boundary layer thickness and higher Mach number are larger than that for other cases.

Acknowledgment

The authors would like to acknowledge the support from Korea Institute of Science and Technology Information under [The Strategic Supercomputing Support Program]. The use of the computing system of the Supercomputing Center is also greatly appreciated.

References

[BCRS05] Bassi, F., Crivellini, A., Rebay, S., Savini, M.: Discontinuous Galerkin solution of the Reynolds-averaged Navier-Stokes and k-ω turbulence model equations. Comput. Fluids 34, 507–540 (2005)

[BR97] Bassi, F., Rebay, S.: A high-order accurate discontinuous finite element method for the numerical solution of the compressible Navier-Stokes equations. J. Comput. Phys. 131, 267–279 (1997)

[BO99] Baumann, C.E., Oden, J.T.: A discontinuous hp finite element method for the Euler and Navier-Stokes equations. Int. J. Numer. Methods Fluids 31, 79–95 (1999)

[CLG04] Chatellier, L., Laumonier, J., Gervais, Y.: Theoretical and experimental investigations of low Mach number turbulent cavity flows. Exp. Fluids 36, 728–740 (2004)

[CLM97] Colonius, T., Lele, S.K., Moin, P.: Sound generation in a mixing layer. J. Fluid Mech. 330, 375–409 (1997)

[Cur55] Curle, N.: The influence of solid boundaries upon aerodynamic sound. Proc. R. Soc. Lond. A 231, 505–514 (1955)

[Fre97] Freund, J.B.: Proposed inflow/outflow boundary condition for direct computation of aerodynamic sound. AIAA J. 35, 740–742 (1997)

[GBJ03] Gloerfelt, X., Bailly, C., Juvé, D.: Direct computation of the noise radiated by a subsonic cavity flow and application of integral methods. J. Sound Vib. 266, 119–146 (2003)

[IH02] Inoue, O., Hatakeyama, N.: Sound generation by a two-dimensional circular cylinder in a uniform flow. J. Fluid Mech. 471, 285–314 (2002)

[Lig52] Lighthill, M.J.: On sound generated aerodynamically: I. General theory. Proc. R. Soc. Lond. A 211, 564–587 (1952)

[NPP07] Nguyen, N.C., Persson, P.-O., Peraire, J.: RANS solutions using high order discontinuous Galerkin methods. AIAA Paper 2007-0914 (2007)

[Roe97] Roe, P.L.: Approximate Riemann solvers, parameter vectors and difference schemes. J. Comput. Phys. 135, 250–258 (1997)

[RCB02] Rowley, C.W., Colonius, T., Basu, A.J.: On self-sustained oscillations in two-dimensional compressible flow over rectangular cavities. J. Fluid Mech. 455, 315–346 (2002)

[SK95] Sherwin, S.J., Karniadakis, G.E.: A new triangular and tetrahedral basis for high-order (hp) finite element methods. Int. J. Numer. Methods Eng. 38, 3775–3802 (1995)

[Wil98] Wilcox, D. C.: Turbulence Modeling for CFD. DCW Industries, Inc., La Cañada, USA (1998)

Far–Field Noise Minimization Using an Adjoint Approach

Markus P. Rumpfkeil and David W. Zingg

University of Toronto Institute for Aerospace Studies
4925 Dufferin Street, Toronto, Ontario, M3H 5T6, Canada
markus@oddjob.utias.utoronto.ca

1 Introduction

In this paper, shape optimization is applied to a blunt trailing edge airfoil in an unsteady turbulent flow environment to minimize the radiated far-field noise using a novel hybrid Unsteady Reynolds-Averaged Navier-Stokes/Ffowcs Williams and Hawkings (URANS/FW-H) optimization algorithm. Airframe-generated noise is an important component of the total noise radiated from commercial aircraft, especially during aircraft approach and landing, when engines operate at reduced thrust, and airframe components (such as high-lift devices) are in the deployed state [SLL03]. Future Federal Aviation Administration noise regulations, the projected growth in air travel, and the increase in population density near airports will require future civil aircraft to be substantially quieter than the current ones. Consequently, the attempt to understand and reduce airframe noise has become an important research topic [SG04].

A typical approach to tackle airframe-generated noise computations is to represent the CFD solution on a reasonable computational mesh that does not extend too far from the aircraft. A near-field plane or surface within the computational mesh can then serve as an interface between the CFD solution and a wave propagation program based on principles of geometrical acoustics and nonlinear wave propagation [SLL03]. The two-dimensional Ffowcs Williams and Hawkings (FW-H) equation in the frequency-domain [Loc00] is the wave propagation formulation of choice in this work.

This paper employs a general framework to derive a discrete adjoint method for the optimal control of unsteady flows [RZ07, RZ08] together with a Newton-Krylov approach to optimization [NZ02, NZ04]. We present several design problems using the novel hybrid URANS/FW-H optimization algorithm after validating the FW-H wave propagation code in the next section.

2 Noise Prediction Validation

A direct comparison between the pressure fluctuations calculated via the FW-H approach and those obtained from a CFD simulation is performed at three

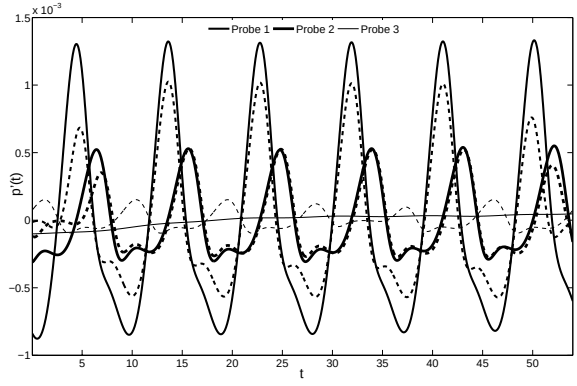

Fig. 1. Comparison of pressure fluctuations calculated by CFD (solid) and FW-H (dashed)

distinct locations with increasing distance from an airfoil. The laminar flow over the single-element NACA 0012 airfoil with a Reynolds number of 800, a free stream Mach number of 0.2 and an angle of attack of 20° is considered. At these conditions the airfoil experiences vortex shedding. A C-mesh with 848×395 nodes and a non-dimensional time step $\Delta t = 0.03$ is used. After the flow solver has reached a periodic steady state, 1800 time steps are taken, which cover about five vortex shedding cycles, and the solution is recorded.

The extracted CFD pressure fluctuations and those computed using the FW-H solver are plotted in Figure 1 for the three probe locations. In two dimensions one expects that the sound intensity, which itself is proportional to the square of the sound pressure, is inversely proportional to the distance of an acoustic point source. This distance law is almost perfectly fulfilled by the pressure fluctuations which are calculated with the FW-H approach.

Comparing the pressure fluctuations probe location by probe location one can make the following observations: At probe location 2, which is about $2c$ below the airfoil, the two pressure records are almost identical, except for the beginning and end of the data, where the necessary window function [Loc00] tarnishes the result from the FW-H approach. The agreement in the first probe location (less than $1c$ below) is also fairly good, except for the overprediction of the amplitude by the CFD calculation. The CFD results at probe location 3 ($30c$ below) are basically useless due to the coarser grid this far away.

3 Results

A NACA 0012 airfoil with a $0.03c$ thick blunt trailing edge in a turbulent flow is investigated. The free-stream flow conditions are given by $M_\infty = 0.2$, $Re = 2 \times 10^6$, $\alpha = 0°$, and the mesh consists of about $36,000$ nodes. As displayed in Figure 2, the comparison of pressure fluctuations calculated by CFD

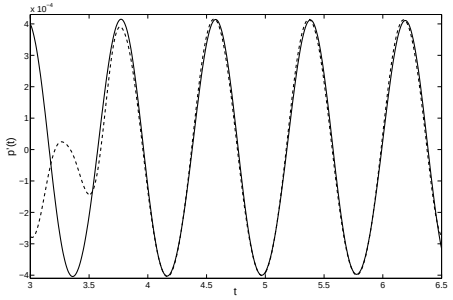

Fig. 2. Comparison of pressure fluctuations calculated by CFD (solid) and FW-H (dashed) about $\frac{1}{3}c$ below the trailing edge of initial airfoil

and FW-H for the initial airfoil show good agreement at a location about $\frac{1}{3}c$ below the trailing edge of the initial airfoil.

First, a remote inverse shape design problem is studied with a discrete cost function J given by

$$J = \frac{1}{2}\Delta t \sum_{timesteps} (p_{obs}^n - p_{obs}^{*n})^2. \tag{1}$$

Here, p_{obs}^n is the pressure at some far-field observer location at time step n obtained from a current airfoil shape, and p_{obs}^{*n} is the target pressure at the same location and time step obtained from the target airfoil shape, which is given through a perturbation in two shape design variables of the initial blunt NACA 0012 airfoil. Both airfoils are shown in Figure 3 and the far-field observer location is $40c$ below the trailing edge.

In order to reduce the computational costs in the actual optimization runs a bigger non-dimensionalized time step of $\Delta t_c = 0.01$ is utilized for the first $N_c = 300$ steps for the adjustment period after a shape modification has taken place, which can be seen in Figure 8. Once the interval where the pressures are compared is reached, a smaller time step $\Delta t = 0.005$ is used for another 700 steps, leading to $N = 1000$ time steps in total for each flow solve covering a time interval of $[0, 6.5]$. The corresponding adjoint equations for this situation are given in Rumpfkeil and Zingg [RZ07, RZ08].

The convergence history of this remote inverse shape design problem with the adjoint approach in comparison to a second-order central finite-difference

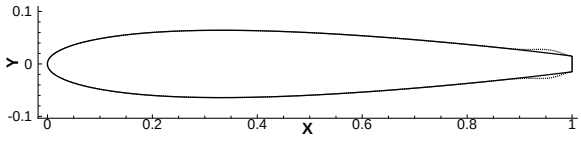

Fig. 3. The initial (solid) and target (dotted) airfoil shapes

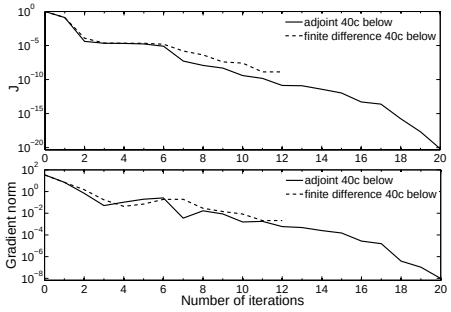

Fig. 4. Convergence history of remote inverse shape design problem

approach with a step size of $h = 10^{-5}$ is shown in Figure 4. The objective function J is always scaled such that its initial value is unity. One can see that the objective functions are driven to small values in about ten design iterations and that the two approaches show a reasonable agreement, which means that the adjoint approach for the gradient calculation is accurate. For example, at the first design iteration the finite difference method (fd) and adjoint method (ad) yield

$$\left(\frac{\partial J}{\partial Y}\right)_{fd} = (-33.53,\, 34.18), \qquad \left(\frac{\partial J}{\partial Y}\right)_{ad} = (-34.36,\, 35.11).$$

The computational time of a gradient computation is about two to three times the time of a flow solve, since the non-linear flow solve problem has a much better initial guess leading to less linear iterations per time step than the linear adjoint problem.

Next, two more practically relevant optimizations are considered with the same flow conditions but two different objective functions:

1. Mean drag $$J_D = \bar{C}_D = \frac{1}{\#\text{ time steps}} \sum_{timesteps} C_D^n \qquad (2)$$

2. Pressure fluctuations $$J_N = \sum_{timesteps} (p_{obs}^n - \bar{p}_{obs})^2 = \sum_{timesteps} (p_{obs}^{'n})^2 \qquad (3)$$

where $\bar{p}_{obs}$ is the mean pressure in the observer location, which is located $40c$ below the trailing edge, $p_{obs}^{'n} = p_{obs}^n - \bar{p}_{obs}$ is the pressure fluctuation in the observer location, and C_D^n is the drag coefficient both at time step n.

Eight B-spline control points are used as shape design variables which are all located in the aft 15 percent of the chord length (four on the upper and four on the lower surface). The unsteady shape optimizations are started from three different initial shapes, which are shown in Figure 5 together with their initial objective function values:

1. The initial airfoil (solid)
2. The airfoil that results from setting all eight design variables to their specified upper bound (dashed)
3. The airfoil that results from setting all eight design variables to their specified lower bound (dotted)

The time horizon and time step sizes are the same as used in the remote inverse shape design presented earlier in this section. Figure 6 presents the final optimized airfoil shapes together with their objective function values. All three initial shapes converge for each objective function to the same respective final shapes shown in dotted and dashed lines for the mean drag and noise minimizations, respectively. As indicated in the figure, the mean drag value of the noise minimized airfoil is slightly higher than the mean drag value of the mean drag minimized airfoil. Conversely, the pressure fluctuations of the mean drag minimized airfoil are a factor of two higher than the ones from the noise minimized airfoil. This shows that noise and drag improvements lead to qualitatively similar results to a first approximation, but they definitely do not yield the same optimized shapes.

The convergence histories of the mean drag minimizations are displayed in Figure 7 (left). The objective function values are always scaled with the mean drag value of the original airfoil $J_D = 2.14 \cdot 10^{-2}$ to make comparisons easier. Since all three initial shapes converge to the same final shape they have the same minimized objective function value which translates into a reduction in mean drag of about 39 percent from the original airfoil. The

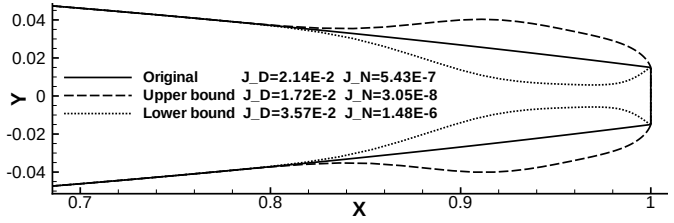

Fig. 5. Initial shapes for the turbulent blunt trailing edge flow optimizations

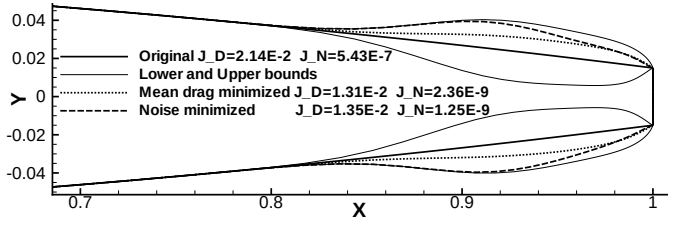

Fig. 6. Final improved airfoil shapes of the turbulent blunt trailing edge flow optimizations

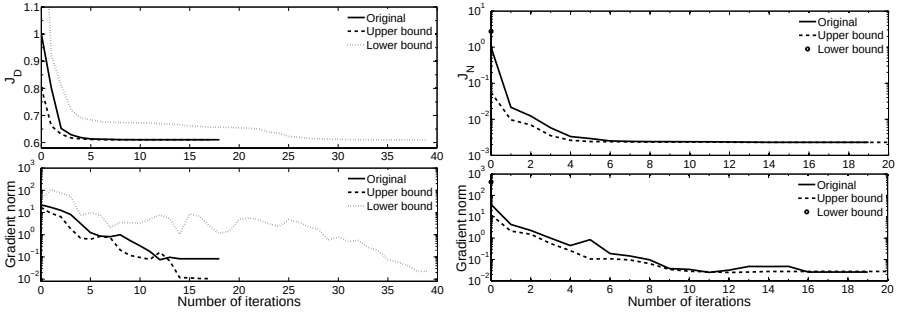

Fig. 7. Convergence histories of the mean drag (left) and noise minimizations (right)

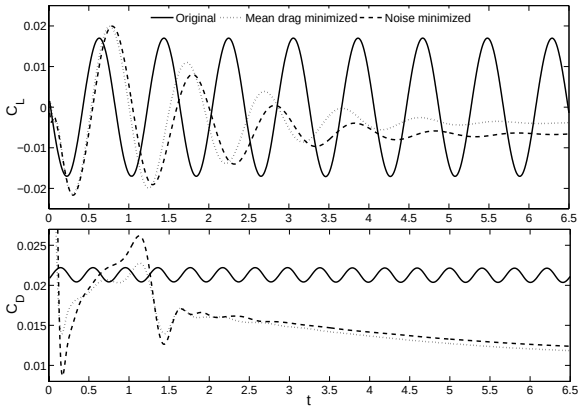

Fig. 8. Time histories of C_L and C_D before and after the optimizations vs. time ($\Delta t = 0.005$)

gradient norms are reduced by three to four orders of magnitude indicating that the optimizer has converged to a minimum in each case.

The convergence histories of the noise minimizations (Figure 7 right) show that the sum of the squared pressure fluctuations for the optimized shape is reduced to 0.23 percent of the original airfoil's value $J_N = 5.43 \cdot 10^{-7}$, which is again used to scale all the objective function values to ease comparisons. Starting from the lower bound leads to a failed line search in the first iteration because all gradients indicate that it would be beneficial to "slim" the airfoil even more which is not allowed by the box constraints imposed on the design variables to avoid grid movement and flow convergence problems. The gradient norms are reduced by two to three orders of magnitude.

The time histories of C_L and C_D for the original blunt trailing edge airfoil before and after the optimizations are shown in Figure 8. One can clearly see the adjustment period for the improved airfoils in the time interval $[0, 3]$

before they reach their new somewhat periodic steady state. A reduced mean drag for both optimized airfoils is also visible, and both objective functions lead to reduced oscillation amplitudes in both lift and drag.

4 Conclusions

The results presented in this paper show that the novel hybrid URANS/FW-H optimization algorithm, which uses a Newton-Krylov approach in combination with a discrete adjoint method, is effective and efficient for practical applications. We proved that it is possible to recover far-field pressure fluctuations via remote inverse shape designs in unsteady turbulent flows, and we were able to minimize the pressure fluctuations at a given far-field observer position in an efficient manner. Our future work will focus on the ability to modify a high-lift airfoil configuration to reduce the radiated noise while maintaining good aerodynamic performance.

References

[Loc00] Lockard, D.P.: An Efficient, Two-Dimensional Implementation of the FW-H Equation. J. of Sound and Vibration 229(4), 897–911 (2000)

[NZ02] Nemec, M., Zingg, D.W.: Newton-Krylov Algorithm for Aerodynamic Design Using the Navier-Stokes Equations. AIAA J. 40(6), 1146–1154 (2002)

[NZ04] Nemec, M., Zingg, D.W.: Multipoint and Multi-Objective Aerodynamic Shape Optimization. AIAA J. 42(6), 1057–1065 (2004)

[RZ07] Rumpfkeil, M.P., Zingg, D.W.: A General Framework for the Optimal Control of Unsteady Flows with Applications. AIAA paper, 2007-1128

[RZ08] Rumpfkeil, M.P., Zingg, D.W.: The Optimal Control of Unsteady Flows with a Discrete Adjoint Method. Optimization and Engineering (2008) doi:10.1007/s11081-008-9035-5

[SG04] Singer, B.A., Guo, Y.: Development of Comp. Aeroacoustics Tools for Airframe Noise Calculations. Int. J. of CFD 18(6), 455–469 (2004)

[SLL03] Singer, B.A., Lockard, D.P., Lilley, G.M.: Hybrid Acoustic Predictions. Comp. and Math. with Applications 46, 647–669 (2003)

“*This page left intentionally blank.*”

Stabilized High-Order Discontinuous Galerkin Methods for Aeroacoustic Investigations

Andreas Richter, Jörg Stiller, and Roger Grundmann

Technische Universität Dresden, Institute for Aerospace Engineering,
01062 Dresden, Germany
andreas.richter4@tu-dresden.de

1 Introduction

Solving the compressible, unsteady Navier-Stokes equations is a powerful method to investigate the acoustic phenomena in technical systems with superimposed meanflow. This includes pipes, bends, but also musical woodwind instruments. Often the acoustics of these systems is treated as an linear-acoustic problem and investigated by solving the Helmholtz equation. This approach neglects interactions between mean flow and acoustic wave, flow phenomena and also nonlinear phenomena like wave steepening. The pressure related to the flow field and the acoustic pressure perturbations that are radiated can vary about four or five order of magnitude. Resolving these effects requires the solution as accurate as possible to avoid numerical dissipation and dispersion errors. We use an explicit, high-order discontinuous Galerkin formulation to minimize these errors.

Nonlinear effects like wave steepening can lead to large gradients in the solution. Among a compact and flexible formulation discontinuous Galerkin methods provide a stable method to resolve these phenomena.

2 Stabilization

Near discontinuities spurious oscillations can occur. To avoid instabilities we use a slope limiting scheme. Following the declaration in Figure 1 the limiter for a scalar value works as follow:

1. Transform the solution coefficients on element Ω_e to the Legendre coefficients $\hat{U}_{ij,e}(t)$.
2. Compute the vector $\mathbf{n}_{ij}$ which defines the plane through the points $\mathbf{x}_{e+i}, \mathbf{x}_{e+j}$ and $\mathbf{x}_e$ (see Figure 1) with

$$\mathbf{n}_{ij} = \frac{(\mathbf{x}_{e+i} - \mathbf{x}_e) \times (\mathbf{x}_{e+j} - \mathbf{x}_e)}{|(\mathbf{x}_{e+i} - \mathbf{x}_e) \times (\mathbf{x}_{e+j} - \mathbf{x}_e)|} \tag{1}$$

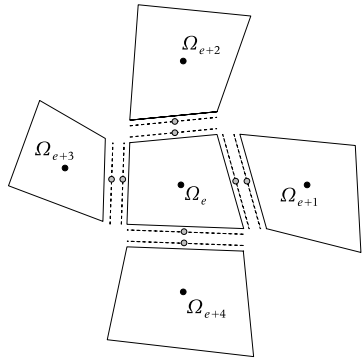

Fig. 1. Slope limiter

The point $\mathbf{x}_{e+i}^T$ bases on the element averages $\bar{x}_{e+i}$, $\bar{y}_{e+i}$ and $\bar{U}_{e+i}$

$$\mathbf{x}_{e+i} = (\bar{x}_{e+i}, \bar{y}_{e+i}, \bar{U}_{e+i}(t));\ \mathbf{x}_e^T = (\bar{x}_e, \bar{y}_e, \bar{U}_e(t)). \tag{2}$$

3. Estimate with
$$(\mathbf{x} - \mathbf{x}_e) \cdot \mathbf{n}_{ij} = 0 \tag{3}$$
the gradients $(\partial_x U_e(t))_k$ and $(\partial_y U_e(t))_k$ with $k = 1 \ldots 4$.
4. Limit the linear gradients $\partial_x U_e(t)$ and $\partial_y U_e(t)$ on Ω_e using the *minmod* function 5 with
$$\begin{aligned} \Pi \partial_x U_e(t) &= \text{minmod}\left(\partial_x U_e(t)\right)_k \\ \Pi \partial_y U_e(t) &= \text{minmod}\left(\partial_y U_e(t)\right)_k . \end{aligned} \tag{4}$$
$$\text{minmod}(a,b) = \begin{cases} \text{sign}(a)\min(|a|,|b|) & \text{if sign}(a) = \text{sign}(b) \\ 0 & \text{else} \end{cases} \tag{5}$$
5. Set all Legendre coefficients except $\hat{U}_{00,e}(t)$, $\hat{U}_{10,e}(t)$ and $\hat{U}_{01,e}(t)$ to zero and adjust the conservation properties.
6. Transform the limited Legendre coefficients $\tilde{U}_{ij,e}(t)$ back to the solution coefficients.

The limiter is applied separately to every characteristic variable. While this limiting procedure reduces the accuracy locally to a first order scheme we implemented a discontinuity detection criterion introduced by Krivodonova et al. [1]. The Figure 2 demonstrates the efficiency of the scheme. The left figure shows a Kelvin-Helmholtz instability at $t = 1$ on the domain $(-1, 1)^2$ with the grid $\Delta x = \Delta y = 1/512$. In the right figure the limiting criterion is illustrated. Only 11.66 % of the elements are marked for limiting. So the limiter works only where it is necessary and conserves the accuracy in the rest of the domain [3].

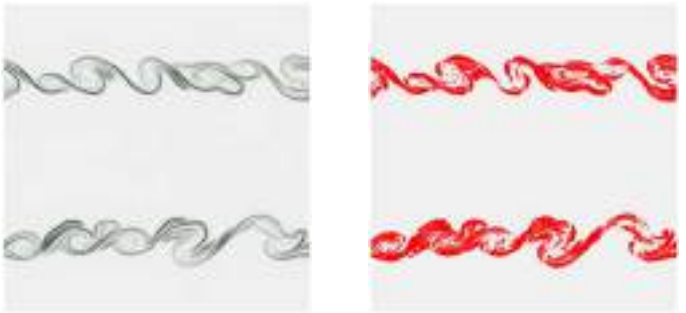

(a) density gradient (b) limiting criterion

Fig. 2. Kelvin-Helmholtz instability: (a) density gradient $\|\nabla\rho\|$; (b) limited elements

3 Stabilized Extrapolation Boundary Conditions

The investigation of open structures needs the implementation of stable and non-reflecting open boundaries. Typically one-dimensional characteristic boundary conditions or buffer zone techniques like perfectly matched layers (PML) are used. While the characteristic treatment produces large artificial reflections, mainly if the wave front leaves the domain with an oblique angle, PML are not available for nonlinear systems with viscous effects. As an alternative we use a local extrapolation at open boundaries in conjunction with the slope limiter described above to avoid instabilities. Figure 3 shows the reflection error as a function of the angle ϕ between the wave normal vector and the boundary normal. Characteristic boundary conditions are compared to the extrapolation boundaries. While for $\phi < 20°$ no significant differences occur, the error evoked by the characteristic treatment increases rapidly, compared to the extrapolation condition.

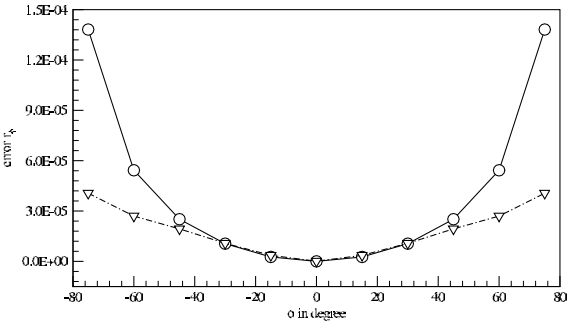

Fig. 3. Reflection error r_ϕ. Circle: characteristic boundary condition, gradient: extrapolation boundary condition

In the Navier Stokes case the same procedure doesn't activate instabilities but leads to a continuous solution growth at open boundaries. To prevent this we use first a weak characteristic treatment which is not stable generally and in the next step also the limiting procedure. This treatment reduces the absorbability only slightly but provides an overall stable boundary treatment.

4 Numerical Tests

4.1 Flow Around a Cylinder at Re=100

To test the numerical behavior of the stabilized extrapolation conditions we solve the flow around an infinite cylinder at $\mathrm{Re} = 100$. Here the typical von Karmann vortex street occurs and leave the domain at the open boundary on the right side (see Fig. 4). While the limited slopes are observable in Fig. 4 (a) and (b) no spurious reflections occurs. It is also remarkable that compared to other boundary schemes no additional effects while long time integration occurs (tested up to $1 \cdot 10^7$ time steps using an explicit Runge-Kutta time integration scheme).

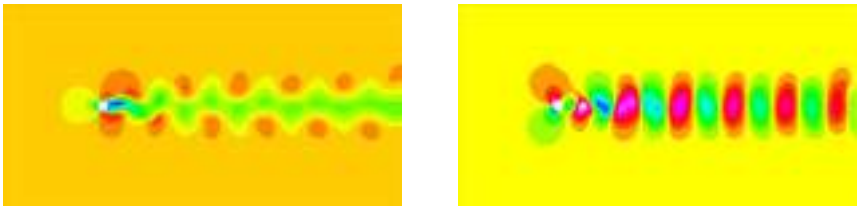

(a) x velocity (b) y velocity

Fig. 4. Flow around a cylinder at $\mathrm{Re} = 100$, time $\mathrm{t} = 200$

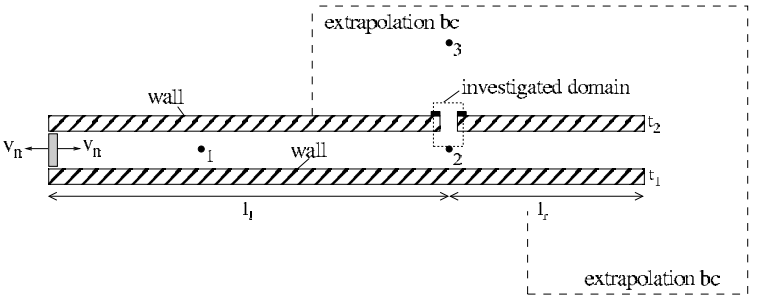

Fig. 5. Configuration tone hole investigation

4.2 Tone Hole Investigations

Based on the numerical scheme we investigated the viscothermal effects at an open tone hole of a flute-like structure. Simultaneous PIV measurements are performed at the University of Edinburgh, School of Physics (see [2]). The configuration is shown in Figure 5. In the experiments a loudspeaker excites the system at the first eigenfrequency. In the numerical experiments the loudspeaker is replaced by a moving, plane wall which oscillates also at the first eigenfrequency. The outer domain is truncated using the stabilized

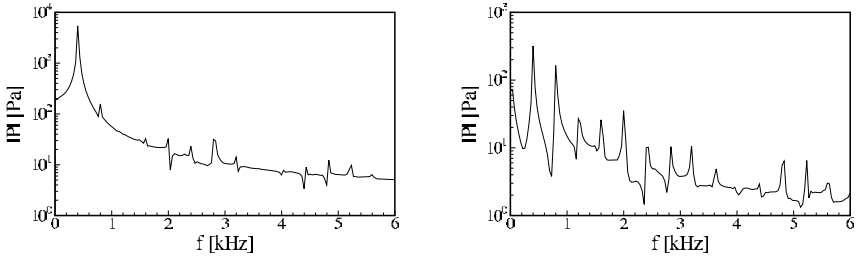

(a) point 1 (b) point 3

Fig. 6. Pressure fluctuations in frequency domain at point 1 and 3

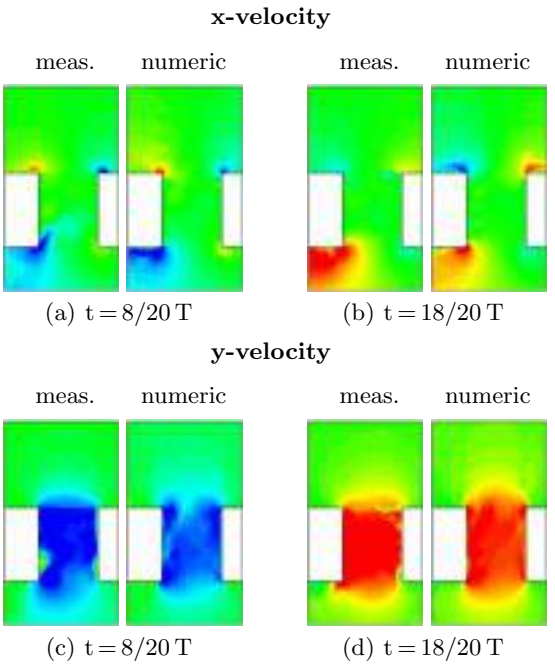

(a) t = 8/20 T (b) t = 18/20 T

(c) t = 8/20 T (d) t = 18/20 T

Fig. 7. Contours of: (a-b) x-velocity $v_x = -5 \ldots 5\ \frac{m}{s}$; (c-d) y-velocity $v_y = -5 \ldots 5\ \frac{m}{s}$

extrapolation boundary conditions described above. The pressure fluctuations at different measurement points are transformed into the frequency domain and shown in Figure 6. Inside the system the fist eigenfrequency at 400 Hz dominates while outside the instrument also the overtones becomes important. Every peak in Figure 6 (b) correlates with an overtone. Additional frequencies which could base on spurious boundary effects are not detectable, the boundary conditions are appropriate for aeroacoustic investigations.

Figure 7 compares the PIV measurements with the achieved numerical results at different time steps. Here a good agreement between the experiments and numerical results can be found.

5 Conclusion

We presented a numerical method to solve the unsteady, compressible Navier-Stokes equations based on high-order discontinuous Galerkin methods. Artificial open boundaries are provided by a stabilized extrapolation condition. The practicability of these method for aeroacoustic investigations is demonstrated while simulating the flow behavior at open, flute-like structures and validated using additional PIV measurements.

Acknowledgment

This work was supported by the German National Science Foundation (Deutsche Forschungsgemeinschaft, DFG) within the project "CFD investigation in fluid dynamic and acoustic phenomena inside the bassoon. We also thank Prof. D. M. Campbell and his team at the University of Edinburgh for supplying the experimental results.

References

1. Krivodonova, L., Xin, J., Remacle, J.-F., Chevaugeon, N., Flaherty, J.E.: Shock detection and limiting with discontinuous Galerkin methods for hyperbolic conservation laws. Appl. Num. Math. 48, 323–338 (2004)
2. MacDonald, R., Campbell, M.: The in uence of mean ow on local non-linear effects at woodwind instrument toneholes. In: ISMA 2007 Barcelona, International Symposium on Musical Acoustics (2007)
3. Richter, A., Stiller, J., Grundmann, R.: Stabilized discontinuous Galerkin methods for ow-sound interaction. Journal of Computational Acoustics 15(1), 123–143 (2007)

Part 4
Aeroacoustics 2

“*This page left intentionally blank.*”

Direct Simulation for Acoustic Near Fields Using the Compressible Navier-Stokes Equation

Yasuo Obikane[1] and Kunio Kuwahara[2]

[1] Institute of Computational Fluid Dynamics 1-16-5 Haramachi, Meguroku-ku, Tokyo 152-0011, Japan
obikane@icfd.co.jp
[2] Institute of Computational Fluid Dynamics 1-16-5 Haramachi, Meguroku-ku, Tokyo 152-0011, Japan
kunio-kuwahara@icfd.co.jp

Abstract. This paper presents direct simulations of acoustic near field around a subsonic resonator by using the compressible Navier-Stokes equation. The direct simulation depends on the size of the resonator and the capability of the PC. In the present paper, we select a recorder, a musical instrument. Though we use regular meshes, the computational region is large enough for prediction of both the flow field and the near field of the recorder. In addition, to ensure the energy transfer among the waves we used the higher order finite difference equation called Multi-Directional-TVD method proposed in 2004 (M.Lee et al.[Ref1]). Our computations were successful in producing acoustic noises.

Keywords: Direct Simulation, Acoustic near field, Compressible Navier Stokes.

1 Introduction

The objectives in the present paper are to find a possibility to simulate the acoustic resonance by instability of flows. We select a recorder, a flute-like musical instrument. The present topics are following.

1.1 Prediction of Acoustic Resonance Phenomena

In Aero-acoustics, most topics of resonance contain several fluid mechanics topics such as instability of flows, formation of large vortex, generation of sounds by interaction of vortex and elastic characteristics of air. The waves seems to be so complex since it contains many time scales, spatial scales, and velocity scales which are related to each other with non-linearity. However, if the resonance occurs, then the full fluid system moves with the same mode by absorbing energy from the source. All large structures such as vortices

are created in the same mode. It is easy to clarify the resonance oscillation. Thus, it is quite promising to develop a design code to realize the resonance for the benchmark test.

1.2 "The Theory of The Fluteh by M.S.Howe

To find the clues it is important to review the theoretical approach of the flute. The reformation on the aero-acoustics and the theory of the flute were done by M.S. Howe (1975)([Ref2]). By assuming the existence of elliptical vortex or oscillation of vertical speed blowing into the mouth of a flute, he obtained a threshold Mach number for generating sound, and predicted the sound power of a flute by using only the opening size (b, d) and the length of flue body(L), and mean speed of the flow(equation(10.53) [Ref2]). The result implies that the generation of sound is not dependant on the geometrical fine structure of the flute. @It does not depend on the thickness and angle nor the angle of attack to the reed which are mostly related to aerodynamic instabilities at the opening. Namely, the results does not depend on the detail mechanism of the instabilities of the shear layer which is the most difficult to be simulated by computers. He concluded the acoustic coupling was the most important.

1.3 Computational Problems for the Compressible Navier Stokes equation(C.N.S.E)

The set of the compressible Navier Stokes equation is well described in many aero-acoustics papers [Ref3]. Here, we just mention the name of equations; the continuity of equation with time derivative of density, and the two dimensional compressible Navier Stokes equation in a flux form, and enthalpy, and the ideal gas equation. Many important works about the boundary conditions for Direct Simulation has been done by K W.Thompson([Ref6]), J.D.Baum([Ref7]), S.K.W. Tam([Ref4]), and T.Pointsot and S.K.Lele ([Ref5]). The method has been well established. However, there are still problems for software designers which boundary conditions and which scheme should be selected for given acoustic problems.

1.4 Numerical Method

The present scheme has the third order non-linear terms, and the fourth order of the Laplace operator which can pack the vortex and sustain the shape of the vortices than the other schemes shown by Lee et all 2004([Ref1]). These Properties seems to be the most important to aeroacoustics because vortices produce sounds. Otherwise, vortices can be easy to penetrate itself to the potential regions, and fade fast. In addition, on the outside of vortex region and no-mean flow acoustics region, the non-linear terms will diminish so the high accuracy of the linear viscous terms will become more important.

1.5 Transition to Turbulence

Designers know that both position and shape of the reed and the shape of outlet are important. These shapes are related to the transition from laminar to turbulence. For example, the most recorders have a trim on the edge of the one side to produce an asymmetry flow where the instability easily causes. The recorder is usually played at the speed from 2 to 20 m/sec, then the Reynolds number of the recorder in the channel of d=2mm becomes 200 to 2000. The Reynolds number is in a typical transition region. Because the transition is a three dimensional phenomena, we are interested in "What can the two dimensional CNSE code do?"([Ref8],[Ref10])

2 Bench Mark Computation

2.1 Bench Mark 1 :Edge-Tone

The first bench mark computation is the edge tone problem which is related to the flute and other reed instruments. We took a simple model as shown in Fig. 1. Because of the regular mesh, we take as many meshes as possible which can model the reed shape. The mesh size is 0.05mm, only 8 points are set in the vertical direction in the channel. The distance from outlet to the reed is 3mm, and the thickness of reed is 1.5mm, the angle of reed (wedge) is 20degrees. The velocity of jet is about 14m/sec. From the Brownfs formula of mode (m), we obtain the frequency of the third mode of 0.466x(m)x(U-0.4)x(1/L-7) = 7285(Hz). The frequencies of the computed wave shown in Fig. 3 are about 7300Hz and 14600Hz which are close to the Brown's results. The present edge-tone has a softer tone than one with a monotone tone. The variance of the pressure (P(t,x,y) - meanP(x,y)) is shown in the Fig. 2. In the both sides we observed the arcs which would generate the sound as monopole since one pack of flow in one direction on each arc was running towards the wall. In the other computation, we also obtained the similar arcs in the same area where the mechanism is needed to be clarified.

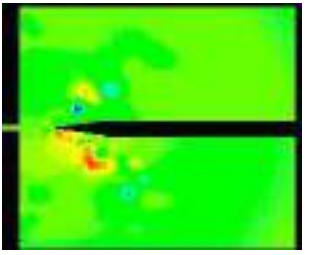

Fig. 1. Egde-Tone Pressure

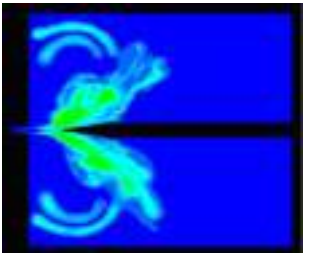

Fig. 2. Egde-Tone Variance

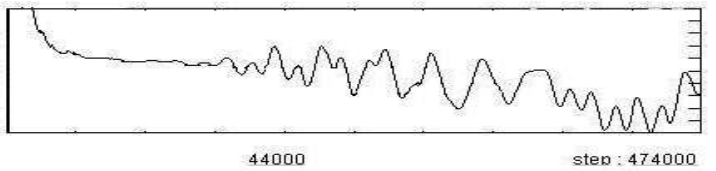

Fig. 3. Pressure variation with time

2.2 Bench Mark 2 :Recorder

The second bench mark test is a sound generated by a recorder, a flute-like instrument like a flute, used mostly by elementary school students. For the simplicity, we compute the flow near the head part of the recorder which includes only a blowing channel and a reed and a short resonance cylinder. The model is one third of the real recorder, and does not include the resonance cylinder part with holes to change the frequency.

Case1. Computational results (with-hand) To make some differences to the other recorder, the outlet of the cylinder was closed by a hand as shown in Fig.4. The vertical wall represents a hand. By the hand, the recorder becomes a closed resonator. The mesh size is 0.25mm, 300x110 grid points. Input speed is about 3m/sec. In the figure, there is a small trim on the corner of the left channel to make the blowing unstable. For case 1, computational results are shown in Figs. 4, 5, 6, 7. The picture in fig. 4 shows a Mach number distribution where the vortex can be seen above the reed. The unstable sinusoidal shear layer discharged from the channel is also observed in Fig. 4. The train of vortexes, which produces sounds, can be seen. We can observe in Figs. 5, 6 the clear difference of frequency distribution between inside of the flute and outside of the flute. In the inside of the cylinder, the frequency band is broader than the outside. In the outside, we observed two major frequencies about 400Hz to 500Hz. The intensities gradually decrease as frequency increases. In the final stage of the computation we observed the cyclic rotational motion of the center of vortex at 12mm from the reed and 10mm above the top of the recorder. The center draws a cyclic circle with the radius about 1mm. The result supports the assumption of Howe's elliptic vortex theory.

Case2. Computational results (no-hand) In the case of the open end (no hand) of the cylinder, the sound is computed. The results are shown in Figs. 8, 9, 10, 11, 12. In Fig.10 two peaks about 400Hz and bi-harmonics frequency 800Hz are observed at a point outside of the cylinder. The sound inside of the cylinder is lower and has a broader band than the outside. This tendency is similar to characteristics of case 1. But, a harmonic frequency is

Fig. 4. Recorder-With-Hand(Mach number)

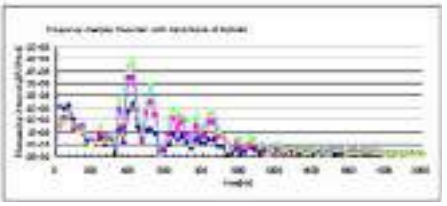

Fig. 5. Recorder-With Hand

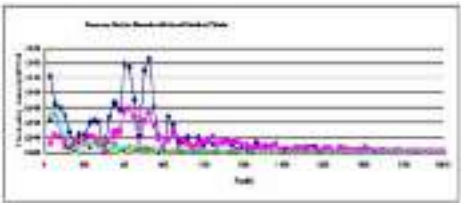

Fig. 6. Recorder-With-Hand

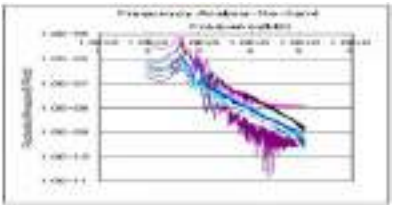

Fig. 7. Recorder-Fluctuating Pressure Spectrum No-Hand

observed in the open case. The spatial distributions of the variance of the pressure are shown in Figs.12,13. Two intense regions are observed above the reed which seems to be a dipole source at the low speed sound generators which is consistent with the traditional acoustics theory by M.J. Lighthill [Ref2].

Case3. Computational results(stable case) By Howefs gthe theory of the fluteh, the flow at very low Mach number(U =0.2 m/sec) could not generate any sound. In the case3 we did not come out any sound because of the stability of jet. We had a steady solution, and no vortex shows up in the domain. However, It is hard to evaluate whether the Howefs potential theory

$$M > 5/7n^2\pi^4(sd/L^2)$$

(eq.10.53. [Ref2]), agree with the present result quantitatively. It seems be the instability problem in the shear layer of which critical velocity depends on the Reynolds number.

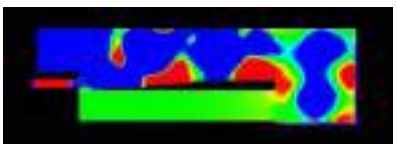

Fig. 8. Recorder-No-Hand

Fig. 9. Recorder-No-Hand

Fig. 10. Recorder-No-Hand

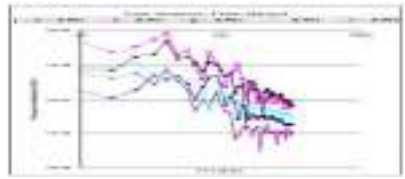

Fig. 11. Recorder-No-Hand

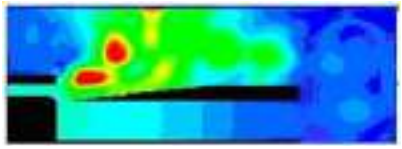

Fig. 12. Recorder-No-Hand

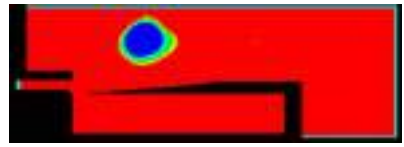

Fig. 13. Recorder-With-Hand

3 Conclusion

1. The regular mesh system can be applied to simulate the resonator with out fine structures of geometry such as a reed instruments at a very low speed.
2. As Howefs theory, once the vortex are generated, the mechanism of the flute sound generation would be governed by vortex interaction even the solver is the Navier Stokes equation. The oscillation of the vortex center seems to support Howe's elliptic theory.
3. With two dimensinal C.N.S.E Keys of instability could be clarified for recorder.
4. However, the modes of edge-tone could not be clarified in the present case, and the further computation should be performed.

References

[Ref1] Lee, M., Kawamura, T., Kuwahara, K., Ooida, J.: Simulation of Unsteady Flows at High Angle of Attack. In: AIAA-2004-2136, 34th AIAA Fluid Dynamics Conference and Exhibit, Portland, Oregon, June 28-1 (2004)

[Ref2] Howe, M.S.: Contributions to the theory of aerodynamics sound, with application to excess jet noise and the theory of the flute. J. Fluid Mech. 71(4), 625–673 (1975)

[Ref3] Schroder, W., Ewert, R., Bui, T.P., Groshel, E.: An LES-APE Approach in Computational Aero-acoustics: Theory and Application, VKI Lecture Series 2006-7 Computational Aeroacoustics (2006)

[Ref4] Tam, C.K.W.: Computational Aeroacoustics: Issues and Methods AIAA Journal 33(10) (October 1995)

[Ref5] Pointsot, T., Lele, S.K.: Boundary conditions for direct simulation of compressible viscous flows. J. Compu. Phys. 101, 104–129 (1992)

[Ref6] Thompson, K.W.: Time Dependent Boundary Condition for hyperbolic Systems. Journal of Comptational Physics 68, 1–24 (1987)

[Ref7] Baum, J.D.: Numerical Investigation of Acoustic Refrection Phenomenon. In: de Vahl Davis, G., Fletcher, C. (eds.) Computational Fluid Dynamics, pp. 249–265 (1988)

[Ref8] Chasnov, J.R.: Decaying Turbulence in Two and Three Dimensions. In: Proceedings of the first AFSOR International Conference on DNS/LES, pp. 57–68 (1997)

[Ref9] Muranaka, H., Nonomura, T., Fujii, K.: Numerical Simulation of the Frequency Charactersitics of Edge Toneh. Transactions of JSCES Paper No. 20050026

[Ref10] Kurotaki, T., Sumi, T., Atobe, T.: Numerical Simulation aroud Airfoil with Natural Transition in High Reynolds Numberh. AIAA Paper 2007-3841

[Ref11] Clercx, H., van Heijst, G., Trieling, R.: Two Dimensional Turbulence, `www.fluid.tue.nl/WDY/2Dturb/bounded/bounded.htm`

“*This page left intentionally blank.*”

Aeroacoustic Simulation in Automobile Muffler by Using the Exact Compressible Navier-Stokes Equation

Yasuo Obikane

Institute of Computational Fluid Dynamics 1-16-5 Haramachi, Meguroku-ku, Tokyo 152-0011, Japan
obikane@icfd.co.jp

Abstract. The noises generated by the flow inside the casing or the noises in the short distance around machines are primary subjects for environmental engineers as well as the noises emitted from factories. In this paper, we developed a simulation software which can show a full development of both flow and sound in an acoustic chamber, especially resonance and attenuation in automobile mufflers. We use the compressible Navier-Stokes equation [CNSE] without the Lighthillfs wave equation. Three bench marks were performed; sound by a point oscillator on a cavity, sound by two jets in both a round chamber and a square chamber. Then, the reactive muffler (Baffled Muffler Design) was computed with perforation on the pipes. In the muffler model, we put artificial oscillations at the inlet to observe the wave characteristics in the perforated muffler. The transmission loss(dB) is about 25 to 34dB which is similar to the experimental results with perforation by Gerges [Ref7]. To observe the development of fluctuating energy with high accuracy, we use the third order finite difference scheme, the Multi-Directional,TVD method proposed in 2004 by Lee et al[Ref1].

Keywords: Automobile muffler, Aero-acoustics, Compressible Navier Stokes.

1 Introduction

Because of the complexity of the configuration of real mufflers, two approaches to the muffler noise problem are used mostly by designers; One is statistical vibration method such as Transfer Matrix Method(TMM) [Ref7]; The other method is to solve flow or acoustic field with CFD [Ref6]. TMM is easy to handle for simple configuration and need measurement data for calibration for each component because of the linearity. CFD is more rigorous and can treat both flows and sounds at one time, but it requires tedious mesh generations and post processing and days CPU time and Giga byte storage.

2 Objectives

In the present paper we compute the automobile muffler flow at low speeds with two dimensional CNSE code[Ref1]. The objectives are following as: To check

1. Realistic computability of forcing oscillations at low speeds
2. Realistic computability of acoustic waves in shear flows with CNSE
3. Confirmation that one code can simulate both low speeds and supersonic.

and our detail research interests are the following;

1. Noise generated by vortex shedding in the wake from the outlet pipe
2. Pulsing motion from the engine at the inlet
3. Wave cancellation by an attached resonator
4. Noise reduction with perforation
5. Two dimensional turbulence in the chamber

3 Governing Equations

We use a two dimensional flux form with four variables (rho,rhou,rhov,rhoE). The flux form of CNSE is well described in many aeroacoustics papers [Ref3]. Here, we just mention the name of equations; the continuity of equation with time derivative of density, and the two dimensional CNSE, and enthalpy, and the ideal gas equation. Many important works about the boundary conditions for direct simulation has been discussed by K.W. Thompson, S.K.W. Tam, and T.Pointsot and S.K.Lele and others. Thus, the computational method has been well established. However, because of the huge storage and small time steps there are still many problems for software designers such as boundary conditions and how many digits should be selected for the given aeroacoustics problems.

4 Numerical Method

The present numerical scheme is discussed by M.Lee, T.Kawamura, K.Kuwahara, and J.Ooida [Ref1]. Therefore, we skip the detail discussion except mentioning the remarks and a drawing in Fig. 1. The schem is the third order for non-linear term, the fourth order for the viscous term, and 17 points are used out of 25 points in 5x5 matrix. The non-linear operator split into two components: Lxy and Lx'y'. Lxy is the operator defined on the coordinates x,y in Cartesian coordinates, and Lx'y' is the operator defined on the coordinates oriented 45 degree to xy coordinates shown in Fig. 1. The operator L is defined as follows: L = 2/3Lxy + 1/3Lx'y'. By adding the oblique direction the operator has been expected to have more accuracy. In ddition, TVD condition is imposed on the scheme. For the boundary condition, we use Dirichlet condition in the Inlet , and Neuman condition on the outlet for the all variables. On the top and bottom boundaries the Neumann conditions

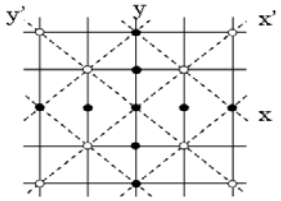

Fig. 1. Multi-Directiona Method

Fig. 2. Point Osc in a Cavity

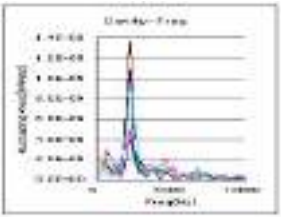

Fig. 3. Frequency Distirbution for one point Osc

were applied. On and in the body we used the incompressible boundary condition u=v=0, the constant density, and the stagnation enthalpy as non heat conducting fluid because of the low Mach number.

5 Bench Mark Computation

5.1 Bench Mark 1: One Point Oscillator on a Cavity

To confirm the propagation property, we pick a one point acoustic oscillator at the mouth of a cavity discussed by A.V. Alexandrov [Ref2]. No external flow is set, and also the initial velocity is zero in all domains. The computational result is shown in Fig. 2. Several small vortexes drawn as small white spots can be seen above the oscillator, and the waves generated are propagated outward. As the oscillator acted as a dipole source and also as a vortex generator, the vortexes were released periodically from the cavity. In Fig.3, a peak frequency is observed at 2200Hz of the generator, but could not see a bi-harmonics frequency. In Fig.4, the spectrum of the pressure fluctuation shows that the low frequency variation decreases in a steeper gradient as frequency increases. The higher frequency varies rather gradually to exponent minus one. These patterns are similar to the spectrum of two dimensional turbulence. [Ref4], [Ref5]. Therefore, the energy cascade may be described by the present code. To make a confirmation, we need further computation for the decay process.

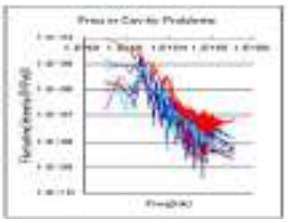

Fig. 4. Freq (log10) in one point Osc

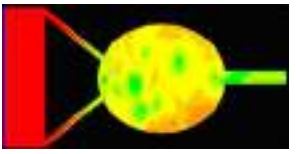

Fig. 5. Pressure Distribution

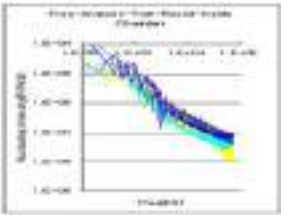

Fig. 6. Freq-Round-Chamber

5.2 Bench Mark 2: Flow Noise by Two Jets in a Round Chamber

It is well known that shear flows change the direction of sound and also dissipate the acoustics energy. In the second bench mark, we compute mixing flows in a round chamber with two nozzles. If the flow is unstable, then vortex shedding is generated, and causes sounds in the chamber. If it is stable, then any sound does not come out from stationary vortexes attached to some parts. The computational results are shown in Fig. 5, 6, 7. The Mach number and the pressure distribution are shown in Figs. 5, 6 respectively. The texture of the picture depends on the slicing scale, and it is hard to draw the sound quantitatively. However, the homogeneity of the distribution of 2D vortexes can be shown in Fig. 5 and they are quite similar to the results in [Ref4]. The large eddies are in the round chamber. The noise level in the outlet pipe is shown in Fig. 7. The level in the lower frequency is one order smaller and wider because of the viscosity and contraction in the outlet pipe. The maximum velocity at the channel was about 20m/sec.

6 Simulation of Automobile Muffler Model

We model a baffled muffler with one resonator room which is most commonly used in the automobiles. The flow is very complex because the muffler has several components such as pipes, baffles, a resonator, and perforated pipes as shown in Fig. 8. In addition, pulsing inlet flows come from the exhaust valves in the engine rooms. By using the model we simultaneously compute the complex flows and the compound acoustics wave with reflected waves which are canceling some parts of the inlet wave in a proper phase. We compute four cases: no forcing oscillation, artificial oscillations with frequencies 580Hz, 1470Hz with the amplitude of 10m/sec, and flow without a resonator room with no oscillation.

6.1 Case1: Artificial(forcing) Oscillation at the Inlet

The computed fluctuating pressures are shown in Figs. 9,10,11. The variation with time clearly shows that each wave has a different phase. The first and the second waves have a similar phase, but the fluctuating pressure in the third

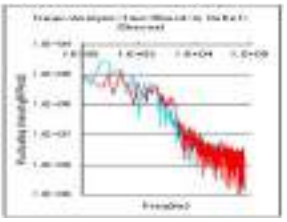

Fig. 7. Freq-In-Outlet

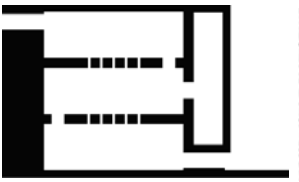

Fig. 8. configuration

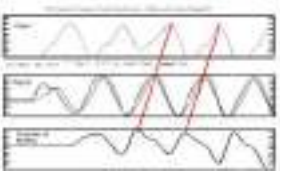

Fig. 9. Time-Variation

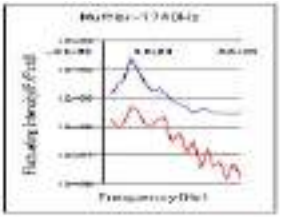

Fig. 10. Muffler-Pulsing motion

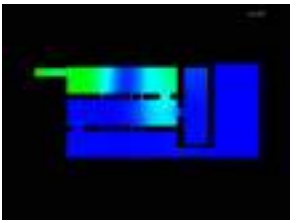

Fig. 11. No-Pulsive Pres-Variance

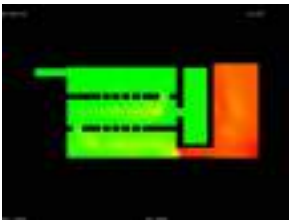

Fig. 12. Pulsive-Pres-Variance

pipe is out of phase. Indeed , the pressure outside of the muffler shows lower fluctuation and off phase from the original oscillation. The spectral patterns are shown in Figs. 9, 10. The transmission losses were about 24.7dB, 33.8dB for 580Hz,1740Hz respectively. The variance of the pressure is shown in Fig. 11, three parts in the first two pipes have higher pressure, but both in the third pipe and the outside area of the muffler, there is no high pressure. Thus, the damping of the muffler is quite effective.

6.2 Case2: No Artificial Oscillation at the Inlet

The variance of pressure is shown in Figs. 12. There, the outside sound power has higher intensity than one of the inside of the chamber. The slowly varying pressure with time can be seen in Fig. 14. It has vortexes which was not shown in the case1 of the artificial oscillation. No spike back pressure was observed. However, in some other computation for the muffler without theresonator, a

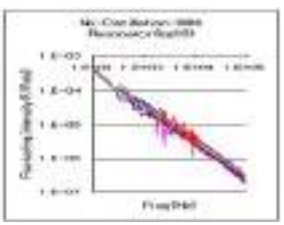

Fig. 13. Freq-No-Osc

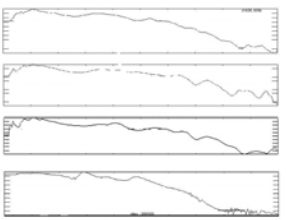

Fig. 14. Time variation Holes

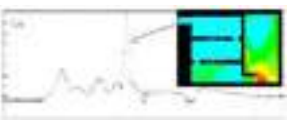

Fig. 15. No-Resonator-No-Osc

Fig. 16. Mach-No-Osc

spike was shown up, and then the spike pressure was instantaneously released at the middle of the computation as shown in Fig. 13, though it has rather larger numerical noises as shown in Fig. 13. In the Fig. 16, the case of no oscillation clearly shows the development of the vortexes in the train of pipes.

7 Conclusion

1. Showed Realistic computability of forcing oscillations at low speeds and acoustic waves in shear flows with the CNSE.
2. Confirmed that one code can simulate both low speeds and supersonic
3. Need more computation in a larger domain to check noise generated by vortex shedding in the wake from the outlet pipe
4. Successfully realized the pulsing motion in the muffler
5. Observed the wave cancellation by an attached resonator.
6. Observed the noise reduction with perforation in different frequencies
7. Seems to observe Two dimensional turbulence in the chamber

References

[Ref1] Lee, M., Kawamura, T., Kuwahara, K., Ooida, J.: Simulation of Unsteady Flows at High Angle of Attack. In: AIAA-2004-2136, 34th AIAA Fluid Dynamics Conference and Exhibit, Portland, Oregon, June 28-1 (2004)

[Ref2] Alexandrov, A.V., Chetverushikin, B.N., Kozubskaya, T.K.: Numerical inverswitgation of viscous compressible gas flows by means of flow field exposure to acoustic radiation. Parallel Computation Fluid Dynamics-Trend and Applications, 267–273 (2001)

[Ref3] Schroder, W., Ewert, R., Bui, T., Groshel, E.: An LES-APE Approach in Computational Aero-acoustics: Theory and Application. VKI Lecture Series 2006-7 Computational Aeroacoustics (2006)

[Ref4] Chasnov, J.R.: Decaying Turbulence in Two and Three Dimensions. In: Proceedings of the first AFSOR International Conference on DNS/LES, pp. 57–68 (1997)

[Ref5] Frisch, U.: Turbulence, The regacy of A.N. Kolmogorov. Cambridge University Press, Cambridge (1995)

[Ref6] Kim, H.S., Hong, J.S., Oh, J.E.: Active Noise Controal with the Active Muffler in Automotive Exhaust Systems. JSME, Series, C, vol. 41(2), pp. 178–1183

[Ref7] Gerges, S.N.Y., Jordan, R., Thieme, F.A., Bento Coelho, J.L., Arenas, J.P.: Muffler Modeling by Transfer Matrix Method and Experimental Verification. J. of the Braz. Soc. of Mech. Sci. and Eng. XXVII(2), 132–140 (2005)

Part 5
Aeroacoustics/Elasticity

“*This page left intentionally blank.*”

Towards Understanding the Physics of Supersonic Jet Screech

Igor Menshov[1], Ilya Semenov[2], Ildar Ahmedyanov[2], Mohammed Khalil Ibrahim[3], and Yoshiaki Nakamura[3]

[1] Keldysh Institute for Applied Mathematics, RAS
menshov@kiam.ru
[2] Institute for Computer Aided Design, RAS
semenov@icad.org.ru
[3] Dep. of Aerospace Eng., Nagoya University
nakamura@nuae.nagoya-u.ac.jp

Introduction. Jet flows have been a subject of intensive theoretical, numerical, and experimental investigations during last several decades. Many fluid dynamicists and specialists in computer simulations have endeavored to learn more about very complicated structures in jet flows. This interest have been in the first turn feeding by the desire to understand basic mechanisms of strong noise generated by high-speed jets, in particular very intense tones known as jet screech.

By present there exists a received theory on what plays a major role in producing jet screech sound. In accordance to this theory that is referred to in literature as feedback loop theory the screech noise occurs due to interactions between jet large-scale turbulent structures and shocks that exist inside the jet (for example, see [1, 4]).

In the present paper, another point of view on the jet screech mechanism is presented. We demonstrate a close correlation between the jet screech phenomenon and a 3D helical instability of the flow, which counters the existing theory of screech generation based on the vortex/shock interaction. We provide numerical, theoretical, and experimental evidence in favor of a quite different mechanism and state that the screech comes from the helical instability that alters the flow, imparting to it the typical shape of a highly rotating drill. And the jet screech has in fact the same nature as the sound produced by a rotating in air drill. We intentionally use a rather simple physical model - 3D compressible ideal fluid (Euler model) - to refine this phenomenon from dissipative processes that may do vague it. The helical mode instability develops mainly due to convective processes; it is inherent the flow itself, and dissipative factors such as heat conduction and viscosity are not dominant.

1 Numerical Evidence

First we present some results of the numerical simulation of a jet flow with using the model of compressible Euler equations. Parameters of this simulation are chosen to fit conditions of the experiment carried out in Nagoya University. We refer this experiment below in Section 3 to compare obtained numerical results with experimental observations.

The problem to be considered is a gas jet emitted from a circular nozzle into an ambient resting medium with pressure P_a and density ρ_a. The exit section diameter $D = 7.8\ mm$, and the nozzle leap thickness is $L = 1.5\ mm$

The jet efflux is modeled by setting a time-independent profile of the longitudinal velocity component $U_e(r)$ (where r is the radial distance) and the values of pressure P_e and density ρ_e at the nozzle exit. Two other velocity components are assumed to be zero.

The velocity profile is analogous to that we used previously for Navier-Stokes simulations [5]:

$$U(r) = 0.5U_e \left\{ 1 + \tanh \left[\frac{25}{4} \left(\frac{R}{r} - \frac{r}{R} \right) \right] \right\} \tag{1}$$

where $R = 0.5D$ is the nozzle exit radius, U_e is the maximal velocity (the velocity at the axis of symmetry). Note that no artificial disturbances are superimposed on the inflow velocity field.

The jet flow is characterized by the nozzle pressure ratio parameter $NPR = P_0/P_a$, where P_0 is the stagnation pressure, and the ratio of the exit pressure to the ambient pressure, P_e/P_a. These parameters are taken to match experimental conditions (Section 3): $NPR = 5$ and $P_e/P_a = 1.73$. Under these conditions the exit Mach number (based on the maximum velocity U_e) $M_e = 1.33$, and $M_j = 1.7$ that equals the isentropically fully expanded jet Mach number.

The inflow gas and the ambient gas are considered in the model of the Euler equations of a calorically perfect gas with the ratio of specific heats $\gamma = 1.4$. The governing equations in the form of conservation laws are written as

$$\partial_t \mathbf{q} + \partial_k \mathbf{f}_k = 0 \tag{2}$$

where $\mathbf{q}$ is the conservative vector, $\mathbf{f}_k$, $k = 1, 2, 3$, are the corresponding flux vectors.

The system of equations (2) is discretized in space with the Godunov finite-volume method. The time integration is performed with the explicit-implicit LU-SGS matrix-free time marching scheme proposed in [2]. This allows us to carry out the calculations with a reasonable time step, which is not restricted by the CFL-condition. At the same time, the scheme minimizes the dissipative error introduced by the implicit component.

The computational domain is represented by two subdomains. One of them is the domain of basic calculations, which expands $17D$ in the radial direction, and $25D$ in the streamwise direction. The second subdomain (so-called

buffer region) adjoins the basic one along the right-hand side boundary and serves to dump the flow and eliminate undesirable reflections from the outflow boundary. The buffer region expands $30D$.

The computational grid is of cylindrical type. The numerical code we have developed to solve the general system of equations (2) can treat computational cells of any polyhedral shape. Therefore, there are no problems occurred when calculating degenerated cells near the longitudinal axis.

The grid of the base domain consists of 480 cells in the streamwise direction, 208 cells in the radial direction, and 112 cells in the angular direction. The grid size (in radius) is $0.014D$ in the jet core; an axial grid size of $0.04D$ is used to accurately resolve the shock wave structure in the region $0 < x/D < 12$. The buffer region is covered by a rather coarse grid of 25 cells in the axial direction, which is generated so that a smooth transition between the base and buffer grids is ensured.

All calculations were carried out with parallel processing on the platform of the MVS-15000BM cluster at Joint Super Computer Center of the Russian Academy of Sciences (JSCC RAS). The cluster consists of 1052 CPU IBM Power PC 4 of an overall peak performance of 10 TFlops. Communications are realized on the base of the Myrinet communication media (2.2 Gb/sec) with a full graph node topology.

The time integration step Δt was 0.5 μs which corresponds to a CFL value of about 50. This choice turned out to be optimal, since it made possible calculations with a single LU-SGS iteration stage.

The results obtained give us grounds to put forward a basically different explanation for the screech nature and to ascertain that the feedback loop, though it can probably be realized, is not related to the mechanism of screech generation. We claim that the screech appears due to the development of helical instability in the jet flow and that its nature is essentially the same as that of the sound produced by a rapidly rotating drill.

Let us consider the numerical modeling results presented in Fig. 1, which shows the instantaneous isosurface of density for $\rho = 1.7\ kg/m^3$, which is intermediate between the ambient gas density ($\rho = 1.17\ kg/m^3$) and the density at the nozzle exit ($\rho = 3.225\ kg/m^3$).

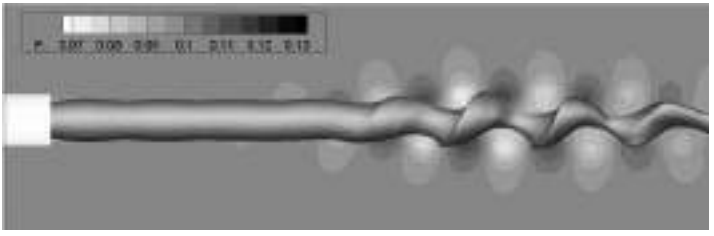

Fig. 1. Isosurface of the gas density $\rho = 1.7 kg/m^3$

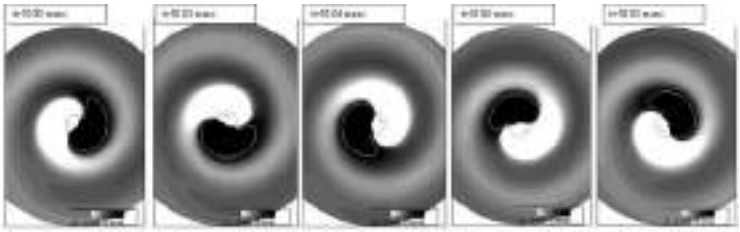

Fig. 2. Jet cross sections for five successive moments, showing the pressure field in the 1.009 $bar < P < 1.018$ bar range and the $\rho = 1.7 kg/m^3$ isosurface sections

This surface can be considered as a kind of visualization of the jet boundary. As can be seen, the axisymmetric jet flow pattern breaks up at a distance of three to four shock cells (these are not shown in the figure; the cell length is about $2D$) and the jet acquires a typical helical drill like shape.

The helical jet shape is unsteady. Figure 2 shows the pressure field in the jet cross section at a distance of $13D$ from the nozzle exit at several successive moments. The cross sections of the aforementioned isosurface $\rho = 1.7 kg/m^3$ are depicted by a gray curve. As one can see, the shape of the isosurface section remains unchanged and only rotates in the space at a constant angular velocity. Thus, this isosurface behaves as the surface of a rigid rotating drill. The rotation frequency, which can readily be determined from Fig. 2, amounts to 10.58 kHz. Thus, we may conclude that the axisymmetric pattern is lost as a result of the development of the helical instability and the jet takes the shape of a rapidly rotating drill. An angular component appears in the jet flow, while the flow character changes from near-rectilinear to helical.

What happens in the ambient gas when the helical instability arises? Obviously, the jet action on the surrounding gas is the same as that of a solid with a similar surface rotating at the same frequency (about 634800 rpm). In other words, if the jet flow region (Fig. 1) is mentally replaced by a solid drill rotating at the indicated frequency, the behavior of the ambient medium will not change significantly.

A rapidly rotating drill produces discrete sound, at a frequency equal to the rotation frequency. The nature of this tone is simple: due to the asymmetry, the cross section of the rotating drill executes periodic upward and downward motions leading to periodic compressions and rarefactions in the ambient gas and the corresponding tonal sound generation.

The mechanism of the supersonic jet screech generation is precisely the same. We ascertain that there is a complete analogy between the sound produced by a rotating drill and the discrete sound of a jet. Let us return to Fig. 1 which shows, together with the instantaneous position of the jet surface ($\rho = 1.7 kg/m^3$ density isosurface), the pressure distribution in the near- field zone in the 0.7 $bar < P < 1.3$ bar range. The compression (dark regions) and rarefaction (light regions) zones produced by the jet due to the helical instability are clearly visible.

2 Theoretical Evidence

The existence of the helical modes in jet flows that was numerically demonstrated in the previous section is theoretically examined by the linear-stability analysis of an axisymmetric columnar jet flow. The flow is characterized by constant pressure and density; the velocity vector has non-zero only longitudinal component that depends on the radius. We consider a two-parametric family of velocity profiles given by Eq. (1) where instead of the factor $\frac{25}{4}$ a parameter θ is used. Another parameter is the Mach number M_j defined by the maximal in the profile velocity.

Linear-stability analysis is carried out for disturbances in the form of harmonics $\exp[i(\lambda t + m\phi + kx)]$. The problem is to find non-trivial solutions of the linearized system of equations. It reduces to an eigenvalue problem for λ

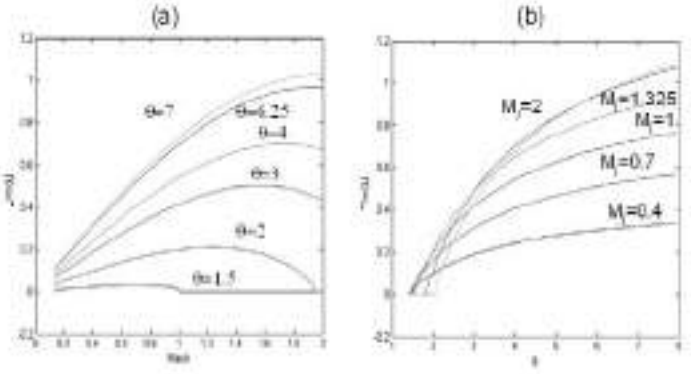

Fig. 3. Growth rate factor for $k = 2$ vs jet Mach number (a) and vs parameter θ

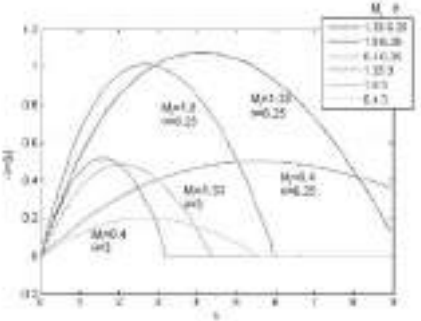

Fig. 4 Growth rate factor vs wavenumber K

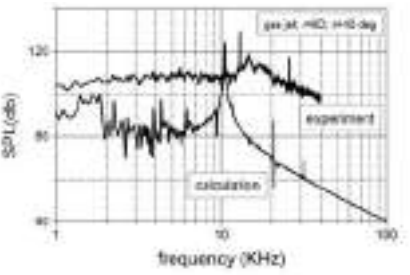

Fig. 5 Comparison experimental and numerical frequency spectra of pressure signal at the observation point $r = 6D,\ \phi = 40deg$

at given values of the wavenumbes m and k (m is an integer). The solution of this problem is quite similar to that we used in [3].

Some results of the linear-stability analysis are shown in Fig. 3. Here we display the growth rate $Im(\lambda)$ as a function of M_j at different values of θ (a), and as a function of θ at different values of M_j (b) for wavenumbers $k = 2$ and $m = 2$. One can see that these helical modes are unstable in a wide range of M_j and θ.

Figure 4 shows $Im(\lambda)$ vs longitudinal wavenumber k, which represents the length scale of the helical mode. There is a maximum in these distributions, which indicates the existence certain step most unstable (dominant) modes. For example, for $M_j = 1.33$ (conditions of the numerical simulation and experiment) and $\theta = 3$ the dominant mode corresponds a value of about $k = 2$.

3 Experimental Evidence

The experiment we refer in this paper was fulfilled in the Fluid Dynamics Lab., Department of Aerospace Eng., Nagoya University. This experiment was to take a high-speed camera visualization of the jet flow and the sound spectrum data at an observation point. The camera used is Photron FASTCAM-SA1 with a peak performance of 675000 frames per seconds. From the video one can see discernable rotor-type movement in the jet at a distance 3-4 shock cells from the nozzle exit. The spectrum data is compared with the numerical data in Fig. 5. One can see a good correlation between the data. Although there is a quantitative difference, qualitatively the data well agree.

4 Conclusion

Numerical, theoretical, and experimental evidence has been given in favor of quite new understanding of the jet screech phenomenon. In contrast to the existing screech theory based on the feedback loop of shock/vortex interactions, we assert that the screech comes out as the result of helical instability which drastically changes the flow and shifts it into a spiral mode; the screech has in fact the BVI nature and is quite similar to the sound generated by a quickly rotating in air drill.

References

1. Tam, C.K.W.: Supersonic jet noise. Annual Review of Fluid Mechanics 27, 17–43 (1995)
2. Menshov, I., Nakamura, Y.: Unconditionally Stable Scheme for Unsteady Compressible Flows. Physics of Fluids 17, 034102-1 – 034102-15 (2005)
3. Menshov, I., Nakamura, Y.: Instability of isolated compressible entropy-stratified vortices. AIAA Journal 42(3), 551–559 (2004)
4. Manning, T., Lele, S.K.: Numerical simulations of shock-vortex interactions in supersonic jet screech. AIAA Paper, No 98-0282, 1–11 (1998)
5. Hashimoto, A., Menshov, I., Nakamura, Y.: Sound emission from the helical mode of supersonic jet. AIAA Paper, No 2004-2656, 1–12 (2004)

Calculation of Wing Flutter Using Euler Equations with Approximate Boundary Conditions

Biao Zhu and Zhide Qiao

National Key Laboratory of Aerodynamic Design and Research, Northwestern Polytechnical University, Xi'an 710072, China
zhubia@gmail.com, zdqiao@nwpu.edu.cn

1 Introduction

Aeroelastic simulation, such as flutter prediction, is an important issue for modern aircraft design. If flutter occurs during flight, it will be lead to disastrous structural failure. So flutter is a catastrophic aeroelastic phenomenon that all flight vehicles must be clear of in their flight envelope.

Recently, there is a considerable interesting in studying the aeroelasticity of an aircraft using unsteady Euler equations or Navier-Stokes equations. Bendiksen and Kousen[1][2] used an explicit time accurate two-dimensional Euler code to study the nonlinear effects in transonic flutter. With their model, they demonstrated the possibility of LCO in a transonic flow. Lee-Rausch and Batina[3][4] developed three-dimensional methods for the Euler and Navier-Stokes equations, respectively, for predicting the flutter boundaries of wings. Alonso and Jameson[5] developed a model which is close to the fully coupled method by solving unsteady Euler equations coupled structural equations. Liu[6] developed a fully coupled method using Jameson's explicit scheme with multigrid method and a finite element structural model. The grids for CFD solver have to be regenerated in total computational field at every real time step, however the grid generating is a time consuming work. So we have to use some new numerical method for aeroelastic simulation to decreasing the calculating time and increasing the calculating efficiency, meanwhile keeping the required precision.

In this paper, we solve the three dimensional unsteady transonic Euler equations coupled with structural equations by using the first-order approximate boundary conditions[7][8][9] to simulate the wing's aeroelasticity. Cell-center finite volume method spatial derivatives, implicit dual-time temporal derivatives and 5-step Runge-Kutta scheme are adopted in the solution of unsteady flow. The techniques of local time stepping and implicit residual smoothing are used to accelerate the convergence rate. Wall boundary conditions are implemented on non-moving mean wall positions, meanwhile the first-order approximate boundary conditions are used in Euler equations on stationary Cartesian grids. This method needn't generate the deforming grids during calculation, thus it needs less demand on CPU time and can be easily deployed in any fluid-structure interaction problem.

2 Numerical Methods

2.1 Governing Equations

The three-dimensional unsteady Euler equations in conservative integral form in the Cartesian coordinate system (x, y, z) are

$$\frac{\partial}{\partial t}\int_V \mathbf{W}dV + \int_S \mathbf{F} \bullet \mathbf{n}dS = 0 \tag{1}$$

where $\mathbf{W}$ denotes the conservative variable and $\mathbf{F}$ is flux vector.

2.2 Approximate Boundary Conditions

A rigid wing pitching around an unswept axis located on the plane $y = 0$ and at $x = x_0$ is considered. The shape of stationary wing is described by $f(x, z)$. The instantaneous position of the wing surface is defined by $F(t, x, z)$. $\alpha_1(t)$ is the instantaneous angle of attack. Under the assumption $|F| \ll 1$, the first-order approximation of the velocity of y component on the wing surface at instant time t is

$$v(t, x, 0, z) = u(t, x, 0, z)F_x + w(t, x, 0, z)F_z + F_t + O(F) \tag{2}$$

where the subscripts x, z and t denote the partial derivatives with respect to x, z and t, respectively.

There are altogether five independent variables in the Euler equation (1), e.g. ρ, u, v, w and p. Then the momentum differential equation in the outward normal direction $\mathbf{n}$ is also used, which gives

$$\mathbf{n} \bullet \left[\frac{\partial \mathbf{q}}{\partial t} + (\mathbf{q} \bullet \bigtriangledown \mathbf{q})\right] = \mathbf{n} \bullet (-\frac{\bigtriangledown p}{\rho}) \tag{3}$$

At the wing surface, $y = F(t, x, z)$ equation (3) is expanded and its first-order approximation is

$$\begin{aligned} p_y(t, x, 0, z) = {} & F_x p_x(t, x, 0, z) + F_z p_z(t, x, 0, z) - \rho(t, x, 0, z) \\ & [F_{tt} + 2F_{tx}u(t, x, 0, z) + 2F_{tz}w(t, x, 0, z) + F_{xx}u^2(t, x, 0, z) + \\ & 2F_{xz}u(t, x, 0, z)w(t, x, 0, z) + F_{zz}w^2(t, x, 0, z)] \end{aligned} \tag{4}$$

Given $f(x, z)$, the instantaneous position of the wing surface $F(t, x, z)$ is expressed implicitly as follows

$$f(x_0 + (x - x_0)\cos\alpha_1 - F(t, x, z)\sin\alpha_1, z) = (x - x_0)\sin\alpha_1 + F(t, x, z)\cos\alpha_1 \tag{5}$$

If there is also plunging with plunging displacement defined as $H(t)$, upward positive, then equation (5) becomes

$$f(x_0 + (x - x_0)\cos\alpha_1 - (F - H)(t, x, z)\sin\alpha_1, z) = (x - x_0)\sin\alpha_1 + (F - H)\cos\alpha_1 \tag{6}$$

Under the wing being thin and undergoing small deformation, the nine derivatives of $F(t, x, z)$ used in equation (2) and (4) can be obtained from equation (6).

2.3 Structural Equation of Motion

The second-order linear structural dynamic governing equation of motion can be written as

$$\mathbf{M}\ddot{\mathbf{z}} + \mathbf{C}\dot{\mathbf{z}} + \mathbf{K}\mathbf{z} = \mathbf{F} \tag{7}$$

where $\mathbf{M}$, $\mathbf{C}$ and $\mathbf{K}$ are mass, damping and stiffness matrices, respectively. $\mathbf{z}$ is displacement vector, and $\mathbf{F}$ is the aerodynamic load. In this study, the data of natural mode shapes and frequencies are calculated by finite-element analysis. In order to solve equation (7), the generalized displacement is introduced. Then the transformed equation can be solved by Newmark method.

3 Results and Discussion

As validations of three-dimensional CFD solver which based on stationary Cartesian grid with the approximate boundary conditions for boundary implementation, the steady state transonic ONERA M6 wing and unsteady transonic LANN wing are calculated first. Finally, the flutter boundary of the AGARD 445.6 Wing is predicted.

3.1 ONERA M6 Wing

The ONERA wing is a classic test wing to validate CFD solver. The standard test condition is Mach number $M_a = 0.8395$ and $\alpha = 3.06°$. The grid dimension is$140 \times 60 \times 40$ in this case.

The computed surface pressure distributions at various cross sections are shown in Fig.1 with the experimental data given by Schmitt et al[10]. The pressure distributions at different cross section are agreement between the computation and experiment. In these figures, the biggest difference occurs at the leading edge region. This is because the singularity exists when the present method used in Cartesian grid for blunt leading edge.

3.2 LANN Wing

The second test case is to validate three dimensional unsteady solver by using LANN wing[11]. The LANN wing oscillates about an unswept axis at 62.1% of its root chord in a pitching motion. The harmonic pitching motion of LANN wing can be described by the following equation.

$$\alpha(t) = \alpha_m + \alpha_0 \sin \omega t$$

In this test case, the free stream Mach number is $M_\infty = 0.822$, and the mean angle of attack $\alpha_m = 0.6°$, the pitching amplitude $\alpha_0 = 0.25°$ and the reduced frequency $k = 0.102$.

In order to compare the pressure distribution of the unsteady computation, Fourier transformation is performed for the unsteady pressure distribution. The first Fourier mode of the unsteady pressure distributions at six span positions is shown

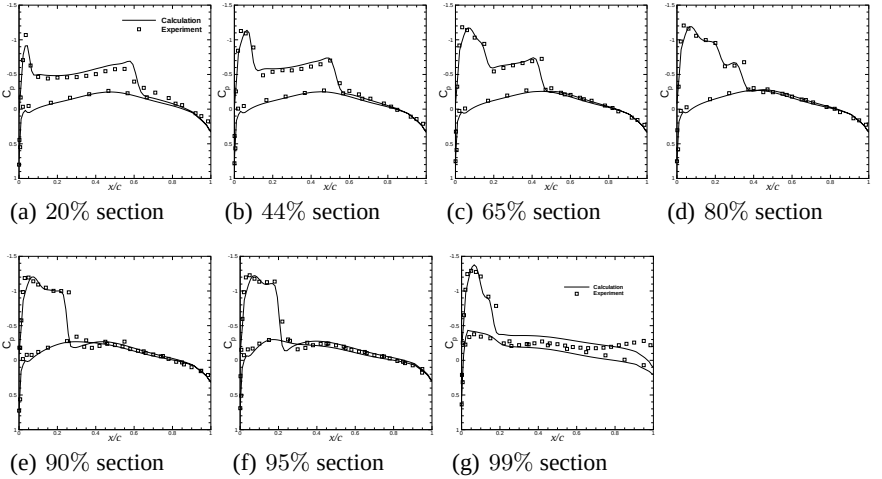

(a) 20% section (b) 44% section (c) 65% section (d) 80% section

(e) 90% section (f) 95% section (g) 99% section

Fig. 1. Pressure distributions on the ONERA M6 wing surface at different cross sections

in Fig.2, where L is the half span. The left is for real component and the right is for imaginary component. The shock wave strength is over predicted by the current approximate method. And the position of shock wave obtained by using current method is behind that of experimental result. However, the position and the strength of the shock wave predicted by the first-order approximate boundary conditions are better agreement with the experimental results than those by the Euler solver with exact boundary conditions.

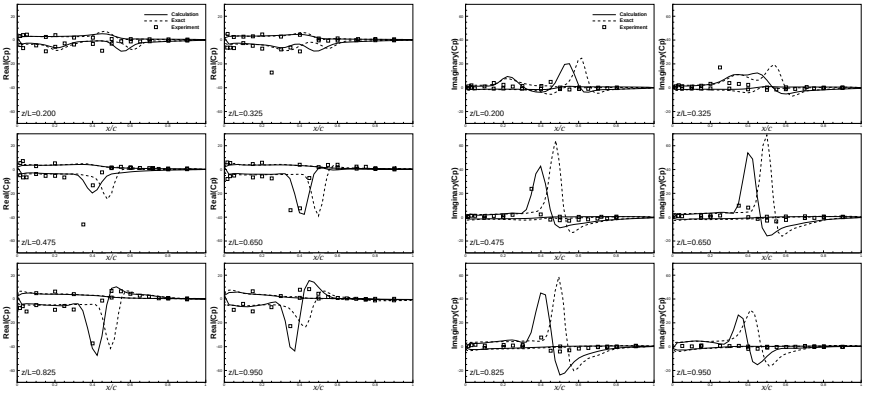

(a) Real component (b) Imaginary component

Fig. 2. Comparison of the first Fourier mode of unsteady pressure for LANN wing

3.3 AGARD 445.6 Wing

The AGARD 445.6 wing is a semi-span model which has a quarter-chord sweep angle of 45°, an aspect ratio of 1.65, a taper ratio of 0.6576, and a NACA 65A004 airfoil cross section. We consider the weakened wing model as listed in [12]. The wing structure is modeled by its first four natural vibration modes in the present computation.

In order to obtain the flutter boundary, the speed index V_f is defined as

$$V_f = \frac{U_\infty}{b\omega_\alpha\sqrt{\mu}}$$

where b is the airfoil half chord, ω_α is natural circular frequency for first torsional modes, μ is mass ratio.

The flutter boundary of the AGARD 445.6 weakened wing model 3 is obtained by the current approximate method on stationary Cartesian grids and shown in Fig.3. In order to validate the accuracy of the current approximate method, the experimental result and Batina's result are shown in Fig.3 too. From the figure, the flutter boundary predicted by the first-order approximate boundary conditions is agreement well with Batina's result and experimental result in subsonic and transonic Mach number range, and departures from the experimental result in supersonic range. The flutter frequency predicted by the first-order approximate boundary conditions is more close to the experimental data than Batina's result.

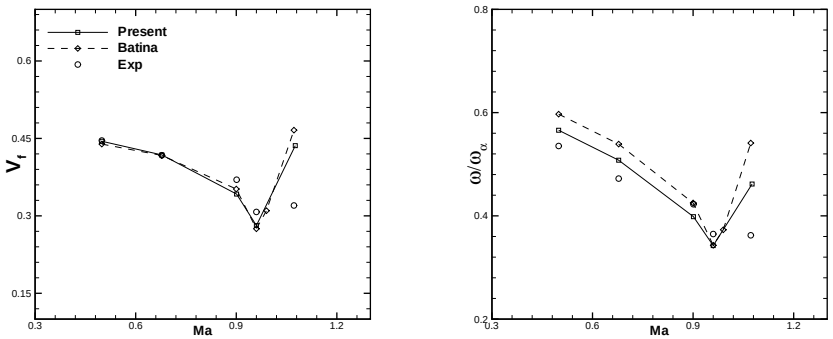

Fig. 3. Comparison of the flutter boundary and flutter frequency of AGARD 445.6 Wing

4 Conclusion

In this paper, we use the first-order approximate boundary conditions to solve the unsteady Euler equations coupled with equations of structural motion to predict the flutter boundary of AGARD wing on stationary Cartesian grids. Using this approximate method, we solve the steady case for ONERA M6 Wing and unsteady case for LANN wing first, finally the aeroelastic properties of AGARD 445.6 wing is predicted. The results obtained by the first-order approximate boundary conditions are

compared well with those obtained by exact boundary conditions and experiment. The comparison preliminarily indicates that the first-order approximate conditions are accurate enough and effective for aeroelastic simulation.

References

[1] Bendiksen, O.O., Kousen, K.A.: Transonic flutter analysis using the Euler equation. AIAA Paper 1987-0911 (1987)
[2] Kousen, K.A., Bendiksen, O.O.: Limit cycle phenomena in computational transonic aeroelasticity. Journal of Aircraft 31, 1257–1263 (1994)
[3] Lee-Rausch, E.M., Batina, J.T.: Wing flutter boundary prediction using unsteady Euler aerodynamic method. Journal of Aircraft 32, 416–422 (1995)
[4] Lee-Rausch, E.M., Batina, J.T.: Wing flutter computations using an aerodynamic model based on the Navier-Stokes equations. Journal of Aircraft 33, 1139–1147 (1996)
[5] Alosnso, J.J., Jameson, A.: Fully-implicit time-marching aeroealstic solutions. AIAA Paper 1987-0911 (1987)
[6] Liu, F., Cai, J., Zhu, Y.: Calculation of wing flutter by a coupled fluid-structure method. Journal of Aircraft 38, 334–342 (2003)
[7] Gao, C., Luo, S., Liu, F.: Calculation of unsteady transonic flow by an Euler method with small perturbation boundary conditions. AIAA Paper 2003-1267 (2003)
[8] Gao, C., Luo, S., Liu, F., Schuster, D.M.: Calculation of airfoil flutter by an Euler method with approximate boundary conditions. AIAA Paper 2003-3830 (2003)
[9] Zhang, Y.H.: Numerical simulations of transonic flow of wing by solving Euler equations with approximate boundary method. MA Thesis, Northwestern Polytechnical University, Xi'an (2005)
[10] Schmitt, V., Charpin, F.: Pressure distributions on the ONERA-m6-wing at transonic Mach. numbers. AGARD-AR 138 (1979)
[11] Zwaan, V.: LANN wing pitching oscillation, Compendium of unsteady aerodynamics measurements. AGARD-R-702 (1985)
[12] Yates Jr., E.C.: AGARD standard aeroelastic configurations for dynamic response, I-Wing 445.6. NASA-TM-100492 (1987)

Direct Computation of Infrasound Propagation in Inhomogeneous Atmosphere Using a Low-Dispersion and Low-Dissipation Algorithm

Christophe Bailly and Christophe Bogey

Laboratoire de Mécanique des Fluides et d'Acoustique, UMR CNRS 5509, Ecole Centrale de Lyon, 69134 Ecully Cedex, France
& Institut Universitaire de France
christophe.bailly@ec-lyon.fr, christophe.bogey@ec-lyon.fr

Summary. Numerical simulations of long-range infrasound propagation involving temperature gradients, realistic atmosphere at high altitude and absorption are reported in this study. A low-dispersion and low-dissipation finite-difference algorithm initially developed for aeroacoustics applications is used to solve the full Navier-Stokes equations including vibrational relaxation effects.

1 Introduction

With the aim of monitoring infrasounds ($f \leq 1$ Hz) generated by supersonic aircrafts, meteors or atmospheric explosions, accurate numerical studies of sound propagation at high altitude in a realistic atmosphere are required to better understand physics. Low-frequency noise can propagate to thousand kilometers in the earth atmosphere, and can be detected passively by ground probes. Due to temperature gradients, sound waves are refracted by stratosphere ($\sim$ 50 km) and thermosphere ($\sim$ 110 km) and are then propagated back to the ground at large distances from the source, typically several hundred kilometers [2]. The mean profile of the sound speed considered in the present work is shown in figure 1. Local minima of the sound speed can be observed, corresponding to channel axes of natural waveguide, and sound waves are refracted towards these axes. This phenomenon is well known in underwater acoustics since the work by Ewing & Worzel [7] about the SOFAR channel in the Atlantic ocean.

The acoustic signature detected at the ground is therefore composed of several wave packets characterized by different arrival times, and is strongly affected by classical absorption, namely viscosity and thermal conductivity [12], by molecular absorption at high altitude, and also by non-linear effects due to the amplification of sound pressure levels in the upper atmosphere [15].

Thanks to the development of accurate time solutions of Navier-Stokes equations for turbulent compressible flows over the last 15 years, and more especially to the dramatic progress in computational acoustics, direct simulations of long-range sound propagation in atmosphere are now reachable, and can provide reference solutions to validate alternative approaches often based on geometrical acoustics, as illustrated by the study of Wochner *et al.* [16] for instance. In the present work, numerical algorithms originally developed for the direct computation of aerodynamic noise are used to advance simulations of outdoor sound propagation including atmospheric effects.

2 Case of the *Misty Picture* experiment

A preliminary simplified simulation of the *Misty Picture* experiment [8] performed at White Sands Missile Range (NM, USA) is reported here. This experiment is currently a reference case for infrasound propagation in the Earth atmosphere [14] as discussed in Gainville *et al.* [9, 10].

2.1 Atmosphere Model

The atmospheric model is built up from a mean temperature profile $\bar{T}$ resulting from measurements for the lower part, and from extrapolations with statistical data for the upper part. These data are provided by Gainville [10]. The mean molecular weight $M = M(z)$ as a function of the altitude z is calculated by following Sutherland & Bass [15], and a perfect gas law is used for $z \leq 180$ km. The pressure profile is then calculated by solving the hydrostatic equation,

$$\ln\left(\bar{p}/p_0\right) = -\frac{g}{R}\int_0^z \frac{M}{\bar{T}}dz$$

where g is the acceleration of gravity, R is the universal gas constant and p_0 is the pressure at the ground. The density profile is thus obtained by using the perfect gas law $\bar{\rho} = \bar{p}M/(R\bar{T})$. As already mentioned in the introduction, the profile of the sound speed $c = (\gamma r T)^{1/2}$ where $\gamma(z)$ is the ratio of specific heats and $r = R/M$, is plotted in figure 1. The two parts of the profile are clearly visible. The jump for $z \simeq 95$ km is linked to the modelling of the molecular weight, and not to the matching between measurements and statistical data.

A classical issue is then the stability [11] of this profile which leads to the examination of the sign of the following quantity,

$$N^2 \equiv -\frac{g}{\bar{\rho}}\frac{d\bar{\rho}}{dz} - \frac{g^2}{\bar{c}^2}$$

and the atmosphere model is stable when $N^2 > 0$. Figure 1 also displays the profile of $N = \mathrm{sgn}(N^2) \times \left|N^2\right|^{1/2}$, where N is known as the Väisälä-Brunt angular frequency. The atmosphere is found unstable at four different locations which means that sound waves passing these regions could generate internal

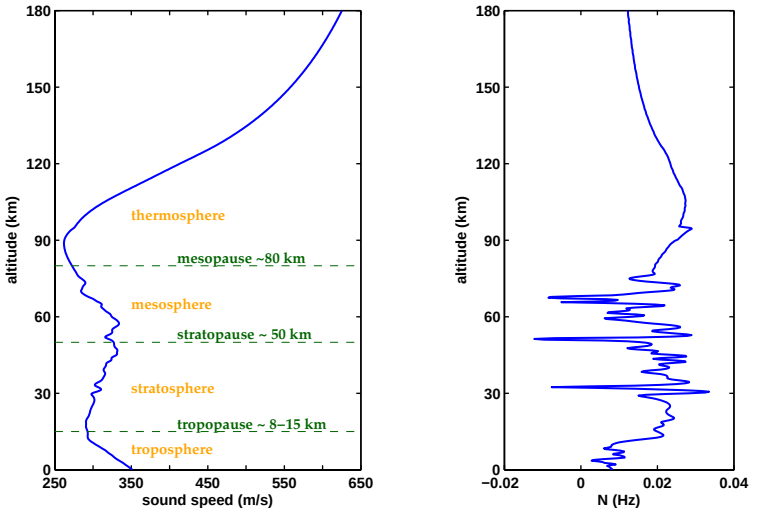

Fig. 1. *Misty picture* experiment, mean flow profiles up to $z = 180$ km. Left, speed of sound c and right, Väisälä-Brunt angular frequency N.

gravity waves. This is not, however, a crucial problem here since the travelling time of an acoustic wavepacket is very small compare to the characteristic time of gravity waves $\tau_g = 2\pi/N \simeq 2\pi/0.02 \simeq 314$ s corresponding to an oscillation period of around 5 minutes.

2.2 Governing Equations and Numerical Algorithm

The more general governing equations are the Navier-Stokes equations,

$$\begin{cases} \dfrac{\partial \rho}{\partial t} + \nabla \cdot (\rho \boldsymbol{u}) = 0, \\ \dfrac{\partial (\rho \boldsymbol{u})}{\partial t} + \nabla p + \nabla \cdot (\rho \boldsymbol{u}\boldsymbol{u}) - \nabla \cdot \boldsymbol{\tau} - \rho \boldsymbol{g} = 0, \\ \dfrac{\partial \left(\rho e_t\right)}{\partial t} + \nabla \cdot [(\rho e_t + p)\boldsymbol{u}] + \nabla \cdot \boldsymbol{q} - \nabla \cdot (\boldsymbol{\tau}\boldsymbol{u}) - \rho \boldsymbol{g} \cdot \boldsymbol{u} = 0 \end{cases}$$

symbolically noted $\mathcal{L}(\boldsymbol{U}) = 0$. In these equations, $\boldsymbol{u}$ denotes the fluid velocity, $\boldsymbol{\tau}$ is the viscous stress tensor, e_t is the total specific energy and $\boldsymbol{q}$ is the heat flux vector. The system can also be linearized around the mean state defined in the previous section, and linearized's Euler equation are recovered by neglected molecular effects.

The considered system is excited by a source term written as $\boldsymbol{S} = s(t) \times F(x, z)$ where F is a space Gaussian function and s is the initial time signature, yielding $\mathcal{L}(\boldsymbol{U}) = \boldsymbol{S}$. In the present study, the simulations are

two-dimensional, x and z denotes respectively the horizontal distance and the altitude, and the function s is given by

$$s(t) = 0.5 \sin(\omega_s t) \left[1 - \cos\left(\frac{\omega_s t}{2}\right)\right] [H(t) - H(t - 2T_s)]$$

where $\omega_s = 2\pi/T_s = 2\pi f_s$, $f_s = 0.1$ Hz, $0 \leq t \leq 2T$ and H stands for the Heaviside function.

The discretization of the governing equations is performed with an optimized eleven-point stencil finite-difference scheme for the spatial derivation associated with a selective filtering [3, 5]. A six-stage low-storage Runge-Kutta algorithm [3] is used for the time integration. Wall boundary conditions are enforced along the line $z = 0$ and non-reflecting boundary conditions are implemented elsewhere by means of the boundary schemes of Berland *et al.* [1]. This numerical algorithm is widely used by the authors for the direct computation of aerodynamic noise, refer to [4] for a recent discussion.

Figure 2 displays snapshots of the calculated fluctuating pressure field normalized by the density, $p'/\sqrt{\rho}$, which is generated by the impulsive source located near the ground. The physical computational domain has the dimensions 450 km $\times$ 180 km. It is discretized with a uniform step size of $\Delta = 300$ m, the time advancement is performed with a CFL number of 0.8 and linearized's Euler equations are solved in this case. Formation of shadow zones corresponding to the two natural wave guides discussed in the

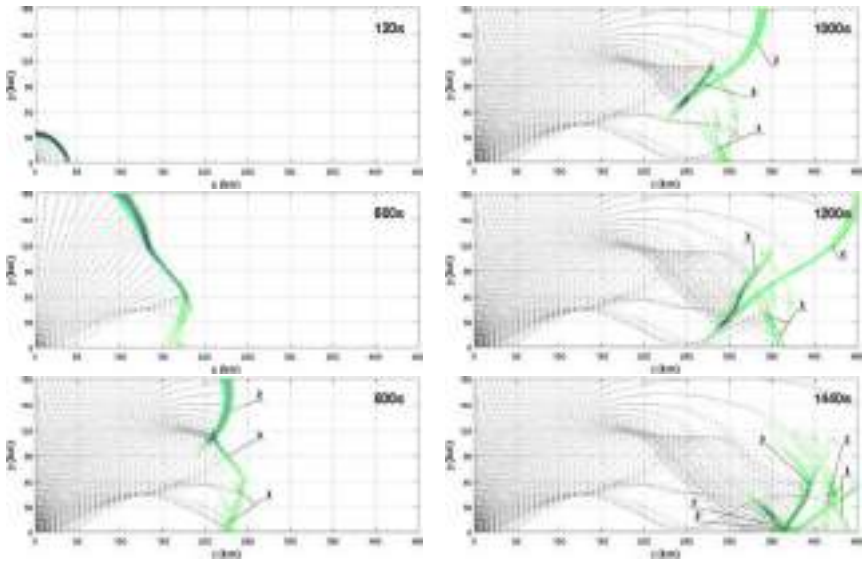

Fig. 2. Snapshots of the computed pressure field normalized by the density, $p'/\sqrt{\rho}$, for different times. A ray-tracing (dashed lines) is also superimposed to support the interpretation. Note that $y \equiv z$ in all theses pictures.

introduction, and of caustics is clearly visible. More precisely, one can distinguish: (1) - stratospheric waves, (2) - thermospheric waves refracted between 120 and 180 km, (2') - ground reflection of waves (2), (3) - thermospheric waves refracted around 115 km and (3') - ground reflection of waves (3). The pressure signatures for a receiver located at $x = 400$ km and at different altitudes have been also analyzed and compared with results obtained by solving the full Navier-Stokes equations.

3 Modelling of Atmospheric Sound Absorption in Time-Dependent Simulations

Sound propagation in the upper atmosphere requires to take into account not only the thermo-viscous effects but also the vibrational relaxation effects [12, 13, 15]. The translational and rotational processes are already included in Navier-Stokes equations through the dynamic viscosity μ and the bulk viscosity μ_b respectively in the viscous stress tensor $\nabla \cdot \boldsymbol{\tau} = \mu\nabla^2\boldsymbol{u} + (\mu/3 + \mu_b)\nabla(\nabla \cdot \boldsymbol{u})$, and a thermal equilibrium is also assumed. Time integration of molecular relaxation effects at near equilibrium state is carried out by introducing a Landau-Teller relaxation equation for each species β,

$$\partial_t(\rho T_\beta) + \nabla \cdot (\rho \boldsymbol{u} T_\beta) = (\rho/\tau_\beta)(T - T_\beta)$$

where T_β denotes the vibration temperature and τ_β is the associated relaxation time. The internal total energy writes thus as the sum of the translational, rotational and vibrational contributions

$$\rho e = \rho e_{tr} + \rho e_{rot} + \rho e_{vib} = \frac{p}{\gamma - 1} + \rho r \sum_\beta X_\beta T_\beta^\star e^{-T_\beta^\star/T_\beta}$$

In this last expression, X_β is the mole fraction and $T_\beta^\star$ is the temperature associated with molecular vibration at equilibrium. Physically, an energy transfer due to the passage of the acoustic wavepacket is produced when the characteristic acoustic time is smaller than the vibrational relaxation time $\tau_\beta = \tau_\beta(p, \mu, X_\beta)$. Preliminary simulations have been performed by rewritting the energy equation for the variable $\rho\check{e}_t \equiv p/(\gamma - 1) + \rho\boldsymbol{u}^2/2$ in order to preserve the formulation of the non-reflecting boundary conditions in the solver.

4 Concluding Remarks

A computational aeroacoustics algorithm has been used to provide reference solutions for long-range propagation in Earths atmosphere at high altitudes. The next step is to implement a shock-capturing procedure [6] since strong non-linear propagation effects occurs because of the amplification of sound pressure levels in the upper atmosphere. Time signatures will be also discussed by comparisons with experimental data.

Acknowledgement

The authors acknowledge the CEA (french atomic agency) for useful discussions through the research group MOPA and financial support, and Olaf Gainville for supplying the data.

References

1. Berland, J., Bogey, C., Marsden, O., Bailly, C.: High-order, low dispersive and low dissipative explicit schemes for multi-scale and boundary problems. J. Comput. Phys. 224(2), 637–662 (2007)
2. Besset, C., Blanc, E.: Propagation of vertical shock waves in the atmosphere. J. Acoust. Soc. Am. 95(4), 1830–1839 (1994)
3. Bogey, C., Bailly, C.: A family of low dispersive and low dissipative explicit schemes for flow and noise computations. J. Comput. Phys. 194(1), 194–214 (2004)
4. Bogey, C., Bailly, C.: Large Eddy Simulations of transitional round jets: influence of the Reynolds number on flow development and energy dissipation. Phys. Fluids 18(6), 065101 (2006)
5. Bogey, C., Bailly, C.: On the application of explicit filtering to the variables or fluxes of linear equations. J. Comput. Phys. 225, 1211–1217 (2007)
6. Bogey, C., de Cacqueray, N., Bailly, C.: Self-adjusting shock-capturing spatial filtering for high-order non-linear computations. AIAA-2008-2968 (2008)
7. Ewing, M., Worzel, J.L.: Long-range sound transmission. The Geological Society of America, Memoir 27 (1948)
8. Test execution report–Misty Picture Event, AD-A283 521, Defence Nuclear Agency, Washington (1987)
9. Gainville, O., Piserchia, P.-F., Blanc-Benon, P., Scott, J.: Ray tracing for long range atmospheric propagation of infrasound. In: 12th AIAA/CEAS Aeroacoustics Conference, AIAA Paper 2006-2451 (2006)
10. Gainville, O.: Modélisation de la propagation atmosphérique des ondes infrasonores par une méthode de tracé de rayons non linéaire. Ph.D. Thesis, EC-Lyon, 2008-2007 (2008)
11. Lighthill, M.J.: Waves in fluids. Cambridge University Press, Cambridge (1978)
12. Lighthill, M.J.: Viscosity effects in sound waves of finite amplitude. In: Surveys in Mechanics, e. b. G. K. B. a. R. M. Davies. Cambridge University Press, Cambridge (1996)
13. Pierce, A.D.: Acoustics, Acoustical Society of America, 3rd edn. (1994)
14. Piserchia, P.-F., Roche, R., Aballea, F., Defrance, J.: Numerical modeling of infrasound propagation at very long distance. In: 11th Long Range Sound Propagation Symposium, pp. 1–2 (2004)
15. Sutherland, L.C., Bass, H.E.: 2004 Atmospheric absorption in the atmosphere up to 160 km. J. Acoust. Soc. Am. 115(3), 1012–1032 (2004); See also Erratum. J. Acoust. Soc. Am., 120(5), 2985 (2006)
16. Wochner, M.S., Atchley, A.A., Sparrow, V.W.: Numerical simulation of finite amplitude wave propagation in air using a realistic atmospheric absorption model. J. Acoust. Soc. Am. 118(5), 2891–2898 (2005)

Part 6
Algorithm 1

“*This page left intentionally blank.*”

Symmetry Preserving Discretization of the Compressible Euler Equations

Emma Hoarau[1], Pierre Sagaut[2], Claire David[2], and Thiên-Hiêp Lê[1]

[1] ONERA, BP 72, 29 avenue de la Division Leclerc, 92322 Châtillon cedex
emma.hoarau@onera.fr
[2] Université Pierre et Marie Curie, 4 place Jussieu, 75005 Paris
sagaut@lmm.jussieu.fr

1 Introduction

Symmetries are transformations which act on the physical variables of a system. They can transform the time, the position, the velocity and the thermodynamical properties (density, pressure) of the physical system. But they do not modify the evolution of the physical system. This work deals with continuous symmetries which are described by the Lie group theory. In physics, symmetries are space-time transformations, such as the Galilean transformations, the Lorentz transformations, the projective transformations, the scaling transformations, the translations.

Symmetry techniques are powerful tools for the differential equation analysis. Symmetries have been used to generate new solutions of complex differential systems. These are special solutions, called *similarity solutions* or invariant solutions, i.e. solutions which remain unchanged when the related symmetries are applied. These explicit solutions can be used to build models for physical experiments, or as reference solutions to evaluate the performance of the numerical methods. They can also be used to understand the physical dynamics of specific phenomena. For instance, symmetries have been used in the turbulence modeling. Razafindralandy and Hamdouni [RH05], Razafindralandy et *al.* [RHO07] have used symmetries to build turbulence model which preserve the features of the turbulent phenomena. Moreover, if the system is derived from a Lagrangian action, Emmy Noether theorem states that each symmetry of the Lagrangian action corresponds to some physical quantity that the system conserves.

In computational aerodynamics, most classical methods, do not preserve the symmetries of the original problem. This leads to the introduction of an additional numerical error, which depends on the amplitude of the transformation. The numerical methods provide an approximate solution of another problem. Oscillations and instabilities may appear. Figures 1 and 2 show the dependency of the numerical solution of the Burgers equation upon the frames stemmed from Galilean transformations. Each frame F_i is corresponds to a specific value of the velocity v_G of the transformation. The Burgers equation is preserved by the Galilean transformations. But oscillations appear when

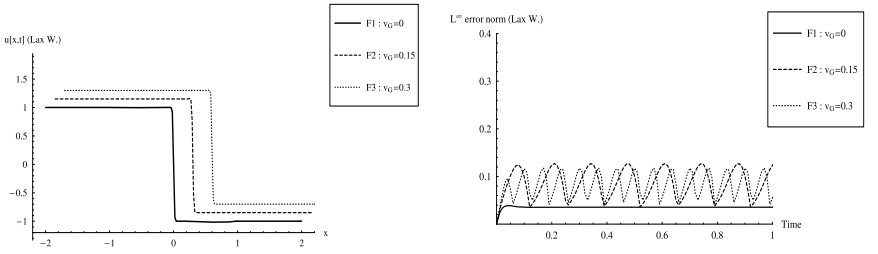

Fig. 1. Numerical results of the Lax Wendroff scheme ($Re_h = 4$, $CFL = 0.5$), at t=1

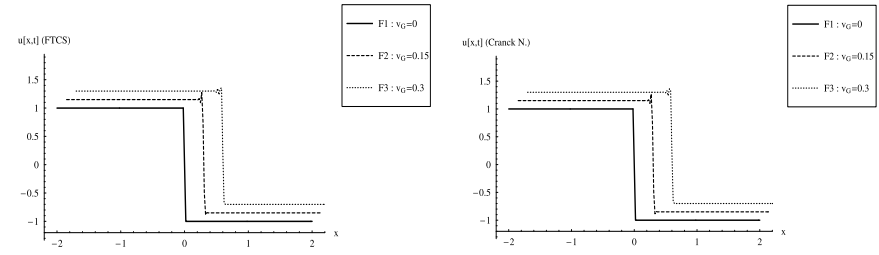

Fig. 2. Space variation of the numerical solutions for the forward-time centered-space method and Crank Nicolson one ($Re_h = 4$, $CFL = 0.5$), at t=1

the discrete variables are transformed. Chhay and Hamdouni characterized this additional error in [CH08] and introduced the concept of the *error of consistency in symmetry*.

This additional error arises, in complex computational codes, when the spatial domain is divided into sub-domains which are in relative motion. For instance in fluid-structure interaction, the fluid follows the solid structure motion. The fluid particles are subjected to transformations. If the numerical method does not inherit the symmetries of the original problem, an additional error is introduced in the numerical solution.

Symmetry preserving schemes belong to the fundamental research in mathematics, which is called *geometric integration*. Symmetry preserving schemes have been implemented for generic problems of mathematical mechanics. It is little known in aerodynamics. The technique has been initiated by Yanenko [YS76] and Shokin [Sho83] in 1976. They proposed a local analysis of the symmetries of finite difference schemes, based on the equivalent differential system. Budd approach [BHR96] has provided schemes preserving scaling transformations, for problems with exponential increase in time. Olver approach [Olv01] is based on the theory of Cartan of moving frame. The classical schemes are invariantized to inherit the symmetries of the original problem.

Our work concentrates on the so-called *method of finite-difference invariants*, introduced by Dorodnitsyn [Dor91]. It is a discretization technique based on a Lie group analysis prolonged to the stencil discrete variables. The obtained scheme is build on an invariant adapted mesh.

The method [BDK97] is implemented to find finite difference approximations of the one-dimensional Euler equations, which govern a compressible and inviscid flow. The approach consists in the building of a discrete invariant model, consistent with the equations. It uses techniques of Lie group application to algebraic equations [Olv86], [Ibr96]. Comparisons between the discrete invariant method and the Lax Wendroff scheme will be realized.

2 Euler Equations

The one-dimensional Euler equations for a compressible inviscid flow is written:

$$\begin{aligned} &\rho_t + \{\rho u\}_x = 0 \qquad (\textit{continuity}) \\ &\{\rho u\}_t + \{\rho u^2 + p\}_x = 0 \qquad (\textit{momentum}) \\ &\{\rho E\}_t + \big\{u\big(\rho E + p\big)\big\}_x = 0 \qquad (\textit{energy}) \\ &\rho e = \frac{p}{\gamma - 1} \qquad (\textit{ideal gas equation}) \end{aligned} \tag{1}$$

ρ, ρu, and E are respectively the density, the momentum and the total energy. The latter is composed of the internal energy and the kinetic energy:

$$E = e + \frac{u^2}{2}$$

x and t are the independent variables. An equivalent closed system involved the dependent variables ρ, u and the pressure p.

System (1) admits six continuous symmetries:

- Spatial and temporal translations
  $(x, t, u, \rho, p) \mapsto (x + \mathbf{a_1}, t, u, \rho, p)$
  $(x, t, u, \rho, p) \mapsto (x, t + \mathbf{a_2}, u, \rho, p)$

- Scaling transformations
  $(x, t, u, \rho, p) \mapsto (\mathbf{a_3}\ x, \mathbf{a_3}\ t, u, \rho, p)$
  $(x, t, u, \rho, p) \mapsto (x, t, u, \mathbf{a_4}\ \rho, \mathbf{a_4}\ p)$
  $(x, t, u, \rho, p) \mapsto (x, \mathbf{a_5}\ t, {\mathbf{a_5}}^{-1}\ u, {\mathbf{a_5}}^2\ \rho, p)$

- *Galilean transformations*
  $(x, t, u, \rho, p) \mapsto (x + \mathbf{a_6}\ t, t, u + \mathbf{a_6}, \rho, p)$

The transformations depend continuously upon the physical variables and the parameters a_i, which provide the amplitudes of the transformations.

3 Discrete Invariant Method

Denote by Σ_h a finite difference scheme for the Euler equations, by z the discrete variables of the stencil $\mathcal{Z}$, and by $\mathcal{F}$ an approximation of the Euler equations. Σ_h can be written as:

$$\begin{aligned} \mathcal{F}(z) &= 0 \\ \Omega(z,h) &= 0 \end{aligned} \tag{2}$$

where Ω defines the finite difference mesh.

The scheme Σ_h is invariant under the symmetries of the Euler equations, if the numerical solution remains the same when the frame is changed under the action of the transformations.

The action of a symmetry is considered to be the motion of the fluid particles, described by the equations. The motion is a flow generated by a vector field, which is called *infinitesimal generator*.

Denote by $\mathbf{L}_\alpha(z)$ the discrete infinitesimal generators related to the symmetries of the Euler equation. The infinitesimal change in the scheme under the flow is written:

$$\mathbf{L}_\alpha(z)\ \mathcal{F}(z) = 0, \quad \mathbf{L}_\alpha(z)\ \Omega(z,h) = 0, \quad \alpha = 1, \ldots, 6 \tag{3}$$

Equations (3) are discrete infinitesimal conditions of invariance. These linear equations easily evaluate the invariance of expressions. They are also used to derive expressions which inherit the symmetries of the original system. The building of the discrete invariant scheme follows the procedure:

- Resolution of the invariance conditions with the unknowns I_k:

  $$\mathbf{L}_\alpha(z)\ I_k(z) = 0$$

  The invariants $I_k(z)$ is determined by an algorithmic procedure, which uses symmetry techniques based on the method of characteristics and techniques of substitution.
- The discrete invariant scheme is written as:

  $$\mathcal{F}(I_1(z), \ldots, I_\theta(z)) = 0$$

  The obtained scheme depends on the discrete invariants $I_k(z)$ and inherit the whole symmetries of Euler equations. $\mathcal{F}$ is chosen in such a way that it is consistent with the Euler equations. θ is the difference between the cardinal number of the stencil and the dimension of the matrix composed of the coefficients of the infinitesimal generators.

The symmetry techniques derive difference equations with Lagrangian formulation, because of the preservation of the Galilean transformation. The numerical method uses an adaptative mesh method. The numerical resolution is simultaneously done for the fixed computational domain, and the moving physical domain. A conservative formulation is adopted.

4 Numerical Results

The numerical test case is the propagation of a linear Gaussian pulse ($L = 0.0625$, $h = 0.001$). The Gaussian pulse is initially located at the center of the domain, at $t = 0$:

$$\rho = 1 + h * \exp\big(-\frac{(x-0.5)^2}{2L^2}\big), \quad u = 0.5, \quad p = \frac{1}{\gamma} + h * \exp\big(-\frac{(x-0.5)^2}{2L^2}\big)$$

Figure 3 shows the evolution of the density at different time steps. The numerical solution of the discrete invariant method agrees well with the exact solution. Figures 4 show the evolution of the L^∞ error norm for the Lax Wendroff scheme and the discrete invariant method in different frames stemmed from Galilean transformations. Each frame corresponds to a specific value

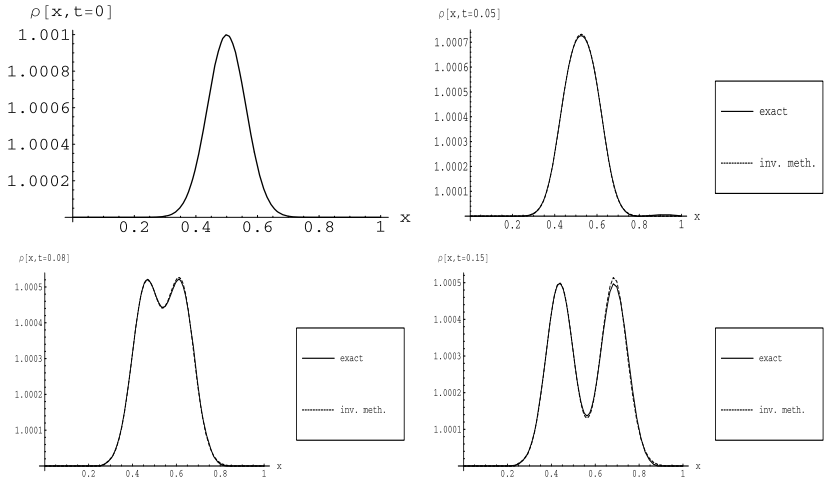

Fig. 3. Propagation of a Gaussian pulse (t=0, t=0.05, t=0.08, t=0.125) with the discrete invariant method

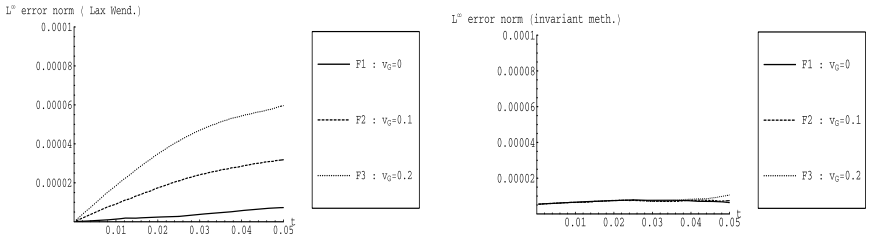

Fig. 4. L^∞ error norm for the Lax Wendroff scheme and the discrete invariant one in the frames F1, F2, F3

of the velocity v_G of the Galilean transformation. The L^∞ error norm for the Lax-Wendroff scheme depends highly on the velocity. With the discrete invariant method, the dependency of the error upon the velocity is visibly minimized. The numerical solution remains the same when the frame changes under the Galilean transformations.

5 Conclusion

Symmetry theory is applied to computational methods, to build numerical scheme which inherit the physical properties of the original equations. Particularly, the discrete invariant method initiated by Dorodnitsyn is implemented for an inviscid and compressible flow. The implementation leads to the minimization of the dependency of the numerical error upon specific frames. In close future, an improvement of the numerical properties of the discrete invariant methods will be studied in order to investigate the treatment of sharp discontinuities. Then the method will be implemented to the Riemann problem, with the propagation of shocks and contact discontinuity.

References

[BDK97] Bakirova, M.I., Dorodnitsyn, V.A., Kozlov, R.: Symmetry-preserving difference schemes for some heat transfert equations. J. Phys. A: Math. Gen. 30, 8139–8155 (1997)

[BHR96] Budd, C.J., Huang, W., Russell, R.D.: Moving mesh methods for problems with blow-up. SIAM J.Sci. Comput. 17(2), 305–327 (1996)

[CH08] Chhay, M., Hamdouni, A.: Consistance en symétrie. Rapport technique, Université de la Rochelle (2008)

[Dor91] Dorodnitsyn, V.A.: Transformation groups in net spaces. J. Sov. Math. 55(1), 1490–1517 (1991)

[Ibr96] Ibragimov, N.H.: CRC Handbook of Lie Group Analysis of Differential Equations, vol. 1,2,3. CRC Press, Boca Raton (1994-1996)

[Olv86] Olver, P.J.: Applications of Lie Groups to Differential Equations. Springer, New-York (1986)

[Olv01] Olver, P.J.: Geometric foundations of numerical algorithms and symmetry. Appl. Alg. Engin. Comp. Commun 11, 417–436 (2001)

[RH05] Razafindralandy, D., Hamdouni, A.: Subgrid models preserving the symmetry group of the navier-stokes equations. Comptes Rendus Mécanique 333, 481–486 (2005)

[RHO07] Razafindralandy, D., Hamdouni, A., Oberlack, M.: Analysis and development of subgrid turbulence models preservingthe symmetry properties of navier-stokes equations. Eur. J. Mech. B Fluid 26, 531–550 (2007)

[Sho83] Shokin, Y.I.: The method of differential approximation. Springer, Heidelberg (1983)

[YS76] Yanenko, N.N., Shokin, Y.I.: Group classification of difference schemes for a system of one-dimensional equations of gas dynamics. Amer. Math. Soc. Transl. 2(104), 259–265 (1976)

A Numerical Diffusion Flux Based on the Diffusive Riemannproblem

Claus-Dieter Munz, Gregor Gassner, and Frieder Lörcher

Institute for Aerodynamics and Gasdynamics, University of Stuttgart, 70569 Stuttgart, Germany
{munz, gassner, loercher}@iag.uni-stuttgart.de

1 Introduction

In finite volume (FV) or discontinuous Galerkin (DG) schemes the approximate solution may jump at the grid cell interface. Any physical phenomena which can not be resolved on the given grid will result in such a jump. If the time evolution of these jumps can be approximated in a stable and consistent way, then the numerical scheme does not generate spurious oscillations and gives meaningful mean values of under-resolved phenomena. In his pioneering work Godunov proposed to approximate the convection flux between grid cells by solving the break down of the jump into different waves. Approximations of this approach are called Godunov-type schemes and are described, e.g., in the book of Toro [TOR99].

In the case of diffusion the situation is different. The usual approach in FV schemes is to reconstruct data at the interface, but under the assumption of continuity. This is motivated by the fact that the solution of the Cauchy problem for diffusion is continuous even for discontinuous initial data. But, this pragmatic approach means that convection and diffusion is treated in different ways. Furthermore, such a finite difference type approximation needs a couple of grid cells within a profile not to generate spurious oscillations at steep viscous profiles. For DG schemes other approaches have been proposed which take into account the jump via some sort of penalization. This idea goes back already to symmetric interior penalty (SIP) of Nitsche [NIT71]. Another technique is based on the reformulation of the parabolic equation to a first order system as proposed in [BR97, CS98].

In the following we propose to follow Godunov's way also for diffusion and to base the flux on the local diffusion of a discontinuity. We look at the exact solution of the so called diffusive generalized Riemann problem. We start with a scalar linear diffusion equation and extent the results to systems of diffusion equations. A linearization leads to the general nonlinear case. We discuss the use of these fluxes in FV and DG schemes and show DG results for the compressible Navier-Stokes equations.

2 The Generalized Diffusive Riemannproblem

Linear Scalar Case

In a first step we consider the one-dimensional scalar linear diffusion problem

$$v_t = (\mu(x)v_x)_x \quad \text{with} \quad \mu(x) = \begin{cases} \mu^+, & \text{for } x > 0, \\ \mu^-, & \text{for } x < 0, \end{cases} \tag{1}$$

with initial values

$$v(x,0) = \begin{cases} u^+ + x\,u_x^+, & \text{for } x > 0, \\ u^- + x\,u_x^-, & \text{for } x < 0. \end{cases} \tag{2}$$

We use the exact solution of this diffusive generalized Riemann problem (dGRP) to get information about the local behavior of the solution at jumps.

To obtain the exact solution we use Laplace transformation. The general solution is first calculated separately in the regions $x < 0$ and $x > 0$ in which the diffusion coefficients are constant. With $w(x,s) := \mathcal{L}\{v(x,t)\}$ the Laplace transformations of initial value problem (1),(2) read as

$$w_{xx}^{\pm} - \frac{s}{\mu^{\pm}} w^{\pm} = -\frac{u^{\pm} + x u_x^{\pm}}{\mu^{\pm}}, \tag{3}$$

where w^+ and w^- denotes the solution for $x > 0$ and $x < 0$, respectively.

The solutions of these two ordinary differential equations contain four constants which are determined by the conditions that the solutions do not grow exponentially for $|x| \to \infty$ and that the solutions as well as the flux $f^d := \mu(x)v_x$ is continuous at $x = 0$. The transformation back results in the flux at $x = 0$

$$f^d(0,t) = \frac{[\![u]\!]\sqrt{\mu^+\mu^-}}{\sqrt{\pi t}(\sqrt{\mu^+} + \sqrt{\mu^-})} + \frac{\sqrt{\mu^+} f^{d-} + \sqrt{\mu^-} f^{d+}}{\sqrt{\mu^+} + \sqrt{\mu^-}}, \tag{4}$$

where $[\![u]\!] = u^+ - u^-$ denotes the jump. This flux is singular at $t = 0$, but the integral average over a finite time step exists as an improper integral

$$g^d := \frac{1}{\Delta t} \int_0^{\Delta t} f^d(0,t)dt = \frac{2\,[\![u]\!]\sqrt{\mu^+\mu^-}}{\sqrt{\Delta t}\sqrt{\pi}(\sqrt{\mu^+} + \sqrt{\mu^-})} + \frac{\sqrt{\mu^+} f^{d-} + \sqrt{\mu^-} f^{d+}}{\sqrt{\mu^+} + \sqrt{\mu^-}} \tag{5}$$

and is defined to be the desired numerical diffusion flux. The state u_{dGRP} at the initial jump is given as

$$u_{dGRP} = \lim_{t \to 0^+} v(0,t) = \frac{\sqrt{\mu^+}u^+ + \sqrt{\mu^-}u^-}{\sqrt{\mu^+} + \sqrt{\mu^-}}. \tag{6}$$

If the diffusion coefficient does not jump, then this expression simplifies to the arithmetic mean of the state left and right, denoted by $\{u\}$. The numerical diffusion flux (5) reads in this case as

$$g^d := \frac{\sqrt{\mu}}{\sqrt{\Delta t \pi}} [\![u]\!] + \frac{1}{2}(f^{d-} + f^{d+}) = \mu \left(\eta \frac{[\![u]\!]}{\Delta x} + \{u_x\} \right). \tag{7}$$

The dGRP flux (7) has a similar form as that of the SIP scheme and may be considered as its mathematical justification due to the behavior of local solutions. The parameter $\eta = \Delta x / \sqrt{\Delta t \mu \pi}$ serves as the penalization parameter. Its minimal value can be determined by considering the stability of the method, see [LGM08].

Linear Systems

We consider next the linear diffusion system

$$U_t - \underline{D}\, U_{xx} = 0, \tag{8}$$

with the assumption that the diffusion matrix $\underline{D}$ is positive semi-definite and diagonalizable. We denote by $\underline{T}$ the right eigenvector matrix and introduce the variables $W = \underline{T}^{-1} U$. This transformation decouples the system and yields for each component of W a scalar linear diffusion equation with diffusion coefficients given by the eigenvalues of $\underline{D}$. For each of these scalar equations, flux (7) is used. After back-transformation into the original variables, the dGRP flux of the linear system (8) reads as

$$\frac{1}{\Delta t} \int_0^{\Delta t} \underline{D}\, U_x(x=0,t)\, dt = \underline{D} \left(\eta \frac{[\![U]\!]}{\Delta x} + \{U_x\} \right). \tag{9}$$

Non-linear Systems

For a non-linear diffusion system

$$U_t - (\underline{D}(U)\, U_x)_x = 0, \tag{10}$$

the exact solution is not longer known. A suitable approach seems to linearize the non-linear system at a state $\widetilde{U} = \widetilde{U}(U^+, U^-)$ and to use the dGRP flux (9) for the resulting linear system. In the simulations for the compressible Navier-Stokes equations shown in the next chapter, we use simply the arithmetic meanvalue $\widetilde{U} = \{U\}$. For cases where the diffusion coefficients have stronger jumps the average given by (6) is more appropriate.

Multi-dimensional Case

The extension to the multidimensional case is straightforward, when we assume that the underlying problem is invariant with respect to rotation. For

the approximation of the diffusion flux $\mathbf{g}^d$ into normal direction at grid cell surface, the gradient of the state variable $\boldsymbol{\nabla} u$ is rotated from the global $\mathbf{x}$-system into the $\boldsymbol{\xi}$-system aligned with normal and tangential directions of the side surface. The transformation can be written as

$$\boldsymbol{\nabla}_{\boldsymbol{\xi}} u = \underline{T}\, \boldsymbol{\nabla}_{\mathbf{x}} u, \tag{11}$$

where the subscripts denote the gradients with respect to the corresponding coordinates. Using the rotational invariance

$$\mathbf{f}^d(u, \boldsymbol{\nabla}_{\mathbf{x}} u) \cdot \mathbf{n} = f_1^d(u, \boldsymbol{\nabla}_{\boldsymbol{\xi}} u) \quad \text{for all } \mathbf{n} \in \mathbb{R}^d, \tag{12}$$

we can write

$$\mathbf{f}^d(u, \nabla_{\mathbf{x}} u) \cdot \mathbf{n} = \mu u_{\xi_1} =: f_{\mathbf{n}}^d. \tag{13}$$

Hence, the multi-dimensional problem can be reduced to a one-dimensional problem into the normal direction ξ_1. In an analogous way we get for the numerical fluxes

$$\mathbf{g}^d(\mu^{\pm}, u^{\pm}, \boldsymbol{\nabla}_{\mathbf{x}} u^{\pm}) \cdot \mathbf{n} =: \mathbf{g}_{\mathbf{n}}^d(\mu^{\pm}, u^{\pm}, u_{\xi_1}^{\pm}) \tag{14}$$

where "$-$" and "$+$" denote the values at the grid cell interfaces from inside and outside of the considered grid cell. More details are given in [GLM08].

3 The Use in High Order DG and FV schemes

The big advantage of the dGRP flux in a FV scheme is that the original reconstruction for advection can directly be used for the diffusion term, too. The functional values at the interface have the order of the reconstruction. Due to the fact that derivatives are involved in the diffusion flux we have to differentiate the local dGRP solution, by which one order of accuracy is lost. Hence, if we perform a polynomial reconstruction of degree k, then the convection flux is of order $k+1$, while the diffusion flux is of order k. This is avoided, if under the assumption of smoothness a second central reconstruction is done for the derivatives at the interface which is up to now the usual approach. But, using the dGRP-flux it becomes possible to approximate a with respect to the given grid steep viscous profile within a few grid cells similar to a shock wave. This may increase the robustness of the calculations.

In a DG scheme the approximation of diffusion terms have an optimal order of convergence, if the approximation is adjoint consistent, see, e.g., [ABCM02]. This can be obtained in the DG variational formulation by applying the integration by parts twice to the diffusion term. For a scalar linear one dimensional diffusion problem, the *novel* weak formulation is given by

$$\int_Q u_t \phi \, dx - \int_{\partial Q} u_x \phi \, ds + \int_{\partial Q} u \phi_x \, ds - \int_Q u \phi_{xx} dx = 0 \tag{15}$$

where Q is an arbitrary grid cell and ϕ denotes a test function. See [GLM07] for details.

4 Example: Compressible Navier-Stokes Equations

We show numerical results for the flow past a sphere at Mach number $M = 0.3$ and Reynolds number $Re = 300$. The sphere has the radius $r = 1$ and is centered at $\mathbf{x} = 0$. This is a calculation with an explicit space-time DG scheme as proposed in [LGM07, GLM08] on which the advection flux and the diffusion flux are combined. The very flexible unstructured grid is shown in figure 1. Prisms around the surface of the body to capture the boundary layer very well are combined with tetrahedrons and then with quite regular "Cartesian" grid cells for the outer flow. Although the mesh is non-conforming, the resulting discretization is fully conservative and high order accurate. To capture the geometry, prims with curved boundaries are used. The results for a simulation with $4th$ order polynomials are listed in Table 1 and show quite good agreement with incompressible reference results In figure 2 the structure of the vortices are shown using the λ_2 vortex detection criterium.

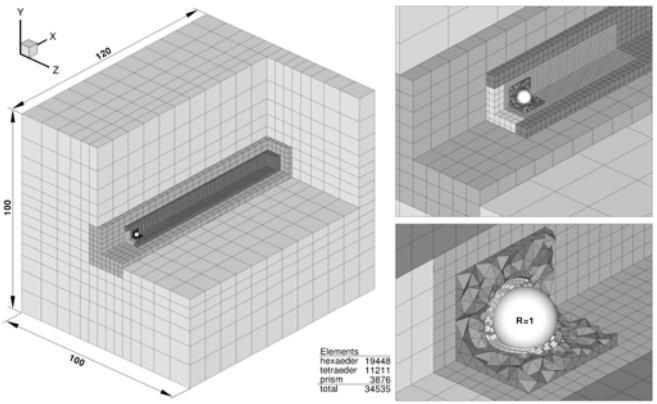

Fig. 1. Unstructured grid

Table 1. Drag coefficient, lifting coefficient and Strouhal number

	C_D	ΔC_D	C_L	ΔC_L	Sr
	0.672	0.0031	−0.065	0.012	0.135
Johnson&Patel [JP99]	0.656	0.0035	−0.069	0.016	0.137
Tomboulides [TOM93]	0.671	0.0028	-	-	0.136

Fig. 2. Isometric view of λ_2 isosurface

References

[ABCM02] Arnold, D.N., Brezzi, F., Cockburn, B., Marini, L.D.: Unified analysis of discontinuous Galerkin methods for elliptic problems. SIAM J. Numer. Analysis 39, 1749–1779 (2002)

[BR97] Bassi, F., Rebay, S.: A High-Order Accurate Discontinuous Finite Element Method for the Numerical Solution of the Compressible Navier-Stokes Equations. J. Comput. Phys. 131, 267–279 (1997)

[CS98] Cockburn, B., Shu, C.-W.: The local discontinuous Galerkin method for time-dependent convection diffusion systems. SIAM J. Numer. Analysis 35, 2440–2463 (1998)

[GLM07] Gassner, G., Lörcher, F., Munz, C.-D.: A contribution to the construction of diffusion fluxes for finite volume and discontinuous Galerkin schemes. J. Comput. Phys. 224, 1049–1063 (2007)

[GLM08] Gassner, G., Lörcher, F., Munz, C.-D.: A discontinuous Galerkin scheme based on a space-time expansion. II. Viscous compressible flow in multi space dimensions. J. of Sci. Comp. 34, 260–286 (2008)

[JP99] Johnson, T.A., Patel, V.C.: Flow past a sphere up to a Reynolds number of 300. J. Fluid. Mech. 378, 19–70 (1999)

[LGM07] Lörcher, F., Gassner, G., Munz, C.-D.: A discontinuous Galerkin scheme based on a space-time expansion. I. Inviscid compressible flow in one space dimension. J. Sci. Comp. 32, 175–199 (2007)

[LGM08] Lörcher, F., Gassner, G., Munz, C.-D.: An explicit discontinuous Galerkin scheme with local time-stepping for general unsteady diffusion equations. J. Comput. Phys. 227, 5649–5670 (2008)

[NIT71] Nitsche, J.A.: Über ein Variationsprinzip zur Lösung von Dirichlet-Problemen bei Verwendung von Teilräumen, die keinen Randbedingungen unterworfen sind. Abh. Math. Sem. Univ. Hamburg 36, 9–15 (1971)

[TOM93] Tomboulides, A.G.: Flow past a sphere up to a Reynolds number of 300. Princeton University, Princeton (1993)

[TOR99] Toro, E.F.: Riemann Solvers and Numerical Methods for Fluid Dynamics. Springer, Heidelberg (1999)

Part 7
Algorithm 2

“*This page left intentionally blank.*”

Enhancement of the Computational Efficiency of UFP via a MWM

Hyung-Min Kang[1], Kyu-Hong Kim[2], Dong-Ho Lee[2], and Do-Hyung Lee[3]

[1] BK21 School for Creative Engineering Design of Next Generation Mechanical and Aerospace Systems, Seoul National University, Seoul, Korea
kangm@snu.ac.kr
[2] School of Mechanical and Aerospace Engineering and Institute of Advanced Aerospace Technology, Seoul National University, Seoul, Korea
aerocfd1@snu.ac.kr, donghlee@snu.ac.kr
[3] Department of Mechanical Engineering, Hanyang University, Ansan, KyungKi-Do, Korea
dohyung@hanyang.ac.kr

1 Introduction

Recently, in Computational Fluid Dynamics (CFD), the computational accuracy and efficiency have been enhanced with the aids of numerical schemes and computing systems. However, for the accurate calculations of flow problems, dense grid points are still needed in the spatial domain. Moreover, the increase of grid points results in the decrement of the size of the cells, which limits the size of time step. Therefore, much computational cost is necessary for accurate calculations of flow problems, especially for unsteady cases.

In spite of needing dense grid systems, it is the waste of the computational resources to use fine grids in the whole domain because the majority of the CFD datasets is smooth region where the accurate solutions can be obtained with relatively coarse grids. Adaptive methods can be a solution for this situation and adaptive wavelet methods have been studied as good adaptive tools. For examples, Holmström proposed the algorithm that uses the interpolating wavelet transformation to organize an adaptive dataset.[Hol99] Sjögreen also used a multi-resolution scheme based on the interpolating wavelet transformation to solve the compressible Euler equations.[Sjö95]

The objective of this study is the improvement of the computational efficiency of unsteady flow problems while the numerical accuracy of a solution is automatically maintained. For achieving this purpose, the threshold value developed in the previous research[KKL08] is extended to unsteady flow problems in order to maintain the spatial and the temporal accuracy of conventional CFD schemes. And the general adaptive wavelet transformation procedure is changed by adopting residual interpolation. Throughout these processes, the accuracy of a conventional solver is conserved and the

computational cost is substantially reduced. In order to demonstrate the efficiency and the accuracy of the developed method, the method is applied to a complicated shock-vortex interaction problem.

2 Implementation of the Modified Wavelet Method

In this research, the two-dimensional Euler equations are used as the governing equations of unsteady flow problems. The generalized coordinate transformed two-dimensional Euler equations are written as Eq. (1).

$$\frac{\partial \overline{Q}}{\partial \tau} = -[\frac{\partial \overline{E}}{\partial \xi} + \frac{\partial \overline{F}}{\partial \eta}] = -R^n_{i,j}, \tag{1}$$

$$with \quad \overline{Q} = \frac{Q}{J},\ \overline{E} = \frac{1}{J}[\xi_t Q + \xi_x E + \xi_y F],\ \overline{F} = \frac{1}{J}[\eta_t Q + \eta_x E + \eta_y F].$$

Here, our objective is to improve the computational efficiency of unsteady flow problems with maintaining the numerical accuracy of conventional solvers. For these purposes, the modified threshold method is applied in order to maintain the spatial and the temporal accuracy of conventional schemes. And the general adaptive wavelet procedure is changed by adopting residual interpolation at the n time step and time integration is performed on the entire domain. The overall procedure of modified adaptive wavelet method is as follows.

First, by the decomposition process, the estimation of flow variables is performed. If we assume that (i, j) cell is even numbered cell and $(i+1, j)$, $(i, j+1)$ and $(i+1, j+1)$ are odd numbered cells, the values at even numbered cell is saved to a point in the coarser level grid. At odd numbered cells, we approximate the original values by interpolating polynomial. In this research, our concentration is focused on unsteady flow problems and a tiny change of flow properties may grow large with the passage of time. Therefore, we use the 6^{th} order of interpolating polynomial in order to capture the tiny variation of flow properties, accurately. The equations with 6^{th} order of accuracy for the approximation procedure of two dimensional flow problems are presented in Eq. (2).

$$\begin{aligned}
\widetilde{Q}^n_{i+1,j} &= \frac{1}{256}(3Q^n_{i-4,j} - 25Q^n_{i-2,j} + 150Q^n_{i,j} + 150Q^n_{i+2,j} - 25Q^n_{i+4,j} + 3Q^n_{i+6,j}) \\
\widetilde{Q}^n_{i,j+1} &= \frac{1}{256}(3Q^n_{i,j-4} - 25Q^n_{i,j-2} + 150Q^n_{i,j} + 150Q^n_{i,j+2} - 25Q^n_{i,j+4} + 3Q^n_{i,j+6}) \\
\widetilde{Q}^n_{i+1,j+1} &= 0.5 \times (\frac{3}{256}Q^n_{i-4,j-4} - \frac{25}{256}Q^n_{i-2,j-2} + \frac{75}{128}Q^n_{i,j} + \frac{75}{128}Q^n_{i+2,j+2} \\
&\quad - \frac{25}{256}Q^n_{i+4,j+4} + \frac{3}{256}Q^n_{i+6,j+6}) + 0.5 \times (\frac{3}{256}Q^n_{i-4,j+6} - \frac{25}{256}Q^n_{i-2,j+4} \cdot \\
&\quad + \frac{75}{128}Q^n_{i,j+2} + \frac{75}{128}Q^n_{i+2,j} - \frac{25}{256}Q^n_{i+4,j-2} + \frac{3}{256}Q^n_{i+6,j-4})
\end{aligned} \tag{2}$$

After the approximation, we calculate the difference values between original values and approximated values as Eq. (3). These routines are performed

multi-resolutionally and consequently, all difference values except the original values in coarsest level grid are calculated.

$$d^n_{i+1,j} = Q^n_{i+1,j} - \widetilde{Q}^n_{i+1,j}, d^n_{i,j+1} = Q^n_{i,j+1} - \widetilde{Q}^n_{i,j+1}$$
$$d^n_{i+1,j+1} = Q^n_{i+1,j+1} - \widetilde{Q}^n_{i+1,j+1} \quad (3)$$

After calculating the difference values, the modified threshold value ϵ' is defined in order to maintain the l^{th} order of spatial accuracy and the m^{th} order of temporal accuracy of the numerical schemes simultaneously, as given by Eq. (4). Based on this value ϵ', we control the flag values of the grid points. If difference value is larger than ϵ', the flag value is determined as 1 and the point is included in $I(\epsilon')$ dataset; if not, the flag value is set as 0 and the point is excluded from $I(\epsilon')$ dataset. Throughout this process, the dataset is adapted to the flow features while maintaining the numerical accuracy of conventional schemes.

$$\epsilon' = min[\epsilon, max((\Delta x)^l, CFL^m \cdot (\Delta x)^m)]. \quad (4)$$

Then, flux values are only calculated at the included cells in $I(\epsilon')$ dataset by the conventional spatial discretization schemes and residual values are computed at these cells. At excluded cells in the dataset, residual values are interpolated by using the same interpolating polynomial as Eq. (2). Here, wavelet transformation and the residual interpolation are performed at the same time. Then, the residual interpolation can be executed based on the $I(\epsilon')$ dataset at n time step and there is no problem due to time discrepancy. And time integration is performed on the whole computational domain until some criteria are satisfied.

3 Numerical Test and Discussion

To demonstrate that the modified adaptive wavelet method enhances the computational efficiency and maintains the numerical accuracy of conventional CFD schemes, it is applied to a shock-vortex interaction problem.[IH99] The computational domain is set as $0 \leq x, y \leq 40$. The Mach number of vortex is 0.39 and the initial vortex core is located at the point (7, 7). This vortex is propagated to a stationary normal shock with the Mach number of 1.29. And the normal shock is inclined by 45 degrees at the point (10, 10).

The governing equations are the two-dimensional Euler equations. For spatial discretization, AUSMPW+ method [KKR01] with the 2^{nd} order MUSCL scheme [Van97] is used. For time integration, the 4^{th} order Runge-Kutta method with CFL=1 is used. ϵ is set as 10^{-5}. Then, the modified threshold value is presented as Eq. (5).

$$\epsilon' = min[10^{-5}, max((\Delta x)^2, CFL^4 \cdot (\Delta x)^4)]. \quad (5)$$

Figure 1 shows adaptive datasets according to the wavelet decomposition level at t=15sec. It can be known that the datasets follow the flow features accurately and many cells are remained near the vortex and shock regions.

In the other smooth regions, the changes of the flow properties are negligible and the remaining cells are sparsely distributed. Also, in these figures, the adaptive datasets between level 3 and 4 are very similar. Therefore, there is a proper level of wavelet decomposition according to the complexity of solutions. In this case, the appropriate wavelet decomposition level is 3.

Throughout the application of modified adaptive wavelet method, the computation becomes about 2.0 times faster when the wavelet decomposition level is 3. The L2 error between the solutions of the conventional solver and the modified adaptive wavelet method is 1.26×10^{-7}. The overall efficiency improvement and the L2 error according to wavelet decomposition level are summarized in Table 1. If the number of the cells becomes large, the higher computational efficiency can be obtained because the portion of the region where the flow properties change smoothly increases and the compression ratio of the wavelet method can be enhanced. Therefore, the present method can become more effective in the flow problems that require a huge number of grid points.

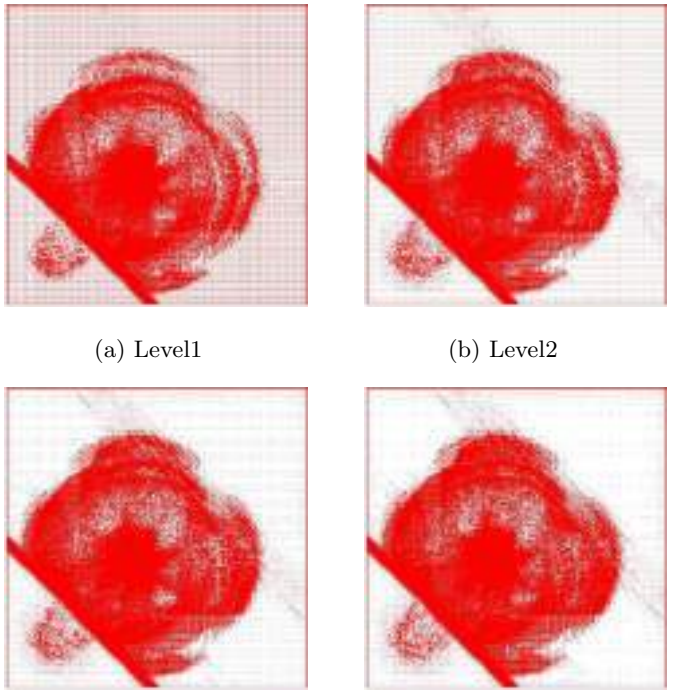

(a) Level1 (b) Level2

(c) Level3 (d) Level4

Fig. 1. Adaptive datasets of shock-vortex interaction problem according to wavelet decomposition level at t=15sec

Table 1. Results of efficiency improvements and L2 error for the shock-vortex interaction problem; Grid size is 481 × 481

Wavelet Decomposition	L2 Error	CPU Time	Time Ratio
Conventional		1162.27	
Level1	3.96E-08	921.75	1.26
Level2	7.08E-08	629.52	1.85
Level3	1.26E-07	581.58	2.00
Level4	2.56E-07	578.70	2.01

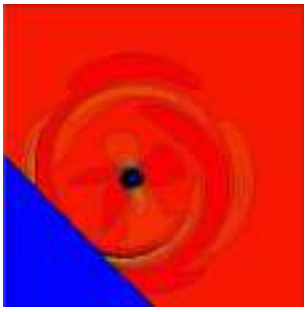

(a) Conventional method

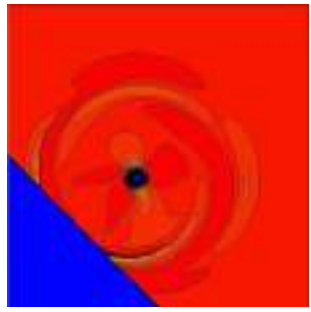

(b) Modified wavelet method

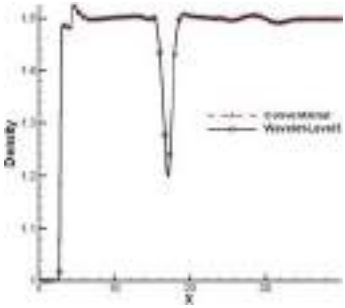

(c) Comparison of density at y=17

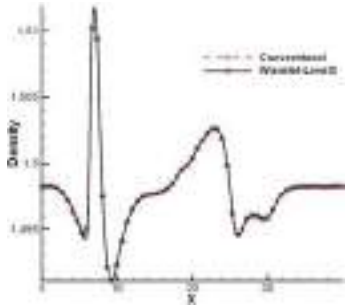

(d) Comparison of density at y=25

Fig. 2. Density plots of shock-vortex interaction problem at t=15sec; the wavelet decomposition level is 3

Figures 2 (a) and (b) show the density distributions of conventional CFD schemes and the modified adaptive wavelet method at t=15sec, respectively. The comparisons of the density distributions at y=17 and y=25 are presented in Figs. 2 (c) and (d), respectively. The density distributions are very similar to each other. Also in Figs. 2 (c) and (d), the original features around the

vortex core or the shock discontinuity region are represented exactly by the modified adaptive wavelet method.

4 Conclusion

Throughout this research, the modified adaptive wavelet method is proposed for the unsteady flow problems in order to increase the overall computational efficiency of a conventional CFD solver while maintaining the original numerical accuracy of CFD schemes. First, the threshold value is modified in order to maintain the spatial and temporal accuracy of conventional CFD schemes, simultaneously. Second, residual interpolation is performed at the n time step, not at the n+1 time step to eliminate the problems due to the time discrepancy. This modified adaptive wavelet method is applied to the shock-vortex interaction problem. And the computational cost is reduced by half with maintaining the numerical accuracy of conventional CFD schemes.

Acknowledgement

This work was supported by the second stage of the Brain Korea 21 Project in 2008. Also, this work was supported by the Korea Science and Engineering Foundation(KOSEF) grant funded by the Korea government(MEST) (No. R01-2006-000-10034-0).

References

[Hol99] Holmström, M.: Solving hyperbolic PDEs using interpolation wavelets. SIAM J. Sci., Comput. 21, 405–420 (1999)

[Sjö95] Sjögreen, B.: Numerical experiments with the multiresolution scheme for the compressible Euler equations. J. Comput. Phys. 117, 251–261 (1995)

[KKL08] Kang, H., Kim, K., Lee, D.: Improvement in computational efficiency of Euler equations via a modified Sparse Point Representation method. Computers & Fluids 37, 265–280 (2008)

[IH99] Inoue, O., Hattori, Y.: Sound generation by shock-vortex interactions. J. Fluid Mechanics 380, 81–116 (1999)

[KKR01] Kim, K., Kim, C., Rho, O.: Methods for the accurate computations of hypersonic flows: I. AUSMPW+ scheme. J. Comput. Phys. 174, 38–80 (2001)

[Van97] Van Leer, B.: Towards the ultimate conservative difference scheme V. A Second-order sequel to Godunov's method. J. Comput. Phys. 135, 229–248 (1997)

A High-Order Accurate Implicit Operator Scheme for Solving Steady Incompressible Viscous Flows Using Artificial Compressibility Method

Kazem Hejranfar[1] and Ali Khajeh Saeed[2]

[1] Associate Professor, Aerospace Engineering Department,
Sharif University of Technology, Iran
[2] MSc. Student, Aerospace Engineering Department,
Sharif University of Technology, Iran

Abstract. This paper uses a fourth-order compact implicit operator scheme for solving 2D/3D steady incompressible flows using the artificial compressibility method. To stabilize the numerical solution, numerical dissipation terms and/or filters are used. Results obtained for test cases are in good agreement with the available numerical and experimental results. A sensitivity study is also conducted to evaluate the effects of grid resolution and pseudocompressibility parameter on accuracy and convergence rate of the solution. The effects of filtering and numerical dissipation on the solution are also investigated.

Keywords: Incompressible flows, Fourth-order implicit operator scheme, Numerical dissipation.

The high-order compact method used herein is an alternating direction implicit operator scheme, proposed by Ekaterinaris (1999, 2000) for computing 2-D compressible flows. In the present study, this numerical scheme is efficiently implemented to solve the incompressible Navier-Stokes equations in the primitive variables formulation using the artificial compressibility method. For space discretizing the convective fluxes, fourth-order centered spatial accuracy of the implicit operators is efficiently obtained by performing compact space differentiation in which the method uses block-tridiagonal matrix inversions. High-order spectral-type low-pass compact filters are used to regularize the numerical solution and eliminate spurious modes. The numerical dissipation terms (6^{th}-order) are also used to stabilize the numerical method. The numerical dissipation term is added to the differenced equations while filtering is a postprocessing procedure. In this study, the high-order compact implicit operator scheme is also extended for computing three-dimensional incompressible flows. A sensitivity study is performed to examine the accuracy and convergence rate of the solution to grid size and the pseudocompressibility parameter β. The effects of filtering and numerical dissipation on the solution are also studied.

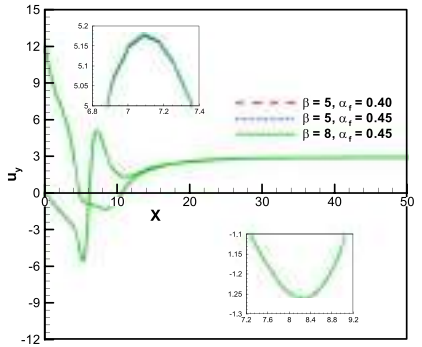

Fig. 1. Effect of β and α_f on wall shear for backward facing step at Re=800

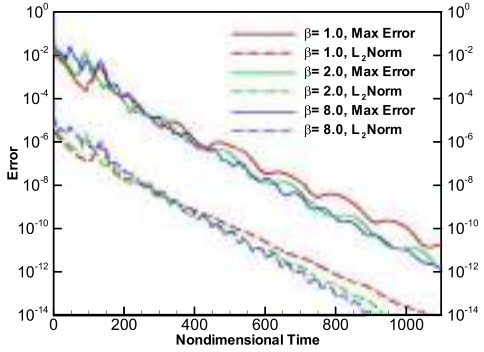

Fig. 2. Effect of β on convergence rate of solution for backward facing step at Re=800

Some of obtained results are presented herein. Figures 1 through 4 show the results for the flow in a 2- D backward facing step. As shown in Figs. 1 and 2, the results are not very sensitive to the values of the pseudocompressibility parameter β and also the filtering coefficient α_f. The results indicate that values of the pseudocompressibility parameter in the range of 2-10 give a faster convergence. Figure 3 illustrates the computed flowfield for the backward facing step shown by the velocity profiles and streamlines for 200$\leq$Re$\leq$1200. As shown in Fig. 4, the present results for reattachment location of the primary recirculating region in the range Re$\leq$400, in which the two-dimensionality of the flow retains, agree with the experiment. The fourth-order accuracy of the method is demonstrated through a grid refinement, as shown in Table 1.

The effects of the filtering coefficient α_f and the numerical dissipation value ϵ_e on the flowfield parameters (L_1,L_2,L_3 see Fig. 4) are presented in Table 2. The results show that a larger value of ϵ_e especially for coarse grid affects the solution. It can be seen that the filtering coefficient in the range $\alpha_f \geq 0.40$ give the reasonable results.

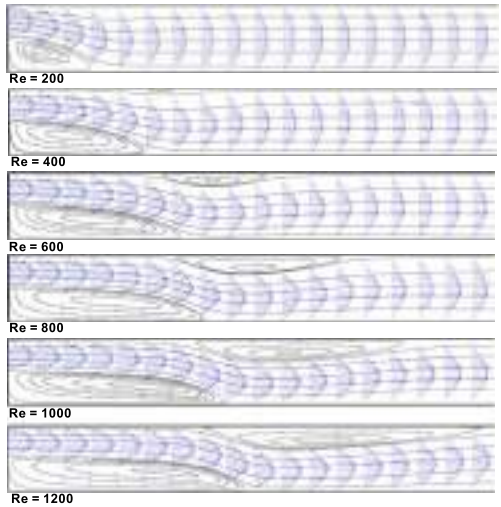

Fig. 3. Computed flowfield for backward facing step shown by velocity profiles and streamlines, Re=200-1200

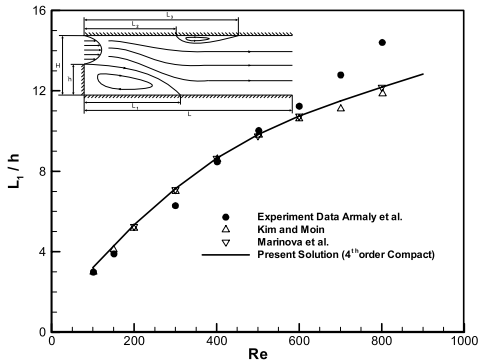

Fig. 4. Comparison of reattachment location for backward facing step flow for different Re

Table 1. Order of accuracy of the numerical method implemented

Grid	$Log(\Delta x)$	$Log\left(L_{2-Norm}\right)$
(300×60)	-0.7781	-5.2164
(600×120)	-1.0791	-6.3832
Order of Accuracy	-	$3.9\sim$

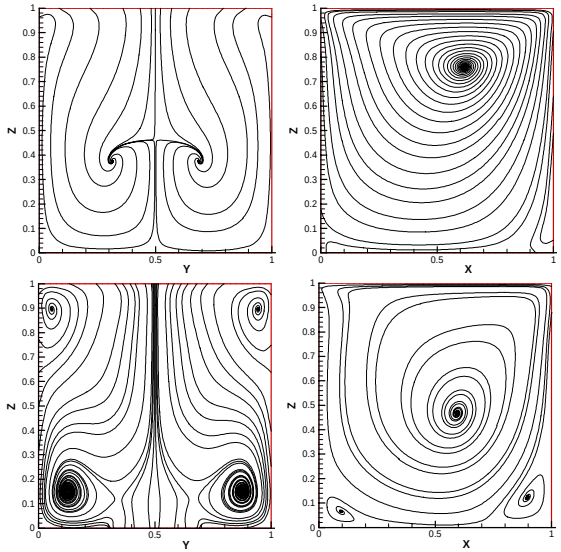

Fig. 5. Computed flowfield for 3-D cavity shown by streamlines at the planes x=0.5 and y=0.5 for Re=100 (top), and 1000 (bottom)

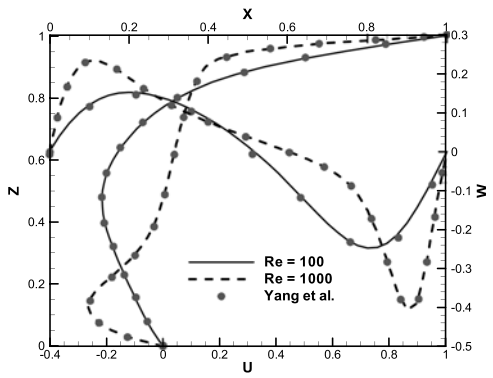

Fig. 6. Comparison of velocity profiles at the mid-planes x=y=0.5 and y=z=0.5 for 3-D cavity flow for Re=100,1000

Figure 5 gives the computed flowfield shown by streamlines at the *y*-*z* (*x*=0.5) and *x*-*z* (*y* =0.5) planes for the 3-D cavity for Re=100,1000. With increasing Re, the centers of the centered vortices in the *y*-*z* plane are considerably moved toward the lower wall and the vortices near the corners grow. Also, the center of primary vortex in the *x*-*z* plane is moved toward the center of the cavity. The present results for the velocity components (*u*,*w*) at the mid-planes (Fig. 6) are in agreement with the available numerical results. The present computations indicate that the

Table 2. Effects of α_f and ϵ_e on flowfield parameters L_1, L_2, L_3 at Re=800

Grid	(300×60)			(600×120)		
Parameter	L_1	L_2	L_3	L_1	L_2	L_3
$\varepsilon_e = 0.0025$	6.138	4.901	10.443	6.108	4.866	10.465
$\varepsilon_e = 0.0050$	6.137	4.900	10.451	6.106	4.864	10.468
$\varepsilon_e = 0.0100$	6.109	4.870	10.458	6.098	4.855	10.471
$\alpha_f = 0.35$	6.098	4.857	10.466	6.093	4.850	10.473
$\alpha_f = 0.40$	6.095	4.853	10.465	6.093	4.850	10.473
$\alpha_f = 0.45$	6.088	4.846	10.463	6.092	4.850	10.472

high-order compact implicit operator scheme used is robust, accurate and efficient for computing the incompressible flow problems.

References

Ekaterinaris, J.A.: Implicit, High-Resolution, Compact Schemes for Gas Dynamics and Aeroacoustics. Journal of Computational Physics 156, 272–299 (1999)

Ekaterinaris J.A.: Implicit high-order accurate in space algorithms for the NavierStokes equations. AIAA Journal 38(6), 1594–1602 (2000)

“*This page left intentionally blank.*”

Development of a Coupled and Unified Solution Method for Fluid-Structure Interactions

V. Sankaran[1], J. Sitaraman[2], B. Flynt[3], and C. Farhat[3]

[1] Aeroflightdynamics Directorate, Ames Research Center, CA, USA
vsankaran@mail.arc.nasa.gov
[2] National Institute of Aerospace, Langley Research Center, USA
jaina@nianet.org
[3] Dept. of Mechanical Engineering, Stanford University, USA
bflynt@stanford.edu, cfarhat@stanford.edu

1 Introduction

Traditional fluid-structure solutions usually involve the use of distinct methodologies and codes, eg., finite-volume for the fluids and finite-element for the structural dynamics [GG92]. Such a strategy consequently involves the use of sub-iterations to ensure temporal accuracy [MM98]. Alternately, a staggered solution procedure that preserves temporal accuracy without sub-iterations may be employed [FL98]. Further, coupled implicit solution schemes have also been developed [FF92]. Despite these developments, issues remain regarding the accuracy of load transfers between the fluid and structural domains as well as the robustness and efficiency of loosely-coupled solution approaches. In this article, we consider a unified formulation that employs finite-volume solutions of both the fluid and structural counterparts and a fully coupled solution of the combined system. Specific attention is paid to the formulation of the interface flux balance between the fluid and structural zones to insure appropriate flux conservation at the interface as well as full implicitness of the non-linear solution procedure. The algorithm is applied to one-dimensional fluid-structure problems to demonstrate the capabilities of the method.

2 Technical Approach

Equations of Motion

The governing equations for coupled fluid, mesh motion and structural dynamics can be expressed using the Arbitrary Lagrangian-Eulerian (or ALE) formulation:

$$\frac{\partial}{\partial t}\int_V Q dV + \int_S E_i' dS_i = \int_S V_i dS_i + \int_V H dV \tag{1}$$

$$Q = \begin{pmatrix} \rho \\ \rho u_j \\ e \\ \rho^f u_j^f \\ d_j^f \\ \rho^s u_j^s \\ d_j^s \end{pmatrix} \qquad E_i' = \begin{pmatrix} \rho(u_i - u_i^f) \\ \rho u_j(u_i - u_i^f) + p\delta_{ij} \\ e(u_i - u_i^f) + pu_i \\ 0 \\ 0 \\ 0 \\ 0 \end{pmatrix} \qquad V_i = \begin{pmatrix} 0 \\ \tau_{ij}' \\ \kappa \partial T/\partial x_i + u_j \tau_{ij} \\ \tau_{ij}^f \\ 0 \\ \tau_{ij}^s \\ 0 \end{pmatrix}$$

$$H = \begin{pmatrix} 0 \\ 0 \\ \Phi \\ f_j^f + b_j^f + cu_j^f \\ u_j^f \\ f_j^s + b_j^s + cu_j^s \\ u_j^s \end{pmatrix}$$

$$\tau_{ij}' = \mu\left(\frac{\partial u_i}{\partial x_j} + \frac{\partial u_j}{\partial x_i}\right) + \delta_{ij}\lambda \nabla \cdot \mathbf{u}$$
$$\tau_{ij}^f = \frac{E^f}{2(1+\nu^f)}\left(\frac{\partial d_i^f}{\partial x_j} + \frac{\partial d_j^f}{\partial x_i}\right) + \delta_{ij}\frac{E^f \nu^f}{(1+\nu^f)(1-2\nu^f)}\nabla \cdot \mathbf{d}^f$$
$$\tau_{ij}^s = \frac{E^s}{2(1+\nu)}\left(\frac{\partial d_i^s}{\partial x_j} + \frac{\partial d_j^s}{\partial x_i}\right) + \delta_{ij}\frac{E^s \nu}{(1+\nu)(1-2\nu)}\nabla \cdot \mathbf{d}^s$$

In the above equation, the first three rows represent the standard fluid dynamics conservation laws, the next two are the pseudo-structural equations used to model the fluid-mesh motion and the last two are the structural equations. The stress terms in each case are also given above.

Preconditioning Formulation

Efficient numerical solution of the unsteady system demands the use of a dual-time scheme with preconditioning scaling of the pseudo-time derivatives:

$$\Gamma_p \frac{\partial}{\partial \tau}\int_V Q_p dV + \frac{\partial}{\partial t}\int_V Q dV + \int_S E_i' dS_i = \int_S V_i dS_i + \int_V H dV \qquad (2)$$

$$\Gamma_p = \begin{pmatrix} \rho_p' & 0 & \rho_T & 0 & 0 & 0 & 0 \\ u_j\rho_p' & \rho\delta_{ij} & u_j\rho_T & 0 & 0 & 0 & 0 \\ h_0\rho_p' - (1-\rho h_p) & \rho u_i & h_o\rho_T + \rho h_T & 0 & 0 & 0 & 0 \\ 0 & 0 & 0 & \frac{\rho^f}{\epsilon^f} & 0 & 0 & 0 \\ 0 & 0 & 0 & 0 & \frac{1}{\epsilon^f} & 0 & 0 \\ 0 & 0 & 0 & 0 & 0 & \frac{\rho^s}{\epsilon^s} & 0 \\ 0 & 0 & 0 & 0 & 0 & 0 & \frac{1}{\epsilon^s} \end{pmatrix}$$

The scalings of the fluid dynamic terms take their standard form (see for example [SZ04]), while the structural scalings are scalings of the time-step based on the eigenvalues of the structural system. In 1D, the eigenvalues are given by the longitudinal seismic velocities, eg., $\pm\sqrt{E^f/\rho^f}$ for the fluid-mesh motion terms. The scaling term is then defined as:

$$\epsilon_f = \frac{V}{\sqrt{E^f/\rho^f}} \qquad (3)$$

A similar expression can be used for the structural equations as well; however, as we will see later, the structural equations are partitioned from the fluid dynamics at the linear solver level for domain decomposition. Therefore, the corresponding pseudo time-step is naturally chosen to be commensurate with the structural eigenvalues, obviating the need for further scaling.

Discrete Formulation

The unified finite-volume formulation of the fluids and structural equation permits a common discretization framework to be employed for the entire system. For instance, the inviscid flux terms can be written as:

$$\mathbf{E'}_{k+1/2} = \frac{\mathbf{E'}_L + \mathbf{E'}_R}{2} - \frac{\Delta x}{2}|\sigma(\mathcal{A}')|(Q_R - Q_L) \tag{4}$$

There are two issues that come up with the discrete formulation. The first has to do with insuring that the discrete geometric conservation law (GCL) is satisfied. Substituting for constant flow into the discrete equations:

$$\frac{3}{2}V^{n+1} - 2V^n + \frac{1}{2}V^{n-1} = u^{n+1}_{f,k+1/2} - u^{n+1}_{f,k-1/2} \tag{5}$$

In other words, GCL is ensured provided the cell volume is updated using the appropriate flux formula for the inter-facial grid velocity terms.

The second issue of concern in Eqn. 4 is the dissipation formulation for the structural flux terms. In Eqn. 1, the structural inviscid fluxes are zero; nevertheless, we note that the structural equations represent a hyperbolic system and the addition of appropriate dissipation terms is necessary for ensuring monotonicity and diagonal dominance. The latter aspect is particularly important for the implicit solution of the combined system. In our work, we choose the absolute values of the structural eigenvalues, $\epsilon^s\sqrt{E^s/\rho^s}$ and $\epsilon^f\sqrt{E^f/\rho^f}$, to define the respective artificial dissipation terms for these equations. Note the presence of the preconditioning scaling terms in the eigenvalue definitions.

Interface Condition

At the fluid structure interface, we must ensure that the flux terms match and that all compatibility constraints are satisfied. Conservation of mass, momentum and energy yield the following:

$$p + \tau'_{nn} = \tau^s_{nn}, \qquad \tau'_{nt} = \tau^s_{nt}, \qquad u_j = u^f_j, \qquad \frac{\partial T}{\partial n} = 0 \tag{6}$$

Finally, the following compatibility conditions relating the structural and fluid-dyamic mesh motions must also be enforced:

$$u^s_j = u^f_j = \frac{\partial d^f_j}{\partial t} = \frac{\partial d^s_j}{\partial t}, \qquad d^s_j = d^f_j \tag{7}$$

In all, the above equations represent seven equations in seven unknowns (in 1D) and 17 equations in 17 unknowns (in 3D). The solution of these equations can be expressed as a single vector equation, which can be solved using Newton's method:

$$\Omega(Q) = 0 \implies \frac{\partial \Omega}{\partial Q} \Delta Q = -\Omega^k \tag{8}$$

where $\Omega(Q)$ represents Eqns. 6-7. The above solution is used to calculate both the fluid and structural fluxes at the fluid-strcture interface and the variables are therefore coupled to the field variables on both sides of the interface. The implicit coupled solution procedure is discussed in the following section.

Implicit Solution Procedure

Implicit solution of the coupled system of equations in Eqn. 2 can be written as:

$$\begin{aligned} \Gamma_p \frac{\partial Q_p V}{\partial \tau} = -\Big[& \tfrac{3Q^{n+1} - 4Q^n + Q^{n-1}}{\Delta t} V^{n+1} + \textstyle\sum_{faces} (\hat{E}_i' S_i)^{n+1} \\ & - \textstyle\sum_{faces} (V_i S_i)^{n+1} - (HV)^{n+1} \Big] = -R^{n+1} \end{aligned} \tag{9}$$

which can be linearized and written in delta form as:

$$\Big[\frac{\Gamma_p}{\Delta \tau} + \Big(\frac{\partial R}{\partial Q_p} \Big)' \Big] (Q_p^{k+1} - Q_p^k) = -\left[\Big(\frac{\partial R}{\partial Q_p} \Big) (Q_p^k - Q_p^l) - R^l \right] \tag{10}$$

We note that the left hand side Jacobians may be approximated for a variety of reasons, but the dual-time iterations still preserve full implicit coupling. In particular, for domain decomposition purposes, it is easiest to solve the fluid and structural sub-systems independently. Thus, the above equation would take the following form:

$$\left[\frac{\Gamma_p}{\Delta \tau_k} + \begin{pmatrix} A' & 0 \\ 0 & D' \end{pmatrix} \right] \Delta_k \begin{pmatrix} Q_f \\ Q_s \end{pmatrix} = -\left[\begin{pmatrix} A & B \\ C & D \end{pmatrix} \Delta_l \begin{pmatrix} Q_f \\ Q_s \end{pmatrix} - R^l \right] \tag{11}$$

where $Q_f = (\rho, \rho u_j, e, \rho^f u_j^f, d_j^f)^T$ and $Q_s = (\rho^s u_j^s, d_j^s)^T$, i.e., the fluid and structural sub-systems respectively. When the pseudo-iterations converge, the fully coupled implicit solution represented on the right-hand side is satisfied, thereby ensuring that no new numerical stability constraints are introduced by the fluid-structure coupling.

3 Results

The coupled implicit fluid-structure algorithm has been implemented in a one-dimensional code for demonstration purposes. Initial verification focused

on the stand-alone versions of the fluid and structural dynamics modules. Figure 1 shows sample convergence performance for steady state structural computations for an elastic beam with a force applied on one end and for unsteady fluid computations of a shock tube. In both cases, these results confirm that the two modules perform as expected.

The individual modules are then combined together using a Python-based framework [AL04], which manages the overall execution and data transfer between the constituent solvers. Representative results for a shock-tube with elastic walls are shown in Fig. 2. Time-accurate computations are performed using the dual-time formulation and the converged pressure field and structural displacement are plotted for several time instances. The pressure solutions show a rarefaction wave moving leftward into the high pressure gas, while a shock and contact discontinuity proceed rightward into the low pressure gas. Eventually, when the shock wave hits the right-wall of the shock tube, it is reflected and then travels leftward back towards the center of the shock tube. When the shock hits the right-wall, the pressure rise in turn causes the beam structure to compress as the wave traverses the beam. It can be observed that as the pressure rises on the right wall, the beam displacement increases. At the highest point shown, the pressure is about 20 atm, which is twenty times compared to the initial pressure (on the right side) of 1 atm. The corresponding beam displacement is observed to be about 25 mm.

These results and more detailed performance estimates (not shown here) confirm that the coupled formulation provides robust and efficient predictions for fluid-structure interaction problems. Current work is focused on extending the analysis to multi-dimensions and to demonstrate the application of the method to more practical problems.

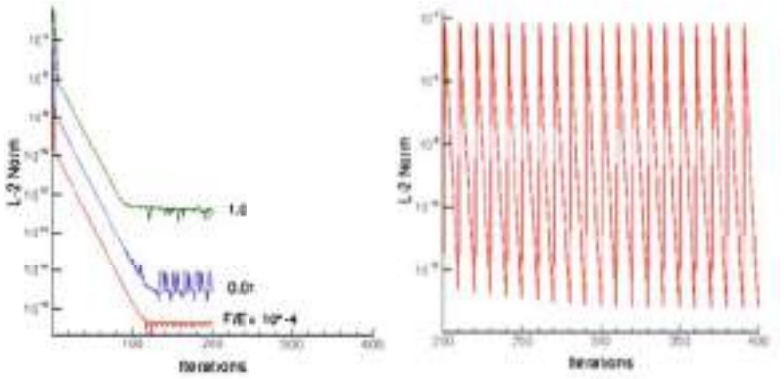

Fig. 1. Convergence rates for stand-alone structural and fluid dynamics modules. Figure shows steady-state structural code performance for an elastic beam (left) and unsteady fluid-dynamics code performance for a shock-tube(right).

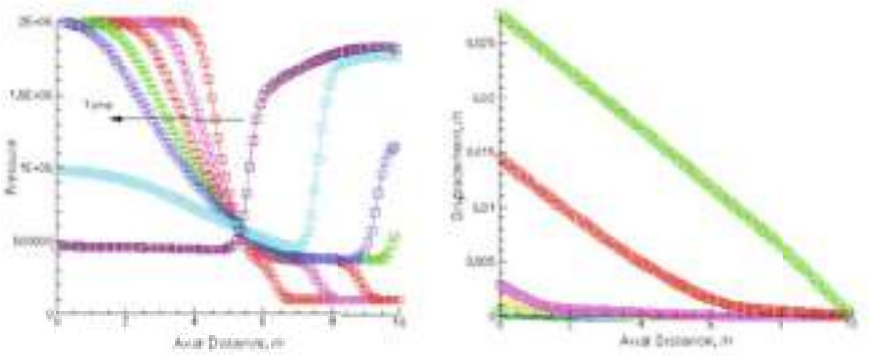

Fig. 2. Sample fluid and structural dynamics results for a 1D shock-tube fitted with an elastic wall at the head-end. Figure shows pressure along the duct at several time-instances (left) and the corresponding structural deflections (right).

Acknowledgment

This work was funded in part by NASA-NRA Grant NNX07AT97A and in part by the US Army Aeroflightdynamics Directorate.

References

[FL98] Farhat, C., Lesoinne, M.: Enhanced Partitioned Procedures for Solving Nonlinear Transient Aeroelastic Problems. AIAA Paper 98-1806 (1998)

[FF92] Felker, F.: A New Method for Transonic Aeroelastic Problems. AIAA Paper 92-2123 (1992)

[GG92] Guruswamy, G.: ENSAERO a Multidisciplinary Program for Fluid/Structural Interaction Studies. Comput. Syst. Eng. 1(2-4), 237–256 (1990)

[MM98] Melville, R.B., Morton, S.A.: Fully Implicit Aeroelasticity on Overset Grid Systems. AIAA Paper 98-0521, Aerospace Sciences Meeting and Exhibit, Reno, NV (1998)

[SZ04] Sankaran, V., Zeng, X., Li, D., Merkle, C.L.: Influence of Large Scale Pressure Changes on Preconditioned Solutions at Low Mach Numbers. AIAA Journal 42(12), 2490–2498 (2004)

[AL04] Alonso, J., LeGresley, P., Weide, E.v.d., Martins, J., Reuther, J.: pyMDO: A Framework for High-Fidelity Multi-Disciplinary Optimization. In: AIAA Paper 2004-4480, 10th AIAA/ISSMO Multidisciplinary Analysis and Optimization Conference, Albany NY (2004)

Part 8
Algorithm 3

“*This page left intentionally blank.*”

Development of AUSM-Type Solver for Analysis of Ideal Magnetohydrodynamic Flows

Sang Hoon Han, Jeong Il Lee, and Kyu Hong Kim

School of Mechanical and Aerospace Engineering, Seoul National University,
Seoul 151-744, Korea
aerocfd1@snu.ac.kr

AUSMPW+ and M-AUSMPW+ were modified to solve the equations of the ideal Magnetohydrodynamics(MHD). Discontinuity-sensing functions in AUSMPW+ and M-AUSMPW+ were newly defined for MHD equations. In order to obtain high resolution results and to satisfy the magnetic divergence free constraint, the OMLP, which is a high order interpolation scheme and a hyperbolic divergence cleaning technique, were applied. One-dimensional Brio and Wu's shock tube problem, two-dimensional interaction of shock and cloud problem were calculated to validate and show the advantages of the newly developed schemes.

1 Introduction

Over the past 20 years, many researchers have been interested in Magnetohydrodynamics(MHD) because of its many possible applications to various fields of science and engineering such as astrophysics, and thermonuclear, electrical and aerospace engineering. In the MHD equations, the magnitudes of all eigenvalues are the same order as that of flow speed with the assumption that the electrical field is known in advance. Thus, most of the numerical schemes for the MHD equations have been based on gas dynamics. Among the many modern upwind schemes for gas dynamics, Roe's approximate Riemann solver was firstly applied to the MHD equations by Brio and Wu.[BW88] After that, many other researchers including Ryu and Jones, Balsara et al., Dai and Woodward, Zachary et al. have used the Roe-type linearized Riemann solver to solve the MHD equations. [RJ95] Basically, Roe-type schemes are more accurate than other upwind-type schemes because all of the discontinuities in the MHD equations can be physically considered by each corresponding eigenvalue. However, they require the complex process of eigen-decomposition for the MHD system and require more computational time, especially for multi-dimensional problems.

As another approximate Riemann solver, the HLL method has been generalized to MHD equations.[Jan00] However, when applied to gas dynamics, HLL essentially made a contact discontinuity smeared since it had no way to recognize the discontinuity. Another representative method of the upwind scheme for gas dynamics is the Flux Vector Splitting(FVS) method, such as the Steger-Warming

scheme. Unfortunately, it cannot be applied directly to the MHD equations because it is not homogeneous of degree one with respect to the state vector. Therefore, MacCormack modified these equations into homogeneous of degree one conservative form by adopting Powell's model and then used the modified Steger-Warming flux splitting algorithm to solve the MHD equations.[Mac98] While this method kept the robustness in capturing the fast shock wave, it had a basic problem: it could not capture a contact discontinuity accurately. As another upwind scheme, the AUSM-type methods were recently developed for gas dynamics. The AUSM-type schemes promise enhanced accuracy over the previous FVS schemes like the van Leer or Steger-Warming scheme and offer simpler implementation compared to the approximate linearized Riemann solver like Roe's FDS. Agarwal et al. firstly applied the original AUSM method with first order spatial accuracy to the MHD equations in a one-dimensional case. Even though it was successfully applied, the AUSM showed a numerical overshoot at a strong shock region. It also generated a relatively more diffusive result at a contact discontinuity than Roe's FDS, which was an interesting result since the AUSM has been known as one of the numerical schemes that can capture a contact discontinuity accurately in gas dynamics.

With respect to spatial discretization, Roe's FDS gives more accurate results than the many modern upwind schemes. However, it requires expensive computational cost, especially when it is applied in multi-dimensional cases. On the other hand, FVS and AUSM-type scheme are more efficient, although they have difficulties in capturing a contact discontinuity accurately.

With recent demand of an accurate calculation with a lower computational cost, a high order spatial calculation of the MHD equations as well as spatial discretization has been studied. Jiang and Wu presented the 5th order WENO finite difference scheme combined with the Lax-Friedrich spatial discretization to calculate ideal MHD equations. Even though it was successfully applied to the MHD equations, the numerical tests seemed to give slightly diffusive results because the Lax-Friedrich scheme intrinsically generated a higher artificial viscosity. With such problems, all of the mentioned schemes have their own weaknesses in accuracy, robustness or efficiency, all of which must be overcome.

The goal of the present paper is 1) to develop a new spatial discretization scheme which can ensure both higher accuracy and efficiency over Roe's scheme and 2) to extend the developed new scheme to higher order spatial accuracy with robustness. To this end, AUSMPW+ and M-AUSMPW+ schemes[KKR01, KK05] were chosen as the base flux function and modified for the MHD calculation. Also, the recently developed high order interpolation scheme, the Optimized Multi dimensional Limiting Process(OMLP) method [KLL08] was adopted into our new scheme to realize stable higher order calculations.

Through the numerical experiments for one-dimensional and two-dimensional cases, our new developed schemes have shown good performances in accuracy, robustness and efficiency.

2 Governing Equations

2.1 Ideal MHD Equations

The ideal MHD equations include the continuity, the momentum, the energy, and the magnetic induction equations. The two dimensional ideal MHD equations in conservative form are as follows.

$$\frac{\partial U}{\partial t}+\frac{\partial F}{\partial x}+\frac{\partial G}{\partial y}=0 \tag{1}$$

The conservative variable vector U and the flux functions F and G are given by

$$U=\begin{bmatrix}\rho\\ \rho u\\ \rho v\\ \rho w\\ B_x\\ B_y\\ B_z\\ \rho e\end{bmatrix},\ F=\begin{bmatrix}\rho u\\ \rho u^2+p_t-B_x^2\\ \rho vu-B_xB_y\\ \rho wu-B_xB_z\\ 0\\ B_yu-B_yv\\ B_zu-B_zw\\ (\rho e+p_t)u-B_x(\vec{V}\cdot\vec{B})\end{bmatrix},\ G=\begin{bmatrix}\rho v\\ \rho uv-B_yB_x\\ \rho v^2+p_t-B_y^2\\ \rho wv-B_yB_z\\ B_xv-B_yu\\ 0\\ B_zv-B_yw\\ (\rho e+p_t)v-B_y(\vec{V}\cdot\vec{B})\end{bmatrix}, \tag{2}$$

where ρ , p , $\vec{V}$, $\vec{B}$, e are density, pressure, velocity field, magnetic field and specific total energy, respectively. Total pressure and specific total energy are given by

$$p_t=p+\frac{1}{2}\left(B_x^2+B_y^2+B_z^2\right), \tag{3}$$

$$\rho e=\frac{1}{2}\rho\left(u^2+v^2+w^2\right)+\frac{1}{2}\left(B_x^2+B_y^2+B_z^2\right)+\frac{p}{\gamma-1}. \tag{4}$$

2.2 Modifying the Ideal MHD Equations (Cleaning Divergence Errors)

Generally, there are no magnetic sources or monopoles in a magnetic field, that is, a magnetic field has to satisfy the following divergence constraint.

$$\nabla\cdot\vec{B}=0. \tag{5}$$

For multi-dimensional problems, however, it is difficult to satisfy the divergence free constraint using conventional numerical MHD solvers. The violation of the divergence constraint in simulations of MHD is due to numerical errors and conservation characteristics in the computations. Since this violation may frequently lead to severe stability problems, many researchers have tried to enforce the divergence-free constraint in their MHD formulations.

In this study, the mixed-type Hyperbolic Divergence Cleaning Method(HDCM) was used to eliminate divergence errors since it can be easily implemented with-out

a great modification of the numerical solver. The modified governing equations of the mixed type HDCM can be written in the following conservative form.[DKK02]

3 Numerical Method

3.1 AUSMPW+/M-AUSMPW+ Scheme of Ideal MHD Equations

The key idea of the AUSMPW+/M-AUSMPW+ scheme is numerical oscillation control by sensing of the discontinuous region and control of advection through the use of pressure-based weighting functions. In order to apply the key idea to the ideal MHD equations, the pressure-based weighting functions f and w should be modified to consider the effect of the magnetic field. Although magnetic field plays important roles as thermal pressure does in MHD, oscillatory behaviors are frequently observed without consideration of the effect of the magnetic field.

The modified numerical flux of AUSMPW+ /M-AUSMPW+ in two dimensions can be given by

$$\mathbf{F}_{\frac{1}{2}} = \overline{M}_L^+ \mathrm{c}_{\frac{1}{2}} \mathbf{\Phi}_{L,\frac{1}{2}} + \overline{M}_R^- \mathrm{c}_{\frac{1}{2}} \mathbf{\Phi}_{R,\frac{1}{2}} + (P_L^+ \mathbf{P_L} + P_R^- \mathbf{P_R}) + \frac{1}{2}(F_{B,L} + F_{B,R}) \tag{6}$$

i) $m_{\frac{1}{2}} = M_L^+ + M_R^- \geq 0$, (7-a)

$$\overline{M}_L^+ = M_L^+ + M_R^- \cdot [(1-w)\cdot(1+f_R) - f_L],$$
$$\overline{M}_R^- = M_R^- \cdot w \cdot (1+f_R).$$

ii) $m_{\frac{1}{2}} < 0$, (7-b)

$$\overline{M}_L^+ = M_L^+ \cdot w \cdot (1+f_L),$$
$$\overline{M}_R^- = M_R^- + M_L^+ \cdot [(1-w)\cdot(1+f_L) - f_R)]$$

- ***Modified pressure- based weight functions w and f ;***

$$f_{L.R} = \begin{cases} (\dfrac{p_{t,L,t,R}}{p_{ts}} - 1) & , p_{ts} \neq 0 \\ 0 & , elsewhere \end{cases}, \quad p_{ts} = P_L^+ p_{t,L} + P_R^- p_{t,R}, \tag{8-a}$$

$$w(p_{t,L}, p_{t,R}) = 1 - \min\left(\frac{p_{t,L}}{p_{t,R}}, \frac{p_{t,R}}{p_{t,L}}\right)^3, \tag{8-b}$$

where $p_{t,L} = p_L + \frac{1}{2}(B_x^2 + B_y^2 + B_z^2)_L$, $p_{t,R} = p_R + \frac{1}{2}(B_x^2 + B_y^2 + B_z^2)_R$.

- ***AUSMPW+ scheme***

$$\mathbf{\Phi}_{L,\frac{1}{2}} = \mathbf{\Phi}_L, \ \mathbf{\Phi}_{R,\frac{1}{2}} = \mathbf{\Phi}_R. \tag{9}$$

- ***M-AUSMPW+ scheme***

$$\mathbf{\Phi}_{L,\frac{1}{2}} = \mathbf{\Phi}_L + \frac{\max\left[0,(\mathbf{\Phi}_R - \mathbf{\Phi}_L)(\mathbf{\Phi}_{L,superbee} - \mathbf{\Phi}_L)\right]}{(\mathbf{\Phi}_R - \mathbf{\Phi}_L)\left|\mathbf{\Phi}_{L,superbee} - \mathbf{\Phi}_L\right|} \min\left[a\frac{\left|\mathbf{\Phi}_R - \mathbf{\Phi}_L\right|}{2}, \left|\mathbf{\Phi}_{L,superbee} - \mathbf{\Phi}_L\right|\right], \quad \text{(10-a)}$$

$$\mathbf{\Phi}_{R,\frac{1}{2}} = \mathbf{\Phi}_R + \frac{\max\left[0,(\mathbf{\Phi}_L - \mathbf{\Phi}_R)(\mathbf{\Phi}_{R,\text{superbee}} - \mathbf{\Phi}_R)\right]}{(\mathbf{\Phi}_L - \mathbf{\Phi}_R)\left|\mathbf{\Phi}_{R,\text{superbee}} - \mathbf{\Phi}_R\right|} \min\left[a\frac{\left|\mathbf{\Phi}_L - \mathbf{\Phi}_R\right|}{2}, \left|\mathbf{\Phi}_{R,\text{superbee}} - \mathbf{\Phi}_R\right|\right], \quad \text{(10-b)}$$

3.2 A High Order Interpolation Scheme: OMLP

OMLP(Optimized Multidimensional Limiting Process) is the high order interpolation scheme. In the OMLP, The mechanism for distinguishing continuous from discontinuous regions, which is based on the Gibbs phenomena in computation, is introduced so that the decision of the distinguishing function can be used to limit the application of MLP to improve the solution accuracy in the continuous region. The details of OMLP are described in Ref. [KLK08]. We combined our new modified AUSMPW+/M-AUSMPW+ schemes with 5^{th} order OMLP.

4 Numerical Results

4.1 Brio and Wu's Shock Tube Test

This shock tube problem was firstly tested by Brio and Wu.[BW88] It has been considered as one of the standard one dimensional MHD test problems because it involves a compound structure that consists of attached shock and rarefaction waves.

The initial conditions of the left and right states are given by

$$(\rho, u, v, w, B_y, B_z, p)_L = [1,0,0,0,1,0,1]$$

$$(\rho, u, v, w, B_y, B_z, p)_R = [0.125,0,0,0,-1,0,0.1]$$

with $B_x = 0.75$ and $\gamma = 5/3$. The CFL number was 0.8, and 400 grid points were used for comparing the numerical flux functions. Figure 1 shows the spatial distributions of density according to the numerical schemes at time t=98.

As shown in Fig. 2, AUSMPW+ shows the most diffusive characteristic, followed by Roe's scheme. M-AUSMPW+ shows a sharper density slope than the other two schemes. Especially, the density slope of M-AUSMPW+ with the 5th-order OMLP is almost twice as steep as that of AUSMPW+ and comparable to that of Roe's scheme on 800 grids. In addition to enhanced accuracy, M-AUSMPW+ showed robustness and stability. Especially, although the 5th-order OMLP was combined with M-AUSMPW+, the calculations were robust and the results were accurate without any numerical oscillations.

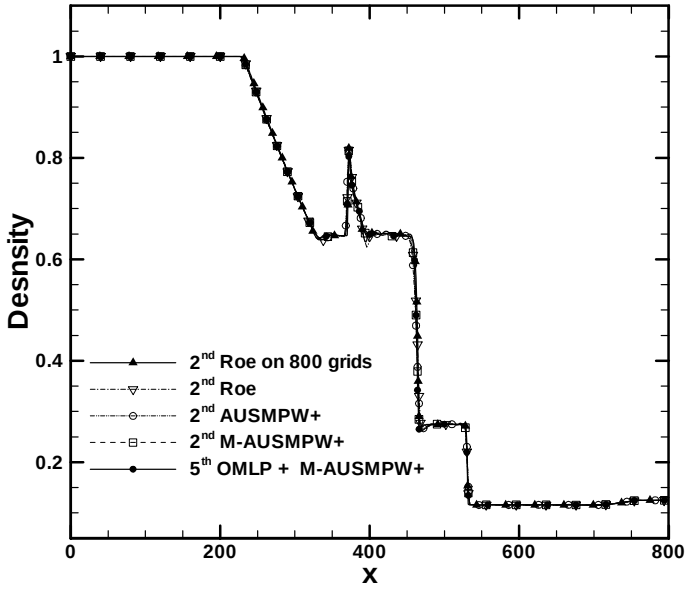

Fig. 1. Density distribution of Brio and Wu's MHD shock tube test at t=98sec

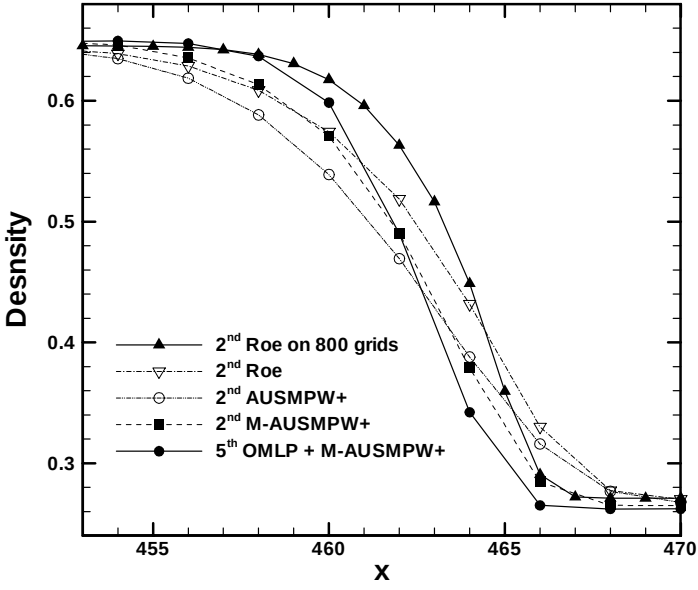

Fig. 2. Comparison of density plots on contact discontinuity between the numerical flux functions

4.2 2-D Cloud and Shock Interactions

The next test case was a problem involving the interactions of a high density cloud with a strong shock wave. The initial conditions contained a discontinuity parallel to the y axis at x = 0.6. The left states and right states across the discontinuity were given by

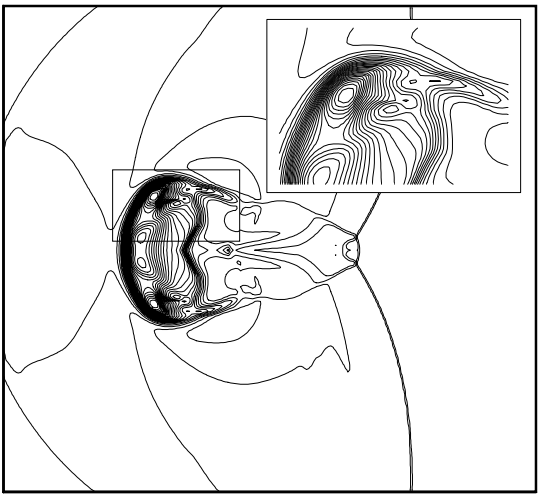

(a) Density contour of Roe with 2nd order and 200X200 grid points.

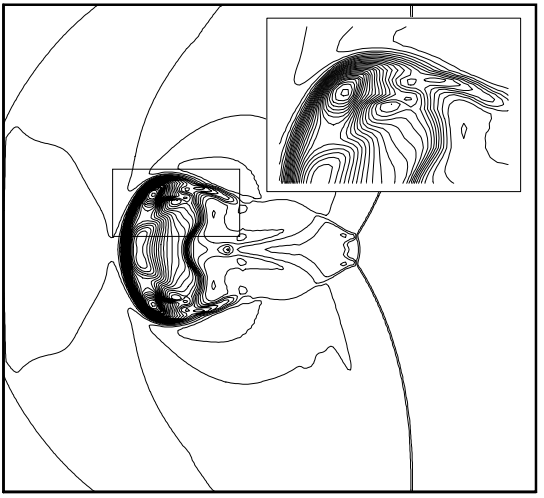

(b) Density contour of M-AUSMPW+ with 2nd order and 200X200 grid points.

Fig. 3. Comparison of density contours between numerical flux functions

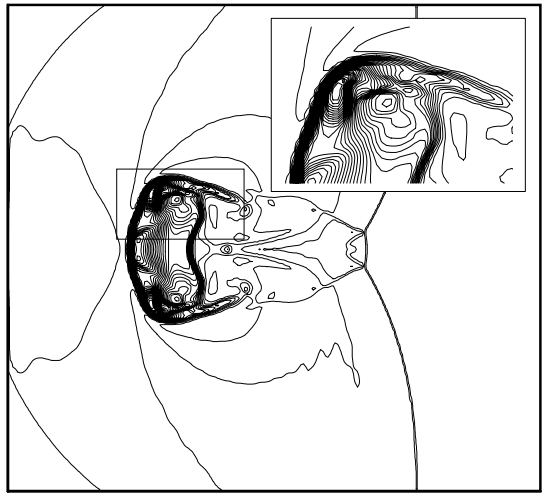

(c) Density contour of M-AUSMPW+ with 5th OMLP/ 200X200 grid points.

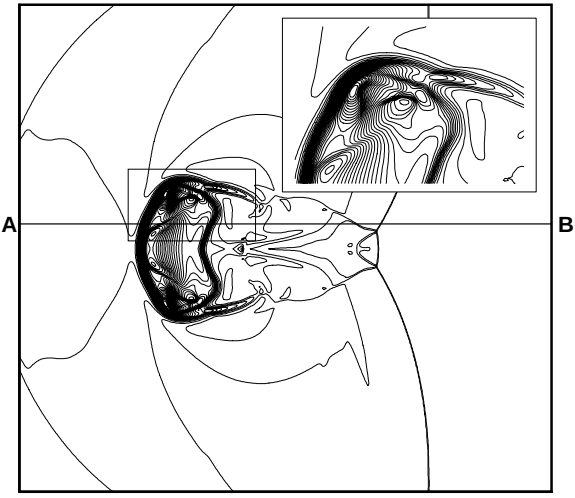

(d) Density contour of Roe with 2nd order and 400X400 grid points.

Fig. 3. (*continued*)

$$(\rho, u, v, w, B_x, B_y, B_z, p)_L = [3.86859,0,0,0,0,7.73718,-7.73718,167.345]$$

$$(\rho, u, v, w, B_x, B_y, B_z, p)_R = [1,-11.2536,0,0,0,2,2,1]$$

In front of the shock wave, the initial spherical cloud with radius of 0.15 was located at (x, y) = (0.8, 0.5). The initial states of the circle were given by

$$(\rho, u, v, w, B_x, B_y, B_z, p)_{circle} = [10,-11.2536,0,0,0,2,2,1]$$

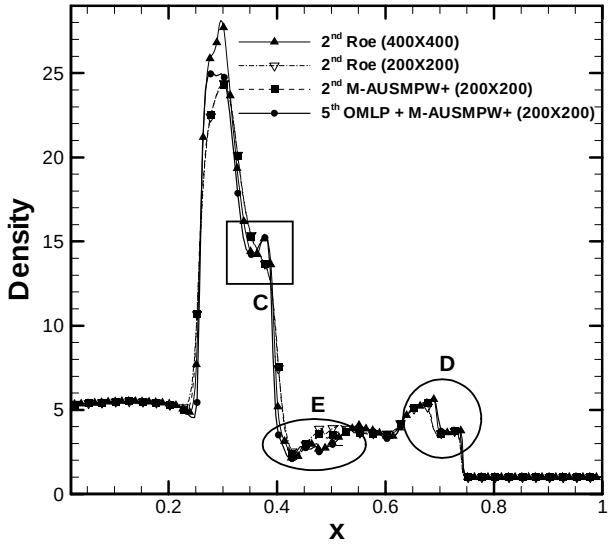

Fig. 4. Comparison of density line plotted along the line AB in Fig. 3(d)

For boundary conditions, the supersonic inflow was applied to the right boundary, and outflow conditions were applied for all other boundaries. The CFL number used for the calculation was 0.6, and the computational domain was with a uniform mesh. The 3rd order TVD Runge-Kutta method was used for time integration. In the present study, the calculations using M-AUSMPW+ and Roe's scheme combined with the van Leer limiter "blew up" after some number of iterations. By applying the minmod limiter, which is more diffusive than the van Leer limiter, numerical calculations were performed successfully. Thus, all of the 2nd order calculations were performed with the minmod limiter in this test case. Even though M-AUSMPW+ with the van Leer limiter failed to calculate this problem, M-AUSMPW+ with the 5th order OMLP succeeded without any difficulty due to the oscillation control ability of the OMLP in multi-dimensions.

Figure 3(d) is the result of Roe's scheme with the minmod limiter and the 400 by 400 grid points, which was used as the reference solution in the present study. As shown in the magnified rectangular region of Figs. 3(a) ~ 3(c), M-AUSMPW+ with the 5th order OMLP in the 200 by 200 grid points clearly resolves the complex patterns including the contact lines and shock waves. For detailed comparisons between the numerical schemes, density line contours are plotted along the line AB in Fig. 3(d). The rectangular(C), circle(D) and elliptic(E) regions in Fig. 4 are enlarged in Figs. 5(a) ~ 5(c), respectively. As shown in Figs. 5(a) ~ 5(c), Roe's FDS and M-AUSMPW+ with the minmod limiter smeared out a local extrema and finally show very different density patterns from that of the reference solution. On the other hand, M-AUSMPW+ with the 5th order OMLP follows the reference solution well even with a quarter grid points.

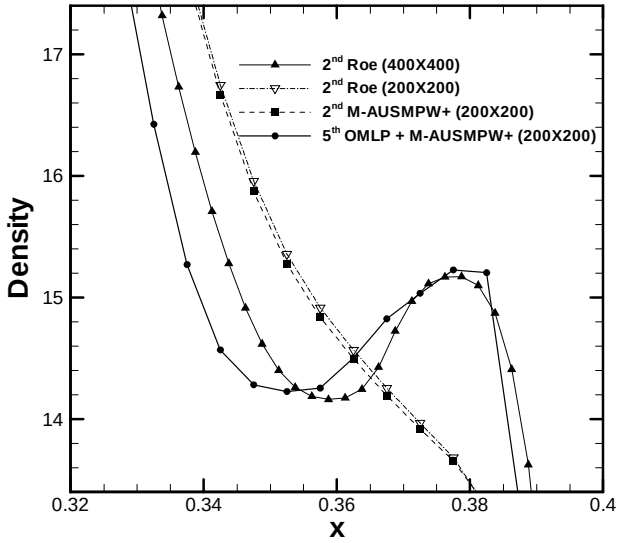

(a) Comparison of density line contours at continuous region(C) in Fig. 4.

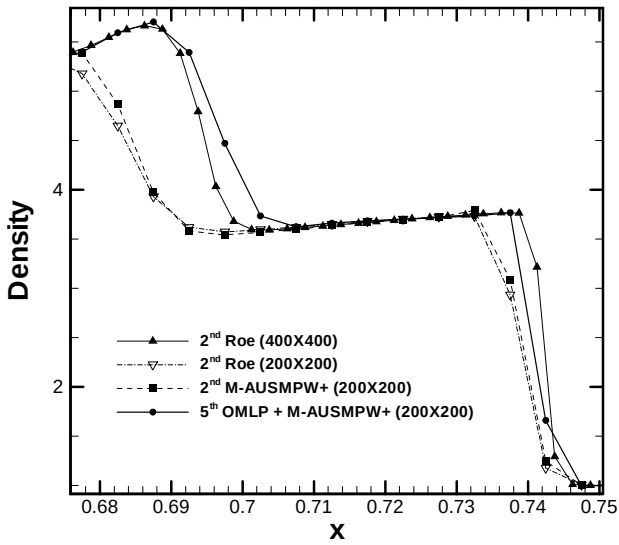

(b) Comparison of density line contours at discontinuous region(D) in Fig. 4.

Fig. 5. Comparison of density line contours between the numerical flux functions

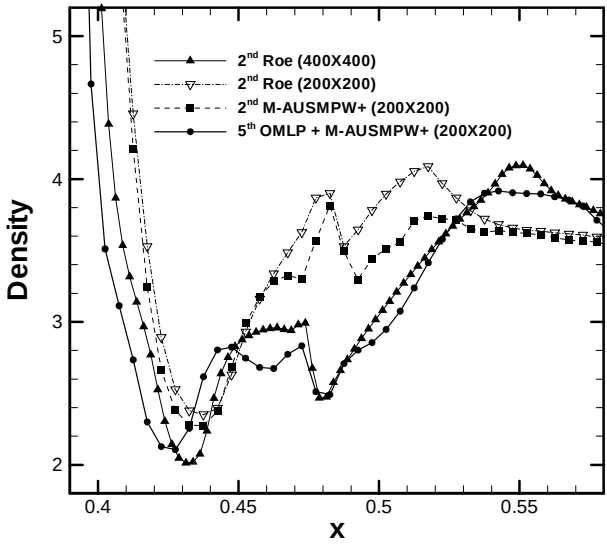

(C) Comparison of density line contours at continuous region(E) in Fig. 4

Fig. 5. (*continued*)

For the computational time, the elapsed time ratio of M-AUSMPW+ to AUSMPW+ was 1.21 and that of Roe's scheme to AUSMPW+ was 1.62 as in Table 1.

Table 1. Required time for calculation of shock-cloud interaction problem

Scheme	AUSMPW+	M-AUSMPW+	Roe's FDS
Time/Iter	1	1.21	1.62

※ 5th order OMLP and 3rd order TVD Runge-Kutta method were employed.

5 Conclusions

The modified AUSMPW+ and M-AUSMPW+ schemes were presented for solving the ideal MHD equations. And they were extended to higher order spatial accuracy by combination with the 5th order OMLP interpolation method. The newly modified M-AUSMPW+ scheme has the following desirable characteristics in solving the MHD equations. First, M-AUSMPW+ guarantees enhanced accuracy especially in a contact discontinuity because it was originally designed to minimize the numerical dissipation. Second, M-AUSMPW+ can reduce numerical oscillations effectively. Third, M-AUSMPW+ shows superior efficiency. Last, M-AUSMPW+ can easily incorporate the high order OMLP interpolation, and it performs numerical calculations robustly. Through the various numerical tests, it is

confirmed that the newly developed M-AUSMPW+ can solve the complicated physical phenomena of MHD systems with enhanced accuracy, robustness, efficiency and high order spatial accuracy.

References

[BW88] Brio, M., Wu, C.C.: An Upwind Differencing Scheme for the Equations of Ideal Magnetohydrodynamics. Journal of Computational Physics 75, 400–422 (1988)

[RJ95] Ryu, D.S., Jones, T.W.: Numerical Magnetohydrodynamics in Astrophysics: Algorithm and Test For One-Dimensional Flow. The Astrophysical Journal 442, 228–258 (1995)

[Jan00] Janhunen, P.: A positive conservative method for magnetohydrodynamics based HLL and Roe methods. Journal Of Computational Physics 160, 649–661 (2000)

[Mac98] MacCormack, R.W.: An Upwind Conservation Form Method For The Ideal MagnetoHydroDynamics Equations. In: 30th Plasmadynamics and Lasers Conference (1998)

[KKR01] Kim, K.H., Kim, C., Rho, O.H.: Methods for the Accurate Computations of Hypersonic Flows: I. AUSMPW+ Scheme. Journal of Computational Physics 174, 38–80 (2001)

[KK05] Kim, K.H., Kim, C.: Accurate, efficient and monotonic numerical methods for multi-dimensional compressible flows Part I: Spatial discretization. Journal of Computational Physics 208, 527–569 (2005)

[KLK08] Kim, S.T., Lee, S.G., Kim, K.H.: Wavenumber-extended high-order oscillation control finite volume shcmes for multi-dimensional aeroacoustic computations. Journal of Computational Physics 227, 4089–4122 (2008)

[DKK02] Dedner, A., Kemm, F., Kroner, D., Munz, C.D., Schnitzer, T., Wesenberg, M.: Hyperbolic Divergence Cleaning for the MHD Equations. Journal of Computational Physics 175, 645–673 (2002)

An Implicit Parallel Fully Compressible Roe Based Solver for Subsonic and Supersonic Reacting Flows

T. Belmrabet[1], M. Talice[2], G. Delussu[2], and S. Hanchi[1]

[1] Fluid Dynamics Laboratory, EMP, Alger, Algeria
toufik_belmrabet@yahoo.fr
[2] Renewable Energy Group, CRS4, Italy
talice@crs4.it

1 Introduction

The extension of the classical Roe's formulation to the numerical integration of fully compressible multi-component reacting flows will be presented. The matrix of the five Navier Stokes equations written in conservative form has been completed with a set of (N - 1) transport equations for the species mass fractions. The Eddy Dissipation Model (EDM) [MH76] has been used as the combustion model of choice, whereas turbulence has been taken into account via the one equation Spalart & Allmaras model. Coupling of the above mentioned modeling represents a challenge per se, as the turbulence mixing time τ_t had to be derived from the only resolved turbulent quantity $\widetilde{\nu}$. The method has been validated against a set of test cases, both in subsonic and supersonic regimes.

2 Theoretical Formulation and Numerical Treatment

2.1 Governing Equations

The fully coupled system of the species conservation, fluid dynamics, and turbulent transport equations can be written in a compact vector form as:

$$\frac{\partial Q}{\partial t} + P \cdot \left(\frac{\partial (F_x - G_x)}{\partial x} + \frac{\partial (F_y - G_y)}{\partial y} + \frac{\partial (F_z - G_z)}{\partial z}\right) = P \cdot S \qquad (1)$$

where details on the arrays of conservative variables Q, convective and diffusion flux vectors, $\overrightarrow{F}$ and $\overrightarrow{G}$, and on the reaction source term $\overrightarrow{S}$, are given in [FMO97]. The Newton's, Fourier's and Fick's laws of viscosity, heat and mass diffusivity, together with two equations of state, close the mathematical model. Dependence on temperature of the specific heat coefficients $C_p i$ for each of the chemical species i, is modeled via a polynomial function of T. In order to extend the method to the low Mach number regime, system

of equations (1) can be preconditioned. The preconditioning matrix is given by $P = M \cdot M_m^{-1}$, where M is the Jacobian matrix of conservative variables vectors $Q = (\rho \quad \rho\overrightarrow{V} \quad \rho E \quad \rho Y_1 \cdots \rho Y_N)^T$ with respect to the vector of the viscous-primitive variables $Q_v = (p \quad V \quad T \quad Y_1 \cdots Y_N)^T$. Matrix M contains arbitrary thermodynamics in terms of derivatives of density and enthalpy with respect to pressure and temperature $(\rho_p, \rho_T, \rho_{Y_i}, h_p, h_T, h_{Y_i})$, while matrix M_m, that is a modified version of M, contains a modified thermodynamics in terms of ρ_p^m. If no modification is applied, $(P = I)$, the original non-preconditioned system form is recovered (see [MDT02] for more implementation details).

2.2 Numerical Modeling

The governing equations are integrated by using a cell-centered finite-volume approach on block structured meshes. Convective inviscid fluxes are approximated by a second order Roe's scheme for multi-species reactive flows, whereas viscous fluxes and source terms are calculated through a standard cell-centered Finite-Volume techniques and are both second order accurate (see [MDT02] for a thorough implementations details).

2.3 Turbulence Modeling

The Spalart Allmaras (SA) turbulence model [SA97] is a one transport equation model for the resolved variable, $\widetilde{\nu}$, which is similar to the eddy viscosity ν_t in regions far from walls. The choice of this model has been suggested for its well known characteristics of robustness and accuracy, as well as because it does not require the use of wall functions in wall bounded flows even on the same kind of grids typically used with algebraic models.

2.4 Combustion Modeling

In industrial applications, the chemical reaction time scale is considerably short and one generally makes the assumption of a total, irreversible and infinitely rapid combustion process. Under this assumption, the reaction rate is mainly controlled by the turbulent mixing time, τ_t, that can be estimated from the turbulence kinetic energy k and its dissipation rate ε as: $\tau_t = \frac{k}{\varepsilon}$. Complete details on the Eddy Dissipation Model (EDM) can be found in the work of Magnussen and Hjertager [MH76].

3 Coupling the EDM Model with the SA Model

The problem is how to go from ν_t or $\widetilde{\nu}$ to $\frac{\varepsilon}{k}$. The idea is to reformulate $\frac{\varepsilon}{k}$ in a quasi LES fashion with the assumption of local equilibrium between the

production of turbulent kinetic energy and its dissipation rate ($P_k = \varepsilon$). In this case the turbulent eddy frequency ($\omega = \frac{1}{C_\mu}\frac{\varepsilon}{k}$) is related to the strain rate via:

$$\omega = \frac{1}{\sqrt{C_\mu}} \cdot |S| \tag{2}$$

where $|S| = \sqrt{(S_{ij} - \frac{1}{3}S_{kk})^2}$ and $S_{ij} = \frac{1}{2} \cdot (\frac{\partial u_i}{\partial x_j} + \frac{\partial u_j}{\partial x_i})$ is the mean strain rate tensor. This formulation is valid only in regions far from walls. In fact, close to walls, strong gradients of the dependent variables occur and the viscous effects on the transport processes are large. It is then necessary to extend the model down to solid walls. A wall function based on a two-layer approach is then used to specify both ε and k in the near-wall region. By following this approach, the computational domain is divided into two regions: a viscosity-affected region (near walls) and a fully-turbulent region (away from walls). The standard coupling (2) is used away from the wall. In the near wall region, the turbulent kinetic energy is computed from the resolved field variables, while the length scale is specified by using reasonably well-established algebraic equations. The boundary between the two regions is determined by a wall-distance-based, local turbulent Reynolds number Re_y. At first ε_{SA} and k_{SA} are evaluated as functions of the resolved field variables. The choice of using $\tilde{\nu}$ and $|\Omega|$ would lead to: $k_{SA} \propto \nu|\Omega|$ and to a dissipation rate $\varepsilon_{SA} \propto \nu|\Omega|^2$. A better choice may be given by: $\varepsilon_{SA} = \nu_l \cdot |\Omega|^2$ and $k_{SA} = \sqrt{\frac{\nu_t \cdot \varepsilon_{SA}}{C_\mu}}$. A local Reynolds number Re_y is then computed, being y the distance to the closest wall: $Re_y = \frac{\sqrt{k_{SA}} \cdot y}{\nu_l}$. In the fully turbulent region ($Re_y > 200$) the quasi LES model (2) is used. In the viscosity-affected near-wall region ($Re_y < 200$), the same approach used in one equation turbulence energy models [W93] is used. By assuming that $\varepsilon \sim \frac{k^{\frac{3}{2}}}{l}$ and by introducing a coefficient λ_ε, the dissipation field can be computed as: $\varepsilon = \lambda_\varepsilon \cdot \frac{k_{SA}^{\frac{3}{2}}}{l_\varepsilon}$. As mentioned in [W93], there are several ways to compute λ_ε and l_ε. Generally, length scale distributions similar to those for mixing-length models are used. Wolfshtein [W69], for low-Reynolds-number flows, introduces a damping factor which resembles a Van Driest function. The chosen λ_ε and l_ε are:

$$\lambda_\varepsilon = 0.5[1 + \tanh(\tfrac{Re_y - 200}{\frac{40}{\tanh(0.98)}})] \quad and \quad l_\varepsilon = y \cdot C_l \cdot (1 - e^{-\frac{Re_y}{A_\varepsilon}})$$

where: $C_l = 0.4187 \cdot C_\mu^{-0.75}$ and $A_\varepsilon = 2 \cdot C_l$

Finally, the inverse of the turbulent mixing time can be computed as:

$$if\{ \begin{array}{ll} Re_y > 200 & \frac{\varepsilon}{k} = \sqrt{C_\mu} \cdot |S| \\ Re_y < 200 & \frac{\varepsilon}{k} = \lambda_\varepsilon \cdot \frac{k_{SA}^{\frac{1}{2}}}{l_\varepsilon} \end{array} \tag{3}$$

4 Test Cases

4.1 Moreau's Combustor

A stream of a fresh premixed mixture of methane and air ($\phi = 0.87$) enters through the inlet's upper part of a 1.3 m long, 0.1 m high, planar combustor of rectangular section. The flame is stabilized via a stream of hot gases, that enters the combustor through its inlet's lower part. A detailed description of the case can be found in [MB76]. Figure 1 shows the computed profiles of temperature and axial velocity at several combustor's cross sections. The agreement with the experiment looks fairly good.

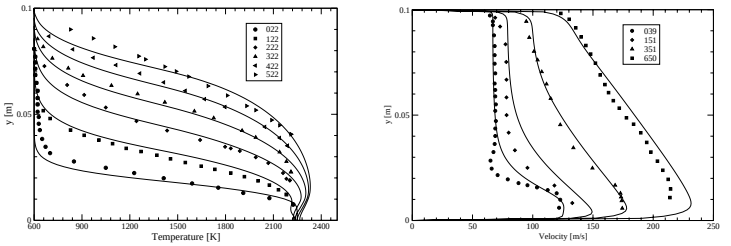

(a) (b)

Fig. 1. Moreau combustor: transverse distribution along the combustor axis of: a) temperature; b) velocity

4.2 Kent's and Bilger's Combustor

Two separated streams of hydrogen and air enter a cylindrical combustor [KB76]. The form of the flame depends on the relative velocity of the two streams. The present calculation is for the velocity ratio (v_{fuel}/v_{air}) of 10. Figures 2 and 3 show the computed axial and radial distributions of temperature and species mole fractions. In the axial direction results appear to be in fairly good agreement with the experiment, while in the radial direction some discrepancy with respect to the experiments is probably due to the insufficient resolution of the turbulent field.

4.3 Supersonic Flow over a Flat Plate with Injection Slot

A stream of hydrogen is injected through a 1 mm hole into a supersonic (M = 2.5) stream of nitrogen over a flat plate. This test case allows to check the method's capability to solve compressible problems. The system of three vortexes shown in figure 4 (a) holds the flame. Iso-lines of temperature are shown in figure 4 (b).

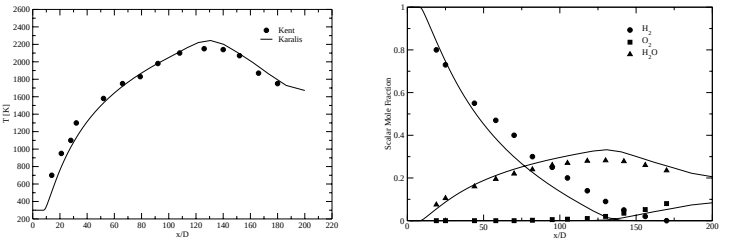

(a) (b)

Fig. 2. Kent combustor: axial distribution of: a) temperature and b) mole fraction of species

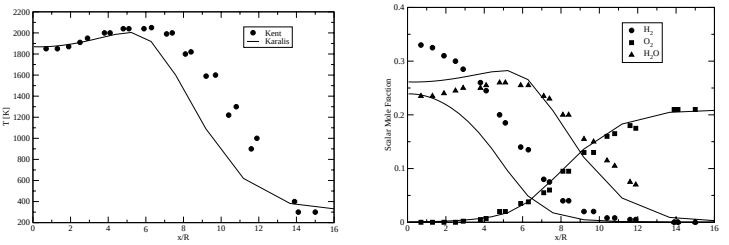

(a) (b)

Fig. 3. Kent combustor: radial distribution of: a) temperature and b) mole fraction of species

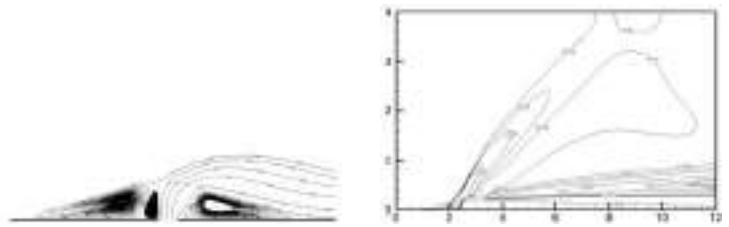

(a) (b)

Fig. 4. Supersonic flow with injection slot: vortex structure in the proximity of the injection slot (a); iso-lines of temperature (b)

5 Conclusion

The coupling of the Spalart and Allmaras turbulence model with a finite-rate (EDM) combustion model has been carried out. The resulting formulation, tested against a variety of compressible and incompressible cases, has given generally more accurate results than those achievable with traditional approaches. Nevertheless, still some problems have been encountered in the limit zone of $Re_y = 200$, which are probably due to a still insufficient

approximation of the mixing length scale. Future work will be devoted to address these problems and to give a sounder theoretical background to the proposed model.

Acknowledgment

Research funded with a grant by the the Italian Ministry of University and Research (MIUR).

References

[W69] Wolfsthein, M.: The velocity and temperature distribution in one-dimensional flow with turbulence augmentation and pressure gradient. Int. J. Heat Mass Transfer 12, 301–318 (1969)

[KB76] Kent, J.H., Bilger, R.W.: Turbulent diffusion flames. In: 14th Int. Symposium on Combustion, The Comb. Inst., pp. 615–625 (1973)

[MH76] Magnussen, B.F., Hjertager, B.H.: On mathematical modeling of turbulent combustion with special emphasis on soot formation and combustion. In: 16th Int. Symposium on Combustion, The Comb. Inst., pp. 719–729 (1976)

[MB76] Moreau, P., Boutier, A.: Laser velocimetry measurements in a turbulent flame. In: 16th Int. Symposium on Combustion, The Comb. Inst., pp. 1747–1756 (1976)

[W93] Wilcox, D.C.: Turbulence modeling for CFD. DCW Industries, Inc., La Cañada (1993)

[SA97] Spalart, P.R., Allmaras, S.R.: A one-equation turbulence model for aerodynamic flows. AIAA Paper 92-0439 (1992)

[FMO97] Fedkiw, R.P., Merriman, B., Osher, S.: High accouracy numerical methods for thermally perfect gas flows with chemistry. J.C.P. 132, 175–190 (1997)

[MDT02] Mulas, M., Chibbaro, S., Delussu, G., Di Piazza, I., Talice, M.: Efficient computations of flows of arbitrary fluids for all regimes of Reynolds, Mach and Grashof numbers. Int. J. of Num. Methods for Heat and Fluid Flow 12-6, 637–657 (2002)

Part 9
Bio-fluid Mechanics 1

“*This page left intentionally blank.*”

Rheology of Blood Flow in a Branched Arterial System with Three-Dimension Model

Ha-Hai Vu[1], Cheung-Hwa Hsu[2], and Yaw-Hong Kang[3]

[1] Mechanical Engineering Department, National Kaohsiung University of Applied Sciences, Kaohsiung 807, Taiwan
vuha_hai@yahoo.com
[2] Mold & Die Engineering Department, National Kaohsiung University of Applied Sciences, Kaohsiung 807, Taiwan
chhsu@cc.kuas.edu.twm
[3] Mechanical Engineering Department, National Kaohsiung University of Applied Sciences, Kaohsiung 807, Taiwan
yhkang@cc.kuas.edu.tw

Summary. Blood flow rheology is a very complex phenomenon. Hemodynamics owns Newtonian or non-Newtonian characteristic is still debatable. There is no model which represents the viscous property of blood is approved by all researchers. Recently, studies related to blood tend to classify blood as non-Newtonian fluid. In this research, power law, Casson and Carreau which are being the most popular non-Newtonian models are applied to investigate the hemodynamics variables that influence formation of thrombosis and predict damageability to blood cell. The branched arterial system is simplified as T-junction geometry and the computational fluid dynamics software Fluent 6.2 with finite volume method is utilized to analyze the blood flow rheology in cases of continuous and pulsatile flow. The analysis results are compared with that of Newtonian model and give out very interesting hemodynamics predictions for each model. The size of recirculation zone is different from each model that is observed significantly. The wall shear stress of Carreau model gets the highest value, 14% in case of continuous flow and around 17% in pulsatile case bigger than that of Newtonian model. The results of pulsatile flow show that the Newtonian model is closed to power law model while the Casson model is similar to the Carreau model.

Keywords: hemodynamics, Newtonian, non-Newtonian, recirculation zone, wall shear stress.

1 Introduction

It is known that about 45% of blood volume contains three main kinds of cells that are known as red blood cells (RBCs), white blood cells and platelets. Normally, the red blood cells occupy from 35% to 50% of the blood, Saladin

et al (2000), so as a result they are important components in determining the flow characteristics of blood. When whole blood is tested in a viscometer, its non-Newton character is revealed, Fung (2004). Thus, generally speaking, blood is non-Newtonian fluid, Quarteroni (2006).

Many studies showed out evidences that blood behaves as a non-Newtonian fluid even in large arteries. It was proved that blood behaves predominantly as a non-Newtonian fluid in most of the cycle period, Rodkiewicz et al (1990). Other studies also gave out conclusions that non-Newtonian viscosity influences hemodynamics factors both in medium and large size arteries, Gijsen et al (1999a, 1999b). The conclusions were consolidated by investigating the non-Newtonian pulsatile blood flow in a bifurcation model with a non-planar branch, Chen et al (2006). Studies suggested that the non-Newtonian property of blood is important in the hemodynamic effect and plays an important role in vascular biology and pathology. With studying of blood flow in right coronary arteries Johnston et al (2006) concluded that the non-Newtonian model is more appropriate than Newtonian to simulate the blood properties.

Several theories have been built to describe the complex behavior of non-Newtonian fluid with varying degrees of success. Recently, Power law and Carreau models, among variety of non-Newtonian models, are the most widely used, Quarteroni et al (2006). In addition Han et al (2001) found that blood flow could be described as a Bingham plastic following the Casson equation.

In present study, the analysis of blood flow phenomena is conducted by using three-dimensional model in both continuous and pulsatile flow cases with utilizing the computational fluid dynamics software Fluent 6.2. Three commonly used non-Newtonian models of Carreau, Casson and power law are still applied to describe the properties of blood.

2 Materials and Methods

2.1 Power Law for Non-Newtonian Viscosity

$$\eta = k\,\dot{\gamma}^{\,n-1} e^{T_0/T} \tag{1}$$

2.2 Carreau Model

$$\eta = \eta_\infty + (\eta_0 - \eta_\infty)[1 + (\dot{\gamma}\,\lambda e^{T_0/T})^2]^{(n-1)/2} \tag{2}$$

2.3 Casson Model

$$\eta = \frac{\tau_0 + k[\gamma^n - (\tau_0/\mu_0)^n]}{\dot{\gamma}} \tag{3}$$

2.4 T-Junction Model

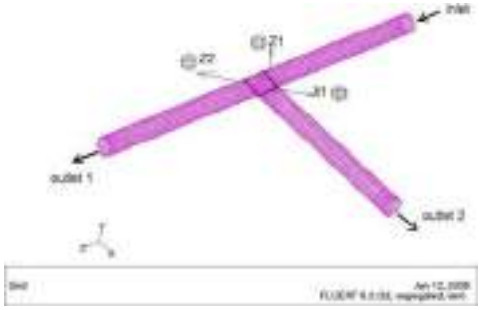

Fig. 1. T-junction model

3 Results and Discussions

Blood flow is demonstrated that the transition from laminar to turbulent only happens at Reynolds numbers of 3200 with vessel diameter about 7 mm, and 500 with vessel diameter about 1 mm, Han et al (2001). With assumption of Reynolds number approximately 480 along with 10 mm artery diameter, we could definitely consider the flow as laminar flow.

The appearance of vortex or recirculation zone is the condition for forming thrombosis. In both steady and unsteady cases, Newtonian as well as non-Newtonian fluids form the recirculation zones at the beginning of branched tube. The Newtonian model provides the largest vortices while the Carreau model gives out smaller size vortices. We focus on only comparing the results between Carreau model which owns the biggest viscosity and Newtonian one with the smallest viscosity.

Blood damage can be categorized as hemolysis, platelet activation, and the formation of thrombus and two of them are mainly caused by shear stress. In our research, different viscous models provide different wall shear stress

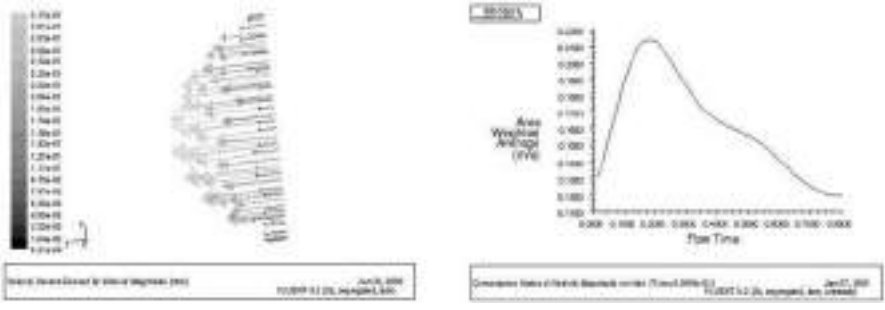

Fig. 2. Parabolic Pulsatile inlet velocities

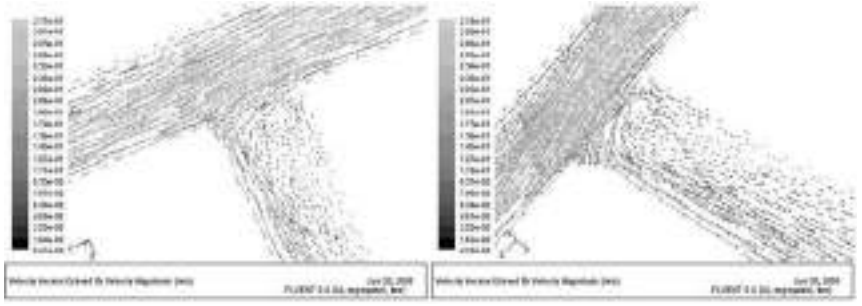

Fig. 3. Velocity distribution-Carreau-Newtonian - Steady

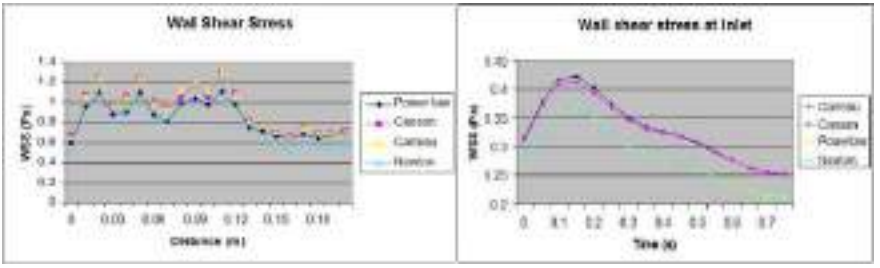

Fig. 4. Wall Shear Stress - Continuous Pulsatile flow

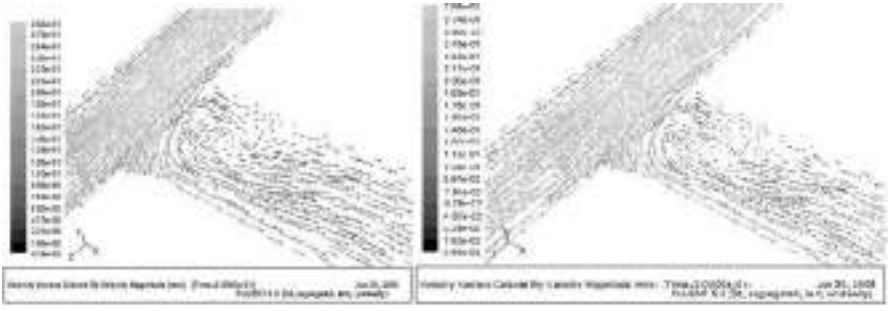

Fig. 5. Velocity distribution-Carreau Newtonian - Unsteady

(WSS) values. The Carreau model shows out the biggest WSS with average value about 14% in steady case and 17% in unsteady case higher than that of Newtonian model. The highest viscosity of Carreau model can account for this behavior. As depicted in Fig.4, while the difference between Newtonian and non-Newtonian models in case of continuous flow is not apparent even though Newtonian model gives out the smallest value, the analysis results

in case of pulsatile flow, especially results of Carreau model, show out much more obviously this difference.

4 Conclusion

In case of continuous flow, the Newtonian model predicts the largest size vortex, while the Carreau model predicts smaller size. Higher WSS value is obtained in case of continuous flow compared with that in case of pulsatile flow, but the difference between Newtonian and non-Newtonian does not reflect obviously. While the Casson model is closed to Carreau model, the Newtonian is similar to power law model.

In case of pulsatile flow, WSS variation of four models highlights that the difference between Newtonian and non-Newtonian models is very obviously. In this case, Newtonian model also provides the largest size of recirculation region, but more obvious than that in case of continuous flow.

In both continuous flow and pulsatile flow cases, Carreau model always predicts the highest value of viscosity and provides the biggest wall shear stress. The advantage of Carreau model might give us the numerical analysis results closer to behavior of nature blood.

Branched artery which is simplified as T-junction mode with angle of 90^0 is the worst case we have studied. This finding helps medical scientist be easier to specify which area inside circulatory system often forms thrombosis.

References

1. Chen, J., Lu, X.Y.: Numerical investigation of the non-Newtonian pulsatile blood flow in a bifurcation model with a non-planar branch. Journal of Biomechanics 39, 818–832 (2006)
2. Easthope, P.: A three-dimensional dyadic Walburn-Schneck constitutive equation for blood. Biorheology 26, 37–44 (1989)
3. Fung, Y.C.: Biomechanics Mechanical Properties of Living Tissues. Springer, Heidelberg (2004)
4. Fung, Y.C.: Biomechanics: Circulation. Springer, Heidelberg (2004)
5. Gijsen, F.J.H., van de Vosse, F.N., Janssen, J.D.: The Influence of the Non-Newtonian Properties of Blood on the Flow in Large Arteries: Steady Flow in a carotid bifurcation model. Journal of Biomechanics 32, 601–608 (1999a)
6. Gijsen, F.J.H., van de Vosse, F.N., Janssen, J.D.: The Influence of the Non-Newtonian Properties of Blood on the Flow in Large Arteries: Unsteady Flow in a 90^0 Curved Tube. Journal of Biomechanics 32, 705–713 (1999b)
7. Han, S.I., Marseille, O., Gehlen, C., Blümich, B.: Rheology of blood by NMR. Journal of Magnetic Resonance 152, 87–94 (2001)
8. Hund, S.J.: Hemodynamic design optimization of a ventricular cannula: Evaluation and implementation of objective functions. Ph.D dissertation, University of Pittsburgh, School of Engineering, U.S.A (2006)
9. Johnston, B.M., Johnston, P.R., Corney, S., Kilpatrick, D.: Non-Newtonian blood flow in human right coronary arteries: Transient simulation. Journal of Biomechanics 39, 1116–1128 (2006)

10. Katritsis, D., Kaiktsis, L., Chaniotis, A., Pentos, J., Efstathopoulous, E.P., Marmarelis, V.: Wall shear stress: Theoretical considerations and methods of measurement. Progress in Cardiovascular Diseases 495, 307–329 (2007)
11. Long, Q.: Numerical investigation of physiologically realistic pulsatile flow through arterial stenosis. Journal of Biomechanics 34, 1229–1242 (2001)
12. Longest, P.W., Kleistreuer, C.: Computational haemodynamics analysis and comparison study of arterio-venous grafts. Journal of Medical Engineering & Technology 24(3), 102–110 (2000)
13. Quarteroni, A.: What mathematics can do for the simulation of blood circulation. AMS Subject Classification: 92C50, 96C10, 76Z05, 74F10, 65N30, 65M60 (2006)
14. Rodkiewicz, C.M., Sinha, P., Kennedy, J.S.: On the Application of a Constitutive Equation for Whole Human Blood. Journal of Biomechanics Engineering 112(2), 198–206 (1990)
15. Saladin, K.S.: Anatomy & Physiology: The unity of form and function. McGraw-Hill, New York (2000)
16. Shibeshi, S.S., Collins, W.E.: The rheology of blood flow in a branched arterial system. National Institutes of Health: Appl. Rheol. 15(6), 398–405 (2005)
17. Valencia, A.A., Guzmán, A.M., Finol, E.A., Amon, C.H.: Blood Flow Dynamics in Saccular Aneurysm Models of the Basilar Artery. Journal of Biomechanical Engineering 128, 516–526 (2006)
18. Fluent 6.2 User's Guide. Fluent Inc. (2005)

The Effect of Curvature and Torsion on Steady Flow in a Loosely Coiled Pipe

Kyung E. Lee[1] and Jung Y. Yoo[1,2]

[1] BK21 School for Creative Engineering Design of Next Generation Mechanical and Aerospace Systems, Seoul National University, Seoul 151-744, Korea
kelee07@snu.ac.kr
[2] School of Mechanical and Aerospace Engineering, Seoul National University, Seoul 151-744, Korea
jyyoo@snu.ac.kr

A number of hemodynamic studies have already indicated that there is a relationship between the development of vascular diseases (e.g., atherosclerosis, intimal hyperplasia and thrombosis) and the local hemodynamic factors. Steady flow in the loosely coiled helical pipes is investigated, which is motivated by physiological and clinical applications. The objective of this study is to improve understanding of the influence of geometrical curvature and torsion on flows in helical pipes, in which the radius of pipe is much larger than the distance from the center of the pipe to the center of the helix. The three-dimensional computations of steady flows in the loosely coiled helical pipe are performed using a Navier-Stokes equation solver, which is based on spectral/hp element method for high accuracy. In this study, it is noted that the position of the maximum axial velocity component is influenced more by the curvature than by the torsion. It turns out that the effect of torsion on the axial flow is relatively minor, although torsion can radically influence the asymmetric pattern of the transverse flow and coherent vortical structures in a helical pipe. The ensuing results can provide hemodynamic information (i.e., vortex formation, mixing performance and wall shear stress distribution) within the loosely coiled vessels, so that clinical applications such as the design of stents and the model of synthetic bypass graft vessel to enhance the mixing of blood flow may be proposed.

1 Introduction

Nowadays, many developed countries face high rates of vascular diseases (e.g., atherosclerosis, intimal hyperplasia, thrombosis). Various medical, numerical and experimental observations have suggested that there is a strong correlation between mechanical factors and preferential sites for the accumulation of lipids in the early stage of atherosclerosis. For one thing, there seems to be a general agreement that wall shear stress affects the development of atherosclerosis. However, there is still uncertainty about the exact mechanism. It is hypothesized that low levels of wall shear stress are atherogenic

[CFS71, KGZG85] and some suggest that the gradient or the level of oscillation of wall shear stress are atherogenic, while others believe that high shear stress can damage the endothelium leading to atherosclerosis [Fry68, BTY83]. It has also been reported that high wall shear stress may have influences on initiation of the disease in the very young, but that low wall shear stress may have influences in adults [NL83, BW98, MCW01]. It is generally accepted that local hemodynamic factors are associated with the formation and the development of atherosclerosis, so that an answer to this question can be given in terms of hemodynamic factors, e.g., velocity, secondary motion, existence of separation, wall shear stress and coherent vortical structure.

The objective of this study is to provide a better understanding of the effects of torsion and curvature on the steady flow in the helical geometries with small amplitude. This further hemodynamic knowledge of flow in helical geometries can subsequently be applied to the optimization of a LITA (left internal thoracic-artery) graft and the design of stents for clinical applications.

2 Numerical Models and Methodology

Steady flow in helical geometries as shown in Figures 1 and 2 is studied. The radius (R) of the helix, the radius (r) of the tube ($4R = r$) and two different pitches ($P = 20r$ and $6r$) are chosen to correspond to physiologically realistic vessels. Hybrid high-order meshes are generated by using modified advancing front technique and the numerical results are achieved by using a Navier-Stokes equation solver, on the basis of spectral/hp element method [KS99]. In this method, vascular geometry can be defined accurately by increasing hybrid elements and high p-convergence is obtained by high polynomial order expansion.

3 Results

Let us show the evolution of steady flow at $Re = 125$ and 500 in a loosely coiled helical pipes (Helix I and II) with different pitches to consider the effects of curvature and torsion, by examining sectional velocity and vorticity profiles, coherent vortical structures and wall shear stress distribution.

Figures 3 and 4 show the wall shear stress normalised by that in the Poiseuille flow at the inlet of a straight pipe at the same Reynolds numbers. The sections of interest in axial velocity, normal vorticity at half-, one-, one & half- and two-turn of helices are presented on the left and right, respectively, at $Re = 125$ and 500. All sections are oriented as shown in Figure 3(b).

In Figures 3 and 4, as Re becomes larger, the effect of curvature and torsion on the flow in helical pipes appears to be more pronounced. In summary,

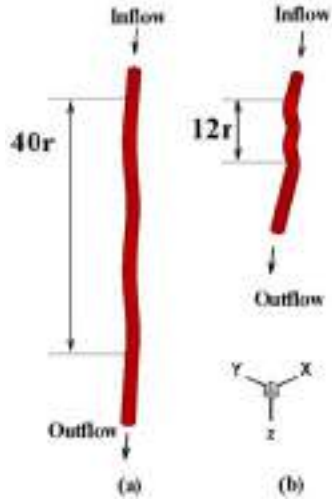

Fig. 1. Two-turn helical models, (a) Helix I, (b) Helix II with different pitches $P = 20r$ and $6r$

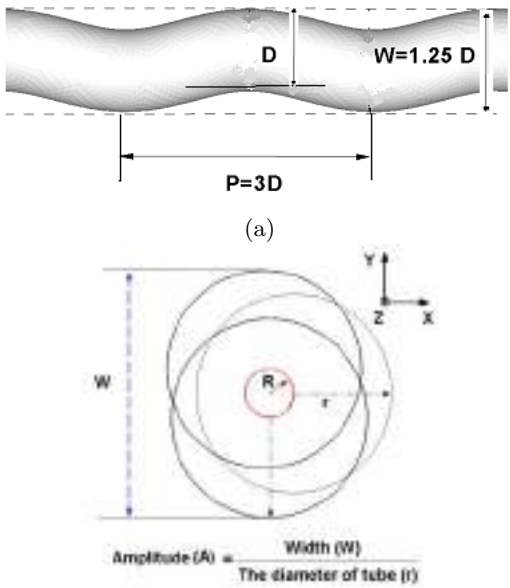

Fig. 2. (a) Side view of two-turn Helix I; (b) Front view of Helix I with the definition of the amplitude of the helix (A)

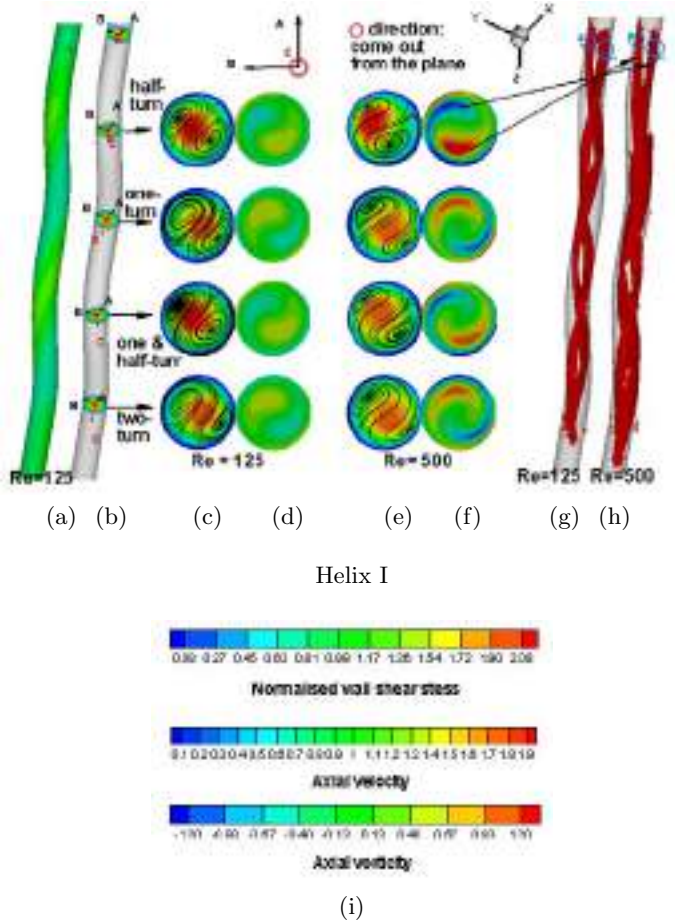

(a) (b) (c) (d) (e) (f) (g) (h)

Helix I

(i)

Fig. 3. Helix I: (a) the normalised wall shear stress, (b) physical orientation of each section, (c) axial velocity at Re = 125, (d) axial vorticity on the cross-sections at Re = 125, (e) axial velocity at Re = 500, (f) axial vorticity on the cross-sections at Re = 500, (g) coherent vortical structure (λ_2 = -0.1) at Re = 125, (h) coherent vortical structure [JH95] (λ_2 = -0.3) at Re = 500 and (i) the scale bars of wall shear stress, axial velocity and normal vorticity

torsion influences strongly on the transverse flow and the coherent vortical structure, although torsion does not affect significantly on the change of the axial flow. In Helix I with small curvature and small torsion, a helical symmetric vorticity pattern is observed. In Helix II with large curvature and large torsion, an asymmetric vorticity pattern presents the dominant single vortex.

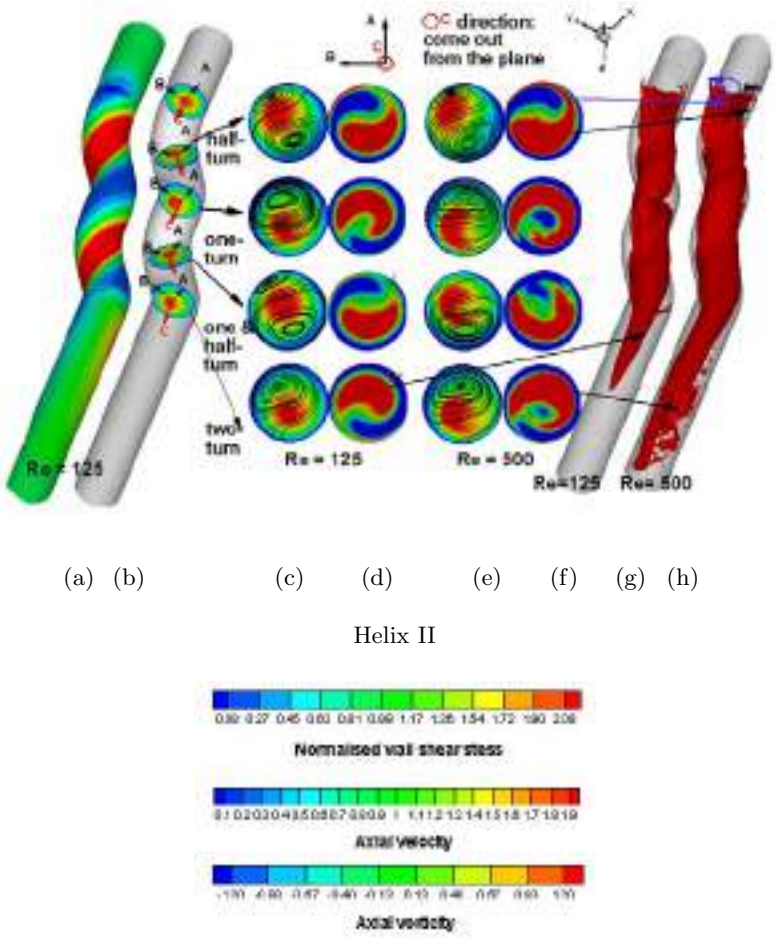

(a) (b) (c) (d) (e) (f) (g) (h)

Helix II

(i)

Fig. 4. Helix II: (a) the normalised wall shear stress, (b) physical orientation of each section, (c) axial velocity at Re = 125, (d) axial vorticity on the cross-sections at Re = 125, (e) axial velocity at Re = 500, (f) axial vorticity on the cross-sections at Re = 500, (g) coherent vortical structure (λ_2 = -0.3) at Re = 125, (h) coherent vortical structure [JH95] (λ_2 = -0.3) at Re = 500 and (i) the scale bars of wall shear stress, axial velocity and normal vorticity

4 Conclusions

The results provide a better understanding of the role of vascular configurations in terms of the curvature and the torsion on the flow. Therefore, these results can suggest clinical applications with consideration of mixing and wall shear stress distribution within the helical shaped vessel.

References

[BTY83] Berger, S.A., Talbot, L., Yao, L.-S.: Flow in curved pipes. Ann. Rev. Fluid Mech. 15, 461–512 (1983)

[BW98] Barnes, S.E., Weinberg, P.D.: Contrasting patterns of spontaneous aortic disease in young and old rabbits, Arterioscler. Thromb. Vasc. Biol. 18, 300–308 (1998)

[CFS71] Caro, C.G., Fitz-Gerald, J.M., Schroter, R.C.: Atheroma and Arterial Wall Shear: Observation, Correlation and Proposal of a Shear Dependent Mass Transfer Mechanism for Atherogenesis. Proceedings of the Royal Society of London (B) 177, 109–159 (1971)

[Fry68] Fry, D.L.: Acute vascular endothelial changes associated with increased blood velocity gradients. Circ. Res. 12, 165–197 (1968)

[JH95] Jeong, J., Hussain, F.: On the identification of a vortex. Journal of Fluid Mechanics 285, 69–94 (1995)

[KGZG85] Ku, D.N., Giddens, D.P., Zarins, C.K., Glagov, S.: Pulsatile flow and atherosclerosis in the human carotid bifurcation. Positive correlation between plaque location and low oscillating shear stress, Arterioscler. Thromb. Vasc. Biol. 5, 293–302 (1985)

[KS99] Karniadakis, G.E., Sherwin, S.J.: Spectral/hp methods for computational fluid dynamics, 2nd edn. Oxford Science Publications (1999)

[MCW01] McGillicuddy, C.J., Carrier, M.J., Weinberg, P.D.: Distribution of lipid deposits around aortic branches of mice lacking LDL receptors and apolipoprotein E. Arterioscler. Thromb. Vasc. Biol. 21, 1220–1225 (2001)

[NL83] Nerem, R.M., Levesque, M.J.: The case for fluid dynamics as a localising factor in atherogenesis. In: Proc. Symposium on fluid dynamics as a localising factor for atherosclerosis, pp. 26–33. Springer, Berlin (1983)

Part 10
Bio-fluid Mechanics 2

“*This page left intentionally blank.*”

Analysis of the Unsteady Flow and Forces in an AAA Endovascular Stent

T. Kim[1], H.A. Dwyer[2], A. Cheer[1], T.B. Howell[3], T. Chuter[3], and D. Saloner[3]

[1] Dept. of Mathematics, University of California, Davis, Davis, California 95616
[2] Dept. of Mech. & Aero. Engr, University of CA, Davis, Davis, CA 95616
[3] University of California, San Francisco, San Francisco, California 94143

Abstract. A detailed unsteady simulation of the flow and the forces on the blood vessels at the iliac bifurcation of the aorta for both healthy and diseased patients is presented. The flow geometry of two patients, one healthy and one diseased, is obtained from CT data, while their blood pressure was measured directly. The simulations using finite volume CFD and overset grid techniques are shown to be very accurate. The abnormal geometry for the abdominal aortic aneurysm patient in this investigation effects the flow patterns resulting in large forces that are shown to be caused primarily by the blood pressure rather than the flow pressure. These forces are directly related to flow area and the direction of the iliac arteries relative to the descending aorta. The fluid flow is disturbed by the vessel geometry in the diseased patient as shown by areas of significant flow recirculation and stagnation.

Keywords: Patient specific AAA stent-graft, computational fluid dynamics, unsteady flow and dynamic forces.

1 Introduction

Over the last decade there has been rapid progress in the technology to repair abdominal aortic aneurysms (AAA) with the use of endovascular stent-grafts ([CRH96], [LL01], [WCM03]). Although the technology is improving, there is pressing need to understand the flow and the forces in individual patients, since individual parameters such as advanced disease, age of the patient and blood pressure can have a significant influence on long term success of the intervention. In the present work, we performed simulations of the flow and calculated the forces on two patients in whom there are large variations in the geometry of the aortic bifurcation leading to the left and right iliac arteries. The geometry of the bifurcations is obtained and modeled from CT scans of the individual patients, one with an endovascular stent-graph and one without ([S04]). This data is used to create three dimensional surface models of the abdominal aorta region (see figure 1). These surfaces are then used to generate the overset mesh system for our computations.

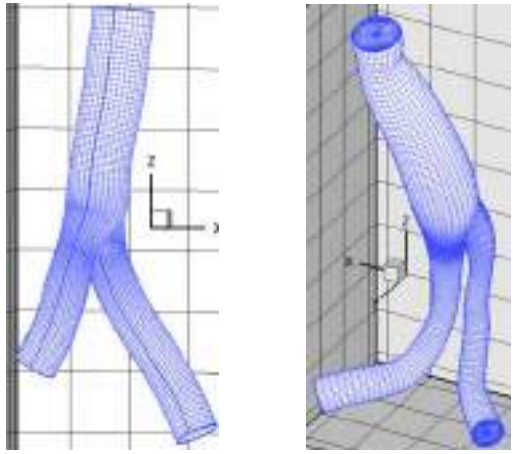

Fig. 1. Surface and Computational grids generated from CT Scans. Healthy Patient (left) and AAA Patient (right).

2 Methods of Approach

The fluid flow in our system is modeled by the incompressible Navier–Stokes equations in dimensionless control volume formulation.

Continuity

$$\iint_S \vec{V} \bullet d\vec{A} = 0 \tag{1}$$

Momentum

$$\frac{\alpha^2}{\mathrm{Re}} \iiint_V \frac{\partial \vec{V}}{\partial t} dV + \iiint_V (\vec{V} \bullet \vec{\nabla}) \vec{V} dV = -\iint_S p \bullet d\vec{A} + \frac{1}{\mathrm{Re}} \iint_S \overline{\overline{\tau}} \bullet d\vec{A} \tag{2}$$

where p is the pressure, $\overline{\overline{\tau}}$ is the viscous stress tensor, R is the inlet radius of the aorta, $\mathrm{Re} = \frac{2R\bar{U}}{\nu}$ the Reynolds number, $\alpha = R\left(\frac{\omega}{\nu}\right)^{1/2}$ is the Womersley parameter [W55], $\bar{U}$ is the maximum inlet velocity, ν is the kinematic viscosity of the fluid, and ω is the inlet pulse frequency (ω=2πf where f is the heart rate). For most applications this system of equations cannot be solved analytically and a numerical method must be employed.

A control volume approach is used to approximate the solution to equations (1) and (2) ([SDC02],[KDC04]). In our numerical simulations, the inlet flow velocity at the proximal end of the vessel is specified as a function of time (figure 2), and the shapes of the velocity profile and the blood pressure phase are assumed to be the same for both subjects. The peak systole average blood velocity in the abdominal aorta is approximately 60 cm/s for a healthy individual and using the actual measured radii for the subjects and the same cardiac output we obtain a peak Reynolds number of Re = 1523 for the stented subject and Re = 2498 for the non–stented subject. The asymmetric shape of the blood pressure curve in figure 2

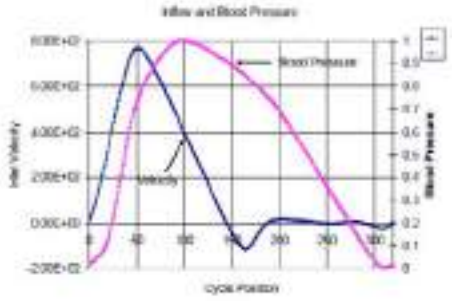

Fig. 2. Inlet velocity profile and blood pressure curve for one cycle. The cardiac cycle starts at 0 and ends at 360.

corresponds to systole (cardiac contraction) and diastole (cardiac filling). A fifty percent split of the flow volume at the bifurcation is assumed at all times during the cardiac cycle. The Womersley number is set at $\alpha = 15$ in both cases. The forces acting on the vessel and the stent-graph are also calculated using a control volume approach.

3 Discussion

Results of our unsteady three dimensional flow simulations indicate very different flow structures and forces between the stented and non-stented subjects. In our calculations the pressure is separated into two parts: the blood pressure and the flow pressure. The sum of these two pressures which represents the actual pressure relative to the pressure outside the vessel wall, is presented in figure 3. When the inlet flow is at its peak, the difference between the maximum and minimum pressure values for the AAA stented patient is about 2.5% of the maximum and for the non-stented patient it is 5.1%. This relatively small change in pressure indicates that any wall motion is primarily due to the overall blood pressure rather than the flow.

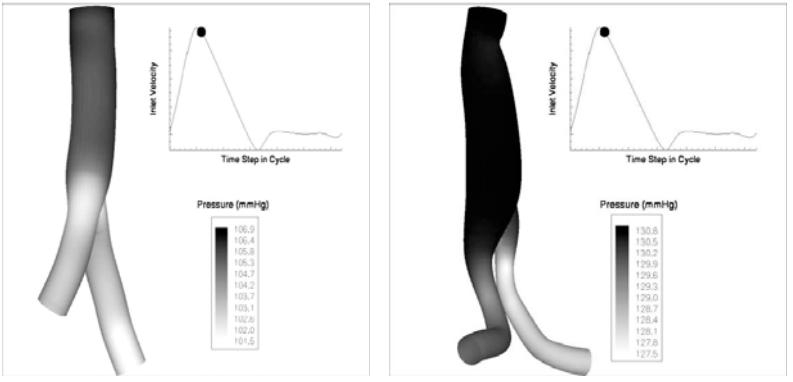

Fig. 3. Pressure along the surface of the vessel at peak flow conditions for healthy patient (left) and stented AAA subject (right)

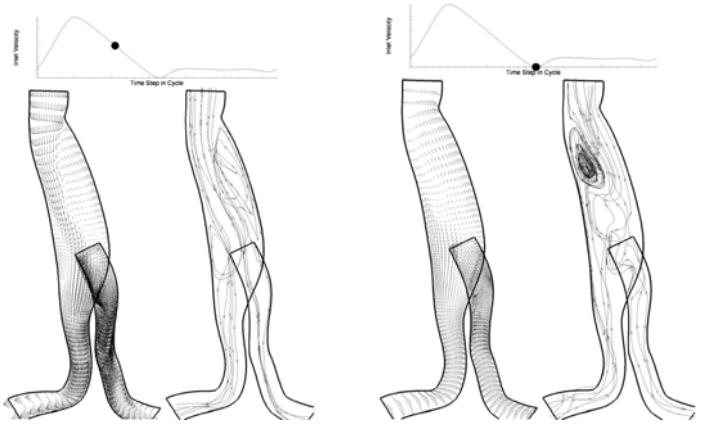

Fig. 4a. Velocity and instantaneous streamlines along the lateral surface at two different times for the stented AAA patient

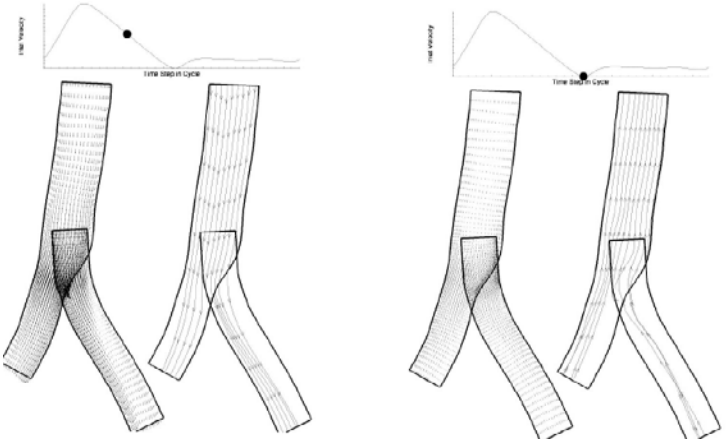

Fig. 4b. Velocity and instantaneous streamlines along the lateral surface at the same two times for the healthy unstented subject

The velocity and instantaneous streamlines at various stages of the cardiac cycle for both subjects are presented in figure 4. The bend in the vessel near the inlet and the expansion of the vessel area after the bend appear to cause a recirculation zone for the stented AAA subject (figure 4a). Large sections of flow separation are not observed in the case of the non-stented subject during most of the cardiac cycle where the geometry is relatively straight and the vessel radius remains relatively constant (figure 4b).

Wall shear stress is calculated and presented in figure 5. The lowest wall shear appears in the region after the entrance bend in the vessel near the inlet for the AAA stented patient. Since the cross-sectional areas in this region expand to over

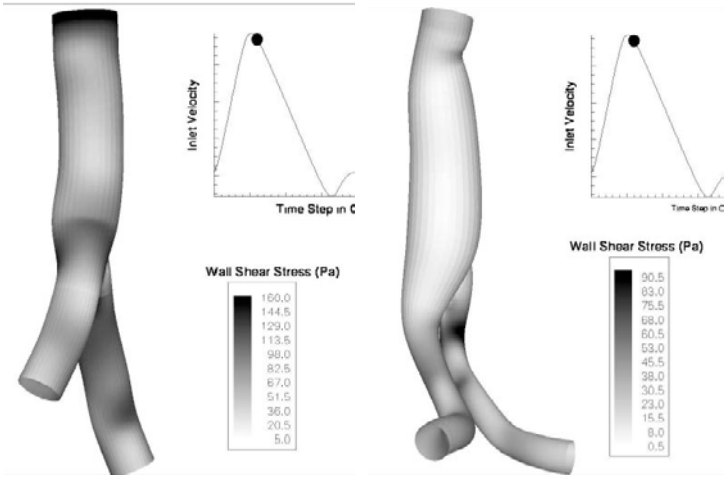

Fig. 5. Wall shear stress for healthy patient (left) and AAA patient (right)

twice the cross-sectional area of the inlet, the velocity in this region must decrease, resulting in lower wall shear stress.

Using a control volume surrounding the stent material, the force needed to keep the stent-graft fixed, the clamping force, is calculated. A time history plot of the various force components is presented in figure 6. In both cases, the blood pressure is the dominate force component indicating that the forces due to the flow are of secondary importance when calculating the overall forces acting on the stent graft vessel. The force magnitude calculated, of almost four Newtons, is similar to that obtained by Liffman et al [LL01], however the mechanism is much different. By doing a comparison of the different forces resulting from fluid flow, the unsteady acceleration terms and the flow pressure gradient are the largest; however they tend to cancel each other out, since flow acceleration and the pressure gradient are strongly connected through the flow dynamics.

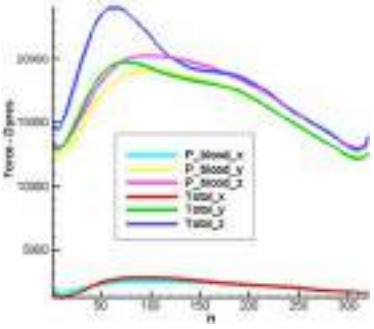

Fig. 6a. Force Components for healthy non- stented patient.

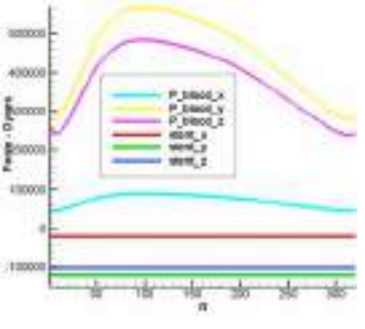

Fig. 6b. Forces AAA patient. Total forces in this case is the sum of P-blood and stent

The clamping force needed to keep the stent graph fixed also has components along all axii, and the relative size is approximately 50% in the vertical or z direction, 40% in the y direction, and 10% in the x direction. For the stent graft patient, the force due to the measured blood pressure is almost two orders of magnitude larger than all the other forces (figure 6b). In the non–stented case, although the blood pressure is still the dominating force component, the flow pressure plays a more significant part of the force on the vessel wall. Furthermore, the magnitude of the clamping force for the stented case is more than an order of magnitude larger than that of the non–stented case.

There are two important factors that explain our results for the force calculations. First, the dominating force is the blood pressure term, and second, the blood pressure term is strongly dependent on the cross-sectional areas of the flow inlet and outlets and their orientation. In the case of the non–stented subject, since the sum of the outlet cross–sectional areas is approximately the same as the inlet area and the normals to the cross–sectional surfaces are nearly parallel, the blood pressure forces on the inlet and outlets nearly cancel each other out. For the stented subject the normals to the inlet and outlets are nearly at right angles to each other and there is very little cancellation between the inlet and outlets of the blood pressure force. If the right and left iliac arteries are artificially bent for the healthy patient, the force magnitude would increase into the range of five Newtons. Therefore, the direction of the iliac arteries relative to the direction of the aorta plays a very significant role on the forces acting on the vessel.

References

[CRH96] Chuter, T., Risburg, B., Hopkinson, B., et al.: Clinical experience with a bifurcated graft system-development and early experience. Cardiovas Surg. 4, 706–712 (1996)

[LL01] Liffman, K., Lawrence-Brown, M., et al.: Analyical modeling and numerical simulation of forces in an endoluminal graft. Journal of EndoVascular Therapy 8, 358–371 (2001)

[WCM03] Walsh, P.W., Chin-Quee, S.C., Moore Jr., J.E.: Flow changes in the aorta associated with the deployment of a AAA stent graft. Med. Engr. & Physics 25, 299–307 (2003)

[S04] Saloner, D.: Private Communication from University of California, San Francisco (2004)

[W55] Womersley, J.R.: Method for the calculation of velocity, rate of flow and viscous drag in arteries when the pressure gradient is known. J. Physiol. 127, 553–563 (1955)

[SDC02] Shahcheraghi, N., Dwyer, H.A., Cheer, A., et al.: Unsteady and three-dimensional simulation of the blood flow in the human aortic arch. Jour. Of Biomedical Engr. 124, 378–387 (2002)

[KDC04] Kim, T., Dwyer, H.A., Cheer, A.Y.: A simulated dye method for flow visualization with a computational model for blood flow. Journal of Biomechanics 37, 1125–1136 (2004)

Part 11
Complex Flow 1

“*This page left intentionally blank.*”

Computation of Low Reynolds Number Aerodynamic Characteristics of a Flapping Wing in Free Flight

Dominic D.J. Chandar and M. Damodaran

School of Mechanical and Aerospace Engineering,
Nanyang Technological University, 50 Nanyang Avenue, Singapore 639798
domi0002@ntu.edu.sg, mdamodaran@ntu.edu.sg

1 Introduction

It is well known from literature that unsteady motions of airfoils and wings create aerodynamic forces suitable thrust and lift forces which propel and sustain insect and bird flight. Most of the experimental studies carried out by Freymuth[1], Jones et al.[2], Lai and Platzer[3] and numerical computations by Liu and Kawachi[4], Wang[5], Lewin and Haj-Hariri[6], have focused on static flapping or active flight while neglecting the dynamics of forward flight. In an experiment by Vandenberghe et al.[7], the problem of forward flight has been discussed in detail with more emphasis on the dynamic motion of a wing undergoing plunging motion. The transition between the state of rest and free flight for a flapping wing is shown to take place at a critical reduced frequency of plunging. Numerical computations in two-dimensions following the lines of Vandenberghe et al.[7] have been performed by Alben and Shelly[8], Chandar and Damodaran[9]. Three-dimensional computations on free flight highlighting the effect of wing rotation modes can be found in Chandar and Damodaran[10]and is extended in the present paper to understand the effect of outer boundaries on trajectories due to flapping motion in two-dimensions and analyze the effect of combined wing rotation on forward flight in three-dimensions.

2 Computational Model

The motion of a wing is governed by the unsteady incompressible Navier Stokes equations coupled with the dynamical equations of motion. The complete description of the numerical method, implementation of the boundary conditions, interpolation on the overlapping mesh and convergence studies, can be found in Henshaw [11], Chandar and Damodaran [9]. However for the

sake of completeness, an outline of the numerical method is provided here. The time dependent incompressible Navier Stokes Equations are given by,

$$\frac{\partial \mathbf{u}}{\partial t} + (\mathbf{u}.\nabla)\,\mathbf{u} + \frac{\nabla p}{\rho} = \nu \Delta \mathbf{u} + \mathbf{F} \tag{1}$$

$$\nabla.\mathbf{u} = 0 \tag{2}$$

Here $\mathbf{u}$ is the velocity vector, p is the pressure, $\mathbf{F}$ is a vector of external forces per unit volume, ν is the kinematic viscosity and ρ is the fluid density. These equations are discretized in space on a system of overlapping meshes. An implicit multi-step method is used for time stepping and second order differences are used for spatial discretization. The pressure is obtained by solving a pressure Poisson equation using the Bi-Conjugate Gradient Stabilized method from *PETSc*(Portable Extensible Toolkit for Scientific Computation) [12]. The acceleration of the body is computed using aerodynamic forces F_A and torques $T = \int_{d\Omega}(r - x_{cm}) \times dF_A$ where r is any point on the body and x_{cm} is the center of mass. This appears in the boundary condition for pressure in the pressure equation. The Navier-Stokes equations are solved numerically with this boundary condition and a new set of forces are obtained. This procedure is repeated over a period of time till the final time of computation. When the meshes move rigidly with the body, the solutions in the region of overlap are interpolated using a Lagrange interpolation formula. The non-dimensional quantities of interest are the Reynolds number $Re = V_p c/\nu$ and the Strouhal number $St = \omega c h_0/V_p$, where V_p is the maximum plunge velocity, c the mean aerodynamic chord, ω the flapping frequency, and h_0 the maximum plunge amplitude.

3 Results and Discussions

Validation cases for the *OverBlown* code can be found in Chandar and Damodaran[9]-[10]. Two sets of computations are shown in this paper to address the effect of (i) location of outer boundaries on estimated aerodynamic coefficients and computed flight trajectories and (ii) wing rotations on computed flight trajectories.

3.1 Effect of Outer Boundary Locations on Computed Aerodynamic Characteristics

This assessment is carried out to study the effect of the extent and location of far-field outer boundary on the computedaerodynamic characteristics and trajectories for a plunging and pitching symmetrical airfoil (10% thick). Three different extents of the outer boundary locations are considered. The width (W) and height (H) of the computational domain for these cases are given by (a) $W = 24c$, $H = 16c$ (b) $W = 12c$, $H = 8c$ and (c) $W = 6c$, $H = 4c$

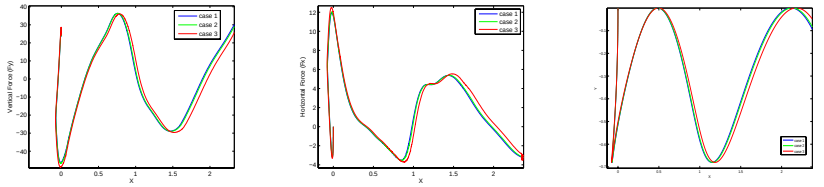

(a) (b) (c)

Fig. 1. Comparison of aerodynamic characteristics of an airfoil in free flight (a) vertical force (b) horizontal force and (c) trajectories for different domains

where c is the airfoil chord. The mesh density is maintained the same in all cases and the minimum mesh spacing from the wall is $5 \times 10^{-4}c$. The airfoil undergoes a combined plunge and pitch oscillation analogous to a flapping wing as described in the next section. The plunge and pitch are governed by the expressions, $h = -h_0(1 - cos2\pi ft)$, $\theta_i = \theta_0(1 - cos2\pi ft)$ respectively with $h_0 = 0.34$, $\theta_0 = 10^o$ and $f = 1.5$ Hz. From the aerodynamic forces, the position of the centre of mass is then obtained by integrating Newton's second law for a rigid body. Figures 1(a)-1(b) show the variation of the vertical and horizontal force components with spatial x-coordinate of the forward flight direction for the three cases. Computations show that these forces are either overestimated or underestimated on a smaller domain. The forces corresponding to case(b) do not differ much from that of case(a) (very large domain) hence the domain corresponding to case(b) would be an optimum choice for economic three-dimensional computations. The computed trajectory corresponding to these three cases are shown in Fig. 1(c). It can be seen that the computed trajectory corresponding to case(c) has a larger wavelength compared to that of case(a) and case(b). This shows that on smaller domains, numerical errors will cause the airfoil to travel slower.

3.2 Effect of Wing Rotations on Computed Trajectories

Of all flapping wing computations available in literature, computing the free flight characteristics is conceivably the most interesting one. By allowing the wing to translate freely, one can get an idea of the trajectory the wings establish and hence monitor its dynamic performance. From existing computations on flapping wings, it is well known that an optimal combination of reduced frequency, amplitude and plunge-pitch phase, gives rise to thrust. But it is unknown what will happen when the body is propelled forward by virtue of this thrust. Static flapping computations have some drawbacks i.e.,(i) they might over/under-estimate the thrust due to the fact that the imposed free-stream velocity is constant. The vortices which are shed as a result of flapping have a fixed residence time within the vicinity of the airfoil or wing (ii) It is unknown whether the lift produced as a result of flapping can sustain the body's weight. These issues are avoided when the wing is set

free to move at a velocity which is determined by the aerodynamic forces. An arbitrary wing consisting of elliptical wing sections with a thickness ratio of 0.1 and a low aspect ratio of 2is considered so that the three-dimensional effects are not negligible and a high density ratio of 10 is chosen to ensure that the wing will move slowly. Choosing a low density ratio wing will result in large accelerations requiring the imposition of very stringent time steps for the computation. The span-wise, chord-wise direction extends along the Z-axis and X-axis respectively as shown in Fig. 2(a)-2(c). Overlapping meshes with 607,000 mesh points are generated for the wing. The wing is enclosed in a box (cartesian mesh) which has all its sides as interpolation boundaries (inner box in Fig. 2(c)). When the wing moves, this box also moves with respect to a stationary cartesian mesh (outer box in Fig. 2(c)) and the interpolation relationship between the outer and inner box is regenerated every time step. The dimensions of the outer box are decided based on the observations from the previous sub-section. The domain corresponding to case(b) is used and the extent of the domain in the span-wise direction is given by $8S$ where S is the wing-span. Rotations about all three axes can be specified and the resulting translational motion be obtained by integrating the rigid body equations. Presently, computations have been carried out for periodic rotations about 2 axes (X and Z) and the position of the wing being constrained to move along X-axis. These are equivalent to plunging and pitching in two-dimensions. The specified rotational motions for the wing follow the equation $\theta_i = \theta_0(1 - cos2\pi ft)$ where θ_i denotes the angular position of the wing about axis 'i' which passes through the point P(0,0,-1) as in Fig.2(a). The Reynolds number and the Strouhal number are computed based on the maximum plunge velocity $V_p = 2\pi\theta_0 Sf$ where S is the wing-span. Based on a flapping amplitude of 10 degrees, kinematic viscosity of $0.01cm^2s^{-1}$ and a Strouhal number of 2, based on maximum arc length traversed by the wing tip, the Reynolds number is 329. Since the wing flaps in zero free-stream velocity, a steady flow initial condition is not required to start the computation at t=0. Three different types of rotation modes are considered namely (a) rotation about X-axis (b) rotation about Z-axis and (c) combined

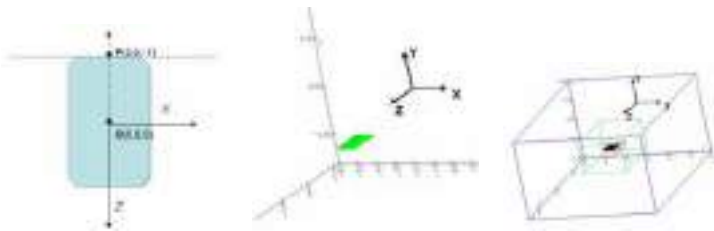

(a) (b) (c)

Fig. 2. Free flight of a flapping wing showing (a),(b) The elliptical cross-section wing of aspect ratio 2 and (c) Mesh block boundaries

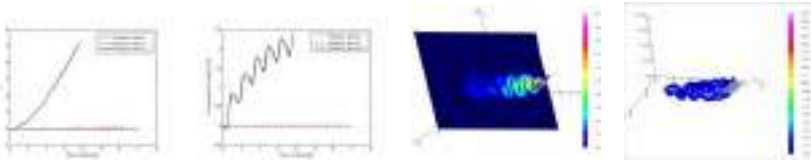

(a) (b) (c) (d)

Fig. 3. Computed (a) trajectory (b) forward speed for a flapping wing with different modes

rotation about X and Z axis. Using approximately 333 time steps per cycle, the solution is computed till the wing reaches the vicinity of the boundary. Figure 3(a)-3(b) shows the computed trajectory and forward speed corresponding to different modes of oscillation. It can be seen that between cycle 4.5 and 5.5 , the combined mode of oscillation propels the wing at an average speed of 2.05 cm/s. This is about 62% of the peak plunge velocity (3.29 cm/s). Whereas rotation about X, Z axis resulted in an average speed of 0.019 cm/s and 0.0013 cm/s respectively. This result confirms the fact that pure plunging motion of the wing (rotation about X-axis) results in higher thrust compared to pure pitching (rotation about Z-axis) at the same reduced frequency. Figure 3(c)-3(d) shows the contours of vorticity magnitude about a plane passing through the mid-section of the wing and iso-surfaces respectively. The wake is partially deflected downwards which indicates lift is being produced. This is also evident from Fig. 4(a) where the time history of lift over one cycle is plotted along with the wing positions at specific times. The region from cycle = 4 to cycle= 4.5 is the downstroke and from cycle=4.5 to cycle = 5 is the upstroke. The average lift in the downstroke is about 8.32 and in the upstroke is about -5.17. Figure 4(b) shows the time history of the horizontal force over one cycle. The numerical values differ from an earlier computation[10] as the pressure forces were not taken into account while calculating the total force. In this case the downstroke produces a thrust of -0.74 whereas the upstroke produces a thrust of 1.25. Hence the conditions for maximizing lift and thrust occur at different phases of the cycle. A possible solution to this problem would be to provide a phase difference between pitch and plunge.

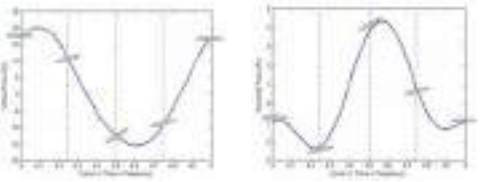

(a) (b)

Fig. 4. Computed aerodynamic forces (a) Vertical force (b) Horizontal force over one cycle of flapping

4 Conclusion

The importance of passive form of flapping flight has been discussed based on the computational study by solving the Navier-Stokes equations on moving overlapping meshes. The effect of the location of the outer boundary on computed solutions show that on a smaller domain, the aerodynamic forces are either over- or under-estimated depending on the position of the airfoil in the oscillation cycle and that the airfoil motion is slower due to boundary interference errors. For three-dimensional wings, it has been shown that more lift is produced in the downstroke than the upstroke and that the combined flapping mode which involves simultaneous rotation about two axes yielded a high forward speed due do higher thrust. By varying the phase between different rotational motions, it might be possible to optimize both thrust and lift either during the downstroke or upstroke. Further research is aimed at analyzing the flexibility of the wing in free flight.

References

1. Freymuth, P.: Propulsive Vortical Signature of Plunging and Pitching Airfoils. AIAA J. 26, 881–883 (1988)
2. Jones, K.D., Dohring, C.M., Platzer, M.F.: Experimental and Computational Investigation of the Knoller-Betz Effect. AIAA J. 37, 1240–1246 (1998)
3. Lai, J.C.S., Platzer, M.F.: Jet Characteristics of a Plunging Airfoil. AIAA J. 37, 1529–1537 (1999)
4. Liu, H., Kawachi, K.: Numerical Study of Insect Flight. J. Comp. Phy. 146, 124–156 (1998)
5. Wang, Z.J.: Vortex Shedding and Frequency Selection in Flapping Flight. J. Fluid Mech. 410, 323–341 (2000)
6. Lewin, G.C., Haj-Hariri, H.: Modelling Thrust Generation of a Two-dimensional Heaving Airfoil in a Viscous Flow. J. Fluid Mech. 492, 339–362 (2003)
7. Vandenberge, N., Zhang, J., Childress, S.: Symmetry Breaking Leads to Forward Flapping Flight. J. Fluid Mech. 506, 147–155 (2004)
8. Alben, S., Shelley, M.: Coherent Locomotion as an Attracting State for a Free Flapping Body. Proceedings of the National Academy of Sciences 102(32), 11163–11166 (2005)
9. Chandar, D., Damodaran, M.: Computational Study of Unsteady Low Reynolds Number Airfoil Aerodynamics Using Moving Overlapping Meshes. AIAA J. 46(2), 429–438 (2008)
10. Chandar, D., Damodaran, M.: Computational Study of the Free Flight of a Flapping Wing in Low Reynolds Numbers. In: 46th Aerospace Sciences Meeting and Exhibit, Reno, NV, AIAA paper 2008-0420 (2008)
11. Henshaw, W.D.: OverBlown, A Fluid Flow Solver for Overlapping Grids. Reference Guide, UCRL-MA 134289, 1–51 (2003)
12. Balay, S., Gropp, W.D., McInnes, L.C., Smith, B.: PETSc 2.0 Users Manual Revision 2.3.3, Argonne National Laboratory, Report AN-95/11, 1–190 (2007)

Application of Window Embedment Grid Technique

Yufei Zhang, Haixin Chen, and Song Fu*

School of Aerospace, Tsinghua University, Beijing, 100084, China
fs-dem@tsinghua.edu.cn

Abstract. An in-house developed multi-block grid CFD code called NSAWET is used for simulations of complex aeronautics configurations. With its Window-Embedment grid technique, the grid generation about complex configuration can be greatly simplified by generating grid about each part of the configuration separately with appropriate grid topology and density. Multi-scale flow field can be well simulated. Both the block number and the grid point number can be dramatically reduced. The code allows exchanging flow information between block interfaces on which points are not one-to-one matched with the technique of Overlap Area-Weighted Reconstruction. A realistic civil transporter configuration is numerically simulated. The results match well with experimental data.

Keywords: Structured grid, window embedment method, vortex generator, civil transporter.

1 Introduction

Compared with the unstructured grid, the structural grid's major drawbacks are its difficulties in process complex geometry and inconveniences in local grid refinement. In modern CFD investigations, more and more multi-scale geometries and the relevant multi-scale flow fields often need to be simulated. For example, some aerodynamics parts are relatively small in size compared with the whole aircraft, such as vortex generators, high-lift devices and external stores. Fine grids are critical to reveal these critical parts' surrounding flow details which are important to the aircraft's overall performance.

In the conventional '1-to-1' multi-block grid technique, because of the strong correlation among grid blocks on the grid point number and grid distribution, the grid clustering in one block often have to be 'broadcasted' to other blocks, leading to waste of grid points and excessively large aspect-ratio of grid cells in the far-field region. What's more, the selections of grid topology for different blocks are also often mutually restricted and not able to suit each block's specific geometry and flow characteristics.

In present study, Window Embedment (WE) grid technique is introduced to deal with the problems of structured grid. Several successful cases of the WE method will be shown in the following sections.

* Corresponding author.

2 Introduction to Window Embedment Grid

The NSAWET (Navier-Stokes Analysis based on Window-Embedment Technique) code is developed for the engineering viscous simulation of realistic aircraft configurations. The Window Embedment technique [CFL03] is the core strategy of the code. As a cure for those structural grid technique's inherent problems, the WE method has been successfully used in several realistic aircraft configurations [CZX06].

Decomposing a complex configuration to simple parts, and generating grid separately, are the basic ideas of the WE method. These ideas come from the Chimera grid. But the WE grid is quite different from the Chimera grid, because the WE grid has clear interfaces between the outer and inner grid. Flow information is interpolated on the grid interfaces. There are two superficial but very important advantages for the WE method. First, with the clear interfaces, the conservation of the flow information is easy to reserve. Second, high accuracy interpolation methods such as ENO and WENO methods are efficacious on the grid interfaces. Flow information between the interfaces is exchanged by the method of overlap area-weighted reconstruction (OAWR) [CFL03]. Moreover, WE grid method is easy to realize local grid refinement, and the total grid point number could be reduced. In the window region, a part of outer block grid is replaced by the inner grid. But it doesn't need to eliminate the part of outer block grid. The part is blocked by setting the timestep to zero. Block number could be dramatically reduced by this method. The array in computer memory of the blocked part is used as ghost cells to change flow information between the outer and inner blocks.

(1). Baseline inlet grid and a window on the grid

(2). Vortex generators mesh and interface of the window

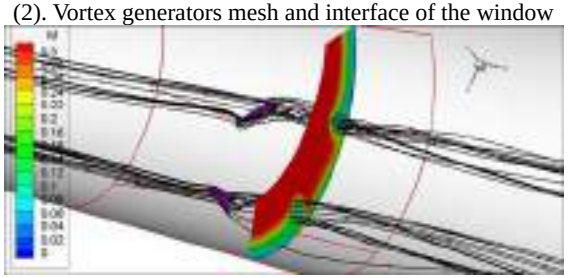

(3). Streamlines and Mach number distributions

Fig. 1 Meshing strategy of WE technique for vortex generators

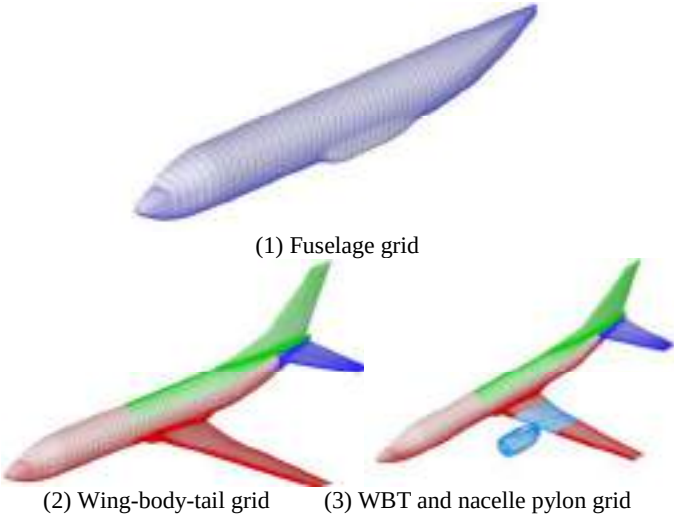

(1) Fuselage grid

(2) Wing-body-tail grid (3) WBT and nacelle pylon grid

Fig. 2. Surface grid of a civil transporter with nacelle and pylon

To explain the meshing strategy of WE technique, the grid generation procedure about vortex generators in a serpentine inlet is used as an example (Fig. 1): First, in Fig. 1 (1), an O-H grid is generated about the baseline inlet; then in Fig. 1 (2), a window is specified on the baseline grid, and H-H grid blocks for the blades of vortex generators are embedded into the window. With such a two-layer embedment, the whole configuration is simulated with high quality grids. The regions of vortex generators are simulated by grids with appropriate density and topology. In the simulation results, as shown in Fig. 1 (3), the streamlines pass through the window smoothly, and the vortex structure after the blades and their effects are clearly revealed.

A more complex example is shown in the Fig. 2. A civil transporter, with nacelle and pylon, is separated as three parts: fuselage, wing (or horizontal and vertical tails), and nacelle. The mesh near the wing is more dense than the fuselage region. Total number of the grid is about 2.5×10^6. Only about 20% of the points are in the fuselage and far-field region; 80% of the grid points are in the window, near the wing and the nacelle.

3 Numerical Methods

3.1 Spatial Schemes

Spatial discretization of NSAWET code is formulated in the frame of the finite volume approach in order to get a highly efficient, robust and accurate solver for engineering application. Two upwind schemes, the Roe's Flux Difference Splitting

(FDS) scheme and the van-Leer's Flux Vector Splitting (FVS) scheme are integrated. Third order MUSCL up-wind bias interpolation is employed to ensure that the schemes are 2nd order accurate on non-uniform and curvilinear grid. Smooth and continuously derivable van Albada limiter is used to restrict the high-order spurious oscillation in the numerical solution. In present study, the Roe's FDS scheme is employed for spatial discretization.

3.2 Turbulence Models

Several two-equation turbulence models are integrated in NSAWET for the closure of Reynolds stress. The k-ε model, k-ω model with its TNT and SST [Men94] variations, and the k-g [XCF05] model are adopted. These models all have the so-called low Reynolds number property. Therefore no wall function is needed. Solving of model equations for k, ωor g is decoupled from those of N-S equations. Second order upwind scheme are used for spatial discretization.

The k-ω SST and k-g models are employed for comparison in present study.

3.3 Time Advancing Schemes

The fully implicit lower-upper symmetric-Gauss-Seidel scheme developed by Yoon and Jameson is integrated as the time stepping method for both N-S equations and the turbulence model equations. In order to achieve 2nd order of temporal accuracy in unsteady computation, dual-time stepping is adopted.

4 Numerical Experiments

4.1 DLR-F4 Wing-Body Configuration

We generated the grid by using the window embedment method. In Fig. 3, field information is exchanged between a span-wise patched C-H and H-H grid interface. The pressure contours on the two sides of the interface are almost identical.

The k-ω SST and k-g turbulence model are compared in the computation, shown in Fig. 4. The shock location predicted by k-ω SST is a little bit downstream to the measured location, while the k-g model matches very well. The result of k-ω SST model shows more serious shock-induced separation and larger wing root separation than that of k-g model.

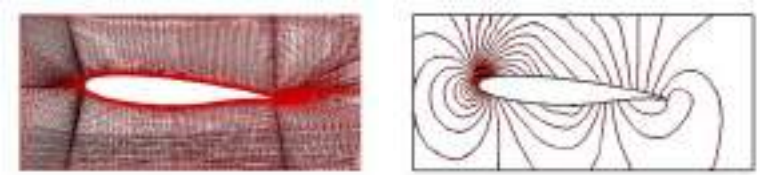

Fig. 3. Grid and pressure distribution on a non-matched interface (DLR-F4 wing-body configuration)

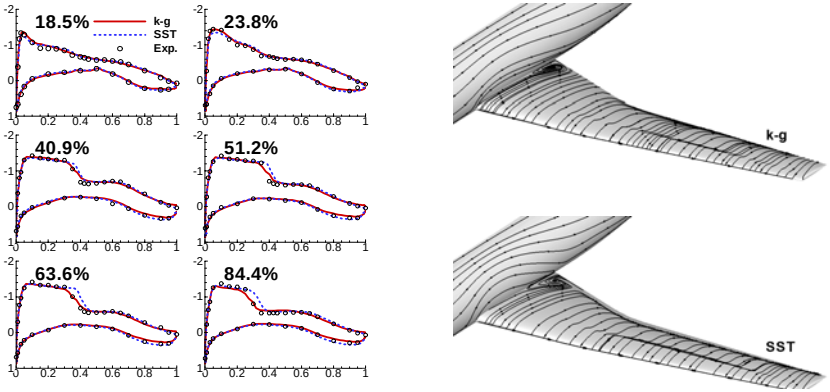

Fig. 4. Comparison of Cp and surface streamline for k-ω SST and k-g model (DLR-F4 model, Ma=0.755, α=0.93°, Re = 3.0×10^6)

4.2 Application for Transporter Simulation

In this section, a realistic modern twin-engine transporter is numerical investigated. The k-ω SST turbulence model is employed for the computation.

The comparisons on wing surface pressure distribution between the wing-body-tail configurations without and with the nacelle-pylon are showed by Cp contours in Fig. 5. In our computation, we need only to turn off/on the window of

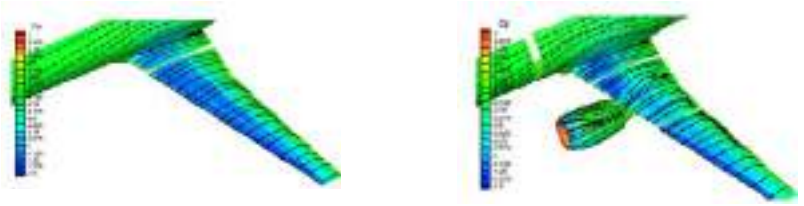

Fig. 5. Comparison of pressure and surface streamline for civil transporter (Ma=0.76, α=4°, Re=5.0×10^6) Left: wing-body-tail; Right: wing-body-tail and nacelle-pylon

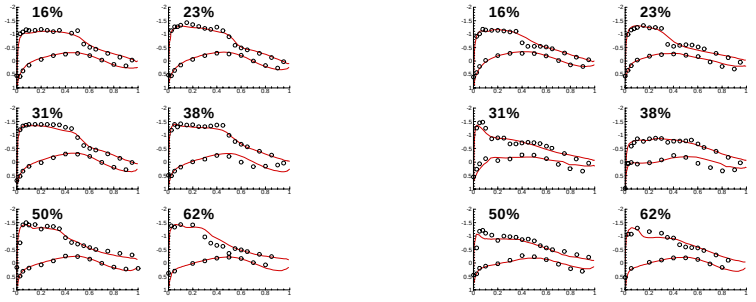

Fig. 6. Comparison of Cp for civil transporter (Ma=0.76, α=4°, Re=5.0×10^6) Left: wing-body-tail; Right: wing-body-tail and nacelle-pylon.

the nacelle and pylon to switch between the two configurations. Fig. 5 shows that the nacelle, without a strake, caused an obvious upper surface separation.

The Cp profiles match well with the measurements, as shown in Fig. 6. Fig. 6 shows that the nacelle reduces the suction peak of the wing, which may decrease lift and increase drag. Similar as section 4.1, the shock position of the SST model results is a little downstream in the wing-body-tail case than the experiment (Fig. 6, the 62% section).

5 Conclusions

The Window Embedment method shows good performance in aeronautics applications. The results of DLR-F4 wing-body and a twin-engine civil transporter show that, the shock locations of SST model are a little bit downstream compared with measurements. At the same time, SST model shows more serious separation than k-g model in the wing-body configurations. The pressure distributions of k-g model match well with the experiments.

References

[CZX06] Haixin, C., Yufei, Z., Zhixiang, X., Song, F.: NSAWET Code and Its Application. In: 5th Asia Workshop on Computational Fluid Dynamics, Xi'an, China (August 2006)

[CFL03] Haixin, C., Song, F., Fengwei, L.: Navier-Stokes Simulations for Transport Aircraft Wing/Body High-Lift Configurations. Journal of Aircraft 40(5), 883–890 (2003)

[Men94] Menter, F.R.: Two-Equation Eddy-Viscosity Turbulence Models for Engineering Applications. AIAA Journal 32(8), 1598–1605 (1994)

[XCF05] Zhixiang, X., Haixin, C., Song, F., Fengwei, L.: Computations with k-g model for complex Configurations at High-Incidence. Journal of Aircraft, 42(2), 462–468 (2005)

Improved Component Buildup Method for Fast Prediction of the Aerodynamic Performances of a Vertical Takeoff and Landing Micro Air Vehicle

Sheila Tobing[1], Tiauw Hiong Go[2], and Roxana Vasilescu[3]

[1] Nanyang Technological University (Singapore)
L060048@ntu.edu.sg
[2] Nanyang Technological University (Singapore)
YongkiGo@ntu.edu.sg
[3] Nanyang Technological University (Singapore)
vasilescu@ntu.edu.sg

Summary. An innovative and efficient method for fast prediction of the aerodynamic performances of a Vertical Takeoff and Landing Micro Air Vehicle (VTOL MAV) during the conceptual design phase is presented in this paper. Characterized by low aspect ratio lifting surfaces and low Reynolds number regime flight, typical MAVs generate complex flow phenomena that cannot be accurately accounted using conventional-aircraft design tools. This complexity of the flow motivates the necessity of using advanced Computational Fluid Dynamics (CFD) tools, even in the conceptual design stage. However, full CFD simulations for predicting the aerodynamic performances of various MAV configurations created during the design stage are not realistic due to time and computational cost constraints. This paper proposes an innovative solution which based on the Component Buildup Method (CBM) to predict the full vehicle aerodynamic performances. In order to include the aerodynamic interferences while still maintaining a low computational cost, an improved CBM (I-CBM) was developed to predict the VTOL MAV aerodynamic performances at various configurations.

1 Background

One of the most common tools used in the aerodynamic prediction during the conceptual design phase of a conventional aircraft is the Component Buildup Method (CBM). In this method, each component of an aircraft is investigated individually and independently. Assuming the validity of superposition principle of aerodynamic effects, the aerodynamic coefficients of a vehicle are calculated by adding the aerodynamic coefficients of its major components. The early formulation of CBM is presented by Pitts, Nielsen, and Kaattari[1] in their paper about the interactions of circular-cylindrical bodies with various types of wings/tails. The authors suggest that the lift of the wing-body-tail combination can be estimated by the sum of lift from

its principal components. CBM is intensively applied and developed for missile/rocket design[2][3]. In the conventional-aircraft design process, Roskam[4] uses CBM to predict the aerodynamic performances of conventional aircraft. Research in the application of CBM in the conceptual design phase of a VTOL MAV has only been done recently. A CBM-based code, AVID OAV, has been developed to predict the aerodynamics of ducted fan MAVs[5]. In predicting the aerodynamic performances, AVID OAV uses empirical instead of computational data. This software is also designed only for ducted-fan MAVs with no wing and inside-the-duct control vanes. In this work, a case where the MAV may be equipped with wings and outside-the-duct control vanes is considered.

2 The Proposed Method

The lack of analytical and empirical models to predict the aerodynamic performances of a VTOL MAV makes a quick design analysis difficult. Thus, the aerodynamic design analysis is usually based more on computational approach (CFD). The VTOL MAV aerodynamics can be simulated fully or per component (CBM). Full configuration simulations are too complex and costly to account for various degrees of freedom in the design envelope. The component simulations (CBM), which will be referred as individual simulation/analysis, are less complex and less costly than the full configuration. However, the results obtained using such method are usually inaccurate due to the negligence of the aerodynamic interferences. A more sophisticated approach, called the Improved Component Buildup Method (I-CBM), is proposed here. In comparison to the original method (CBM), the I-CBM includes the interference effects by introducing the correction models. In I-CBM, similar to the CBM, the VTOL MAV is decomposed into its major components: duct, wing, stator, horizontal and vertical tails. In I-CBM, the aerodynamic performances of the VTOL MAV are calculated by adding the duct-wing (coupled) results and the corrected-CBM results of the rest of the components (Fig. 1).

Three types of analysis are performed in this study: full configuration, individual and coupled duct-wing. The full configuration analysis is the reference for all the simulations (Fig. 2). In the individual analysis, each component of the VTOL MAV is simulated individually and independently. Thus, each component in the individual analysis experiences flows with freestream

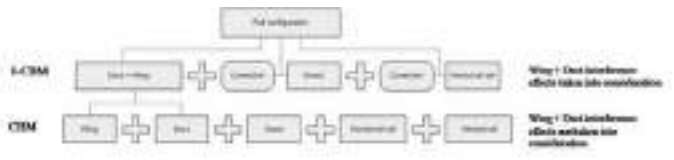

Fig. 1. Schematic diagram of different computation methods

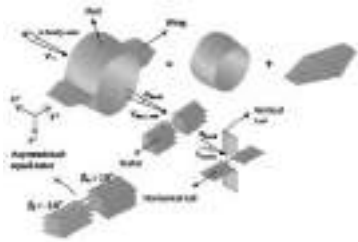

Fig. 2. Full configuration of the VTOL MAV

angles-of-attack (α). The full configuration analysis includes all the components of the VTOL MAV, such that the flow around a component is perturbed by other components. The perturbed angle-of-attack is termed as local angles-of-attack (α_{local}) in this study. The duct-wing coupled analysis is performed to study the aerodynamic interference effects between the two components. In all equations, lift and drag are referred as forces and symbolized by F.

The duct has an aligning effect to the x-body axis for the flow that passes through it (Fig. 2). Therefore, the local flow entering the stator is straighten in the direction of the x-body axis, despite of the angle-of-attack of the freestream flow. The stator which has a cascade configuration will further change the direction of the flow before it passes the horizontal and vertical tails. As a result of lower local angles-of-attack, the stator and the tails produce lower drag and also lower lift compared to the individual analysis results for the same freestream angle of attack.

Three parameters are introduced in the analysis: α, β and δ (1). The freestream angle-of-attack (α) of the VTOL MAV is the relative angle between the x-body axis and the freestream velocity vector. The second parameter (β) is the setting angle of the stators, whereas β_L is for the left plane and β_R is for the right. The setting angle of the horizontal tail is symbolized as δ.

$$\begin{aligned} C_F(\alpha, \beta_L, \beta_R, \delta) = {} & C_{F_{Duct+Wing}}(\alpha) + C_{F_{Stator}}(\alpha, \beta_L, \beta_R) \\ & + C_{F_{Horizontal-Tail}}(\alpha, \beta_L, \beta_R, \delta) \end{aligned} \tag{1}$$

Based on β_L - β_R configuration, the computational model for stator can be divided into three different categories: symmetrical, asymmetrical-equal and asymmetrical-unequal. The horizontal tail tested has δ of $-2°$, $0°$ and $2°$.

- Symmetrical $\beta_L = \beta_R \rightarrow$ 0° - 0° and 5° - 5°
- Asymmetrical-equal $\beta_L = -\beta_R \rightarrow -5°$ - 5° and $-10°$ - 10°
- Asymmetrical-unequal $\beta_L \neq \beta_R \rightarrow 0°$ - 5° and 10° - 0°

3 Validation

A total of 24 computational models are created to validate I-CBM. Using a RANS solver, FLUENT, each model is tested for three different

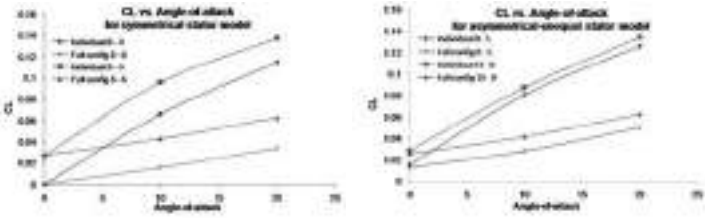

Fig. 3. Lift of the symmetrical and asymmetrical-unequal stator models

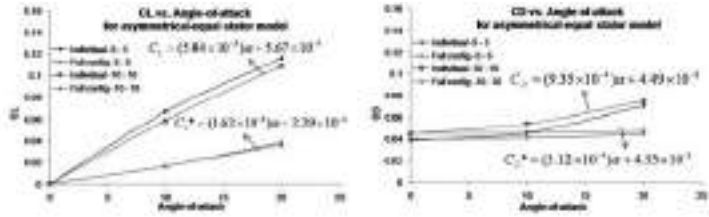

Fig. 4. Lift and drag of the asymmetrical-equal stator models

angles-of-attack of 0°, 10° and 20°. The individual and full configuration simulation results of a particular component are compared to build the correction models. The corrected equations are taken from the linear approximation of the full configuration analysis and marked with "$*$" in Fig. 4 and 5. In this work, the corrected equations are for α range from 0° to 10°.

The computational results of the duct-wing configuration show that the lift and drag predictions for the individual simulations (CBM) are significantly higher than the coupled (I-CBM) or the full configuration (Table 1). On the contrary, the lift predictions for the coupled duct-wing and the full configuration models are in a very good agreement. Both the coupled and full computational models include the interference effects, and thus the coupled configuration must be used to accurately predict the aerodynamic properties of the duct-wing configuration (2).

$$C_{F_{Duct\ and\ Wing}} \neq C_{F_{Duct}} + C_{F_{Wing}}$$

$$C_{F_{Duct\ and\ Wing}} = C_{F_{Duct+Wing(coupled)}} \tag{2}$$

The lift and drag predictions of the individual symmetrical stator model (CBM) are higher than the full configuration. A consistent pattern of deviation of the individual (CBM) simulation results from the full configuration ones is also found in the aerodynamics coefficient predictions (Fig. 3). It is also found that the equation for the the full configuration analysis has significantly lower lift and drag curve-slopes compared to the individual one (3). These findings show that the freestream angle-of-attack has a small influence

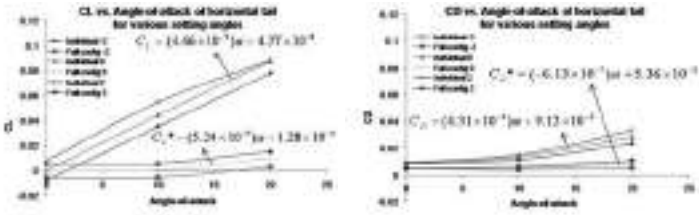

Fig. 5. Lift and drag predictions of the horizontal tail for various δ

Table 1. Aerodynamic performances for α of 10° for various methods of prediction

Method	Total C_D	Total C_L	Error (%)	
Full configuration	0.0819	0.5233	Total C_D	Total C_L
I-CBM (Coupled Duct & Wing)	0.0916	0.5294	11.84	1.16
CBM (Uncoupled/Individual Duct & Wing)	0.1244	0.7953	51.89	51.97

Table 2. Comparison of results for α of 10°

	CBM		I-CBM		Full Model	
	C_L	C_D	C_L	C_D	C_L	C_D
Wing	0.527	0.065	0.529	0.092		
Duct	0.268	0.059				
Horizontal tail	0.045	0.013	*0.001*	*0.005*		
Vertical tail	0.003	0.009	0.003	0.009		
Stator	0.059	0.054	*0.016*	*0.046*		
Total (CBM)	0.902	0.202	0.550	0.152	0.547	0.141
Error (%)	64.70	43.34	0.41	8.12	-	-

on the aerodynamic performances of the stator because the duct redirects the flow before it reaches the stators. Similar findings are observed in the computational results of the asymmetrical-equal and asymmetrical-unequal models (Fig. 4).

$$\frac{\partial C_{F^*_{Stator}}}{\partial \alpha} \lll \frac{\partial C_{F_{Stator}}}{\partial \alpha} \tag{3}$$

$$\frac{\partial C_{F^*_{Horizontal-Tail}}}{\partial \alpha} \lll \frac{\partial C_{F_{Horizontal-Tail}}}{\partial \alpha} \tag{4}$$

The aerodynamic performances of the horizontal tail are not fully dictated by the freestream angle-of-attack. One can notice from the variations of the C_L vs. α and the C_D vs. α curves in Fig. 5 that the drag and the lift of the horizontal tail with various setting angles (δ) only change slightly with

the increase of the freestream angle-of-attack. These results show that the stator redirects the flow before it passes the horizontal tail, generates a lower local angle-of-attack, which leads to a lower drag and a lower lift produced by the horizontal tail (4).

After the duct-wing coupled model is analyzed and the correction model for stator and horizontal tail are formulated, the I-CBM can be applied to predict the aerodynamic performances of the VTOL MAV. The corrected values, italicized in Table 2, are calculated using the correction models. The rest of the components are computed individually and independently. As shown in Table 2, I-CBM gives significantly more accurate results compared to CBM. The CBM overpredicts the total lift and the total drag of the VTOL MAV by more than 60% and 40% respectively. Using the I-CBM, the total lift for the MAV is overpredicted by less than 1%, while the total drag is overpredicted by 8%.

4 Conclusions

Two main points are taken from this study. First, the duct and wing are inseparable due to the strong interference effects between them. The separation of the duct and the wing leads to significant error in predicting the vehicle's aerodynamic performances using the CBM. Second, the rest of the components can be analyzed individually and independently by applying the correction models. Therefore, I-CBM by taking into consideration the duct-wing interference effects and the correction models for the stator and the horizontal tail, proved to be a fast and reasonably accurate approach to predict the aerodynamic performances of the VTOL MAV.

References

1. Pitts, W.C., Nielsen, J.N., Kaattari, G.E.: Lift and center of pressure of wing-body-tail combinations at subsonic, transonic, and supersonic speeds. Technical Report NACA-TR-1307, NACA (1957)
2. Bennett, B.K.: Conceptual design synthesis tool for arbitrary-body missiles. In: 15th Applied Aerodynamics Conference, number AIAA-1997-2281, Atlanta, GA, June 23-25. AIAA (1997)
3. Stremel Jr., P.M., Faltz, J.A., Hegedus, M.C., Mendenhall, M.R., Perkins, S.C.: Engineering analysis for rocket sled aerodynamics. In: 44th AIAA Aerospace Sciences Meeting and Exhibit, number AIAA-2006-664, January 9-12, AIAA (2006)
4. Roskam, J.: Part VI: Preliminary Calculation of Aerodynamic, Thrust and Power Characteristics. Number TL671.2.R821 in Airplane Design. Roskam Aviation and Engineering Corporation, Lawrence, Kansas (1985)
5. Guerrero, I., Londenberg, K., Gelhausen, P., Myklebust, A.: A powered lift aerodynamic analysis for the design of ducted fan uavs. In: 2nd AIAA "Unmanned Unlimited" Systems, Technologies, and Operations, number AIAA 2003-6567, San Diego, CA, September 15-18, pp. 2003–6567. AIAA (2003)

Part 12
Complex Flow 2

“*This page left intentionally blank.*”

Numerical Investigation of the Tip Leakage Flow in a Multistage High Pressure Compressor

N. Gourdain[1], M. Stoll[2], M. Montagnac[1], and J.F. Boussuge[1]

[1] CERFACS, Computational Fluid Dynamics Team, 42 Avenue Gaspard Coriolis, Toulouse, 31057, France
nicolas.gourdain@cerfacs.fr
[2] Stuttgart University, Stuttgart, 70049, Germany
stollmi@gmx.de

This study takes place in the frame of a research project to simulate the flow in a multistage High Pressure Compressor (HPC). The present paper focuses on the effect of tip gap deteriorations that occur in a high pressure compressor due to thermal constraints. To simulate this challenging industrial problem, the compressor is considered with two radial tip gap dimensions. The flow is computed by the mean of a 3D unsteady RANS calculation and is compared with experimental measurements, showing that a good decription of the mean flow is obtained with the proposed numerical model. The results show that the last stage is responsible for the loss of stability. An increase of the radial tip gap leads to a dramatic reduction of operability (by 20%), pressure ratio and efficiency. Finally, detailed investigation of the flow at off-design conditions are presented to obtain a better understanding of the flow in this multistage compressor.

1 Introduction

To answer to the objectives in terms of pollutant emissions and economical constraints, the design of the next engine generation points toward compact, high efficiency and large operability configurations. To achieve these challenging goals, an increase in performances of the critical component like the compressor is thus a necessary step. Unfortunately, some phenomena that take place in a modern gas turbine engine are still not well understood, especially in a multistage compressor. It is now well established that overall performances of a compressor are strongly dependent on the flow behavior near end walls [DE07]. Moreover, the compressor operability is directly linked to the tip clearance dimension [IKY+04] but this radial gap varies in size, mainly due to thermal constraints and deterioration. Even if the impact of this process is not easy to estimate, it must be taken into account at the design stage,

resulting in an increase of the surge margin (about 30% of the total margin) and thus an increase of the engine specific consumption. Moreover, many authors such as Crook *et al.* [CGTA93] and Hoying [Hoy96] have clearly shown that the tip leakage region exhibit usually the first signs of instabilities for most of the subsonic and transonic compressors. Indeed, a better description of tip leakage flows can give valuable information to design high efficiency and more stable compressor. These last few years, the development of reliable numerical tools (Computational Fluid Dynamics) and high performance computers led to significant progress to study turbomachine flow problems.

To simulate very complex flows that occur in turbomachine, few authors have recently shown that a balance between a correct physical description and the time calculation can be found. For example, Hathaway *et al.* [HHCW04] have investigated the development of instabilities in a full helicopter multistage compressor and a simulation of a rotating stall phenomenon has been done by Gourdain *et al.* [GBM$^+$06] in a full subsonic compressor stage. Both studies have been performed thanks to an unsteady RANS method. A higher level in terms of very large system simulation has been reached by Schluter *et al.* [SAKVDW05] with the simulation of a full aircraft gas turbine, using an inventive RANS/LES coupling strategy.

Even if the unsteady RANS approach is very costly, it is still the most appropriate method to describe the flow in a multistage compressor, at any operating point. Based on this state of the art, it is proposed in this paper to investigate the unsteady flow of a three-stage compressor, with a particular interest for the flow evolution after a deterioration of the tip gap in the two last rotors. The test case and the numerical method are presented in the first section. Due to natural periodicity, only a 22.5° sector is sufficient to take into account all the rotor-stator interaction phenomena. However a good balance has to be found between precision and simulation cost to represent the flow in such a system. To obtain a validation of the numerical model, experimental data are used to compare mean aerodynamic values. Then results obtained for both configurations (with small and large radial tip gaps) are presented and analyzed in a second section. Finally the paper focuses on off-design operating conditions. The interest is to point out the effect of the tip gap dimension on the tip leakage flow features and on the compressor stability. As a consequence, useful information is expected for the design of the next engine generation, thanks to a better quantification and prediction of the tip gap deterioration effects.

2 Methodology

2.1 Compressor Test Case

The test case used for this study is a slightly transonic multistage compressor, designed for studying aerothermal and aerodynamic effects. The configuration is representative of a high pressure compressor core of a modern gas turbine

Table 1. Blade number of the compressor rows

	IGV	R1	S1	R2	S2	R3	S3
Number of blades	32	64	96	80	112	80	128

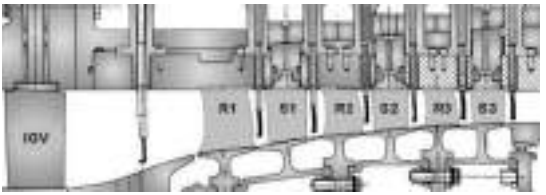

Fig. 1. Axial view of the investigated multistage compressor

and is installed on a 2.05 MW test facility equipped with wire probes and Laser Doppler Velocimetry. Measurements have been performed by Ottavy *et al.* [OTVA06] and Vouillarmet *et al.* ([VOP06]) at different operating points, from chock to stall. This axial compressor is composed of six rows and one Inlet Guide Vane (IGV). The number of blades of each row is indicated Table 1 and an axial view of the compressor is shown on Fig. 1. The rotor blade shape is a forward swept design that promotes both efficiency and operability.

The nominal rotational speed is 11,500 rpm, corresponding to a relative tip Mach number at the first stage of 0.92, so the flow is transonic in the first stage and mainly subsonic in the two other ones. In order to investigate the specific role of the tip leakage effects, two configurations of the same compressor are tested. The first one is the original version of the compressor (small radial tip gap) while the second one corresponds to the same compressor after a deterioration. Thermal constraints are usually more importants for the last stages. To represent this phenomenon, the radial tip gap is increased but only for the two last rotors. Relative dimensions of the tip gap l, expressed as a fraction of the blade span H, are indicated Table 2 for each rotor. For industrial reasons, all the data presented in this paper are normalized with respect to the maximum experimental value. That means the mass flow is expressed as a fraction of the experimental chocked mass flow and experimental maximum pressure ratio and efficiency are equal to 1.0. Moreover, experimental data are available only for the original configuration with the smallest radial tip gaps.

2.2 Numerical Method

The flow solver used is the *elsA* software that solves the Reynolds-Averaged Navier-Stokes equations using a cell centered approach on multi-block structured meshes [CV08]. Convective fluxes are computed thanks to a third order

Table 2. Radial tip gaps for both configurations

Blade row	Configuration 1	Configuration 2
R1	l/H=1.2%	l/H=1.2%
R2	l/H=1.7%	l/H=2.5%
R3	l/H=2.1%	l/H=2.7%

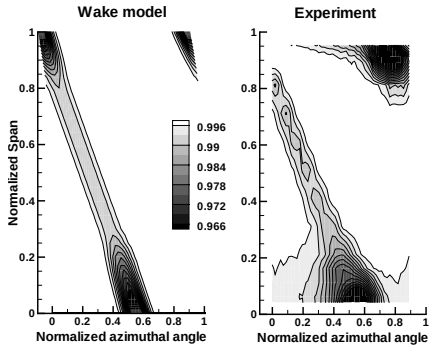

Fig. 2. Comparison of the wake model with experiments (compressor inlet, total pressure)

Roe scheme with a Harten entropic correction [Roe81] and diffusive fluxes are computed with a 2nd order centered scheme. A second order Dual Time Stepping (DTS) method is considered for the time integration [Jam91]. The time marching for the inner loop is performed by an efficient implicit time integration scheme, based on the backward Euler scheme and a scalar LU-SSOR method [YJ87]. Convergence acceleration techniques such as local time stepping method are also used. To reach a converged state, the number of sub-iterations for the inner loop is defined to obtain at least two orders of reduction for the residuals magnitude. The turbulent viscosity is computed with the two equations model of Wilcox [Wil88] based on a $k-\omega$ formulation and the flow is assumed to be fully turbulent since the Reynolds number based on chord is around 10^6.

For practical reasons of CPU resources, the whole experimental domain can not be simulated. First the IGV is not represented but is taken into account by means of an analytical model. The hypothesis is that the flow distortion generated by the IGV is mainly induced by the presence of wakes. This behavior is modeled according to the self similarity law of Lakshminarayana and Davino [LD79] that describes the spatial evolution of a wake with a simple Gaussian function (Eq. 1). Experimental data obtained at the nominal operating point are then used to fit the model constants as the azimuthal wake extension L and the total pressure deficit δp_{wake}. A comparison of the model with experiments is presented Fig. 2. As it can be shown, the wake model

is able to reproduce the main features of the inlet flow, especially at mid-span. These differences observed near the hub are due to a recirculating high temperature flow in the facility that is not considered by the analytical law. Finally, the wake model is used to define the upstream injection condition through the values of total pressure P_t, total temperature T_t and velocity direction α.

$$P_t(\theta) = P_{t0}\left\{1 - \delta P_{wake} exp\left[-\alpha\left(\frac{\theta}{L/2}\right)^2\right]\right\} \quad (1)$$

P_{t0} : reference total pressure
δP_{wake} : total pressure deficit
α : form factor ($\alpha = 0.693$)
θ : azimuthal coordinate
L : wake extension

Second, it is assumed that a good description of the deterministic stresses is the most important parameter to compute correctly the aerodynamical stability limit [GBL05], meaning the duct length has no real impact on the surge line position. Indeed only a part of the inlet and outlet ducts is modeled. However a sufficient distance is considered between the boundary conditions and the blade rows to avoid numerical reflexion problems. A particular feature of the present compressor is that a periodicity between the different blade rows exist. Thus only a $2\pi/16$ sector periodicity can be considered (22.5 degrees) to represent all the rotor-stator interactions. The main limitation is that no tangential wavelength greater than a sixteenth of the circumference can develop. Indeed, the numerical model is not able to compute a realistic unstable phenomenon (rotating stall or surge).

The flow domain is discretized with a multi-block approach, using an O-H meshing strategy for each passage of the compressor. A view of the mesh is presented Fig. 3. The typical dimensions of a blade passage mesh are 85, 33 and 57 points, respectively in the axial, tangential and radial directions. An O-H mesh with 13 points in the radial direction is used to discretize the radial tip gap. To obtain a good balance between CPU cost and precision, a wall law approach is applied [GH01] with a fixed wall cell size that corresponds to a mean normalized wall distance y^+ of 20. The same meshing strategy is used for both studied configurations, leading to a total nodes number of 8.4 millions to discretize the three stages. The number of mesh points and the normalized wall distance y^+ are kept constant but the dimension of the mesh cells inside the tip leakage is thus slightly increased in the case of the large tip gap. A standard condition of spatial periodicity is considered for the lateral boundaries and a sliding mesh condition with non abutting points is applied at the rotor/stator interface. The main advantage of this approach is to be conservative in the case of plane interfaces (which is roughly the case here). Moreover this boundary condition is optimized in terms of time and memory requirements since only 2D interpolation coefficients are needed. To

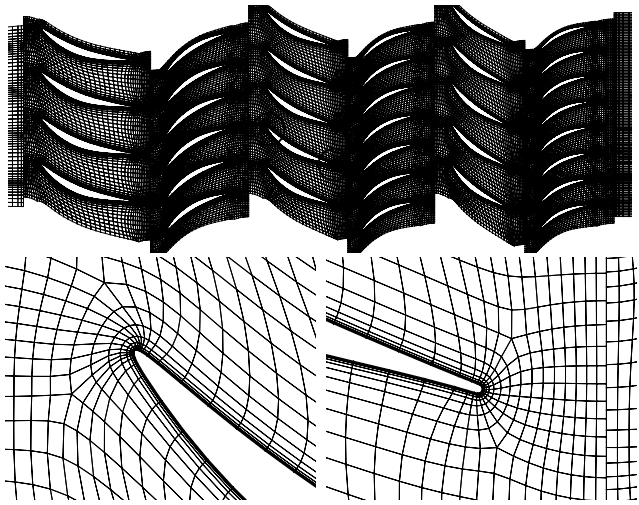

Fig. 3. View of the whole mesh at mid-span and details near the leading and trailing edges (1 point over 2)

model the outlet duct, a throttle condition is coupled with a simplified radial equilibrium. Then the characteristic of the compressor is described from the choked point to the stall inception point, simply by increasing the value of the throttle parameter λ.

2.3 Numerical Model Validation and Results

The numerical model is used to perform unsteady calculations thanks to 4 processors of a NEC SX8 supercomputer (corresponding to a 128 Gflops peak power). The numerical simulation shows that a periodic state is reached after one compressor rotation at choked conditions while more than four rotations are needed for a near stall operating point. A validation of the numerical model is then obtained by a comparison of the numerical data with experimental measurements. The total-to-total pressure ratio and the polytropic efficiency are plotted on Fig. 4 with respect to the mass flow. Experimental data are indicated only for the small tip gap version while numerical data are shown both for small and large tip clearance cases. All data are time and space averaged. The first thing is to evaluate the capacity of the model to compute the surge line position. Nevertheless an assumption is necessary to estimate the stability of an operating point, since the experimental time needed to obtain instabilities can be very important (more than hundreds of rotor revolutions), and thus can not be simulated for practical reason of time. For a given operating point, up to four rotations are simulated. If a periodic state is reached at the end of this time, the computed point is assumed to be stable. The comparison with the experimental measurements shows that the

compressor operability, defined as the difference between the chocked mass flow and the last stable operating point mass flow, is correctly estimated by the simulation (relative error is less than 1.5%). The numerical model is also able to represent correctly the pressure and efficiency evolutions with respect to the mass flow. The chocked mass flow is only a little bit over estimated (+0.6%) and the stability limit is slightly under predicted (-0.7%). These small differences are probably due to the coarse mesh used that is not sufficient to compute the smallest details of the flow. Another approximation is the inlet boundary condition that has been fitted only for the nominal operating point, meaning that the inlet flow characteristics are possibly not properly modeled far from the nominal conditions. However, this short comparison validates the numerical model and shows clearly that the mean flow characteristics are accurately simulated in this three-stage compressor.

An investigation of the differences between small and large tip clearance cases indicate that an increase of the tip gap leads to a reduction of the maximum pressure ratio Pi_{max} (by 2.9%) and the maximum efficiency (by 1.1%). At nominal operating point, mass flow, pressure ratio and efficiency are slightly decreased (respectively -1%, -0.4% and -0.5%). These differences tend to increase when the mass flow is reduced while no impact is observed at choked flow conditions. But the main effect of larger tip clearance is to reduce strongly the compressor operability (by about 20%). The reasons of this dramatic performance drop are deeper investigated in the next section, with a particular attention for the tip leakage flow phenomena.

3 Flow Analysis

The flow analysis focuses on the mechanisms leading to a reduction of the operability when the tip gap dimension is increased. Many previous works have suggested that the most destabilizing effects are induced by the tip leakage flows [CGTA93] [Hoy96]. Indeed the present study focuses mainly on the mechanisms near the casing that potentially lead to a loss of stability.

3.1 Investigation of the Small Tip Clearance Case

Figure 5 shows an instantaneous flow field of axial velocity at near stall operating point, corresponding to a normalized mass flow ϕ of 0.949. The interest is to show how the flow reacts when the balance between the momentum of the main flow and the tip leakage flow is reduced. At the investigated operating point, no sign of massive separations is highlighted, meaning the compressor operates in stable conditions. However, regions of low axial momentum are observed near the casing, mainly due to the tip leakage flow. A high intensity vortex develops near the leading edge of each rotor blade and is driven by the main flow in the channel. As a consequence of the low static pressure in the vortex core, it tends to capture all the low kinetic energy

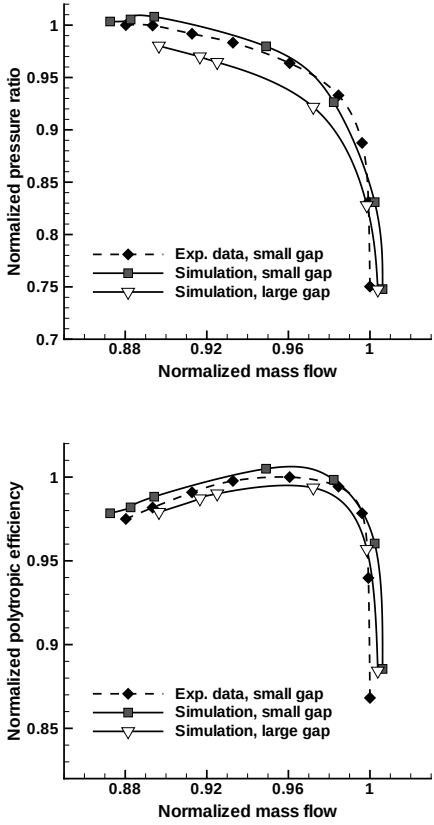

Fig. 4. Comparison of the experimental and numerical compressor performances (up: pressure ratio, down: efficiency)

material of the near region around it. Indeed the trajectory of this vortex is correlated with the deficit of axial momentum in the channel. A second small intensity vortex is also observed along the rotor suction side. This is a consequence of the tip clearance jet flow that emerges from the blade suction side. The interaction between the tip leakage boundary layer and the suction side boundary layer induces the development of a high helicity region just under the tip leakage jet, near the blade suction side. This tip leakage vortex is then also associated with a local loss of kinetic energy and flow blockage. But this secondary flow, induced by the tip clearance, is found to be small with respect to the vortex that develop near the leading edge. This tip flow topology shown here has already been observed in the literature [GMB07] and is close to the model proposed by Kang *et al.* [KHC93]. Althought the same phenomena exists for each of the three rotor rows, it is clear that the largest region of low axial velocity develops in the rotor of the last stage.

Compared with the other rows, the last rotor exhibits the lowest pressure ratio but also the highest relative tip clearance (l_{gap}/H=2.1%). So, in this case the larger relative tip gap induces a higher momentum tip leakage flow that is not balanced by the lower pressure gradient. As a consequence, a stronger flow deviation and axial velocity deficit is observed in the last rotor, compared to the two first stages.

Another mechanism that explains the development of low axial momentum regions is the high incidence on the rotor leading edge and the reduction of the main flow axial momentum that occur at off-design conditions. This phenomenon generates a high pressure gradient that tends to increase the tip leakage momentum and to push the tip clearance flow upstream the rotor. As a consequence, the location of the blocked flow region at partial mass flow is closer to the leading edge than at nominal operating conditions. At this point, the behavior of the flow in the rotor passages has also a large effect on the stator flow. In fact, the result of the strong flow incidence at the rotor exit is an increase of potential effects, leading to a deficit of axial momentum in the rotor-stator inter row region. This mechanism is particularly observed in the last stator and tends to generate a coupling with the tip leakage flow. An increase of the flow unsteadiness is also detected when the flow travels towards to the compressor exit. Between the first rotor and the last stator the mass flow oscillation has been increased by more than a factor three. It is mainly due to the periodic coupling between wakes, potential effects and tip vortices.

This part shows clearly that the most limiting phenomenon for operability is the low axial momentum region induced by the tip leakage flow of the third rotor. This flow is responsible for an increase of the flow angle at the rotor leading edge and also at following stator leading edge. At the lowest mass flow, a major separation of the boundary layer occurs on the last stage rows and reversed flows lead to a complete loss of aerodynamic stability.

Fig. 5. Instantaneous axial velocity flow field, partial mass flow operating point (small tip gap configuration, h/H=94%)

3.2 Investigation of the Large Tip Clearance Case

To point out the flow differences between the two configurations, it has been chosen to compare the same operating point rather than a given mass flow. It means that aerodynamic conditions like flow angle and pressure ratio are not identical for both cases. But the outlet boundary condition that models the flow at the exit is the same, i.e. the throttle position is fixed. This choice has been done to simulate the behavior of the compressors in the same system. As previously, an axial velocity flow field is used to identify the blocked flow regions at partial mass flow ($\phi = 0.925$) and is shown Fig. 6. The flow topology is basically the same than for the small tip gap configuration. The main difference observed is an increase of the tip leakage flow momentum for rotors 2 and 3.

It has been shown in the previous section that the impact of larger tip gap increases when the mass flow is reduced. At partial mass flow, the flow blockage near the casing of the two last rotors leads to a dramatic drop in terms of mass flow, reducing also the main flow momentum. The consequence is that the tip leakage vortex tends to move closer to the rotor leading edge. Moreover, the large tip gap configuration leads to an increase by +90% of the blocked section in the last stage. Another point of interest is the high unsteadiness of the flow, especially in the last stage. As shown Fig. 6, the instantaneous flow is similar for all passages for a given row of the two first stages. However, important differences are noticed in the passages of the third stage. In fact, the rotor-stator interactions generate coupled unsteady rotating waves. These structures have a large influence dowstream and are responsible for a variation of the tip leakage vortex position. The flow angle at the stator leading edge is also periodically increased and an unsteady separation occurs in the stator.

Fig. 6. Instantaneous axial velocity flow field, partial mass flow operating point (large gap configuration, h/H=94%)

This section points out that an increase of the tip gap induces the development of large low momentum areas near the casing. Moreover, the last stage is largely affected by the unsteady flow generated by the rotor-stator interactions of the previous stages.

Finally, this work shows that the row with the largest tip gap has always the most destabilizing effect (the third rotor in the present case). Moreover a coupling between the rotor and adjacent stator is observed, especially at partial mass flow. The flow of the last stages also impacts upstream rows and this interaction leads to a complex system for which the contribution of each row can not be separated from the contribution of the other rows.

4 Conclusion

A numerical simulation has been presented to investigate the flow in a multistage axial compressor. The comparison between the numerical results and the experimental data has shown the model is able to compute correctly the main characteristics of the flow, like pressure ratio and efficiency. Moreover, the stability limit and the choked line position are well estimated by unsteady calculations. Then two configurations of the compressor have been investigated in order to point out the effect of a tip gap deterioration. The results analysis shows clearly that an increase of the radial tip gap has a destabilizing effect on the rotor flow. At partial mass flow, an increase of +30% of the last rotor tip gap leads to an increase of +90% of the flow blockage. This behavior points out the mismatching of the last rotor when the tip gap dimension is modified. In this condition the compressor operability is reduced by -20% compared to the reference case and a large decrease of pressure ratio and efficiency is also observed. This study also show that a complex interaction exists between the different blade rows. At partial mass flow these interactions tend to increase in terms of magnitude and the flow in the last stages becomes highly unsteady. In this case, a good understanding of the flow can be obtained only by the simulation of the whole system. Finally, the present paper points out the most destabilizing flow regions and highlights the rows that have to be controlled to obtain the best benefit on pressure ratio, efficiency and operability.

Acknowledgement. Important contributions have been provided by Xavier Ottavy and André Vouillarmet (LMFA) with experimental data. These people are gratefully acknowledged. No numerical study can be achieved without a good support from the software developers. Thanks to the *elsA* community for developing efficient methods in the numerical code that was used for this study. A particular acknowledgement is adressed to Michel Gazaix from Onera for helpful comments and suggestions. Finally, thanks to SNECMA for giving authorization to use the compressor geometry and for support.

References

[Ada84] Adamczyk, J.J.: Model Equation for Simulating Flows in Multistage Turbomachinery. Technical Memorandum 86869, NASA (1984)

[CGTA93] Crook, A.J., Greitzer, E.M., Tan, C.S., Adamczyk, J.J.: Numerical Simulation of Compressor Endwall and Casing Treatment Flow Phe- nomena. ASME Journal of Turbomachinery 115(3), 501–512 (1993)

[CV08] Cambier, L., Veuillot, J.P.: Status of the elsA CFD Software for Flow Simulation and Multidisciplinary Applications. In: 46th AIAA Aerospace Science Meeting and Exhibit, Reno. AIAA 2008-664 (January 2008)

[DE07] Domercq, O., Escuret, J.F.: Tip Clearance Effect on High- Pressure Compressor Stage Matching. Jouranl of Power and Energy 221(6), 759–767 (2007)

[DS79] Denton, J.D., Singh, U.K.: Time Marching Methods for Turbomachinery Flow Calculations. VKI Lecture Series 1979-7, Belgium (1979)

[EAM77] Erdos, J.I., Alzner, E., McNally, W.: Numerical Solution of Periodic Transonic Flow Through a Fan Stage. AIAA Journal 15(11), 1559–1568 (1977)

[GBL05] Gourdain, N., Burguburu, S., Leboeuf, F.: Rotating Stall Simulation and Analysis in an Axial Compressor. In: 17th International Symposium on Air Breathing Engine, Munich, Germany, ISABE Paper 2005-1138 (2005)

[GBM+06] Gourdain, N., Burguburu, S., Michon, G.J., Ouayahya, N., Leboeuf, F., Plot, S.: About the Numerical Simulation of Rotating Stall Mechanisms in Axial Compressors. In: ASME Turbo Expo, Barcelona, Spain, ASME paper GT2006-90223 (2006)

[GH01] Goncalves, E., Houdeville, R.: Reassessment of the wall functions approach for RANS computations. Aerospace Science and Technology 5, 1–14 (2001)

[GMB07] Gourdain, N., Montagnac, M., Boussuge, J.F.: Numerical Simulation of an Axial Compressor with Non Axisymmetric Casing Treatment. In: 2nd European Conference for Aerospace Sciences, (124), Brussels, Belgium (2007)

[GVDWA+07] Gopinath, A., Van Der Weide, E., Alonso, J.J., Jameson, A., Ekici, K., Hall, K.C.: Slides - Three-Dimensional Unsteady Multi-Stage Turbomachinery Simulations using the Harmonic Balance Technique. In: 45th AIAA Aerospace Sciences Meeting and Exhibit, Reno, Nevada, AIAA Paper 2007-0892 (January 2007)

[He97] He, L.: Computational Study of Rotating-Stall Inception in Axial Compressors. Journal of Propulsion and Power 13(1), 31–38 (1997)

[HHCW04] Hathaway, M.D., Herrick, G., Chen, J., Webster, R.: Time Accurate Unsteady Simulation of the Stall Inception Process in the Compression System of a US Army Helicopter Gas Turbine Engine. In: Proceedings of the DoD 2004 Users Group Conference, Washington, DC, USA, pp. 182–193. IEEE Computer Society, Los Alamitos (2004)

[Hoy96] Hoying, D.A.: Blade Passage Flow Structure Effects on Axial Compressor Rotating Stall Inception. Ph.D. Thesis, Massachusetts Insti- tute of Technology, Cambridge, MA (1996)

[IKY+04] Inoue, M., Kuroumaru, M., Yoshida, S., Minami, T., Yamada, K., Furukawa, M.: Effect of Tip Clearance on Stall Evolution Process in a Low-Speed Axial Compressor Stage. In: ASME Turbo Expo., Vienna, Austria, ASME paper GT2004-53354 (2004)

[ISN05] Iyengar, V., Sankar, L., Niazi, S.: Assessment of the Self Recir- culating Casing Treatment Concept to Axial Compressors. In: 43rd AIAA Aerospace Sciences Meeting and Exhibit, Reno, USA Kingdom, AIAA Paper 2005-0632 (2005)

[Jam91] Jameson, A.: Time Dependent Calculations Using Multigrid, with Ap- plications to Unsteady Flows Past Airfoils and Wings. AIAA Paper AIAA-91-1596 (1991)

[KHC93] Kang, S., Hirsch, C., Cumpsty, N.A.: Experimental Study on the 3D Flow Within a Compressor Cascade with Tip Clearance. Journal of Turbomachinery 115, 444–452 (1993)

[LD79] Lakshminarayana, B., Davino, R.: Mean velocity and decay characteristics of the guidevane and stator blade wake of an axial flow compressor. In: American Society of Mechanical Engineers, Gas Tur- bine Conference and Exhibit and Solar Energy Conference, San Diego, Calif (1979)

[OTVA06] Ottavy, X., Trebinjac, I., Vouillarmet, A., Arnaud, D.: Laser measurements in high speed compressors for rotor-stator interaction analysis. Measurement Science and Technology 12, 310–317 (2006)

[Roe81] Roe, P.L.: Approximate Riemann Solvers, Parameter Vectors and Difference Schemes. Journal of Computational Physics 43, 357–372 (1981)

[SAKVDW05] Schluter, J., Apte, S., Kalitzin, G., Van Der Weide, E.: Large-scale integrated LES-RANS simulations of a gas turbine Engine. Annual Research Briefs, Stanford University (2005)

[TS62] Tyler, J.M., Sofrin, T.G.: Axial Flow Compressor Noise Studies. SAE Transactions 70, 309–332 (1962)

[VOP06] Vouillarmet, A., Ottavy, X., Paoletti, B.: Campagne d'Essais au Banc ECL 2 MW, Compresseur CREATE-2, Rapport final de synthese. Confidential report DOC-RAP-019 (2006)

[Wil88] Wilcox, D.C.: Reassessment of the Scale-Determining Equation for Advanced Turbulence Models. AIAA Journal 26, 1299–1310 (1988)

[WK04] Wilke, I., Kau, H.P.: A Numerical Investigation of the Flow Mechanisms in a High Pressure Compressor Front Stage With Axial Slots. Journal of Turbomachinery 126(3), 339–349 (2004)

[YJ87] Yoon, S., Jameson, A.: An LU-SSOR Scheme for the Euler and Navier-Stokes Equations. In: AIAA 25th Aerospace Sciences Meeting, number AIAA-87-0600, Reno, Nevada, USA, January 12-15 (1987)

“*This page left intentionally blank.*”

Part 13
Complex Flows 3

“*This page left intentionally blank.*”

Computational and Experimental Studies of Fluid Flow and Heat Transfer in a Calandria Based Reactor

S.D. Ravi[1], N.K.S. Rajan[2], and P.S. Kulkarni[3]

[1] Dept. of Aerospace Engg., IISc, Bangalore, India
ravi@cgpl.iisc.ernet.in
[2] Dept. of Aerospace Engg., IISc, Bangalore, India
nksr@cgpl.iisc.ernet.in
[3] Dept. of Aerospace Engg., IISc, Bangalore, India
psk@aero.iisc.ernet.in

Abstract. CFD investigations are carried out to study the heat flux and temperature distribution in the calandria using a 3-Dimensional RANS code. Internal flow computations and experimental studies are carried out for a calandria embedded with a matrix of tubes working together as a reactor. Numerical investigations are carried on the Calandria reactor vessel with horizontal inlets and outlets located on top and the bottom to study the flow pattern and the associated temperature distribution. The computations have been carried out to simulate fluid flow and convective heat transfer for assigned near-to working conditions with different moderator injection rates and reacting heat fluxes. The results of computations provide an estimate of the tolerance bands for safe working limits for the heat dissipation at different working conditions by virtue of prediction of the hot spots in the calandria. The isothermal CFD results are validated by a set of experiments on a specially designed scaled model conducted over a range of flows and simulation parameters. The comparison of CFD results with experiments show good agreement.

Keywords: Calandria, Reactor, Complex flow, RANS.

1 Introduction

The present world demands an environmental friendly power generation for which Nuclear power plant is a suitable alternative. The nuclear power is associated with a scare regarding its safety during operation, hence there is need to analyze flow pattern and heat transfer in Calandria or any heat exchanger used in these systems.

A numerical simulation is a very useful tool to compute the distributions of thermal and hydraulic flows in the complex geometry. However, the CFD

results need to be supplemented by experimental data in order to validate the different models approaches in obtaining the solution.

CFD results are validated with results of specially conducted experiments which have further provided optimum operating parameters for numerical simulation for better understanding of the working of nuclear reactor.

2 Calendria Model and Mesh Generation

The nature of flow pattern in Calandria has significant effect on safe operation of reactor vessel in PHWR's. Hence to get an insight into the problem of flow in calandria vessel, laboratory experiments have been conducted. Aprototype of the Calandria for experimental study and a Calandria model for numerical simulation have been designed. It is also necessary to ensure Geometric similarity, Kinematic similarity and Dynamic similarity between the model and prototype to understand flow patterns. Since the flow is axis-symmetric the analysis is carried out only for half portion. A 3-D view of the Calandria model is shown in Fig.1(a) [Raj89, IAE02].

Fig.1(b) shows the computational mesh for analysis of the fluid dynamics and heat transfer characteristics inside the calandria model. In the core region, 69 fuel channels with 21mm of square pitch are simulated so it is possible to observe the flow behaviors around the channels. The total cell number is about 205, 205 consisting of structured meshes and to save the calculation time.

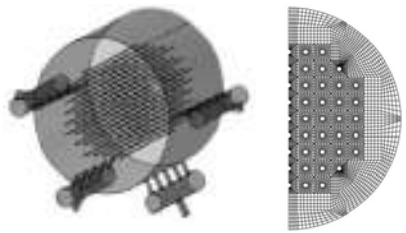

(a) (b)

Fig. 1. (a) 3-D view of the Calandria model. (b) Structured mesh model.

3 Governing Equations and Boundary Condition

A 3D-RANS code having upwinding implicit scheme and $k-\omega$ approach for turbulence is used for the numerical solution. The Reynolds-Averaged Navier-Stokes Equations are solved for steady, compressible viscous flow. The governing equations used are the conventional standard sets that include:

Continuity equation:

$$\frac{\partial \overline{U}_j}{\partial x_j} = 0 \tag{1}$$

Momentum equation:

$$\frac{\partial}{\partial t}\left(\rho\overline{U}_i\right) + \frac{\partial}{\partial x_j}\left(\rho\overline{U}_i\overline{U}_j\right) = -\frac{\overline{p}}{\partial x_i} - \frac{\partial}{\partial x_j}\left(\tau_{ij} + \rho\overline{u_i^{"}u_j^{"}}\right) \tag{2}$$

Energy equation:

$$\frac{\partial}{\partial t}\left(\rho\overline{h}\right) + \frac{\partial}{\partial x_j}\left(\rho\overline{U}_j\overline{h}\right) = -\frac{\overline{p}}{\partial x_j}\left(\overline{Q}_j + \rho\overline{u_j^{"}h^{"}}\right) \tag{3}$$

The boundary conditions and initial conditions used include (a) no slip, impermeable and adiabatic walls; (b) At inlet and outlet ports, mass flow rate conditions based on incoming and outgoing incompressible fluid are imposed. The mass flow rate at inlet and outlet are chosen to be equal. Diminishing residual criteria of the variables is used for the convergence with a limit of RMS residuals falling below 10^{-4}.

4 Results of Experimental and Computational Analysis

It can be seen from Fig.2 and Fig.3 that numerically simulated results match very well with experimental data [RKR03, MSH06]. Steady state observation shows that flow patterns are linearly proportional to the injection of velocities. It can be seen that streamlines and velocity distribution match in the experimental data. It is observe that fuel channels in the vessels enhance the mixing and diffuses the strong circulation zones. 3D-RANS code with various turbulence models has been used for computations. It is found that $K-\omega$ model perform better than other models when compared with experimental results.

4.1 Computational Results

Computations for isothermal and non-isothermal cases are made to understand the basic flow physics and convective heat transfer in the calandria. The flow structure and temperature distribution have been captured spatially. The non- isothermal analysis is made with an assumption that the fuel

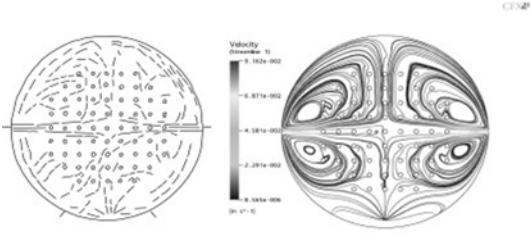

Fig. 2. Streamline plot comparision

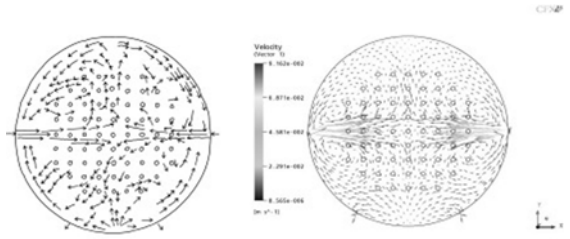

Fig. 3. Vector plot comparision

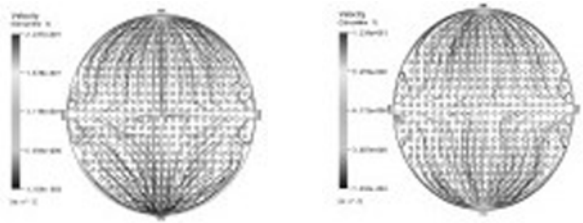

(a) (b)

Fig. 4. (a) Isothermal flow pattern for $Re = 1.69 \times 10^7$, with fuel channels. (b) Non-isothermal flow pattern for $Re = 1.69 \times 10^7$, with fuel channels.

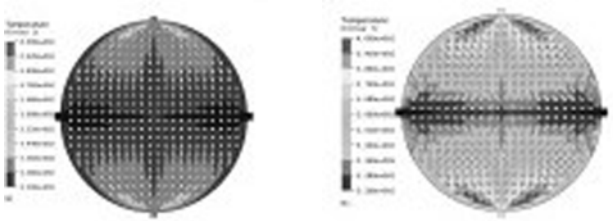

(a) (b)

Fig. 5. (a) Temperature distribution at $Re = 1.69 \times 10^7$ with 300MW thermal dissipation. (b) Temperature distribution at $Re = 1.69 \times 10^7$ with 1200MW thermal dissipation.

channel surfaces are giving out uniform heat flux. It is observed that the flow pattern and the velocity profiles Fig4(a) and Fig.4(b). This observation turns out to be strengthened with the observation that the temperature distribution patterns remaining nearly unchanged at different heat dissipation levels Figs.5(a) and 5(b). It is found that the inlet velocity and heat load are the major parameters affecting on the formation of flow patterns. Fig.6(a) and Fig.6(b) shows the effect of inlet velocity on pipe wall temperature and Heat load on pipe wall temperature.

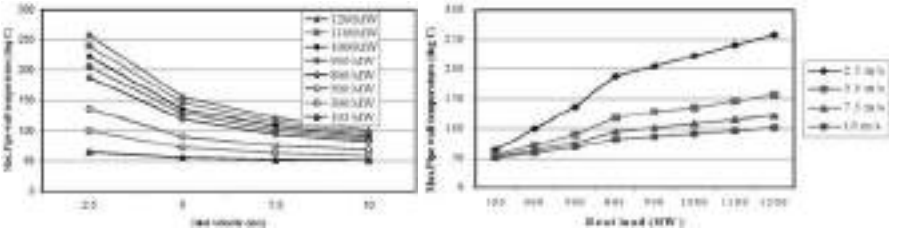

(a) (b)

Fig. 6. (a) Effect of inlet velocity on pipe wall temperature. (b) Effect of Heat load on pipewall temperature.

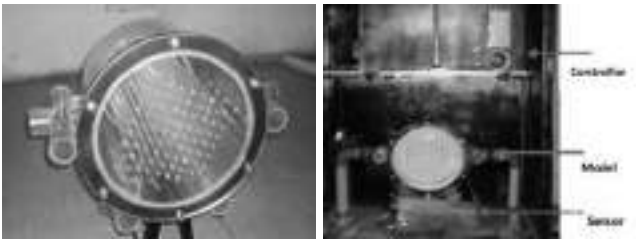

(a) (b)

Fig. 7. (a) Model of the Calandria fabricated with Acrylic material. (b) Different parts of the experimental set-up-with calandria model.

4.2 Experimental Results

The developed model constructed by transparent acrylic material for the Experimental study [Raj89] is shown in Fig.7(a). Fig.7(b) shows the Different parts of the experimental set-up with Calandria model. A series of photograph of the steady state flow were taken in the range of flow rate 0.03562 kg/s of water that correspond to the fluid velocities (at injection) of 1.3 m/s and bulk Reynolds number of 3.965×10^5 respectively. Fig.8 shows the Photographs taken with different speed of strobe.

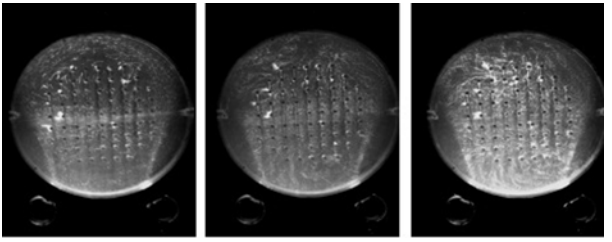

Fig. 8. Photographs taken with different speed of strobe

5 Conclusions

CFD analysis is carried out to study the mass flux and temperature distribution in the calandria using CFX-10 as an analysis tool. Internal flow computations are carried out for a calandria embedded with a matrix of tubes carrying nuclear reacting media. Increase in Reynolds number as mass flow rate is increased, does not have a significant change in the structure of the flow pattern. This is an important input to heat transfer studies to be carried out that indicates the forced convection dominating the heat transfer. The results of computation provide an estimate of the tolerance bands of safe working limits for the heat dissipation for different working conditions, by virtue of locating the hot spots in the calandria. The work assumes significance for preliminary design considerations of the reactors and for detailed and critical parametric analysis that prove to be expensive without CFD tools.

References

[Raj89] Rajan, N.K.S.: Experimental and Computational Studies of Fluid Dynamics and Heat Transfer in Spherical Vessels. Ph.D Thesis, Department of Aerospace Engineering, Indian Institute of Science, Bangalore, India (1989)

[IAE02] International Atomic energy Agency Vienna: Heavy water reactors status and projected development. Technical reports series no. 407, 16–32 (2002)

[RKR03] Tupake, R.S., Kulkarni, P.S., Rajan, N.K.S.: Numerical Analysis of Heat and Mass Transfer in a Calandria Based Reactor. In: 5th Asian CFD Conference, Bussan, Korea (2003)

[MSH06] Kim, M., Yu, S.-O., Kim, H.-J.: Analyses on fluid flow and heat transfer inside Calandria vessel of CANDU-6 using CFD. Nuclear Engineering and Design (236), 1155–1164 (2006)

Part 14
Complex Flows 4

“*This page left intentionally blank.*”

Propulsion by an Oscillating Thin Airfoil at Low Reynolds Number

Roel Müller[1], Akira Oyama[2], Kozo Fujii[2], and Harry Hoeijmakers[1]

[1] University of Twente,
PO Box 217, 7500 AE, Enschede, the Netherlands
r.a.j.muller@alumnus.utwente.nl,
h.w.m.hoeijmakers@ctw.utwente.nl
[2] JAXA Institute of Space and Astronautical Science,
Sagamihara, Kanagawa, 229-8510, Japan
oyama@flab.isas.jaxa.jp, fujii@flab.isas.jaxa.jp

Abstract. This paper describes an investigation of the mechanisms producing thrust for an airfoil performing a pitching or heaving motion in a low Reynolds-number flow ($Re = 1000$, based on chord length) by analysis of numerically obtained flow fields and forces on the airfoil. For heaving motion the dependence on reduced frequency and non-dimensional heaving amplitude are examined. For pitching motion the reduced frequency and the center of rotation are varied. The vortex generated by the leading edge is found to be determinant for thrust by heaving motion. Pitching propulsion is shown to be an effect of coupled acceleration and inclination of the airfoil.

Keywords: Flapping wing propulsion, Low Reynolds number, Heaving wing, Pitching wing.

1 Introduction

At low Reynolds numbers conventional wings produce relatively small lift and substantial drag. However, large insects and small birds realize high lift combined with flapping propulsion and great agility at the same low Reynolds numbers. These characteristics make flapping flight very attractive for micro air vehicles (MAVs), but equally so for aircraft designed for planetary research on Mars. Due to the low density of the Martian atmosphere, an aircraft of practical dimensions would encounter the same low Reynolds number.

The aerodynamics for flapping flight at these low Reynolds numbers is however not yet well understood and it is not clear how thrust is generated exactly [PJ06]. 3D Flapping flight of MAVs is described by many parameters (angular amplitudes, frequency, phase shifts) which make it difficult to determine which parameters govern the flow field.

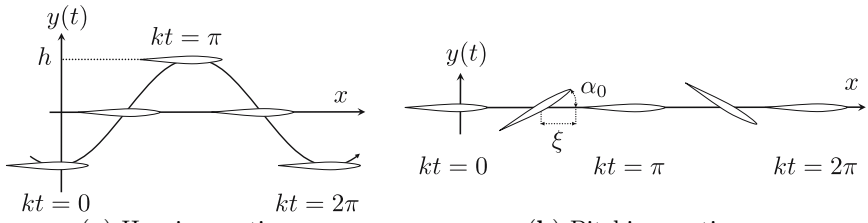

(**a**) Heaving motion (**b**) Pitching motion

Fig. 1. Parameters for both oscillating motions

Therefore this research concerns analysis of basic motions. Thrust generation by a simple heaving airfoil (Fig. 1a) and a purely pitching airfoil (Fig. 1b) are examined, to detemine the variation with the parameters ξ, k and h independently. The results is helpful in obtaining insight in more complex cases.

For heaving motion the varied parameters are reduced frequency $k = \frac{2\pi fc}{U_\infty} \in (0.2, 4)$ and nondimensional amplitude h chordlength $h \in (0.125, 2.5)$. For pitching motion the reduced frequency $k \in (0.2, 6)$, the pitching amplitude $\alpha_0 \in (10°, 30°)$ and the center of rotation (between leading edge (LE) and trailing edge (TE), expressed by $\xi \in (0, 1)$) are varied.

2 Computational Method

Flow fields for these cases are obtained using a computational method based on one used for a variety of CFD studies, most recently [Oya07]. Besides the flow fields, the time history of thrust/drag of the airfoil, divided in a friction and pressure part, is used to analyze the results.

The governing equations are the Navier Stokes equations for incompressible flow. These were solved using a pseudo two-dimensional, pseudo-compressibility method. The convective terms are evaluated by Roe's scheme, while MUSCL interpolation based on the primitive variables is used to evaluate the fluxes at the grid interface. The viscous terms are discretisized by a second order central difference scheme. Time integration is carried out by means of a first-order lower-upper symmetric Gauss-Seidel (LU-SGS) implicit time integration scheme. Laminar flow of a Newtonian fluid is assumed.

3 Test Case

The computations were carried out using a C-shaped grid with 100 cells in radial and 268 in tangential direction. For every motion, 6000 time steps covering 3 cycles were simulated, the last cycle being used for analysis.

Accuracy was checked using a grid with doubled resolution. However, this showed better conservation of vortices and earlier flow separation. This caused only minor changes in far as thrust generating phenomena or the comparison of different cases are concerned. The absolute value of the thrust coefficient did however change up to 0.5 in some cases.

The range of design variables is representative for insects and some small birds and it is comparable with previous research focussing on insects, small birds and MAV development.

4 Heaving Motion

Figure 2 shows the dependance of $C_{T,av}$ on the parameters k and h. For $k > 1$ and $h < 2$, thrust increases strongly as the value of the parameters increase. In these cases thrust can be explained by one mechanism. For lower values of k, the airfoil does not shed the strong vortices needed to propell the wing. For higher values of h however, the structure of the flowfield is lost due to the the excessive motion of the airfoil.

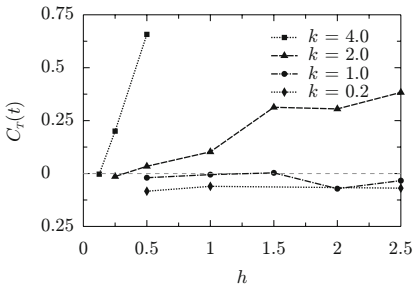

Fig. 2. Time-averaged thrust coefficient $C_{T,av}$ for different values of k and h

Heaving motion generates thrust when a vortex is generated at the LE and stays close to the airfoil, as shown in Fig. 3. Examination of the flow fields shows that such a vortex causes low pressure near the nose of the airfoil, generating thrust by suction. This vortex also induces a strong flow opposite to the free stream. This flow causes friction in upstream direction, which again is thrust. Both phenomena generate thrust of a similar order of magnitude. For comparison, the development with time of thrust due to pressure and friction is included in Fig. 3.

Figure 3a shows an airfoil simultaneously propelled by a LE vortex and hindered by a vortex shed at the TE. In Fig. 3b the effect of the LE vortex is maximal. Figure 3c–d show how the vortex travels along the airfoil. First the thrust by pressure decreases, as the vortex still induces a thrust-generating flow. Later the vortex travels around the TE and merges with the trailing edge vortex generated at that moment, which causes drag.

Vortices generated at the TE have the exact opposite effect of LE vortices, but since TE vortices travel away from the airfoil, their influence is smaller.

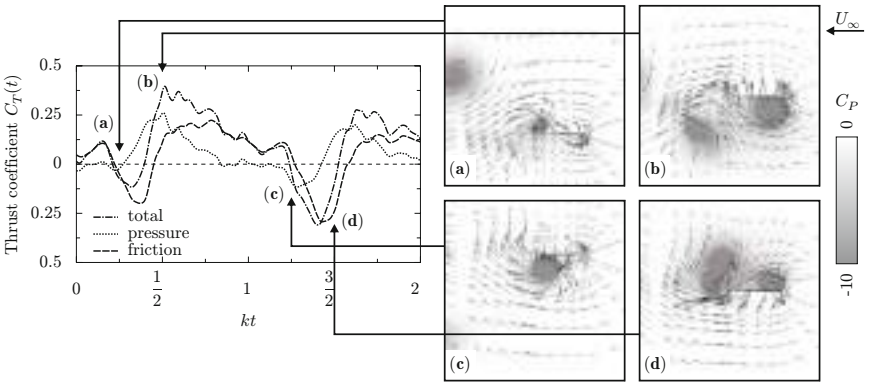

Fig. 3. Plunging airfoil propelled by a LE vortex ($k = 2$, $h = 1$)

5 Pitching Motion

Usually pitching around the LE is favorable for thrust, as seen in Fig. 4. For pitching around the LE ($\xi = 0$), as for the heaving motion, higher values of k give more thrust. $k = 4$ is the first value for which positive thrust is found. Similar to h, higher values of α_0 cause more thrust as well.

In the case of $k = 0.2$ and $k = 1$, pitching around the TE ($\xi = 1$) delivers more thrust. This seems to match the findings of heaving motion, for which thrust was generated by vortices at the moving LE. For higher values of k new mechanisms have to be found.

For pitching motion the time history of the thrust/drag shows relatively little influence of friction. At lowest frequencies, the airfoil shows a quasi-steady behavior, for which drag depends mostly on the momentary inclination of the airfoil, i.e. increasing inclination gives an increase in drag. As the frequency increases, the free stream velocity loses influence compared to the influence of the pressure difference over the airfoil opposing the pitching motion. When the

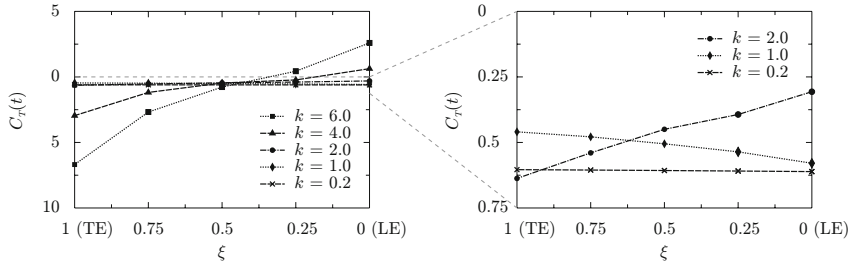

(**a**) All values of k (**b**) Lower values of k

Fig. 4. Time-averaged thrust coefficient $C_{T,av}$ for different values of ξ and k

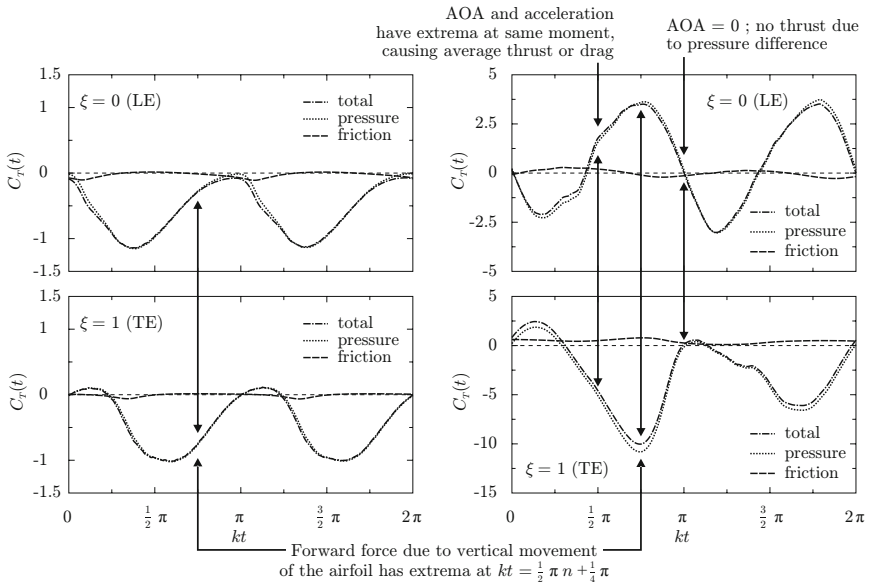

(**a**) $k = 1$, $\alpha_0 = 30°$ (**b**) $k = 4$, $\alpha_0 = 30°$

Fig. 5. Time history of thrust for pitching around either LE or TE

airfoil is horizontal at $k = n\pi$, this does not cause any horizontal force. Since the airfoil does not move at $kt = n\pi + \frac{1}{2}\pi$, the influence of pressure on the airfoil due to the pitching motion is largest at $kt = \frac{1}{2}n\pi + \frac{1}{4}\pi$. This can already be seen at $k = 1$, as Fig. 5a shows. This effect gives thrust in a certain part of the cycle, but drag in another part of the cycle. Even though this effect stays dominant in the pressure thrust as a function of time, it does not give thrust on average, which however can be observed for higher values of k.

At even higher frequencies the average thrust for pitching around the LE is understood to be an effect of inertia of the fluid around the airfoil, as shown in Fig. 5b and schematically in Fig. 6.

When the airfoil rotates around the LE, it is accelerating upward when at maximum angle attack. Due to inertia of the fluid around the airfoil, the pressure on the top side of the airfoil in higher, which causes thrust. When the angle of attack is negative, the same effect still produces thrust. For pitching around the TE the effect is opposite however, and only drag is produced.

The effect of vortices on the pressure on a pitching airfoil is smaller than on a heaving airfoil. As seen in Fig. 7a, for pitching around the leading edge, this is because the leading edge is not moving, and therefore little vorticity is shed. Figure 7b shows how pitching around the trailing edge does generate a large LE vortex, but this vortex is relatively far away from the airfoil and has little influence on the pressure on the wing surface.

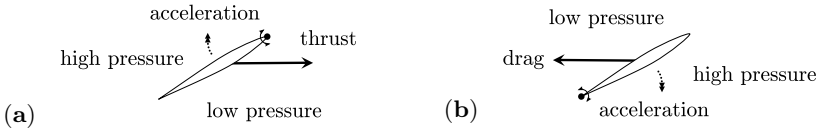

Fig. 6. At maximum angle of attack an airfoil is either: (**a**) propelled by positive vertical acceleration when pitching around the LE or (**b**) hindered by negative vertical acceleration when pitching around the TE

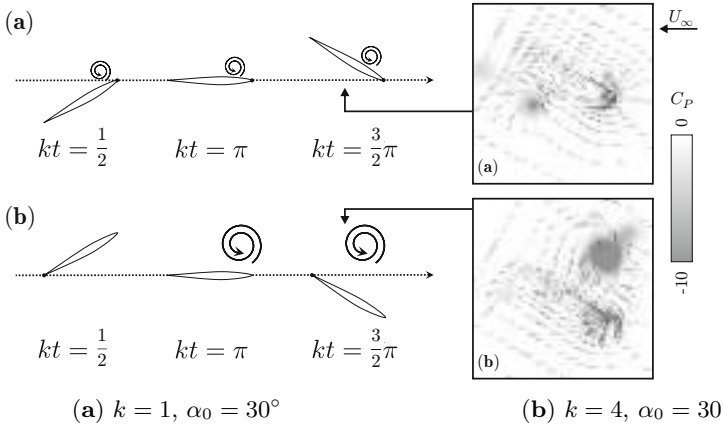

(**a**) $k = 1$, $\alpha_0 = 30°$ (**b**) $k = 4$, $\alpha_0 = 30°$

Fig. 7. In comparison with heaving, vortices play a smaller role for pitching motion

6 Summary and Further Research

The above identifies and explains the contributions of heaving and pitching to the thrust generated by an airfoil. It must however be realized that these phenomena are discussed on a qualitative basis. For engineering purposes quantitative analysis of more accurate simulations is required. These could include a wider range of parameters. The (symmetric) problems at hand did not allow an investigation of the effect of oscillation on the lift of the airfoil. For application in aviation this would be of great importance.

References

[PJ06] Platzer, M.F., Jones, K.D.: Flapping Wing Aerodynamics, Progress and Challenges. In: 44th AIAA Aerospace Sciences Meeting and Exhibit (2006)

[Oya07] Oyama, A., Okabe, Y., Fujii, K., Shimoyama, K.: A Study on Flapping Motion for MAV Design Using Design Exploration. In: AIAA Infotech@Aerospace 2007 Conference and Exhibit (2007)

Residual Currents around Plural Asymmetrical Structures in Oscillatory Flow Fields

Rusdin Andi[1], Hideo Oshikawa[2], Akihiro Hashimoto[3], and Toshimitsu Komatsu[4]

[1] Department of Maritime Engineering, Graduate School of Engineering, Kyushu University
suiri21@civil.kyushu-u.ac.jp
[2] Department of Urban and Environmental Engineering, Faculty of Engineering, Kyushu University
oshikawa@civil.kyushu-u.ac.jp
[3] Department of Urban and Environmental Engineering, Faculty of Engineering, Kyushu University
ahashimo@civil.kyushu-u.ac.jp
[4] Department of Urban and Environmental Engineering, Faculty of Engineering, Kyushu University
komatsu@civil.kyushu-u.ac.jp

1 Introduction

In the resent years, water deterioration by pollution in a stagnant sea area like a semi-enclosed bay occurs mainly due to the lack of water exchange with the open sea. Komatsu *et al.* [KYG97] suggested to use unidirectional residual currents generated by asymmetrical structures which are put on the sea bottom in order to activate substance transport in a tidal field. In addition, Komatsu *et al.* [KSK01] also proposed to apply this method to control sediment transport in wave fields. Moreover, Kawano *et al.* [KHF06] proposed the specific pipe called One-Way Pipe, which can generate residual currents in a wave field by a number of asymmetrical structures set inside the pipe. It is expected to activate water exchange with the open sea by putting a series of One-Way Pipes from the inside end of the bay to the baymouth.

Oscillatory flows with plural asymmetrical structures are computed in order to estimate the effectiveness of the methods using the asymmetrical structures in a wave field. Oshikawa *et al.* [OSK04] performed a laboratory experiment in a wave tank with a number of asymmetrical structures to examine the characteristics of residual currents. They investigated the effects of three-dimensional asymmetrical structures on the residual currents by using quarter spheres. In addition, they discussed the effects of some parameters, such as the Keulegan-Carpenter number and the space between asymmetrical structures. However, their results have not been verified with a wide range of conditions because it was difficult to set optional experimental conditions in the physical experiments. Therefore, we performed numerical simulations which could provide ideal conditions.

2 Computational Method

The vertical two-dimensional numerical simulation based on the Reynolds-averaged Navier-Stokes equations (:RANS) and the k-ε turbulent model is used to simulate oscillatory flows around the structures. At the top of the computational domain, the free slip boundary is set for the flow velocity, and the zero normal gradient condition is used for the pressure. The velocity components and pressures at the left side and the right side open boundaries are based on the analytical solutions which are sinusoidal functions for an oscillatory flow. The numerical solver originally based on the CADMAS-SURF code [CDI01] is the same as that used in the study by Rusdin *et al*. [ROH07].

Computational conditions are decided in consideration with the laboratory experiments by Oshikawa *et al*. [OSK04]. In the simulation 12 quarter-cylinder shaped structures are set longitudinally at the bottom of the computational domain, and cases with different in-line spaces between the structures are compared under some flow conditions which are given by the Keulegan-Carpenter number ($KC=U_0k/T$), the Reynolds number ($Re=U_0k/\nu$) and water depth relative to the size of the structure, h/k. U_0, T, h and ν denote the amplitude of the x-directional oscillating velocity at the water surface, an oscillatory period, a water depth and a coefficient of kinematic viscosity, respectively. The definitions of k and s can be found in Fig. 1, where k is the height of the structures and s is the longitudinal distance between the structures. In this study, h (=30.0cm), k (=2.1cm) and ν (=0.01cm^2/s) are constant.

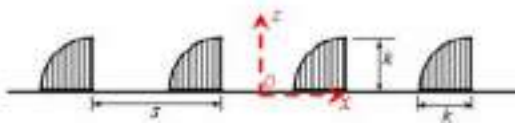

Fig. 1. Shape of the asymmetrical structures and definitions of s and k

3 The Effects of the Asymmetrical Structures

In this case, the positive residual currents and the negative residual hydrodynamic force are produced near the asymmetrical structures. In this study, the residual current is defined as the Eulerian velocity averaged over one period of an oscillatory flow, and the residual hydrodynamic force is calculated by averaging hydrodynamic force on one structure over the same period. In the case of KC=9.9, Re=4351 and s/k=4, the time series of the normalized horizontal velocity at the open boundary, u_o/U_0, and that between two structures, u/U_0 at x/k=0, and the normalized horizontal hydrodynamic force on the middle structure of the computational domain, F^*, are drawn in Fig. 2, where the hydrodynamic force are normalized by $0.5\rho kU_0^2$ and ρ denotes the density of fluid. The vertical position of the velocity measured is taken at the height of the structure, z/k=1. There is the large difference between the velocities in the range from t/T=0.58 to 1.14 (=0.14) because the flow passes from the vertical edge side to the circular one for the each structure in the time. The difference creates a residual current near the structures

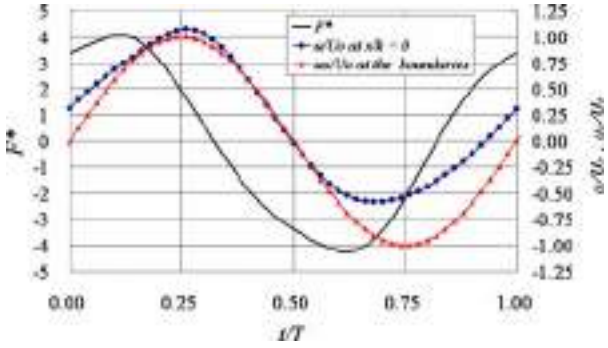

Fig. 2. Time series of the horizontal hydrodynamic force and velocities

because the residual current of u_o is perfectly 0. In this case, the normalized residual current, u^*/U_0, is 0.20. Similarly, residual hydrodynamic force, f^*, is generated by the structures as the absolute value of the negative peak of F^* is larger than that of the positive one. In this case f^* is -0.042. On the sign, a negative residual hydrodynamic force corresponds to a positive residual current.

The computational results are considerably reliable. In the case of KC=9.9, Re=4351 and s/k=2.5, the comparison of dimensionless horizontal residual currents u^*/U_0 at x/k=0 between the computational results and the experimental ones [OSK04] are shown in Fig. 3. The vertical profile of u^*/U_0 in the computation is quite similar to that in the experiment. Especially the maximum value of u^*/U_0 in the simulation almost agrees with that in the experiment. In addition, in such a small s/k, negative residual currents are found near the bottom from the simulation as the indication by Oshikawa *et al.* [OSK04].

The residual currents are significantly influenced by KC. Fig. 4 presents the vertical profiles of u^*/U_0 at x/k=0 for various KC in the case of Re=4351 and s/k=10. Although the asymmetrical structures produce positive residual currents near the bottom in all cases, the vertical profiles remarkably depend on KC. The maximum value of u^*/U_0 in each vertical profile varies with the KC. In addition, the zero crossing location of each vertical profile increases with KC.

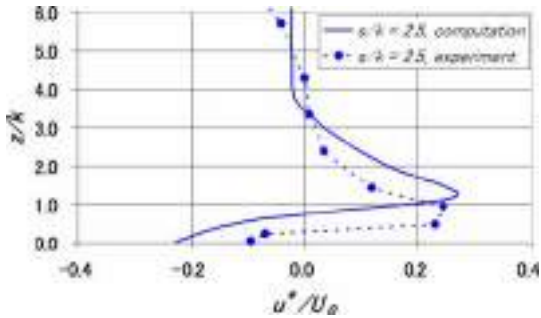

Fig. 3. Comparison of vertical profiles of the horizontal residual currents between the computational results and the experimental ones [OSK04]

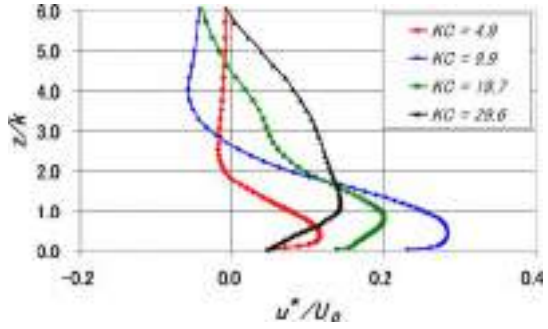

Fig. 4. Vertical profiles of u^*/U_0 for Re=4351 and s/k=10 with various KC

4 The Effects of the Space between the Structures

Fig. 5 shows the velocity vectors and the streamlines of the residual currents normalized by U_0 in cases of s/k=2 and 4, for KC=9.9 and Re=4351. Both cases indicate that the positive horizontal residual currents are produced near the structures until z/k=3 in the case of s/k=2 and z/k=4 in the case of s/k=4. However, there is the obvious difference on the number of eddies. Only one eddy is generated between a sequence of two structures in the case of s/k=2 while three eddies are generated in the case of s/k=4.

The amplitude of the horizontal hydrodynamic force on the middle structure increases with s/k in the conditions of $2 \leq s/k \leq 8$. The time series of dimensionless horizontal hydrodynamic force F^* for KC=9.9 and Re=4351 with various s/k are given in Fig. 6. As a reference, the case with only one structure set in the computational domain is included, which corresponds to the infinite s/k. The figure shows that the amplitude of F^* becomes larger with KC up to s/k=8. However, F^* does not vary so much in the cases where $s/k \geq 8$ as the results in the cases of s/k=8 and s/k=12 are almost the same as that of the single structure.

The horizontal residual velocity is remarkably affected up to a few times the structure height. The dimensionless horizontal residual currents u^*/U_0 at x/k=0 in the each case of s/k=2, 6, 10, 16 with KC=9.9 and Re=4351 are illustrated in Fig. 7. The maximum u^*/U_0 are found in the case of s/k=10. In the small space with s/k=2, the negative residual currents are generated near the bottom as mentioned above. However,

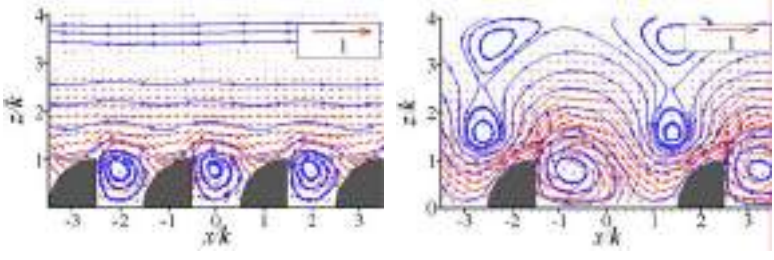

Fig. 5. Vectors and streamlines of the residual currents. The left figure illustrates the case with s/k=2 and the right one illustrates the case with s/k=4.

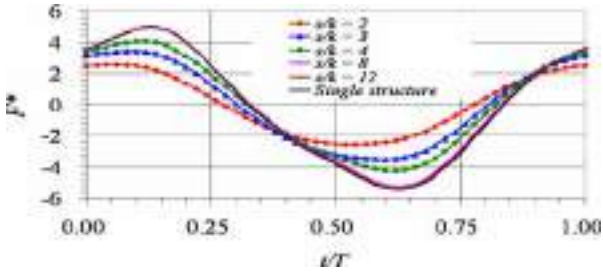

Fig. 6. Time series of F^* with different *s/k* for *KC*=9.87 and *Re*=4351

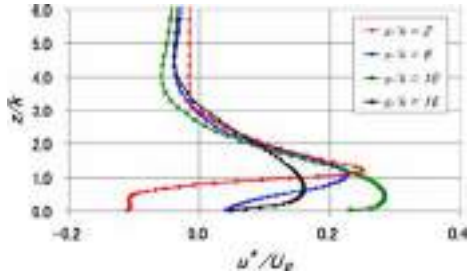

Fig. 7. Vertical profiles of u^*/U_0 at *x/k*=0 for *KC*=9.9 and *Re*=4351

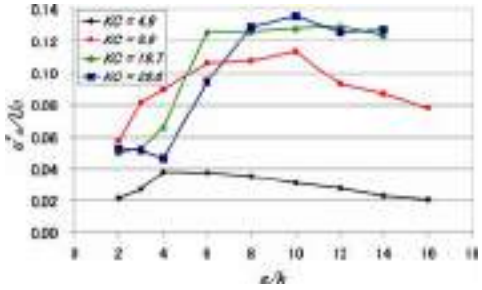

Fig. 8. Representative horizontal residual velocity for different *s/k* and *KC*

there is little difference between the vertical profiles in the range where *z/k* is larger than about 3. This value is correspondent to each zero crossing position except for the one for the negative u^*/U_0 in the small *s/k*.

The horizontal residual currents around the structures are relatively large in the conditions of $6 \leq s/k \leq 10$. It is extremely important to determine the most effective *s/k* for practical use of the methods, e.g. the One-Way Pipe. In this research, a local averaged horizontal velocity u^*_a, which is a representative residual velocity around the structures, is used to estimate an appropriate *s/k*. u^*_a is vertically averaged up to the three times *k* from the bottom, and the length horizontally averaged over is correspondent to the two times *s* in the middle of the computational domain. Therefore, the size of the area for spatial averaging of u^* is different for each case of *s/k*. Fig. 8 shows u^*_a

$/U_0$ in the cases of Re=4351. The u^*_a/U_0 significantly increases with KC in the conditions of $4.9 \leq KC \leq 19.7$, however the difference of u^*_a/U_0 between KC=19.7 and KC=29.6 in each s/k is relatively small. The s/k where u^*_a/U_0 takes each maximum value depends on KC. The case with small KC (KC=4.9) has the maximum u^*_a/U_0 at s/k=4, while the case with large KC (KC=29.6) has the maximum u^*_a/U_0 at s/k=10 and has the minimum at the s/k=4. Therefore, s/k should be practically taken to be from 6 to 10 depending on KC because u^*_a/U_0 is relatively large in the conditions of $6 \leq s/k \leq 10$ with any KC.

5 Conclusions

The plural asymmetrical structures put in a wave field can produce a unidirectional residual current in any space between the structures. The oscillatory flows with a series of quarter-cylinder shaped structures were investigated by using the numerical simulation. The computational results considerably agreed with the experimental ones by Oshikawa *et al*. [OSK04].

The horizontal unidirectional residual currents around the structures are relatively large in the range where the in-line space between the structures relative to their height, s/k, is approximately from 6 to 10. The residual currents are affected not only by s/k but also by flow conditions, especially the Keulegan-Carpenter number KC. Therefore, each asymmetrical structure should be practically set so that s/k corresponds to values from 6 to 10 in consideration with KC corresponding to dominant waves in a sea.

References

[KHF06] Kawano, T., Hatta, M.P., Fujita, K., Matsuda, J., Oshikawa, H., Komatsu, T.: Characteristics of Wave-Induced Residual Currents in the One-Way Pipe. Annual Journal of Hydraulic Engineering, JSCE 50, 1435–1440 (2006) (in Japanese)

[KYG97] Komatsu, T., Yano, S., Gug, S., Kohashi, N.: Control and Creation of Tidal Residual Current in a Semi-Enclosed Bay by Bottom Roughness with Directional Resistance Characteristics. In: Proc. of the 27th Congress of IAHR, B, pp. 653–658 (1997)

[KSK01] Komatsu, T., Saita, T., Kohashi, N., Adachi, T., Shibata, T.: Control of Sediment Transport by BaNK Blocks with Directional Resistance Properties. In: Proc. 29th IAHR, Theme E, pp. 340–346 (2001)

[OSK04] Oshikawa, H., Shibata, T., Komatsu, T.: Characteristics of Wave-Induced Residual Currents due to Plural Submerged Asymmetrical Roughness. Annual Journal of Hydraulic Engineering, JSCE 48 (2004) (in Japanese)

[ROH07] Rusdin, A., Oshikawa, H., Hashimoto, A., Komatsu, T.: Numerical simulations of oscillatory flows around a submerged asymmetrical structure. In: Proceedings of 5th International Symposium on Earth Science and Technology, pp. 189–196 (2007)

[CDI01] CDIT: Research and development of numerical wave channel. Coastal Dev. Inst. Technol., CDIT Libr. 12 (2001) (in Japanese)

Part 15
Compressible Flow 1

“*This page left intentionally blank.*”

Stability of the MUSCL Method on General Unstructured Grids for Applications to Compressible Fluid Flow

F. Haider[1], Jean-Pierre Croisille[2], and B. Courbet[1]

[1] Onera Département de simulation numérique des écoulements et aéroacoustique 29 rue de la Division Leclerc 92320 Châtillon France
florian.haider@onera.fr, bernard.courbet@onera.fr

[2] Laboratoire Mathématiques et Applications, UMR 7122, Université Paul Verlaine Bât. A, Ile du Saulcy 57045 Metz France
jean-pierre.croisille@math.univ-metz.fr

1 Introduction

Practical applications have motivated various extensions of the Muscl finite-volume method to general unstructured meshes and the Muscl approach is at the heart of many solvers for compressible gas dynamics. On unstructured grids, many stability results rely explicitly on slope limiters, see for example the maximum principle in [1] and the convergence results in [2, 5]. Limiters are non-linear methods in the sense that they give non-linear schemes even when they are applied to linear equations. Their importance lies mainly in applications to non-linear gas dynamics involving steep gradients and shocks. However, in order to analyze the properties of a numerical scheme, it remains important to study its behaviour in the case of the linear advection equation. In the absence of slope limiters, the spatial discretization of the linear advection equation with constant coefficients results in a linear semi-discrete equation.

The purpose of the present work is a theoretical and numerical analysis of this semi-discrete equation in order to examine the influence of the grid type, the reconstruction method and the stencil size on the linear stability of the Muscl scheme on unstructured grids. The goal is to identify the slope reconstruction methods and the stencil sizes that lead to stable discretizations of linear advection. In applications to compressible gas dynamics, these methods can be expected to be more robust and accurate than schemes that are stabilized only by slope limiters. The present study is motivated by numerical experiments in three-dimensional applications to internal flows and aerothermochemistry with the package Cedre developed by Onera. We refer to [3, 4] for more details.

2 Slope Reconstruction on General Unstructured Meshes

This section presents a general approach to slope reconstruction on unstructured grids. Throughout this paper the boundary conditions are assumed to be periodic. We consider a general unstructured grid of a cube $\Omega \subseteq \mathbb{R}^d$ consisting of N general polyhedra $\mathcal{T}_\alpha$ with barycenter $\mathbf{x}_\alpha$ and d-volume $|\mathcal{T}_\alpha|$. The face $\mathcal{A}_{\alpha\beta}$, with barycenter $\mathbf{x}_{\alpha\beta}$, has a normal vector $\mathbf{n}_{\alpha\beta}$ oriented from cell $\mathcal{T}_\alpha$ to $\mathcal{T}_\beta$. The length of $\mathbf{n}_{\alpha\beta}$ equals the surface $|\mathcal{A}_{\alpha\beta}|$. The set of the cell indices of the direct neighbors of cell $\mathcal{T}_\alpha$ is denoted $\mathbb{V}_\alpha$. Furthermore, we define $\mathbf{h}_{\alpha\beta} = \mathbf{x}_\beta - \mathbf{x}_\alpha$ for all cells $\mathcal{T}_\alpha$ and $\mathcal{T}_\beta$ and $\mathbf{k}_{\alpha\beta} = \mathbf{x}_{\alpha\beta} - \mathbf{x}_\alpha$ for all adjacent cells $\mathcal{T}_\alpha$ and $\mathcal{T}_\beta$. Whenever two cells have no common interface, $\mathbf{n}_{\alpha\beta} \triangleq 0$ and $\mathbf{k}_{\alpha\beta} \triangleq 0$. In addition, $\mathbf{n}_{\alpha\alpha} \triangleq 0$, $\mathbf{k}_{\alpha\alpha} \triangleq 0$ and $\mathbf{h}_{\alpha\alpha} \triangleq 0$. This allows to drop the neighborhood in all sums and to write $\sum_\beta$ instead of $\sum_{\beta\,\in\mathbb{V}_\alpha}$. The reconstruction of a slope $\boldsymbol{\sigma}_\alpha$ in each cell $\mathcal{T}_\alpha$ allows to compute second order accurate values

$$u_{\alpha\beta} = u_\alpha + \boldsymbol{\sigma}_\alpha \cdot \mathbf{k}_{\alpha\beta} \tag{1}$$

at the barycenter $\mathbf{x}_{\alpha\beta}$ of the cell interface $\mathcal{A}_{\alpha\beta}$. The most general linear slope reconstruction method can be written as

$$\mathfrak{u} \mapsto \boldsymbol{\sigma}_\alpha(\mathfrak{u}) = \sum_\beta \mathbf{s}_{\alpha\beta}(u_\beta - u_\alpha) \tag{2}$$

where the $\mathbf{s}_{\alpha\beta}$ are coefficient vectors in cell $\mathcal{T}_\alpha$ and $\mathbf{s}_{\alpha\beta} \triangleq 0$ by definition if cell $\mathcal{T}_\beta$ is not in the reconstruction stencil of cell $\mathcal{T}_\alpha$. Second order accuracy requires that (2) reproduce the slope of polynomials of degree one. This is equivalent to the following consistency condition for the coefficients $\mathbf{s}_{\alpha\beta}$

$$\boldsymbol{\sigma} = \sum_\beta \mathbf{s}_{\alpha\beta}\,(\mathbf{h}_{\alpha\beta} \cdot \boldsymbol{\sigma}) \quad \text{for all}\, \boldsymbol{\sigma} \in \mathbb{R}^d\,. \tag{3}$$

Let m be the number of cells in the reconstruction stencil of cell $\mathcal{T}_\alpha$ and $\mathbb{W}_\alpha \triangleq \{\beta_1, \beta_2, \ldots, \beta_m\}$ the cell indices in that stencil. On cell $\mathcal{T}_\alpha$, the unknown vectors $\mathbf{s}_{\alpha\beta}$, $\beta \in \mathbb{W}_\alpha$, form the columns of a $d \times m$ matrix S_α. Similarly, the vectors $\mathbf{h}_{\alpha\beta}$, $\beta \in \mathbb{W}_\alpha$, form the rows of the $m \times d$ matrix H_α. Now the consistency condition (3) can be written as the matrix equation with unknown S_α

$$S_\alpha H_\alpha = \mathrm{I}_{d\times d}\,. \tag{4}$$

The least-squares slope coincides with the pseudo-inverse of H_α that is also the minimum Frobenius norm solution of (4), see [3]. It is given by

$$S_\alpha^{\mathrm{ls}} = \left(H_\alpha^t H_\alpha\right)^{-1} H_\alpha^t\,.$$

Another method is based on the well-known Green Theorem and results in

$$S_\alpha^{\mathrm{gr}} = \left(N_\alpha^t H_\alpha\right)^{-1} N_\alpha^t$$

where the matrix N_α has the row vectors

$$\mathbf{n}'_{\alpha\beta} = \frac{\|\mathbf{a}_{\alpha\beta}\|}{\|\mathbf{h}_{\alpha\beta}\|}\mathbf{n}_{\alpha\beta}$$

and $\mathbf{a}_{\alpha\beta}$ is the orthogonal projection of $\mathbf{k}_{\alpha\beta}$ on $\mathbf{h}_{\alpha\beta}$, see [3].

3 Stability Analysis of the MUSCL Scheme

The application of the MUSCL scheme to the linear advection equation $\partial_t u(\mathbf{x},t) + \mathbf{c}\cdot\boldsymbol{\nabla} u(\mathbf{x},t) = 0$ with periodic boundary condition results in a linear dynamical system (*method of lines*)

$$\frac{\mathrm{d}u_\alpha(t)}{\mathrm{d}t} = \sum_\beta J_{\alpha\beta} u_\beta(t)\ ;\ 1 \le \alpha \le N. \tag{5}$$

The definition $\mathbf{s}_\alpha \triangleq \sum_\beta \mathbf{s}_{\alpha\beta}$ allows to write the MUSCL operator J in (5) as

$$\begin{aligned} J_{\alpha\beta} = &-|\mathcal{T}_\alpha|^{-1}\left\{\sum_\gamma (\mathbf{c}\cdot\mathbf{n}_{\alpha\gamma})_+ \delta_{\alpha\beta} + (\mathbf{c}\cdot\mathbf{n}_{\alpha\beta})_- + \right. \\ &+\sum_\gamma (\mathbf{n}_{\alpha\gamma}\cdot\mathbf{c})_+ \mathbf{k}_{\alpha\gamma}\cdot\mathbf{s}_{\alpha\beta} - \sum_\gamma (\mathbf{n}_{\alpha\gamma}\cdot\mathbf{c})_+ \mathbf{k}_{\alpha\gamma}\cdot\mathbf{s}_\alpha\,\delta_{\alpha\beta} - \\ &\left.-\sum_\gamma (\mathbf{n}_{\gamma\alpha}\cdot\mathbf{c})_+ \mathbf{k}_{\gamma\alpha}\cdot\mathbf{s}_{\gamma\beta} + (\mathbf{n}_{\beta\alpha}\cdot\mathbf{c})_+ \mathbf{k}_{\beta\alpha}\cdot\mathbf{s}_\beta\right\}. \end{aligned} \tag{6}$$

The time derivative of the quadratic energy function of (5) can be written as a sum

$$\frac{\mathrm{d}}{\mathrm{d}t}E(t) = \sum_{\alpha=1}^N |\mathcal{T}_\alpha| \frac{\mathrm{d}}{\mathrm{d}t}\left(|u_\alpha(t)|^2\right) = \sum_{\alpha=1}^N \Phi_\alpha(\mathbf{u}) \tag{7}$$

where

$$\begin{aligned} \Phi_\alpha(\mathbf{u}) = \sum_\beta (\mathbf{c}\cdot\mathbf{n}_{\alpha\beta})_+ \Bigg[&\underbrace{-(u_\beta - u_\alpha)^2}_{\mathrm{I}} + \\ &\underbrace{+2\sum_\gamma (u_\beta - u_\alpha)\, r_{\beta\gamma}^{(\alpha)} (u_\gamma - u_\alpha)}_{\mathrm{II}}\Bigg]. \end{aligned} \tag{8}$$

Note that the first term is always non-positive whereas the second term can be positive. The elements $r_{\beta\gamma}^{(\alpha)} \triangleq \mathbf{k}_{\alpha\beta} \cdot \mathbf{s}_{\alpha\gamma}$ in the second part of (8) form the entries of a local geometric matrix R_α attached to the cell $\mathcal{T}_\alpha$. If K_α is the matrix whose rows are the vectors $\mathbf{k}_{\alpha\beta}$ for $\beta \in \mathbb{V}_\alpha$ then $R_\alpha = K_\alpha S_\alpha$. The dimensionless operator R_α is invariant under scaling of the grid and defines the linear mapping $R_\alpha : (u_\gamma - u_\alpha)_{\gamma \in \mathbb{W}_\alpha} \mapsto (u_{\alpha\beta} - u_\alpha)_{\beta \in \mathbb{V}_\alpha}$ where $u_{\alpha\beta}$ is defined by (1). We summarize the main results of our study, see [3, 4], as follows.

Theorem 1 (Stability of the First Order Finite Volume Scheme). *If all reconstruction coefficients* $\mathbf{s}_{\alpha\gamma}$ *are zero then* $\frac{d}{dt}E(t) \leq 0$ *on arbitrary polyhedral meshes regardless of the velocity* $\mathbf{c}$ *and the space dimension* d. □

Theorem 1 and (8) suggest to choose reconstruction coefficients that minimize an appropriate matrix norm of $R_\alpha = K_\alpha S_\alpha$ under the constraint (4).

Theorem 2 (Minimization Property of the Least-squares Reconstruction). *The least-squares reconstruction minimizes each singular value of* $K_\alpha S_\alpha$ *and therefore all unitarily invariant matrix norms, in particular the Spectral, Frobenius, and the Trace norms among the matrices satisfying (4).*

For the least squares reconstruction, the influence of the stencil size on the matrix R_α is characterized by

Theorem 3 (Influence of the Stencil Size on the Reconstruction Matrix). *Let* $\tilde{S}_\alpha$ *be the least-squares slope reconstruction matrix. If cells are added to the reconstruction stencil, then the singular values as well as all unitarily invariant matrix norms of* $R_\alpha = K_\alpha \tilde{S}_\alpha$ *are non-increasing. Furthermore, if* $\{\beta_1, \ldots, \beta_k\}$ *are the indices of the newly added cells and if the family of vectors* $\{\mathbf{h}_{\alpha\beta_1}, \ldots, \mathbf{h}_{\alpha\beta_k}\}$ *has full rank* d *then all unitarily invariant matrix norms as well as all strictly positive singular values of* $R_\alpha = K_\alpha \tilde{S}_\alpha$ *are strictly decreasing.*

Theorems 2 and 3 allow the following practical conclusions that have been tested numerically in Sect. 4. First, the least-squares reconstruction should provide better stability than alternative reconstruction methods. Second, larger stencil sizes should increase the linear stability of the MUSCL scheme.

4 Numerical Computation of Spectra of MUSCL Operators

This section presents the numerical computations of spectra of (6) on the unit square and the unit cube. The purpose of these calculations is to look for a correlation between the values of R_α and the appearance of unstable eigenmodes and to test the conclusions at the end of Sect. 3. The test cases include different grid types, reconstruction methods and stencil sizes.

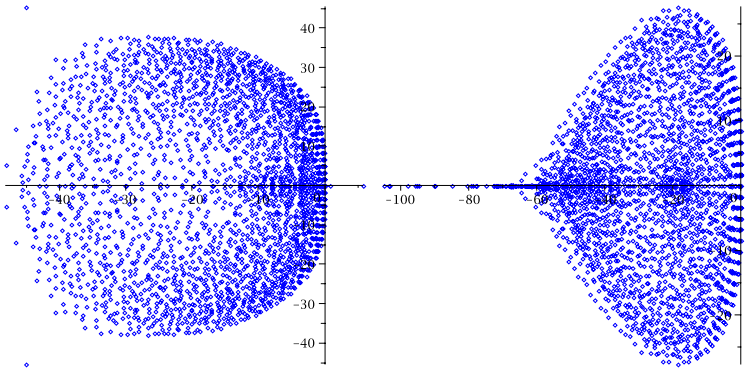

(a) First neighborhood (b) Second neighborhood

Fig. 1. Spectra of the operator (6) for a tetrahedral grid : Least-squares reconstruction on the first and second neighborhood. For the former, two unstable eigenmodes are visible on the right of the imaginary axis.

A program computes for each test case the matrix of (6) and its spectral abscissa, defined by $\omega_J = \max\{\Re(\lambda) | \lambda \in \sigma(J)\}$ as well as the spectral norm of $R_\alpha = K_\alpha S_\alpha$ for each cell $\mathcal{T}_\alpha$. The numerical computations reveal a strong correlation between the values of R_α and the existence of unstable eigenvalues λ with $\Re(\lambda) > 0$. The latter appear only on grids with cells where the spectral norm of R_α approaches or exceeds 1. Recall that the matrix R_α is dimensionless and scaling invariant. The case where the largest values of R_α have been observed is the first neighborhood slope reconstruction in three dimensions on tetrahedra and prisms. For this case, the least-squares as well as the Green slope produce a small number of unstable eigenmodes. For second neighborhood stencils, the second order accurate slope can also produce unstable modes on tetrahedra that appear together with values of $\|R_\alpha\| > 1$. For all other cases, the values of $\|R_\alpha\|$ are smaller than 1 and no unstable modes occur.

5 Applications to Compressible Gas Dynamics

The conclusions of Sect. 3 have been used to enhance the solver Cedre. However, for an industrial software like Cedre that handles large unstructured grids it is better to avoid large reconstruction stencils. We have therefore adopted a new method that can be implemented by means of the first neighborhood connectivity. In a first step, the algorithm computes in each cell a slope using the least-squares reconstruction on the first neighborhood. In a second step, the algorithm takes a weighted average of these slopes over the first neighbors of each cell. Numerical computations of spectra for the operator (6) show that this leads to a stable Muscl discretization of linear

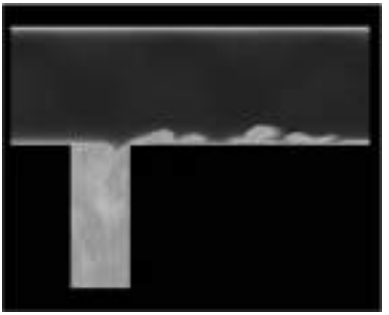

Fig. 2. Entropy for the flow over a deep 3D cavity, see [6]

advection. The method has recently been tested with CEDRE on unstructured three-dimensional grids for the subsonic flow over a deep cavity and for a supersonic jet [4]. In the case of the cavity, the new slope reconstruction is stable without any slope limitation on tetrahedral grids. Previously, this was only the case for simulations on structured grids [6]. In the case of the jet, slope limiting is necessary only inside the nozzle and this leads to much better results [4]. In previous computations, structured blocks had to be used inside the tetrahedral grid in order to obtain good results [7].

References

1. Barth, T., Ohlberger, M.: Finite Volume Methods: Foundation and Analysis. In: Stein, E., De Borst, R., Hughes, T.J.R. (eds.) Encyclopedia of Computational Mechanics. Wiley, New York (2004)
2. Chainais-Hillairet, C.: Second Order Finite Volume Schemes for a Nonlinear Hyperbolic Equation: Error Estimate. Math. Meth. Appl. Sci. 23(5), 467–490 (2000)
3. Haider, F., Croisille, J.P., Courbet, B.: Stability Analysis of the Cell Centered Finite-Volume MUSCL Method on Unstructured Grids (submitted, 2008)
4. Haider, F.: Discrétisation en maillage non structuré et applications LES. Thesis, University Paris 6 (2008)
5. Kröner, D.: Numerical Schemes for Conservation Laws. John Wiley and Sons/B.G. Teubner, Chichester/Stuttgart (1997)
6. Larchevâque, L., Sagaut, P., Mary, I., Labbé, O., Comte, P.: Large-eddy simulation of the compressible flow over a deep, open cavity. Phys. Fluids 15(1), 193–210 (2003)
7. Lupoglazoff, N., Rahier, G., Vuillot, F.: Application of the CEDRE Unstructured Flow Solver to Jet Noise Computations. In: First European Conference for Aerospace Sciences (EUCASS), Moscou, Russie (2005)

Time-Accurate Computational Analysis of the Flame Trench

Cetin Kiris[1], William Chan[1], Dochan Kwak[1], and Jeffrey Housman[2]

[1] NASA Ames Research Center, Moffett Field, CA 94035, USA
Cetin.C.Kiris@nasa.gov
[2] Department of Mechanical and Aeronautical Engineering,
University of California Davis,
Jeffrey.A.Housman@nasa.gov

Abstract. Time accurate simulations are performed to analyze the effects of the exhaust plumes generated by the Space Shuttle's Solid Rocket Boosters (SRBs) on the Mobile Launch Platform (MLP) and flame trench. The subsequent ignition overpressure (IOP) waves are generated by the interaction of the plume with the trench. These IOP waves travel from the flame trench to the launch vehicle, and may cause stability problems during takeoff. Computed results for one configuration of the Space Shuttle (STS-1) and three MLP configurations for a single SRB (used to represent Ares-Ix) are compared.

1 Introduction

The purpose of this study is to characterize the ignition overpressure phenomenon during takeoff of new and existing launch vehicles. During ignition of the rocket propulsion system, transient pressure waves are initiated by the interaction of the exhaust plume with the flame trench. These ignition overpressure waves are generated during the initial buildup of thrust, in which mass is suddenly injected into the confined volume of the flame trench under the launch platform. The additional mass displaces the air within the trench causing a piston-like action and produces compression waves which travel up and down the trench. The traveling compression waves, along with their reflections, generate a series of strong pressure waves which travel back through the inlet of the trench towards the launch vehicle, where they may affect the stability of the vehicle during takeoff. For more details on the ignition overpressure phenomenon see Jones [1]. In order to assess the effects of the ignition overpressure waves on new and existing launch vehicles, time accurate simulations of the flame trench are performed for the Space Shuttle configuration and various MLP configurations with a single SRB, used to represent a preliminary design for Ares Ix. The SRB nozzle conditions are impulsively started with full thrust conditions (physically these conditions are

achieved in approximately 0.3 seconds) and it is observed that IOP waves obtained from the Shuttle simulation correlate well with STS-1 flight data (the water suppression system was not implemented during the STS-1 launch), Ryan *et al* [2]. The impulsive start conditions are used consistently throughout the simulations in order to assess the magnitude of the IOP waves. CFD simulations for the single SRB are performed for each configuration and a trend analysis of the IOP behavior is assessed.

2 Computational Model

The computational geometry for the launch site simulations includes the flame trench, the surrounding ground terrain, the Mobile Launch Platform, two plume deflectors, and the launch vehicle. Launch vehicles used in the simulations include a simplified Space Shuttle configuration with one external tank (ET) and two SRBs, and a preliminary Ares-Ix configuration consisting of one SRB rocket. The MLP for the Space Shuttle configuration contains two openings for the SRB plumes. For the single SRB configuration, various MLP options were investigated including either one of two openings, and with one or two deflectors. In order to provide high fidelity simulations of the plumes, various support structures in the MLP opening are modeled in the computational geometry and grid systems.

Structured viscous overset grid systems were built to model the different launch site configurations described above. A grid generation script based on the Chimera Grid Tools (CGT) script library, see Chan [3], was developed to create the various grid systems. The overset grid and scripting approach are particularly well-suited for this problem since they facilitate easy modifications to the grids to accommodate different options for the launch vehicle, MLP and deflectors. The Space Shuttle grid system contains 129 grids and

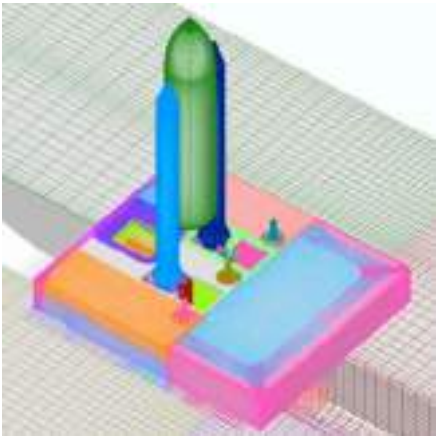

Fig. 1. Overset grid system of Shuttle, MLP, and flame trench

92 million grid points, see Figure 1. Grid systems for the single SRB with various MLP options contain 92 to 120 grids, and 73 to 87 million grid points.

3 OVERFLOW Solver

The CFD code OVERFLOW developed at NASA, see Buning [4], is used in simulating the exhaust plume iteraction with the flame trench. OVERFLOW is an implicit structured overset Reynolds Averaged Navier Stokes (RANS) solver. For the results reported here second-order centeral differencing with explicit artificial dissipation was used along with dual time stepping and the Spalart-Allmaras one equation turbulence model. Physical time steps on the order of 10^{-5} seconds and 20 to 40 subiterations per time step of the diagonalized implicit scheme were chosen to accurately represent the pressure waves and converge the numerical solution. The subiteration procedure consists of a right hand side evaluation followed by inversion of the diagonalized form of the approximate factored left hand side operator. The solver is made parallel through domain decomposition and uses the MPI message passing standard. The reported results were run on the Columbia supercomputer, at NASA Ames Research Center, on 128 processors. The overall simulation of two seconds of physical time required several weeks of wall clock time.

4 Two-SRB Results

In order to validate the geometric model and computational procedure, the IOP waves genenerated during ignition of STS-1 (without the water suppression system) was simulated first. The physics of the IOP phenomenon for this configuration has been well analyzed and documented as in Ryan *et al* [2]. Instaneous pressure contours of the IOP waves along with temperature contours of the exhaust jets are displayed in Figure 2. From these contour

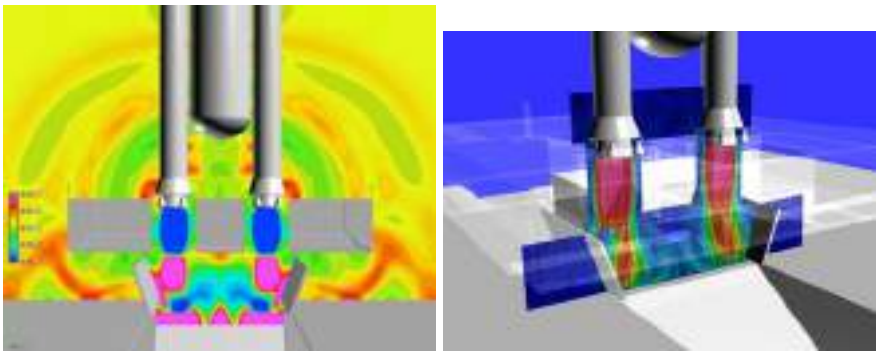

Fig. 2. Instantaneous IOP waves (left) and temperature contours (right) for the Shuttle configuration

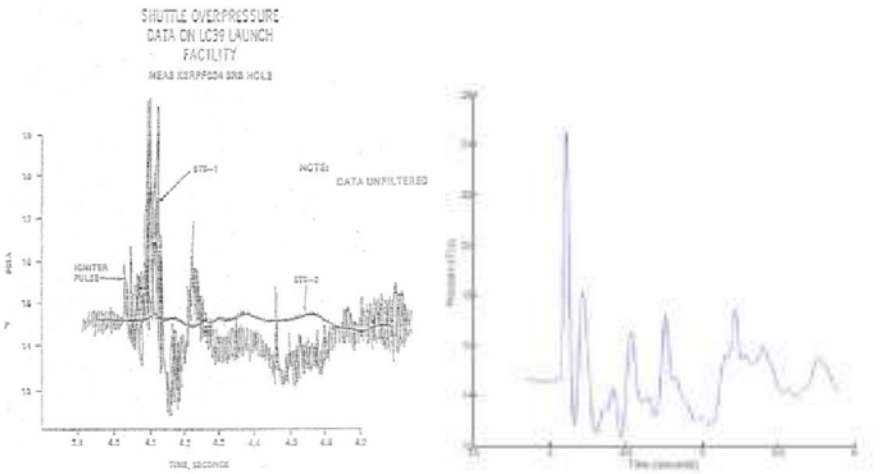

Fig. 3. STS-1 IOP comparison between flight data, Ryan [2] (left) and CFD prediction (right)

plots it is observed that large pressure waves are reflected from the trench, travel back towards the SRBs, and along the sides of the launch vehicle. Additionally, complicated vortical structures are observed as the plume enters the trench. In Figure 3 the pressure at a point on the launch vehicle is plotted versus time, where the recorded flight data is on the left and the current CFD prediction is on the right. Good agreement between the peak pressure levels is observed, qualitative agreement is also good provided the acoustic noise is removed from the flight data.

5 Single SRB Results

As a result of the good comparison between the predicted CFD results and the recorded flight data for the two SRB scenario, the computational model was modified to study the effects that different MLP configurations have on the IOP waves for a single rocket (represented here by a modified SRB). The purpose of this study is to analyze the IOP phenomenon for three MLP configurations. These include an unmodified MLP with the unused hole kept open and the deflector,located below the hole and directing flow into the trench, is retained, a configuration with the hole kept open and the associated deflector is removed, and a configuration where the entire unused hole is closed. Figure 4 shows pressure contours on a cutting plane at two different times for the three different configurations. From the images it is observed that in each configuration the IOP waves with the peak values are reflected from its own exhaust hole. In Figure 5 the unsteady pressure at a point on the SRB is plotted versus time for each of the three configurations as well as the

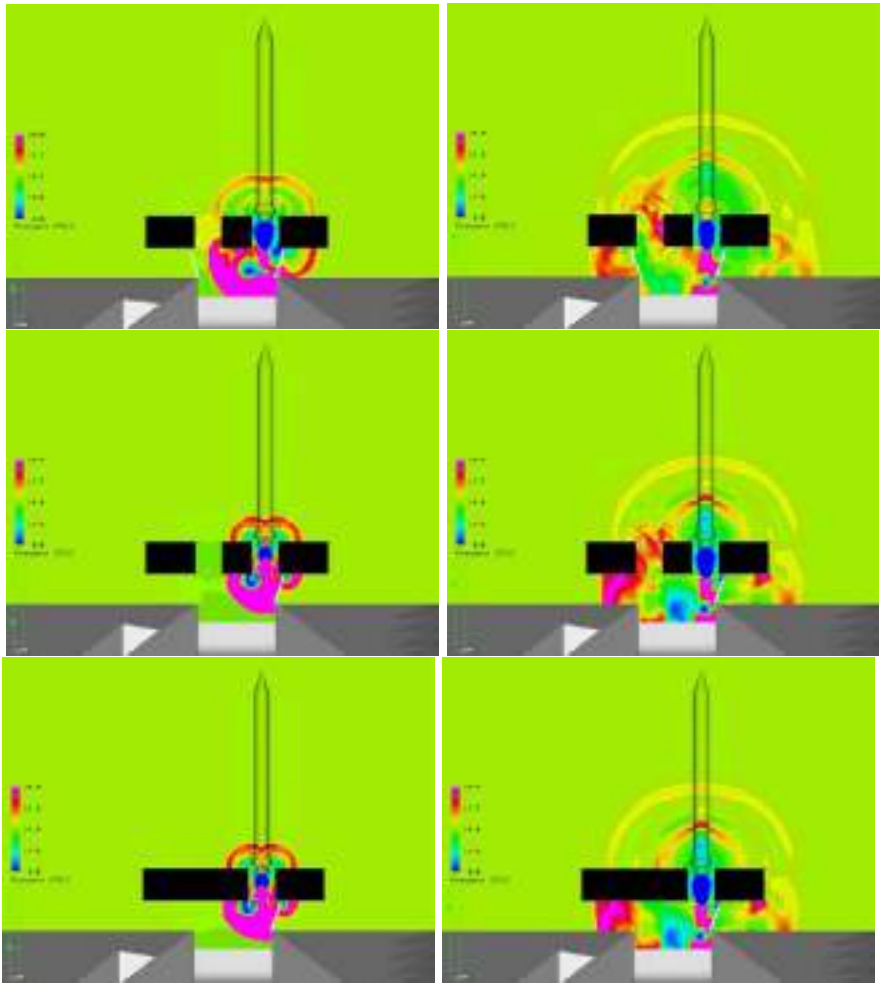

Fig. 4. Instantaneous IOP waves at two different times for a single SRB with MLP configured with open hole and deflector (top), open hole and no deflector adjact to hole (middle), and closed hole with no deflector (bottom)

results from the STS-1 simulation. Comparing the predicted pressure peaks with the STS-1 data, it is observed that similar IOP behavior is generated by all three configurations, and none of the configurations lead to significantly larger peak pressures than those experienced by STS-1 (when the IOP water supression system is excluded from the model).

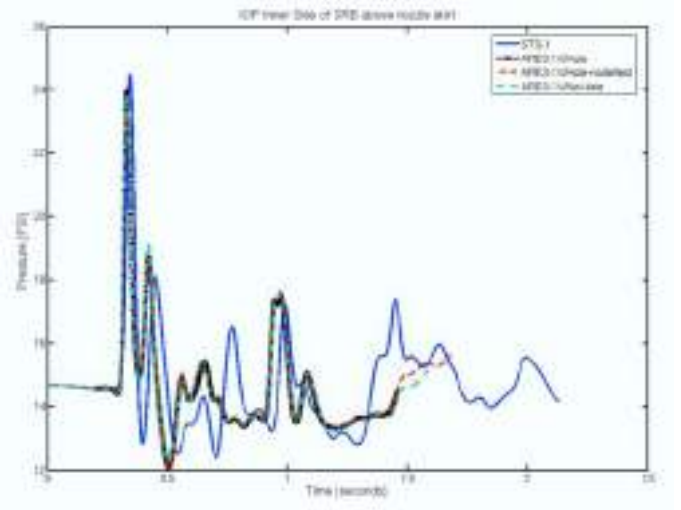

Fig. 5. Comparison of predicted IOP waves on inner side of SRB for STS-1 and single SRB using three MLP configurations

6 Summary

Time-accurate CFD simulations of the launch pad flame trench were presented using the Shuttle configuration and three different MLP configurations for a single SRB. The predicted IOP waves compared well with flight data for the Shuttle configuration. Computations for the single SRB showed similar IOP patterns for each MLP configuration and the STS-1 results. Addition of the water suppresion system will likely reduce the IOP effects. Including the suppresion system into the CFD model requires the addition of multiphase capabilities and is the subject of future study.

Acknowledgements

This work has been funded by NASA Kennedy Space Center (KSC). Special thanks to Dr. Bruce Vu, Michael Lonergan, and Shaun Green of KSC. Visualization support has been provided by Tim Sandstrom and David Ellsworth from the NAS Visualization group at NASA Ames Research Center. Ground terrain grid generation support was provided by Raymond Chow of University of California Davis.

References

1. Jones, J.H.: Scaling of Ignition Startup Pressure Transients in Rocket Systems as Applied to the Space Shuttle Overpressure Phenomenon. In: APL JANNAF 13th Plume Technol. Meeting, vol. 1, pp. 371–392 (1982)

2. Ryan, R.S., Jones, J.H., Guest, S.H., Struck, H.G., Rheinfurth, M.H., Verderaime, V.S.: Propulsion System Ignition Overpressure for the Space Shuttle. Technical Memorandum 82458, NASA (1981)
3. Chan, W.M.: Advances in Software Tools for Pre-processing and Post-processing of Overset Grid Computations. In: Proceedings of the 9th International Conference on Numerical Grid Generation and Field Simulation (2005)
4. Buning, P.G., Jespersen, D.C., Pulliam, T.H., Klopfer, G.H., Chan, W.M., Slotnick, J.P., Krist, S.E., Renze, K.J.: OVERFLOW User's Manual Version 1.8aa. Internal Report NASA Ames Reseach Center (2003)

“*This page left intentionally blank.*”

Very High Order Residual Distribution Schemes for Steady Flow Problems

Adam Larat, Rémi Abgrall, and Mario Ricchiuto

INRIA Bordeaux Sud-Ouest, Projet Scalapplix

Despites the progress made in CFD over the years, the methods still need improvement because the computed flow problems are becoming more and more complex. One of the way to improve methods is to increase accuracy. In this paper, we present a numerical scheme that can handle unstructured meshes, have a very compact stencil (hence easy to parallelize) and is non oscillatory. This paper presents the third order version of the method, but *a priori* any order of accuracy can be achieved. This goals can also be achieved in principle with the Discontinous Galerkin schemes; but our method is a non DG one. It uses conformal finite elements, hence enabling a considerable decrease of degrees of freedom, especially in 3D, with respects to the DG schemes. We first sketch design principles, then describe the scheme for the Euler and Navier Stokes equations. Two and three dimensional examples are given.

We are looking for the solutions of a steady conservation law inside a given domain $\Omega \in \mathbb{R}^d$, $d = 1, 2, 3$:

$$\overrightarrow{\nabla} \cdot \overrightarrow{\boldsymbol{\mathcal{F}}}(u) = 0, \quad \text{in } \Omega \text{ with boundary conditions.} \tag{1}$$

with $u : \mathbb{R}^d \longrightarrow \mathbb{R}^m$ and $\overrightarrow{\boldsymbol{\mathcal{F}}} = (f_1, \cdots, f_d) : \mathbb{R}^m \longrightarrow (\mathbb{R}^m)^d$, a given non-linear flux. We consider either the Euler Equations: $\overrightarrow{\boldsymbol{\mathcal{F}}} = \overrightarrow{\boldsymbol{\mathcal{F}}}^{\text{adv}}$ for perfect fluids, or the Navier-Stokes Equations with a constant viscosity and Prandlt number $\overrightarrow{\boldsymbol{\mathcal{F}}} = \overrightarrow{\boldsymbol{\mathcal{F}}}^{\text{adv}} - \overrightarrow{\boldsymbol{\mathcal{F}}}^{\text{diff}}$ for viscous fluids. The x, y, z Jacobians of these fluxes with respect to the conservative variables are written $\mathrm{A}_i = \frac{\partial f_i}{\partial u}$. If $\mathbf{n}$ is a vector, we define the matrix $\mathrm{K}_{\mathbf{n}} = \sum_{i=1}^{d} \mathrm{A}_i n_i$. We consider wall, inflow and outflow boundary conditions.

1 Description of the Scheme

The continuous domain Ω is approximated by an unstructured conformal mesh $\mathcal{M}_h$ with triangles in 2D and tets in 3D. The extension to quads/hex is straightforward. The parameter h is a characteristic mesh size, e.g. say the largest element diameter.

1.1 Numerical Approximation, Degrees of Freedom

In the present case (third order), the degrees of freedom are localized at the vertices of the mesh and the mid–points of the edges ($N = 6$ in 2D, 10 in 3D). We denote them generically by σ. The $\mathbb{P}^k$ continuous Lagrangian basis function associated to the DoF σ is φ_σ. It is a continuous function that is second degree polynomial on each element. For any degree or freedom σ', it satisfies $\varphi_\sigma(\sigma') = \delta_{\sigma\sigma'}$ where $\delta_{\sigma\sigma'}$ is the Kronecker symbol. Note that φ_σ is zero except on the triangles that share σ. We approximate a solution by its $\mathbb{P}^k$ Lagrange interpolation $u_h = \sum_{\sigma\in\mathcal{M}_h} u_\sigma \varphi_\sigma$.

1.2 Residual Computation and Distribution

The driving idea of a Residual Distribution Scheme is to approximate equation (1) at each degree of freedom σ by a relation of the form

$$\sum_{T\in\mathcal{M}_h,\sigma\in T} \Phi_\sigma^T = 0 \tag{2}$$

such that the residuals Φ_σ^T satisfy the following design principle:

- Conservation:

$$\sum_{\sigma\in T} \Phi_\sigma^T = \Phi^T := \int_T \overrightarrow{\nabla}\cdot\overrightarrow{\boldsymbol{\mathcal{F}}}(u)dx = \int_{\partial T} \overrightarrow{\boldsymbol{\mathcal{F}}}(u)\cdot\mathbf{n}dl$$

  where $\mathbf{n}$ is the outward unit vector normal to the boundary ∂T. The integral is evaluated by mean of a third order accurate quadrature formula over the edges/faces of ∂T.
- The scheme (2) defines a numerical solution denoted by u^h that is oscillation free and third order accurate when the exact one is smooth.

In practice, we start from a first order scheme, say the following Lax Friedrichs one:

$$\Phi_i^{T,L} = \frac{1}{N}\left(\Phi^T + \alpha_T \sum_{\sigma'\in T}(u_\sigma - u_{\sigma'})\right)$$

where α_T is larger that the maximum spectral radii of the matrices $\mathrm{K}_{\mathbf{n}}$ scaled by the lenght/area of ∂T. This produces a stable and (very) dissipative scheme. We then construct a set of residuals that produces a third order accurate solution. Following [4], we know when third order accuracy is met, the solution of (2) satisfies $\Phi_i^T = \mathcal{O}(h^{d+2})$, where d is the spatial dimension. Since the integration rule over ∂T is third order accurate, the condition on the residual is achieved thankx to a set of uniformly bounded matrices β_σ^T such that

$$\Phi_\sigma^T = \beta_\sigma^T \Phi^T \text{ with } \beta_\sigma^T = \frac{\max(x_\sigma, 0)}{\sum_{\sigma'\in T}\max(x_{\sigma'},0)}, \quad x_\sigma = \frac{\Phi_\sigma^{T,L}}{\Phi^T}. \tag{3}$$

Again, the conservation constraint is met, and one can show (see [2] for details) that the solution of (2) with these residual preserves a local maximum principle. In the case of the Euler equations, this method is applied on the characteristic variables and going back to the conservative ones, enables to define a set of matrices β_σ^T that have formaly the same properties.

In practice, (2) is solved by the following iterative relaxation method

$$u_\sigma^{n+1} - u_\sigma^n = \omega_\sigma \sum_{T \in \mathcal{M}_h, \sigma \in T} \Phi_\sigma^T(u_h^n) \tag{4}$$

or better by its linearised implicit version. The boundary conditions are weakly imposed. Details can be found in [2].

2 Numerical Simulations for the Non Viscous Problem

Let us first consider the scalar transport problem

$$\overrightarrow{\lambda} \cdot \overrightarrow{\nabla} u = 0, \ \overrightarrow{\lambda} = (-y, x)^T. \qquad u = g, \text{ on the inflow boundary} \tag{5}$$

We solve this problem on $[0;1]^2$, taking for g a $\mathcal{C}^2$ compactly supported function. We obtain the result of Figure 1-(a). The isolines indicate the existence of "wiggles", they are not an indication of a stability problem but the evidence of a convergence problem: we are not solving (2) but an approxiamtion of it, because the scheme (4) is not converging. This can be clearly seen on the upper curve of 1-(c). Our scheme is not dissipative enough.

A cure to this problem is obtained by adding a stabilization term coming from SUPG formulation. We add to (3) the term

$$D_\sigma^T = h\theta\left(u_h\right) \int_T (\boldsymbol{\lambda} \cdot \boldsymbol{\nabla} u)\ (\boldsymbol{\lambda} \cdot \boldsymbol{\nabla} \varphi_\sigma) dx, \qquad \boldsymbol{\lambda} = \frac{\partial \overrightarrow{\boldsymbol{\mathcal{F}}}}{\partial u} \tag{6}$$

The parameter θ is chosen to be approximately 1 in the smooth regions of the solution and 0 in the non smooth ones. Anyway, a good choice is still $\theta = 1$: the new term do not kill the non oscillatory behavior of the scheme. More fancy choices help in solving very strong shocks, see [1, 2] for details. The practical computation of (6) is explored in [3]. This formulation can be extended immediately to the system case. As we can see on 1–(b) and (c), the use of this term helps tremendously to reach full convergence and obtain a much nicer solution.

Then we present solutions of our high order methods on a transonic inviscid NACA problem: Ma $= 0.8$, $\alpha = 2°$. On Fig. 2 are represented both 2^{nd} and 3^{rd} order simulations. The isolines are much smoother for the third order solution and we can notice that the shocks are also better represented.

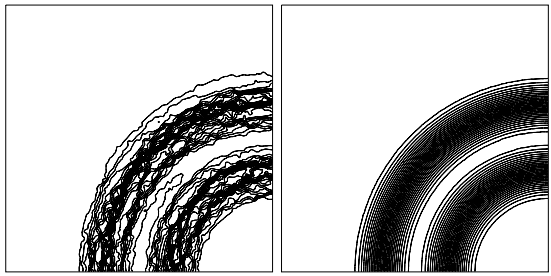

(a) (b)

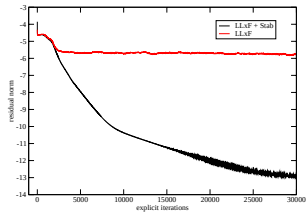

(c)

Fig. 1. Solutions and convergence histories for problem (5). (a): Formulation (2)–(3), (b): Formulation (2)–(3) with (6) ($\theta = 1$). (c): convergence history

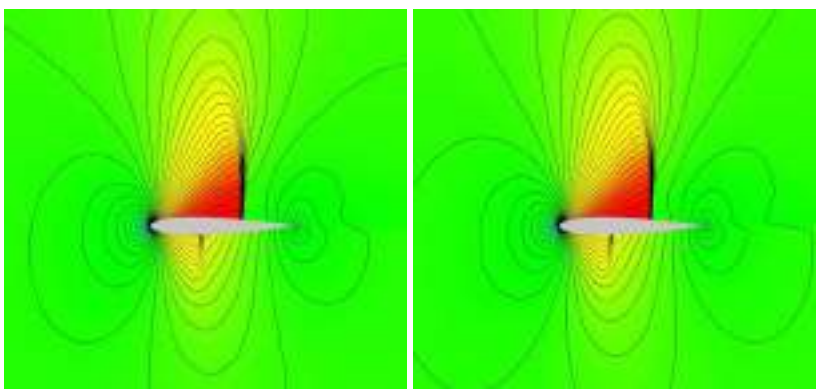

2^{nd} order, Mach Number Isolines 3^{rd} order, Mach Number Isolines

Fig. 2. 2^{nd} and 3^{rd} order simulations on a Naca0012. Ma=0.8, $\alpha = 2°$

3 Navier-Stokes Problems

We are now interested in simulation of Navier-Stokes problems. This section presents our current numerical strategy. We see the Navier Stokes equations

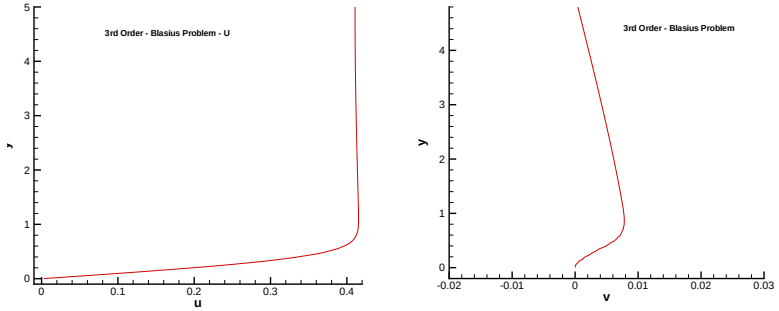

U profil V profil

Fig. 3. Blasius Problem. Cut following a straight line x =cste

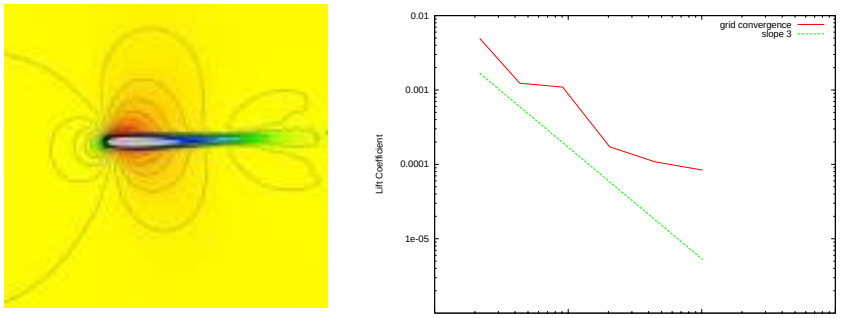

Solution : Colour = Mach; Isolines = Rho Grid convergence

Fig. 4. Viscous NACA 00012 problem : Ma = 0.5, $\alpha = 0°$, Re = 500

as the Euler equations plus a dissipation term. The discretisation of the Euler term has already been described. The dissipative term is approximated by a simple Galerkin approximation. The contribution of the diffusive term to the DoF σ is: $V_\sigma = -\int_\Omega \overrightarrow{\nabla\varphi_\sigma} \cdot \overrightarrow{\boldsymbol{\mathcal{F}}}^{\text{diff}} dx$ which is splitted as the sum (with few terms) of the integrals on the elements T where φ_σ is not identicaly zero. This term should be evaluated by an exact Gaussian integral quadrature but it is rather expensive. In order to simplify this, we also use the following decomposition per component of the diffusive flux:

$$\overrightarrow{\boldsymbol{\mathcal{F}}}_i^{\text{diff}}(x) = \sum_{j=1}^{d} \left(K_{ij} \cdot U_{,j}\right)(x) = K_{ij}(x) \cdot \sum_{k \in T} U_k \left(\varphi_k\right)_{,j}(x).$$

Then one can rewrite the Galerkin formulation into a ratherless costly form: $V_\sigma = \sum_{\sigma \in \mathcal{D}_i} \sum_{\sigma \in T} \mathcal{M}_{ik} U_k$ where $\mathcal{D}_i$ is the support of φ_σ.

This formulation has been used on several viscous problems. The first one is the well–known Blasius problem, which is well solved by the 3^{rd} order scheme as can be seen on 3.

We have also computed viscous NACA 00012 problems: $\text{Ma} = 0.5$, $\alpha = 0°$, $\text{Re} = 500$. As $\alpha = 0°$, we should have a good estimation of grid convergence by representing the lift coefficient with respect to the grid characteristic size h. That is done on Figure 4. The scheme has actually a good behaviour on the coarser mesh, but the finer the grid, the worse the convergence rate becomes. This observation has been done on several cases. A cure to this problem is under investigation.

4 Conclusion

We have presented the current state of our third order Residual Distribution scheme for hyperbolic and viscous problems. It has been illustrated by several standard test cases. 3D problems are presented in [2]. The results are satisfactory but still need improvement in the viscous case.

Acknowledgements

A. Larat has been financed by the EU STREP ADIGMA under contract number 030719 (AST5-CT-2006-030719).

References

1. Abgrall, R.: Essentially non-oscillatory residual distribution schemes for hyperbolic problems. J. Comput. Phys. 214(2), 773–808 (2006)
2. Abgrall, R., Larat, A.: M Ricchiuto. Construction of very high order resid- ual distribution schemes for steady invicid fow problems. J. Comput. Phys. (submitted)
3. Abgrall, R., Larat, A., Ricchiuto, M., Tavé, C.: A simple construction of very high order non oscillatory compact schemes on unstructured meshes. Computers and Fluids (in press) (2009)
4. Abgrall, R., Roe, P.L.: High-order fluctuation schemes on triangular meshes. J. Sci. Comput. 19(1-3), 3–36 (2003)

Part 16
Compressible Flow 2

“*This page left intentionally blank.*”

Shocks in Direct Numerical Simulation of the 3-D Spatially Developing Plane Mixing Layer

Qiang Zhou[1], Feng He[2], and M.Y. Shen[3]

[1] School of Aerospace, Tsinghua University Beijing 100084, China
zhouqiang04@mails.tsinghua.edu.cn
[2] School of Aerospace, Tsinghua University Beijing 100084, China
hefeng@tsinghua.edu.cn
[3] School of Aerospace, Tsinghua University Beijing 100084, China

Three-dimensional direct numerical simulations are performed for the spatially-developing plane mixing layer at convective Mach number 1.2. The shocks are generated by organized vortex structures and turbulent motions after the breakdown of large structures into small vortices. A simple and effective criterion based on dilation is used for shock identification. The 3-D view of shocks are obtained. It is shown that the origin of most of shocks in the mixing layer is closely bound up with vortices. Different types of shocks are illustrated based on their different generation mechanisms.

1 Introduction

In high-speed mixing layers, the structure of turbulence is strongly affected by compressibility. The occurrence of shocks has been shown when convective mach number is higher than 0.7 in two-dimensional simulations [L89]. However, in simulations of three-dimensional compressible mixing layers, shocks will not be captured until the convective mach number reaches a higher value of 1.2 [VG95, KS02, FL06]. In experimental investigations the existence of shocks has been confirmed by powerful visualization and measurements techniques [P95, RMH02]. In most of previous work, numerical simulations are done in a temporal frame. In this paper we report the occurrence of shocks in a spatially developing compressible mixing layer at $Mc = 1.2$ (Mach number of upper layer and lower layer is 4.8 and 2.4 respectively).

2 Basic Equations, Initial Conditions and Numerical Methods

The physical model used is the full Navier-Stokes equation. The law of state for perfect gases is used to relate the state variables. The Prandtl number is set to 0.75, and the nondimensional viscosity has a power law dependence on the nondimensional temperature as $\mu = T^{0.768}$.

The latest developed high-order high-resolution hybrid scheme 7P7Om2-WENO (r=5) [ZYHS07] is used for spatial discretization of the convective flux. Actually, the

switch for WENO schemes does not turn on since no shocks with strong intensity occur in the simulation. For viscous flux terms, the explicit central eighth-order scheme is adopted. The time integration is performed by means of a eight-stage, fourth-order, strong-stability-preserving Rung-Kutta scheme [SR03]. The code is validated by comparing the computed results for a 2-D time-developing mixing-layer with Ref. [SR90].

In the simulation, periodic boundary condition is imposed in the spanwise direction (z), non-reflecting boundary conditions are implemented in the normal direction (y) and the outflow boundary. At the inflow boundary the mixing layer is periodically strongly forced by a pair of most unstable oblique waves of equal amplitudes (the amplitude is 0.2 relative to the mean profile) from linear stability analysis. Here, the unperturbed inflow profile is a computed solution of the compressible boundary-layer equations [SR90]. Our simulations are executed in the domain $[0, 16L_1] \times [-L_2/2, L_2/2] \times [0, L_3]$, where $L_1 = 2\pi/\alpha = 22.61, L_2 = 100, L_3 = 2\pi/\beta = 12.57$. The α and β correspond to the streamwise and spanwise wavenumber of the most unstable oblique mode from linear stability analysis [SR90]. The Reynolds number used in this simulation is 300. The vorticity thickness of the unperturbed inflow profile and the velocity of the upper layer are used as the characteristic length and velocity respectively. Several mesh sizes were used up to obtain independency of the solution. For the present study the mesh size is $720 \times 251 \times 50$, which is fine enough to compute all relevant scales.

3 Computational Results

3.1 Visualization of Shocks

To our knowledge, shocks in three-dimensional compressible mixing layer were first captured by Vreman et al. [VG95]. However, until recently, no general criterion has been established for shock identification. In most investigations, shocks are shown in two-dimensional slices, which can be somewhat misleading because the shape of the shock surface may be highly three-dimensional. In the present paper, as Vreman et al. did in Ref. [VG95], we locate the shock using iso-surfaces of dilation $\nabla \cdot \mathbf{u}$. In the computation, shocks usually have a thickness of about three grids. So they can be shown as three-dimensional flakes. In the center of the shock body, the dilation attains a peak value, and the iso-surface of some higher value (higher value means lower compressibility due to that the dilation in the shock body is negative) will organize as a coat covering the shock, from which we can easily get the three-dimensional shape of the shock. If an appropriate value for the iso-surface is used, the strength of the shock can be obtained quantitatively. For more clear information about the shock, the Rankine-Hugoniot relations should be used.

In Fig. 1 (top view) and Fig. 2 (3-D view), vortex structures are shown using the iso-surface of swirl strength of 0.007 with gray color, from which we can see the full developing process of instability, formation of λ vortices and hairpin vortices. The large vortex structures finally break into small vortex structures and the flow turns into turbulence.

We locate shocks using the iso-surface of $\nabla \cdot \mathbf{u} = -0.04$ with black color, which are shown in Fig. 3. We can see that these black iso-surfaces do construct many bodies of flake. Density and pressure can be extracted from the two sides of the flakes to check if they are satisfied with Rankine-Hugoniot relations. After the check, we conclude that these iso-surfaces do locate the shocks. From Fig. 3, it can be seen that shocks are abundant in three different domain of the mixing layer. Domain A is not far from the inflow boundary. λ vortices start to form in this domain. Domain B is close to but in front of the transition region, in which large vortices with high vorticity are abundant. The third domain C is the turbulence region of the mixing layer.

Fig. 1. Vortex structures (top view), visualized by the iso-surface of swirl strength of 0.007

Fig. 2. Vortex structures (3-D view), visualized by the iso-surface of swirl strength of 0.007

Fig. 3. Shocks in the mixing layer (3-D view), visualized by the iso-surface of $\nabla \cdot \mathbf{u} = -0.04$

Fig. 4. Illustration for bluff-body shocks (side view)

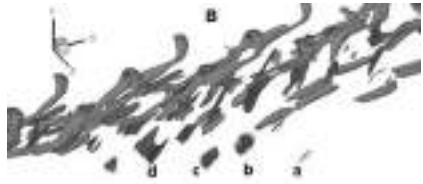

Fig. 5. Illustration for bluff-body shocks (3-D view)

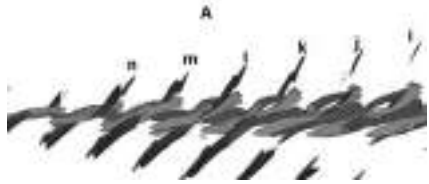

Fig. 6. Illustration for bluff-body shocks in domain A, $\nabla \cdot \mathbf{u} = -0.02$ (side view)

Fig. 7. Illustration for counter-rotating-vortices shocks (top view)

3.2 Categorization of Shocks

Shocks in the supersonic mixing layer is abundant and complex, however, based on the generation mechanism, we can basically classify them into three types.

For the first type, let we see Fig. 4 (side view) and focus our attention on shocks a, b, c, and d in domain B. It is clearly that their formation mechanism shows good agreement with the scenario of flow around a bluff body. This type of shocks has been founded in previous experiments and numerical simulations (see [RMH02] and [FL06]). Here the "bluff bodies" are several pairs of inclined streamwise vortices. Shocks of this type usually show up outside of the mixing layer. Note that in Fig. 4 the shocks are illustrated by the iso-surface of dilation of -0.04, their strength is relatively weak in comparison to the shocks in the interior of the mixing layer, which can be visualized by -0.075 and even much lower values. The maximum value of the ratio of the pressure before and behind shocks a, b, c, and d is about 1.32. In domain A, there also exist shocks of this type (see Fig. 6), in which λ vortices work as bluff bodies. The shocks (shocks i to n) on the upside of the mixing layer are relatively weaker than those on the underside, they do not show up until the dilation is set to -0.02. On the upside, The maximum value of the pressure ratio when crossing the shock is only about 1.25. It is may because that λ vortices move

Fig. 8. Illustration for counter-rotating-vortices shocks (3-D view)

Fig. 9. Illustration for turbulence shocks

a bit faster than the mean velocity of the upper and lower layers' fluids. We will call this type of shocks bluff-body shock in the rest of the paper.

Shocks of the second type are the strongest shocks in the mixing layer. They reside in the interior of the mixing layer. In Fig. 7 (top view), we can see that a shock, named *e*, is located between two legs of a hairpin vortex. These two legs are indeed a pair of counter-rotating vortices. They induce the fluid between them to accelerate to a relatively high velocity, then shock *e* occures since the velocity of the fluid has to be reduced in order to reach the high pressure domain between large structures. In Fig. 7, there are another two shocks *f* and *h*, they are actually different parts of a same shock due to the periodicity in direction *z*. See Fig. 8, another view of these shocks, it can be clearly seen that the shock body *e* is not a flat but a curved plane. Moreover, its shape is strongly confined by the creator, the vortices nearby. Shocks of this type are very strong. Actually, the strongest shocks in the simulation belongs to this type, they reside in domain B, a region just before the flow's breakdown to turbulence. The maximum value of the pressure ratio when crossing the shock is about 3.2. Shocks of this type also appearance in domain A, where the corresponding counter-rotating vortices are legs of λ vortices. We will call this type of shocks counter-rotating-vortices shock (CRV shock for short) in the rest of the paper.

Shocks of the third type are located only in domain C, which is the region of turbulence. Transition to turbulence occurs between domain B and C. We find no shocks in the transition region. So shocks in domain C are not the remains of those in domain B. Indeed, they are brand-new, generated by the vortices in turbulence. Surprisingly, these shocks have almost the same shape and orientation, which is not consistent with the results of the time-developing simulations [VG95, KS02]. Most shocks in this domain have a flat slender-strip body and is sloped about 40^o – 50^o with respect to the flow direction. They basically have no spanwise structures (see

Fig. 3 and Fig. 9). Clearly, it can be seen that all these shocks are generated by counter-rotating vortices and that those vortices have almost the same orientation with the shocks. We conjecture that simulations with higher Reynolds number and more periods in spanwise direction may obtain more complex shocks in this domain. So the generation and the behavior of shocks in turbulence need more careful analysis in the future. We can call shocks of this type turbulence shocks later on.

4 Conclusion

In this paper we report the occurrence of shocks in a spatially developing compressible mixing layer at $Mc = 1.2$. Shocks are visualized using the iso-surfaces of dilation. It is proven that this method is very effective. We can obtain the 3-D shape of the shock conveniently. It is shown that the origin of most of shocks in the mixing layer is closely bound up with vortices. Classification of these shocks is attempted. Based on their generation mechanisms, we categorize them into three main types: bluff-body shocks, CRV shocks and turbulence shocks.

Acknowledgement

The computations were (partly) supported by the Computing Facility for Computational Mechanics, Institute of Mechanics, Chinese Academy of Sciences. The authors are grateful for the support of the National Natural Science Foundation of China (No. 90305014).

References

[FL06] Fu, S., Li, Q.B.: Numerical simulation of compressible mixing layers. Int. J. Heat Fluid Flow 27, 895–901 (2006)

[L89] Lele, S.: Direct numerical simulation of compressible free shear flows, AIAA Paper No. 89-0374 (January 1989)

[KS02] Kourta, A., Sauvage, R.: Computation of supersonic mixing layers. Phys. Fluids 14, 3790–3797 (2002)

[P95] Papamoschou, D.: Evidence of shocklets in a counterflow supersonic shear layer. Phys. Fluids 7, 233–235 (1995)

[RMH02] Rossmann, T., Mungal, M.G., Hanson, R.K.: Evolution and growth of large-scale structures in high compressibility mixing layers. J. Turbulence 3, 009 (2002)

[SR90] Sandham, N.D., Reynolds, W.C.: Compressible mixing layer: linear theory and direct simulation. AIAA J. 28, 618–624 (1990)

[SR03] Spiteri, R.J., Ruuth, S.J.: Non-linear evolution using optimal fourth-order strong-stability-preserving RungeCKutta methods. Math. Comput. Simul. 62, 125–135 (2003)

[VG95] Vreman, B., Kuerten, Geurts, B.: Shocks in direct numerical simulation of the confined three-dimensional mixing layer. Phys. Fluids 7(9), 2105–2107 (1995)

[ZYHS07] Zhou, Q., Yao, Z.H., He, F., Shen, M.Y.: A new family of high-order compact upwind difference schemes with good spectral resolution. J. Comp. Phys. 227(2), 1306–1339 (2007)

Calculation of Aerodynamic Performance of Propellers at Low Reynolds Number Based on Reynolds-Averaged Navier-Stokes Equations Simulation

Xu Jianhua, Song Wenping, and Han Zhonghua

National Key Laboratory of Aerodynamic Design and Research, College of Aeronautics, Northwestern Polytechnical University, Xi'an 710072, China
jianhua19492002@163.com, wpsong@nwpu.edu.cn, hanzh@nwpu.edu.cn

1 Introduction

Propellers used for MAVs(Micro Air Vehicles), UAVs(Unmanned Aerial Vehicles) and HAAs(High Altitude Airships) operate at low Reynolds number. Thus, the momentum-blade element theory[1] which is widely used in the aerodynamic design and calculation of propellers is restricted.Numerical simulations based on Euler/N-S equations are very effective in the study of detailed information of flow around propellers[2], especially useful in aerodynamic optimizations of propellers.

Based on this point, a new numerical method is developed to simulate the aerodynamic performance of propellers at low Reynolds number using RANS equations coupled with Baldwin-Lomax algebraic turbulence model. The improved LU-SGS scheme is utilized for time integral. When the yaw angle is zero, the fluid is quasi-steady in rotary frame fixed to propellers. So, only one of the blades is modeled, and the influence of other blades is accounted for using periodic boundary conditions. The influence of hub and blade roots is neglected.

Chimera-grid methodology is used to effectively capture the viscous effect near the propeller blade and implement the periodic boundary conditions[3]. In order to improve the efficiency, RANS equations are solved on blade grid and Euler equations are solved on background grid. The numerical results agree well with the experimental data that proves the new method introduced is valid.

2 Governing Equations

In rotary frame fixed to propellers, and the governing equations can be written as follows[3]:

$$\frac{\partial}{\partial t}\iiint_{\Omega}\mathbf{W}dv+\iint_{\partial\Omega}\mathbf{H}\bullet\mathbf{n}dS-\beta\iint_{\partial\Omega}\mathbf{H}_{v}\bullet\mathbf{n}dS+\iiint_{\Omega}\mathbf{G}dv=0 \qquad (1)$$

where,$\mathbf{W} = (\rho, \rho u, \rho v, \rho w, \rho E, \rho H)$. $\mathbf{H}$, $\mathbf{H}_v$ and $\mathbf{G}$ are inviscid flux, viscous flux and Coriolis force flux, respectively. RANS equations are solved on propeller grid, herein $\beta = 1$ and Euler equations are solved on background grid, herein $\beta = 0$

3 Numerical Method

Assume $\mathbf{Q}_{i,j,k}$, $\mathbf{Q}v_{i,j,k}$ and $\mathbf{G}_{i,j,k}$ indicate inviscid flux term, viscous flux term and Coriolis force flux term. Eq. (1) can be discretized as follows by adding dissipative term $\mathbf{D}_{i,j,k}$:

$$\Omega_{i,j,k}\frac{d}{dt}\mathbf{W}_{i,j,k} + \mathbf{Q}_{i,j,k} - \beta\mathbf{Q}v_{i,j,k} + \mathbf{G}_{i,j,k} - \mathbf{D}_{i,j,k} \tag{2}$$

Replace the time derivative in Eq. (2) with a first-order forward difference. Then, Viscous flux and Coriolis force flux are discretized with explicit scheme. An implicit form is reached:

$$\Omega_{i,j,k}\frac{\Delta\mathbf{W}_{i,j,k}}{\Delta t} + \mathbf{Q}^{m+1}_{i,j,k} - \beta\mathbf{Q}v^{m}_{i,j,k} + \mathbf{G}^{m}_{i,j,k} - \mathbf{D}^{m}_{i,j,k} \tag{3}$$

where, $\Delta\mathbf{W}_{i,j,k} = \mathbf{W}^{m+1}_{i,j,k} - \mathbf{W}^{m}_{i,j,k}$

Then, linearize the inviscid flux and ignore the second-order and higher-order terms, we obtain:

$$\begin{aligned}\mathbf{Q}^{m+1}_{i,j,k} = \mathbf{Q}^{m}_{i,j,k} &+ (\mathbf{A}\Delta\mathbf{W})_{i+\frac{1}{2},j,k} - (\mathbf{A}\Delta\mathbf{W})_{i-\frac{1}{2},j,k} \\ &+ (\mathbf{B}\Delta\mathbf{W})_{i,j+\frac{1}{2},k} - (\mathbf{B}\Delta\mathbf{W})_{i,j-\frac{1}{2},k} \\ &+ (\mathbf{C}\Delta\mathbf{W})_{i,j,k+\frac{1}{2}} - (\mathbf{C}\Delta\mathbf{W})_{i,j,k-\frac{1}{2}}\end{aligned} \tag{4}$$

where, $\mathbf{A}$ is Jacobian matrix that normal to the grid surface in ξ direction, which is defined as $\mathbf{A} = \frac{\partial(\mathbf{H}\bullet\mathbf{n})}{\partial\mathbf{W}}$. The definitions of $\mathbf{B}$ and $\mathbf{C}$ are similar. Then Eq. (3) can be written as follows:

$$\begin{aligned}\Omega_{i,j,k}\frac{\Delta\mathbf{W}_{i,j,k}}{\Delta t} + (\mathbf{A}\Delta\mathbf{W})_{i+\frac{1}{2},j,k} - (\mathbf{A}\Delta\mathbf{W})_{i-\frac{1}{2},j,k} + (\mathbf{B}\Delta\mathbf{W})_{i,j+\frac{1}{2},k} - (\mathbf{B}\Delta\mathbf{W})_{i,j-\frac{1}{2},k} \\ + (\mathbf{C}\Delta\mathbf{W})_{i,j,k+\frac{1}{2}} - (\mathbf{C}\Delta\mathbf{W})_{i,j,k-\frac{1}{2}} = \mathbf{RHS}^{m}_{i,j,k}\end{aligned} \tag{5}$$

where, $\mathbf{RHS}^{m}_{i,j,k} = -(\mathbf{Q}^{m}_{i,j,k} - \beta\mathbf{Q}v^{m}_{i,j,k} + \mathbf{G}_{i,j,k} - \mathbf{D}^{m}_{i,j,k})$

Jacobian matrices are split as follows and an improved LU-SGS scheme is achieved[4]:

$$\mathbf{A}^{\pm} = \frac{\mathbf{A} \pm [\alpha r_A + \frac{\gamma\mu}{\rho Pr}(\xi_x^2 + \xi_y^2 + \xi_z^2)]\mathbf{I}}{2}$$

$$\mathbf{B}^{\pm} = \frac{\mathbf{B} \pm [\alpha r_B + \frac{\gamma\mu}{\rho Pr}(\eta_x^2 + \eta_y^2 + \eta_z^2)]\mathbf{I}}{2} \tag{6}$$

$$\mathbf{C}^{\pm} = \frac{\mathbf{C} \pm [\alpha r_C + \frac{\gamma\mu}{\rho Pr}(\zeta_x^2 + \zeta_y^2 + \zeta_z^2)]\mathbf{I}}{2}$$

where, α is a constant no less than 1.0 and 1.01 is used in this paper. r_A, r_B and r_C are spectral radius of Jacobian matrices. $\gamma = 1.4$ is the ratio of specific heats. μ is coefficient of viscous. ρ is density. Pr is Prandtl number.

The influence of spectral radius of viscous Jacobian matrices is considered in above method, so stability can be maintained even over much larger values of time step Δt. For quasi-steady fluid in this paper, we let $\Delta t \longrightarrow$ infinity.

Finally, an improved LU-SGS scheme is achieved as follows:

$$(\mathbf{L} + \mathbf{D})\mathbf{D}^{-1}(\mathbf{D} + \mathbf{U})\Delta\mathbf{W}_{i,j,k} = \mathbf{RHS}_{i,j,k} \tag{7}$$

$$\mathbf{L} = -(\mathbf{A}^{+}_{i-1,j,k} + \mathbf{B}^{+}_{i,j-1,k} + \mathbf{C}^{+}_{i,j-1,k})$$

$$\mathbf{D} = [\alpha(r_A + r_B + r_C) + \frac{\gamma\mu}{\rho Pr}S]\mathbf{I}$$

where,

$$\mathbf{U} = -(\mathbf{A}^{-}_{i+1,j,k} + \mathbf{B}^{-}_{i,j+1,k} + \mathbf{C}^{-}_{i,j+1,k})$$

$$S = (\xi_x^2 + \xi_y^2 + \xi_z^2 + \eta_x^2 + \eta_y^2 + \eta_z^2 + \zeta_x^2 + \zeta_y^2 + \zeta_z^2)$$

Then, the sweep process is similar to the basic LU-SGS scheme.

4 Grid System and Boundary Conditions

The grid system consists of two chimera grids: the blade grid and the background grid. Where, the blade grid has a C-H topology and contains 741741 points($169 \times 57 \times 77$) : 169 points on the chordwise direction (129 points on the blade surface), and 77 points in the spanwise direction (57 points on the blade surface) and 57 points in the direction orthogonal to the blade surface. The blade surface grid in the spanwise direction is almost regular, with a slight clustering at blade tip. The background grid

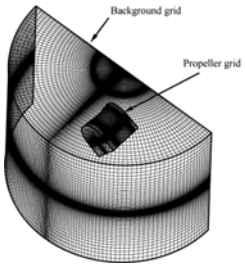

Fig. 1. Sketch map of chimera grids

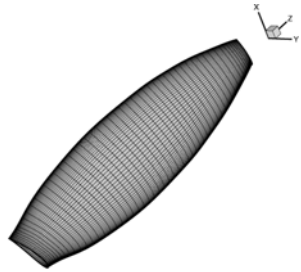

Fig. 2. Blade surface grid

has an O-H topology and contains 1087669 points ($121 \times 89 \times 101$): 121 points on the rotational direction, and 89 points on the wind direction and 101 points on the radial direction. For the case of two blades, the computational domain is restricted to one 180 degrees azimuthal sector. Trilinear interpolation method is used for the connection between the overset grids. An distance decreasing method is used for searching hole points and donor cells[5].The sketch map of Chimera-grids is shown in Figure 1, and the blade surface grid is shown in Figure 2.

Boundary conditions: non-slip boundary condition is applied on blade surface. Periodic boundary conditions are used on rotationally symmetric surfaces.

5 Numerical Results and Analysis

A study on the comparison between the common used five-step Runge-Kutta time stepping scheme and the improved LU-SGS scheme is made when the wind speed is 13m/s, the advanced ratio is 0.81, and the Reynolds number is 2.7×10^5 (based on the chord length at the relative radius equate to 0.75). Comparison of convergent history between the two schemes is shown in Figure 3. Obviously, it converges much faster and better by using the improved LU-SGS scheme than that of five-step Runge-Kutta time stepping scheme. Therefore, all the studies made in this paper are based on the improved LU-SGS scheme.

Then, the flow around the propeller is simulated when the wind speed is 15m/s, the advanced ratio is 0.74, and the Reynolds number is 3.3×10^5. The convergent history of thrust coefficient and efficiency is shown in Figure 4 and the vorticity iso-surface is shown in Figure 5. Several observations can be made. First, well defined vortical structures are shed from the blade tips.In additional, the vortical wake is plotted at the end of the 1213rd iteration when the solution is convergent and the aerodynamic forces which satisfy the engineering precision are obtained.It will continue to develop as the computation is continued for more iterations. However, for some other cases, the vortices are diffused. This may be due to the grid quality and numerical dissipation which need to be studied further.

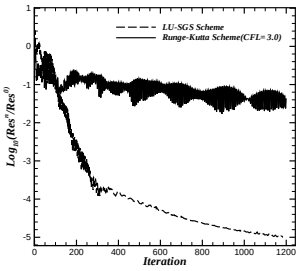

Fig. 3. Comparison of convergent history between the two schemes

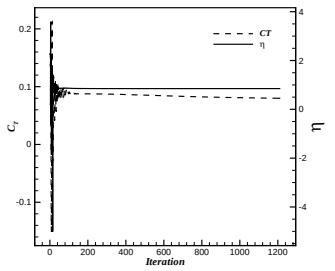

Fig. 4. Convergent history of thrust coefficient and efficiency

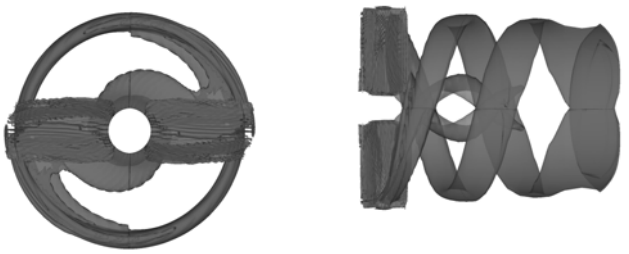

Fig. 5. Vorticity iso-surface

The above cases show high efficiency of the improved LU-SGS scheme and capability of vortex capturing. These conclusions ensure the high effectiveness and precision. Then, a series of advanced ratios J are calculated when the wind speed is 13m/s. The Reynolds number varies between 2.7×10^5 and 8.0×10^5 . Comparisons between the calculation and experimental data of thrust coefficients, power coefficients, efficiencies and torques are shown in Figures 6-9. The numerical results agree well with the experiment data proves the new method.

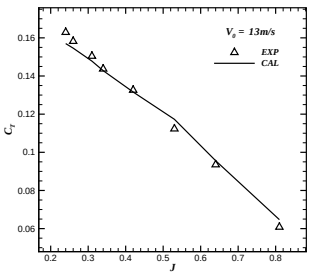

Fig. 6. Comparison of efficiencies between calculation and experimental data

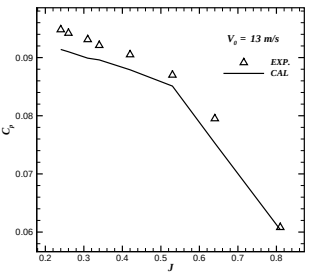

Fig. 7. Comparison of torques between calculation and experimental data

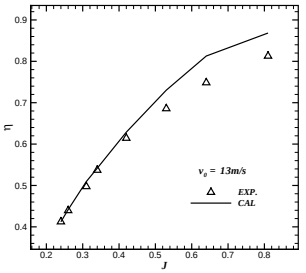

Fig. 8. Comparison of efficiencies between calculation and experimental data

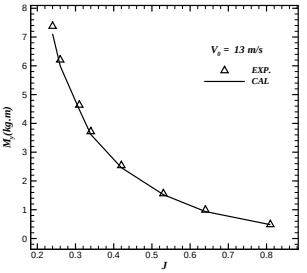

Fig. 9. Comparison of torques between calculation and experimental data

6 Concluding Remarks

A new numerical simulation method has been developed to calculate the aerodynamic performance of propellers at low Reynolds number using RANS equations coupled with Baldwin-Lomax algebraic turbulence model. The improved LU-SGS scheme is utilized for time integral which converges faster and better than the common used five-step Runge-Kutta time stepping scheme. Chimera-grid methodology is used to effectively and precisely capture the vortical wake. The numerical results agree well with the experiment data. Therefore, it can be used as a reference in the design of propellers at low Reynolds number.

References

[1] Peiqing, L.: Theory and applications of propellers. Beihang University Press (2006)
[2] Boyle, F.: Efficient solution of the Navier-Stokes equations for transonic propeller flows. AIAA Paper, 2003-4083 (2003)
[3] Ai-ming, Y., Zhi-de, Q.: A NewWay of Simulation the Flow Field of a Lifting Rotor in Hover. Journal of Northwestern Polytechnical University 18(4), 579–582 (2000)
[4] Zhonghua, H.: Efficient Method for Simulation of Viscous Flows past Helicopter Rotors and Active Flow Control (PHD). Northwestern Polytechnical University, Xian (2007)
[5] Wenqing, Y., Bifeng, S., Wenping, S.: Distance Decreasing Method for Chimera-grid. In: The Thirteenth National Conference on Computational Fluid Dynamics. Dandong, Liaonin, China, July 18-21 (2007)

Mathematical Modeling of Supersonic Turbulent Flows in a Channel of Variable Cross-Section with Mass Supply

N.N. Fedorova, I.A. Fedorchenko, and M.A. Goldfeld

Khrisianovich Institute of Theoretical and Applied Mechanics,
Siberian Branch of Russian Academy of Sciences (ITAM SB RAS),
4/1 Institutskaya str., Novosibirsk, 630090, Russia
nfed@itam.nsc.ru

1 Introduction

To effective operation of scramjet combustion chamber, the full mixing of air and fuel as well as mixture ignition and stable burning have to be organized. The whole physical problem is very complex and depends on numerous factors. Implementation of fuel supply in supersonic flow is one of the most important problems since it governs the state of fuel-air mixing and the quantity of enriched mixture to come into the ignition region. At the same time, to stabilize combustion, the fuel-air mixing within the flameholding region must be appropriate and controllable over a wide range of operating conditions.

In order to promote engine performance, fuel and air must be properly mixed in the near field of fuel injection. One of the simplest ways is to use the backward facing step (BFS). Generating a recirculation zone, BFS provide hot mixture into the flow and, under the certain temperature and mixture concentration conditions serves as a flame holder.

This approach provides sustained combustion but has a disadvantage of relatively high stagnation pressure losses. In recent years, a cavity flame holder has been investigated and found to significantly improve mixing efficiency with significantly lower pressure losses [GBM01]. The present work focuses on the fundamental investigations of flowfield in channel with BFS / open cavity with different injection schemes, based on the use of sonic gas (fuel) jets.

2 Problem Statement and Flow Condition

In the paper, turbulent supersonic flows in a model combustion chamber are studied experimentally and numerically. The experiments were performed at ITAM SB RAS in the IT-302M hotshot wind tunnel with arc heating. Contoured nozzles were manufactured for Mach numbers M_∞=2, 2.5, 3 and used in the present tests. In real conditions, incoming Mach numbers before the expansion region were a little bit lower then designed values because of a thick boundary layer on channel walls. The test conditions and variation of flow parameters during the test time operation are listed in Table 1. Here P0 and T0 stand for

Table 1. Incoming flow condition

M_∞	P0, MPa	T0, K	$Re_1, 10^6$/m	P_∞, kPa	δ, mm
2	2÷0.62	2000÷1420	40÷20	192	3.8
2.33	2.7÷0.94	2300÷1850	30÷10	138	5.6
2.8	4.0÷1.35	2700÷2000	20÷6	134	5.9

stagnation pressure and temperature and Re_1 is a Reynolds number per m. Since main flow parameters were changing during experimental runs in hot short wind tunnel, some intermediate values were chosen for computations. Chosen for specific computation values of static pressure P_∞ and boundary layer thickness before the expansion are also shown in a Table 1.

Installation of injectors, pressure taps, thermocouples, and gas sampling for measurements were available in the bottom wall of channel. At the tests, pressure distributions along the channel wall and flow visualization were obtained under various flow conditions and fuel injector positions.

The chamber geometry varies by changing the flame-holding configuration from BFS to cavity, and also by varying L/d, δ/h ratios and θ value, where d is a channel width, h is a cavity depth/step height, L is a cavity length, θ is an angle of the cavity aft ramp and δ is a boundary layer thickness before the expansion. The flows are investigated experimentally and numerically with / without taking into account the mass supply into the supersonic turbulent boundary layer.

3 Method of Computation

The computations were conducted with the help of in-house computer code for solving non-stationary averaged Navier-Stokes equations complemented with the two-equation k-ω turbulence model [Wil93]. For a temporal approximation, a four-step finite-difference scheme of splitting according spatial variables was used [BF96]. At each fractional step the finite-difference scheme was realized by scalar sweeps. The TVD-scheme of Flux Vector Splitting by van Leer of the third order of accuracy has been used for the approximation of convective terms. The viscous

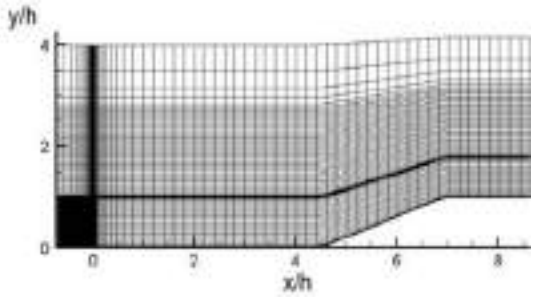

Fig. 1. Primary computational grid for a cavity problem

terms have been approximated with the central finite-difference relations of second order of accuracy.

The calculation domain did not include the whole model but the part of it contacted directly to the expansion part. The regular quadrangular grid condensed toward the rigid walls was composed in the computation domain. The most of computations were performed on a grid consisted of 500×350 nodes. In the Fig. 1, a grid pattern for a channel with a cavity with every fifth grid line is shown.

The inlet (left) section of the computational domain was chosen downstream from the laminar/turbulent transition region and far upstream from the expansion corner. The profiles of all the gas-dynamical and turbulent parameters were obtained from boundary-layer computations and specified at the entrance of computational domain. To resolve a laminar sublayer, total number of grid points there were about 10 and the condition $y_1^+ \le 1$ was kept for incoming turbulent boundary layers.

At rigid surface no-slip velocity and temperature conditions of two types were specified. The first type was the adiabatic temperature condition $\partial T / \partial n \big|_{wall} = 0$, and the second type was constant temperature $T \big|_{wall} = T_w$. Since the flow was supersonic at the outlet, extrapolation conditions were used there. The waves reflected from the top channel wall didn't come to the region of interest, so, to decrease the number of grid points, the inviscid reflection conditions were prescribed at the top boundary.

4 Test Computations

Previously, the computer code was successfully applied for modeling the Shock Wave /Boundary Layer Interactions in such configurations as impinging shock wave [FFS01], inlets [BFGF04], etc.

To verify the code for flows with jet injection, some test computations were conducted. First, a problem of air injection into a still gas has been investigated. It is known that in case of supersonic under-expanded jets, a multi-barrel structure of the flow arises. The calculations for the case of jet Mach number 1 and pressure ratio of the jet and the ambient media 3.5 performed in a frame of laminar Navier-Stokes equations have reproduced this multi-barrel structure. Comparison of the Mach number distribution along the symmetry axis resulted from the present calculations and the empiric relation [DL84] is presented in Fig. 2, a. Satisfactory agreement on both Mach distribution and size of the barrel is observed.

Numerical simulation of the sonic air injection normal to the supersonic $M_\infty=6$, $Re_1=21.1\ 10^6$ 1/m flow along the flat plate has been carried out under the condition of Sterrett *et al* [SBAR67] experiments. Parameters of the primary

Table 2. Parameters of the primary and secondary flows

Parameter	Primary flow	Jet
Total pressure, MPa	2.16	0.73
Static temperature, K	57.7	250

(freestream) and secondary (injected) flows are presented in Table 2. Regular rectangular grid has toward the wall and near jet slot refinement. The jet axis locates at x=0 and jet slot is 1.37 mm width with 20 grid points. Initially, computation grid consists of 200 grid points in streamwise, 150 nodes in normal directions and is extended during the calculation process both in x and y directions due to the flow evolution.

The flowfield realized in this case has a complex structure including shock waves, supersonic and subsonic zones and strong separation. In Fig. 2, b, Mach number contours for this problem is demonstrated. Front of the leading shock wave is influenced by both an essential boundary layer separation and shock arising due to the jet presence. Computed wave structure agrees qualitatively with that described in the experiments [SBAR67].

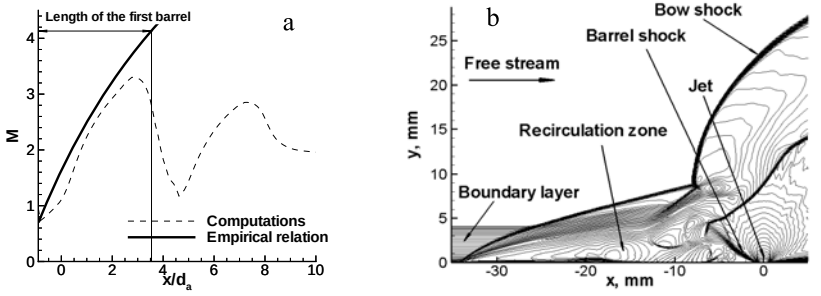

Fig. 2. Mach number distribution along the axis for a sonic jet into a still air (a) and Mach number contours for a normal sonic jet into M=6 flow (b)

5 Numerical Results

The code was applied to model the supersonic flow in channel with BFS and cavity at M_∞=2, 2.33 and 2.8 without fuel injection. The first case to report is M_∞=2 with adiabatic and cold wall temperature T_w varying from 300K to 1200K. The calculations have shown that temperature factor influences significantly on all flow parameters in the recirculation zone.

Temperature flowfields presented in Fig. 3 for case of adiabatic (a) cold wall (b) conditions together with streamlines demonstrate that the highest temperature occurs in the reattachment region. Temperature in the recirculation zone is much lower for T_w=500 K than that for adiabatic condition. Significant reconstruction in the streamlines pictures can be seen. Under adiabatic conditions (Fig. 4, a), a three-vortex configuration is formed in the separation zone with the small clockwise vortex in the inner corner, rather big counter clockwise middle vortex with temperature of about 1000K and the clockwise vortex adjusted to the external flow. With T_w decreasing, the first vortex disappears, the second vortex reduces in sizes and the third external vortex grows (Fig. 4, b). These results are of great importance for hot-shot wind tunnel for which cold wall temperature condition is typical. As the present computations have shown, cold wall temperature

conditions may cause decreasing temperature in the recirculation zone and yhen lead to the fuel ignition delay or suppressing.

In Fig. 4 the pressure distributions along the surface are presented for channel with BFS at M_∞=2.33 (a) and 2.8 (b) under cold wall conditions: T_w=300. Here the *x*-axis is directed along the wall, point *x*/*h*=0 corresponds to the expansion corner, point *x*/*h*=1 is the internal compression corner. Pressure is normalized by it value before the expansion. Comparison of the results demonstrates reasonable agreement.

The computations of flow in channel with a cavity were performed under the same experimental conditions and on the grid presented in Fig. 1. The numerical results are in qualitative agreement with the experimental data. But the computations have revealed the necessity of the primary grid adaptation to resolve all the flow features. Special attempts should be applied to model unsteady behavior of a flow over an open cavity.

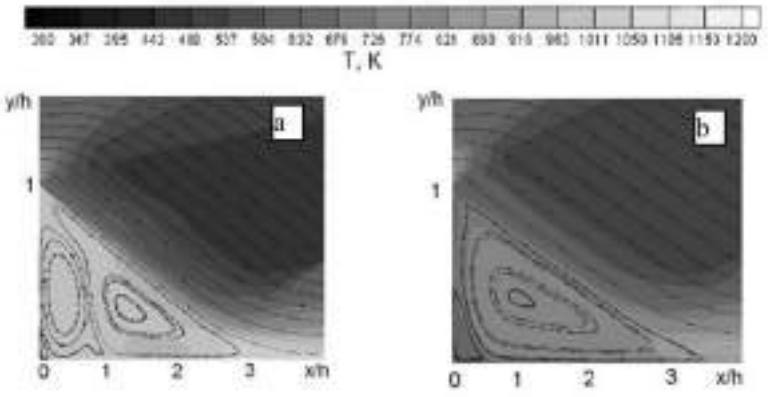

Fig. 3. Temperature fields and streamlines in vicinity of BFS at M_∞=2 under adiabatic (a) and cold wall Tw=500 (b) conditions

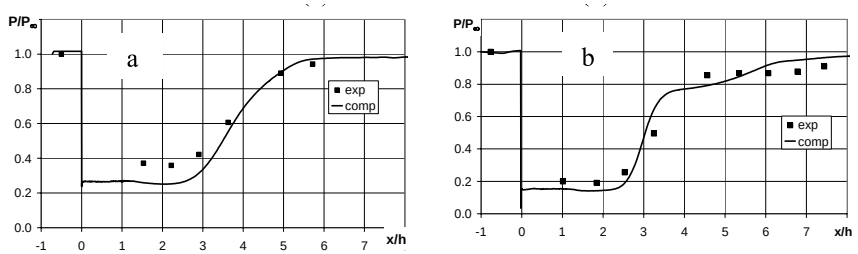

Fig. 4. Experimental and computed static pressure distributions along BFS surface at M_∞=2.33 (a) and 2.8 (b)

6 Conclusions and Future Work

Turbulent supersonic flows in a plane channel with an abrupt expansion are studied numerically on the basis of RANS model supplemented with turbulent model by Wilcox. Numerical procedure and in-house code were tested on flows with Shock wave/Turbulent boundary layer interaction and sonic jet injection into still and supersonic flow. Results of numerical simulation of high-enthalpy turbulent supersonic flows are presented conducted under conditions of experiments in the hot–shot wind tunnel. Influence of incoming Mach number, temperature factors and channel geometry on flowstructure is investigated.

Further work plan includes the simulation of sonic jet injection to a channel with BFS and cavity. Different scheme of the fuel supply will be studied numerically. The particle traces of the gas injected into the main flow will be constructed and residence time in the recirculation zone will be evaluated. Grid adaptation to the peculiarity of a complex flowstructure will be performed.

Acknowledgements. This work was supported financially by Russian Foundation for Basic Research grant 07-08-00420.

References

[GBM01] Gruber, M.R., Baurle, R.A., Mathur, T., Hsu, K.-Y.: Fundamental Studies of Cavity-Based Flameholder Concepts for Supersonic Combustors. Journal of Propulsion and Power 17, 146–153 (2001)

[Wil93] Wilcox, D.C.: Turbulence modeling for CFD. DCW Ind. Inc., La Canada (1993)

[BF96] Borisov, A.V., Fedorova, N.N.: Numerical simulation of turbulent flows near the forward-facing steps. Thermophysics and Aeromechanics 4(1), 69–83 (1996)

[FFS01] Fedorova, N.N., Fedorchenko, I.A., Shuelein, E.: Experimental and numerical study of oblique shock wave / turbulent boundary layer interaction at M=5. Comp. Fluid Dyn. Journ. 10(3), 376–381 (2001)

[BFGF04] Bedarev, I.A., Fedorova, N.N., Goldfeld, M.A., Falempin, F.: Mathematical Modeling of Supersonic Turbulent Flows in Inlets with Rotating Cowl. In: Groth, C., Zingg, D.W. (eds.) Computational Fluid Dynamics 2004, pp. 295–300. Springer, Heidelberg (2006)

[DL84] Dulov, V.G., Lukianov, G.A.: Gasdynamics of outflow processes. Novosibirsk (1984) (in Russian)

[SBAR67] Sterrett, J.R., Burber, J.B., Alston, D.W., Romeo, D.J.: Experimental investigation of secondary jets from two-dimensional nozzles with various exit mach numbers for hypersonic control application. NASA TN D-3795 (1967)

Efficient Numerical Simulation of Dense Gas Flows Past Airfoils and Wings

Pietro Marco Congedo[1], Paola Cinnella[1], and Christophe Corre[2]

[1] Università del Salento, Dipartimento di Ingegneria dell'Innovazione, Via Monteroni, 73100 Lecce, Italy
[2] LEGI, Domaine universitaire B.P.53, 38041 Grenoble, France
pietcong@in.dii.unile.it, paola.cinnella@unile.it, christophe.corre@hmg.inpg.fr

1 Introduction

Dense gases are single-phase vapors whose properties deviate significantly from the ideal gas law, operating at temperatures and pressures of the order of magnitude of the critical ones. Bethe-Zel'dovich-Thompson (BZT) fluids, which can be commercially available heat transfer fluids, form a particular class of dense gases for which nonclassical gasdynamic behaviors are theoretically predicted: they display a Fundamental Derivative of Gasdynamics $\Gamma = 1 + \frac{\rho}{c}\left(\frac{\partial c}{\partial \rho}\right)_S$, with ρ the fluid density, c the sound speed, and S the entropy, that becomes negative in a range of thermodynamic conditions above the liquid/vapor coexistence curve. In that case, the compression shocks of the perfect gas theory violate the entropy inequality and are therefore inadmissible. Such non-classical phenomena have several practical outcomes: prominent among them is an active research effort to reduce losses caused by wave drag and shock/boundary layer interactions in turbomachines and nozzles, with particular application to Organic Rankine Cycles (ORCs). The complexity of setting up experimental studies with such dense gases [1] has motivated the development of numerical tools to analyze their performance, assess their interest and define their optimal conditions of use. This study deals with the extension to dense gas flow computations of a low-cost preconditioned implicit scheme previousy developed for perfect gas flows [2].

2 Governing Equations and Thermodynamical Model

Let us first focus on the $3D$ Euler equations written in conservative form:

$$\frac{\partial W}{\partial t} + \nabla \cdot F^E = 0, \tag{1}$$

where $W = (\rho, \rho u, \rho v, \rho w, \rho E)^T$ is the vector of conservative variables and $F^E = (f^E(W), g^E(W), h^E(W))$. Alternatively, the system can be expressed

in quasi-linear form using entropic variables $V = (p, u, v, w, S)$, with $dS = dp - c^2\, d\rho$:

$$\frac{\partial V}{\partial t} + A^e \frac{\partial V}{\partial x} + B^e \frac{\partial V}{\partial y} + C^e \frac{\partial V}{\partial z} = 0, \tag{2}$$

where the entropic Jacobian matrices are such that $A^e = \frac{df^E}{dV}$, $B^e = \frac{dg^E}{dV}$, $C^e = \frac{dh^E}{dV}$. The condition number of system (1) or (2) is defined as the ratio of the largest to the smallest eigenvalue of the system; a high condition number translates into a poor convergence to a steady-state when time-marching is applied to solve the system. Since the eigenvalues of the Euler system are given by $\lambda_1 = \underline{V} \cdot \underline{\kappa} - c = V_\kappa - c$, $\lambda_{2,3,4} = V_\kappa$ and $\lambda_5 = V_\kappa + c$ where $\underline{V}$ is the local velocity vector and $\underline{\kappa}$ an arbitrary unit vector, the condition number for (1) or (2) becomes large when the local Mach number goes to zero or is close to unity. A better efficiency for these flow conditions can be recovered by solving, instead of (2):

$$P_e^{-1} \frac{\partial V}{\partial t} + A^e \frac{\partial V}{\partial x} + B^e \frac{\partial V}{\partial y} + C^e \frac{\partial V}{\partial z} = 0, \tag{3}$$

where the preconditioning matrix P_e^{-1} is the one proposed by Turkel [3]:

$$P_e = \begin{bmatrix} \beta^2 & 0 & 0 & 0 & 0 \\ -\dfrac{\alpha u}{\rho a^2} & 1 & 0 & 0 & 0 \\ -\dfrac{\alpha v}{\rho a^2} & 0 & 1 & 0 & 0 \\ -\dfrac{\alpha w}{\rho a^2} & 0 & 0 & 1 & 0 \\ 0 & 0 & 0 & 0 & 1 \end{bmatrix} \tag{4}$$

with β^2 and α free parameters to be chosen so as to minimize the condition number of the preconditioned system (3). The eigenvalues of the preconditioned system are $\widetilde{\lambda}_1 = \widetilde{\underline{V}} \cdot \underline{\kappa} - \widetilde{c} = \widetilde{V}_\kappa - \widetilde{c}$, $\widetilde{\lambda}_{2,3,4} = V_\kappa$, $\widetilde{\lambda}_5 = \widetilde{V}_\kappa + \widetilde{c}$ with the preconditioned local velocity and speed of sound respectively given by:

$$\widetilde{V}_\kappa = \tfrac{1}{2}\, z\, V_\kappa \,,\, \widetilde{c} = \tfrac{1}{2}\sqrt{z^2 V_\kappa^2 + 4\beta^2 (c^2 - V_\kappa^2)} \tag{5}$$

where $z = 1 - \alpha + \beta^2$. If α, β are chosen such that $\alpha = 1 + \beta^2$ and $\beta^2 = M^2/(1 - M^2)$, then the condition number grows as $O(1/\sqrt{1 - M^2})$ instead of $O(1/(1 - M^2))$ when the local Mach number $M \to 1^-$ [3], yielding an improved convergence for transonic flows.

If the preconditioning is applied to the conservative form of the Euler system, the system to solve reads:

$$P_c^{-1} \frac{\partial W}{\partial t} + \nabla \cdot F^E(W) = 0 \,, \tag{6}$$

with $P_c = \left(\dfrac{\partial W}{\partial V}\right) P_e \left(\dfrac{\partial V}{\partial W}\right)$. In this study, Martin-Hou's (MAH) thermal equation of state (EOS) is used to model the dense gas thermodynamic behaviour: it relies on a 5 virial expansion terms to describe the relationship

between pressure, density and temperature $p = p(\rho, T)$. It is complemented with a caloric EOS linking internal energy with density and temperature $e = e(\rho, T)$ (see for instance [4] for more details). Combining both EOS, it is formally possible to express p as $p(\rho, e)$ or $p = \Pi(W)$ (see also [5]). The matrices $\dfrac{\partial V}{\partial w}$, $\dfrac{\partial w}{\partial V}$ can then be written in terms of the partial derivatives of Π with respect to density and total energy: Π_ρ, $\Pi_{\rho E}$. The preconditioning matrix P_c is derived from these expressions and definition (4); it takes the form $P_c = I + (\beta^2 - 1)Q_c$, with Q_c displaying the following properties: *i)* $Q_c^2 = Q_c$, *ii)* the product of Q_c with a column vector X is easily computed as

$$(\beta^2 - 1)Q_c\, X = \chi \begin{pmatrix} (\beta^2 - 1) \\ u\zeta \\ v\zeta \\ w\zeta \\ (\beta^2 - 1)\left(\dfrac{c^2 - \Pi_\rho}{\Pi_{\rho E}}\right) + q^2\zeta \end{pmatrix} \tag{7}$$

with $\chi = \dfrac{\Pi_{\rho E}}{c^2}\left(\dfrac{\Pi_\rho}{\Pi_{\rho E}}X^{(1)} - uX^{(2)} - vX^{(3)} - wX^{(4)} + X^{(5)}\right)$ and $\zeta = \beta^2 - 1 - \alpha$. This relationship generalizes the one given in [3] for perfect gases and will be used in the next section when deriving a low-cost implicit discretization for (6). The partial derivatives Π_ρ and $\Pi_{\rho E}$ are given by:

$$\Pi_{\rho E} = \frac{1}{\rho C_v}\left(\frac{\partial p}{\partial T}\right)_\rho, \; \Pi_\rho = \left(\frac{\partial p}{\partial \rho}\right)_T + \Pi_{\rho E}\left(\frac{V^2}{2} - e - \rho\left(\frac{\partial e}{\partial \rho}\right)_T\right)$$

where $\left(\dfrac{\partial p}{\partial T}\right)_\rho$, $\left(\dfrac{\partial p}{\partial \rho}\right)_T$ and $\left(\dfrac{\partial e}{\partial \rho}\right)_T$ are readily obtained from MAH thermal and caloric EOS.

3 Space and Time Discretization

The integral form of the preconditioned system (6) is discretized on a general unstructured grid using a standard finite volume approach expressed as:

$$(P_c^{-1})_i^n \frac{\Delta W_i^n}{\Delta t_i^n} = -\frac{1}{|\Omega_i|}\sum_k \left(\mathcal{H}_{i,k}^E\right)^n \;\; S_{i,k} = -\mathcal{R}_i^n, \tag{8}$$

where n is the time step counter, $\Delta(\cdot)^n = (\cdot)^{n+1} - (\cdot)^n$, $|\Omega_i|$ is the volume of the i^{th} control cell and index i, k on the numerical flux $\mathcal{H}^E$ refers to the center of the k^{th} interface of the i^{th} grid cell with surface $S_{i,k}$. The numerical flux approximating the normal physical flux $F^E \cdot \underline{n}$ through a face is computed as:

$$\mathcal{H}_{i,k}^E = \mathcal{H}^E(W_{i,k}^L, W_{i,k}^R)$$

where $W_{i,k}^{L/R}$ are linearly reconstructed states in the cells i and $o(i,k)$ sharing the interface i, k. The numerical flux formula used in the present study is

the modified HLLC scheme proposed in [6]; it relies on characteristic speeds which are computed from the preconditioned eigenvalues defined by (5). A fast convergence to steady state is obtained by coupling the above explicit scheme with a simple implicit stage, based on a first-order Rusanov numerical flux adapted to take into account the preconditioning matrix applied to the Euler system:

$$D_i^n \Delta W_i^n + \sum_k \left(\Delta F^E_{o(i,k)} \right)^n \cdot \underline{n}_{i,k} \ \sigma_{i,k} - \sum_k C^n_{i,k} \Delta W^n_{o(i,k)} = -\mathcal{R}_i^n \quad (9)$$

where $\sigma_{i,k} = \frac{S_{i,k}}{2|\Omega_i|}$ and the coefficients $C^n_{i,k}$ and D^n_i are defined by:

$$C^n_{i,k} = \left(P_c^{-1} \widetilde{\rho}^E_\perp\right)^n_{i,k} \sigma_{i,k} \ , \ D^n_i = \left(\frac{P_c^{-1}}{\Delta t}\right)^n_i + \textstyle\sum_k C^n_{i,k}$$

with $\widetilde{\rho}^E_\perp = |\tilde{V}_n| + \tilde{c}$. Scheme (9) can be rewritten as:

$$\Delta W_i^n = (D_i^n)^{-1} \ \mathrm{RHS}_c + (D_i^n)^{-1} \ (P_c^{-1})^n_i \ \mathrm{RHS}_d \quad (10)$$

where the contributions to the right-hand-side are split into:

$$\mathrm{RHS}_c = -\mathcal{R}_i^n - \textstyle\sum_k \left(\Delta F^E_{o(i,k)} \right)^n \cdot \underline{n}_{i,k} \ \sigma_{i,k} \ , \ \mathrm{RHS}_d = \textstyle\sum_k (\widetilde{\rho}^E_\perp)_{i,k} \ \sigma_{i,k} \ \Delta W^n_{o(i,k)}$$

and $D^n_i = a^n_i \left(P_c^{-1}\right)^n_i$, with the scalar coefficient a defined by $a^n_i = \frac{1}{\Delta t^n_i} + \sum_k \sigma_{i,k} (\tilde{\rho}^E_\perp)^n_{i,k}$. Taking advantage of the properties $i)$ and $ii)$ for Q_c, the implicit scheme is computed using the following simple form:

$$\Delta W_i^n = \frac{1}{a_i^n} \left[\mathrm{RHS}_c + \mathrm{RHS}_d\right] + \phi \begin{pmatrix} (\beta^2 - 1) \\ u\zeta \\ v\zeta \\ w\zeta \\ (\beta^2 - 1) \left(\dfrac{c^2 - \Pi_\rho}{\Pi_{\rho E}} \right) + q^2 \zeta \end{pmatrix}^n_i \quad (11)$$

with

$$\phi = \frac{\Pi_{\rho E}}{c^2} \left(\frac{\Pi_\rho}{\Pi_{\rho E}} RHS_c^{(1)} - u \ RHS_c^{(2)} - v \ RHS_c^{(3)} - w \ RHS_c^{(4)} + RHS_c^{(5)} \right).$$

The extra-cost induced by the preconditioning is thus reduced to the inexpensive computation of the product between ϕ and the column vector in (11). For practical purpose, this implicit stage is solved using a Point-Jacobi relaxation.

4 Numerical Results

The scheme defined by (11) with an explicit stage based on the HLLC scheme is used for computing the inviscid flow of a dense gas (PP10) at $M_\infty = 0.84$ and 3.06 degrees of incidence over the ONERA M6 wing. The thermodynamic

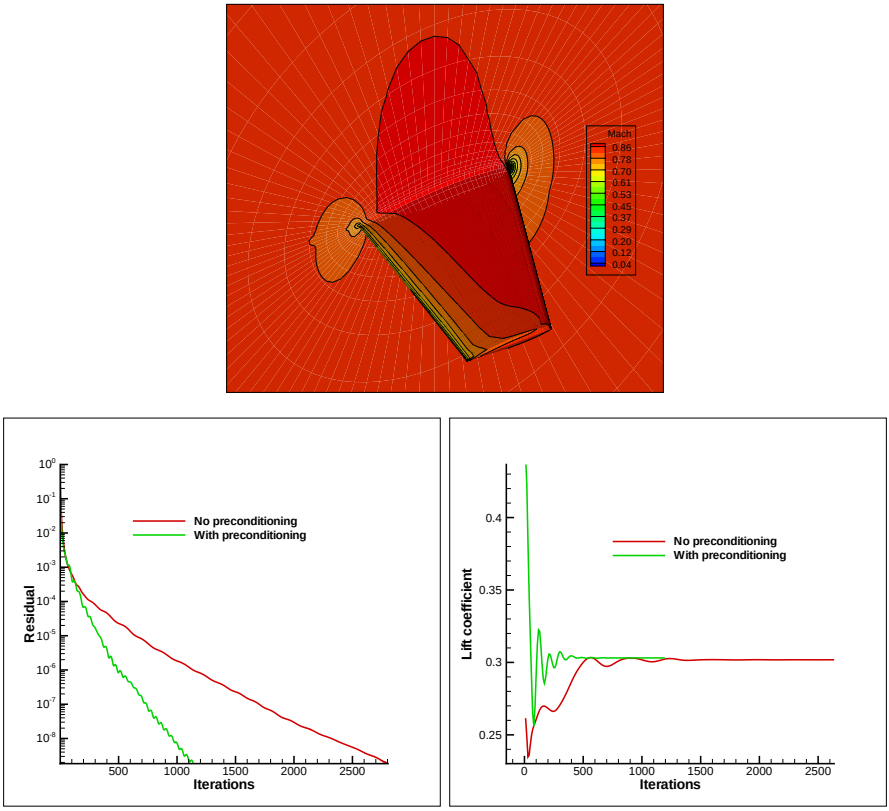

Fig. 1. $3D$ inviscid computation of a dense gas flow over the ONERA M6 wing. Solution and convergence history without and with preconditioning (residual and lift coefficient evolution)

conditions are such that $p_\infty/p_c = 1.00$, $\rho_\infty/\rho_c = 0.752$, corresponding to $\Gamma_\infty = 0.461$ which implies significant BZT effects. The flow is computed on a coarse grid made of 48000 hexahedral cells and the scheme is applied either with no preconditioning ($\beta^2 = 1$) or with Turkel preconditioning where β^2 has been bounded using the following formula [7]:

$$\beta^2 = min\left(max\left(\frac{M^2}{1-M^2}, M_\infty^2\right), 1\right) \tag{12}$$

with $\alpha = 1 + \beta^2$. The implicit treatment (11) is applied with $\Delta t \to \infty$ and 14 Point-Jacobi subiterations. The non-preconditioned and preconditioned schemes yield almost the same steady solution; the computed Mach contours with the preconditioned solver are presented in Fig.1: large regions of the flow display Mach number values close to unity which means β^2 as computed by (12) remains below unity in many grid cells, making the preconditioning effective. The use of such preconditioning yields a higher convergence rate

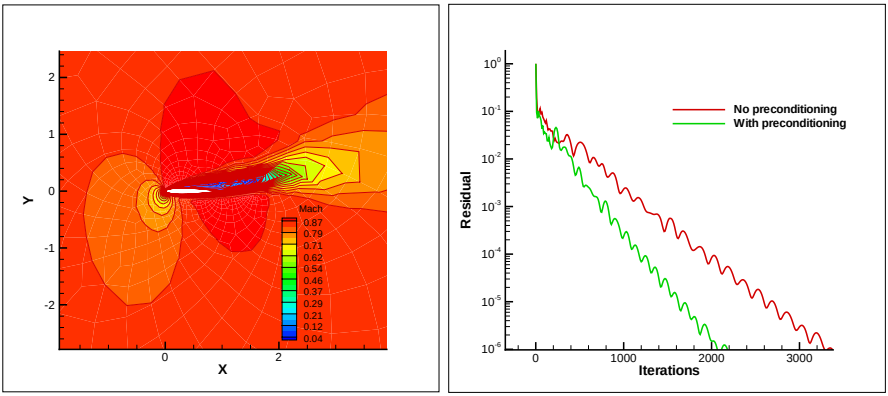

Fig. 2. $2D$ laminar computation of a dense gas flow over the NACA0012 airfoil. Solution and convergence history without and with preconditioning

which, taking into account the modest overcost (a few %) induced by the preconditioning thanks to the use of (11), translates into a 50% reduction of the computational cost for reaching a steady-state. Though not detailed here for lack of space, the implicit treatment (11) has been extended to the Navier-Stokes equations. The laminar flow at $M_\infty = 0.85$, $Re = 1000$ and 10 degrees of incidence over the NACA0012 airfoil is computed for PP10 with $p_\infty/p_c = 1.008$, $\rho_\infty/\rho_c = 0.676$ on a grid made of 6400 triangular cells. The convergence history displayed in Fig.2 demonstrates the net efficiency gain offered by preconditioning for the dense gas flows under study holds in the viscous case.

References

1. Colonna, P., Guardone, A., Nannan, N.R.: Siloaxes: A new class of candidate BZT fluids. Phys. Fluids 19, 086102–086111 (2008)
2. Kloczko, T., Corre, C., Beccantini, A.: Low-cost implicit schemes for all-speed flows on unstructured meshes. International Journal for Numerical Methods in Fluids (2008); published on line: DOI 10.1002/fld.1730
3. Turkel, E.: Preconditioning techniques in CFD. Annual Review of Fluid Mechanics 31, 385–416 (1999)
4. Cinnella, P., Congedo, P.M.: Aerodynamic performance of transonic dense gas flows past an airfoil. AIAA J. 43(2), 370–378 (2005)
5. Colonna, P., Rebay, S.: Numerical simulation of dense gas flows on unstructured grids with an implicit high resolution upwind Euler solver. International Journal for Numerical Methods in Fluids 46, 735–765 (2004)
6. Luo, H., Baum, J.D., Löhner, R.: Extension of Harten-Lax-van Leer scheme for flows at all speeds. AIAA J. 43(6), 1160–1166 (2005)
7. Turkel, E., Radespiel, R., Kroll, N.: Assessment of preconditioning methods for multidimensional aerodynamics. Computers and Fluids 26(6), 613–634 (1997)

A Dual-Time Implicit Upwind Scheme for Computing Three-Dimensional Unsteady Compressible Flows Using Unstructured Moving Grids

Kazem Hejranfar and Mohammad-Hadi Azampour

Aerospace Engineering Department, Sharif University of Technology, Tehran, Iran
khejran@sharif.edu

1 Introduction

Although computational fluid dynamics (CFD) has achieved a substantial amount of attention in the recent years, it is still far from being a maturing subject for simulation of unsteady flows around geometrically complex and largely moving and deforming bodies. Such flows are often encountered at various important engineering problems such as flutter, store separation, oscillating and flapping wings. The flow simulation for these problems poses a variety of challenges for computational methods. Firstly, a robust mesh deformation technique is necessary for maintaining a suitable descritization of the evolving computational domain. In addition, an appropriate numerical algorithm is required to integrate the governing equations in time and space. Therefore, in order to develop an efficient unsteady flow solver, both mesh deformation and flow solution aspects must be considered, as well as the interaction between these two areas.

In this paper, a dual-time implicit upwind scheme for solving unsteady inviscid compressible flowfield around pitching airfoils and wings using unstructured moving meshes is presented. The Arbitrary Lagrangian-Eulerian form of the Euler equations is discretized in real time based on the efficient upwind AUSM+ scheme. The present solution procedure provides a robust and accurate flow solver for computing unsteady compressible flowfeild around moving complex geometries.

2 Mesh Movement Strategy

Unstructured grid methods have the potential to handle complex geometries. Furthermore, the ability to adapt unstructured grids near regions of computational interest with large gradients has added to its popularity. However, developing a robust grid movement strategy for unstructured grids, which maintains the same nodal connectivity and that is computationally efficient, is still an active area of research in CFD.

Linear spring analogy is the oldest and simplest strategy to deform the unstructured mesh points. The linear spring analogy proposed by Batina [Bat90] has been widely used, due primarily to simplicity of implementation and computational efficiency. In this method, each edge of the grid is modeled as a linear tension spring which stiffness is proportional to the inverse of the edge length. Thus, for the edge connecting the nodes i and j, the stiffness C_{ij} of the spring is $C_{ij} = 1/l_{ij}^2$.

When the boundaries of a computational domain perform movements, the following equations for the interior nodes displacements are solved iteratively until all the forces are in equilibrium

$$\Delta x_i^{n+1} = \frac{\sum_j C_{ij} \Delta x_j^n}{\sum_j C_{ij}}, \quad \Delta y_i^{n+1} = \frac{\sum_j C_{ij} \Delta y_j^n}{\sum_j C_{ij}}, \quad \Delta z_i^{n+1} = \frac{\sum_j C_{ij} \Delta z_j^n}{\sum_j C_{ij}}, \tag{1}$$

where j is the notation for all nodes connected to node i. Indeed, we seek for a position of node i in which the summations of the images of all the forces acting on it in x, y and z directions tend to zero. The above equations require only a few Jacobi iterations to achieve an acceptable level of accuracy, therefore, this method is computationally efficient.

From Eq. 1, it is obvious that the behavior of a network of springs can not be modeled, because there is no interaction between the x, y and z coordinates. To overcome this deficiency, Burg [Bur04] proposed a new formulation for the forces acting on the nodes which can model the behavior of a network of springs

$$\mathbf{F}_{ij} = [F_x^i, F_y^i, F_z^i, F_x^j, F_y^j, F_z^j]^T = \left[\mathbf{R}_{ij} C_{ij} \mathbf{R}_{ij}^T\right] \mathbf{q}_{ij} = \mathbf{K}_{ij} \mathbf{q}_{ij} \tag{2}$$

in which the displacement matrix $\mathbf{q}_{ij}$, and the rotation matrix $\mathbf{R}_{ij}$, are

$$\mathbf{q}_{ij} = [\Delta x_i, \Delta y_i, \Delta z_i, \Delta x_j, \Delta y_j, \Delta z_j]^T \tag{3}$$

$$\mathbf{R}_{ij} = [-\cos\theta \sin\Phi, -\sin\theta \sin\Phi, -\cos\Phi, \cos\theta \sin\Phi, \sin\theta \sin\Phi, \cos\Phi]^T \tag{4}$$

In this formulaion, when a displacement in a direction is applied to node j, then it results in a displacement in all directions for node i.

Both representations of the linear spring analogy, however, may produce grids with negative volume elements. In other words, nodes cross-over the faces. Herein, similar to Singh's work [SNB95], to maintain the quality of grids near moving surface, the nodes outside a certain distance from the moving body are allowed to rotate while rigidly moving the points attached to and near the object in motion.

3 Solution Algorithm

Governing Equations

The governing equations are the three-dimensional time-dependent compressible Euler equations in the non-dimensional conservative form. The computational domain consists of unstructured tetrahedral cells. The integral form of these equations over the control volume Ω with the boundary $\partial\Omega$ are

$$\frac{\partial}{\partial t}\iiint_{\Omega}\mathbf{Q}dV+\oiint_{\partial\Omega}\mathbf{F}\left(\mathbf{Q}\right).\hat{\mathbf{n}}\;dS=0 \tag{5}$$

where

$$\mathbf{Q}=\begin{bmatrix}\rho\\ \rho u\\ \rho v\\ \rho w\\ E\end{bmatrix},\quad \mathbf{F}\left(\mathbf{Q}\right).\hat{\mathbf{n}}=\left(\mathbf{U}.\hat{\mathbf{n}}\right)\begin{bmatrix}\rho\\ \rho u\\ \rho v\\ \rho w\\ \rho H\end{bmatrix}+p\begin{bmatrix}0\\ \hat{n}_x\\ \hat{n}_y\\ \hat{n}_z\\ x_t\hat{n}_x+y_t\hat{n}_y+z_t\hat{n}_z\end{bmatrix} \tag{6}$$

Here, $\mathbf{Q}$ denotes the solution vector of conservative variables, $\mathbf{F}\left(\mathbf{Q}\right)$ is the inviscid flux vector, V is the cell volume, and $\hat{\mathbf{n}}\;dS$ is the vector element of a surface area with outward unit normal vector $\hat{\mathbf{n}}\left(\hat{n}_x,\hat{n}_y,\hat{n}_z\right)$. In addition, p, ρ, E and H denote the pressure, density, total energy per unit volume and total enthalpy per unit mass, respectively. Also, (u,v,w) are the Cartesian velocity components, and the normal velocity component, $\mathbf{U}.\hat{\mathbf{n}}$, is

$$\mathbf{U}.\hat{\mathbf{n}}=(u-x_t)\hat{n}_x+(v-y_t)\hat{n}_y+(w-z_t)\hat{n}_z \tag{7}$$

This formulation is called Arbitrary Lagrangian-Eulerian form of the Euler equations that can be used for moving grid problems.

Spatial Discretization

By applying Eq. 5 independently to each tetrahedral cell, the following set of ordinary differential equations is obtained

$$\frac{d}{dt}\left(\mathbf{Q}_jV_j\right)+\mathbf{R}(\mathbf{Q})=0,\quad \text{where}\quad \mathbf{R}(\mathbf{Q})=\sum_{k=1}^{4}\mathbf{F}_k.\hat{\mathbf{n}}\;dS_k \tag{8}$$

Here, $\mathbf{R}(\mathbf{Q})$ is the steady residual of cell j, $\mathbf{F}_k$, is the flux vector through the face k of cell j, and dS_k is the area of face k. In the present work, the AUSM+ scheme is used to compute the flux vector $\mathbf{F}_k$ in Eq. 8. In this scheme, the flux vector at a cell interface is given by

$$\mathbf{F}_k=\begin{cases}\rho_L\,\tilde{a}\,M_k\,\mathbf{\Phi}_L+\mathbf{g}\,p_k & if\quad M_k\geq 0\\ \\ \rho_R\,\tilde{a}\,M_k\,\mathbf{\Phi}_R+\mathbf{g}\,p_k & else\end{cases} \tag{9}$$

where

$$\mathbf{g}=\left[0,\hat{n}_x,\hat{n}_y,\hat{n}_z,x_t\hat{n}_x+y_t\hat{n}_y+z_t\hat{n}_z\right]^T,\quad \mathbf{\Phi}=\left[1,u,v,w,H\right]^T \tag{10}$$

Also, the interface Mach number M_k and the interface pressure p_k are evaluated using the weighted averages of the left and right states. In Eq. 9, $\tilde{a}$ is the numerical speed of sound. Details of the formulation of the AUSM+ scheme used can be found in [CL03] and [HA07]. The higher order accuracy

of the flow variables at each cell face is computed by the MUSCL formulation [Van79].

At the moving body surface, the flow tangency boundary condition is used for the inviscid flow. This is implemented by eliminating the convective fluxes across the faces of the mesh which lie on the wing surfaces. The treatment of the far-field boundary condition is based on the one-dimensional Reimann invariants normal to the far-field boundary

Implicit Time Integration

For unsteady calculations, a dual-time second-order implicit scheme is used as follows

$$V_j^{n+1}\frac{\partial \mathbf{Q}_j^{n+1}}{\partial \tau} + \mathbf{R}^*(\mathbf{Q}_j^{n+1}) = 0 \tag{11}$$

$$\mathbf{R}^*(\mathbf{Q}_j^{n+1}) = \frac{3\ V_j^{n+1}\mathbf{Q}_j^{n+1}}{2\Delta t} - \frac{2\ V_j^{n}\mathbf{Q}_j^{n}}{\Delta t} + \frac{V_j^{n-1}\mathbf{Q}_j^{n-1}}{2\Delta t} + \mathbf{R}_j(\mathbf{Q}^{n+1}) \tag{12}$$

where τ is the fictitious pseudo-time and the residual $\mathbf{R}^*$ is the unsteady solution of Eq. 8. Eq. 11 can be solved by using an efficient time-marching method designed to solve steady-state problems, utilizing the acceleration techniques. In the present study, the local pseudo-time stepping and residual smoothing are used to accelerate the convergence rate of the solution.

The Geometric Conservation Law (GCL) is applied to avoid the numerical errors due to the analytical calculation of the cell volumes [Ili98].

4 Results and Discussion

To validate the solution algorithm, the unsteady transonic flow at $M_\infty = 0.8$ around a rectangular half-span pitching wing is studied. The wing has the NACA 64A010 airfoil section and a complete aspect ratio of 4 which subjected to a forced, sinusiodal pitching motion ($\alpha = 1.0^\circ \sin(\omega t)$ and $\kappa = \omega c/2U_\infty = 0.135$). The unstructured grid over this wing is shown in Fig. 1 that contains

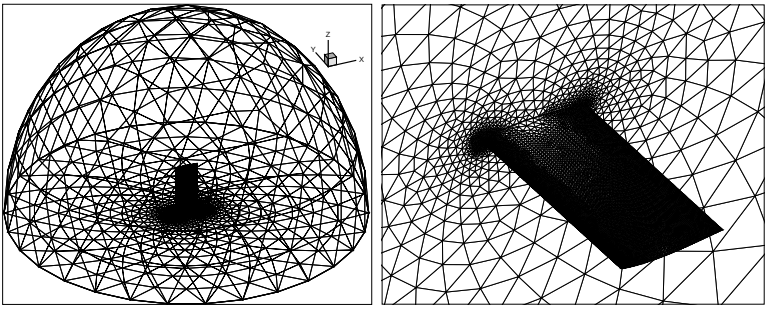

Fig. 1. Unstructured grids around NACA 64A010 rectangular wing

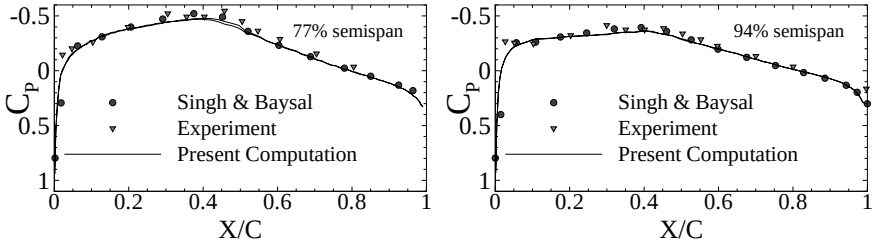

Fig. 2. Mean surface pressure coefficient distributions over the NACA 64A010 wing

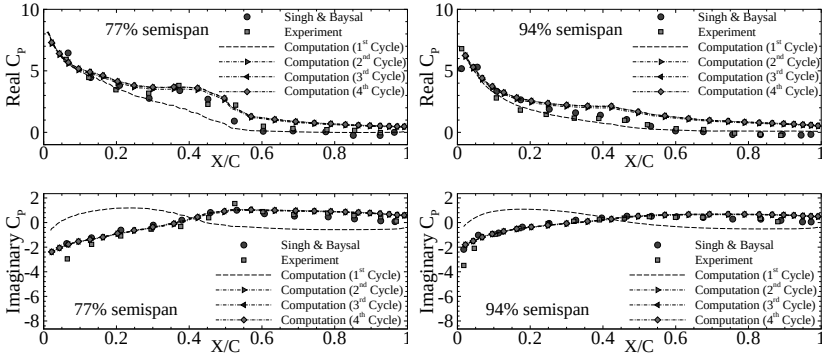

Fig. 3. Real and imaginary parts of unsteady pressure coefficient over the wing

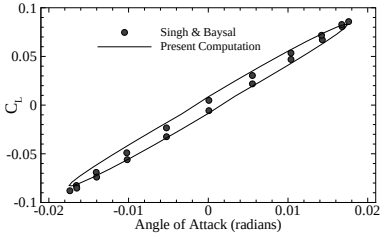

Fig. 4. Comparison of lift coefficient for unsteady flow around the wing

49359 nodes and 235510 tetrahedral elements. For this harmonic case, it is possible to decompose the pressure coefficient history computed in time domain as follows

$$Cp(t) = Cp_m + Cp_{\mathrm{Re}} \sin(\omega t) + Cp_{\mathrm{Im}} \cos(\omega t) \tag{13}$$

where Cp_m is the mean surface pressure coefficient, and Cp_{Re} and Cp_{Im} are the real and imaginary parts of the surface pressure coefficient which can be computed by the following relation

$$\begin{matrix}\mathrm{Re}\\ \mathrm{Im}\end{matrix}\{Cp\} = \frac{2}{\alpha(t_2 - t_1)} \int_{t_1}^{t_2} Cp(\tau) \left\{ \begin{matrix}\sin\\ \cos\end{matrix} (\omega\tau) \right\} d\tau \tag{14}$$

The time-accurate calculations are performed for four cycles which presented in Figs. 2 and 3 and the results are compared with the numerical solution by Sigh [SNB95] and the experimental data by Mabey [MWP88]. In Fig. 2 the computed mean surface pressure coefficient distributions in two different sections of wing (77% and 94% semispan) are compared with the available results which shows good agreement. In Fig. 3, the computed real and imaginary parts of the surface pressure coefficient distributions at the desired sections are presented. It is found that the unsteady results for the first cycle is not accurate for the harmonic solution. The calculated results for cycles 2-4 are nearly the same and agree well with the available results. In Fig. 4, the variation of the lift coefficient vs. the angle of attack of the wing is shown which is in agreement with the results by Singh [SNB95]. The present solution procedure provides a robust and accurate flow solver for computing unsteady three-dimensional compressible flowfeild around moving complex geometries.

References

[Bat90] Batina, J.T.: Unsteady Euler airfoil solutions using unstructured dynamic meshes. AIAA Journal 28(8), 1381–1388 (1990)

[Bur04] Burg, C.O.E.: A Robust Unstructured Grid Movement Strategy using Three-Dimensional Torsional Springs. AIAA Paper-2004-2529

[CL03] Chima, R.V., Liou, M.S.: Comparison of the AUSM+ and H-CUSP Schemes for Turbomachinery Applications. NASA/TM-2003-212457, AIAA-2003-4120

[HA07] Hejranfar, K., Azampour, M.H.: A Dual-Time Implicit Upwind Scheme for Computing Unsteady Compressible Flows over Oscillating Airfoils Using Unstructured Moving Grids. In: 6th International Conference of the Iranian Aerospace Society, Iran (2007)

[Ili98] Illinca, A., Illinca, C.: Geometric Conservation Laws for Three-Dimensional Unstructured Moving Grid. CFD 1998 (1998)

[MWP88] Mabey, D.G., Welsh, B.L., Pyne, C.R.: A summary of measurement of steady and oscillatory pressure on a rectangular wing. Aeronautical Journal 92(911), 10–28 (1999)

[SNB95] Singh, K.P., Newman, J.C., Baysal, O.: Dynamic Unstructured Method for Flows Past Multiple Objects in Relative Motion. AIAA Journal 33(4), 641–649 (1995)

[Van79] Van Leer, B.: Towards the Ultimate Conservative Difference Scheme, V: A Second Order Sequel to Godunov's Method. Journal of Computational Physics 32, 101–136 (1979)

Part 17
Error Estimation and Control

“*This page left intentionally blank.*”

Problems Associated with Grid Convergence of Functionals

Manuel D. Salas[1] and Harold L. Atkins[2]

[1] NASA Langley Research Center
m.d.salas@nasa.gov
[2] NASA Langley Research Center
harold.l.atkins@nasa.gov

Summary. The current use of functionals to evaluate order-of-convergence of a numerical scheme can lead to incorrect values. The problem comes about because of interplay between the errors from the evaluation of the functional, e.g., quadrature error, and from the numerical scheme discretization. Alternative procedures for deducing the order-property of a scheme are presented. The problem is studied within the context of the inviscid supersonic flow over a blunt body; however, the problem and solutions presented are not unique to this example.

Keywords: Code verification, grid convergence, supersonic blunt-body, drag functional.

1 Introduction

Computational Aerodynamicists conduct most of their grid convergence studies by studying the behavior of solution functionals, e.g., drag, lift and moment coefficients, as the computational grids are refined. Functionals are used for several reasons: first, their accurate evaluation is of intrinsic value; and second, they provide a means of determining convergence properties of a numerical scheme without looking directly at hundreds of thousands of field point values. Ideally, an error measure should be used to examine order-properties of grid convergence studies; however, exact solutions are usually not available for flows of practical interest. Therefore, estimating convergence properties using functionals is frequently the only course of action available.

However, there are some subtle problems associated with the use of functionals for grid convergence studies, and if these problems are not recognized and resolved, the results that follow from the use of functionals can be very misleading. It is the purpose of this paper to expose these problems, and where possible, suggest solutions.

There are many aspects of a numerical order-properties analysis that must be done correctly in order for the analysis to be reliable. Paramount among

these are: that grid refinements must be uniform, preferably with grids sequences that are hierarchical; and the iterative methods used to solve the discrete equations on a given grid must be sufficiently converged, preferably with residuals reduced several orders of magnitude below the solution error. Of course, this is complicated by the fact that the errors are not known a priori.

The problems that are associated with the use of functionals for the study of grid convergence rates are illustrated with numerical results from the computation of a blunt-body in an inviscid supersonic stream. However, it should be emphasized that the problems discussed are not unique to the blunt-body problem, indeed they are not unique to fluid mechanics, and may occur in any grid convergence study involving functionals. The particular case studied is the Mach 6 flow of an inviscid gas over a circular cylinder. In the numerical implementation the problem is solved as a time dependent problem with the bow shock wave fitted as a boundary of the flow. By fitting the shock, the numerical scheme acts only on a smooth flow region. Thus, the computation is limited to the layer bounded by the bow shock, the circular cylinder, the symmetry line, and a supersonic outflow boundary imposed at some $\theta = \theta_{\max}$, see Fig. 1.

The physical plane is transformed to a computational plane where N and M mesh points are uniformly distributed between the body and the shock and between the symmetry line and the outflow line, respectively. The predictor/corrector MacCormack scheme [1] is used for the numerical integration of the Euler equations.

Table 1 shows results obtained with a series of grids. The number of mesh points corresponding to each k^{th} grid are $\mathrm{N}_k = 3 \times 2^k$ and $\mathrm{M}_k = 5 \times 2^k$. Columns 2 and 3 display the inviscid drag coefficient computed with the trapezoidal rule (TR) and with Simpson's rule (SR). The drag coefficient order-of-convergence is given by

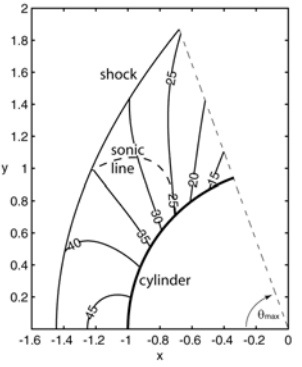

Fig. 1. Supersonic blunt-body flow field, showing isobars, $M_\infty = 6$

Table 1. $M_\infty = 6$ cases investigated. For the three finest grids the trapezoidal rule (TR) computed drag is not monotone and for both quadrature rules the computed drag exhibits super-convergence.

k	C_d (TR)	C_d (SR)	p(TR)	p(SR)
1	1.8755919	1.8767669	1.92	1.90
2	1.8706109	1.8709412	2.73	2.58
3	1.8692925	1.8693766	4.03	3.25
4	1.8690942	1.8691147	—	—
5	1.8690821	1.8690872		
6	1.8690859	1.8690872		

$$p_k = \log_2 \left[\frac{C_{d,k} - C_{d,k+1}}{C_{d,k+1} - C_{d,k+2}} \right], \tag{1}$$

and is shown in the last two columns. The order-of convergence for $k = 3$ for TR and SR shows a large discrepancy and both results are significantly greater than the formal order of the scheme which is second order. For $k = 4$, the drag coefficient is not monotone and the order-of-convergence evaluation fails. (Note that the order-of-convergence for grid k depends on the solutions from grids k, $k + 1$, and $k + 2$).

To establish that there is reason to suspect these results, consider the behavior of the error norm in total temperature. For this problem in the steady state, the total enthalpy, and hence the total temperature, is constant. The L_2 and L_∞ norms of the total temperature error are shown in Fig. 2. The order-of-convergence based on the L_2 and L_∞ norms is 2.03 and 1.84, respectively. These are in fairly good agreement with the formal order of the scheme. Why then is the order-of-convergence of the drag functional misbehaving?

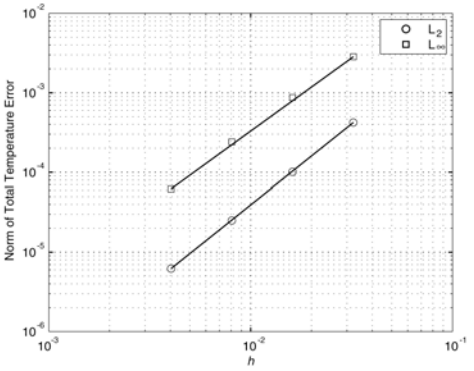

Fig. 2. L_2 and L_∞ of total temperature error for entire shock layer, based on results from grids $k = 3, 4, 5$, with $h_k = 1/\sqrt{N_k M_k}$

2 Order-Of-Convergence of Functionals

To answer the last question, first consider the following question: If the surface pressure converges with order p, what should the expected order-of-convergence of the drag-functional be? To this end, let the computed surface pressure, P_c, normalized by the free stream pressure, P_∞, be given by $P_c/P_\infty = P_e/P_\infty + \alpha(\theta)h^p$, where P_e is the exact surface pressure. The sectional drag coefficient is defined by

$$C_d = \int_0^{\theta_{\max}} (P_c/P_\infty - 1)\, b(\theta)\cos(\theta)d\theta / \left(\tfrac{1}{2}\gamma M_\infty^2 A_{ref}\right) \tag{2}$$

where γ is the ratio of specific heats, M_∞ is the free stream Mach number, $b(\theta)$ is the body radius, and A_{ref} is a reference surface area, here taken as the projected plan-form area. Therefore, $C_d = C_{d,e} + \Gamma h^p$ where Γ is a constant and $C_{d,e}$ is the exact value of the drag coefficient; therefore, the drag-functional should converge with order p.

3 The Problem with Quadrature

If it is assumed that the pressure order-of-convergence behaves like the total temperature order-of-convergence, then the result just obtained for drag is not consistent with the results of Table 1. The problem lies in the numerical integration of (2). The integration is *approximated* by a quadrature taken over M equally spaced intervals on the surface of the cylinder, i.e. $\int_0^{\theta_{\max}} f d\theta \approx \sum_1^{M+1} a_i f_i$. The quadrature has a leading error of order h^q. It is easy to show that $C_d = C_{d,e} + \beta_q h^q + \Gamma h^p + O(h^{q+p})$, where β_q is a constant and q equals 2 for TR and 4 for SR. Using this relation for C_d in (1) we find

$$\bar{p} = p + \log_2 \left\{ \frac{2^{p-2}\beta_q \left[1 - 2^q\right] + h^{p-q}\Gamma \left[1 - 2^p\right]}{2^{2(p-2)}\beta_q \left[1 - 2^q\right] + h^{p-q}\Gamma \left[1 - 2^p\right]} \right\}, \tag{3}$$

where h is the coarse grid spacing. Here $\bar{p}$ is the *computed* order-of-convergence and the $\log_2$-term is an error brought about by the interplay between the quadrature error and algorithmic error. In the limit $h \to 0$, the $\bar{p}$ behavior is given by $\bar{p} \to q$ if $p \geq q$, and $\bar{p} \to p$ if $p < q$. However, in a computation h will always be finite and having $p < q$ is not a guarantee that the $\log_2$-term will be small.

4 How to Eliminate the Quadrature Error

A solution to the quadrature problem can be found by studying (1). Consider the numerator. The numerator is the difference between the drag coefficients of the medium (k+1) and coarse (k) grids. The medium grid has a quadrature error of order $(h/2)^2$, while the coarse grid has a quadrature error of order h^2.

These errors do not cancel out and their interplay with the algorithmic error causes some (not all) of the problems in the results of Table 1. The solution is to implement the quadrature in such a way that the quadrature errors of the medium and coarse grids cancel. To do this, evaluate both the medium and coarse grid quadratures using an h interval, i.e., use only every other point of the medium grid. The same idea is applied to the denominator by evaluating both the medium and fine grid quadratures using an $h/2$ interval.

5 Higher-Order Algorithmic Error Model

The actual algorithmic error in any numerical solution on any given grid contains a full hierarchy of errors that are unknown, but are generally assumed to be of the form $C_{d,k} = C_{d,ex} + \sum_{n=p}^{\infty} \alpha_n h_k^n$, where p is the unknown actual order of the numerical method. The standard method for deducing order properties from grid convergence, described earlier, is obtained by fitting a single error mode of the form $C_{d,k} = C_{d,ex} + \alpha h_k^p$ to the actual error. For sufficiently small h, the actual error is dominated by the lowest order term, and the single mode model provides an accurate prediction of the order-of-convergence. However, for larger h above this asymptotic region, multiple error modes are competing, and their projection onto a single mode can be erroneous. Consider then a two-mode error model:

$$C_{d,k} = C_{d,ex} + \alpha_1 h_k^p + \alpha_2 h_k^{p+1}. \tag{4}$$

For this model, using a sequence of four grids (k through k+3), where $h_{k+1}/h_k = h_{k+2}/h_{k+1} = h_{k+3}/h_{k+2} = 1/2$, we find the order-of-convergence to be

$$p = \log_2 \left[\frac{3\Delta_{k+1}}{4\Delta_{k+2}} \pm \sqrt{\left(\frac{3\Delta_{k+1}}{4\Delta_{k+2}}\right)^2 - \frac{\Delta_k}{2\Delta_{k+2}}} \right], \tag{5}$$

where $\Delta_i = C_{d,i} - C_{d,i+1}$. The "+" sign is the appropriate choice when in or near the asymptotic region. It is important to monitor the ratio

$$\frac{\alpha_2 h_k}{\alpha_1} = \frac{4(1-2^p)}{(1-2^{p+1})} \frac{(\Delta_k - 2^p \Delta_{k+1})}{(2^{p+1}\Delta_{k+1} - \Delta_k)}. \tag{6}$$

Table 2. Drag order-of-convergence using higher order method and coarse grid interval, $k = 3$, for quadrature rules

k	C_d (TR)	C_d (SR)	p(TR)	p(SR)
3	1.8692925	1.8693766	1.674	1.681
4	1.8690328	1.8691145		
5	1.8690056	1.8690872		
6	1.8690056	1.8690871		

When the magnitude of this ratio is less than one, the one-mode error model is valid. With a two-mode error model and eliminating the quadrature error as previously described, we obtain the results listed in Table 2. For more details see [2].

6 Conclusions and Recommendations

With the increased reliance in both science and engineering on the numerical solution of partial differential equations, the subject of code verification has become increasingly significant. An important element of code verification is the study of grid convergence. Most studies today of this subject have been at best superficial and in many cases painfully inadequate. This paper is an attempt to reverse this trend by first highlighting a series of problems that exist in the standard order-of-convergence analysis, particularly as it relates to the evaluation of functionals, and second by providing a number of solutions and workarounds to these problems. It is important to distinguish between a code verification effort and an effort to determine if a particular solution to a specific problem is sufficiently accurate for some intended use. The two tasks are very different. A rigorous grid convergence and order-of-convergence study can aid in determining if an algorithm has been implemented correctly. However, such a rigorous study requires grids of the same family and grid refinements that are uniform, preferably with grids sequences that are nested. In the second task, limited time and resources often lead to compromising one or more attributes of a rigorous study. While non-uniform mesh refinement may lead to some improvement in the solution, order-of-convergence properties computed from non-uniform refinements or ill-converged solutions sets are meaningless. Whenever possible, error norms should be used to establish the order-of-convergence. The higher order analysis developed in Sect. 5 is the best way to evaluate if the asymptotic range has been reached or if more levels of grid refinement are needed to reach it. It should be part of any rigorous grid convergence study. Reference [2] provides a more in depth study of these issues.

References

1. MacCormack, R.W.: The effect of viscosity in hypervelocity impact cratering. AIAA Paper No. 69-354 (1969)
2. Salas, M.D., Atkins, H.L.: On problems associated with grid convergence of functionals. Comp. & Fluids (to appear) (2008)

Accuracy Analysis Based on a Posteriori Error Estimates of SemiGLS Stabilization of FEM for Solving Navier-Stokes Equations

Pavel Burda[1], Jaroslav Novotný[2], and Jakub Šístek[1]

[1] Dept. of Math., Czech University of Technology, Karlovo nám. 13, CZ-12135 Praha 2, Czech Republic
burda@marian.fsik.cvut.cz, sistek@seznam.cz
[2] Institute of Thermomechanics, Czech Academy of Science, Dolejškova 5, CZ-18200 Praha 8, Czech Republic
novotny@bivoj.it.cas.cz

Summary. The accuracy of the stabilized finite element solution of incompressible flow problems with higher Reynolds numbers is studied. We use a modification of the Galerkin Least Squares Method called semiGLS. A posteriori error estimates are used as the principal tool for the accuracy analysis. The problem of singularities is considered. Numerical results are presented.

Keywords: FEM, Incompressible flow, Stabilization, SemiGLS, A posteriori estimates.

1 Introduction

It is well known that finite element method (FEM) in its standard form (e.g. the mixed FEM version) suffers from numerical oscillations and other instabilities when applied to problems of flows with high Reynolds numbers. Stabilization techniques for FEM are commonly accepted tools for solving these problems. However, when applying the stabilization technique we observe quite significant loss of accuracy in the solution, cf. e.g. [BNŠ06Sw], where the *semiGLS* method was discussed. In this paper we focus primarily on the analysis of accuracy of the *semiGLS* method. We make use of a posteriori error estimates of the finite element solution in order to trace the loss of accuracy of the stabilized algorithm.

2 Mixed FEM Formulation

Let Ω be an open bounded domain in $\mathbb{R}^2$ filled with an incompressible viscous fluid. Steady flow is governed by the following Navier-Stokes system,

$$(\mathbf{u} \cdot \nabla)\mathbf{u} - \nu \Delta \mathbf{u} + \nabla p = \mathbf{f} \quad \text{in } \Omega, \tag{1}$$

$$\nabla \cdot \mathbf{u} = 0 \quad \text{in } \Omega, \tag{2}$$

with appropriate conditions on the boundary Γ. Here $\mathbf{u}$ is the vector of flow velocity, p is the pressure normalized by the density, ν is the kinematic viscosity, $\mathbf{f}$ is the density of volume forces.

Using the variational formulation of problem (1)–(2) and mixed FEM, we come to the discrete weak steady Navier-Stokes problem. We work with Taylor-Hood finite elements P_2P_1 and/or Q_2Q_1 on triangles or quadrilaterals, respectively. These satisfy the Babuška-Brezzi condition.

3 SemiGLS Stabilized Formulation

We recall the *semiGLS* stabilization technique, which was described in [BNŠ06Sw] as a modification of Galerkin Least Squares method, proposed by [HFH89]. Applying this stabilization to the momentum equation (1) and adding the continuity equation (2), we introduce the stabilized problem:

Find $\mathbf{u}_h \in V_{gh}$ and $p_h \in Q_h$ satisfying $\forall \mathbf{v}_h \in V_h, \quad \forall \psi_h \in Q_h$,

$$\int_\Omega \big((\mathbf{u}_h \cdot \nabla)\mathbf{u}_h \cdot \mathbf{v}_h + \nu \nabla \mathbf{u}_h : \nabla \mathbf{v}_h + \psi_h \nabla \cdot \mathbf{u}_h - p_h \nabla \cdot \mathbf{v}_h\big) \mathrm{d}\Omega$$

$$+ \sum_{K=1}^{N} \int_{T_K} \left[(\mathbf{u}_h \cdot \nabla)\mathbf{u}_h - \nu \Delta \mathbf{u}_h + \nabla p_h\right] \cdot \tau \left[(\mathbf{u}_h \cdot \nabla)\mathbf{v}_h - \nu \Delta \mathbf{v}_h + \nabla \psi_h\right] \mathrm{d}\Omega$$

$$= \int_\Omega \mathbf{f} \cdot \mathbf{v}_h \mathrm{d}\Omega + \sum_{K=1}^{N} \int_{T_K} \mathbf{f} \cdot \tau \left[(\mathbf{u}_h \cdot \nabla)\mathbf{v}_h - \nu \Delta \mathbf{v}_h + \nabla \psi_h\right] \mathrm{d}\Omega,$$

Here $\mathbf{u}_h = (u_{h1}, u_{h2})$, V_{gh}, Q_h, V_h are proper finite element spaces, and τ is a positive stabilization parameter, cf. [BNŠ06Sw] where the potential of the *semiGLS* method was demonstrated also on practical problems.

Although stabilization terms should vanish in the limit for $h \to 0$ (the exact solution) satisfying the formal consistency, the approximate solution does not reach this limit. So these terms remain present in the practically solved equations and modify them slightly. We take this as the substantial source of the loss of accuracy.

4 A Posteriori Error Estimates

For evaluating the achieved accuracy of the approximate solution, we use the following error estimator that represents the relative error on the finite element T_K,

$$\mathcal{R}^2(u_{1h}, u_{2h}, p_h, T_K) = \frac{|\Omega|\ \mathcal{E}^2(u_{1h}, u_{2h}, p_h, T_K)}{|T_K| \|(u_{1h}, u_{2h}, p_h)\|^2_{V,\Omega}}. \tag{3}$$

This is based on the following a posteriori error estimates that were derived and tested for Taylor-Hood elements in [BNS03],

$$\|(e_{u_1}, e_{u_2}, e_p)\|^2_{V,T_K} \leq \mathcal{E}^2(u_{1h}, u_{2h}, p_h, T_K), \tag{4}$$

where

- (u_1, u_2, p) denotes the exact solution
- (u_{1h}, u_{2h}, p_h) denotes the approximate solution computed by FEM
- $(e_{u_1}, e_{u_2}, e_p) = (u_1 - u_{1h}, u_2 - u_{2h}, p - p_h)$ denotes the error of approximate solution
- $\|u_{1h}, u_{2h}, p_h\|^2_{V,\Omega} = \|u_{1h}\|^2_{1,\Omega} + \|u_{2h}\|^2_{1,\Omega} + \|p_h\|^2_{0,\Omega}$ where
- $\|u_{1h}\|_{1,\Omega}$,$\|u_{2h}\|_{1,\Omega}$ mean Sobolev $H^1(\Omega)$ norms
- $\|p_h\|_{0,\Omega}$ means the $L_2(\Omega)$ norm
- $|\Omega|, |T_K|$ mean the area of the domain Ω, and the element T_K, respectively

The term on the right hand side of the inequality (4) is evaluated as

$$\mathcal{E}^2(u_{1h}, u_{2h}, p_h, T_K) = C\Big[h_K^2 \int_{T_K} \left(r_1^2(u_{1h}, u_{2h}, p_h) + r_2^2(u_{1h}, u_{2h}, p_h)\right) \mathrm{d}\Omega + \int_{T_K} r_3^2(u_{1h}, u_{2h}, p_h) \mathrm{d}\Omega\Big],$$

where $r_1(u_{1h}, u_{2h}, p_h), r_2(u_{1h}, u_{2h}, p_h)$ are residuals of the momentum equation (1), $r_3(u_{1h}, u_{2h}, p_h)$ is the residual of the continuity equation (2), see [BNŠ06Gh].

The constant C is a delicate task in a posteriori error estimates. We refer to [BNS03], where we show its derivation for the case of non-stabilized finite element method. In this paper we work with the error in a relative sense: using the above estimator we are able to show the relative error on finite elements, and so reveal the distribution of the error in the solution domain. This is important especially for flows with high Reynolds number.

5 Numerical Results and Accuracy Analysis

5.1 Steady Flow in Lid Driven Cavity

Comparison of a posteriori error estimates for the problem of the lid driven cavity at Reynolds number 10,000 is presented in Figure 1. The mesh is uniform, 64×64 elements. In the plots, AEE is an abbreviation for *a posteriori error estimator*. We compare solution without stabilization (left) to the solution by semiGLS (right). In both cases, highest errors are at upper corners which is caused by the presence of singularities in the exact solution at these two corners. The a posteriori error estimates confirm these singularities. On the other hand on Figure 1 we can observe the well-known fact that we pay for stabilization by the loss of accuracy. The inaccuracy of the stabilized solution is spread on the whole domain. We can also observe the "leading role" of pressure in the inaccuracy: where the pressure has higher gradients there the inaccuracy of the stabilized solution is higher, cf. Fig. 2.

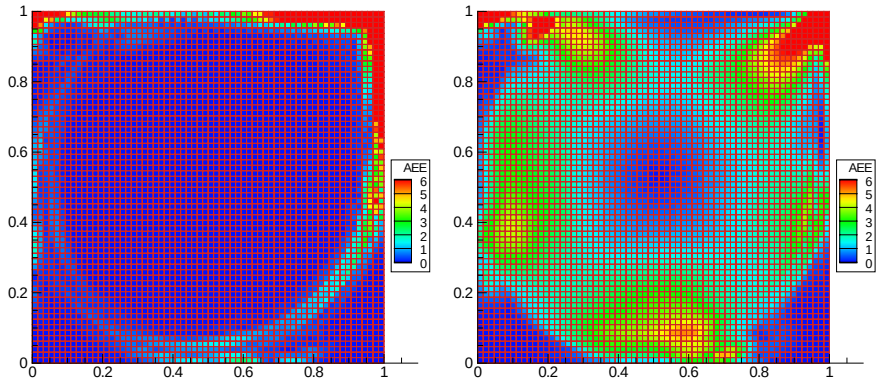

Fig. 1. A posteriori errors on elements, cavity problem, Re = 10,000, without stabilization (left) and by *semiGLS* method (right)

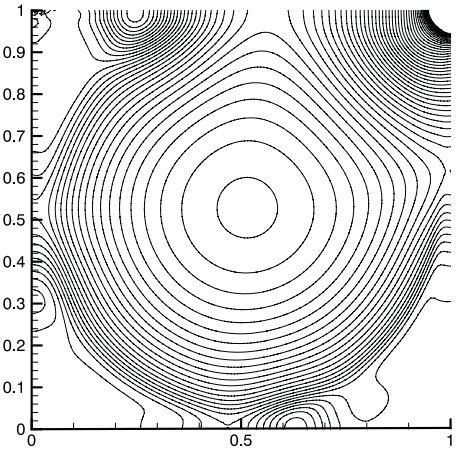

Fig. 2. Pressure contours, cavity problem, Re = 10,000, without stabilization

5.2 Steady Flow in Channel with Sudden Extension of Diameter

In Figure 3, we give results for a channel with abrupt changes of diameter. Here again, the exact solution attains singularities in the two nonconvex corners. But here the mesh is refined in the vicinity of these nonconvex corners which restrains the influence of the singularity on the finite element solution; the algorithm for designing properly refined mesh was described in [BNŠ05].

There is also a straightforward way to evaluate the loss of accuracy. It is based on comparison of discrete norms of approximate solutions obtained with and without stabilization, see [BNŠ06Sw]. In Table 1 we show the differences of solutions obtained by the semiGLS method from those obtained by the Newton

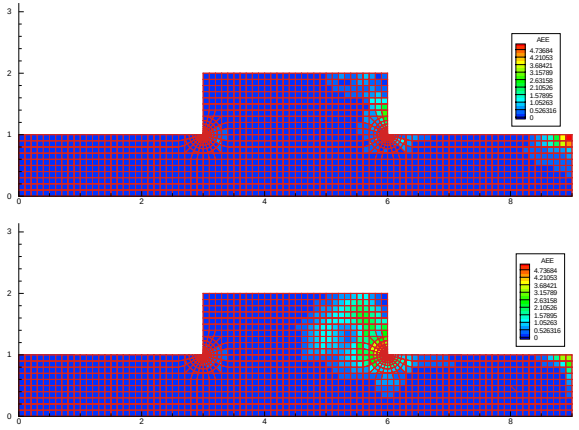

Fig. 3. A posteriori errors in the channel: mixed method without stabilization (top) and *semiGLS* method (bottom), Re = 1,000

Table 1. Differences between solutions obtained with and without stabilization

	64×64	128×128	channel
$\delta_{u_{h1}}$ [%]	39.07	21.42	0.0718
$\delta_{u_{h2}}$ [%]	49.12	22.24	2.7202
δ_{p_h} [%]	137.10	42.82	0.5139

method: first two columns for cavity, third column for the channel. We can observe again that in the case of the channel, where the mesh is adjusted to the singularities near corners, the differences are much lower.

Let us note that the calculations for our analysis were done for quite low Reynolds numbers. The reason is in the existence of steady solution for comparison of errors with stabilized solutions. The results of semiGLS stabilization on problems with much higher Reynolds numbers are given e.g. in [BNŠ06Sw].

6 Conclusion

The loss of accuracy is inherited in the stabilized method and could be hardly suppressed. However, using the new approach presented in this paper, we can evaluate its distribution and therefore get the idea about its effect.

In Figures 1, 3 we can observe, that the error can spread to a larger area when using *semiGLS*. Similar behaviour was observed also for other stabilization techniques, such as *SUPG* method. However, one should note that the precision of the stabilized solution is much higher in case of the channel on Figure 3 where the mesh is refined towards the singulalarity, compared to

the case of cavity on Figure 1 where the mesh is uniform regardless of the singularities in upper corners.

Although a posteriori error estimates give important information on the distribution of the error, still the problem of accuracy in the stabilized FEM deserves more complex analysis.

Acknowledgement. This work has been supported by the GACR grant No. 106/08/0403 and by the State Research Project No. MSM 684 0770010.

References

[BNS03] Burda, P., Novotný, J., Sousedík, B.: A posteriori error estimates applied to flow in a channel with corners. Mathematics and Computers in Simulation 61, 375–383 (2003)

[BNŠ05] Burda, P., Novotný, J., Šístek, J.: Precise FEM solution of a corner singularity using an adjusted mesh. Int. J. Numer. Meth. Fluids 47, 1285–1292 (2005)

[BNŠ06Sw] Burda, P., Novotný, J., Šístek, J.: On a modification of GLS stabilized FEM for solving incompressible viscous flows. Int. J. Numer. Meth. Fluids 51, 1001–1016 (2006)

[BNŠ06Gh] Burda, P., Novotný, J., Šístek, J.: Semi-GLS stabilization of FEM applied to incompressible flows with higher Reynolds numbers. In: Burda, P. (ed.) ICCFD4, Fourth Internat. Conf. on Computational Fluid Dynamics, Ghent, Belgium, July 10-14 (2006) (to appear in the proceedings by Springer)

[BNŠ08] Burda, P., Novotný, J., Šístek, J.: Accuracy of semiGLS stabilization of FEM for solving Navier-Stokes equations and a posteriori error estimates. In: ICFD Conference on Numerical Methods for Fluid Dynamics, Int. J. Numer. Meth. Fluids, vol. 56, pp. 1167–1173 (2008)

[HFH89] Hughes, T.J.R., Franca, L.P., Hulbert, G.M.: A new finite element formulation for computational fluid dynamics: VIII. The Galerkin/least-squares method for advective-diffusive equations. Comput. Methods Appl. Mech. Engrg. 73, 173–189 (1989)

Residual Adaptive Computations of Complex Turbulent Flows

N. Ganesh[1], K. Ravindra[2], and N. Balakrishnan[3]

[1] Indian Institute of Science, Bangalore-12
ganesh@aero.iisc.ernet.in
[2] Simulation&Innovation Engineering Solutions, Bangalore-12
deepu.ravindra@gmail.com
[3] Indian Institute of Science, Bangalore-12
nbalak@aero.iisc.ernet.in

Summary. A new adaptive algorithm for computing turbulent flows past high–lift devices is proposed. The adaptive algorithm is based on a recently developed residual error estimator, which is capable of detecting sources of error. The error estimator can be effectively employed in the absence of discontinuous flow features for both refinement and derefinement. The new adaptation algorithm is employed within a RANS framework to study the physics of flow past a three–element take–off configuration.

1 Introduction

Flow past multi–element airfoils is quite complex due to the presence of boundary layer transition, separation and reattachment, wake–boundary layer and shock–boundary layer interactions and unsteadiness at higher angles of attack. Accurate predictions of lift and drag are critically dependent on how well the flow features are resolved and therefore on the computational mesh employed. Mesh generation for multi–element airfoils is a formidable task and no single mesh is optimal over the large range of angles of attack typically encountered by such configurations. Adaptive meshes offer a viable and economical alternative to handle these problems. The key to success of any adaptive algorithm are the sensors that can detect the error. Error estimators are a natural choice as sensors because of their ability to provide reasonable estimates of the error in the domain that can be used to design a "termination criterion" for adaptation. A residual error estimator referred to as $\Re$–parameter, developed by the authors [1] is particularly attractive because of its ability to detect error sources in addition to providing a criterion to decide on the sufficiency of grid resolution. The residual estimator is inexpensive, works well in regions devoid of discontinuities and limiters and can be used effectively for both refinement and derefinement for flows past high–lift configurations.

2 Residual Error Estimation

In this section, we briefly discuss the residual error estimation for steady–state fluid flow problems. Consider the governing conservation equations expressed in an integral form over a finite volume Ω_i bounded by surface Γ_i,

$$I_i[U] = \frac{1}{\Omega_i} \oint_{\Gamma_i} \mathbf{F} \cdot \mathbf{d}\Gamma = 0 \tag{1}$$

The discrete approximation to the above equation reads,

$$\delta_i^1[u] = 0 \tag{2}$$

In **Eq.(1)**, U represents the exact solution and $\mathbf{F} = \mathbf{F}(U)$ represents the flux vector, while in **Eq.(2)** δ_i^1 represents a discrete approximation to I_i and u is the numerical solution. The fundamental idea in the design of the $\Re$–parameter is to *exploit the imbalance* that would arise if the exact operator, I operated on the numerical solution, u. We then have,

$$I_i[u] = R_i^1[u] \tag{3}$$

However, in working with a discretised domain, an estimate of this error can be obtained using another discrete operator δ_i^2 approximating I.

$$\delta_i^2[u] = R_i^1[u] + R_i^2[u] \tag{4}$$

If $R^1 \sim \mathbf{O}(\mathbf{h^m})$ and $R^2 \sim \mathbf{O}(\mathbf{h^n})$, the necessary condition for the $\Re$–parameter to be an estimate of the local truncation error is $m < n$. In the present procedure, a linear reconstruction (m=1) is employed to obtain the solution while a quadratic reconstruction (n=2) with a three–point Gaussian quadrature for flux integration, is used to estimate the errors.

The $\Re$–parameter is computed as the RMS value of the continuity, momentum and energy residuals. The residual estimation procedure is generic and can be applied to any system of equations.

3 Adaptation Algorithm

The success of any AMR algorithm is critically dependent on the criterion employed for refinement/derefinement. We develop a new isotropic h–refinement algorithm purely based on the residual error estimator in the present work. The refinement/derefinement criterion hinges on the following hypothesis.

Hypothesis. *For a grid l^p at any level p ($p \geq 1$), the volumes which continue to remain at the initial level (p=0), have the lowest values of the $\Re$–parameter.*

Furthermore, the residual estimate can be related to the characteristic length scale for each cell as $\Re = \mathrm{X(h)\ h}$, where X(h) is the "Dissipation Function" and depends on the solution derivatives. Such a representation is

more general and accounts for the non–integral nature of the slope of the error curve. The readers are referred to [1] for a detailed discussion.

We define a threshold value of the parameter, $\Re^* = \frac{1}{2}\left(||\Re||_1 + ||\Re||_\infty\right)$, the norms being taken over a stencil comprising of cells at initial (or base) level and where limiters are not operational. For every cell at grid level l, we then calculate the dissipation function X^l , 'cell threshold length' h^* and threshold dissipation function X^* (using values at levels l and $(l-1)$) as below.

$$X^l = \frac{\Re^l}{h^l} \qquad h^* = \frac{\Re^*}{X^*} \qquad X^* = 2 \times X^l - X^{l-1}$$

It must be emphasised that while the threshold value of the $\Re$–parameter is a global quantity, the threshold length scale is local to every cell in the domain. The refinement/derefinement criterion are given as follows.

Refinement criterion. *A volume c on a grid l^p (p≥1) is flagged for refinement iff the characteristic length scale h_c associated with the volume satisfies $h_c > h_c^*$.*

Derefinement criterion. *A volume c on a grid l^p (p≥1) is flagged for derefinement iff the characteristic length scale h_c associated with the volume satisfies $2 \times h_c \leq h_c^*$.*

On the base level grid l^0, it is however necessary to have a separate refinement criterion. This is achieved by flagging a fixed percentage of cells where the $\Re$–parameter is maximum. It must be emphasised that it is desirable to refine a larger percentage of volumes to begin with, in order to detect flow features, as the derefinement criterion will subsequently remove the over–adapted regions automatically. In addition to the above basic criterion, a series of smoothing rounds are necessary to ensure good grid quality.

4 Grid and Solution Methodology

The starting grid is a hybrid mesh comprising of 50666 volumes. On this initial grid, quadrilateral cells used for filling the viscous wall layers are carefully generated to resolve the laminar sublayer. These cells are therefore not included in the refinement/derefinement procedure. Nevertheless, refinement of these cells in order to satisfy the smoothness criterion of atmost one hanging node for a given edge is permitted. The rest of the computational domain are filled with triangles. The first grid spacing off the wall is $5{\times}10^{-6}$ and the farfield is set at 150 chords. In this sense, a good initial grid is a prerequisite for a meaningful adaptive strategy.

The in–house developed flow solver HIFUN–2D based on cell–centered finite volume framework is used for steady–state computations. Inviscid fluxes are computed using the Roe's flux difference splitting scheme [2], while the viscous fluxes are computed using diamond path reconstruction [9]. Solution

monotonicity is enforced using the Venkatakrishnan limiter [3] and implicit time–stepping based on Symmetric Gauss-Seidel (SGS) relaxation is employed for convergence acceleration [5]. A point vortex correction is employed at the farfield boundary, while wall fluxes are computed based on pressure extrapolation. Turbulence is modelled using the one–equation Spalart–Allmaras model [4]. The flow equations are solved in a decoupled manner from the turbulence model equations. A point–transition strategy [8], which zeroes out the turbulence production term is employed for transition specification.

5 Numerical Simulations

The proposed adaptive strategy is employed to investigate the lift characteristics and drag polar of the three–element NHLP airfoil, typical of a take–off configuration. The freestream conditions correspond to a Mach number of 0.197 and Reynolds number of 3.52 million. In the computations performed in this work, transition is set at 12.5% chord on both surfaces of the main element, while the slat and flap are run "fully turbulent". Two levels of refinement/derefinement are performed at eight angles of attack (viz. 12^o,16^o,18^o,20^o,22^o,23^o,24^o and 25^o). The number of volumes on the final level adapted grid is approximately 4,10,000 for all angles of attack. Fig.1 shows the initial and adapted meshes for α=20^o. The mach contours on these grids are shown in Fig.2. It is evident that the wakes and the confluent boundary layer are captured accurately on the adapted meshes. The adaptive strategy leads to better predictions of the wake deficit (Fig.3)

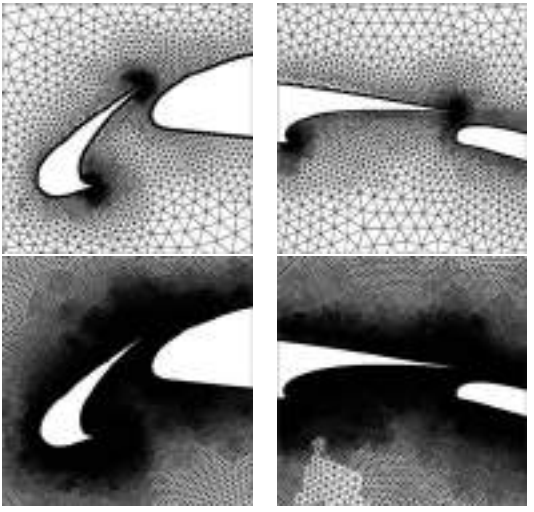

Fig. 1. Initial hybrid mesh (Top) and Adapted mesh at final level (Bottom) close to the slat (Left) and close to the flap (Right) ($\alpha = 20^o$)

Fig. 2. Mach contours on the final level adapted grid: Full view (Left), close to slat (Center) and close to flap (Right) ($\alpha = 20^o$). Contour levels are 0:0.01:1.03

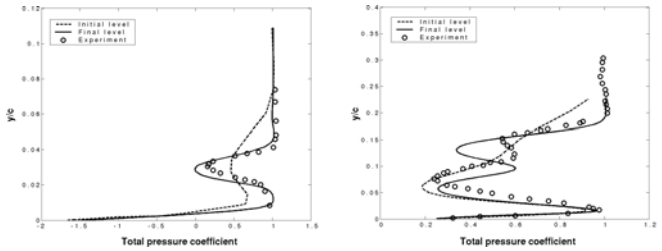

Fig. 3. Total pressure coefficient profiles at x/c = 0.35 (Left) and x/c=1.215 (Right) for α=20^o

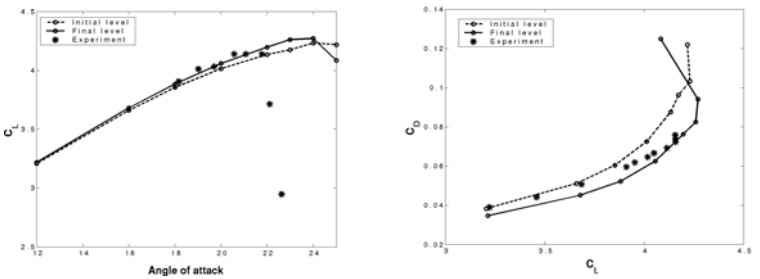

Fig. 4. C_L–α curve (Left) and Drag polar (Right)

and consequently the lift characteristics and drag polar (Fig.4). Table 1 shows the comparison of $C_{L,max}$ and stall angle with experiments and other computations. Though the slope of the lift curve in the linear regime is in good agreement with experiments [6], maximum lift and stall angle are overpredicted, consistent with other computations [7]. Grid adaptation is seen to

Table 1. Comparison of stall angle and maximum lift coefficient

	$C_{L,max}$	Stall angle
Experiment [6]	4.16	21.7^o
Present(HIFUN–2D)	4.27	24.0^o
CFL3D [7]	4.32	24.0^o

significantly improve the drag predictions, while the predictions of lift characteristics show only marginal improvement.

6 Conclusion

A new adaptive algorithm based on the residual error estimator is developed to handle flow past high–lift configurations. Application of the strategy to the NHLP test case amply demonstrate that the adaptive algorithm does well to predict the stall angle, maximum lift and drag polar with reasonable accuracy. The present work demonstrates that the adaptive algorithm can indeed be employed as a cheap yet effective engineering tool for high–lift computations. The adaptive strategy in conjunction with advances in transition and turbulence modelling is expected to be employed for realistic predictions of high–lift configurations in the near future.

References

1. Ganesh, N., et al.: Proceedings of ICCFD4, CFD 2006. Springer, Heidelberg (2006)
2. Roe, P.L.: J. Comp. Phys. 104 (1993)
3. Venkatakrishnan, V.: J. Comp. Phys. 118, 120–130 (1995)
4. Spalart, P.R., Allmaras, S.R.: La Recherche Aerospatiale (1994)
5. Nikhil., V.: Shende, PhD Thesis, IISc (2006)
6. Rumsey, C.: Private communication (2008)
7. Fejtek, I.: AIAA 1997–1932 (1997)
8. Rumsey, C., et al.: NASA Tech. Report (1997)
9. Munikrishna, N.: PhD Thesis, IISc (2008)

Part 18
Flow Control/Instability

“*This page left intentionally blank.*”

Active Control of Transitional Channel Flows with Pulsed and Synthetic Jets Using Vortex Methods

Emmanuel Creusé[1], André Giovannini[2], and Iraj Mortazavi[3]

[1] LAMAV & INRIA Lille Nord Europe, Université de Valenciennes, 59313 Valenciennes Cedex 09, France
ecreuse@univ-valenciennes.fr
[2] IMFT UMR CNRS, 118, route de Narbonne, 31062 Toulouse, France
giova@imft.fr
[3] IMB & INRIA Université Bordeaux I, 351, cours de la Libération, 33405 Talence, France
Iraj.Mortazavi@math.u-bordeaux1.fr

Abstract. In this work a vortex method is used to simulate and control an incompressible two-dimensional transitional flow over a backward-facing step. Two different control strategies are implemented to modify the shedding, the recirculation zone behind the step and the transport in the channel. The first technique consists in using a pulsing inlet velocity and the second one is based on local oscillating jets implemented on the step vertical wall. The influence of these controls on the flow behavior is carefuly investigated. Both, open-loop and closed-loop active control approaches are performed.

Keywords: Vortex method, closed and open-loop active control, backward-facing step.

1 Context and Aim of the Study

The aim of the present work is to develop two different active control strategies to manipulate the flow characteristics inside a backward-facing step channel with a transitional flow regime: 1) using pulsed inlet velocities, with open and closed-loop frequency choices; 2) implementing two jets to the vertical step wall with open-loop or closed-loop action into the lower and upper levels of the step. This work follows the primary results obtained by the authors in a previous paper for laminar flows [3]. Here, the impact of the control on several flow characteristics like vorticity, energy, fluctuations, velocity gradients etc. is carefully analysed. Reynolds numbers are $Re = 500$ and $Re = 2000$.

2 Numerical Scheme

The numerical simulations are performed using a Vortex-In-Cell method [2]. In VIC calculations, an Eulerian grid is implemented in order to compute efficiently the velocity field on the Lagrangian particles. The goal is to obtain a fast computation of the particle velocities in regular bounded domains. Here, fast Poisson solvers enable fast velocity evaluations. Compared with pure finite-difference methods, VIC methods offer the advantage of a robust and accurate treatment of the convective part of equations with time steps not constrained by convective CFL conditions [1]. The simulations are validated, comparing them to existing experimental and numerical literature and grid convergence analysis ensured. Appropriate sets of space and time numerical parameters are selected in order to achieve accurate control strategies [4].

3 Control Strategies

The control is performed either by taking an oscillating inlet velocity $\mathbf{u}(t) = (u_{in}(t), 0)^T$, instead of the uncontrolled uniform velocity boundary condition simulation (Fig. 1, $Control_1$), or by two small jets implemented on the upper and lower parts of the step (Fig. 1, $Control_2$). Both, open and closed-loop controls are used and compared. The open loop studies are performed for a wide range of parameters to get the most efficient ones. These values are then compared to the closed-loop control to verify its efficiency.

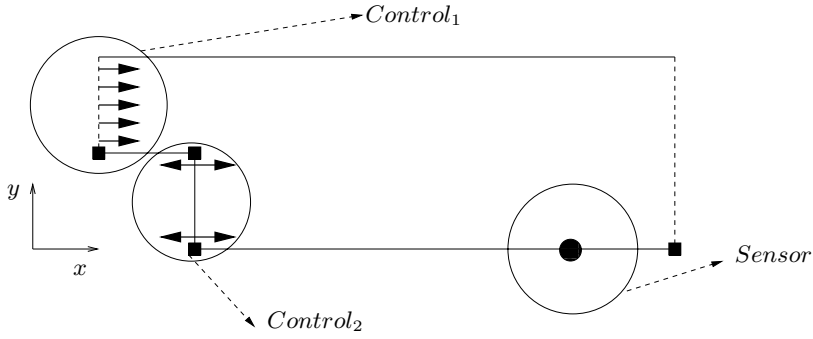

Fig. 1. Control devices on the step geometry

The control effect is focused on the vortex shedding, transport phenomena and the step recirculation zone behavior. One of the main targets is to reduce the recirculation area and length, then to decrease the trapped particles and to improve the transport of vortices [5]. In order to quantify this control, several time dependent fonctionals are studied [4]. These functionals are the recirculation area length $L_r(t)$, the total enstrophy in the domain that measures the

vorticity of the flowfield and the near wall recirculation area intensity that corresponds to the level of shear forces.

4 Numerical Results

4.1 First Control Type

The first control (Fig. 1, $Control_1$) is achieved oscillating the inlet velocity profile $u_{in}(t) = 1.0 + A\cos(2\,\pi\,f\,t)$. The frequency f and the amplitude A of this oscillating flow are obtained either by an extensive parametric study (open-loop control OLC) or implementing the dominant frequencies of the vorticity formation and transport in the pulsing flow as the reference value (closed-loop control CLC).

For the open-loop control an extremum value for each time-averaged functional for a frequency nearly equal to the basic fundamental frequency of the flow, namely $f \approx 0.14$ is achieved (see Fig. 2). On the other hand, the efficiency of the control almost linearly increases with the increasing values of the amplitude until a "plateau".

The closed-loop control consists in using the fundamental frequencies of flow shedding or transport in order to fit the oscillation frequency. The frequency measuring sensors may be implemented on the wall (non-intrusive sensors) or inside the flow field (intrusive sensors). The main advantage of the closed-loop control is that the control frequency is taken directly from the principal flow frequencies and avoids the heuristic trial and error approaches with high computational cost needed for open-loop methods. In the non-intrusive closed-loop control the quantity $\partial^2 u/\partial y^2$ is connected to the wall tangent pressure gradient. The closed-loop control consists in taking $u_{in}(t) = 1.0 + M\left(\partial^2 u/\partial y^2(t)\right)_{S_n}$, where S_n is a point on the bottom wall (see the location of the sensor on Fig. 1), and $M = 2.5.10^{-3}$ is chosen to make vary the inlet velocity in the same range as for the open loop case.

The results show that the closed-loop control is efficient since each obtained functional value as well as average and instantaneous fields are close to the best results achieved by the open-loop control. As the figure 3 shows the averaged recirculation zones are remarquably reduced and concentrated in a small area behind the step using this closed-loop control.

These results are then compared to those obtained using intrusive sensor. More precisely, we now induce at the entry of the domain the velocity :

$$u_{in}(t) = 1.0 + M\left(u_{S_i}(t) - \overline{u_{S_i}}\right),$$

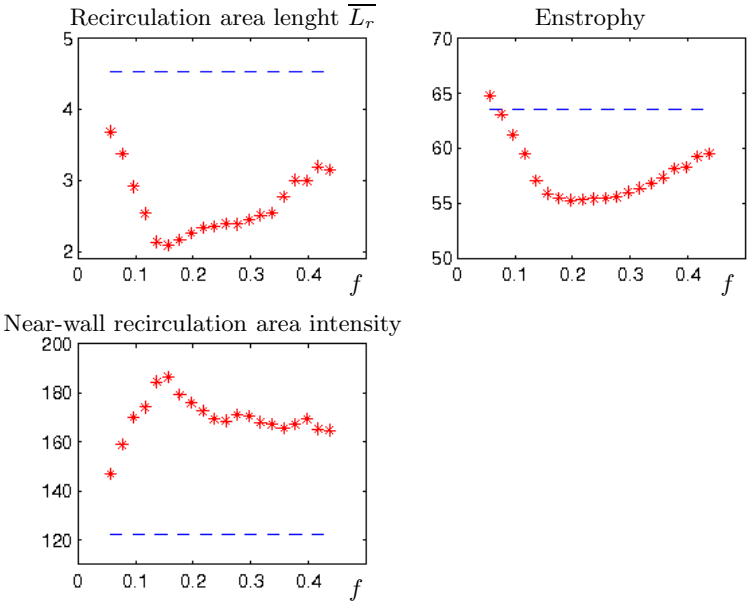

Fig. 2. Value of the functionals. Top left : Recirculation area lenght. Top right : Enstrophy. Bottom left : Near-wall recirculation intensity. In dashed-blue line : The value corresponding to uncontrolled flow.

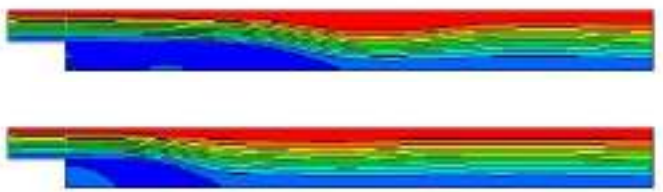

Fig. 3. Mean streamlines for uncontrolled (up) and non-intrusive CLC (down) regimes

where $u_{S_i}(t)$ is the horizontal velocity at a given point inside the flow, $\overline{u_{S_i}}$ its time-averaged value recorded during an uncontrolled simulation, and M a parameter chosen to tune the amplitude of the signal (which has to be the same as in the non intrusive case). It shows the higher efficiency of the intrusive control compared to non intrusive one : the time-averaged value L_r is respectively equal to 2.71 in the non intrusive case and 2.38 in the intrusive one (4.51 for the uncontrolled flow). Indeed, in the intrusive configuration the

sensors are placed inside the flow that is less perturbated by the wall effects. This can be understood by looking at the value of $u_{in}(t)$ in both cases (see Fig. 4).

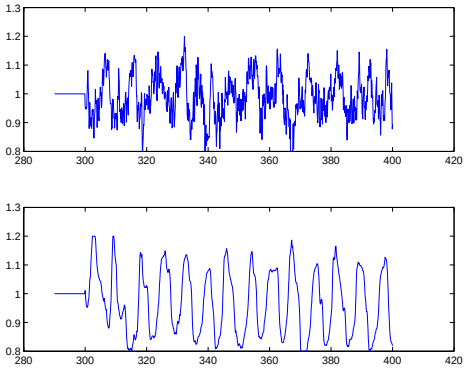

Fig. 4. Signal of $u_{in}(t)$ for closed-loop control : with non intrusive sensor (top) and with intrusive sensor (bottom)

4.2 Second Control Type

In the second type of control, two small jets are implemented on the upper and lower parts of the vertical step (Figure 1, $Control_2$). The main target of this approach is to influence directly the vortex shedding and the recirculation zone: the upper jet changes the shedding dynamics and the lower one perturbates and pushes away the recirculation zone. The actuators placed in the close vicinity of the bottom and the top of the step, blow or expell an horizontal flow inside the flow.

In this study, different possibilities as steady open-loop, active open-loop and active closed-loop actuators are applied to this configuration and their efficiency is verified. The inlet velocity is taken equal to unity; u_{ju} and u_{jb} correspond to the uniform jet velocities respectively on the top and the bottom of the step. Then, the oscillation, according to the control technique, is imposed to these velocities. Moreover, the computations are performed with both pulsed and synthetic jets. In the first case, in both devices the jet varies between 0 and $|2A|$, with a negative jet in the upper side of the step and a positive one in the lower part. In the second, the jet varies between $-A$ and A and there is no absolutely positive or negative device, even they never coincide to each other.

For this kind of control, as the figure 5 shows, the best closed-loop results are achieved, taking $(u_{ju}, u_{jb}) = (-1.0, 0.5)$ as the initial conditions and implementing the pulsed jets. A lot of detailed results are available in [4].

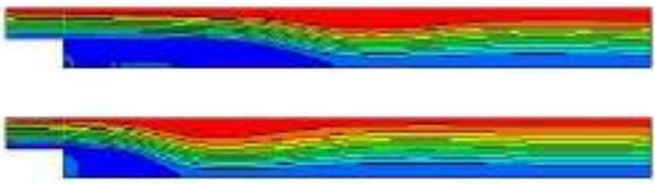

Fig. 5. Mean streamlines for uncontrolled (up) and CLC with pulsed step jets (down) regimes

5 Conclusion

In this work, both open and closed-loop control methods were applied to control a backward-facing step flow using a Vortex-In-Cell method. Two control configurations the first one correponding to a pulsing inlet flow and the second one to jets introduced into the lower and upper parts of the step were studied, . The first strategy showed that the natural fundamental frequency of the flow offers the characteristic value to tune the pulsing frequency. The control is therefore based on this value whatever the used devices. We also observed the efficiency of implementing the intrusive sensors. For the second strategy, the best control is achieved with a high velocity negative upper jet compared to a positive bottom jet. This result was also true for oscillating jets. It was verified that an automatic closed-loop approach can provide a control as efficient as the best open-loop control.

References

1. Cottet, G.-H., Koumoutsakos, P.: Vortex methods. Cambridge Univ. Press, Cambridge (2000)
2. Christiansen, J.P.: Numerical Simulation of Hydrodynamics by the Method of Point Vortices. J. Comp. Phys. 13, 363–379 (1971)
3. Creusé, E., Mortazavi, I.: Simulation of low Reynolds number flow control over a backward-facing step using pulsed inlet velocities. Applied Math. Research Express 4, 133–152 (2004)
4. Creusé, E., Giovannini, A., Mortazavi, I.: Vortex simulation of active control strategies for transitional backward-facing step flows. Computers and Fluids (in press) (2008)
5. Kaiktsis, L., Monkewitz, P.: Global destabilization of flow over a backward-facing step. Phys. Fluids 15, 3647–3658 (2003)

Numerical Analysis of Control Problems for Stationary Models of Hydrodynamics and Heat Transfer

Gennady Alekseev and Dmitry Tereshko

Institute of Applied Mathematics FEB RAS, Vladivostok, Russia
alekseev@iam.dvo.ru

In the last years much effort was focused on inverse identification problems for models of hydrodynamics and heat transfer [AT90, GHS91, AM94, GHS93, IR98, Ale98, LI00, Ded07]. In these problems the unknown densities of boundary or distributed sources, the coefficients of model differential equations or boundary conditions are recovered from additional information on the solution to the original boundary value problem. Importantly, inverse problems can be reduced to corresponding extremum problems by choosing a suitable minimized cost functional that adequately describes the inverse problem in question [Ale01, Ale07a, Ale07b]. As a result, both control and inverse problems can be analyzed by applying a unified approach based on the constrained optimization theory in Hilbert or Banach spaces.

In this paper extremum problems for the stationary model of heat convection in a viscous incompressible heat-conducting fluid are considered. We formulate theorems about solvability of these problems, the validity of the Lagrange principle for them and a regularity condition for a Lagrange multiplier. Finally we discuss some results of numerical experiments.

1 Statement of the Direct Boundary Problem

Let Ω be a bounded domain in the space $\mathbf{R}^m, m = 2, 3$ with Lipschitz boundary Γ. We consider the boundary value problem for the stationary Navier-Stokes equations

$$-\nu\Delta\mathbf{u} + (\mathbf{u}\cdot\nabla)\mathbf{u} + \nabla p = \mathbf{f}, \;\; \operatorname{div}\mathbf{u} = 0 \text{ in } \Omega, \quad \mathbf{u} = \mathbf{g} \text{ on } \Gamma \tag{1}$$

which describes the steady flow of the viscous incompressible fluid through the domain Ω. Here $\mathbf{u}$ and p denote the velocity and pressure fields respectively, $\mathbf{f}$ is a given body force, ν is the kinematic viscosity coefficient, $\mathbf{g}$ is a given vector-function on Γ. The density constant is taken to be 1. In the case where thermal effects are essential we have to add the heat transfer equation

$$-\lambda\Delta T + \mathbf{u}\cdot\nabla T = f \text{ in } \Omega \tag{2}$$

together with the boundary conditions

$$T = \psi \text{ on } \Gamma_D, \;\; \partial T/\partial n = \chi \text{ on } \Gamma_N \tag{3}$$

to the system (1). Here λ is the thermal conductivity coefficient, ψ is a given function on a part Γ_D of Γ, χ is a function given on another part $\Gamma_N = \Gamma \backslash \Gamma_D$ of Γ, $\mathbf{n}$ is the unit outer normal and the body force $\mathbf{f}$ in (1) is defined by $\mathbf{f} = -\mathbf{G}\beta T$, where $\mathbf{G}$ is the gravitational acceleration vector, β is the volumetric thermal expansion coefficient. We shall refer to problem (1) as Problem 1 and to (1)–(3) with $\mathbf{f} = -\mathbf{G}\beta T$ as Problem 2.

We will make use of Sobolev spaces. In particularly we need the function spaces $H^1(\Omega)$, $\mathbf{H}^1(\Omega)$, $L^2(\Omega)$, $\mathbf{H}^{1/2}(\Gamma)$, $H^{1/2}(\Gamma_D)$ and their subspaces

$$\mathcal{T} = \{\theta \in H^1(\Omega) : \theta|_{\Gamma_D} = 0\}, \;\; L_0^2(\Omega) = \{r \in L^2(\Omega) : \int_\Omega r d\Omega = 0\},$$

$$\mathbf{H}_0^1(\Omega) = \{\mathbf{v} \in \mathbf{H}^1(\Omega) : \; \mathbf{v}|_\Gamma = 0\}.$$

The inner products and norms in $L^2(\Omega)$ or $L^2(\Gamma_N)$ are denoted by $(\cdot,\cdot)$, $\|\cdot\|$ or $(\cdot,\cdot)_{\Gamma_N}$, $\|\cdot\|_{\Gamma_N}$. The norm in $H^1(\Omega)$ and $\mathbf{H}^1(\Omega)$ is denoted by $\|\cdot\|_1$.

We assume that

(i) Ω is a bounded domain in $\mathbf{R}^3$ with a Lipschitz boundary $\Gamma \in C^{0,1}$ consisting of N connected components Γ_i, where $i = 1, 2, .., N$; the open segments Γ_D and Γ_N of Γ obey the conditions $\Gamma_D \in C^{0,1}$, meas $\Gamma_D > 0$ and $\Gamma = \overline{\Gamma_D} \cup \overline{\Gamma_N}$.

We set $\mathcal{T} = \{\varphi \in H^1(\Omega) : \; \varphi|_{\Gamma_D} = 0\}$, $\mathbf{H}_0^1(\Omega) = \{\mathbf{v} \in \mathbf{H}^1(\Omega) : \; \mathbf{v}|_\Gamma = 0\}$, $L_0^2(\Omega) = \{p \in L^2(\Omega) : \;\; (p, 1) = 0\}$, $\tilde{\mathbf{H}}^1(\Omega) = \{\mathbf{v} \in \mathbf{H}^1(\Omega) : \;\; \mathbf{v} \cdot \mathbf{n}|_{\Gamma_N} = 0, \;\; (\mathbf{v}, \mathbf{n})_{\Gamma_i} = 0, \;\; i = 1, 2, \ldots, N\}$, $\tilde{\mathbf{H}}^{1/2}(\Gamma) = \{\mathbf{v}|_\Gamma : \;\; \mathbf{v} \in \tilde{\mathbf{H}}^1(\Omega)\}$. Let in addition to assumption (i) the following conditions take place:

(ii) $f \in L^2(\Omega)$, $\psi \in H^{1/2}(\Gamma_D)$; (iii) $\mathbf{g} \in \tilde{\mathbf{H}}^{1/2}(\Gamma)$, $\chi \in L^2(\Gamma_N)$.

The following technical lemma holds (see [AT08]):

Lemma 1. *Under conditions (i) there exist constants $\delta_i > 0$, $\gamma_i > 0$ and $\beta_i > 0$ such that*

$$(\nabla \mathbf{v}, \nabla \mathbf{v}) \geq \delta_0 \|\mathbf{v}\|_1^2 \;\; \forall \mathbf{v} \in \mathbf{H}_0^1(\Omega), \;\; (\nabla T, \nabla T) \geq \delta_1 \|T\|_1^2 \;\; \forall T \in \mathcal{T},$$

$$|((\mathbf{u} \cdot \nabla)\mathbf{v}, \mathbf{w})| \leq \gamma_0 \|\mathbf{u}\|_1 \|\mathbf{v}\|_1 \|\mathbf{w}\|_1 \;\; \forall \mathbf{u}, \mathbf{v}, \mathbf{w} \in \mathbf{H}^1(\Omega),$$

$$|(\mathbf{u} \cdot \nabla \varphi, \eta)| \leq \gamma_1 \|\mathbf{u}\|_1 \|\varphi\|_1 \|\eta\|_1, \;\; |(\beta \varphi \mathbf{G}, \mathbf{v})| \leq \beta_1 \|\varphi\|_1 \|\mathbf{v}\|_1. \tag{4}$$

Let $X = \tilde{\mathbf{H}}^1(\Omega) \times L_0^2(\Omega) \times H^1(\Omega)$, $Y = \mathbf{H}^{-1}(\Omega) \times L_0^2(\Omega) \times \tilde{\mathbf{H}}^{1/2}(\Gamma) \times \mathcal{T}^* \times H^{1/2}(\Gamma_D)$. The weak formulation of Problem 2 is given as follows: to seek a triple $(\mathbf{u}, p, T) \in X$ such that

$$\nu(\nabla \mathbf{u}, \nabla \mathbf{v}) + ((\mathbf{u} \cdot \nabla)\mathbf{u}, \mathbf{v}) - (p, \mathrm{div}\mathbf{v}) = -(\beta T \mathbf{G}, \mathbf{v}) \;\; \forall \mathbf{v} \in \mathbf{H}_0^1(\Omega),$$

$$\lambda(\nabla T, \nabla S) + (\mathbf{u} \cdot \nabla T, S) = (f, S) + (\chi, S)_{\Gamma_N} \;\; \forall S \in \mathcal{T},$$

$$\mathrm{div}\, \mathbf{u} = 0 \text{ in } \Omega, \;\; \mathbf{u} = \mathbf{g} \text{ on } \Gamma, \;\; T = \psi \text{ on } \Gamma_D. \tag{5}$$

2 Control Problems

Our goal is the study of control problems for the models under consideration. The problems consist in minimization of certain cost functional depending on the state and controls. As the cost functionals we choose some of the following ones:

$$I_1(\mathbf{u}) = \frac{1}{2}\int_{\Omega_0} |\mathbf{u} - \mathbf{u}_d|^2 d\Omega, \quad I_2(\mathbf{u}) = \frac{1}{2}\int_{\Omega_0} |\operatorname{rot}\mathbf{u} - \zeta_d|^2 d\Omega.$$

Here Ω_0 is a subdomain of Ω. The functionals J_1 and J_2 where functions $\mathbf{u}_d \in \mathbf{L}^2(\Omega_0)$ and $\zeta_d \in \mathbf{L}^2(\Omega_0)$ interpreted as measured velocity and vorticity fields are used to study the inverse problem for the models in questions. As the control we choose the function $\mathbf{g}$ for Navier-Stokes model and the pair $(\mathbf{g}, \chi)$ for heat convection model.

In order to formulate an extremum problem for the model (1)–(3) we split the set of all data of Problem 2 into two groups: the group of controls containing the functions $\mathbf{g} \in \mathbf{H}^{1/2}(\Gamma)$ and $\chi \in L^2(\Gamma_N)$ which play the role of controls and the group of fixed data comprising the invariable functions f and ψ. We assume that the controls $\mathbf{g}$ and χ vary in some convex sets $K_1 \subset \mathbf{H}^{1/2}(\Gamma)$ and $K_2 \subset L^2(\Gamma_N)$. The mathematical statement of the optimal control problem is as follows: seek a pair $(\mathbf{x}, u)$, where $\mathbf{x} = (\mathbf{u}, p, T) \in X$, and $u = (\mathbf{g}, \chi) \in K = K_1 \times K_2$ such relations (5) are satisfied and

$$J_i(\mathbf{x}, u) = I_i(\mathbf{x}) + \frac{\mu_1}{2}\|\mathbf{g}\|^2_{\mathbf{H}^{1/2}(\Gamma)} + \frac{\mu_2}{2}\|\chi\|^2_{\Gamma_N} \to \inf. \tag{6}$$

Here μ_1, $\mu_2 \geq 0$ are nonnegative constants.

According to the theory of extremal problems [IT79], we introduce an element $\mathbf{y}^* = (\xi, \sigma, \zeta, \theta, \zeta_1) \in Y^*$, to which we refer below as the conjugate state or Lagrange multiplier.

The following theorems establish sufficient conditions for solvability and local uniqueness in problem 2 and for solvability and the validity of the Lagrange principle and the regularity of the Lagrange multiplier. The proofs of the theorems are simular to those of the corresponding results in [Ale01].

Theorem 1. *Under conditions (i)–(iii) problem 2 has for any control* $(\mathbf{g}, \chi) \in K$ *weak solution* $(\mathbf{u}, p, T)$ *that satisfies the estimates* $\|\mathbf{u}\|_1 \leq M_{\mathbf{u}}$, $\|p\| \leq M_p$, $\|T\|_1 \leq M_T$ *where* $M_{\mathbf{u}}(u)$, $M_p(u)$ *and* $M_T(u)$ *are continuous nondecreasing functions of the norms of* $\mathbf{g}$, f, ψ *and* χ. *If additionally* $\mathbf{g}$, f, ψ *and* χ *are small in the sense that*

$$\frac{\gamma_0}{\delta_0\nu} M_{\mathbf{u}}(u) + \frac{1}{\delta_0\nu}\frac{\beta_1\gamma_1}{\delta_1\lambda} M_T(u) < 1, \tag{7}$$

then the weak solution to problem 2 is unique for any $u \in K$.

Theorem 2. *Let in addition to (i), (ii)* $\mu_1 > 0$, $\mu_2 > 0$. *Then the control problem (6) has at least one solution.*

Theorem 3. *Let under conditions (i), (ii)* $(\hat{\mathbf{x}}, \hat{u}) = (\hat{\mathbf{u}}, \hat{p}, \hat{T}, \hat{\mathbf{g}}, \hat{\chi})$ *be a local minimizer in problem (6) and let the functional* J *be continuously differentiable with respect to* $\mathbf{x}$ *at the point* $\hat{\mathbf{x}}$ *for any element* $u \in K$ *and be convex with respect to* u *for every point* $\mathbf{x} \in X$. *Then there exists a nonzero Lagrange multiplier* $(\lambda_0, \mathbf{y}^*) = (\lambda_0, \xi, \sigma, \zeta, \theta, \zeta_1) \in \mathbf{R}^+ \times Y^*$ *that satisfies the Euler-Lagrange equation*

$$\nu(\nabla \mathbf{w}, \nabla \xi) + ((\hat{\mathbf{u}} \cdot \nabla)\mathbf{w}, \xi) + ((\mathbf{w} \cdot \nabla)\hat{\mathbf{u}}, \xi) + \kappa(\mathbf{w} \cdot \nabla \hat{T}, \theta) - (\sigma, \operatorname{div} \mathbf{w}) +$$

$$\langle \zeta, \mathbf{w} \rangle_\Gamma + \lambda_0 \langle J'_{\mathbf{u}}(\hat{\mathbf{x}}, \hat{u}), \mathbf{w} \rangle = 0 \ \forall \mathbf{w} \in \tilde{\mathbf{H}}^1(\Omega), \quad (r, \operatorname{div} \xi) = 0 \ \forall r \in L_0^2(\Omega),$$

$$\kappa[\lambda(\nabla \tau, \nabla \theta) + \lambda(\hat{\alpha}\tau, \theta)_{\Gamma_N} + (\hat{\mathbf{u}} \cdot \nabla \tau, \theta) + \langle \zeta_1, \tau \rangle_{\Gamma_D}] +$$

$$(\beta \tau \mathbf{G}, \xi) + \lambda_0 \langle J'_T(\hat{\mathbf{x}}, \hat{u}), \tau \rangle = 0 \ \forall \tau \in H^1(\Omega). \tag{8}$$

for the conjugate state $\mathbf{y}^*$ *and satisfies the minimum principle*

$$\langle \zeta, \mathbf{g} - \hat{\mathbf{g}} \rangle_\Gamma + \kappa(\chi - \hat{\chi}, \theta)_{\Gamma_N} \le \lambda_0 [J(\hat{\mathbf{x}}, u) - J(\hat{\mathbf{x}}, \hat{u})] \ \forall u \in K. \tag{9}$$

Here $\langle \zeta, \cdot \rangle_\Gamma = \langle \zeta, \cdot \rangle_{\tilde{\mathbf{H}}^{1/2}(\Gamma)^* \times \tilde{\mathbf{H}}^{1/2}(\Gamma)}$, $\langle \zeta_1, \cdot \rangle_{\Gamma_D} \equiv \langle \zeta_1, \cdot \rangle_{H^{1/2}(\Gamma_D)^* \times H^{1/2}(\Gamma_D)}$ and κ is a dimensional parameter. The dimension $[\kappa]$ is chosen so that the dimensions of the values ξ, σ, θ for the conjugate state coincide with those of the corresponding values $\mathbf{u}$, p, T of the basic state. Relations (8) together with inequality (9) and weak statement (5) constitute an optimality system.

Theorem 4. *Let the assumptions of Theorem 2 be satisfied and inequality (7) holds for all* $u \in K$. *Then any nontrivial Lagrange multiplier satisfying (8) is regular; i.e. it has the form of* $(1, \mathbf{y}*)$ *and is uniquely determined.*

3 Numerical Analysis

The most interesting question is following: can we minimize "velocity" functionals I_1, I_2 by "temperature" boundary control χ when the function $\mathbf{g}$ is fixed? Therefore in this section we shall use only one control χ. In addition we assume that the set K_2 coincides with all space $L^2(\Gamma_N)$. Then the minimum will be reached in an internal point of set K and it is possible to replace the minimum principle (9) with identity $(\mu\chi - \theta, \psi)_{\Gamma_N} = 0 \ \ \forall \phi \in L^2(\Gamma_N)$. Having expressed from this relation χ by formula $\chi = \theta/\mu$ we can eliminate the control χ from the optimality system. We shall write down the received relations in the form of the operator equation $\Phi(\mathbf{u}, p, T, \xi, \sigma, \theta) = 0$. For its numerical solution the iterative algorithm based on the Newton's method is proposed. This algorithm consists of the following steps:

1. For given $(\mathbf{u}_0, p_0, T_0, \xi_0, \sigma_0, \theta_0)$ and supposing $\mathbf{u}_n$, p_n, T_n, ξ_n, σ_n and θ_n are known, we define $\tilde{\mathbf{u}}$, $\tilde{p}$, $\tilde{T}$, $\tilde{\xi}$, $\tilde{\sigma}$, $\tilde{\theta}$ by solving the following problem

$$\Phi'(\mathbf{u}_n, p_n, T_n, \xi_n, \sigma_n, \theta_n)(\tilde{\mathbf{u}}, \tilde{p}, \tilde{T}, \tilde{\xi}, \tilde{\sigma}, \tilde{\theta}) = -\Phi(\mathbf{u}_n, p_n, T_n, \xi_n, \sigma_n, \theta_n).$$

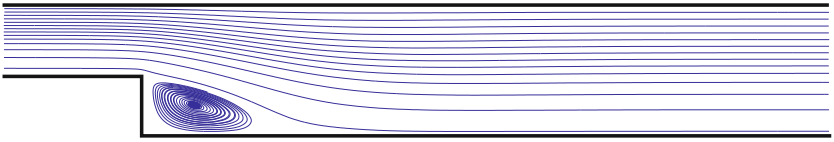

Fig. 1. Streamlines for uncontrolled flow (Re=200)

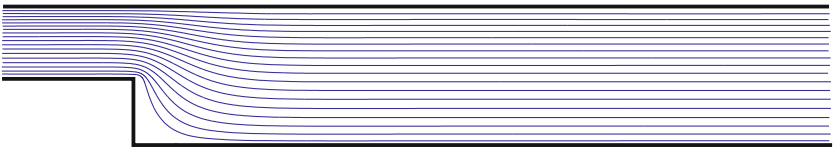

Fig. 2. Streamlines for controlled flow (Re=200)

2. Then we calculate new guesses $\mathbf{u}_{n+1}$, p_{n+1}, T_{n+1}, ξ_{n+1}, σ_{n+1}, θ_{n+1} for $\mathbf{u}$, p, T, ξ, σ, θ as

$$\mathbf{u}_{n+1} = \mathbf{u}_n + \tilde{\mathbf{u}},\ p_{n+1} = p_n + \tilde{p},\ T_{n+1} = T_n + \tilde{T},$$

$$\xi_{n+1} = \xi_n + \tilde{\xi},\ \sigma_{n+1} = \sigma_n + \tilde{\sigma},\ \theta_{n+1} = \theta_n + \tilde{\theta}.$$

3. If the condition $\|T_{n+1} - T_n\| < \varepsilon$ for some sufficiently small number ε is not satisfied, then we go to step 1.

We used free software Freefem++ (www.freefem.org) for the discretization of direct boundary-value problems by the finite element method.

The computational experiments showed that if the initial guess is selected sufficiently close to the exact solution, then the algorithm converges for several iterations. The regularization parameter μ_2 plays an important role. If its values are relatively large then we can not obtain small values of functionals J_i. But, from other side, the very small values of the regularization parameter can lead to the instability and oscillations in the numerical solution.

We consider the functional J_1. Following example is connected with the vortex reduction in the backward-facing-step channel by means of the "temperature" boundary control χ. The initial flow without controls is the solution of the nonlinear problem (5) with $f = 0$, $\psi = 0$, $\alpha = 0$, $\chi = 0$ and Reynolds number $\mathrm{Re} = 200$. The streamlines for this case are shown in Figure 1.

One can see that it is complicated flow with a vortex in the corner. The desired flow $\mathbf{u}_d$ is the solution of the linear Stokes equations.

We want to receive the solution $\mathbf{u}$ of the nonlinear problem (5) with Reynolds number $\mathrm{Re} = 200$ closed to desired velocity field $\mathbf{u}_d$. For this purpose we solve the extremum problem (6) with the functional J_1 and boundary control χ. The received flow is shown in Figure 2. Similar results have been received for the functional J_2 in the case of the vorticity minimization ($\zeta_d = 0$).

Looking at this flow we can see that in this problem the "temperature" control χ allows to create a velocity field with desired properties.

Acknowledgments. This work was supported by Federal Agency on Science and Innovations (project no. NSh-2810.2008.1) and Far Eastern Branch of the Russian Academy of Sciences (projects no. 06-I-P22-086, 06-II-SO-03-010, 06-III-A-01-011, 06-III-A-03-072).

References

[AT90] Abergel, F., Temam, R.: On some control problems in fluid mechanics. Theoret. Comput.Fluid Mech. 1, 303–325 (1990)

[GHS91] Gunzburger, M.D., Hou, L., Svobodny, T.P.: Analysis and finite element approximation of optimal control problems for the stationary Navier-Stokes equations with distributed and Neumann controls. Math. Comp. 57, 123–151 (1991)

[AM94] Alekseev, G.V., Malikin, V.V.: Numerical analysis of optimal boundary control problems for Navier-Stokes equations. Comp. Fluid Dynamics J. 3, 1–26 (1994)

[GHS93] Gunzburger, M.D., Hou, L., Svobodny, T.P.: The approximation of boundary control problems for fluid flows with an application to control by heating and cooling. Comput. Fluids. 22, 239–251 (1993)

[IR98] Ito, K., Ravindran, S.S.: Optimal control of thermally convected fluid flows. SIAM J. Sci. Comput. 19, 1847–1869 (1998)

[Ale98] Alekseev, G.V.: Solvability of stationary boundary control problems for heat convection equations. Sib. Math. J. 39, 844–858 (1998)

[LI00] Lee, H.-C., Imanuvilov, O.Y.: Analysis of optimal control problems for the 2-D stationary Boussinesq equations. J. Math. Anal. Appl. 242, 191–211 (2000)

[Ded07] Dede, L.: Optimal flow control for Navier-Stokes equations: Drag minimization. Int. J. Numer. Meth. Fluids. 55, 347–366 (2007)

[Ale01] Alekseev, G.V.: Solvability of inverse extremal problems for stationary heat and mass transfer equations. Sib. Math. J. 42, 811–827 (2001)

[Ale07a] Alekseev, G.V.: Uniqueness and stability in coefficient identification problems for a stationary model of mass transfer. Dokl. Math. 76, 797–800 (2007)

[Ale07b] Alekseev, G.V.: Coefficient inverse extremum problems for stationary heat and mass transfer equations. Comp. Math. Mathem. Phys. 47, 1055–1076 (2007)

[IT79] Ioffe, A.D., Tikhomirov, V.M.: Theory of Extremal Problems. North Holland, Amsterdam (1979)

[AT08] Alekseev, G.V., Tereshko, D.A.: Analysis and optimization in viscous fluid hydrodynamics. Dalnauka, Vladivostok (2008)

Frictional and Radiation Dampings on Shear Instability

Camilo E. Pinilla, Salem Bouhairie, and Vincent H. Chu

McGill University, Department of Civil Engineering and Applied Mechanics, Montreal, Canada H3A 2K6
vincent.chu@mcgill.ca

The effects of the friction and radiation dampings on shear instabilities were analysed using quasi-Direct Numerical Simulation (DNS) of a one-layer shallow-water model. The initial exponential growth rate of the instabilities were determined from the simulations over a wide range of conditions. The merging of eddies and the formation of shocklets were also simulated as nonlinear processes subsequent to the instabilities. The results were correlated with two dimensionless parameters. One of the parameter is the convective Froude number Fr_c which characterizes the radiation damping of flow disturbance energy, and correlates an analogous effect in compressible flow that is dependant on the Mach number. The other dimensionless parameter is the friction number which correlates the local damping of disturbance energy due to friction. Details of the linear and nonlinear developments of the instabilities are successfully simulated, and correlated with the two dimensionless parameters.

1 Introduction

Shear stability is a problem fundamental to understand a variety of processes in science and engineering. The classical approach to the problem is to impose normal modes of perturbations to the base flow. In this method, the governing equations of the flow are linearized. The eigenvalues associated with the modes are determined from the linear equations, so that the stability or the instability of the shear flow can be assessed. This normal mode approach (NMA) is based on a linear approximation. Weak nonlinear developments of shear flow instabilities can be derived at considerable expenses by perturbation expansion from the linear problem. An alternative approach to analyzing the shear stability problem is quasi-Direct Numerical Simulation (DNS) of two-dimensional depth-averaged equations of shallow flow. The method is equally efficient for both the initial linear problem and the nonlinear development. In shallow water, the surface gravity waves and the shear instability are components of the same flow, but occupy very different

widths of the shear flow. These components were accurately determined in the present quasi-DNS by selecting the correct computational domain. The numerical scheme for the DNS was based on the finite volume formulation with quadratic upstream interpolation and a total variation diminishing (TVD) procedure to manage spurious oscillations. The accuracy of the scheme was validated by first comparing the numerical results with those obtained by the NMA. The simulations produced the linear instabilities at within a short time period. Nonlinear instabilities occurred after a long time period, resulting in nonlinear processes such as the merging of eddies and the formation of the shocklets (hydraulic jumps) simulated by DNS.

2 Formulation

The equations governing the shear flow in one layer of shallow water are:

$$\frac{\partial h}{\partial t} + \frac{\partial hu}{\partial x} + \frac{\partial hv}{\partial y} = 0 \tag{1}$$

$$\frac{\partial u}{\partial t} + u\frac{\partial u}{\partial x} + v\frac{\partial u}{\partial y} - fv = -g\frac{\partial (h + z_o)}{\partial x} + \frac{\tau_{sx} - \tau_{bx}}{\rho h} \tag{2}$$

$$\frac{\partial v}{\partial t} + u\frac{\partial v}{\partial x} + v\frac{\partial v}{\partial y} + fu = -g\frac{\partial (h + z_o)}{\partial y} + \frac{\tau_{sy} - \tau_{by}}{\rho h} \tag{3}$$

where (u, v) = x- and y-components of the depth-averaged velocity, h = depth of the layer, z_o= bottom elevation, (τ_{sx}, τ_{sy}) = x- and y-components of driving force, (τ_{bx}, τ_{by}) = x- and y-components of the resistance force, g = gravity and f = coriolis parameter. These equations model the stratified flow of one layer, if g is replaced by the reduced gravity $g' = g\Delta\rho/\rho$. The layer can be a dense current in the atmosphere where its fluid is heavier than the fluid above the layer, or a surface current in the lakes and oceans where the its fluid is lighter than the fluid below the layer. Therefore, the simulation results obtained from these equations are generally applicable to free-surface flows in shallow river waters and coastal currents, as well as one-layer stratified flows in the atmosphere, lakes and oceans.

The numerical computations were carried out using the finite volume method in a staggered grid. The control volumes for the solution of the continuity equation and the momentum equations are staggered as shown in Figure 1(a). Values on the face of the control volume are first determined by quadratic interpolation, as shown in Figure 1(b). The spurious numerical oscillations if any are controlled by revising the face values to achieve TVD [BC06]. To account for the energy dissipation across the shocklets, the DNS are carried out using a momentum conserved formulation. The dimensionless parameters identified with the shear instability of the gravity waves are

$$\mathrm{Fr}_c = \frac{U_1 - U_2}{c_1 + c_2} = \text{convective Froude number}, \quad \mathrm{S} = \frac{\hat{G}}{\hat{U}\,\hat{U}_y} = \text{friction number}. \tag{4}$$

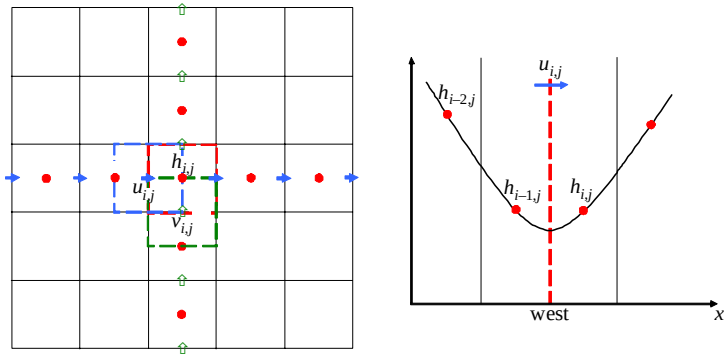

Fig. 1. (a) Staggered Grid. (b) Quadratic upstream interpolation for the west face of the control volume used to solve the continuity equation.

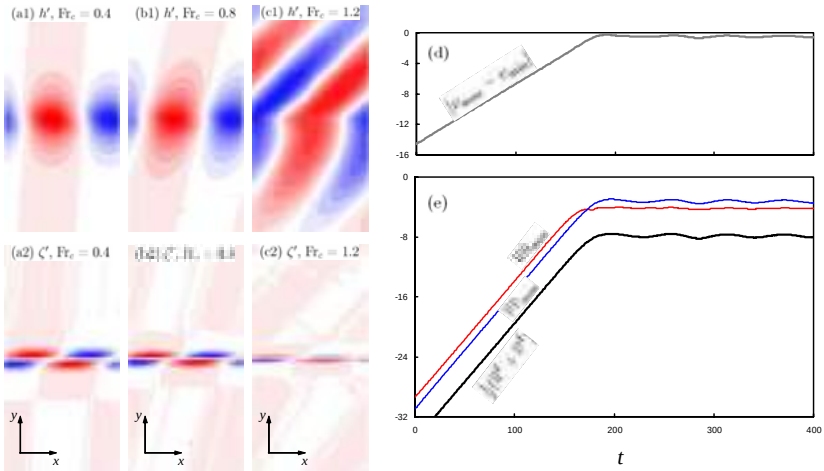

Fig. 2. Surface wave, h', and vorticity, ζ', profiles: (a) $\mathrm{Fr}_c = 0.4$, (b) $\mathrm{Fr}_c = 0.8$, (c) $\mathrm{Fr}_c = 1.2$. (d) The semi-logarithmic plot of $|v_{\max} - v_{\min}|$ has an initial slope of α. (e) All quadratics, $\overline{uu}_{\max}$, $\overline{vv}_{\max}$ and $\frac{1}{2}(\overline{u}^2 + \overline{v}^2)$, have the same initial slope of 2α.

In the expressions for Fr_c and S, $c_1 = \sqrt{gH_1}$, $c_2 = \sqrt{gH_2}$, are the celerities of the gravity waves; U_1 and U_2 are the velocity in the free streams; $\hat{U}$ and $\hat{U}_y$ are the velocity and its gradient at the inflection of the base-flow velocity profile. The subscripts correspond to the lateral free streams 1 and 2 on both sides of the mixing plane. Figure 2 (a), (b) and (c) show plan views of contours delineating depth fluctuation profile, h', and the vorticity fluctuation profile, ζ', for the shear flows having convective Froude numbers $\mathrm{Fr}_c = 0.4$, 0.8 and 1.2, respectively. The region of greatest vorticity reduces with the increasing the Froude number. The vorticity fluctuations ζ' define the shear instability,

while the depth fluctuations h' define the surface gravity waves. These two components do not necessarily occupy the same region. At Froude number $\mathrm{Fr}_c = 1.2$, the surface waves were excited and subsequently dominated a region much greater than that of the shear instabilities. The computational domain for the DNS extended from y = -192 to +192, in order to accomodate the surface waves.

3 Stability

From the DNS results, the growth rate of the shear instability, α, was determined by fitting the initial exponential growth on the semi-logarithmic plots, as shown in Figure 2 (d) and (e). The results are shown in Figure 3, where the growth rates α are correlated with the wave number k, the Froude number Fr_c, and the friction number S. Figure 3 (a) shows the analogy between the one-layer gravity stratified flows with the compressible flow. The points in the figure show the DNS results obtained for the gravity-stratified flows having convective Froude numbers Fr_c = 0.01, 0.4, 0.8 and 1.2. These are compared with the lines in the figure for compressible flows having convective Mach numbers, Ma_c = 0.01, 0.4, 0.8 and 1.2, obtained by the NMA of Sandham and Reynolds [SR91]. The close analogy between the instabilities

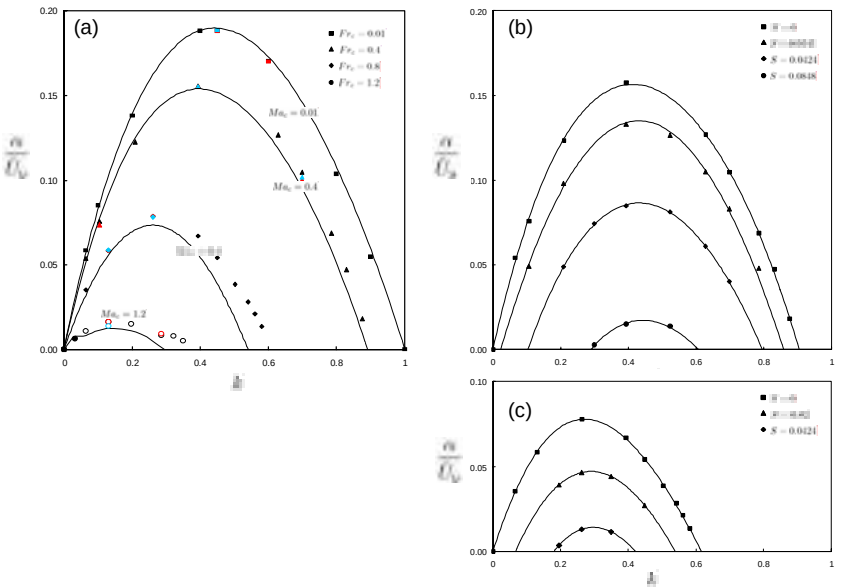

Fig. 3. (a) Rate of the initial exponential growth for flow with S = 0. Data show analogous dependence on the convective Froude number Fr_c and convective Mach number Ma_c. (b) Dependence on friction number; Fr_c = 0.4 and (c) Fr_c = 0.8.

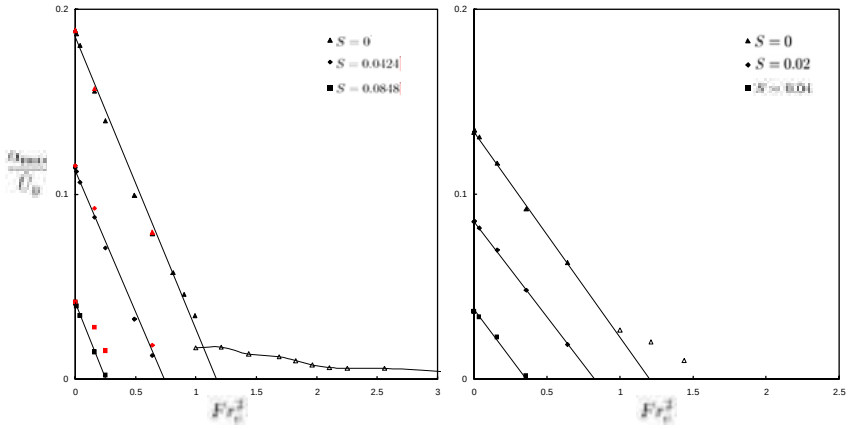

Fig. 4. Maximum growth rate $\alpha_{\max}$ as a function of the convective Froude number Fr_c and friction number S; (a) constant depth, (b) variable depth

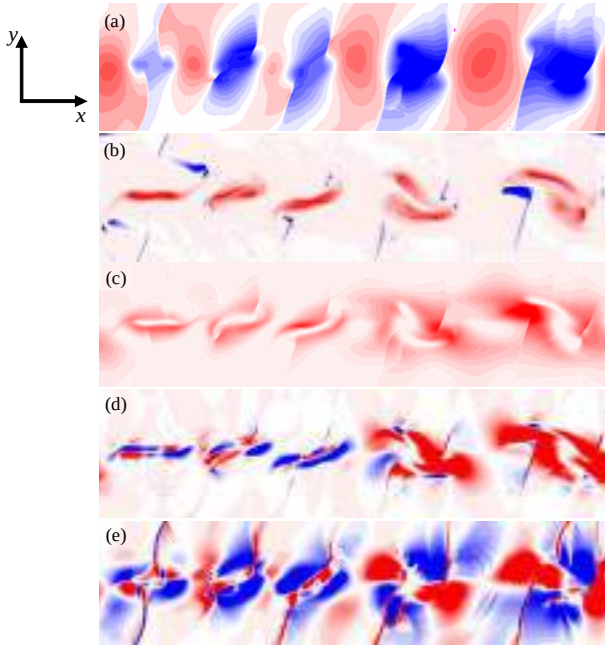

Fig. 5. Nonlinear development subsequent to the shear instability at Froude number $Fr_c = 0.8$; (a) free surface elevation, (b) vorticity, (c) turbulence intensity, (d) production, and (e) radiation

of the gravity stratified flow and the compressible flow is due to the remarkable similarity in the radiation damping of flow disturbance energy between the two flows. Given the Fr_c and S, a maximum growth rate was obtained. Figure 4 shows the maximum rate $\alpha_{\max}$, normalized by $\hat{U}_y$. Growth rate dependence on the convective Froude number Fr_c and friction number S is similar for both constant depth and variable depth. For subcritical instability, the general dependence on convective Froude number and friction number is

$$\frac{\alpha_{\max}}{\hat{U}_y} = 0.18\,[1 - \frac{S}{S_{crit}} - \frac{Fr_c^2}{Fr_{crit}^2}] \qquad \text{if} \qquad Fr_c < 1, \tag{5}$$

where S_{crit} and Fr_{crit} are respectively the critical values of the friction number and convective Froude number, when the growth rate of the disturbance's amplitude is reduced to zero.

Similar correlations with the convective Froude number and the friction number have been obtained for nonlinear development of the shear flow subsequent to the shear instabilities. When eddies and shocklet merge, as shown in Figure 5, the energy dissipation across the hydraulic jumps become significant. The full details of these and other DNS results were presented at the conference.

4 Conclusion

Shear instability and its subsequent nonlinear development over a wide range of conditions were determined by a quasi-DNS using a one-layer shallow model. The results are consistent with previous studies by the NMA [CW91] [SR91], and are successfully correlated with the friction and radiation dampings using two dimensionless parameters: Fr_c and S.

References

[BC06] Bouhaire, S., Chu, V.H.: Heated wake by deferred corrected ULTRA. In: Proc. 4th International Conference on Computational Fluid Dynamics, Ghent, Belgium, p. 6 (2006)

[CW91] Chu, V.H., Wu, J.-H., Khayat, R.E.: Stability of transverse shear flows in shallow open channels. J. Hydraulic Engineering 117(10), 1370–1388 (1991)

[SR91] Sandham, N.D., Reynolds, W.C.: Three-dimensional simulations of large eddies in the compressible mixing layer. J. Fluid Mechanics 224, 133–158 (1991)

FSI Analysis of HAR Wing at Low Speed Flight Condition

JeongHwa Kim[1], Y.-J. Park[1], H.-M. Kang[2], S. Jun[1], and Dong-Ho Lee[3]

[1] School of Mechanical and Aerospace Engineering, Seoul National University, Seoul, Korea
dubhe48@snu.ac.kr, heatfin@snu.ac.kr, ellga5@snu.ac.kr
[2] BK21 School for Creative Engineering Design of Next Generation Mechnical and Aerospace Systems, Seoul National University Seol, Korea
kangm@snu.ac.kr
[3] Institute of Advanced Aerospace Technology,
School of Mechanical and Aerospace Engineering, Seoul National University, Seoul, Korea
donghlee@snu.ac.kr

1 Introduction

Fluid-Structure coupling analysis is required to handle a interaction between the analysis of fluid mechanics and structural analysis. (In this study, the analysis of fluid mechanics is as follows: aerodynamic analysis) Because of inconsistency of aerodynamic grid and structural mesh, each result of analysis needs to be converted to be holding a compatibility of another analysis. Therefore, the Fluid-Structure Interaction (FSI) problem makes lots of difficulties and more studies are required.

High-aspect-ratio wing is applied in HALE (high-altitude, long endurance) aircraft commonly. Because HALE aircraft requires large lift to drag ratio and weight reduction, aspect ratio of wing is very large and structure of wing is flexible. This kind of wing deflects largely in normal operations.

Recently, many researchers have studied the HALE aircraft. Schoor and Flotow [SF90] researched the aeroelastic analysis for human-powered aircraft with high-aspect-ratio wing using linear beam model and two-dimensional aerodynamic model. Patil et al. [PHC01] studied the static aeroelastic and flutter analysis for high-aspect-ratio wing of HALE aircraft. Tang and Dowell [TD01] published the aeroelastic analysis using nonlinear beam model neglecting high order of geometrical nonlinearities over third order terms and ONERA aerodynamic stall model. Also they compared flutter instability boundary and Limit-Cycle Oscillations (LCO) caused by geometric structural nonlinearity with experimental results. Patil and Hodges [PH04] researched the aeroelastic analysis using nonlinear structural model and three-dimensional aerodynamic model. Yoo et al. [YLL04] studied the nonlinear static aeroelastic analysis using the transonic small disturbance (TSD) and large deflection beam theory.

The aerodynamic analyses for aeroelastic analysis of HALE aircraft wing have been based on the low fidelity models, such as either two-dimensional aerodynamic model or three-dimensional panel method. However, these approaches have some difficulties to consider the thickness and the camber of airfoil. Hence, the Computational Fluid Dynamics (CFD) technique needs to analyze aerodynamic loads more accurately. In this study, CFD analysis is used for aerodynamic model based on three-dimensional Euler equation. Finite Element Method (FEM) is applied to structural analysis, which uses beam element.

2 VMT Method

In VMT method, V represents Shear force, M for Moment and T for Torque. The VMT is the method used to transfer the aerodynamic load distribution into FEM mesh, to satisfy the force equilibrium in each airfoil section. In structural analysis, because the aerodynamic loads work dominantly in the direction of lift, analysis can be executed to focus only on the lift. However there is a great deal of complexity in the relation between CFD grid and FEM mesh. Thus, transfer of lift is difficult. To transfer lift distribution from CFD grid to FEM mesh, the VMT method is required.

Firstly, V, M and T of whole wing are calculated using aerodynamic loads distribution. Next, weighting factor $w_i = ax + by + c$, or coefficients a, b, and c are calculated to obtain the nodal forces of FEM mesh. (x and y are nodal coordinates of the FEM mesh.)

The VMT method can be expressed as follows.

$$\begin{cases} \sum_{i=1}^{N} f_i w_i = a\sum_{i=1}^{N} f_i x_i + b\sum_{i=1}^{N} f_i y_i + c\sum_{i=1}^{N} f_i = V \\ \sum_{i=1}^{N} f_i w_i y_i = a\sum_{i=1}^{N} f_i x_i y_i + b\sum_{i=1}^{N} f_i y_i^2 + c\sum_{i=1}^{N} f_i y_i = M \\ \sum_{i=1}^{n} f_i w_i x_i = a\sum_{i=1}^{N} f_i x_i^2 + b\sum_{i=1}^{N} f_i x_i y_i + c\sum_{i=1}^{N} f_i x_i = T \end{cases} \tag{1}$$

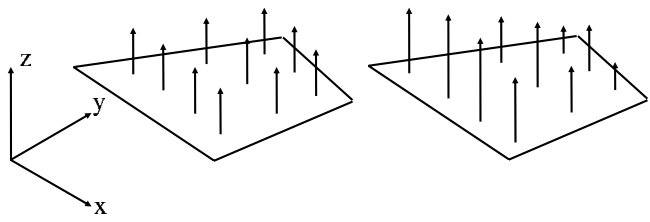

Fig. 1. Aerodynamic loads($F_z = p_i$) and nodal loads($F_z = f_i w_i$)

3 Transfer of Structure's Displacement

We assume that the configuration of the wing section does not change. This assumption is based on the fact that the spanwise bending and torsional motion are dominant among the wing deformations. The translation and rotation of wing section are caused by wing deformation.

After calculating the displacement of the structural model, we used method which maintains the configuration of the wing section and transfers the translation and the rotation of the section. The surface grid is moved with this method, volume grid is regenerated using the surface grid.

4 Fluid-Structure Interaction Analysis

In this study, I used a static aeroelastic analysis to solve the fluid-structure interaction problem. The static aeroelastic analysis analyzes the wing deformation, caused by static loads. For example, gravity force, steady state aerodynamic loads are static loads. The aerodynamic loads make structural deformations, and these structural deformations also affect the next aerodynamic loads. To find a solution, we evaluate the structural and aerodynamic problems, repeatedly, because these processes interact with each other. In general, loose coupling and strong coupling approach are most conventional methodologies in solving the static aeroelastic problem. This study uses loose coupling to analyze aeroelastic problem.

5 Wing Model

My numerical example is based on the experimental wing model studied by Tang and Dowell. The wing is rectangular, untwisted, flexible, and high-aspect ratio wing with a slender body at the tip. Physical Representation of the wing model is shown in Fig. 2.

Span length is 0.4508m, chord length is 0.0508m, and mass of slender body at tip is 0.0417kg. Further information is given in the reference [TD01].

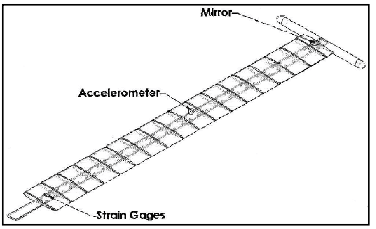

Fig. 2. Physical representation of wing model

The wing section is NACA 0012 airfoil. Root-support mechanism is a socket that allows a change in the steady angle of attack at the root. Therefore, the cantilevered condition is selected as the boundary condition for structural analysis. Because the lift is dominant in this system, which laterally acts on the wing, the beam element are used.

6 Results

In this section, static deflection under gravity loading and static aeroelastic deflections of wing will be presented. Static aeroelastic analysis is performed in two flow conditions.

1) Mach number = 0.1, angle of attack = 2.2 deg.
2) Mach number = 0.1, angle of attack = 1.0 deg.

Because the effect of aerodynamic loads is small, the slender body of the tip was not considered for aerodynamic analysis.

6.1 Static Deflection under Gravity Loading

This analysis was performed to validate structural model and to obtain the initial state. Tip deflection is -59.2mm, this value is approximately 0.06m. This result is similar to experimental data reported by Tang and Dowell [TD01]. Therefore, we can conclude that the structural wing model is well built.

6.2 Static Aeroelastic Deflections of the Wing

The results are shown in Fig. 4. and Fig. 5. for an angle of attack 2.2 deg. Fig. 4. shows shape deformations of wing model, and Fig. 5. shows the converged state of the wing tip deflection. After the wing tip is repeatedly deflected upward and downward during the transient state, a converged shape is obtained. However, quantities of deflection change are decreased gradually. Converged tip deflection 110.0mm is almost equal to experimental data reported by Tang and Dowell [TD01].

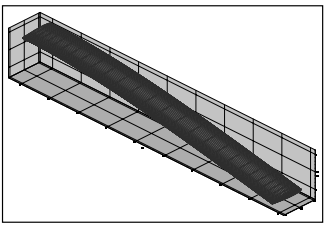

Fig. 3. Initial shape under gravity loading only

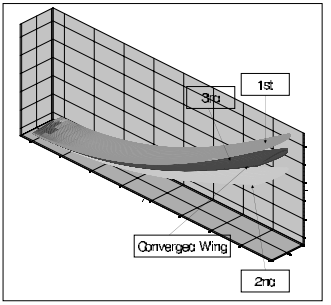

Fig. 4. Static aeroelastic deflection of the wing for angle of attack 2.2 deg

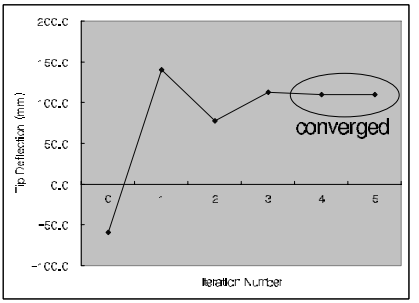

Fig. 5. Converged state of the wing for angle of attack 2.2 deg

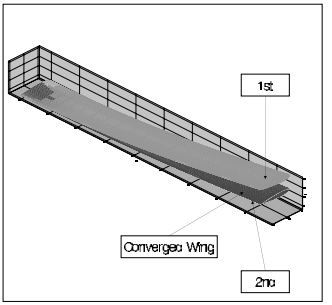

Fig. 6. Static aeroelastic deflection of the wing for angle of attack 1.0 deg

Fig. 6. and Fig. 7. show the static aeroelastic deflection at the tip for an angle of attack 1.0 deg. At flow velocity 34.5m/s (M = 0.1), the aerodynamic forces provide minimum lift to overcome the effect of gravity. Compare to the results for an angle of attack 2.2 deg., the magnitude of the converged static aeroelastic deflections is less than those for the angle of attack 2.2 deg.

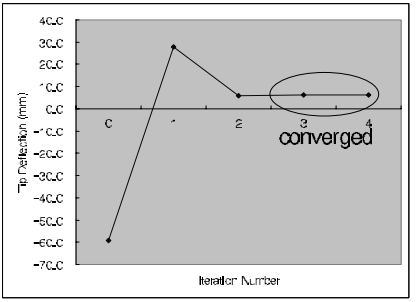

Fig. 7. Converged state of the wing for angle of attack 1.0 deg

7 Conclusions

Fluid-Structure Interaction analysis has been conducted on a high-aspect ratio wing that has a beam-like structural behavior. The high-aspect ratio wing showed the corresponding large deflections under the aerodynamic loads. And the effect of large deflections changed the aerodynamic loads. It is a typical behavior of the fluid-structure interaction problems.

Static aeroelastic study has been performed using 3-dimensional Euler solver and nonlinear FEM solver. And from this study, the VMT method and loose coupling approach are very successful in solving the fluid-structure interaction analysis.

Acknowledgement. This work was supported by Defense Acquisition Program Administration and Agency for Defense Development under the contract UD070041AD. And this work was supported by the second stage of the Brain Korea 21 Project in 2008.

References

[PHC01] Patil, M.J., Hodges, D.H., Cesnik, C.E.S.: Nonlinear Aeroelasticity and Flight Dynamics of High-Altitude Long-Endurance Aircraft. Journal of Aircraft 38(1), 88–94 (2001)

[TD01] Tang, D., Dowell, E.H.: Experimental and Theoretical Study on Aeroelastic Response of High-Aspect-Ratio Wings. AIAA Journal 39(8), 1430–1441 (2001)

[SF90] van Schoor, M.C., von Flotow, A.H.: Aeroelastic Characteristics of a Highly Flexible Aircraft. Journal of Aircraft 27(10), 901–908 (1990)

[PH04] Patil, M.J., Hodges, D.H.: On the importance of aerodynamic and structural geometrical nonlinearities in aeroelastic behavior of high-aspect-ratio wings. Journal of Fluids and Structures (19), 905–915 (2004)

[YLL04] Yoo, J.-H., Lim, I.-G., Lee, I.: Nonlinear Static Aeroelastic Analysis of a High-Aspect-Ratio Wing with Large Deflection Effects. Journal of the Korean Society for Aeronautical and Space Sciences 34(3), 31–36 (2006)

Part 19
Flow in Porous Media

“*This page left intentionally blank.*”

3-D Numerical Simulation of Main Sieve Diaphragm with Three Types Passageway Design in a Gas Mask Canister

Chun-Chi Li[1], Jr-Ming Miao[1], Chin-Chiang Wang[2], Yin-Chia Su[2], and Tzu-Yi Lo[2]

[1] Department of Mechatronic, Energy and Aerospace Engineering, Chung Cheng Institute of Technology, National Defense University, Taiwan, R.O.C. davidli@ndu.edu.tw

[2] Master Program of Mechanical Engineering, Chung Cheng Institute of Technology, National Defense University, Taiwan, R.O.C.

Summary. This paper focuses on the passageway design of the main sieve diaphragm that is the key point to reduce the pressure drop of a gas mask canister. Three types of the passageways are designed to explore the aerodynamic behaviors of the flow inside a canister. The models include the hole, rib-strip and honeycomb types. The 3-D numerical simulations of flows have been applied to determine the pressure drops in the models. The simulation results reveal the smallest pressure drops on the passageway of honeycomb type, because the structure of honeycomb type is stronger enough to avoid the deformation of the main sieve diaphragm. So the passageway of honeycomb type can provide larger channel area and more uniform channel distribution to reduce the pressure drop. The analysis of the flow structure, such as the velocity profile and the distribution of dead zone in the models, is also studied.

Keywords: main sieve diaphragm, gas mask canister, porous media, air age.

1 Introduction

After the 911 terror-attack, the gas masks are not only for soldiers to use in the battle fields, but also for people to regard these masks as necessities for their daily lives. Therefore, the gas masks are bringing the potential commercial opportunities in the markets. On the basis of the design of gas mask and in addition to confirming the standard of toxic filtering, the low pressure drop of respiratory is the other considerable factor. The pressure drop of a gas mask mainly results from inhaling gas through the canister. The canister generally consists of the filter layer and activated carbon layer. Both layers are defined as porous media significantly causing the pressure drop. The filter layer consists of multi-pleated filter papers enabling to block suspended particles. The activated carbon layer can functionally adsorb and filter toxic gases. Generally, to connect the filter layer and the activated carbon layer is

a main sieve diaphragm that is an only passageway to permit gas entering activated carbon layer.

To the design of this kind of porous media filters, like gas mask canister or industrial filters, the aerodynamic behaviors of fluids, such as pressure drop and flow structure, are the most vital factors in the flow dynamic system [1]. The flow structures should prevent from forming the preferential flow and the dead zone. Due to the opaqueness of the absorbent, it would not be experimentally observed the inner flow structures through the sizes and locations of the preferential flow and dead zones. It will be helpful to explore the aerodynamic characteristics of the flow field for the references of the design and improvement, through employing the CFD tools to analyze the flow variables in porous media inside the filter. According to the fluid dynamics of porous media, it generally obeys the Darcy's equation at low Reynolds number. In this equation, the pressure drop is satisfied with the linear relation as below.

$$-\Delta P/L = (\mu/\kappa)V_s \tag{1}$$

where ΔP is the pressure drop of porous medium zone, L is the length in flow direction, κ is the permeability, μ is the fluid viscosity and V_s is the superficial velocity entering porous medium zone.

When the superficial velocity or Reynolds number increases, the inertia effect is gradually to increase. A second order parabolic equation can describe the inertia effect that is called the Forchheimer's equation, shown as below.

$$-\Delta P/L = \alpha\mu V_s + \beta\rho V_s^2 \tag{2}$$

where α is the reciprocal permeability of porous material, it also called viscous parameter. β is usually called the inertial parameter.

Previous authors have used CFD tools to analyze porous filters, but their primary focus was to analyze the fluids flow through different arrays of the spatial microstructure of a filter media in 2-D or 3-D simulations [2-4].The point which most previous studies have in common is that they focused on a single type of porous media. However, very little existing literature analyzes the aerodynamic characteristics of a gas mask canister. Therefore, the topic of the aerodynamic behavior of a gas mask canister with two kinds porous materials is worthy of further research.

Li & Miao, used CFD to simulate a gas mask canister containing two porous media [5]. The passageway of main sieve diaphragm in the canister was hole type. The effects of the distribution and area of holes in the main sieve diaphragm and the thickness of the activated carbon layer on the pressure drop and the aerodynamic flow behavior inside the canister body were determined. The results revealed the flow structures in the activated carbon layer were dominated by the passageway distribution of main sieve diaphragm. Better hole distribution and a larger hole area corresponded to a lower pressure drop, a smaller dead zone, and a higher adsorption time. In present study, we design three types of the passageways to explore the aerodynamic behaviors of

the flow inside a canister. The design of passageway on main sieve diaphragm should be optimized by considering not only how to reduce the pressure drop and the weight of activated carbon layer, but also the structural strength and the limitations of the manufacturing technique used. The analysis of the flow structure, such as the velocity profile and the distribution of dead zone in the models, is also studied.

2 Problem

2.1 Governing Equations

The governing equations herein include the continuity and momentum equations, both of which obey the conservation principle,

$$\frac{\partial}{\partial x_i}(\rho u_i) = 0 \ , \tag{3}$$

$$\frac{\partial}{\partial x_j}(\rho u_i u_j) = -\frac{\partial P}{\partial x_i} + \frac{\partial \tau_{ij}}{\partial x_j} + \rho g_i - \frac{\partial}{\partial x_j}(\rho \overline{u_i' u_j'}) + S_i \ , \tag{4}$$

where ρ is the fluid density; u_i is the velocity component in the i direction;p is the pressure; τ_{ij} is the viscosity shear stress tensor; g_i is the acceleration due to gravity in the i direction; $\rho\overline{u_i' u_j'}$ is the Reynolds stress term, related to the mean flow by the Boussinesq hypothesis when the flow is not laminar, and S_i is a source term that describes the pressure gradient in the porous medium, and is defined by Eq. (2) and is assumed to be isotropic. The turbulent model is adopted the $\kappa-\varepsilon$ turbulent model with low-Reynolds number[6]. The working gas is air, for which $\rho = 1.225 kg\, m^{-3}$ and $\mu = 1.7894 \times 10^{-5} kg\, m^{-1} s^{-1}$.

The air age equation is

$$\frac{\partial}{\partial x_i}(\rho u_i \tau) = \frac{\partial}{\partial x_i}(\frac{\mu_{eff}}{\sigma_\tau}\frac{\partial_\tau}{\partial x_i}) + \rho \ , \tag{5}$$

where τ is the air age; $\mu_{eff} = \mu_l + \mu_t$ (where μ_{eff} is effective viscosity, μ_l is molecular viscosity and μ_t is turbulent viscosity) and $\sigma_\tau = 1$ is the turbulent Schmidt number.

2.2 Boundary Conditions and Numerical Method

At the inlet of the canister, a constant velocity value is imposed. The outlet boundary condition is the outlet pressure boundary. The no-slip condition was assumed at the solid wall. The central axial plane of the canister is regarded as a symmetrical boundary.

The 3-D numerical simulations of flows have been applied to determine the pressure drops in the models. The flow variables in present models are solved by the Navier-Stokes equations adding to the low Reynolds number

$\kappa - \varepsilon$ turbulent model. The pressure gradient is calculated by Forchheimer's equation to add to the source term of the momentum equation. The air age is employed to represent the resident time of gas in a canister. The finite volume method based on the cell center is used in the models. We discretize the integral form governing equations based on unstructured tetrahedron grid. The convection term is discretized by the one-order upwind scheme and the viscous term is discretized by central differential scheme. The solution algorithm for pressure-velocity coupling is the SIMPLE algorithm and related discretization algebraic equations are solved using the TDMA method.

2.3 Grid Configuration

According to the research of Li & Miao, we know the passageway design of the main sieve diaphragm that is the key point to reduce the pressure drop of a canister. In this paper, three types of passageways are designed to explore the aerodynamic behaviors of the flow inside a canister. The mesh of models including the hole, rib-strip and honeycomb types are shown in Figure 1. All the results presented here are grid-independent. The residual convergence criterion in all cases was less than 1×10^{-4}.

3 Result and Discussion

We used curve fitting to estimate the viscous and inertia parameters of the porous media in accordance with the experimental data. The simulation results of the estimated inertial and viscosity parameters in the Forchheimer's equation are in good agreement with the experiment. The more details see the [5]. In the following simulations, the same parameters are used. Figure 2(a-c) shows the velocity contours of hole, honeycomb and rib-strip types at the flow rate of 30 L/min. Figure 2(a) shows that since the outermost holes are sealed and and the porous flow causes momentum loss, the

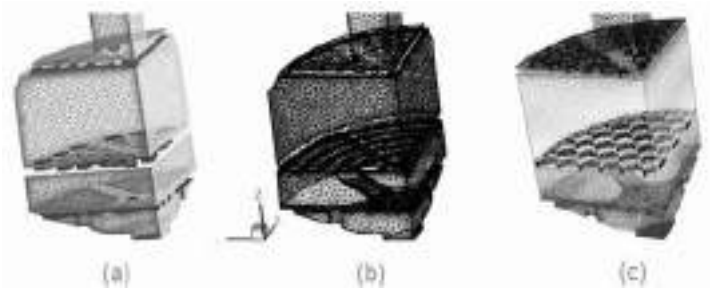

Fig. 1. Mesh system of three types of passageways on a gas mask canister. ((a) hole type, (b) rib-strip-type and (c) honeycomb type).

gas flowing through the open holes of the main sieve diaphragm does not easily flow past the outer part of the activated carbon layer. Thus, a larger low-velocity zone called dead zone forms in this area. Figure 2(b) shows that the rib-strip design of the main sieve diaphragm in models H_1, the original low-velocity region in Fig 2(a) decreases in size. Figure 2(c) shows that the honeycomb design of the main sieve diaphragm in models J_1, the low-velocity region almost disappears.

Employing the flow variable distributions described by the air age index, it is much easier to judge the position of the dead zone through observing the flow structure inside the activated carbon layer. Figure 3(a-c) appears the contours of air ages of the hole, rib-strip and honeycomb types. Models A_1, with sealed outermost holes, clearly have a large zone of higher air age outside the activated carbon layer (Fig. 3(a)). The gas cannot flow easily through this zone, and a large dead zone is formed. Figure 3(b) shows that the original dead zone in Fig 3(a) apparently shrinks, but a little dead zone still exists at the corner of wall. Figure 3(c) shows that the dead zone almost disappears in Model J_1. Figure 4 shows the velocity profile of three type passageways. The velocity profile of honeycomb type is more uniform than those of others. The local parts of high or low velocity profiles form the preferential flow or the dead zones result in increasing the pressure drops of a canister.

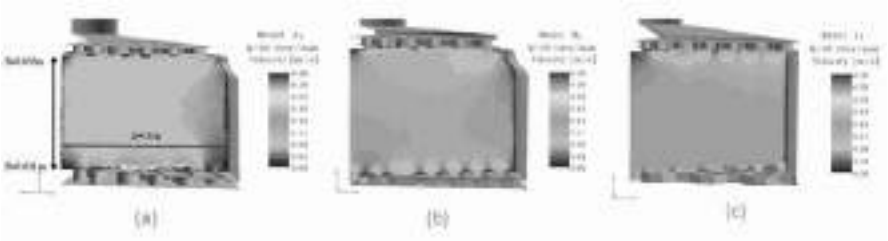

Fig. 2. The velocity contours in the activated carbon layer under the condition of flow rate, 30 L/min. ((a) hole type, (b) rib-strip-type and (c) honeycomb type).

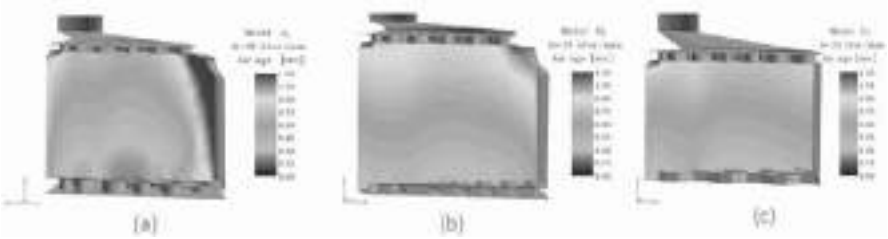

Fig. 3. The air age contours in the activated carbon layer under the condition of flow rate, 30 L/min. ((a) hole type, (b) rib-strip-type and (c) honeycomb type).

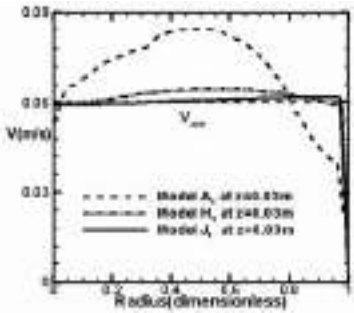

Fig. 4. Velocity profile of three types of models at 30 L/min

4 Conclusion

Equations for a porous medium describe the relationship between the superficial velocity and the pressure drop from a macro perspective. A higher superficial velocity corresponds to a greater pressure drop. According to the continuity equation, the product of the superficial velocity and the flow-through area yields the volumetric flow rate. Consider model A_1 as an example: the passageway of main sieve diaphragm yields a non-uniform velocity profile. Fluid does not flow easily into the resulting low-velocity zone, yielding a dead zone. Hence, the overall superficial velocity in the activated carbon layer increases, increasing the pressure drop. In contrast, the passageway of honeycomb design yields a more uniform velocity profile, as in model J_1, reducing the size of the dead zone, and reducing the superficial velocity in the activated carbon layer, thereby reducing the pressure drop. Using the advantages of CFD, the positions of the dead zones and the preferential flow can be identified, providing great assistance in the design of improved main sieve diaphragms.

To summarize the research results, the conclusions can be obtained as follows: comparing with the three types of the passageways, because the structure of honeycomb type is stronger enough to avoid the deformation of main sieve diaphragm, so the main sieve diaphragm of the honeycomb type own the larger channel area and better channel distribution to reduce the pressure drop.

References

1. Subrenat, A., Bellettre, J., Le Cloirec, P.: 3-D numerical simulations of flows in a cylindrical pleated filter packed with activated carbon cloth. Chemical Engineering Science 58(22), 4965–4973 (2003)
2. Dhaniyala, S., Liu, B.Y.H.: An asymmetrical, three-dimensional model for fibrous filters. Aerosol Science and Technology 30(4), 333–348 (1999)
3. Liu, Z.G., Wang, P.K.: Numerical investigation of viscous flow fields around multifiber filters. Aerosol Science and Technology 25(4), 375–391 (1996)

4. Thomas, D., Contal, P., Renaudin, V., Penicot, P., Leclerc, D., Vendel, J.: Modelling pressure drop in HEPA filters during dynamic filtration. Journal Aerosol Science 30(2), 235–246 (1999)
5. Li, C.C., Lio, K.C.: Aerodynamic behavior of a gas mask canister containing two porous media. Chemical Engineering Sci. (submitted) (2008)
6. Jones, W.P., Launder, B.E.: The calculation of low-Reynolds-number phenomena with a two-equation model of turbulence. Int. Journal Heat Mass Transfer 16(6), 1119–1130 (1973)

“*This page left intentionally blank.*”

Pore Scale Simulation of Combustion in Porous Media

May-Fun Liou and HyoungJin Kim

NASA Glenn Research Center, Cleveland, OH 44135, USA

Abstract. This paper describes an improved methodology for studying combustion in porous media in pore scale. Porous media combustion is one technology having advantages over the conventional combustion system. Examples of combustion in porous media are presented to show the potential application of the present mesh-based microstructure representation algorithm (MBMRA).

Keywords: Porous media, Mesh refinement, Combustion, Flame.

1 Introduction

The combustion research in porous medium has been conducted from the early development. The applications range broadly from internal combustion engines to nuclear waste storage tanks. In simulating flows in natural or manufactured porous materials, fluid and thermal transport are usually modeled using the continuum approach in terms of appropriate averaged parameters in which the real pore structure and the associated length scales are not considered; instead their effects are accounted for by averaging over the pores in a global manner. However, those averaged parameters can only be obtained by experiments and are strongly dependent on the types of microstructure and operating conditions. Often, the models are grossly simplified and do not account for the effects of micro-scales acted on meso or macro scales. The dispersion effect, which significantly changes the behavior of mass and thermal transport, is difficult to be adequately quantified by experiments or global theories.

In conventional CFD approach, a prescribed physical domain of porous medium with existing fluid-solid interface is mapped onto a computational domain, which is then geometrically discretized by mesh generation. This would become a formidable task if hundreds or thousands of pores of irregular shapes were to be mapped. To overcome this hurdle, we have developed a mesh-based microstructure representation algorithm (MBMRA) [1].

In this paper, we present an improved MBMRA over the earlier development by incorporating a mesh adaptation scheme. The local refinement of mesh in the surroundings of a solid structure in the porous media offers an efficient grid distribution and a cost-effective use of computing time. The degree of refinement is based on the minimum distance from solid cells, and the refinement is typically done by connecting midpoints of cell edges (thus, a triangle is divided into 4 subelements in 2D). A smoothing mechanism is added to blend fine meshes into coarse ones smoothly. The refinement is completed by a bisection refinement

(dividing into 2 sub-elements) to eliminate hanging nodes. A refined two-dimensional unstructured triangular mesh MBMRA is illustrated in Fig. 1. The shaded area in (a) is a sample solid which is composed of three triangular cells. After the refining processes described above, new meshes are produced, shown in (b), and their corresponding connectivity are rebuilt. Also, the sample solid has increased its mesh from three triangular cells to 26 elements which allow a more effective conjugate heat transfer simulation.

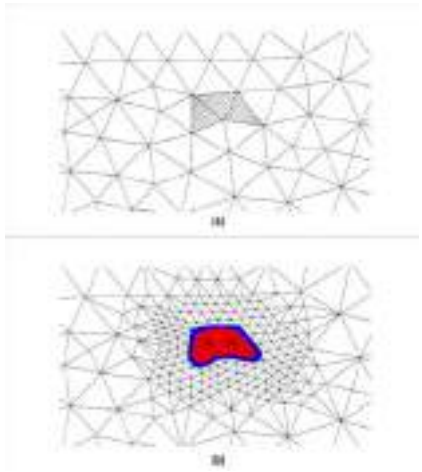

Fig. 1. (a) Original MBMRA mesh distribution around a sample solid; (b) Refined mesh distribution of the same solid sample

1.1 Test Case

NASA's National Combustion Code (NCC) is a set of tools for analyzing and designing combustion systems over a wide range of Mach numbers. Its chemistry tool permits users an arbitrary number of reactions and species. It is used to incorporate the MBMRA methodology because it has been subject to validation tests for a broad range of combustion problems. In this study, both non-reacting and reacting flows are used for validation.

First, a two dimensional flow over a circular cylinder is considered to test the ability of the refined MBMRA for capturing an unsteady flow around a single solid body at a higher Reynolds number. This is a standard benchmark case for unsteady flow problem, and various experimental and computational references are available in the open-literature, e.g., Roshko [2] and Visbal [3].

A cylinder of diameter of 0.1 m is considered. A triangular mesh of 11736 cells is generated originally, with 1074 solid elements representing the cylinder. Refinement as aforementioned is applied surrounding the cylinder to help facilitate solution convergence and reduce numerical oscillations. A total of 18002 elements are used in the computation, see Fig. 2. The insert at the right upper corner of Fig. 2 shows the mesh zoomed around the solid cylinder. The first grid

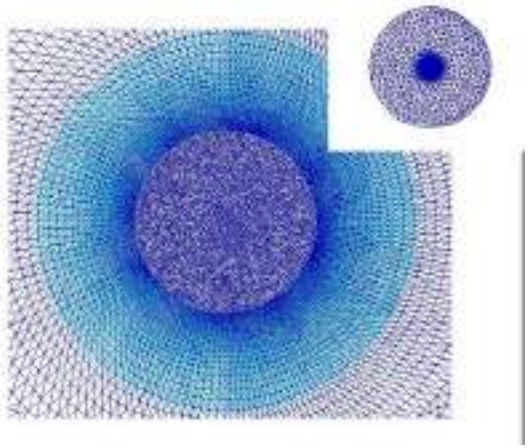

Fig. 2. A triangular mesh over the circular cylinder, consisting of a refined mesh, in cyan color, around the cylindrical solid – enlarged view given in the inset

spacing away from the cylinder, Δy_w, is $5x10^{-4}$ m. The adiabatic and no-slip conditions are imposed on the surface of cylinder. The left half of the outermost grids is assigned the inflow conditions (u = 0.1 m/s, v = 0 m/s, ρ = 0.187 kg/m3) while the other half is imposed with a fixed pressure p and with extrapolations of other variables from their interior values. The resulting Re_D (Reynolds number based on diameter) is 64, lying in the range in which the existence of unsteady vortex shedding is ensured.The contours of longitudinal velocity component u are plotted in Fig. 3. The contours indicate that the flowfield is fully developed. A small reversed flow, denoted by the dark blue color, is formed behind the cylinder. The computed Strouhal number (St) is 0.161, a close agreement with the experimental values of 0.16-0.17, reported by Roshko [2]. Thus, this MBMRA generated single solid body case provides a quantitative comparison with experimental data.

Next, the Sandia's piloted methane-air flame D, which consists of a main jet with a mixture of 25% methane and 75% air by volume, is simulated. It has been demonstrated that NCC can provide numerical results in excellent agreement, in terms of temperature and species, with the experimental results by Norris et al. [4]. In addition, an open flame calculation through a porous zone, as described in Sandia's flame, is compared with the Sandia test results. Figure 4 shows the resulting temperature contours for this case. The top plot shows the steady state solution of Snadia D-Flame while the bottom plot indicates the flame was deflected by the existence of porous medium situated at the center of the flow domain. A case of the flame burning inside a channel was studied with a 10 steps, 12 species finite-rate chemistry. The results without and with a porous medium of porosity 0.95 are shown in Fig. 5 (a) and (b) respectively. Similar to the Sandia case, the closed flame in channel is deflected through the porous zone. In this section, the MBMRA technique has been applied in dealing with non-reacting and reacting flows in porous medium.

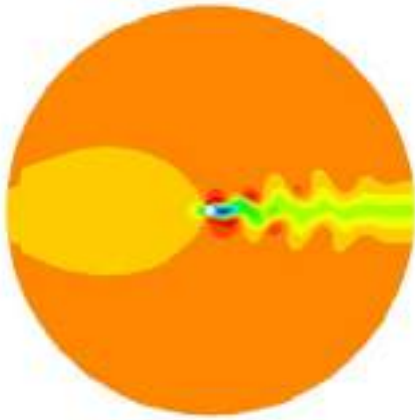

Fig. 3. Velocity contours showing vortex-shedding behind a circular cylinder (Re_D=64)

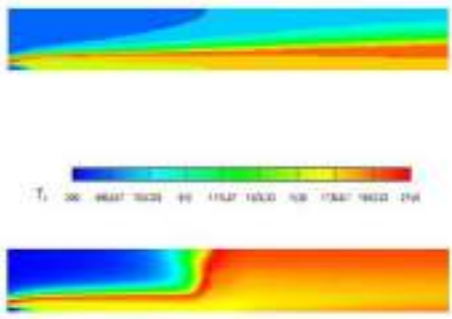

Fig. 4. Temperature contours. Top: Sandia's D-Flame; Bottom: Flame through a porous zone in the open flame case.

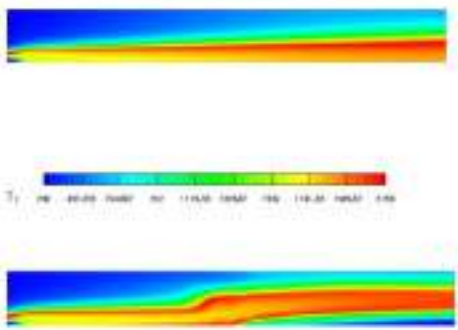

Fig. 5. Top: Flame propagating into porous zone inside a channel; Bottom: Flame propagating in clean/non-porous channel at steady state

2 Dump Combustor

Dump combustors are widely used in modern air breathing propulsion systems for its geometrical characters. A sudden expansion in dump combustor usually causes flow to separate and creates a low speed recirculation zone. A well-designed dump combustor will provide reactants sufficient residence time in the vortex to fully react, thus producing a larger energy conversion and a wider stable operating condition. We consider a dump combustor with a swirler mixing the combustion air radially and axially with the premixed and pre-heated methane fuel. A low Reynolds number κ- ε turbulent model and the Magnussen eddy dissipation model are used. The Magnussen chemistry model, a simplified chemical kinetic mechanism, is governed by flow field turbulence quantities. Figure 6 shows the computational domain of 21,000 cells. Particle traces are displayed with the axial velocity contours in Fig. 7 to show the effect of swirler. Figure 8 shows the temperature contours and fuel mass fraction at mid-plane (y = 0) of this combustor. Magnussen model, known for predicting a fast heat release, has resulted in high velocities in the swirler zone and high temperatures in the same area as shown in Figs. 7 and 8.

To enhance the mixing of fuel and oxidant, a section of porous material with porosity of 0.485 is inserted at the ignition zone of this dump combustor, as shown in Fig. 6. The porous material is Silicon Nitride (Si3N4), which has the following thermal properties, heat conductivity (K) of 25 W/K-m and heat capacity (Cp) of 0.5 KJ/(Kg-K). There are additional 30,000 computational elements after refining meshes around solid structures within porous zone. Figure 9 shows the location of the porous medium by plotting iso-surface of density. The red color indicates solid and blue for air. The rest of colors show where the intertwining flow passages. The same flow and boundary conditions as the clean dump combustor are applied in this porous combustor. Figure 10 is a cross sectional cut (y-z plane) of the porous region.

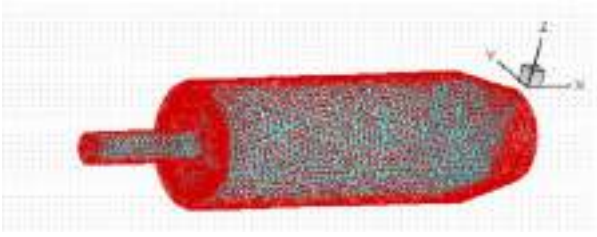

Fig. 6. Computational mesh used for the dump combustor analyses. The cyan color indicate the plane of y = 0.

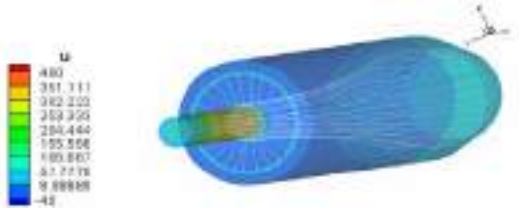

Fig. 7. Particletraces through the inlet and radial swirler surface plotted with contours of axial velocity

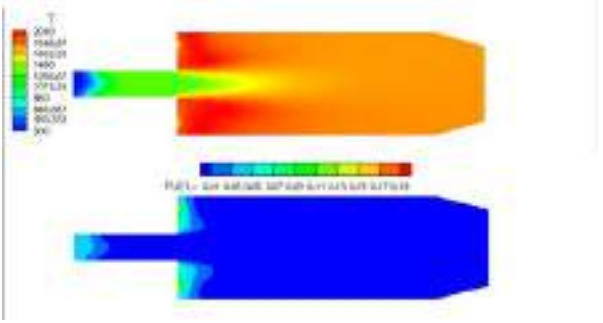

Fig. 8. Chemical reaction results in a dump combustor, contours of temperature and fuel mass fraction distributions in the y = 0 plane

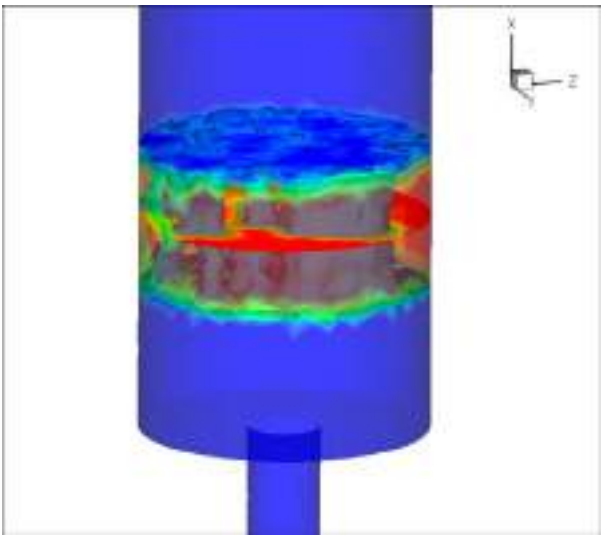

Fig. 9 Using porous microstructure as a mixer in dump combustor: density contours of gas-phase (air) and solid-phase (Si3N4)

The results obtained indicates that the inserted porous structure increases the mixing of fuel and oxidant, as shown in particles tracing through the entire flow field in Fig. 11. It is also displayed in terms of turbulent kinetic energy (κ) in Fig. 12. The top plot in Fig. 12 is the κ-contours from the porous case comparing to the clean dump combustor shown in the bottom figure. The intensified turbulent activity inside the porous medium is obvious. In addition to turbulence, the propensity of a combustion system to burn is also dependent on other factors, such as fuel type, calorific value, mixture, pressure, velocity, and enclosure geometry. In this porous geometry, the added ignition heat is conducted away sufficiently fast that the temperature is reduced below thse spontaneous ignition temperature. The flame was quenched right after igniting this rapidly burning explosive mixture because of sufficient cooling by solid structures.

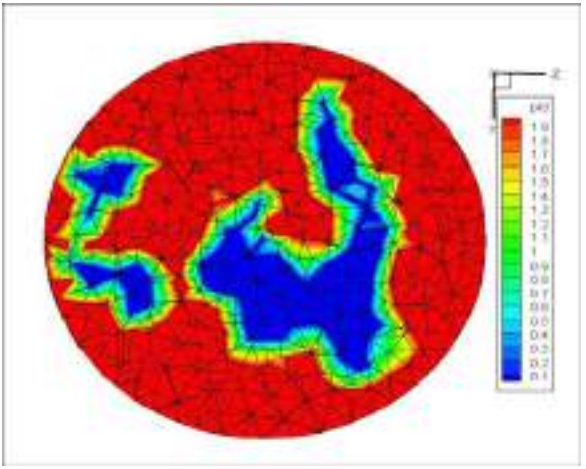

Fig. 10. Cross section of the porous structure in terms of pid (property identification), solid has a pid of 2 while fluid has a pid equal to 1

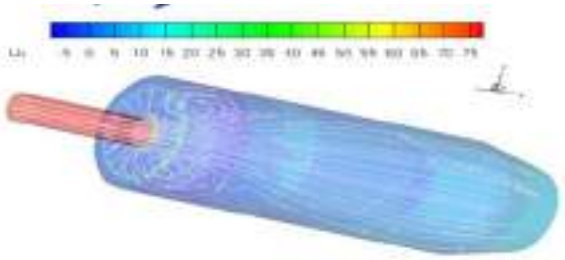

Fig. 11. Traces of particles released at the inlet and swirler surfaces, showing re-circulation in the porous zone

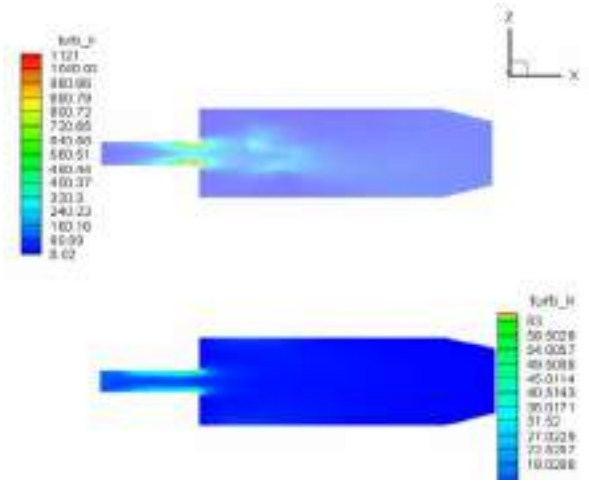

Fig. 12. Contours of turbulent kinetic energy

3 Anderson's Burner (Hydrogen/Air Combustor)

The high cost and reliability of jet fuel has pushed the aerospace industry to renew its interest in using hydrogen as fuel. There are advantages of reduction of particulate emission, elimination of carbon related emission and coking. The concept of using hydrogen as a practical fuel in gas turbine combustor started in

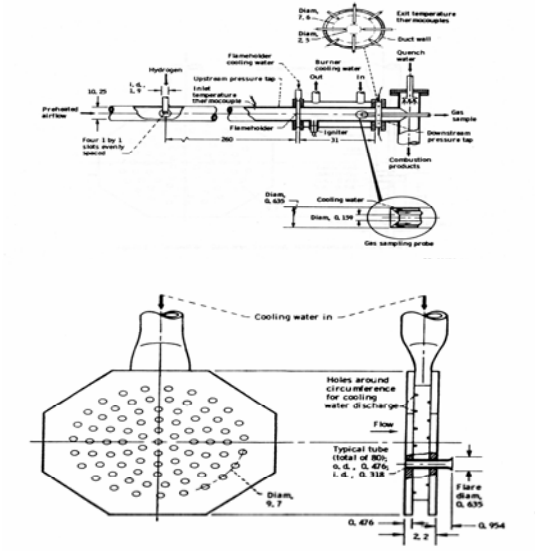

Fig. 13. Schematic of the hardware and set up and an enlarged view of the flame holder in Anderson's hydrogen/air burner experiment

early 1950's. There were previous experimental efforts[5,6] and recent numerical analyses[7] which provides ample knowledge in developing quick mixing, low emissions and high performance fuel injector and mixer.

Note that the flame holder consists of eighty small tubes, shown in Fig. 13, and each cross section is 92% blocked. This specific blockage prevents flashback but causes a 25% to 40% pressure drop. Further information in experimental set up and hardware uses is given in [5]. A three-dimensional 1.3 millions unstructured mesh, seen in Fig. 14, is used to represent half of the geometry in the CFD studies on the assumption that flow is symmetric inside the burner. To reduce the

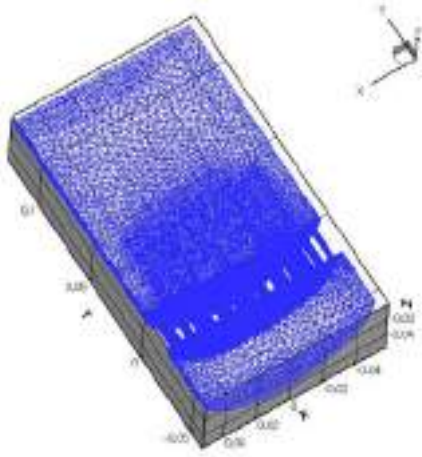

Fig. 14. Grid used in computing Anderson's burner

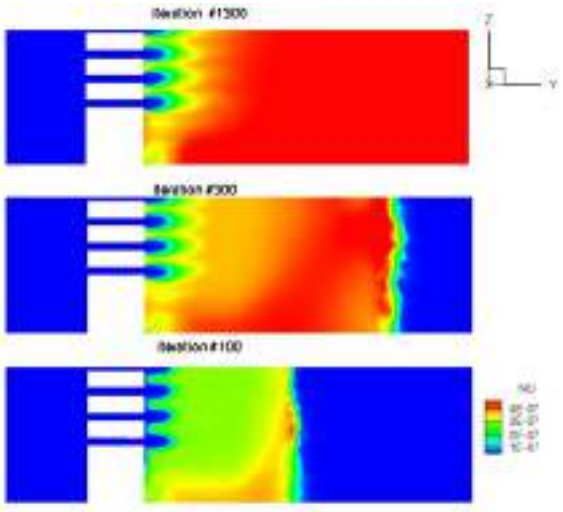

Fig. 15. Product NO in contours of mass fraction at the $x = 0$ plane, indicating the flame front moving downstream as solutions progress to steady state

computational cost of representing a full reaction mechanism, NCC's intrinsically low-dimensional manifold (ILDM) procedure [4] is used in this study. Two cases with different equivalence ratios are computed by matching with those experimental conditions listed in Table 1. The numerical results were in good agreement with experimental data for peak temperatures and NOx along the centerline of burner [7]. Figure 15 presents the flame front traveled from the 100th iteration after ignition to the stage that flame held at steady state. A two dimensional model of Anderson burner is used to study the morphology of porous structure in flame holding. Similarly, unstructured grid for half of the burner is needed because of symmetry. Basically, it is a 2-D channel with a 2-D flame holder. Mesh refinement around solid structure, colored in cyan in Figs. 16 and 18, is applied. Figure 16 shows the location of solid (in red) in a geometry of 15 tubes flame holder located behind the ignition zone. After ignition, the premixed H_2/air burned behind the flame holder. The flame was flashback to tiny channels after being blocked by the porous region, as shown in Fig. 17. The other case is a geometry of reduced number of channels, from 15 to 7, in the flame holder while keeping their size unchanged. It is intended to use porous solids to enhance flow recirculation behind the flame holder. In Fig. 18 it is seen that the flame from the tiny channels is moved to the solid structures and held there. This flame-holding is displayed in the contours of temperature in Fig. 19. The top plot is the 2D model with porous medium and the bottom figure is the results from a clean channel.

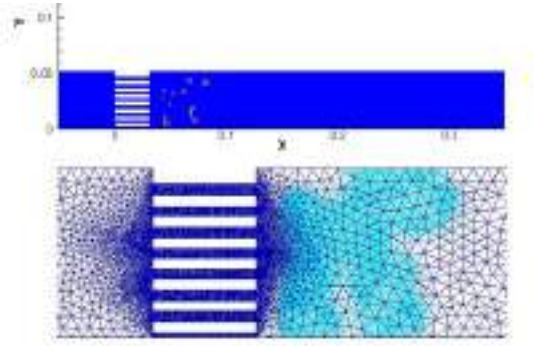

Fig. 16. Anderson's 2-D model with 15 flame holder tubes and porous medium located behind ignition zone

Table 1. Conditions used in computing the Anderson case

Inlet mixture temperature	Burner pressure	Reference velocity	Equivalence ratio
700 K	3.8x105 N/ m^2	18 m/sec	0.4
600 K	3.8x105 N/ m^2	17 m/sec	0.25

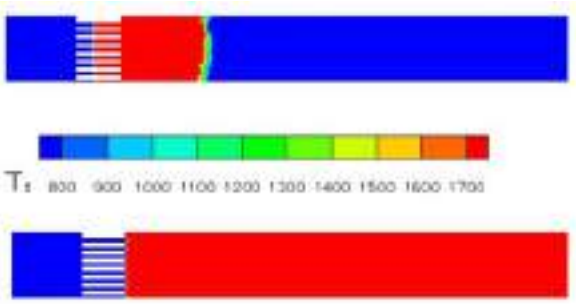

Fig. 17. Temperature contours; Top: fame stopping at the porous structure and flushbacking into flame holder. Bottom: flame held at flame holder in clean channel.

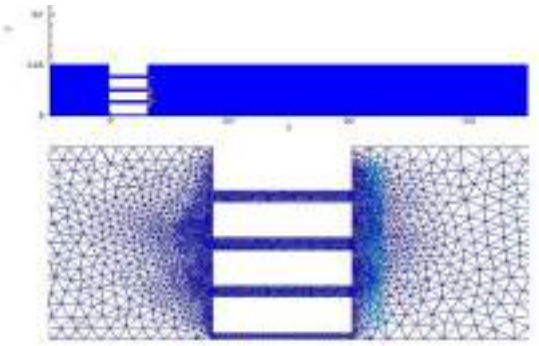

Fig. 18. Geometry of 2-D model with reduced number of channels and solids inside ignition zone

Fig. 19. Contours of temperature; Top: flame held at solids. Bottom: flame held at flame holder in clean channel

4 Summary

In this paper, the MBMRA technique is used in several combustor configurations to study flame propagation characteristics of different fuels in arbitrary porous

media, which act as a premixer or as a flame holder. The flame studied is deflected by the porous media and the flame temperature is lower than those without it. It also demonstrated that the porous structure can enhance the recirculating/mixing feature and intensify the turbulent flow quantities, thus advantageous for diffusion flame. But, it also can quench the flame if the thermal characteristics of solid material or the morphology of pores can not sustain the combustion. In the future, consideration of refinement based on the local Reynolds number will be included so that relevant scales of the flow can be adequately resolved.

Acknowledgement

The authors would like to thank Dr. T.H. Shih at Glenn Research Center for providing the 3D mesh and numerical set-up of the Anderson burner case.

References

1. Liou, M.-F., Greber, I.: An innovative technique for simulating pore-scale transport phenomena in porous media: mesh-based microstructure representation algorithm. In: ICCFD4 (2006)
2. Roshko, A.: On the development of turbulent wakes from vortex streets, NACA TN-2913 (1953)
3. Norris, A.T., Chen, K.H., Raju, M.S.: Chemical kinetics in the National Combustion Code., AIAA-2000-0334
4. Visbal, M.R.: Evaluation of the Implicit Navier-Stokes solver for some unsteady separated flows. AIAA Paper 85-1501 (1985)
5. Anderson, D.N.: Emission of oxides of nitrogen from an experimental premixed hydrogen burner. NASA TM X-3393 (1976)
6. Norgen, C.T., Ingebo, R.D.: Emission of nitrogen oxides from an experimental hydrogen-fueled gas turbine combustor. NASA TM X-2997 (1974)
7. Shih, T.-H., Norris, A., Iannetti, A., Marek, J., Liu, N.-S., Smith, T., Povinelli, L.: A study of hydrogen/air combustor using NCC. AIAA 2001-0808 (2001)

Combined Finite Element - Particles Discretisation for Simulation of Transport-Dispersion in Porous Media

H. Beaugendre[1], A. Ern[2], and S. Huberson[3]

[1] Université de Bordeaux, UMR 5251, INRIA Bordeaux Sud-Ouest, 351 cours de la Libération, 33405 Talence Cedex, France
Heloise.Beaugendre@math.u-bordeaux1.fr
[2] CERMICS, Ecole Nationale des Ponts et Chaussées, Université Paris-Est, 6 et 8 avenue Blaise Pascal, 77455 Marne la Vallée Cedex 2, France
ern@cermics.enpc.fr
[3] LEA, Université Poitiers-ENSMA, téléport 2, Boulevard Marie et Pierre Curie, BP30179, 86962 Futuroscope Chaseneuil Cedex
serge.Huberson@univ-poitiers.fr

1 Introduction

Combining finite element together with particle methods provide one of the best compromise for solving transport problem in porous media. Saturated or non-saturated flows are determined by boundary condition and the media permeability.[1] For real terrain, permeability can consist in various almost constant and imbricated zones with complex shapes. Thus, it is of some interest that the boundary between two adjacent zones coincides with a natural mesh interface and that each element is entirely contains in one such zone. Beside this, solving transport equation by means of particle methods offers two distinctive advantages. The method is unconditionally stable when applied to a pure convective equation, and it does not contain any numerical diffusion if the particle trajectories are correctly computed. Therefore the combination of finite elements and particle method appears to be a straightforward application of the principle : "the right method at the right place".

Although the previous statement provide a consistent basis to build a numerical model, there still remain some options in the choice of the two components themself. To start with, it has long been recognised that the computed flow must satisfied as much as possible the divergence free condition; this can be achieved by selecting a non-conforming or mixed method. Second, there exist many way to design particles methods for the convective part as well as for the dispersion term. For the first one, a so-called streamline method can be used as an alternative to the more classical time integration. For the last one, there is a profusion of model including random walk, particle

[1] This work was partially supported by GDR MOMAS-CNRS.

mesh, particle strength exchange and dispersion velocity among others. Our purpose is to compare some of these different strategies in order to provide as clear as possible criteria to be used when designing a solver. Three different points will be successively addressed hereafter : the finite element scheme, the particle trajectories computation and the dispersion simulation.

2 Finite Element Flow Computation

The first point was adressed by considering two finite element schemes to approximate the flow, the usual conforming scheme and a non-conforming scheme (Beaugendre 2006). The latter is quite similar to the more usual mixed hybrid finite element method: it uses one degree of freedom per mesh face and produces a discrete flow field with continuous normal component. The difference with the mixed hybrid finite element approach is that the present scheme can be interpreted as a finite volume box scheme where the mean of governing equations is considered elementwise. Figure 1 shows an example of computed potential flow for the lense test-case.

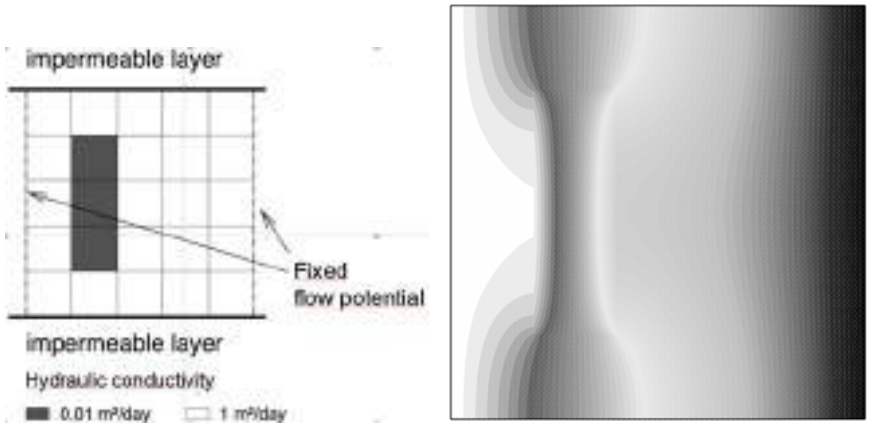

Fig. 1. a) Schematic representation of the domain for the lense test case; b) Flow potential distribution

3 The Streamlines Method

The trajectories computation was based on the flow computed with the previous finite element method. This is a two steps procedure. First the location of the particle on the finite element mesh have to be determined, second the trajectories of the particle across the resulting element has to be computed. The first step was achieved by superimposing a regular cartesian grid to the finite element mesh. The cartesian grid cells are selected as small as possible

so that a large number of cells cover one single element. Therefore, a particle contains in one grid cell is usually contained by no more than one element. The trajectory computation was performed by using two alternative procedures. The first one consists in a numerical time integration of the differential equation $dX/dt = U$ as usual in particles method. The second consist in using the polynomial form of the velocity field on each element to compute the local streamlines and then the particle trajectory across this element. Associated to this calculation is a time interval corresponding to the particle sojourn within this element also called flight-time. The whole procedure constitutes the streamline method (Matringe 2006).

The resulting method was applied to different test-cases. On figure 2, we present the lense test case streamlines computed from the potential obtained with the conforming and non conforming method. Three different meshes were used in order to point out the convergence of the two method. It was observed that the non-conforming scheme always provide the best streamlines pattern.

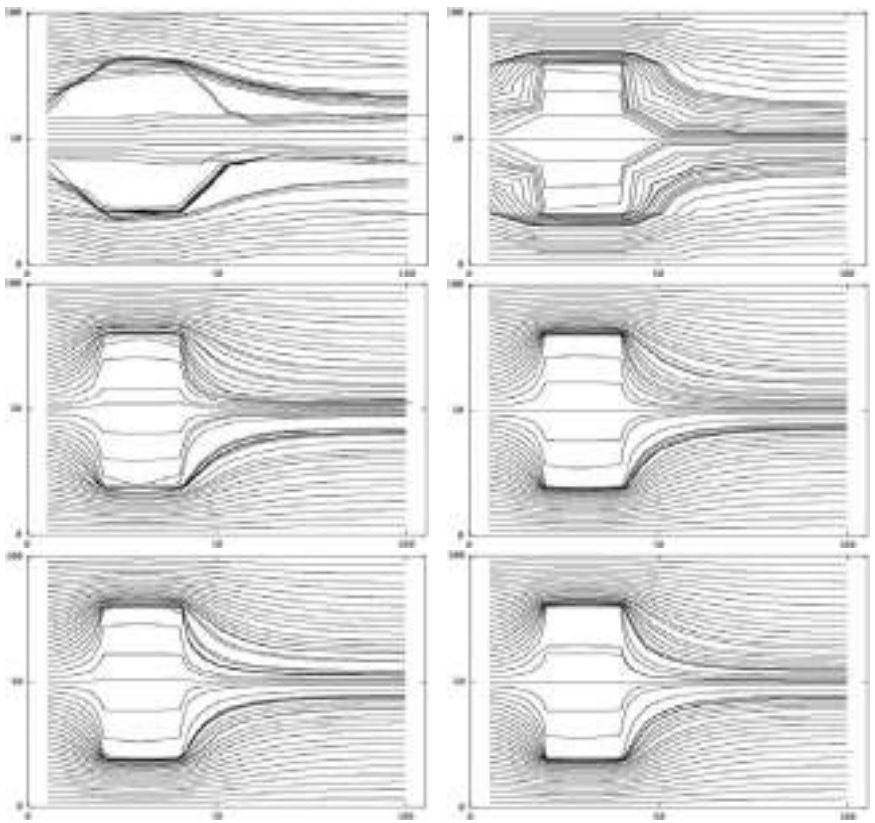

Fig. 2. Comparison of the computed trajectories with non-conservative (left) and conservative (right) flow fields. From top to bottom, finer meshes are used.

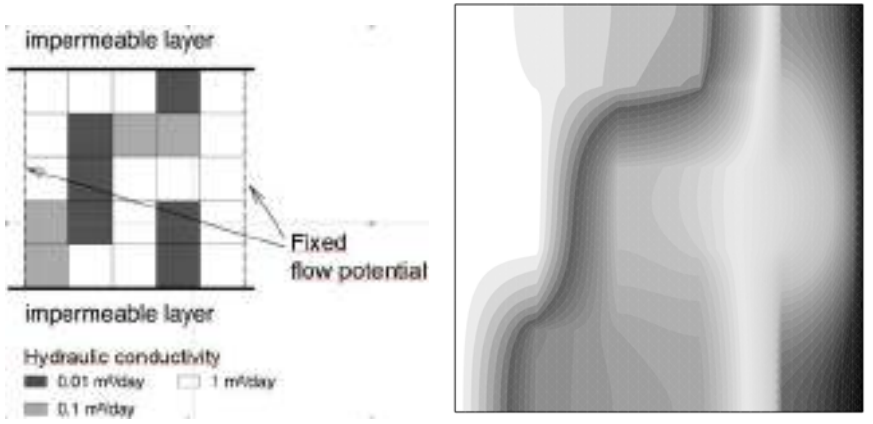

Fig. 3. a) Schematic representation of the domain for the multi-conductivity test case; b) Flow potential distribution

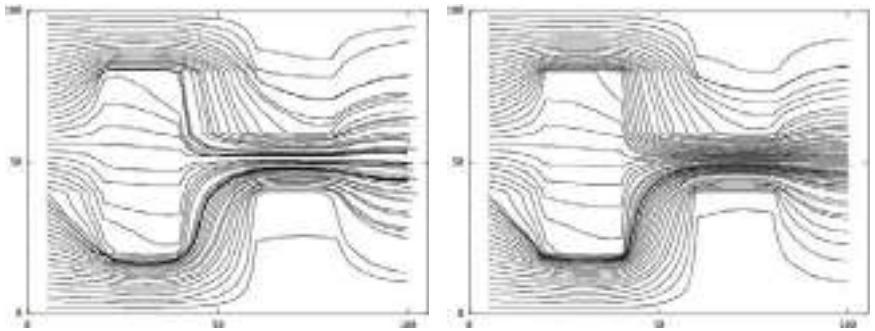

Fig. 4. Computed trajectories for the non-conservative (left) and conservative (right) flow fields

The second test case - figure 4 corresponds to a similar configuration, but uses a fully unstructured mesh. It can be observed from the computed streamlines compared to that of figure 2 that the method still works in this case.

4 Dispersion

The dispersion simulation can be based on many different methods. In the present work, two methods were particularly investigated: the diffusion velocity method and the particle strength exchange (PSE) method. The first one was selected because it yields modified streamlines, keeping constant the weight associated to each particles weither the second keep the streamlines unchanged and only modifies the particles weight. The first method was assumed to be in agreement with the streamline method concept. It consists in an algebraic manipulation of the original convection-dispersion equation in order to obtain a pure transport equation where the velocity consist in two

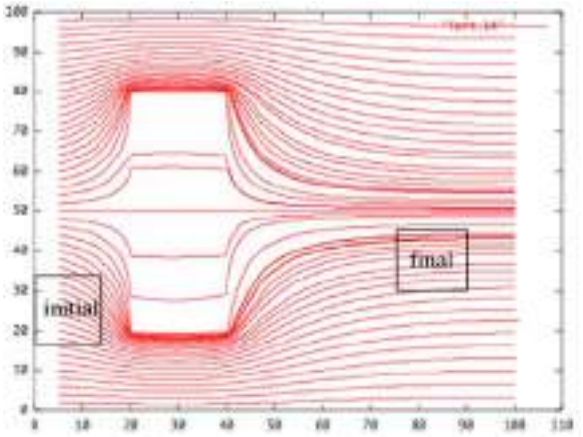

Fig. 5. PSE dispersion. The square indicate the initial and final location of the particle set.

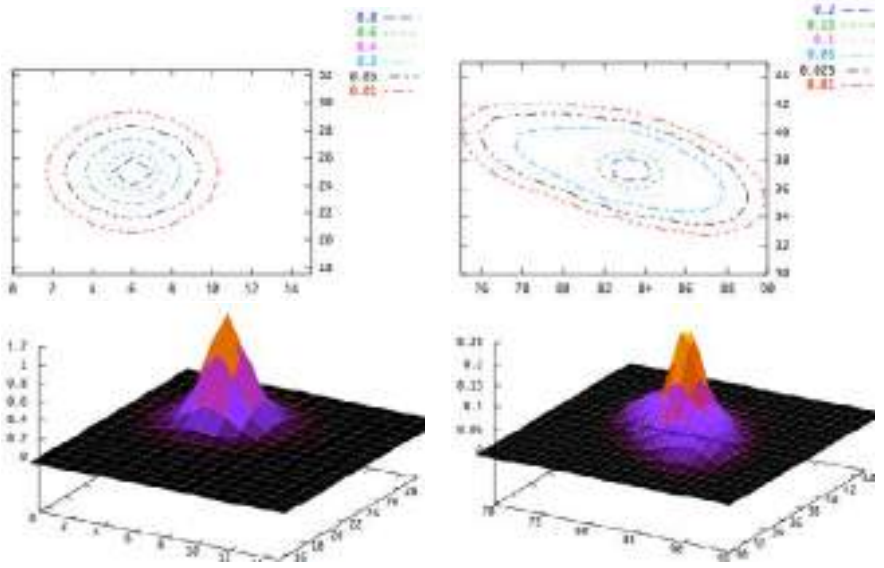

Fig. 6. PSE dispersion : Initial (left) and final(right) concentration

parts, the original velocity component computed with finite elements and a dispersion component which is proportional to the ratio of the gradient by local value of the transported quantity. The method was found to work well in a previous study (Beaudoin 2003) and can be easily combined with any of the two procedures used for the computation of the trajectories. The implementation of the PSE method reduces to the addition of the computation of

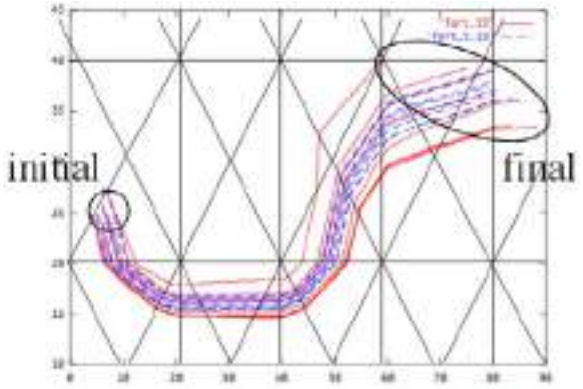

Fig. 7. velocity dispersion : selection of eight particles modified trajectories. dash-lines : original streamlines, continuous lines : modified streamlines.

the particles weight at each time step. It has to be noticed that both method necessitates to have a common time-stepping for all the particle which was not the case when only streamlines were computed.

Eventually, it was found that the PSE metod was the best candidate for extending the streamline method to the case of dispersive flows. The possibility to display initialy the particles along pre-computed streamlines enables to reduce the additional computational work to the particle weights. The application of the velocity diffusion do not permit to keep the same streamlines set for all the computation and, therefore, was found much more CPU-time consuming. It can be obviously guessed that the same drawback definitely plague the application of the Monte-Carlo simulation of dispersion.

References

[BE06] Beaugendre, H., Ern, A.: Finite volume box scheme for a certain class of nonlinear conservative laws in mixed form. In: ICCFD, The Fourth International Conference on Computational Fluid Dynamics, Ghent, Belgium. Springer, Heidelberg (2006)

[BHE03] Beaudoin, A., Huberson, S., Rivoalen, E.: Simulation of anisotropic diffusion by means of a diffusion velocity method. J. Comput. Phys 186, 102–113 (2003)

[MJT06] Matringe, S., Juanes, R., Tchelepi, A.: Robust streamline tracing for the simulation of porous media flow on general triangular and quadrilateral grids. J. Comput. Phys. 219, 992–1012 (2006)

Part 20
Flow with Non-flat Wall

“*This page left intentionally blank.*”

A Numerical-Asymptotic Method for Computation of Infinite Number of Eddies of Viscous Flows in Domains with Corners

Alexander V. Shapeev[1] and Ping Lin[1,2]

[1] Department of Mathematics, National University of Singapore, 2, Science Drive 2, Singapore 117543
shapeev@gmail.com

[2] Division of Mathematics, University of Dundee, 23 Perth Road, Dundee, Scotland DD1 4HN, UK
plin@maths.dundee.ac.uk

1 Introduction

Two-dimensional flows of a viscous fluid near a corner between two steady rigid planes was first examined by Moffatt [Mof64]. He established that when the angle between the planes is less than a certain critical angle, any flow near the corner consists of infinite series of eddies with decreasing size and intensity as the corner point is approached.

One of the most famous examples of flow in domain with corners is a flow in the lid-driven cavity. The lid-driven cavity problem has become a benchmark problem for researchers to test performance of numerical methods designed for computation of viscous fluid flows. Particularly, among other criteria, researchers examine the accuracy of their methods based on how accurately the corner eddies can be computed. However, in the most of previous works only a few eddies were computed. In addition, the accuracy of finding intensity and position of the smaller eddies was less than the accuracy for the larger eddies.

The aim of this paper is to develop a systematic method that can accurately compute position and intensity of infinite series of eddies in addition to computing the other main features of flow in domains with corners. The proposed method is based on a standard C^1-continuous finite element discretization (namely, Argyris elements) applied to the stream function equation. In order to compute infinite series of eddies, the exponential mesh refinement near the corners is used together with the special elements at the corners of the domain with basis functions taken from Moffatt's asymptotics. We present the results of application of the proposed method to the lid-driven cavity problem, though the method can be applied to any kind of problems in domains with corners. The computations indicate that the proposed method allows one to accurately compute the infinite series of eddies, with the relative error of finding intensity and position of different eddies being independent of their size.

2 Computational Method

The problem of viscous fluid flow is governed by the boundary-value problem for the Navier-Stokes equations, which in 2D can be written in the form of a single equation for the stream function φ:

$$\begin{cases} \Delta\Delta\varphi + \mathrm{Re}\left(\dfrac{\partial\Delta\varphi}{\partial x}\dfrac{\partial\varphi}{\partial y} - \dfrac{\partial\Delta\varphi}{\partial y}\dfrac{\partial\varphi}{\partial x}\right) = 0, \quad (x,y) \in \Omega, \\ \varphi|_{\partial\Omega} = 0, \quad \left.\dfrac{\partial\varphi}{\partial n}\right|_{\partial\Omega} = u_s, \end{cases} \tag{1}$$

where Re is the Reynolds number, domain $\Omega = [0,1] \times [0,1]$, $\partial\Omega$ is the boundary of Ω, and u_s is a tangential velocity on the boundary: $u_s = 1$ for $y = 1$, and $u_s = 0$ otherwise.

To accurately resolve the corner eddies in a flow, we should consider the structure of the flow in the vicinity of the corners. As was found by Moffatt, any flow near the corner with angle smaller than the critical one consists of a series of eddies with decreasing size and intensity as the corner point is approached [Mof64]. The first (i.e. largest) eddies can be affected by the flow far from the corner as well as by the nonlinear forces. However, such impact on the smaller eddies can be neglected and therefore their behavior is expected to be close to the behavior of the family of asymptotic solutions found by Moffatt [Mof64]. To summarize, the flow domain consists of

1. the part without the corner eddies,
2. the part with relatively large corner eddies that might not be well described by the asymptotic solution due to the impact of the flow far from the corner as well as the impact of the nonlinear forces, and finally
3. the part with relatively small eddies that are well described by the Moffatt's asymptotic solution.

To construct a mesh, the domain is decomposed into several subdomains according to the structure of the flow: the main subdomain without the corner eddies, the near-corner subdomains with relatively large corner eddies and the corner subdomains with the small eddies. Thus, the domain is decomposed into $1 + 2N_c$ subdomains, where N_c is the number of corners. A typical domain decomposition near a corner is shown in figure 1(a). There is one main subdomain (tagged with "M" in figure 1(a)), one near-corner subdomain per each corner between rigid walls (tagged with "NC" in figure 1(a)), and one corner subdomain per each corner between rigid walls (tagged with "C" in figure 1(a)).

The discretization in the main subdomain is done on the uniform mesh and is based on Argyris elements (the standard C^1-continuous, P_5 finite elements on a triangular mesh). The discretization in the near-corner subdomain (trapezium $ABGF$ in figure 1(a)) is also based on Argyris elements and is done on the exponentially graded mesh. The mesh in the near-corner subdomain is chosen to be conforming with the mesh in the main subdomain and therefore no additional techniques are involved to couple the solutions

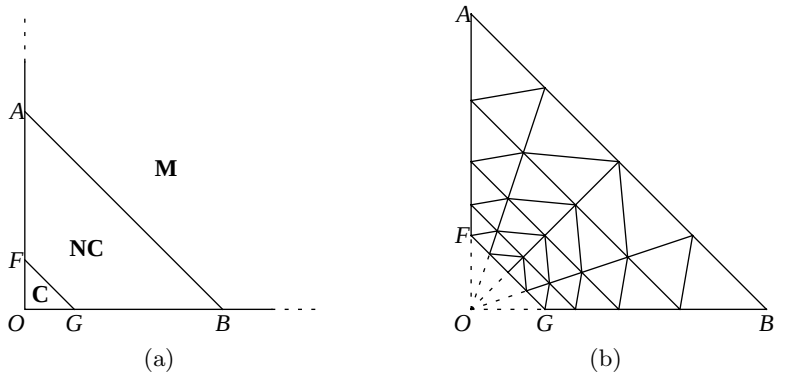

Fig. 1. (a) domain decomposition near the corner; **(b)** mesh of the near-corner subdomain (right)

in these two subdomains. The typical mesh in the near-corner subdomain is shown in figure 1(b).

We assume that in the corner subdomain (triangle OFG in figure 1(a)), the asymptotic expansion of the flow gives a sufficiently accurate approximation to the exact solution. Therefore, the solution basis in the corner triangle OFG is chosen to be a set of only two functions, which are the real and the imaginary part of the Moffatt's asymptotic solution. Certain matching conditions are introduced to the finite element formulation to ensure the approximate conformity of the finite element basis across the edge FG.

The nonlinear system of algebraic equations resulted from the discretization is solved using Newton's iteration. The linearized system of algebraic equations is solved by the unsymmetric multifrontal method implemented in UMFPACK software package.

In the lid-driven cavity flow problem there are flow singularities in the upper corners. The technique we use to treat the corner singularities is similar to the technique we use to compute the corner eddies. Namely, we perform the same mesh refinement and we match the asymptotic expansion at the corner triangle with the solution at the near-corner subdomain.

3 Lid-Driven Cavity Problem

The lid-driven cavity flow consists of the primary eddy (denoted as PE), a series of bottom left corner eddies (denoted as BL1, BL2, ..., BLk, ...), and a series of bottom right corner eddies (denoted as BR1, BR2, ..., BRk, ...). The eddies are numbered in order of decreasing size. For high Reynolds numbers, the top left eddies (TL1 and TL2) can also appear in the flow.

The lid-driven cavity problem was computed using the method described above. The computations were done on four different meshes denoted as M1,

Table 1. Parameters of meshes used

Mesh	Triangles	DOF	Reduced DOF	Corner triangle size
M1	388	2078	1490	0.016
M2	2052	10126	8578	0.0039
M3	10244	48334	44482	0.00098
M4	49156	226574	217346	0.00024

M2, M3 and M4. The parameters such as number of triangles, number of degrees of freedom (DOF) and size of a leg of the corner triangle (i.e. length of OG in figure 1(b)) are presented in table 1. The fourth column (reduced DOF) is the number of degrees of freedom after application of the boundary conditions and the matching conditions on the interface between corner and near-corner subdomains.

The present results were compared with the results of Barragy and Carey [BC97], which were found to be the most accurate results containing up to the 4th corner eddies. The absolute difference between the present work and [BC97] in stream function at the location of the eddies is less than 10^{-5}. The finest mesh used in [BC97] had 132098 degrees of freedom and a finest effective mesh size of about 0.00026.

Intensity and position of some of the eddies in the present computations of the flow with Re=2500 for different mesh refinements and the results of Barragy and Carey [BC97] are presented in table 2. The data indicate that the present results of computing both the large (i.e. PE) and the small (i.e. BL3) eddies for Re=2500 converge fast and are more accurate than the results of Barragy and Carey. However, it should be admitted that the results of [BC97] for very high Reynolds numbers ($\mathrm{Re} \geq 10000$) have somewhat better accuracy in computing the large eddies, which is attributed to the uniform mesh being used in the main subdomain in the present method. Barragy and Carey used the graded mesh which might resolve the boundary layers near the walls better.

It is interesting to examine the relative error of finding intensity and position of different corner eddies depending on the mesh and compare it with the results of Barragy and Carey. The error was estimated as the difference with the present solution on the finest mesh M4. The estimated relative error for $\mathrm{Re} = 2500$ thus computed for the eddies BL1-BL4 is presented in table 3. As can be seen from table 3, the method of Barragy and Carey (as well as all the methods available in the literature and known to us) produces the relative error which increases for the smaller eddies. On the contrary, the present method allows us to compute the whole infinite series of eddies, and the relative error of finding the eddies' intensity and position decreases uniformly for all the eddies as the mesh is refined. That is, there is a bound on the relative error of finding the eddies' intensity and position, this bound is independent of size and intensity of the particular eddy and decreases as the

Table 2. Comparison of results for eddies PE and BL3 for Re=2500 for different refinements with Barragy and Carey [BC97]

PE	φ	x	y
M1	-0.1229531	0.5232264	0.5433070
M2	-0.1214925	0.5197949	0.5439642
M3	-0.1214695	0.5197760	0.5439257
M4	-0.1214690	0.5197769	0.5439244
Barragy&Carey	-0.1214621	0.5188822	0.5434181
BL3	φ	x	y
M1	$7.062414 \cdot 10^{-13}$	0.0003730432	0.0003730432
M2	$7.758873 \cdot 10^{-13}$	0.0003711063	0.0003711063
M3	$7.750788 \cdot 10^{-13}$	0.0003708568	0.0003708568
M4	$7.751069 \cdot 10^{-13}$	0.0003708612	0.0003708595
Barragy&Carey	$7.595817 \cdot 10^{-13}$	0.0003884944	0.0003884944

Table 3. Estimated relative error of finding eddies' intensity for Re=2500

	BL1	BL2	BL3	BL4
present, M1	0.077583	0.088858	0.088846	0.088846
present, M2	0.00086856	0.0010060	0.0010069	0.0010069
present, M3	0.000031924	0.000036335	0.000036188	0.000036189
Barragy&Carey	0.00010006	0.00060359	0.020030	-

Table 4. Intensity and position of all eddies for Re=2500

	φ	x	y
PE	-0.1214690	0.5197769	0.5439244
BL1	0.0009311474	0.08424181	0.1110062
BL2	$-2.811158 \cdot 10^{-8}$	0.006129716	0.006158831
BL3	$7.751069 \cdot 10^{-13}$	0.0003708612	0.0003708595
BL4	$-2.137191 \cdot 10^{-17}$	0.00002238491	0.00002238491
BR1	0.002662432	0.8344014	0.09075692
BR2	$-1.226678 \cdot 10^{-7}$	0.9904594	0.009384439
BR3	$3.381770 \cdot 10^{-12}$	0.9994289	0.0005710737
BR4	$-9.324506 \cdot 10^{-17}$	0.9999655	0.00003446937
TL1	0.0003434479	0.04300225	0.8893601
BLk	$5.892847 \cdot 10^{-22}\, \Phi^{k-5}$	$1.351140 \cdot 10^{-6}\, R^{k-5}$	$1.351140 \cdot 10^{-6}\, R^{k-5}$
BRk	$2.571033 \cdot 10^{-21}\, \Phi^{k-5}$	$1 - 2.080551 \cdot 10^{-6}\, R^{k-5}$	$2.080551 \cdot 10^{-6}\, R^{k-5}$

mesh is refined. This is a distinctive feature of the proposed method, which is a result of appropriate mesh refinement near the corners as well as coupling the approximate solution with the exact asymptotics.

The present method allows us to compute intensity and position of all the eddies present in the flow. The results for Re=2500 are given in table 4.

The fifth corner eddies (BL5 and BR5) as well as the smaller eddies (sixth, seventh, etc.) were computed for the first time in the present work. The relative difference between computations of these eddies on the meshes M3 and M4 was found to be relatively small (about 10^{-4}), which indicates the accuracy of the present results.

4 Conclusion

The method of computing infinite series of corner eddies in viscous fluid flows in domains with corners was proposed. The method is based on Argyris finite element discretization for the stream function formulation of the Navier-Stokes equations, exponential mesh refinement near corners, and asymptotics of the flow near corners. The method was applied a benchmark problem of the lid-driven cavity flow. The results of computations demonstrate high accuracy of the present method, show that the method can accurately compute the infinite series of eddies, and indicate that the relative error of finding eddies' intensity and position decreases uniformly as the mesh is refined (i.e. the error of finding intensity and position of different eddies does not depend on their size). The comparison with the results available in the literature shows that the present method produces solutions of the same or better accuracy than the existing methods.

Acknowledgement

This research is partially supported by the Singapore Academic Research Funds R-146-000-064-112 and R-146-000-099-112.

References

[BC97] Barragy, E.B., Carey, G.F.: Stream function-vorticity driven cavity solution using p finite elements. Computers & Fluids 26(5), 453–468 (1997)

[Mof64] Moffat, H.K.M.: Viscous and resistive eddies near a sharp corner. J. Fluid Mech. 18, 1–18 (1964)

Part 21
Higher-Order Method 1

“*This page left intentionally blank.*”

Implicit High-Order Compact Differencing Methods: Study of Convergence and Stability

Meng-Sing Liou[1] and Angelo Scandaliato[2]

[1] NASA Glenn Research Center, Cleveland, OH 44135, USA
meng-sing.liou@nasa.gov
[2] Ohio Aerospace Institute, Cleveland, OH 44142, USA
angelo.scandaliato@oai.org

Summary. Compact differencing can deliver high-order accuracy using only a limited span of stencils, but incurring a costly matrix inversion. Hence, use of a stable implicit time discretization becomes favorable in order to offset the computation cost by allowing a large time step. A practical way to reduce the burden of inverting a large matrix from multidimensional problems is to split the implicit operator into a series of smaller operators. Undesirable consequences can surface, such as (1) loss of stability, and/or (2) loss of accuracy. Here, we propose a consistent implicit compact method and study the stability and accuracy of steady and unsteady solutions.

1 Introduction

Approximating derivatives with the use of high-order methods has several advantages, one of which is efficiency in the sense that with only a moderate increased effort it leads to convergence to the "true" solution at a fast rate. This means that fewer discrete points are needed for the same level of accuracy or a more accurate solution is obtained with the same number of grid points, in comparison with low-order methods.

Interest in high-order accurate methods has surged recently because of its efficiency and necessity for some applications in CFD, in which accuracy appears to be critical. Examples include turbulence simulation and aeroacoustics. Methods being intensively studied at the present time still have shortcomings. For example, a quick reduction of stable time step is found in the discontinuous Galerkin methods. Compact differencing methods are based on a known structure of stencils, thus restricting its use to structured grids only.

The approximate factored scheme proposed by Beam and Warming [1] is a popular implicit scheme for allowing a large time step. However, temporal accuracy is lost due to various approximations; a dual time scheme is often employed to restore the accuracy, but requires subiterations between physical time steps. Some fundamental issues remain to be clarified, with respect to

spatial and temporal convergence and stability. For example, inconsistent discretizations of spatial derivatives for the implicit (LHS) and explicit (RHS) operators can lead to degradation of stability and spatio-temporal accuracy.

In this paper, we present the analysis for the scalar convection-diffusion equation and extend it to Navier-Stokes equations. We begin with the stable Crank-Nicolson implicit method for any dimensions; the spatial derivatives are then approximated with the compact schemes, because of its ease of extending to very high orders of accuracy, say 10th and above and its compatibility with implicit formulation. We pay special attention to the following aspects: (1) clarification of "delta-form" vs. "direct-from", here "direct form" referring to solving the unknown itself, rather than the difference of unknowns at two consecutive time levels, (2) spatial and time convergence, (3) extension to a system of equations, and (4) effects of tridiagonal and pentadiagonal Padé schemes on stability and convergence.

2 Formulation

Let us consider the constant-coefficient scalar convection-diffusion equation,

$$\frac{\partial}{\partial t}\varphi + L(\frac{\partial}{\partial x_i}, \frac{\partial^2}{\partial x_j \partial x_i})\varphi = 0 \tag{1}$$

where the spatial derivatives operator,

$$L\varphi = \sum_{i=1}^{3} c_i \frac{\partial}{\partial x_i}\varphi - \nu \sum_{i=1}^{3}\sum_{j=1}^{3} \frac{\partial^2 \varphi}{\partial x_j \partial x_i} \tag{2}$$

contains the usual convection and diffusion terms, and also mixed derivatives to mimic terms involved in the compressible Navier-Stokes equations. We shall consider how these types of terms can be handled and whether any approximation (such as time delayed) of it would affect stability.

Apply the Crank-Nicolson (C-N) discretization, we get

$$\triangle\varphi^n = \varphi^{n+1} - \varphi^n = \frac{k}{2} L(\varphi^{n+1} + \varphi^n), \quad k = t^{n+1} - t^n. \tag{3}$$

Use p-th order accurate compact differencings for first and second derivatives on a domain with a constant spacing $h = x_{j+1} - x_j$ for $1 \le j \le J$,

$$\frac{\partial \varphi}{\partial x_i} \Rightarrow \mathcal{L}_i\{\frac{\partial \varphi_j}{\partial x_i}\} = \mathcal{R}_i\{\varphi_j\}, \quad \frac{\partial^2 \varphi}{\partial x_i^2} \Rightarrow \mathcal{L}_{ii}\{\frac{\partial^2 \varphi_j}{\partial x_i^2}\} = \mathcal{R}_{ii}\{\varphi_j\}, \quad i = 1, 2, 3 \tag{4}$$

where the notation $\{\circ\}$ represents a vector containing a set of variable values at all discrete points. The difference matrices $\mathcal{L}_i, \mathcal{R}_i, \mathcal{L}_{ii}, \mathcal{R}_{ii}$ are diagonal, tri- or penta-diagonal in our case. The notation for subscripts "i" and "ii" serves two purposes: the first denotes directions $1 \le i \le 3$ and the second indicates

the order of derivatives, i.e., a single subscript denotes a first derivative while a double subscript refers to a second derivative. After substitution, we have

$$\left[I + \frac{k}{2}\sum_{i=1}^{3}(\mathcal{B}_i - \mathcal{B}_{ii})\right]\{\varphi_{ijk}^n\} = \left[I - \frac{k}{2}\sum_{i=1}^{3}(\mathcal{B}_i - \mathcal{B}_{ii})\right]\{\varphi_{ijk}^n\} \tag{5}$$

where the spatial derivatives are approximated by

$$\mathcal{B}_i = c_i\mathcal{L}_i^{-1}\mathcal{R}_i, \quad \mathcal{B}_{ii} = \nu\mathcal{L}_{ii}^{-1}\mathcal{R}_{ii}, \quad i = 1, 2, 3 \tag{6}$$

The above discretization has the following properties: (1) the accuracy is $O((k^2 + h^p))$, (2) it is unconditionally stablefor any time step k.

There are also two issues concerning this equation: (1) it is costly to invert the LHS matrix for a multidimensional problem, and (2) the steady state solution is dependent on the time step k and is $O(k^2)$, in this case.

To address the first issue, the main idea is to break the costly unwieldy operator into a sequence of small simpler operators, so that the overall computation is still much cheaper. This splitting is usually based on the coordinate direction in the spatial derivatives, as in the case of alternating direction [2] or fractional step [3].

Splitting of Operators

The coordinate splitting gives,

$$\prod_{i=1}^{3}\left[I + \frac{k}{2}(\mathcal{B}_i - \mathcal{B}_{ii})\right]\{\varphi_{ijk}^{n+1}\} = \prod_{i=1}^{3}\left[I - \frac{k}{2}(\mathcal{B}_i - \mathcal{B}_{ii})\right]\{\varphi_{ijk}^n\} \tag{7}$$

The splitting error, in reference to the unsplit form (5), involves product of matrices $\mathcal{B}_i$ and $\mathcal{B}_{ii}$ and is at most as large as the time discretization error. Hence the split form maintains the same formal order of accuracy.

Interestingly, if further splitting is carried out by separating convection and diffusion derivatives, the resulting split scheme

$$\prod_{i=1}^{3}(I + \frac{k}{2}\mathcal{B}_i)(I - \frac{k}{2}\mathcal{B}_{ii})\{\varphi_{ijk}^{n+1}\} = \prod_{i=1}^{3}(I - \frac{k}{2}\mathcal{B}_i)(I + \frac{k}{2}\mathcal{B}_{ii})\{\varphi_{ijk}^n\} \tag{8}$$

is also unconditionally stable for any dimensions and for any CFL ($= c_i k/h$) and Fourier numbers ($= \nu k/h^2$), see You [4] and Zhao et al. [5]. We note that the unconditional stability is achieved in (5-8) by maintaining *consistent* operations for the corresponding terms on the LHS and RHS. If this consistency is broken, serious ramifications on stability can appear. Since the solution $\{\varphi_{ijk}^{n+1}\}$ is solved directly in (5), (7) and (8), it is called *direct method*.

The above splitting is good for unsteady solution since the formal order of accuracy remains. Unfortunately, it loses accuracy for steady solution, because the solution is always time-dependent to the order of k^2, thus when $O(k^2) >> O(h^p)$ - a desirable condition for seeking steady-state solutions , the extra work done to gain benefits of high order spatial differencing is now in vain.

Steady State Solution: Delta Form

The second issue concerns the steady-state solution; following the idea of Beam and Warming [1], the equation is recast such that the solution satisfies the discrete version of spatial derivatives only, as $\triangle\varphi^n$ diminishes,

$$\left[I + \frac{k}{2}\sum_{i=1}^{3}(\mathcal{B}_i - \mathcal{B}_{ii})\right]\{\triangle\varphi^n_{ijk}\} = -k\sum_{i=1}^{3}(\mathcal{B}_i - \mathcal{B}_{ii})\{\varphi^n_{ijk}\} \tag{9}$$

Here, the increment of variable, $\{\triangle\varphi^n_{ijk}\}$ is solved, thus called delta method. In what follows, we are concerned with the issues of stability, accuracy of time-dependent and steady-state solutions, and computational efficiency.

Notice that the above equation is identical to (5), hence retaining the same stability and accuracy, but adding the property of having the steady-state solution independent of time step. This is a very desirable property because the steady-state solution is wanted by using as large a time step as possible.

For the sake of computation efficiency, we again apply coordinate splitting,

$$\prod_{i=1}^{3}(I + \frac{k}{2}(\mathcal{B}_i - \mathcal{B}_{ii}))\{\triangle\varphi^n_{ijk}\} = -k\sum_{i=1}^{3}(\mathcal{B}_i - \mathcal{B}_{ii})\{\varphi^n_{ijk}\} \tag{10}$$

To further reduce computational cost incurred by the matrix operations on the LHS, it is interesting to observe that one can find an implicit compact operator common for both $\mathcal{L}_i$ and $\mathcal{L}_{ii}$. That is to say, $\mathcal{L}_i = \mathcal{L}_{ii}$ as given in [6], but at the expense of reducing accuracy by one order from the individually-derived matrices on the same stencil configuration. In fact, we now have odd-valued orders of accuracy, e.g., $O(h^7)$. The resulting algebraic equation becomes,

$$\prod_{i=1}^{3}(I+\frac{k}{2}\mathcal{L}_i^{-1}\,(c_i\mathcal{R}_i-\nu\mathcal{R}_{ii}))\{\triangle\varphi^n_{ijk}\} = -k\sum_{i=1}^{3}\mathcal{L}_i^{-1}\,(c_i\mathcal{R}_i-\nu\mathcal{R}_{ii})\{\varphi^n_{ijk}\} \tag{11}$$

In what follows, we present results to comment on accuracy and stability; the results are obtained for a 2D convection-diffusion equation, unless noted.

Accuracy: direct vs delta forms

First, we show in Fig. 1 the effect of using this "hybrid" compact differencings on accuracy. We see the resolution of the present method in the wavenumber domain is quite good. Moreover, computational results show an extremely fast reduction of error for the 3rd-order and 7th-order schemes and the efficiency of the 7th-order scheme shows the dominating advantage.

Figure 2 compares the convergence rates of three approximations: (1) LHS uses explicit $O(h^2)$ and RHS uses Pade's $O(h^4)$, (2) LHS and RHS use the same 3-3 stencil, implicit compact $O(h^3)$ scheme, and (3) LHS and RHS use the same 5-5 stencil implicit compact $O(h^7)$ scheme. Some striking results are observed: (1) there's an optimal CFL number for convergence in each group, (2) the level of error at convergence is proportional to the spatial

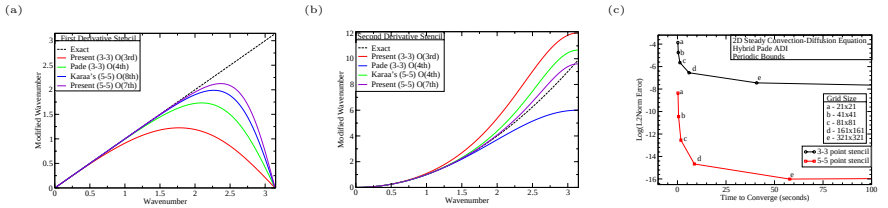

Fig. 1. Resolution accuracy of compact differencings for (a) first- and (b) second-order derivatives; (c) reduction of errors between present 3-3 and 5-5 formulas

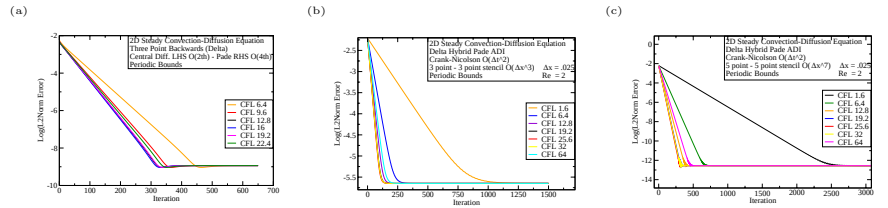

Fig. 2. Convergence history for a 2D convection-diffusion equation: (a) explicit (1-3 stencils); (b) tridiagonal (3-3 stencils); (c) pentadiagonal (5-5 stencils)

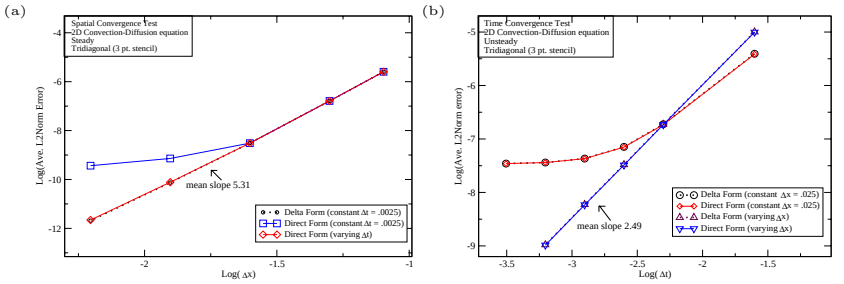

Fig. 3. Convergence study of the direct and delta forms for (a) steady and (b) unsteady solutions of a 2D convection-diffusion equation

discretization accuracy, and (3) the 5-5 scheme is the best by considering accuracy and number of iterations at convergence.

In Fig. 3, we show convergence of steady and unsteady solutions by using the direct and delta forms. We see in (a) the "delta form" converges at a rate of 5th-order, better than the theoretical 4th order accuracy for a 3-point stencil Padé scheme, while the "direct form" coincides at larger spatial steps ($\Delta x = h$), but deteriorates considerably at fine steps. However, it's also shown that the "direct form" can be made to give identical convergence if the temporal error is reduced to the level of spatial error by varying time step (k)

such that $O(k^2) = O(h^4)$. In (b), the time-convergence (reducing k) of both forms are shown; now the "delta form" has no advantages, behaving exactly the same as the direct form while keeping h constant. On the other hand, if h is reduced at the same rate as the temporal error, then the convergence maintains at a constant rate (≈ 2.5), again displaying super-convergence. It is clear that spatio-temporal errors must be synchronized. This finding, to our knowledge, has not been reported in the literature.

The convergence study of 2D linearized Navier-Stokes equations was conducted, the trends are identical to that in Fig. 3, thus they are omitted here.

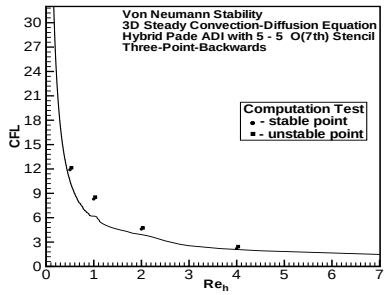

Fig. 4. Stability map for the 3D 3-level backward time differencing

Stability: effects of splitting and stencil
Splitting of the LHS operators alone compromises the stability. With ADI splitting on the delta form, the impact of splitting only begins in 3D equations with a loss of stability, see Fig. 4. The stability boundary in a Re_h vs CFL map is shown for the three-level backward implicit scheme, where $Re_h = c_i h/\nu$. The result for the C-N scheme is similar (and not shown), but with smaller stability region. The result clearly shows that the stable time-step (expressed in terms of CFL) is affected by the cell Reynolds number Re_h and interestingly it is reasonably large, but quickly reduces to $CFL \approx 1$. The trend is confirmed by computation, in which the stable and unstable points are depicted. How to recover the stability in 3D while maintaining a steady-state solution using compact scheme remains a subject of interest.

References

[1] Beam, R., Warming, R.: J. Comput. Phys. 16, 393–402 (1978)
[2] Douglas Jr., J., Gunn, J.E.: Numer. Math. 6, 428–453 (1964)
[3] Yanenko, N.: USSR Comp. Math. 3, 1094–1100 (1963)
[4] You, D.: J. Comput. Phys. 214, 1–11 (2006)
[5] Zhao, J., Dai, W., Niu, T.: Nemer. Meth. Partial Diff. Eqn. 23, 949–959 (2007)
[6] Karra, S.: Int. J. Numer. Meth. Fluids (to appear)

A NLFD-Spectral Difference Scheme for Unsteady Flows

Jean-Sebastien Cagnone[1] and Siva K. Nadarajah[2]

[1] Department of Mechanical Engineering, Mcgill University, Montreal, QC, H3A 2S6, Canada
jean-sebastien.cagnone@mail.mcgill.ca
[2] siva.nadarajah@mcgill.ca

1 Introduction

Computation of periodic flows using a time-accurate integration scheme is a costly procedure. Often, much effort is devoted to resolving the initial transients and finally capturing a full flow cycle. Moreover, if the flow phenomena has complex features which only very fine grids can resolve, then the prohibitive cost of each time step may lead to unacceptably large computational times. Notably, leading edge vortex shedding, flutter conditions and rotorcraft aerodynamics remain very challenging cases that would benefit from more efficient solution techniques.

To alleviate the cost of periodic flow modeling, Hall introduced [HTC00] the Harmonic Balance method, later pursued by McMullen & Jameson [MJA01] as the Non-Linear Frequency Domain (NLFD). By representing the flow solution as a Fourier expansion, this method allows for precise results while requiring only a limited number of harmonics.

In this work, we combine the NLFD time representation to the Spectral Difference (SD) scheme of Wang et al. [WLM07]. The spectral difference is a high order, conservative scheme for conservation laws in differential form, similar to the discontinuous Galerkin and spectral volume methods. Combining the SD and the NLFD schemes leads to a high-order, fully compact numerical procedure to solve periodic Euler flows at high resolution, using only a reduced number of degrees of freedom. An implicit LU-SGS technique is also presented to allow an efficient solution of the NLFD equations.

2 Scheme Formulation

The basis of the SD method of order k is a superposition of two grids within each cell. The first one, formed by the Gauss-Chebyschev quadrature points, is chosen such that it supports a polynomial solution of degree $k-1$. This polynomial is then used to reconstruct the fluxes on a second grid formed by the Gauss-Lobbato points. On this grid, the fluxes form a polynomial of

degree k that is then differentiated to obtain the residual. At the edges of the flux grid, the numerical flux is evaluated through a Riemann solver providing the inter-element coupling and the upwinding necessary for stability. The analytical flux function may be used at the inner nodes as the solution is continuous within each element. In accordance with the method of lines, the discretization results in a set of ODE's to which an integration method may be applied:

$$w_t + R(w) = 0. \tag{1}$$

If a time accurate approach is chosen, the residual is integrated forward in time using a Runge-Kutta (RK) scheme. Here, we choose to adopt a time spectral method where periodicity of the state and residual vectors is assumed. These vectors can be represented by independent Fourier series and substituted in the governing equation to yield a separate equation for each mode. Adding a pseudo-time derivative, we iteratively solve those equations to steady state:

$$\hat{w}_\tau + ik\hat{w}_k + \hat{R}_k = 0. \tag{2}$$

The solution technique uses a pseudo-spectral method that can be described as follows: the residual is computed for each real space instances and transported to Fourier space, along with the state vectors. Equation (2) can then be solved to retrieve new Fourier coefficients for the flow solution. Finally, the updated flow is brought back to real space for a residual evaluation. To efficiently solve the equation corresponding to each wave number, the implicit LU-SGS solver of Sun et al. [SWK07] is adapted to our purpose. Solving (2) implies driving the real and imaginary part of each mode to zero:

$$\frac{\partial \hat{w}_{\mathbf{R}}}{\partial \tau} + \hat{R}_{\mathbf{R}} - k\hat{w}_{\mathbf{I}} = 0,$$
$$\frac{\partial \hat{w}_{\mathbf{I}}}{\partial \tau} + \hat{R}_{\mathbf{I}} + k\hat{w}_{\mathbf{R}} = 0.$$

To keep those equations decoupled and preserve the simplicity of the method, the source term is kept explicit, all other terms being treated implicitly. We linearize the residual, distinguishing between the cell's and the neighbor's contribution:

$$\frac{\hat{w}_c^{n+1} - \hat{w}_c^n}{\Delta\tau} + \frac{\partial \hat{R}_c}{\partial \hat{w}_c}\left[\hat{w}_c^{n+1} - \hat{w}_c^n\right] + \sum_{nb \neq c} \frac{\partial \hat{R}_c}{\partial \hat{w}_{nb}}\left[\hat{w}_{nb}^{n+1} - \hat{w}_{nb}^n\right] = -\hat{R}_c^n - ik\hat{w}_c^n.$$

For more efficiency, the scheme employs a Gauss-Seidel approach. Noting s the sweep iteration and $*$ the latest available update, we transfer the neighbor's contribution to the right-hand side:

$$\left(\frac{I}{\Delta\tau} + \frac{\partial \hat{R}_c}{\partial \hat{w}_c}\right)\left[\hat{w}_c^{n+1} - \hat{w}_c^n\right]^{s+1} = -\sum_{nb \neq c} \frac{\partial \hat{R}_c}{\partial \hat{w}_{nb}}\left[\hat{w}_{nb}^{n+1} - \hat{w}_{nb}^n\right]^* - \hat{R}_c^n - ik\hat{w}_c^n.$$

Sun proposes a simplification to approximate the neighbors contribution, and we refer to his paper for the complete derivation. Once applied, the scheme simplifies to:

$$\left(\frac{I}{\Delta\tau}+\frac{\partial\hat{R}_c}{\partial\hat{w}_c}\right)\left[\hat{w}_c^{n+1,s+1}-\hat{w}_c^{n+1,s}\right]=-\hat{R}_c^*-\frac{\left[\hat{w}_c^{n+1}-\hat{w}_c^n\right]^s}{\Delta\tau}-ik\hat{w}_c^n. \quad (3)$$

The left-hand side of (3) is assembled and stored in factorized LU form for the real and imaginary part of each mode. Using a symmetric sweeping pattern, we solve each cell sequentially by performing triangular solves until the time step is deemed sufficiently converged. Finally, we mention that the Fourier space Jacobians can be easily obtained by taking advantage of the pseudo-spectral NLFD approach. Indeed, using the chain rule we write

$$\frac{\partial\hat{R}}{\partial\hat{w}}=\sum_{r=1}^{n}\frac{\partial\hat{R}}{\partial R_r}\frac{\partial R_r}{\partial w_r}\frac{\partial w_r}{\partial\hat{w}}, \quad (4)$$

where the summation is effectuated over the real space instances. Noticing that $\partial\hat{R}/\partial R$ and $\partial w/\partial\hat{w}$ are simply the coefficients forming the basis functions of the forward and inverse Fourier transforms, we conclude that the spectral Jacobians are easily calculated as a linear combination of the real space Jacobians. This method is significantly simpler than formally expressing $\hat{R}$ as a function of $\hat{w}$ and taking the appropriate derivatives.

3 Numerical Results

3.1 Vortex Advection

To numerically evaluate the accuracy of our SD Euler solver, we perform the vortex advection problem, a common test case for high order solvers. In a mean diagonal flow $(\rho,u,v,p)=(1,1,1,1)$, perturbations are added such that an isentropic vortex is created and passively advected downstream. This exact solution is then used to assess the amount of numerical diffusion introduced by the scheme.

$$(\delta u,\delta v)=\frac{\varepsilon}{2\pi}e^{\frac{1}{2}(1-r^2)}(-\bar{y},\bar{x}),\quad \delta T=-\frac{(\gamma-1)\varepsilon^2}{8\gamma\pi^2}e^{(1-r^2)},\quad \varepsilon=5. \quad (5)$$

The simulation is run using a 14×14 square domain using progressively finer structured grids until $t=2$. First-through fifth-order SD schemes are tested using the Roe flux and a third-order TVD-RK scheme. As Fig. (1a) shows, the measured error decays at the expected rate for all SD formulations and near-ideal orders of convergence are recovered, albeit for a slight inaccuracy in the coarse first-order results. Figure (1b) shows error as a function of the number of degrees of freedom of the solution. For the same number of unknowns, the high-order SD schemes are much more accurate than their lower order counterpart, demonstrating the benefits of p- over h- refinement.

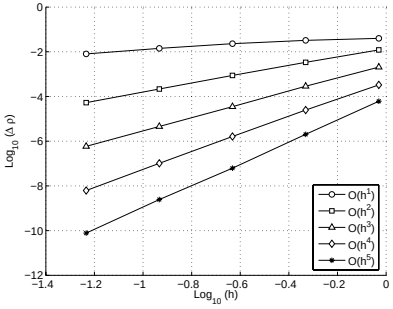

(a) $L2$ error against mesh size

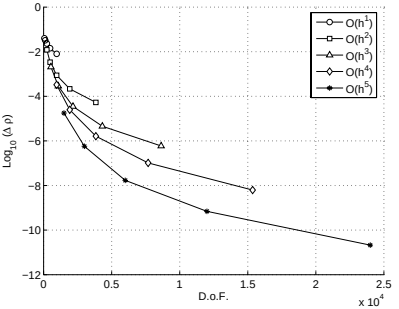

(b) $L2$ error against d.o.f

Fig. 1. Vortex advection accuracy study

3.2 Steady Subsonic Airfoil

In the following test, first-through fifth-order SD schemes are used to solve the inviscid, steady flow around a NACA0012 airfoil in subsonic regime, $M_\infty = 0.4$ and $\alpha = 5^o$. The simulation is effectuated on an very coarse grid of 32×8 using Rusanov's numerical flux. The solid wall is presented as quadratic segments using a higher-order boundary representation. To numerically quantify the solution accuracy, the entropy production in the solution are compared. Figure (2) shows the error as a function of the scheme order. The spectral (exponential) decay of the entropy error under p-refinement is clearly noticeable.

3.3 Pitching Subsonic Airfoil

As a demonstration problem for the NLFD-SD scheme, a NACA64A010 airfoil undergoing a sinusoidal motion is simulated. Flow parameters are:

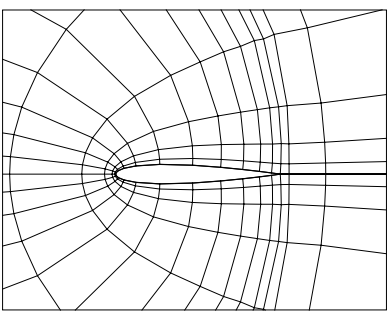

(a) Grid 32×8

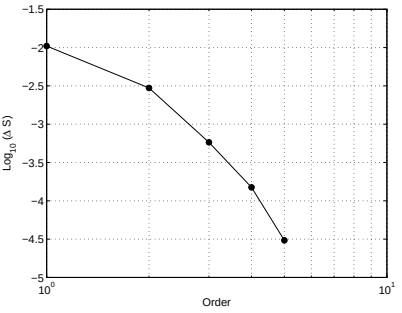

(b) $L2$ error against order

Fig. 2. Steady subsonic airfoil

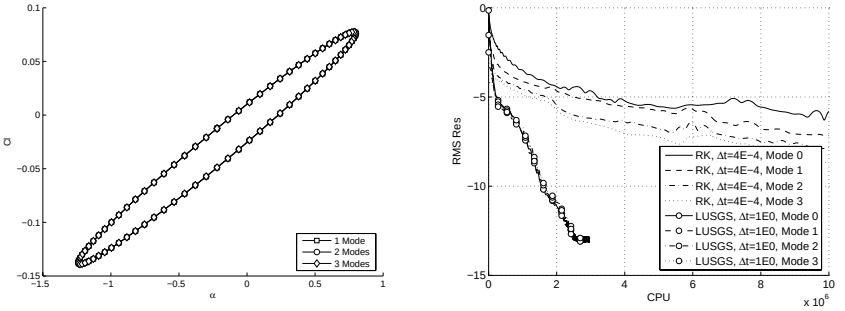

(a) Lift hysteresis (b) Convergence

Fig. 3. Pitching subsonic airfoil

$$M_\infty = 0.502,\ \bar{\alpha} = -0.22^o,\ \alpha_o = 1.02^o,\ \omega_r = 0.1 \tag{6}$$

This corresponds to the $CT = 2$ case of Davis [Dav82], whose experimental results will be used for validation purposes. The simulation is run using the third-order SD scheme on a 128×32 grid, using explicit and implicit methods. Figure (3a) presents the lift hysteresis obtained with 1, 2 and 3 modes above the fundamental frequency. As it can be noticed, the three curves are nearly indistinguishable, suggesting that a single mode is sufficient to capture the lift history. Since one mode requires only three time steps in real space, it can be concluded that the NLFD is a large improvement over time accurate methods. Figure (3b) compares the residual convergence of the three mode simulation when using the LU-SGS and five-step RK integration schemes. The implicit solver displays an improvement of more that an order of magnitude over the explicit scheme. Finally, Fig. (4) presents the real and imaginary part of the first mode of c_p, showing a good agreement with the experimental data.

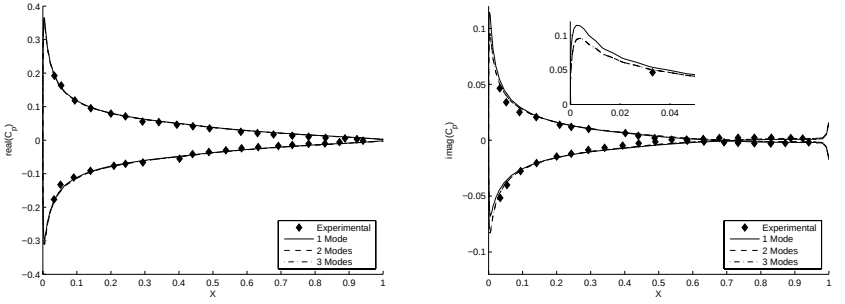

(a) real($\hat{c_p}$) (b) imag($\hat{c_p}$)

Fig. 4. First mode of the pressure distribution

The detail frame in Fig. (3b) confirms that one mode captures the general pressure trend. The curves representing the two and three modes simulations are completely overlapping, proving that mode-independence is achieved and that two modes are sufficient to get converged pressure distributions.

4 Conclusion

The present investigation describes the NLFD-SD high-order scheme for the solution of periodic inviscid flows. By combining high-order SD spatial discretization and a Fourier space description of the flow, high resolution may be achieved in both time and space dimensions. Subsonic inviscid simulations realized with a limited number of harmonics on relatively coarse meshes were in good agreement with experimental values. Lastly, the implicit driver was found to be at least an order of magnitude faster than its explicit counterpart, making the high-order NLFD-SD a competitive solution technique.

References

[HTC00] Hall, K.C., Thomas, J.P., Clark, W.S.: Computation of unsteady nonlinear flows in cascades using a harmonic balance technique. Technical report, 9th International Symposium on Unsteady Aerodynamics, Aeroacoustics and Aeroelasticity of Turbomachines (2000)

[MJA01] McMullen, M., Jameson, A., Alonso, J.: Acceleration of convergence to a periodic steady state in turbomachinery flows. AIAA paper 01-0152 (2001)

[WLM07] Wang, Z.J., Liu, Y., May, G., Jameson, A.: Spectral Difference Method for Unstructured Grids II: Extension to the Euler Equations. Journal of Scientific Computing 32, 457–471 (2007)

[SWK07] Sun, Y., Wang, Z.J., Liu, Y., Chen, C.L.: AIAA paper No. 2007-0313 (2007)

[Dav82] Davis, S.S.: NACA 64A101 (NASA Ames model) Oscillatory Pitching. Compendium of unsteady aerodynamic measurements (1982)

Part 22
Higher-Order Method 2

“*This page left intentionally blank.*”

High-Order-Accurate Fluctuation Splitting Schemes for Unsteady Hyperbolic Problems Using Lagrangian Elements

G. Rossiello, P. De Palma, G. Pascazio, and M. Napolitano

Dipartimento di Ingegneria Meccanica e Gestionale,
Centro di Eccellenza in Meccanica Computazionale,
Politecnico di Bari, Via Re David 200, 70125 Bari, Italy
g.rossiello@poliba.it, depalma@poliba.it, pascazio@poliba.it, napolita@poliba.it

1 Introduction

Fluctuation splitting (FS) schemes have been developed in order to solve complex flows, using unstructured grids, more accurately than standard schemes, while employing a compact stencil. FS schemes, which can be viewed as an efficient implementation of finite elements within a residual distribution framework, have been applied with success to solve steady and unsteady, continuous and discontinuous compressible flows, see, e.g., [Bon05, Dep05]. In particular, for the case of unsteady advection problems, the authors derived the conditions to obtain consistent mass matrices [Dep05] and the sufficient conditions for an FS scheme to be (r+1)-th-order accurate in both space and time [Ros07]. Most importantly, they have proven that the explicit FS Lax–Wendroff scheme [Str94], being one of the FS scheme satisfying the above conditions, is an extremely efficient scheme with second-order accuracy in both space and time on a general triangulation composed by linear elements [Ros08]; indeed a remarkable result. This paper proceeds from the aforementioned studies to provide an analysis of FS schemes based on Lagrangian triangular elements, which allow one to achieve higher-order accuracy, while retaining the advantage of the compactness of the original schemes designed for linear elements. In particular, as done for the case of linear elements in [Dep05, Ros07], for the present case of triangular Lagrangian ones, the consistency conditions for the mass matrix are derived, together with those to be satisfied in order for mass lumping to preserve the accuracy of the scheme. After a brief description of the theory, numerical results are presented for two linear explicit schemes of Lax–Wendroff's type, which are seen to obey the theoretical prediction of [Ros08]. A more thorough analysis of the theory is presented in [RosSu], whereas its numerical validation will be provided in the near future.

2 Analysis

Consider the two-dimensional scalar conservation law:

$$\frac{\partial u}{\partial t} + \boldsymbol{\nabla} \cdot \mathbf{F} = 0 \ , \tag{1}$$

with $\quad u \colon \Theta \to \mathbb{R}, \ \Theta = \Omega \times [0, +\infty[, \ \Omega \subseteq \mathbb{R}^2, \quad \mathbf{F} = (f(u), g(u))^{\mathcal{T}} \ .$

For linear advection, the flux vector can be expressed as $\mathbf{F} = \boldsymbol{\lambda} u$, where $\boldsymbol{\lambda} = (a, b)^{\mathcal{T}}$ is the advection velocity. The spacial computational domain, Ω, is divided into cell-vertex triangular Lagrangian elements, T; the vertices are labeled i, j, k, and the generic node (degree of freedom) is numbered σ. For a p^{th}-order element, the number of nodes is equal to $\nu = (p+1)(p+2)/2$.

FS discretizations[1] of hyperbolic equations are obtained by distributing the fluctuation, namely, the element residual,

$$\Phi^T = \phi^T + \psi^T = \int_T \boldsymbol{\nabla} \cdot \mathbf{F}^h(u^h) \ \mathrm{d}\Omega + \int_T \frac{\partial u^h}{\partial t} \ \mathrm{d}\Omega, \tag{2}$$

among the nodes σ, using suitable weight functions, ω_σ:

$$\begin{gathered} \Phi_\sigma^T = \psi_\sigma^T + \phi_\sigma^T, \quad \phi_\sigma^T = \int_T \omega_\sigma \ \boldsymbol{\nabla} \cdot \mathbf{F}^h(u^h) \ \mathrm{d}\Omega, \quad \psi_\sigma^T = \int_T \omega_\sigma \ \frac{\partial u^h}{\partial t} \ \mathrm{d}\Omega, \\ \text{with} \quad \sum_{\sigma \in T} \omega_\sigma(\mathbf{x}) = 1, \quad \forall \, \mathbf{x} \in T, \quad \text{so that} \quad \sum_{\sigma \in T} \Phi_\sigma^T = \Phi^T, \end{gathered} \tag{3}$$

where u^h and $\mathbf{F}^h$ are the discrete counterparts of u and $\mathbf{F}$, respectively, h representing the spacial increment, and ϕ_σ^T, ψ_σ^T are the steady and unsteady signals from triangle T to node σ, respectively.

Then, the system of n_{DOF} equations to be solved is obtained by summing up for each node σ all signals from the triangles sharing it:

$$\Phi_\sigma = \sum_{T \ni \ \sigma} \Phi_\sigma^T = 0. \tag{4}$$

For the steady term, it can be shown [RosSu] that the fluctuation reads:

$$\phi^T = \sum_{\sigma \in T} \mathbf{F}_\sigma \cdot \int_T \boldsymbol{\nabla} N_\sigma \ \mathrm{d}\Omega = \sum_{\sigma \in T} u_\sigma \boldsymbol{\lambda} \cdot \int_T \boldsymbol{\nabla} N_\sigma \ \mathrm{d}\Omega = \sum_{\sigma \in T} k_\sigma^\star u_\sigma, \tag{5}$$

where N_σ are the shape functions and $k_\sigma^\star$ are generalized inflow parameters equal to linear combinations of the well known vertices-inflow parameters of

[1] Here, for the sake of brevity, only a finite difference discretization in time is employed since no major differences arise when considering a space-time approach [Ros08].

linear-reconstruction FS schemes, $k_i = \boldsymbol{\lambda} \cdot \mathbf{n}_i/2$. Starting from equation (3), an elemental convection matrix can be defined,

$$\left\{\phi_\delta^T\right\} = \left[\mathbf{C}_{\delta\sigma}\right]\left\{u_\sigma\right\} = \left[\beta_\delta^T \ \mathcal{K}_{\delta\sigma}^\star\right]\left\{u_\sigma\right\} = \begin{bmatrix} \beta_1^T \mathcal{K}_{11}^\star & \dots & \beta_1^T \mathcal{K}_{1\nu}^\star \\ \vdots & \ddots & \vdots \\ \beta_\nu^T \mathcal{K}_{\nu 1}^\star & \dots & \beta_\nu^T \mathcal{K}_{\nu\nu}^\star \end{bmatrix} \begin{Bmatrix} u_1 \\ \vdots \\ u_\nu \end{Bmatrix}, \tag{6}$$

where $\beta_\delta^T = \dfrac{1}{S_T}\displaystyle\int_T \omega_\delta \ \mathrm{d}\Omega$ and $\mathcal{K}_{\delta\sigma}^\star = \boldsymbol{\lambda} \cdot \boldsymbol{\nabla} N_\sigma(\mathbf{x}^\star) S_T$, with $\mathbf{x}^\star \in T$ given by the mean-value theorem. The coefficients of the convection matrix must satisfy the following conditions to provide a consistent and conservative FS discretization. For each row of $\mathbf{C}$,

$$\sum_{\sigma\in T} \boldsymbol{\nabla} N_\sigma = 0 \Longrightarrow \sum_{\sigma\in T} \mathcal{K}_{\delta\sigma}^\star = 0. \tag{7}$$

Furthermore, from equations (5) and (6):

$$\phi^T = \sum_{\sigma\in T} u_\sigma \ k_\sigma^\star \quad = \sum_{\delta\in T} \phi_\delta^T = \sum_{\delta\in T} \beta_\delta^T \sum_{\sigma\in T} \mathcal{K}_{\delta\sigma}^\star u_\sigma = \quad \sum_{\sigma\in T} u_\sigma \sum_{\delta\in T} \beta_\delta^T \mathcal{K}_{\delta\sigma}^\star. \tag{8}$$

Thus, for each column of the elemental convection matrix:

$$\sum_{\delta\in T} \beta_\delta^T \mathcal{K}_{\delta\sigma}^\star = k_\sigma^\star. \tag{9}$$

Finally, $\displaystyle\sum_{\delta\in T} \beta_\delta^T = 1$, since $\displaystyle\sum_{\delta\in T} \omega_\delta(\mathbf{x}) = 1, \quad \forall\, \mathbf{x} \in T.$

Considering, now, the discretization of the unsteady residual, one has:

$$\psi_\delta^T = \int_T \omega_\delta \frac{\partial u^h}{\partial t} \mathrm{d}\Omega = \sum_{\sigma\in T} \frac{\partial u_\sigma}{\partial t} \int_T \omega_\delta \, N_\sigma \, \mathrm{d}\Omega = \sum_{\sigma\in T} m_{\delta\sigma}^T \frac{\partial u_\sigma}{\partial t}, \tag{10}$$

where $m_{\delta\sigma}^T$ are the components of the element mass matrix which can be written as [Ros08]:

$$m_{\delta\sigma}^T = \int_T \omega_\delta \, N_\sigma \, \mathrm{d}\Omega = N_\sigma(\mathbf{x}_\delta^\star) \int_T \omega_\delta \, \mathrm{d}\Omega = \gamma_{\delta\sigma} \, \beta_\delta^T \, S_T, \tag{11}$$

where $\mathbf{x}_\delta^\star \in T$ and $N_\sigma(\mathbf{x}_\delta^\star) = \gamma_{\delta\sigma}$. The constraints to be satisfied by the mass-matrix coefficients for the scheme to be consistent and conservative are now recalled [Dep05]. Since $\sum_\sigma N_\sigma = 1$,

$$\sum_\sigma m_{\delta\sigma}^T = \sum_\sigma \int_T \omega_\delta \, N_\sigma \, \mathrm{d}\Omega = \int_T \omega_\delta \, \mathrm{d}\Omega = \beta_\delta^T \, S_T. \tag{12}$$

Moreover, using equation (11), one has

$$\sum_\sigma m_{\delta\sigma}^T = \sum_\sigma \gamma_{\delta\sigma} \, \beta_\delta \, S_T \Longrightarrow \sum_\sigma \gamma_{\delta\sigma} = 1, \quad \text{for} \quad \delta = 1, ..., \nu. \tag{13}$$

Furthermore, since $\sum_{\delta} \omega_\delta = 1$, for conservation:

$$\psi^T = \sum_{\delta} \int_T \omega_\delta \frac{\partial u^h}{\partial t} \mathrm{d}\Omega = \int_T \frac{\partial u^h}{\partial t} \mathrm{d}\Omega = \sum_{\sigma} \frac{\partial u_\sigma}{\partial t} \int_T N_\sigma \mathrm{d}\Omega = \sum_{\sigma} \frac{\partial u_\sigma}{\partial t} \eta_\sigma S_T. \tag{14}$$

On the other hand, using equations (10) and (11),

$$\sum_{\delta} \int_T \omega_\delta \frac{\partial u^h}{\partial t} \mathrm{d}\Omega = \sum_{\delta} \sum_{\sigma} m^T_{\delta\sigma} \frac{\partial u_\sigma}{\partial t} = \sum_{\delta} \sum_{\sigma} \frac{\partial u_\sigma}{\partial t} \gamma_{\delta\sigma} \beta^T_\delta S_T \,. \tag{15}$$

Comparing the right hand sides of the last two equations, the following conservation constraints are obtained:

$$\sum_{\delta} \gamma_{\delta\sigma} \beta^T_\delta = \eta_\sigma, \quad \text{for} \quad \sigma = 1, ..., \nu. \tag{16}$$

Classical FS schemes, written in the form

$$\boldsymbol{\Phi}^T_\delta = \beta^T_\delta \boldsymbol{\Phi}^T, \tag{17}$$

satisfy the above conditions for consistency and conservation: starting from equation (2) and using equations (5) and (6) for ϕ^T and ϕ^T_δ and equations (14) and (10) for ψ^T and ψ^T_δ, equations (17) provides:

$$\mathcal{K}^\star_{\delta\sigma} = k^\star_\sigma, \quad \text{and} \quad \gamma_{\delta\sigma} = \eta_\sigma. \tag{18}$$

Conditions (7) and (9) are thus satisfied, being $\sum_{\delta \in T} \beta^T_\delta = 1$, $\sum_{\sigma \in T} k^\star_\sigma = 0$ and $\sum_{\sigma \in T} \eta_\sigma = 1$. Therefore a scheme defined by equation (17) is consistent and conservative; on the other hand, its associate algebraic system (4) is indeterminate when employing Lagrangian elements with $p \geq 2$ (see [RosSu] for details).

2.1 Mass Lumping and Explicit Schemes

Generalizing to a p^{th}-order reconstruction the analysis provided in [Ros08] for $p = 1$, mass lumping, namely, $\gamma_{\delta\sigma} = \delta_{\delta\sigma}$, automatically satisfies condition $\sum_\sigma \gamma_{\delta\sigma} = 1$ and requires that $\beta_\delta = \eta_\delta$ for consistency (see equation (16)).

Starting from these results, the FS Lax–Wendroff explicit scheme is proven to be second-order-accurate in space and time over general unstructured grids. For a linear reconstruction, the consistent mass lumping requires $\beta_\sigma = \eta_\sigma = 1/3$, indicating that the space distribution derives form the Galerkin weight functions. Assuming a linear reconstruction of the flux function in time, the following signal is obtained:

$$\boldsymbol{\Phi}^{n+1}_\delta = \sum_{T \ni \delta} \left[\psi^{T,n+\frac{1}{2}}_\delta + \phi^{T,n+\frac{1}{2}}_\delta \right] = S_\sigma \frac{u^{n+1}_\sigma - u^n_\sigma}{\Delta t} + \frac{1}{3} \sum_{T \ni \sigma} \phi^{T,n+\frac{1}{2}} = 0. \tag{19}$$

In order to derive an explicit scheme, performing a Taylor expansion in time for $\boldsymbol{\lambda} \cdot \boldsymbol{\nabla} u^{n+\frac{1}{2}}$ and integrating in space using $\omega_\delta = N_\delta$, the following approximation of $\phi_\delta^{T,n+\frac{1}{2}}$ is obtained:

$$\frac{1}{3}\phi_\delta^{T,n+\frac{1}{2}} = \frac{1}{3}\phi_\delta^{T,n} + \frac{k_\delta}{2\Delta \mathrm{t}}\phi_\delta^{T,n} = \beta_\delta^{LW}\phi^{T,n}, \tag{20}$$

where β_δ^{LW} is the distribution coefficient of the FS Lax–Wendroff (LW) scheme [Str94]. The proposed analysis for consistent mass lumping allows one to derive a family of high-order-accurate explicit schemes which differ in the discretization of the time derivative and in the time approximation of the steady term. For example, a two-point-backward discretization of the time derivative leads to an alternative FS scheme (LW2) (see [Ros08] for details) which also enjoys second-order accuracy.

3 Results

The accuracy of the two LW and LW2 schemes has been verified by computing the unsteady linear advection, with $\boldsymbol{\lambda} = (1, 2)$, of the double-sine-shaped function,

$$u = \sin^2(2\pi x)\, \sin^2(2\pi y),$$

over the unit square $[0, 1]^2$. Two set of meshes have been employed for discretizing the computational domain, called A and B. Each coarsest mesh has 32 cells along each edge of the computational domain: the coarsest mesh A is an unstructured mesh, obtained by a triangulation with a non uniform discretization of the edges of the computational square, which is made up of regular triangles having largely different sizes, see figure 1 (left); the coarsest mesh B is a considerably skewed mesh obtained by a perturbed structured

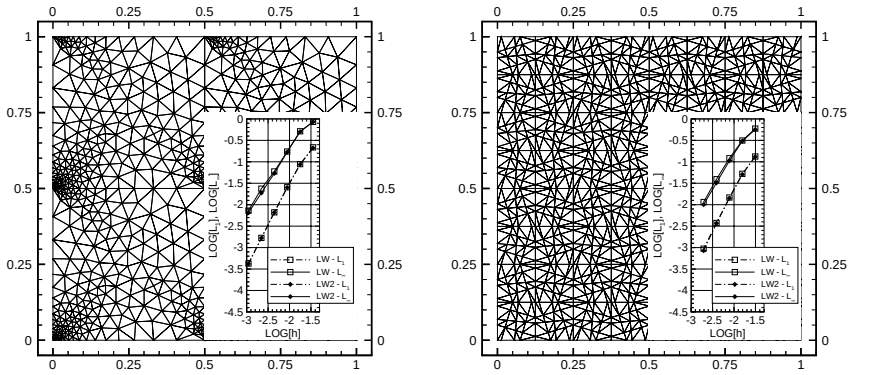

Fig. 1. Linear advection: Coarsest mesh A ($h_1 = 3.534 \cdot 10^{-2}$) (left) and coarsest mesh B ($h_1 = 3.125 \cdot 10^{-2}$) (right)

module, shown in figure 1 (right). Starting from each coarsest mesh, four refined meshes were obtained by mapping it onto each region obtained by dividing the computational domain into 4, 16, 64, and 256 identical squares, ($h_i = h_1/4^i$ for $i = 1, ..., 4$), with $h_1 = 1/\sqrt{N_T}$, N_T being the total number of triangles of the corresponding coarsest mesh. It is noteworthy that such a refinement does not preserve the shape of each cell, locally, thus providing a very severe test for the order of accuracy of the schemes.

The logarithms of the L_1 and L_∞ norms of the numerical errors are reported in figure 1, which confirms the predicted order of accuracy of the schemes.

References

[Bon05] Bonfiglioli, A., De Palma, P., Pascazio, G., Napolitano, M.: An implicit fluctuation splitting scheme for turbomachinery flows. ASME J. Turbomach. 127, 395–401 (2005)

[Dep05] De Palma, P., Pascazio, G., Rossiello, G., Napolitano, M.: A second-order-accurate monotone implicit fluctuation splitting scheme for unsteady problems. J. Comput. Phys 208, 1–33 (2005)

[Ros07] Rossiello, G., De Palma, P., Pascazio, G., Napolitano, M.: Third-order-accurate fluctuation splitting schemes for unsteady hyperbolic problems. J. Comput. Phys 222, 332–352 (2007)

[Str94] Struijs, R.: A multidimensional upwind discretization method for the Euler equations on unstructured grids, Ph. D. thesis, von Karman Institute for Fluid Dynamics (1994)

[Ros08] Rossiello, G., De Palma, P., Pascazio, G., Napolitano, M.: Second-order-accurate explicit fluctuation splitting schemes for unsteady problems, Computers & Fluids (in press) (2008)

[Red93] Reddy, J.N.: An introduction to finite element method, 2nd edn. McGraw Hill, New York (1993)

[RosSu] Rossiello, G., De Palma, P., Pascazio, G., Napolitano, M.: Analysis of high-order fluctuation splitting schemes for hyperbolic problems. J. Comput. Phys. (submitted)

Assessment of High-Order Algorithms for Aeroacoustic Computation of Shock-Containing Flows

J. Berland, T. Le Garrec, X. Gloerfelt, and V. Daru

SINUMEF, Arts et Métiers ParisTech, 151 Boulevard de l'Hôpital, 75014 Paris, France

1 Introduction

This work is interested in the design of discretization tools ensuring high order of accuracy for both discontinuous and smooth solutions. These developments are motivated by the desire to achieve aeroacoustic calculations of supersonic turbulent flows such as for instance supersonic jets, transonic airfoils or supersonic opened cavities.

Since the earliest stages of computational aeroacoustics (CAA), the need for algorithms exhibiting high accuracy over a large range of wavenumbers has been recognized [Tam95a]. Schemes with large stencils are therefore commonly implemented in order to perform simulations of the generation of sound waves by turbulent flows. In particular, Dispersion-Relation-Preserving (DRP) schemes have been developped in order to meet the stringent requirements of CAA [BB04, TW93]. These algorithms are based on large stencils whose coefficients are optimized in the Fourier space to ensure low dissipative and low dispersive properties. The DRP discretization tools are especially well suited for long range propagation and aeroacoustic calculations, but do not have shock-capturing specific features. When encountering flow with discontinuities, high-order algorithms may indeed fail to describe the solution because of their inability to deal with the spurious oscillations generated by the Gibbs phenomenon in the neighborhood of strong gradients. This issue may be circumvented by employing specific shock-capturing schemes, *e.g.* the Essentially NonOscillary (ENO) or the Weighted ENO (WENO) differentiation methods [HEOC87]. These approaches are however not suitable for aeroacoustic applications since they can introduce too much artificial dissipation strongly altering the features of the acoustic waves.

An alternative technique proposed by Jameson et al. [JST81] is to combine high-resolution central difference schemes with a selective adaptive smoothing term. Kim & Lee [KL01] extended Jameson's algorithm by designing an adaptive control of the damping terms. This Adaptive Nonlinear Artificial Dissipation (ANAD) aims at damping out spurious oscillations generated close to the shock waves while keeping acoustic waves unaffected. The

dissipation term is indeed expressed as the combination of a second- and a fourth-order damping term. A nonlinear function, relying on a shock sensor, then locally regulates the magnitude of the second- and fourth-order dissipations according to the rate of change of the pressure gradient. This class of algorithms is appealing because of its simplicity and its low requirement in computational cost. The method furthermore turned to be efficient for several CAA applications [KL01, ELC07, MBM07].

Adaptive Nonlinear Selective Filtering (ANSF) techniques are also available for calculation of flows with discontinuities. ANSF techniques share strong similarities with ANAD algorithms. Smoothing terms are nevertheless no longer considered as artificial damping terms. Instead, a signal processing operation is applied after each time step in order to adjust the solution near discontinuities. The method relies on an algebraic algorithm theoretically able to handle any kind of discontinuity. Such a shock-capturing scheme has been recently proposed by Bogey et al. [BCB08].

Another promising family of shock capturing schemes can be derived using flux-limiting procedures. Daru & Tenaud [DT04] recently introduced a new set of high-order upwind-limited schemes. The procedure of limitation allows to obtain a monotonicity-preserving (MP) algorithm while maintaining high-order of accuracy. The numerical flux combines a high-order flux function to a Roe's scheme, and is designed so that the Monotonicity-Preserving (MP) conditions are fulfilled [SH97]. Test cases relying on calculations of supersonic cavity flows furthermore demonstrated that these algorithms were suitable for CAA applications [DG07].

Three shock capturing techniques, the ANAD algorithms of Kim & Lee [KL01], the ANSF technique of Bogey et al. [BCB08] and the MP scheme of Daru & Tenaud [DT04], are therefore available for aeroacoustic calculations involving shocks. The present work is an attempt to provide a comprehensive comparison between these approaches.

2 Shock-Capturing Algorithms

For sake of brievity, the algorithms themselves are not provided in details but full descriptions of the schemes may be found in the works cited in what follows. The following discretization schemes are assessed in the present study: the 11-point optimized finite differences along with the 11-point optimized selective filter of Bogey & Bailly [BB04] (refered to as DRP11), the 11th-order one-step monotonicity-preserving algorithm of Daru & Tenaud [DT04] [DT04] (refered to as OSMP11), the adaptive damping scheme of Kim & Lee [KL01] with the 11-point optimized selective filter of Bogey & Bailly [BB04] as a background filter (refered to as ANAD), and the adaptive nonlinear selective filtering of Bogey et al. [BCB08] (refered to as ANSF).

3 Test Cases

3.1 Shock Wave Interacting with a Density Disturbance (1D)

A one-dimensional test case, initially proposed by Shu & Osher [SO89] is first solved. A moving Mach 3 shock wave interacts with a sinusoidal density profile. The solution is computed up to $t = 1.8$ using 200 grid points, for the DRP11, the OSMP11, the ANAD and the ANSF algorithms. The resulting density distributions close to the shock are plotted in figure 1. One may observe that the DRP11 and the OSMP11 yield rather similar results. The density disturbance is well preserved in the neighborhood of the discontinuity. As concern the ANAD and ANSF schemes, it turns out that they may introduce too much dissipation. In particular, for $5.5 < x < 7.5$ the amplitude of the high-frequency oscillations are particularly underestimated.

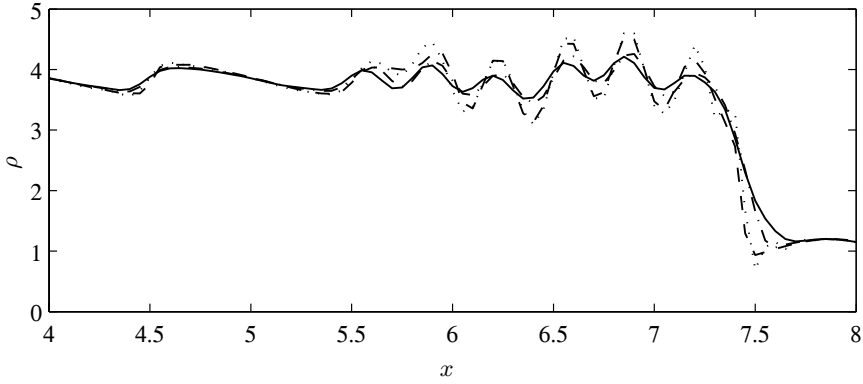

Fig. 1. Pressure distribution for the 1D shock-turbulence interaction, obtained for various numerical algorithms. · · · · ·, DRP11 ; –·–·–, ANAD ; ———, ANSF ; – – – –, OSMP11

3.2 Transonic Airfoil (2D)

A two-dimensional steady test case is now considered in order to assess the algorithms in a more realistic context. The inviscid flow around a NACA0012 airfoil is solved. The angle of attack is $\alpha = 1.0°$ and the freestream Mach number M_∞ is taken to be equal to 0.85. Under these operating conditions, compression shocks emerge on both pressure and suction sides of the airfoil. This flow configuration has been widely used to benchmark shock-capturing numerical techniques, as for instance in the works of Yee et al. [YH87].

Coordinate transformation is utilized in order to perform the calculation using a curvilinear physical space. The mesh has a C-shape and makes use of 241×301 grid points. The domain extends from $-6c$ to $+4c$ in the streamwise

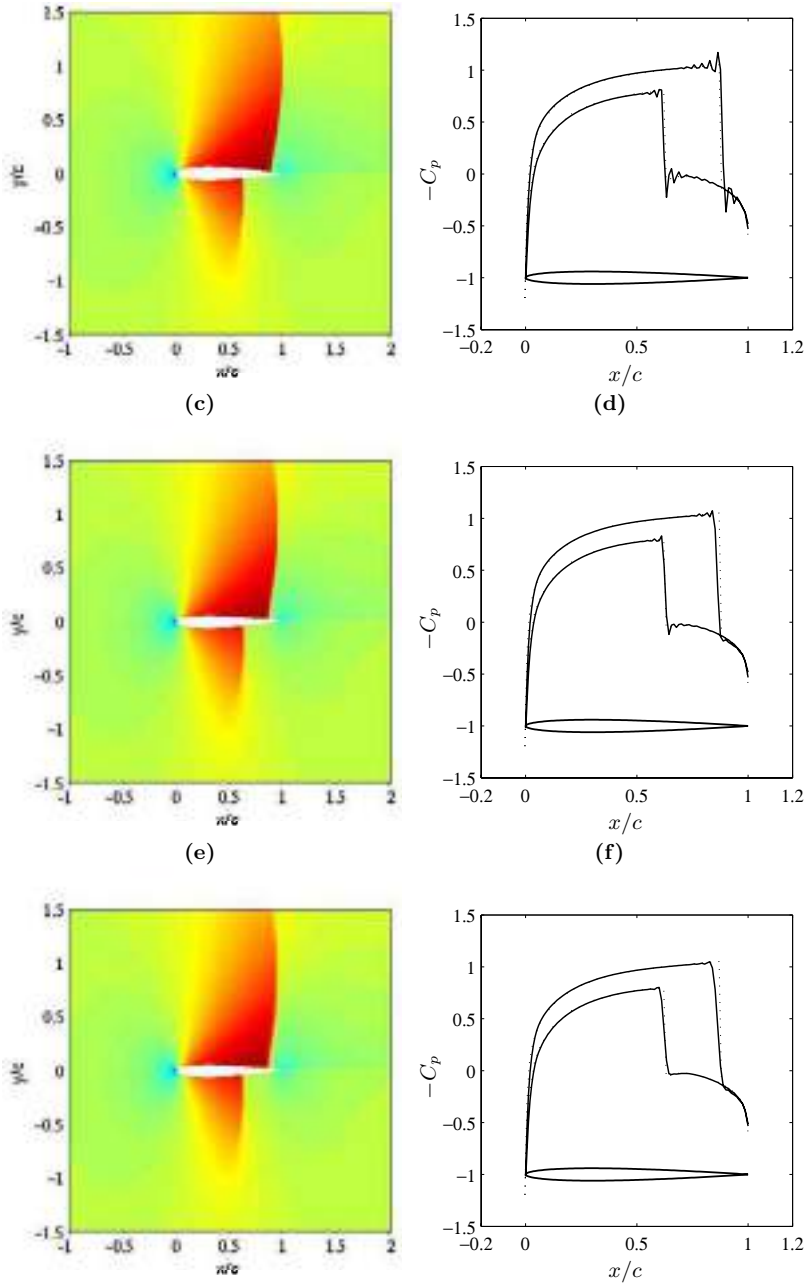

Fig. 2. Mach colormap and pressure coefficient distribution computed for various numerical algorithms, for the NACA0012 airfoil with $M_\infty = 0.85$, $\alpha = 1.0°$. **(a)-(b)**, DRP11 scheme; **(c)-(d)**, ANAD scheme; **(e)-(f)**, ANSF scheme. Colorscale based on the Mach number from 0 (blue) to 1.5 (red). Line styles for the pressure coefficient: ———, present calculations; ·····, reference data of Yee & Harten [YH87].

direction, and ranges from $-6c$ to $+6c$ in the transverse direction, where c is the chord length. The flow around the airfoil is computed using the 11-point optimized DRP11 schemes [BB04], the ANAD algorithm of Kim & Lee [KL01]and the ANSF technique of Bogey et al. [BCB08].

The Mach number field is represented in figures 2.a, 2.c and 2.e, for the DRP11 scheme, the ANAD scheme and the ANSF scheme, respectively. For the three numerical algorithms the Mach number distributions appear to be very similar. Flow acceleration is visible on either side of the airfoil and the Mach number eventually becomes greater than one in some regions around the airfoil. Two shocks are observed, one around $x/c \sim 0.9$ on the suction side, and another around $x/c \sim 0.6$ on the pressure side.

The pressure coefficient distributions around the airfoil is now presented in figures 2.b, 2.d and 2.f, for the DRP11 scheme, the ANAD scheme and the ANSF scheme, respectively. As a guideline, the results of Yee & Harten [YH87] using ARC2D with a grid refined in the neighborhood of the shocks (560×65 nodes) are also presented. An overall agreement is observed. In particular, the shock locations are correctly reproduced for all the numerical methods, including the DRP11 schemes in figure 2.b. It is worth noting that even though the optimized schemes do not have any specific features aiming at capturing flow discontinuities, the pressure coefficient distribution is still in good agreement with the data of Yee & Harten [YH87]. Gibbs oscillations are nonetheless visible but it seems that they do not have a negative impact on the global solution. According to figure 2.d and figure 2.f, Gibbs oscillations are severely reduced with the ANAD or the ANSF schemes. Away from the shocks, the pressure coefficient does not seem to be affected by the shock-capturing. On the other hand, around the discontinuities, the solution is clearly smoother than the one obtained with the DRP11 schemes alone. Some small residual oscillations are however still visible in figure 2.d for the ANAD scheme. For the ANSF algorithm in figure 2.f, the solution is completely smooth but the shock lies over a larger number of grid points.

The calculations with the shock-capturing algorithms ANAD and ANSF therefore appear to correctly reproduce the features of the flow around the transonic airfoil.

4 Conclusion

The shock-capturing abilities of three numerical algorithms, namely, the ANAD algorithms of Kim & Lee [KL01], the ANSF technique of Bogey et al. [BCB08] and the MP scheme of Daru & Tenaud [DT04], have been investigated. The simulation of the interaction of a shock wave interacting with a density disturbance showed that the ANAD and ANSF schemes might be slightly over-dissipative. On the other hand, inviscid calculations of the flow around a transonic airfoil using the ANAD and ANSF techniques turn out to provide correct results.

References

[BB04] Bogey, C., Bailly, C.: A family of low dispersive and low dissipative explicit schemes for flow and noise computations. J. Comput. Phys. 194, 194–214 (2004)

[BCB08] Bogey, C., de Cacqueray, N., Bailly, C.: Self-adjusting shock-capturing spatial filtering for high-order non-linear computations. In: 14th AIAA/CEAS Aeroacoustics Conference Proceedings, 5-7 May, Vancouver, British Columbia, Canada, AIAA Paper 2008-2968 (2008)

[DT04] Daru, V., Tenaud, C.: High order one-step monotonicity-preserving schemes for unsteady compressible flow calculations. J. Comput. Phys. 193(2), 563–594 (2004)

[DG07] Daru, V., Gloerfelt, X.: Aeroacoustic computations using a high-order shock-capturing scheme. AIAA J. 45(10), 2474–2486 (2007)

[ELC07] Emmert, T., Lafon, P., Bailly, C.: Computation of aeroacoustic phenomena in subsonic and transonic ducted flow. In: 12th AIAA/CEAS Aeroacoustics Conference, 8-10 May, Cambridge, Massachusetts, USA, AIAA Paper 2007-3429 (2007)

[HEOC87] Harten, A., Engquist, B., Osher, S., Chakravarthy, S.: Uniformly high order essentially nonoscillatory schemes. J. Comput. Phys. 71(2), 231–303 (1987)

[JST81] Jameson, A., Schmidt, W., Turkel, E.: Numerical solutions of the Euler equations by finite volume methods using Runge-Kutta time stepping schemes. In: 14th AIAA Fluid and Plasma Dynamics Conference Proceedings, 23-25 June, Palo Alto, California, USA, AIAA Paper 1981–1259 (1981)

[KL01] Kim, J.W., Lee, D.J.: Adaptive nonlinear artifical dissipation model for computational aeroacoustics. AIAA J. 39(5), 810–818 (2001)

[MBM07] Moase, W.H., Brear, M.J., Manzie, C.: The forced response of choked nozzles and supersonic diffusers. J. Fluid Mech. 585, 281–304 (2007)

[SO89] Shu, C.W., Osher, S.: Efficient implementation of essentially non-oscillatory shock-capturing schemes, II. J. Comput. Phys. 83, 32–79 (1989)

[SH97] Suresh, A., Huynh, H.: Accurate monotonicity-preserving schemes with Runge-Kutta time stepping. J. Comput. Phys. 136(1), 83–99 (1997)

[TW93] Tam, C., Webb, J.: Dispersion-Relation-Preserving finite difference schemes for computational acoustics. J. Comput. Phys. 107, 262–281 (1993)

[Tam95a] Tam, C.K.W.: Computational aeroacoustics: issues and methods. AIAA J. 33(10), 1788–1797 (1995)

[Tam95b] Tam, C.K.W.: Benchmark problems and solutions. In: ICASE/LaRC Workshop on Benchmark Problems in Computational Aeroacoustics, NASA CP 3300, 1–13 (1995)

[YH87] Yee, H., Harten, A.: Implicit TVD schemes for hyperbolic conservation laws in curvilinear coordinates. AIAA J. (25), 266–274 (1987)

A Dynamic Spatial Filtering Procedure for Shock Capturing in High-Order Computations

Christophe Bogey[1], Nicolas de Cacqueray[2], and Christophe Bailly[3]

[1] Laboratoire de Mécanique des Fluides et d'Acoustique, UMR CNRS 5509, Ecole Centrale de Lyon, 69134 Ecully Cedex, France
christophe.bogey@ec-lyon.fr
[2] Laboratoire de Mécanique des Fluides et d'Acoustique, UMR CNRS 5509, Ecole Centrale de Lyon, 69134 Ecully Cedex
nicolas.cacqueray@ec-lyon.fr
[3] Laboratoire de Mécanique des Fluides et d'Acoustique, UMR CNRS 5509, Ecole Centrale de Lyon, 69134 Ecully Cedex
& Institut Universitaire de France
christophe.bailly@ec-lyon.fr

Summary. A shock-capturing method is developed for high-order non-linear computations. It consists in applying an adaptative second-order conservative filtering to handle discontinuities, in combination with a background selective filtering to remove grid-to-grid oscillations. The magnitude of the shock-capturing filtering is determined dynamically from the flow solutions using a procedure based on a Jameson-like shock detector. Results obtained for a shock-propagation problem are shown to assess the validity of the method.

1 Introduction

The need for filtering high-frequency waves is a recurrent issue in high-order simulations, which has led to the design of selective filters, e.g. by Lele [10], Visbal & Gaitonde [14] and Bogey & Bailly [2]. These filters can be used for strongly non-linear problems, such as the generation of screech noise in supersonic jets as performed in [1], but it is generally recognized that they are not well suited to solutions including discontinuities. Near shocks, high-order schemes might indeed generate spurious Gibbs oscillations due to spectral truncation in the wavenumber space. Therefore the usual approach to ensure stability for shocked flows is based on shock-capturing schemes. Such schemes might however be too dissipative for unsteady problems. In that case, their spectral properties have to be analysed [11], and their accuracy has to be checked by solving demonstrative test cases [6].

An alternative approach consists in developing an adaptative shock-capturing filtering, which is also appropriate for high-order simulations, as done for instance by Tam & Shen [13] and by Kim & Lee [9]. In the present study, a spatial filtering is thus proposed to deal with shocks in high-order

non-linear computations in which a background selective filtering is implemented to remove grid-to-grid oscillations. To smooth shocks, the filtering is of second order, and its magnitude is adjusted dynamically from the flow variables so that it is negligible for linear propagation and for vortical disturbances. A procedure of shock detection is especially proposed so as to evaluate the filtering amplitude from the magnitude of the high wavenumbers of the solutions. In order to obtain a strong conservative form, the filtering procedure is also written as the difference between damping fluxes taken at the interface of two adjacent cells.

In what follows, the shock-capturing method is first presented, and solutions calculated for a shock-propagation problem are then shown. More details about the method and results obtained for other test cases including linear sound propagation, vortex convection, shock-acoustic interactions in a transonic nozzle and shock-vortex interactions can be found in [5].

2 Shock-Capturing Methodology

A procedure of shock detection is first derived to estimate the strength of the shock-capturing filtering from the flow variables, so that it should be significant around discontinuities but negligible everywhere else. More precisely, in order to indicate the presence of shocks, a shock detector, roughly similar to that formulated by Jameson *et al.* [8] making use of the second derivative of pressure, is evaluated from the magnitude of the high-wavenumber components of a variable that can be either pressure or dilatation.

In some cases the use of pressure to detect shocks might however not be appropriate for distinguishing between turbulent fluctuations and shocks in an unambiguous manner. To deal with this deficiency, as also suggested by Ducros *et al.* [7], a possibility is to take into account the local property of compressibility. This led us here to perform the shock detection from dilatation $\Theta = \nabla \cdot \mathbf{u}$ rather than from pressure.

To determine the shock sensor, the high-wavenumber components are first extracted from variable Θ using a Laplacian filter, yielding, at node i

$$D\Theta_i = \frac{1}{4}\left(-\Theta_{i+1} + 2\Theta_i - \Theta_{i-1}\right) \tag{1}$$

The magnitude of the high-passed filtered dilatation is then calculated as

$$D\Theta_i^{magn} = \frac{1}{2}\left[\left(D\Theta_i - D\Theta_{i+1}\right)^2 + \left(D\Theta_i - D\Theta_{i-1}\right)^2\right] \tag{2}$$

and the shock sensor is defined as the ratio r expressed as

$$r_i = \frac{D\Theta_i^{magn}}{c_i^2/\Delta x^2} + \epsilon \tag{3}$$

where $c_i^2 = \gamma p_i/\rho_i$ is the square of the sound speed, Δx is the mesh spacing, and $\epsilon = 10^{-16}$ is introduced to avoid numerical divergence later in equation (4).

Once the value of the shock detector r is known, the strength of the filtering has to be given. In the present approach, a threshold parameter r_{th} is used to specify the regions where the shock-capturing filtering is employed. The filtering magnitude is evaluated by the function

$$\sigma_i^{sc} = \frac{1}{2}\left(1 - \frac{r_{th}}{r_i} + \left|1 - \frac{r_{th}}{r_i}\right|\right) \tag{4}$$

For $r_i \leq r_{th}$, the filtering magnitude is $\sigma_i^{sc} = 0$ as required. For $r_i > r_{th}$, that is when the level of the high-wavenumber components of dilatation are appreciable, one gets $0 < \sigma_i^{sc} < 1$, and in particular $\sigma_i^{sc} \to 1$ for $r_i \to +\infty$. The threshold parameter r_{th} is typically to be set between 10^{-6} and 10^{-4}, a lower value corresponding to an application of the shock-capturing filtering on a wider region. In this way, the second-order filter is only switched on when the dilatation gradients are strong.

The shock-capturing filtering is applied at each time step just after the background selective filtering removing grid-to-grid oscillations. Since its magnitude depending on the shock detection varies, the filtering operation is written in a conservative form as the difference between two damping fluxes taken at the interface of two adjacent cells as recommended by Kim & Lee [9] for instance. At point i on an uniform grid, the conservative variables U are thus filtered explicitly to yield

$$U_i^{sc} = U_i - \left(\sigma_{i+\frac{1}{2}}^{sc} D_{i+\frac{1}{2}}^{sc} - \sigma_{i-\frac{1}{2}}^{sc} D_{i-\frac{1}{2}}^{sc}\right) \tag{5}$$

where the filtering strength $0 \leq \sigma^{sc} \leq 1$ is specified by the dynamic procedure presented previously, and the damping functions $D_{i+\frac{1}{2}}^{sc}$ and $D_{i-\frac{1}{2}}^{sc}$ are estimated from the variables U using the following interpolations

$$D_{i+\frac{1}{2}}^{sc} = \sum_{j=1-n}^{n} c_j U_{i+j} \qquad \text{and} \qquad D_{i-\frac{1}{2}}^{sc} = \sum_{j=1-n}^{n} c_j U_{i+j-1} \tag{6}$$

To determine the coefficients c_j of the $2n$-point interpolation defining the damping functions, one considers the non-conservative form of the filtering

$$U_i^{sc} = U_i - \sigma_i^{sc} \sum_{j=-n}^{n} d_j U_{i+j} \tag{7}$$

and notes that equations (5) and (7) must be equivalent when the filtering magnitude is uniform. For a given n, the coefficients c_j are then directly obtained from the coefficients d_j of the corresponding non-conservative centered filter. The values found for the standard 2nd-order filter, here referred to as Fo2, are collected in Table 1.

Table 1. Coefficients c_j for conservative shock-capturing filtering: standard 2nd-order filter (Fo2), and optimized 2nd-order filter (Fopt), with $c_{1-j} = -c_j$

	Fo2	Fopt
c_1	1/4	−0.210383
c_2	0	0.039617

The coefficients c_j calculated for another second-order filter are also reported in the Table. This filter was built up in [5] using an optimization procedure in the wave-number space so that it displays dissipation features similar to those of the standard filter Fo2, but generates reduced phase errors. Phase errors are indeed induced by the variations of the filtering magnitude.

3 Application to a Shock-Propagation Problem

The shock-capturing methodology is now implemented to solve the shock-propagation problem proposed by Tam [12], based on the one-dimensional Euler equations. The spatial derivatives are computed using eleven-point low-dispersion centered finite-differences, and the time integration is performed using a six-stage low-dissipation Runge-Kutta algorithm, designed in [2]. The grid spacing is uniform with $\Delta x = 1$, and the time step is $\Delta t = 0.8$. A background selective filtering is carried out using a eleven-point filter of order 6 optimized in the wavenumber space [5], with a uniform magnitude equal to 1, at each grid point every time step. The shock-capturing methodology is then applied. Note that the present discretization methods have been successfully used to perform accurate Large-Eddy Simulations of three-dimensional turbulent flows and their radiated noise [1, 3].

The pressure solution calculated at $t = 200$ using selective filtering of the fluxes as discussed in [4], without shock-capturing, is presented in figure 1(a). The pressure pulse has been dispersed, which suggests that filtering the fluxes is not appropriate when strong non-linear effects take place.

The solutions obtained using selective filtering of the variables, alone or in combination with the shock-capturing filtering, are then displayed in figures 1(b), 1(c) and 1(d). The pressure pulse has become triangular in shape at $t = 200$ due to non-linear effects. In figure 1(b), without using shock-capturing, a shock is indeed visible at $x \simeq 249\Delta x$, but it is surrounded by Gibbs oscillations because of the spectral truncation of the solution.

In figures 1(c) and 1(d), using shock-capturing, the pressure pulse however does not exhibit oscillations around the shocks which are rather sharp. The Gibbs oscillations have then been removed by the second-order filter. More precisely, as demonstrated in [5], the second-order shock-capturing filtering applies near the discontinuity, but its magnitude is nil everywhere else.

In addition the location of the shocks is found to differ when non-conservative or conservative filtering procedures are implemented, with shocks

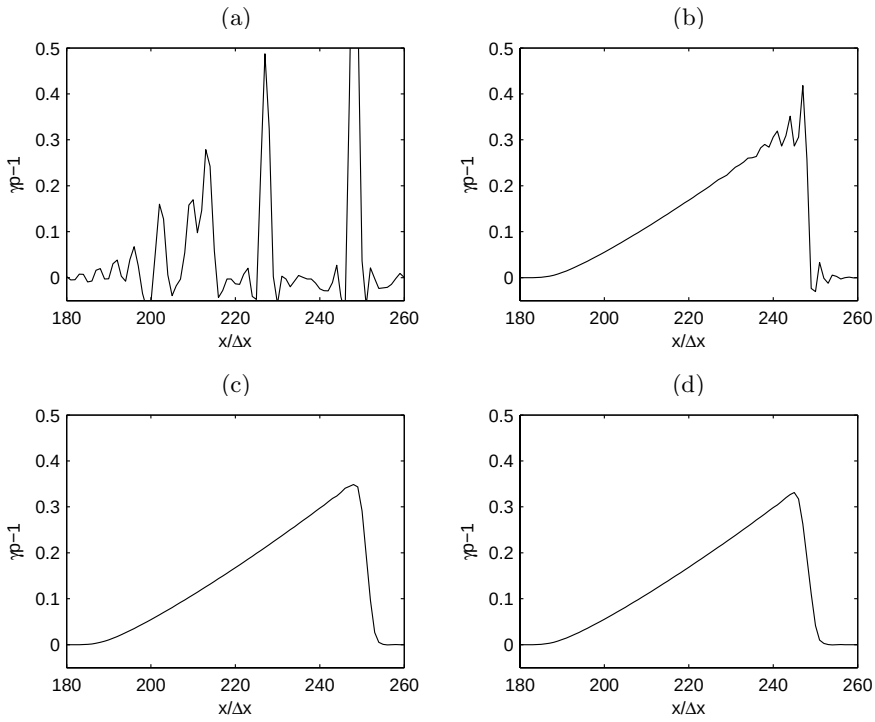

Fig. 1. Shock propagation. Pressure computed at $t = 200$: (a) selective filtering of the fluxes without shock-capturing, (b) selective filtering of the variables without shock-capturing, (c) selective filtering of the variables and non-conservative shock-capturing filtering, (d) selective filtering of the variables and conservative shock-capturing filtering, using filter Fo2 and a threshold parameter $r_{th} = 10^{-5}$

that are situated at $x \simeq 252\Delta x$ in figure 1(c) but $x \simeq 249\Delta x$ in figure 1(d). This result illustrates the fact that that the use of the conservative form of the filtering is required to properly calculate the speed of the shock propagation.

4 Concluding Remarks

A methodology based on an adaptative spatial filtering has been developed to capture shocks in non-linear problems which have to be computed using low-dissipation schemes such as aeroacoustic problems. In order to optimize the efficiency of the approach, the different components of the shock-capturing procedure, including the shock detection from the flow variables, the determination of the filtering strength from the shock detector and the second-order filter applied around the shocks, have been considered. The method has been then applied to linear test cases and to non-linear problems involving shocks, as described in detail in [5]. The results obtained show

that it takes into account shocks in a proper manner, while being of easy implementation and of reasonable cost.

Acknowledgement. The second author is grateful to the Centre National d'Etudes Spatiales (CNES) for financial support. Computations were performed on the Nec-SX8 at the Institut du Développement et des Ressources en Informatique Scientifique (IDRIS - CNRS).

References

[1] Berland, J., Bogey, C., Bailly, C.: Numerical study of screech generation in a planar supersonic jet. Phys. Fluids 19, 75105 (2007)
[2] Bogey, C., Bailly, C.: A family of low dispersive and low dissipative explicit schemes for flow and noise computations. J. Comput. Phys. 194(1), 194–214 (2004)
[3] Bogey, C., Bailly, C.: Large Eddy Simulations of transitional round jets: influence of the Reynolds number on flow development and energy dissipation. Phys. Fluids 18(6), 065101 (2006)
[4] Bogey, C., Bailly, C.: On the application of explicit filtering to the variables or fluxes of linear equations. J. Comput. Phys. 225, 1211–1217 (2007)
[5] Bogey, C., de Cacqueray, N., Bailly, C.: Self-adjusting shock-capturing spatial filtering for high-order non-linear computations. AIAA-2008-2968 (2008)
[6] Daru, V., Gloerfelt, X.: Aeroacoustic computations using a high-order shock-capturing scheme. AIAA Journal 45(10), 2474–2486 (2007)
[7] Ducros, F., Ferrand, V., Nicoud, F., Weber, C., Darracq, D., Gacherieu, C., Poinsot, T.: Large-eddy simulation of the shock/turbulence interaction. J. Comput. Phys. 152(2), 517–549 (1999)
[8] Jameson, A., Schmidt, W., Turkel, E.: Numerical solutions of the Euler equations by finite volume methods using Runge-Kutta time-stepping schemes. AIAA-81-1259 (1981)
[9] Kim, J.W., Lee, D.J.: Adaptative nonlinear artificial dissipation model for Computational Aeroacoustics. AIAA Journal 39(5), 810–818 (2001)
[10] Lele, S.K.: Compact finite difference schemes with spectral-like resolution. J. Comput. Physics 103(1), 16–42 (1992)
[11] Pirozzoli, S.: On the spectral properties of shock-capturing schemes. J. Comput. Physics 219, 489–497 (2006)
[12] Tam, C.K.W.: Benchmark problems and solutions. In: ICASE/LaRC Workshop on CAA, NASA CP, vol., 3300, pp. 1–13 (1995)
[13] Tam, C.K.W., Shen, H.: Direct computation of nonlinear acoustic pulses using high order finite difference schemes. AIAA-93-4325 (1993)
[14] Visbal, M.R., Gaitonde, D.V.: High-order-accurate methods for complex unsteady subsonic flows. AIAA Journal 37(10), 1231–1239 (1999)

A Discontinuous Galerkin Method Based on a Gas Kinetic Scheme for the Navier-Stokes Equations on Arbitrary Grids

Hong Luo[1] and Kun Xu[2]

[1] North Carolina State University, Raleigh, NC, 27695, USA
hong_luo@ncsu.edu
[2] Hong Kong University of Science and Technology, Hong Kong, China
makxu@ust.hk

1 Introduction

In recent years, the discontinuous Galerkin methods (DGM) have received increasing attention in computational fluid dynamics due to many attractive features they possess. However, DGM have a number of weaknesses that have to be addressed, before they can be applied to flow problems of practical interest in a complex configuration environment. In particular, how to efficiently discretize diffusion terms required for the Navier-Stokes equations remains one of unresolved issues in the DGM. DGM are indeed a natural choice for the solution of hyperbolic problems, such as the compressible Euler equations. However, the DG formulation is far less certain and advantageous for the compressible Navier-Stokes equations, where dissipative fluxes exist. A severe difficulty raised by the application of the DGM to the Navier-Stokes equations is the approximation of the numerical fluxes for diffusion terms, that has to properly resolve the discontinuities at the interfaces. Taking a simple arithmetic mean of the solution derivatives from the left and right is inconsistent, because the arithmetic mean of the solution derivatives does not take into account a possible jump of the solutions. A number of numerical methods have been proposed in the literature, such as those by Bassi and Rebay [bassi], Cockburn and Shu[cockburn], Baumann and Oden[baumann] and many others. Arnold et al. have analyzed a large class of discontinuous Galerkin methods for second-order elliptic problems in a unified formulation in Reference [arnold]. All these methods have introduced in some way the influence of the discontinuities in order to define correct and consistent diffusive fluxes. More recently, van Leer and Lo[vanleer] proposed a recovery-based DG method for the diffusion equation using the recovery principle, and Gassner et al[Gassner] introduced a numerical scheme based on the exact solution of the diffusive generalized Riemann problem for the discontinuous Galerkin methods. Unfortunately, all these methods seem to require substantially more computational effort than the classical continuous finite

element methods, which are naturally suited for the discretization of elliptic problems.

In this work, a discontinuous Galerkin Method is presented for the solution of the compressible Navier-Stokes equations on arbitrary grids, where the numerical fluxes at the interface are evaluated using a gas-kinetic Bhatnagar-Gross-Krook (BGK) formulation[liu]. The idea behind this approach is to combine the robustness of the BGK scheme with the accuracy of the DG methods in an effort to develop a more accurate, efficient, and robust method for numerical simulations of viscous flows in a wide range of flow regimes. The developed method is used to compute a variety of viscous flow problems on arbitrary grids. The numerical results obtained by this BGKDG method are extremely promising and encouraging in terms of both accuracy and robustness, indicating its ability and potential to become not just a competitive but simply a superior approach than the current available numerical methods.

2 Numerical Method

The governing Navier-Stokes equations are discretized using a newly developed DG method on arbitrary grids[luo08]. Unlike the traditional discontinuous Galerkin methods, where either standard Lagrange finite element or hierarchical node-based basis functions are used to represent numerical polynomial solutions in each element, this DG method represents the numerical polynomial solutions using a Taylor series expansion at the centroid of the cell, which can be further expressed as a combination of cell-averaged values and their derivatives at the centroid of the cell. The unknowns to be solved in this formulation are the cell-averaged variables and their derivatives at the center of the cells, regardless of element shapes. As a result, this formulation is able to provide a unified framework, where both cell-centered and vertex-centerd finite volume schemes can be viewed as special cases of this discontinuous Galerkin method by choosing reconstruction schemes to compute the derivatives, offer the insight why the DG methods are a better approach than the finite volume methods based on either TVD/MUSCL reconstruction or ENO/WENO reconstruction, and possesses a number of distinct, desirable, and attractive features and advantages, which can be effectively used to address the shortcomings of the DG methods. First, the same numerical polynomial solutions are used for any shapes of elements, which can be triangle, quadrilateral, and polygon in 2D, and tetrahedron, pyramid, prism, and hexahedron in 3D. Using this formulation, DG method can be easily implemented on arbitrary meshes. The numerical method based on this formulation has the ability to compute 1D, 2D, and 3D problems using the very same code, which greatly alleviates the need and pain for code maintenance and upgrade. Secondly, cell-averaged variables and their derivatives are handily available in this formulation. This makes implementation of WENO limiter straightforward and efficient that is required to eliminate non-physical oscillations in the vicinity of discontinuities. Thirdly, the basis

functions are hierarchic. This greatly facilitates implementation of p-multigrid methods and p-refinement.

Unlike the traditional discontinuous Galerkin methods, where a Local Discontinuous Galerkin (LDG) formulation is usually used to discretize the viscous fluxes in the Navier-Stokes equations, a BGK scheme is used in this DG method to compute the fluxes which not only couples the convective and dissipative terms together, but also includes both discontinuous and continuous representation in the flux evaluation at a cell interface through a simple hybrid gas distribution function. BGKDG formulation is especially attractive for the Navier-Stokes equations, as there is no need to compute the viscous fluxes at the interfaces, thus significantly reducing the computational costs. In the BGK formulation, the fluxes at the interface for the Euler and Navier-Stokes equations are constructed based on the integral solution of the BGK model, which requires both conservative variables and their derivatives. In this regard, the BGK formulation bears a strong resemblance to the generalized Riemann solver in the evolution of fluxes at the interface. However, the BGK formulation offers a much deeper physical insight in the construction of a DG method for the convection-diffusion problems. It should be pointed out that the BGK scheme, recognized as being expensive in comparison with the traditional upwind methods for computing numerical fluxes, makes a comeback in the context of DG formulation, as it does not require a separate computation of viscous fluxes at the interfaces. A recently developed, fast, low-storage p-multigrid (p=polynomial degree)[luoaiaa08] is used for obtaining steady state solutions to the governing compressible Navier-Stokes equations. A Hermite polynomial WENO limiter[luo07] is used to eliminate the non-physical spurious oscillations in the vicinity of discontinuities.

3 Numerical Examples

The developed method is used to compute a variety of viscous flow problems on arbitrary grids. A few examples are presented here to illustrate the high accuracy and robustness of this DG method for a wide range of flow regimes from subsonic to hypersonic.

A. Laminar flow past a flat plate

This test case is chosen to assess the accuracy of the numerical solution obtained by the BGKDG method for solving the Navier-Stokes equations. The mesh used to compute the flat plate boundary layer contains 120 cells and 30 cells in the x- and y-direction, respectively. The numerical solution is presented at a Mach number of 0.2, and Reynolds number of 100,000 based on the freestream velocity and the length of the flat plate using DG(P1) and DG(P2) methods. Fig. 1 compares the profiles of velocity component in the x-direction at five locations obtained by DG(P1) and DG(P2) solutions with Blasius solution, respectively, while the velocity profiles in the y-direction obtained by DG(P1) and DG(P2) solutions are compared with Blasius

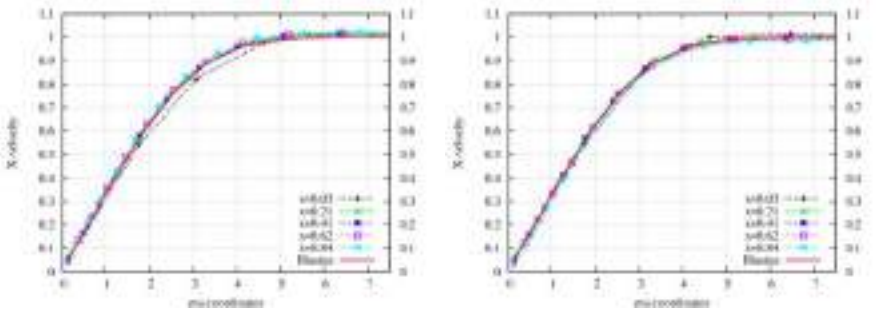

Fig. 1. Comparison of the velocity profiles in the x-direction at different x-locations obtained using the DG(P1) (left) and DG(P2) (right) solutions with Blasius solution

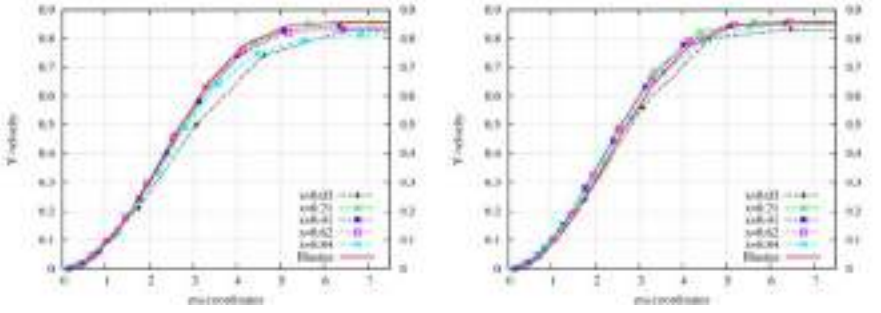

Fig. 2. Comparison of the velocity profiles in the y-direction at different x-locations obtained using the DG(P1) (left) and DG(P2) (right) solutions with Blasius solution

solution in Figure 2. Both DG(P1) and DG(P2) solutions resolve boundary layers very accurately, even with as few as four cells in the boundary layer. What demonstrates the high accuracy of DG solutions is that they give the accurate prediction of velocity profiles not only in the x-direction, but also in the y-direction, which is extremely difficult to predict accurately.

B. Hypersonic laminar flow past a circular cylinder

This test case is taken from the experiment done by Wieting34, where the flow condition is given as M_∞=8.03, T∞=124.94 K, Tw=294.44 K, Re = 1.835x105. Fig. 3 shows the mesh used in the computation, the computed pressure, and temperature contours in the flow field, respectively. Fig. 4 compares the computed normalized pressure and heat flux at the cylindrical surface with the experimental data, where a fairly good agreement can be observed. This example clearly indicates the potential and promise of the DG method for accurate and reliable prediction of heat flux in the hypersonic regime.

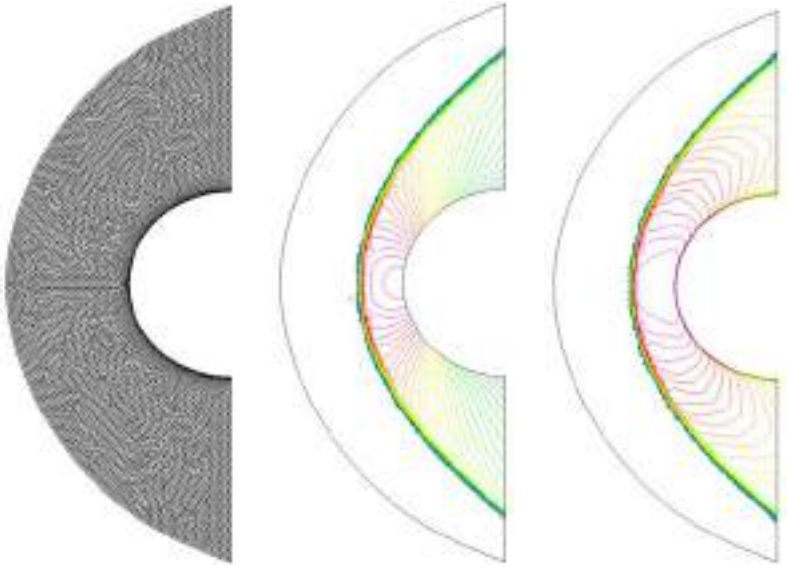

Fig. 3. Comparison of the computed head flux (left) and pressure distributions along the cylindrical surface with the experimental data

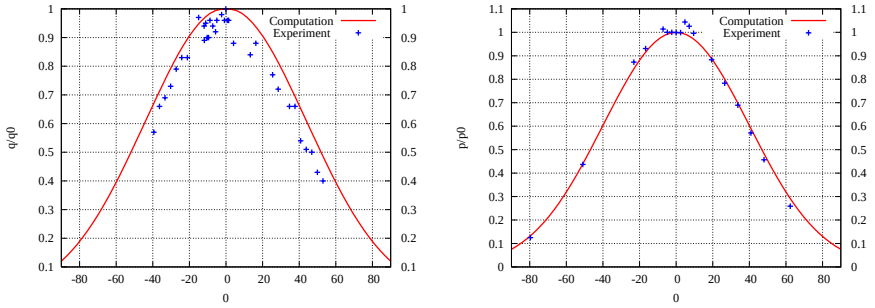

Fig. 4. Comparison of the computed head flux (left) and pressure distributions along the cylindrical surface with the experimental data

4 Conclusions

A discontinuous Galerkin method based on a Taylor basis has been extended for solving the compressible Navier-Stokes equations on arbitrary grids. Unlike the traditional discontinuous Galerkin methods which normally use a local discontinuous Galerkin formulation to discretize the viscous fluxes, the present DG method uses BGK formulation for the discretization of the

Navier-Stokes equations, which has the ability of treating both convective and dissipative effects together using a gas-kinetic distribution function. As a result, there is no need to compute the viscous fluxes at the interfaces separately, thus significantly reducing the computational costs. The developed method has been used to compute a variety of viscous flow problems on arbitrary grids. The numerical results obtained by the BGKDG method are extremely promising and encouraging, indicating its ability and potential to become not just a competitive but simply a superior approach than the current available numerical methods. Further effort will be focused on conducting a systematic study on accuracy, convergence, and cost between BGKDG and LDG methods for solving the Navier-Stokes equations and extending this BGKDG method for three dimensional problems.

References

[bassi] Bassi, F., Rebay, S.: A High-Order Accurate Discontinuous Finite Element Method for the Numerical Solution of the Compressible Navier-Stokes Equations. Journal of Computational Physics 131, 267–279 (1997)

[cockburn] Cockburn, B., Shu, C.W.: The Local Discontinuous Galerkin Method for Time-dependent Convection-Diffusion System. SIAM, Journal of Numerical Analysis 16 (2001)

[baumann] Baumann, C.E., Oden, J.T.: A Discontinuous hp Finite Element Method for the Euler and Navier-Stokes Equations. International Journal for Numerical Methods in Fluids 31 (1999)

[arnold] Arnold, D.N., Brezzi, F., Cockburn, B., Marini, L.D.: Unified Analysis of Discontinuous Galerkin Methods for Elliptic Problem. SIAM, Journal of Numerical Analysis 39, 1749–1779 (2002)

[vanleer] van Leer, B., Lo, M.: A Discontinuous Galerkin Method for Diffusion Based on Recovery, AIAA paper 2007-4083 (2007)

[Gassner] Gassner, G., Lorcher, F., Munz, C.D.: A Contribution to the Construction of Diffusion Fluxes for Finite Volume and Discontinuous Galerkin Schemes. Journal of Computational Physics 224, 1049–1063 (2007)

[liu] Liu, H., Xu, K.: A Runge-Kutta Discontinuous Galerkin Method for Viscous Flow Equations. Journal of Computational Physics 224, 1223–1242 (2007)

[luo08] Luo, H., Baum, J.D., Löhner, R.: A Discontinuous Galerkin Method Based on a Taylor Basis for the Compressible Flows on Arbitrary Grids. Journal of Computational Physics (in press) (2008), doi:210.1016/j.jcp.2008.06.035

[luo07] Luo, H., Baum, J.D., Löhner, R.: A Hermite WENO-Based Limiter for DG Methods on Unstructured Grids. Journal of Computational Physics 225, 686–713 (2007)

[luoaiaa08] Luo, H., Baum, J.D., Löhner, R.: Fast, p-Multigrid Discontinuous Galerkin Method for Compressible Flows at All Speeds. AIAA Journal 46, 635–652 (2008)

Recovery Discontinuous Galerkin Jacobian-Free Newton-Krylov Method for All-Speed Flows

HyeongKae Park, Robert Nourgaliev, Vincent Mousseau, and Dana Knoll

Idaho National Laboratory Multiphysics Methods Group,
Idaho Falls, ID, 83415-3840, USA
Ryosuke.Park@inl.gov, Robert.Nourgaliev@inl.gov,
Vincent.Mousseau@inl.gov, Dana.Knoll@inl.gov

1 Introduction

There is an increasing interest to develop the next generation simulation tools for the advanced nuclear energy systems. These tools will utilize the state-of-art numerical algorithms and computer science technology in order to maximize the predictive capability, support advanced reactor designs, reduce uncertainty and increase safety margins. In analyzing nuclear energy systems, we are interested in compressible low-Mach number, high heat flux flows with a wide range of Re, Ra, and Pr numbers. Under these conditions, the focus is placed on turbulent heat transfer, in contrast to other industries whose main interest is in capturing turbulent mixing. Our objective is to develop single-point turbulence closure models for large-scale engineering CFD code, using Direct Numerical Simulation (DNS) or Large Eddy Simulation (LES) tools, requireing very accurate and efficient numerical algorithms.

The focus of this work is placed on fully-implicit, high-order spatiotemporal discretization based on the discontinuous Galerkin method solving the conservative form of the compressible Navier-Stokes equations. The method utilizes a local reconstruction procedure derived from weak formulation of the problem, which is inspired by the recovery diffusion flux algorithm of van Leer and Nomura [VN05] and by the piecewise parabolic reconstruction [CW84] in the finite volume method. The developed methodology is integrated into the Jacobian-free Newton-Krylov framework [KK04] to allow a fully-implicit solution of the problem.

2 Jacobian-Free Newton-Krylov Framework

The Jacobian-free Newton-Krylov (JFNK) [KK04] framework enables a fully-coupled solution of the nonlinear system. JFNK is a combination of quadratically convergent Newton's method and a Krylov subspace method [Saa03]. In each Newton iteration, the following linear system of equations is solved:

$$J^k \delta \mathbf{U}^k = -Res(\mathbf{U}^k) \tag{1a}$$

$$\mathbf{U}^{k+1} = \mathbf{U}^k + \delta \mathbf{U}^k \tag{1b}$$

where, the superscript k denotes the k^{th} Newton iterate. $J \equiv \frac{\partial Res}{\partial U}$ is the Jacobian matrix and $Res(\mathbf{U}^k)$ denotes the nonlinear residual functions. Computation of the Jacobian matrix can be prohibitively expensive. The JFNK method eliminates the direct computation of the Jacobian matrix by taking advantage of the fact that Krylov methods require only matrix-vector product to perform the iterations. To this end, the Jacobian-vector product is approximated by the forward finite difference of the form:

$$J\mathbf{v} \approx \frac{Res(\mathbf{U} + \varepsilon \mathbf{v}) - Res(\mathbf{U})}{\varepsilon} \tag{2}$$

With this formulation, the linear system of equations can be solved by providing only subroutines for the nonlinear residual function evaluation. Thus, the JFNK framework provides a powerful platform to include a variety of nonlinear phenomena, especially useful for multiphysics simulations. This "Jacobian-free" version of Krylov methods can also be applied to the preconditioned system, which is the key to efficient numerical algorithm[1]. The Jacobian-vector product of the (right-) preconditioned system can be expressed as:

$$JM^{-1}\mathbf{v} \approx \frac{Res(\mathbf{U} + \varepsilon M^{-1}\mathbf{v}) - Res(\mathbf{U})}{\varepsilon} \tag{3}$$

3 Recovery Discontinuous Galerkin Method

The "recovery" discontinuous Galerkin (rDG) method was first introduced by van Leer and Nomura [VN05] for a diffusion operator. Their idea was to approximate a diffusion flux at cell edges by a higher-order reconstruction of the solution. As we found out, the concept of "recovery" can be extended to the advection and reaction operators. The rDG for the advection operator may be considered as the generalization of the Piecewise Parabolic finite volume method (PPM) [CW84]. In rDG, the higher-order solution within a cell is reconstructed by utilizing the solutions at the immediate neighboring cells. To do so, we first define the "recovered" function in cell i as:

$$\tilde{\mathbb{U}}_i(x) = \sum_{n=0}^{R} \tilde{\mathbb{U}}_i^n \mathfrak{L}_n(x) \tag{4}$$

where $\tilde{\mathbb{U}}_i^n$ is the coefficient of the n^{th}-order recovered function $\tilde{\mathbb{U}}_i(x)$. The recovered function is the R^{th}-order polynomial, where $R = 3p + 2$, and p

[1] For recent developments of the physics-based preconditioning in nuclear reactor applications, see [PNM08].

is the order of the original DG method. The coefficients are computed by enforcing the following weak formulations:

$$\int_{\mathcal{I}_m} \mathfrak{L}_n(x)\,\tilde{\mathbb{U}}_m(x)\,dx = \int_{\mathcal{I}_m} \mathfrak{L}_n(x)\,U_m(x)\,dx \quad \begin{matrix} m=i,i\pm1 \\ \text{and} \\ n=0,\ldots,p \end{matrix} \tag{5}$$

where U_m is the original DG solution in cell m. Eq. (5) produces the $(R+1)\times(R+1)$ system of equations, which can be solved analytically. Since the weak statements are used in reconstruction, the procedure is conservative and the first p-moments of the recovered coefficients are equal to those of the original DG solution. The advantage of the rDG is that the higher-order corrections are used only to compute the numerical fluxes at cell edges or integral reaction terms which appears upon DG discretization. As a result, it does not increase the number of unknowns of the solved nonlinear system.

Two-dimensional extension of rDG. The recovery procedure discussed above can be extended to two-dimensional problems. The lowest order discretization rDG_0(=PPM) uses the direction-by-direction recovery procedure; therefore it is only 1^{st} order in the cross derivatives. The recovered in-cell solution of the high-order rDG, on the other hand, includes high-order cross-derivative terms, as well as normal derivatives. The key to this procedure is the choice of degrees of freedom (DoF) that avoids a null space. Fig. 1 shows our choice of DoF from neighboring cells in rDG_1, and Eq. (6) expresses the resulting recovered function.

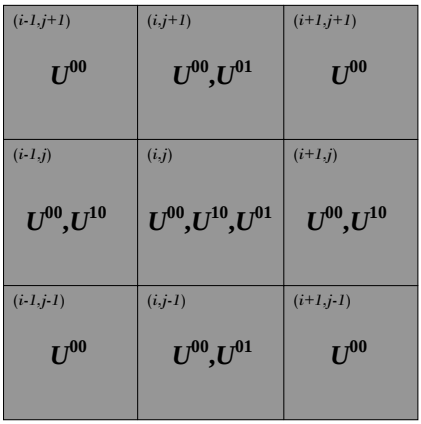

$$U_{i,j}(x,y) = U_{ij}^{00} + U_{ij}^{10} + U_{ij}^{01}$$

Fig. 1. The choice of the in-cell solution reconstruction for rDG_1

$$
\begin{aligned}
\tilde{\mathbb{U}} = {} & \tilde{\mathbb{U}}^{00}\mathfrak{L}_0(x)\mathfrak{L}_0(y) \\
& + \tilde{\mathbb{U}}^{10}\mathfrak{L}_1(x)\mathfrak{L}_0(y) + \tilde{\mathbb{U}}^{01}\mathfrak{L}_0(x)\mathfrak{L}_1(y) \\
& + \tilde{\mathbb{U}}^{20}\mathfrak{L}_2(x)\mathfrak{L}_0(y) + \tilde{\mathbb{U}}^{02}\mathfrak{L}_0(x)\mathfrak{L}_2(y) + \tilde{\mathbb{U}}^{11}\mathfrak{L}_1(x)\mathfrak{L}_1(y) \\
& + \tilde{\mathbb{U}}^{30}\mathfrak{L}_3(x)\mathfrak{L}_0(y) + \tilde{\mathbb{U}}^{03}\mathfrak{L}_0(x)\mathfrak{L}_3(y) + \tilde{\mathbb{U}}^{12}\mathfrak{L}_1(x)\mathfrak{L}_2(y) + \tilde{\mathbb{U}}^{21}\mathfrak{L}_2(x)\mathfrak{L}_1(y) \\
& + \tilde{\mathbb{U}}^{40}\mathfrak{L}_4(x)\mathfrak{L}_0(y) + \tilde{\mathbb{U}}^{04}\mathfrak{L}_0(x)\mathfrak{L}_4(y) + \tilde{\mathbb{U}}^{22}\mathfrak{L}_2(x)\mathfrak{L}_2(y) \\
& + \tilde{\mathbb{U}}^{50}\mathfrak{L}_5(x)\mathfrak{L}_0(y) + \tilde{\mathbb{U}}^{05}\mathfrak{L}_0(x)\mathfrak{L}_5(y) \\
& + O(\Delta x^6, \Delta y^6, \Delta x^3\Delta y, \Delta x\Delta y^3) \qquad (6)
\end{aligned}
$$

where the subscripts denote the order of polynomial in x- and y-direction, respectively. From Eq. (6), it is clear that the reconstructed function is the 6^{th} order accurate in x- and y-direction and the 4^{th} order accurate in cross-derivative terms.

4 Numerical Examples

In this section, we demonstrate high-order convergence of the rDG by solving the one- and two-dimensional Navier-Stokes equations. As the first example, we use a one-dimensional manufactured solution [NTP08]. Fig. 2 (left) shows the density error vs. total number of DoFs, used for rDG_{0-3}. All spatial discretizations exhibit nearly theoretical convergence rates. Fig. 2 (right) shows the convergence of five fully implicit time integration schemes, which also demonstrates the expected convergence rates.

The next example is the 2-D traveling wave problem, defined as

$$u(x, y, t) = 1 + 2\cos(2\pi(x - t))\sin(2\pi(y - t)) \qquad (7a)$$

$$v(x, y, t) = 1 - 2\sin(2\pi(x - t))\cos(2\pi(y - t)) \qquad (7b)$$

$$P(x, y, t) = P_0 - (\cos(4\pi(x - t)) + \cos(4\pi(y - t))) \qquad (7c)$$

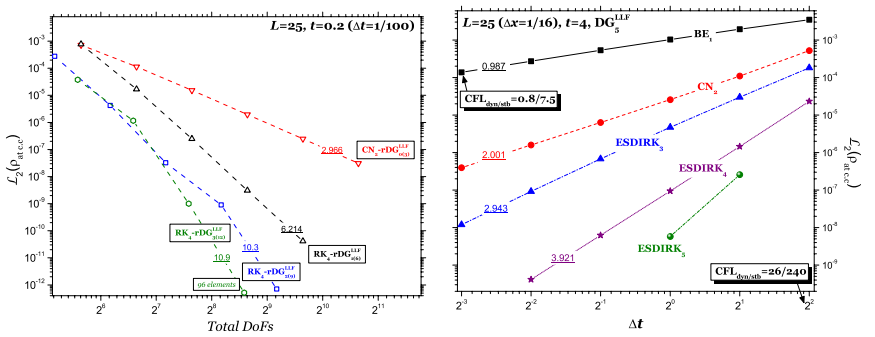

Fig. 2. Spatial (left), and temporal (right) convergence tests for rDG_{0-3}

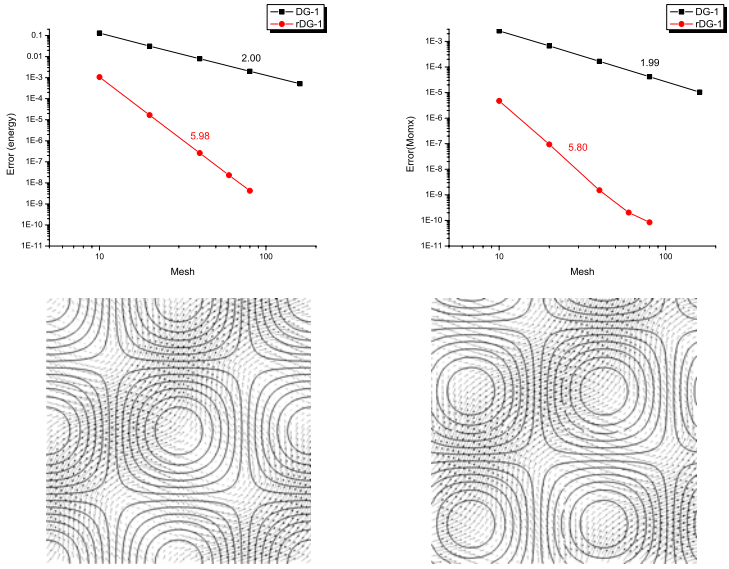

Fig. 3. Grid convergence of rDG for total energy (upper left), and x-momentum (upper right). Vorticity and velocity fields are shown at t=0.0 (bottom left), t=0.15 (bottom right) .

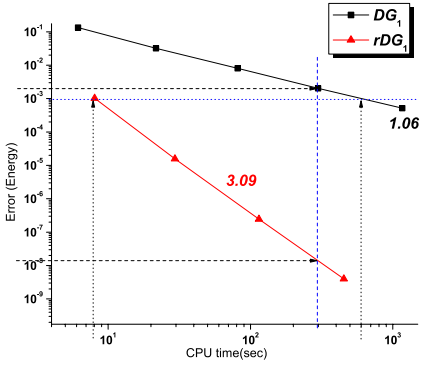

Fig. 4. Error vs. CPU time for the traveling-wave problem

Fig. 3 summarizes the convergence studies, comparing the DG_1 with rDG_1, for total energy and x-momentum variables. Samples of the velocity and vorticity fields at t=0.0 and t=0.15 are shown at the bottom. As can be seen from Fig. 3, the convergence rates are the 2^{nd} and the 6^{th} order for DG_1 and rDG_1, respectively. A significant increase in accuracy is gained. Fig. 4 shows the efficacy (accuracy vs. CPU time), comparing the DG_1 with the

rDG_1. Since the average number of the GMRES and Newton iterations does not increase in this problem, the CPU time solely depends on the number of nonlinear function evaluations. As one can see from Fig. 4, up to five orders of magnitude more accurate result can be obtained with same CPU time, On the other hand, to obtain the same accuracy, thr rDG_1 is ≈ 100 times faster than the DG_1.

5 Conclusion

In this work, we have developed very high-order spatial discretization scheme for hyperbolic and reaction operators based on the recovery of DG method. Numerical examples demonstrated nearly theoretical convergence for the smooth-flow tests. A significant saving in the computational time has been achieved. The recovery procedure uses only the immediate neighbors to estimate higher order correction terms in the solution, which can be utilized for *a posteriori* error indicator and subsequent mesh adaptivity. The next step is to extend the procedure to unstructured grids as well as to the three-dimensional problems.

Acknowledgment. This manuscript has been authored by Battelle Energy Alliance, LLC under contract No. DE-AC07-05ID14517 (INL/CON-08-14501) with the U.S. Department of Energy. The United States Government retains and the publisher, by accepting the article for publication, acknowledges that the United States Government retains a nonexclusive, paid-up, irrevocable, world-wide license to publish or reproduce the published form of this manuscript, or allow others to do so, for United States Government purposes.

References

[KK04] Knoll, D.A., Keyes, D.: Jacobian-free Newton-Krylov Methods: A Survey of Approaches and Applications. Journal of Computational Physics 193, 357 (2004)

[CW84] Colella, P., Woodward, P.R.: The Piecewise Paraboilic Method (PPM) for Gas-Dynamical Simulations. Journal of Computational Physics 54, 174 (1984)

[VN05] van Leer, B., Nomura, S.: Discontinuous Galerkin for Diffusion. In: 17th AIAA Computational Fluid Dynamics Conference Tronto, Ontario, Canada (2005)

[NTP08] Nourgaliev, R.R., et al.: Direct Numerical Simulation of Interfacial Flows: Implicit Sharp-Intrface Method (I-SIM). In: 46th AIAA Aerospace Sciences Meeting and Exhibit, Reno, Nevada (2008)

[Saa03] Saad, Y.: Iterative Methods for Sparse Linear Systems, 2nd edn. SIAM, philadelphia (2003)

[PNM08] Park, H., et al.: Jacobian-free Newton-Krylov discontinuous Galerkin method and physics-based preconditioning for nuclear reactor simulations. In: International Conference on the Physics of Reactors (PHYSOR 2008), Interlaken, Switzerland (2008)

Part 23
Higher-Order Method 3

“*This page left intentionally blank.*”

A Characteristic-Wise Hybrid Compact-WENO Scheme for Solving the Navier-Stokes Equations on Curvilinear Coordinates

Zhensheng Sun[1] and Yu-Xin Ren[2]

[1] Department of Engineering Mechanics, Tsinghua University, Beijing 100084, China
szs07@mails.tsinghua.edu.cn
[2] Department of Engineering Mechanics, Tsinghua University, Beijing 100084, China
ryx@tsinghua.edu.cn

A hybrid compact-WENO scheme for viscous flow simulations on the curvilinear coordinates is presented. The inviscid fluxes are computed by the 5th-order hybrid compact-WENO scheme. An improved Roe type character-wise decomposition approach is used to extend the hybrid scheme into system of equations. The compact schemes for discretizing the metrics terms that appear in the inviscid and viscous fluxes are also constructed. After applying the present scheme to some standard test cases to verify the code, we use the present method to simulate the interaction between the reflect shock wave and the incident boundary layer. The effects of the grid density and the Reynolds number are considered.

1 Introduction

Accurate and efficient simulation of turbulence flow fields involving shock waves represents a significant challenge for numerical schemes. The numerical schemes should be highly accurate to capture shock waves as well as the multi-scale smooth flow structures. In recent years, many efforts have been devoted in developing schemes with these properties.

Among others, the hybridization of the high order compact scheme and the high resolution shock capturing scheme is a promising approach. This type of hybrid schemes takes the advantages of the compact schemes in smooth flow regions and the high resolution shock capturing schemes near the flow discontinuities. Adams and Shariff [AS96] have developed a hybrid compact-ENO scheme which is composed of the non-conservative compact upwind scheme for the smooth region and the shock-capturing ENO scheme that is used near the discontinuities. Pirozzoli [P02]has derived a hybrid compact-WENO schemes in which a conservative approach for the compact scheme

rather than a non-conservative one was developed to make coupling with the WENO scheme much easier and the numerical oscillation level much lower. Ren et al [RLZ03] have improved the hybrid compact-WENO in several ways. They designed a continuous weight function to avoid the abrupt transition from one sub-scheme to another. The Roe type, characteristic-wise decomposition approach rather than the Lax-Friedrichs flux splitting was used to reduce the numerical dissipation. This characteristic-wise hybrid scheme has shown remarkable improvement in resolutions.

In the present paper, the characteristic-wise hybrid scheme is extended to solve viscous flow in curvilinear coordinate. The inviscid fluxes are computed by the 5th-order hybrid compact-WENO scheme. An improved Roe type character-wise decomposition approach is used to extend the hybrid scheme into system of equations. The sixth order central difference scheme is used for viscous flux computation. On the curvilinear coordinates, one important problem is to design the discretization of the geometrical metrics so that the desired accuracy can be ensured. In this paper, the compact schemes for discretizing the metrics terms that appear in the inviscid and viscous fluxes are constructed. After applying the present scheme to some standard test cases to verify the code, we use the present method to simulate the interaction between the reflect shock wave and the incident boundary layer. The effects of the grid density and the Reynolds number are considered. The numerical results show very good resolution to the shock and shear waves.

2 Numerical Method

In the present paper, the numerical scheme will be designed to solve the 2-dimensional compressible Navier-Stokes equations in strong conservative form on general curvilinear coordinates (ξ ,η):

$$\frac{\partial \hat{U}}{\partial t} + \frac{\partial \hat{F}}{\partial \xi} + \frac{\partial \hat{G}}{\partial \eta} = \frac{1}{\mathrm{Re}} \left(\frac{\partial \hat{F}_v}{\partial \xi} + \frac{\partial \hat{G}_v}{\partial \eta} \right)$$

Further details of the equations can be found in [ATP84].

On the curvilinear coordinates, one important problem is to design the discretization of the geometrical metrics so that the desired accuracy can be ensured. The metric terms are computed by the 6-th order conservative central compact scheme. Taking $\frac{\partial x}{\partial \xi}$ as an example:

$$\frac{\partial x}{\partial \xi}|_{j,k} = \hat{x}_{j+1/2,k} - \hat{x}_{j-1/2,k}$$

where $\hat{x}_{j+1/2,k}$ is obtained by the solution of the following compact scheme.

$$\tfrac{1}{3}\hat{x}_{j-1/2,k} + \hat{x}_{j+1/2,k} + \tfrac{1}{3}\hat{x}_{j+3/2,k} = \tfrac{1}{36}x_{j-1,k} + \tfrac{29}{36}x_{j,k} + \tfrac{29}{36}x_{j+1,k} + \tfrac{1}{36}x_{j+2,k}$$

Then the metrics are employed to evaluate the Jacobian J :

$$J = \begin{vmatrix} \frac{\partial x}{\partial \xi} & \frac{\partial x}{\partial \eta} \\ \frac{\partial y}{\partial \xi} & \frac{\partial y}{\partial \eta} \end{vmatrix} = \frac{\partial x}{\partial \xi}\frac{\partial y}{\partial \eta} - \frac{\partial x}{\partial \eta}\frac{\partial y}{\partial \xi}$$

The inverse metrics such as $\frac{\partial \xi}{\partial x}$ can thus be computed using the general relationship of the coordinate transformation:

$$\frac{\partial \xi}{\partial x} = J^{-1}\frac{\partial x}{\partial \xi}\ \frac{\partial \xi}{\partial y} = -J^{-1}\frac{\partial x}{\partial \eta}, \frac{\partial \eta}{\partial x} = -J^{-1}\frac{\partial y}{\partial \xi}\ \frac{\partial \eta}{\partial y} = J^{-1}\frac{\partial x}{\partial \xi}$$

The inviscid fluxes are computed using an improved version of the characteristic hybrid compact-WENO scheme [RLZ03]. For simplicity, we present the scheme by omitting the subscript k without ambiguity. For the $i-$th characteristic variable of the flux $\hat{F}$ defined by $w_m^{(i)} = L_{j+1/2}^{(i)} F_m, (i = 1, 2, 3, 4; m = j-1, \ldots j+2)$, the hybrid scheme reads:

$$\sigma_{j+1/2}^{(i)}\phi_{j+1/2}^{(i)}\hat{w}_{j-1/2}^{(i)} + \hat{w}_{j+1/2}^{(i)} + \sigma_{j+1/2}^{(i)}\psi_{j+1/2}^{(i)}\hat{w}_{j+1/2}^{(i)} = \hat{c}_{j+1/2}^{(i)} \tag{1}$$

where $\sigma_{j+1/2}^{(i)}$ is the weight which can be found in [RLZ03] and

$$\phi_{j+1/2}^{(i)} = \tfrac{1}{3} + \tfrac{s_{j+1/2}^{(i)}}{6},\ \psi_{i+1/2} = \tfrac{1}{3} - \tfrac{s_{j+1/2}^{(i)}}{6},\ s_{j+1/2}^{(i)} = sign(\lambda_{j+1/2}^{(i)})$$

$$\hat{c}_{j+1/2}^{(i)} = \sigma_{j+1/2}^{(i)}\hat{b}_{j+1/2}^{(i)} + (1 - \sigma_{j+1/2}^{(i)})\hat{w}_{j+1/2}^{(i),WENO} \tag{2}$$

$$\hat{b}_{j+1/2}^{(i)} = (\tfrac{1}{18}w_{j-1}^{(i),+} + \tfrac{19}{18}w_j^{(i),+} + \tfrac{5}{9}w_{j+1}^{(i),+}) + (\tfrac{5}{9}w_j^{(i),-} + \tfrac{19}{18}w_{j+1}^{(i),-} + \tfrac{1}{18}w_{j+2}^{(i),-}) \tag{3}$$

In these equations, $\lambda_{j+1/2}^{(i)}$ and $L_{j+1/2}^{(i)}$ are respectively the $i-$th eigenvalue and left eigenvector. Further details of Eq. (2) and Eq. (3) are as follows. For a chosen threshold value $\eta_{j+1/2}$, if $min(|\lambda_j^{(i)}|, |\lambda_{j+1}^{(i)}|) > \eta_{j+1/2}$, then

$$w_m^{(i),+} = \begin{cases} L_{j+1/2}^{(i)}F_m, if\lambda_j^{(i)} > 0, \\ 0, \qquad\qquad otherwise; \end{cases}$$

$$w_m^{(i),-} = \begin{cases} 0, \qquad\qquad if\lambda_j^{(i)} > 0, \\ L_{j+1/2}^{(i)}F_m, otherwise; \end{cases}$$

$$\hat{w}_{j+1/2}^{(i),WENO} = \hat{w}_{j+1/2}^{(i),WENO-Roe}$$

otherwise,

$$w_m^{(i),+} = \frac{L_{j+1/2}^{(i)}F_m + \lambda_m^{(i)}L_{j+1/2}^{(i)}U_m}{2}$$

$$w_m^{(i),-} = \frac{L_{j+1/2}^{(i)}F_m - \lambda_m^{(i)}L_{j+1/2}^{(i)}U_m}{2}$$

$$\hat{w}_{j+1/2}^{(i),WENO} = \hat{w}_{j+1/2}^{(i),WENO-LF}.$$

The WENO-Roe and WENO-LF stand for the original Roe type WENO flux and WENO flux based on the Lax-Friedrich flux splitting, see [JS96]. It can be seen that the entropy-fix has been considered in these procedures. When the eigenvalues are small enough, the right-hand side of Eq. (1) is computed by the Lax-Friedrichs flux for both the compact and the WENO sub-schemes, which is different with [RLZ03] where the entropy-fix was only applied to the WENO sub-scheme. This improvement makes the present scheme being more robust than the scheme of [RLZ03]. The final step of the inviscid flux computation is to arrange Eq. (1) for all characteristic fields into a block-tridiagnal system of equations that can be solved to obtain the numerical flux in the physical space.

This viscous fluxes are computed by 6-th order central difference scheme. The third order TVD Runge-Kutta scheme [JS96]is used for the time integration.

3 Numerical Tests

The first test case is a flat plate boundary layer problem with $Ma = 0.2$ and $Re = 10^4$. A nonuniform rectangle mesh with 70×110 cells (Figure 1)is used in the simulation. Non-dimensional u velocity profiles are shown at $x/L = 0.3$ and are compared with Blasius profiles in Figure 2. A good agreement between these two results can be seen.

This second case is a two dimensional laminar flow impinged by an oblique shock upon a flat plate causing a boundary layer to separate near the impinging region. A nonuniform rectangle grid is used in the simulation. The angle between the incident shock and the horizontal line is32.6°. Computational results in Figure 3 are obtained at $Ma = 2.0$and $Re = 2.96e^5$ and compared with some experimental results in Figure 4. The agreement is also very good.

After applying the present scheme to above standard test cases to verify the code, we use the present method to simulate the interaction between the reflect shock wave and the incident boundary layer. The flow conditions are taken from [DT00]. For the $Re = 200$ case, the computations have been

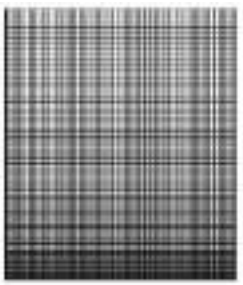

Fig. 1. Flat plate grids

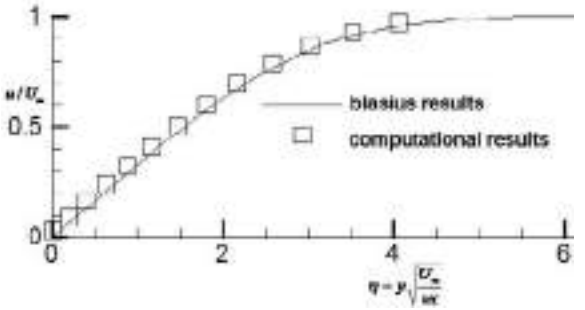

Fig. 2. u velocity distributions at $x/L = 0.3$

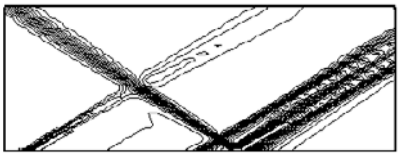

Fig. 3. Pressure contour

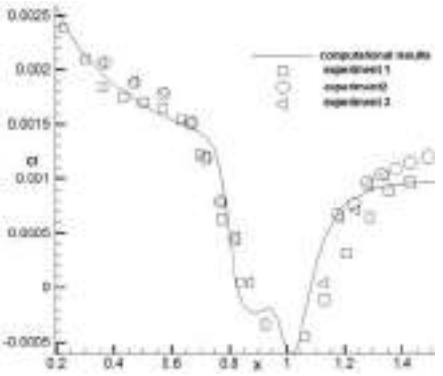

Fig. 4. Skin friction coefficient

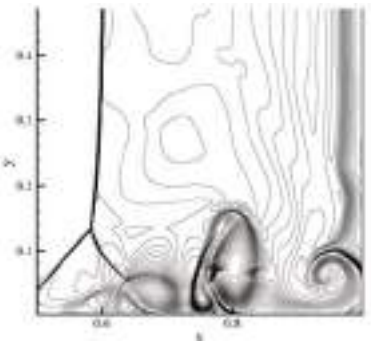

Fig. 5. $Re = 200$, density contour of reflect shock wave interacting with incident boundary layer at $t = 1.0$, mesh number 250×125

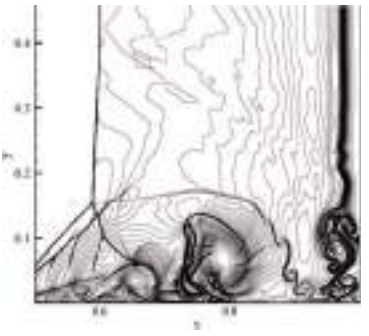

Fig. 6. $Re = 1000$, density contour of reflect shock wave interacting with incident boundary layer at $t = 1.0$, mesh number 1000×500

performed on the 250×125 , 500×250 and 1000×250 nonuniform grids. The numerical results are almost the same and the one on the 250×125 grid is shown in Figure 5. The advantage of the scheme on curvilinear coordinates is that the nonuniform grids can be used in simulation. By clustering the grids near the boundary layer, fast grid convergence can be achieved. For a comparison, it is reported in [SY03] that the grid convergence can be reached on a 1000×500 grid for the second order MUSCL scheme and on a 500×250 grid for the $5-$th order WENO scheme and high order ACM filter scheme.

When the Reynolds number is increased to 1000, the flow structures are much more complicated. The boundary layer separates at several points, giving rise to development of lots of vortex and large compressibility effects. The flow is suspected to be unstable according to [DT00]. No grid convergence study is done in the present paper for this case. However, according to the

numerical results shown in Figure 6 which is computed on a 1000×500 grid, the present scheme can capture very rich small scale flow structures. This indicates that the present scheme can compute the multi-scale flows with shock waves in very high resolution.

4 Conclusions

In this paper, the hybrid compact-WENO scheme has been extended to solve the N-S equations on curvilinear coordinates. Firstly, we construct the six-order central compact scheme to discrete the geometrical metrics to obtain the desired accuracy. Secondly, an improved Roe type, 5-th order characteristic-wise compact scheme is designed to combine with the 5-th order WENO scheme to form a hybrid compact-WENO scheme with improved entropy-fix procedure. Thirdly, the six-order central difference scheme is used for viscous flux computation. Numerical tests show that the present scheme can achieve very high resolution for complex flow structures with shock waves.

Acknowledgements. This work was supported by Project-10572075 of NSFC.

References

[AS96] Adams, N.A., Shariff, K.: A high-resolution hybrid compact-ENO scheme for shock-turbulence interaction problems. J. comput. Phys. 127, 27–51 (1996)

[ATP84] Anderson, D.A., Tannehill, J.C., Pletcher, R.H.: Computational Fluid Mechanics and Heat Transfer. McGraw-Hill, New York (1984)

[DT00] Daru, V., Tenaud, C.: Evaluation of TVD high resolution schemes for unsteady viscous shocked flows. Comput. Fluids 30, 89–113 (2007)

[JS96] Jiang, G.S., Shu, C.W.: Efficient implementation of weighted ENO schemes. J. Comput. Phys. 126, 202–228 (1996)

[L03] Lele, S.K.: Compact finite difference schemes with spectral-like resolution. J. Comput. Phys. 103 (1992); conservation laws, J.Comput. Phys. 192, 365–386 (2003)

[SY03] Sjögreen, B., Yee, H.C.: Grid convergence of high order methods for multiscale complex unsteady viscous compressible flows. J. Comput. Phys. 185, 1–26 (2003)

[P02] Pirozzoli, S.: Conservative hybrid compact-WENO schemes for shock-turbulence interaction. J. Comput. Phys. 178, 81–117 (2002)

[RLZ03] Ren, Y.X., Liu, M., Zhang, H.: A characteristic-wise hybrid compact-WENO scheme for solving hyperbolic laws. J.Comput. Phys. 192, 365–386 (2003)

High-Order Central ENO Finite-Volume Scheme with Adaptive Mesh Refinement for the Advection-Diffusion Equation

Lucian Ivan and Clinton P.T. Groth

University of Toronto Institute for Aerospace Studies,
4925 Dufferin Street, Toronto, Ontario, M3H 5T6, Canada
lucian.ivan@utoronto.ca, groth@utias.utoronto.ca

1 Scope

High-order methods are being actively pursued in an effort to reduce the cost of large-scale scientific computing applications. Moreover, for complex flows both high-order discretizations and adaptive mesh refinement (AMR) may be required. For hyperbolic conservation laws, the challenge has been to achieve accurate discretizations while coping in a reliable and robust fashion with discontinuities and shocks. For elliptic equations, it is desirable that the discretization procedure remain accurate while satisfying a maximum principle, even on stretched/distorted meshes [Coi94, DABLP99].

In spite of the many successful high-order methods proposed for both structured and unstructured meshes [HEOC87, Abg94, HS99, CS89, Bar93, OV02] and their application to complex engineering problems even in combination with AMR procedures [MJ06, WA06, BC05], there is still no consensus for robust, efficient, and high-order-accurate schemes that fully deal with all of the aforementioned issues and are applicable to more arbitrary meshes.

This study considers the development and application of a high-order central essentially non-oscillatory (CENO) finite-volume procedure with AMR to the advection-diffusion equation. A consistent order of discretization error is sought for both hyperbolic and elliptic terms.

2 High-Order CENO Scheme

The two-dimensional advection-diffusion equation considered is given by

$$\frac{\partial u}{\partial t} + \underbrace{\boldsymbol{\nabla} \cdot (\mathbf{V}(x,y,u)\, u)}_{advective(hyperbolic)} = \underbrace{\boldsymbol{\nabla} \cdot (\kappa(x,y,u)\, \boldsymbol{\nabla} u)}_{diffusive(elliptic)} + \underbrace{\phi(x,y,u)}_{source}, \qquad (1)$$

where u is the solution (a scalar quantity), $\mathbf{V}$ is the advection velocity vector, κ is the diffusion coefficient, ϕ is a non-linear source term and x and y are the two spatial coordinates. Based on the relative magnitudes of the advective

and diffusive fluxes, the solutions of this equation can range from those having a more hyperbolic nature and governed by wave propagation phenomena to those having a more elliptic nature and governed by diffusive processes.

High-order solutions of (1) are sought here by applying a finite-volume spatial discretization procedure in conjunction with high-order polynomial solution reconstruction, upwind discretization of the hyperbolic flux, and centrally weighting discretization of the elliptic flux. The semi-discrete form of the finite-volume formulation applied to (1) for a cell (i,j) of a two-dimensional multi-block mesh composed of quadrilateral computational cells is given by

$$\frac{d\bar{u}_{i,j}}{dt} = -\frac{1}{A_{i,j}} \sum_{l=1}^{N_f} \sum_{m=1}^{N_G} \left(\omega \mathbf{F} \cdot \mathbf{n}\, \Delta\ell\right)_{i,j,l,m} + \frac{1}{A_{i,j}} \int_{\mathcal{V}_{i,j}} \phi_{i,j}(x,y,u) dv = R_{i,j}\,, \quad (2)$$

where each cell has $N_f = 4$ faces and a N_G-point Gaussian quadrature numerical integration procedure is used to evaluate the solution flux, the sum of the advective and diffusive fluxes $\mathbf{F} = \mathbf{F_a} + \mathbf{F_d} = \mathbf{V}u - \kappa\, \boldsymbol{\nabla} u$, through each face. The variable $\bar{u}_{i,j}$ is the average solution scalar, $A_{i,j}$ is the cell area, ω is the quadrature weighting coefficient, $\Delta\ell$ and $\mathbf{n}$ are the length of the cell face and unit vector normal to the cell face, respectively. Analytical or numerical integration can be performed to calculate the integral of the particular non-linear source term, $\phi_{i,j}$, for cell (i,j). In this work, either a two- or four-stage standard Runge-Kutta scheme is used to integrate the system of ordinary differential equations given by (2), depending on the desired accuracy.

The hyperbolic fluxes, $\mathbf{F_a} \cdot \mathbf{n} = u\,\mathbf{V} \cdot \mathbf{n}$, at each quadrature point are determined from the left and right solution values, u_l and u_r, as follows:

$$\mathbf{F_a} \cdot \mathbf{n} = \begin{cases} u_l\,(\mathbf{V} \cdot \mathbf{n}) & \text{if} \quad \mathbf{V} \cdot \mathbf{n} \;\geq\; 0, \\ u_r\,(\mathbf{V} \cdot \mathbf{n}) & \text{if} \quad \mathbf{V} \cdot \mathbf{n} \;<\; 0. \end{cases} \quad (3)$$

The solution states, u_l and u_r, are determined by performing piecewise k-order polynomial solution reconstruction within each computational cell. Herein, the k-order CENO reconstruction proposed by Ivan and Groth is used [IG07].

The high-order central ENO (CENO) method is not based on either selecting or weighting reconstructions from multiple stencils. Instead, a hybrid solution reconstruction procedure is used that combines the high-order k-exact least-squares reconstruction technique of Barth [Bar93] based on a fixed central stencil with a monotonicity preserving limited piecewise linear least-squares reconstruction algorithm [Bar93]. The limited reconstruction procedure is applied to computational cells with under-resolved solution content and the unlimited k-exact reconstruction scheme is used for cells in which the solution is fully resolved. Switching in the hybrid procedure is determined by a solution smoothness indicator. Note that for smooth and hyperbolic problems, a k-order reconstruction produces a $k+1$-order accurate spatial discretization. A detailed description of the CENO reconstruction

procedure and of the smoothness indicator is given in the paper by Ivan and Groth [IG07].

As previously mentioned, the proposed discretization seeks to obtain a global k-order accurate scheme on arbitrary meshes. This implies the use of a k-order accurate gradient for the diffusive flux evaluation, which here is derived from a $k+1$-order accurate reconstruction. For this reason, even if a quartic ($k=4$) reconstruction has the potential to generate a 5th-order discretization of the hyperbolic flux in combination with at least three quadrature points ($N_G=3$), it will only be 4th-order accurate for the elliptic flux discretization. Therefore, two quadrature points ($N_G=2$) are sufficient to obtain a global 4th-order accurate scheme with a piecewise quartic reconstruction.

In a similar manner to hyperbolic fluxes, numerical elliptic fluxes, $\mathbf{F_d}\cdot\mathbf{n} = -\kappa\,\boldsymbol{\nabla} u\cdot\mathbf{n}$, must be evaluated at each quadrature point. Having determined the left and right solution reconstructions, $u_l^k(\mathbf{r})$ and $u_r^k(\mathbf{r})$, the solution gradient at the inter-cellular face is obtained as the arithmetic mean of the reconstruction gradients and thus, the flux at the calculation point, $\mathbf{r}$, is evaluated as

$$\mathbf{F_d}\cdot\mathbf{n} = -\kappa\,\left[\frac{1}{2}\,\left(\boldsymbol{\nabla} u_l^k(\mathbf{r}) + \boldsymbol{\nabla} u_r^k(\mathbf{r})\right)\right]\cdot\mathbf{n}\,. \tag{4}$$

The accuracy of (4) can be easily observed to be k-order accurate. To infer other properties such as positivity (i.e. local satisfaction of a discrete maximum principle) or non-existence of odd-even solution decoupling, it is convenient to apply the elliptic discretization to the Laplace operator and analyse the influence coefficient of each entry in the supporting stencil [Coi94]. Note that for a given discretization the influence coefficients depend only on the mesh geometry and not on the actual solution. As proposed by Coirier [Coi94], the positivity of the scheme can be characterized in terms of α_0 and $\tilde{\alpha}_{\min}$ coefficients. Ideally, $\alpha_0 < 0$ for stability and $\tilde{\alpha}_{\min} = 0$ for positivity [DABLP99].

In the current work, different mesh geometries were analysed including Cartesian, stretched, and randomly disturbed quadrilateral grids. The analysis has shown that odd-even solution decoupling does not occur. In terms of the stability and positivity, it was found that $\alpha_0 < 0$ but $\tilde{\alpha}_{\min} < 0$ for discretizations of all order, unfortunately implying that, while stable, none of the discretizations satisfy a discrete maximum principle. Note that for square Cartesian meshes, values for $\tilde{\alpha}_{\min}$ are found to be -0.823 for $k=2$, -0.362 for $k=3$ and -0.854 for $k=4$ when inverse distance geometric weighting is used in the k-exact reconstruction. However, the positivity can be improved by using an inverse distance squared geometric weighting, for which $\tilde{\alpha}_{\min}$ was found to be -0.051 for $k=2$, -0.247 for $k=3$ and -0.324 for $k=4$. For non-Cartesian meshes, large variations in the value of $\tilde{\alpha}_{\min}$ are possible ($-5 < \tilde{\alpha}_{\min} < 0$), depending on the regularity and topology of the mesh.

High-order treatment of boundary conditions (BCs) is crucial for developing high-order accurate schemes. Herein, high-order BCs have been imposed by making use of extra rows of ghost cells or by constraining the least-squares reconstruction in cells adjacent to boundaries as described in [OV02].

A flexible block-based hierarchical data structure is used in conjunction with the CENO scheme described above to facilitate automatic solution-directed mesh adaptation on body-fitted multi-block quadrilateral mesh. In this work, an h-refinement criterion based on the solution smoothness indicator is used to control the refinement of AMR mesh. The AMR CENO algorithm and the refinement criterion are described in details in [IG07].

3 Numerical Results

The accuracy of the hybrid CENO algorithm was first assessed based on the circular advection at constant angular velocity of the smooth inflow variation $u(x,0) = e^d \sin^6(\pi\, d)$ if $d \in [0:1]$, otherwise 0, where $d = x - 0.3$. The predicted solution distribution for this problem using the quartic CENO reconstruction on a 80×80 Cartesian mesh is shown in Fig. 1. The error norms for both 4th-order versions ($k=3$ and $k=4$) of the proposed CENO scheme are also depicted in Fig. 1. As the mesh is refined, the slopes of the L_1-, L_2- and L_∞-norms approach in the asymptotic limit -4.53, -4.55 and -4.58 for the cubic reconstruction ($k=3$), and -4.94 in all error norms for the quartic reconstruction ($k=4$), respectively, indicating that the expected theoretical order of accuracy has been achieved in each case.

The high-order CENO scheme was also applied in conjunction with AMR to a problem similar to the previous one. In this case the inflow function was $u(x,0) = e^{2\,d} \sin^6(2\,\pi\, d)$ if $d \in [0:0.8]$, otherwise 0, where $d = x - 0.4$. This function exhibits two smooth extrema and a discontinuity close to the second peak. Figure 2 shows the final solution profile along the cross-section

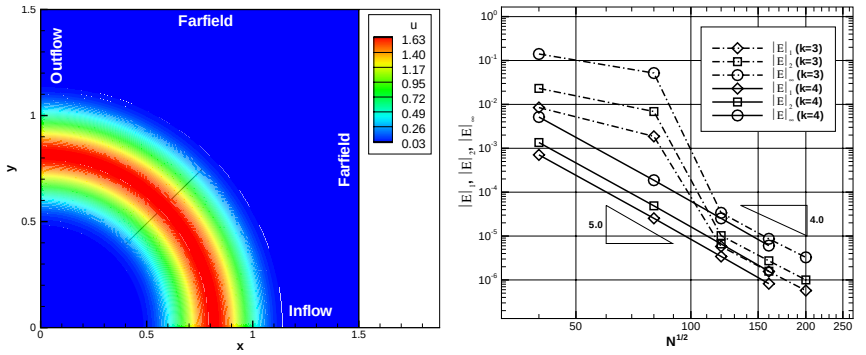

Fig. 1. Predicted 4th-order ($k=4$) CENO solution (left) and L_1, L_2 and L_∞ error norms for $k=3$ and $k=4$ CENO reconstructions (right)

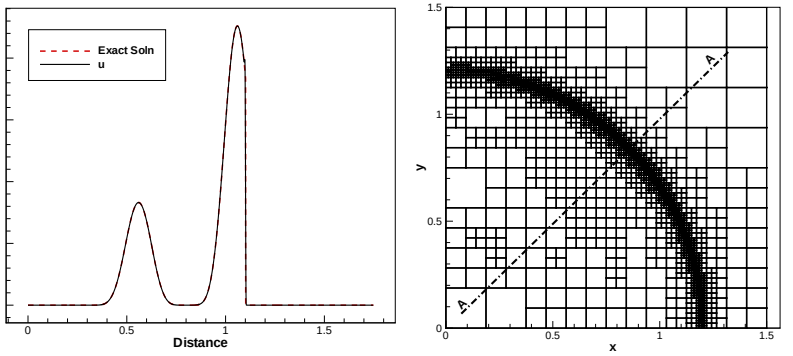

Fig. 2. Comparison of 4th-order ($k=3$) AMR CENO solution on the final mesh and exact solution along A-A (left) and final mesh with 2,911 10×10 blocks (right)

A-A compared against the exact solution and the final multi-block AMR mesh and the location of line A-A. The results clearly show that the proposed AMR scheme in conjunction with the h-refinement criteria based on the smoothness indicator of the hybrid CENO reconstruction is capable of refining both under-resolved (inaccurate) and non-smooth regions of the solution and will not unnecessarily refine resolved solution content. The smooth peaks are all well captured whereas the solution discontinuity is well identified by the smoothness indicator and well resolved by the AMR procedure.

The numerical scheme was also tested for solutions to the Laplace equation for the curved boundary domain shown in Fig. 3. Dirichlet BCs were implemented based on the exact solution $u(x,y) = e^{\mu x}\ (\cos(\mu y) + 2\sin(\mu y))$, $\mu = 1.5$. A 4th-order solution to this problem and the L_1, L_2, and L_∞ error norms for cubic and quartic interpolants are also shown in Fig. 3. The slopes of the L_1- and L_2-norms reach in the asymptotic limit -3.86 and -3.85 for $k=3$ and -3.86 and -3.81 for $k=4$, respectively. Even if the orders of accuracy for these two interpolants are essentially the same and close to the theoretical value, there is about one order of magnitude difference between the absolute error values, demonstrating the benefits of using a quartic interpolant.

The proposed scheme is now applied to problems involving different ratios of advection and diffusion terms as determined by the Péclet number (Pe). Solution of (1) with $\mathbf{V} = (v_0, 0)$ and $\kappa(x,y) = 0.01$, for the BCs shown in Fig. 4 is considered for Pe = 0.1, Pe = 1, and Pe = 10, depending on v_0.

Figure 4 shows the numerical solution obtained for Pe = 10 on an 80×40 Cartesian mesh and the error norms for the three Péclet numbers. The results show that the errors generated by the quartic polynomial are consistently lower than those of the cubic interpolant by at least one order of magnitude for all cases and obtain the theoretical accuracy in all error norms. Thus, the L_1-norm for $k=4$ is -4.02 (Pe=0.1), -4.30 (Pe=1.0) and -3.92 (Pe=10.0), respectively. In the case of cubic interpolant, the L_1-norm is -3.92 (Pe=0.1), -3.88 (Pe=1.0)

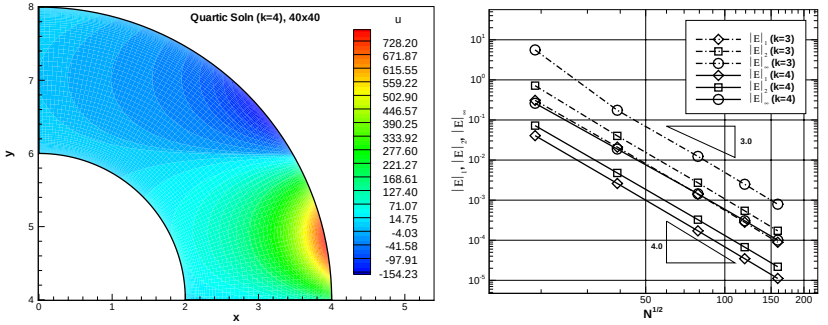

Fig. 3. Fourth-order ($k = 4$) solution to the Laplace equation on a 40×40 grid (left) and L_1-, L_2- and L_∞ error norms for cubic and quartic interpolants (right)

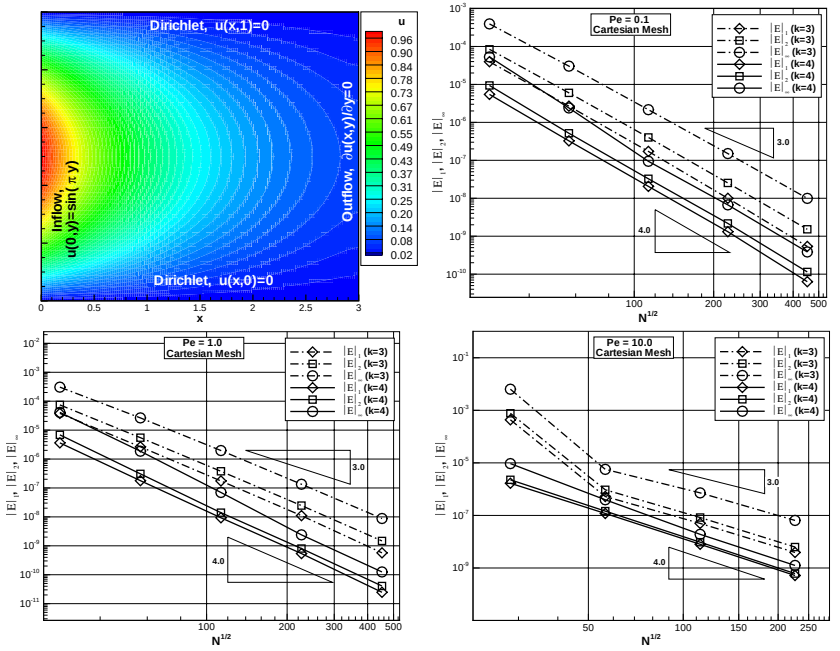

Fig. 4. Fourth-order solution for a channel flow problem with Pe = 10 (upper-left) and L_1-, L_2- and L_∞ error norms obtained with cubic ($k = 3$) and quartic ($k = 4$) interpolants for Pe = 0.1 (upper-right), Pe = 1 (lower-left) and Pe = 10 (lower-right)

and -3.53 (Pe = 10.0), respectively. It can be also seen in the error plots that, for the same accuracy level, the cubic interpolant requires almost twice as many cells as the quartic one. Taking into account that both reconstructions have

identical stencils, the only extra cost associated with quartic reconstruction is to determine and store five additional derivatives.

4 Concluding Remarks

A high-order finite-volume scheme with AMR for the advection-diffusion equation has been proposed with a number of desirable features. Future research will extend the algorithm to the solution of the full Navier-Stokes equations.

References

[Abg94] Abgrall, R.: J. Comput. Phys. 114, 45–58 (1994)
[BC05] Barad, M., Colella, P.: J. Comput. Phys. 209, 1–18 (2005)
[Bar93] Barth, T.J.: AIAA, Paper 93-0668 (1993)
[CS89] Cockburn, B., Shu, C.-W.: Math. Comput. 52, 411 (1989)
[Coi94] Coirier, W.J.: PhD thesis, University of Michigan (1994)
[DABLP99] Delanaye, M., Aftomis, M.J., Berger, M.J., Liu, Y., Pulliam, T.H.: AIAA, Paper 99-0777 (1999)
[HEOC87] Harten, A., Enquist, B., Osher, S., Chakravarthy, S.R.: J. Comput. Phys. 71, 231–303 (1987)
[HS99] Hu, C., Shu, C.-W.: J. Comput. Phys. 150, 97–127 (1999)
[IG07] Ivan, L., Groth, C.P.T.: AIAA, Paper 2007-4323 (2007)
[MJ06] May, G., Jameson, A.: AIAA, Paper 2006-304 (2006)
[OV02] Ollivier-Gooch, C.F., Van Altena, M.: J. Comput. Phys. 181, 729 (2002)
[WA06] Wolf, W.R., Azevedo, J.: AIAAJ, 44(10), 2295–2310 (2006)

“*This page left intentionally blank.*”

Part 24
Hypersonic and Reacting Flows

“*This page left intentionally blank.*”

Active Control of Hypersonic Shock Layer Instability: Direct Numerical Simulation and Experiments

T.V. Poplavskaya[1,2], A.N. Kudryavtsev[1], S.G. Mironov[1,2], and I.S. Tsyryulnikov[1]

[1] Khristianovich Institute of Theoretical and Applied Mechanics, Siberian Branch of RAS, Novosibirsk 630090, Russia
popla@itam.ncs.ru, alex@itam.nsc.ru, mironov@itam.nsc.ru
[2] Novosibirsk State University, Novosibirsk 630090, Russia

1 Introduction

When a flying vehicle moves with a high velocity in the upper layers of the atmosphere, a viscous shock layer is formed in the vicinity of its leading edges. The viscous shock layer consists of a thick boundary layer and a thin zone of inviscid flow behind the bow shock wave. The receptivity of a hypersonic shock layer to external and internal disturbances plays an important role in formation of a spectrum of initial disturbances and influences laminar-turbulent transition in a hypersonic boundary layer. In this connection, the investigation of wave processes in a hypersonic shock layer and development of methods of controlling their intensity is an important scientific problem.

The previous results of experimental and theoretical research and control methods developed refer to the boundary–layer flow and cannot be directly transposed to a hypersonic shock layer. The flow in a hypersonic shock layer has some specific features: the influence of a closely located shock wave on the evolution of disturbances, significant nonparallelism of the flow, and a high degree of rarefaction. The present paper describes comprehensive numerical and experimental investigations of evolution of disturbances generated in the hypersonic viscous shock layer on a flat plate by external acoustic waves and by perturbations introduced into the shock layer from the surface of model. The active control of intensity of pulsations is possible because both external acoustic waves and the periodic controlled disturbances introduced on the plate surface generate, in a shock layer, entropy-vorticity disturbances with identical spatial distributions and phase velocities.

The analysis of the laminar-turbulent transition in the boundary layer is traditionally started from the problem of receptivity, i.e., excitation of instability waves by external disturbances. Elucidation of the ways and reasons for the emergence of disturbances in the shock layer, i.e., the process of generation of disturbances in the shock layer, is the essence of the problem of

shock-layer receptivity. The study of boundary–layer–type subsonic flows [KKL82] is based on a convenient classification of the mechanisms of receptivity to external disturbances with subdivision into localized and distributed mechanisms. The same classification can be used for hypersonic flows. Two limiting cases of excitation of disturbances in the viscous shock layer can be distinguished: continuous (distributed) generation in an extended flow region and localized generation by spatially concentrated forcing. The present activities were aimed at numerical and experimental investigations of distributed and localized receptivity of the shock layer on a flat plate at high Mach numbers and moderate Reynolds numbers.

2 Methods of Investigation

With allowance for the moderate magnitude of local Reynolds numbers typical of the viscous shock layer, the most adequate approach to the problem of numerical simulation seems to be the direct numerical simulation (DNS) of disturbances on the basis of solving the full unsteady Navier-Stokes equations. Two–dimensional Navier-Stokes equations written in the form of conservation laws are solved by high–order shock–capturing schemes. Details of the numerical method can be found in [KMP06,KMPT06]. First, the steady flow is calculated. The results of simulations turned out to be in good agreement with the mean density in the shock layer measured in experiments by the electron-beam fluorescence method [KMP06]. Then the problem of interaction of the viscous shock layer with disturbances of different types, which are introduced by imposing appropriate time–dependent boundary conditions, is solved.

Measurements of characteristics of mean flow and density pulsations were measured by the method of electron-beam fluorescence of nitrogen [MM00] at hypersonic wind tunnel T-327A of ITAM SB RAS. A flat plate model $240mm$ long with a sharp leading edge $100mm$ wide was inserted into a hypersonic flow with a Mach number $M_\infty = 21$, unit Reynolds number $Re_{1\infty} = 6 \times 10^5 m^{-1}$, and stagnation temperature $T_0 = 1200K$; the temperature factor of the surface was $T_w/T_0 = 0.26$.

3 Disturbances

3.1 Distributed Receptivity

The external acoustic disturbances excited in the experiments were slow acoustic waves generated by the turbulent boundary layer formed on the nozzle walls.

In numerical simulations of the problem of shock-layer interaction with external acoustic disturbances, the variables on the left boundary of the computational domain were set in the form of a superposition of the steady main

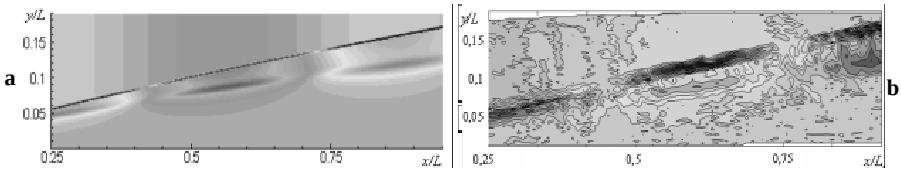

Fig. 1. Isolines of instantaneous density fluctuations for a slow external acoustic wave on the basis of DNS (a) and in experiment (b) at $M_\infty = 21, Re_L = 1.44 \times 10^5, T_w = 300K, A = 0.003, f = 9kHz, \theta = 0^\circ$

flow and a plane monochromatic acoustic wave characterized by the amplitude A, frequency f, and angle of propagation θ.

Figure 1 shows the instantaneous fields of density fluctuations in the shock layer for a slow external acoustic wave, which were obtained in computations (a) and experiments (b). The spatial patterns of the fields of fluctuations are in good agreement. The most intense density fluctuations are observed on the shock wave and on the edge of the viscous boundary layer. The magnitude of the maximum of fluctuations on the boundary-layer edge is several times lower than the amplitude of density fluctuations on the shock wave. Disturbances of the entropy-vortex mode still dominate in the shock layer, which is evidenced by the data on the field of vorticity fluctuations and by the analysis with the use of the linear theory of interaction [MW68].

3.2 Localized Receptivity

Internal perturbations localized near the leading edge were generated by an obliquely cut cylindrical aerodynamic whistle located under the plate [MT06]. Disturbances of the periodic blowing–suction type were simulated by imposing the boundary condition for the transverse mass flow on a certain area of the plate surface [KMPT06]. After introduction of disturbances, the Navier-Stokes equations were integrated until the unsteady solution reached a steady periodic regime.

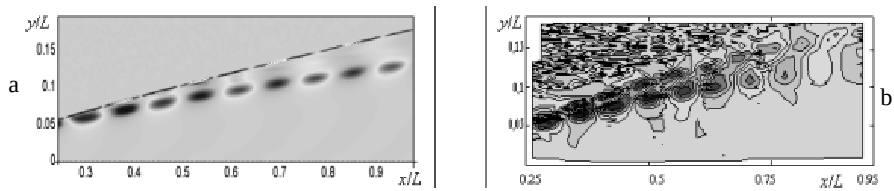

Fig. 2. Isolines of instantaneous density fluctuations induced by a whistle (periodic blowing-suction) on the basis of DNS (a) and in experiment (b) at $M_\infty = 21, Re_L = 1.44 \times 10^5, T_w = 300K, A = 0.003, f = 38.4kHz$

The isolines of density fluctuations obtained in computations (Fig. 2a) and experiments (Fig. 2b) show that the most intense density fluctuations are observed on the shock wave and on the edge of the viscous boundary layer, similar to the case of distributed receptivity, i.e., the field of fluctuations generated by a local source of the blowing–suction type is similar to the field of fluctuations generated by external acoustic disturbances.

The main specific feature inherent in the formation of the field of density fluctuations during shock-layer interaction with external acoustic disturbances and internal disturbances of the periodic blowing–suction type is the mechanism of generation of entropy-vortex disturbances and their propagation inside the shock layer. This is also confirmed by the linear theory of interaction of plane waves with the shock wave [MW68].

4 Active Control

An obvious consequence is the possibility of suppression of fluctuations generated by external disturbances by artificially inserted internal disturbances with a properly chosen phase and amplitude of blowing–suction. The principle opportunity of suppression and amplification of disturbances using simultaneous influence on the shock layer of external acoustic waves and a blowing - suction near the plate leading edge has been first demonstrated numerically.

As is evidenced by the computed results (Fig. 3), periodic blowing–suction of the gas near the leading edge initiated in-phase or in antiphase with respect to the external fast acoustic wave with a properly chosen blowing–suction amplitude can suppress or amplify the development of instability in the shock layer, which arises under the action of free-stream acoustic disturbances, i.e., active control of the flow in the shock layer can be ensured. Similar results were obtained in DNS [F07] for external slow acoustic waves.

The possibility of controlling the intensity of fluctuations in a hypersonic shock layer on a flat plate was also demonstrated in experiments for fast

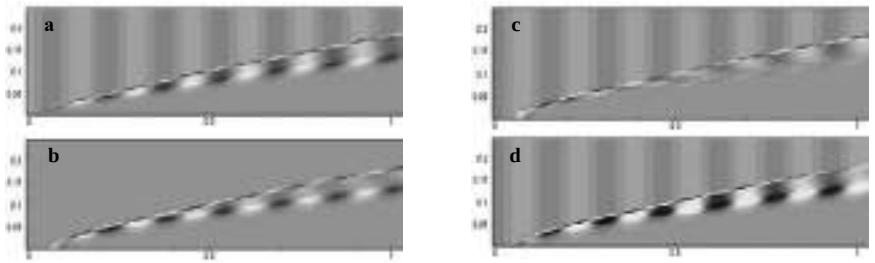

Fig. 3. Fields of instantaneous density fluctuations in a shock layer for $M_\infty = 21, Re_L = 1.44 \times 10^5, T_w = 300K, f = 38.4kHz$: (a)- slow acoustic wave $\theta = 0°$, $A = 0,001$; (b) - blowing-suction $A = 0,06$; (c) - antiphase action; (d) - in-phase action

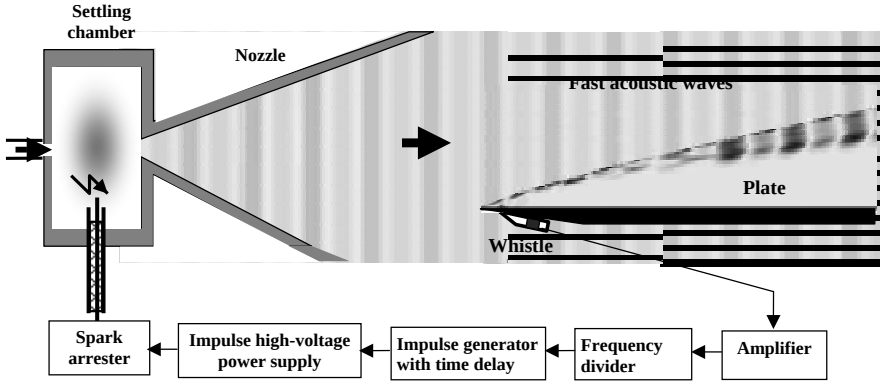

Fig. 4. Arrangement of the experiment

external acoustic waves. The idea of this experiment is illustrated in Fig. 4. Periodic acoustic waves are generated in a hypersonic flow, which interact with the shock layer on the plate and generate fluctuations in the shock layer. The oblique gas-dynamic whistle located under the plate near its tip also excites periodic pressure perturbations in the shock layer. If the frequencies of external flow disturbances and of perturbations excited by the whistle are identical, a certain relation between the phases of these disturbances may lead to interference suppression (amplification) of fluctuations in the boundary layer on a flat plate. As an illustration, Fig. 4 shows suppression of density fluctuations in the shock layer at the time when the perturbations excited by the whistle have covered half of the plate length.

For a frequency $f = 37.5kHz$, Fig. 5 shows the experimental curves for the amplitude of density fluctuations on the edge of the boundary layer on the plate ρ'/ρ'_{max} in the cross section $x/L = 0.63$ versus the time shift $\triangle\tau$ between external flow disturbances and perturbations generated by the

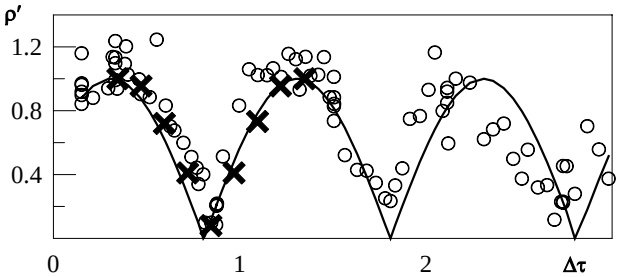

Fig. 5. Amplitude of density fluctuations on the boundary-layer edge versus the delay of the initial disturbances

whistle. Here ρ'_{max} is the level of density fluctuations on the boundary-layer edge in the case of an in-phase action of the external acoustic wave and periodic blowing–suction. The relation between the amplitudes of external and internal disturbances allows almost complete suppression of perturbations in the shock layer. The solid curve in Fig. 5 approximates the experimental values in accordance with the law of interference of two sinusoidal waves of identical frequency and amplitude.

For comparison, Fig. 5 shows the DNS data (marked by crosses) for the shock layer under the action of fast acoustic waves propagating at a zero angle to the external flow centerline with a frequency $f = 37.5kHz$. The initial amplitudes of the fast external acoustic wave and periodic blowing–suction were chosen with the aim of suppressing the fluctuations and have the values of 0.0017 and 0.0694, respectively. The numerical values are seen to be in good agreement with the measured data.

This work was supported by the Russian Foundation for Basic Research (Grant No. 05–08–33436).

References

[KKL82] Kachanov, Y.S., Kozlov, V.V., Levchenko, V.Y.: Emergence of Turbulence in the Boundary Layer. Nauka, Novosibirsk (1982)

[MT06] Mironov, S.G., Tsyryulnikov, I.S.: Experimental study of the evolution of periodic controlled disturbances in a hypersonic viscous shock layer on a flat plate. Teplofiz. Aeromekh 3, 353–360 (2006)

[KMP06] Kudryavtsev, A.N., Mironov, S.G., Poplavskaya, T.V., Tsyryulnikov, I.S.: Experimental study and direct numerical simulation of the evolution of disturbances in a viscous shock layer on a flat plate. J. Appl. Mech. Tech. Phys. 5, 617–627 (2006)

[KMPT06] Kudryavtsev, A.N., Mironov, S.G., Poplavskaya, T.V., Tsyryulnikov, I.S.: Direct numerical simulation of receptivity of a hypersonic shock layer to natural and artificial disturbances. Vych. Tekhnol. 11(Pt. 1), 108–116 (2006)

[MM00] Mironov, S.G., Maslov, A.A.: An experimental study of density waves in hypersonic shock layer on a flat plate. Phys. Fluids A. 6, 1544–1553 (2000)

[MW68] McKenzie, J.F., Westphal, K.O.: Interaction of linear waves with oblique shock waves. Phys. Fluids. 11, 2350–2362 (1968)

[F07] Fomin, V.M., Kudryavtsev, A.N., Maslov, A.A., Mironov, S.G., Poplavskaya, T.V., Tsyryulnikov, I.S.: Active control of disturbances in a hypersonic shock layer. Dokl. Ross. Akad. Nauk. 2, 190–193 (2007)

Part 25
Immersed Boundary Method/Cartesian Grid Method 1

“*This page left intentionally blank.*”

A Hierarchical Nested Grid Approach for Local Refinement Coupled with an Immersed Boundary Method

Xudong Zheng[1], Rajat Mittal[1], and Yifan Peng[2]

[1] Department of Mechanical and Aerospace Engineering, The George Washington University, Washington, D.C., 20052, USA
xudohg@gwu.edu, mittal@gwu.edu

[2] Department of Civil Engineering National Chi-Nan University, Puli, 545, Taiwan(ROC)

1 Introduction

The immersed boundary method (IBM) has gained tremendous popularity in recent years due to its ability to deal with highly complex moving boundary problems. Since IBMs usually employ body non-conformal Cartesian grids, providing high resolution selectively to localized regions (such as the boundary layer on the body) has been one of the major shortcomings of this method. Introduction of local grid refinement into the IBM would therefore significantly enhance the capability of the method. In the current paper, we present a new local refinement technique that is specifically designed to work effectively with our existing sharp-interface immersed boundary method ([Bozkurttas05], [Mittal08]).

There are two fundamentally different approaches to local-refinement ([Michael99]). In the first approach, the mesh with local refinement is treated as one single unstructured mesh and the connectivity between the cells can either be implicit or explicit (as with a quadtree or octree structure). The second approach employs finer block meshes which are considered to be "nested" or "embedded" onto the coarser mesh. In the former approach, it is easy to develop highly complex local refinement topologies but since the grid structure is lost, one cannot take advantage of powerful block iterative and geometric multi-grid scheme for solving the discretized equations. In the latter approach, it is relatively difficult to work with complex refinement topologies but since the structured nature of the grid topology is maintained, one has access to all of the powerful solution methodologies that are available for such grids.

In the current effort we have developed a new nested grid refinement procedure that provides a high level of flexibility in local refinement which retains the advantages of a structured grid topology. In order to implement this method we introduce a new date structure we call an "Eulerian global map" to manage the connectivity between the nested refined grid blocks. The use of this data structure simplifies the local refinement approach and proves to

be robust even for highly complex refinement topologies. In addition, a level-set is used to determine the criteria for refinement and cell blanking used to construct nested grid with curvilinear shapes.

2 Numerical Methodology

2.1 Underlying Numerical Scheme

In current study, the incompressible Navier-Stokes equations are solved with an immersed boundary method.

$$\frac{\partial u_i}{\partial x_i} = 0 \tag{1}$$

$$\frac{\partial u_i}{\partial t} + \frac{\partial (u_i u_j)}{\partial x_j} = -\frac{\partial p}{\partial x_i} + \frac{1}{Re}\frac{\partial^2 u_i}{\partial x_j x_j} \tag{2}$$

where p is the pressure and u velocity vector , respectively. The equations are discretized in space using a cell–centered, non–staggered arrangement of the primitive variables u_i and p. In addition to the cell-center velocities, the face-center velocity, U_i(only the component normal to the cell face) are computed and stored. A second–order fractional step method is used to integrate the equation in time. The advection term is linearized using a second–order Adams–Bashforth scheme. Also, an implicit Crank–Nicolson scheme is employed to discretize the diffusion term and to eliminate the viscous stability constraint. The resulting finite difference scheme is shown as follows:

$$\frac{u_i^* - u_i^n}{\Delta t} + \frac{1}{2}(3N_i^n - N_i^{n-1}) = \frac{1}{2}(D_i^* + D_i^n) \tag{3}$$

$$\frac{1}{\rho}\frac{\delta}{\delta x_i}\left(\frac{\delta p_i^{n+1}}{\delta x_j}\right) = \frac{1}{\Delta t}\frac{\delta U_i^*}{\delta x_i} \tag{4}$$

$$u_i^{n+1} = u_i^* - \Delta t \frac{1}{\rho}\left(\frac{\delta p^{n+1}}{\delta x_i}\right)_{cc} \tag{5}$$

$$U_i^{n+1} = U_i^* - \Delta t \frac{1}{\rho}\left(\frac{\delta p^{n+1}}{\delta x_i}\right)_{fc} \tag{6}$$

where $N_i = \delta(U_j u_i)/\delta x_j$, $D_i = \delta(\delta u_i/\delta x_j)/\delta x_j$ $\delta/\delta x_j$ represents a second-order central difference. The intermediate face-velocity $U^*$is computed by interpolating the neighboring intermediate cell-center velocity u^*. In the above equation, cc stands for cell-center, fc stands for face-center. A line–SOR scheme is used to solve the advection–diffusion equation and an alternating–direction, geometric multi-grid with a line–SOR smoother is used to solve the pressure Poisson equation. The boundary representation is implemented by sharp interface immersed boundary method. A 3D ghost-cell methodology has been developed to satisfy the exact boundary condition on the boundary surfaces by linear interpolation[Mittal08].

2.2 Grid Refinement Strategy

In the local refinement procedure, all of nested meshes are in principle rectangular in shape. Finer (child) meshes are completely embedded inside some next level coarser (parent) mesh and the fine mesh resolution is exactly twice that of the coarse mesh. Any given mesh refinement level can have multiple (sibling) meshes of various shapes. A level set based on distance from the immersed boundary is used to determine which cells of the fine nested meshes are active and which are to be deactivated. This allows us to effectively have complex shaped nested meshes. For each refinement layer, an Eulerian global map is created, which covers the whole domain. Each nested block mesh is given a unique ID and every grid location in the map stores the corresponding block index ID. Since only one integer (or short) variable is stored, the memory usage for this map is relatively small. With this data structure, the information regarding the location and relation of nested mesh blocks is easily to get without searching the tree structure and the interpolation becomes straight forward and robust even for complex grid topologies.

An iterative approach is adopted for solving the governing equations on the nested mesh wherein we iterate successively between the meshes of different refinement levels till convergence. In order to pass information from one mesh to another, we employ a single layer of "ghost-cells" around each mesh block and a linear 2nd-order scheme is used for the interpolation interpolation. A separate conservative interpolation scheme is used to transfer the fluxes (convective, diffusive and pressure gradient) between the blocks. The ghost-cells values are transferred from coarse block to fine block and the fluxes are transferred from fine block to coarse block. The solving procedure is shown as follows:

1. Start
2. Specify initial conditions, u^n, U^n, p^n, and physical boundary conditions
3. Setup "global map" according to the block topologies.
4. Identity the ghost-cell and conservative faces and store the connectivity for interpolation
5. $t = t + \delta t$
6. The advection-diffusion step.
   6.1 Compute ghost cell velocity u^n, and face velocity U^n convective flux $U^n u^n$, diffusive flux $\delta u^n / \delta x$ at block interfaces.
   6.2 Compute N_i^n, N_i^{n-1}, D_i^n for each block.
   6.3 Solve Advection-Diffusion equation for each block.
   6.4 Compute ghost cell velocity u^*, diffusive flux $\delta u^* / \delta x$ at block interfaces.
   6.5 If u^* are converged for all of blocks then proceed to next step, or return to step 6.3.
7. Compute U^* and Recompute U^* at conservative interfaces for each block.

8. The pressure possion step.
   8.1 Solve possion equation for each block.
   8.2 Compute ghost-cell pressure p^{n+1}, and pressure gradient $\delta p^{n+1}/\delta x$ at block interfaces for each block.
   8.3 If p^{n+1} is converged for all of blocks then proceed to next step, or return to step 8.1 .
9. Velocity correction.
   9.1 Compute u^{n+1} and U^{n+1} for each block.
   9.2 Recompute u^{n+1} and U^{n+1} at interfaces based on conservative pressure gradient and pressure ghost value for each block.
10. If stationary boundary goto step 5.
11. If moving boundary, move the boundaries and surrounding blocks. goto step 3.

3 Results and Discussion

Several test cases have been included here to demonstrate the capabilities of the method. The first test case is that of the 2D cavity driven flow. For this case, one layer grid refinement is used and the refinement region is 0.16 away from outer boundaries(Figure 1 (a)). The case is simlated with $Re = 100$. The Figure 1 (c) and (d) shows that u and v centerline velocities match previous study and they do not show any discontinuity at block interfaces. The second test case is of a 2D flow past a cylinder at $Re = 100$. For this case, a three layer nested grid refinement is used(Figure 2 (a)). The first refinement

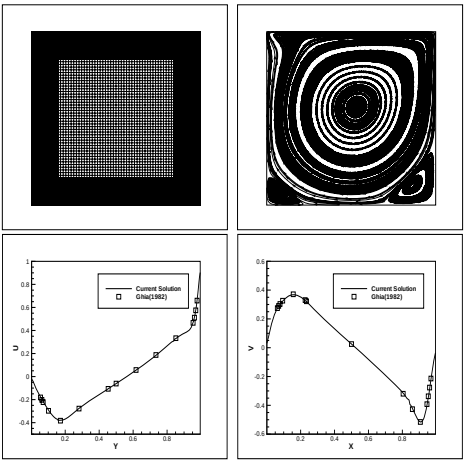

Fig. 1. 2D driven cavity flow (a) mesh configuration (b) streamlines (c) comparison of u at vertical center line (d) v at horizontal center line

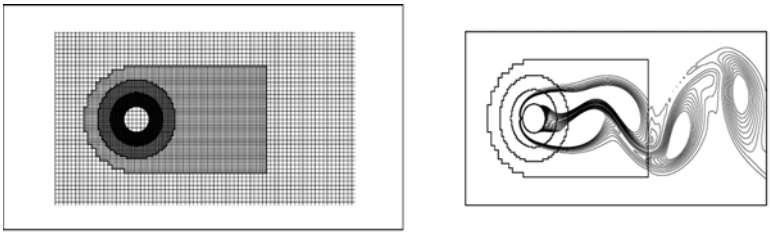

Fig. 2. 2D simulations of flow past circular cylinder (a) Three-level nested mesh used in current simulation (b) contours of instantaneous spanwise vorticity.

level has a C type shape so as to capture the flow around the cylinder and the wake. Two other levels of refinement are used which tighly surround the circular cylinder. The inner one is $0.5d$ away from the cylinder and the outer one is $1.0d$ way from the cylinder. Figure 2 (b) shows the instantaneous vorticity for this case and it shows vortex shedding from the cylinder. The third case is of a 3D flow past a sphere at $Re = 300$. For this case, a three layer nested grid refinement is used(Figure 3 (a)). First a rectangular grid refinement block is created to capture the wake. Then a two-layer level-set refinement block is created where the inner one is $0.5d$ away from the sphere, the outer one is $1.0d$ distance from the sphere. Figure 3 (b) shows the vortex structures created in the wake of the sphere and the vortex topology is inline with previous studies[Mittal02] The last case is of 2D flow past a cylinder at $Re = 100$ with moving nested grids. Two concentric elliptic type blocks are created surrounding the cylinder (Figure 4) and a sinusoidal rotary motion is given to these two blocks to demonstrate the moving block ability. As can be seen from the figure, the results look reasonable with the moving blocks.

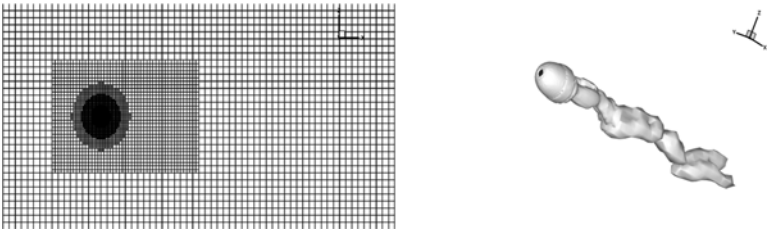

Fig. 3. 3D simulations of flow past sphere (a) Three-level nested mesh used in current simulation (b) Isosurface of maximum eigenvalue of velocity gradient.

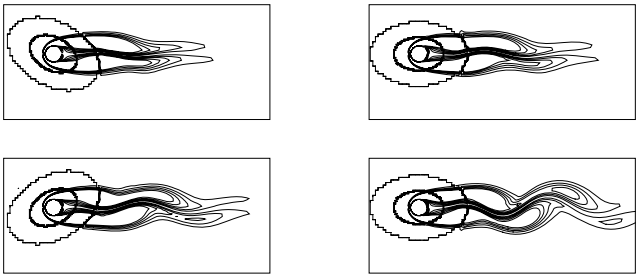

Fig. 4. Instantenous vorticity contour of 2D simulations of flow past cylinder with moving concentric blocks

4 Conclusions

A new local-grid refinement approach that employs a hierarchical nested grid approach has been developed and applied to a sharp interface immersed boundary solver. The key feature of the methodology is that the structured grid approach is retained at all the refinement levels and this allows us to use powerful line-SOR schemes and a geometric multigrid method. A set of simulations of canonical flows have been conducted and these indicate that the solver accurately reproduces the key features of the flows.

References

[Bozkurttas05] Bozkurttas, M., Dong, H., Seshadri, V., Mittal, R., Najjar, F.: Towards Numerical Simulation of Flapping Foils on Fixed Cartesian Grids. AIAA Paper 2005-0079 (2005)

[Michael99] Michael, J.A., et al.: Adaptive Cartesian Mesh Generation. In: Handbook of Grid Generation, vol. 22. CRC Press, Boca Raton (1999)

[Mittal02] Mittal, R., Wilson, J.J., Najjar, F.M.: Symmetry properties of the transitional sphere wake. AIAA Journal 40, 579–582 (2002)

[Mittal08] Mittal, R., Dong, H., Najjar, F.M., Vargas, A., Loebbecke, A.V.: A versatile sharp interface immersed boundary method for incompressible flows with complex boundaries. J. Comput. Phy. 227, 93–102 (2008)

A New Cartesian Grid Method with Adaptive Mesh Refinement for Degenerate Cut Cells on Moving Boundaries

Hua Ji[1], Fue-Sang Lien[2], and Eugene Yee[3]

[1] Waterloo CFD Engineering Consulting Inc., Waterloo, ON, N2T 2N7, Canada
huaji2005@gmail.com
[2] University of Waterloo, Waterloo, ON, N2L 3G1, Canada
fslien@mecheng1.uwaterloo.ca
[3] Defence R&D Canada – Suffield, P.O. Box 4000, Medicine Hat, AB, T1A 8K6, Canada
eugene.yee@drdc-rddc.gc.ca

1 Introduction

The cut-cell method has become increasingly popular in recent years for treating complex boundaries due to its computational efficiency relative to other approaches [Aft99, Joh98]. However, a major difficulty in the application of cut-cell methods arises from the presence of degenerate cells and/or very small cells in the Cartesian grid.

Virtually all cut-cell methods use a Volume-of-Fluid (VOF) method to reconstruct the boundary of the degenerate cell. Although this approach is relatively simple to implement, it has the drawback that it may severely violate the geometric fidelity of the irregular boundary and, hence, affect the accuracy of the solution. Another approach for dealing with a degenerate split cell is to divide this cell into several separate computational cells. This approach is less robust and computationally expensive, and also has the disadvantage that it results in very complex computational molecules involving complicated relationships between a node and its neighboring nodes [Day98].

In this paper, we formulate a new robust and efficient cut-cell method for the moving boundary problem on an arbitrary complex domain.

2 Numerical Methods

2.1 Representation and Tracking of an Irregular Moving Boundary

Because the boundary can move and the Cartesian grid does not have to conform to the boundary, an ordered list of marker points are used to represent the boundary. Instead of using piecewise linear segments to represent the

boundary curve, a set of connected polynomials is constructed using marker points to provide a parametric representation of the boundary curve. The geometric properties associated with this boundary can be computed based on cubic splines.

2.2 Discretization of the Governing Equation

We consider an initial-value problem given by

$$\frac{\partial \phi}{\partial t} + D\nabla^2 \phi = f, \tag{1}$$

where t is the time, D is the diffusion coefficient and f is a source term. The source term f is evaluated at the centroid of each cell. For the transient term $\frac{\partial \phi}{\partial t}$, a three-level implicit method that is second-order accurate is used.

In a cell, the discrete equivalent of the diffusion term in Eq. (1) can be written as follows:

$$D \oint_S \nabla \phi \cdot \vec{n}\, ds = D \sum_d l_d \nabla_d \phi + D \int_B \nabla \phi \cdot \vec{n}\, ds, \tag{2}$$

where d is a generic label for a coordinate direction, B is the portion of the boundary curve that intersects a cut-cell, and the gradient ∇_d is evaluated at the midpoint of a cell face in the direction d of the fluid domain. Here, we have split the gradient fluxes into two contributions.

To evaluate the gradient fluxes of ϕ through the cell faces in the fluid domain, let us consider 2 neighboring cells at the same grid refinement level. Each cell can be either (1) a regular Cartesian cell, (2) a regular cut-cell, (3) a degenerate no-split cut-cell or, (4) a degenerate split cut-cell, yielding sixteen possible combinations. Here, we only discuss two selected cases. The evaluation of the cell-face gradient fluxes can be determined for the remaining twelve cases analogously to the two cases discussed below (see also [Ji06]).

The first case considers degenerate no-split and split cut-cells as illustrated in Figs. 1 and 2, respectively. The gradient flux of ϕ at the east face (F_e) is evaluated as:

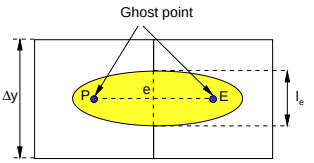

Fig. 1. Evaluation of the gradient flux of ϕ through the face between two neighboring degenerate no-split cut-cells at the same grid refinement level

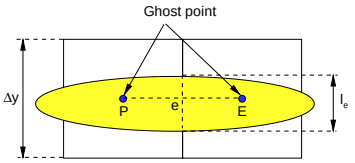

Fig. 2. Evaluation of the gradient flux of ϕ through the face between two neighboring degenerate split cut-cells at the same grid refinement level

$$F_e = (\triangle y - l_e)\nabla_e \phi = \frac{\phi_E - \phi_P}{x_E - x_P}(\triangle y - l_e)\,. \tag{3}$$

Here, the concept of a "ghost point" is used in order to improve the robustness of the present approach in treating degenerate split/no-split cut-cells.

In the second case, the two neighboring cells are a regular cut-cell (left) and a degenerate no-split cut-cell (right), as shown in Fig. 3. The gradient flux of ϕ on the east face (F_e) can be evaluated as follows:

$$F_e = \left(\frac{\phi_E - \phi_P}{x_E - x_P}\right) l_e + \frac{l_e}{x_E - x_P}\left[\left(\frac{\partial \phi}{\partial y}\right)_E (y_{e'} - y_E) - \left(\frac{\partial \phi}{\partial y}\right)_P (y_{e'} - y_P)\right]. \tag{4}$$

The node P in Fig. 3 is the centroid of the regular cut-cell. However, the centroid of the degenerate no-split cut-cell (node E), which is considered as a "ghost point" here, is the same as the centroid of the corresponding regular Cartesian cell. For the neighboring cells at different grid refinement levels, the gradient flux of ϕ can still be evaluated using either Eq. (3) or (4), depending on the particular case.

In Eq. (2), we also need to evaluate the gradient flux of ϕ through the boundary curve B of the cut-cell. For Neumann boundary conditions, the gradient of ϕ at each marker point along the boundary curve, represented by a cubic spline, is known. If we assume that the variation of the gradient $\nabla\phi \cdot \vec{n}$

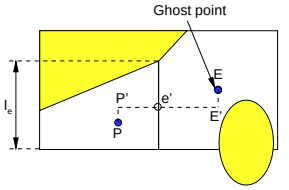

Fig. 3. Evaluation of the gradient flux of ϕ through the face between regular and degenerate no-split cut-cells at the same grid refinement level

between any two adjacent marker points is linear, the second term on the RHS of Eq. (2) can be evaluated using Simpson's 3/8 rule. Without the need to split the cut-cell into smaller cells and to treat each cell individually, our proposed approach can be applied to the cut-cells that intersect a boundary curve at any number of points. Furthermore, our approach results in an evaluation of the gradient flux of ϕ through the boundary curve that is second-order accurate owing to the assumption of the linear variation of $\nabla\phi \cdot \vec{n}$ along any section of the boundary curve between two adjacent marker points.

3 Numerical Results

To evaluate the numerical accuracy of the proposed method, we consider as the first case, a Poisson equation with the exact solution $\phi = \sin(3\pi x)\sin(3\pi y)$. The interior boundary curve for this example is a very thin ellipse, which is rotated 45° in the counter-clockwise direction as shown in Fig. 4 for $L = 6$ (L denotes the level of grid refinement). In this example, the boundary curve cannot be adequately resolved even for the finest mesh used (viz., $L = 8$). It should be noted that the VOF-based cut-cell method cannot solve this challenging problem without using a split-cell method.

Table 1 shows the variation of the L_p-norm of the solution error obtained using our proposed methodology for this example. Here, r_p is a measure of the rate of convergence of the solution (with respect to the L_p-norm), whereby $r_p = n$ indicates that the solution methodology possesses an n-th order of accuracy. From the tabulated information, it can be seen that our solution methodology is second-order accurate (approximately or better) in the L_1- (not shown) and L_2-norms. However, the solution methodology is less than second-order accurate in the L_∞-norm. This is because the L_∞-norm of the solution error is controlled by the error in one or more degenerate cut-cells for this example.

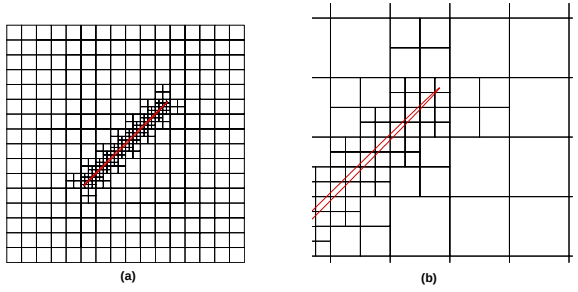

Fig. 4. The global mesh with a locally refined mesh for $L = 6$ for an interior boundary curve that is a thin rotated ellipse ('thin' boundary curve)

Table 1. Numerical accuracy test for Poisson equation applied to the domain with an interior boundary curve that is a thin rotated ellipse ('thin' boundary curve)

Level	$\|\varepsilon\|_2$	r_2	$\|\varepsilon\|_\infty$	r_∞
5	6.71×10^{-2}		1.42×10^{-1}	
6	1.65×10^{-2}	2.03	4.26×10^{-2}	1.67
7	4.19×10^{-3}	1.97	1.37×10^{-2}	1.55
8	1.09×10^{-3}	1.92	4.69×10^{-3}	1.46

For the second case, we consider a moving boundary problem. For this case, we use the following source term in Eq. (1) (with $D = 1$):

$$f(x, y, t) = \frac{4(x^2 + y^2 - 5(t+1))}{125\pi(t+1)^3} \exp\left(-\frac{x^2 + y^2}{5(t+1)}\right). \tag{5}$$

The solution domain is the region exterior to an elliptical boundary curve, defined at the initial time $t = 0$ as:

$$\frac{(x-p)^2}{a} + \frac{(y-q)^2}{b} = 1, \tag{6}$$

with $p = 0.5 - 6\gamma$, $q = 0.5 - 5\gamma$, $a = \frac{3}{2}\gamma$, $b = \gamma$, and $\gamma = \frac{\sqrt{2}}{15}$.

Dirichlet boundary conditions are imposed on the sides of the unit square. Neumann boundary conditions were specified along the interior elliptical boundary curve. The global mesh is two levels of refinement less than the locally refined mesh used for the cut-cells. The solution is advanced in time from $t = 0$ to $t = 0.5$.

The advection of the marker points on the boundary curve are computed using an explicit second-order accurate Runge-Kutta method. The horizontal and vertical velocities of the moving boundary curve are $u = -0.1$ and

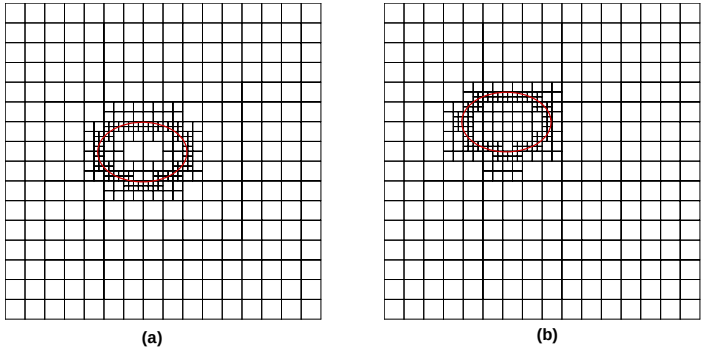

Fig. 5. A moving boundary problem showing (a) the initial grid at $t = 0$ and (b) the final grid at $t = 0.5$ for a local refinement level $L = 6$

Table 2. Numerical accuracy test for an unsteady problem applied to the domain with a moving elliptical interior boundary curve

Level	$\|\varepsilon\|_1$	r_1	$\|\varepsilon\|_2$	r_2	$\|\varepsilon\|_\infty$	r_∞
5	6.00×10^{-4}		6.00×10^{-4}		6.11×10^{-4}	
6	1.55×10^{-4}	1.94	1.55×10^{-4}	1.94	1.56×10^{-4}	1.96
7	3.93×10^{-5}	1.97	3.93×10^{-5}	1.97	3.96×10^{-5}	1.97
8	9.90×10^{-6}	1.98	9.90×10^{-6}	1.98	9.97×10^{-6}	1.99

$v = 0.2$, respectively. A multigrid acceleration method is used to solve the discretized system of equations at each time step.

Figure 5 shows the initial grid at $t = 0$ and final grid at $t = 0.5$. Table 2 summarizes the L_p-norms of the solution error at $t = 0.5$ as a function of the grid resolution. The results in this table clearly demonstrate that our solution methodology is second-order accurate in both time and space.

4 Conclusions

We present a new robust and efficient Cartesian grid method for solving a moving boundary problem on an arbitrary complex domain. The gradient fluxes through all sections of the boundary curve in a cut-cell are computed using surface integrals, with the important consequence that all cut-cells (including the degenerate cut-cells) in the solution domain can be treated similarly. The concept of a "ghost point" is introduced when evaluating the gradient fluxes in the fluid domain for degenerate (split and no-split) cut-cells in order to increase the robustness of the present approach [viz., there is no need to deal with each of the (usually small) split cut-cells individually]. Two cases are used to demonstrate the accuracy and efficiency of our proposed solution methodology for both fixed and moving boundary problems.

References

[Aft99] Aftosmis, M.J., et al.: Proceedings of the Thermal and Fluids Analysis Workshop, NASA Marshall Spaceflight Center, Huntsville, AL (1999)

[Day98] Day, M.S., et al.: Embedded boundary algorithm for solving the Poisson equation on complex domains, Tech. Report LBNL-41811 (1998)

[Ji06] Ji, H., Lien, F.S., Yee, E.: Int. J. Numer. Methods Fluids 52, 723 (2006)

[Joh98] Johansen, H., Colella, P.: Journal of Computational Physics 147, 60 (1998)

Building-Cube Method for Incompressible Flow Simulations of Complex Geometries

Shun Takahashi, Takashi Ishida, and Kazuhiro Nakahashi

Department of Aerospace Engineering, Tohoku University, Japan
takahasi@ad.mech.tohoku.ac.jp

In this paper, two numerical results obtained by Building-Cube Method which is based on an equally-spaced Cartesian mesh method are presented. One is a flow simulation around the Ahmed body which is a simplified automobile model. The accuracy of the present numerical method is discussed by comparing with the experimental result. Another one is a flow simulation around a formula-1 race car for demonstrating the capability of the present method to treat 3D complicated geometries.

1 Introduction

At present, CFD using unstructured mesh is commonly used to simulate around 3D arbitrary geometries owing to the flexibility in mesh generations. The unstructured-mesh CFD, however, has some disadvantages. The mesh generation is still time consuming for engineering uses. Spatial accuracy of the unstructured-mesh CFD is usually at most second order and to implement spatial higher order schemes is painfully expensive. Recently, Cartesian-mesh method is spreading gradually [1][2][3], because of the advantages about quick and robust mesh generation, easy implementation of spatially higher order schemes, and so on.

The Building-Cube Method [4] (BCM) was proposed based on equally-spaced Cartesian mesh method to aim for high-resolution computations around complex geometries. In this method, whole computational domain is divided into a number of sub-domains of cuboids called as cubes. Each cube has equally-spaced Cartesian mesh, called as cells, in it. By using the same number of cells in all cubes, it is simple to keep load balance among all cubes in the use of large scale computers with massively parallel processors (MPP).

In this paper, a BCM flow solver for the incompressible Navier-Stokes equations is discussed with two large-scale computations. One is a flow simulation around the Ahmed body for evaluation of the accuracy of the present method. Another one is a flow simulation around a formula-1 race car to investigate the applicability and robustness of the present method for analyses around 3D arbitrary geometries. These computations have been conducted

by using NEC SX-9 vector-parallel supercomputers installed on Cyberscience Center of Tohoku University.

2 Numerical Method

2.1 Mesh Generation

In the BCM, the computational mesh consists of two sets, cubes which are the computational sub-domains, and equally-spaced Cartesian mesh called as cells in each cube. Then BCM mesh generation is classified into two procedures of cube generation and cell generation. In these procedures, Tomas Möllar's intersection check, fully threaded tree (FTT) data structure and OpenMP parallel processing are exploited for robust and fast mesh generation [5]. Typical time to generate BCM mesh for about 100 million cells is less than 10 minutes on Dual quad-core 64 bit PC.

2.2 Solution Algorithm

In this paper, 3D incompressible Navier-Stokes equations (Eq.(1)) are solved by fractional-step method with staggered arrangement.

$$\begin{cases} \frac{\partial \mathbf{u}}{\partial t} + \left(\mathbf{u}\cdot\nabla\right)\mathbf{u} = -\nabla p + \frac{1}{\mathrm{Re}}\nabla^2\mathbf{u} \\ \nabla\cdot\mathbf{u} = 0 \end{cases} \tag{1}$$

In the fractional-step method, three processes of Eqs. (2)-(4) are implemented sequentially at each time step [6][7][8]. In this paper, second order accurate Adams-Bashforth explicit time integration is implemented in solving the temporal velocity field $\mathbf{u}^*$ in Eq. (2). Here the convection term $\mathbf{A}$ and diffusion term $\mathbf{B}$ are discretized by third order upwind finite difference scheme [9] and second order central finite difference scheme respectively. In the process of Eq. (3), the pressure filed p^{n+1} is solved by Poisson equation. In solving incompressible Navier-Stokes equations, most of computational cost is paid for the procedure. Therefore Red-Black SOR method is used to exploit vector processing of SX-9. Moreover pressure perturbation in incompressible flow field should be propagated to far field at once ideally. Then flow information of each cube is exchanged between adjacent cubes because BCM mesh is multi-block structure of cubes. Finally real velocity field $\mathbf{u}^{n+1}$ is solved by Eq. (4).

$$\frac{\mathbf{u}^* - \mathbf{u}^n}{\Delta t} = -\left(\frac{3}{2}\mathbf{A}^n - \frac{1}{2}\mathbf{A}^{n-1}\right) + \left(\frac{3}{2}\mathbf{B}^n - \frac{1}{2}\mathbf{B}^{n-1}\right) \tag{2}$$

$$\nabla^2 p^{n+1} = \frac{1}{\Delta t}\nabla\cdot\mathbf{u}^* \tag{3}$$

$$\frac{\mathbf{u}^{n+1} - \mathbf{u}^*}{\Delta t} = \nabla p^{n+1} \tag{4}$$

Detail of the present computational method is described in [10]. In the present computations, wall object is expressed by simple staircase pattern. Hence nonslip boundary condition of velocity and non gradient to normal direction boundary condition of pressure are applied to staircase cells directly.

3 Numerical Results

3.1 Flow Simulation Around Ahmed Body

Ahmed body, which is a simplified automobile model, has been investigated by many experiments and simulations [11][12][13] In the present paper, a model with 35 degrees was employed for comparisons of velocity profile on symmetrical plane. Total number of cubes is 3,048 and each cube has 32^3 cells in it. Total number of cells is 99,876,864 (about 0.1 billion). The minimum spacing near the wall boundary is 1.2×10^{-3} base on overall length of the model which corresponds to 1.3×10^{-3} meter in the real scale. Reynolds number is 2.8 million based on the overall length. Ground boundary is treated as a nonslip boundary. A constant velocity condition is applied at the inflow boundary, and a constant pressure condition is applied to the outflow boundary. On other outer boundaries, velocity and pressure are calculated by linear extrapolation. In this simulation, any turbulence model was not used.

In Figure 2, black diamonds and red lines indicate the experimental and the present computed results of the u-velocity on the symmetrical plane. At upstream region of the model, a slight discrepancy is observed between the present result and the experiment. The computed result shows a boundary layer separation on the upper surface near the front. The separation affects to the downstream above the model. In the diagonal part to wake region, the present result shows relatively good agreement with the experimental result.

The boundary layer separation in the upstream region appeared in the present computation may be due to the lack of mesh resolution for the thin turbulent boundary layer at this Reynolds number. It caused a laminar separation because of no turbulence model. Therefore some kinds of turbulence model such as the Smagorinsky model for LES may be required in the present method.

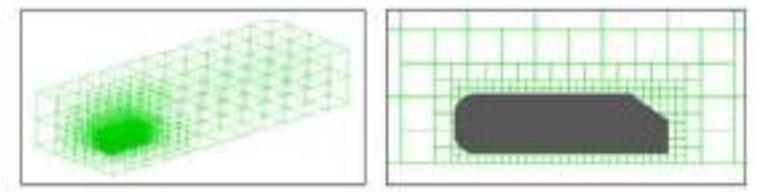

Fig. 1. Computational mesh around Ahmed body

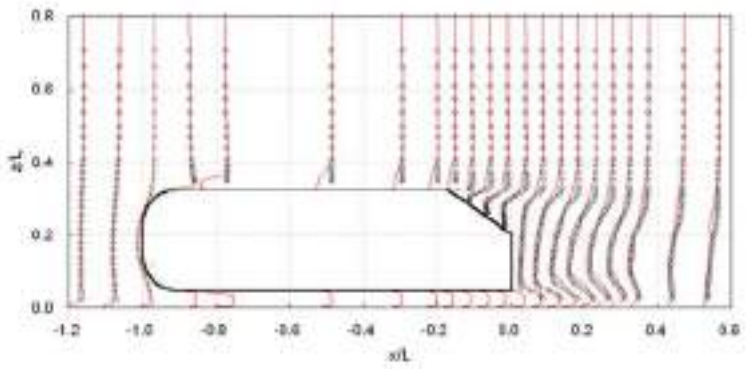

Fig. 2. Comparison of velocity profile on symmetrical plane

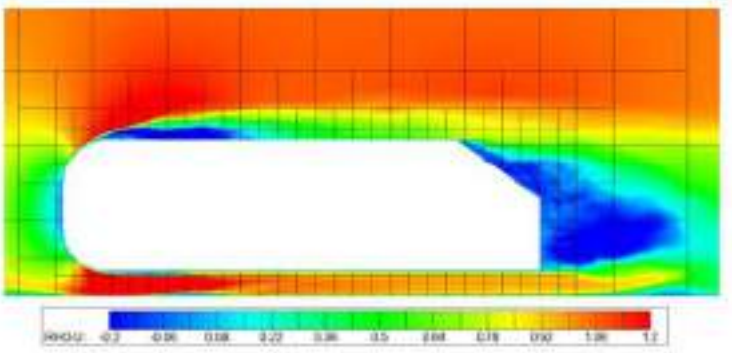

Fig. 3. U-velocity distribution on symmetrical plane

3.2 Flow Simulation Around Formula-1 Model

The present method was applied to flow fields around a formula-1 race car as shown in Fig. 4 for the capability demonstration. Total number of cubes is 5,930, and each cube has 32^3 cells. Total number of cells is 194,314,240 (about 0.2 billion). The Minimum spacing near the wall boundary is 7.3×10^{-4} based on overall length which corresponds to about 3.5×10^{-3} meter in the real scale. Reynolds number is 14.9 million based on overall length [14]. The computational mesh was generated in about 10 minutes even for this complicated model. In this simulation, wheels and ground boundaries are treated as simple nonslip boundaries. A slight gap was inserted between the wheels and the ground for keeping computational stability.

Typical flow features such as flow accelerations over the front-wing and under the body, and inflow to the diffuser were qualitatively well captured. But the magnitude of flow acceleration was relatively small because of the treatment of wheels and ground boundary. Moving boundary treatment should be included for more realistic solution.

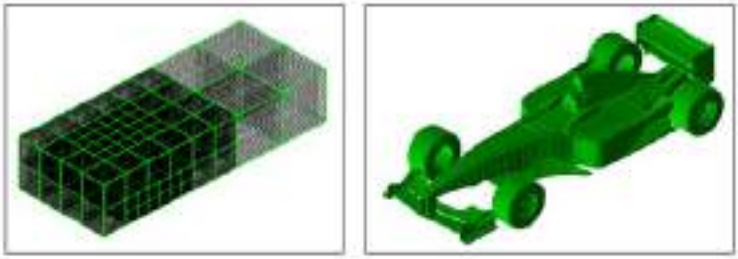

Fig. 4. Computational mesh around formula-1 car

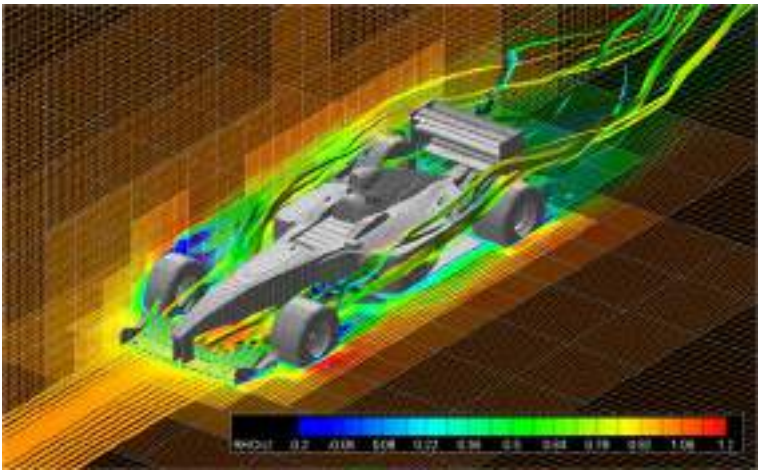

Fig. 5. Flow visualization around formula-1 car

4 Conclusions

Incompressible flow simulations by Building-Cube Method were performed around two kinds of objects. One was Ahmed body model, in which flow separation was overestimated. LES or any other turbulence model should be implemented for more accurate solution. Another one was formula-1 race car model as an example of complicated geometries.

Acknowledgement

Present computations were conducted on NEC SX-9 at Cyberscience center of Tohoku University. We gratefully acknowledge the help of all staff members of the center.

References

[1] Aftosmis, M.J.: Solution Adaptive Cartesian Grid Methods for Aerodynamic Flows with Complex Geometries, VKI Lecture Series, 1997-02 (1997)
[2] Ye, T., Mittal, R., Udaykumar, H., Shyy, W.: An accurate Cartesian grid method for viscous incompressible flows with complex immersed boundaries. JCP 156, 209–240 (1999)
[3] Hartmann, D., Meinke, M., Schröder, W.: An adaptive multilevel multigrid formulation for Cartesian hierarchical grid methods. Computer and fluids 37, 1103–1125 (2008)
[4] Nakahashi, K.: High-Density Mesh Flow Computations with Pre-/Post-Data Compressions, AIAA paper, 2005-4876 (2005)
[5] Ishida, T., Takahashi, S., Nakahashi, K.: Efficient and Robust Cartesian Mesh Generation for Building-Cube Method. Journal of Computational Science and Technology 2, 4 (2008)
[6] Kim, J., Moin, P.: Application of a Fractional-Step Method to Incompressible Navier-Stokes Equations. JCP 59, 308–323 (1985)
[7] Perot, J.B.: An Analysis of the Fractional Step Method. JCP 108, 51–58 (1993)
[8] Dukowicz, J.K., Dvinsky, A.: Approximate Factorization as a High Order Splitting for the Implicit Incompressible Flow Equations. JCP 102, 336–347 (1992)
[9] Kawamura, T., Kuwahara, K.: Computation of high Reynolds number flow around circular cylinder with surface roughness, AIAA paper, 84-0340 (1984)
[10] Takahashi, S., Ishida, T., Nakahashi, K.: Dynamic Load Balancing for Flow Simulation Using Adaptive Refinement, AIAA paper, 2008-920 (2008)
[11] Ahmed, S.R., Ramm, G., Faltin, G.: Some salient features of the time averaged ground vehicle wake. SAE paper no. 840300 (1984)
[12] Lienhart, H., Stoots, C., Becker, S.: Flow and turbulence structures in the wake of a simplified car model (Ahmed model). DGLR Fach Symp. der AGSTAB (2000)
[13] Hinterberger, C., García-Villalba, M., Rodi, W.: Large Eddy Simulation of flow around the Ahmed body, Trucks, Buses, Trains. Lecture Notes in Applied and Computational Mechanics / The Aerodynamics of Heavy Vehicles. Springer, Heidelberg (2004)
[14] Kamatsuchi, T.: Turbulent Flow Simulation around Complex Geometries with Cartesian Grid Method, AIAA paper, 2007-1459 (2007)

Part 26
Immersed Boundary Method/Cartesian Grid Method 2

“*This page left intentionally blank.*”

Assessment of Regularized Delta Functions and Feedback Forcing Schemes for an Immersed Boundary Method

Soo Jai Shin, Wei-Xi Huang, and Hyung Jin Sung

Dep. of Mech. Eng., KAIST, Daejeon 305-701, Korea
hjsung@kaist.ac.kr

We present an improved immersed boundary method for simulating incompressible viscous flow around an arbitrarily moving body on a fixed computational grid. To achieve a large CFL number and to transfer quantities between Eulerian and Lagrangian domains effectively, we combined the feedback forcing scheme of the virtual boundary method with Peskin's regularized delta function approach. Stability analysis of the proposed method was carried out for various types of regularized delta function. The stability regime of the 4-point regularized delta function was much wider than that of the 2-point delta function. An optimum regime of the feedback forcing is suggested on the basis of the analysis of stability limits and feedback forcing gains. The proposed method was implemented in a finite difference and fractional step context. The proposed method was tested on several flow problems and the findings were in excellent agreement with previous numerical and experimental results.

1 Introduction

An immersed boundary(IB) method using momentum forcing in the Navier-Stokes equations has received much attention because it can handle easily viscous flow over or inside complex geometries with Cartesian grids which generally do not coincide with the body surface. The IB method can be classified into two categories, depending on how momentum forcing is applied [1]. One is discrete forcing approach and the other is continuous forcing approach. Compare with discrete forcing approach, continuous forcing approach is easy to be expanded in three dimensional cases and straightforward in flows with moving boundaries due to its simple formation. Details about comparison of two approach can be found in Mittal et al. [1] Continuous forcing approach can be divided in two method : Peskins IB method and the virtual boundary method. Peskins IB method was first proposed by Peskin to simulate flows inside a moving heart. The basic idea is to determine a singular force distribution at arbitrary Lagrangian positions and to apply it to the flow equations in

the fixed reference frame via a regularized delta function. The careful design of Peskins delta function is vital to the efficiency of the method. Goldstein et al. [2] developed a virtual boundary method that employs a feedback forcing to enforce the no-slip condition at immersed boundaries embeded in the fluid domain. Saiki and Biringen [3] modified the virtual boundary formulation and proposed the so-called area-weighted virtual boundary method. Several papers using this method have reported that this method suffers from a very strict time-step restriction since the amplitude of the feedback forcing needs to be large for proper operation, resulting in a very stiff system. But Lee [4] relieves time restriction by investigating the stability characteristics of the virtual boundary method. He simulated turbulent flows with complex boundaries using an order-one CFL number. In the present study, we compare two methods which are thought almost same by most people and combine beneficial things of these methods for better performance. And we analyze stability of present method to relieve time restriction. The present method is applied to flow around several different moving problems.

2 Numerical Approach

In the present study, we present an immersed boundary method on the basis of Navier-Stokes solver adopting the fractional step method and a staggered Cartesian grid system. The fluid motion is defined on an Eulerian Cartesian grid and the fluid-solid interface is discretized using a Lagrangian grid fixed on the body. And the fluid-solid interface force is explicitly calculatied using a feedback law as shown Eq. (1)

$$\mathbf{F} = \alpha \int (\mathbf{U}(\mathbf{X_l}) - \mathbf{U_d}(\mathbf{X_l}))dt + \beta(\mathbf{U}(\mathbf{X_l}) - \mathbf{U_d}(\mathbf{X_l})) \tag{1}$$

The regularized delta function is employed to transfer quantities between Lagrangian and Eulerian locations in Eqs. (2) and (3), respectively,

$$\mathbf{U}(\mathbf{X_l}) = \sum \mathbf{u}(\mathbf{x})\delta_h(\mathbf{x} - \mathbf{X_l})h^3 \tag{2}$$

$$\mathbf{f}(\mathbf{x}) = \sum_{l=1}^{N_L} \mathbf{F}(\mathbf{X_l})\delta_h(\mathbf{x} - \mathbf{X_l})\Delta V_l \tag{3}$$

In the present study, four types of regularized delta functions are chosen as shown in Fig.1

$$\delta_h(\mathbf{x}) = \frac{1}{h^3}\,\phi(\frac{x_1}{h})\phi(\frac{x_2}{h})\phi(\frac{x_3}{h}) \tag{4}$$

Note that all four types of delta function have the property

$$\sum \delta_h(\mathbf{x} - \mathbf{X})h^3 = 1 \tag{5}$$

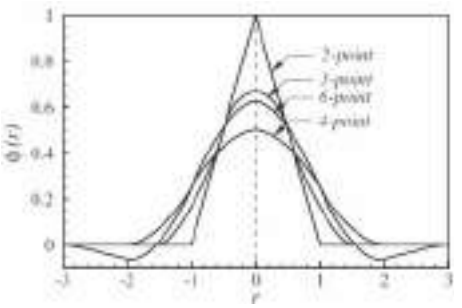

Fig. 1. Four types of regularized delta function

which is the discrete analogue of the basic property of the Dirac delta function. In Fig.1, the value of $\phi(r)$ is maximum at $r = 0$ for all functions and the value of $\phi(0)$ decreases as the points of the delta function increase, except for the 6-point delta function. These properties are kernels of the stability analysis.

3 Stability Analysis

Stability analysis of the proposed method was carried out for various types of regularized delta function. Figure 2 shows the stability regimes of different types of delta functions for the case in which the Lagrangian domain is a line immersed in a 2-D flow. The flow is stable in the region below the line, and unstable above the line. The stability regimes are wider for the smaller

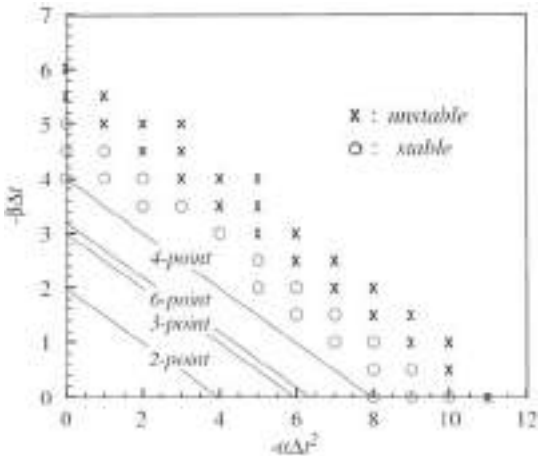

Fig. 2. Stability regimes in two-dimensional flow for several types of delta function

value of $\phi(0)$ in the regularized delta functions. Compared with the 2-point regularized delta function, the stability region of the 4-point regularized delta function is twice as wide in each direction($-\alpha\Delta t^2$, $-\beta\Delta t$). To validate the numerical analysis, simulations of a moving cylinder in a 2-D flow using the 4-point regularized delta function were carried out for different $-\alpha\Delta t^2$ and $-\beta\Delta t$. Stable and unstable cases are denoted by circles and crosses, respectively, in Fig. 2. The analytical solution is in good agreement with the numerical results obtained using the present IB method.

4 Results and Discussion

4.1 Stationary Cylinder in a Free-Stream at Re=100

We used a computational domain of $0 \leq x, y \leq 8$ and a cylinder with diameter d=0.30 whose center is located at (1.85,4.0). A Dirichlet boundary condition($u/u_\infty = 1, v = 0$) was used at the inflow and far-field boundaries, and a convective boundary condition was used at the outflow boundary. Table 1 shows the drag and lift coefficients, C_D and C_L, obtained using the proposed method, as well as the Strouhal number defined from the oscillation frequency of the lift force. The drag and lift forces were obtained by integrating all the momentum forcing applied on the boundary. Parameters such as the mesh width h, time step Δt, and feedback forcing gain α were selected to match the conditions of Lai and Peskin [5] and a 4-point regularized delta function was employed [5]. To compare the present method with Peskins IB method, we used feedback forcing gains of $\alpha = -4.8 \times 10^4$ and $\beta = 0$. Table 1 indicates that the value of $\alpha = -4.8 \times 10^4$ used in the present method is large enough to obtain reliable results. By contrast, the results of Lai and Peskin [5] using $\kappa = 4.8 \times 10^4$ deviate somewhat from the other results, especially those obtained in the same study using $\kappa = 9.6 \times 10^4$. These findings are consistent with previous reports showing that compared with the value of $-\alpha$ in the virtual boundary method, a larger value of the stiffness coefficient κ in Peskins IB method is required to ensure accurate results for a rigid boundary problem [1]. Since we tested the stability region of feedback forcing gains (α,β) with the 4-point regularized delta function (see Fig. 2), we used a computational time step of 1.2×10^2($-\alpha\Delta t^2$=6.912) to be consistent with $-\alpha\Delta t^2 \leq 8$. As a consequence, the present results are in good agreement with those of Lai and Peskin [5], even though the computational time step of the present method ($\Delta t = 1.2 \times 10^{-2}$) is about an order of magnitude larger than that of Lai and Peskin ($\Delta t = 9.6 \times 10^{-4}$). The maximum Courant-Friedrichs-Lewy (CFL) number in the present simulations exceeded 1 due to the adoption of the feedback forcing scheme and the optimization of parameters by stability analysis.

Table 1. Comparison of drag coefficient, lift coefficient, and Strouhal number with those obtained in previous studies

	h	κ or $-\alpha$	Δt	C_D	C_L	St	CFL
Case 1	$\frac{1}{64}$	4.8×10^4	1.2×10^{-2}	1.44	0.35	0.168	1.35
Case 2	$\frac{1}{64}$	4.8×10^4	6.0×10^{-3}	1.44	0.35	0.168	0.7
Case 3	$\frac{1}{64}$	4.8×10^4	6.0×10^{-3}	1.37	0.34	0.163	0.7
Lai and Peskin [5]	$\frac{1}{128}$	4.8×10^4	1.8×10^{-3}	1.52	0.29	0.155	-
Lai and Peskin [5]	$\frac{1}{128}$	9.6×10^4	9.0×10^{-4}	1.45	0.33	0.165	-

4.2 Transverse Oscillation of a Circular Cylinder

The proposed method was applied to a periodic transverse oscillation of a circular cylinder in a free-stream. The behavior of the l_2-norm error (a measure of the no-slip condition along the IB) of the streamwise virtual surface velocity is shown in Fig.3 for three different forcing gains with the 3-point regularized delta function. The error converges to a smaller value for larger $-\alpha\Delta t^2$, as observed for the stationary problem, and the error decays rapidly for larger $-\beta\Delta t$. Since the initial decays of the error are important in compensation of the boundary condition in moving boundary problems, the error also converges to a smaller value for larger $-\beta\Delta t$. Accordingly, $-\alpha\Delta t^2$ and $-\beta\Delta t$ should be as large as possible to decrease the error

The time history of the drag coefficient is illustrated in Fig. 4 for four types of delta function with the same forcing gains. As the number of points in the regularized delta function increases, the non-growing oscillations decrease. This suggests that the 4-point regularized delta function with large forcing gains yield better results.

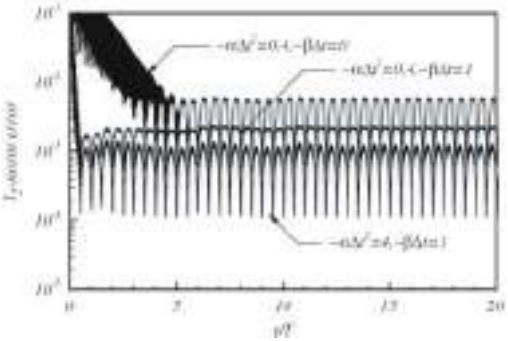

Fig. 3. l_2-norm error of the virtual surface velocity in the streamwise direction normalized by the free-stream velocity u_∞ for three different forcing gains

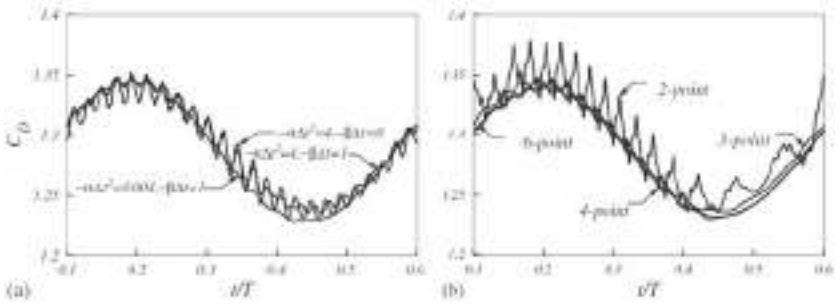

Fig. 4. Time history of the drag coefficient for different types of delta function with $-\alpha\Delta t^2$=0.4 and $-\beta\Delta t$=1

5 Conclusions

We analyzed the stability regimes of the feedback forcing gains in the proposed method for several types of delta function. The stability region of the 4-point regularized delta function was much wider than that of the 2-point delta function. The effects of regularized delta functions and feedback forcing gains (α, β) were also investigated. For the regularized delta function supported by more points, its non-growing oscillations became smaller. On the other hand, the l_2-norm error converged to a smaller value for larger $-\alpha\Delta t^2$ and decayed faster for larger $-\beta\Delta t$. In the stationary boundary problem, $-\beta\Delta t$ influenced only the initial behavior of the error, whereas in the moving boundary problem the error also converged to a smaller value for larger $-\beta\Delta t$. On the basis of the stability analysis of the present method, we can recommend an optimum region of the feedback forcing gains that enables the use of a large CFL number and decreases the l_2-norm error and non-growing oscillations

References

1. Mittal, R., Iaccarino, G.: Immersed boundary methods. Annual Review of Fluid Mechanics 37, 239–261 (2005)
2. Goldstein, D., Handler, R., Sirovich, L.: Modeling a no-slip flow boundary with an external force field. J. Comput. Phys. 105, 354–366 (1993)
3. Saiki, E.M., Biringen, S.: Spatial simulation of a cylinder in uniform flow: application of a virtual boundary method. J. Comput. Phys. 123, 450–465 (1996)
4. Lee, C.: Stability characteristics of the virtual boundary method in three-dimensional applications. J. Comput. Phys. 184, 559–591 (2003)
5. Lai, M.-C., Peskin, C.S.: An immersed boundary method with formal second-order accuracy and reduced numerical viscosity. J. Comput. Phys. 160, 705–719 (2000)

Simulation of a Flow around a Car, Using Cartesian Coordinates

Akiko Mano[1] and Kunio Kuwahara[2]

[1] Institute of Computational Fluid Dynamics, 1-16-5 Haramachi, Meguro-ku, Tokyo 152-0011, Japan
mano@icfd.co.jp
[2] Institute of Computational Fluid Dynamics, 1-16-5 Haramachi, Meguro-ku, Tokyo 152-0011, Japan
kunio_kuwahara@icfd.co.jp

This paper introduces a computational technique to compensate for the added numerical diffusion that is generated when uniform Cartesian coordinates are used to describe the flow around bluff bodies. Because of the staircase-like representation of the surface object, it was found that the added surface "roughness" causes larger than expected separation region for some test cases. In order to control the velocity profile in the boundary layer, a *blvr* (boundary layer velocity ratio) is defined, and it is used to set the negative value of the viscosity along the surface. Numerical solutions of the governing Navier-Stokes equations are carried out in a uniform Cartesian coordinates using a multi-directional finite difference scheme with a third-order upwinding. No explicit turbulence model is incorporated into the model.One example, a flow around a car, using this technique is presented. We get numerical value of coefficient of drag, 0.234. This agrees with experimental value, 0.245 very well.

1 Introduction

Many simulations of a flow past streamlined body have been carried out, mostly using a finite-difference method in a body-fitted coordinate system [KK04]. Simulations of bluff bodies are less frequent because of difficulties in solver implementation and grid generation. It is often acknowledged, that grid generation is one of the most difficult and manpower consuming parts when dealing with body-fitted coordinates. On the other hand, many important applications involve flow around a bluff body, i.e. flow around a car. The simplest way to avoid all these complications would be to employ a Cartesian coordinate system in which the body is represented by creating a masking data (voxel) on the grid coordinates.[BKK03] However, this approach results in lack of resolution near the boundary of the object. If the object is visualized, it looks like a staircase structure. By using multi-directional finite differences,[Kuw99], [KK02] a smoother representation of the staircase

boundary is achieved, but the resolution problem is not completely solved. In problems involving separation depending on the resolution of the boundary layer, simulations predict larger than expected areas of separation. This is due to the numerical diffusion caused by the roughness on the boundary. To resolve the behavior of the flow along the staircase boundary, we introduce a negative viscosity[KKB06] on the surface of the body to compensate for the numerical diffusion. In the present paper, one example, a flow around a car, using this technique is presented.

2 Computational Method

The governing equations are the incompressible Navier-Stokes equations. In Cartesian coordinates system, they can be written as it follows,

$$\frac{\partial u_1}{\partial x_1} + \frac{\partial u_2}{\partial x_2} + \frac{\partial u_3}{\partial x_3} = 0 \tag{1}$$

$$\frac{\partial u_i}{\partial t} + u_j \frac{\partial u_i}{\partial x_j} = -\frac{\partial p}{\partial x_i} + \frac{\partial}{\partial x_j} \left\{ \frac{1}{Re} \left(\frac{\partial u_i}{\partial x_j} + \frac{\partial u_j}{\partial x_i} \right) \right\} \tag{2}$$

For high-Reynolds number flow, time-dependent computations are required owing to the strong unsteadiness. Presently, a finite-difference method is employed to discretize the basic equations and they are solved using the projection method (Chorin[Cho68], and Takami and Kuwahara[TK74]). The pressure field is obtained by solving the following Poisson's equation:

$$\triangle p = -div(\mathbf{u} \cdot grad\mathbf{u}) + \frac{D^n}{\delta t}, \quad D = div\mathbf{u} \tag{3}$$

where n is the time step and δt is the time increment. D^{n+1} is assumed to be zero, but D^n is retained as a corrective term.

In the present paper, a multi-directional finite difference method is implemented when discretizing the governing equations. In case of 2-dimensional computations, when structured grid points are given, the black points in Fig. 1(a) are usually used to approximate the derivatives at the central point (system A). If we introduce another 45° rotated local grid system, the white points in Fig. 1(b), can be used to approximate the derivative at the central point (system B). In order to improve the derivative value at the central point, the values of both systems are combined. If a ratio A: B=2:1 is adopted, the resulting finite difference scheme for the Laplacian coincides with the well-known 9 point formula with fourth-order accuracy. This method improves the rotational invariance of the coordinate system, and then those cases where flow direction is not parallel to the grid location are better simulated. In 3 dimensions, three different grid systems are used. Each grid system is obtained by rotating a perpendicular plane 45° with respect to each coordinate axis. One of such systems is shown in Fig. 1(c).

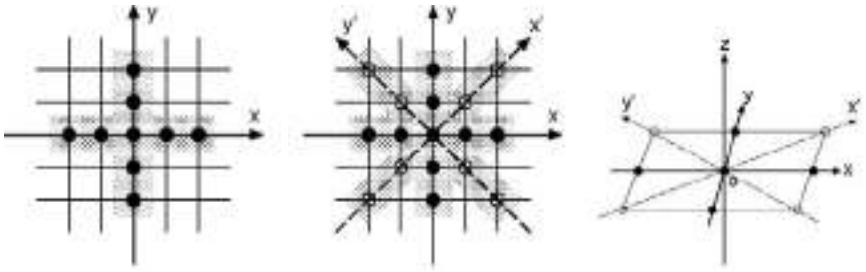

(a) System A. (b) System B. (c) System Z:x'-y'-z.

Fig. 1. System for multi-directional scheme

Space derivatives are discretized using a three-point central difference approximation with exception of the convective terms. For the convective terms, a third-order upwind scheme is used to stabilize the computation (Kawamura[KK84]). It has been found to be the most suitable for high-Reynolds number flow computations. The second-order Crank-Nicolson implicit scheme is used for time integration. The equations are iteratively solved at each time step by SOR method. A multi-grid method is utilized to solve the Poisson's equation.

Negative viscosity

In the Cartesian coordinate system, the body is represented as a set of voxels at the grid points with their values set on/off (a binary operator) to indicate its presence. As stated before, the surface of the body resembles a staircase. After computations are carried out, larger than expected regions of separations are observed. This is due to the numerical diffusion caused by the surface roughness. Therefore, a special treatment of the boundary conditions is needed in order to properly simulate these types of flows. The present technique introduces a negative value of the viscosity on the surface of the body to compensate for the numerical diffusion. At high-Reynolds number, turbulence in the free space is simulated without using an explicit turbulence model in these computations. Viscous effects are limited only within the boundary

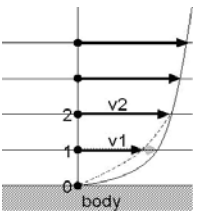

Fig. 2. Boundary layer velocity ratio ($blvr$). $blvr = v1/v2$

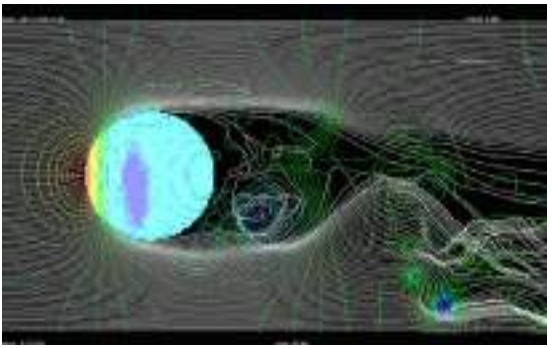

(a) *blvr* =0.60 (larger separation areas).

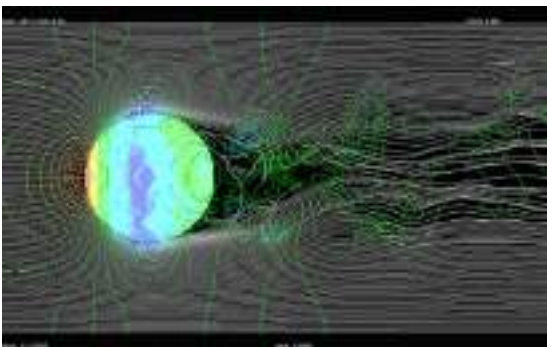

(b) *blvr* =0.70 (Separation is reduced).

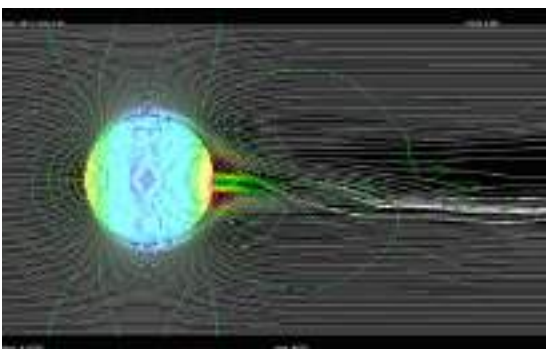

(c) *blvr* =0.75 (Separation is reduced much ferther.).

Fig. 3. Flow around a sphere in each *blvr*; pressure field and stream lines

layer. Therefore, a simple model is made for the boundary layer to account for the viscous effect.

It is important to point out that this negative viscosity has no definitive physical meaning, and how to determine its value represent a big challenge.

If the absolute value is large enough, the flow near the boundary accelerates and separation is reduced. On the other hand, if the absolute value is small, the separation region becomes larger. Therefore, research in a proper way to determine this value is been undertaken. The velocity profile in the boundary layer is closely related to the negative viscosity. The present paper defines a *blvr* (boundary layer velocity ratio) that it is used to determine the proper value of the negative viscosity (See Figure 2). The *blvr* is the ratio of the averaged velocity between the two points nearest to the surface ($blvr = v1/v2$). If *blvr* is 0.5, the local flow Reynolds number is 0.0. On the other hand, if it is 1.0, a free-slip condition is imposed $blvr = v1/v2$ on the surface. Therefore, the value of the *blvr* should Figure 2. Boundary layer velocity fall between 0.5‘1.0. Presently, the value of the negative viscosity ratio (*blvr*) is a function of this parameter.

Examples of 3-dimensional simulation of flow around a sphere with using the negative viscosity are visualized. Figure 3 explains the effect of the negative viscosity, and *blvr* in Fig. 3 (a)‘(c) are 0.60, 0.70 and 0.75 respectively.

3 Computational Results

Figure 4 shows computational grid and a body represented by a set of voxels for simulation of a flow around a streamlined car in uniform stream. (The body used the shape data of the low resistance body having been distributed by Society of Automotive Engineers of Japan, Inc. for the bench mark[Soc08].) In order to properly simulate these types of flows, the computation started to

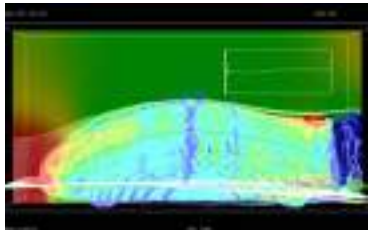

Fig. 4. Flow around a car; pressure field and stream lines in Stage 4 (See table 1)

Table 1. In the computations around a car, Calculation area, calculation lattice intervals and *blvr* in each stage

Stage	Calculation area[m]	Calculation lattice interval[mm]	*blvr*
1	8×4×2	30	0.8
2	4×2×1	16	0.75
3	2×1×0.5	8	0.725
4	1s×0.5×0.5	4	0.725

carry out with a large area and coarse grid, and shifted to a narrowness region, fine grid gradually. The *blvr* ratchet down (See Table 1). In coarse grid, the separation region is larger than in fine grid. So we have to start large *blvr*. The *blvr* in Fig. 4 is 0.725. We get numerical value of coefficient of drag, 0.234. That's good agreement with experimental value, 0.245.

4 Conclusion

Three dimensional flows around bluff bodies were simulated in Cartesian coordinate system. In this system, the separation was effectively reduced by using the negative viscosity. We get numerical value of coefficient of drag, which agrees with experimental value, very well. In the future, we plans to research in a proper way to determine the negative viscosity automatically. And we want to finish to run a simulation of D'Alembert's paradox.

References

[KK04] Komurasaki, S., Kuwahara, K.: Implicit Large Eddy Simulation of a Subsonic Flow around NACA0012 Airfoil. AIAA Paper.2004-0594 (2004)

[BKK03] Bethancourt, A., Kuwahara, K., Komurasaki, S.: Grid Generation and Unsteady Flow Simulation around Bluff Bodies. AIAA Paper.2003-1129 (2003)

[Kuw99] Kuwahara, K.: Unsteady Flow Simulation and Its Visualization. AIAA Paper.99-3405 (1999)

[KK02] Kuwahara, K., Komurasaki, S.: Simulation of High Reynolds Number Flows Using Multidirectional Upwind Scheme. AIAA Paper. 2002-0133 (2002)

[KKB06] Kuwahara, K., Komurasaki, S., Bethancourt, A.: Simulation of a Flow around a Bluff Body Using Cartesian Coordinates. JAXA Special Publication. 25-28 (2006)

[Cho68] Chorin, A.J.: Simulation of High Reynolds Number Flows Using Multidirectional Upwind Scheme. Math. Comp. 22. pp. 745 (1968)

[TK74] Takami, H., Kuwahara, K.: Numerical Study of Three-Dimensional Flow within a Cubic Cavity. J. Phys. Soc. Japan. 37.6 (1974)

[KK84] Kawamura, T., Kuwahara, K.: Computation of high Reynolds number flow around a circular cylinder with surface roughness. AIAA Paper. 84-0340 (1984)

[Soc08] Society of Automotive Engineers of Japan, Inc. Technical Report Series No.42 (2008)

Numerical Simulation of Parachute Inflation Process

Masaya Miyoshi, Koichi Mori, and Yoshiaki Nakamura

Department of Aerospace Engineering, Nagoya University, Nagoya, Japan
miyoshi@fluid.nuae.nagoya-u.ac.jp

Abstract. In the present study the parachute deformation and motion in the process of inflation are simulated by implementing the immersed boundary technique in fluid-structure coupling solver, where velocity vector is given in a virtual cell as boundary condition. The main focus is on examining the process of canopy inflation; first the canopy is inflated in the normal direction to the uniform flow (in the lateral direction), and then its apex is pulled by a vortex ring generated by the canopy's outer surface due to its negative pressure. After finishing the inflation process, the canopy moves in the tangential direction to the spherical surface, the center of which is located at the payload location. This motion is caused by the breakup of an initial axisymmetric vortex, followed by vortices generated from the shear layer. The predicted maximum parachute opening force is twice as large as the payload force in the steady state, which is in good agreement with experiment.

1 Introduction

Parachutes are usually used to decelerate high speed flying objects. It has many attractive advantages such as compact size and light weight. However, the dynamic behavior of a parachute system shows complicated phenomena such as the deformation of parachute shape, the non-axisymmetric flow field, and the interaction between the parachute structure and the surrounding flow. The phenomenon in inflation process is complicated, because a large deformation of the parachute occurs. In addition, the maximum parachute opening force[1] and the onset of parachute canopy instability are seen in this process. The peak of parachute opening force is important from the canopy and payload structural requirement[2].

Several methods to analyze parachute dynamics have been developed so far, where the parachute opening phase is modeled by the fluid-structure coupling method. However, in computational simulation the problem is simplified by using rigid or axisymmetric parachute models. Johari et al.[3] analyzed the flow field around a rigid parachute in an impulsively started flow and showed the non-axisymmetric flow field behind the canopy induces side

force. Dreprov et al.[4] and Benney et al.[5]simulated the parachute opening process by using simplified, axisymmetric models. However, problem of these simulations neglect the interactions between the non-axisymmetric flow field and canopy flexible structure.

In the present study, the inflation of a flexible parachute canopy is computed by using a 3D Navier-Stokes solver along with a nonlinear mass-spring-damper model. The results are compared with the experimental data by the low speed wind-tunnel.

2 Numerical Method and Conditions

The low subsonic flow around a parachute is computed using the pseudo-compressibility method. The governing equations are composed of the continuity equation and the Navier-Stokes equations. These equations are written as

$$\frac{\partial p}{\partial t} + \beta \nabla \cdot \mathbf{u} = 0 \tag{1}$$

$$\frac{\partial \mathbf{u}}{\partial t} + (\mathbf{u} \cdot \nabla)\,\mathbf{u} = -\frac{1}{\rho}\nabla p + \nu \nabla^2 \mathbf{u} \tag{2}$$

where β is the artificial compressibility parameter. These equations are solved in time using an implicit time integration scheme, LU-SGS, where subiteration is performed. The CFD solver incorporated in the present solver has been validated by Hashimoto et al[6].

In order to deal with the moving boundary, the immersed boundary method is employed on a Cartesian grid. The boundary condition at the canopy's surface is calculated by the method proposed by Ochi[7]. In the case of solid boundary, this method can approximately provide velocity vector in a virtual cell, which is used to calculate inviscid terms. The virtual cell is a cell containing a control point. This method has been modified so as to treat the moving boundary. The velocity vector in the virtual cell is written as

$$\mathbf{V}_j = \mathbf{V}_i - 2\,(\mathbf{V}_i \cdot \mathbf{n}_j)\,\mathbf{n}_j + \mathbf{V}_w \tag{3}$$

where $\mathbf{V}_j$ is the velocity vector in the virtual cell j, $\mathbf{V}_i$ is the velocity vector in the real cell i adjoining the virtual cell, $\mathbf{n}_j$ is a unit normal vector to the canopy surface, and $\mathbf{V}_w$ is the canopy velocity vector.

The structure dynamics of the parachute is solved by a mass-spring-damper (MSD) model[5]. The parachute is modeled as an aggregate of control points connected by springs and dampers. The spring force acts only when the distance between two control points is greater than the constructed distance, since the canopy fabric cannot support compressive forces. The force of gravity and the fluid force supplied by the pressure difference across the surface act to each control point. The equations to calculate the parachute model are solved in time using the explicit second-order Runge-Kutta method.

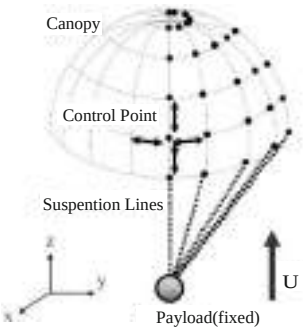

Fig. 1. Parashute model

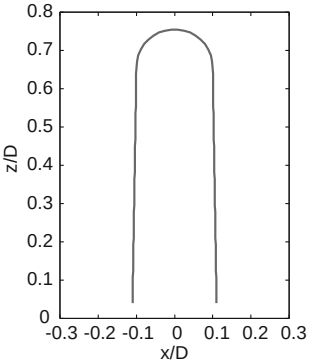

Fig. 2. Initial canopy shape in the $y/D = 0$ cross section

In order to solve the fluid and structure equations simultaneously, the weak coupling method is employed. The data of structure displacement as well as the velocity and pressure on the surface are transferred between the flow and structure solvers.

The present computational model is connected by suspension lines to a payload and inflated by the freestream. The payload with no mass and no volume is fixed in the wind tunnel. The initial canopy shape is modeled as a folded canopy just after deployment, as shown in Fig.2. The fully-opened canopy shape is a hemisphere with a diameter of $0.15m$($D = 0.15$). The actual folded canopy has wrinkles near its edges, but they are neglected in this simulation; the canopy surface is assumed to be smooth and represented by 8464 control points.

The freestream velocity is $U = 20.0m/s$, and the force of gravity acts in the negative z direction. The Reynolds number is $Re = 2 \times 10^5$, which is based on the fully-opened canopy diameter D and the freestream velocity U. This simulation treats the case where the canopy suddenly appears in the uniform flow and starts to be deformed.

3 Results

Time variations of the canopy inflation are shown in Fig. 3, where the color represents the magnitude of pressure differences across the canopy surface, where the dark color corresponds to high pressure. The canopy keeps opening from $t = 0.000sec$ through $t = 0.0619sec$ by the pressure differences that increase with time. After the canopy diameter reaches its maximum, D, (Fig. 3(e)), it decreases due to the inner tension of the canopy(Fig.3(f)). Eventually, it converges to D, where there is an equilibrium state between the tensions and pressure differences. The canopy top continues to move in the negative z direction after $t = 0.0619sec$. Then, it moves back and the

Fig. 3. Time-variation of canopy shape

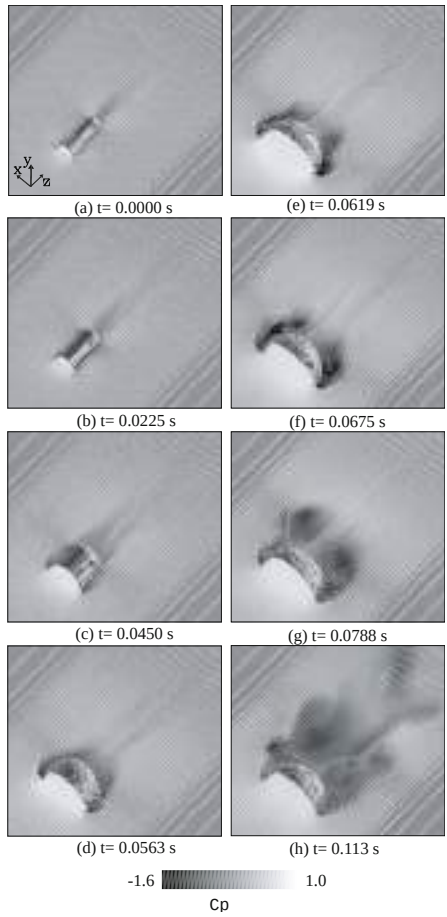

Fig. 4. Velocity vectors and pressure distribution in the x-z plane

canopy takes its regular shape (a hemisphere). In addition, the canopy moves in the tangential direction to the spherical surface with its center at the payload location.

Time variations of the velocity vectors and pressure distributions in the x-z plane are shown in Fig. 4. From $t = 0.000sec$ through $t = 0.0563sec$, the bigger the canopy diameter, the smaller the pressure on the outer side of the canopy is; i.e., the pressure difference between the inner and outer canopy increases, which accelerates increase in the diameter. After the canopy diameter reaches it maximum, D, an axisymmetric vortex ring is generated in the near wake of the canopy and its the negative pressure pulls the apex of the canopy. At $t = 0.0788sec$ the vortex ring breaks up and a non-axisymmetric

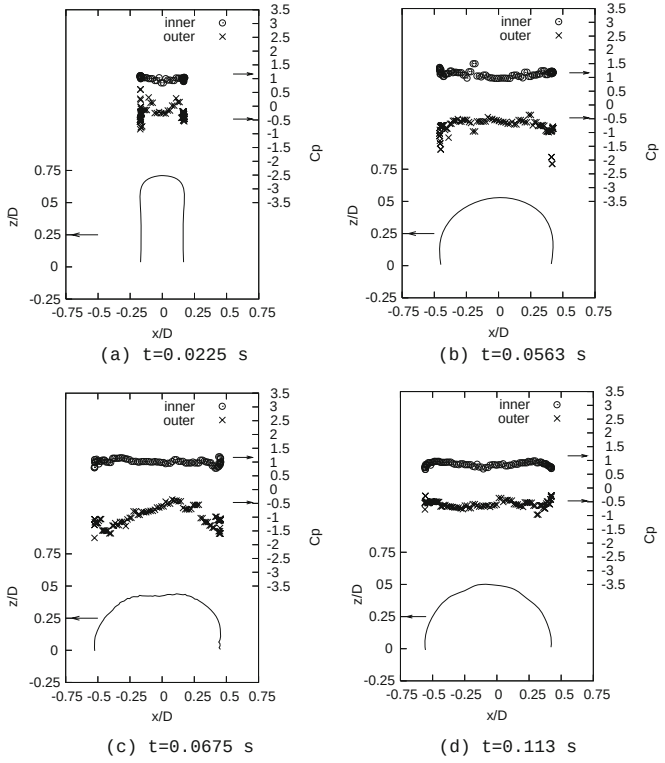

Fig. 5. Pressure distributions

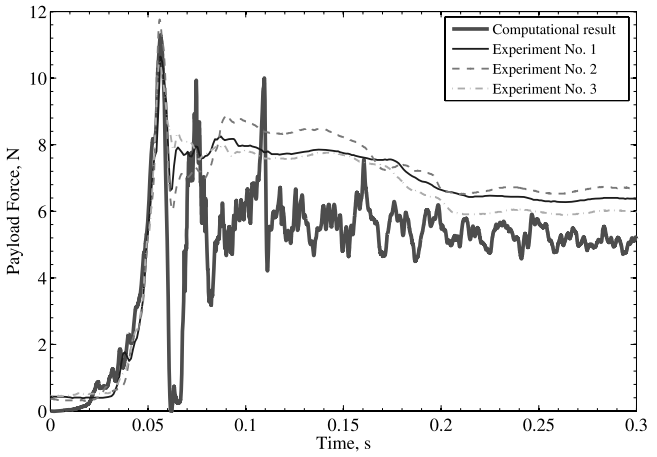

Fig. 6. Time history of payload force

wake is generated, which causes the side force to act on the canopy. As a result the canopy is forced to move in the tangential direction to the spherical surface, the center of which is located at the payload location.

The history of the payload force, which is estimated to act on the payload from the tensions of the suspension lines, is shown in Fig. 6. The experimental data is also shown for comparison. These experiments are examined in the low speed wind-tunnel at Nagoya University. The flow condition and the fully-opened parachute shape are the same as those of the computational parachute model, but only the direction of the gravity is different in that the gravity doesn't act in negative z direction in Fig. 1. Fig. 6. represents that the computational result and shows qualitative agreement with experimental data. The maximum opening force is twice as large as the payload force in the steady state which appears at $t = 0.0565sec$ (during the canopy opening). And it is in good agreement with the measured force in experiments. It appears ($t = 0.0560sec$) slightly before the diameter reaches its maximum ($t = 0.0619sec$).

4 Conclusions

The deformation and motion of three-dimensional parachute model during the inflation process is simulated by using Cartesian grid with the immersed boundary method. The canopy was first inflated in the normal direction to the uniform flow and then its apex was pulled by a vortex ring produced above the canopy. At steady state, the canopy comes to take its regular shape (a hemisphere). After that the canopy started to tilt and the breakup of a vortex ring near the wake of the canopy take place. The maximum predicated parachute opening force, which governs canopy and payload structural requirement, is in good agreement with experimental data.

References

1. Heinrich, H.G., Noreen, R.A.: J. of Aircraft 7(4) (1970)
2. Lee, C.K.: J. of Aircraft 26(5) (1989)
3. Johari, H., Stein, K., Tezduyar, T.: J. of Aircraft 38(6) (2001)
4. Dneprov, I.V.: AIAA Paper 93-1237
5. Benney, R.J., Stein, K.R.: J. of Aircraft 33(4) (1996)
6. Hashimoto, A., Furuta, Y., Yagi, N., Nakamura, Y.: AIAA paper 2006-3215 (2006)
7. Ochi, A., Nakamura, Y.: The Japan Society of Fluid Mechanics. In: 19th CFD symposium (2005) (in Japanese)

A Finite-Volume Method for Convection Problems with Embedded Moving-Boundaries

Yunus Hassen[1,2] and Barry Koren[1,2]

[1] Centrum Wiskunde & Informatica, Amsterdam, the Netherlands
[2] Faculty of Aerospace Engineering, TU Delft, Delft, the Netherlands
yunus.hassen@cwi.nl, barry.koren@cwi.nl

Summary. An accurate method, using a novel immersed-boundary approach, is presented for numerically solving linear, scalar convection problems. Moving interior boundary conditions are embedded in the fixed-grid fluxes in the direct neighborhood of the moving boundaries. Tailor-made limiters are derived such that the resulting scheme is monotone. The results obtained are very accurate, without requiring much computational overhead. It is anticipated that the method can readily be extended to real fluid-flow equations.

Keywords: Immersed-boundary method; Hyperbolic conservation laws; High-order schemes; Monotonicity; Flux limiters.

1 Introduction

The immersed-boundary method, in general, is a method in which boundary conditions are indirectly incorporated into the governing equations. It has first been introduced by Peskin [4], and currently many varieties of it exist.

Immersed-boundary methods are very suitable for simulating flows around flexible, moving and/or complex bodies. Basically, the bodies of interest are just embedded in non-deforming Cartesian grids that do not conform to the shape of the body. The governing equations are modified to include the effect of the embedded boundaries. Doing so, mesh (re)generation difficulties associated with body-fitted grids, are obviated; and, the underlying regular fixed grid allows to use a simple data structure as well as simpler numerical schemes over a majority of the domain.

Our approach uses a cell-centered finite-volume discretization. The governing partial differential equations are discretized using a standard finite-volume method (FVM) away from the embedded body (EB). Near the EB, a special FVM is derived which takes the prescribed interior boundary conditions into account.

The article begins with the problem description and with some standard finite-volume results. The following sections detail: the special fluxes that take

the effects of the embedded boundaries into account, monotonicity domains, the temporal discretization and time adaptivity. Finally, some numerical results, based on the present approach, and concluding remarks are given.

2 Model Equation

Consider the scalar, linear convection equation:

$$c_t + f_x = 0, \quad f = f(c) := uc, \tag{1}$$

where $c(x,t)$ is the scalar field, u the flow velocity, which is assumed to be constant and positive, and $f(c)$ the flux function. The independent variables x and t represent space and time, respectively. We take $x \in [0,1]$.

Eq. (1) is hyperbolic. The initial solution $c(x,0) = c_0(x)$ simply propagates unchanged with the velocity u: $c(x,t) = c_0(x-ut)$. We consider two initial solutions, each with two interior, moving EBs. The solution at the left and right of each EB is prescribed. The two moving embedded-boundaries have arbitrary initial locations (x_1 and x_2, $x_1 \neq x_2$). The initial solutions read:

$$c_0(x) = \begin{cases} 0, & \text{if } x_1 \le x \le x_2, \\ 1, & \text{elsewhere;} \end{cases} \quad \text{and} \quad c_0(x) = \begin{cases} 0, & \text{if } x_1 \le x \le x_2, \\ \frac{1}{2}(1-\cos(2\pi x)), & \text{elsewhere.} \end{cases} \tag{2}$$

The cosine function in (2) exploits the advantage that higher-order accurate numerical schemes have in non-constant, smooth solution regions. Model equation (1) is approximated in a periodic domain, allowing us to time-step for as long as we want for a finite spatial domain.

2.1 Standard FVM Results

The unit domain is divided into N non-overlapping cells of uniform size. Let $h = 1/N$ be the cell width, $x_i = (i-1/2)h$ the cell-center coordinates and $x_{i+\frac{1}{2}} = ih$ the cell-face coordinates for $i = 1, 2, ..., N$. Let the discrete solution in cell i, at time level n, be denoted as $c_i^n = c(x_i, t^n)$. Then the semi-discrete finite-volume form of (1) reads:

$$h\frac{\mathrm{d}c_i}{\mathrm{d}t} + (f^n_{i+\frac{1}{2}} - f^n_{i-\frac{1}{2}}) = 0. \tag{3}$$

Eq. (3) is solved by approximating the fluxes at the cell faces and by time-stepping the temporal part. These fluxes, at time level n, are computed (dropping the index n, for convenience) as $f_{i+\frac{1}{2}} = uc_{i+\frac{1}{2}}$, where $c_{i+\frac{1}{2}}$ is the cell-face state at $i+1/2$, which can be approximated in a variety of ways. For example, for $u > 0$, $c_{i+\frac{1}{2}} = c_i$ and $c_{i+\frac{1}{2}} = c_i + \frac{1+\kappa}{4}(c_{i+1} - c_i) + \frac{1-\kappa}{4}(c_i - c_{i-1})$ are two classical cell-face states, computed with the first-order upwind- and van Leer's κ-scheme [6], respectively. Note that, with no EB in the neighborhood, $\kappa \in [-1, 1]$.

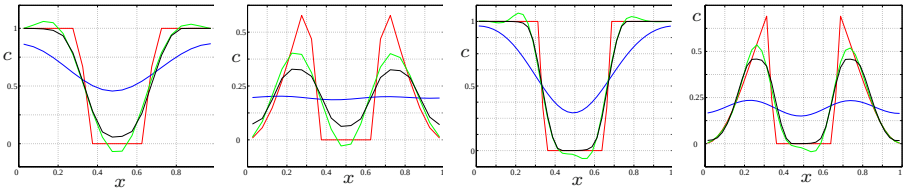

(a) On a 20-cell grid (b) On a 40-cell grid

Fig. 1. Standard finite-volume solutions after one full-period. Red: exact discrete, blue: first-order upwind, green: unlimited $\kappa = \frac{1}{3}$, and black: limited $\kappa = \frac{1}{3}$ schemes.

The κ-schemes yield non-monotone discretizations. Several algorithms have been proposed in the literature that yield higher-order accurate, monotone solutions. Most of these algorithms exploit the inherent monotonicity of the first-order upwind scheme. The best known representatives of these algorithms are the limited schemes following Sweby's total-variation diminishing (TVD) theory [5].

$c_{i+\frac{1}{2}}$ can be written in the limited form as $c_{i+\frac{1}{2}} = c_i + \frac{1}{2}\phi(r_{i+\frac{1}{2}})(c_i - c_{i-1})$, where $\phi(r)$ is the limiter function and $r_{i+\frac{1}{2}} = \frac{c_{i+1}-c_i}{c_i-c_{i-1}}$ its monotonicity argument. Here we specifically adopt the limiter proposed by Koren [3] as the standard limiter. It gives a monotone third-order accurate net flux in a cell, by resembling the $\kappa = \frac{1}{3}$-scheme.

Now, for later comparison purposes, we will show what the solutions are when using the standard finite-volume discretizations described above, methods in which no embedded-boundary conditions are imposed. For the time integration, the three-stage Runge-Kutta scheme RK3b from [2] is employed. For both initial solutions (2), we consider the locations of the EBs to be at $x_1 = \frac{1}{3}$ and $x_2 = \frac{2}{3}$. Furthermore, we take $u = 1$, and we compute the solution at $t = 1$, the time at which the solution has made a single full-period. For both the first-order upwind and the $\kappa = \frac{1}{3}$ (unlimited and limited) schemes, the computations are performed on a grid with 20 and 40 cells. The solutions are depicted in Fig. 1. The time steps have been taken sufficiently small to ensure that in all cases the temporal discretization errors are negligible with respect to the spatial discretization errors.

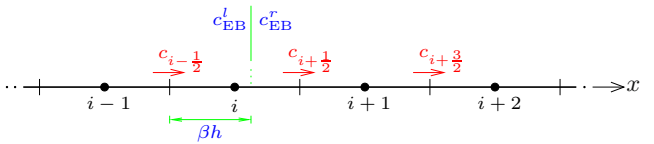

Fig. 2. EB situated in cell i at time t, its associated solution values, and the affected cell-face states

3 Fluxes with Embedded Moving-Boundary Conditions

The sharp discontinuities of the initial solutions (2) are considered as infinitely thin bodies going with the flow and the boundary conditions associated with these are embedded in the fixed-grid fluxes. Here, the embedded-boundary conditions are user-specified and enforced to remain intact to the EB and unchanged at all times. The solution values on the left and right sides of the EB are designated as $c^l_{\rm EB}$ and $c^r_{\rm EB}$, respectively (Fig. 2).

For an EB situated in cell i, with its coordinate $x_{\rm EB} = x_{\rm EB}(t)$ given, its relative position with respect to the cell face $x_{i-\frac{1}{2}}$ is βh, where:

$$\beta = \frac{x_{\rm EB} - x_{i-\frac{1}{2}}}{h}, \qquad \beta \in [0,1]. \tag{4}$$

There is no information flow across the EB. Fluxes on one side of the EB are all computed based on the information on the same side and the additional interior boundary condition on the respective side of the EB. In general, when considering three-point upwind-biased interpolation for the fluxes, three cell-face states ($c_{i-\frac{1}{2}}$, $c_{i+\frac{1}{2}}$ and $c_{i+\frac{3}{2}}$) are affected by the presence of a single EB (in cell i) and these are the cell-face states of interest that are especially modified (Fig. 2). $c_{i-\frac{1}{2}}$ and $c_{i+\frac{3}{2}}$ are written as optimally blended, three-point upwind-biased interpolation formulae:

$$c_{i-\frac{1}{2}} = c_{i-1} + \frac{1}{1+2\beta}\frac{1+\kappa_{i-\frac{1}{2}}}{2}(c^l_{\rm EB} - c_{i-1}) + \frac{1-\kappa_{i-\frac{1}{2}}}{4}(c_{i-1} - c_{i-2}), \tag{5a}$$

$$c_{i+\frac{3}{2}} = c_{i+1} + \frac{1+\kappa_{i+\frac{3}{2}}}{4}(c_{i+2} - c_{i+1}) + \frac{2}{3-2\beta}\frac{1-\kappa_{i+\frac{3}{2}}}{4}(c_{i+1} - c^r_{\rm EB}). \tag{5b}$$

Since we do not draw information across the EB, no upwind-biased interpolation formula can be derived for $c_{i+\frac{1}{2}}$. Non-equidistant central interpolation is applied to compute $c_{i+\frac{1}{2}}$.

The blending parameters $\kappa_{i-\frac{1}{2}}$ and $\kappa_{i+\frac{3}{2}}$ are optimized such that the net fluxes in cells $i-1$ and $i+2$, respectively, are as accurate as possible. The net flux in cell i cannot be optimized due to the presence of the EB with its discontinuous solution behavior. Deriving the modified equations in cells $i-1$ and $i+2$, and equating the leading term of the truncation errors to zero, we get:

$$\kappa_{i-\frac{1}{2}} = \frac{7-6\beta}{9+6\beta}, \ \ \kappa_{i-\frac{1}{2}} \in [\tfrac{1}{15}, \tfrac{7}{9}] \quad \text{and} \quad \kappa_{i+\frac{3}{2}} = \frac{7-6\beta}{15-6\beta}, \ \ \kappa_{i+\frac{3}{2}} \in [\tfrac{1}{9}, \tfrac{7}{15}]. \tag{6}$$

The reasons to consider the net flux in cell $i+2$ instead of that of cell $i+1$, for optimizing $\kappa_{i+\frac{3}{2}}$, are given in [1]. The formulae for the EB-affected cell-face states are summarized, in terms of the parameter β, as:

$$c_{i-\frac{1}{2}} = c_{i-1} + \frac{8}{(3+6\beta)(3+2\beta)}(c^l_{\rm EB} - c_{i-1}) + \frac{1+6\beta}{18+12\beta}(c_{i-1} - c_{i-2}), \tag{7a}$$

$$c_{i+\frac{1}{2}} = c^r_{\rm EB} + \frac{2-2\beta}{3-2\beta}(c_{i+1} - c^r_{\rm EB}), \tag{7b}$$

$$c_{i+\frac{3}{2}} = c_{i+1} + \frac{11-6\beta}{30-12\beta}(c_{i+2} - c_{i+1}) + \frac{4}{(9-6\beta)(5-2\beta)}(c_{i+1} - c^r_{\rm EB}). \tag{7c}$$

Note that it is assumed that two successive EBs are sufficiently far apart, such that a given cell-face state is affected by only one EB. Recall that all but the EB-affected fluxes are computed with a standard scheme.

4 Temporal Discretization

After substituting the appropriate discretizations for the spatial operator in the semi-discrete equation (3), it is integrated in time using an explicit method: either the Forward Euler or the RK3b [2] scheme. The later gives a third-order accuracy in time.

4.1 Monotonicity and Limiters

Noting that the EB-affected cell-face states (7) are higher-order accurate and linear, wiggles are imminent. These wiggles can be suppressed by carefully constraining the convective cell-face states. We define non-standard monotonicity arguments, $\tilde{r}_{i-\frac{1}{2}}$ and $\tilde{r}_{i+\frac{3}{2}}$, and derive the limited forms of $c_{i-\frac{1}{2}}$ and $c_{i+\frac{3}{2}}$ (see [1] for details). $c_{i+\frac{1}{2}}$, however, is not limited as we can not define a monotonicity argument $\tilde{r}_{i+\frac{1}{2}}$. After enforcing appropriate monotonicity requirements [1], the resulting limiter-functions $\tilde{\phi}(\tilde{r})$ are fully constrained, as:

$$0 \leq \tilde{\phi}(\tilde{r}_{i-\frac{1}{2}}) \leq \frac{2}{\nu} - 2 \quad \text{and} \quad \frac{\tilde{\phi}(\tilde{r}_{i-\frac{1}{2}})}{\tilde{r}_{i-\frac{1}{2}}} \leq 1 + 2\beta, \tag{8a}$$

$$-1 \leq \tilde{\phi}(\tilde{r}_{i+\frac{3}{2}}) \leq \frac{3-2\beta}{\nu} - 1 \quad \text{and} \quad 4 - \frac{2}{\nu} \leq \frac{\tilde{\phi}(\tilde{r}_{i+\frac{3}{2}})}{\tilde{r}_{i+\frac{3}{2}}} \leq 2, \tag{8b}$$

where $\nu = \frac{u\tau}{h}$ is the CFL number. The ν-dependent, EB-sensitive bounds (8) yield a monotonicity preserving scheme for $\nu \leq \frac{1}{2}$. Typical limiters, satisfying these special bounds, are depicted in Fig. 3.

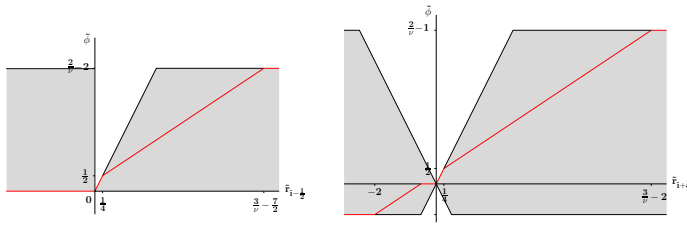

Fig. 3. Typical EB-sensitive limiters and the corresponding monotonicity domains for the EB-affected cell-face states $c_{i-\frac{1}{2}}$ (left) and $c_{i+\frac{3}{2}}$ (right), for $\beta = \frac{1}{2}$

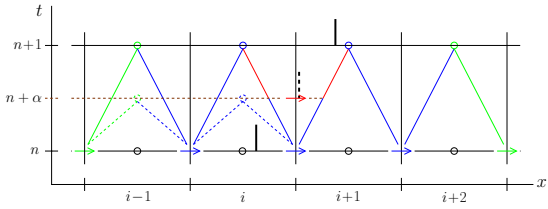

Fig. 4. Stencil for local adaptivity in time. The standard, modified and the intermediate cell-face states are designated in green, blue, and red, respectively.

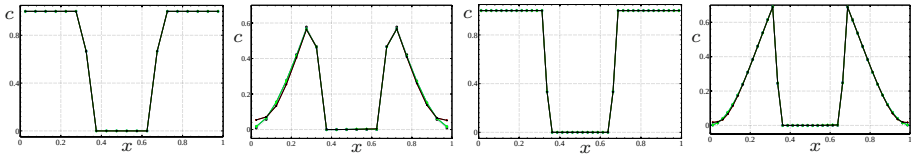

(a) On a 20-cell grid (b) On a 40-cell grid

Fig. 5. Immersed-boundary solutions after one full-period. ○: exact discrete, □: unlimited higher-order upwind-biased with Forward Euler, ∗: limited ditto, ◇: unlimited higher-order upwind-biased with RK3b, ×: limited ditto.

4.2 Local Adaptivity in Time

If an EB is situated in such a way that $x^n_{\mathrm{EB}} \in [x_{i-\frac{1}{2}}, x_{i+\frac{1}{2}})$ and $x^{n+1}_{\mathrm{EB}} \in [x_{i+\frac{1}{2}}, x_{i+\frac{3}{2}})$, there is an abrupt change in $c_{i+\frac{1}{2}}$ when going from t^n to t^{n+1} (see Fig. 4). To account for this change, time adaptivity is introduced by first computing the time fraction α at which the EB crosses $x_{i+\frac{1}{2}}$, as:

$$\alpha = \frac{x_{i+\frac{1}{2}} + \epsilon - x^n_{\mathrm{EB}}}{u\tau}, \qquad \alpha \in (0,1). \tag{9}$$

Next, the intermediate cell-face state $c^{n+\alpha}_{i+\frac{1}{2}}$ is computed. Note that the EB is placed at infinitesimal distance ϵ off $x_{i+\frac{1}{2}}$, in the direction of the flow. Then the cell-face state $c^n_{i+\frac{1}{2}}$ is recomputed as the weighted average:

$$c^n_{i+\frac{1}{2}} := \alpha c^n_{i+\frac{1}{2}} + (1-\alpha) c^{n+\alpha}_{i+\frac{1}{2}}. \tag{10}$$

Finally, solution updating, in Forward Euler, is continued everywhere, using the time-adapted cell-face state, with the regular time step τ. For RK3b, we do not yet resort to the temporal local-adaptivity. We instead split the regular time step τ into smaller time steps, depending on the number of EBs crossing cell faces, and update the intermediate solutions everywhere.

5 Results and Conclusion

We present numerical results to validate the immersed-boundary approach introduced in this work. We take the same data as in § 2.1. The results obtained, shown in Fig. 5, are remarkably accurate. They show a significant improvement in resolution over those computed using the standard methods (Fig. 1). For the more discriminating initial solution, the cosine-cavity in (2), the numerical results of the limited higher-order upwind-biased schemes are slightly deficient at the peripheries. This is due to the property of limiters that they clip physically relevant extrema. Apparently, the deficiency diminishes with decreasing grid size.

The essence of the present approach is that moving bodies are embedded in a regular fixed grid and specific fluxes in the vicinity of the embedded boundary are intelligently computed in such a way that they accurately accommodate the boundary conditions valid on the moving EB. Then, over the majority of the domain, where we do not have influence of the EBs, we use standard methods on the underlying regular fixed grid. Excellent results are achieved, without much computational overhead. We foresee that the numerical methods introduced here can readily be extended to real fluid-flow equations.

References

1. Hassen, Y., Koren, B.: ACOMEN 2008 Proceedings, Liège, Belgium (2008)
2. Hundsdorfer, W., et al.: J. Comput. Phys. 117, 35–46 (1995)
3. Koren, B.: Notes on Numerical Fluid Mechanics 45, 117–138 (1993)
4. Peskin, C.S.: J. Comput. Phys. 10, 252–271 (1972)
5. Sweby, P.: SIAM J. Num. Anal. 21, 995–1011 (1984)
6. van Leer, B.: Lect. Appl. Math., vol. 22- part 2, pp. 327–336. AMS, RI (1985)

“*This page left intentionally blank.*”

Part 27
Kinetic Approach

“*This page left intentionally blank.*”

Computation of Shock Structure in Diatomic Gases Using the Generalized Boltzmann Equation

R.K. Agarwal[1] and Felix G. Tcheremissine[2]

[1] Washington University in St. Louis, St. Louis, MO 63130, USA
rka@wustl.edu
[2] Russian Academy of Sciences, Moscow, Russia
cherem@ccas.ru

The paper describes the methodology for computing hypersonic non-equilibrium shock wave flows of diatomic gases using the Generalized Boltzmann Equation (GBE) including both the vibrational - translational (VT) and rotational - translational (RT) relaxations.

1 Introduction

The shock structure in nonequilibrium hypersonic flows that includes both the vibrational - translational (VT) and rotational - translational (RT) energy transfers is computed by applying a three-stage splitting procedure to the GBE [Bey2000] which is the same as the Wang-Chang Uhlenbeck equation [Che02] except that it includes the degeneracy of rotational levels. The three stages consist of the free molecular transport, VT relaxation, and RT relaxation. For the VT relaxation, GBE is always solved. For the RT relaxation, two approaches are employed. In the first approach, for the RT relaxation GBE is solved. This approach is computationally very intensive since it requires solving the complete GBE for both vibrational and rotational degrees of freedom. In the second approach, a two-level BGK type model of RT relaxation is employed. The second approach is significantly more efficient (about 20 times faster than the first approach). The paper describes the two-level RT relaxation model. The model is validated by by comparing the results for the shock structure with the complete GBE solution for RT relaxations. Computations are then performed for the shock structure at high Mach numbers accounting for both the vibrational and rotational excitations; the second approach is employed for computing the RT relaxations. For solving the GBE, The computational framework available for the classical Boltzmann equation [Che04] is extended by including both the rotational and vibrational degrees of freedom in the GBE.

2 Technical Approach

The GBE can be written as

$$\frac{\partial f_i}{\partial t} + \boldsymbol{\xi} \frac{\partial f_i}{\partial \mathbf{x}} = R_i \tag{1}$$

The collision operator is given by

$$R_i = \sum_{jkl} \int_{-\infty}^{\infty} \int_0^{2\pi} \int_0^{b_m} (f_k f_l \omega_{ij}^{kl} - f_i f_j) P_{ij}^{kl} g b db d\varphi d\xi_j \qquad (2)$$

Here f_i is the distribution function for the energy level i, P_{ij}^{kl} is the probability of the transfer from levels i, j to the levels k, l, and the factor $\omega_{ij}^{kl} = (q_k q_l)/(q_i q_j)$; q_i being the degeneration of the rotational energy level. For simple levels, the GBE changes to the WC-UE. We consider molecular Nitrogen having the Lennard-Jones potential (6, 12) with the depth of the energy hole $\varepsilon = 91K$, degeneration of rotational level $q_i = 2i+1, i = 0,1,..\infty$, and the rotational energy of the level $e_{ri} = \varepsilon_0 i(i+1),\ \varepsilon_0 = 2.9K$. The molecular interaction during the collision consists of two phases. In the first phase, the molecules interact in an elastic manner according to the molecular potential. This stage determines the deviation angle of the relative velocity. In the second stage, the modulus of the relative velocity changes according to the energy conservation equation. For the transition probabilities P_{ij}^{kl} we apply the formulae given in [Bey2000] that are obtained by fitting the experimental data of molecular dynamics simulations of interactions of rigid rotors that model N_2 molecules.

$P_{ij}^{kl} = P_0 \omega_{ij}^{kl} [\alpha_0 \exp(-\Delta_1 - \Delta_2 - \Delta_3 - \Delta_4) + \frac{1}{\alpha_0} \exp(-\Delta_3 - \Delta_4)]$, where

$\Delta_1 = |\Delta e_1 + \Delta e_2| / e_{tr0},\ \Delta_2 = 2|\Delta e_2 - \Delta e_1| / e_{tot}$

$\Delta_3 = 4|\Delta e_1| / (e_{tr0} + e_{ri}),\ \Delta_4 = 4|\Delta e_2| / (e_{tr0} + e_{rj})$

$\Delta e_1 = e_{ri} - e_{rk},\ \Delta e_2 = e_{rj} - e_{rl},\ \alpha_0 = 0.4 e_{tot} / e_{tr0}$

$e_{tr0} = m g^2 / 4,\ e_{tot} = e_{tr0} + e_{ri} + e_{rj}$.

The energy conservation law in a collision selects virtual collisions with non zero probability. From the equation $m g_{ij}^2 / 4 + e_{ri} + e_{rj} = m g_{kl}^2 / 4 + e_{rk} + e_{rl}$, it can be shown that $P_{ij}^{kl} > 0$, if $g_{kl}^2 \geq 0$, otherwise $P_{ij}^{kl} = 0$. The elastic collision is a particular case of this collision. The probabilities obey the normalization condition: $\sum_{k,l} P_{ij}^{kl} = 1$. The kinetic equation (1) is solved by the splitting scheme. At a time step $\tau \ll \tau_0$, where τ_0 is a mean inter-collision time, equation (1) is replaced by the sequence of equations;

(a) $\frac{\partial f_i}{\partial t} + \xi \frac{\partial f_i}{\partial \mathbf{x}} = 0$ (b) $\frac{\partial f_i}{\partial t} = R_i$

The collision operator R_i is evaluated at the uniform grid S_0 in the velocity space by the conservative projection method proposed in [Che06].

3 Two Level Kinetic Model for RT Relaxation in a Gas

The proposed model equation is aimed at simplifying the simulation of the rotational-translational (RT) energy exchange in a gas. Such simplification is highly needed for complex processes in which rotational excitation is accompanied by the vibration - translational (VT) energy transfer. The model consists of 2 levels: the ground level with the rotational energy $\varepsilon_1 = 0$ and the exicted level with some energy $\varepsilon_2 > T_{\max}$, where $T_{\max}$ is the maximum temperature in the problem under consideration. We call the proposed model as "2LRT" model. The distribution function is also composed of two parts, f_1 and f_2 with corresponding populations of the levels n_1 and n_2. The gas density is $n = n_1 + n_2$ and the rotational energy is $E_{rot} = \varepsilon_2 n_2$. Let the density of the gas at some point be n, the kinetic energy E_{kin}, and the rotational energy E_{rot}. One can then determine the populations of the levels by the simple formulas $n_2 = E_{rot} / \varepsilon_2$ and $n_1 = n - n_2$. Maximal value of E_{rot} is given by $E_{rot} = nT_{\max}$, therefore $n_2 < nT_{\max} / \varepsilon_2$, and one obtains $0 < n_2 < n$ and $n_1 > 0$. Having E_{kin}, one can determine the equilibrium temperature, $T_{eq} = 2(E_{kin} + E_{rot})/5n$ and the equilibrium rotational populations $n_{2,eq} < nT_{eq} / \varepsilon_2$, $n_{1,eq} = n - n_{2,eq}$. These parameters determine the equilibrium distribution functions $f_{1,M}$ and $f_{2,M}$. For construction of the model equation we begin with the Wang Chang–Uhlenbeck equation (WC-UE) for the considered 2 levels system $(\{i, j, k\} = 1, 2)$.

$$\partial f_i / \partial t = \sum_{j,k,l} \int p_{i,j}^{k,l} (f_k f_l - f_i f_j) g_{i,j} b db d\varphi d\xi_j \tag{3}$$

In equation (3), we replace the collision operator by an elastic collision operator Q_{el} and the non-elastic operator Q_r. The elastic operator is the same as the Boltzmann collision integral for a two-component gas mixture:

$$Q_{i,el} = \sum_j \int (f_i' f'_j - f_i f_j) g_{i,j} b db d\varphi d\xi_j \tag{4}$$

The non-elastic operator is taken in a relaxation form:

$$Q_{r,i} = -\nu_r (f_i - f_{i,M}^*) \tag{5}$$

It was found by a number of numerical experiments that the choice for $f_{i,M}^*$ in equation (5) as the Maxwellian distribution functions $f_{i,M}$ is possible, but is not the best. The function $f_{i,M}^*$ represents the elliptic distribution defined by the diagonal elements of the temperature tensor.

$$f_{i,M}^{*} = n_{i,eq}\left(\frac{m}{2\pi k}\right)^{3/2}\left(T_{xx}^{*}T_{yy}^{*}T_{zz}^{*}\right)^{-1/2}\exp\left(-mc_x^2/2kT_{xx}^{*} - mc_y^2/2kT_{yy}^{*} - mc_z^2/2kT_{zz}^{*}\right) \quad (6)$$

where $c_x = \xi_x - u, c_y = \xi_y - v, c_z = \xi_z - w$, and u, v, w are the components of the bulk velocity vector. The components T_{aa}^{*} of the temperature tensor are defined by self-similar transformation of the initial components as

$$T_{aa}^{*} = T_{aa}\left(T_{eq} / T_{kin}\right) \quad (7)$$

The use of the function given in equation (6), instead of the Maxwellian, means that the inelastic operator Q_r preserves to some extent the shape of the distribution function in the velocity space. The RT relaxation frequency can be defined as a part of the relaxation frequency ν of the BGK model equation

$$\nu_r = a_1 \nu . \quad (8)$$

The non-elastic operator contributes to the evolution of the velocity distribution function toward the equilibrium state. To take into account its influence one should diminish the elastic collision operator by a factor $(1 - a_2\nu_r)$, $0 < a_2 < 1$. Finally, the proposed RT relaxation model contains two operators, the inelastic operator given by equation (5) with the frequency given by the equation (8), and the elastic operator $Q_{i,el}^{*} = (1 - a_2\nu_r)Q_{i,el}$. The coefficients a_1 and a_2 can be determined from comparisons of the solutions of the proposed model with solutions of the WC-UE equation.

4 Computation of Shock Structure

The shock structure is formed as a final stage of the evolution of a discontinuity in the initial distribution function. The problem is considered for the interval $-L_1 \le x \le L_2$ with the discontinuity at $x = 0$. The initial distribution function on both sides of discontinuity is described by the velocities and spectral levels:

$$f_i^{1,2}(\xi, x) = n^{1,2}\left[m/(2\pi T^{1,2})\right]^{3/2}\exp\left[-\frac{m(\xi - u^{1,2})^2}{2T^{1,2}}\right]\frac{2i+1}{Q_r}\exp\left(-\frac{e_{ri}}{T^{1,2}}\right)$$

where Q_r denotes the statistical sum. Parameters $(n, T, u)^{1,2}$ are defined by the Rankine-Hugoniot relations with $\gamma = 7/5$. At the boundary, the initial distribution function is kept constant. Figure 1 shows the shock structure in nitrogen for Mach 10. Comparison for density distribution at Mach 10 between the computation and experimental data [Als76] shows excellent agreement. In Figure 1, the shock structure in nitrogen was computed for RT relaxation using the complete collision integral in the GBE. Next, we perform the same computations with 2LRT model. Figure 2 shows the comparison of results between the 2LRT model and the solution of GBE. The graphs for flow variables computed with the 2LRT model are marked by stars. The agreement is reasonable. It gets better at lower Mach numbers.

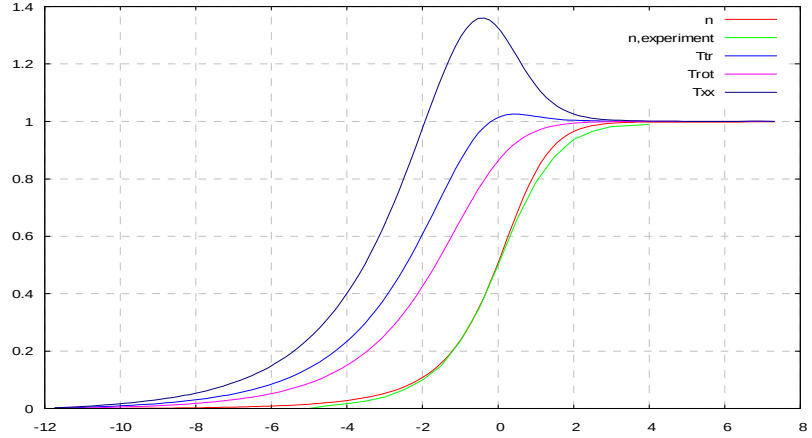

Fig. 1. Shock Structure in nitrogen for M=10 obtained with GBE; n = computed density, n, experiment = experiment density, T = total temp, Txx = translational temp, Trot = rotational temp (normalized)

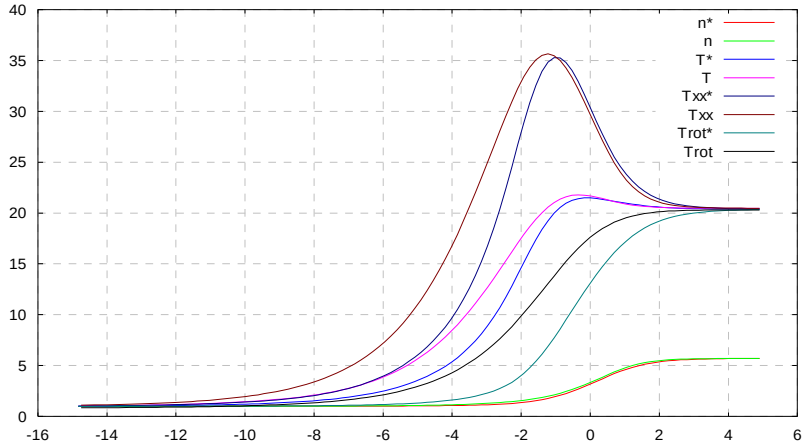

Fig. 2. Comparison of Shock Structure in nitrogen at M =10 computed with GBE and 2LRT model (shown by *)

Finally, we consider the gas with both rotational and vibrational degrees of freedom. The vibrational spectrum for nitrogen has the energy quantum of 3340K. As mentioned above in the introduction, VT transfers are computed using the GBE and the RT transfer are computed using the two-level kinetic model for efficient computations. The vibration energy is computed by the expression $E_{vib} = \sum_{j=0}^{j=j_m} j\varepsilon_{vib} n_j$ Assuming that the vibrations possess two degrees of freedom, one can associate the vibration energy with the classic vibrational

temperature $T_{vib,cl} = E_{vib} / k$. This temperature measures the amount of energy stored in the vibrations. From the viewpoint of quantum mechanics, the vibrations form the Bose gas in which the temperature in the thermodynamic equilibrium is related to the vibrational energy by the formula $E_{vib} = \dfrac{\varepsilon_{vib}}{\exp(\varepsilon_{vib} / kT_{vib,q}) - 1}$.

In the classical limit, one obtains $T_{vib,q} \to T_{vib,cl}$. In Figure 3, we present both vibration temperatures along with the density, kinetic translational, longitudinal translational and rotational temperatures. It should be noted that the quantum vibrational temperature reaches the thermodynamic equilibrium value, but the classic vibrational temperature is below this limit.

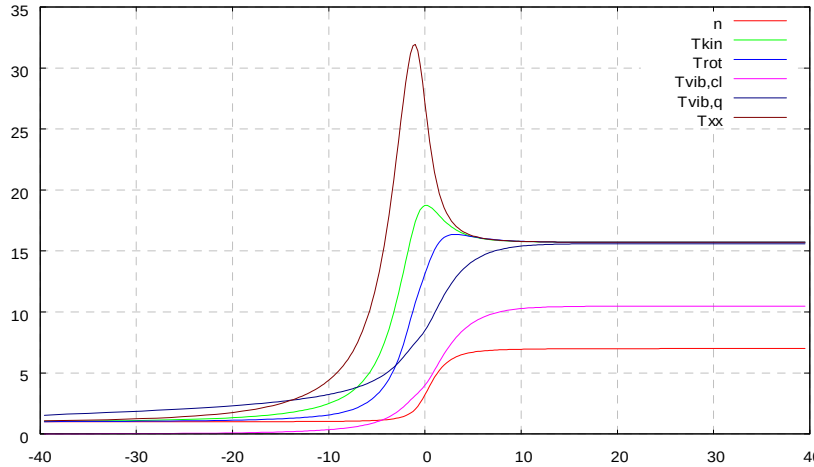

Fig. 3. Shock structure in nitrogen at M =10 with both RT and VT relaxations

Acknowledgements

This work was sponsored (in part) by the Air Force Office of Scientific Research. The authors are grateful to AFOSR Program Manager Dr. John Schmisseur and Dr. Eswar Josyula of AFRL for support and helpful discussions.

References

[AIs76] Alsmeyer, H.: Density profiles in argon and nitrogen shock waves measured by the absorption of an electron beam. J. Fluid Mech. 74, 497–513 (1976)

[Bey00] Beylich, A.: An interlaced system for nitrogen gas. In: Proc. of CECAM Workshop, ENS de Lyon, France (2000)

[Che02] TCheremisin, F.G.: Solution of the Wang Chang – Uhlenbeck Master Equation. Doklady Physics 47, 872–875 (2002)

[Che06] Tcheremissine, F.G.: Solution of the Boltzmann Kinetic Equation for high speed flows. Comp. Math. and Math. Phys. 46, 315–329 (2006)

A High-Order Accurate Gas-Kinetic BGK Scheme

Qibing Li and Song Fu

Department of Engineering Mechanics, Tsinghua University,
Beijing 100084, China
lqb@tsinghua.edu.cn

1 Introduction

During the past decade, the gas-kinetic BGK scheme has been developed rapidly [1]. The scheme is based on the Bhatnagar-Gross-Krook (BGK) model of Boltzmann equation. The good performance behavier, such as the positivity preserving property and the inherent satisfaction of the entropy condition, guarantees the scheme to yield more reliable numerical results for a wide range of flow physics [2, 3], including the high-speed turbulent mixing layer [4] and decaying homogeneous isotropic turbulence [5].

In computational aeroacoustics, it is a challenge to accurately predict the sound generation. To capture both the amplitude and frequency contents of the wave, a high-accuracy numerical scheme is required. The same situation is encountered when simulating the instability of a flow. The BGK scheme is a finite volume method and mostly second-order both in spatial and temporal directions, it is thus worth to improve its accuracy to study those flows. Currently, the genuinely multidimensional scheme has become a hotspot for its accuracy or efficiency for steady-state flow when compared to classical finite-volume method. For a gas-kinetic scheme, based on microscopic particle distribution function, the multidimensional version can be easily constructed with the inclusion of the tangential slopes of conservative variables in the flux at a cell interface [6]. The scheme shows better performance in the prediction of the flow sensitive to the accuracy of the stress or wall variable gradient calculation, when compared with the corresponding quasi-one-dimensional extension and directional splitting scheme.

In this paper the high-order accurate multidimensional gas-kinetic BGK scheme for subsonic flow is developed and, primarily, validated with circular pulse propagation and the radiation interference from three baffled pistons.

2 A High-Order Accurate BGK Scheme

2.1 Fundamental of Gas-Kinetic BGK Scheme

The BGK scheme is briefly described as follows. First, the BGK-Boltzmann equation is written as

$$\frac{\partial f}{\partial t} + u_i \frac{\partial f}{\partial x_i} = (g - f)/\tau \tag{1}$$

where $i = 1, 2$ for two-dimensional flow and $\tau = \mu/p$ is the particle collision time. $f = f(\mathbf{x}, t, \mathbf{u}, \xi)$ is the gas distribution function, and g is the equilibrium state approached by f, assumed to be a Maxwellian distribution,

$$g = \rho(\lambda/\pi)^{(K+2)/2} \mathrm{e}^{-\lambda(|\mathbf{u}-\mathbf{U}|^2+\xi^2)}, \tag{2}$$

where $\xi^2 = \xi_1^2 + \xi_2^2 + \ldots + \xi_K^2$ represents the internal energy of particles, and $\lambda = \rho/(2p)$. The total number of degrees of freedom, K, in ξ is equal to $(4 - 2\gamma)/(\gamma - 1)$ for a 2-D flow. During the particle collisions, f and g satisfy the conservation constraint,

$$\int (g - f)\boldsymbol{\psi} \mathrm{d}\Xi = \mathbf{0} \tag{3}$$

at any point in space and time for the conservation of mass, momentum and energy. Here $\mathrm{d}\Xi = \mathrm{d}u_1 \mathrm{d}u_2 \mathrm{d}\xi$ is the volume element in the phase space with $\mathrm{d}\xi = \mathrm{d}\xi_1 \mathrm{d}\xi_2 \ldots \mathrm{d}\xi_K$, and $\boldsymbol{\psi}$ is the vector of moments,

$$\boldsymbol{\psi} = (\psi_1, \psi_2, \psi_3, \psi_4)^T = (1, \mathbf{u}, (|\mathbf{u}|^2 + \xi^2)/2)^T. \tag{4}$$

From Eqs. (1) and (3), the finite volume formulation of the BGK scheme is formed as

$$(\mathbf{Q}^*)_{lm}^{n+1} = (\mathbf{Q}^*)_{lm}^{n} + \frac{1}{S_{lm}} \oint_{\partial\Omega_{lm}} \int_{t^n}^{t^n + \Delta t} \mathbf{F}^* \mathrm{d}t \mathrm{d}l \tag{5}$$

where Ω_{lm} is a computational cell indexed by l and m with the area S_{lm} and boundary $\partial\Omega_{lm}$. The superscript '$*$' represents the variable in the global coordinates. The flux $\mathbf{F}^*$ is calculated through the coordinate transformation from that in the local coordinates $\mathbf{F}$. For convenience, the calculation of $\mathbf{F}$ is presented through an example at a cell interface $x_{l+1/2} = 0$, $-\Delta y/2 \le y_m \le \Delta y/2$. The relations between the distribution function f and the macroscopic conservative quantities $\mathbf{Q}$ and the flux $\mathbf{F}$ are given by

$$\mathbf{Q} = (\rho, \rho U, \rho V, \rho\varepsilon)^T = \int f\boldsymbol{\psi} \mathrm{d}\Xi, \quad \mathbf{F} = \int uf\boldsymbol{\psi} \mathrm{d}\Xi. \tag{6}$$

The BGK equation (1) has the integral solution for constant collision time,

$$f(\mathbf{x}, t, \mathbf{u}, \xi) = \frac{1}{\tau} \int_0^t g(\mathbf{x}', t', \mathbf{u}, \xi) e^{-(t-t')/\tau} \mathrm{d}t' + \mathrm{e}^{-t/\tau} f_0(\mathbf{x} - \mathbf{u}t, \mathbf{u}, \xi) \tag{7}$$

where $\mathbf{x}' = \mathbf{x} - \mathbf{u}(t - t')$ is the trajectory of a particle motion and f_0 is the initial gas distribution function at the beginning of each time step ($t = 0$).

If f_0 and g are known, the time dependent distribution function f can be easily deduced through the above expression, avoiding the great difficulty to

solve the BGK equation directly. This is adopted by the gas-kinetic BGK scheme, with the key to construct f_0 and g around the cell interface $(l + 1/2, m)$ according to the Chapman-Enskog expansion. Once f is obtained, the fluxes across the cell interface can be calculated with Eq. (6) and the conservative variables at the next time step can be calculated via the finite volume formulation (5). Details can be found in the corresponding reference.

2.2 Extension to High-Order Accuracy

Till now, the existing BGK scheme is mostly second-order accurate both in spatial and temporal directions. Many attempts were employed to improve the accuracy, such as that with high-order reconstruction of conservative variables at cell interface [7], but the scheme is still second-order, due to the evolution of gas flow, or the distribution function f is only second-order. In the present study, the high-order accurate f is considered through the expansion to third-order in both spatial and temporal directions,

$$f_0(\mathbf{x}, 0, \mathbf{u}, \xi) = g_0 \left[(1 + a_k x_k + (a_i a_j + b_{ij}) x_i x_j/2 - \tau \left(a_k u_k + A + (a_i A + C_i + u_j(a_i a_j + b_{ij}) x_i)\right)\right] \quad (8)$$

$$g(\mathbf{x}, t, \mathbf{u}, \xi) = g_0 \left[1 + a_k x_k + At + (a_i a_j + b_{ij}) x_i x_j/2 + (A^2 + B')t^2/2 + (a_k A + C_i) x_k t\right] \quad (9)$$

where g_0 is the initial local Maxwellians. The local terms a_i, b_{ij}, C_i, B' and A are from the Taylor expansion of a Maxwellian and take the form, $a = a^{(\alpha)}\psi_\alpha$, $\alpha = 1, 2, 3, 4$, where all coefficients, $a^{(\alpha)}, \ldots, A^{(\alpha)}$, are local constants from the first and second derivatives of g. These coefficients, as well as g_0 are related to the reconstructed conservative variables $\mathbf{Q}$ and their slopes, which can be evaluated through the condition on Chapman-Enskog expansion, same as that in BGK-Burnett method [8].

Then the distribution function at the cell interface can be deduced,

$$f(\mathbf{0}, t, \mathbf{u}, \xi) = g_0 \left[(1 - \tau a_k u_k + (-\tau + t)A + (-\tau t + t^2/2)(A^2 + B') - \tau t(a_k A + C_k)u_k - \tau t B''\right] . \quad (10)$$

It should be noted that it is difficult to achieve high-order reconstruction of macro conservative variables in curvilinear mesh. In the present study, the least-square method is adopted and the coefficients can be calculated in advance for only one time to decrease the computational cost. The present scheme is truely multidimensional, as the solution (7) allows the movement of particles in any direction. That is, it simulates a multidimensional transport process across a cell interface.

3 Numerical Results

The scheme is applied to the study of two-dimensional circular pulse propagation and the nonlinear radiation interference from three baffled pistons

[9, 10]. In the first case, The initial pressure pulse in a uniform fluid is set as $p = 1/\gamma + 0.01 \exp[-\ln 2\ (x^2 + y^2)/0.2^2]$ with density $\rho = 1$ and velocity $u = v = 0$. Uniform cell size, $\Delta x = \Delta y = 0.05$ is adopted. The Reynolds number $Re = \rho cL/\mu = 5000$. Figure 1 shows the results for the first test case, from which good agreement can be seen with the existing study with LBM and DNS [9] .

In the second case, three pistons located at $y = 0$, with the half length a and the distance between two neighbors $d = 4a$. They vibrate in a uniform flow $(p = 1/\gamma, \rho = 1, u = v = 0)$ with the movement $v = V_0 \cos(\omega t)$ and $\omega a/c = 2$. The Reynolds number $Re = \rho ac/\nu = 5000$. 200×200 computational cells are adopted with minimal cell sizes $\Delta x_m = 0.07$ and $\Delta x_m = 0.04$. When the vibration of pistons is weak, the linear radiation interference occurs. When the signal strength is moderate, the waves' dissipation becomes

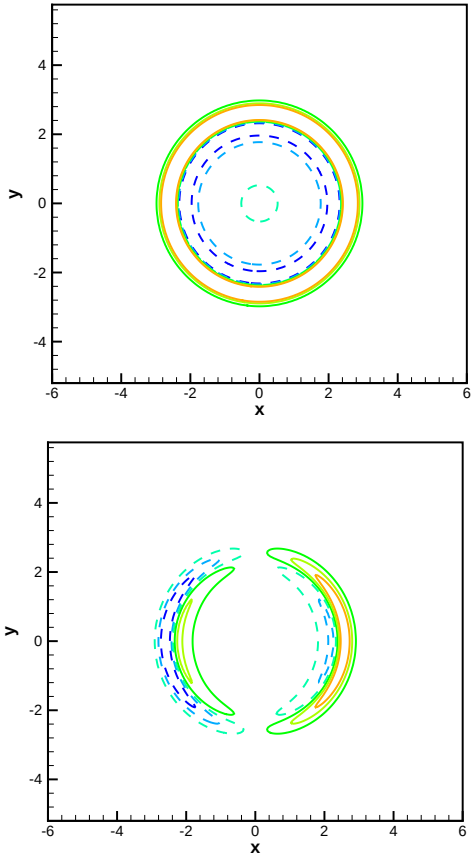

Fig. 1. Pressure (top) and velocity (bottom) fluctuations at t=2.5. Solid contours are positive levels and dashed negative. Six contours are equally distributed between $\pm 2.5 \times 10^{-4}$ for pressure and $\pm 6.25 \times 10^{-4}$ for velocity.

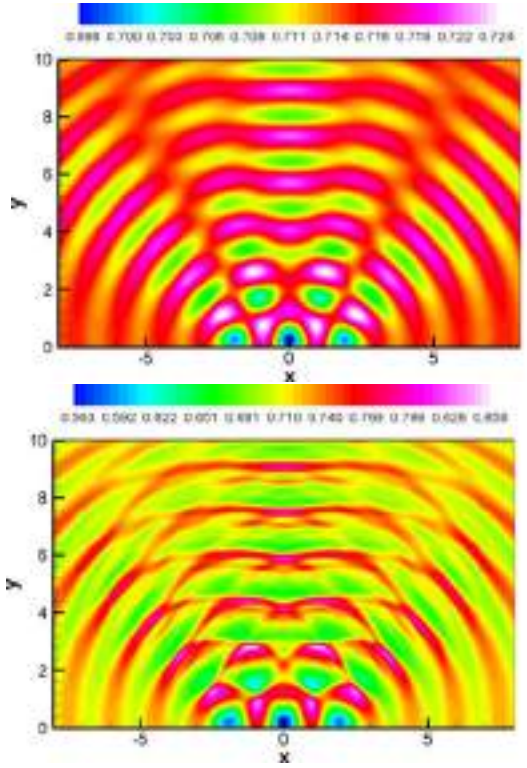

Fig. 2. Radiated wave (pressure contours) from array of the three baffled pistons at t=12: the top figure is for $V_0 = 0.01c$ and the bottom $V_0 = 0.1c$

stronger, and the maxima and minima following the directivity pattern of the sources can be seen (Fig. 2), agreeing with the study of Popescu et al. [10].

The performance of the multidimensional scheme is also primarily evaluated in the present study, compared with the corresponding directional splitting method and the simple treatment with only the adoption of high-order-accurate interpolation in the reconstruction of conservation variables at a cell interface [7]. For the simulation of circular pulse propagation with a coarse mesh, the present study shows that the high-order multidimensional scheme can yields much better results.

It should be mentioned that the explicit reconstruction in the present new scheme, as well as the usual BGK scheme, is correlated with only several cells around a cell interface, thus the scheme inherits the good parallel performance when compared with a compact finite-volume scheme [11].

4 Conclusions

The high-order accurate gas-kinetic BGK scheme is presented developed through the expansion of velocity distribution function to high order in both

spatial and temporal directions. Primary test cases show that the present scheme is a good choice when investigating the flow with multiscale structure, such as aeroacoustics. However, for flow with discontinuity, the high-order scheme required further study.

References

1. Xu, K.: A gas-kinetic BGK scheme for the Navier-Stokes equations, and its connection with artificial dissipation and Godunov method. J. Comput. Phys. 171, 289–335 (2001)
2. Li, Q.B., Fu, S., Xu, K.: A compressible Navier-Stokes flow solver with scalar transport. J. Comput. Phys. 204, 692–714 (2005)
3. Xu, K., Mao, M., Tang, L.: A multidimensional gas-kinetic BGK scheme for hypersonic viscous flow. J. Comput. Phys. 203, 405–421 (2005)
4. Fu, S., Li, Q.B.: Numerical simulation of compressible mixing layers. Int. J. Heat Fluid Flow. 27, 895–901 (2006)
5. Kerimo, J., Girimaji, S.S.: Boltzmann-BGK approach to simulating weakly compressible 2D turbulence: comparison between lattice Boltzmann and gas kinetic methods. J. Turbulence 8(46) (2007)
6. Li, Q.B., Fu, S.: On the multidimensional gas-kinetic BGK scheme. J. Comput. Phys. 220, 532–548 (2006)
7. Xu, K., He, X.: Lattice Boltzmann method and gas-kinetic BGK scheme in the low-Mach number viscous flow simulations. J. Comput. Phys. 190, 100–117 (2003)
8. Xu, K., Li, Z.: Microchannel flow in the slip regime: gas-kinetic BGK-Burnett solutions. J. Fluid Mech. 513, 87–110 (2004)
9. Li, X.M., Leung, R.C., So, R.M.C.: One-step aeroacoustics simulation using lattice Boltzmann method. AIAA J. 44, 782–789 (2006)
10. Popescu, M., Vedder, R., Shyy, W.: A finite volume-based high-order, Cartesian cut-cell method for wave propagation. Int. J. Numer. Meth. Fluids 56, 1787–1818 (2008)
11. Pereira, J.M.C., Kobayashi, M.H., Pereira, J.C.F.: A fourth-order-accurate finite volume compact method for the incompressible Navier-Stokes solutions. J. Comput. Phys. 167, 217–243 (2001)

Part 28
Micro/Nano Fluid Mechanics 1

“*This page left intentionally blank.*”

Numerical Simulations of Three Dimensional Micro Flows

Charles-Henri Bruneau, Thierry Colin, and Sandra Tancogne

University of Bordeaux, 351 Cours de la Liberation, 33405 Talence (France)
Inria Bordeaux Sud Ouest team MC2
lastname@math.u-bordeaux1.fr

1 Introduction

Microfluidics deal with the manipulation and the control of liquids in channels about a hundred of microns. The consideration of various experimental configurations leads to several regimes of flows: jets, droplets or plugs [3]. Indeed, the use of coflows or drippings find his interest in various applications ([6], [4]): ink jet printing or spray atomization for example. So, it is necessary to control the evolution of a diphasic jet in a view to produce droplets of different shapes and volumes. The created microdroplets are often employed for their internal dynamic to mix products that are generally toxic and expensive. In this work, numerical results of diphasic flows in square micro channels are presented. At the scale, the flow are generally laminar and the movement of the interface between the two fluids is controlled by the effect of the surface tension.

As the breaking jet, due to the Rayleigh-Plateau instability, is only observable thanks to a tridimensional modeling. All numerical simulations are done in tridimensional cartesian meshes. So, the aim is first to study the breaking jet phenomenon, when confinement and effects due to the surface tension are predominant. Then, the second point is to analyze the internal dynamic of the created droplets. Finally, a numerical result corresponding to the coalescence of microdroplets is shown. The interface liquid-liquid is followed thanks to the Level Set method coupled to the one-fluid formulation of Stokes equation for diphasic flows.

2 Modeling

2.1 The Stokes Equations for Diphasic Flows in Microfluidic

We consider the Stokes equations for two fluids in a bounded domain $\Omega \in \mathcal{R}^3$. The two fluids, respectively called internal (i) and external (e), occupy at each time t the domains $\Omega_i(t)$ and $\Omega_e(t)$ such that $\Omega = \Omega_i(t) \cup \Omega_e(t)$. The interface $\Gamma(t)$ between the two fluids is defined like $\Gamma(t) = \bar{\Omega}_i(t) \cap \bar{\Omega}_e(t)$.

So, the hydrodynamic model is the following

$$\begin{cases} div(2\eta D(U)) = \nabla P + \gamma\kappa\delta_\Gamma \mathbf{n}_\Gamma \text{ in } \Omega \\ \nabla.U = 0 \text{ in } \Omega \end{cases} \tag{1}$$

where $D(U)$ is the deformation rate tensor given by $D(U) = \frac{\nabla U + (\nabla U)^T}{2}$, η is the dynamic viscosity such that

$$\eta = \begin{cases} \eta_i & \text{in the internal flow} \\ \eta_e & \text{in the external flow} \end{cases} \tag{2}$$

and $\gamma\kappa\delta_\Gamma \mathbf{n}_\Gamma$ denotes the surface tension contribution at the interface with γ the surface tension coefficient between the two fluids, κ the mean curvature of the interface Γ, δ_Γ is the Dirac mass on Γ

$$\delta_\Gamma = \begin{cases} 1 & \text{at the interface,} \\ 0 & \text{elsewhere,} \end{cases} \tag{3}$$

and $\mathbf{n}_\Gamma$ is the unit vector normal to the interface Γ.

2.2 The Level Set Method: Parametrization of the Interface

Our objective is to follow the evolution in the time interval $(0, T)$ of the interface between the two fluids. Several methods could have been chosen (VOF, Lagrangian, Level Set ..). In our work, the interface is modeled by the level function $\phi(t, x, y, z)$ [7]. At the initial time, ϕ is zero at the interface, negative in one phase and positive in the other:

$$\phi(0, x, y, z) = \begin{cases} < 0 \text{ in flow i,} \\ > 0 \text{ in flow e,} \\ 0 \quad \text{at the interface } \Gamma. \end{cases} \tag{4}$$

Its motion is governed by an advection equation

$$\begin{cases} \partial_t \phi + (U.\nabla)\,\phi = 0 & \text{in } \Omega \times (0, T) \\ \phi(t = 0) = \phi(0, x, y, z) & \text{in } \Omega \end{cases} \tag{5}$$

Such a modeling implies the properties of the Level Set function to be respected at each time step. In particular, the fact that the interface is represented by the zero value of the function ϕ:

$$\forall t \geq 0, \quad \Gamma(t) \; = \; \{(x, y, z),\ \phi(t, x, y, z) = 0\}\,. \tag{6}$$

When ϕ is known, the unit normal $\mathbf{n}_\Gamma$ at the interface and the curvature κ are computed as follow,

$$\mathbf{n}_\Gamma = \left.\frac{\nabla\phi}{|\nabla\phi|}\right|_{\phi=0} \text{ and } \kappa = \nabla.\left.\left(\frac{\nabla\phi}{|\nabla\phi|}\right)\right|_{\phi=0}. \tag{7}$$

3 The Numerical Method

Now, we proceed to the discretization of the equations introduced in the previous section. For the presentation of the whole algorithm, we refer the reader to [8].

3.1 The Advection Equation

The time discretization of the advection equation (5) is explicit and a classical Euler scheme is used:

$$\phi^{n+1} = \phi^n - \Delta t(U^n.\nabla)\phi^n \tag{8}$$

with Δt the time step, $n+1$ the new iteration at $t^{n+1} = (n+1)\Delta t$. This choice is associated to a restriction on the time step (the classical CFL condition) in order to ensure the stability and so the convergence.

The space discretization is made with a five order WENO scheme [5].

3.2 The Hydrodynamic Part

The discretization of the incompressible Stokes equations is classical. The finite volume method on structured staggered grids is considered (Patankar, 1980). Although, the Stokes equation is a stationary equation, an explicit time discretization of the capillary unknowns is proposed with the following scheme:

$$\begin{array}{rcl} \nabla.(2\eta^n D(U^{n+1})) & = & \nabla P^{n+1} + \gamma\kappa^n\delta(\phi^n)\nabla\phi^n, \\ \nabla.U^{n+1} & = & 0. \end{array} \tag{9}$$

In the Stokes equation, the explicit treatment of the term associated to the surface tension required a stability criterion to maintain the convergence of the method. Commonly, the criterion proposed by Brackbill, Kote and Zemach is used [1]. Recently, a less restrictive stability condition was proposed by Galusinski and Vigneaux [2].

4 The Rayleigh-Plateau Instability

4.1 Experimental Considerations

The numerical simulations proposed are based on the following experimental configuration [3], the jet is generated with a cylindrical capillary centred in a square capillary.

In this configuration, several kinds of microdroplets can be observed varying the internal or the external flow rate of the fluids.

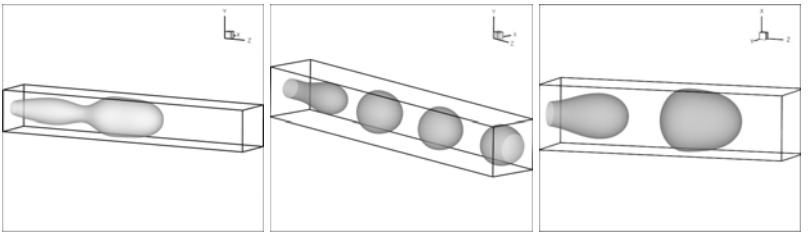

Fig. 1. From left to right: an oscillating jet, a succession of droplets and a plug

4.2 Jets, Droplets and Plugs

Numerically, the same configuration is adopted. The external microchannel has a square section $S_c = 550\ \mu m$ and the radius of the cylindrical tube is $R_i = 105\ \mu m$. The inner fluid has a viscosity $\eta_i = 55mPa.s$ and the outer one $\eta_e = 235mPa.s$. The surface tension between the two fluids is $\gamma = 24mN/m$. In Fig. 1, the flow rates are the following: ($Q_i = 7500\mu L/h$, $Q_e = 6000\mu L/h$), ($Q_i = 2500\mu L/h$, $Q_e = 3000\mu L/h$) and ($Q_i = 2500\mu L/h$, $Q_e = 5500\mu L/h$). According to these flow rates, differents regimes are respectively observed as in the experiments: an oscillating jet, droplets and a plug.

In microfluidic experiments, the droplets are confined and the surface tension drives their shapes. These droplets are used as microreactors or micromixers. To understand their internal dynamic, it is interesting to know the droplets velocity field in their own referential. The shape of the previous plug is plotted on (Fig.2). It shows the effects due to the square section of the external capillary. In the plane (x,y), the shape of the plug is not anymore circular (Fig. 2 on the right) and the external flow circulates only by the corners of the microchannel.

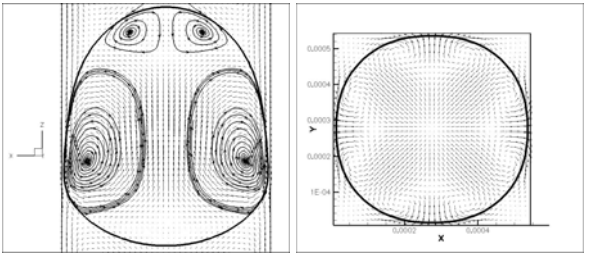

Fig. 2. Example of the use of droplets as micromixers (shape of the droplets in different slices, velocity field in the droplet frame of reference and few streamlines). Left: shape and velocity field in the plane(x,z); right: view of the plug in the plane(x,y).

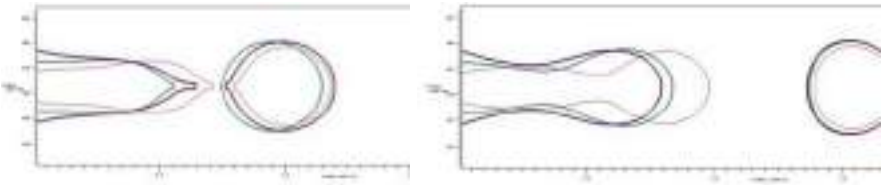

Fig. 3. Relation between the section of the injector and the volume of the created droplet: representation of three different configurations

4.3 Discussions

In [8], it is proposed an approach based on the linear theory of stability to introduce a stability criterion. Thanks to this one, the flow regime (jet or droplet) can be predicted knowing the dimension of the external capillary and the properties of the two fluids. In addition, the stability length corresponding to the length of the jet just before the creation of the microdroplet can be computed. However, the study is based on the knowledge of the steady state and the perturbation of this one. In order to be as realistic as possible, it could be necessary to take into account the radius of the internal injector. In Fig. 3, three representations of the flow are plotted. The properties of the two fluids are defined in subsection 4.2. The external capillary is about $650\mu m$ of section and the diameter of the injector is respectively $60\mu m$, $120\mu m$ and $273\mu m$. These numerical results show that there exists a stability area since the stability length is approximately the same in each case. Generally, for this kind of configuration, the jet tends towards the steady state solution before the break-up. In addition, the smallest injector creates the smallest droplet that it is explained by the higher velocity and the fact that the stability length is a little bit higher.

5 The Particular Case of a T-Junction

The analysis of the break-up of a diphasic jet shows that the Level Set method manages well the topological changes. At the stage, the study of the micro-

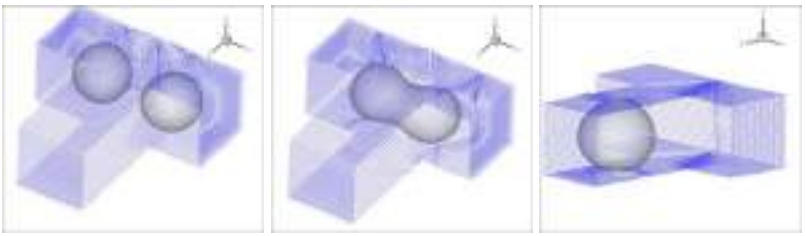

Fig. 4. Coalescence of two microdroplets in a T-junction

droplets is expanded to an other configuration frequently employed for bench by scientists: the coalescence of the droplets. The technical points (meshing generation and implementation) are presented in [8]. In a T-junction (Fig.4), the continuous phase is injected by two branches of the T and is ejected by the third one.

6 Conclusion

The Level Set method proposed by Osher and Sethian is used in order to follow the interface between two flows such that their movement is mostly governed by the pressure gradient and the surface tension. This method gives results in good agreement with the experiments because the main quantities like the curvature and the unit normal are well computed. This study allows to analyze the breaking jet phenomenon and gives access to quantities like the pressure and the velocity of the droplet when it is created. We take a special care on the representation of the internal capillary employed as an injector and we can in this way compared the volumes of the microdroplets for several radius of injectors. First results concerning the coalescence of two microdroplets in a T-junction are proposed.

References

1. Brackbill, J.U., Kothe, D.B., Zemach, C.: A Continuum Method for Modeling Surface Tension. Journal of Computational Physics 100(2) (1992)
2. Galusinski, C., Vigneaux, P.: Level-Set method and stability condition for curvature-driven flows. C. R. Acad. Sci. Paris, Ser. I 344(11), 703–708 (2007)
3. Guillot, P., Colin, A.: Stability of jet in confined pressure-driven biphasic flows at low Reynolds number. Phys. Rev. Lett. 99, 104502 (2007)
4. Guillot, P., Panizza, P., Salmon, J.-B., Joanicot, M., Colin, A., Bruneau, C.-H., Colin, T.: Viscosimeter on a Microfluidic Chip. Langmuir 22 (2006)
5. Jiang, G.S., Shu, C.W.: Efficient Implementation of Weighted ENO Schemes. Journal of Computational Physics 126 (1996)
6. Sarrazin, F., Prat, L., Casamatta, G., Joanicot, M., Gourdon, C., Cristobal, G.: Micro-drops approach in micro-reactors: mixing characterisation, La Houille Blanche (2006)
7. Sussman, M., Smereka, P., Osher, S.: A level set approach for computing solutions to incompressible two-phase flow. J. Comput. Phys. 114, 146–159 (1994)
8. Tancogne, S.: Calcul numérique et Stabilité d'écoulements diphasiques tridimensionnels en Microfluidique. Thése de Doctorat - Univ. Bordeaux 1 (2007)

Optimization of Ribbed Microchannel Heat Sink Using Surrogate Analysis

Afzal Husain[1] and Kwang-Yong Kim[2]

[1] Inha University, Incheon, Korea
afzal19@inhaian.net

[2] Inha University, Incheon, Korea
kykim@inha.ac.kr

Abstract. The present study deals with three-dimensional fluid flow and heat transfer in a ribbed microchannel heat sink. The design variables affecting the heat transfer performance have been studied in the light of thermal resistance and pumping power and surrogate-based optimization is performed using radial basis neural network. The decrease of the thermal resistance is observed with increase of mass flow rate at the expense of higher pumping power due to rib structures. The difference between thermal resistance of ribbed microchannel and smooth microchannel reduces with increase of pumping power. The ratio of the rib width-to-height is found to be more sensitive than the other two design variables related to rib height, pitch and microchannel width.

1 Introduction

The increased circuit density in ultra large-scale integration (ULSI) technologies and device miniaturization have motivated many researchers to utilize alternative cooling technologies. Moreover, limitations of space in micro-devices lead to the new designs for minichannel heat sinks. Advanced micro- and nano-fabrication processes have yielded microchannels having a high surface area to volume ratio and opened the doors for implementing new designs in silicon based micro cooling systems. In the past two decades various studies have been performed comprising experimental [KMII98], analytical [KHGJ4] and numerical [WJ03] techniques. The focus of most of these studies has been development of the mathematical model and optimization of the design. The increasing demand for higher heat flux removal motivated the researchers to look for alternative designs to enhance the performance of the microchannel heat sinks. In this line Wei and Joshi [LG05] optimized the stacked microchannel heat sink and suggested that shorter the length of stacked microchannel smaller the thermal resistance. Wei et al. [WJL07] studied heat transfer enhancement with a dimpled surface for steady, laminar flow in a rectangular microchannel. Cheng [C07] investigated two-layer stacked microchannel heat sink with enhanced mixing passive microstructures. These microstructures on the channel wall led to higher heat transfer rate and lower thermal resistance.

These studies have motivated the application of micro-rib in microchannel heat sink for heat transfer augmentation in microcooling devices.

In the present work ribbed microchannel heat sink has been optimized for minimum thermal resistance and pumping power. The fluid flow is assumed to be steady, incompressible, and laminar and a finite volume general purpose Navier-Stoke solver is used to carry out the numerical analysis. Radial Basis Neural Network (RBNN) [O96] is used to construct the response function to search optimum design through sequential quadratic programming (SQP)in MALTAB [MAT04] on the basis of discrete numerical analysis.

2 Problem Description and Numerical Analysis

A rectangular microchannel heat sink model studied by Husain and Kim [HK08a] has been taken to optimize using RBNN. The staggered micro-ribs are placed on both side walls of the microchannel which comprise large part of the channel surface area subjected to wall heat transfer as shown In Fig. 1. The governing equations for steady, incompressible and laminar flow and conjugate heat transfer in the microchannel are solved at constant fluid (water) properties using commercial code CFX 11.0 [CFX06]. A uniform heat flux is applied at the bottom of the microchannel heat sink to elucidate the effect of rib structures on thermal resistance and pumping power required to drive the coolant.

A single microchannel has been taken to study utilizing the symmetry of the parallel channels. The full length of the single microchannel has been taken to study conjugate heat transfer under practical boundary conditions for the heat flux at the fluid-solid interface as discussed by Husain and Kim [HK08a]. No-slip condition is applied at the interior walls of the channel, i.e. $u = 0$. The thermal conditions in the z-direction are $-k\frac{\partial T_s}{\partial z} = q$ at $z = 0$ and $\frac{\partial T_s}{\partial z} = 0$ at $z = l_z$. Three design variables, $h_r/w_c(= \theta)$, $w_r/h_r(= \phi)$, and $w_c/p_r(= \eta)$,and two performance functions, overall thermal resistance and pumping power to drive the coolant, are employed to study the microchannel heat sink. The overall thermal resistance is defined as:

$$R_{th} = \frac{\Delta T_{max}}{qA_s} \tag{1}$$

where ΔT_{max} is the maximum temperature rise in the heat. The pumping power required to drive the fluid through microchannel heat sink can be evaluated as:

$$P = Q_c \Delta P. \tag{2}$$

where Q_c is defined as the flow-rate through the microchannels and ΔP is the pressure drop. These performance functions are calculated by solving Navier-Stokes and energy equations at specified design points.

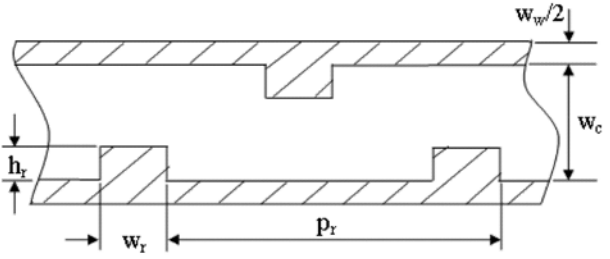

Fig. 1. Schematic of rib structure

3 Optimization Procedure

A Three-level fractional factorial design is used to select the design points in the design range $\theta = 0.3{-}0.5, \phi = 0.5{-}2.0, \eta = 0.056{-}0.112$. The design space is selected through some preliminary calculations within the geometric and flow constraints. The performance functions, thermal resistance and pumping power are evaluated at these design points through numerical analysis. A single objective function, f is formed combining the two performance functions applying a weighting factor, wf as:

$$f = R_{th} + wf.P \tag{3}$$

The composite objective function f is then optimized using the RBNN. The optimization procedure and the construction of the surrogate model RBNN is explained in detail in the previous study by Husain and Kim [HK08b].

4 Results and Discussion

The grid independence is carried out and a grid of $501 \times 45 \times 61$ is used for a typical case of design variables $\theta = 0.3$, $\phi = 1.25$, and $\eta = 0.084$. The validation of the numerical scheme is carried out in a previous study by Husain and Kim [HK08a]. The ribbed channel shows lower temperature rise as compared to smooth microchannel. The ribbed microchannel heat sink has been analyzed and compared with the smooth microchannel heat sink in terms of thermal resistance and pumping power as shown in Fig. 2. The thermal resistance of the ribbed microchannel decreases at a faster rate than the smooth microchannel with increase of mass flow rate as shown in Fig. 2(a). On the other hand, pumping power of the ribbed microchannel increases at much faster rate than smooth microchannel. Thermal resistance of the ribbed microchannel is generally higher than smooth microchannel at low pumping power however the thermal resistance of the ribbed microchannel heat sink decreases with increase of pumping power at a faster rate than smooth microchannel and after a certain pumping power ribbed microchannel

heat sink offers lower thermal resistance than smooth microchannel heat sink at the same pumping power as shown in Fig. 2(b). Therefore, the application of the rib structures in a microchannel strongly depends upon the pumping source available to drive the coolant.

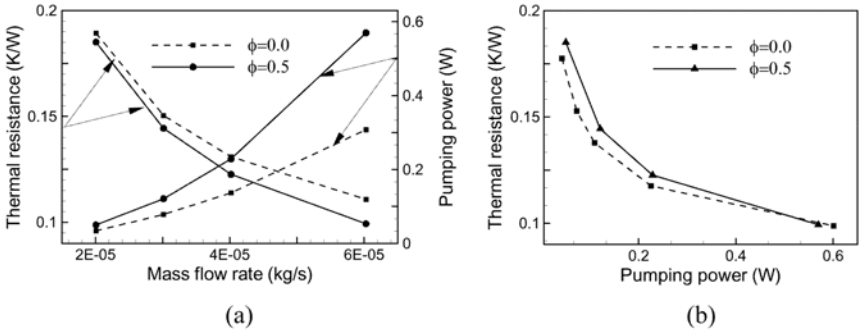

Fig. 2. (a) Variations of thermal resistance and pumping power with mass flow rate in smooth ($\phi = 0.0$) and ribbed microchannels ($\theta = 0.3$, $\phi = 0.5$ and $\eta = 0.112$) (b) Variations of thermal resistance with pumping power in smooth ($\phi = 0.0$) and ribbed microchannels ($\theta = 0.3$, $\phi = 0.5$ and $\eta = 0.112$)

The surrogate model, RBNN is trained for the specified error goal and assigned spread constant and optimization is performed for the composite objective function with the help of SQP in MATLAB. Fig 3 shows the variation of the optimum design variables and objective functions (composite objective function f, thermal resistance Rth, and pumping power P) with the change in weighting factor. Objective function f is optimized with different weighting factors and the values of thermal resistance and pumping power have been found at the corresponding set of optimum design points with the help of RBNN. The separate RBNNs are constructed for thermal resistance and pumping power. As the contribution of the pumping power increases to the objective function with increase of weighting factor, the values of design variables corresponding to optimum objective function decreases due to the adverse effect of design variables on the pumping power.

The contribution of an independent design variable to the variance of the objective function is checked by sensitivity analysis by varying the design variables around the optimum values as shown in Fig. 4. Each design variable is varied ∓ 20 percent from the optimum value while keeping the other variables fixed. The objective function values at these sets of design variables are calculated using constructed RBNN model. The objective function increases sharply with a change in ϕ while keeping the other variables fixed at optimum values. On the other hand, any change of θ or η has a less effect on the objective function for the fixed values of other two variables. It can be seen that the optimal design is highly sensitive to ϕ as compared to θ and η near

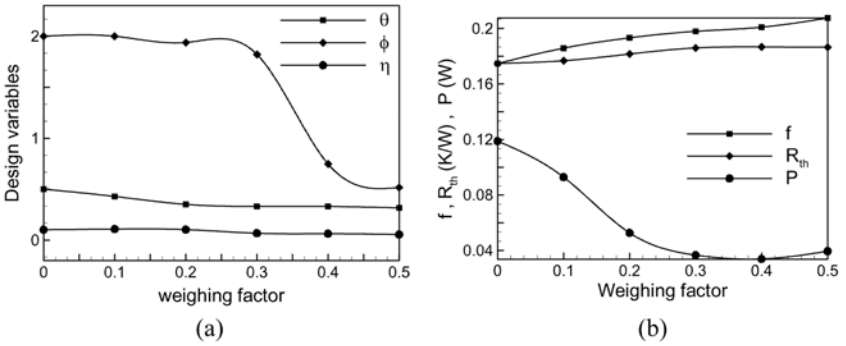

Fig. 3. Variation of optimum point (a) design variables and (b) objective functions, with the weighting factor

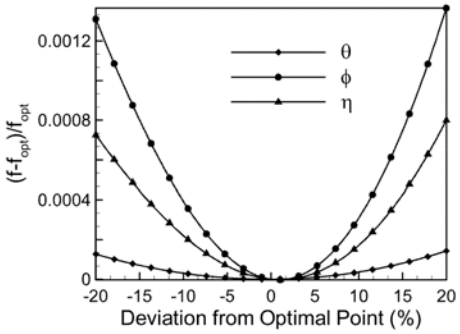

Fig. 4. Sensitivity analysis of ribbed microchannel

the optimum point. Therefore, the design variable θ and η can be suitably adjusted to obtain minimum thermal resistance under any design constraint.

5 Conclusion

The application of the staggered-ribs in the microchannel heat sink has been explored with the help of numerical analysis. Three design variables related to micro-rib height, width, pitch and channel width are selected to analyze the rib effectiveness and their effect on thermal resistance and pumping power. It is observed that the performance of the microchannel heat sink can be increased significantly with the application of rib. The rib microstructures decrease thermal resistance at the expense of much higher pumping power than the smooth microchannel based on mass flow rate analysis. The pumping

power analysis shows that at higher pumping power ribbed microchannel offers lower thermal resistance than smooth microchannel. Therefore, application of the rib structures in microchannel heat sink strongly depends on the pumping source. The design variable rib width-to-height ratio is found to be more sensitive than rib width-to-height ratio and channel width-to-pitch of the rib ratio near the optimum design.

References

[KMII98] Kawano, K., Minakami, K., Iwasaki, H., Ishizuka, M.: Development of Micro Channels Heat Exchanging. In: Nelson Jr., R.A., Swanson, L.W., Bianchi, M.V.A., Camci, C. (eds.) Application of Heat Transfer in Equipment Systems, and Education, ASME, New York, HTD-361-3/PID-3, pp. 173–180 (1998)

[KHGJ4] Knight, R.W., Hall, D.J., Goodling, J.S., Jaeger, R.C.: Heat Sink Optimization with Application to Microchannels. IEEE Trans. Compon., Hybrids, Manufact. Technol. 15(5), 832–842 (1992)

[WJ03] Wei, X., Joshi, Y.: Optimization Study of Stacked Micro-channel Heat Sinks for Micro-electronic Cooling. IEEE Trans. Compon. Packag. Technol. 26(1), 55–61 (2003)

[LG05] Liu, D., Garimella, S.V.: Analysis and Optimization of the Thermal Performance of Microchannel Heat Sinks. International Journal for numerical methods in Heat and Fluid flow 15(1), 7–26 (2005)

[WJL07] Wei, X.J., Joshi, Y.K., Ligrani, P.M.: Numerical Simulation of Laminar Flow and Heat Transfer Inside a Microchannel With One Dimpled Surface. Journal of Electronic Packaging 129, 63–70 (2007)

[C07] Cheng, Y.J.: Numerical Simulation of stacked microchannel heat sink with mixing-enhanced passive structure. Int. Comm. Heat Mass Trans. 34, 295–303 (2007)

[O96] Orr, M.J.L.: Introduction to radial basis neural networks, Center for cognitive science, Edinburgh University, Scotland, UK (1996), `http://anc.ed.ac.uk/RBNN/`

[MAT04] MATLAB®, The language of technical computing, Release 14. The Math Works Inc (2004)

[HK08a] Husain, A., Kim, K.Y.: Microchannel heat sink with designed roughness: analysis and optimization, Journal of Thermophysics and Heat Transfer (to be published) (2008)

[CFX06] CFX-11.0, Solver Theory, ANSYS (2006)

[HK08b] Husain, A., Kim, K.Y.: Shape Optimization of Micro-channel Heat sink for Micro Electronic Cooling. IEEE Trans. Compon. Packag. Technol. 31(2), 322–330 (2008)

Part 29
Micro/Nano Fluid Mechanics 2

“*This page left intentionally blank.*”

Conformations of PMMA Thin Films on an Au (111) Substrate: Chain-Length and Tacticity Effects

Ming-Liang Liao[1,*], Shin-Pon Ju[2], Ching-Ho Cheng[2], Wen-Jay Lee[2], and Jee-Gong Chang[3]

[1] Department of Aircraft Engineering, Air Force Institute of Technology, Taiwan, R.O.C.
minsliao@gmail.com
[2] Department of Mechanical and Electro-Mechanical Engineering, Center for Nanoscience and Nanotechnology, National Sun-Yat-Sen University, Taiwan, R.O.C.
[3] National Center for High-Performance Computing, Taiwan, R.O.C.

Abstract. Chain-length and tacticity effects on conformations of poly(methyl methacrylate) (PMMA) thin films on an Au (111) substrate at room temperature were investigated by means of molecular dynamics (MD) simulations. The MMA oligomers were found to exhibit a flattened conformation parallel to the Au substrate in the contact region and a little flattened conformation in the surface region for both the short-chain and the long-chain thin films. The flattened conformation remains in the bulk region for the long-chain case, but it is not present in the bulk region of the short-chain film.

1 Introduction

Conformations of poly(methyl methacrylate) (PMMA) thin films on a solid substrate are an interesting issue of researchers. In a recent study, Zhang et al. [Zha02] employed reflection-absorption infra-red and surface-enhanced Raman scattering spectroscopy to examine the orientation of the bulk and the interface of an atactic PMMA thin film dip-coated onto a silver-particle deposited substrate.

Regarding the numerical studies, the molecular dynamics (MD) simulation technology is a powerful numerical method. It can offer detailed interfacial behavior, at an atomic level, of a polymer thin film on a solid substrate. Recently, Lu and Tung [Lu05] have utilized an MD simulation technique to examine the tacticity effect on the free volume morphology of PMMA membranes.

In this paper we investigated conformations of an MMA-oligomer thin film on an Au (111) substrate. The influence of the chain length and tacticity of MMA oligomers on the conformations was examined.

2 Simulation Model

The MD simulation model used in the present research consists of an MMA-oligomer thin film and an Au substrate on which the MMA oligomers are deposited. There are three different groups of interactions existing in the simulation

* Corresponding author.

model, including 1) the intra- and intermolecular interactions of MMA oligomers; 2) the interaction of Au atoms; 3) the interaction between the MMA oligomers and the Au atoms. In the current MD simulations, three different potentials were employed to model the three groups of interactions. First, the ENCAD (Energy Calculations and Dynamics) potential [Lev95] was chosen to model the atomic interactions between the intra- and intermolecular interactions of the MMA oligomers. The interactions between the Au atoms of the substrate were described by the tight-binding potential [Cle93], whereas the Dreiding force field [May90] was used to model the interactions between the MMA oligomers and the Au atoms.

The MMA-oligomer thin film was assumed to be made of MMA oligomers having m repeat units (i.e., with a chain length of m). Three kinds of MMA-oligomer thin films with m = 5 and 20, respectively, were considered in the current study to examine chain-length effects on the conformations of the thin films. A total number of 1200 repeat units of the MMA monomer were used for each kind of the MMA-oligomer thin film. For investigation of tacticity effects on the conformations, three types of MMA-oligomer thin films were examined. They were supposed to be made of the three stereoisomers of PMMA (i.e., the isotactic, syndiotactic, and atactic isomers), respectively. The substrate consists of 8976 Au atoms and has a length of 110 Å, a width of 98 Å, and a thickness of 14 Å. Periodic boundary conditions in the in-plane (x-y) directions were imposed in the present simulations.

At the beginning of the MD simulations, velocities of all atoms were randomly assigned according to a Maxwell distribution, and the velocity-rescaling thermostat [Hai92] was used to maintain the Au substrate at the target temperature. The thermostat was implemented by assigning the top five layers of the Au substrate as the thermal control layers, with the bottom layer of the Au substrate being as the fixed layer. The time integration of Newton's equations of motion was carried out with the aid of the Verlet algorithm [Hai92] to obtain the new velocity and position of each atom. A time step of 10^{-15} s (1 fs) was selected during the time integration. In addition, a canonical (NVT) ensemble was employed in the MD simulations. The simulations lasted for 500 ps at the target temperature and data from the last 50 ps were collected and averaged to examine the simulation results.

3 Results and Discussion

To examine conformations of the MMA-oligomer thin films, mean square radii of gyration of the MMA oligomers along the film thickness were utilized. For observation of mean square radii of gyration of the MMA oligomers along the film thickness, the thin film was split into several layers parallel to the Au substrate with a layer thickness of 5 Å.

Through-thickness variations in the in-plane and the transverse components of the mean square radii of gyration for the short-chain MMA-oligomer thin films (with m = 5) of different tacticity are shown in Fig. 1. It should be noted that all the values in the figure have been normalized with respect to the mean square radius of gyration of the corresponding thin film. As can be seen, there are five pairs of data for each case of the figure. The first pair is in the contact region, the middle two pairs are in the bulk region, and the last two pairs are in the surface region.

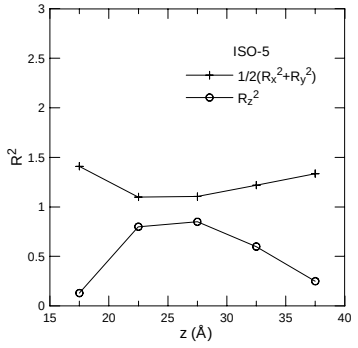

(a) isotactic

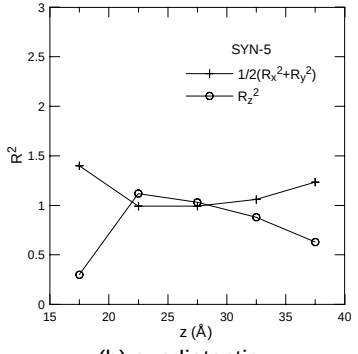

(b) syndiotactic

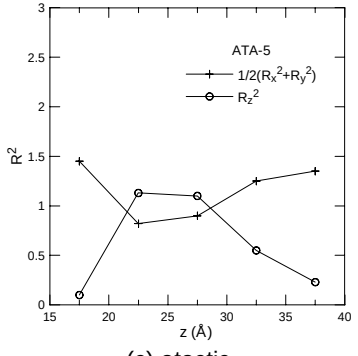

(c) atactic

Fig. 1 Components of mean square radii of gyration for the short-chain thin films with m=5 of different tacticity; (a) isotactic, (b) syndiotactic, (c) atactic

It is evident that the in-plane component of the mean square radius of gyration in the contact region is much larger than the transverse component, regardless of tacticity of the MMA-oligomer thin films. This indicates that the MMA oligomers in the contact region have a conformation that is compressed in the transverse (z) direction and elongated in the in-plane (x-y) direction. Namely, they exhibit a

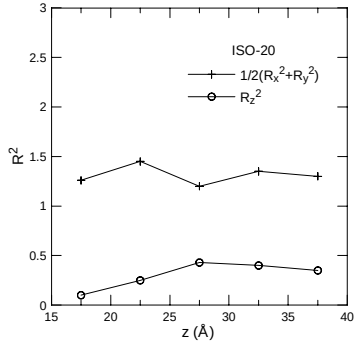

(a) isotactic

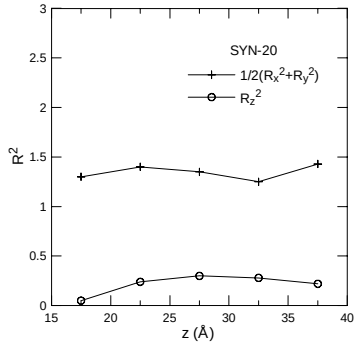

(b) syndiotactic

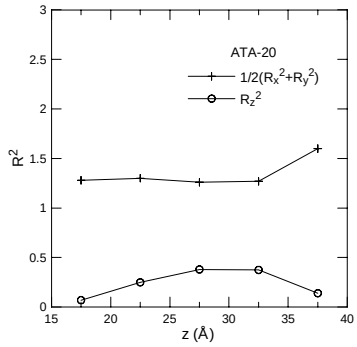

(c) atactic

Fig. 2. Components of mean square radii of gyration for the long-chain thin films with *m*=20 of different tacticity; (a) isotactic, (b) syndiotactic, (c) atactic

flattened conformation parallel to the Au substrate. In the bulk region, the MMA oligomers have nearly equal in-plane and transverse components of the mean square radii of gyration, irrespective of tacticity of the thin film. This implies that the flattening conformation in the contact region is not present in the bulk region and the MMA oligomers have a conformation resembling that of bulk PMMA, in

which the PMMA molecules orientate in a random manner. The MMA oligomers in the surface region were found to have the in-plane components of mean square radii of gyration greater than the transverse components. This signifies that the oligomers in the surface region also have a quite flattened conformation. However, as can be seen from Fig. 1, the flattened conformation of the surface oligomers is less parallel to the Au substrate as compared to that for the contact region. The conformations attained in the present study for the short-chain MMA-oligomer thin films were found to much resemble those of an MMA-monomer thin film deposited on an Au (111) substrate, which was examined in our previous research [Ju07]. This may suggest that a short-chain MMA-oligomer thin film behaves like an MMA-monomer thin film when they are deposited on an Au substrate individually.

Fig. 2 shows the in-plane and the transverse components of the mean square radii of gyration for the long-chain MMA-oligomer thin films (with m = 20) of different tacticity. As in the short-chain case, the in-plane component of the mean square radius of gyration in the contact region was noticed to be much greater than the transverse component, regardless of tacticity of the thin film. The MMA oligomers in the contact region hence have a flattened conformation parallel to the Au substrate.

As opposite to those for the short-chain case (Fig. 1), the in-plane component of the mean square radius of gyration for the MMA oligomers in the bulk region of the long-chain thin film is also much greater than the transverse component. This indicates that the MMA oligomers in the bulk region of the long-chain thin film also have a flattened conformation parallel to the Au substrate, as against the random orientation of the oligomers in the bulk region of the short-chain thin film. The flattened conformation is ascribed to the difficulty for the long molecular chain to orientate randomly in the bulk region of the long-chain thin film. It was noticed that the flattened conformation in the bulk region is similar to that observed in the bulk region of a PMMA thin film deposited on a silver substrate [Zha02].

The MMA oligomers in the surface region of the long-chain thin film was also found to have a quite flattened conformation but less parallel to the Au substrate, as can be seen from the comparison of the in-plane and the transverse components of the mean square radii of gyration for the MMA oligomers in the surface region of the long-chain thin film. From results of Fig. 2, it should be noted that tacticity of the long-chain thin film also has unclear effects on the conformations of the MMA oligomers.

4 Conclusions

From the results of the present simulations, it is clear that the MMA oligomers were observed to have a flattened conformation parallel to the Au substrate in the contact region and a little flattened conformation in the surface region for both the short-chain and the long-chain thin films. The flattened conformation prevails in the bulk region of the long-chain thin films, but it does not appear in the bulk region of the short-chain thin film, in which the MMA oligomers have almost equal

mean square radii of gyration in the in-plane as well as the transverse directions and thus have a random orientated conformation—a characteristic resembling bulk MMA.

Acknowledgments

The authors gratefully acknowledge the support provided to this research by the National Science Council of the Republic of China under Grant No. NSC-95-2221-E-110-070 and NSC-96-2221-E-344-003.

References

[Cle93] Cleri, F., Rosato, V.: Tight-binding potentials for transition metals and alloys. Phys. Rev. B 48, 22–33 (1993)

[Hai92] Haile, J.M.: Molecular Dynamics Simulation. Wiley–Interscience, New York (1992)

[Ju07] Ju, S.P., Lee, W.J., Cheng, C.H.: Molecular dynamics investigation into the effect of temperature on the structure and properties of methyl methacrylate thin films on an Au (111) surface. Langmuir 23, 8067–8073 (2007)

[Lev95] Levitt, M., Hirshberg, M., Sharon, R., Daggett, V.: Potential energy function and parameters for simulations of the molecular dynamics of proteins and nucleic acids in solution. Comput. Phys. Commun. 91, 215–231 (1995)

[Lu05] Lu, K.T., Tung, K.L.: Molecular dynamics simulation study of the effect of PMMA tacticity on free volume morphology in membranes. Korean J. Chem. Eng. 22, 512–520 (2005)

[May90] Mayo, S.L., Olafson, B.D., Goddard III, W.A.: DREIDING: a generic force field for molecular simulations. J. Phys. Chem. 94, 8897–8909 (1990)

[Zha02] Zhang, J.M., Zhang, D.H., Shen, D.: Orientation study of atactic poly (methyl methacrylate) thin film by SERS and RAIR spectra. Macromolecules 35, 5140–5144 (2002)

Part 30
Multiphase Flow 1

“*This page left intentionally blank.*”

Numerical Method for Flows of Arbitrary Substance in Arbitrary Conditions

Satoru Yamamoto and Takashi Furusawa

Dept. of Computer and Mathematical Sciences, Tohoku University,
Sendai 980-8579, Japan
yamamoto@caero.mech.tohoku.ac.jp

1 Introduction

A numerical method which can be applied to the simulation of flows of arbitrary substance in arbitrary conditions is presented. This method is based on the preconditioning method proposed by the authors [1]. The preconditioning method can enable compressible flow solvers to calculate incompressible flow problems. Natural convection can be also calculated by the preconditioning method without the Boussinesq approximation.

Substances have their own thermophysical properties. Those properties are changed according to bulk conditions. Most of the existing flow solvers assuming ideal gas or incompressible fluid cannot calculate such real flow problems. We should introduce additional mathematical models approximating those thermophysical properties to simulate flows of arbitrary substance in arbitrary conditions accurately. We have calculated carbon-dioxide flows in a square cavity and in a pipe using the preconditioning method [2] and Peng-Robinson equation of state. All of numerical approaches we know applying to flows of arbitrary substance seem to employ a flow solver and an equation of state specialized to each flow of a substance. It means that the equation of state should be changed if the substance is changed. We guess that the development of the new code spends a lot of times and costs.

In this paper, we employ a database for thermophysical properties named PROPATH [3] developed by Kyushu University. In PROPATH, thermophysical models for 48 substances are programmed in wide-range pressure and temperature conditions. All of these models have been verified and validated as the most accurate model in chemical engineering. For examples, equation of state(EOS) for carbon-dioxide employed in PROPATH was standardized by International Union of Pure and Applied Chemistry(IUPAC) [4]. As EOS for water, a unified model at the International Association for the Properties of Water and Steam(IAPWS) IF-97 [5] is employed. PROPATH can cover all the states except for solid, that is gas, liquid and supercritical fluid. Each model is defined as a function of pressure and temperature. All the thermophysical properties used in the present computational code are referred

from PROPATH as a function. The most distinguished point of the present work is the coupling between the preconditioning method and PROPATH. All of thermophysical properties such as density, thermal conductivity, specific heats, and molecular viscosity in the code are replaced by the functions. Also all the derivative functions such as those of density and enthalpy with respect to temperature and pressure are also calculated by the combinations among functions in PROPATH. As one of special features in PROPATH, the name of each function is specified as a same name in all substances. The set of functions for each substance is contained in one library file. Therefore, the working substance can be easily changed to a different substance only if the library file is changed to that for the different substance when the computational code is compiled with the library file, *.lib for the substance.

The present method is applied to flows of arbitrary substance in several conditions to show the capability and the extensity of the method. As gas conditions at atmospheric pressure and temperature, natural convective problems of carbon-dioxide, water vapor, methane, and helium in gas conditions, are first calculated and compared with each other. As a special liquid condition at atmospheric pressure and temperature, natural convection assuming cold water near 4°C is calculated and compared with the experimental and numerical results. As a two-phase flow condition between supercritical fluid and subcritical liquid, a mixing flow of supercritical water and water liquid in a T-shaped channel is calculated and compared with flows in different conditions.

2 Numerical Methods

The present preconditioning method is applied to the 2D compressible Navier-Stokes equations in curvilinear coordinates. The detail expression was presented in Ref [1]. The numerical flux is derived as a preconditioned flux-vector splitting form. This form is further extended to an implicit scheme as the preconditioned LU-SGS scheme.

All the thermophysical models programmed in the present computational code are referred from PROPATH as an external function. Thermophysical properties for 48 substances are prepared in PROPATH. Most of those models are approximated by equations derived as a polynomial from the existing theoretical equations or experimental data.

As a typical model, that for carbon-dioxide is only explained herein. Equation of state(EOS) for carbon-dioxide was standardized by International Union of Pure and Applied Chemistry(IUPAC) [4]. The EOS model is defined by

$$p = \rho RT[1 + \omega \sum_{i=0}^{9} \sum_{j=0}^{J_i} a_{ij}(\tau - 1)^j(\omega - 1)^i] \tag{1}$$

where $\omega = \rho/\rho^*$ and $\tau = T^*/T$. The coefficients a_{ij} and the number J_i are defined in Ref. [4]. Actually in this case, $\rho^* = 468[\mathrm{kg/m^3}]$ and $T^* = 304.21[\mathrm{K}]$.

PROPATH can calculate thermophysical properties for 48 substances accurately. Thermophysical properties such as specific heat at constant volume and that at constant pressure can be derived using Eq.(1).

As another substance, EOS for water was standardized by International Association for the Properties of Water and Steam(IAPWS) IF-97 [5].

The molecular viscosity and the thermal conductivity for carbon-dioxide and water are also defined by a polynomial equation.

3 Numerical Examples

As the first numerical example assuming a gas condition at atmospheric temperature and pressure, natural convective problems in a square cavity for different substances are calculated and those calculated results are compared with each other. The working substances are carbon-dioxide, water vapor, methane, and helium. The length of the boundaries is fixed to 0.020[m]. The bulk pressure is 0.104[MPa]. The temperature at the left and the right boundaries are 420[K] and 380[K], respectively. In these conditions, all cases result in natural convection of gas.

Figure 1 shows the calculated temperature contours for four substances. Almost the same distributions are obtained in the cases of carbon-dioxide, water vapor, and methane. Exactly, the Rayleigh numbers in these cases are slightly different from each other, but the numbers are close to $Ra = 10^4$.

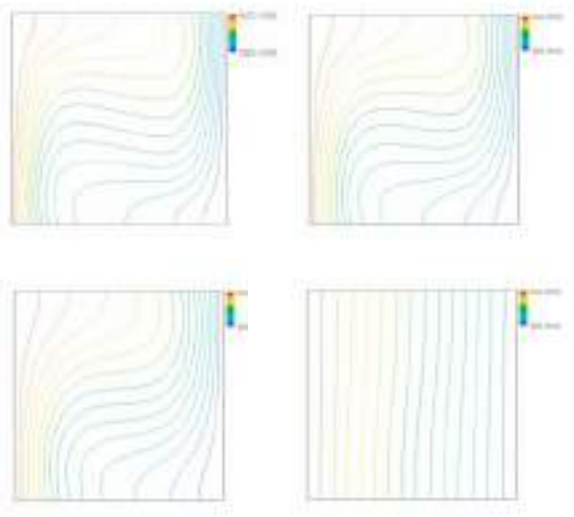

Fig. 1. Calculated temperature contours of natural convection in a square cavity(atmospheric gas conditions) (Upper left: carbon-dioxide, upper right: water vapor, lower left: methane, lower right: helium)

It is found that the gradient of temperature contours near the center of the convection is slightly different from each other.

On the other hand in the case of helium, the distribution is quite different from other three substances. This result suggests that the thermal conductivity dominates the flow field significantly compared with the convection. The Rayleigh number of the present case for helium results in a very lower number than those in other three cases.

As a liquid condition at atmospheric temperature and pressure, natural convection assuming cold water near 4°C is calculated. Generally, water liquid in atmospheric conditions may be calculated as an incompressible fluid without compressibility. However, water has trivial compressibility exactly even though it is liquid. Especially, an anomalous property of cold water near 4°C has been reported by Banaszek et al. [6]. It is due to the structure of the molecular combination between hydrogen and oxygen atoms. The density of water liquid has a maximum peak value at 4°C. As boundary conditions, the temperatures at the left and the right boundaries are fixed to 10°C and 0°C. The bulk pressure is 0.104[MPa].

Figure 2(a) shows the calculated temperature and the corresponding velocity vectors. The temperature distributions in Fig.2(a) indicate that the water liquid near 4°C induces a gravitational flow and the flow separates toward left and right directions near the bottom boundary. Buoyancy effect usually induces an uprising flow when the fluid is heated. If water is cooled locally, the local water moves downward also due to the gravity force. However in this case, water liquid located near the corner at the right and bottom boundaries moves upward, although the temperature at the right boundary is 0°C which is colder than that at the left boundary. An additional smaller vortex near the corner is observed as well as a main convective vortex. This flow property may be due to a gravitational flow where the temperature is near 4°C and the water has a little higher density.

Figure 2(b) shows the calculated vertical velocities on the horizontal centerline compared with the experimental and the numerical results reported by Banaszek et al. [6]. Two computational grids which have 61x61 and 101x101

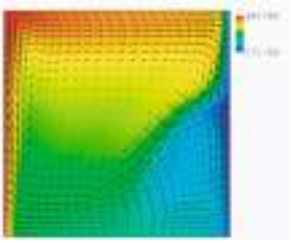

Fig. 2(a). Calculated velocity vectors and temperature contours

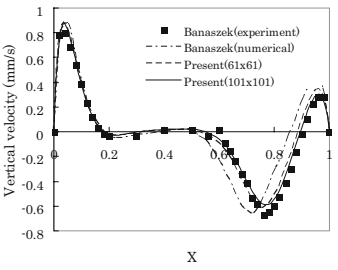

Fig. 2(b). Calculated velocity distributions at the horizontal centerline

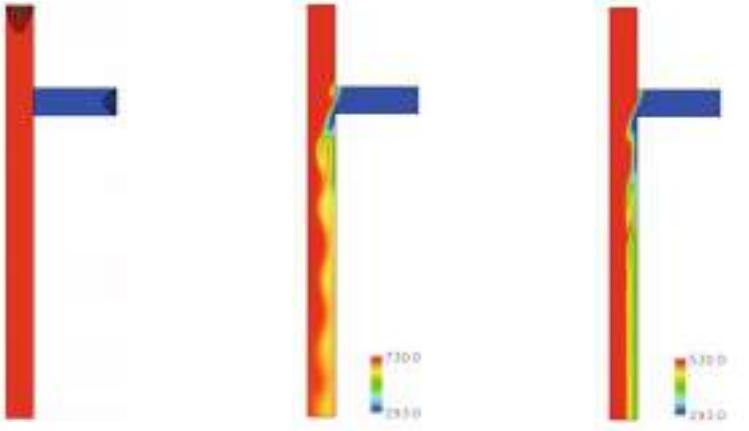

(a) Flow schematic (b) Supercritical inlet (c) Subcritical inlet

Fig. 3. Schematic and calculated temperature contours

grid points are used in the present calculations. Both calculated values obtained by the present method are in better agreement with the experiments than those calculated by Banaszek.

As the last case, the calculation of a two-phase flow of supercritical water and water liquid through a T-shaped channel is introduced. This flow problem is currently one of topics for chemical engineers to make nano particles in supercritical water. The flow schematic is shown in Fig.3(a). A laminar flow without the gravity force is assumed. The longitudinal channel is a main channel and the lateral channel is a sub-channel connected to the main channel. Inlet temperature and the pressure of the main channel are fixed to 730[K] and 30[MPa]. These values indicate that the flow through the main channel is in a supercritical condition. Inlet temperature of the sub-channel is 293[K] and the pressure is the same value with that of the main channel. The flow through the sub-channel is in a liquid condition. Therefore, the supercritical water through the main channel is to be interacted with the water liquid from the sub-channel.

Figure 3(b) shows the calculated temperature contours. The water liquid encounters the supercritical water at the T-junction and the two-phase flow streams downward. The flow has a periodical oscillation originally generated near the T-junction. In the mixing region, the critical point between the supercritical water and the water liquid is certainly located. At the transitional region, thermophysical properties change rapidly.

On the other hand, Fig. 3(c) shows the calculated temperature contours of the flow in a liquid condition. The inlet temperature of the main channel is reduced to 530[K]. As compared with Fig. 3(b), the temperature shown in Fig.3(c) has no oscillated pattern. The difference between Fig.3(b) and 3(c) may be due to the density difference in the two-phase flow. In the case of

Fig. 3(b), the density changes rapidly at the critical point and the magnitude is quite large. Also we obtain that the specific heat has relatively high and peak values at the critical point.

4 Conclusion

The preconditioning method developed by the authors was applied to a new method coupled with the database of thermophysical properties, PROPATH, and the present method could calculate flows assuming several substances in several conditions. In the case of natural convection assuming cold water near 4°C in atmospheric conditions, the calculated results were in good agreement with the experimental data reported by Banaszek et al. and the anomalous property observed in the cold water could be accurately simulated. In the case of the T-shaped channel, a two-phase flow between supercritical water and water liquid was successfully captured by the present method. Rapid changes for thermal properties such as density, thermal conductivity, and the specific heat at the critical region could be also calculated without any numerical problems.

References

1. Yamamoto, S.: Preconditioning Method for Condensate Fluid and Solid Coupling Problems in General Curvilinear Coordinates. J. Comp. Phys. 207, 240–260 (2005)
2. Yamamoto, S., Toratani, M., Sasao, Y.: Preconditioning Method Applied to Near-Critical Carbon-Dioxide Flows in Micro-Channel. JSME Int. J., Series B 48, 532–539 (2005)
3. A Program Package for Thermophysical Properties of Fluids(PROPATH), Ver.12.1, PROPATH GROUP
4. Angus, S., et al.: International Thermodynamic Table of the Fluid State-3 Carbon Dioxide, IUPAC, vol. 3 (1976)
5. Japan Society of Mechanical Engineers, 1999 JSME Steam Tables (1999)
6. Banaszek, J., Jaluria, Y., Kowalewski, T.A., Rebow, M.: Semi-implicit FEM Analysis of Natural Convection in Freezing Water. Numerical Heat Transfer, Part A 36, 449–472 (1999)

Fully-Implicit Interface Tracking for All-Speed Multifluid Flows

Robert Nourgaliev, Samet Kadioglu, and Vincent Mousseau

Idaho National Laboratory, Reactor Physics & Design Department,
Multiphysics Methods Group
robert.nourgaliev@inl.gov, samet.kadioglu@inl.gov,
vincent.mousseau@inl.gov

A new interface tracking method for all-speed multi-fluid flows is introduced. The key feature of the method is that the interface motion and fluid dynamics are fully-(non-linearly)-coupled, which allows to completely eliminate operator-splitting temporal errors. The direct benefits of this treatment are *a)* the method is *L*-stable, permitting time steps controlled only by accuracy requirements; *b)* the method is high-order-accurate in time; *c)* the method is fully-conservative, even at the interface, and robust (no pressure-velocity oscillations, in difference to previous attempts for conservative interface tracking). The keys to these advantages are the high-order sharp cut-cell-based interface treatment combined with implicit Runge-Kutta (ESDIRK) scheme within the physics-based-preconditioned Jacobian-free Newton-Krylov method (JFNK) [KK03]. Interfaces are tracked by hybridizing the Lagrangian Marker tracking with the Eulerian JFNK-based Re-Distancing/Level-Set algorithm (MRD/LS) [NKMK08]; all non-linearly coupled with the JFNK-based "recovery Discontinuous Galerkin" (rDG-JFNK) for all-speed fluid flows [NTPMK08, PNMK08].

1 Introduction

This work is motivated by the need for Direct Numerical Simulation (DNS) of boiling multiphase flows in nuclear reactor safety applications. Among the usual DNS-requirements for high-fidelity of spatiotemporal discretization, we would like to account for compressibility of both liquid and gas (vapor), in a wide range of Mach numbers. Conservation of mass, momentum and energy is of outmost importance – especially at the interface with phase change, which makes the traditional explicit non-conservative treatment of the compressible multi-material interface [AK01, NDT06] unacceptable. Furthermore, it is required to properly account for viscosity and heat conduction effects, as well as phase change (boiling/condensation). These stringent physical modeling requirements impose severe limitations on the currently available multi-fluid flow simulation methods, all based on operator-splitting of the interface

motion (modeled by either Level Set, Volume Tracking or Front-Tracking) and fluid dynamics (explicit Godunov-based; semi-implicit SIMPLE- or Approximate Projection-based) algorithms.

We approach this challenge by developing the fully-coupled algorithm (denoted hereafter as I-SIM, or *Implicit Sharp Interface Method*). The whole non-linear system (interface tracking + cut-cell remeshing + fluid solver) is solved using an implicit Runge-Kutta scheme [BCVK02], within the framework of the Jacobian-Free Newton-Krylov method [KK03]. This allows us to avoid stability issues due to the stiffness of the compressibility effects, diffusion (viscosity/heat conduction) operators, high-acoustic impedance interface, and phase change. Interface jump conditions are treated sharply, with the 3$^{\text{rd}}$-order accuracy in space [NLT08].

The contribution/outline of the current paper is the following. First, we describe the basic principles of the I-SIM, in Section 2. Second, we demonstrate the benefits (robustness, accuracy, conservation) of the fully-coupled simulations using multi-fluid 1D manufactured and shock-tube problems, in Section 3. Finally, in Section 4, we show preliminary results for two-dimensional simulations, focussing here on sharp implicit interface kinematics treatment with a hybrid of the marker tracking and the Level-Set-based re-distancing algorithm (MRD/LS).

2 Numerical Method (Summary)

The basic idea of our implicit interface tracking method is outlined in Fig. 1. Interface kinematics is treated in a Lagrangian framework, by placing markers at the interface, as in Front Tracking (FT) algorithms. However, in

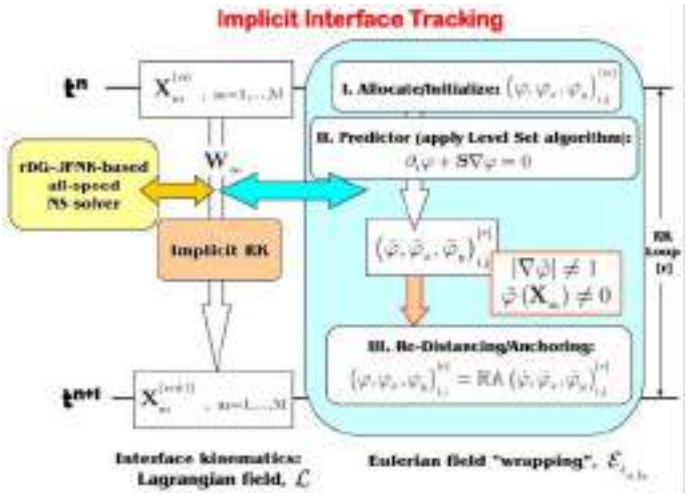

Fig. 1. Outline of the implicit interface tracking algorithm (I-SIM)

difference to FT, the markers are not connected, to avoid complexity. Instead, the interface topology and geometry are treated in an Eulerian framework, by "wrapping" a signed distance function φ (Level Set, LS) around markers, re-distancing/anchoring ($\mathbb{RA}$) LS each time the markers move. This $\mathbb{RA}$ operator is designed in such a way, so the markers reside on the zero-level of φ (by "anchoring" the LS, [NKMK08]) and φ satisfies the Eikonal equation, $|\nabla\varphi| = 1$ (by re-distancing the LS). This is achieved by combining the PDE-based re-initialization with the 3^{rd}-order interpolation at interfacial cells. The $\mathbb{RA}$ operator is convergent in pseudo-time, which ensures the 1^{st}-order spatial convergence in curvature [NKMK08]. This is in contrast to traditional LS treatments (PDE-RI/LS), which do not converge in pseudo-time due to the interface drift problem, and are non-convergent (spatially) in curvature. To enforce efficiency, we developed the implicit pseudo-time discretization within the JFNK method, as described in [NKMK08].

Marker-field motion is treated implicitly, fully-coupled with the fluid dynamics solver and the MRD/LS algorithm, within the JFNK framework [KK03], see Fig. 1. This allows us to eliminate operator-splitting temporal errors, and makes the method high-order-accurate in time. Moreover, since the *L*-stable *Explicit, Singly Diagonal Implicit Runge-Kutta (ESDIRK)* scheme is employed for temporal discretization, the method is robust and suitable for problems with multiple time scales. As a fluid dynamics solver, we developed the all-speed fully-coupled implicit method, based on *recovery Discontinuous Galerkin* (rDG) spatial discretization of both hyperbolic and diffusion (viscous stress and heat conduction) operators. In the present study, we show only one-dimensional examples for coupling interface (marker) motion with fluid dynamics (Section 3). Two-dimensional rDG-JFNK all-speed solver is presented in [PNMK08]. Its coupling with the MRD/LS interface tracking and 2D cut-cell treatments [NLT08] will be presented elsewhere.

3 One-Dimensional Tests

First, we demonstrate that our method is indeed high-order-accurate in both time and space, using a "Manufactured Problem" introduced in [NTPMK08]. This is a problem for traveling disturbances in density and velocity, with two embedded characteristic time scales for pressure waves, and it includes both significant viscous dissipation and heat conduction. Spatial convergence is shown in Fig.2a. It can be seen that our high-order rDG method is very accurate, converging with nearly-theoretical convergence rates at the asymptotic-grid range (the 3^{rd}-order for piecewise-constant, the 6^{th}-order for linear, the 9^{th}-order for quadratic and the 12^{th}-order for cubic rDG). Temporal convergence is shown in Fig.2b, which also demonstrates that the method converges with nearly-theoretical rates, and operator-splitting errors are completely eliminated.

Multi-fluid shock-tube problems are presented in Fig.3. As one can see, the method is very accurate and robust in a wide range of shock speeds and

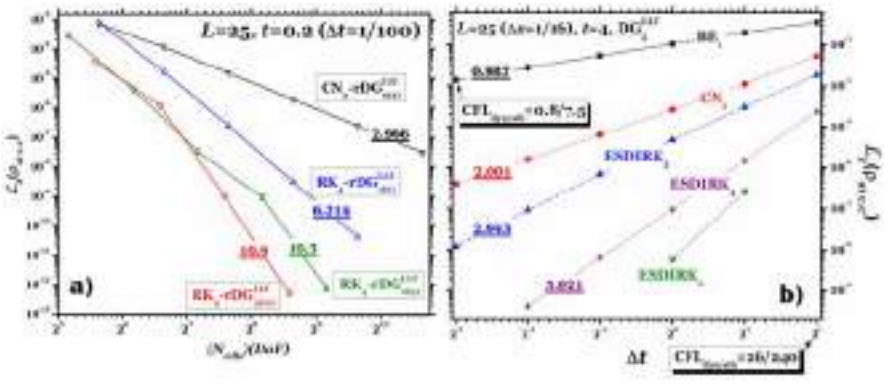

Fig. 2. Low-speed ($M \approx 0.1$) manufactured solution [NTPMK08]. a) Convergence in space. b) Convergence in time.

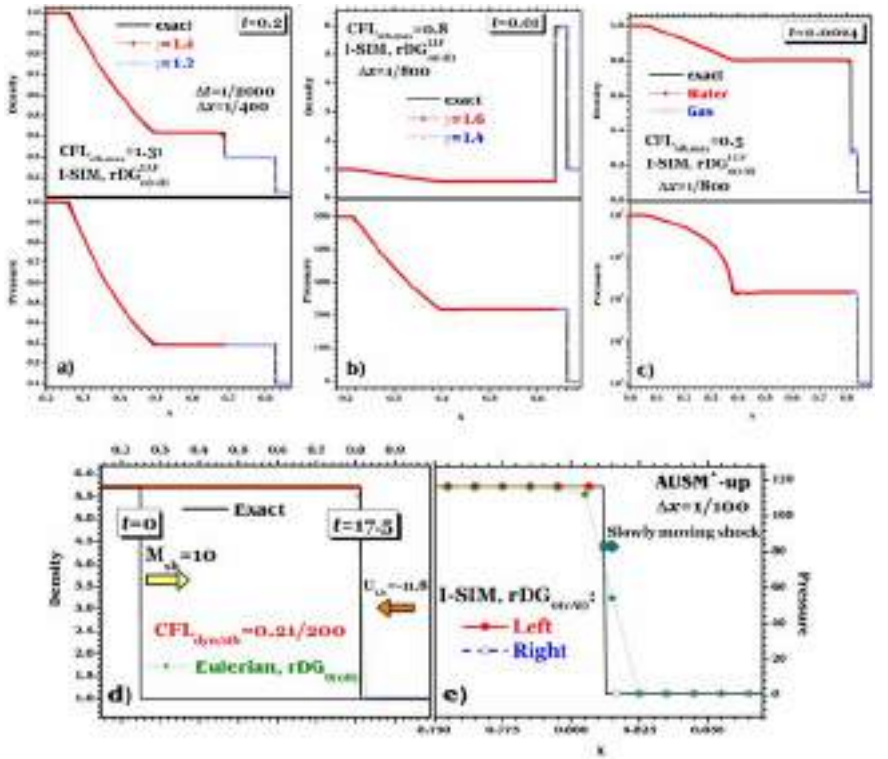

Fig. 3. a) Two-gas Sod's test; b) Stiff two-gas shock tube problem; c) Stiff liquid-gas shock tube problem; d,e) Implicit shock tracking problem.

stiffness of the interface. Importantly, our algorithm is fully-conservative (to machine accuracy), and robust, without well-known pressure-velocity oscillation problems [AK01]. This is achieved by combining the cut-cell treatment of near-interfacial cells with the implicit ESDIRK discretization. Due to the implicit discretization, we can step over the CFL stability limits, choosing the time step based on accuracy requirements (in the example of Fig.3(d,e), it was the resolution of the (slow) shock speed).

4 2D Interface Kinematics by MRD/LS

Our final numerical example is a modified "Time-reversed single-vortex problem", originally introduced by Rider&Kothe. The dynamics of the severe interface (ellipse) stretching/tearing computed with our MRD/LS algorithm is shown in Fig.4(a-e). By the time $t = 4$, the interface becomes sub-grid. The usual LS method will result in severe mass losses. Our method however works very well, as the interface kinematics is controlled by marker-field, which is very easy/cheap to ensure well-resolved. As one can see from Fig.4e, by the end of the stretching cycle ($t = 8$), the mass and shape of the interfacial

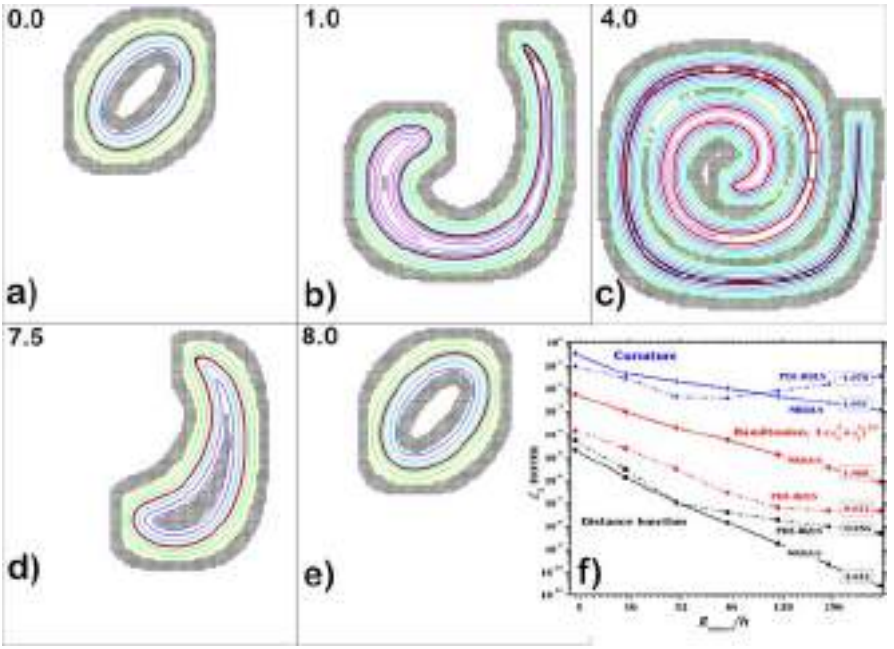

Fig. 4. a-e) Performance of the implicit MRD/LS algorithm for a time-reversed single vortex problem ($T = 8$, $h = \frac{1}{100}$) [NKMK08]. f) Grid convergence for the Level Set, Normals (Hamiltonian) and interface curvature – a comparison of the MRD/LS and the PDE-RI/LS methods.

structure are fully preserved. We would like to emphasize, that the distance-property of the LS is well-maintained, by converging the re-distancing operator to a complete pseudo-time steady-state. Thus, we can demonstrate convergence in curvature, Fig.4f. In contrast, the PDE-RI/LS method is diverging in curvature, as the steady-state is not achievable, setting the "floor" of temporal discretization errors. More on comparison of the MRD/LS and the PDE-RI/LS can be found in [NKMK08].

5 Conclusion

We have demonstrated that the high-fidelity fully-coupled implicit multi-fluid simulations are possible, and advantageous; providing the robustness and accuracy needed for Direct Numerical Simulations of compressible (all-speed) multiphase flows. While significantly more complex compared to traditional methods, the benefits of fully-coupled non-linear solvers for multi-fluid flows are evident, enabling to robustly and accurately incorporate viscous, heat transfer and phase change effects, necessary for realistic simulations of boiling multiphase flows.

Acknowledgement. This manuscript has been authored by Battelle Energy Alliance, LLC under Contract No. DE-AC07-05ID14517 (INL/CON-08-14470) with the U.S. Department of Energy. The United States Government retains and the publisher, by accepting the article for publication, acknowledges that the United States Government retains a nonexclusive, paid-up, irrevocable, world-wide license to publish or reproduce the published form of this manuscript, or allow others to do so, for United States Government purposes.

References

[AK01] Abgrall, R., Karni, S.: Computations of compressible multifluids. J. Comp. Phys. 169, 594–623 (2001)

[BCVK02] Bijl, H., Carpenter, M.H., Vatsa, V.N., Kennedy, C.A.: Implicit time integration schemes for the unsteady compressible Navier-Stokes equations: laminar flow. J. Comp. Phys. 179, 313–329 (2002)

[KK03] Knoll, D.A., Keyes, D.: Jacobian-Free Newton-Krylov methods: A survey of approaches and applications. J. Comp. Phys. 193, 357–397 (2003)

[NLT08] Nourgaliev, R.R., Liou, M.-S., Theofanous, T.G.: Numerical prediction of interfacial instabilities: Sharp Interface Method (SIM). J. Comp. Phys. 227, 3940–3970 (2008)

[NDT06] Nourgaliev, R.R., Dinh, T.-N., Theofanous, T.G.: Adaptive characteristics-based matching for compressible multifluid dynamics. J. Comp. Phys. 213, 500–528 (2006)

[NTPMK08] Nourgaliev, R.R., Theofanous, T.G., Park, H., Mousseau, V., Knoll, D.: Direct numerical simulation of interfacial flows: Implicit Sharp-Interface Method (I-SIM). In: AIAA 2008-1453, 46rd AIAA Aerospace Sciences Meeting and Exhibit, January 7-10, Reno, NV, USA (2008)

[NKMK08] Nourgaliev, R.R., Kadioglu, S., Mousseau, V., Knoll, D.A.: Marker Re-Distancing/Level Set (MRD/LS) method for high-fidelity implicit interface tracking. SIAM J. Scientific Comp. (under review) (2008)

[PNMK08] Park, H., Nourgaliev, R.R., Mousseau, V., Knoll, D.: Recovery Discontinous Galerkin – Jacobian-Free Newton Krylov (rDG-JFNK) method for all-speed Navier-Stokes equations. In: Intern. Conf. on Comput. Fluid Dyn., ICCFD5, Seoul, Korea, July 7-11 (2008)

“*This page left intentionally blank.*”

Development of Surface-Volume Tracking Method Based on MARS

Taku Nagatake, Zensaku Kawara, and Tomoaki Kunugi

Department of Nuclear Engineering, Kyoto University, Yoshida, Sakyo, Kyoto 606-8501, Japan

1 Introduction

The MARS (Multi-interfaces Advection and Reconstruction Solver)[1] is one of the direct numerical methods for multiphase flow solvers with a volume tracking procedure for free surface or interface deformation. The main feature of the MARS is 1) a precise conservation of volume of fluid (VOF), 2) a surface-volume tracking procedure with a precise linear interface calculation and 3) a representation of the interface/surface within one or two control volumes. Since this method has been developed on a staggered structure-grid system, it is difficult to perform the computation with high accuracy in a complicatedcomputational domain. Therefore, it is necessary to develop a new version of the MARS on the unstructured grid system. In this study, a new version of the MARS based on collocated structure-grid system has been developed. In order to validate this procedure, the well-known as the "Dam breaking problem" was chosen and unmerically solved. On the other hand, the experiments of this problem with the same configuration of the solution domain as the numerical simulation were conducted, and the numerical and experimental results were compared with each other.

2 Numerical Method

The first version of the MARS on unstructured grid system has been developed on collocated structure-grid system (see figure1). If the staggered grid system on unstructured grid system is used, the numerical algorithm will be very complicated and need a lot of computational memory. However, it is well-known that the "checker board error" of pressure field when the pressure Poison equation is solved is inevitable if all variables are defined on the same collocation point due to the uncoupling of velocity and pressure. In order to avoid this error, the solver of the pressure Poison equatin based on a fractional-step method is modified by Rhie & Chow method (1983)[2]. The actual precedure is as follows: 1) Velocity is calculated at a cell center at first, 2) Velocity at a cell-face can be interpolated by using this cell-center velocity. The direction of this cell-face-center velocity is normal to the cell

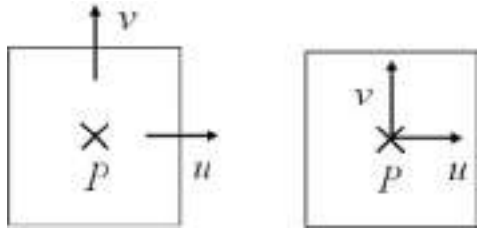

Fig. 1. Variable location

face, 3) Pressure poison equation can be solved by using this cell-face-center velocity, and 4) Cell-face-center velocity and pressure at the new time step are corrected, and 5) Cell-center velocity can be interpolated by using the cell-face velocity. In this interpolation procedure, the mass flow rate at the cell-face is expressed by the following equation:

$$\tilde{u}_{i+1/2} = \frac{\rho_i \tilde{u}_i + \rho_{i+1} \tilde{u}_{i+1}}{\rho_i + \rho_{i+1}} \tag{1}$$

In the MARS, the VOF function f is transferred by below equation:

$$\frac{\partial F}{\partial t} + (\boldsymbol{u} \cdot \nabla) = \frac{\partial F}{\partial t} + \nabla \cdot (F\boldsymbol{u}) - F \nabla \cdot \boldsymbol{u} = 0 \tag{2}$$

From the viewpoint of the conservation VOF function, it is necessary that the velocity field $\boldsymbol{u}$ has to be satisfied a solenoidal condition based on the pressure Poison equation. Therefore, the velocity at cell-face-center is used for solving the equation1.

In the MF analysis, it is necessary to include a surface tension force as a body force in the momentum eqeuation. In this study, the CSF model (Continuum Surface Force model, Brackbill, et al, 1992)[3] was applied. In the CSF model, there are two methods for the calculation of surface normal vector: ALE-like and MAC-like definitions. The ALE-like surface normal vector is defined at a node and at a cell-face-center as for the MAC-like definition. In this study, the ALE-like definition was chosen because of the accuracy.

3 Validation of the Algorithm with Dam Breaking Problem

In order to validate the present numerical procedure, the numerical simulation and the experiments were carried out for the "Dam breaking problem". Figure 2 shows the calculation domain. The computational domain is height of liquid column $2L_0 = 5.0$[cm] ($L_0 = 2.5$[cm]), the time step 1.0×10^{-4}[s], and the mesh number is 50 (in width) $\times$100 (in length) $\times$100 (in height). The no-slip velcity conditions are imposed on the walls. The working fluids are the air for the gas and the water for the liquid.

The flow visualization experiment was performed using the same shape and sizes as the computational domain. The acrylic resin container was used as a test section. This container was divided into two sections (a liquid column section was filled with water and a vacancy section with air) by a partition plate covered with a rubber to prevent the water leakage from the end of this plate put on the bottom wall of the container. The water level in the liquid column section was kept constant before its break by pulling-up the partition plate quickly.

In this study, the time period of pulling the plate up is set 0.024 [s] (case1 and case2) and 0.042 [s] (case3). The time period of the bottom edge of the plate reaches on the top of the liquid column. In the case2, the rubber with hydrophobic coating was used. The water behaviors in the container were recorded with an ultra high-speed video camera (Phantom 7.1, vision Research Co. with maximum 160 kfps). In this experiment, since the leakage of water was inevitable during the time period of pulling the partition plate up, this leakage caused to misread the speed and the position of the flowing water-front on the bottom wall of the container. In order to remove these errors, the experimental results were corrected by removing the length of the leaked water existed in front of the "real" water-front in the recorded images.

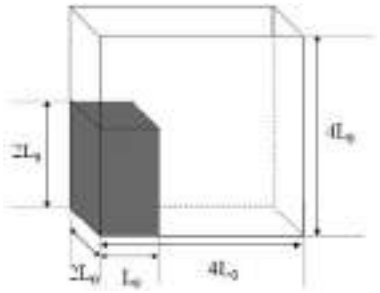

Fig. 2. Calculation domain

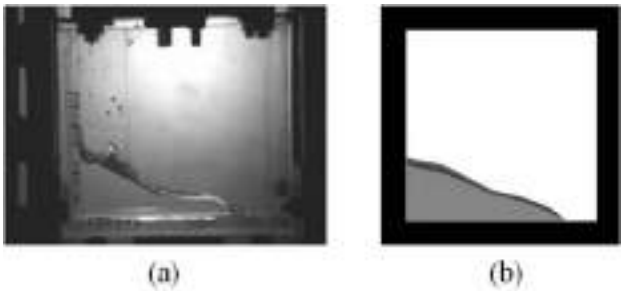

Fig. 3. The shapes of gas-liquid interface at 0.1[s] (a)Experimental result (b)Numerical result

4 Results and Discussion

Figure 3 shows the shape of interface: (a)numerical result and (b)experimental one (case1) at $t = 0.1$[s]. Figure 4 shows the comparison of the water-front position varying with time between the numerical and experimental results. In this figure, the horizontal axis denotes the non-dimensional time T^* and the vertical axis denotes the non-dimensional water fromt position X^*. These non-dimensional parameters are defined as follows:

$$X^* = X/L_0 \tag{3}$$

$$T^* = T\sqrt{ng/L_0} \tag{4}$$

where X is the water-front position, T time, n the aspect ratio of liquid column and g is gravity acceleration. In this study, n is 2.0. In the early stage ($T^* < 2.0$), the numerical results are different from the experimental data. This is because the leakage water volume is inevitable in the experiment during the pulling-up period of the partition plate. In the developed stage ($T^* > 2.0$), the numerical result almost agrees with the experimental data in case2. Figure5 shows the comparison of the water-front velocity. In this figure, the horizontal axis denotes the dimensionless time and the vertical axis denotes the dimensionless velocity dX^*/dT^*. In the developed stage, the numerical results in case1 and case2 agree well, and it measn that the terminal velocity of the water-front in these cases are the same. This is because the time period of pulling the plate up was longer than ohter cases, and the plate affected the behavior of water surface. The processes of pulling the plate up in cases 1 and 2 did not affect the behavior of water surface than that in case3.

In order to correct these results, the effect of the process of pulling the plate up is removed from the experimental results as follows (see figure 6): When the opening area between the partition plate and the bottom wall of the container is small, i.e., in the early stage, the hydrostatic pressure works the water at

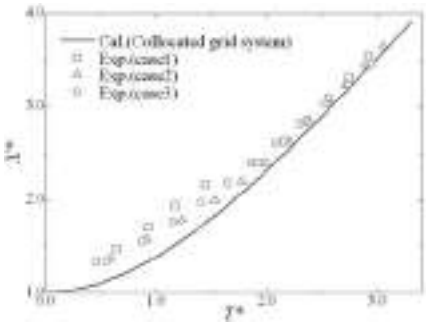

Fig. 4. Time histories of water-front position

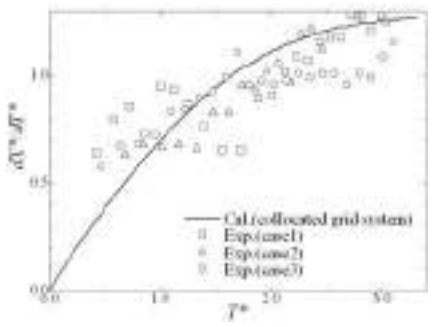

Fig. 5. Time histories of water-front velocity

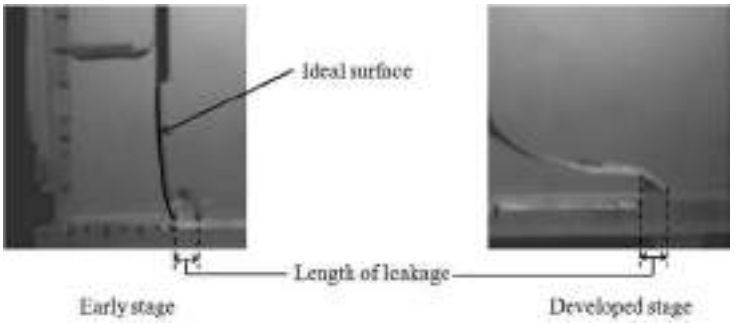

Fig. 6. Correction of liquid flow shape

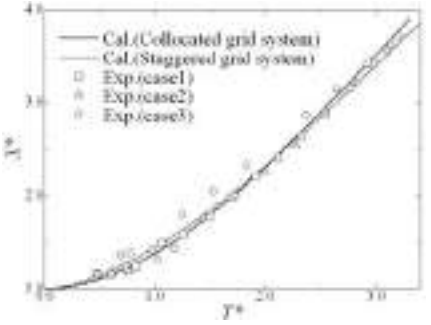

Fig. 7. Time histories of corrected water-front position

this area and some water leaks before the main water movement: the recorded water-front is ahead of an ideal one. Since it is difficult to predict the ideal position of the water-front, the ideal water-front position was measured by using the spline fitting curve of the water surface to be intersected at the bottom wall. If the opening area becomes large, the water leakage volume compared to total water movement volume becomes negligible, and the water surface becomes close to the ideal shape. Next in the developed stage, it seems that the length of water leakage volume is just added at the ideal water-front position because both velocities of the leakage and main water parts are almost the same. Therefore, the length of the leakage water volume in the early stage can be subtracted from the water-front position recorded in the images.

Figure7 shows the copmarison between the numerical results and corrected experimental data. In this figure, the numerical simulations were performed with the present collocated grid system and the staggered grid system (i.e., the original MARS), respectively. Both numerical results are in very good agreement with the experimental results in cases 1 and 2. In the early stage, the water-front based on the staggered grid system is developed faster than that based on the collocated one. In the developed stage, the water-front

result based on the collocated grid is developed faster than that based on the staggered one. The water-front in case3 is different from other results because that, as mentioned before, the process of pulling the plate up affects the water behavior for long time compared to other cases. This effect cannot be removed in this correction method, so that this is a big remaining issue of this kind of experiments in the future.

5 Conclusion

In the present study, the collocated MARS was developed and validated with the "Dam Breaking Problem."

1) Dam breaking experiment was performed, and the correction method of the experimental results was considered. This correction method can be removed the effect of pulling the partition plate up on the water surface behavior.
2) It is confirmed that the algorithm based on the collocated grid system proposed in this study can be performed with high accuracy compared to the original MARS by validating the "Dam break" experimental data.

It is expected that the unstructured/collocated MARS developed in this study can be applied to many MF problems with enough accuracy in the future.

References

1. Kunugi, T.: MARS for Multiphase Calculation. Computational Physics 9, 536–571 (2001)
2. Rhie, C.M., Chow, W.L.: Numerical Study of the Turbulent Flow Past an Airfoil with Trailing Edge Separation. AIAA Journal 21(11), 1525–1532 (1938)
3. Brackbill, J.U., et al.: A Continuum Method for Modeling Surface Tension. Journal of Computational Physics 100, 335–354 (1992)

Part 31
Multiphase Flow 2

“*This page left intentionally blank.*”

Adaptive Moment-of-Fluid Method for Multi-Material Flow

Hyung Taek Ahn[1] and Mikhail Shashkov[2]

[1] School of Naval Architecture & Ocean Engineering, University of Ulsan
Ulsan, Korea
htahn@ulsan.ac.kr
[2] Theoretical Division, Group T-7, Los Alamos National Laboratory
Los Alamos, New Mexico, U.S.A.
name@email.address

Abstract. A novel adaptive mesh refinement (AMR) strategy based on the Moment-of-Fluid (MOF) method for volume-tracking dynamic interface computation is presented. The Moment-of-Fluid method is a new interface reconstruction and volume advection method using volume fraction as well as material centroid. The mesh refinement is performed based on the error indicator, the deviation of the actual centroid obtained by interface reconstruction from the reference centroid given by moment advection process. Using the AMR-MOF method, the accuracy of volume-tracking computation with evolving interfaces is improved significantly compared to other published results.

Keywords: Adaptive Mesh Refinement (AMR), Volume-of-Fluid (VOF), Moment-of-Fluid (MOF), Volume Tracking, Multi-phase flow, Multi-material flow.

1 Backgrounds

One of popular strategy of improving accuracy in computational physics is using adaptive mesh refinement (AMR). Although the flows with evolving interface is considered a very appropriate class of problem with potential adaptivity, the application of AMR on such problem is relatively rare compared to the flow problems without interfacial phenomena. Here, we present a novel adaptive mesh refinement technique based on the moment-of-fluid method (AMR-MOF) for multi-phase/multi-material interfacial flow simulation.

The MOF method [1, 2, 4, 5] can be thought of as a generalization of VOF method. In VOF method, volume (the zeroth moment) is advected with local velocity and the interface is reconstructed based on the updated (reference) volume fraction data. In MOF method, volume (zeroth moment) as well as centroid (ratio of the first moment with respect to the zeroth moment) are advected and the interface is reconstructed based on the updated moment data (reference volume and reference centroid). In the MOF method, the computed interface is chosen to match the reference volume exactly and to provide the best possible approximation to the reference centroid of the material.

By using the centroid information, the volume tracking with dynamic interfaces can be computed much more accurately. Furthermore with this conceptual extension of using the moment data, the interface in a particular cell can be reconstructed independently from its neighboring cells. With the advantages of MOF method over the VOF method, our opinion is that the MOF method is a next generation volume-tracking interfacial flow computation method evolved from VOF method.

In this paper, we present a very accurate and efficient adaptive mesh refinement strategy for volume-tracking interfacial flow computations based on the moment-of-fluid method.

2 AMR-MOF

In general required level of mesh adaptation has to depend on the complexity of the interface, two immediate examples being *curvature* and *topology* of the interface. Fig. 1 illustrates representative interface features.

We note that all features illustrated in Fig. 1 are in subcell scale (their length scale is less then those of unrefined mesh) and also independent from

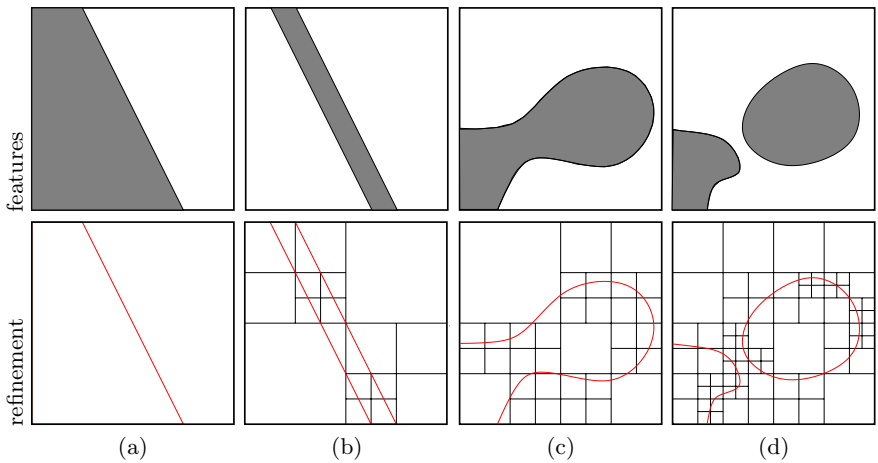

Fig. 1. Subcell scale interface features with different curvature and topology. Top row – material configuration, bottom row – possible AMR-MOF refinement pattern. Four representative interface features within a square cell are illustrated: (a) one piece of the material inside the cell — interface is the segment of the straight line (curvature is zero); (b) two disjoint pieces of the white material — subcell thickness filament of dark material, curvature has meaning only for each segment of the straight line and equal to zero, but one curvature per cell does not make sense; (c) one piece of dark material with complicated shape, only average averaged curvature makes sense; (d) disjoint pieces of dark material (subcell size droplet), each of pieces has high average curvature.

the features of their neighboring cells (neighboring cell may not have similar features). It is interesting to note that after we have created illustrative Fig. 1.

3 Static Interface Reconstruction

The statement of the problem for AMR-MOF static interface reconstruction is as follows: for given original material configuration, represent the reconstructed material region by PLIC on adaptively refined mesh.

The flow-chart for the static AMR-MOF interface reconstruction of a given geometry is presented in Fig. 2. We note that the static AMR-MOF interface reconstruction, described in Fig. 2 is only for the *initial* representation of given material configuration on AMR mesh. In this Section we present static interface reconstruction for multi-element airfoil configuration. The AMR-MOF reconstruction starts with a single cell $[0, 1]^2$ - level-0 mesh. Adaptive refinement is performed up to level-8 from the level-0 mesh. First six levels of AMR-MOF interface reconstruction is displayed in Fig. 3.

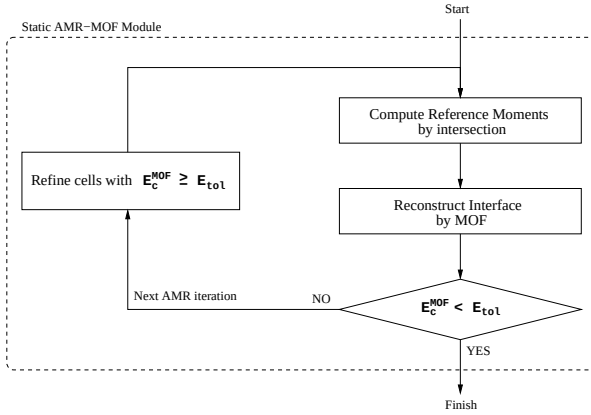

Fig. 2. Flow-chart for static AMR-MOF interface reconstruction for initial representation of material configuration on AMR mesh

4 Dynamic Interface Reconstruction

The algorithm of the AMR-MOF for dynamically evolving interface is illustrated in Fig. 4.

The reversible vortex problem is presented with longer period, $T = 8$. Time steps of $\Delta t = \frac{1}{32}$ (total number of time stepping, $n_t = 256$) is used for all AMR-MOF computation. The result of AMR-MOF computation, with maximum refinement up to level-4, is displayed in Fig. 5 at various time steps.

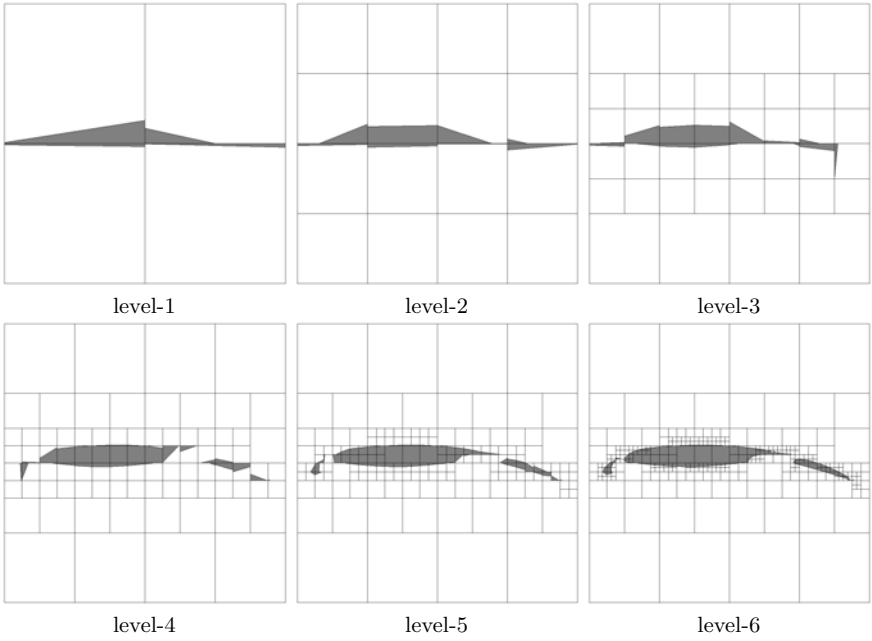

Fig. 3. AMR-MOF interface reconstruction of multi-element airfoil configuration starting with one cell, i.e. the level-0 mesh is 1×1 covering the domain of $[0, 1]^2$. Different levels of AMR-MOF reconstruction process are displayed. $E_{tol} = 1.e\text{-}15$ is used as the refinement criterion.

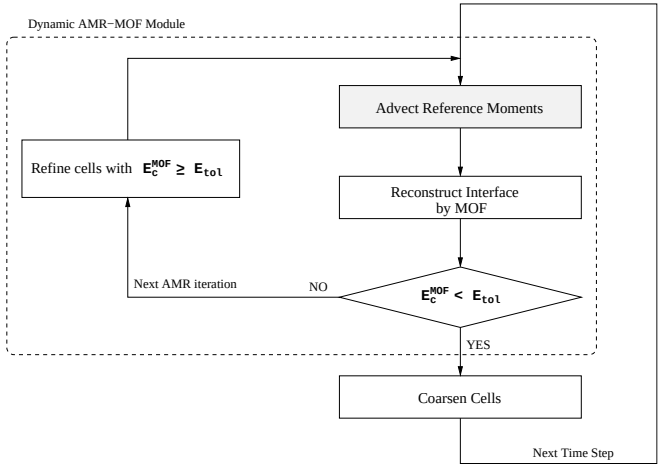

Fig. 4. Flow-chart for dynamic AMR-MOF interface reconstruction and moment advection. The difference of the dynamic AMR-MOF module from the static AMR-MOF module, as shown in Fig. 2, is reference moment computation step. For dynamic case, the reference moment is computed by advection step, as indicated with gray box.

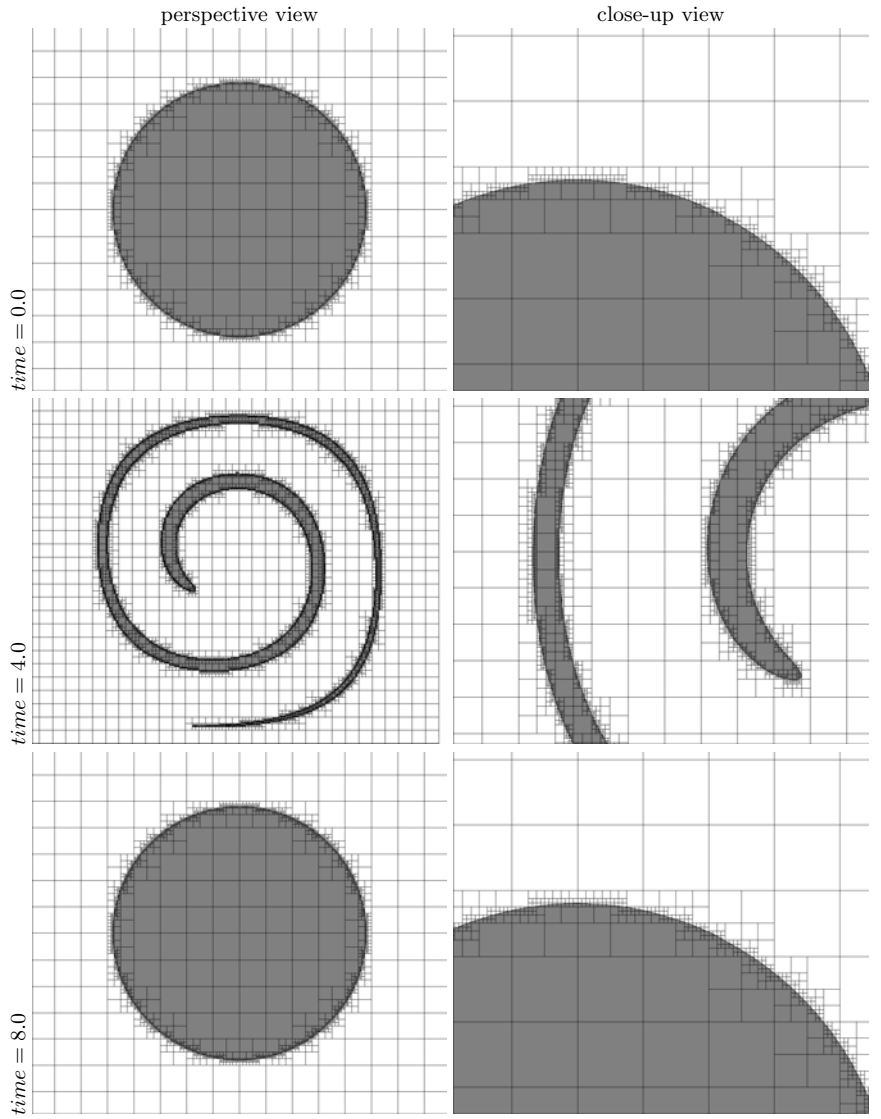

Fig. 5. Single vortex flow, $T = 8$. Level-0 mesh is 32^2 and maximum 4 level of AMR is allowed (maximum effective mesh resolution is 512^2). $E_{tol} = 1.e\text{-}20$ is used as the refinement criterion

5 Conclusion

A new adaptive mesh refinement strategy based on the moment-of-fluid method was presented. Numerical examples demonstrate that error in the centroid position can correctly detect not only regions with high curvature of the interface but also regions with subcell structures like filaments. In [3] we have coupled standard MOF without AMR with with incompressible Navier-Stokes solver for two materials. In the future we planning to couple AMR-MOF with incompressible Navier-Stokes AMR solver.

References

1. Ahn, H.T., Shashkov, M.: Geometric algorithms for 3d interface reconstruction. In: Brewer, M.L., Marcum, D. (eds.) Proceedings of the 16th International Meshing Roundtable, pp. 405–422. Springer, Heidelberg (2007)
2. Ahn, H.T., Shashkov, M.: Multi-material interface reconstruction on generalized polyhedral meshes. Journal of Computational Physics 226, 2096–2132 (2007)
3. Ahn, H.T., Shashkov, M., Christon, M.A.: The moment-of-fluid method in action. Communications in Numerical Methods in Engineering, Report of Los Alamos National Laboratory, LA-UR-07-6854 (to appear) (2008)
4. Dyadechko, V., Shashkov, M.: Moment-of-fluid interface reconstruction. Technical Report LA-UR-05-7571, Los Alamos National Laboratory (2005)
5. Dyadechko, V., Shashkov, M.: Reconstruction of multi-material interfaces from moment data. Journal of Computational Physics (2008) doi:10.1016/j.jcp.2007.12.029

Numerical Simulation of Underfill Flow in Flip-Chip Packaging

Tomohisa Hashimoto[1], Keiichi Saito[2], Koji Morinishi[3], and Nobuyuki Satofuka[4]

[1] Department of Mechanical Engineering, Kinki University, 3-4-1 Kowakae, Higashi-Osaka, Osaka, 577-8502, Japan
hasimoto@mech.kindai.ac.jp
[2] Plamedia Corporation, Honcho, Nakano-ku, Tokyo, 164-0012, Japan
saito@plamedia.co.jp
[3] Department of Mechanical and System Engineering, Kyoto Institute of Technology, Matsugasaki, Sakyo-ku, Kyoto, 606-8585, Japan
morinisi@kit.ac.jp
[4] The University of Shiga Prefecture, 2500 Hassaka-cho, Hikone-shi, Shiga, 522-8533, Japan
satofuka.n@office.usp.ac.jp

1 Introduction

In flip-chip packaging technology, the underfill encapsulation is one of the important processes to obtain a significant improvement in fatigue lifetime for the solder joints between IC chip and substrate. The advanced design of electronic devices aiming at the enhancement of the performance involves the increase of the number of solder bumps, smaller size of the IC chip and smaller gap height between IC chip and substrate. That leads to making various problems caused by the flow behavior, such as voids in underfill and mis-placed IC chip. The numerical analysis is more and more strongly required for simulating the underfill flow behavior, including the condition of dispensing the underfill material on the substrate. In fact, it is desirable to predict the filling time, the final fillet shape formed around IC chip and the occurrence of air trap especially around the solder bump in the underfill process, considering the effect of contact angle, viscosity and surface tension of the underfill material for increasing the reliability of flip-chip packaging.

We developed a numerical method for simulating the underfill flow in flip-chip packaging, especially for designing the optimum condition of solder joint performance [1]. The two types of processes for applying the underfill encapsulant to the gap between IC chip and substrate are presented. One is conventional capillary flow type and the other is no-flow type. The both underfilling processes are illustrated in Fig. 1. In the capillary flow type, multiple processing steps are involved. The solder joints between IC chip and substrate are formed, which is called solder bump reflow, and then thermosetting epoxy resin is driven into the cavity by capillary action. After the resin is completely

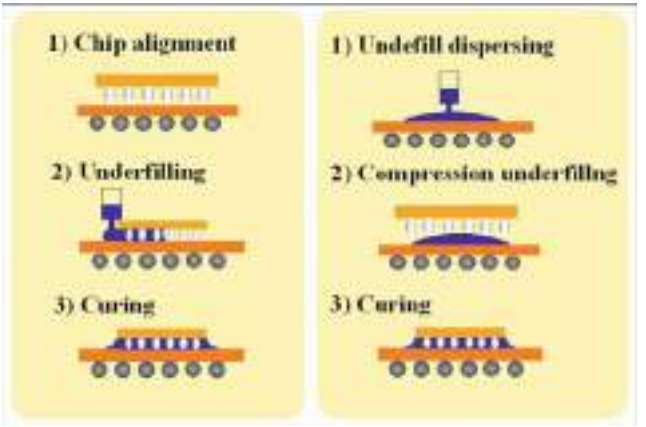

Fig. 1. The underfilling processes of conventional capillary flow type (left) and no-flow type (right)

filled, the assembly is taken to an oven where the resin is cured. On the other hand, the no-flow type was invented to reduce the processing steps in the capillary flow type, which provides cost savings. The epoxy resin is directly dispensed on the substrate and is compressed by pre-heated IC chip. While the IC chip is mounted on the substrate, the solder joints are formed with curing of the resin. We need to understand the flow behavior and filling time of underfill material for various solder bump patterns; solder bump diameter, bump pitch and gap height, taking the drag force acting on the solder bump into account. In the underfill flow analysis, the governing equations for three-dimensional incompressible flow are solved by using the finite difference method (FDM) incorporating the pseudo compressibility approach [2] on a non-uniform Cartesian grid. In the numerical method, a central difference scheme with artificial dissipation is used for the spatial discretization. The forward Euler explicit method is used as an iterative scheme in the pseudo time integration method. Our basic concept of numerical approach to the underfill encapsulation process can be found in [3, 4]. The level set method [5] is used as an interface capturing algorithm to represent the gas-liquid interface. The continuum surface force (CSF) model [6] is used for treating the surface tension. It is assumed that temperature distribution in the underfill material is uniform. The power-law model is adopted as a constitutive equation for treating the mould flow behavior of non-Newtonian fluid. The simulations especially in the no-flow type are carried out by coupling the Navier-Stokes equations and the equations of motion of IC chip.

In this paper, the effect of capillary action, viscosity and surface tension on the flow behavior in the underfilling process of conventional capillary flow type are discussed.

2 Numerical Simulation of Capillary Flow Undefill

As one of the analytical models for the conventional capillary flow type, as shown in Fig. 2, a semi-spherical liquid dispensed on the substrate near the IC chip is driven into the cavity with a gap height between IC chip and substrate by capillary action. The solder bump in the gap is modeled as the rectangular cylinder. In this model, the surface tension is caused by prescribing the contact angle on the surface of IC chip and substrate. The effect of gravity force is included. The dimension of die is about 1.0mm $\times$ 1.0mm, and the gap height between IC chip and substrate is about 0.1mm. The array pattern of solder bump is 5×5. The bump diameter is 0.1mm and the bump pitch is 0.2mm. The number of grid points is about 37000. By using this model, the fillet shape formed around the IC chip and the effect of contact angle, viscosity and surface tension on the underfill flow behavior were investigated. In the properties of gas and liquid, the density, viscosity and surface tension are shown in Table 1.

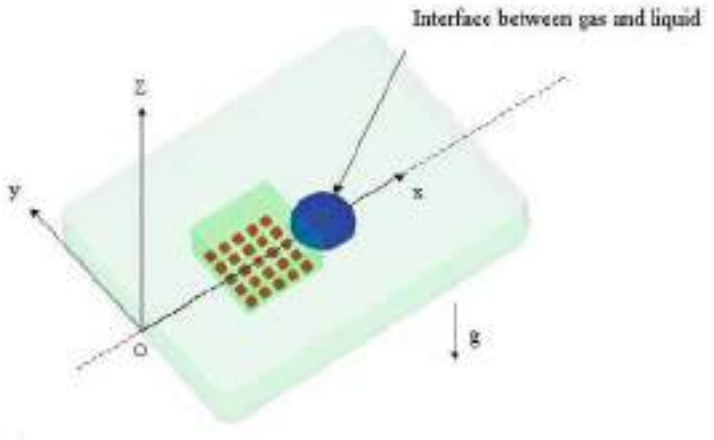

Fig. 2. The analytical model for the conventional capillary flow type

Table 1. Viscosity and surface tension

	solder bump pattern	viscosity [Pa · s]	surface tension [N/m]
case1	-	1.5×10^{-2}	1.0×10^{-2}
case2	5×5	1.5×10^{-2}	1.0×10^{-2}
case3	5×5	1.5×10^{-3}	1.0×10^{-2}
case4	5×5	1.5×10^{-3}	1.0×10^{-3}
case5	5×5	1.5×10^{-2}	1.0×10^{-1}

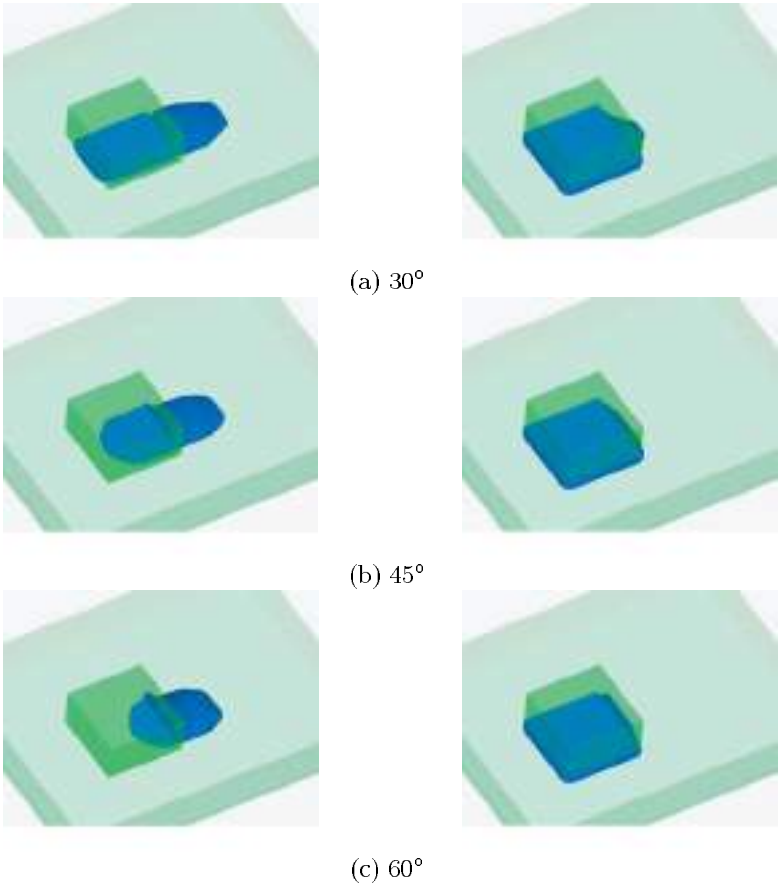

(a) 30°

(b) 45°

(c) 60°

Fig. 3. The comparison of propagating interface at 0.1s (left) and the final fillet shape (right) for the different three contact angles (case1)

3 Numerical Results

In the case1, the solder bump between IC chip and substrate is neglected and the flow front profile and filling time are evaluated by changing the contact angle. The filling times of the contact angles of 30°, 45° and 60° are about 1.0s, 1.2s and 1.4s, respectively. The instantaneous propagating gas-liquid interface at 0.1s and the final fillet shape obtained from the three contact angles are compared in Fig. 3. It is observed that as the contact angle becomes larger, the filling time is longer due to decrease of the flow velocity, and that the final fillet shapes for the three contact angles are different, depending on the collapse of semi-spherical liquid and the spread especially in the plus direction of x-axis. It is found that the effect of capillary action on the flow

Fig. 4. The final fillet shape (case2)

Fig. 5. The close-up view of propagating interface (case2)

Fig. 6. The final fillet shape (case3)

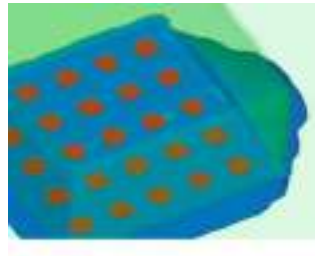

Fig. 7. The close-up view of the final fillet shape (case3)

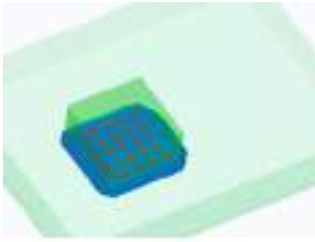

Fig. 8. The final fillet shape (case4)

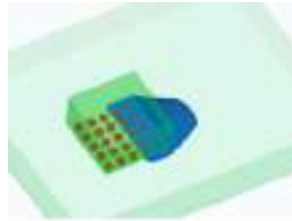

Fig. 9. The final fillet shape (case5)

behavior is one of the most important factors in predicting the filling time and the final fillet shape. In the case2-5, the solder bump of rectangular cylinder between IC chip and substrate is considered and the effect of viscosity and surface tension of liquid on the flow behavior is investigated, fixing the contact angle 30°. In the case2, where the viscosity and surface tension are the same as the case1, the final fillet shape and the close-up view in the instantaneous flow front are shown in Fig. 4 and Fig. 5, respectively. The filling time is about 3.5s. It is confirmed that the curve of flow front is a meniscus. In the

case3, only the viscosity in the case2 is changed by a factor of 0.1. The final fillet shape and the close-up view are shown in Fig. 6 and Fig. 7, respectively. The filling time is about 1.5s, which becomes shorter than that of the case2 due to increase of the flow velocity. It is observed that some air traps occur in the rear of solder bump, especially on the center line indicated by a dotted line in Fig. 2.

It is considered that when an air is trapped around a solder bump, the flow front attach the neighboring solder bump in the downstream direction before the flow goes around completely along the solder bump. That is the reason why the flow velocity in the minus direction of x-axis becomes much faster than that in the direction of y-axis. In the case4, only the surface tension in the case3 is changed by a factor of 0.1. The filling time is about 1.0s, which becomes shorter than that of the case3. The good final fillet shape is obtained as shown in Fig. 7, because the spread of liquid is smaller than those obtained from the case2-3 and there is no air trap as can be seen in the case3. In the case5, only the surface tension in the case2 is changed by a factor of 10.0. The final fillet shape is shown in Fig. 8. This result shows that the gap between IC chip and substrate can not be completely filled with the liquid.

4 Conclusions

It is observed that the capillary action, viscosity and surface tension are important factors affecting on the filling time and final fillet shape. It is possible to simulate the occurrence of air trap around the solder bump. In the future work, the numerical results should be confirmed by comparing with the available experimental data.

References

[1] Hashimoto, T., Tanifuji, S., Morinishi, K., Satofuka, N.: Numerical simulation of conventional capillary flow and no-flow underfill in flip-chip packaging. Computers & Fluids 37(5), 520–523 (2008)
[2] Rogers, S.E., Kwak, D.: Upwind differencing scheme for the time-accurate incompressible Navier-Stokes equations. AIAA Journal 28, 253–262 (1990)
[3] Hashimoto, T., Morinishi, K., Satofuka, N.: Numerical simulation of unsteady flow around deformable elastic body under fluid dynamic force. In: ECCOMAS 2004, Paper 364, pp. 1–19 (2004)
[4] Hashimoto, T., Morinishi, K., Satofuka, N.: Numerical simulation for impact of elastic deformable body against rigid wall under fluid dynamic force. In: ICCFD3, pp. 375–380 (2004)
[5] Sussman, M., Smeraka, P., Osher, S.: J. Comput. Phys. 114, 146–159 (1994)
[6] Brackbill, J.U., Kothe, D.B., Zemach, C.: J. Comput. Phys. 100, 335–354 (1992)

Simulation of Water Advancing over Dry Bed Using Lagrangian Blocks on Eulerian Mesh

Lai Wai Tan, Camilo E. Pinilla, and Vincent H. Chu

McGill University, Department of Civil Engineering and Applied Mechanics, Montreal, Canada H3A 2K6
vincent.chu@mcgill.ca

Lagrangian Blocks on Eulerian Mesh (LBEM) simulations of water advancing over dry bed are conducted using blocks as the computational elements. The non-negative nature of the blocks have allowed the LBEM simulation to be carried out without the oscillation problem that has limited the applicability of many existing computational schemes. At the leading edge of the water, the velocity is maximum and friction is the dominant effect. The simulation for the dominant friction effect at the wave front is carried out for the release of water from (i) dam-break outflow, (ii) levee overflow, and (iii) sump overflow. Despite the geometric difference, all three flows have the maximum velocity at the wave front following identical asymptotic trend at large time.

1 Introduction

Prediction of the water advancing over dry bed is crucial to understanding a variety of engineering problems including flooding over lands and wave run-up over beaches. Since velocity usually is highest at the leading edge, the frontal region is often the area of significant erosion. Reliable and robust computational schemes are required before the erosion problem can be correctly simulated [BS07, FC02, RBT03]. In a finite-volume formulation, as a consequence of spurious numerical oscillations, the water depth at the leading edge of the front may become negative leading to collapse of the computation. Flux limiters are required to control the numerical oscillations, and an artificial wet bed also is required to prevent the water depth from becoming negative during the simulation. Figure 1 shows the simulation of the dam-break waves by finite volume method (FVM). Flux limiters (MINMOD, MUSCL, SMART, Superbee, Ultimate-Quickest, Ultra-Quick, and Van Leer) and an artificial wet bed are employed to suppress the spurious oscillations. The wet bed produces an artificial surge waves which may affect the accuracy of the numerical simulation. The surge height is 0.67 m for an artificial wet-bed depth of 0.01 m, and 0.24 m for a wet-bed depth of 0.001 m, under a 10 m height of water behind the dam [Sto57]. The selection for the wet-bed is part of the task in the simulation by the FVM. The depth must be small

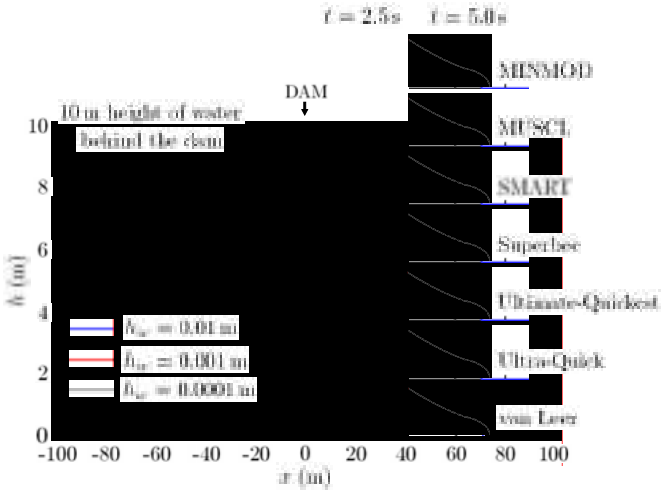

Fig. 1. Results obtained by FVM using three artificial wet bed depths $h_w = 0.01$ m, 0.001 m, and 0.0001 m; friction coefficient $c_f = 0.0038$ at $t = 2.5$ s and 5.0 s

enough to prevent significant formation of the surge, but must not be too small to avoid the collapse of the computation. The decision for the depth of the wet bed is particularly a difficult task, when the simulation is for water over variable topography.

Numerical methods have been developed for simulation of the wave front without the artificial wet bed. The Lagrangian Blocks on Eulerian Mesh (LBEM) is one such methods. It is an extension of the Lagrangian Block Method (LBM), which has been successfully implemented in the turbulence simulations [CA01, CA02]. The method is complimentary to other interface-tracking algorithms, including the level-set and the volume-of-fluid methods. Figure 2 shows the LBEM simulation obtained using large blocks. The LBEM is stable and robust despite the very large blocks used in these simulations.

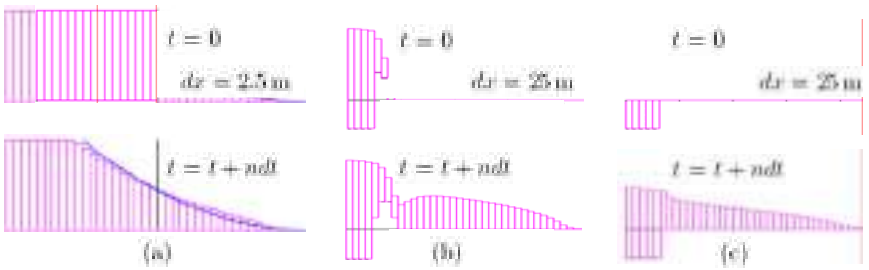

Fig. 2. LBEM simulations of the wave fronts on dry bed produced by the release of water from **(a)** dam-break outflow, **(b)** levee overflow, and **(c)** sump outflow

Figure 2a shows the close agreement of dam-break wave simulation with the exact solution by Ritter [Rit92]. The non-negative nature of the blocks has allowed the LBEM simulation to be carried out without the numerical oscillation problem.

2 LBEM Formulation

The Lagrangian blocks are contiguous elements defined to satisfy the requirement of fluid continuity. Figure 3a shows the blocks on the Eulerian mesh.

A block of fluid is defined by its depth h_i and width w_i. At the beginning of the computation time step t, the edges of the blocks fit the Eulerian mesh, i.e. $x_i^n = x_i$, $x_{i+1}^n = x_{i+1}$ and $w_i^n = x_{i+1}^n - x_i^n$. At the end of the time step $t + \Delta t$, the block will either be stretched or compressed as the edges of the block moves to the new positions x_i^{n+1} and x_{i+1}^{n+1}. The forces on the blocks are calculated assuming hydrostatic pressure variation over depth (Fig. 3b). To satisfy the continuity for volume conservation,

$$(x_i^{n+1} - x_{i+1}^{n+1})h_i^{n+1} = (x_i^n - x_{i+1}^n)h_i^n \tag{1}$$

The edge position of the block x_i at time $t + \Delta t$ are calculated by integrating the following momentum equation with time using the Lagrangian method:

$$\frac{Du_i}{Dt} = -g\,\frac{h_i - h_{i-1}}{x_{i+1}^n - x_i^n} - gS_f, \tag{2}$$

where $u_i = dx_i/dt$ = velocity, and $S_f = c_f u_i|u_i|/(2gh)$ = friction slope. The mass and momentum in the blocks are recasted onto the Eulerian mesh at each time step by the second moment method [EM72].

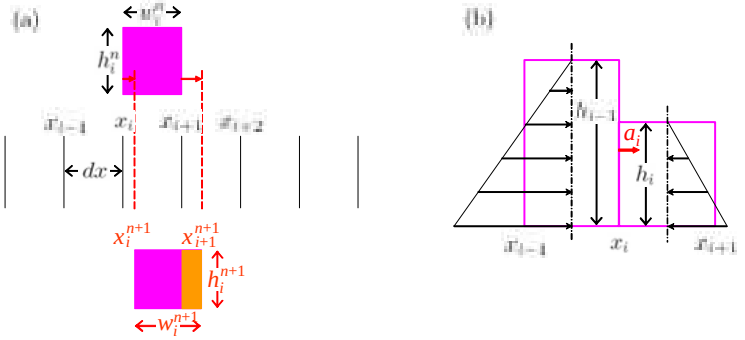

Fig. 3. (a) Movement of the Lagrangian blocks and redistribution of the mass in the blocks onto the fixed Eulerian mesh **(b)** Hydrostatic pressure forces on the upstream and downstream faces of the blocks

3 Friction Effect on Dam-Break Wave

Figure 4 shows the LBEM simulation results obtained for the dam-break wave. At the leading edge of the advancing front, the water depth is zero and the velocity is the highest. The wave front would advance on the horizontal bed with a velocity equal to $2\sqrt{gh_0}$ according to Ritter, if friction were ignored [Rit92]. In reality, friction is always the dominant effect at the front. The role of the friction, and the inertia effect, have been discussed by Whitham using the boundary-layer approximation [Whi55], by Hogg and Pritchard in terms of inner-and-outer expansion [HP04], and by Sakkas and Strelkoff using the method of characteristics [SS73]. The relationship of these previous analytical and semi-analytical results with the present numerical results is important to understand the erosional processes at the front, and has been presented at length in the conference.

The outflow is maximum at the location of dam removal. If friction is ignored, this maximum outflow is

$$q_{\max} = \frac{8}{27}\sqrt{gh_0^3} \tag{3}$$

Friction reduces this flowrate once the friction effect at the front has reached the location of the dam's removal (see Fig. 4c). In fact, the asymptotic profile of the advancing front is determined by this outflow $q_{\max}$.

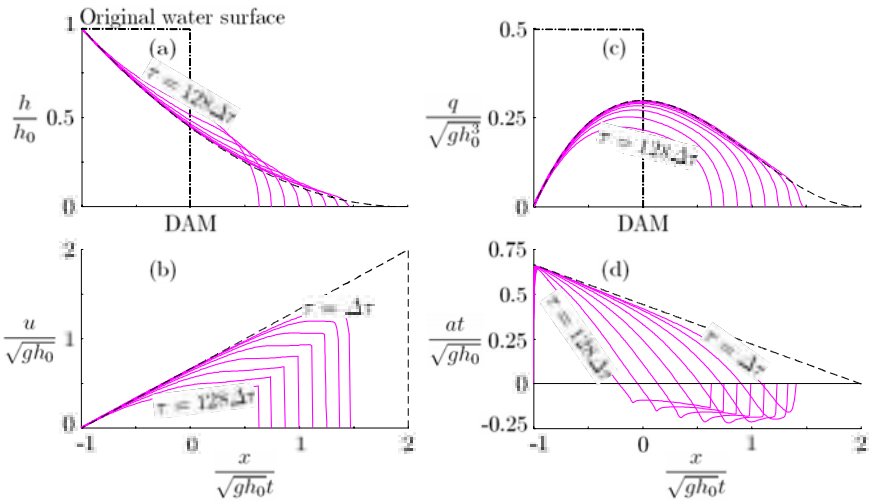

Fig. 4. Resistance effect on dam-break wave of $h_0 = 0.22\,\text{m}$, $c_f = 0.0038$ and $dx = 0.01\,\text{m}$; **(a)** depth **(b)** velocity **(c)** discharge, and **(d)** acceleration profiles, at $\tau = n\Delta\tau$ ($n = 1, 2, 4, 8, 16, 32, 64, 128$) where $\tau = c_f/2\sqrt{g/h_0}t$ and $\Delta\tau = 0.0127$

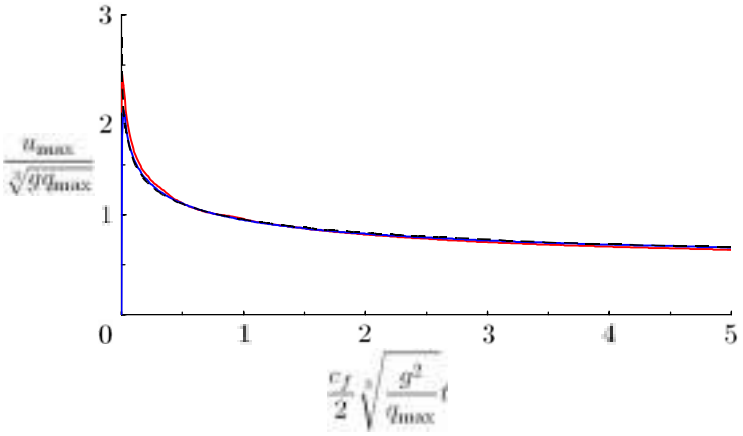

Fig. 5. Maximum erosional velocity over frictional bed $c_f = 0.0038$. Simulation results obtained for **(a)** dam-break outflow (*dashed line*), **(b)** levee overflow with height of levee = 1.0 (*red*), and **(c)** sump overflow with rising velocity = 1.6 (*blue*)

4 Summary of Results Based on $q_{\max}$

To demonstrate the dependence on $q_{\max}$, a number of numerical simulations has been conducted for wave fronts produced by other outflow geometries. The conditions of these simulations for (i) dam-break outflow, (ii) levee overflow, and (iii) sump overflow are summarized in Table 1.

Figure 5 shows the results correlated with the outflow rate $q_{\max}$. All simulation results fall onto the same curve when the maximum wave front velocity is normalized by the velocity scale $\sqrt[3]{gq_{\max}}$, and the time normalized by the

Table 1. Physical problems considered in obtaining a unified result of dimensionless frictional time scale for water advancing over dry bed

Parameters	Dam-break outflow	Levee overflow	Sump overflow
Friction coefficient c_f	0.0038 0.019 0.038	0.0038 0.019 0.038	0.0038 0.019 0.038
Height of levee $h_L/\sqrt[3]{q_{\max}^2/g}$		1.00 0.50 0.25	
Rising velocity $v_R/\sqrt[3]{gq_{\max}}$			1.6 0.8 0.4

time scale $1/[(c_f/2)\sqrt[3]{g^2/q_{\max}}]$. The asymptotic behaviour of the front is determined by the maximum rate $q_{\max}$, of the outflow at the control section.

5 Conclusion

The wet-and-dry interface across the water wave front has been successfully simulated by the LBEM without the use of flux limiter and artificial wet bed. The results for the dam-break outflow are consistent with the analytical and semi-analytical solutions to the problem [TC07]. The simulations of levee overflow and sump overflow using large blocks have demonstrated the versatility of the method for practical applications. The method is now ready for generalization to two-dimensional outflow on complex terrains.

References

[BS07] Begnudelli, L., Sanders, B.F.: Conservative wetting and drying methodology for quadrilateral grid finite-volume models. J. Hydr. Engng. 133(3), 312–322 (2007)

[CA01] Chu, V.H., Altai, W.: Simulation of shallow transverse shear flow by generalized second moment method. J. Hydr. Res. 39(6), 575–582 (2001)

[CA02] Chu, V.H., Altai, W.: Simulation of turbulence and gravity interfaces by Lagrangian block method. In: Comp. Fluid Dynamics 2002, pp. 299–304. Springer, New York (2002)

[EM72] Egan, B.A., Mahoney, J.R.: Numerical modeling of advection and diffusion of urban source pollutant. J. Appl. Meteorology 11, 312–322 (1972)

[FC02] Fraccarollo, L., Capart, H.: Riemann wave description of erosional dam-break flows. J. Fluid Mech. 461, 183–228 (2002)

[HP04] Hogg, A.J., Pritchard, D.: The effects of hydraulic resistance on dam-break and other shallow inertial flows. J. Fluid Mech. 501, 179–212 (2004)

[RBT03] Rogers, B.D., Borthwick, A.G.L., Taylor, P.H.: Mathematical balancing of flux gradient and source terms prior to using Roe's approximate Riemann solver. J. Comp. Physics 192, 422–451 (2003)

[Rit92] Ritter, A.: Die fortpflanzung der wasserwellen. Zeitschrift des Vereines Deutscher Ingenieure 36(33), 947–954 (1892)

[SS73] Sakkas, J.G., Strelkoff, T.: Dam-break flood in a prismatic dry channel. J. Hydr. Div., ASCE 99(HY12), 2195–2216 (1973)

[Sto57] Stoker, J.J.: Water waves. Interscience, Hoboken (1957)

[TC07] Tan, L.W., Chu, V.H.: Dam-break flood waves on dry and sloping bed using Lagrangian Block Method. In: 5th Int. Symp. on Env. Hydr., Arizona, December 4-7 (2007)

[Whi55] Whitham, G.B.: The effects of hydraulic resistance in the dam-break problem. Proc. Roy. Soc. (London) A227, 399–407 (1955)

Time-Derivative Preconditioning for Single and Multicomponent Flows

Jeffrey A. Housman[1], Cetin C. Kiris[2], and Mohamed M. Hafez[3]

[1] Department of Mechanical and Aeronautical Engineering,
University of California Davis,
jhousman@ucdavis.edu
[2] NASA Ames Research Center,
Moffett Field, CA 94035, USA
Cetin.C.Kiris@nasa.gov
[3] Department of Mechanical and Aeronautical Engineering,
University of California Davis,
mhafez@ucdavis.edu

Abstract. A time-derivative preconditioned system of equations suitable for the numerical simulation of single and multicomponent inviscid flows at all speeds is formulated. For low speed multicomponent flow, a preconditioned nonconservative discretization method is described which preserves pressure and velocity equilibrium across fluid interfaces. This method is extended to transonic and supersonic flows using a hybrid approach that combines conservative and nonconservative formulations. Both multicomponent (multiple fluids) and multiphase (same fluid in different phases) can be solved using the proposed methods.

1 Introduction

Many propulsion related flow applications require modeling of multicomponent and multiphase flows over a wide range of Mach numbers. For example, the low speed flow of liquid propellants through the Low Pressure Fuel Turbopump (LPFTP) in the Space Shuttle Main Engine (SSME), see Kiris *et al.* [1]. Another example is the ignition overpressure suppression system activated during the launch of a space vehicle. As a first step towards modeling these complex flow applications, a time-derivative preconditioned numerical method for the simulation of inviscid multicomponent and multiphase compressible fluids obeying an arbitrary equation of state is described.

Time-marching numerical methods used to solve the compressible equations become inefficient and lose accuracy when applied to low speed flow applications, see Merkle and Choi [2]. In addition, application of conservative numerical methods to multicomponent flows produce nonphysical pressure and velocity oscillations across fluid interfaces, see Karni [3]. In this work, a time-derivative preconditioned system of equations for inviscid multicomponent flow is described along with a characteristics-based nonconservative

numerical method, which eliminates nonphysical behavior across fluid interfaces. The nonconservative method is an extension of the Split Coefficient Matrix (SCM) method, developed by Chakravarthy *et al.* [4], to low speed flows. In order to model flows containing shocks, a novel hybrid approach which combines a conservative and nonconservative method is described.

2 Governing Equations

The time-derivative preconditioned system of equations for an inviscid N-component mixture of compressible fluids written in strong conservation law form for a two-dimensional generalized curvilinear coordinate system are

$$\Gamma_p \frac{\partial \hat{Q}}{\partial s} + \frac{\partial \hat{W}}{\partial t} + \frac{\partial \hat{F}}{\partial \xi} + \frac{\partial \hat{G}}{\partial \eta} = 0 \tag{1}$$

where

$$\begin{aligned}
\hat{Q} &= J^{-1} \left(p, u, v, T, Y_1, \cdots, Y_{N-1}\right)^T, \\
\hat{W} &= J^{-1} \left(\rho, \rho u, \rho v, \rho H - p, \rho Y_1, \cdots, \rho Y_{N-1}\right)^T, \\
\hat{F} &= \left(\rho \hat{U}, \rho \hat{U} u + \hat{\xi}_x p, \rho \hat{U} v + \hat{\xi}_x p, \rho \hat{U} H - \hat{\xi}_t p, \rho \hat{U} Y_1, \cdots, \rho \hat{U} Y_{N-1}\right)^T \\
\hat{G} &= \left(\rho \hat{V}, \rho \hat{V} u + \hat{\eta}_x p, \rho \hat{V} v + \hat{\eta}_x p, \rho \hat{V} H - \hat{\eta}_t p, \rho \hat{V} Y_1, \cdots, \rho \hat{V} Y_{N-1}\right)^T
\end{aligned}$$

Standard notation is used for the fluid dynamic variables p pressure, (u, v) Cartesian velocity components, T temperature. The mixture fluid properties ρ mixture density, $H = h + (u^2 + v^2)/2$ mixture total enthalpy, and Y_i the mass fraction of the i^{th} fluid component for $i = 1, \cdots, N-1$. Note the N^{th} component mass fraction is given by the saturation condition $Y_N = 1 - \sum_{i=1}^{N-1} Y_i$. The mixture properties and their partial derivatives with respect to pressure and temperature, along with the scaled metric terms and contravariant velocities, are described in Housman [5]. Additionally, the local time-derivative preconditioning matrix is derived in Housman [6] for a single component fluid and extended to a multicomponent fluid in [7] and [8].

3 Numerical Method

Three discretization strategies are outlined for the convective flux derivatives. These include a well known conservative precondition Roe method (PROE), a novel nonconservative preconditioned Split Coefficient Matrix method (PSCM), and a hybrid conservative/nonconservative method (HYBR) which combines the two approaches and is approapriate for multicomponent flow problems at all speeds. Once the spatial derivatives have been discretized using one of three methods, efficient time marching numerical methods are used to solve either the steady or unsteady equations.

3.1 Conservative Formulation

The conservative preconditioned Roe method, described in van Leer, Lee, and Roe [9], utilizes the standard conservative finite difference form of the discrete equations where the preconditioned numerical flux is

$$\tilde{F}_{j+1/2} = \frac{1}{2}\left[\hat{F}(Q_{j+1}) + \hat{F}(Q_j) - \left(\Gamma_p|\Gamma_p^{-1}\hat{A}|\right)_{j+1/2}(Q_{j+1} - Q_j)\right], \quad (2)$$

where Γ_p and $|\Gamma_p^{-1}\hat{A}| = \hat{R}_\xi|\hat{\Lambda}_\xi|R_\xi^{-1}$ are evaluated at the density weighted symmetric average.

3.2 Nonconservative Formulation

The nonconservative formulation is based on a preconditioned version of the SCM method which starts with the quasi-linear form of the equations. Once the preconditioned flux Jacobians have been factored using their eigenvalue decomposition, and split into there positive and negative eigenvalue contributions, the nonconservative positive and negative flux derivatives are defined as

$$\left(\partial\hat{F}/\partial\xi\right)^{\pm} \doteq \hat{R}_\xi\hat{\Lambda}_\xi^{\pm}\hat{R}_\xi^{-1}\left(\partial Q/\partial\xi\right). \quad (3)$$

These positive and negative flux derivatives are then discretized using an upwind biased method.

3.3 Hybrid Formulation

The hybrid method, which combines the conservative preconditioned Roe and the nonconservative preconditioned SCM methods, uses local changes in the mass fraction variable to determine if a sharp interface is present, see Karni [10]. Once a sharp interface is detected the discrete equations are locally switched from conservative to nonconservative form, such that pressure and velocity equilibrium across the fluid interface is preserved. The hybrid method can formally be written as

$$\frac{\partial\hat{Q}}{\partial s} + \phi\Gamma_p^{-1}\left[\text{PROE}\right] + (1-\phi)\left[\text{PSCM}\right]. \quad (4)$$

Using any of the three approaches the semi-discrete form of the equations are discritized in pseudo-time s using an implicit Euler discretization and solved using an inexact Newton method with alternating line implicit Jacobi relaxation. Typically three relaxation sweeps are taken at each nonlinear iteration. Details of the algorithm and the dual time stepping procedure used for unsteady cases are described in Housman [5].

4 Results

In order to test the accuracy of the different appoaches, two multicomponent Riemann problems are solved, and an exact solution is used for comparison. First order discretization in both space and time are used to observe the true dissipative nature of the approaches. To distinquish between the methods the preconditioned Roe method is denoted PROE, a nonpreconditioned Roe method by QROE, the preconditioned SCM method by PSCM, and the hybrid method by HYBR. Next the steady single phase flow of air over a NACA0012 airfoil is computed for varying Mach numbers to demonstrate the Mach independent convergence of the PROE and PSCM methods. Which are the two methods combined to form the hybrid method, it is important to recall that the hybrid method reduces to the conservative PROE method when applied to single phase flows. Finally, the noncavitating and cavitating flow of liquid water through a channel containing a NACA0015 hydrofoil is simulated and compared to experimental data. The two dimensional results are computed with third-order upwind biased differencing in space and the minmod limiter for flows containing sharp fluid interfaces.

4.1 Riemann Problems

As alluded to in the introduction, conservative methods produce nonphysical pressure and velocity oscillations across moving component contact discontinuities when both γ and the temperature vary across the interface. Two one-dimensional Riemann problems are used to demonstrate this. The initial data for the first case is given by $(\rho_L, u_L, p_L, Y_L, \gamma_L)^T = (1.0, 1.0, 1.0, 1.0, 1.6)^T$ and $(\rho_R, u_R, p_R, Y_R, \gamma_R)^T = (0.1, 1.0, 1.0, 0.0, 1.2)^T$. Figure 1 plots the pressure and velocity at $t = 0.25$ seconds. The second case consists of a left moving rarefaction, a right moving contact, and a right moving shock. The initial data is $(\rho_L, u_L, p_L, Y_L, \gamma_L)^T = (1.0, 0.0, 1.0, 1.0, 1.6)^T$ and $(\rho_R, u_R, p_R, Y_R, \gamma_R)^T = (0.125, 0.0, 0.1, 0.0, 1.2)^T$. Figure 2 plots the velocity over the domain and

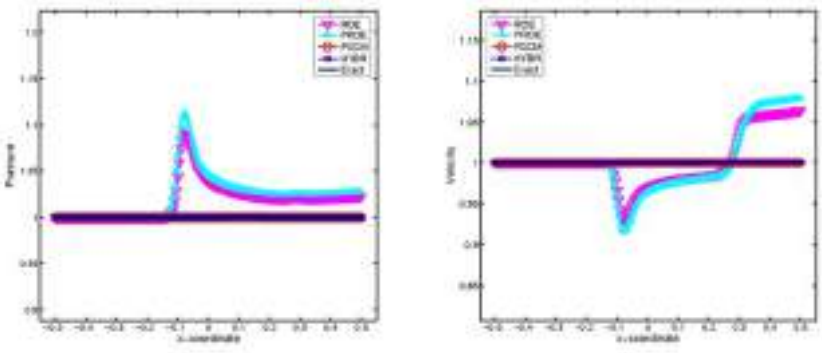

Fig. 1. Results for Riemann problem I: Pressure (left) and Velocity (right)

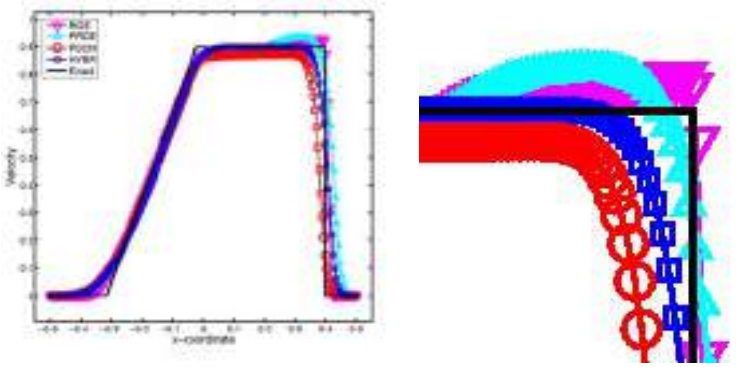

Fig. 2. Results for Riemann problem II: velocity (left) and close-up of velocity (right)

close-up to the non-physical jump. This nonphysical pressure and velocity jump across the contact, incurred by the conservative methods, is clearly observed in both solutions. While the nonconservative approach preserves the pressure and velocity equilibrium the Rankine-Hugonoit jump conditions are not satisified across the shock in the second case. The superiority of the hybrid approach is demonstrated, in that correct shock jumps and locations are obtained and nonphysical jumps across the fluid interface are suppressed.

4.2 NACA0012 Airfoil

Simulations of external flow of an inviscid single component gas (air) around a NACA0012 airfoil, for a wide range of subsonic free-stream Mach numbers are reported. The purpose of this case is to demonstrate the Mach independent convergence of the PROE and PSCM methods for subsonic flow and compare the solutions of the conservative and nonconservative approaches at low speeds. Note the HYBR method is equivalent to the PROE method for single component flows. The case was originally proposed by Rizzi and Viviand [11] and modified here by considering a series of subsonic free-stream

Table 1. Number of iterations required to reduce the maximum residual eight orders of magnitude for steady flow around a NACA0012 airfoil

M_{ref}	QROE	PROE	PSCM
0.5	306	306	331
0.1	325	262	228
0.01	> 1000	262	228
0.001	> 1000	336	257

Mach numbers. A single structured C-grid consisting of 169×65 grid points clustered near the airfoil is used. Convergence results for free-stream Mach numbers of $M_{ref} = 0.5, 0.1, 0.01, 0.001$ and zero angle of attack are reported in Table 1. Both Mach independent convergence and approximately the same convergence rates are acheived by the conservative and nonconservative preconditioned methods, while the nonpreconditioned method fails to converge as the Mach number approaches zero.

4.3 NACA0015 Hydrofoil

In this case liquid water flowing through a channel containing a NACA0015 hydrofoil is simulated at both noncavitating and cavitating conditions. This case was proposed as a benchmark problem by Salvetti and Beux [12] as part of the Numerical Workshop conducted as the conference on *Mathematical and Numerical Aspects of Low Mach Number Flows*. For details on the test case, the phase change model, and the particular equations of state used, see Housman [5]. A structured overset grid system consisting of 22205 grid points is used to discretize the domain. Figure 3 displays the CP curves on the surface of the airfoil for both the noncavitating and cavitating cases. It is observed that similar results are obtained using either the PROE, PSCM, or HYBR methods, and each compare well with the experimental results. While simuliar solutions are obtained, superior sub-iteration convergece was obtained using the nonconservative and hybrid methods for cavitating conditions.

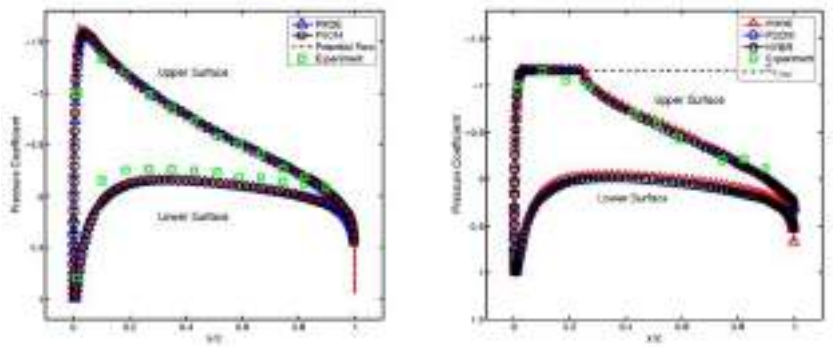

Fig. 3. Coefficient of pressure on the upper and lower surface of the NACA0015 hydrofoil contained in a channel: (left) noncavitating and (right) cavitating

5 Summary

A time-derivative preconditioned system of equations appropriate for multicomponent/multiphase flows is described, along with three discretization strategies. Each of the preconditioned methods achieve Mach independent

convergence. The hybrid method was shown to preserve pressure and velocity equilibrium across fluid interfaces and obtain the correct weak solution when shocks are present, and cavitating multiphase capabilities were demonstrated.

References

1. Kiris, C., Kwak, D., Chan, W., Housman, J.: High Fidelity Simulations for Unsteady Flow Through Turbopumps and Flowliners. Computers and Fluids 37, 536–546 (2007)
2. Merkle, C.L., Choi, Y.H.: Computation of Low Speed Compressible Flows with Time-Marching Methods. International Journal for Numerical Methods in Engineering 25, 292–311 (1985)
3. Karni, S.: Multicomponent Flow Calculations by a Consistent Primitive Algorithm. Journal of Computational Physics 112, 31–43 (1994)
4. Chakravarthy, S.R., Anderson, D.A., Salas, M.D.: The Split-Coefficient Matrix Method for Hyperbolic Systems of Gas Dynamics. In: 18th AIAA Aerospace Sciences Meeting, AIAA-80-0268 (January 1980)
5. Housman, J.: Time-Derivative Preconditioning Method for Multicomponent Flow. PhD thesis, University of California Davis (2007)
6. Housman, J., Kiris, C., Hafez, M.: Preconditioned methods for simulations of low speed compressible flows (accepted for publication in Computers and Fluids) (in print) (2008)
7. Housman, J., Kiris, C., Hafez, M.: Time-Derivative Preconditioning Method for Multicomponent Flow part i: Riemann problems (accepted for publication to Journal of Applied Mechanics) (in print) (2008)
8. Housman, J., Kiris, C., Hafez, M.: Time-Derivative Preconditioning Method for Multicomponent Flow part ii: Two-dimensional applications (accepted for publication to Journal of Applied Mechanics) (in print) (2008)
9. van Leer, B., Lee, W.T., Roe, P.L.: Characteristic Time-Stepping or Local Preconditioning of the Euler Equations. In: AIAA Computational Fluid Dynamics Conference, Honolulu, AIAA-91-1552-CP (1991)
10. Karni, S.: Hybrid Multifluid Algorithms. SIAM Journal of Scientific Computing 17(5), 1019–1039 (1996)
11. Rizzi, A., Viviand, H. (eds.): Numerical Methods for the Computation of Inviscid Transonic Flows with Shock Waves. Notes on Numerical Fluid Mechanics, vol. 3. Vieweg (1981)
12. Salvetti, M.-V., Beux, F.: Liquid Flow Around Non-Cavitating and Cavitating NACA0015 Hydrofoil. In: Numerical Workshop Problem from Mathematical and Numerical Aspects of Low Mach Number Flows Conference, Porquerolles, France (2004)

“*This page left intentionally blank.*”

Part 32
Multiphase Flow 3

“*This page left intentionally blank.*”

High-Speed Jet Formation after Solid Object Impact

Stephan Gekle[1], José Manuel Gordillo[2], Devaraj van der Meer[1], and Detlef Lohse[1]

[1] Physics of Fluids, University of Twente, The Netherlands
[2] Grupo de Mecánica de Fluidos, Universidad de Sevilla, Spain

1 Introduction

A spectacular example of free surface flow is the impact of a solid object on a liquid: At impact a splash is created and a surface cavity (void) emerges which then collapses creating an upwards and downwards jet at singularity and entraining a giant bubble [1, 3]. The impact of a circular disc leads to an especially impressive jet. Using boundary-integral techniques we illucidate the mechanism that turns the diverging radial motion of the collapsing cavity into the vertical upshoot of a fast and thin jet.

Jet formation in the present context stands out from previously studied mechanisms. It does not originate from a flow pattern whose principal direction prior to jet formation already points along the jet axis, such as the collapse of bubbles near a solid wall, jetting induced by pressure waves or the thick Rayleigh jets observed for raindrops falling on a lake surface in e.g. [4]. Neither is it created by concurrence of capillary waves – as for "champagne bubbles" rupturing near a free surface – or Faraday waves in a vertically shaken fluid container. Instead, the purely inertial focussing makes the present phenomenon more reminiscent of the very violent jet of fluidized metal observed during the collapse of "lined cavities" in military and mining operations, see e.g. [2].

2 Methods

Since the process admits a potential flow description we choose an axisymmetric boundary-integral method including surface tension. This method is very powerful for accurately predicting the evolution of complicated free surfaces with high computational efficiency as it requires information only from the fluid boundaries. Careful surface surgery is required as the cavity pinches off and the purely radial flow almost instantly diverts into the vertical motion of the up- and downward jets. To resolve the small-scale features during pinch-off and jet formation adaptive grid refinement is employed with node

densities spanning four orders of magnitude. While boundary-integral methods are very powerful in describing surface phenomena they are known to be vulnerable to numerical instabilites, which we overcome by innovative smoothing techniques. Numerical tracer particles visualize the distribution of liquid during jet formation.

3 Results

The process of impact and jet formation is illustrated in Fig. 1. The disc speed is constant throughout. After impacting on a semi-infinite water pool a cavity several disc radii deep emerges (a). Hydrostatic pressure pushes the surface inward leading to the pinch-off of a large bubble halfway down the cavity (b). This pinch-off point constitutes a finite-time singularity with diverging radial velocity. The energy contained in the mass of inwards rushing fluid is thus focussed on a single point leading to the two enormously fast and thin fluid jets shooting up- and downwards from the pinch-off point in Fig. 1 (c) and (d).

Immediately after cavity closure the pinch-off location turns into a stagnation point surrounded by a locally hyperbolic flow pattern. Intuitively one might expect the incoming liquid being deflected by the stagnation point to cause the formation of the two jets. Our results show that this is *not* the

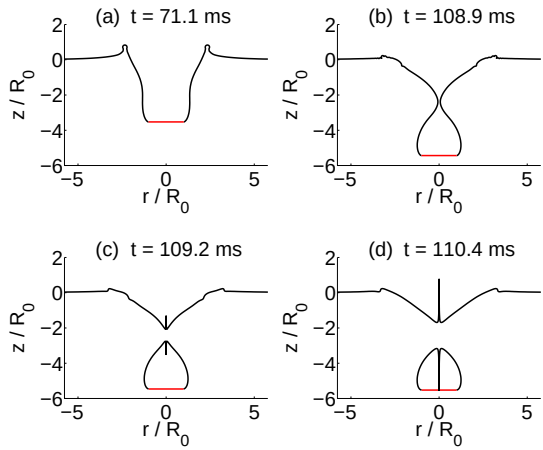

Fig. 1. Surface profiles (black) showing the cavity created after the impact of the disc (red) in (a), its collapse due to hydrostatic pressure (b) and the resulting creation of two thin and fast jets, (c) and (d). Note the extremely short time scale of jet formation: the jet grows above the original surface in less than 1% of the total time after impact. Units are normalized by the disc radius $R_0 = 2\text{cm}$, the impact speed is $V_0 = 1\text{m/s}$.

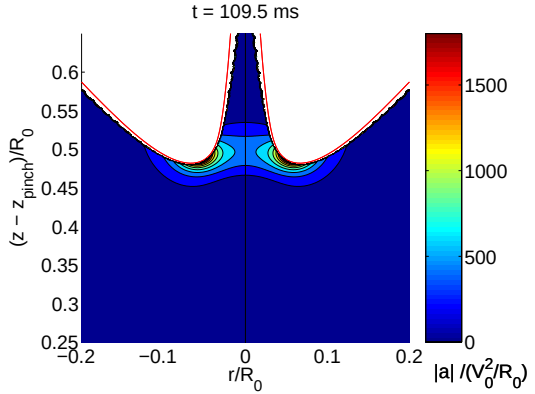

Fig. 2. The material acceleration $a = DV/Dt$ is confined to a small region around the jet base. As the liquid rushes in towards the axis of symmetry its radial momentum is diverted upwards into the jet. The stagnation point at (0,0) is not shown, since it lies far too deep to influence the process longer than in the first instances after pinch-off.

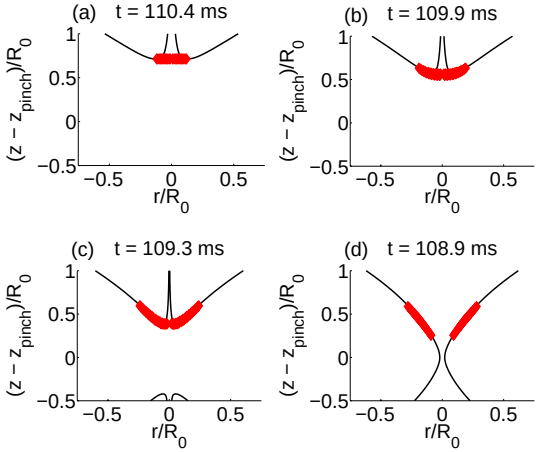

Fig. 3. A line of tracer particles is placed at the base of the jet (a). Going forward in time, these particles would move upwards into the jet. Reversing the flow field and stepping backwards in time, (b) and (c), allows us to follow the tracers and to illustrate their region of origin (d). Repeating this process for different starting times demonstrates that the entire jet originates from a similar thin band straddling the surface of the collapsing bubble (not shown here for clarity).

case. Jet formation turns out to be a very local process with the vertical acceleration of the fluid occuring almost exclusively around the base (surface minimum/maximum for the upward/downward jet, respectively) of the jet as shown in Fig. 2.

This result implies that the liquid contained in the jet cannot originate from an extended bulk region around the pinch-off point, but rather from a very thin layer of fluid straddling the surface of the original collapsing bubble, see Fig. 3.

4 Conclusions

Using boundary integral simulations we illucidate the mechanism responsible for the ejection of thin high-speed jets after the impact of solid objects on a water surface. Surprisingly, the formation of the jet is not related to the stagnation point at the closing location of the collapsing cavity, but due only to the inertial focussing of the colliding liquid at the base of the jet. Despite the whole liquid bulk being set into motion by hydrostatic pressure, the jet, nevertheless, is shown to feed exclusively from a very thin layer of fluid on the surface of the collapsing cavity.

References

1. Bergmann, R., van der Meer, D., Stijnman, M., Sandtke, M., Prosperetti, A., Lohse, D.: Giant bubble pinch-off. Phys. Rev. Lett. 96, 154505 (2006)
2. Birkhoff, G.D., MacDonald, D.P., Pugh, W.M., Taylor, G.I.: Explosives with lined cavities. J. Appl. Phys. 19, 563–582 (1948)
3. Gekle, S., van der Bos, A., Bergmann, R., van der Meer, D., Lohse, D.: Noncontinuous froude number scaling for the closure depth of a cylindrical cavity. Phys. Rev. Lett. 100, 084502 (2008)
4. Morton, D., Rudman, M., Liow, J.L.: An investigation of the flow regimes resulting from splashing drops. Phys. Fluids 12, 747–763 (2000)

Numerical Study on Population Balance Approaches in Modeling of Isothermal Vertical Bubbly Flows

Sherman C.P. Cheung[1], G.H. Yeoh[2], J.Y. Tu[1], E. Krepper[3], and D. Lucas[3]

[1] School of Aerospace, Mechanical and Manufacturing Engineering, RMIT University, Victoria 3083, Australia
chipok.cheung@rmit.edu.au, jiyuan.tu@rmit.edu.au
[2] Australian Nuclear Science and Technology Organisation (ANSTO), PMB 1, Menai, New South Wales 2234, Australia
Guan.Yeoh@ansto.gov.au
[3] Institute of Safety Research, Forschungszentrum Rossendrof e.V., P.O. Box 510 119, 01314 Dresden, Germany
e.krepper@fzd.de, d.lucas@fzd.de

Practicing engineers are constantly confronted with the prospect of solving complex gas-liquid bubbly flow problems in real industrial systems. The use of population balance models coupled with the two-fluid model presents the most viable way of handling such flows. The homogeneous MUltiple-SIze-Group (MUSIG) model has recently become a widely adopted population balance approach whereby the continuous bubbles size range can be represented by a series of discrete classes. The improved inhomogeneous MUSIG model extends the capability of accounting different bubble shapes and travelling gas velocities. Conversely, the Average Bubble Number Density (ABND) model represents another simpler approach in handling bubble interactions in complex gas-liquid bubbly flow. The capability of these three population balance models is assessed. Particular emphasis is directed towards the possible handling of bubbly-to-slug transition flow conditions. Numerical predictions are compared against experimental data obtained from Lucas et al. [1] and Hibiki et al. [2]. Shortcomings and applicability of these models for industrial applications are also discussed.

1 Introduction

Complex gas-liquid bubbly flow structures are featured in many practical applications. Industrial systems that purposefully promote large interfacial areas for gas-liquid mass transfer and efficient mixing for competing gas-liquid reactions are extensively employed especially in the chemical, petroleum, mining and pharmaceutical industries. The population balance approach, which allows the evaluation of averaged bubble size distribution with appropriate considerations of bubble interactions, is increasingly being adopted to model the aforementioned systems.

The recent numerical studies based on the MUltiple-SIze-Group (MUSIG) model has typified the application of population balance approach in bubbly flow simulations [3-5]. In the homogeneous MUSIG model, the continuous size range

of bubbles can be discretized into a number of discrete size classes. For each class, a scalar equation is solved to accommodate the population changes caused by intra/inter-group bubble coalescence and break-up. The capability of the MUSIG model can be further extended to account different bubble shapes with different travelling velocities. The inhomogeneous MUSIG model developed by Krepper et al. [6], which consisted of sub-dividing the dispersed phase into N number of velocity fields, demonstrated the practicability of such an extension. This flexibility represents a robust feature for bubbly flows modelling.

Excessive computational calculations to solve a large number of bubble classes with the inclusion of different bubble shapes with different travelling velocities may however significantly overwrite the potential benefits that the MUSIG models originally intended to achieve. Recently, an Average Bubble Number Density (ABND) equation, which is equivalent to the interfacial area transport equation, has been proposed in our previous study [7]. The ABND aims at condensing the representation of the bubble size distribution into a single average scalar (i.e. bubble number density) –another simpler approach for solving the population balance equation. The main focus in this paper is directed towards comparing the capability of the three population balance approaches (i.e. homogeneous MUSIG, inhomogeneous MUSIG and ABND models) to resolve various isothermal various flow conditions. Predictions of these models are compared against two different experimental data of isothermal gas-liquid bubbly flow by Lucas et al. [1] and Hibiki et al. [2].

2 Mathematical Models

The three-dimensional two-fluid model is adopted to solve the ensemble-averaged of mass and momentum equations governing each phase. Denoting the liquid as the continuum phase (α_l) and the vapour (i.e. bubbles) as disperse phase (α_g), these equations can be found as follow

$$\frac{\partial(\rho_i \alpha_i)}{\partial t} + \nabla \cdot (\rho_i \alpha_i \vec{u}_i) = 0 \tag{1}$$

$$\frac{\partial(\rho_i \alpha_i \vec{u}_i)}{\partial t} + \nabla \cdot (\rho_i \alpha_i \vec{u}_i \vec{u}_i) = -\alpha_i \nabla P + \alpha_i \rho_i \vec{g} + \nabla \cdot \left[\alpha_i \mu_i^e \left(\nabla \vec{u}_i + (\nabla \vec{u}_i)^T\right)\right] + F_i \tag{2}$$

The total interfacial force F_i is formulated according to appropriate consideration of different sub-forces affecting the interface between each phase. For the liquid phase, the total interfacial force is given by:

$$F_{\mathrm{lg}} = F_{\mathrm{lg}}^{\mathrm{drag}} + F_{\mathrm{lg}}^{\mathrm{lift}} + F_{\mathrm{lg}}^{\mathrm{lubrication}} + F_{\mathrm{lg}}^{\mathrm{dispersion}} \tag{3}$$

The sub-forces appearing on the right hand side of the above equation are: drag force, lift force, wall lubrication force and turbulent dispersion force. More detail descriptions of these sub-forces can be found in Anglart and Nylund [8]. Note that for the gas phase: $F_g = -F_{lg}$.

2.1 Population Balance Approaches

Averaged Bubble Number Density (ABND) Model

In the ABND model, the population balance of dispersed bubbles is represented by an average quantity of bubble number density, *n*, which is mainly governed by the bubble coalescence and breakage mechanism. The average bubble number density transport equation can be thereby expressed as follow:

$$\frac{\partial n}{\partial t} + \nabla \cdot \left(\vec{u}_g n \right) = \phi_n^{RC} + \phi_n^{TI} \tag{4}$$

where ϕ_n^{RC} and ϕ_n^{TI} are the bubble number density changes due to random collision and turbulent induced breakage. The phenomenological mechanism of coalescence and breakage source terms need closure to describe the spatial evolution of the gas phase. The coalescence and breakage kernels proposed by Yao and Morel [9] are employed and incorporated within the ABND model.

MUltiple SIze Group (MUSIG) Model

For the MUSIG model, to ensure overall mass conservation for all poly-dispersed vapour phases, the above bubble number density equation can be re-expressed in terms of the volume fraction and size fraction of the bubble size class *i*, $i \in [1, M_j]$, of velocity group *j*, $j \in [1, N]$ according to:

$$\frac{\partial \rho_j \alpha_j f_i}{\partial t} + \nabla \cdot \left(\rho_g \alpha_j f_i \vec{u}_j \right) = S_{j,i} \tag{5}$$

On the right hand side of the equation, the term $S_{j,i} = \left(P_C + P_B - D_C - D_B \right)$ represents the net mass transfer rate of the bubble class *i* resulting from the source of P_C, P_B, D_C and D_B, which are the production rates due to coalescence and breakage and the death rate due to coalescence and breakage of bubbles evaluated according to the kernels proposed by Prince and Blanch [10] and Luo and Svendsen [11] respectively.

3 Numerical Details

The generic CFD code ANSYS-CFX 11 was utilised to handle the two sets of equations governing conservation of mass and momentum. Numerical simulations of two experiments were performed on a 60^o radial sector of the pipe with symmetry boundary conditions imposed at the end vertical sides. At the pipe outlet, a relative averaged static pressure of zero was specified. In modelling bubble induced turbulent flow, the Shear Stress Transport (SST) model was adopted while the effect of bubbles on liquid turbulence was handled by the Sato's bubble-induced turbulent viscosity model. For the simulation of Hibiki's experiment [2], uniformly distributed superficial liquid and gas velocities, void fraction and bubble size (i.e. 3mm) were specified at inlet. Bubble size in the range of 0-10 mm

was discretised into 10 bubble groups. These 10 size groups were further divided into two velocity fields in the *inhomogeneous* MUSIG model. For the TOPFLOW experiment by Lucas et al. [1], bubbles were injected from 12 equally-spaced mass point sources at circumvent of the pipe while the bubble size were specified according to experimentally measured size. Twenty bubbles groups were employed to discretized the bubble range from 0-60mm where the first 2 groups assigned to the first velocity field and the other 18 to the second velocity field. Reliable convergence were achieved within 2500 iterations when the RMS (root mean square) pressure residual dropped below 1.0×10^{-7}. A fixed physical time scale of 0.002s was adopted for all steady state simulations.

4 Results and Discussions

Fig. 1 depicts the measured and predicted bubble size distribution and radial gas volume fraction profiles for the test case TOPFLOW 118 with two different gas

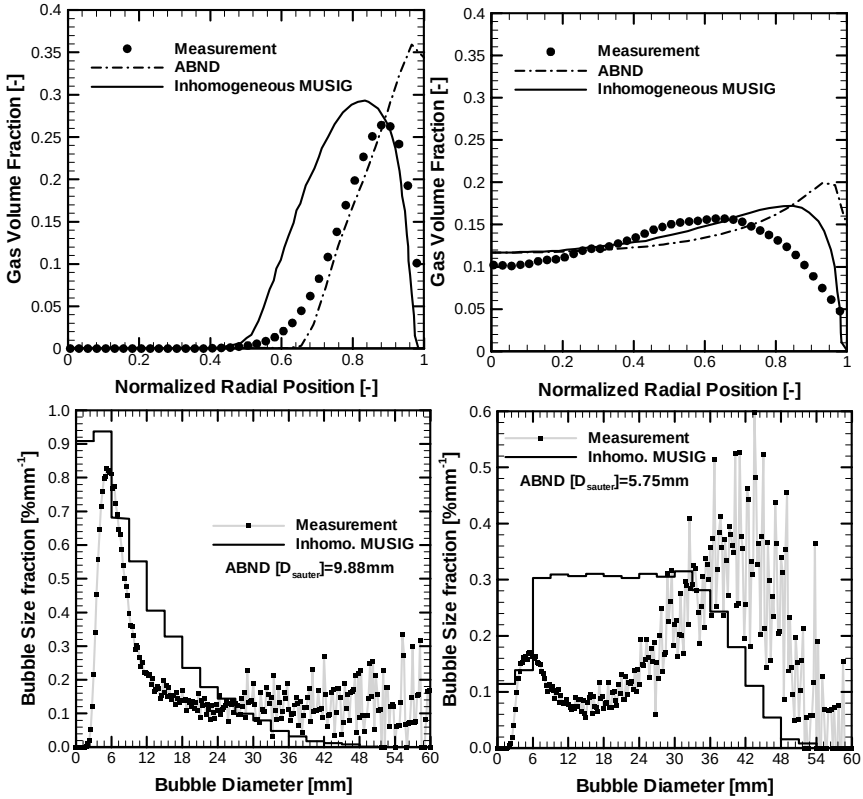

Fig. 1. Predicted and measured bubble gas volume fraction and bubble size distribution profiles for the test case TOPFLOW 118 with gas injection inlet locations 0.335m (left) and 1.552m (right)

injection inlet locations (i.e. 0.335m and 1.552m). In general, predicted gas volume fraction profiles of both ABND and inhomogeneous MUSIG model are in satisfactory agreement with the experimental result, while results of the inhomogeneous MUSIG model appear marginally superior to those of the ABND model. Evolution of the bubble size distribution is adequately captured by the inhomogeneous MUSIG model. Meanwhile, the ABND model tends to under-predict the Sauter mean diameters (see also in figure).

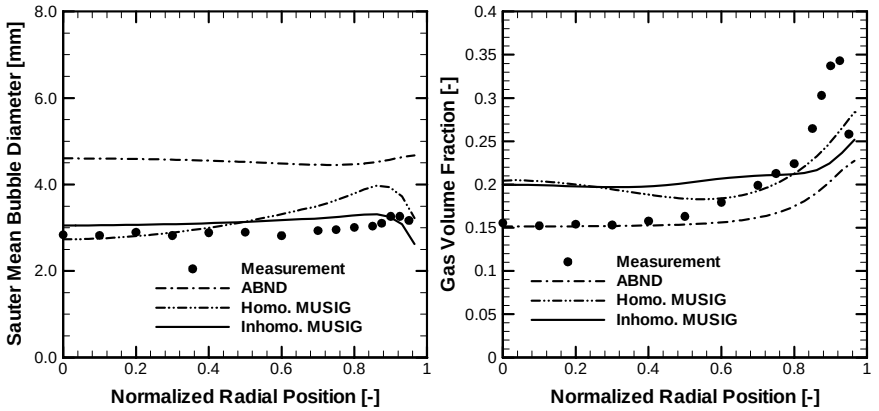

Fig. 2. Predicted and measured Sauter mean bubble diameter (left) and gas volume fraction profile (right) at the measuring station of bubbly-to-slug transition flow condition $<j_g>$=0.242m/s and $<j_f>$=0.986m/s

The measured and predicted local radical gas volume fraction and Sauter mean bubble diameter profile at the measuring station (i.e. z/D=53.5) for experiment by Hibiki et al. [2] are illustrated in Fig. 2. Comparing the predicted Sauter mean diameters, the inhomogeneous MUSIG model was found to yield comparatively better prediction when compared against the measured data. This could be attributed to the means of splitting the bubble velocity with two independent fields which facilitated the model to re-capture the separation of small and big bubbles caused by different lift force actuation. Nevertheless, notable discrepancies were found when comparing against the gas volume fraction profile. As depicted, volume fractions of both models were obviously over-predicted at the channel core but under-predicted at the wall region. This could be attributed to the interfacial force models which have been developed principally for isolated bubbles rather than on a swarm or cluster of bubbles. Direct applications of these models for high void fraction conditions, where bubbles are closely packed, become invalid and introduce uncertainties in the model calculations [12]. Moreover, the existing kernels which only featured coalescence due to only random collision and breakage due to turbulent impact for spherical bubbles may have to be extended to account for additional bubble mechanistic behaviours for cap/slug bubbles in bubbly-to-slug transition flow conditions.

5 Conclusions

The ABND model, coupled with the two-fluid model is presented and compared against the MUSIG model and two experimental data by Lucas et al. [1] and Hibiki et al. [2]. The comparison shown that ABND models can be considered as a viable option especially for industrial practitioners who demand a rapid design tool in simulating bubbly flows with reasonable accuracy. For the case of acquiring highly accurate mean bubble Sauter diameter distribution, the homogenous/inhomogeneous MUSIG model serves as a better alternative approach in handling such flows.

References

[1] Lucas, D., Krepper, E., Prasser, H.M.: Modeling the evolution of bubbly flow along a large vertical pipe. Nuclear Tech. 158, 291–303 (2007)
[2] Hibiki, T., Ishii, M., Xiao, Z.: Axial interfacial area transport of vertical bubble flows. Int. J. of Heat & Mass Trans. 44, 1869–1888 (2001)
[3] Olmos, E., Gentric, C., Vial, C., Wild, G., Midoux, N.: Numerical simulation of mult iphase flow in bubble column. Influence of bubble coalescence and break-up. Chem. Eng. Sci. 56, 6359–6365 (2001)
[4] Pochorecki, R., Moniuk, W., Bielski, P., Zdrojkwoski, A.: 2001 Modelling of the coa lescence/redisperison processes in bubble columns. Chem. Eng. Sci. 56, 6157–6164 (2001)
[5] Yeoh, G.H., Tu, J.Y.: Thermal-hydrodynamic modelling of bubbly flows with heat and mass transfer. AIChE J. 51, 8–27 (2005)
[6] Krepper, E., Lucas, D., Prasser, H.: On the modelling of bubbly flow in vertical pipes. Nucl. Eng. Design. 235, 597–611 (2005)
[7] Cheung, S.C.P., Yeoh, G.H., Tu, J.Y.: On the modeling of population balance in isothermal vertical bubbly flows – average bubble number density approach. Chem. Eng. & Proc. 62, 4659–4674 (2007)
[8] Anglart, H., Nylund, O.: CFD application to prediction of void distribution in two-phase bubbly flows in rod bundles. Nucl. Sci. & Eng. 163, 81–98 (1996)
[9] Yao, W., Morel, C.: Volumetric interfacial area prediction in upwards bubbly two-phase flow. Int. J. Heat Mass Trans. 47, 307–328 (2004)
[10] Prince, M.J., Blanch, H.W.: Bubble coalescence and break-up in air sparged bubble columns. AIChE J. 36, 1485–1499 (1990)
[11] Luo, H., Svendsen, H.: Theoretical model for drop and bubble break-up in turbulent dispersions. AIChE J. 42, 1225–1233 (1996)
[12] Simonnet, M., Gentric, C., Olmos, E., Midoux, N.: Experimental determination of the drag coefficient in a swarm of bubbles. Chem. Eng. Sci. 62, 858–866 (2007)

Direct Numerical Simulation of Cavitation Noise for a 3D Circular Cylinder Cross-Flow

Youngmin Bae[1], Jung H. Seo[1], Young J. Moon[1], and Byeong Rog Shin[2]

[1] Korea University, Seoul, 136-713, Korea
yjmoon@korea.ac.kr

[2] Changwon National University, Changwon, 641-773, Korea
brshin@changwon.ac.kr

In this study, cavitation noise for a circular cylinder cross-flow is directly simulated for Reynolds number based on the cylinder diameter, $Re_D = 200$ and 3900, and cavitation number, $\sigma = 0.7 \sim 2$. The cavitating flow and noise are predicted by the compressible Navier-Stokes equations written for the two-phase fluid, employing a density-based homogeneous equilibrium model with a linearly-combined equation of state. To resolve the linear and non-linear waves in the cavitating flow, a sixth-order compact central scheme is utilized with a selective spatial filtering technique. It is observed that, at sub- and super-critical cavitation numbers, the cavitating flow and noise characteristics are significantly changed by the shock waves due to the collapse of the cloud cavitation in the wake. It is also shown that spanwise flow structures over the cylinder is quite coherent to the strength of monopole shock waves.

1 Introduction

Cavitation bubbles formed by a breakdown of cavitation sheet or collapse of vortex cavities are often responsible for the generation of loud noise and erosion damages, especially when they collapse coherently. There have been some experimental works by Resiman et al. [1] and Levy et al. [2] to measure the cavitation noise with the sources identified. Cavitation experiments, especially for the cavitation noise, are, however, still quite difficult and numerical simulation is thereby important not only for the prediction but also for the investigation of the flow physics.

In the present study, a two-phase cavitating flow and noise from a circular cylinder are directly simulated with a density-based homogeneous equilibrium model [3]. The governing equations are the compressible Navier-Stokes equations written for the mixture fluid, in which the two-phase flow physics is treated by a linearly-combined equation of state to simulate the cavitating flow and the cavitation noise as well.

Numerical schemes are also an important issue for direct simulation of cavitating flow noise. A numerical scheme should be able to capture the steep

gradients of cavitating flow as well as high-frequency physical waves. In this regard, we consider a high-order central compact scheme with a selective filtering technique [4], which is shown to be effective and easy to apply to the present governing equations, as compared to other high-order upwind schemes [5, 6].

In the present study, the cavitating flow noise from a circular cylinder is investigated by the proposed direct numerical simulation procedure. The source mechanism and characteristics of the cavitation noise are examined for different cavitation numbers with discussion on the relation between the spanwise coherence of the cloud cavitation and the strength of shock waves.

2 Computational Methods

2.1 Density- Based Homogeneous Equilibrium Model

In the present study, a homogeneous equilibrium model proposed by Shin et al. [3] is employed. In the homogeneous medium, the mixture density ρ can be expressed by a linear combination of densities in the liquid-phase ρ_l and gas-phase ρ_g as

$$\rho = (1-\alpha)\,\rho_l + \alpha\rho_g \tag{1}$$

where α is a void fraction (gas volume fraction). The relation between the local void fraction α and the quality (gas mass fraction) Y is given by

$$\rho\,(1-Y) = (1-\alpha)\,\rho_l \quad and \quad \rho Y = \alpha\rho_g \tag{2}$$

The equations of state for a pure liquid [7] and an ideal gas are written as

$$\begin{array}{c} p + p_c = \rho_l K\,(T + T_c) \quad for \quad Y = 0 \\ p = \rho_g RT \quad for \quad Y = 1 \end{array} \tag{3}$$

where p and T are the static pressure and temperature, p_c, T_c, K are the pressure, temperature and liquid constant for the liquid state, and R is the gas constant. Using these two equations and the local equilibrium assumption, the equation of state, Eq. (1) for a locally homogeneous gas-liquid two-phase medium can be written as

$$\rho = \frac{p\,(p+p_c)}{K\,(1-Y)\,p\,(T+T_c) + RY\,(p+p_c)\,T} \tag{4}$$

The speed of sound for the isothermal condition is derived as

$$c^2 = \frac{Y\{R\,(p+p_c) - Kp\} + Kp}{Y\{R\,(p+p_c)^2 - Kp^2\} - \rho KRY\,(1-Y)\,p_c T_c + Kp^2} \cdot \frac{p\,(p+p_c)}{\rho} \tag{5}$$

The constants p_c, K and T_c for water in Eq. (5) were estimated as 1944.61 MPa, 472.27 J/KgK and 3837 K, respectively.

Based on the above mathematical modeling, which is under an isothermal condition and neglects the surface tension assuming a high Weber number, the governing equations for the mixture mass, momentum, and gas-phase mass conservation can be written as

$$\begin{aligned} \frac{\partial \rho}{\partial t} &= -\frac{\partial \rho u_j}{\partial x_j} \\ \frac{\partial \rho u_i}{\partial t} &= -\frac{\partial \rho u_i u_j}{\partial x_j} - \frac{\partial p}{\partial x_i} + \frac{\partial \tau_{ij}}{\partial x_j} \\ \frac{\partial Y}{\partial t} &= -\frac{\partial \left(\rho u_j Y\right)}{\partial x_j} \end{aligned} \tag{6}$$

The stress tensor τ can be expressed by

$$\tau_{ij} = \mu \left(\frac{\partial u_i}{\partial x_j} + \frac{\partial u_j}{\partial x_i} - \frac{2}{3} \frac{\partial u_k}{\partial x_k} \delta_{ij} \right) \tag{7}$$

where the mixture viscosity μ is given by [8]

$$\mu = (1 - \alpha)\left(1 + 2.5\alpha\right)\mu_l + \alpha \mu_g \tag{8}$$

The governing equations are spatially discretized with a sixth-order compact finite difference scheme [9] and integrated in time by a four-stage Runge-Kutta method. For the far-field boundary condition, an energy transfer and annihilation (ETA) boundary condition [10] with buffer zone is used to eliminate any reflection of the out-going waves.

2.2 Selective Spatial Filtering

A numerical instability could arise even in the smooth solution because the compact scheme has no diffusion errors. Moreover, on the solution of cavitating two-phase flows, there are steep gradients including shock waves. When a compact scheme is used for such region, the solution will be suffered by severe oscillations. In order to suppress such numerical errors, a spatial filtering proposed by Gaitonde et al. [11] is applied in a selective manner.

The general formulation is given by

$$\alpha_f \tilde{f}_{i-1} + \tilde{f}_i + \alpha_f \tilde{f}_{i+1} = \sum_{n=0}^{N/2} \frac{a_n}{2} \left(f_{i+n} + f_{i-n} \right) \tag{9}$$

where N is the order of spatial filtering and the coefficients a_n can be found in reference [11]. The high-order spatial filtering is only dissipative for very high wave numbers, so it is ideal for smooth regions to suppress the high-frequency numerical errors with minimizing the dissipation of physical waves.

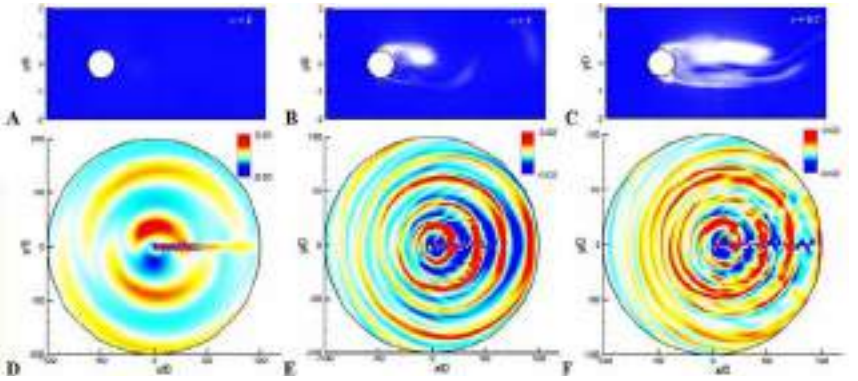

Fig. 1. Cavitating flow and noise over a 2D cylinder for $Re_D = 200$ and cavitation numbers, $\sigma = 2$ (left), 1 (middle), and 0.7 (right); A, B, and C: void fraction (contours between 0 and 1), D, E, and F: pressure fluctuation normalized by $\rho_0 u_0^2$

On the other hand, a more diffusive filtering (e.g. second-order) is required to suppress the oscillation errors for the region where steep gradients exist. Therefore we apply a tenth-order filtering with $\alpha_f = 0.49$ for smooth regions and a second-order filtering with $\alpha_f = 0.2$ for regions with steep gradients.

In order to estimate a smoothness of local solution, the following criterion is used [4]:

$$D_2 = |f_{i+1} - 2f_i + f_{i-1}|$$
$$\begin{cases} D_2 \geq C_s\,(f_{\max} - f_{\min}) & 2^{nd}\ order\ filtering \\ D_2 < C_s\,(f_{\max} - f_{\min}) & 10^{th}\ order\ filtering \end{cases} \tag{10}$$

where f_{max} and f_{min} are the global maximum and minimum values. The constant C_s controls the oscillation errors and resolutions of the high-frequency 'physical' waves so that we use C_s of 0.1 for the selective filtering. For more details, see the reference [4].

3 Results and Discussion

First, we examined the transient characteristics of cavitating flow and noise from a 2D circular cylinder. A direct numerical simulation has been conducted for several cavitation numbers, $\sigma = 2$ (non-cavitating flow), 1 (sub-critical cavitation), and 0.7 (super-critical cavitation). A bubbly flow over the cylinder with ambient void fraction of $\alpha = 0.01$ is assumed for an isothermal state at T_0=293 K, while the Reynolds number of the flow is limited to $Re_D = 200$ to exclude any turbulent nature of the flow.

Figure 1 presents the instantaneous void fraction and pressure fluctuation fields around the cylinder for each cavitation number. For large cavitation number ($\sigma = 2$), cavitation bubbles are not generated because the static pressure do not drop below the vapor pressure p_v. Thereby, the flow patterns,

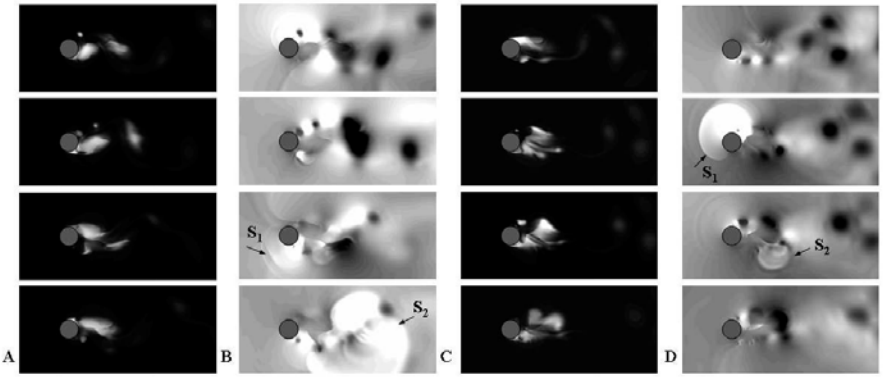

Fig. 2. Cavitating flow and noise over a 2D circular cylinder (A and B) and a 3D circular cylinder (C and D) for $Re_D = 3900$ and $\sigma = 1$; A and C: void fraction, B and D: pressure fluctuation (contours between -0.2 and 0.2)

aerodynamic forces, and Strouhal number of the Karman vortex shedding frequency ($St = 0.19$) are very similar to those of single phase flow. For this case, the noise is purely from the surface dipole and has a spectral peak at the vortex shedding frequency. But for smaller cavitation numbers, the static pressure drops below the vapor pressure at the cylinder surface and also in the shed vortices via phase-change. At $\sigma = 1$, cavitation bubbles are periodically generated by fluctuations of pressure due to the vortex shedding, though a mean pressure itself does not reach the vapor pressure. In this case, the dominant noise is the monopole-like shock waves generated by collapse of alternating cavitation bubble so that the peak is observed at the double of the vortex shedding frequency ($St = 0.32$). For $\sigma = 0.7$, the mean pressure on the cylinder surface drops below p_v and cavitation bubbles are widely distributed with large values of void fraction. As a result, peaks are made not only by the alternate collapse of the cavitation bubble but also by the low frequency behavior of the elongated vortex cavity at super-critical cavitation numbers ($\sigma = 2$). It is interesting to note that, the shedding frequency decreases with the cavitation number (e.g. $St = 0.19$, 0.16 and 0.13 for $\sigma = 2$, 1, and 0.7), because the vortex shedding is delayed due to the formation of cavitation bubble. It is also found that the aerodynamic forces are severely affected by the shock waves generated by the coherent collapse of cloud cavitation in the wake, and the noise level for the cavitating flow case ($\sigma = 1$ and $\sigma = 0.7$) is much larger than that for the non-cavitating case ($\sigma = 2$).

Figure 2 shows a transient process of shock wave generation during the collapse of cavitation bubble for $Re_D = 3900$ and $\sigma = 1$. In early stage, the sheet cavitation is breaking-off by the vortex shedding and cloud cavitations are formed. As soon as the pressure is recovered at the cylinder surface, the front bubble cloud collapses and emits a shock wave (S_1). The sub-cloud exposed to

the surrounding high-pressure fluids is then ruptured in the wake, generating another pressure pulse (S_2). It is worth to note that separated sub-cloud shows somewhat different structures for a 3D case compared with 2D. This change of cavitation structures is associated with spanwise coherence of cloud cavitation, and may result in the change of cavitation noise characteristics.

4 Summary and Conclusions

In this study, cavitation noise for a circular cylinder is directly simulated for $Re_D = 200$ and 3900, and cavitation number, $\sigma = 0.7 \sim 2$. The computed results show that, the cavitating flow and noise characteristics are significantly changed by the shock waves due to the collapse of the cloud cavitation in the wake. In the future study, more comprehensive explanation on the 3D characteristics of cavitating flow and noise will be presented with discussion on the spanwise flow structures over the cylinder and their coherences to the pressure fluctuations at the far-field.

References

1. Resiman, G.E., McKenney, E.A., Brennen, C.E.: Cloud cavitation on an oscillating hydrofoil. In: 20th ONR Symposium on Naval Hydrodynamics, pp. 78–89 (1994)
2. Levy, M., Kjeldsen, M., Arndt, R.E.A.: Clouid cavitation noise. In: APS, 53rd Annual Meeting of the Division of Fluid Dynamics (2000)
3. Shin, B.R., Iwata, Y., Ikohagi, T.: Numerical simulation of unsteady cavitating flows using a homogeneous equilibrium model. Comput. Mech. 30, 388–395 (2003)
4. Seo, J.H., Moon, Y.J.: Direct simulation of cavitating flow noise. In: 13th AIAA/CEAS Aeroacoustics Conference (2007)
5. Jiang, G.S., Shu, C.W.: Efficient implementation of weighted ENO schemes. J. Comput. Phys. 126, 202–228 (1996)
6. Ren, Y., Liu, M., Zhang, H.: A characteristic-wise hybrid compact-WENO scheme for solving hyperbolic conservation laws. J. Comput. Phys. 192, 365–386 (2003)
7. Chen, Y., Heister, S.D.: A numerical treatment for attached cavitation. ASME J. Fluids Eng. 116, 613–618 (1994)
8. Beattie, D.R.H., Whalley, P.B.: A simple two-phase flow frictional pressure drop calculation method. Int. J. Multiphase Flow 8, 83–87 (1982)
9. Lele, S.K.: Compact finite difference scheme with spectral-like resolution. J. Comput. Phys. 103, 16–42 (1992)
10. Edgar, N.B., Visbal, M.R.: A general buffer zone-type non-reflecting boundary condition for computational aeroacoustics. In: 9th AIAA/CEAS Aeroacoustics Conference (2003)
11. Gaitonde, D.V., Shang, J.S., Young, J.L.: Practical aspects of higher-order numerical schemes for wave propagation phenomena. Int. J. Numer. Meth. Engng. 45, 1849–1869 (1999)

Numerical Method for Shock-Cavitation Bubble Interaction Problems

Byeong Rog Shin[1] and Young-Joon An[2]

[1] Department of Mechanical Engineering, Changwon National University, Changwon 641-773, Korea
brshin@changwon.ac.kr
[2] Graduate School of Changwon National University, Changwon 641-773, Korea

A numerical method for gas-liquid two-phase flow is applied to solve shock-bubble interaction problems. The present method employs a finite-difference Runge-Kutta method and Roe's flux difference splitting approximation with the MUSCL-TVD scheme. A homogeneous equilibrium cavitation model is used. By this method, a Riemann problem for shock tube was computed for validation. Then, shock-bubble interaction problems between cylindrical bubbles located in the liquid and incident liquid shock wave are computed.

1 Introduction

Cavitation is well encountered in the flow of hydromachines. When cavitation occurs and collapses near solid surfaces, it causes the noise, vibration and damage to hydraulic machine systems.

To understand the behavior of collapsing of cavitation bubbles, some efforts to propose cavity flow model for numerical simulations [1-3] and, analytical and experimental method for shock-bubble interaction problems [4] have been made. Recently, present author has proposed a mathematical cavity flow model [5,6] based on a homogeneous equilibrium model taking account of the compressibility of the gas-liquid two-phase media. With this model, the mechanism of developing cavitation has been investigated through the application to a couple of cavitating flows around a hydrofoil [7,8].

The purpose of this paper is to extend to a shock-bubble interaction problem with a high-order Runge-Kutta method and MUSCL TVD solution method for stable and accurate treatment of gas-liquid nterfaces considered by contact discontinuity. As numerical examples, one-dimensional (1-D) gas-liquid two-phase shock tube problems are computed to investigate detailed unsteady shock wave phenomena. And then, numerical investigation for shock-bubble interaction problems between cylindrical single cavitation bubble located in the liquid and incident liquid shock wave are solved.

2 Homogeneous Cavitation Model

Gas-liquid two-phase flow of cavity flow is possible to model into an pseudo single-phase flow by using concept of the homogeneous equilibrium model [3] in which thermodynamic equilibrium is assumed and velocity slip between both phases is neglected.

Under this model concept, the pressure for gas-liquid two-phase media is determined by using a combination of two equations of state for gas phase and liquid phase, that is written as follows:

$$\rho = \frac{p(p+p_c)}{K(1-Y)p(T+T_c) + RY(p+p_c)T} \tag{1}$$

3 Numerical Method

By using above cavitating flow model the 2-D governing equations for the mixture mass, momentum, energy and the gas-phase mass conservation can be written in the curvilinear coordinates (ξ, η) as follows:

$$\frac{\partial \boldsymbol{Q}}{\partial t} + \frac{\partial \boldsymbol{E}}{\partial \xi} + \frac{\partial \boldsymbol{F}}{\partial \eta} = \frac{\partial \boldsymbol{E}_v}{\partial \xi} + \frac{\partial \boldsymbol{F}_v}{\partial \eta} + \boldsymbol{S} \tag{2}$$

where $\boldsymbol{Q}$ is an unknown variable vector, $\boldsymbol{E}$, $\boldsymbol{F}$ are flux vectors and $\boldsymbol{E}_v$, $\boldsymbol{F}_v$ are viscous terms. $\boldsymbol{S}$ is the source term. For instance, $\boldsymbol{Q}$, $\boldsymbol{E}$ and $\boldsymbol{E}_v$ are [8],

$$\boldsymbol{Q} = J\begin{pmatrix} \rho \\ \rho u \\ \rho v \\ e \\ \rho Y \end{pmatrix}, \quad \boldsymbol{E} = J\begin{pmatrix} \rho U \\ \rho u U + \xi_x p \\ \rho v U + \xi_y p \\ \rho U H \\ \rho U Y \end{pmatrix}, \quad \boldsymbol{E}_v = J\begin{pmatrix} 0 \\ \xi_x \tau_{xx} + \xi_y \tau_{xy} \\ \xi_x \tau_{yx} + \xi_y \tau_{yy} \\ \xi_x T_{11} + \xi_y T_{22} \\ \xi_x \Re Y_x + \xi_y \Re Y_y \end{pmatrix}$$

The hydraulic flow with hydraulic transients and hydroacoustics such as cavitating flow has compressible flow characteristic at low Mach number. For this kind of flow, a compressible flow model that includes a preconditioning method is advantageous.

Applying the preconditioning method to Eq.(2), we obtain 2-D preconditioned governing equations with unknown variable vectors $\boldsymbol{W} = [p, u, v, T, Y]^T$ written in curvilinear coordinates as follows [8]:

$$\Gamma^{-1}\frac{\partial \boldsymbol{W}}{\partial \tau} + \Gamma_w^{-1}\frac{\partial \boldsymbol{W}}{\partial t} + \frac{\partial (\boldsymbol{E} - \boldsymbol{E}_v)}{\partial \xi} + \frac{\partial (\boldsymbol{F} - \boldsymbol{F}_v)}{\partial \eta} = \boldsymbol{S} \tag{3}$$

In this study, τ is pseudo-time and Γ_w^{-1} is a transform matrix of the Jacobian matrix $\partial \boldsymbol{Q}/\partial \boldsymbol{W}$. The preconditioning matrix Γ^{-1} is formed by the addition of the vector $\theta[1, u, v, H, Y]^T$ to the first column of the Γ_w^{-1}.

Fundamental equations (2) and (3) are solved by using appropriate numerical methods such as finite-difference method with TVD Runge-Kutta method.

Then, Roe's flux difference splitting (FDS) method with the MUSCL-TVD scheme [9] is applied to enhance the numerical stability, especially for steep gradients in density and pressure near the gas-liquid interface. Therefore, the derivative of the flux vector, for instance, $\boldsymbol{E}$ with respect to ξ at point i can be written with the numerical flux as $(\partial \boldsymbol{E}/\partial \xi) = (\boldsymbol{E}_{i+1/2} - \boldsymbol{E}_{i-1/2})/\Delta\xi$ and then, the approximate Riemann solver based on the Roe's FDS is applied as shown in Ref[8].

In the numerical integration of governing equations (3), the 4th-order TVD Runge-Kutta explicit method is used.

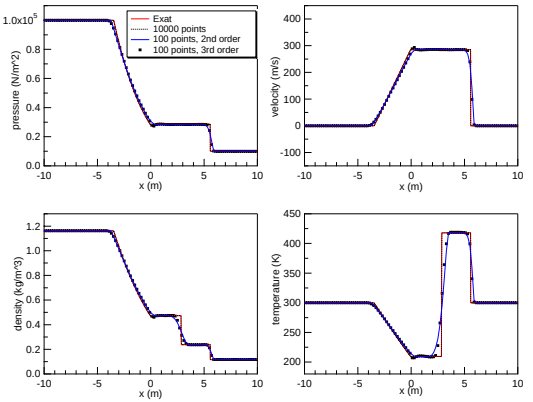

Fig. 1. Computational results of pressure, density, velocity and temperature distribution for ideal gas at $\alpha = 100\%$

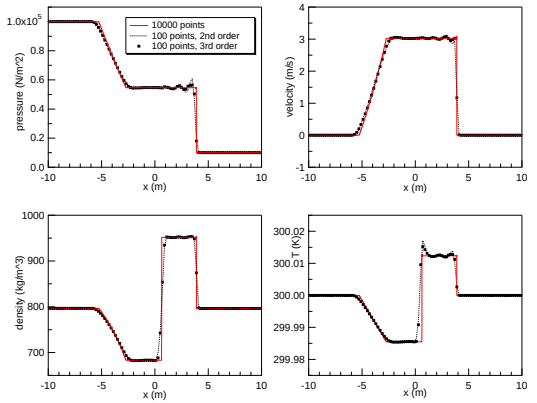

Fig. 2. Computational results of pressure, density, velocity and temperature distribution for gas-liquid 2-phase media at $\alpha = 20\%$

4 Numerical Results

At first, the present computational method has been validated by using the Riemann problem suggested by Sod[10] as a standard test problem. The domain is $x[-10\text{m}, 10\text{m}]$. In this case Eq. (3) is reduced to 1-D Euler equation without preconditioning. Initial conditions of left (L)- and right (R)-hand side at discontinuous surface ($x = 0\text{m}$) at $T = 300\text{K}$ are as followings.

$$p_L = 0.1\text{MPa},\ \text{u}_\text{L} = 0\ \text{m/s},\ \alpha_\text{L} = \alpha$$
$$p_R = 0.01\text{MPa},\ \text{u}_\text{R} = 0\ \text{m/s},\ \alpha_\text{R} = \alpha$$

Figure 1 shows comparisons with exact solution for shock tube problem of ideal gas ($\alpha = 100\%$) with the ratio of specific heats $\gamma = 1.4$ at $t = 0.01\text{s}$. The results obtained by present high-order numerical method for gas-liquid two-phase flow with grid points of 10000 are almost coincide with exact solutions. The result by 100 points is also fairly well predicted except small dissipation at discontinuity. In this figure symbols represent computed results on the real grid points obtained by third-order MUSCL TVD scheme. Results by both second-order and third-order show a monotonic solution without numerical oscillation. But, third-order is closer to the exact solution than the second-order even they have same grid points of 100.

Based on the validity of the present method, the present high-order method was applied to compressible gas-liquid two-phase shock tube flow in thermal process with arbitrary void fraction to investigate the characteristics of pressure waves propagating in the gas-liquid two-phase medium.

Figure 2 shows calculated results for gas-liquid two-phase medium at void fraction of $\alpha = 20\%$. In this case compression wave is propagating with decreasing the void fraction because the compression wave compresses the two-phase medium. However expansion wave shows the opposite behavior with increasing the void fraction, resulting the contact discontinuity exists and propagates toward right-hand side by the wave induced velocity. In this computation, the result obtained by using 10000 grid point is regarded as a exact solution. According to the present investigation, induced velocity showed a tendency of increasing at large void fraction.

Next, present numerical method applyed to shock-bubble interaction problems between stationary or incident liquid shock wave and cylindrical cavitation bubbles located in the liquid. A square domain with a base of 4 times of bubble diameter (d) and 401×401 grid points are used. As an initial condition, a single bubble with void fraction of $\alpha = 1$ is located in the center of a stationary flow field with $\alpha = 0$ at isothermal condition. The initial pressure of gas in bubble was taken as 0.1MPa. A uniform pressure of 10MPa was given around the bubble. Figure 3 shows a time evolution of bubble collapsing process. Bubble is gradually shrunken by the initial pressure difference up to almost terminal stage of collapse. At this time preessure in the bubble reaches maximum value around 240MPa and a rebound shock wave occurs.

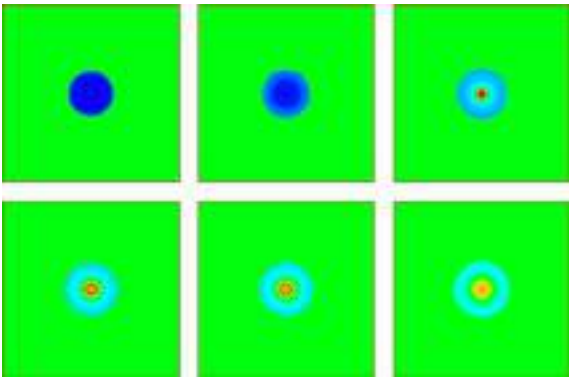

Fig. 3. Collapse of a bubble in a hydrostatic pressure field and a rebound (red: 240MPa, Green: 10MPa, blue: 0.1MPa)

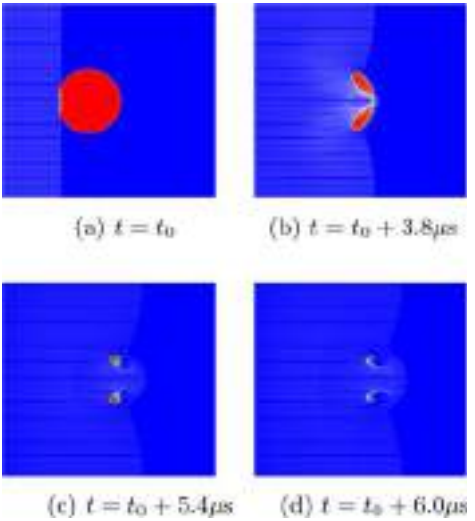

Fig. 4. Time evolution of velocity vectors and void fraction distribution (red: $\alpha = 1.$, blue: $\alpha = 0.$)

Then this wave propagates to liquid region and the bubble is expended with time.

Another shock-bubble interaction problem between cylindrical bubble located in the liquid and incident liquid shock wave are computed. In this case, in the flow field with uniform pressure of 0.1MPa incident liquid shock wave with a high pressure of 100MPa is placed at $3d$ upstream from single bubble center. Figure 4 shows time evolution of velocity vectors and void fraction distribution around cavitation bubble in the collapsing process. When incident shock wave impacts on the bubble the shock wave is diffracted around bubble

and it propagates toward downstream. Due to the pressure difference between back and forth of shock plane, the bubble is asymmetrically contracted with concave shape. A sort of microjet is formed and eventually it impinges on the rear surface of the bubble with reflection shock wave. Bubble collapsing behavior, shock-bubble interaction and shock transmission/reflection pattern are well simulated in these applications.

5 Conclusions

A high resolution numerical method for gas-liquid two-phase flow is applied to solve shock-bubble interaction problems. From the numerical example of gas-liquid two-phase 1-D shock tube problems, it is confirmed that the present numerical method quite well simulates unsteady phenomena of the shock waves. It showed a successive application to two-phase shock tube flows in comparison with exact solutions. At shock-bubble interaction problems bubble collapsing behavior is investigated and shock-bubble interaction and shock transmission/reflection pattern are well simulated.

Acknowledgements

A part of this research is financially supported by Underwater Vehicle Research Center (UVRC), DAPA of Korea.

References

1. Singhal, A.K., et al.: Multi-Dimensional Simulation of Cavitating Flows Using a PDF Model for Phase Change. ASME Paper FEDSM97-3272 (1997)
2. Merkle, C.L., et al.: Computational Modeling of the Dynamics of Sheet Cavitation. In: Proc., 3rd Int., Sympo. on Cavitation, vol. 2, pp. 307–311 (1998)
3. Shin, B.R., et al.: A Numerical Study of Unsteady Cavitating Flows Using a Homogenous Equilibrium Model. Computational Mechanics 30, 388–395 (2003)
4. Bourne, N.K., Field, J.E.: Shock-Induced Collapse of Single Cavities in Liquids. J. of Fluid Mech. 244, 225–240 (1992)
5. Shin, B.R., Ikohagi, T.: Numerical Analysis of Unsteady Cavity Flows Around a Hydrofoil. ASME Paper FEDSM 99-7215 (1999)
6. Shin, B.R.: Numerical Analysis of Unsteady Cavitating Flow by a Homogeneous Equilibrium Model. In: 31st AIAA Fluid Dyn. Conf., AIAA Paper 2001-2909, pp. 1–10 (2001)
7. Iga, Y., et al.: Numerical Study of Sheet Cavitation Break-off Phenomenon on a Cascade Hydrofoil. ASME J. Fluid Engng. 125, 643–651 (2003)
8. Shin, B.R., et al.: Application of Preconditioning Method to Gas-Liquid Two-Phase Flow Computations. ASME J. Fluid Engng. 126, 605–612 (2004)
9. van Leer, B.: Towards the Ultimate Conservative Difference Scheme V. A Second-Order Sequel to Godunov's Method. J. Comput. Phys. 32, 101–136 (1979)
10. Laney, C.B.: Computational Gasdynamics. Cambridge Univ. Press, Cambridge (1998)

Part 33
Optimization 1

“*This page left intentionally blank.*”

A Low Dissipative Discrete Adjoint m-KFVS Method

N. Anil[1], N.K.S. Rajan[2], Omesh Reshi[3], and S.M. Deshpande[4]

[1] Dept. of Aerospace Engg., IISc, Bangalore, India
anil@aero.iisc.ernet.in
[2] Dept. of Aerospace Engg., IISc, Bangalore, India
nksr@cgpl.iisc.ernet.in
[3] EIS, TCS, Mumbai, India
omeshreshi@gmail.com
[4] Engineering Mechanics Unit, JNCASR, Bangalore, India
smd@jncasr.ac.in

Keywords: m-KFVS, MCIR splitting, optimal control of numerical dissipation.

1 Introduction

The kinetic schemes [Des95], also known as Boltzmann schemes are based on the moment-method-strategy, where an upwind scheme is first developed at the Boltzmann level and after taking suitable moments we arrive at an upwind scheme for the governing Euler or Navier-Stokes equations. The Kinetic Flux Vector Splitting (KFVS) scheme [Des86], which belongs to the family of kinetic schemes is being extensively used to compute inviscid as well as viscous flows around many complex configurations of practical interest over the past two decades. To resolve many flow features accurately, like suction peak, minimising the loss in stagnation pressure, shocks, slipstreams, triple points, vortex sheets, shock-shock interaction, mixing layers, flow separation in viscous flows require an accurate and low dissipative numerical scheme. The first order KFVS method even though is very robust suffers from the problem of having much more numerical diffusion than required, resulting in very badly smearing of the above features. However, numerical dissipation can be reduced considerably by using higher order kinetic schemes. But they require more points in the stencil and hence consume more computational time and memory. The second order schemes require flux or slope limiters in the neighbourhood of discontinuities to avoid spurious and physically meaningless wiggles or oscillations in pressure, temperature or density. The limiters generally restrict the residue fall in second order schemes while in first order schemes residue falls up to machine zero. Further, pressure and density contours or streamlines are much smoother for first order accurate schemes than second order accurate schemes. A question naturally arises about the

possibility of constructing first order upwind schemes which retain almost all advantages mentioned above while at the same time crisply capture the flow features. In the present work, an attempt has been made to address the above issues by developing yet another kinetic scheme, known as the low dissipative modified KFVS (m-KFVS) method [Ani08] based on modified CIR (MCIR) splitting with molecular velocity dependent dissipation control function.

2 m-KFVS Method

We now present the basics of m-KFVS method with respect to $1D$ Euler equations. Consider the modified CIR (MCIR) split [RD07, Ani08] $1D$ Boltzmann equation in the Euler limit

$$\frac{\partial F}{\partial t} + \frac{v + |v|\phi}{2}\frac{\partial F}{\partial x} + \frac{v - |v|\phi}{2}\frac{\partial F}{\partial x} = 0 \tag{1}$$

where, F is the Maxwellian distribution function and ϕ is the dissipation control function, given by $\phi = e^{-\alpha|v|}$. The corresponding modified partial differential equation is given by

$$\frac{\partial F}{\partial t} + v\frac{\partial F}{\partial x} = \frac{\Delta x}{2}|v|\phi\frac{\partial^2 F}{\partial x^2} + O\left(\Delta x\right)^2 \tag{2}$$

It can be observed that $\alpha = 0$ gives the first order KFVS method while $\alpha \to \infty$ corresponds to central differencing scheme, which is unstable. A detailed mathematical analysis and the relevant physical arguments for the choice of ϕ are presented in [Ani08]. Taking moments of eq. (1), we get the m-KFVS Euler equations

$$\frac{\partial U}{\partial t} + \frac{\partial}{\partial x}\left(Gm^{+}\right) + \frac{\partial}{\partial x}\left(Gm^{-}\right) = 0 \tag{3}$$

Here, $Gm^{\pm}$ are the modified KFVS fluxes, which are functions of the dissipation control parameter, α. When $\alpha = 0$, we regain the usual KFVS fluxes. Thus, by suitably choosing α $(0 \leq \alpha < \infty)$, the numerical dissipation at each point or

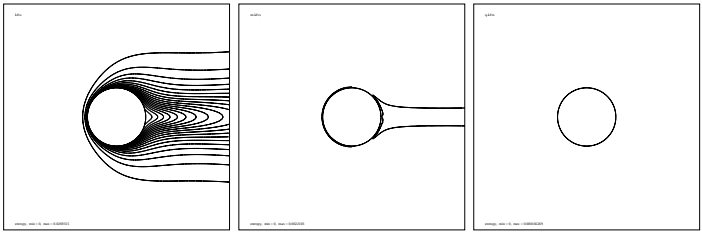

Fig. 1. Subsonic flow past a circular cylinder, $M_\infty = 0.38$ and $AoA = 0^o$. From left to right: Entropy contours based on first order KFVS, low dissipative m-KFVS and second order accurate q-KFVS methods.

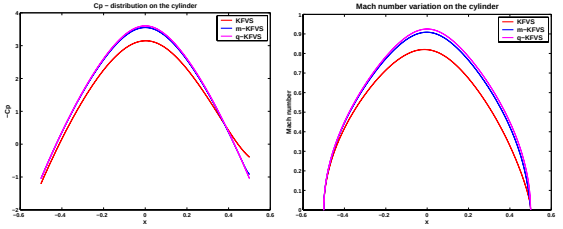

Fig. 2. Subsonic flow past a circular cylinder, $M_\infty = 0.38$ and $AoA = 0^o$. From left to right: C_p distribution and Mach number variation on the cylinder surface based on KFVS, m-KFVS and q-KFVS methods.

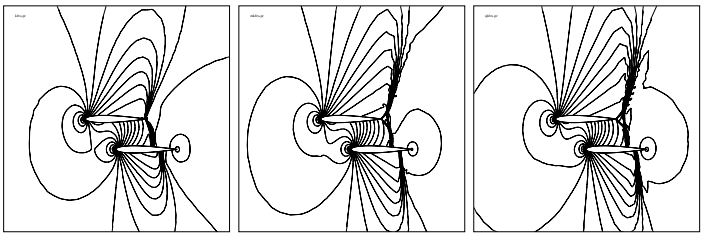

Fig. 3. Transonic flow past bi-NACA airfoil, $M_\infty = 0.85$ and $AoA = 0^o$. From left to right : Pressure contours based on KFVS, m-KFVS and q-KFVS methods.

cell in the computational domain can be reduced considerably by still using the first order stencil. The dissipation control parameter α at grid point or cell centre (in finite volume method) constitute a dissipation control vector. We then have a distributed control on the numerical diffusion or equivalently on the entropy generated by numerical diffusion. The cell-centred finite volume method based on m-KFVS has been successfully applied to many standard test cases for inviscid flows and some of the results are presented in Figs. (1), (2) and (3). These plots clearly show that the m-KFVS method captures the flow features much more accurately than the first order KFVS method and are comparable to second order accurate q-KFVS method.

3 Optimal Control of Numerical Dissipation

Although, the m-KFVS method resolves the flow features more accurately compared to KFVS and near second order accuracy has been achieved in smooth regions, the numerical dissipation generated may not be minimal and hence the dissipation control parameter, α is in general not optimal. It is tempting therefore to ask a pertinent question, whether we can find optimal α-distribution, which gives minimum numerical dissipation. One of the ways of attaining the above objective is by posing the minimisation of numerical dissipation in m-kFVS method as an optimal control problem

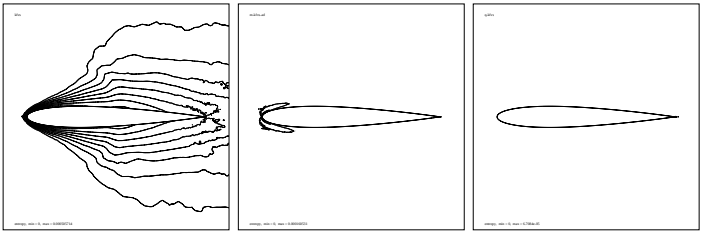

Fig. 4. Low subsonic flow past NACA 0012 airfoil, $M_\infty = 0.1$ and $AoA = 0^o$. Left to right : Entropy contours Based on KFVS, m-KFVS-adjoint and q-KFVS methods.

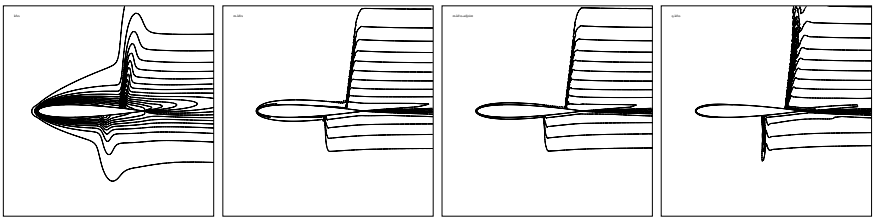

Fig. 5. Transonic flow past NACA 0012 airofoil, $M_\infty = 0.85$ and $AoA = 1^o$. Left to right : Entropy contours based on KFVS, m-KFVS, m-KFVS-adjoint and q-KFVS methods.

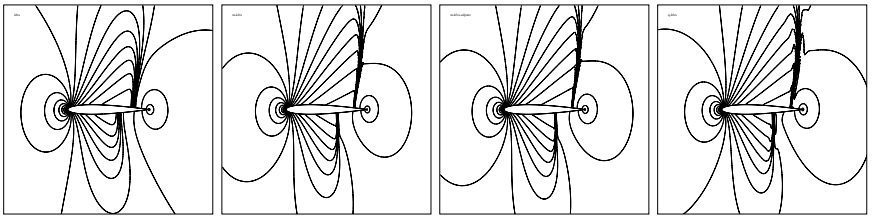

Fig. 6. Transonic flow past NACA 0012 airfoil, $M_\infty = 0.85$ and $AoA = 1^o$. Left to right : Pressure contours based on KFVS, m-KFVS, m-KFVS-adjoint and q-KFVS methods.

[ARO07, Ani08], where the control variables are the dissipation control vector, α. The number of control variables is equal to the number of cells in the computational domain, as each cell has one dissipation control variable. In the present work, the objective is to minimise the numerical dissipation generated by m-KFVS method and hence a natural choice for the cost function is a measure of change in entropy, which has to be minimised subject to the governing state equations as constraint. The discrete form of the cost function [ARO07, Ani08] is defined as the sum of the squares of change in

entropy at all cells in the computational domain, that is,

$$I = I\left\{U\left(\alpha\right)\right\} = \sum_{i=1}^{N} \left(\frac{\Delta S}{R}\right)_i^2, \quad \left(\frac{\Delta S}{R}\right)_i = ln\left(\frac{p}{\rho^\gamma}\right)_i - ln\left(\frac{p}{\rho^\gamma}\right)_\infty \tag{4}$$

Here, U is the conserved vector, α is the dissipation control variable, N is the total number of cells in the computational domain and $\frac{\Delta S}{R}$ is the change in entropy at any cell. The conditions at ∞ are given by freestream conditions. The cost function has to satisfy the governing state equations as constraint. In the present work, we have used the gradient based optimisation method, which requires the evaluation of sensitivity gradients to obtain the minimum value of cost function. The sensitivity gradients of the cost function w.r.t. the control variables are obtained by using discrete adjoint approach. The automatic differentiation tool *Tapenade* [HP04] has been used to ease the development of discrete adjoint solvers. The method of steepest descent is used as an optimisation solver to find the direction, which results in optimal α.

In isoentropic flows, the only contribution to the cost function comes from the numerical change in entropy as the physical change in entropy is zero. Therefore, the cost function can be driven to its minimal value zero on that grid using optimisation solver. In flows with discontinuities such as shocks, both the physical and numerical entropy contribute to the cost function. Also, the numerical entropy cannot evidently be driven to zero. However, it can be driven

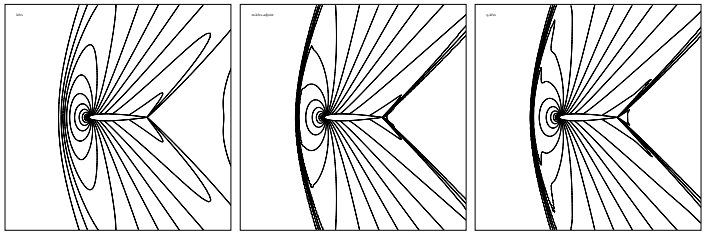

Fig. 7. Supersonic flow past NACA 0012 airfoil, $M_\infty = 1.2$ and $AoA = 0^o$. Left to right : Pressure contours based on KFVS, m-KFVS-adjoint and q-KFVS methods.

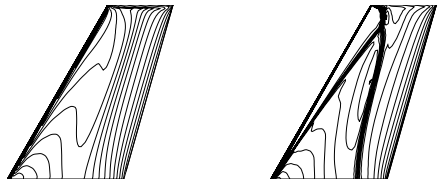

Fig. 8. Transonic flow past Onera M6 wing, $M_\infty = 0.84$ and $AoA = 3.06^o$. Left to right: Pressure contours on the upper surface of the wing based on KFVS and m-KFVS-adjoint methods.

Table 1. Low subsonic flow past NACA 0012 airfoil, $M_\infty = 0.1$ and $AoA = 0^o$. Comparison of maximum entropy change in the computational domain.

Scheme	KFVS	m-KFVS	m-KFVS-adjoint	q-KFVS
Max. entropy	5.0571×10^{-4}	2.3984×10^{-4}	1.6053×10^{-4}	6.7084×10^{-5}

Table 2. Supersonic flow past a NACA 0012 airfoil with $M_\infty = 1.2$ and $AOA = 0^o$. Comparison of lift and drag coefficients.

Scheme	KFVS	m-KFVS	m-KFVS-adjoint	q-KFVS	AGARD
C_L	0.000168	0.000049	0.000039	0.000063	0.0
C_D	0.1023	0.0966	0.0958	0.0968	0.0946 - 0.0960

to entropy produced by shocks plus a small amount necessary for stability and for obtaining wiggle free solution near shocks. The numerical results based on m-KFVS-adjoint method are shown in Figs. (4) to (8) and Tables (1) and (2). These results clearly demonstrate that the optimisation procedure further reduces the numerical dissipation in m-KFVS method and hence results in more accurate solution. It has been observed that the number of optimisation cycles, which results in minimal numerical dissipation depends on the initial α-distribution. Numerical experiments have shown that $2-3$ cycles of optimisation are adequate if initial α-distribution is chosen from the converged m-KFVS solution. The present work can be referred as numerical scheme optimisation.

On the whole, it can be summarised that the m-KFVS method, which is formally first order accurate inherits robustness, smoothness of contours and high residue fall from first order KFVS, and has accuracy, crispness and sharpness of second order q-KFVS method.

References

[ARO07] Anil, N., Rajan, N.K.S.: Omesh Reshi and Deshpande, S.M.: Adjoint based optimal control of dissipation in kinetic schemes. In: Proceedings of the 7th Asian CFD Conference, Bangalore, India, November 26-30 (2007)

[Ani08] Anil, N.: Optimal Control of Numerical Dissipation in modified KFVS (m-KFVS) using Discrete Adjoint Method. PhD Thesis, Indian Institute of Science, Bangalore, India (2008)

[Des86] Deshpande, S.M.: Kinetic theory based new upwind methods for inviscid compressible flows. AIAA paper 1986-0275 (1986)

[Des95] Deshpande, S.M.: Kinetic flux splitting schemes. In: Hafez, M.M., Oshima, K. (eds.) Computational Fluid Dynamics Review, pp. 161–181. John Wiley & Sons, Chichester (1995)

[HP04] Hascoet, L., Pascual, V.: TAPENADE 2.1 user's guide. INRIA Project Report No. 0300 (2004)

[RD07] Ramesh, V., Deshpande, S.M.: Unsteady flow computations for flow past multiple moving boundaries using LSKUM. Computers and Fluids 36(10), 1592–1608 (2007)

Second Order Sensitivities for Shape Optimization in the Presence of Shocks

Eyal Arian[1] and Angelo Iollo[2]

[1] Computational Mathematics, The Boeing Company, MC 7L-21 PO Box 3707, Seattle, WA 98124-2207, USA
eyal.arian@boeing.com
[2] Institut de Mathématiques de Bordeaux, UMR 5251 CNRS, Université de Bordeaux and INRIA Futurs, Equipe-Projet MC2, 33405 Talence cedex, France
angelo.iollo@math.u-bordeaux1.fr

Summary. We compute the analytical Hessian for an optimal shape design problem governed by the quasi-one-dimensional Euler equations. We derive the Hessian explicitly for this case, and propose two formulations that can be applied in general to CFD. One method is less costly than the other but may be less stable as the analysis indicates. We present results pertinent to a problem involving a shock showing the interest of using second order information in the minimization.

Keywords: Aerodynamic Optimization, Hessian, Adjoint method, Compressible Euler Flow.

1 Introduction

Industrial aerodynamic optimization problems are large scale ill-conditioned problems, with many inequality constraints, that require significant computational resources. In reality there are not enough resources and time to achieve complete convergence and only improved design is possible. The state-of-the-art practice is to use the adjoint method to compute the reduced gradient, and quasi-Newton method is used to accelerate the convergence. Quasi-Newton approximates the Hessian (or its inverse) by a low rank update method (rank-2 in most cases), taking the identity matrix to be the initial guess. That choice corresponds to having the gradient as the initial search direction in the optimization process, which can serve as a very poor search direction.

In industrial aerodynamic design the number of design variables is in the hundreds, and there are not enough resources for more than $O(10)$ optimization iterations, resulting in poor convergence of rank-2 quasi-Newton methods. Therefore, we think that a better approximation of the Hessian is essential to achieve convergence. Such an approximation can serve as the initial guess for a quasi-Newton method.

The Hessian for such problems is typically highly ill-conditioned as analyzed for example by Arian & Ta'asan (1999). For such problems the gradient pre-multiplied by the approximated inverse of the Hessian serves as an excellent search direction close enough to the solution as demonstrated by Arian & Vatsa (1999). However, the techniques used in these references are not practical in the industrial setting in which the governing state equations are more difficult to analyze. In practice we would like to use the available information, such as sensitivities and adjoint solutions, to generate an approximated Hessian numerically.

To this end, in this work we report three different ways to compute the Hessian for an optimal shape design problem governed by the quasi-one-dimensional Euler equations. That model problem is simple enough to be solved analytically but still retain the complexity of fluid dynamics that makes it interesting. The first approach is specific to the problem under scrutiny, whereas the other two can be applied in general. All of the approaches are consistent, as shown in [arianiollo]. In this paper we actually use the analytical Hessian in an optimization problem with shocks, to demonstrate its application and its effectiveness on convergence

2 Problem Definition

We consider the compressible Euler equations in a quasi-one-dimensional approximation. The flow takes place inside a nozzle of height $h(x)$, where x is the spatial coordinate. The optimal design problem consists of minimizing an objective function, $J(U)$, subject to state equations:

$$\begin{array}{c} \min_{h(x)} J(U) \\ R(U,h) = 0 \end{array} \tag{1}$$

with

$$R(U,h) = \frac{d}{dx}(hF) - \frac{dh}{dx}P, \tag{2}$$

and

$$U = (\rho, \rho q, \rho E)^T, \qquad F = (\rho q, \rho q^2 + p, \rho H q)^T, \qquad P = (0, p, 0),$$

where p is the static pressure, and ρH is the total enthalpy density.

In the following numerical example, the objective function is defined to be the integral of the negative pressure distribution across the domain. The reduced gradient and Hessian are calculated by first and second order perturbations, respectively, to the non-linear problem at a given design point. The perturbation of the original minimization problem results in the following linear sub-problem:

$$\begin{array}{c} \min_{\tilde{h}} J(U+u) \\ Lu - f = 0 \end{array} \tag{3}$$

where U is given, u is a perturbation to U, $f = f(\tilde{h})$, and $\tilde{h}$ is perturbation of h. The channel height, $h(x)$, is composed of a seed height function, $h_0(x)$, perturbed by a sum of N fixed shape basis functions, $h_i(x)$, with the coefficients, c_i, serving as the design variables:

$$h(x) = h_0(x) + \sum_{i=1}^{N} c_i h_i(x).$$

The linear operator, L, has the following explicit form,

$$Lu = \frac{d}{dx}(hAu) - \frac{dh}{dx}Bu,$$

where $A = \partial F/\partial U$ and $B = \partial P/\partial U$. The right hand side of the linearized problem has the following explicit form:

$$f = \frac{d\tilde{h}}{dx}P - \frac{d}{dx}(\tilde{h}F) \tag{4}$$

The boundary conditions for the above perturbation equations, $Lu - f = 0$, depend on the boundary conditions of the unperturbed problem.

3 Direct and Adjoint Based Methods for Hessian Computation

In this simple model problem the gradient as well as the Hessian can be computed by the implicit function theorem, since the solution of the flow in the nozzle can be computed at the cost of solving a non-linear equation in the flow variables at each point of the domain, see [arianiollo] for details. Indeed, in the case of flows with shocks, it is possible to compute first and second derivatives of the shock position with respect to the design variables.

In practice the Hessian can not be calculated directly. We propose two methods to approximate the Hessian by solving sensitivity and adjoint equations. These methods can be applied for massive problems for which the flow is approximated using CFD. The first method requires solving the adjoint-sensitivity equations in addition to the standard sensitivity equations and adjoint equation ($O(2N + 1)$ linear solutions) while the second method requires only the sensitivity and adjoint equations ($O(N + 1)$ linear solutions). Both methods use the following representation of the Hessian,

$$\frac{d^2J}{dc_i dc_j} = \int_\Omega \Big[\Big(\frac{dv}{dc_j}\Big)^T f_i + v^T \frac{df_i}{dc_j}\Big] dx, \tag{5}$$

where v satisfies the adjoint equation $L^*v = \frac{\partial p}{\partial U}$, $f_i = \frac{\partial R}{\partial c_i}$ depends on the state solution.

We observe that the term f_i is discontinuous at the shock (Heaviside function) and the adjoint v has a log singularity at the throat but is continuous

at the shock. The term df_i/dc_j contains a delta function at the shock since it contains a derivative of the pressure, p, that in turn contains a Heaviside function.

The first method consists of a manipulation of the above formula taking advantage of the adjoint problem to the governing problem, see [arianiollo] for details. The second method uses a representation that can be derived from Eq.5 by further analysis of the adjoint-sensitivities, dv/dc_j, and eliminating the need to solve N linear equations for these sensitivities. In this case, the Hessian can be represented in the following matrix-vector form:

$$\frac{d^2J}{dc_i dc_j} = \int_\Omega \begin{bmatrix} \frac{dU}{dc_i} \\ 1 \end{bmatrix}^T \left\{ \begin{bmatrix} \frac{\partial^2 p}{\partial U^2}^T & 0 \\ 0 & 0 \end{bmatrix} - v \otimes \begin{bmatrix} \frac{\partial L^*}{\partial U} & \frac{\partial L^*}{\partial c_j} \\ \frac{\partial L}{\partial c_i} & 0 \end{bmatrix} \right\} \begin{bmatrix} \frac{dU}{dc_j} \\ 1 \end{bmatrix} dx \qquad (6)$$

The notation $\otimes$ is introduced in order to clarify the application of the operators in the integrand on the sensitivities and adjoint variables. It should be interpreted as follows:

$$v \otimes \frac{\partial L^*}{\partial U}\frac{dU}{dc_j} = \frac{\partial L^*}{\partial U}\Big(\frac{dU}{dc_j}\Big) \cdot v$$
$$v \otimes \frac{\partial L^*}{\partial c_j} = \frac{\partial L^*}{\partial c_j}\Big(v\Big)$$
$$v \otimes \frac{\partial L}{\partial c_i}\frac{dU}{dc_j} = v \cdot \frac{\partial L}{\partial c_i}\Big(\frac{dU}{dc_j}\Big)$$

where the parenthesis $A(x)$ denotes the action of an operator A on x, and the dot $v \cdot x$ denotes a dot product between v and x.

The cost of the second method consists of solving N linear sensitivity equations, and 1 additional adjoint equation, all together $O(N+1)$ linear equations. Although the second method seems to have an advantage over the first with regards to computational cost, we suspect that it is likely to be more unstable in practice, since some of the terms involve multiplication of delta functions at the shock. This is not the case for the Hessian representation of the first method given in Eq.(5).

4 Numerical Test Demonstrating the Impact of the Hessian on Convergence of Transonic Optimal Design

We demonstrate the effectiveness of the second order sensitivity information on an optimal shape design problem governed by the quasi-one dimensional Euler equation. In the numerical test we compute the Hessian using the direct approach as described in detail in [arianiollo]. Total enthalpy is set to 4, total pressure at inlet is 2, the pressure at the exit is 1.6. That choice of parameters and the initial shape guarantees the flow to be transonic and that it contains a shock. We minimize the following objective functional,

$$\min_{c_k} \int_{-1}^{1} -p dx + \mu \sum_{i=1}^{N} c_i^2,$$

where the first term is the integral of the (negative) pressure, and the second term is a regularization term to prevent highly oscillatory solutions (we choose $\mu = 1/20$). The coefficients c_k are relative to a spline representation of the perturbation of the initial geometry $h_0(x)$. The collocation points of such splines are $N = 12$ in this case, and they are uniformly distributed between $1/10$ and $1/2$, i.e., the interval where the geometry is perturbed. We have that $\forall x \in \Omega$, $\Omega = [-1, 1]$ and $h_0(x) = 2$ for $-1 \leq x < -1/2$, $h_0(x) = 1 + \sin^2(\pi x)$ for $-1/2 \leq x \leq 1/2$, and $h_0(x) = 2$ for $1/2 < x \leq 1$.

Minimizing the negative pressure term in the objective function is equivalent to maximizing the pressure, which tends to increase the region of the nozzle that has relatively high pressure.

We apply both Newton's method and gradient descent method. For the Newton's method the Hessian is determined exactly at every iteration. The convergence results are shown in Fig. 1, depicting the L_2 norm of the error, in log scale, as a function of iteration number. Using the Hessian the error is reduced by a factor 0.1 at every iteration, after the first three iterations, while only by a factor of about 0.85 when using the gradient only.

In Fig. 2, the error (depicted by 'o') is compared with the negative gradient '+', and gradient pre-multiplied by the inverse of the Hessian '*'. Clearly the inverse of the Hessian is "correcting" the gradient direction to point to the error.

Finally, in Fig. 3 and Fig. 4 the nozzle hight $h(x)$ and the pressure distribution $p(x)$ are given, respectively. The dashed line depicts the quantities before optimization and the solid line depicts the optimal solution. Since the initial geometry is obtained by a random perturbation of the splines coefficients, the initial shape is oscillatory, whereas the final result is much smoother thanks to the regularization term.

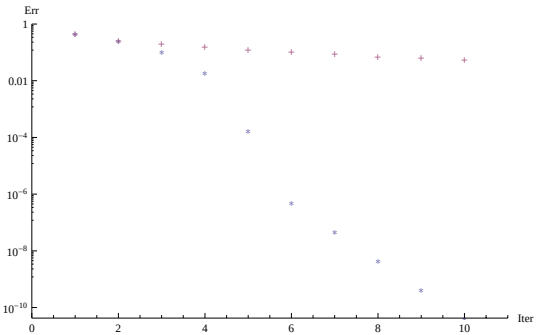

Fig. 1. Convergence history in a Log plot using Gradient Descent and Hessian

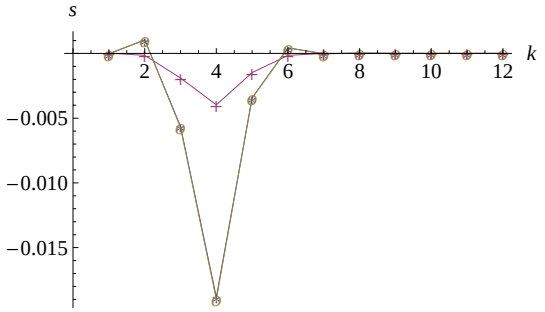

Fig. 2. After three Newton iterations the gradient is give by '+', the error by 'o', and the gradient pre-multiplied by the inverse of the Hessian is depicted by '*'.

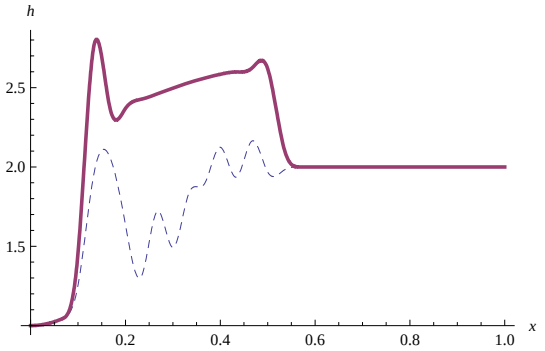

Fig. 3. The initial geometry, $h(x)$, is depicted by dashed line, and the optimal solution is depicted by the solid line

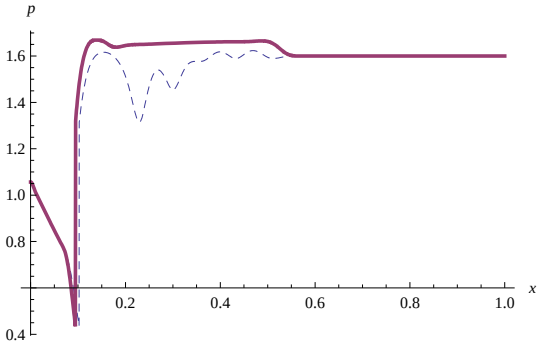

Fig. 4. The initial pressure distribution, $p(x)$, is depicted by dashed line, and the optimal solution is depicted by the solid line

References

[arianiollo] Arian, E., Iollo, A.: Analytic Hessian Derivation for the quasi-one-dimensional Euler Equations, Boeing Technical Report, CM-08-004 (2008)

[taasan] Arian, E., Ta'asan, S.: Analysis of the Hessian for Aerodynamic Shape Optimization: Inviscid Flow. Computers & Fluids 28(7), 853–877 (1999)

[vatsa] Arian, E., Vatsa, V.: A Preconditioning Method for Shape Optimization Governed by the Euler Equations. International Journal of Computational Fluid Dynamics 12, 17–27 (1999)

“This page left intentionally blank.”

Strategies for Robust Convergence Characteristics of Discrete Adjoint Method

Byung Joon Lee[1] and Chongam Kim[2]

[1] Postdoctoral Research Fellow, mecha777@hitel.net
[2] Associate Professor, chongam@snu.ac.kr
School of Mechanical and Aerospace Eng., Seoul National University, Seoul, Korea

1 Introduction

Recently, aerodynamic shape design works with adjoint approach are popularly carried out by many researchers because the adjoint formulation can provide accurate sensitivities without additional computational time cost accompanied with the increase of the number of design variables. [LKJ04]

However, the adjoint approach still has several unsettled problems to be extensively applied to various aerodynamic shape optimization applications. Most of all, the adjoint solver often shows too poor convergence characteristics to provide sufficiently accurate gradient information in complicated configuration design problems. The convergence of the adjoint solver is mainly affected by that of baseline flow solver. Therefore, the flow phenomenon itself such as a severe flow expansion, large separation and strong shock waves or the numerical schemes applied to the baseline solver can be the causes. In addition, the convergence characteristics of an adjoint solver are extremely affected by the poor mesh quality from grid generator or modifier during the design process.

In the present study, the increase of robustness in the sensitivity analysis with discrete adjoint formulation is achieved by introducing volume-integrated objective functions and a numerical dissipation term to enhance the diagonal dominance of the adjoint Jacobian matrix. The performances of present approaches are validated through 2- and 3-D sensitivity analyses and design applications where the adjoint solver hardly converges.

2 Sensitivity Analysis via Volume Integrated Functions

The differentiation of surface-integrated objective functions have conventionally non-zero value only on the wall boundary of adjoint formulation as given in Eqs.(1)-(2). In the inner computational domain the adjoint vectors are evaluated by Eq.(1).

$$\left(\frac{I}{J\Delta t} + \left[\frac{\partial R}{\partial Q} \right]^T_{VL} \right) \Delta\Lambda = -\left[\frac{\partial R}{\partial Q} \right]^T \Lambda^m \tag{1}$$

Here, the matrix *I* indicates an identity matrix and *J* is Jacobian. The van-Leer flux Jacobian which is conventionally used in the flow solver is indicated by $[\partial R/\partial Q]$. The boundary condition on the surface can be given as follows.

$$\left[\frac{\partial R}{\partial Q}\right]^T \Lambda + \left[\frac{\partial R_B}{\partial Q}\right]^T \Lambda_B + \left\{\frac{\partial F}{\partial Q}\right\} = \{0\}^T \qquad \text{(on the wall)} \tag{2}$$

where subscript *B* represents the boundary cell. *R*, *Q* and *F* denote the discrete residual equation, flow variable vector and the objective function respectively. The differentiated objective function term, $[\partial F/\partial Q]$, has non-zero value on the wall boundary only. Therefore, the time-marching processes on the inner computational domain and other boundary regions except wall boundary region are mainly governed by the differentiated flux terms, $[\partial R/\partial Q]$, of the discretized governing equations. Thus, any discontinuous perturbation of the differentiated flux terms caused by highly non-linear flow phenomenon and/or low quality of mesh distribution may affect stability of the time marching process of adjoint vector. On the other hand, the volume-integrated objective functions can play a role of a constant-valued source term which can stabilize the time marching process as given in Eq.(3).

$$\left(\frac{I}{J\Delta t} + \left[\frac{\partial R}{\partial Q}\right]_{VL}^T\right)\Delta\Lambda = -\left[\frac{\partial R}{\partial Q}\right]^T \Lambda^m - \left[\frac{\partial F}{\partial Q}\right]^T \tag{3}$$

In Eq.(3), the objective function, especially drag coefficient, can be defined in the inner computational domain by a volume integrated form. The drag coefficient via volume-integration of entropy variation derived by Paparone et al.[LR03] can be given by Eq. (4).

$$F = V_\infty \int_\Omega \nabla \cdot \left(\rho g \bar{V}\right) d\Omega \tag{4}$$

where Ω defines the computational domains divided by the sensing terms into wave and viscous drag regions. The entropy variation function *g* is defined by Eq.(5) as follows.

$$g\left(\Delta s / \mathbb{R}\right) = -f_{s1}(\Delta s / \mathbb{R}) - f_{s2}(\Delta s / \mathbb{R})^2 \tag{5}$$

Here, f_{s1} and f_{s2} correspond to the coefficients of the first and the second order terms of Taylor series expansion for non-dimensional velocity with respect to entropy variation. $\mathbb{R}$ is the universal gas constant and *s* denotes entropy. In the present paper, the effects of volume-integrated drag coefficient for sensitivity analysis codes are presented for a 2-D transonic airfoil. Figure 1 shows the comparison of the residual history of the present adjoint solvers via surface integrated and volume integrated drag coefficients. The time iterative calculation is performed with a same CFL number over NACA0012 airfoil at the free-stream condition that Mach number is 0.7, angle of attack is 3.1° and Reynolds number is 9 million. The size of O-type mesh system is (320x128) which is too fine to provide the flow solver with sufficient amount of numerical dissipation for securing good convergence. Conventionally, in case that good convergence characteristics of

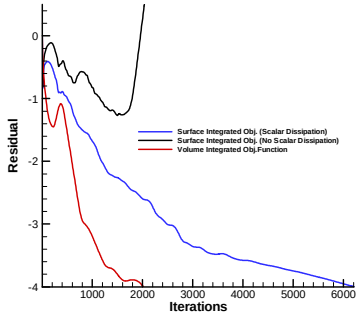

Fig. 1. Comparison of the Residual History [CFL#=5.0]

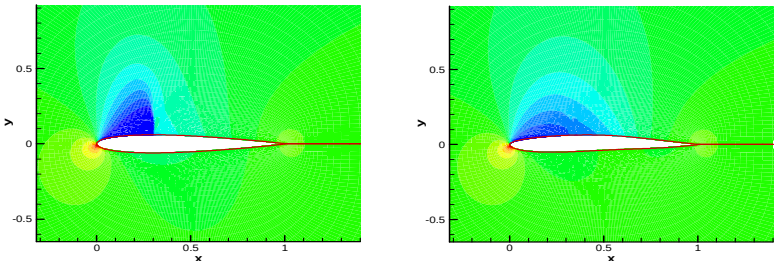

Fig. 2. Comparison of Pressure Contours [Baseline(Left) and Designed (Right)]

flow solver is not secured even though the solution shows fairly good accuracy, the adjoint solver hardly converges as shown in Fig. 1. On the other hand, the volume integrated objective function case converges very well. In this test case, the design optimization with gradient based method can be carried out by the volume integrated objective function case only. For the test case, a drag minimization with maintaining lift coefficient is performed. Through 12 design iterations, drag coefficient can be diminished by 32% during the lift coefficient slightly increases. The shock waves on the upper surface of the airfoil are weakened fundamentally by comparing it with the baseline model as shown in Fig. 2.

3 Enhancement of Diagonal Dominance of Adjoint Matrix

For the second strategy, a Jameson-type numerical dissipation is considered for the discrete adjoint formulation. In case that the solution from the baseline solver is evaluated using 5 stencils for 3rd order spatial accuracy which is common in conventional CFD solvers, the adjoint Jacobian matrix for 1-D problem can be represented by Eq. (6)

$$\left[\frac{\partial R}{\partial Q}\right]^T = \begin{bmatrix} \ddots & & & & & & & & & & & & \\ & \ddots & & & & & & & & & & & \\ & & \ddots & & & & & & & & & & \\ & & & \ddots & & & & & & & & & \\ & & & & \ddots & & & & & & & & \\ & & & & & \ddots & & & & & & & \\ & & & & & & \ddots & & & & & & \\ & & & & & & & \ddots & & & & & \\ & & & & & & & & \ddots & & & & \\ & & & & & & & & & \ddots & & & \\ & & & & & & & & & & \ddots & & \\ & & & & & & & & & & & \ddots & \\ & & & & & & & & & & & & \ddots \end{bmatrix} \tag{6}$$

where $\varepsilon = 0$ in case of original adjoint formulation and $\varepsilon > 0$ in case of the modified adjoint formulation. To modify the adjoint matrix to have more diagonal dominance, a difference type symmetric equation such as numerical dissipation is needed. In the present work, 4th order numerical dissipation which is represented by the variable *G* is considered as shown in Eq.(7).

$$\begin{aligned} SD_i = {} & \varepsilon_{i+1/2} G_{i+2} - \left(3\varepsilon_{i+1/2} + \varepsilon_{i-1/2}\right) G_{i+1} + \left(3\varepsilon_{i+1/2} + 3\varepsilon_{i-1/2}\right) G_i \\ & - \left(\varepsilon_{i+1/2} + 3\varepsilon_{i-1/2}\right) G_{i-1} + \varepsilon_{i-1/2} G_{i-2} \end{aligned} \tag{7}$$

where $\varepsilon_{i+1/2}$ is the coefficient term for dissipation at the cell interface and a newly defined variable for dissipation G is

$$G_i = \partial R_i / \partial Q_i \cdot \lambda_i \tag{8}$$

The dissipation term is added to RHS of the discrete adjoint equation as an anti-diffusion term to enhance the diagonal terms as shown in Eq.(9).

$$\begin{aligned} RHS_i - SD_i = {} & -\left(\left(1+\varepsilon_{i+\frac{1}{2}}\right)\frac{\partial R_{i+2}}{\partial Q_i}\right)\lambda_{i+2}^m - \left(\left(1-3\varepsilon_{i+\frac{1}{2}} - \varepsilon_{i-\frac{1}{2}}\right)\frac{\partial R_{i+1}}{\partial Q_i}\right)\lambda_{i+1}^m \\ & - \left(\left(1+3\varepsilon_{i+\frac{1}{2}} + 3\varepsilon_{i-\frac{1}{2}}\right)\frac{\partial R_i}{\partial Q_i}\right)\lambda_i^m - \left(\left(1-\varepsilon_{i+\frac{1}{2}} - 3\varepsilon_{i-\frac{1}{2}}\right)\frac{\partial R_{i-1}}{\partial Q_i}\right)\lambda_{i-1}^m - \left(\left(1+\varepsilon_{i-\frac{1}{2}}\right)\frac{\partial R_{i-2}}{\partial Q_i}\right)\lambda_{i-2}^m \end{aligned} \tag{9}$$

The diagonal dominance of the adjoint Jacobian matrix can be tested by a conventional stability condition as shown in Eq. (10). The ratio, *A'*, of the diagonal term to the summation of off-diagonal terms for the modified Jacobian matrix can be easily known that it is always smaller than that of original adjoint Jacobian matrix, *A*. The condition represents that the modified adjoint matrix can have more diagonal dominance and it is directly related to the stable convergence characteristics of adjoint solver.

$$A' = \frac{\left|\frac{\partial R_i}{\partial Q_i}\right|}{\left\{\frac{\left(1+\varepsilon_{i+\frac{1}{2}}\right)}{\left(1+3\varepsilon_{i+\frac{1}{2}}+3\varepsilon_{i-\frac{1}{2}}\right)}\left|\frac{\partial R_{i+2}}{\partial Q_i}\right| + \frac{\left(1-3\varepsilon_{i+\frac{1}{2}}-\varepsilon_{i-\frac{1}{2}}\right)}{\left(1+3\varepsilon_{i+\frac{1}{2}}+3\varepsilon_{i-\frac{1}{2}}\right)}\left|\frac{\partial R_{i+1}}{\partial Q_i}\right| + \frac{\left(1-\varepsilon_{i+\frac{1}{2}}-3\varepsilon_{i-\frac{1}{2}}\right)}{\left(1+3\varepsilon_{i+\frac{1}{2}}+3\varepsilon_{i-\frac{1}{2}}\right)}\left|\frac{\partial R_{i-1}}{\partial Q_i}\right| + \frac{\left(1+\varepsilon_{i-\frac{1}{2}}\right)}{\left(1+3\varepsilon_{i+\frac{1}{2}}+3\varepsilon_{i-\frac{1}{2}}\right)}\left|\frac{\partial R_{i-2}}{\partial Q_i}\right|\right\}}$$

$$\geq \frac{\left|\frac{\partial R_i}{\partial Q_i}\right|}{\left\{\left|\frac{\partial R_{i+2}}{\partial Q_i}\right| + \left|\frac{\partial R_{i+1}}{\partial Q_i}\right| + \left|\frac{\partial R_{i-1}}{\partial Q_i}\right| + \left|\frac{\partial R_{i-2}}{\partial Q_i}\right|\right\}} = A, \quad if\ 0 < \varepsilon \ll 1 \tag{10}$$

The definition of the coefficient for the dissipation can be given by Eqs.(11)~(14). The proper scaling of the dissipative terms is accomplished through the factors as follow.

$$\varepsilon_{i+1/2} = \varepsilon^{(4)} C_{i+1/2}, \text{ and } C_{i+1/2} = \frac{1}{2}\left[C_{\xi_{i+1}} + C_{\xi_i}\right],$$

$$\text{where } C_\xi = e_\xi \varphi_\xi, \text{ and } \varphi_\xi = \sqrt{1+(e_\eta / e_\xi)^\sigma} \text{ (2-D case)} \tag{11}$$

Moreover, *e* is the spectral radius of the flux Jacobian matrices in the body-fitted curvilinear directions that conform to the body surface. A conservative estimate of this spectral radius is constructed according to the following formula,

$$e = u \cdot \hat{n} + a\sqrt{n_x^2 + n_y^2} \tag{12}$$

where *a* is the speed of sound at the center of the cell, and *n* is the average of the directed area vectors of the two faces in the ξ-direction. The 2nd and 4th order coefficients are as follow.

$$\varepsilon^{(2)} = k^{(2)} \max(\nu_{i,j}, \nu_{i+1,j}) \tag{13}$$

where $\nu_{i,j} = \left|\frac{\frac{\partial C_{D_{i+1,j}}}{\partial p_{i+1,j}} - 2\frac{\partial C_{D_{i,j}}}{\partial p_{i,j}} + \frac{\partial C_{D_{i-1,j}}}{\partial p_{i-1,j}}}{\frac{\partial C_{D_{i+1,j}}}{\partial p_{i+1,j}} + 2\frac{\partial C_{D_{i,j}}}{\partial p_{i,j}} + \frac{\partial C_{D_{i-1,j}}}{\partial p_{i-1,j}}}\right|$, and $C_{D_{i,j}}$ is the volume integrated drag coefficient on Cell (*i,j*). The 4th order coefficient can be given by Eq.(14).

$$\varepsilon^{(4)} = \max(0, (k^{(4)} - \varepsilon^{(2)})) \tag{14}$$

In order to prevent the deterioration of the accuracy by the dissipation term, the coefficient, $\varepsilon^{(2)}$ is taken proportional to the normalized 2nd difference of volume integrated sensitivity which acts as a sensor that turns off around the boundary of entropy drag.

In order to quantify an adequate size of dissipation, the gradients according to the coefficients are compared with those of no dissipation case in a low anlge of attack case in Fig. 3. As shown in Fig.3, the $k^{(4)} = 1/128$ case shows quite reasonable accuracy. Therefore, hereafter, the sensitivity analysis and design works in the present work are performed with $k^{(4)} = 1/128$ case. However, the determination

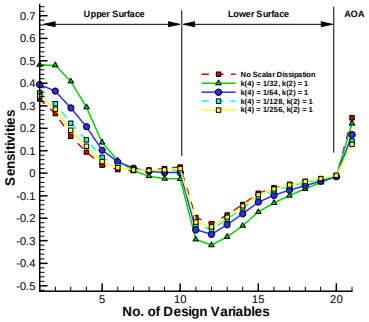

Fig. 3. Comparison of Accuracy

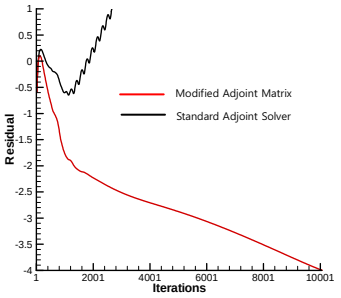

Fig. 4. Comparison of Residual History [ONERA-M6, CFL#=5.0]

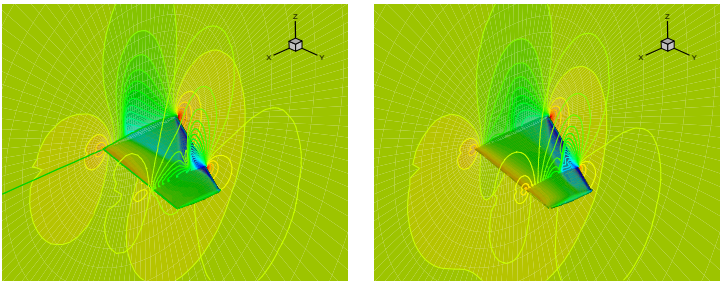

Fig. 5. Comparison of Pressure Contours [Baseline(Left) and Designed (Right)]

of the coefficient is still problem-dependant. According that the dissipation increases, the adjoint Jacobian matrix can have more diagonal dominance but the accuracy of the gradients decreases. The sensitivity analyses and design optimization works are carried out for transonic flows in 2- and 3-D applications where the flow solver shows residual oscillation just below 4^{th} order and the adjoint solver diverges. The test case of 2-D problem is same to the volume integrated adjoint problem. In 3-D case, the present approach is tested in the free-stream condition that Mach number is 0.84, angle of attack is 5.6°, the Reynolds number is 14.6 million. As shown in Fig. 1 and 4, in both cases, the modified adjoint formulation via numerical dissipation show good convergence characteristics in comparison with the original adjoint form. A drag minimization with maintaining lift coefficient is carried out for 3-D wing design problem. Figure 5 shows the pressure distributions around the baseline and designed wings. Through the design optimization, the drag coefficient can be diminished by 17.5% while the lift coefficient remains at the initial value.

4 Conclusion

Two strategies for improving the convergence characteristics of discrete adjoint solver are suggested. The volume integrated objective function can play a role of source term for the discrete adjoint formulation which can stabilize the convergence characteristics. By using the volume integrated form of drag coefficient, sensitivity analysis and design optimization can be successfully performed with the low quality mesh system where the adjoint solver with surface integrated objective function hardly converges. However, the volume integrated form for the lift and induced drag is not known yet. It needs further studies to be extended to 3-D problems. As an alternative, the adjoint Jacobian matrix can be modified to have more diagonal dominance by using the Jameson-type numerical dissipation. The stability condition can reveal the modified adjoint matrix can have more diagonal dominance than the original adjoint matrix has. Through 2- and 3-D sensitivity analyses and design optimization applications, the present approach shows that it can secure robust convergence characteristics for discrete adjoint solver.

References

[LKJ04] Leoviriyakit, K., Kim, S., Jameson, A.: Aero-Structural Wing Planform Optimization Using the Navier-Stokes Equations, AIAA 2004-4479

[LR03] Paparone, L., Tognaccini, R.: Computational Fluid Dynamics-Based Drag Prediction and Decomposition. AIAA J. 41(9), 1647–1657 (2003)

“*This page left intentionally blank.*”

On the Reliability of the Aerodynamic Analysis Using a Moment Method

Jaehun Lee[1], Hee Youb Kang[2], Jang Hyuk Kwon[3], and Byung Man Kwak[4]

[1] Department of Aerospace & Systems Engineering, KAIST, Daejeon, Korea
jaehun.lee@gmail.com
[2] Department of Mechanical Engineering, KAIST, Daejeon, Korea
hykang@kaist.ac.kr
[3] Department of Aerospace & Systems Engineering, KAIST, Daejeon, Korea
jhkwon@kaist.ac.kr
[4] Department of Mechanical Engineering, KAIST, Daejeon, Korea
bmkwak@khp.kaist.ac.kr

In this study, the reliability analysis was performed for the aerodynamic analysis. Among various reliability analysis methods, the moment method was used and results were compared with other reliability methods. The reliability of aerodynamic analysis of a 2D airfoil and a 3D wing were considered. In the case of the 2D airfoil, the reliability was computed by parameterizing an airfoil shape using the PARSEC function and considering uncertainties of its shape. In the case of 3D wing, the reliability was computed by considering uncertainties of flow conditions. Compared with other methods, it was found that the moment method predicted the probability accurately.

1 Introduction

Reliability analysis computes how much the system is reliable using statistical methods. Reliability analysis becomes popular because it reflects more physical phenomena which possess uncertainty. Popular reliability analysis methods are MCS(Monte Carlo simulation), FORM(first order reliability method) and moment methods.

Reliability analysis is commonly used in the structural analysis and its use in the aerodynamic analysis is recent. Possible uncertainty of aerodynamic analysis is a wing shape and flow conditions. It will be useful to consider such uncertainty in the aerodynamic analysis. Ahn et al. conducted RBDO of a 3D wing using FORM[Ahn2005]. In their study, parameters related with the planform shape only such as the sweepback angle and the taper ratio were considered. Recently Sobieczky proposed the PARSEC function to approximate the shape of an airfoil with certain parameters[Sobieczky98].

In this study, reliability analysis was performed for the aerodynamic analysis using the moment method. Reliability of aerodynamic performances was computed by considering uncertainty of an airfoil shape and uncertainty of flow conditions of a 3D wing.

2 Reliability Analysis

In reliability analysis, the reliability is defined as follows:

$$Reliability = 1 - P_f \tag{1}$$

In (1), P_f is called the probability of failure and it is the probability of a limit state function g being violated. If the region which satisfies $g > 0$ is a feasible region, the probability of failure is defined as follows:

$$P_f = P(g \leq 0) \tag{2}$$

2.1 Monte Carlo Simulation

MCS computes the reliability with a repeated random sampling and it requires a large number of computations. MCS computes the probability of failure with the following formula:

$$P_f = \frac{1}{N} \sum_{i=1}^{N} I\left[g(x(i))\right] \tag{3}$$

where N is the sample size , $x(i)$ is the i^{th} random variable, and I is an indicator function whose value is 1 when $g > 0$, zero otherwise. Since random numbers used in MCS can be different according to the algorithm of the random number generation, the prediction of MCS can be placed within a certain range. It is called a confidence interval and calculated with the following formula:

$$P_f - \sqrt{\left(\frac{P_f(1-P_f)}{N}\right)} * z_\alpha \;\leq\; P_f \;\leq\; P_f + \sqrt{\left(\frac{P_f(1-P_f)}{N}\right)} * z_\alpha \tag{4}$$

where z_α is called as z critical value and its value is assumed as 1.96 for the 97.5% confidence interval[Devore2000].

2.2 First Order Reliability Method

FORM is a method that approximates the limit state function as a linear equation and finds the most probable point(MPP) in a reduced space and it is the nearest point to satisfy the limit state function. FORM requires to find β which means a distance from the origin to MPP and it is called the reliability index. It is defined as

$$\beta = \|u\| = \sqrt{u^T u} \tag{5}$$

In (5), u is a $n \times 1$ vector and it is called a transformed variable and defined as follows:

$$u = \frac{x - \mu}{\sigma} \tag{6}$$

where x is a random variable, μ is a mean vector, and σ is the standard deviation vector. When x has a normal distribution, the probability of failure is computed as follows:

$$P_f = \Phi(-\beta) \tag{7}$$

2.3 Moment Method

Moment methods directly find the probability distribution from statistical moments. Statistical moments are defined as follows:

$$M_k = \int_{-\infty}^{\infty} (x-\mu)^k f(x) dx \tag{8}$$

M_k is the k^{th} central moment, x is the random variable, and $f(x)$ is the probability distribution or probability density function(PDF). (8) can be calculated numerically with a quadrature rule.

$$E\{g^k\} = \int_{-\infty}^{\infty} [g(x)]^k \phi(x) dx \cong \sum_{i=1}^{m} w_i [g(l_i)]^k \tag{9}$$

where w_i means the i^{th} integration weight and l_i means the i^{th} integration point. Rahman and Xu proposed a method to determine the general levels and weights for non-normal distribution, which is called MBQR[Rahman2004].

After computing l_i and w_i, the statistical moments of the limit state function is calculated by quadrature rule. From the calculated moment, the PDF of the limit state function is estimated by the Pearson system. It finds the probability density function f which satisfies the following differential equation.

$$\frac{df(x)}{f(x)dx} = -\frac{\overline{x}+a}{c_0 + c_1\overline{x} + c_2\overline{x}^2} \tag{10}$$

where $\overline{x}$ means $x-\mu$. There are 7 types of solutions depending on the roots of $c_0 + c_1\overline{x} + c_2\overline{x}^2$ and more thorough explanations can be found in references[Seo2002, Lee2006]. The current moment method will be denoted as the Pearson system.

3 Flow Analysis

A parallelized flow solver for the Navier-Stokes equations is used in the aerodynamic analysis. The governing equations are as follows:

$$\frac{\partial q}{\partial t} + \frac{\partial f_i}{\partial x_i} = \frac{\partial f_{vi}}{\partial x_i} \tag{11}$$

$$q = \begin{pmatrix} \rho \\ \rho u_1 \\ \rho u_2 \\ \rho u_3 \\ \rho E \end{pmatrix}, \; f_i = \begin{pmatrix} \rho u_i \\ \rho u_i u_1 + \delta_{i1} p \\ \rho u_i u_2 + \delta_{i2} p \\ \rho u_i u_3 + \delta_{i3} p \\ \rho u_i H \end{pmatrix}, \; f_{vi} = \begin{pmatrix} 0 \\ \sigma_{ij}\delta_{i1} \\ \sigma_{ij}\delta_{i2} \\ \sigma_{ij}\delta_{i3} \\ u_j\sigma_{ij} + k\frac{\partial T}{\partial x_i} \end{pmatrix} \tag{12}$$

The flow region is discretized spatially by the finite volume method and the Roe's FDS and TVD are used in calculating the numerical flux. The multigrid method with mesh sequencing is used to accelerate the convergence of the steady calculation[Park2004]. DACE tool is used to replace the flow analysis when the computing time is large[Lophaven2002].

4 Reliability of Flow Analysis

4.1 2D Airfoil

For the numerical test, the reliability analysis was applied to a two-dimensional aerodynamic analysis. To consider the uncertainty of airfoil shape, the PARSEC function is used. RAE2822 was used in the aerodynamic analysis. The Mach number was 0.73 and the angle of attack was 2.78°. The limit state function was assigned for the lift coefficient to be greater than a reference value.

$$P_f = P(C_l - C_{l,Ref} \leq 0) \tag{13}$$

All parameters are assumed as standard normal random variables. At first, 4 parameters were tested for different DOE(design of experiment) levels and their means and standard deviations are shown in Table 1.

Table 1. Mean and standard deviation of 4 parameters

	X_{up}	Z_{up}	Z_{XXup}	r_{le}
μ	0.42896	0.06301	-0.42818	0.008187
σ	0.01	0.001	0.01	0.001

Table 2. Probability of failure for 4 parameters, $C_{l,Ref} = 0.98C_{l,\mu}$

Level	Pearson	MCS (97.5% confidence interval)
3	0.1032	0.107
5	0.0957	(0.0878,0.1262)
7	0.0971	

Test results are shown in Table 2. $C_{l,Ref}$ is assumed as 98% of C_l at the mean value. In the moment method, the probability of failure converged near the lower bound of confidence interval of MCS as the DOE level increases.

4.2 3D Wing

The reliability analysis was applied to the aerodynamic analysis of a 3D wing. Since the computing time is large in this case, the DACE is used to replace the flow analysis. The $k-\omega$ turbulence model is used to consider the effect of viscosity[Park2004]. Probabilities of failure of following limit state functions are calculated.

$$P_{f,C_L} = P(C_L - C_{L,Ref} \leq 0) \tag{14}$$

Table 3. Mean and standard deviation of flow conditions

	M	AOA
μ	0.8395	3.06
σ	0.01	0.01

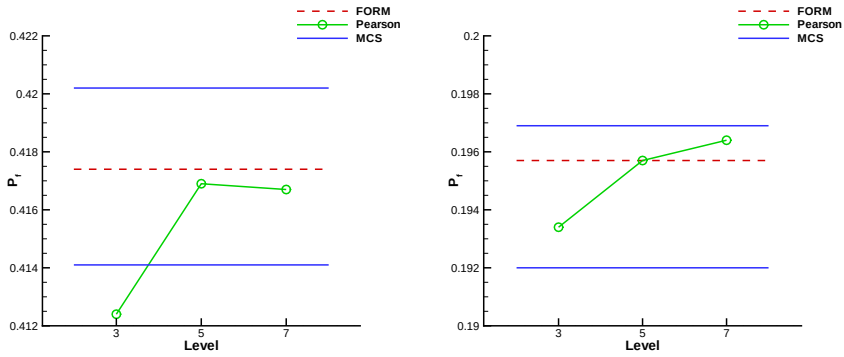

Fig. 1. Probability of failure for the lift and the drag

$$P_{f,C_D} = P(-C_D + C_{D,Ref} \leq 0) \tag{15}$$

Parameters considered here are Mach number and the angle of attack. Mean values and standard deviations are as follows:

Test results are shown in Fig. 1. Both FORM and the moment method predict the probability of failure within the confidence intervals of MCS. The drag shows a higher probability of failure, and it may be originated from the generation of a shock which will be sensitive to the flow conditions.

5 Conclusion

The reliability of aerodynamic analysis was computed using the Pearson system. The probability of failure of the aerodynamic performance was computed and the prediction was compared with MCS and FORM. Comparing with FORM, the Pearson system predicted the probability of failure relatively accurately. It is expected that the Pearson system can be used for the reliability based design optimization.

References

[Ahn2005] Ahn, J., Kim, S., Kwon, J.H.: Reliability-based wing design optimization using trust region-sequential quadratic programming framework. Journal of Aircraft 42, 1331–1336 (2005)

[Devore2000] Devore, J.L.: Probability and statistics for engineering and the sciences, Duxbury (2000)

[Lee2006] Lee, S.H., Kwak, B.M.: Response surface augmented moment method for efficient reliability analysis. Structural Safety 28, 261–272 (2006)

[Lophaven2002] Lophaven, S.N., Nielsen, H.B., Sϕndergaard, J.: A Matlab kriging toolbox version 2.0 (2002)

[Park2004] Park, S.H., Kwon, J.H.: Implementation of $k-\omega$ Turbulence models in an implicit multigrid method. AIAA Journal 42, 1348–1357 (2004)

[Rahman2004] Rahman, S., Xu, H.: A univariate dimension-reduction method for multi-dimensional integration in stochastic mechanics. Probabilistic Engineering Mechanics 19, 393–408 (2004)

[Seo2002] Seo, H.S., Kwak, B.M.: Efficient statistical tolerance analysis for general distributions using three-point information. International Journal of Production Research 40, 931–944 (2002)

[Sobieczky98] Sobieczky, H.: Parametric airfoils and wings. Notes on Numerical Fluid Mechanics 68, 71–88 (1998)

Part 34
Optimization 2

“*This page left intentionally blank.*”

Uncertainty Based MDO of UAS Using HAPMOEA

D.S. Lee[1], K. Srinivas[1], L.F. Gonzalez[2], and J. Periaux[3]

[1] School of AMME, University of Sydney, NSW 2006, Australia
c.lee@usyd.edu.au, k.srinivas@usyd.edu.au
[2] Queensland University of Technology
l.gonzalez@qut.edu.au
[3] CIMNE/UPC, Barcelona, Spain and INRIA Sophia OPALE Project Associate
jperiaux@gmail.com

CFD has been successfully used in the optimisation of aerodynamic surfaces using a given set of parameters such as Mach numbers and angle of attack. While carrying out a multidisciplinary design optimisation one deals with situations where the parameters have some uncertainty attached. Any optimisation carried out for fixed values of input parameters gives a design which may be totally unacceptable under off-design conditions. The challenge is to develop a robust design procedure which takes into account the fluctuations in the input parameters. In this work, we attempt this using a modified Taguchi approach. This is incorporated into an evolutionary algorithm with many features developed in house. The method is tested for an UCAV design which simultaneously handles aerodynamics, electromagnetics and maneuverability. Results demonstrate that the method has considerable potential.

1 Introduction

This paper develops a methodology for uncertainty based Multidisciplinary Design Optimisation (U-MDO) and is an extension to Lee et al. [1], and Srinivas et al. [2]. It couples a CFD software, a Radar Cross Section (RCS) analysis tool, an advanced evolutionary optimiser and the concept of robust/uncertainty strategy [3] to produce a set of optimal -stable designs. The approach is demonstrated on its application to Unmanned (Combat) Aerial Vehicle (UAV/UCAV) to maximise its performance and survivability. UCAVs have high industrial demands in the area of military and natural disaster monitoring (forest fire, flood, earthquake, etc.). For this optimisation, four main objectives are considered; the first is to maximise an aerodynamic performance at cruise condition, the second is to produce a low observability at mono and bi-static radar signature aircraft against enemy radar system. The third is to have extreme manoeuvrability. Finally the fourth is to have a robust design that has good characteristics in terms of performance and sensitivity at variable flight conditions and frequencies.

2 Methodology

The method couples the Hierarchical Asynchronous Parallel Multi-Objective Evolutionary Algorithms (HAPMOEA software) with several analysis tools. The HAPMOEA [7] is based on the well known Darwinian principle and implemented with Evolution Strategies [4]. The core of this method incorporates the concepts of Covariance Matrix Adaptation, CMA [5], Distance Dependent Mutation, DDM [4]. At the top level of this method, the asynchronous parallel computation [6], multi-fidelity hierarchical topology and Pareto tournament selection are implemented. In the bottom level, the method does two major search operations (Mutation and combination) under Pareto-game strategy. In the middle level, the method couples evolutionary optimiser (HAPMOEA), analysis tools and statistical design tool taking into account uncertainty.

3 Real World Design Problem

Analysis and Formulation

The vehicle considered is a Joint Unmanned Combat Air Vehicle (J-UCAV) that is similar in shape to Northrop Grumman X-47B [9]. The wing planform is assumed to be of an arrow shape with jagged trailing edge. The aircraft maximum gross weight is approximately 21,045 kg and empty weight is 16,955 kg. The wing design parameters for the baseline wing configuration are illustrated in Fig. 1. In this test case, the fuselage extends from 0 to 25% of the half span. The crank positions are at 46.4% and 75.5% of half span. The inboard and outboard sweep angles are 55^o and 29^o, while the taper ratios are 20 and 2% of c_{Root}. It is assumed that the baseline design contains three types of aerofoils at root (NACA 66-021), crank1 (NACA 67-1015), crank2 (NACA 67-008) and tip (NACA 67-008). The mission profile of UCAV considers Reconnaissance, Intelligence, Surveillance and Target Acquisition (RISTA) is as illustrated in Fig. 2 and is divided into eight sectors.

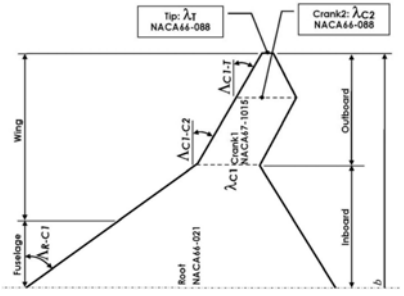

Fig. 1. Wing Geometry

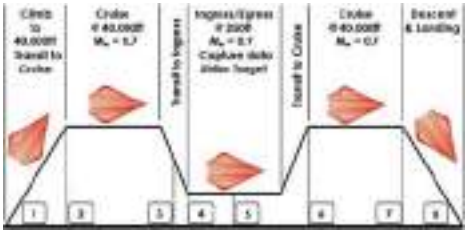

Fig. 2. Mission profile

Problem Definition

Objective 1 refers to aerodynamic quality (eq. 1) at the variability of flight conditions and is expressed in terms of mean and variance of inverse L/D ratios. The mean and variance of the turning radius (r) at 45^o bank angle formulate the quality of manoeuvrability (eq. 2). Electro-magnetic (RCS) quality (eq. 3) at the variability of radar frequencies is in terms of mean and variance of mono ($Sector2$) and bi-static ($Sector4$) radar signatures. The fitness functions for objectives are;

$$f_1 = min\left(\frac{-1}{Aerodynamic_{Quality}}\right) \tag{1}$$

where $Aerodynamic_{Quality} = \left(\ln\left(\overline{1/(L/D)}\right) + \ln\left(\delta\left(1/(L/D)\right)\right)\right)$,

$$\overline{1/(L/D)} = \frac{1}{K}\left(\sum_{i=1}^{K}\left(\frac{1}{(L/D)_i}\right)\frac{M_{\infty i}^2}{M_s^2}\right)$$

$$\delta 1/(L/D) = \frac{1}{K-1}\sum_{i=1}^{K}\left(\frac{1}{(L/D)_i}\frac{M_{\infty i}^2}{M_s^2} - \overline{\frac{1}{(L/D)}}\right)^2$$

$$f_2 = min\left(Maneuverability_{Quality}\right) = min\left(\overline{r} + \delta r\right) \tag{2}$$

where r is the instantaneous turning radius at bank anlge 45^o and defined as; $r = {V_\infty}/{\omega}$, $\omega = {\left(g\sqrt{n^2-1}\right)}/{V_\infty}$, $n = {qC_L}/{(W/S)}$.

$$f_3 = min\left(RCS_{Quality}\right) \tag{3}$$

where $RCS_{Quality}$ can be defined as;

$$RCS_{Quality} = \left(\overline{RCS_{Mono}} + \delta RCS_{Mono}\right) + \left(\overline{RCS_{Bi}} + \delta RCS_{Bi}\right)$$

Mono-static Radar conditions: $\theta = [0^o : 3^o : 360^o]$ *and* $\phi = [0^o : 0^o : 0^o]$.
Bi-static Radar conditions: incident angles are $\theta = 135^o$, $\phi = 90^o$

$$\theta = [0^o : 3^o : 360^o],\ \phi = [0^o : 0^o : 0^o]$$

The variable flight and radar frequency conditions are;

$$M_{\infty i} \in [0.8195,\ 0.8295,\ M_s = 0.8395,\ 0.8495,\ 0.8595] \quad and\ \alpha = 4.3^o$$

$$F_{\infty i} \in [1.0,\ 1.25,\ F_s = 1.5,\ 1.75,\ 2.0]$$

Table 1. UCAV wing design variables

Variables	S_1	S_2	S_3	λ_{C1}	λ_{C2}	Λ_{R-C1}	Λ_{C1-C2}	Λ_{C2-T}
Lower	50.46	10.09	5.05	0.15	0.15	49.5^o	25^o	25^o
Upper	63.92	16.82	10.09	0.45	0.45	60.5^o	35^o	35^o

Design Variables

Four aerofoils at root, crank 1, crank 2 and tip sections are considered for optimisation and the Control Points (CPs) for aerofoil design are sixty eight (4 sections × 17 CPs). The wing planform shape is parameterised by considering eight design variables including three wing sectional areas, three sweep angles and two taper ratios are considered and the upper and lower bounds of these variables are described in table 1 where the sectional areas (S) are in m^2 and one geometrical constraints is applied $\lambda_{C2} \leq \lambda_{C1}$. These lead to the different span length (b) and Aspect Ratio (AR).

Results

The algorithm was run approximately for 945 function evaluations and took 150 hours on two 2.4 GHz processors. The resulting Pareto set is shown in Fig. 3 where the best solution (Pareto member 1) for fitness functions 1 is marked as inverse triangle and triangle is the best solution (Pareto member 3) for fitness function 2. Square represents the best solution (Pareto member 10)

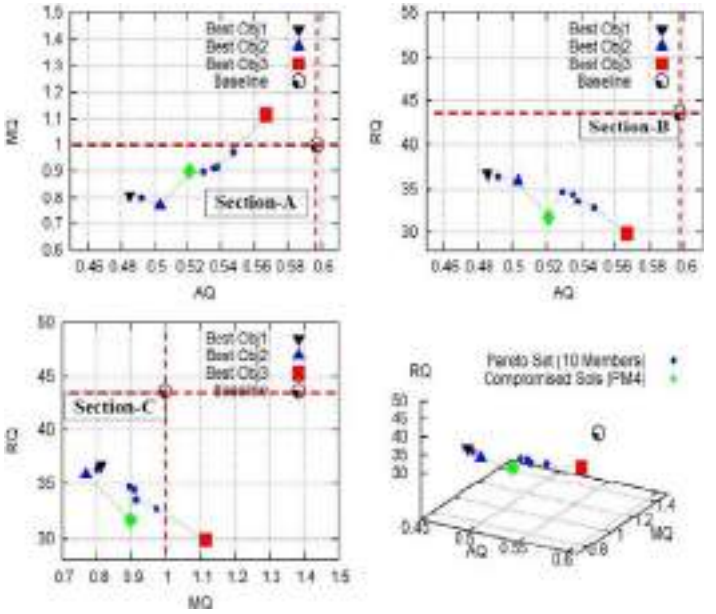

Fig. 3. Pareto non-dominated solutions for U-MDO of UCAV

Table 2. Comparison of the objectives

Description	Baseline	ParetoM1	ParetoM3	*ParetoM*4	ParetoM10
AQ	0.597	0.485 (-19%)	0.503 (-16%)	0.521(−13%)	0.566 (-5%)
MQ	0.998	0.822 (-18%)	0.768 (-23%)	0.899(−10%)	1.114 (+12%)
RQ	43.63	36.77 (-8%)	35.86 (-18%)	31.68(−27%)	29.83 (-32%)

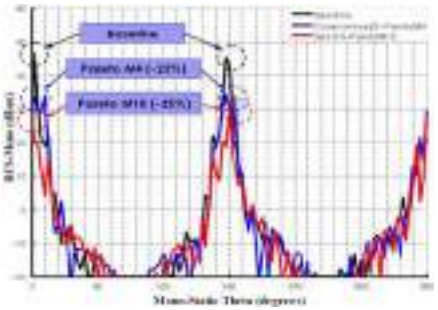

Fig. 4. Mono-static radar signature

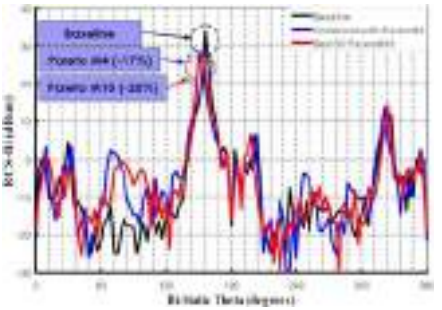

Fig. 5. Bi-static radar signature

for fitness function 3. It can be seen that the baseline UCAV dominates Pareto member 10 in the aspect of maneuverability quality as shown in Section-A and Section-C. However, all Pareto members dominate the baseline UCAV in aspect of the quality of cruise aerodynamics and electro-magnetics in terms of performance (mean) and sensitivity/stability (variance).

The best solutions (Pareto members 1, 3 and 10) and Pareto member 4 are selected to compare the aerodynamic, maneuverability and RCS quality to the baseline UCAV in table 2. All Pareto members exhibit improved quality in aerodynamic parameters. With regards to maneuverability quality, Pareto member 10 is dominated by the baseline design while Pareto member 10 has 32% less chance to be detected to enemy radar system when compared to the baseline UCAV. Pareto member 4 is selected as a compromised solution for further evaluation since it makes an improvement at all aspects of aerodynamic, maneuverability and electro-magnetic qualities.

Figure 4 shows the comparison of mono-static RCS at the standard design frequency ($1.5GHz$) between Pareto member 4 (compromised solution), Pareto member 10 (best solution for fitness function 3) and the baseline design. Pareto member 4 and 10 produce 25 and 35% lower mono-static radar signature when compared to the baseline design. The bi-static radar signatures obtained by Pareto members 4, 10 and the baseline design is shown Fig. 5. The results show that the Pareto members 4 and 10 has lower observability by 17 and 20% when compared to the baseline design. Therefore, they

will have less chance to be detected to enemy radar systems at *Sector* 2 and *Sector* 4.

4 Conclusions

HAPMOEA coupled to CFD and robust design technique has capabilities to generate a set of useful Pareto non-dominated solution that has unique character in the aspects of aerodynamic performance, manoeuvrability and electro-magnetics. The numerical results show a broad applicability of methodology for MDO design problems and benefit of using CFD, and the importance of integrating robust/uncertainty concepts. Future work will focuses on game strategies including Nash and Pareto to speed up optimisation convergence of MO and MDO with uncertainty design problems.

References

1. Lee, D.S., Gonzalez, L.F., Srinivas, K., Auld, D.J., Periaux, J.: MultiObjective and Multidisciplinary Design and Optimisation of Blended Wing-Body UCAV using Hierarchical Asynchronous Evolutionary Algorithms. In: 45th AIAA Aerospace Sciences Meeting and Exhibit, Grand Sierra Resort Hotel (Formerly Reno Hilton) Reno, Nevada January 8-11 (2007)
2. Srinivas, K., Lee, D.S., Gonzalez, L.F., Periaux, J.: Multidisciplinary Design Optimisation Of Joint UCAV Using HAPMOEA with Uncertainty. In: WEHSFFC and ECCOMA, Moscow, Russia, November 19-22 (2007)
3. Clarich, A., Pediroda, V., Padovan, L., Poloni, C., Periaux, J.: Application Of Game Strategy In Mulit-Objective Robust Design Optimisation Implementing Self-Adaptive Search Space Decomposition By Statistical Analysis. In: European Congress on Computational Methods in Applied Sciences and Engineering, July 24-28 (2004)
4. Michalewicz, Z.: Genetic Algorithms + Data Structures = Evolution Programs. Artificial Intelligence. Springer, Heidelberg (1992)
5. Hansen, N., Muller, S.D., Koumoutsakos, P.: Reducing the Time Complexity of the Derandomized Evolution Strategy with Covariance Matrix Adaptation (CMA-ES). Evolutionary Computation 11(1), 1–18 (2003)
6. Van Veldhuizen, D.A., Zydallis, J.B., Lamont, G.B.: Considerations in Engineering Parallel Multiobjective Evolutionary Algorithms. IEEE Transactions on Evolutionary Computation 7(2), 144–173 (2003)
7. Lee, D.S., Gonzalez, L.F., Whitney, E.J.: Multi-objective, Multidisciplinary Multi-fidelity Design tool: HAPMOEA - User Guide (2007)
8. Lee, D.S.: Uncertainty Based Multiobjective and Multidisciplinary Design Optimization in Aerospace Engineering, The Univ. of Sydney, Sydney, NSW, Australia, section 9.3, pp. 269–307 (2008)
9. Northrop Grumman, `http://www.is.northropgrumman.com/systems/nucasx47b.html`

The Optimum Design of a Propeller Energy-Saving Device by Computational Fluid Dynamics

Ching-Yeh Hsin, Bo-Hong Lin, and Chung-Ching Lin

Department Of Systems Engineering and Naval Architecture,
National Taiwan Ocean University, Keelung, Taiwan
hsin@mail.ntou.edu.tw

Abstract. The design of a propeller energy-saving device, PBCF, by computational fluid dynamics is presented in this paper. The key design points of PBCF are first pointed out, and the effectiveness of different geometry settings are investigated from computational results. It is found that the pitch angle and the installed angle of fins are the most important design points of PBCF. A design procedure is developed by using both the boundary element method and RANS method. From the computational results, both the force predictions and the detail flow visualizations show that a correctly designed PBCF is an effective energy-saving device.

Keywords: propeller design, energy-saving, propeller boss cap fins, PBCF.

1 Introduction

In this paper, the analysis and design of a propeller energy-saving device, "Propeller Boss Cap Fins" (PBCF), is presented. PBCF is an energy-saving device which the normal propeller hub replaced by a hub with fins attached (Fig. 1). The number of fins is usually the same as the number of propeller blades. PBCF was developed twenty years ago ([Ouc88] and [Ouc89]), and used widely recently due to the high oil price. A 2% ship speed increase and 4~5% fuel saving are reported by using the PBCF, and the installation fee can be recouped in six months for a large containership. The purpose of this paper is to study the functions of PBCF, and try to develop a design procedure by computations.

2 Geometric Parameters

For the conventional propellers, the lifting-line method is first applied to the design of the propeller loading distribution, and the lifting-surface method is then adopted for the propeller blade geometry designs. For the energy-saving devices, besides its geometry is not conventional, it is usually very sensitive to the geometry changes. Therefore, critical geometric parameters will be selected, and the parametric analysis will be done. In the PBCF computations, we have first identified the geometric parameters to analyze the geometric effects ([LCC06] and [LBH07]), and these parameters are shown as follows (Fig. 2):

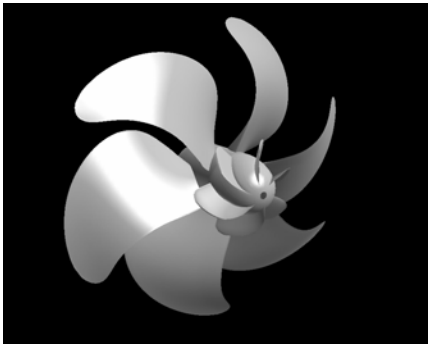

Fig. 1. The computer depiction of a propeller with the PBCF

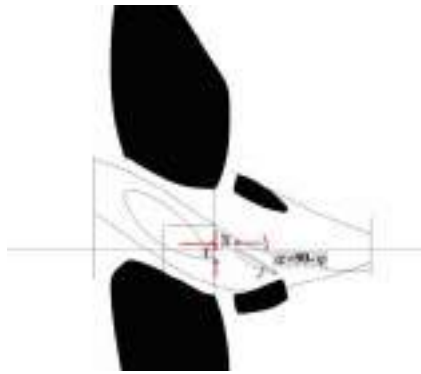

Fig. 2. The geometric parameters of the PBCF

- The fin geometry
- The axial position of the PBCF
- The circumferential position of the PBCF
- The pitch angle of the PBCF
- The installation angle of the PBCF

The detailed descriptions of these geometric parameters can be seen in [HCY08]. Once the geometric parameters are identified, computational tools will be used to make the parametric studies.

3 Parametric Analysis

The potential flow boundary element method is first used to analyze the geometric effects. We first find that the radius of the fin should be set as 20% to 25% of the propeller radius. For the axial position, we find that the propeller blade and the PBCF blade should be kept as close as possible, and 5% of the propeller radius is selected. The circumferential position of the PBCF blade does not affect the efficiency much from the computational results. The pitch angle of the PBCF does affect the efficiency a lot, and 90-degress pitch angle provides the best performance from the potential flow computational results. This is obviously not physically true, and it is because that the potential flow boundary element method cannot accurately predict the performance. The reasons are that first the wake geometry of the propeller is given by a simple wake alignment procedure, and it does not include the PBCF effect. Secondly, the potential flow cannot predict viscous phenomena such as the boundary layer and the separations, and therefore the forces on the PBCF increases monotonically as the angle of attack increases. On the other hand, from the computational results of the RANS method, there is an optimum “pitch angle” for the PBCF. Therefore, the viscous flow method is necessary in the design of the PBCF. We then used the PBCF presented by

Dr. Ouchi to investigate the pitch and the installation angles of the PBCF. We first find that the fins of PBCF should be planar, and then find that the PBCF is not necessary to be arranged perpendicular to the hub surface, and we call this angle "installation angle". The critical geometric parameters of PBCF thus should be the "pitch angle" and the "installation angle".

4 Computational Results

The commercial software FLUENT is used for the viscous flow computations, and GRIDGEN is used to generate the grid system. In order to accurately compare the efficiencies of propellers with and without the PBCF, also the effects of different PBCF geometries, we developed a grid system which the grids around the propeller blade and the PBCF are independent to each other. Because the grids around the propeller and the PBCF are independent to each other, a different PBCF can be replaced without changing the propeller grids, and the "PBCF zone" will be filled with grids for propellers without the PBCF.

The PBCF in Ouch's paper was first tested. Table 1 shows the numerical results, and in order to further understand the effects of PBCF, the flow field downstream is studied. Fig, 3 shows the axial velocities downstream with and without the PBCF, and one can see that the axial velocities near hub have been reduced by the PBCF. Fig 4 shows the tangential velocities downstream with and without the PBCF. It is clear that the tangential velocities have been reduced by PBCF, and this means that the energy loss due to the rotation has been recovered. Fig. 5 shows the vorticity strength downstream with and without the PBCF, and the vorticity strength is apparently reduced by PBCF.

The viscous flow computations are then used to assist the PBCF design for a containership propeller, and this propeller is referred as propeller "CV1700" in this paper. CV1700 is a well designed containership propeller, and its K-J chart is shown in Fig. 6. In Fig. 6, "BEM" represents the computational results from the potential flow boundary element method, and "FLUENT" represents the computational results from the viscous flow computations. One can see that the computational results from both methods are within reasonable accuracy. In the design procedure, we have used both the boundary element method and the viscous flow RANS method. Although the potential flow boundary element method cannot accurately represent the flow field, it can still provide a quick and qualitative comparison between different PBCF geometries. We use the boundary

Table 1. The computational forces and efficiencies of propeller "Ouchi" with and without the PBCF

	K_T PROP	K_Q *10 PROP	η PROP	K_T PBCF	K_Q *10 PBCF	η TOTAL
w/o PBCF	0.1515	0.2881	0.5859	0	0	0.5859
with PBCF	0.1559	0.2877	0.6037	-0.0035	-0.0026	0.5955
effic. gain						1.64%

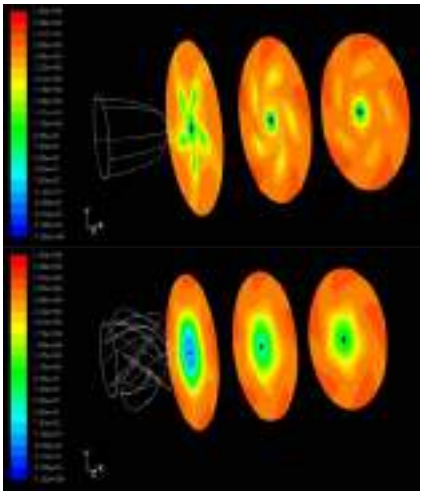

Fig. 3. The contours of axial velocity downstream for a propeller without (above) and with (below) PBCF

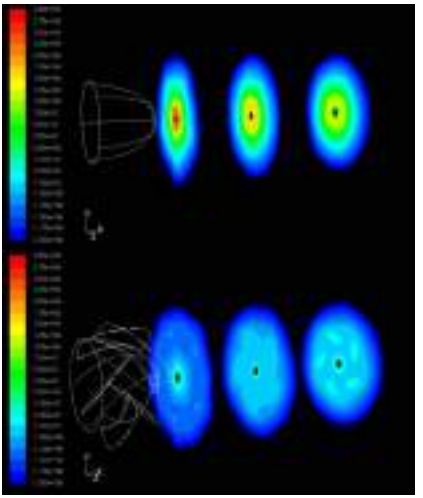

Fig. 4. The contours of tangential velocity downstream for a propeller without (above) and with (below) PBCF

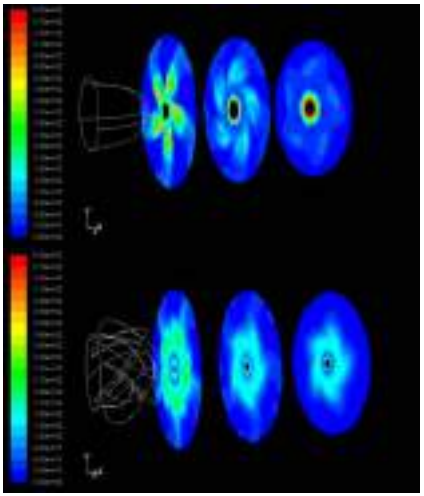

Fig. 5. The contours of vorticity strength downstream for a propeller without (above) and with (below) PBCF

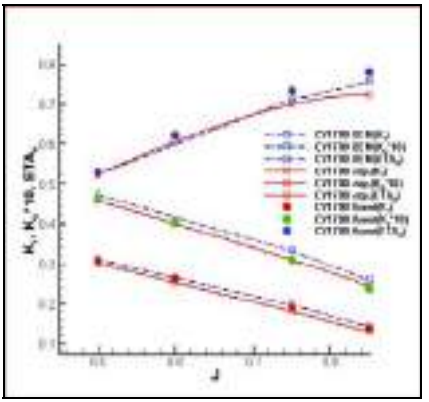

Fig. 6. The K-J chart of the propeller CV1700 from the experimental data and the computational results

element method to make the parametric studies of different combinations of geometric parameters, and several combinations are selected as "better designs". The viscous flow method is then used to make the final design among these. The reason to use this design procedure is to gain both the design efficiency and the design accuracy [TJC05]. Table 2 shows the computational results of the propeller without the PBCF, and with the designed PBCF. After adding the PBCF, a

Table 2. The computational forces and efficiencies of propeller "CV1700" with and without the PBCF

	K_T PROP	K_Q *10 PROP	η PROP	K_T PBCF	K_Q *10 PBCF	η TOTAL
w/o PBCF	0.1929	0.3123	0.7373	0	0	0.7373
with PBCF	0.1961	0.3147	0.7438	0.0003	-0.0011	0.7476
effic. gain						1.40%

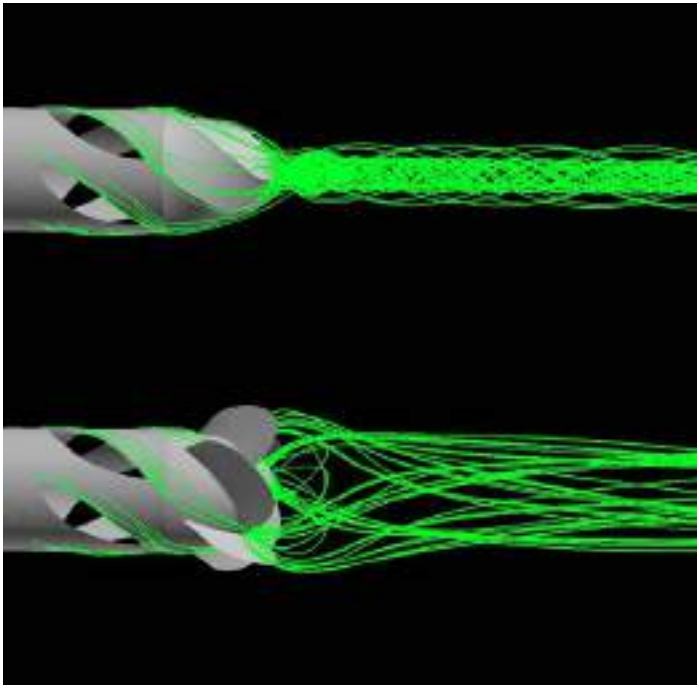

Fig. 7. The hub vortex of the propeller CV1700 without PBCF (above) and with a designed PBCF (below)

1.4% efficiency gain is obtained for this propeller. Fig. 7 shows the hub vortex of the propeller without and with the designed PBCF, and one can see that the PBCF does reduce the hub vortex. Notice that a conventional MAU section is used for the propeller Ouchi, and the efficiency is about 60%. For the CV1700 propeller, a NACA66 thickness and the a=0.8 mean-line are used, and the efficiency is above 70%. Even they are very different, computational results of both propellers show that the PBCF can increase the total efficiency.

5 Conclusions

In this paper, the energy-saving device, PBCF, is studied. The effectiveness of different geometry settings of PBCF are investigated from computational results,

and it is found that the pitch angle and the installation angle of fins are the most important design parameters of PBCF. Two different propellers with the PBCF are computed and presented in this paper. One is the propeller reported in papers by Ouchi. etc., and the other one is a containership propeller. For the containership propeller, the PBCF is also designed. In the design procedure, both the boundary element method and the RANS method are used. For two propellers, both the force predictions and the detail flow visualizations from computations show that a correctly designed PBCF is an effective energy-saving device.

Acknowledgements

The authors would like to express their gratitude to Dr. Ouchi Kazuyuki for providing the PBCF related information.

References

[HCY08] Hsin, C.-Y., Lin, B.-H., Chang, C.-H., Lin, C.-C.: The Analysis and Design of PBCF by Computations. In: Proc. of the 4th Asia-Pacific Workshop on Marine Hydrodynamics (APHydro 2008) (2008)

[LBH07] Lin, B.-H.: Investigations of the computational predictions to the effectiveness of propeller energy saving devices, M.S. Thesis, Dept. of Systems Engineering and Naval Architecture, National Taiwan Ocean University, Keelung (in Chinese) (2007)

[LCC06] Lin, C.-C.: Effects of the Geometry Variations to the Propeller Performance, M.S. Thesis, Dept. of Systems Engineering and Naval Architecture, National Taiwan Ocean University, Keelung (in Chinese) (2006)

[Ouc88] Ouchi, K., Ogura, M., Kono, Y., Orito, H., Shiotsu, T., Tamashima, M., Koizuka, H.: A Research and Development of PBCF (Propeller Boss Cap Fins) — Improvement of Flow from Propeller Boss. Journal of Society of Naval Architects of Japan 163 (1988)

[Ouc89] Ouchi, K., Tamashima, M., Kawasaki, T., Koizuka, H.: A Research and Development of PBCF (Propeller Boss Cap Fins) — 2nd Report: Study on Propeller Slipstream and Actual Ship Performance. Journal of Society of Naval Architects of Japan 165 (1989)

[TJC05] Tu, J.-C.: Designs by Analysis Results of The Potential and Viscous Flow Computations, M.S. Thesis, Dept. of Systems Engineering and Naval Architecture, National Taiwan Ocean University, Keelung (in Chinese) (2005)

Part 35
Rotor Aerodynamics

“*This page left intentionally blank.*”

An Analysis on the Helicopter Rotor Aerodynamics in Hover and Forward Flight Using CFD/Time-Marching-Free-Wake Coupling Method

Seong Yong Wie[1], Dong Kyun Im[2], Eugene Kim[3], Jang Hyuk Kwon[4], and Duck Joo Lee[5]

[1] Department of Aerospace Engineering, KAIST, Daejon, Korea
wsy278@kaist.ac.kr
[2] Department of Aerospace Engineering, KAIST, Daejon, Korea
poong04@kaist.ac.kr
[3] Department of Aerospace Engineering, KAIST, Daejon, Korea
eng11@kaist.ac.kr
[4] Department of Aerospace Engineering, KAIST, Daejon, Korea
jhkwon@kaist.ac.kr
[5] Department of Aerospace Engineering, KAIST, Daejon, Korea
djlee@kaist.ac.kr

In this study, a helicopter rotor is simulated by tightly coupled CFD/Free-wake method to describe wake characteristics. Rotor blade and flow field aerodynamics are calculated by CFD, and wake motions are simulated by Time-Marching-Free-Wake(TMFW) method. This tightly coupled CFD/Free-wake method can describe wake characteristics as well as rotor aerodynamic properties. Using this coupling analysis, hovering is analyzed for accurate aerodynamics. In forward flight, rotor blade has pitching and flapping motions. To simulate moving blades, moving overset grid technique is applied to the coupling method. For validation, all of numerical results are compared with experimental results.

1 Introduction

Helicopter rotor wake is more complex than fixed wing's wake because wake generated by rotating blades has a spiral motion. Particularly tip vortices generated from blade tip have very strong circulation strength. These rotor wakes and tip vortices make characteristics of inflow which decides rotor performance. For that reason, description of rotor wake is most important thing to simulate rotor aerodynamic characteristics. Conventional rotor CFD has a difficulty to simulate rotor wake due to numerical dissipation. This dissipation causes diminishing flow vorticity. The numerically diminished flow can't sufficient induced velocity and inflow deciding rotor aerodynamic performance.

To overcome this problem, vortex capturing method, grid adaptation and vortex model have been studied.

In this paper, Time-Marching-Free-Wake(TMFW) method is used to describe wake effects. TMFW can compute rotor wake without numerical dissipation because free-wake is lagrangian approach method. And it is faster than conventional CFD because TMFW not use grid system.[1] But TMFW is difficult to simulate transonic and viscous effects such as shock and dynamics stall. These problems can be overcome by coupling with Rotor CFD. In this paper, Rotor CFD is tightly coupled TMFW at each computational time step. The TMFW coupled with CFD can describe inboard vortices as well as tip vortices. Therefore, detailed geometry of the wake can be predicted. The wake characteristics obtained TMFW can provide induced velocity required rotor CFD calculaton.

The CFD/TMFW coupling method is applied to predict hover, forward flight. In forward flight, blades move with pitching and flapping motion. To consider blade motion, moving overset technique is used. And parallel computation technique is used to accelerate computational speed.

2 Methodology

2.1 Numerical Method

3dimensional unsteady Euler equation is govering equation. Finite Volume method (FVM) is used to discritize governing equation. In this FVM, cell centered method is used. Roe's FDS(Flux Difference Splitting) and van Leer's MUSCL(Monotone Upstream Scheme for Conservation) is used for inviscid flow calculation, and van Alada's limiter is used for stability. For time marching, DADI(Diagonalized Alternating Direction Implicit) is used. To improve time accuracy, dual time stepping is applied. And multigrid method and local time stepping are used to accelerate convergence. To consider blade motion, moving overset grid technique is applied.

Time-Marching-Free-Wake

Wake is described by vortex filaments. Generally, induced velocity of vortex filaments is obtained from Biot-Savart law. Generally, vortex filaments are described to the straight filaments. But vortex filaments have curved shape because rotor tip vortices and wake have a spiral motion. In addition, curved vortex filament can generate self-induced velocity which is required for description of wake movement. In this study, parabolic blending function is applied to the curved line interpolation. This parabolic blending interpolation can describe the circular line and give clear curved line without non-intuitive tangential vector to the line. Induced velocity of curved vortex line can be obtained from Moore-Rosenhead equation,

$$\mathbf{V}_{ind} = \int_C \frac{\mathbf{r}}{(|\mathbf{r}|^2 + \mu_s^2)} \times \Gamma \frac{\partial y(\xi, t)}{\partial \xi} d\xi \tag{1}$$

y is position on the curved line coordinate. And μ_s is Rosenhead's cut-off variable for singularity removal. In the present work, cut-off variable is set to be 0.1 of the chord length. This interpolation technique is only applied to the trailing vortex filaments which is perpendicular to the trailing edge.

Tightly Coupling Method

CFD/TMFW can consider wake description as well as compressible and viscous effects. Specially, inflow variation induced by wake is described with azimuth. This coupling method uses lifting line and boundary correction approach. Trailed vortex information of TMFW comes from lifting line which represents aero-load of CFD. This trailed vortex strength is deference between sectional aerodynamic forces. Wake represented by vortex filament bundles can decide induced velocity of arbitrary space position. For that reason, diminished inflow in CFD calculation is corrected by adding induced velocity of TMFW. Induced velocity is imposed at the boundary of CFD domain at

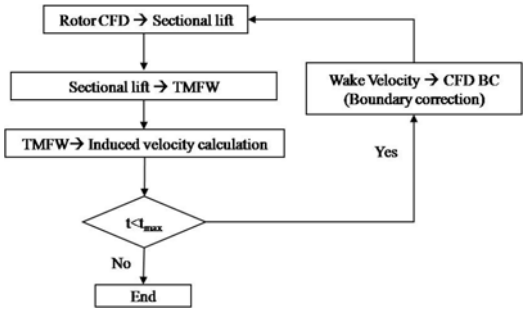

Fig. 1. Procedure of CFD/TMFW Coupling Method

Fig. 2. Wake description in CFD domain

Table 1. Thrust coefficient

Present	Experiment
0.00467	0.00459

each time. Fig.1 indicates schematics of coupling process. Fig.2 shows wake of TMFW in CFD domain.

3 Numerical Results

Using coupling method, hover and forward flight simulation are performed. In hover flight calculation, Caradonna and Tung's rotor model[2] is used. And AH-1G rotor model[3] is used in forward flight. These numerical results are compared with experimental data.

Hover Flight

Rotor blade pitch angle is 8degree. And tip Mach number is 0.439. Total computation revolution is 10. Grid system shown Fig.3 It is composed of

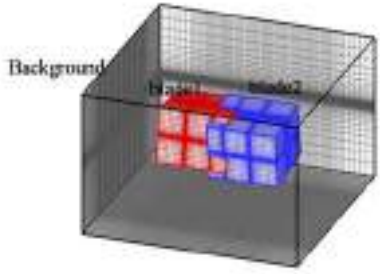

Fig. 3. Grid system

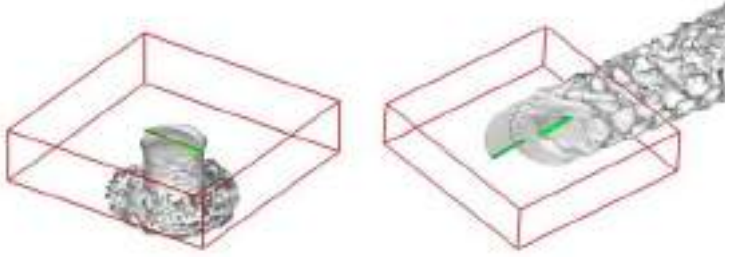

Fig. 4. Wake geometry in hover and forward flight

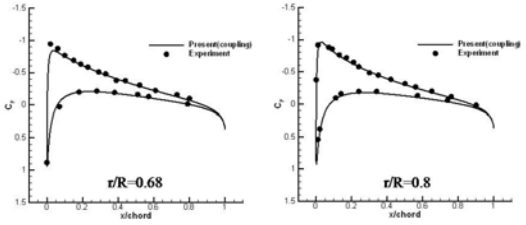

Fig. 5. Pressure coefficient in hover flight

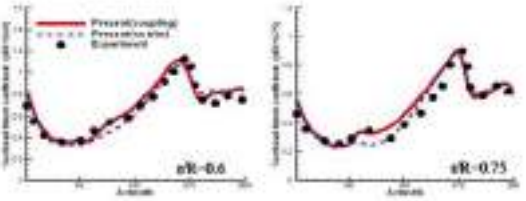

Fig. 6. Sectional lift coefficient

5 blocks. 5 block grids organize 3 bodies. 2 bodies describe 1 blade. 1 body represent background. The number of One Blade grid nodes is $2\times19\times67\times105$. And Background grid node number is $71\times89\times89$. Fig.4 shows rotor wake geometry in the CFD domain. In fig.5, pressure coefficients are compared with experimental data. And table.1 is total thrust coefficient of present and experimental data.

Forward Flight

Tip Mach number of AH-1G is 0.65. Advance ratio is 0.19. And thrust coefficient is 0.00464. This rotor blade has a pitching and flapping motion with azimuth(ψ). Pitch angle is $\theta = \theta_0 + \theta_{1c}\cos(\psi) + \theta_{1s}\sin(\psi)$. Flapping angle is $\beta = \beta_0 + \beta_{1c}\cos(\psi) + \beta_{1s}\sin(\psi)$. Blade motion is determined by rotor trimming. Table 2 is control angle of blade.

Table 2. Pitch and flapping angle

degree	θ_0	θ_{1c}	θ_{1s}	β_0	β_{1c}	β_{1s}
Present	6.2	1.38	-5.19	0	2.13	-0.15
Exp.	6	1.7	-5.5	0	2.13	-0.15

4 Conclusion

In this study, CFD/TMFW coupling method was deveploed to simulate unsteady rotor aerodynamics efficiently. Using this method, hover and forward rotor was simulated. And this numerical results was vailidated through the comparision with experimental data. It is suitable for predicting unsteady rotor aerodynimics and noise, because CFD/TMFW coupling method is more efficient and accurate than conventional rotor CFD.

Acknowledgement

This study has been supported by the KARI under KHP Dual-Use Component Development Program funded by the MOCIE.

References

1. Wie, S.Y., Im, D.K., Kwon, J.H., Lee, D.J.: A Study on the Far-Field Boundary Condition Effects of CFD/Time-Marching-Free-Wake Coupled Method. In: AHS Specialist'conference, Korea (2007)
2. Caradonna, F.X., Tung, C.: Experimental and Analytical Studies of a Model Helicopter Rotor in Hover. NASA TM-81232 (1982)
3. Cross, J.L., Watts, M.E.: Tip Aerodynamics and Acoustics Test: A Report and Data Survey. NASA-RP-1179, NASA Ames Research Center (December 1988)

Part 36
Turbulence Modeling and Simulation 1

“*This page left intentionally blank.*”

Stochastic-Determinism Approach for Simulating the Transition Points in Internal Flows with Various Inlet Disturbances

Ken Naitoh[1], Yuki Nakagawa[2], and Hiromu Shimiya[1]

[1] Waseda University, Tokyo, Japan
k-naito@waseda.jp
[2] Tokyo Gas, Inc. (Waseda University until March 2008)

1 Introduction

Large eddy simulation (LES) and direct numerical simulation (DNS) have been done for the transition to turbulence in straight channels. [MOIN82], [KAWAMURA85] However, these previous computations employ the cyclic boundary conditions between the inlet and outlet of the analytical domain, which can not simulate the transition position in space.

In the present research, the transition to turbulence in a straight channel is computed without using the cyclic boundary condition on inlet and outlet. Laminar flow computed in the upstream domain of the channel drastically changes to the turbulent flow in the middle part of the channel for Re $>$ 10,000. The transition point moves according to increasing inlet-fluctuations of velocites.

2 Governing Equation and Numerical Method

Reseachers on computational fluid dynamics mostly has devoted efforts to reduction of numerical errors, based on mathematics. However, the numerical errors should be used adequately on the basis of physical evaluation, because we can not simulate the unstable flows such as Karman vortex streets without numerical disturbances. Theoretical models such as the RNG theory [YAKHOT86] also include stochastic disturbances in the deterministic Navier-Stokes equation. Thus, the key point to go further is that we should find the appropriate relation between the numerical errors in the analytical domain and the physical fluctuations. Here, we propose the methodology of stochastic determinism, based on the deterministic Navier-Stokes equation and stochastic artificial disturbances.

Basically, the multi-level formulation including the Navier-Stokes equation [NAITOH92] is employed, which can calculate spatial derivatives of physical quantities and integrated quantities accurately. (Eqs. 1 and 2).

$$F_k = 0, \text{ (for } k = 1 - 4) \tag{1}$$

$$
\begin{aligned}
F_1 &\equiv \tfrac{Dv_i}{Dt} + \tfrac{\partial}{\partial x_i} p - \tfrac{1}{Re} \tfrac{\partial^2}{\partial x_j^2} v_i, \\
F_2 &\equiv \tfrac{\partial v_i}{\partial x_i}, \\
F_3 &\equiv \tfrac{\partial^2}{\partial x_i^2} p + \tfrac{\partial}{\partial t} (\tfrac{\partial}{\partial x_i} v_i) + \tfrac{\partial}{\partial x_i} (u_j \tfrac{\partial}{\partial x_j} v_i), \\
F_4 &\equiv \textstyle\int_{V_m} \tfrac{\partial v_i}{\partial x_i} dV
\end{aligned}
\tag{2}
$$

where V_m, p, t, x_i, Re, and u_i $(i = 1, 2, 3)$ denote control volume, pressure, time, Cartesian coordinate, Reynolds number, and velocity component for i-direction, respectively. The volume V_m can be taken at several sizes from a cell to the overall volume of the channel. Turbulence model is not used in the present report. Boundary and initial conditions are in Eq. (3),

$$
\begin{aligned}
&u_1 = U_o + \delta, v_2 = 0, \tfrac{\partial p}{\partial x_1} = 0, \text{(Inlet boundary condition)}, \\
&\tfrac{\partial v_1}{\partial x_1} = 0, \tfrac{\partial v_2}{\partial x 1} = 0, \tfrac{\partial p}{\partial x_1} = 0, \text{(Outlet boundary condition)}, \\
&u_1(t = 0) = U_o, u_2(t = 0) = 0, \text{(Initial condition)}
\end{aligned}
\tag{3}
$$

where Uo and δ denote the constant inlet-velocity and velocity fluctuation at inlet given by random number genertor, respectively. The non-slip boundary condition is put on the solid walls.

Finite-difference scheme with a third-order of accuracy [KAWAMURA85] is used for the convection term in F_1 and also the other terms are with second order of accuracy, while the Euler scheme is employed for temporal development. The numerical algorithm for Eqs. (1) and (2) is based on the MAC method [HARLOW65], while the accurate evaluations for spatial gradients and space-integrals of physical quantities are included. [NAITOH92]

Discretization of Eqs. (1) and (2) due to the finite-difference operator Γ consequently leads to Eq. (4) having numerical errors of ϵ_k. We use the numerical errors as physical fluctuations adequately.

$$
\Gamma[F_k] = \epsilon_k, \text{ (for } k = 1 - 4) \tag{4}
$$

where average-quantity of ϵ_2 $(= \sum_{n=1,N} |\frac{\partial v_j}{\partial x_j}| \delta x / N)$ is proportional to δ corresponding to actual inlet-fluctuation of velocity, where N and δx denote the total number of grids and grid size. ($\epsilon_2 = C_e\ \delta$, where C_e is an arbitrary constant. C_e=1.0 is in this report.) In the present research, homogeneous and orthogonal grid system is used to compute accurately vortices. The magnitude of ϵ_2 can be controlled by the number of iterations in the successive over relaxation (SOR) method. [NAITOH92] The value ϵ_4 is controlled as is close to zero in this research, while the volume V_m is that between the inlet surface and each surface which is orthogonal to the channel axis of x_1. Velocity u_1 is corrected at each grid point $P(i_1, i_2, i_3)$ by using

$$
\begin{aligned}
&u_1(t + \delta t, i_1, i_2, i_3) = u_1^*(t + \delta t, i_1, i_2, i_3) \\
&+ C_x \textstyle\sum_{i_2=1,I_2,i_3=1,I_3} ((Uo - u_1^*(t + \delta t, i_1, i_2, i_3)) \delta x_2 \delta x_3) / S(i_1)
\end{aligned}
\tag{5}
$$

where $u_1(t + \delta t, i_1, i_2, i_3), u_1^*(t + \delta t, i_1, i_2, i_3), C_x (< 1.0)$, and $S(i_1)$ denote the velocity corrected, the velocity obtained by F_1, an arbitrary constant, and

the surface at i_1, respectively. Values ϵ_1 and ϵ_3 are determined by the finite difference method employed.

3 Computational Results

Figure 1 shows the velocity distributions computed for Re =20,000, where the ratio of the inlet-fluctuation and the inlet-velocity, δ/Uo, is with 0.03 percent. The number of grids is 2,503 x 53 x 53, while grid size δx_i is 0.02 for each direction and time increment δt is 0.002. We can see the transition from laminar flow to turbulence in Fig. 1. Figure 2 shows the iso-contours of velocity at some cross-sections. Figure 3 shows the time-averaged velocity computed and the corresponding experimental data taken by Nikuradse [NIKURADSE32]. Computations fairly agree with the experiment. Figure 4 shows the time-dependent velocities computed, which are turbulent after t = 30 at x_1/D = 40. The fluctuations within a constant level after t =50 in Fig. 4 also imply that the present computations essentially simulate physical turbulence. The fluctuation level agrees fairly well with the well-known result of Kawamura. [KAWAMURA85] Figure 5 shows the vorticity distributions while varying the inlet fluctuations. Then, the transition point from laminar to turbulent flow moves, according to increasing velocity-fluctuations at the inlet. Figure 6 shows the energy spectrum for the computational result shown in Fig. 4. The present code also simulates the Karman vortex street and a low Reynolds number flow. (Figs. 7 and 8)

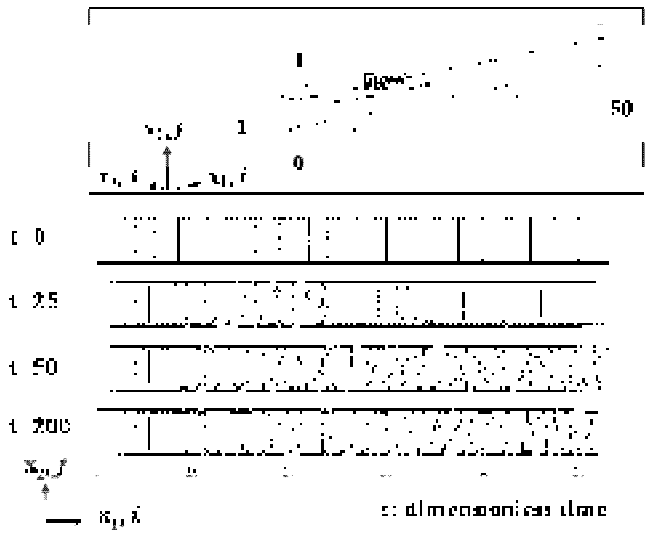

Fig. 1. Velocity distributions of u_1 in the cross-section of x_3 /D=0.5 and x_1 /D=0-50 until t = 200. (Inlet fluctuation is 0.03 percent of U_0. Re=20,000. Grid points = 2503 x 53 x 53.) (D denotes the channel width.)

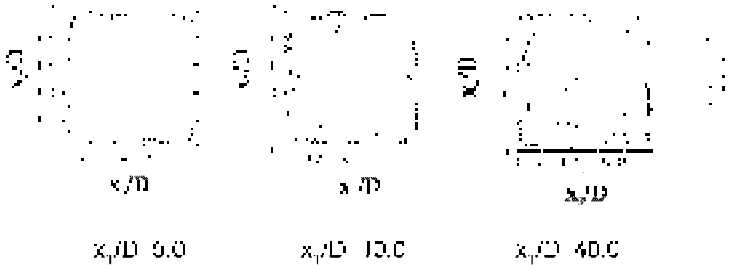

Fig. 2. Iso-contours of velocity in the cross-sections of $x_1/D = 5$, 10, and 40 at t = 200. (Inlet fluctuation is 0.03 percent. Re=20,000. Grid points = 2503 x 53 x 53.)

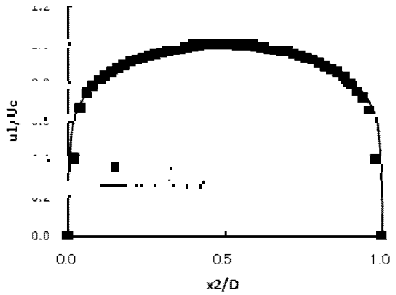

Fig. 3. Time-averaged velocity at the cross-section of $x_3/D = 0.5$ at $x_1/D = 40$. in case of inlet-fluctuation =0.03 percent.Experiment by [NIKURADSE32]

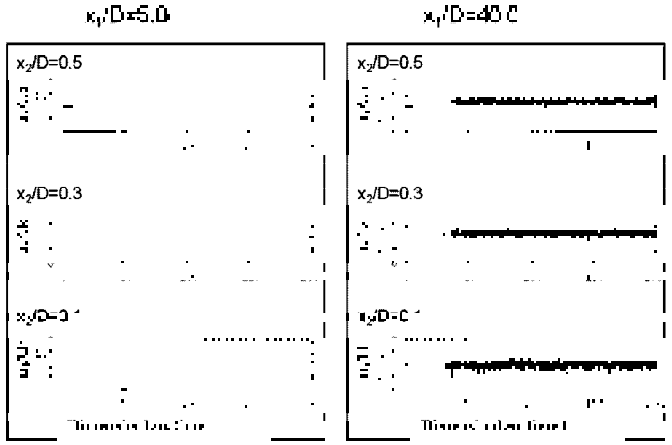

Fig. 4. Time-evolutions of velocities at three points of $x_2/D = 0.1$, 0.3, and 0.5. (Left) at the dimensionless distances x_1/D =5, (Right) at the dimensionless distances x_1/D =40. (Re=20,000. Grid points = 2503 x 53 x 53.)

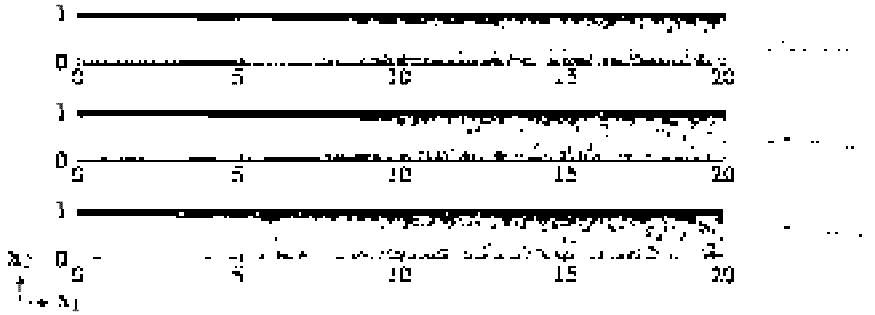

Fig. 5. Vorticity distributions computed in the cross-section of $x_3/D = 0.5$ for $x_1/D < 20.0$ at t = 200, while varying inlet fluctuations. (Re=20,000. Grid points = 2503 x 53 x 53.)

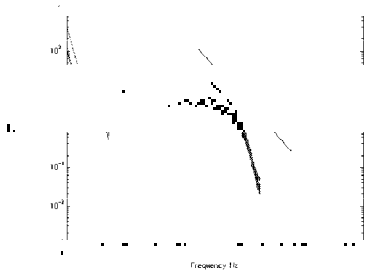

Fig. 6. Energy spectrum of turbulence computed for t=100 - 200. Upper line for x_2/D =0.1. Middle line for x_2/D =0.3. Lower line for x_2/D =0.5. (Re=20,000. Grid points = 2503 x 53 x 53.)

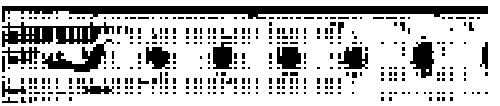

Fig. 7. Vorticity distributions of the Karman vortex streets around a square. (Re=2000. Grid Points = 103 x 3003. δx_1=δx_2=0.01.δt=0.001.)

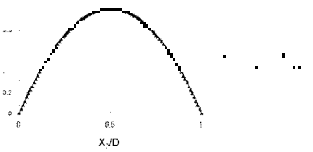

Fig. 8. Flow in a channel at low Reynolds number. (Re = 200. Grid points: 1,003 x 103. δx_1=δx_2=0.01. δt=0.001.)

4 Conclusion

The present approach makes it possible to predict the spatial transition points from laminar flow to turbulence in the internal flows, for the inlet fluctuations less than a few percents of the main velocity at inlet, Uo.

Acknowledgement. The authors express sincere thanks for their help on using the super computer of Osaka University, Cybermedia center. (http://www.hpc.cmc.osaka-u.ac.jp/j/)

References

[HARLOW65] Harlow, F.H., Welch, J.E.: MAC Numerical calculation of Time-dependent Viscous Incompressible Flow of Fluid with Free Surface. Physics of Fluid 8, 12 (1965)

[KAWAMURA85] Kawamura, K., Kuwahara, K.: Direct simulation of a turbulent inner flow by finite-difference method, AIAA paper 85-0376 (1985)

[MOIN82] Moin, P., Kim, J.: Numerical investigation of turbulent channel flow. J. Fluid Mech. 118, 341–377 (1982)

[NAITOH92] Naitoh, K., Kuwahara, K.: Large eddy simulation and direct simulation of compressible turbulence and combusting flows in engines based on the BI-SCALES method. Fluid Dynamics Research 10, 299–325 (1992)

[OOIDA03] Ooida, J., Kuwahara, K.: Implicit LES of Turbulence Generated by a Lattice. AIAAPaper2003-4097 (2003)

[YAKHOT86] Yakhot, V., Orszag, S.: Renormalized group analysis of turbulence. J. Sci. Computing 1 (1986)

[NIKURADSE32] Nikuradse, J.: Gesetzmassigkeiten der turbulenten Stromung in glatten Rohren. Forschungs-Arb. Ing.-Wesen, No. 356 (1932)

Investigation of an Anisotropic NS-α Model for Wall-Bounded Flows

K. Andrea Scott and Fue-Sang Lien

Department of Mechanical Engineering, University of Waterloo, Waterloo, ON, N2L 3G1, Canada
ka3scott@engmail.uwaterloo.ca, fslien@uwaterloo.ca

1 Introduction

The NS-α model is a turbulence model that has different origins than RANS and LES, and is not dissipative in nature. Instead of starting with the Navier-Stokes equations, the governing equations can be derived by applying Hamilton's principle to an averaged Lagrangian [H99]. The resulting momentum equations contain two velocity fields, u_i and $\tilde{u}_i$, where $\tilde{u}_i$ is smoother than u_i via an inversion of the Helmholtz operator. For the isotropic case the parameter that arises in the averaging procedure is a scalar, α, and can be interpreted as a filter width. It can be expected that there will be many situations where it may not be appropriate to maintain an isotropic value of α, e.g. near a solid wall. To extend the range of applicability of the model, we investigate the use of an anisotropic NS-α equation as a subgrid model for LES in this paper.

2 Model Formulation

The Eulerian-averaged equations from Holm [H99] are used as a starting point. In the development of these equations from Hamilton's principle the Lagrangian is averaged at a fixed field point. The Eulerian-averaged equations are,

$$\partial_i \tilde{u}_i = 0, \tag{1}$$

$$\partial_t u_i + \tilde{u}_j \partial_j u_i + u_k \partial_i \tilde{u}_k = -\partial_i P + \nu \partial_{kk} u_i - \frac{1}{2} \partial_i \langle \xi_k \xi_l \rangle \partial_k \tilde{u}_m \partial_l \tilde{u}_m, \tag{2}$$

where P is a pressure-like variable.

$$P = p - \frac{1}{2} \tilde{u}_i \tilde{u}_i - \frac{1}{2} \langle \xi_k \xi_l \rangle \partial_k \tilde{u}_m \partial_l \tilde{u}_m. \tag{3}$$

In the above equation set the angle brackets $\langle \cdot \rangle$ denote an average over short-time or small-scale fluctuations of the flow (see Holm [H99]) and the relationship between the smoothed and unsmoothed velocities is

$$u_i = \underbrace{\left(1 - \partial_k \left(\langle \xi_k \xi_l \rangle \partial_l\right)\right)}_{H,\ \text{Helmholtz operator}} \tilde{u}_i. \tag{4}$$

In Eq. (4), $\tilde{u}$ is a smoothed velocity and $\langle \xi_k \xi_l \rangle$ is the smoothing scale. For the isotropic model $\langle \xi_k \xi_l \rangle = \alpha^2 \delta_{kl}$. The momentum equation can also be written in momentum-conservation form as [CHMZ99],

$$\partial_t u_i + \tilde{u}_j \partial_j u_i = -\partial_i p + \partial_j \left(\langle \xi_k \xi_j \rangle \partial_i \tilde{u}_m \partial_k \tilde{u}_m\right) + \nu \partial_{kk} u_i. \tag{5}$$

To develop an equation with the smoothed velocity as the dependent variable, which is more familiar to the LES-community, we use the commutator between the substantial derivative and the smoothing operator. For example, we would like to have a substantial derivative written entirely in terms of the smoothed velocity. This is done by rewriting the advective terms in Eq. (5) in the following form

$$\partial_t u_i + \tilde{u}_j \partial_j u_i = [D/Dt, H]\tilde{u}_i + H\left(\partial_t \tilde{u}_i + \tilde{u}_j \partial_j \tilde{u}_i\right). \tag{6}$$

$[D/Dt, H]\tilde{u}_i = D/Dt(H(\tilde{u}_i)) - H(D/Dt(\tilde{u}_i))$ and the advecting velocity in the substantial derivative is the smoothed velocity. The momentum equation Eq. (5) can then be written

$$\begin{aligned} \partial_t \tilde{u}_i + \tilde{u}_j \partial_j \tilde{u}_i = H^{-1}\{&-\partial_i p + \partial_j \left(\langle \xi_k \xi_j \rangle \partial_i \tilde{u}_m \partial_k \tilde{u}_m\right) \\ &+\nu \partial_{kk} u_i - [D/Dt, H]\tilde{u}_i\}. \end{aligned} \tag{7}$$

We found the commutator can be expressed

$$\begin{aligned} [D/Dt, H]\tilde{u}_i = &\partial_j \left(\langle \xi_k \xi_l \rangle \partial_k \tilde{u}_i \partial_l \tilde{u}_j + \langle \xi_j \xi_l \rangle \partial_k \tilde{u}_i \partial_l \tilde{u}_k\right) \\ &-\partial_j \left[\frac{D\langle \xi_j \xi_l \rangle}{Dt} \partial_l \tilde{u}_i\right]. \end{aligned} \tag{8}$$

The last term on the RHS of Eq. (8) can *in theory* be neglected because each component of the particle displacement is transported by the mean flow like a scalar [H99]. To maintain a reasonable computational cost, we retain only the diagonal components of $\langle \xi_k \xi_l \rangle$, which will be referred to as α_k^2 hereafter. Note that no Einstein summation convention is applied to α_k^2 in the remainder of the paper. With the above simplifications the momentum equation can be written

$$\partial_t \tilde{u}_i + \partial_j \tilde{u}_i \tilde{u}_j = -\partial_i \tilde{p} + \nu \partial_{kk} \tilde{u}_i - H^{-1}(\partial_j m_{ij}). \tag{9}$$

with the subgrid force

$$\begin{aligned} \partial_j \left(m_{ij}\right) &= \partial_j \left(\alpha_k^2 \delta_{kl} \partial_k \tilde{u}_i \partial_l \tilde{u}_j + \alpha_l^2 \delta_{lj} \partial_k \tilde{u}_i \partial_l \tilde{u}_k - \alpha_k^2 \delta_{kj} \partial_i \tilde{u}_m \partial_k \tilde{u}_m\right) \\ &= \partial_j \left(A_{ij} + B_{ij} - C_{ij}\right). \end{aligned} \tag{10}$$

Here, A_{ij} is the anisotropic gradient model, $A_{ij} + B_{ij}$ is similar to a Leray model[1] and the NS-α model is comprised of all three terms. We found that when α_k^2 is constant the subgrid model can also be written as the sum of a gradient term and a vortex force

$$\partial_j m_{ij} = 2A_{ij} - \boldsymbol{u}^{ST} \times \tilde{\boldsymbol{\omega}} \tag{11}$$

where $u_i^{ST} = \alpha_k^2 \partial_{kk} \tilde{u}_i$. This form is useful for physical interpretation of the model results.

The implementation of the subgrid model involves an explicit filter, expressed as the inverse Helmholtz operator, H^{-1} in Eq. (9). This filter can either be applied by using Helmholtz inversion or by using an equivalent operator, usually taken to be a box filter [GH2006]. We found little difference between the two in their effect on the mean flow and second-order turbulence statistics. However, the box filter was much more computationally efficient. With the box filter the model overhead was 30%, similar to that reported in other studies [PHW2008], while solution of the Helmholtz equation using a conjugate gradient solver led to an overhead of 90%.

3 Description of the Test Cases

The application of the NS-α model to a practical problem is studied here using two test cases. The first is a lid-driven cubic cavity flow at a Reynolds number of 10,000, where the Reynolds number is based on the lid velocity and cavity length. The three-dimensional cavity flow is a challenging test case for a subgrid model due to the lack of homogeneous directions, the presence of both laminar and turbulent flow regions and the anisotropic nature of the flow. Results are presented for a 48^3 mesh with $CFL \sim 1$.

The second test case is a plane-channel flow at a Reynolds number of $Re_\tau = 180$ where Re_τ is based on the channel half-height and the friction velocity $u_\tau = \sqrt{\tau_w}$, where τ_w is the wall shear stress. The domain used for the channel flow is $(L_x, L_y, L_z) = (4\pi, 2, 3\pi/2)$ with $(N_x, N_y, N_z) = (32, 48, 32)$. The mesh is stretched in the wall-normal direction (y), and uniform in the streamwise (x) and spanwise (z) directions.

Since α_k^2 is a smoothing scale it is most intuitive to start with a simple definition based on the grid size. For the anisotropic case it is related to the grid spacing. For example, $\alpha_k^2 = C\left(h_k^2\right)$, where h_k is the grid spacing in the k-direction and C is a constant denoting what fraction of the grid spacing to use. Because α_k^2 can be related to the filter width, Δ_k, of a box filter via $\alpha_k^2 = \Delta_k^2/24$, we choose $C = 1/6$, which corresponds to a filter width which is twice the grid size.

[1] It is not identical to the Leray model because $\partial_i \tilde{u}_i = 0$ was applied in deriving the commutator, while for the Leray model inompressibility is enforced on the unsmoothed velocity [GH2006].

The simulations are carried out using the STREAM code [L92], which is a colocated finite-volume method. A second-order time stepping scheme is used and the advection schemes are QUICK for the cavity flow, and second order central-differencing for the channel flow.

4 Results

Preliminary results for the lid-driven cavity flow with α_k^2 based on the mesh found that the wall jet was consistently pushed too far out from the wall. This is shown as the dotted line in the mean flow profile in Figure 1. This problem was traced back to a discontinuity introduced when the normal component of α_k^2 is set to zero at a solid boundary, which is the boundary condition used in the derivation of the governing equations [H99]. For the cavity flow the mesh is stretched in the plane of the primary recirculation cell and is uniform across the span, thus there is a severe discontinuity at the endwalls.

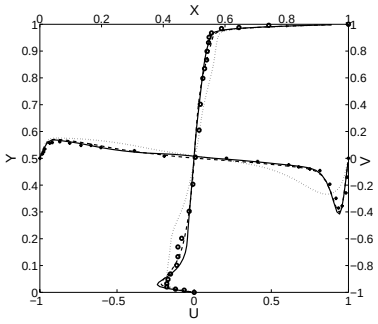

(a) mean

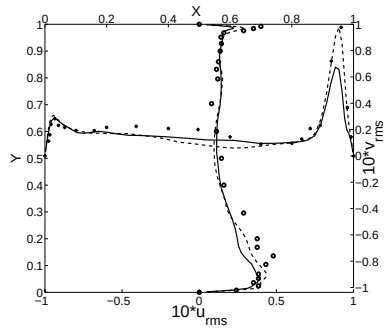

(b) rms

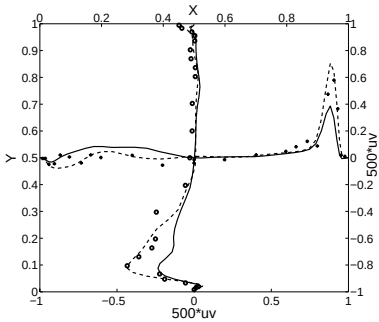

(c) shear stress

Fig. 1. Profiles on the midplane; ——— no model; – – – – model with α_k^2 based on Eq.(12); ····· α_k^2 based on the mesh (shown for mean flow only); symbols: experiment [PK89]

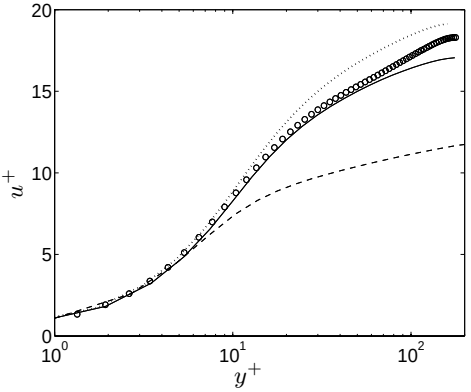

Fig. 2. Velocity profile for 32^3 mesh. Results are similar on finer mesh. Symbols are DNS data [KMM87]; ····· no model; – – – – model with α_k^2 based on the mesh; ——— α_k^2 based on Eq.(12).

This created numerical oscillations in the spanwise direction that led to a generation of numerical (not physical) $\boldsymbol{u}_{ST}$ (see Eq. 11). The oscillations themselves contribute to the generation of streamwise vorticity which is then tilted into the vertical direction, leading to a mixing out of the mean flow profile as seen in Figure 1.

As an alternative to having α_k^2 based strictly on the mesh spacing, we have proposed a definition of α_k^2 which incorporates the properties of the resolved flow as follows:

$$\alpha_k^2 = \frac{H_k(\mathbf{x}, \Delta, t)}{\tilde{g}_{ij}\tilde{g}_{ij}}, \quad \tilde{g}_{ij} = \frac{\partial \tilde{u}_i}{\partial x_j}, \tag{12}$$

where H_k is,

$$H_k = \max\left[(\delta_x \tilde{u}_k)^2, (\delta_y \tilde{u}_k)^2, (\delta_z \tilde{u}_k)^2\right]. \tag{13}$$

We can see in Figure 1 that this eliminates the erroneous mean flow profiles. The results with the model in terms of mean flow and rms profiles also show a significant improvement over those when no model is used, indicating the necessity of a subgrid model for this flow.

For the channel flow problems of a different nature were encountered with the mesh based definition of α_k^2. In this case the grid is refined in the wall normal direction so there is not a significant discontinuity at the wall. However, the vortex force leads to an additional tilting of streamwise vorticity in the near-wall region that manifested itself in high skin friction and a severe undershoot of the mean flow profile, as can be seen in Figure 2. With the flow-dependent definition of α_k^2 (modified to not include the contribution from $\delta_y \tilde{u}$) the results are substantially improved.

Promising results have been reported in the literature in using the NS-α model for isotropic turbulence [CHMZ99] and a transitional mixing layer

[GH2006]. This work represents a preliminary step towards extending the range of applicability of the NS-α model to include wall-bounded flows. We were not able to obtain a converged result for the isotropic model for these test cases, and therefore decided to develop an anisotropic one. The anisotropic model runs stably, but we found using a mesh-based definition of α_k^2 did not produce good results. A simple definition of α_k^2 based on the flow gradients led to significant improvements. Various future directions are possible. A more theoretically-based method to determine α_k^2 may prove to be more robust over a wide variety of flows. On the more practical side, applying the model to high Reynolds number boundary layers using simple wall models [Sa2002] would be useful.

Acknowledgements

This work has been supported by Natural Science and Engineering Research Council of Canada (NSERC) and was made possible by the facilities of the Shared Hierarchical Academic Research Computing Network (SHARCNET) and Western Canada Research Grid (WESTGRID).

References

[CHMZ99] Chen, S., Holm, D.D., Margolin, L.G., Zhang, R.: Direct numerical simulations of the Navier-Stokes alpha model. Physica D 133, 66–83 (1999)

[GH2006] Geurts, B.J., Holm, D.D.: Leray and LANS-alpha modelling of turbulent mixing. Journal of Turbulence 7, 1–33 (2006)

[H99] Holm, D.D.: Fluctuation effects on 3D Lagrangian mean and Eulerian mean fluid motion. Physica D 133, 215–269 (1999)

[KMM87] Kim, J., Moin, P., Moser, R.: Turbulence statistics in fully developed channel flow at low Reynolds number. Journal of Fluid Mechanics 177, 133–166 (1987)

[L92] Lien, F.S.: Computational modelling of 3D flow in complex ducts and passages. PhD thesis, University of Manchester (1992)

[PHW2008] Petersen, M.R., Hecht, M.W., Wingate, B.A.: Efficient form of the LANS-alpha turbulence model in a primitive equation ocean model. Journal of Computational Physics 227, 5717–5735 (2008)

[PK89] Prasad, A.K., Koseff, J.R.: Reynolds number and end-wall effects on a lid-driven cavity flow. Physics of Fluids A 1, 208–218 (1989)

[Sa2002] Sagaut, P.: Large Eddy Simulation for Incompressible Flows. Springer, Heidelberg (2002)

Computing Turbulent Flows Using Meshless Solver LSFD-U

N. Munikrishna[1] and N. Balakrishnan[2]

[1] NASA Glenn Research Center, Cleveland, USA
munikrishnanagaram@oai.org
[2] Indian Institute of Science, Bangalore, India
nbalak@aero.iisc.ernet.in

Summary. This work deals with computing turbulent flows using meshless solver. An objective way of generating suitable point distribution employing hybrid cartesian mesh strategy is evolved. Exploiting certain basic features of the point distribution, a meshless solver, LSFD-U for RANS calculations is developed. To the best of our knowledge, this work, for the first time has demonstrated the capability of meshless solvers in not only generating a good C_p distribution but also in producing an excellent match of the skin friction profile for turbulent flows.

1 Introduction

Meshless solvers requiring only cloud of grid points for solution update have great potential in computing flow past complex real life configurations. Generating suitable point distribution is an important component for the success of any strategy employing meshless solver. Cartesian mesh happens to be the most natural option for obtaining required point distribution for meshless solvers. In our view, there are no major issues in simulating inviscid and laminar viscous flows using meshless solvers along with cartesian distribution of points[Muni06]. The real difficulty pertains to the use of cartesian meshes for simulating turbulent flows because it is impractical to resolve a turbulent boundary layer using an all cartesian mesh strategy. The only reasonable way available is to use a hybrid strategy wherein the viscous region is filled with body-fitted mesh with high aspect ratio cells and the inviscid region is filled with unit aspect ratio cartesian mesh. Though the hybrid cartesian mesh based finite volume schemes have existed[Phil99,Michel99], handling the interface region between body-fitted and cartesian mesh blocks becomes quite complex, particularly for three dimensional calculations. In this context, the ability of meshless solvers to operate on arbitrary distribution of points becomes important. Exploiting this feature associated with the meshless solvers, we propose a way of generating suitable point distribution for

simulating turbulent flows employing hybrid cartesian mesh strategy. In addition to the point generation strategy, we have evolved efficient, cheap and robust discretization procedures exploiting the structure associated with the mesh data and developed meshless solver, LSFD-U for RANS calculations. The efficacy of the meshless solver LSFD-U along with point generation strategy is demonstrated by solving turbulent flow problems.

2 LSFD-U

The compressible Navier-Stokes equation in divergence form reads,

$$U_t + (f + F)_x + (g + G)_y \ = 0, \tag{1}$$

where, U is vector of Conserved variables, f & g are inviscid fluxes and F & G represent the viscous fluxes. The stencil of grid points used in solution update at a node i is shown in figure 1a. The solution procedure associated with LSFD-U(Upwind-Least Squares Finite Difference(LSFD-U)) as applied to a general point distribution involves method of least squares for discretizing spatial derivatives. Inviscid flux discretization[Sridar03] consists of the following steps: (1) determination of the upwind fluxes f_J and g_J, along the coordinate directions, at the fictitious interface J, using an upwind scheme and with the appropriate choice for the left and right states in conjunction with a suitable reconstruction procedure (2) computing the flux derivatives at node i employing method of least squares. In our previous works[Anup04,Muni06], we have evolved four different consistent viscous discretization procedures based on quadratic least squares procedure and they were analysed for positivity as applied to a discrete Laplacian[Coirier94]. The procedure which is found to be more positive and computationally efficient is applied for discretizing viscous flux derivatives. This procedure simply involves the use of gradients and Hessians obtained from a quadratic least squares procedure in discretizing the viscous flux derivatives associated with a generalised point distribution. Other discretization strategies evolved exploiting the local structure in the hybrid cartesian grid are presented in section 4. Solution is updated using the numerical flux derivatives in conjunction with a suitable time integration procedure.

Fig. 1. a. Point cloud b. Structured type point c. Closed Path

3 Point Generation

The point generation involves a hybrid cartesian distribution and consists of four steps: (1) generating body-fitted grid blocks around each component of the geometry using any of the conventional structured mesh generators(presently we use a hyperbolic mesh generator), allowing the different grid blocks to overlap (2) identifying the region of overlap and deleting certain portion of the overlap region (3) filling the remaining computational domain with recursively generated cartesian mesh around the last layer of the structured grid block (4) all the cartesian points falling interior to the structured grid block and certain cartesian points falling in close vicinity of the last layer of structured grid block are identified using geometric search algorithms and deleted. The above described steps can be appreciated from the figure 2.

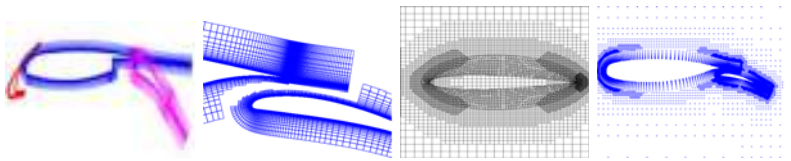

Fig. 2. Different stages in generating hybrid cartesian point distribution

While the discretization procedures developed based on method of least squares explained in section 2 are capable of operating on any cloud of points, there are serious difficulties in their use for the points present in the structured grid block involving highly anisotropy in the point distribution[Muni07]. For the purpose of evolving alternative discretization procedures, the points present in the distribution are sorted as structured, cartesian, hanging, general and boundary type at the pre-processing stage depending on the structure associated with the support points.

4 LSFD-U Flow Solver

Exploiting the structure associated with the grid data, we have evolved robust and efficient discretization procedures for different point types. It is very important to emphasize that use of the strategies exploiting basic features of the grid data, does not in any way compromise on the generality of the flow solver.

Points identifiable with South(S), East(E), North(N) and West(W) neighbourhood fall under this category; points present in the interior to the structured grid block naturally belongs to this type. Because these points are

derived from a body-fitted grid, they exhibit an alignment with streamwise coordinate. Exploiting this feature, we solve the governing equations in a locally rotated coordinate system,(ξ, η) identified with support points, $\frac{\partial \tilde{U}}{\partial t} + \frac{\partial(\tilde{f}+\tilde{F})}{\partial \xi} + \frac{\partial(\tilde{g}+\tilde{G})}{\partial \eta} = 0$, where, $\tilde{U} = [\rho\ \rho\tilde{u}\ \rho\tilde{v}\ e]^T$ is the vector of conserved variable. Referring to figure 1b, the ray iE represents the ξ direction and η represents the normal direction to it. The concept of introducing fictitious interface within the LSFD-U procedure for determining inviscid flux derivatives(explained in section 2) becomes convenient to evolve a simple and robust inviscid discretization procedure suitable for structured type points. As shown in figure 1b, the fictitious interfaces represented with s, e, n, w are located at the projection of the mid-point of the ray joining the node with its neighbour along the coordinate direction. Inviscid fluxes are computed at the fictitious interface using any upwind flux formula and flux derivatives are determined employing simple 1D least squares formula:

$$\tilde{f}_{\xi_i} = \frac{\sum_J \Delta\tilde{f}_J \Delta\xi_J}{\sum_J \Delta\xi_J^2}; \quad J \in [e, w], \qquad \tilde{g}_{\eta_i} = \frac{\sum_J \Delta\tilde{g}_J \Delta\eta_J}{\sum_J \Delta\eta_J^2}; \quad J \in [n, s]. \tag{2}$$

Discretization of the viscous flux derivatives require first and second derivatives of the solution values. The two major hurdles associated with any viscous discretization procedure developed based on method of least squares are the non-positivity of the discretization scheme and ill-conditioning of the geometric matrix associated with the least squares procedure. Therefore, we have employed a Green-Gauss theorem based gradient finding procedure[Jawahar00,Muni07] for determining first and second derivatives of the solution values. It should be remarked that this viscous discretization procedure is found to be positive as applied to a discrete Laplacian and it renders the code required robustness for simulating turbulent flows.

For the cartesian points(cartesian type or Hanging type), wherever there is neighbourhood available in coordinate direction, simple 1D finite difference procedures are used for approximating the solution derivatives. The other derivatives are computed using a modified least squares procedure by treating the derivatives obtained using finite differencing as known quantities. The details of the discretization procedures may be had from reference[Muni07]. The general type points present in the cartesian grid block in the interface region do not show any structured data dependency. Generalised finite difference procedure explained in section 2 are used only for the general type points.

5 Numerical Results

To demonstrate the efficacy of the LSFD-U based RANS solver along with point generation strategy, we have solved standard viscous flow test cases. Roe scheme is used for computing inviscid interfacial fluxes. Baldwin-Lomax

Table 1. Details of Freestream Conditions and Point Distributions

Geometry	M_∞	Re_∞	α	Grid and number of points	number of wall points	Reference data
NACA 0012	0.502	2.91x10^6	1.77^o	G1, 25269	298	Phillippe[Phil99]
RAE 2822	0.676	5.7x10^6	1.92^o	G2, 25404	300	Cook[Cook]
NLR 7301	0.185	2.51x10^6	6^o	G3, 34205	300 + 200	Berg[Berg]
Biplane	0.8	500	10^o	G4, 19974	198 + 198	Jawahar[Jawahar00]

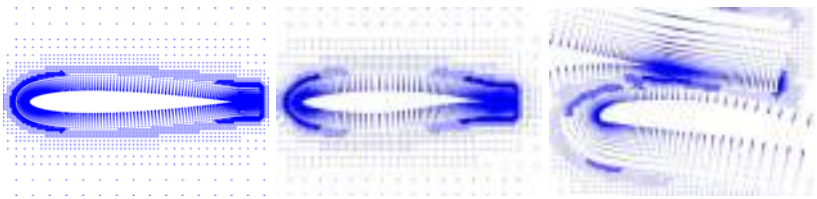

Fig. 3. Hybrid cartesian Point Distributions G1,G2,G3

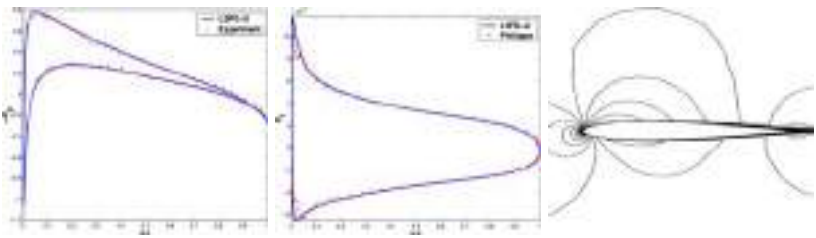

a. $-C_p$ distribution b. C_f distribution c. Mach contours

Fig. 4. Turbulent flow past NACA 0012: $M_\infty = 0.502, Re_\infty = 2.91\text{x}10^6, \alpha = 1.77^o$

turbulence model is employed for computing eddy viscosity. The SGS implicit relaxation procedure[Muni07] is used for accelerating the convergence to steady state. No slip and adiabatic boundary conditions are imposed on the wall boundary and the normal pressure gradient is set to zero. Riemann invariant boundary condition is employed at the farfield points. Details of the free stream conditions and point distributions employed are shown in table 1.

The hybrid cartesian point distributions used for turbulent computations are shown in figure 3. The numerical results obtained for turbulent flow past NACA 0012 and RAE 2822 airfoil are shown in figures 4 and 5 respectively. The capability of the LSFD-U solver for simulating flows involving complex geometries is demonstrated by solving turbulent flow past NLR 7301 airfoil with slotted flap(refer to figure 6) and laminar flow over a NACA 0012 biplane configuration(refer to figure 7). In all the cases, an excellent agreement is

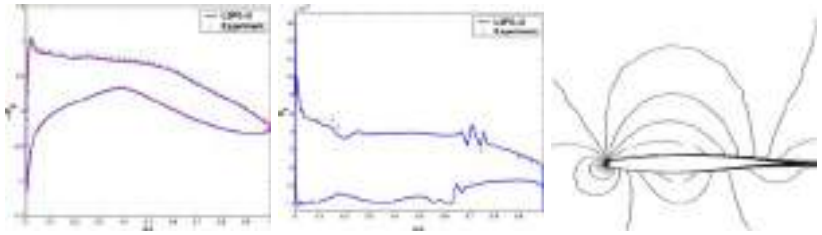

a. $-C_p$ distribution b. C_f distribution c. Mach contours

Fig. 5. Turbulent flow past RAE 2822: $M_\infty = 0.676, Re_\infty = 5.7\text{x}10^6, \alpha = 1.92^o$

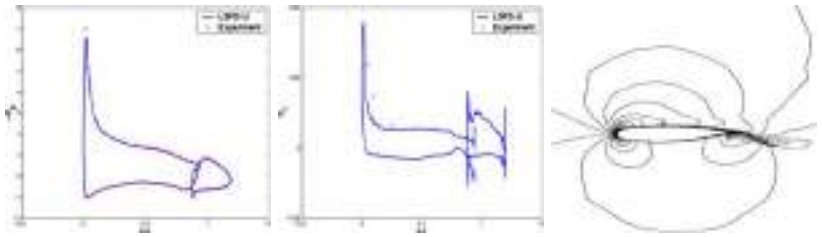

a. $-C_p$ distribution b. C_f distribution c. Mach contours

Fig. 6. Turbulent flow past NLR 7301: $M_\infty = 0.185, Re_\infty = 2.51\text{x}10^6, \alpha = 6^o$

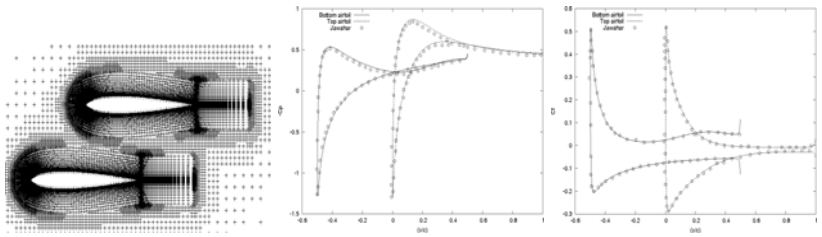

a. Point Distribution, G4 b. $-C_p$ distribution c. C_f distribution

Fig. 7. Laminar flow past NACA 0012 Biplane : $M_\infty = 0.8, Re_\infty = 500, \alpha = 10^o$

observed between the computed surface coefficients with standard numerical and/or experimental data.

6 Conclusions

In this work, we have proposed an objective strategy involving hybrid cartesian mesh to generate suitable point distribution for simulating turbulent flows using meshless solvers. Exploiting certain basic features of the grid data, simple, cheap and robust discretization procedures are evolved and LSFD-U meshless RANS solver is developed. The numerical results clearly establishes

the efficacy of the LSFD-U solver for simulating flows around complex aerodynamic bodies.

Acknowledgments

The authors thank Vikram Sarabhai Space Center (VSSC), Thiruvananthapuram, India for the support it provided under the RESPOND program through the schemes project ISRO 069 for executing the work presented in this paper.

References

[Muni06] Munikrishna, N., Karthikeyan, N., Balakrishnan, N.: CFD 2006. Springer, Berlin (2006)
[Phil99] Phillippe, G.: Ph.D. Thesis, University De Liege (1999)
[Michel99] Delanaye, M., et al.: AIAA Paper 99-0777 (1999)
[Sridar03] Sridar, D., Balakrishnan, N.: Journal of Computational Physics. 189, 1–23 (2003)
[Anup04] Ninawe, A., Munikrishna, N., Balakrishnan, N.: CFD 2004. Springer, Berlin (2004)
[Coirier94] Coirier, W.J.: Ph.D. Thesis, The University of Michigan (1994)
[Jawahar00] Jawahar, P., Kamath, H.: Journal of Computational Physics 164, 165–203 (2000)
[Muni07] Munikrishna, N.: Ph.D. Thesis, Dept. of Aerospace Engineering, IISc, Bangalore (2007)
[Cook79] Cook, P.H.: Report No: AR 138, AGARD (1979)
[Berg79] van den Berg, B.: Report No: NLR TR-79009 U, Dutch Aerospace Lab (NLR) (1979)

“*This page left intentionally blank.*”

Parallel Adaptive Mesh Refinement Scheme for LES of Turbulent Premixed Flames

C.P.T. Groth, W. Lin, F.E. Hernández-Pérez, S.A. Northrup, and Ö.L. Gülder

University of Toronto Institute for Aerospace Studies 4925 Dufferin Street, Toronto, Ontario, M3H 5T6, Canada
groth@utias.utoronto.ca

1 Introduction and Scope

A block-based adaptive mesh refinement (AMR) algorithm is proposed for performing large-eddy simulations (LES) of turbulent premixed combustion using body-fitted multi-block hexahedral computational mesh. The AMR framework is combined with a high-resolution finite-volume scheme with limited linear reconstruction and a parallel implicit time-marching scheme to solve the Favre-filtered Navier-Stokes equations for a thermally perfect compressible reactive mixture. A flexible block-based octree data structure is used to facilitate automatic solution-directed mesh adaptation according to physics-based refinement criteria. The data structure also enables an efficient and scalable parallel implementation via domain decomposition. The use of body-fitted mesh permits the use of anisotropic grids and resolution of thin boundary, mixing, and shear layers. The implicit formulation makes use of a dual-time-stepping-like approach, Jacobian-free inexact Newton method, and preconditioned generalized minimal residual (GMRES) algorithm to solve the system of nonlinear algebraic equations arising from the temporal discretization procedure. An additive Schwarz global preconditioner is used in conjunction with block incomplete LU type preconditioners for each sub-domain. Both the thickened-flame and flame-surface-density subfilter-scale models are considered for representing turbulence-chemistry interactions. Numerical results for a methane-air slot burner demonstrated the potential of the approach for performing LES of turbulent premixed flames.

2 LES Modelling

In LES, a separation of scales is achieved via a low-pass filtering procedure. Scales larger than the filter size, Δ, are resolved, whereas scales smaller than Δ are modelled. Relevant flow quantities, ϕ, are filtered or Favre-filtered yielding $\overline{\phi}$ or $\widetilde{\phi}$, respectively. The Favre-filtered form of the Navier-Stokes

equations for a compressible, reactive, thermally perfect, gaseous mixture are given by

$$\frac{\partial}{\partial t}\left(\bar{\rho}\right) + \frac{\partial}{\partial x_i}\left(\bar{\rho}\tilde{u}_i\right) = 0\,, \tag{1}$$

$$\frac{\partial}{\partial t}\left(\bar{\rho}\tilde{u}_i\right) + \frac{\partial}{\partial x_j}\left(\bar{\rho}\tilde{u}_i\tilde{u}_j + \delta_{ij}\bar{p} - \check{\tau}_{ij}\right) = A_1 + A_2\,, \tag{2}$$

$$\frac{\partial}{\partial t}\left(\bar{\rho}\tilde{E}\right) + \frac{\partial}{\partial x_i}\left[\left(\bar{\rho}\tilde{E} + \bar{p}\right)\tilde{u}_i + \check{q}_i\right] - \frac{\partial}{\partial x_j}\left(\check{\tau}_{ij}\tilde{u}_i\right) = B_1 + B_2 + B_3 + B_4 + B_5 + B_6\,, \tag{3}$$

$$\frac{\partial}{\partial t}\left(\bar{\rho}\tilde{Y}_k\right) + \frac{\partial}{\partial x_i}\left(\bar{\rho}\tilde{Y}_k\tilde{u}_i\right) + \frac{\partial \check{\mathcal{J}}_{k,i}}{\partial x_i} = \overline{\dot{\omega}}_k + C_1 + C_2\,, \tag{4}$$

where $\bar{\rho}$ is the filtered mixture density, $\tilde{u}_i$ is the Favre-filtered mixture velocity, $\bar{p}$ is the filtered mixture pressure, $\tilde{Y}_k$ is the Favre-filtered mass fraction of species k, $\tilde{E}$ is the Favre-filtered total mixture energy (including chemical energy) given by $\tilde{E} = \sum_{k=1}^{N}\tilde{Y}_k(\check{h}_k + \Delta h^0_{f,k}) - \bar{p}/\bar{\rho} + \widetilde{u_i u_i}/2$, $\check{h}_k$ and $\Delta h^0_{f,k}$ are the sensible enthalpy and heat of formation for species k, respectively, and $\overline{\dot{\omega}}_k$ is the filtered reaction rate. The filtered equation of state has the form $\bar{p} = \bar{\rho}R\tilde{T} + D_1$. The resolved viscous stress tensor, $\check{\tau}_{ij}$, the resolved total heat flux, $\check{q}_i$, and the resolved species diffusive fluxes, $\check{\mathcal{J}}_{k,i}$, are evaluated in terms of the filtered quantities as: $\check{\tau}_{ij} = 2\check{\mu}(\check{S}_{ij} - \delta_{ij}\check{S}_{ll}/3)$, $\check{q}_i = -\check{\kappa}\partial\tilde{T}/\partial x_i + \sum_{k=1}^{N}\check{h}_k\check{\mathcal{J}}_{k,i}$, $\check{\mathcal{J}}_{k,i} = -\bar{\rho}\check{D}_k\partial\tilde{Y}_k/\partial x_i$, where $\tilde{T}$ is the mixture temperature, $\check{\mu}$ is the mixture viscosity, $\check{\kappa}$ is the mixture thermal conductivity, and $\check{D}_k$ is the diffusivity of species k, and $\check{S}_{ij} = (\partial\tilde{u}_i/\partial x_j + \partial\tilde{u}_j/\partial x_i)/2$.

The terms A_1, A_2, B_1, B_2, B_3, B_4, B_5, B_6, C_1, C_2, and D_1, arise from the low-pass filtering process and require modelling. In most LES, the terms A_2, B_2, B_3, B_5, C_2, and D_1 are neglected [VV02]. The non-negligible terms are $A_1 = -\partial[\bar{\rho}(\widetilde{u_i u_j} - \tilde{u}_i\tilde{u}_j)]/\partial x_j$, $B_1 = -\partial[\bar{\rho}(\widetilde{hu_i} - \tilde{h}\tilde{u}_i)]/\partial x_i$, $B_4 = -\partial[\bar{\rho}(u_j\widetilde{u_j u_i} - \tilde{u}_j\tilde{u}_j\tilde{u}_i)/2]/\partial x_i$, $C_1 = -\partial[\bar{\rho}(\widetilde{Y_k u_i} - \tilde{Y}_k\tilde{u}_i)]/\partial x_i$ (B_6 is related to C_1), and must be modelled for closure of the filtered equation set. The subfilter stresses, $\sigma_{ij} = -\bar{\rho}(\widetilde{u_i u_j} - \tilde{u}_i\tilde{u}_j)$, are generally modelled using an eddy-viscosity model with $\sigma_{ij} = 2\bar{\rho}\nu_t(\check{S}_{ij} - \delta_{ij}\check{S}_{ll}/3) + \delta_{ij}\sigma_{ll}/3$. The eddy viscosity, ν_t, is prescribed herein by using a one-equation model. Standard gradient-based approximations are used in this work for the modelling of the subfilter-scale fluxes B_1, B_6, and C_1: $\bar{\rho}(\widetilde{hu_i} - \tilde{h}\tilde{u}_i) = -(\check{C}_p\bar{\rho}\nu_t/\mathrm{Pr}_t)\partial\tilde{T}/\partial x_i$ and $\bar{\rho}(\widetilde{u_i Y_k} - \tilde{u}_i\tilde{Y}_k) = -(\bar{\rho}\nu_t/\mathrm{Sc}_t)\partial\tilde{Y}_k/\partial x_i$, where Pr_t and Sc_t are subfilter-scale turbulent Prandtl and Schmidt numbers. The subfilter turbulent diffusion term, B_4, is modelled using $-\bar{\rho}(u_i\widetilde{u_i u_j} - \tilde{u}_i\tilde{u}_i\tilde{u}_j)/2 = \sigma_{ij}\tilde{u}_i$.

3 Thickened Flame Model

The challenge in LES for reactive flows is to accurately model the influence of the subfilter-scale turbulence on the filtered reaction rates, $\overline{\dot{\omega}}_k$. This is

particularly challenging for turbulent premixed combustion where the flame thickness, δ, is 0.1–1.0 mm, which is in many cases smaller than practical filter widths. One approach to modelling the turbulence/chemistry interaction for premixed flames is offered by the so-called thickened flame model. In the thickened flame model, the flame front structure is artificially thickened so it can be resolved on a LES mesh, but such that the laminar flame speed remains unaltered. An increase in flame thickness by a factor F with a constant flame speed, can be achieved by multiplying the molecular diffusivity D by F, and the reaction rate $\dot{\omega}$ by $1/F$. An efficiency factor, E_{F}, is also introduced to account for the resulting decrease in the Damkhöler number, Da, for the flame [CDVP00]. The modified species mass fraction equation takes the form

$$\frac{\partial}{\partial t}\left(\bar{\rho}\tilde{Y}_k\right) + \frac{\partial}{\partial x_i}\left(\bar{\rho}\tilde{Y}_k\tilde{u}_i\right) = \frac{E_{\mathrm{F}}\overline{\dot{\omega}}_k}{F} + \frac{\partial}{\partial x_i}\left[E_{\mathrm{F}}F\bar{\rho}\left(\check{D}_k + \frac{\nu_t}{\mathrm{Sc}_t}\right)\frac{\partial\tilde{Y}_k}{\partial x_i}\right], \quad (5)$$

where the filtered reaction rates, $\overline{\dot{\omega}}_k$, are now calculated directly using Arrhenius law reaction rates evaluated in terms of resolved quantities. To correct the flame Damkhöler number and incorporate the influences of the unresolved turbulent field on the chemical kinetics, the efficiency factor, E_{F}, is evaluated herein using the power-law flame wrinkling model of Charlette *et al.* [CMV02]

4 Flame Surface Density Model

A second approach to subfilter-scale modelling for turbulent premixed flames is to ignore for the internal flame structure represent the combustion occurring at the thin flame front in terms of a reaction progress variable that quantifies the conversion of reactants to products. One possible definition of a progress variable, c, is provided by a reduced fuel mass fraction, $c = (Y_F - Y_F^u)/(Y_F^b - Y_F^u)$, where Y_F, Y_F^u and Y_F^b are respectively the local, unburnt and burnt fuel mass fractions [VV02]. The progress variable takes on values in the range $0 \leq c \leq 1$ with $c = 0$ in the fresh gases and $c = 1$ in the fully burnt gases. Gaseous mixture composition at any location can then be specified directly in terms of $\tilde{c}$. A transport equation for the progress variable can be written as

$$\frac{\partial}{\partial t}\left(\bar{\rho}\tilde{c}\right) + \frac{\partial}{\partial x_i}\left(\bar{\rho}\tilde{c}\tilde{u}_i\right) = \frac{\partial}{\partial x_i}\left(\frac{\bar{\rho}\nu_t}{\mathrm{Sc}_t}\frac{\partial\tilde{c}}{\partial x_i}\right) + \rho_r s_{\mathrm{L}}\bar{\rho}\tilde{\Sigma}\,, \quad (6)$$

where ρ_r is the reactants density, $\tilde{\Sigma}$ is the Favre-filtered flame surface area per unit mass of the mixture, and the product, $\bar{\rho}\tilde{\Sigma}$, is the flame surface area per unit volume or flame surface density (FSD). The quantity, $\tilde{\Sigma}$, includes contributions from the resolved and the unresolved subfilter scales and a means of specifying the FSD is required for closure. The modelled transport equation for the FSD proposed by Hawkes and Cant [HC01] is used here.

5 Parallel Implicit AMR Finite-Volume Scheme

The filtered Navier-Stokes equations and subfilter-scale model equations are solved by applying a finite-volume method in which the conservation equations are integrated over hexahedral cells of body-fitted multi-block mesh. The finite-volume formulation applied to cell (i, j, k) can be expressed as

$$\Gamma_{i,j,k} \frac{d\mathbf{U}_{i,j,k}}{dt} = -\frac{1}{\mathcal{V}_{i,j,k}} \sum_{l} \left(\mathbf{F} \cdot \mathbf{n}\, \Delta A\right)_{i,j,k,l} + \mathbf{S}_{i,j,k} = \mathbf{R}_{i,j,k}(\mathbf{U}) \,, \qquad (7)$$

where $\mathbf{U}$ is the vector of solution variables, $\mathbf{F}$ is the flux dyad containing contributions from the inviscid and viscous terms, $\mathbf{S}$ is the vector of source terms including terms associated with finite rate chemistry, $\mathcal{V}_{i,j,k}$ is the volume of cell (i, j, k), and ΔA and $\mathbf{n}$ are the area of the cell face and unit vector normal to the cell face, respectively, and $\mathbf{R}_{i,j,k}(\mathbf{U})$ is the residual vector. Local preconditioning technique as proposed by Weiss and Smith [WS95] is used to alleviate numerical difficulties for low-Mach-number, nearly incompressible flows. The preconditioning matrix, $\boldsymbol{\Gamma}$, helps control numerical stiffness and dissipation, making the solution of the governing equations more tractable. The inviscid (hyperbolic) component of the numerical fluxes are determined using the least-squares piecewise limited linear solution reconstruction procedure of Barth [Bar93] and Riemann solver based flux functions. The limiter of Venkatakrishnan [Ven93] is used. An extension of the approximate linearized Riemann solver of Roe [Roe81] is used to account for mixture composition. The viscous (elliptic) component of the face fluxes are evaluated by employing the approach of Mathur and Murthy [MM97].

The spatial discretization procedure described above allows for solution-directed block-based AMR and an efficient and highly scalable parallel implementation has been achieved via domain decomposition [GG08]. In particular, a flexible block-based hierarchical octree data structure has been developed and is used to facilitate automatic solution-directed mesh adaptation on multi-block body-fitted hexahedral mesh according to physics-based refinement criteria. Local refinement and coarsening of the mesh is carried out by division and merging of solution blocks, respectively. A domain decomposition procedure is used where the solution blocks making up the computational mesh are distributed equally among available processors, with more than one block permitted per processor. A Morton ordering space filling curve is used to provide nearest-neighbour ordering of the solution blocks in the multi-block hexahedral AMR mesh for more efficient load balancing [ABM04].

The semi-discrete form of the governing equations given in Eq. (7) form a coupled set of non-linear ordinary differential equations. For unsteady flows, time-dependent solutions are obtained by employing a dual-time-stepping-like procedure. In this approach, a modified residual is defined by $\mathbf{R}^*(\mathbf{U}^{(n+1)}) = (3\mathbf{U}^{(n+1)} - 4\mathbf{U}^{(n)} + \mathbf{U}^{(n-1)})/(2\Delta t) + \mathbf{R}(\mathbf{U}^{(n+1)}) = 0$, where an implicit second-order backward discretization of the time derivative has been

used. Newton's method is applied to the solution of the non-linear algebraic equations above. This requires the solution of the following linear system:

$$\left[\left(\frac{3}{2\Delta t}\right)\mathbf{I}+\frac{\partial \mathbf{R}}{\partial \mathbf{U}}\right]\triangle \mathbf{U}^{(n+1,k)}=\mathbf{J}\Delta \mathbf{U}^{(n+1,m)}=-\mathbf{R}^{*}(\mathbf{U}^{(n+1,m)}), \qquad (8)$$

which must be solved at each Newton iterative step, m, for the solution change $\Delta\mathbf{U}^{(n+1)} = \mathbf{U}^{(n+1)} - \mathbf{U}^{(n)}$ at time level n. With the previous time step as an initial estimate, $\mathbf{U}^{(n+1,m=0)} = \mathbf{U}^{(n)}$, successively improved estimates for the solution, $\mathbf{U}^{(n+1,m)}$, are obtained by solving Eq. 8, where $\mathbf{J}$ is the modified residual Jacobian. The procedure is repeated until $||\mathbf{R}^{*}(\mathbf{U}^{(n+1,m)})||_2 < \epsilon||\mathbf{R}^{*}(\mathbf{U}^{(n)})||_2$ where ϵ is some small parameter (typically, $\epsilon \approx 10^{-2}$–10^{-3}).

Each step of Newton's method requires the solution of the large, sparse, and non-symmetric linear system $\mathbf{Jx} = \mathbf{b}$. A preconditioned restarted version of the GMRES algorithm, GMRES(m_g), is used, where m_g is the number of steps after which the method is restarted [Saa96]. An inexact Newton method is adopted in which the GMRES iterations are not fully converged at each Newton step. The iterations are carried out only until $||\mathbf{R}^{*} + \mathbf{J}\Delta\mathbf{U}||_2 \leq \zeta||\mathbf{R}^{*}||_2$, where ζ is typically in the range 0.01–0.5. Preconditioning is required for GMRES to be effective. Right preconditioning of the form $(\mathbf{JM}^{-1})(\mathbf{Mx}) = \mathbf{b}$ is used where $\mathbf{M}$ is the preconditioning matrix. An additive Schwarz global preconditioner with variable overlap [Saa96, KK04] is used in conjunction with local preconditioning based on a block-fill ILU(f) or BFILU(f) factorization of an approximate Jacobian for each subdomain. Here, f is the level of fill. This combination of preconditioning is compatible with the block-based AMR and domain decomposition and facilitates parallel implementation. A "Jacobian-free" approach is also adopted in which numerical differentiation is used to approximate the matrix-vector product $\mathbf{JM}^{-1}\mathbf{x}$.

6 Numerical Results

LES predictions are now considered for a slot burner [FDCD05]. The burner consists of a rectangular slot (slot area 0.025 m × 0.05 m) flanked by two pilot flames to anchor the central flame and shield it from the surroundings. The two pilot flames, each 0.025 m × 0.05 m, are approximated by a uniform co-flow of hot combustion products at a velocity of 14.46 m/s. For the central burner, a uniform mean inflow of 12 m/s with superimposed fluctuating turbulent field is prescribed. The fresh gas at the inflow is a methane-air premixed stoichiometric mixture with temperature $T = 298$ K. The methane-air chemistry is represented simply by a one-step mechanism as described by Westbrook and Dryer [WD81]. The inflow turbulence is generated by employing the procedure of Rogallo [Rog81]. Inflow conditions at any instant in

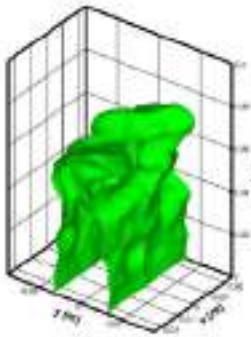

Fig. 1. Predicted instantaneous flame surface at time $t = 4$ ms represented by the iso-surface of fuel mass fraction, $Y_{\mathrm{F}} = 0.0275$ obtained using the thickened flame model.

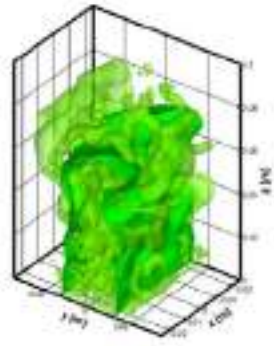

Fig. 2. Predicted flame interaction with turbulent structures as represented by the Q-criterion iso-surface, $Q = 11,000$, at time $t = 4$ ms obtained using the thickened flame model.

time are obtained from this synthetic field using Taylor's hypothesis. The integral length scale of the inflow turbulence is $L = 6.2$ mm and the turbulence intensity is $u' = 1.44$m/s ($u'/s_{\mathrm{L}} = 3.8$). The computational domain was 0.075 m wide, 0.05 m deep, and 0.10 m high. Subsonic inflow boundary conditions were applied at the inlet and subsonic outflow conditions were imposed on the remainder of the domain. For the thickened flame model, a grid consisting of $96 \times 64 \times 128 = 786,432$ cells and $F = 8$ were used and $\Delta = 2\Delta x$.

LES predictions of the slot burner flame obtained using the thickened-flame model at time $t = 4$ ms are shown in Figs. 1 and 2. The instantaneous flame surface is shown in Fig. 1 and this iso-surface, along with surfaces corresponding to a constant value of the Q-criterion, are shown in Fig. 2. The latter depicts the interaction of the turbulent structures with the flame. The initially planar flame near the inlet exhibits a strong interaction with the turbulence, becoming well wrinkled. The predicted flame has an approximately parabolic shape that is mostly convex towards the combustion products. Turbulent structures passing through the flame front are significantly diminished by heat release and expansion of the fluid. A similar set of LES predictions for the slot burner flame was obtained using the FSD model but are not shown. Overall, the predictions for both the thickened-flame and FSD models agree well with the trends observed experimentally [FDCD05].

7 Conclusions

A parallel implicit AMR scheme has been proposed for performing LES of turbulent premixed flames. Initial numerical simulations for a slot burner have demonstrated the potential of the approach.

References

[ABM04] Aftosmis, M., Berger, M., Murman, S.: Paper 2004-1232, AIAA (2004)
[Bar93] Barth, T.J.: Paper 93-0668, AIAA (1993)
[CDVP00] Colin, O., Ducros, V., Poinsot, T.: Phys. Fluids 12, 1843 (2000)
[CMV02] Charlette, F., Meneveau, Veynante, D.: Combust. Flame 131, 159 (2002)
[FDCD05] Filatyev, S., Driscoll, J., Carter, Donbar: Combust. Flame 141, 1 (2005)
[GG08] Gao, X., Groth, C.P.T.: Paper 2008-1017, AIAA (2008)
[HC01] Hawkes, E.R., Cant, R.S.: Combust. Flame 126, 1617–1629 (2001)
[KK04] Knoll, D.A., Keyes, D.E.: J. Comput. Phys. 193, 357–397 (2004)
[MM97] Mathur, S.R., Murthy, J.Y.: Numer. Heat Trans. 31, 191–215 (1997)
[Roe81] Roe, P.L.: J. Comput. Phys. 43, 357–372 (1981)
[Rog81] Rogallo, R.S.: NASA Technical Memorandum 81315 (1981)
[Saa96] Saad, Y.: Iterative Methods for Sparse Linear Systems. PWS (1996)
[Ven93] Venkatakrishnan, V.: Paper 93-0880, AIAA (January 1993)
[VV02] Veynante, D., Vervisch, L.: Prog. Energy Combust. Sci. 28, 193 (2002)
[WD81] Westbrook, C.K., Dryer, F.L.: Combust. Sci. Tech. 27, 31–43 (1981)
[WS95] Weiss, J.M., Smith, W.A.: AIAA J. 33(11), 2050–2057 (1995)

“*This page left intentionally blank.*”

Part 37
Turbulence Modeling and Simulation 2

“*This page left intentionally blank.*”

The Characteristic Analysis of Fire-Driven Flow Simulation Code (FDS) for Railway Tunnel

Yong-Jun Jang and Hag-Beom Kim

Environmental Research Department, Korea Railroad Research Institute,
#360-1, Woulam-Dong, Uiwang-City, Kyounggi-Do, 437-757, Korea
jangyj@krri.re.kr, kimhb31@krri.re.kr

Abstract. The performance and applicability of FDS code is analyzed for flow simulation in railway tunnel. RANS and DNS's results are compared with FDS's. AJL non-linear $k-\varepsilon$ model is employed to calculate the turbulent flow for RANS. DNS data by Moser et al. are used to prove the FDS's applicability in the near wall region. Parallel plate is used for simplified model of railway tunnel. Geometrical variables are non-dimensionalized by the height (H) of parallel plate. The length of streamwise direction is 50H and the length of spanwise direction is 5H. Selected Re numbers are 10,667 for turbulent flow and 133 for laminar low. The characteristics of turbulent boundary layer are introduced. AJL model's predictions of turbulent boundary layer are well agreed with DNS data. However, the near wall turbulent boundary layer is not well resolved by FDS code. Half-Slip (default) conditions are imposed on the wall but wall functions based on log-law are not employed by FDS. The heavily dense grid distribution in the near wall region is necessary to get correct flow behavior in this region for FDS.

1 Introduction

Research on the phenomenon of fire in railway tunnels and underground space has been actively conducted since the 2003 Daegu subway fire disaster in Korea. Due to the danger and constraints involved in using experimental techniques to study fire-driven flow in tunnel, simulation methods are being vigorously developed instead[1]. As for simulation methods, the RANS(Reynolds Averaged Navier Stocks) technique in the FLUENT, START CD series and the LES(Large Eddy Simulation) technique in FDS code developed by NIST of the U.S. are the mainstream.

Compared with LES, RANS has the advantage of being accessible to the general public because of its fast calculation time and small calculation capacity, whereas it has the disadvantage of being vulnerable in the flow field where massive vortices occur such as wake flow[2]. The CFD method that can make up for this disadvantage is the LES technique, which is employed by FDS code. Developed in the early days to research the atmosphere, the LES technique began to be applied to the general fluid and mechanical fields in the 1980s. The advantages of LES have been recognized as suitable for analyzing the flow field in which massive vortices occur such as fire-driven flow, and the phenomenon of unsteady flow

is pre-dominant[3]. However, one drawback of LES is that compared with RANS, it requires a longer calculation time. Another serious drawback is that its flow prediction capability in the near wall region is markedly less than RANS. To overcome this weakness, methods of significantly increasing the number of grids in the near wall region are being used, but it only increases the calculation time exponentially, drawing unfavorable comments on the desirability of its practical applications [2]. Therefore, when employing FDS code that uses the LES technique, it is necessary that such LES advantages be utilized, while avoiding its disadvantages. Unfortunately, many researchers are using FDS in spaces surrounded by walls (such as tunnel wall) without understanding the vulnerabilities of FDS pointed out above, against which some measures are in order.

This research carried out a comparative analysis of the results of RANS and DNS (Direct Numerical Simulations) in a space surrounded by walls to verify the performance of FDS in the same area. As for the turbulent model of RANS, reports [4,5,6,7] were made of successful RSM (Reynolds Stress Model) which is the most sophisticated model in RANS, but for the purpose of reducing calculation time, the AJL model [8], a recently developed non-linear turbulence model, was used. Also, for comparison with the results of DNS, the data from Moser et al. [9] was employed.

2 Flow Conditions and Numerical Method

2.1 Flow Conditions

Using the shape of a railway tunnel as surrounded by walls requires a considerable calculation time. This research adopted as a railway model a three-dimensional parallel plate that obtained DNS results [9] to ensure reduced calculation time and precise comparison as shown in Figure 1. 'H' for the height of the parallel plate, '5H' for the spanwise direction, and '50H' for the main streamwise direction(X) were chosen. In the case of turbulent flow, the flow develops completely at 13H, according to the empirical formula [10]. Therefore 50H is judged to be sufficient for the length of the main streamwise direction. As for the flow model, the turbulent flow of Re = 10,667 and the laminar flow of Re = 133 were simulated. The number of Re chosen for the turbulent flow is the one to be compared with the results of DNS.

In the case of FDS, the default conditions of uniform flow were used at the entrance as boundary conditions; while at the exit, the 'OPEN' conditions of FDS were used. On the side, the symmetrical 'MIRROR' conditions were employed. RANS was calculated two-dimensionally and the turbulent and laminar flow were calculated based on the same Re number as FDS.

In the same flow structure, the results of DNS correspond to $\mathrm{Re}_\tau = u_\tau \delta / \nu = 590$ (δ means channel half-width), which represents Re = 10,667 of this research. In RANS and DNS, X and Y stand for the main streamwise and the wall (height) direction, respectively.

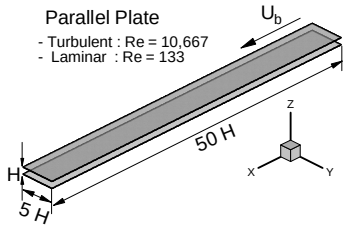

Fig. 1. 3-D parallel-plate structure for simplified railway tunnel

2.2 Grid Generation

FDS uses the orthogonal coordinate system as default conditions. In LES, grid space is a very important variable and if set too wide, the results may be no more satisfactory than RANS. This research used 512 grids in X direction, 64 in Y direction, and 128 in Z direction (4.2 million grids in total), and the grid spaces of $\Delta x^+ \sim 39$, $\Delta y^+ \sim 31$, $\Delta z^+ \sim 3$ were established, fulfilling the space requirements for the parallel plate flow suggested in Temmerman et al.[11]. As for the boundary condition on the wall, the default conditions of FDS were used. For RANS, a total of 3,600 grids were used, and flow analysis was carried out in the near wall sub-layers, maintaining $y^+ (= y u_r / \nu) \le 1$ (Y is in the wall direction in RANS.)

2.3 Governing Equation

The LES governing equation for FDS shown below was obtained by filtering the momentum equation.

$$\frac{D\overline{U_i}}{Dt} = -\frac{1}{\rho}\frac{\partial \overline{P}}{\partial x_i} + \frac{\partial}{\partial x_j}\left\{\nu\left(\frac{\partial \overline{U}_i}{\partial x_j} + \frac{\partial \overline{U_j}}{\partial x_i}\right) - \tau_{ij}\right\}, \quad \tau_{ij} = \overline{U_i U_j} - \overline{U_i}\,\overline{U_j} \tag{1}$$

Here τ_{ij} represents sub-grid scale (SGS) stress.

$$\tau_{ij} - \frac{1}{3}\delta_{ij}\tau_{kk} = -2\nu_t \overline{S_{ij}}, \quad \overline{S_{ij}} = \frac{1}{2}\left(\frac{\partial \overline{U_i}}{\partial x_j} + \frac{\partial \overline{U_j}}{\partial x_i}\right)$$

Here ν_t should be modeled and FDS utilizes the following general-purpose Smagorinsky model [11].

$$\nu_t = (C_s \overline{\Delta})^2 \left|\overline{S}\right|, \quad \left|\overline{S}\right| = (2S_{ij}S_{ij})^{1/2}, \quad \overline{\Delta} = (\Delta x \Delta y \Delta z)^{1/3} \tag{2}$$

And C_s = 0.2 (FDS default condition) was used.

For calculating RANS, a non-linear $k-\varepsilon$ turbulent flow model (AJL [8]) was employed.

2.4 Numerical Method

The user manual was consulted for FDS calculation. RANS calculation was carried out utilizing 'STREAM' [12,13,14] code based on non-orthogonal coordinate system, collocated grid system, and FVM.

3 Results and Discussion

Fig. 2 is a typical result of the turbulent flow in a parallel plate. A comparative analysis of the results of the AJL model and DNS was carried out. Fig. 2(a) exhibits the mean velocity of the turbulent boundary layer in log scale, meaning $U^+ = U/U_\tau$, $Y^+ = yU_\tau/\nu$. Here U_τ means friction velocity. According to Kays & Crawford [10], U_τ shows the value of about 0.06 at Re = 10,667. As shown by the turbulence theory [10], the mean velocity at the laminar sub-layer of the turbulent flow is $U^+ = Y^+$, and that which exceeds this region is called a log-region, for which a relative equation of $U^+ = 2.44 \ln Y^+ + 5.0$ is obtained. The DNS results exactly agree with the theory and the AJL model also shows a considerable degree of exactitude. Fig. 2(b) shows again the same result as (a) in y scale with a good visual representation of the shape of the turbulent flow. Here, we can see the turbulent boundary layer is very thin. Fig. 2(c) indicates the shear stress distribution. A high level of shear stress is generated in the near wall region and the results of

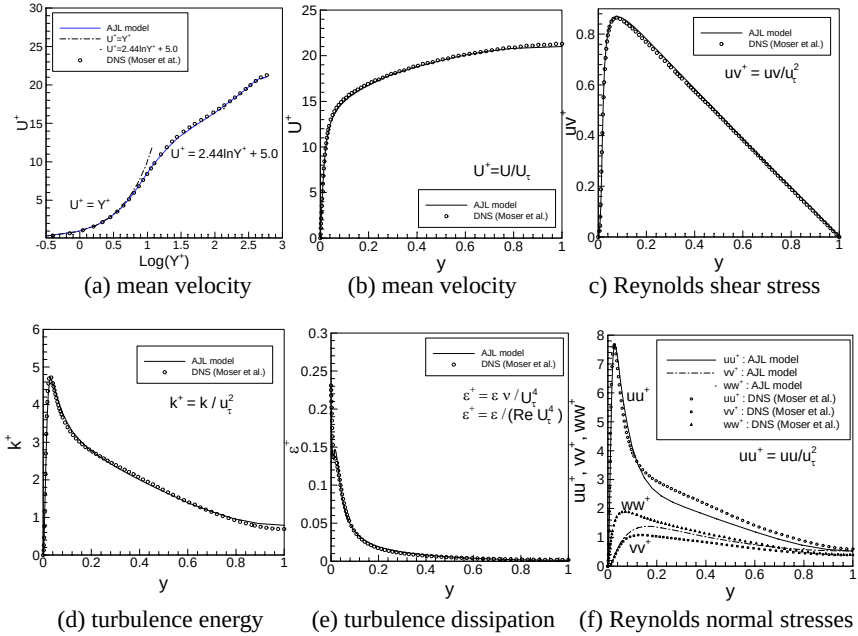

(a) mean velocity (b) mean velocity c) Reynolds shear stress

(d) turbulence energy (e) turbulence dissipation (f) Reynolds normal stresses

Fig. 2. Prediction of turbulent boundary layer in parallel plate using RANS (AJL)

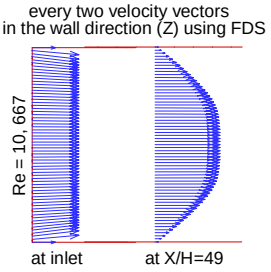

Fig. 3. Velocity distribution using FDS at the inlet and fully developed point

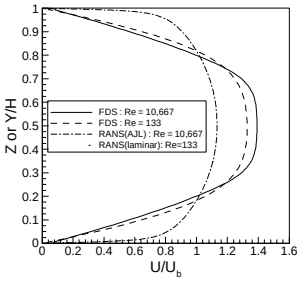

Fig. 4. Comparison between FDS and RANS results

DNS and the AJL model are consistent. Fig. 2(d) shows the turbulent kinetic energy, which reveals a very high level of kinetic energy in the near wall region of great shear stress. The AJL model agrees well with DNS. Fig. 2(e) shows the turbulence dissipation, which is strong in the near wall region. Fig. 2(f) is the predicted result of normal stress, which reveals a strong anisotropy of the turbulence stress. It is in this very aspect that the non-linear model has the advantage, but the linear model is incapable of predicting such anisotropy of the turbulence stress. This anisotropic characteristic of turbulent flow in the near wall region should be well predicted with LES (FDS). A comprehensive view of the turbulent boundary layer using RANS reveals that the result of the employed model (AJL) corresponds well with that of DNS and leads to the conclusion that it is suitable for examining the performance of the FDS code.

Fig. 3 shows the mean velocity vector using FDS at the inlet and fully developed point in the parallel plate. The default conditions of uniform flow are given at the inlet and the flow is developed from a certain distance. Fig. 4 is a graph that compares the results of FDS with those of RANS. The flow condition was compared at the turbulent flow (Re = 10,667) and at the laminar flow (Re = 133), respectively. First, in the turbulent flow, the results of FDS differ from those of RANS. As examined above, a thin boundary layer has to appear in the near wall region like the results of RANS, but the FDS results of the turbulent flow exhibit a flow similar to the laminar flow of RANS, which means turbulence was not generated in the near wall region in FDS calculation. As explained above, in calculating turbulence in FDS, the wall condition was used as default conditions. The results concerning the FDS flow at Re = 133 in the same number of grids (4.2 million) and structure didn't agree well with the results of RANS, either. In Fig. 5, the results of FDS in the parallel plate were analyzed using a log-scale in comparison with the results of DNS. The FDS turbulent flow was similar to the results of DNS in laminar sub-layer, but the results were completely different in the log-region.

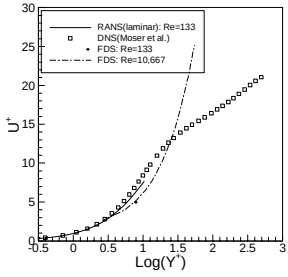

Fig. 5. Comparison between FDS and DNS's results in log-scale

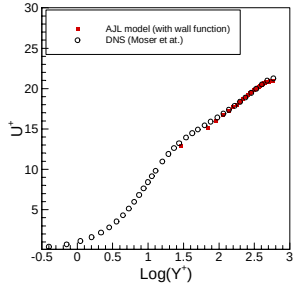

Fig. 6. Mean velocity profile using wall function in RANS (AJL)

The reason for these kinds of results is that when using default conditions in FDS, flow does not completely stick to the wall, but the 'half-slip' condition is given. In general, the 'slip' condition is given when using wall functions in the near wall. When wall functions are used, the turbulent flow is generated in the area exceeding Y^+ = 11 as shown in Fig. 6. Fig. 6 is the calculation result using wall functions in RANS (which used the AJL model). The results of this research, which calculated the turbulent flow using FDS by adjusting the grid distribution in a variety of ways, confirm that wall functions are not employed in FDS. Therefore, the dense arrangement of grids is essential to achieve the correct turbulent flow behavior in the near wall region with FDS. However, this is actually beyond the scope of industrial applicability.

To overcome such vulnerabilities in the near wall region in FDS, it is recommended that, if possible, the simulation of the flow be carried out in a place where contact with the wall can be limited.

4 Conclusion

This research evaluated the simulation performance capability of FDS in a simplified model of a railway tunnel. For this purpose, the results of RANS and DNS in the same space were comparatively analyzed and Re = 10,667 for the turbulent flow and Re = 133 for the laminar flow were applied, respectively. As for the RANS model, the non-linear $k-\varepsilon$ AJL model [8] was used. For DNS, the data from Moser et al. [9] were used.

The calculation results using the default conditions of FDS were not consistent with the results of RANS and DNS in the same space, and the correct turbulent flow behavior was unavailable in the near wall region. Also, FDS did not use wall functions, but a 'half-slip' condition was employed in the near wall region, which made it impossible to form a log-region characteristic of the turbulent flow. Therefore, to avoid such vulnerabilities of FDS in the near wall region, the flow analysis should be made, if possible, in the space where contact with the wall is limited.

References

[1] Ko, S.-W., Ko, K.-H., Ryou, H.-S.: Numerical Study on Fire Suppression using a Water-mist System Considering Droplet Breakup. Journal of The Korean Society for Railway 9(6), 625–629 (2006)

[2] Jang, Y.J., Leschziner, M.A., Abe, K., Temmerman, L.: Investigation of anisotropy-resolving turbulence models by reference to highly-resolved LES data for separated flows. Flow, Turbulence and Combustion 69, 161–203 (2002)

[3] Dejoan, A., Jang, Y.J., Leschziner, M.A.: Comparative LES and Unsteady RANS Computations for a Periodically-Perturbed Separated Flow Over a Backward-Facing Step. Journal of Fluids Engineering (ASME) 127, 872–878 (2005)

[4] Chen, H.C., Jang, Y.J., Han, J.C.: Computation of Heat Transfer in Rotating Two-Pass Square Channels by a Second-Moment Closure Model. Int. J. Heat and Mass Transf. 43(9), 1603–1616 (2000)

[5] Jang, Y.J., Chen, H.C., Han, J.C.: Computation of Flow and Heat Transfer in Two-Pass Channels with 60 deg Ribs. J. Heat Transfer (ASME) 123(3), 563–575 (2001)

[6] Jang, Y.J., Chen, H.C., Han, J.C.: Flow and Heat Transfer in a Rotating Square Channel with 45 deg Angled Ribs by Reynolds Stress Turbulence Model. J. Turbomachinery (ASME) 123(1), 124–132 (2001)

[7] Jang, Y.J., Leschziner, M.A.: An Investigation of Higher-Order Closures in The Computation of the Flow Around a Generic Car Body. In: ECCOMAS 2004 Congress, Jyväskylä Paviljonki International Congress Centre and University of Jyväskylä, Finland, July 24–28 (2004)

[8] Abe, K., Jang, Y.J., Leschziner, M.A.: An investigation of wall-anisotropy expressions and length-scale equations for non-linear eddy-viscosity models. International Journal of Heat and Fluid Flow 24, 181–198 (2003)

[9] Moser, R.D., Kim, J., Mansour, N.N.: Direct numerical simulation of turbulent channel flow up to = 590. Physics of Fluids 11(4), 943–945 (1999)

[10] Kays, W.M., Crawford, M.E.: Convective Heat and Mass Transfer, 3rd edn. McGraw Hill, New York (1993)

[11] Temmerman, L., Leschziner, M.A., Mellon, C.P., Frohlich, J.: Investigation of wall-function approximation and subgrid-scale models in large eddy simulation of separated flow in a channel with streamwise periodic constrictions. International Journal of Heat and Fluid Flow 24, 157–180 (2003)

[12] Lien, F.S., Leschziner, M.A.: A general non-orthogonal collocated finite algorithm for turbulent flow at all speeds incorporating second-moment turbulence-transport closure, Part 1: Computational implementation. Comput. Methods Appl. Mech. Engr. 114, 123–148 (1994a)

[13] Lien, F.S., Leschziner, M.A.: Upstream monotonic interpolation for scalar transport with application to complex turbulent flows. International Journal of Numerical Methods in Fluids 19, 527–548 (1994b)

[14] Jang, Y.J.: Three-Dimensional Flow Analysis around Rolling Stock with Square Cross Section Using Low Re k-ε. Journal of The Korean Society for Railway 9(6), 772–777 (2006)

“*This page left intentionally blank.*”

Part 38
Upwind Scheme 1

“*This page left intentionally blank.*”

Discontinuous Fluctuation Distribution for Time-Dependent Problems

Matthew Hubbard

School of Computing, University of Leeds, Leeds, LS2 9JT, UK
meh@comp.leeds.ac.uk

1 Introduction

For some years now, the fluctuation distribution approach to approximating multidimensional systems of conservation laws has been able to produce accurate simulations of complex steady state fluid flow phenomena using unstructured meshes [DSA00]. More recent research has illustrated their potential for providing a similar level of accuracy in the simulation of time-dependent problems (see the notes in [VKI05] for a recent overview of such methods). Even so, computational simulation of compressible fluid flow problems is still dominated by the finite volume approach.

This is changing, with the emergence of the discontinuous Galerkin (DG) approach, which can be treated as a natural generalisation of the finite volume technique which accounts directly for variation of the solution within each mesh cell rather than dealing with cell-averaged values. Fluctuation distribution schemes do, however, have inherent advantages over finite volume and discontinuous Galerkin schemes, both of which use numerical fluxes across cell boundaries in the update of the dependent variables. They instead consider how the variation within each cell (loosely speaking, a generalised flux *difference*) should affect the local evolution of the dependent variable. Fluctuation distribution schemes are also typically designed to incorporate the most important underlying physical processes: making use of the fluctuation/flux difference instead of the flux provides an environment in which it is simpler to accurately model, not only genuinely multidimensional flow physics, but also source terms when these represent processes which have a natural balance with the fluxes.

Since they are essentially alternative formulations of continuous finite element methods, existing fluctuation distribution schemes are similarly restricted by the continuity imposed on the numerical solution. This can make it difficult to apply h- and p-adaptivity or construct high order schemes which are free of numerically induced oscillations. Recent research, presented in [Hub07, Hub08], has led to the proposal of a *discontinuous* fluctuation distribution scheme, designed to overcome such problems. It provides an alternative discontinuous model to DG which avoids the construction of numerical

fluxes and has been successfully used to design a second order accurate, positive algorithm (a generalisation of the PSI scheme) which can be applied to the Euler equations of gas dynamics. This paper will discuss the extension of these schemes to time-dependent problems, and present preliminary results for scalar conservation laws in one space dimension.

2 Discontinuous Fluctuation Distribution

Consider the scalar conservation law governing the evolution of an unknown quantity $u(\mathbf{x}, t)$ and given by

$$u_t + \boldsymbol{\nabla} \cdot \mathbf{f} \;=\; 0 \qquad \text{or} \qquad u_t + \boldsymbol{\lambda} \cdot \boldsymbol{\nabla} u \;=\; 0 \tag{1}$$

on a domain Ω, with boundary conditions imposed on the inflow part of $\partial\Omega$ and appropriate initial conditions. Here $\boldsymbol{\lambda} = \partial \mathbf{f}/\partial u$ defines the advection velocity associated with the conservation law (1).

These equations will be approximated by discretising an integrated form of the conservation law, assuming that the representation of u is piecewise polynomial with discontinuities allowed at the interfaces between the cells of the computational mesh. Integrating the spatial derivative terms over the whole domain gives

$$\int_\Omega \boldsymbol{\nabla} \cdot \mathbf{f} \; d\Omega \;=\; \sum_{j=1}^{N_c} \int_{C_j} \boldsymbol{\nabla} \cdot \mathbf{f} \; d\Omega \;+\; \sum_{k=1}^{N_f} \lim_{\epsilon \to 0} \int_{{F_k}^\epsilon} \boldsymbol{\nabla} \cdot \mathbf{f} \; d\Omega \,, \tag{2}$$

in which N_c, N_f are the numbers of cells and faces in the mesh, respectively, and the final term represents the integrals over the interfaces, which are being treated as limiting cases of degenerate cells whose widths (ϵ) perpendicular to the adjacent cell faces tend to zero.

Now assume that, in d space dimensions, the computational mesh cells are d-dimensional simplices, that u varies linearly with these cells, and that an appropriate (conservative) linearisation exists for the system [VKI05]. The cell spatial fluctuations can now be written

$$\phi_j \;=\; -\int_{C_j} \boldsymbol{\nabla} \cdot \mathbf{f} \; d\Omega \;=\; \oint_{\partial C_j} \mathbf{f} \cdot \mathbf{n} \; d\Gamma \;=\; -\frac{1}{2} \sum_{i \in C_j} u_i \, \widetilde{\boldsymbol{\lambda}} \cdot \mathbf{n}_i \,, \tag{3}$$

where the symbol $\widetilde{\;}$ indicates an appropriately linearised quantity. The index i loops over the vertices of the mesh cell and $\mathbf{n}_i$ is the inward unit normal to the i^{th} face (opposite the i^{th} vertex) multiplied by the length of that edge. The interface spatial fluctuations can also be evaluated exactly, giving

$$\psi_k \;=\; -\lim_{\epsilon \to 0} \int_{{F_k}^\epsilon} \boldsymbol{\nabla} \cdot \mathbf{f} \; d\Omega \,, \;=\; \int_{F_k} [\mathbf{f} \cdot \mathbf{n}] \; d\Gamma \;=\; -\frac{1}{2} \sum_{i \in F_k} [u_i] \, \widehat{\boldsymbol{\lambda}} \cdot \mathbf{n} \,, \tag{4}$$

where $\widehat{\boldsymbol{\lambda}}$ represents a second (different) set of conservatively averaged values, and $[\;\;]$ represents the jump in a quantity across an interface (where u_i is

considered to be dual-valued), the sign of the difference being dictated by the direction chosen for $\mathbf{n}$. This term is simply the integral over the interface of the flux difference across it.

Each mesh node corresponds to many cell vertices and multiple values of u. When all of the cell- and interface-based fluctuations are distributed, each u_i^j (the value associated with vertex i of cell j) can receive contributions from precisely one cell and d interfaces (subject to the application of boundary conditions). When this is combined with a simple forward Euler discretisation of the time derivative it leads to an iterative update of the form

$$(u_i^j)^{n+1} \;=\; (u_i^j)^n + \frac{(d+1)\Delta t}{S_j}\left(\alpha_i^j \phi_j + \sum_{k=1}^{d} \alpha_i^k \psi_k\right), \tag{5}$$

in which Δt is the time-step, S_j is the volume of cell j, $\alpha_i^{j/k}$ are the distribution coefficients which indicate the appropriate proportions of the fluctuations to be sent from cell j/interface k to vertex i of cell j. Conservation is assured as long as $\sum_{i\in C_j} \alpha_i^j = \sum_{i\in F_k} \alpha_i^k = 1,\ \forall j,k,$ *i.e.* the whole of each fluctuation is distributed to the cell vertices. The precise properties of the scheme depends on the choice of the distribution coefficients. In particular, the discontinuous PSI scheme described in [Hub07, Hub08] is conservative, positive for an appropriate limit on Δt, given by

$$\Delta t \;\leq\; \frac{S_j/(d+1)}{\sum_{l\in C_j}(k_l^j)^+} \qquad \forall \text{ cells } j\,, \tag{6}$$

linearity preserving (and hence second order accurate for piecewise linear u), compact, upwind and continuous. Note that $k_l = \frac{1}{2}\boldsymbol{\lambda}\cdot\mathbf{n}_l$ are the standard inflow parameters which govern the upwinding.

2.1 Time-Dependent Problems

The development of time-dependent fluctuation distribution schemes in which u is continuous has tended to treat the time derivative in a slightly different manner to the spatial derivatives (see, for example, [AM03, RCD05]). However, for the purposes of this discussion the time dimension will be treated precisely as an additional spatial dimension, in which the solution is being advected with speed $\lambda_t = 1$. Equation (1) can now be written as

$$\boldsymbol{\nabla}^t\cdot\mathbf{f}^t \;=\; 0 \qquad \text{or} \qquad \boldsymbol{\lambda}^t\cdot\boldsymbol{\nabla}^t u \;=\; 0\,, \tag{7}$$

in which $\boldsymbol{\nabla}^t$, $\mathbf{f}^t$ and $\boldsymbol{\lambda}^t$ have all been augmented appropriately. The discontinuous fluctuation distribution schemes outlined earlier in Section 2 can now be applied to these equations, albeit on a $d+1$-dimensional space-time mesh.

2.2 One Space Dimension

The new scheme is most easily illustrated in one space dimension. Figure 1 shows two possible configurations for the discretisation of a rectangular space time block of dimensions $\Delta x \times \Delta t$, in which it is subdivided into two triangles. The interfaces between the triangles, at which the discontinuities occur, are indicated by the dashed rectangles. The reverse configuration also illustrates the behaviour of the distribution when the flow velocity is in the opposite direction. The arrows indicate the upwind directions in which the fluctuations are distributed and, importantly, show that since $\lambda_t = 1$, upwinding always sends the fluctuations arising from the discontinuities at a fixed time level forward in time. This allows the solution to be found sequentially, stepping forward in time and solving at each time level instead of having to approximate the full space-time domain at once.

The system can now be approximated at the new time level by iterating the following to convergence:

$$(u_i^j)^{(m+1)} \;=\; (u_i^j)^{(m)} + \frac{2\Delta\tau}{\Delta x \Delta t}\left(\alpha_i^j \phi_j + \sum_{k=1}^{d} \alpha_i^k \psi_k\right). \tag{8}$$

The values of u_5 and u_6 (see Figure 1) form the solution at the new time level. Note that this method is positive for *any* value of Δt, though the above iteration is only positive at each stage for values of $\Delta\tau$ governed by (6).

The time derivative does not have to be treated exactly like the space derivatives. Using the approach typical of the continuous time-dependent schemes [AM03, RCD05] (which do not usually subdivide the space-time cells into simplices) to distribute the cell fluctuations in the discontinuous

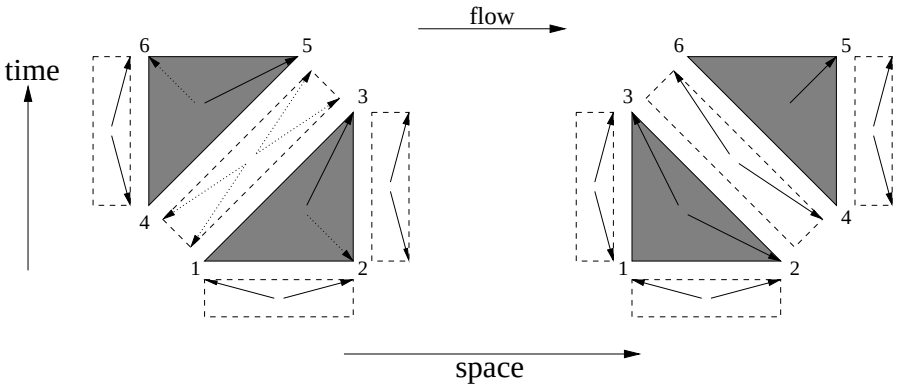

Fig. 1. Fluctuation distribution for a one-dimensional space-time block for flow from left to right (showing both orientations for the diagonal). Solid arrows show vertices to which a proportion of the fluctuation will always be distributed. Distribution indicated by the dotted arrows is dependent on the magnitude of the velocity $\boldsymbol{\lambda}$.

case leads to a scheme which is only first order accurate. It is not yet clear why this should be so and other possibilities are being investigated to try to remove the asymmetry which appears in the mesh of simplices.

3 Numerical Results

The one-dimensional scalar advection equation was modelled, with

$$u(x,0) \;=\; \begin{cases} G(x) & \text{for } 0 \le x \le 1 \\ 0 & \text{elsewhere,} \end{cases} \tag{9}$$

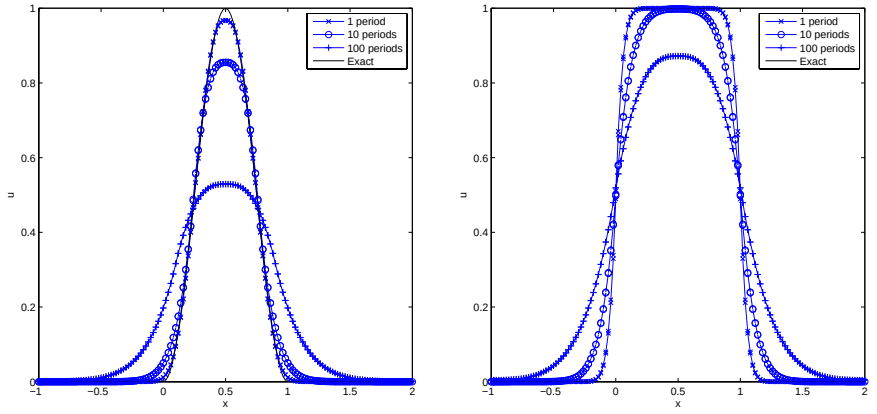

Fig. 2. Numerical approximation of the scalar advection equation for a smooth (left) and a discontinuous (right) initial profile after 1, 10 and 100 periods

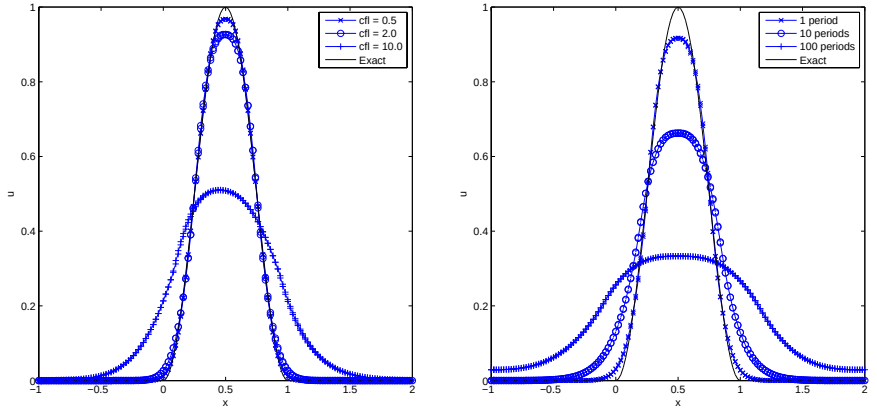

Fig. 3. Numerical approximation of the scalar advection equation for a smooth initial profile for different CFL numbers (left) and for $\lambda = -1$ (right)

being advected with a constant velocity ($\lambda = 1$) across the domain $[-1, 2]$. Periodic boundary conditions are applied and uniform space-time meshes are used to produce all of the following results. Figure 2 shows the outcomes for two initial profiles, $G(x) = \cos^2((x - 0.5)\pi)$ and $G(x) = 1$, obtained on a 151 node uniform spatial mesh with a CFL of 0.5. The effect of increasing the CFL number and reversing the advection velocity are illustrated in Figure 3. The scheme has also been applied successfully to the one-dimensional inviscid Burgers' equation.

4 Summary

A framework has been proposed for the development of fluctuation distribution schemes for approximating time-dependent problems when the underlying representation of the dependent variable is allowed to be discontinuous across space-time mesh interfaces. It has been successfully applied to one-dimensional, scalar problems, for which second order accuracy in space and time and unconditional L^∞ stability have been verified. Further work is required to apply the approach in higher space dimensions and improve the efficiency of the approach, as well as removing the asymmetry inherent in the current space-time mesh used.

References

[AM03] Abgrall, R., Mezine, M.: Construction of second order accurate monotone and stable residual distribution schemes for unsteady flow problems. J. Comput. Phys. 188, 16–55 (2003)

[AS08] Abgrall, R., Shu, C.-W.: Development of residual distribution schemes for the Discontinuous Galerkin methods: the scalar case with linear elements. Commun. Comput. Phys. (to appear)

[DSA00] Deconinck, H., Sermeus, K., Abgrall, R.: Status of multidimensional upwind residual distribution schemes and applications in aeronautics. AIAA paper 2000–2328 (2000)

[Hub07] Hubbard, M.E.: A framework for discontinuous fluctuation splitting. Int. J. Numer. Meth. Fluids 56, 1505–1311 (2008)

[Hub08] Hubbard, M.E.: Discontinuous fluctuation distribution. J. Comput. Phys. (submitted to)

[RCD05] Ricchiuto, M., Csík, Á., Deconinck, H.: Residual distribution for general time-dependent conservation laws. J. Comput. Phys. 209, 249–289 (2005)

[VKI05] High Order Discretization Methods. 34th Computational Fluid Dynamics course, von Karman Institute for Fluid Dynamics, Lecture Series (2005)

Weighted Compact Schemes for Shock / Boundary Layer Interaction

Peng Xie[1], Maria Oliveira[2], Jianzhong Su[3], and Chaoqun Liu[4]

[1] University of Texas at Arlington, PhD student
pxie@smu.edu
[2] University of Texas at Arlington, PhD student
oliveira@uta.edu
[3] University of Texas at Arlington, Professor
su@uta.edu
[4] University of Texas at Arlington, Professor
cliu@uta.edu

Abstract. In this paper, we introduce a new type of weighted, finite-difference schemes. The basic idea comes from the compact schemes discussed in Lele's[lele92] paper and the weighted compact schemes proposed in Jiang's[jiang01] paper. The purpose of this new scheme is to achieve spectral-like resolution and high order of accuracy in smooth regions and to keep the ability to capture shocks without sacrificing the order of accuracy too much. This is really a hybrid scheme that the flux of the conservative Navier-Stokes equations is given by weighted compact scheme (WCS) but with some components from 5^{th} order WENO (Jiang et al [jiang96]). The former gives sharp shock and high resolution, but the later provides necessary dissipation to avoid non-physical oscillations. In the paper, a sixth-order weighted compact scheme and corresponding 5^{th} order WENO are combined following this basic idea. Numerical tests show that the new scheme has improved performance for the problems of two-dimensional shock/boundary layer interaction including test cases with incident shock and double cones. The scheme is especially appropriate for the problems of shock/boundary layer, shock/vertex or shock/turbulence interaction.

1 Introduction

Compact schemes are very popular in the simulations of transitional and turbulent flows because they can provide better spectral resolution and high order accuracy without increasing the width of stencils. However, the traditional compact schemes don't work well with shock waves. The Weighted Compact Scheme (WCS) proposed in [jiang01] is constructed by introducing the idea of WENO scheme to the standard compact schemes. By combining several candidate stencils, the WCS can not only preserve high order accuracy and good spectral resolution in smooth regions, but also keep a sharp transition near the shock without spurious oscillations. The numerical tests in one-dimensional problems are very successful. Unfortunately,

the implementation of Weighted Compact Scheme to two- and three-dimensional flows with wall boundary conditions shows that the scheme does not work well near shock waves. To overcome this problem, a second order smart filter is applied to the small regions near the shock waves. In this way, the oscillations are eliminated while the overall resolution and order of accuracy become questionable. The numerical investigation of shock/boundary layer interaction has been difficult because both strong discontinuity (shock waves) and complicated vortex structure (separation, transition, turbulence) exist. The difference schemes are required to capture the shock and resolve the small scale structures simultaneously. The adverse pressure gradient caused by an incident shock over a laminar boundary layer may lead to a flow separation. The pressure disturbance may propagate upstream through the subsonic region of the boundary layer and enlarge the separation region. As the boundary layer gets thickened, a family of compression waves, or sometimes a separation shock, is formed and make the pressure over the boundary layer increase. This pressure increase leads to a reattachment of the separated boundary layer. For some flows of high Reynolds number, the separation bubble will be unstable and the pressure along the wall surface fluctuates.

2 Hybrid Weighted Compact-ENO Scheme

The 5th order WENO can be written:

$$\hat{F}^{weno}_{j+1/2} = \omega_{0,j+1/2}\left(\frac{1}{3}F_{j-2} - \frac{7}{6}F_{j-1} + \frac{11}{6}F_j\right) + \omega_{1,j+1/2}\left(-\frac{1}{6}F_{j-1} + \frac{5}{6}F_j + \frac{1}{3}F_{j+1}\right) + \omega_{2,j+1/2}\left(\frac{1}{3}F_j + \frac{5}{6}F_{j+1} - \frac{1}{6}F_{j+2}\right) + \ldots$$

$$\omega_k = \frac{\gamma_k}{\sum_{i=0}^{2}\gamma_i},\ \gamma_k = \frac{C_k}{(\varepsilon + IS_k)^p},\ C_0 = \frac{1}{10}, C_1 = \frac{6}{10}, C_2 = \frac{3}{10}$$

$$IS_i = \int_{x_{j-1/2}}^{x_{j+1/2}} \sum_{k=1}^{2} [p_2(x)^{(k)}]^2 h^{2k-1} dx$$

$$IS_0 = \frac{13}{12}(f_{j-2} - 2f_{j-1} + f_j)^2 + \frac{1}{4}(f_{j-2} - 4f_{j-1} + 3f_j)^2$$

$$IS_1 = \frac{13}{12}(f_{j-1} - 2f_j + f_{j+1})^2 + \frac{1}{4}(f_{j-1} - f_{j+1})^2$$

$$IS_2 = \frac{13}{12}(f_j - 2f_{j+1} + f_{j+2})^2 + \frac{1}{4}(f_{j+2} - 4f_{j+1} + 3f_j)^2$$

The weighted compact scheme (WCS) can be written as:

$$\hat{F}^{WCS}_{j+1/2} = \vartheta_{0,j+1/2}\left(\frac{1}{2}F_{j-1} + \frac{5}{2}F_j + 2\Delta x \bullet F'_j\right)/3 + \vartheta_{1,j+1/2}\left[\frac{3}{4}(F_{j+1} + F_j) + \frac{1}{4}\Delta x F'_j - \frac{1}{4}\Delta x F'_{j+1}\right]/1.5 + \vartheta_{2,j+1/2}\left(\frac{1}{2}F_{j+2} + \frac{5}{2}F_{j+1} - 2\Delta x \bullet F'_{j+1}\right)/3$$

$$\vartheta_k = \frac{\gamma_k}{\sum_{i=0}^{2}\gamma_i},\ \gamma_k = \frac{C_k}{(\varepsilon + IS_k)^p},\ C_0 = \frac{1}{18}, C_1 = \frac{8}{9}, C_2 = \frac{1}{18}$$

Since the WENO scheme is too dissipative for small length scales, but WCS has some oscillations around the shock, we combine the two schemes with weights to form a hybrid scheme:

$$\hat{F}_{j+1/2}^{hybrid} = \sigma_{wcs}\hat{F}_{j+1/2}^{wcs} + (1-\sigma_{wcs})\hat{F}_{j+1/2}^{weno}$$

Let us first pick: $\sigma_{wcs} = 0.7$ to see what happens to 1-D shock tube problem

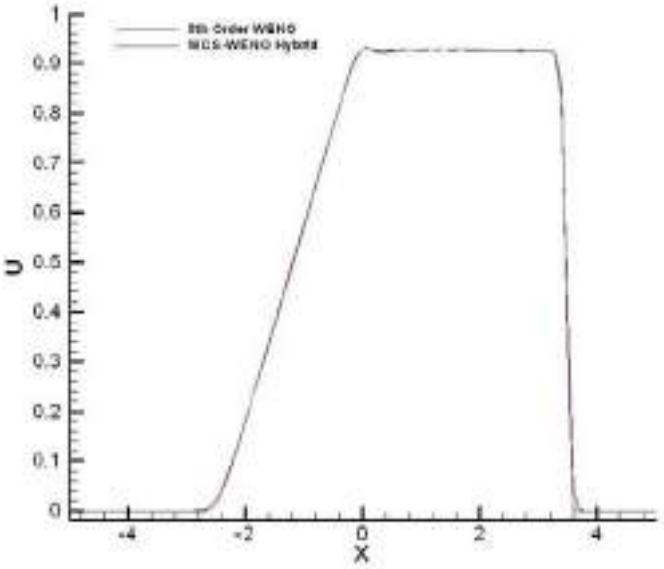

Fig. 1. Comparison of 5th order WENO and WCS-WENO hybrid schemes for 1-D shock tube problem at t=2 (Grid number N=100)

From Figure 1, we can find the WENO scheme (red) smeared the shock and expansion waves and has oscillation after the expansion wave. The improvement by the WCS-WENO hybrid scheme (blue) is very visible.

3 Weighted Compact – ENO for Incident Shock / Boundary Layer Interaction

3.1 Numerical Girds for the Main Flow Solver

In order to resolve the separated boundary layer and separation bubble, the numerical grid is stretched in wall-normal direction. The overall grid is shown as follows,

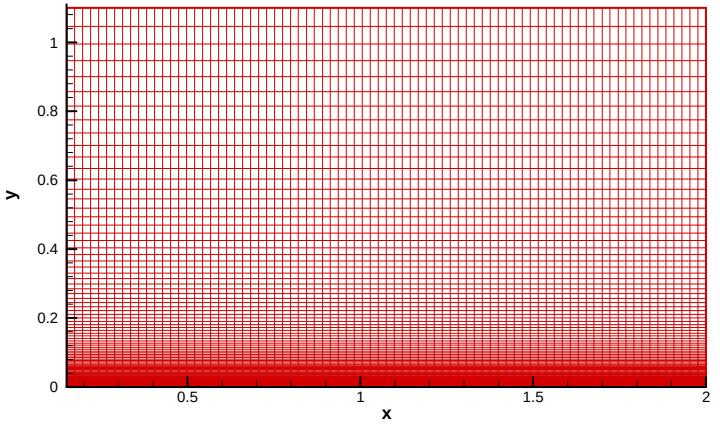

Fig. 2. Stretched Grids

3.2 Initial and Boundary Conditions for the Main Flow Solver

The inflow boundary is given by the profile of the previous inflow generator. The oblique shock is given such that the flow deflection angle is ten degrees. At wall surface, adiabatic and non-slip boundary condition is employed. Non-reflection boundary condition is used at outflow boundary to avoid non-physical reflections.

3.3 Preliminary Numerical Results (Scaled by a Factor of 3 in y-Direction)

(i) Fine Grid (241x141)

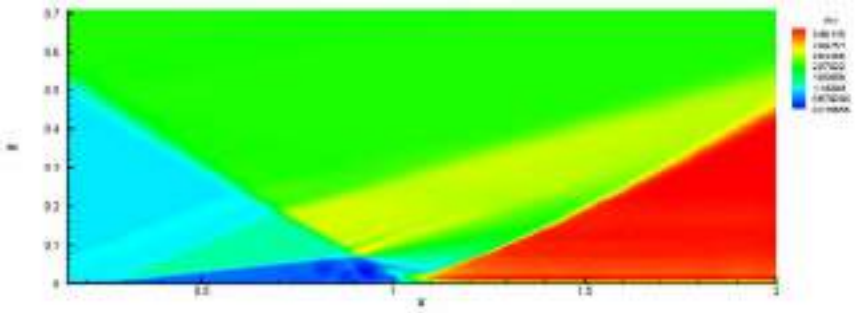

Fig. 3. Density contours

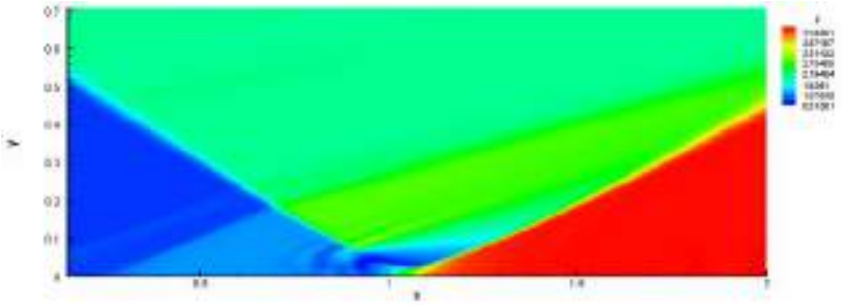

Fig. 4. Pressure Contours

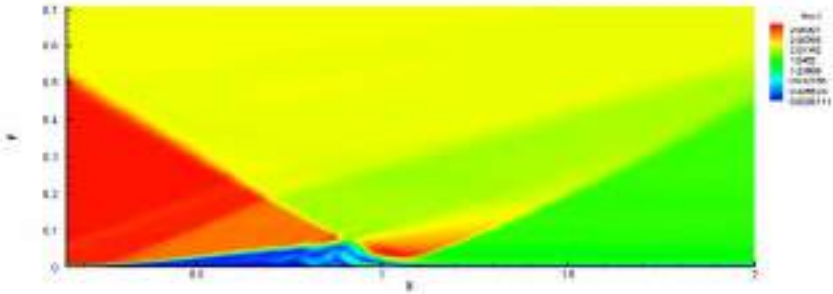

Fig. 5. Mach number contour

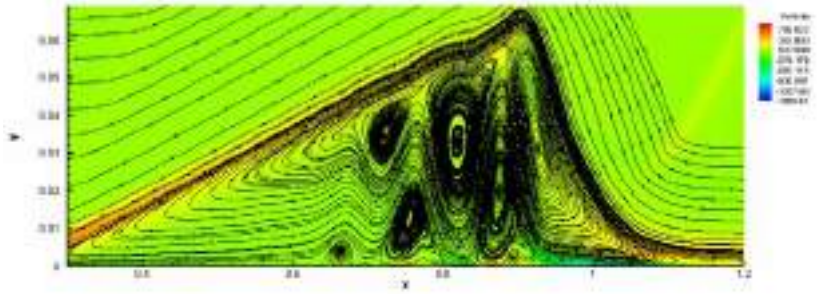

Fig. 6. Vorticity contours and stream line:

(ii) Coarse Grid (121x141) Hybrid:

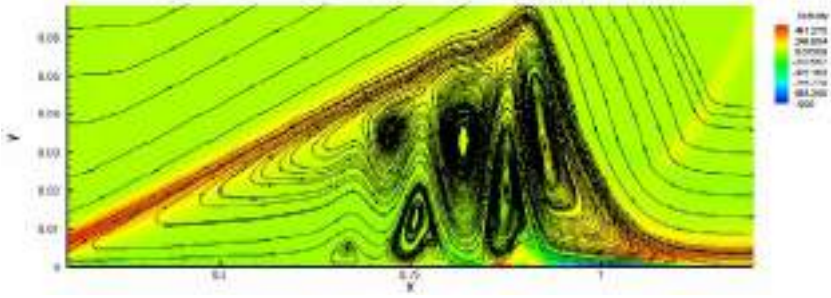

Fig. 7. Vorticity contours and stream line

(iii) Coarse Grid (121x141) WENO:

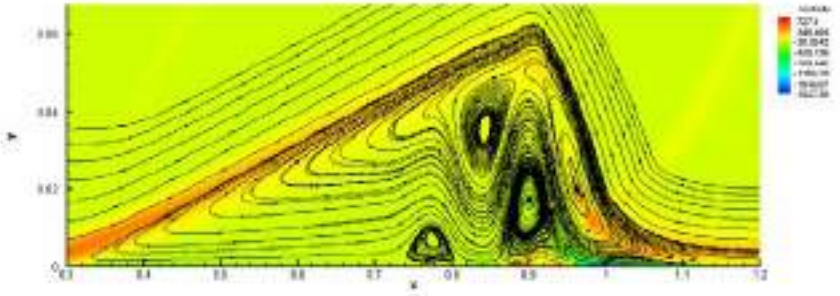

Fig. 8. Vorticity contours and stream line

4 Concluding Remarks

The computational results show the hybrid weighted compact –WENO scheme has much higher resolution than the 5^{th} order WENO scheme for both shock tube problem and incident shock – boundary layer interaction while no visible non-physical oscillations are observed.

References

[lele92] Lele, S.K.: Compact finite difference schemes with spectral-like resolution. Journal Computational Physics 103, 16–42 (1992)

[jiang01] Jiang, L., Shan, H., Liu, C.: Weight Compact Scheme for Shock Capturing. International Journal of Computational Fluid Dynamics 15, 147–155 (2001)

[jiang96] Jiang, G.S., Shu, C.W.: Efficient implementation of weighted ENO scheme. J. Comput. Phys. 126, 202–228 (1996)

The Riemann Problem for Reynolds-Stress-Transport in RANS and VLES

N. Ben Nasr[1], G.A. Gerolymos[2], and I. Vallet[3]

[1] Institut d'Alembert, Case 161, Université Pierre et Marie Curie, 75005 Paris, France
nabil.ben_nasr@upmc.fr
[2] Institut d'Alembert, Case 161, Université Pierre et Marie Curie, 75005 Paris, France
georges.gerolymos@upmc.fr
[3] Institut d'Alembert, Case 161, Université Pierre et Marie Curie, 75005 Paris, France
isabelle.vallet@upmc.fr

Summary. The present paper examines the Riemann problem for the numerical solution of the Reynolds-averaged Navier-Stokes equations with Reynolds-stress closure. Considering both the conservative convective fluxes and the Reynolds-stress production terms the Riemann problem presents 6 states, separated by waves. An HLLC–RSM approximate Riemann solver is developed.

1 Introduction

Recent work on the numerical computation of the Navier-Stokes equations with Reynolds-stress model (RSM) 7-equation turbulence closures, both in a Reynolds-averaged (RSM–RANS) framework, or in continuous RANS-to-DNS RSM–VLES approaches [1], has produced numerical methods which allow the evaluation and improvement of these advanced closures. However, especially when RSM–VLES approaches are concerned, it is important to use low-diffusion [2] high-order schemes.

The use of low-diffusion approximate Riemann solvers (ARSs) using a passive-scalar approach for the Reynolds-stresses [3, 4] fails even for simple subsonic flows (Fig. 1). In a recent work [5] this was related to the incorrect treatment of the contact discontinuity. In a classic low-diffusion solver, the massflux has no dissipation for a stationnary contact discontinuity [2] and treating the Reynolds-stresses as passive scalars yields to the incorrect condition that pressure is continuous across a contact discontinuity, whereas the correct conditon is that $\bar{p} + \bar{\rho} r_n n$ should be continuous. One solution is to use a hybrid scheme, with a dissipative massflux for the Reynolds-stress transport equations [5]. This solution can be used with a variety of ARSs for

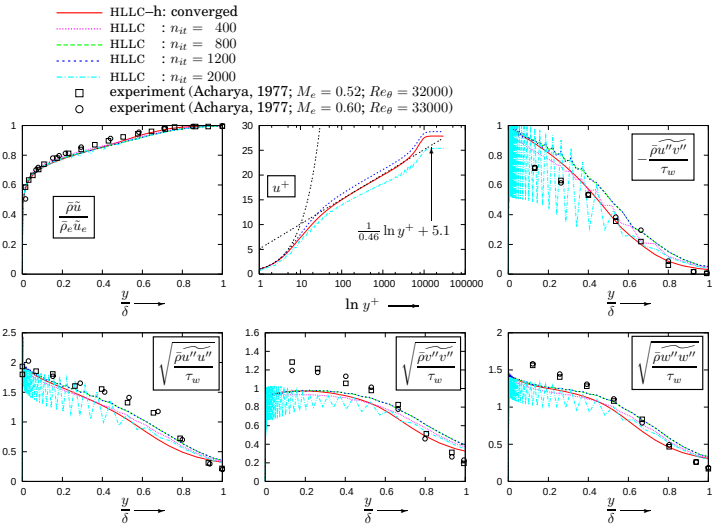

Fig. 1. Mean-mass-flux $\bar\rho\tilde u$, logarithmic law u^+, and Reynolds-stresses for near-zero-pressure-gradient boundary-layer flow, using the HLLC ARS with the passive-scalar approach for the Reynolds-stresses (comparison with measurements of Acharya[6] at $M_e = 0.22$; $Re_\theta = 21000$, and at $M_e = 0.6$; $Re_\theta = 33000$).

the meanflow equations, and yields to robust schemes applicable to complex flows [5].

In the present work we examine the Riemann problem for RST, and develop an HLLC–RSM flux for the coupled system of equations.

2 Reynolds-Stress Transport

2.1 The Complete Set of Equations

The equations are separated into a convective part (time-derivatives and first-derivatives), a diffusive part $\underline{D}$ (second-derivatives), and source-terms $\underline{S}$ (which do not contain derivatives, or are modelled terms such as the rapid part of redistribution).

$$\frac{\partial}{\partial t}\begin{bmatrix}\bar\rho\\ \bar\rho\tilde u_i\\ \bar\rho\tilde h_t-\bar p\\ \bar\rho r_{ij}\\ \bar\rho\varepsilon_u\end{bmatrix}+\frac{\partial}{\partial x_\ell}\begin{bmatrix}\bar\rho\tilde u_i\\ \bar\rho\tilde u_i\tilde u_\ell+\bar p\delta_{i\ell}+\bar\rho r_{i\ell}\\ \bar\rho\tilde h_t\tilde u_\ell+\bar\rho r_{k\ell}\tilde u_k\\ \bar\rho r_{ij}\tilde u_\ell\\ \bar\rho\varepsilon_u\tilde u_\ell\end{bmatrix}+\begin{bmatrix}0\\ 0\\ 0\\ -P_{ij}\\ 0\end{bmatrix}=\underline{D}+\underline{S}\qquad(1)$$

where the red terms correspond to the coupling of the Reynolds-stress with the meanflow equations (through the convective fluxes), while the green terms correspond to nonconservative terms coming form $-P_{ij}=\bar\rho r_{i\ell}\partial_{x_\ell}\tilde u_j+\bar\rho r_{j\ell}\partial_{x_\ell}\tilde u_i$ (exact terms).

2.2 Eigenvalues and Eigenvectors

Retaining the production terms in the RST, the system can be recast in matrix form

$$\frac{\partial \underline{v}}{\partial t} + \underline{\underline{A}}_{\ell} \frac{\partial \underline{v}}{\partial x_{\ell}} = 0 \tag{2}$$

where $\underline{\underline{A}}_{\ell} \in \mathbb{R}^{12\times 12}$ are nonstrictly hyperbolic matrix (12 real eigenvalues with multiplicity) which are not Jacobians of a flux-vector (nonconservative system). Considering, without loss of generality $\underline{\underline{A}}_{x}$

$$\underline{\underline{Ax}} = \begin{pmatrix} \tilde{u} & \bar{\rho} & 0 & 0 & 0\,0\,0\,0\,0\,0\,0 \\ \frac{r_{xx}}{\bar{\rho}} & \tilde{u} & 0 & 0 & \frac{1}{\bar{\rho}}\,1\,0\,0\,0\,0\,0 \\ \frac{r_{yx}}{\bar{\rho}} & 0 & \tilde{u} & 0 & 0\,0\,1\,0\,0\,0\,0 \\ \frac{r_{zx}}{\bar{\rho}} & 0 & 0 & \tilde{u} & 0\,0\,0\,0\,0\,0\,1 \\ 0 & \gamma\bar{p} & 0 & 0 & \tilde{u}\,0\,0\,0\,0\,0\,0 \\ 0 & 2r_{xx} & 0 & 0 & 0\,\tilde{u}\,0\,0\,0\,0\,0 \\ 0 & r_{yx} & r_{xx} & 0 & 0\,0\,\tilde{u}\,0\,0\,0\,0 \\ 0 & 0 & 2r_{yx} & 0 & 0\,0\,0\,\tilde{u}\,0\,0\,0 \\ 0 & 0 & r_{zx} & r_{yx} & 0\,0\,0\,0\,\tilde{u}\,0\,0 \\ 0 & 0 & 0 & 2r_{zx} & 0\,0\,0\,0\,0\,\tilde{u}\,0 \\ 0 & r_{zx} & 0 & r_{xx} & 0\,0\,0\,0\,0\,0\,\tilde{u} \\ 0 & 0 & 0 & 0 & 0\,0\,0\,0\,0\,0\,0 \end{pmatrix} \quad ; \quad \underline{v} = \begin{pmatrix} \bar{\rho} \\ \tilde{u} \\ \tilde{v} \\ \tilde{w} \\ \bar{p} \\ r_{xx} \\ r_{xy} \\ r_{yy} \\ r_{yz} \\ r_{zz} \\ r_{zx} \\ \varepsilon* \end{pmatrix} \tag{3}$$

it is straightforward to show that the eigenvalues are

$$\lambda_{\mathrm{L}} = \tilde{u} - \sqrt{\breve{a}^2 + 3r_{xx}} \tag{4a}$$

$$\lambda_{l*} = \tilde{u} - \sqrt{r_{xx}} \tag{4b}$$

$$\lambda_{*} = \tilde{u} \tag{4c}$$

$$\lambda_{r*} = \tilde{u} + \sqrt{r_{xx}} \tag{4d}$$

$$\lambda_{\mathrm{R}} = \tilde{u} + \sqrt{\breve{a}^2 + 3r_{xx}} \tag{4e}$$

The analysis of a similar reduced problem by Berthon et al. [7] reveals that the Riemann problem solution for this system is composed by 2 genuinely nonlinear (GNL) waves and 3 linearly degenerate contact discontinuities (Fig. 2), thus containing 6 instead of 4 possible states for the construction of an HLLC-type flux.

2.3 Approximate Jump Relations

The nonconservative products are treated by connecting states across the discontinuity with a linear path [7]. In that case, the jump relations across a discontinuity with speed S, separating states 1 and 2, read

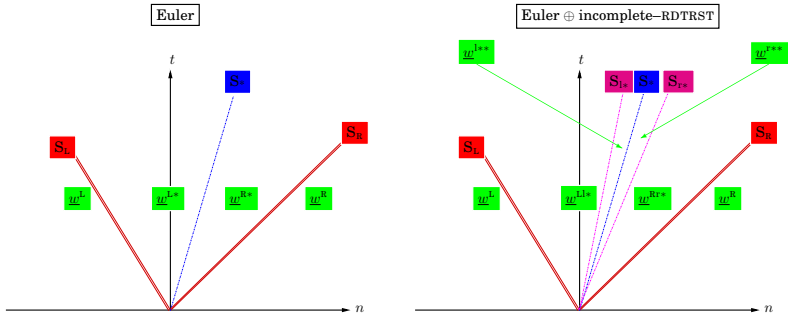

Fig. 2. Riemann problem wave system for the Euler equations[4] (2 GNL-waves and 1 LD contact discontinuity) and for the coupled Euler/RSM equations[7] (2 GNL-waves and 3 LD contact discontinuities)

$$(\mathrm{S}-\tilde{u}_2)\bar{\rho}_2=(\mathrm{S}-\tilde{u}_1)\bar{\rho}_1 \tag{5a}$$
$$(\mathrm{S}-\tilde{u}_1)\bar{\rho}_1\Delta\tilde{u}=\Delta\bar{p}+\Delta[\bar{\rho}r_{xx}] \tag{5b}$$
$$(\mathrm{S}-\tilde{u}_1)\bar{\rho}_1\Delta\tilde{v}=\Delta[\bar{\rho}r_{xy}] \tag{5c}$$
$$(\mathrm{S}-\tilde{u}_1)\bar{\rho}_1\Delta\tilde{w}=\Delta[\bar{\rho}r_{zx}] \tag{5d}$$
$$(\mathrm{S}-\tilde{u}_1-\Delta\tilde{u})\Delta[\bar{\rho}r_{xx}]=\bar{\rho}_1 r_{xx_1}\Delta\tilde{u}+(2\bar{\rho}_1 r_{xx_1}+\Delta[\bar{\rho}r_{xx}])\Delta\tilde{u} \tag{5e}$$
$$(\mathrm{S}-\tilde{u}_1-\Delta\tilde{u})\Delta[\bar{\rho}r_{xy}]=\bar{\rho}_1 r_{xy_1}\Delta\tilde{u}+(\bar{\rho}_1 r_{xy_1}+\tfrac{1}{2}\Delta[\bar{\rho}r_{xy}])\Delta\tilde{u}+(\bar{\rho}_1 r_{xx_1}+\tfrac{1}{2}\Delta[\bar{\rho}r_{xx}])\Delta\tilde{v} \tag{5f}$$
$$(\mathrm{S}-\tilde{u}_1-\Delta\tilde{u})\Delta[\bar{\rho}r_{yy}]=\bar{\rho}_1 r_{yy_1}\Delta\tilde{u}+(2\bar{\rho}_1 r_{xy_1}+\Delta[\bar{\rho}r_{xy}])\Delta\tilde{v} \tag{5g}$$
$$(\mathrm{S}-\tilde{u}_1-\Delta\tilde{u})\Delta[\bar{\rho}r_{yz}]=\bar{\rho}_1 r_{yz_1}\Delta\tilde{u}+(\bar{\rho}_1 r_{xy_1}+\tfrac{1}{2}\Delta[\bar{\rho}r_{xy}])\Delta\tilde{w}+(\bar{\rho}_1 r_{zx_1}+\tfrac{1}{2}\Delta[\bar{\rho}r_{zx}])\Delta\tilde{v} \tag{5h}$$
$$(\mathrm{S}-\tilde{u}_1-\Delta\tilde{u})\Delta[\bar{\rho}r_{zz}]=\bar{\rho}_1 r_{zz_1}\Delta\tilde{u}+(2\bar{\rho}_1 r_{zx_1}+\Delta[\bar{\rho}r_{zx}])\Delta\tilde{w} \tag{5i}$$
$$(\mathrm{S}-\tilde{u}_1-\Delta\tilde{u})\Delta[\bar{\rho}r_{zx}]=\bar{\rho}_1 r_{zx_1}\Delta\tilde{u}+(\bar{\rho}_1 r_{zx_1}+\tfrac{1}{2}\Delta[\bar{\rho}r_{zx}])\Delta\tilde{u}+(\bar{\rho}_1 r_{xx_1}+\tfrac{1}{2}\Delta[\bar{\rho}r_{xx}])\Delta\tilde{w} \tag{5j}$$
$$(\mathrm{S}-\tilde{u}_2)\bar{\rho}_2\varepsilon_2^*=(\mathrm{S}-\tilde{u}_1)\bar{\rho}_1\varepsilon_1^* \tag{5k}$$

Also, obviously (Eq. 5k) ε^* is a passive scalar for this system of equations.

2.4 Approximate Jump Relations for $\lambda \neq \tilde{u}$

A straightforward solution can be obtained for $\Delta[\bar{\rho}r_{xx}]$ from (Eq. 5e), for $\lambda \neq \tilde{u}$,

$$\Delta[\bar{\rho}r_{xx}]=\frac{3\bar{\rho}_1 r_{xx_1}\Delta\tilde{u}}{S-\tilde{u}_1-2\Delta\tilde{u}} \tag{6a}$$

Approximate Jump Relations for $\lambda = \tilde{u} \pm \sqrt{\breve{a}^2+3r_{xx}}$

In that case all the other approximate jump-relations (Eqs. 5) can be expressed as functions of $\Delta\tilde{u}$

$$\Delta\tilde{v} = \frac{2\bar{\rho}_1 r_{xy_1}\Delta\tilde{u}}{(S-\tilde{u}_1-\frac{3}{2}\Delta\tilde{u})(S-\tilde{u}_1)\bar{\rho}_1-(\bar{\rho}_1 r_{xx_1}+\frac{1}{2}\Delta[\bar{\rho}r_{xx}])} \tag{7a}$$

Approximate Jump Relations for $\lambda = \tilde{u} \pm \sqrt{r_{xx}}$

In this case (LD-wave) it is reasonable to assume that

$$\mathrm{S} = \tilde{u}_1 \pm \sqrt{r_{xx_1}} = \tilde{u}_2 \pm \sqrt{r_{xx_2}} \tag{8}$$

Using these relations (Eq. 8), in conjunction with the density jump relation (Eq. 5a), in the equations for $\Delta[\rho r_{xx}]$ (Eq. 6a), $\Delta\tilde{u}$, and in the x-momentum jump-relation (Eq. 5b) yields

$$r_{xx_1} = r_{xx_2} \tag{9a}$$
$$\tilde{u}_1 = \tilde{u}_2 \tag{9b}$$
$$\rho_1 = \rho_2 \tag{9c}$$
$$\rho_1 r_{xx_1} = \rho_2 r_{xx_2} \tag{9d}$$
$$p_1 = p_2 \tag{9e}$$

$$\pm\bar{\rho}_1\sqrt{r_{xx_1}}\Delta\tilde{v} = \Delta[\rho r_{xy}] \tag{10a}$$
$$\pm\bar{\rho}_1\sqrt{r_{xx_1}}\Delta\tilde{w} = \Delta[\rho r_{zx}] \tag{10b}$$

2.5 Approximate Jump Relations for $\lambda = \tilde{u}$

On the contact discontinuity corresponding to the eigenvalue $\lambda = \tilde{u}$, it is reasonable to assume

$$\mathrm{S}_* = u_{\mathrm{L}**} = u_{\mathrm{R}**} = u_* \tag{11}$$

as in the case of the HLLC ARS for the Euler equations [4, 8]. Then the approximate jump relations become

$$\bar{p}_{\mathrm{L}**} + \bar{\rho}_{\mathrm{L}**} r_{xx_{\mathrm{L}**}} = \bar{p}_{\mathrm{R}**} + \bar{\rho}_{\mathrm{R}**} r_{xx_{\mathrm{R}**}} \tag{12a}$$
$$\bar{\rho}_{\mathrm{L}**} r_{xy_{\mathrm{L}**}} = \bar{\rho}_{\mathrm{R}**} r_{xy_{\mathrm{R}**}} \tag{12b}$$
$$\bar{\rho}_{\mathrm{L}**} r_{zx_{\mathrm{L}**}} = \bar{\rho}_{\mathrm{R}**} r_{zx_{\mathrm{R}**}} \tag{12c}$$
$$\tilde{u}_{\mathrm{L}**} = \tilde{u}_{\mathrm{R}**} \tag{12d}$$
$$\tilde{v}_{\mathrm{L}**} = \tilde{v}_{\mathrm{R}**} \tag{12e}$$
$$\tilde{w}_{\mathrm{L}**} = \tilde{w}_{\mathrm{R}**} \tag{12f}$$

2.6 Closure Relations for the HLLC–RSM Flux

Using the the jump-relations across the 2 GNL-waves we can determine the various states in the HLLC–RSM ARS, *viz*

$$\mathrm{S}_* = \frac{[\bar\rho_{\mathrm{L}}(\mathrm{S}_{\mathrm{L}}-\tilde u_{\mathrm{L}})\tilde u_{\mathrm{L}}-(\bar p+\bar\rho r_{xx})_{\mathrm{L}}]-[\bar\rho_{\mathrm{R}}(\mathrm{S}_{\mathrm{R}}-\tilde u_{\mathrm{R}})\tilde u_{\mathrm{R}}-(\bar p+\bar\rho r_{xx})_{\mathrm{R}}]}{\bar\rho_{\mathrm{L}}(\mathrm{S}_{\mathrm{L}}-\tilde u_{\mathrm{L}})-\bar\rho_{\mathrm{R}}(\mathrm{S}_{\mathrm{R}}-\tilde u_{\mathrm{R}})} \tag{13a}$$

$$\bar\rho_{\mathrm{LL}*}r_{xx_{\mathrm{LL}*}} = \bar\rho_{\mathrm{L}*}r_{xx_{\mathrm{L}*}} = \frac{3\bar\rho_{\mathrm{L}}r_{xx_{\mathrm{L}}}(\mathrm{S}_*-\tilde u_{\mathrm{L}})}{\mathrm{S}_{\mathrm{L}}-\tilde u_{\mathrm{L}}-2(\mathrm{S}_*-\tilde u_{\mathrm{L}})} \tag{13b}$$

$$\bar p_{\mathrm{LL}*} = \bar p_{\mathrm{L}*} = (\bar p+\bar\rho r_{xx})_{\mathrm{L}} + (S_*-\tilde u_{\mathrm{L}})\rho_{\mathrm{L}}(S_{\mathrm{L}}-\tilde u_{\mathrm{L}}) - \frac{3\bar\rho_{\mathrm{L}}r_{xx_{\mathrm{L}}}(\mathrm{S}_*-\tilde u_{\mathrm{L}})}{\mathrm{S}_{\mathrm{L}}-\tilde u_{\mathrm{L}}-2(\mathrm{S}_*-\tilde u_{\mathrm{L}})} \tag{13c}$$

Obviously for the HLLC–RSM ARS the tangential velocities are not passive scalars. They are continuous across the $\lambda=\tilde u$ LD-wave, but not across the $\lambda=\tilde u\pm\sqrt{\breve a^2+3r_{xx}}$ GNL-waves nor across the $\lambda=\tilde u\pm\sqrt{r_{xx}}$ LD-waves. Using the appropriate jump relations for $\tilde v$ (Eqs. 12b, 12e, 10b, 7a) it follows that

$$\tilde v_{\mathrm{L}*} = \tilde v_{\mathrm{R}*} = \frac{\left(\bar\rho_{\mathrm{LL}*}\sqrt{r_{xx_{\mathrm{LL}*}}}\tilde v_{\mathrm{LL}*}+\bar\rho_{\mathrm{RR}*}\sqrt{r_{xx_{\mathrm{RR}*}}}\tilde v_{\mathrm{RR}*}+\bar\rho_{\mathrm{RR}*}r_{xy_{\mathrm{RR}*}}-\bar\rho_{\mathrm{LL}*}r_{xy_{\mathrm{LL}*}}\right)}{\bar\rho_{\mathrm{LL}*}\sqrt{r_{xx_{\mathrm{LL}*}}}+\bar\rho_{\mathrm{RR}*}\sqrt{r_{xx_{\mathrm{RR}*}}}} \tag{14}$$

with a similar relation for $\tilde w$. The above relations completely define the HLLC–RSM flux.

3 Conclusions

Reynolds-stresses transport cannot be accomodated, in low-diffusion (contact-discontinuity resolving) ARSs, by simply using the passive scalar approach. In the present work we developed an HLLC–RSM ARS for RST.

References

[1] Gerolymos, G.A., Sénéchal, D., Vallet, I.: RSM–VLES multiblock implicit solver using high-order upwind schemes. In: AIAA Fluid Dynamics Conference, San Fransisco, CA, USA, June 5–8, AIAA Paper 2006–3909, 36 (2006)

[2] Liou, M.S.: Mass flux schemes and connection to shock instability. J. Comp. Phys. 160, 623–648 (2000)

[3] Batten, P., Leschziner, M.A., Goldberg, U.C.: Average-state jacobians and implicit methods for compressible viscous and turbulent flows. J. Comp. Phys. 137, 38–78 (1997)

[4] Toro, E.F.: Riemann Solvers and Numerical Methods for Fluid Dynamics. Springer, Berlin (1997)

[5] Gerolymos, G.A., Vallet, I.: Low-diffusion approximate Riemann solvers for Reynolds-stress transport. In: AIAA Computational Fluid Dynamics Conference, Miami, FL, USA, June 25-28, AIAA Paper 2007–4467, 18 (2007)

[6] Acharya, M.: Effects of compressibility on boundary-layer turbulence. AIAA J. 15(3), 303–304 (1977) (also AIAA paper 76–334, 1976)
[7] Berthon, C., Coquel, F., Herard, J.M., Uhlmann, M.: An approximate solution of the riemann problem for a realisable second-moment turbulent closure. Shock Waves 11, 245–269 (2002)
[8] Batten, P., Clarke, N., Lambert, C., Causon, D.M.: On the choice of wave speeds for the HLLC Riemann solver. SIAM J. Sci. Comp. 18, 1553–1570 (1997)

“*This page left intentionally blank.*”

Part 39
Upwind Scheme 2

“*This page left intentionally blank.*”

Improving Monotonicity of the 2^{nd} Order Backward Difference Time Integration Scheme by Temporal Limiting

T. Wuilbaut and H. Deconinck

von Karman Institute for Fluid Dynamics, Waterloosesteenweg,
72, 1640 Sint-Genesius-Rode, Belgium
wuilbaut@vki.ac.be

This work focuses on the behaviour of the 2^{nd} order accurate backward difference time integration scheme (BDF2) when used to solve unsteady hyperbolic conservation laws, including the compressible Euler equations, in the presence of strong gradients. This scheme is 2^{nd} order, *A-stable* but not monotonicity preserving [Ferziger and Perić(2002)]. The objective of this work is therefore to develop a time integration scheme based on BDF2 that preserves the monotonicity of the solution for moderately high CFL numbers ($CFL = \mathcal{O}(10)$) when used in combination with spatial TVD discretizations. We address the problem of monotone time integration using limiting techniques inspired from the finite-volume space discretizations methods. Similarly, we limit (in time) by blending the BDF2 time-integration scheme with a 1^{st} order accurate, *A-stable* and positive (and therefore monotonicity preserving) scheme. The temporal scheme described is independent from the spatial discretization scheme and from the TVD limiter used, as well as from the spatial computational stencil.

Consider the semi-discretization of a system of ordinary differential equations:

$$\frac{dU}{dt} + R(U) = 0 \tag{1}$$

in which U is the vector of unknowns and R is a particular space discretization operator. Solving equation (1) using the BDF2 time integration scheme, one obtains for a discretization point i:

$$\frac{U_i^{n+1} - U_i^n}{\Delta t} + \theta_i\left(\frac{U_i^{n+1} - 2U_i^n + U_i^{n-1}}{2\Delta t}\right) = -R_i(U^{n+1}) \tag{2}$$

In Eq.(2), we introduced a blending coefficient $\theta \in [0, 1]$ such that when $\theta = 1$ the scheme coincides with the 2^{nd} order BDF2 scheme while when $\theta = 0$ the scheme becomes a 1^{st} order Backward Euler scheme.

The coefficient θ is constructed such that the resulting scheme will be of order two in smooth flows ($\theta = 1$) while reducing to 1^{st} order in the vicinity of discontinuities ($\theta = 0$).

Consistency

Following [Beam and Warming(1982)], the most general consistent two-step method can be written under the form:

$$(1+\xi)U^{n+1}-(1+2\xi)U^{n}+\xi U^{n-1} = \Delta t[\Theta R^{n+1}+(1-\Theta+\phi)R^{n}-\phi R^{n-1}] \quad (3)$$

where ξ, Θ and ϕ are arbitrary real numbers.

The proposed scheme can be rewritten using the latter notation with $\xi = \frac{1}{2}\theta$, $\Theta = 1$ and $\phi = 0$. The scheme is therefore consistent for all values of $\theta \in [0., 1.]$.

Absolute Stability

Following [Beam and Warming(1982)], a Linear Multi Step method described by Eq.(3) is A-stable if and only if:

$$\Theta \geq \phi + \frac{1}{2} \quad (4)$$

$$\xi \geq -\frac{1}{2} \quad (5)$$

$$\xi \leq \Theta + \phi - \frac{1}{2} \quad (6)$$

We can verify that those conditions are fulfilled for any value of the blending coeficient θ with $\xi = \frac{1}{2}\theta$, $\Theta = 1$ and $\phi = 0$.

Monotonicity

The 1^{st} order Backward Euler scheme is unconditionally positive and, combined with a 2^{nd} order TVD Finite Volume method (or any TVD and therefore monotone method), will preserve the monotonicity of the solution. By using the unconditionnally positive Backward Euler scheme at the discontinuities, we will show that we obtain a monotone scheme.

1 Blending Coeficient

We make use of the *minmod()* limiter described in [Roe(1986)] to construct the blending coefficient θ. This limiter is defined by:

$$minmod(r) = \begin{cases} 1 & \text{if } 1 < |r| \text{ and } r > 0 \\ r & \text{if } |r| < 1 \text{ and } r > 0 \\ 0 & \text{if } r < 0 \end{cases}$$

where r is the ratio of temporal slopes, defined at any given point i as:

$$r_i = \frac{\frac{U_i^{n+1} - U_i^n}{\Delta t^{n+\frac{1}{2}}}}{\frac{U_i^n - U_i^{n-1}}{\Delta t^{n-\frac{1}{2}}}} \tag{7}$$

Finally, we define the blending parameter θ_i as:

$$\theta_i = \frac{minmod(r_i)}{max(1, |r_i|)} \tag{8}$$

In Eq.(8), *minmod()* is used as a shock detector. Compared to shock detectors usually described in the literature, we don't use any spatial information. The blending coefficient only depends on the evolution of the variable in time. This approach is general and does not depend on the discretized equations.

In Eq.(8), the division by $max()$ is introduced to obtain a symetric blending parameter. We define symmetry by:

$$\theta(r) = \theta(\frac{1}{r}) \tag{9}$$

We will show in a later section that this property is needed to avoid phase error.

Using the definition (8), the blending parameter θ only equals one (and the scheme is therefore only 2^{nd} order accurate) when the variation of the variable in time is constant. In all other cases, some amount of dissipation is introduced.

In order to reduce the dissipation introduced when $\theta < 1$, we can modify Eq.(8) to obtain:

$$\theta_i = \sqrt{\frac{minmod(r_i)}{max(1, |r_i|)}} \tag{10}$$

We can assume that no unphysical oscillation will appear at a given point i before its corresponding discontinuity. We use this property to define a shock detector that will only be active after a discontinuity has been detected. For a given point, the second-order scheme is used until a decrease of the absolute variation of the variable is observed. Then, the blending factor definition previously described is used. This leads to a low-dissipation scheme by limiting the extra dissipation in a specific region of the shock. This definition is described in (12). Similarly, in order to show the effect of the non-symmetry of the scheme, we define a scheme in which the modified time integration scheme is used only when the absolute variation of the variable increases (11). These alternate definitions can be expressed by:

$$\theta_i = \begin{cases} \sqrt{\frac{1}{r_i}} & if\ |r_i| \geq 1 \\ 1 & if\ |r_i| < 1 \\ 0 & if\ r_i < 0. \end{cases} \tag{11}$$

and

$$\theta_i = \begin{cases} \sqrt{r_i} & if\ |\frac{1}{r_i}| \geq 1 \\ 1 & if\ |\frac{1}{r_i}| < 1 \\ 0 & if\ r_i < 0. \end{cases} \tag{12}$$

2 Results

The time-integration scheme proposed is tested with the blending coeficient 10 on a series of testcases with scalar advection and Euler equations and the accuracy and the monotonicity are assessed for large time steps. For all testcases, the proposed modified *BDF* scheme is used together with a 2^{nd} order cell-centred finite-volume discretization, with a Roe flux splitter and the limiter described in [Barth and Jespersen(1989)].

Scalar Advection

In a first testcase, we compare the result of the proposed scheme to the classical BDF2 scheme on a linear advection of a square pulse testcase (Fig.(1)) for a timestep corresponding to $CFL = 1$. Using the new scheme, the accuracy is preserved and the solution obtained is monotone whilst the classical BDF2 is highly oscillatory (even at $CFL = 1$). The discontinuities have the correct magnitude and position.

Sod Shock Tube

We show the result of the proposed scheme compared to the classical BDF2 scheme for a 1D Sod shock-tube problem from [Sod(1978)] (Fig.(2)) using a timestep of $\Delta t = 0.01s$ corresponding to $CFL_{max} = 5.8$. Again, monotonicity is recovered and the discontinuities are sharper.

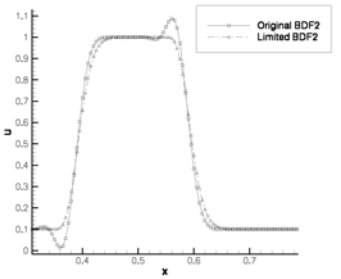

Fig. 1. Comparison of the BDF2 and limited BDF2 solutions for a 1D scalar advection problem

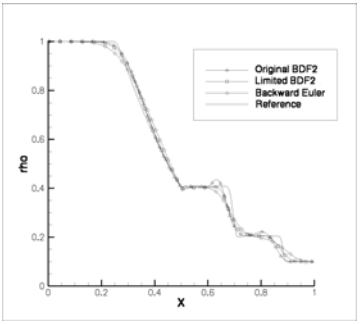

Fig. 2. Comparison of the BDF2, limited BDF2 and Backward Euler solutions (density) for a 1D Sod shock tube ($t = 0,2s$ and $CFL_{max} = 5.8$)

Burgers Equation

We consider Burgers equation and show the influence of the non-symmetric schemes using the blending coeficients of 11 and 12. These modifications will respectively be named *Mod.A* and *Mod.B*. On Fig.(3), we observe that the results obtained with both non-symmetric schemes result in a very inaccurate prediction of the shock location and strength.

Due to the non-symmetric blending coeficient, shocks are not smeared uniformly but ahead or after the shock. The non-symmetric schemes introduce a leading or lagging phase error that accumulates due to the non-linearities of the physical model and should therefore not be allowed when defining blending factor.

Slow Shock Hitting a Wedge

In this testcase from [Ricchiuto(2005)], we consider the interaction of a slow shock hitting a wedge. We compute the solution up to time $t = 1s$ with a

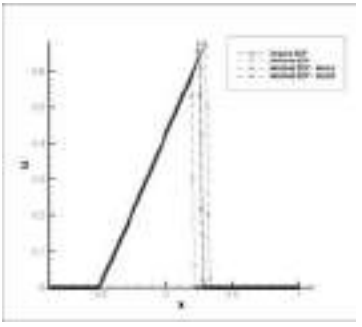

Fig. 3. Burgers Equation - Time $= 1,2s$ - Influence of the non-symmetry of the blending parameter

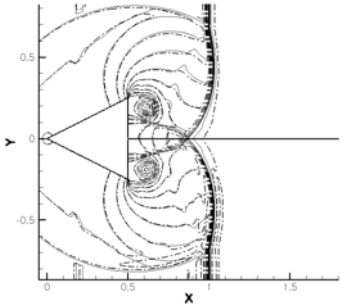

Fig. 4. Density contours of the BDF2 (dashed-bottom), limited BDF2 (dashed-top) solutions compared to the reference solution (solid) for a shock-wedge interaction problem ($CFL_{max} = 5$)

timestep corresponding to $CFL_{max} = 5$ and compare it with the solution obtained with $CFL_{max} = 0.1$, which we use as a reference (Fig.2). The solution obtained with the classical BDF2 shows the presence of spurious oscillations which spoil the accuracy of the solution around the shock. Using the limited scheme, the solution is monotone and the main features of the flow are preserved.

References

[Barth and Jespersen(1989)] Barth, T., Jespersen, D.: The design of application of upwind schemes on unstructured grids. AIAA Paper 1989-0366 (1989)

[Beam and Warming(1982)] Beam, R., Warming, R.: Implicit numerical methods for the compressible navier-stokes and euler equations. In: Computational Fluid Dynamics Course, vol. 4. von Karman Institute for Fluid Dynamics (1982)

[Ferziger and Perić(2002)] Ferziger, J., Perić, M.: Computational Methods for Fluid Dynamics. Springer, Heidelberg (2002)

[Ricchiuto(2005)] Ricchiuto, M.: Construction and Analysis of Compact Residual Discretizations for Conservation Laws on Unstructured Meshes. PhD thesis, Université Libre de Bruxelles, Chaussée de Waterloo, 72, 1640 Rhode-St-Genèse, Belgium (2005)

[Roe(1986)] Roe, P.: Characteristic-based schemes for the euler equations. Ann. Rev. Fluid Mech. 18, 337 (1986)

[Sod(1978)] Sod, G.: A survey of several finite difference methods for systems of nonlinear hyperbolic conservation laws. Journal of Computational Physics 27, 1–31 (1978)

The Finite Volume Local Evolution Galerkin Method for Solving the Euler Equations

Yutao Sun[1] and Yu-Xin Ren[2]

[1] Department of Engineering Mechanics, Tsinghua University, Beijing 100084, China
syt02@mails.tsinghua.edu.cn
[2] Department of Engineering Mechanics, Tsinghua University, Beijing 100084, China
ryx@tsinghua.edu.cn

This paper presents a finite volume local evolution Galerkin (FVLEG)scheme for solving the gas dynamic Euler equations. The FVLEG scheme is the simplification of the finite volume evolution Galerkin (FVEG) method for solving nonlinear Hyperbolic systems. In FVEG scheme, a necessary step is to compute the dependent variables at cell interfaces at $t_n + \tau$ $(0 < \tau \leq \Delta t)$ by using an approximate evolution operator. In the present paper, a new evolution operator suitable for piecewise smooth data is derived. Furthermore, we construct the FVLEG scheme by taking $\tau \to 0$ in the new evolution operators. The FVLEG scheme greatly simplifies the evaluation of the numerical fluxes. It is also well suited with the semi-discrete finite volume method, making the flux evaluation being decoupled with the reconstruction procedure while maintaining the genuine multidimensional nature of the FVEG methods. It is shown that FVLEG scheme can obtain comparable numerical result in terms of accuracy and resolution when compare with FVEG schemes while the efficiency is much higher.

1 Introduction

In this paper, we study the finite volume scheme for solving the two dimensional gas dynamic Euler equations which, in integral form, can be written as

$$\frac{\partial}{\partial t}\int_{\Omega_{i,j}} \mathbf{U}\mathrm{dxdy} + \oint_{\partial\Omega_{i,j}} \mathbf{H}\cdot\mathbf{n}\mathrm{dl} = 0 \tag{1}$$

where Ω_{ij} is the control volume, $\partial\Omega_{ij}$ is the boundary of Ω_{ij} and $\mathbf{H} = \mathbf{Fi}+\mathbf{Gj}$ is the tensor of the fluxes. The finite volume balance equation of Eq. (1) on a quadrilateral control volume is

$$\frac{\partial \bar{\mathbf{U}}_{ij}}{\partial t} = -\frac{1}{\bar{\Omega}_{ij}}\sum_{k=1}^{4}\int_{I_k} \mathbf{H}\cdot\mathbf{n}\mathrm{d}l \tag{2}$$

where $\bar{\mathbf{U}}_{\mathbf{ij}} = (\int_{\mathbf{\Omega_{ij}}} \mathbf{U}\mathrm{d}\mathbf{x}\mathrm{d}\mathbf{y})/\bar{\mathbf{\Omega}}_{\mathbf{ij}}$ and $\bar{\Omega}_{ij} = \int_{\Omega_{ij}} \mathrm{d}x\mathrm{d}y$ are respectively the cell average of the conservative variables and cell volume, I_k is the $k-$th interface of the control volume, and $\int_{I_k} \mathbf{H} \cdot \mathbf{n}\mathrm{d}l$ is the flux across $I_k (k = 1, ..., 4)$.

The general procedure to evaluate the numerical flux can be described by

$$\hat{\mathbf{H}}_{I_k} = \int_{I_k} \mathbf{H}(\mathbf{E}_\tau \mathbf{R}_\Omega \bar{\mathbf{U}}^n) \cdot \mathbf{n}\mathrm{dl}$$

where R_Ω is the reconstruction operator which transforms the cell averages of the conservative variables to their spatial distributions usually in terms of the piecewise polynomial functions, and E_τ is the evolution operator at $t_n + \tau$ with $0 < \tau \leq \Delta t$. It is well known that it is advantageous to take the multidimensional effects in to consideration when design the evolution operators for computing the numerical fluxes. The FVEG scheme [LSW02] is one of such kind of genuine multidimensional methods. The FVEG method is the application of the evolution Galerkin (EG) procedure [LMW00] in the finite volume framework. The EG method is based on the exact integral equations derived from the general theory of bicharacteristics for linear (or linearized) hyperbolic systems. These integral equations are further approximated by approximate evolution operators (E_τ) in such a way that all of the infinitely many directions of the propagation of bicharacteristics are explicitly taken into account. These approximated evolution operators are then used to compute the interfacial dependent variables for the evaluation of the numerical fluxes. For second order scheme, $\tau = \Delta t/2$ is used.

The FVEG schemes have been studied extensively from theoretical as well as numerical point of view and applied to various applications. It is shown that the FVEG schemes yield better accuracy and resolution than some well known finite difference and finite volume schemes. However, the FVEG schemes are much more complicated in implementation than traditional finite volume schemes and are computationally more expensive. In the present paper, a new evolution operator suitable for piecewise smooth data is derived. Furthermore, we construct the FVLEG scheme by taking $\tau \to 0$ in the new evolution operators. The FVLEG scheme greatly simplifies the evaluation of the numerical fluxes. It is also well suited with the semi-discrete finite volume method, making the flux evaluation being independent of the reconstruction procedure while maintaining the genuine multidimensional nature of the FVEG methods. The performance of the proposed scheme is studied by solving several test cases.

2 Numerical Methods

2.1 A Comparison between the FVEG and FVLEG Methods

FVEG schemes are Lax-Wendroff type fully discrete schemes. For a temporally second order scheme, FVEG schemes can be written in the following form:

$$\bar{\mathbf{U}}_{i,j}^{n+1} = \bar{\mathbf{U}}_{i,j}^{n} - \frac{\Delta t}{\bar{\Omega}_{ij}} \sum_{k=1}^{4} \int_{I_k} \mathbf{H}(E_{\Delta t/2} R_\Omega \bar{\mathbf{U}}^{\mathbf{n}}) \cdot \mathbf{n} \mathrm{d}l \tag{3}$$

where $E_{\Delta t/2}$ is the approximate evolution operator to compute the intermediate value of the solution at $t_{n+1/2} = t_n + \Delta t/2$ on cell interface I_k using $R_\Omega \bar{\mathbf{U}}^n$ as the initial condition. On the other hand, FVLEG scheme is a semi-discrete (method of line) approach, in which Eq. (2) is treated as a system of ordinary differential equations (ODEs) with respect to the time after the spatial discretization. And the system of ODEs is integrated with a certain algorithm to obtain the numerical solutions. For example, the second order Runge-Kutta scheme can be used for a temporally second order finite volume scheme:

$$\begin{aligned}
\bar{\mathbf{U}}_{ij}^{(0)} &= \bar{\mathbf{U}}_{ij}^{n} \\
\bar{\mathbf{U}}_{ij}^{(1)} &= \bar{\mathbf{U}}_{ij}^{(0)} - \tfrac{\Delta t}{\Omega_{ij}} \sum_{k=1}^{4} \textstyle\int_{I_k} \mathbf{H}(E_0 R_\Omega \bar{\mathbf{U}}^{(0)}) \cdot \mathbf{n} \mathrm{d}l \\
\bar{\mathbf{U}}_{ij}^{(2)} &= \tfrac{1}{2} \bar{\mathbf{U}}_{ij}^{(0)} + \tfrac{1}{2} \left(\bar{\mathbf{U}}_{ij}^{(1)} - \tfrac{\Delta t}{\Omega_{ij}} \sum_{k=1}^{4} \textstyle\int_{I_k} \mathbf{H}(E_0 R_\Omega \bar{\mathbf{U}}^{(1)}) \cdot \mathbf{n} \mathrm{d}l \right) \\
\bar{\mathbf{U}}_{ij}^{n+1} &= \bar{\mathbf{U}}_{ij}^{(2)},
\end{aligned} \tag{4}$$

where E_0 is the approximate evolution operator to compute the solution at $t_n^+ = t_n + 0$ on cell interface I_k . It clear that for the semi-discrete finite volume scheme, the interfacial dependent variables need only to be evolved for an infinite small period of time to compute the numerical fluxes, whereas for the fully discrete approach, the interfacial dependent variables need to be evolved for an finite period of time. We will see later in this section that the use of the semi-discrete approach greatly simplifies the evaluation of numerical fluxes and makes it straightforward to apply the numerical scheme on general shaped control volumes.

It is clear that the main difference between FVEG and FVLEG schemes is the approximate evolution operators which are in close relation with the time integration algorithm. In the next subsection, the approximate evolution operator E_0 for the FVLEG scheme will be presented. To complete this general introduction, we note that the reconstruction procedure of [RS06] is used to construct the spatially second order FVLEG scheme; and the numerical flux in Eq. (4) is approximately evaluated by using the Simpson rule:

$$\begin{aligned}
&\textstyle\int_{I_k} \mathbf{H}(E_0 R_\Omega \bar{\mathbf{U}}) \cdot \mathbf{n} \mathrm{d}l \approx \\
&\quad \left(\mathbf{H}\left(E_0^{k,1} R_\Omega \bar{\mathbf{U}} \right) + 4\mathbf{H}\left(E_0^{k,c} R_\Omega \bar{\mathbf{U}} \right) + \mathbf{H}\left(E_0^{k,2} R_\Omega \bar{\mathbf{U}} \right) \right) \cdot \mathbf{n}_k \Delta l_k / 6,
\end{aligned}$$

where Δl_k is the length of the I_k interface, the superscripts $(k,1)$,$(k,2)$ represent two end points of I_k interface and the superscript(k,c) stands for the midpoint of the I_k interface . This is also the approach using by [LSW02] in which it is shown that the use of the Simpson rule to approximate the cell interface integral in the flux computation can lead to a scheme which is monotonic under certain conditions.

2.2 The Approximate Evolution Operators for the FVLEG Scheme

In [LSW02], the exact evolution operators are derived for the linearized Euler equations using the bicharacteristic theory, which, taking the density and the $x-$ component of velocity as examples, are:

$$\rho(P) = \rho(P') - \frac{p(P')}{\tilde{a}^2} + \frac{1}{2\pi}\int_0^{2\pi}\left[\frac{p(Q)}{\tilde{a}^2} - \frac{\tilde{\rho}}{\tilde{a}}u(Q)\cos\theta - \frac{\tilde{\rho}}{\tilde{a}}v(Q)\sin\theta\right]d\theta$$
$$- \frac{\tilde{\rho}}{\tilde{a}}\frac{1}{2\pi}\int_0^{2\pi}\int_t^{t+\tau} S\left(\mathbf{r} - [\tilde{\mathbf{u}} - \tilde{a}\mathbf{n}(\theta)]\times(t+\tau-\zeta), \zeta, \theta\right)d\zeta d\theta,$$

$$u(P) = \frac{1}{2\pi}\int_0^{2\pi}\left[-\frac{p(Q)}{\tilde{\rho}\tilde{a}}\cos\theta + u(Q)\cos^2\theta + v(Q)\sin\theta\cos\theta\right]d\theta$$
$$+ \frac{1}{2\pi}\int_0^{2\pi}\int_t^{t+\tau}\cos\theta S\left(\mathbf{r} - [\tilde{\mathbf{u}} - \tilde{a}\mathbf{n}(\theta)]\times(t+\tau-\zeta), \zeta, \theta\right)d\zeta d\theta$$
$$+ \frac{1}{2}u(P') - \frac{1}{2\tilde{\rho}}\int_t^{t+\tau} p_x\left(\mathbf{r} - \tilde{\mathbf{u}}\times(t+\tau-\zeta), \zeta\right)d\zeta,$$

where

$$\mathbf{r} - [\tilde{\mathbf{u}} - \tilde{a}\mathbf{n}(\theta)]\times(t+\tau-\zeta) =$$
$$(x - (\tilde{u} - \tilde{a}\cos\theta)(t+\tau-\zeta), y - (\tilde{u} - \tilde{a}\cos\theta)(t+\tau-\zeta)).$$

In these equations, the variables with tilde are the reference states where the the Euler equations is linearized. $P = (x, y, t+\tau)$ is the location where the dependent variables are to be evaluated. According to the bicharacteristic theory, the Mach cone or the bicharacteristic cone from P intersects the $x-y$ plane at time t to form a circle denoted by $Q(\theta) = (x - (\tilde{u} - \tilde{a}\cos\theta)\tau, y - (\tilde{v} - \tilde{a}\sin\theta)\tau, t)$. $P' = (x - \tilde{u}\tau, y - \tilde{v}\tau, t)$ is at the center of $Q(\theta)$. S is the source term, see [LSW02] for the detailed formulation. It is currently impossible to get an explicit solution of these equations. Therefore, certain approximate operators which are termed as EG1 through EG5 in [LMW00, LMW04, LS06] have been constructed to get the approximate explicit solutions. These approximate solutions are the basis of the FVEG method. When these approximate evolution operators with $\tau = \Delta t/2$ are applied to the piecewise polynomial data obtained by the reconstruction procedure, these approximate solutions are served as $E_{\Delta t/2}R_\Omega\bar{\mathbf{U}}^n$ in Eq. (3).

The simplest way to construct the approximate evolution operator E_0 in FVLEG is to set $\tau = 0$ in E_τ. In other words, we can use the approximate evolution operators EG1 through EG5 developed directly to construct theE_0 by simply taking $\tau = 0$. However, when closely examining the approach for deriving EG1 through EG5, we find that, strictly speaking,these operators

can be only applied to smooth initial conditions. Therefore, in the present paper, E_0 applicable to piecewise smooth functions is constructed. The details of derivation can be found in [SR08] and are omitted here. The final form of E_0 for the density and the $x-$ component of velocity are:

$$\rho(P) = \rho(P') - \frac{p(P')}{\tilde{a}^2} + \frac{1}{2\pi}\sum_{i=1}^{N}[\frac{p_i}{\tilde{a}^2}(\theta_{ie} - \theta_{ib}) - \frac{\tilde{\rho}}{\tilde{a}}u_i(\sin\theta_{ie} - \sin\theta_{ib}) + \frac{\tilde{\rho}}{\tilde{a}}v_i(\cos\theta_{ie} - \cos\theta_{ib})] \quad (5)$$

$$u(P) = \frac{1}{\pi}\sum_{i=1}^{N}[-\frac{p_i}{\tilde{\rho}\tilde{a}}(\sin\theta_{ie} - \sin\theta_{ib}) + u_i(\frac{\theta_{ie} - \theta_{ib}}{2} + \frac{\sin 2\theta_{ie} - \sin 2\theta_{ib}}{4}) - v_i\frac{\cos 2\theta_{ie} - \cos 2\theta_{ib}}{4}], \quad (6)$$

where θ_{ib} and θ_{ie} are the angles of the intersection points between $Q(\theta)$ and cell interfaces. For the E_0 at P_0 (corresponding to P in Eq. (5) and Eq. (6))which is the end point of an interface of the quadrilateral control volumes, the evaluation of θ_{ib} and θ_{ie} is shown in Figure 1. The subscript i stands for the $i-th$ out of the four control volumes surrounding P_0 with its interfaces intersect $Q(\theta)$ at θ_{ib} and θ_{ie}. Using the procedures of this section, we cast the computation of the integrals in E_τ into the evaluation of θ_{ib} and θ_{ie} inE_0. This practice simplifies the evaluation of the numerical fluxes and makes the present scheme more efficient than the FVEG schemes.

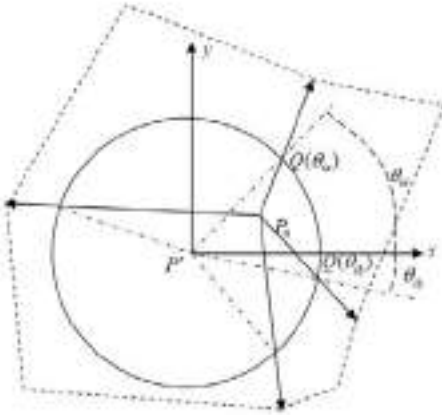

Fig. 1. Possible intersections between the Mach cone and the edges of the control volumes

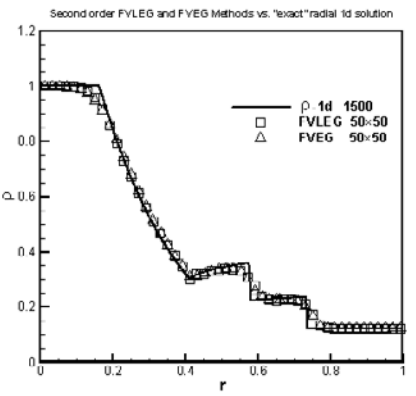

Fig. 2. The comparison of the density distribution between the present scheme and the FVEG scheme

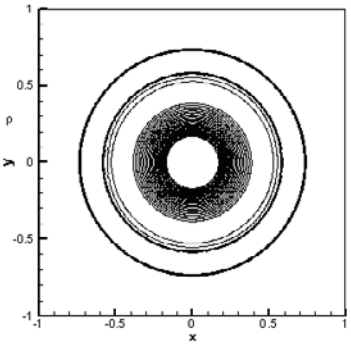

Fig. 3. The density contours of case (1)

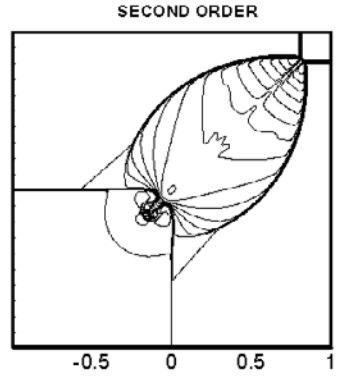

Fig. 4. The density contours of case (2)

3 Numerical Results

In this section, the numerical results of three test cases are presented. These test cases are respectively: (1) the radially symmetric flow [LSW02], (2) the two dimensional Riemann problem [LSW02], and (3) the odd-even grid perturbation problem [Q94]. The detailed initial conditions can be found in the corresponding references.

For the test case (1), the numerical result is compared with that obtained using FVEG scheme and is shown in Figure 2. It is shown that the present scheme is at least as accurate as the FVEG scheme. Figure 3 shows the density contours at time $T = 0.2$ by the second order FVLEG scheme. These results show good multidimensional resolution and preservation of radial symmetry of the numerical solution. The density contours of test case (2) are presented in Figure 4. The flow structures are correctly captured by the present scheme and the resolution of the present scheme is at least as high as the results of the FVEG3 scheme reported in [LSW02]. Moreover, the present scheme produces very clean slip lines, whereas in [LSW02], some wiggles are present at the slip lines for the second order scheme. Figure 5 shows the density contours of test case (3) which is compared with the results of Roe scheme.

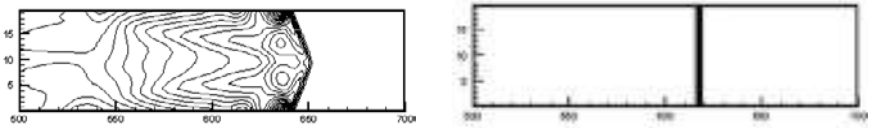

(a) Roe scheme (b) Present scheme

Fig. 5. The density contours of test case (3)

The odd-even decoupling phenomenon presented in the Roe scheme is not founded in the present numerical solutions of the FVLEG scheme.

4 Conclusions

This paper presents a finite volume local evolution Galerkin scheme for solving the gas dynamic Euler equations. The FVLEG scheme simplifies the construction and implementation of the FVEG schemes while maintaining the multi-dimensional nature in numerical flux evaluation. The performance of the proposed scheme is studied by solving several test cases. It is shown that FVLEG scheme can obtain comparable numerical result in terms of accuracy and resolution when compare with FVEG schemes while being more efficient.

Acknowledgements. This work was supported by Project-10572075 of NSFC.

References

[LMW00] Lukáčová-Medvid'ová, M., Morton, K.W. Warnecke, G.: Evolution Galerkin Methods for hyperbolic systems in two space dimensions. Math. Compt. 69, 1355–1384 (2000)

[LMW04] Lukáčová-Medvid'ová, M., Morton, K.W., Warnecke, G.: Finite volume evolution Galerkin (FVEG) methods for hyperbolic problems. SIAM J. Sci. Comput. 26, 1–30 (2004)

[LSW02] Lukáčová-Medvid'ová, M., Saibertová, J., Warnecke, G.: Finite volume evolution Galerkin methods for nonlinear hyperbolic systems. J. Comput. Phys. 183, 533–562 (2002)

[LS06] Lukáčová-Medvid'ová, M., Saibertová, J.: Finite volume schemes for multi-dimensional hyperbolic systems based on the use of bicharacteristics. Applications of Mathematics 51, 205–228 (2006)

[Q94] Quirk, J.: A contribution to the great Riemann solver debate. Int. J. Numer. Methods Fluid Dyn. 18, 555–574 (1994)

[RS06] Ren, Y.X., Sun, Y.T.: A multi-dimensional upwind scheme for solving Euler and Navier-Stokes equations. J. Comput. Phys. 219, 391–403 (2006)

[SR08] Sun, Y.T., Ren, Y.X.: The Finite Volume Local Evolution Galerkin Method for Solving the Hyperbolic Conservation Laws. J. Comput. Phys. (submitted)

“*This page left intentionally blank.*”

Time-Implicit Approximation of the Multi-pressure Gas Dynamics Equations in Several Space Dimensions

Christophe Chalons[1], Frédéric Coquel[2], and Claude Marmignon[3]

[1] Université Paris Diderot-Paris 7, 75005 Paris
chalons@math.jussieu.fr
[2] CNRS & Univ. Pierre et Marie Curie Paris 6, 75005 Paris
coquel@ann.jussieu.fr
[3] ONERA, BP 72, 92322 Châtillon Cédex, France
claude.marmignon@onera.fr

1 Introduction

We are interested in the numerical approximation of the PDE system

$$\begin{cases} \partial_t \rho + \nabla.(\rho\,\mathbf{w}) = 0, \qquad t > 0, \quad \mathbf{x} \in \mathcal{D} \subset R^d, \\ \partial_t(\rho\,\mathbf{w}) + \nabla.(\rho\,\mathbf{w}\otimes\mathbf{w} + \sum_{j=1}^{N} p_j(\rho,\epsilon_j)\ \mathbf{I_d}) = \frac{1}{Rey}\nabla.(\sum_{j=1}^{N}\mu_j(\rho,\epsilon_j)\sigma), \\ \\ \partial_t(\rho\,\epsilon_i) + \nabla.(\rho\,\epsilon_i\,\mathbf{w}) + p_i(\rho,\epsilon_i)\nabla.\mathbf{w} = \frac{1}{Rey}\mu_i(\rho,\epsilon_i)\ \sigma : \nabla\mathbf{w}, \quad i = 1,...,N, \end{cases} \tag{1}$$

with $\sigma = (\nabla\mathbf{w} + {}^t\nabla\mathbf{w}) - \dfrac{2}{3}\nabla.\mathbf{w}\ \ \mathbf{I_d}$.

Here, ρ denotes the density of a compressible material with velocity $\mathbf{w} \in R^d$ and modelled by N independent internal energies $\rho\epsilon_i$. The corresponding pressure and viscosity laws are denoted $p_i(\rho,\epsilon_i)$ and $\mu_i(\rho,\epsilon_i)$.

In the case of a single internal energy ($N = 1$), the above system is equivalent to the usual Navier-Stokes equations in conservative form. But for larger values of N, the proposed model does not rewrite in general in conservative form. Several models from the Physics of complex compressible mixtures enter the proposed setting. Let us quote for instance mixtures of charged particules and multicomponent flows (see [CC1] for instance). In these frameworks, the Reynolds number Rey is usually large and (1) has to be understood in the limit $1/Rey \to 0$. This gives rise to extended Euler equations [CC1]. From a numerical standpoint, the difficulty stems from the lack of conservative reformulation which makes challenging the numerical capture of shock waves. Indeed, in a nonconservative setting, shock discontinuities turn out to be very sensitive to the numerical diffusion of the scheme. In [CC1], [CC2], a full set of generalized jump conditions motivated by a sharp analysis of the viscous shock profiles has allowed to control this sensitiveness. Fig. 1 highlights the benefit of the proposed methods over the classical flow solver in the capture of

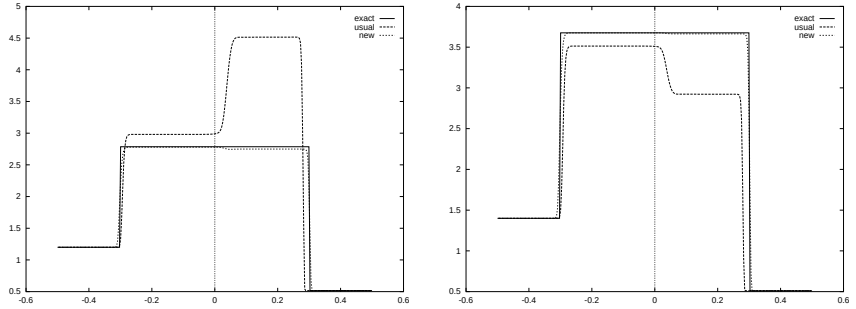

Fig. 1. Pressure p_1 (left) and p_2 (right)

shock solutions. In their design principle, these methods are explicit in time. By contrast, the present work is concerned with large time stepping *implicit* strategies. To achieve this goal, we introduce a new set of generalized jump conditions that are well suited to derive a time-implicit scheme. We then devise a linearized time-implicit solver for the sake of efficiency. This solver is shown to preserve the positivity of each internal energy ϵ_i provided that the total internal energy stays positive. At last, numerical evidences prove that the proposed scheme allows to obtain perfectly stationary solutions.

2 A Tractable Equivalent Reformulation

The derivation of an efficient time implicit method for approximating the solutions of (1) relies on a convenient reformulation of the equations. With this in mind, we state the following result :

Lemma 1. *The smooth solutions of (1) satisfy the following equation on the total internal energy* $\rho\epsilon = \sum_{j=1}^{N} \rho\epsilon_j$ *:*

$$\partial_t \rho\epsilon + \nabla.\ \rho\epsilon\mathbf{w} + \sum_{j=1}^{N} p_j \nabla.\ \mathbf{w} = (\sum_{j=1}^{N} \mu_j)(\frac{1}{Rey}\ \sigma : \nabla\mathbf{w}), \tag{2}$$

and the additional conservation law for the total energy $\rho E = \frac{1}{2}\frac{||\rho\mathbf{w}||^2}{\rho} + \rho\epsilon$ *:*

$$\partial_t \rho E + \nabla.\ (\rho E + \sum_{j=1}^{N} p_j)\mathbf{w} = \frac{1}{Rey}\ \ \nabla.\ ((\sum_{j=1}^{N} \mu_j)\sigma.\mathbf{w}). \tag{3}$$

Moreover, the N specific entropies S_i *defined by the second principle of Thermodynamics obey*

$$\partial_t S_i + \mathbf{w}.\nabla S_i = -\frac{\mu_i}{\rho T_i}(\frac{1}{Rey}\ \ \sigma : \nabla\mathbf{w}), \quad i = 1, ..., N, \tag{4}$$

$$and \quad \partial_t ln\frac{S_i}{S_N} + \mathbf{w}.\nabla ln\frac{S_i}{S_N} = C_i(\partial_t \rho\epsilon + \nabla.\ \rho\epsilon\mathbf{w} + \sum_{j=1}^{N} p_j \nabla.\ \mathbf{w}), \qquad (5)$$

$$where\ C_i = \frac{1}{\rho\sum_{j=1}^{N}\mu_j}\Big(\frac{\mu_N}{T_N S_N} - \frac{\mu_i}{T_i S_i}\Big),\ i = 1, ..., N-1.$$

We underline that (3) is in general the only additional *conservation* law satisfied by the smooth solutions of (1). Equations (2), (4) or (5) are indeed in nonconservative form. Observe also that the entropy laws (4) readily yield

$$\partial_t ln\frac{S_i}{S_N} + \mathbf{w}.\nabla ln\frac{S_i}{S_N} = \frac{1}{\rho}\Big(\frac{\mu_N}{T_N S_N} - \frac{\mu_i}{T_i S_i}\Big)\Big(\frac{1}{Rey}\ \sigma : \nabla\mathbf{w}\Big), \qquad (6)$$

while (5) immediately follows from (2) since

$$\frac{1}{Rey}\ \sigma : \nabla\mathbf{w} = \frac{1}{(\sum_{j=1}^{N}\mu_j)}\Big(\partial_t \rho\epsilon + \nabla.\ \rho\epsilon\mathbf{w} + \sum_{j=1}^{N} p_j \nabla.\ \mathbf{w}\Big). \qquad (7)$$

From a numerical point of view, the main advantage of the laws (5) in comparison to (2) or (4) lies in the fact that they do not involve the product of the small parameter $1/Rey$ with the stiff term $\sigma : \nabla\mathbf{w}$ anymore.

This brief discussion suggests to consider ρ, $\rho\mathbf{w}$, ρE and the $(N-1)$ quantities $X_i = ln\frac{S_i}{S_N}$ as the main unknowns of the model. This admissible change of variables leads to the following equivalent reformulation of (1), that we now write in the asymptotic regime of very large Reynolds numbers $(1/Rey << 1)$:

$$\begin{cases} \partial_t \rho + \nabla.\ \rho\mathbf{w} = 0, \\ \partial_t \rho\mathbf{w} + \nabla.\ (\rho\mathbf{w}\otimes\mathbf{w} + \sum_{j=1}^{N} p_j(\rho,\epsilon_j)\ \mathbf{I_d}) = 0 \\ \partial_t \rho E + \nabla.\ (\rho E + \sum_{j=1}^{N} p_j(\rho,\epsilon_j))\mathbf{w} = 0, \\ \partial_t X_i + \mathbf{w}.\nabla X_i = C_i(\partial_t \rho\epsilon + \nabla.\ \rho\epsilon\mathbf{w} + \sum_{j=1}^{N} p_j(\rho,\epsilon_j)\nabla.\ \mathbf{w}), \quad i = 1, ..., N-1. \end{cases} \qquad (8)$$

Here, the total internal energy in the $(N-1)$ last equations is such that $\rho\epsilon = \rho E - ||\rho\mathbf{w}||^2/(2\rho)$, and each internal energy ϵ_i (needed to evaluate the pressures $p_j(\rho,\epsilon_j)$) is recovered by solving in S_N the following equation :

$$\rho\epsilon = \sum_{i=1}^{N-1} \rho\epsilon_i(\rho, S_N exp(X_i)) + \rho\epsilon_N(\rho, S_N). \qquad (9)$$

To conclude this section, we briefly point out the relationships between the additional laws (5) and the so-called generalized jump conditions proposed in [CC1], [CC2]. In these works, the shock solutions of the inviscid limit model (1) obtained in the limit $Rey \to \infty$ are defined by an analysis of the viscous shock profiles. Here, starting from (6) we get

$$\partial_t \rho X_i + \nabla.\ \rho X_i\mathbf{w} = \Big(\frac{\mu_N}{T_N S_N} - \frac{\mu_i}{T_i S_i}\Big)\Big(\frac{1}{Rey}\ \sigma : \nabla\mathbf{w}\Big) \quad i = 1, ..., N-1, \quad (10)$$

and $(N-1)$ additional generalized jump relations are recovered by integrating (10) along a planar viscous profile propagating at speed σ in a given normal direction $\mathbf{n}$. More precisely, if we denote $\mathbf{U}_-$ and $\mathbf{U}_+$ the end states, we have

$$\begin{aligned} &-\sigma\big(\rho X_i(\mathbf{U}_+) - \rho X_i(\mathbf{U}_-)\big) + (\rho X_i \mathbf{w}.\mathbf{n})(\mathbf{U}_+) - (\rho X_i \mathbf{w}.\mathbf{n})(\mathbf{U}_-) \\ &= \int_{\text{viscous profile}} \Big(\frac{\mu_N}{T_N S_N} - \frac{\mu_i}{T_i S_i}\Big)\Big(\frac{1}{Rey}\ \sigma : \nabla \mathbf{w}\Big)\ d\xi, \quad 1 \leq i \leq N-1. \end{aligned} \tag{11}$$

It is shown in [CC1] how to evaluate the right hand side of these $(N-1)$ generalized jump relations, so as to completely characterize the shock solutions of (1) in the asymptotic regime $Rey \to \infty$. Using (7) to define the singular product $\frac{1}{Rey}\ \sigma : \nabla \mathbf{w}$ in the additional laws (5) can be understood as a convenient and consistent way to replace the role played by such a product in the right hand side of (11). In practice, numerical solutions obtained by a time-explicit finite volumes scheme applied to (8) are in very good agreement with the exact solutions characterized by the jump relations (11) (see again Fig. 1).

3 Numerical Approximation

The first three equations in (8) are coupled, in a strong nonlinear way, to the $(N-1)$ last equations by the total internal energy $\rho\epsilon = \rho E - ||\rho \mathbf{w}||^2/(2\rho)$. Our numerical scheme proposes to avoid this coupling using a prediction-correction strategy.

Roughly speaking, the prediction step intends to update the conservative unknowns ρ, $\rho\mathbf{w}$ and ρE in a consistent way and assuming that each X_i is advected by the flow. The correction step will restore the correct evolution of the X_i whereas the density, momentum and total energy will be unchanged. Let us give a bit more detailed description of the prediction-correction strategy we propose. It is a matter of advancing a given discrete solution $\mathbf{U}_h^n = (\rho_h, (\rho\mathbf{w})_h, (\rho E)_h, (X_i)_h)(\mathbf{x}, t^n)$ at time t^n to the next time level t^{n+1}.

Prediction step $(t^n \to t^{n+1-})$: In this step, we solve the Cauchy problem

$$\begin{cases} \partial_t \rho + \nabla.\ \rho\mathbf{w} = 0, \\ \partial_t \rho\mathbf{w} + \nabla.\ (\rho\mathbf{w} \otimes \mathbf{w} + \sum_{j=1}^N p_j(\rho, \rho\epsilon_j)\ \mathbf{I_d}) = 0, \\ \partial_t \rho E + \nabla.\ (\rho E + \sum_{j=1}^N p_j)\mathbf{w} = 0, \\ \partial_t X_i + \mathbf{w}.\nabla X_i = 0, \quad i = 1, ..., N-1, \end{cases} \tag{12}$$

for the initial data $\mathbf{U}_h(\mathbf{x}, t^n)$. This step is treated using a *time implicit* finite volume method in order to avoid too small time steps due to the standard CFL restriction. In practice, we use a relaxation approximation of (12) which permits a natural decoupling between the first three equations associated with ρ, $\rho\mathbf{w}$ and ρE and the $(N-1)$ last ones. The reader is referred to [CCM2] for the details (see also [CCM1]).

Correction step $(t^{n+1-} \to t^{n+1})$: As expected, the updated values of the density, momentum and total energy are kept unchanged, that is

$$\rho_h^{n+1} = \rho_h^{n+1-}, \quad (\rho \mathbf{w})_h^{n+1} = (\rho \mathbf{w})_h^{n+1-}, \quad (\rho E)_h^{n+1} = (\rho E)_h^{n+1-} \tag{13}$$

where $\mathbf{U}_h^{n+1-} = (\rho_h, (\rho \mathbf{w})_h, (\rho E)_h, (X_i)_h)(\mathbf{x}, t^{n+1-})$ denotes the solution obtained at the end of the prediction step. By contrast, the $(X_i)_{1 \le i \le N-1}$ are going to be redefined according to the expected time evolutions

$$\partial_t X_i + \mathbf{w}.\nabla X_i = C_i(\partial_t \rho\epsilon + \nabla.\ \rho\epsilon \mathbf{w} + \sum_{j=1}^{N} p_j \nabla.\ \mathbf{w}), \quad i = 1, ..., N-1, \tag{14}$$

with $(X_i)_h(\mathbf{x}, t^n)$ as initial data.

With this in mind, we first stress that the total internal energy $\rho\epsilon$ is already known at time t^{n+1} by (13), namely :

$$(\rho\epsilon)_h^{n+1} = (\rho E)_h^{n+1} - ||(\rho \mathbf{w})_h^{n+1}||^2/(2\rho_h^{n+1}). \tag{15}$$

The time derivative $\partial_t \rho\epsilon$ in the right-hand side of (14) is thus known at the end of the prediction step and is given by $((\rho\epsilon)_h^{n+1} - (\rho\epsilon)_h^n)/\Delta t$. The spatial derivatives $\nabla.\ \rho\epsilon\mathbf{w} + \sum_{j=1}^{N} p_j \nabla.\ \mathbf{w}$ are treated in a consistent way from the solution $\mathbf{U}_h(\mathbf{x}, t^{n+1-})$ (see [CCM2] for the details) and to simplify the discussion we introduce the notation

$$-\big(\nabla.\ \rho\epsilon\mathbf{w} + \sum_{j=1}^{N} p_j \nabla.\ \mathbf{w}\big)_h^{n+1-} = \Big((\rho\epsilon)_h^{n+1-} - (\rho\epsilon)_h^n\Big)/\Delta t.$$

We eventually end up with the following (not yet fully) discrete form of (14) :

$$\partial_t X_i + \mathbf{w}.\nabla X_i = C_i\Big((\rho\epsilon)_h^{n+1} - (\rho\epsilon)_h^{n+1-}\Big)/\Delta t$$

for $i = 1, ..., N-1$. These advection equations (whose source terms are actually known at the end of the prediction step) are again solved in a time implicit way, leading to a set of updated values $\{X_i(\mathbf{x}, t^{n+1})\}_{i=1,...,N-1}$. The updated solution $\mathbf{U}_h(\mathbf{x}, t^{n+1})$ is then at hand. Nevertheless, in order to be able to restart the algorithm at the next time iteration we need to define each internal energy $\rho\epsilon_i(\mathbf{U}_h(\mathbf{x}, t^{n+1}))$ according to the closure law (9). In other words, we have to solve in $(S_N)_h^{n+1}$ the nonlinear equation

$$\frac{(\rho\epsilon)_h(\mathbf{x}, t^{n+1})}{\rho_h^{n+1}} = \sum_{i=1}^{N-1} \epsilon_i(\rho_h^{n+1}, (S_N)_h^{n+1} exp(X_i)_h^{n+1}) + \epsilon_N(\rho_h^{n+1}, (S_N)_h^{n+1}). \tag{16}$$

Its well-posedness is the matter of the next statement.

Lemma 2. *Assume that the total internal energy $(\rho\epsilon)_h(\mathbf{x}, t^{n+1})$ is positive. Then, the nonlinear algebraic equation (16) admits a unique solution $(S_N)_h^{n+1}$ and allows to define the N positive internal energies $(\epsilon_i)_h^{n+1}$:*

$$(\epsilon_i)_h^{n+1} = \epsilon_i(\rho_h^{n+1}, (S_N)_h^{n+1} exp(X_i)_h^{n+1}) > 0, \quad i = 1, ..., N. \tag{17}$$

4 Numerical Illustration

An example is given on Fig. 2 which shows the results obtained by this solver on a bidimensional computation around a cylinder. The Mach number is approximately equal to 10 (see [CCM2] for the details).

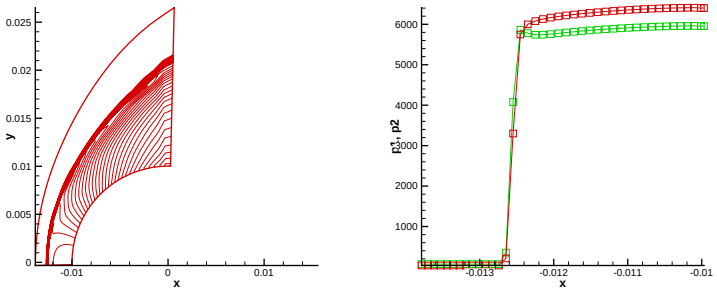

Fig. 2. Density (iso-values) and pressures on the stagnation line

References

[CC1] Chalons, C., Coquel, F.: The Riemann problem for the multi-pressure Euler system. Journal of Hyperbolic Differential Equations 2(3), 745–782 (2005)

[CC2] Chalons, C., Coquel, F.: Navier-Stokes equations with several independent pressure laws and explicit predictor-corrector schemes. Numer. Math. 101(3), 451–478 (2005)

[CCM1] Chalons, C., Coquel, F., Marmignon, C.: Well-balanced time implicit formulation of relaxation schemes for the Euler equations. SIAM J. Sci. Comput. 30(1), 394–415 (2007)

[CCM2] Chalons, C., Coquel, F., Marmignon, C.: Large time-step numerical approximation of the multi-pressure gas dynamics equations in several space dimensions (in preparation)

Smoothness Monitors for Compressible Flow Computation

Bjorn Sjogreen[1] and H.C.Yee[2]

[1] Lawrence Livermore National Laboratory
sjogreen2@llnl.gov
[2] NASA Ames Research Center
helen.m.yee@nasa.gov

Abstract. In [SY04, YS07] and references cited therein, the authors introduced the concept of employing multiresolution wavelet decomposition of computed flow data as smoothness monitors (flow sensors) to indicate the amount and location of built-in numerical dissipation that can be eliminated or further reduced in shock-capturing schemes. Studies indicated that this approach is able to limit the use of numerical dissipation with improved accuracy compared with standard shock-capturing methods. The studies in [SY04, YS07] were limited to low order multiresolution redundant wavelets with low level supports and low order vanishing moments. The objective of this paper is to expand the previous investigation to include higher order redundant wavelets with larger support and higher order vanishing moments for a wider spectrum of flow type and flow speed applications. Studies show that the higher order wavelets with larger support and higher order vanishing moments indicate an improvement relative to the lower order cases.

1 Redundant Wavelets

Assume that we are given a grid function u_j, $j = 1, \ldots, J$ on a grid $x_j = (j-1)\Delta x$. The goal is to detect regions where the grid function does not represent a smooth function on the scale Δx. In theory the degree of smoothness of a function can be deduced from its wavelet coefficients. Here, the basics of the redundant wavelet analysis is briefly summarized [D92].

Basic Wavelet Relations: The wavelet coefficient at x_j on scale m for a function $u(x)$ is defined by

$$w_{m,j}(u) = \int \psi_{m,j}(x)u(x)\,dx,$$

where the wavelet function is

$$\psi_{m,j}(x) = \frac{1}{2^m}\psi((x - x_j)/2^m).$$

It is a scaled and translated version of a mother wavelet function $\psi(x)$. $\psi(x)$ is localized around $x = 0$. Associated with the wavelet function is a scaling function $\phi(x)$. Similar to the wavelet coefficients, the associated scaling function coefficients are

$$f_{m,j}(u) = \int \phi_{m,j}(x)u(x)\,dx,$$

where $\phi_{m,j}(x) = 1/2^m\phi((x - x_j)/2^m)$. Furthermore $\phi(x)$ and $\psi(x)$ are such that the relations

$$\phi(x) = \sum_n a_n\phi(2x - n\Delta x) \qquad \psi(x) = \sum_n b_n\phi(2x - n\Delta x) \tag{1}$$

hold. The sums above are taken over a finite number of terms. Equations (1) give

$$w_{m+1,j} = \tfrac{1}{2}\textstyle\sum_n b_n f_{m,j+n2^m} := D(m)f_{m,j} \tag{2}$$

$$f_{m+1,j} = \tfrac{1}{2}\textstyle\sum_n a_n f_{m,j+n2^m} := A(m)f_{m,j}. \tag{3}$$

Thus, the wavelet and scaling coefficients on scale $m + 1$ are obtained by applying difference operators to the scaling coefficients on scale m. In (2) we denoted the wavelet operator on scale m by $D(m)$ to stress that this operator is usually a differentiation. The scaling function operator on level m, $A(m)$, is usually an averaging operator. The given grid x_j is at scale $m = 0$. The grid function u_j is given at this scale. No information is given about u_j on the smaller scales ($m < 0$). The wavelet decomposition is called redundant if one computes 2J values at scale 1, namely the J wavelet coefficients $w_{1,j}$ and the J scaling functions $f_{1,j}$. This is more information than necessary to represent the original J grid function values. The wavelet decomposition is more often defined without redundancy, i.e., as an expansion in basis functions, by localizing the wavelet coefficients at every second grid point. The J/2 wavelet coefficients and J/2 scaling function values are obtained. With this approach the regularity estimate at a grid point would depend on how the point is aligned with the coarsened grids. Furthermore, the regularity of the wavelet function itself would affect the maximum Lipschitz exponent (regularity estimate) that can be estimated [D92]. For the analysis of u_j, we usually approximate $f_{0,j} = u_j$. From $f_{0,j}$, equations (2) and (3) give $f_{m,j}$ and $w_{m,j}$ for all scales $m > 0$. We focus below on choices for $D(0)$ and $A(0)$. On the coarser scales (2) and (3) define $D(m)$ and $A(m)$ for $m > 0$. For non-periodic boundaries, the difference operators need to be modified at the boundaries. Due to a space limitation, the formulas are not included here (see [SY04] for lower order wavelets).

Vanishing Moments: A wavelet function $\psi(x)$ has k vanishing moments if

$$\int x^n\psi(x)\,dx = 0, \quad n = 0, 1, 2, \ldots, k - 1.$$

The wavelet theory says, see, e.g., [D92, MH92], that a redundant wavelet with k vanishing moments can be used to estimate the number of derivatives of a function, up to the kth derivative, because then the wavelet coefficients $w_{m,j}$ will depend on the scale as $2^{m\alpha}$, where $\alpha < k$ is the Lipschitz exponent of u_j near x_j. The test cases below illustrate the B-spline wavelets. The formula and test results using the redundant form of Harten multiresolution wavelets will be reported in a forthcoming article.

B-spline Wavelets: The Nth degree B-spline wavelet with k vanishing moments have a scaling function whose Fourier transform is

$$\hat{\phi}(\omega) = \left(\frac{\sin \omega/2}{\omega/2}\right)^N \tag{4}$$

and wavelet function with Fourier transform is

$$\hat{\psi}(\omega) = (i\omega)^k \left(\frac{\sin \omega/4}{\omega/4}\right)^{N+k}. \tag{5}$$

We assume that N and k are even numbers. Fourier transformation of (1), use of (4) and (5), and comparison with (2) lead to the difference operators

$$D(0) = (\Delta_+ \Delta_-)^{k/2} \qquad A(0) = (A_+ A_-)^{N/2},$$

where the backward and forward undivided difference operators are

$$\Delta_- u_j = u_j - u_{j-1} \qquad \Delta_+ u_j = u_{j+1} - u_j,$$

and the backward and forward averaging operators are

$$A_- u_j = (u_j + u_{j-1})/2 \qquad A_+ u_j = (u_{j+1} + u_j)/2.$$

The first operators are

$$\begin{aligned}
A(0)u_j &= u_j && (N = 0)\\
A(0)u_j &= (u_{j+1} + 2u_j + u_{j-1})/4 && (N = 2)\\
A(0)u_j &= (u_{j+2} + 4u_{j+1} + 6u_j + 4u_{j-1} + u_{j-2})/16 && (N = 4)
\end{aligned}$$

and

$$\begin{aligned}
D(0)u_j &= u_{j+1} - 2u_j + u_{j-1} && (k = 2)\\
D(0)u_j &= u_{j+2} - 4u_{j+1} + 6u_j - 4u_{j-1} + u_{j-2} && (k = 4).
\end{aligned}$$

The wavelet operators are approximations of the kth derivative, e.g.,

$$u_{j+2} - 4u_{j+1} + 6u_j - 4u_{j-1} + u_{j-2} \approx \Delta x^4 u_{xxxx}(x_j).$$

The averaging operators $A(0)u_j$ are all second order accurate approximations of the point value u_j.

The operators for odd k or N are analogous. The wavelet operators are approximations of odd order derivatives centered at half points. For example, the operators with $k = 3$ are

$$A(0)u_{j+1/2} = (u_{j+2} + 3u_{j+1} + 3u_j + u_{j-1})/8$$
$$D(0)u_{j+1/2} = (u_{j+2} - 3u_{j+1} + 3u_j - u_{j-1}).$$

Regularity Estimate: The grid size at scale m is $2^m \Delta x$. This implies that $(\Delta_- \Delta_+)^{k/2} u_j$ will depend on the scale as $(2^m \Delta x)^k = 2^{mk} \Delta x^k$ if u_j is sampled from a k times differentiable function. According to the theory, [D92, MH92], the local regularity should be measured over the domain of dependence of the point x_j. We define

$$d_{m,j} = \max\{|w_{m,n}| \ \ |n : j \ \text{ in stencil for } \ w_{m,n}\}.$$

If $d_{m,j}$ depend on the scale as $2^{\alpha m}$, then α is the local Lipschitz exponent at x_j of the analyzed function. We use a least squares fit to the model $\log_2 d_{m,j} = \alpha m + c$ to estimate the slope α. With two, three, and four scales this gives the estimates

$$\alpha \approx \log_2(d_{1,j}/d_{0,j}),$$
$$\alpha \approx \frac{1}{2} \log_2(d_{2,j}/d_{0,j}),$$

and

$$\alpha \approx (3 \log_2(d_{3,j}/d_{0,j}) + \log_2(d_{2,j}/d_{1,j}))/10$$

respectively. It is also necessary to avoid division by zero and/or taking the logarithm of zeros. Therefore, if $|w_{m,j}| < 2^{mk}\epsilon$, we set $w_{m,j}$ to $2^{mk}\epsilon$ for some given tolerance ϵ.

2 Test Cases

Due to space limitation, as an illustration, we select for any non-negative even numbers N and k, the B-spline wavelet operator pair

$$D(0) = (\Delta_+ \Delta_-)^{k/2} \quad A(0) = (A_+ A_-)^{N/2}$$

and the multiresolution wavelet operator pair

$$D(0) = \frac{1}{d_0}(\Delta_+ \Delta_-)^{k/2} \quad A(0) = I - D(0),$$

where d_0 is the coefficient in front of u_j in $(\Delta_+ \Delta_-)^{k/2}$. We will test these operators for different values of k and N, and for different number of scales.

Examples using the redundant form of Harten multiresolution wavelets will be reported in a forthcoming article.

Performance of Smoothness Monitors using B-Splines on a Given Data: The given data indicates in the top left of Fig. 1 is the density of a computed solution of a standard 1-D inviscid shock-turbulence interaction test case in gas dynamics. A Mach 3 shock moves to the right into a sinusodial entropy wave. The interaction amplifies the entropy waves and oscillations of higher frequency develop. A few weaker shocks are located behind the physical oscillation region. The solution (given data) in Fig. 1a was computed by the 5th-order WENO scheme on a very fine grid. A good detector should be able to detect the leading shock wave, but classify the physical oscillations ($0.5 < x < 2.4$ and $x > 2.4$) as smooth regions. Samples of estimated regularity exponents "α" are shown in Figs. 1b–1d with the original function shown in black. We investigate the influence of the parameters N, k, and the number of scales (or levels) used for the B-spline wavelets. In all experiments shown, $\epsilon = 10^{-3}$. Figure 1b shows that the estimated α becomes smaller when the B-spline order N is increased (Note that the oscillatory part is classified as regular). In figure 1c, we vary the number of levels (or scales) from two to four. The estimated α becomes lower when the number of levels increases at

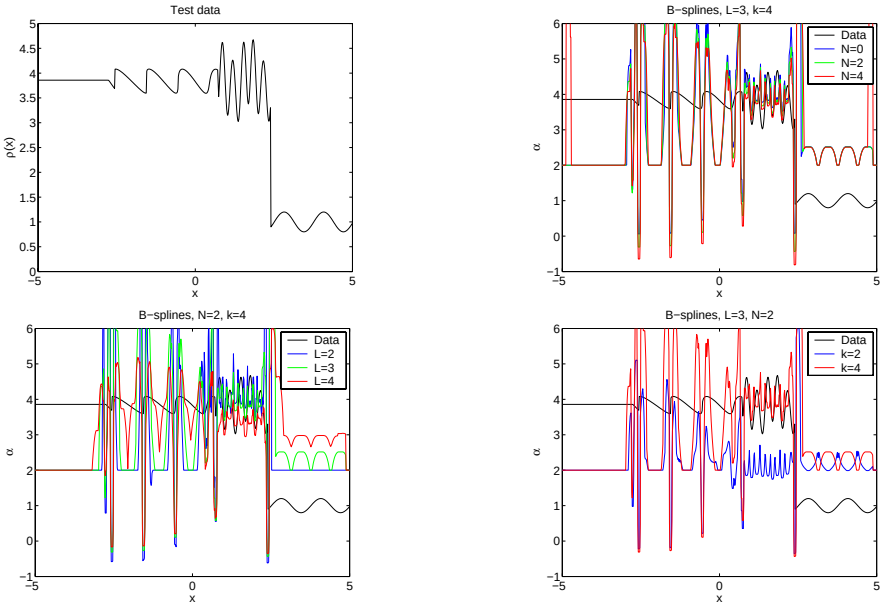

Fig. 1. a) (top left) Test function with jumps and smooth physical oscillations. b) (top right) Estimated α when the B-spline order N varies. c) (bottom left) Estimated α when the number of wavelet levels varies. d) (bottom right) Estimated α when the number of vanishing moments, k, varies.

the oscillations, but at the jumps the estimated α is higher for a larger number of levels. Finally, Fig. 1d shows the α estimate for $k = 2$ and $k = 4$ with N and the number of levels unchanged. Here α is larger for $k = 4$, except at the jump where α is almost unchanged. The influence of the number of vanishing moments is clearly visible for the oscillations. The trends in Figs. 1b–1d were the same for all choices of the fixed parameters. At shock locations, the higher the N, k and L values, the lower the value of α's (near zero or negative spikes). At the physical oscillation region, for all of the studied N, k and L values, the values of α remain positive for the entire region (above 2 in this case). As a second test case to examined how the α behaves at regions of spurious high frequency oscillations (completely due to the numerics), we examined the regularity of the data obtained from the pure convection of a 2-D vortex (inviscid) by the 8th-order central spatial scheme without numerical dissipation added. In this case the exact solution is smooth and a good scheme is expected to convect the vortex without distortion for certain reasonable time lengths. Due to the lack of numerical dissipation and the nonlinearity of the Euler equations, in this case, spurious high frequency oscillation occurs at very early stages of time evolution. The oscillation becomes more pronounced as time progresses and the solution eventually diverges. The data we obtained is at the early stage of the spurious high frequency oscillation. We examined the same N, k and L values. It turns out that at the spurious high frequency oscillation regions, unlike physical oscillations, the αs in this entire region are negative. Thus, the use of α as a flow sensor is a clear cut indication (especially for higher N, k, L values) of the locations of discontinuities (shocks and contacts), physical oscillations and spurious high frequency oscillations.

High Order Filter schemes with Flow Sensors as Part of the Definition of the Filter Numerical Dissipation: The term "smoothness monitor" or "flow sensor" used here is different from a limiter in the sense that, in addition to the built-in limiter existing in shock-capturing schemes,

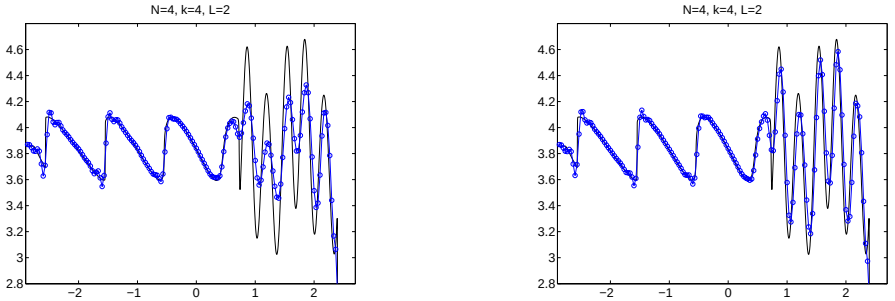

Fig. 2. a) (left) Density by the filter scheme using B-spline wavelet with $N = 2, k = 2, L = 2$ as a flow sensor. b) (right) Density by the filter scheme using B-spline wavelet with $N = 4, k = 4, L = 2$ as a flow sensor.

we use a flow sensor as an adaptive procedure to analyze the computed data to indicate the amount and location of built-in numerical dissipation that can be eliminated or further reduced. For a chosen numerical dissipation term, after incorporating the flow sensor as part of the definition of the numerical dissipation, a less dissipative numerical dissipation model emerges. The improved numerical dissipation model can be used as the replacement of the existing numerical dissipation term. Alternatively, the improved dissipation model can be used to construct a new scheme. An efficient approach is to apply the improved numerical dissipation model as a filter step in conjunction with high order non-dissipative central (compact or non-compact) spatial base schemes. Figure 2 shows the solution of the same 1-D shock-turbulence problem computed by the filter scheme with the 8th-order central spatial base scheme and the dissipative portion of a 2nd-order TVD scheme as part of the filter with $N = 2, k = 2, L = 2$ and $N = 4, k = 4, L = 2$ as B-spline wavelet flow sensors. The limiter is the van Albada limiter for the nonlinear field and super B limiter for the linear field. The slight oscillation around the weak shock regions is typical of the super B limiter effect. The results indicate that higher order N and k values provide higher accuracy solution in the physical oscillation region with similar accuracy around the shock regions. With this adaptive numerical dissipation control of our filter scheme, the accuracy is greatly improved compare with the 5th-order WENO, and it is comparable to a 7th-order WENO scheme using the same grid. However, the 7th-order WENO scheme requires more than three times the CPU time than that of the filter scheme.

Concluding Remarks: The above test cases indicate that the use of multiresolution redundant wavelet decomposition of computed data is a good smoothness monitor with distinct characteristics of Lipschitz exponent for discontinuities (shocks and contacts), physical oscillation and spurious high frequency oscillation (due to the numerics). The smoothness monitors are useful as data analysis and as part of an improved numerical dissipation model or filter scheme. More detailed studies, including complex shock/contact/turbulence interactions and 3-D Navier-Stokes computations will be reported in a forthcoming article.

References

[D92] Daubechies, I.: Ten Lectures on Wavelets. SIAM, Philadelphia (1992)

[MH92] Mallat, S., Hwang, W.L.: Singularity Detection and Processing with Wavelets. IEEE Trans. Inform. Theory 38, 617–643 (1992)

[SY04] Sjögreen, B., Yee, H.C.: Multiresolution Wavelet Based Adaptive Numerical Dissipation Control for Shock-Turbulence Computation. J. Scient. Computing 20, 211–255 (2004)

[YS07] Yee, H.C., Sjögreen, B.: Development of Low Dissipative High Order Filter Schemes for Multiscale Navier-Stokes/MHD Systems. J. Comput. Phys. 225, 910–934 (2007)

“*This page left intentionally blank.*”

Part 40
Wake Flow

“*This page left intentionally blank.*”

Proper Orthogonal Decomposition of Unsteady Heat Transfer from Staggered Cylinders at Moderate Reynolds Numbers

Sirod Sirisup and Saifhon Tomkratoke

Large-Scale Simulation Research Laboratory, National Electronics and Computer Technology Center 112 Thailand Science Park, Klong 1, Klong Luang, Pathumthani 12120, Thailand
{sirod.sirisup,saifhon.tomkratoke}@nectec.or.th

Summary. The characteristics of forced convection heat transfer from a pair of circular cylinders in staggered arrangements with heated upstream cylinder are investigated. The longitudinal separation to cylinder diameter ratio and the transverse separation to cylinder diameter ratio are varied from 2.5 to 5 and from 0.5 to 1, respectively. Three-dimensional direct numerical simulations (DNS) have been performed using the spectral/hp element method with the Reynolds numbers, Re, of 500 and 1000 and the Prandtl number, Pr, of 0.71. The identification of major spatially distributed features is done by extracting the proper orthogonal decomposition (POD) modes from ensemble of simulation solutions. The correlation between flow, heat transfer characteristics and POD modes is discussed.

1 Introduction

Analysis of wake vortex dynamics has long been major subject of interest to engineers and scientists for many years. Understanding wake dynamics behind a bluff body has been great challenge for decades. Despite of its simple geometry, circular cylinder wake flows exhibit rich flow features and yet have many direct engineering and science applications. The alternate shedding pattern of vortices in the wake region, leads to large fluctuating pressure forces in a direction transverse to the flow and may cause vortex-induced vibrations which in some cases can trigger structural failures, [Wil96]. The phenomena of vortex dynamics near wall or behind a bluff body plays important role in the change of heat transfer characteristics, [Fie98]. For example, in a heated circular cylinder, thermal energy is trapped in the viscous layer of the cylinder which released through the separation of viscous layer from the rear surface in the form of narrow pathways directed away from the cylinder wall, [BC06]. The phenomena of wake vortex dynamics between a pair of cylinders placed either inline or staggered can play important role in the change of heat transfer characteristics of the cylinders. Moreover, deeply

understand transport/dispersion mechanism of mass or pollutants can be drawn from studies of heat transfer mechanism because the mechanism of mass/pollutants transfer mimics those of heat transfer [BC06]. The purpose of this study is to characterize forced convection heat transfer due to the wake vortex dynamics in three-dimensional circular cylinders placed in staggered arrangement through direct numerical simulation.

The proper orthogonal decomposition (POD) method is a statistical tool used to identify low-dimensional descriptions for multidimensional systems, [HLB98]. The method has been successfully applied in wide range of scientific applications, for example, fluid flows, biomechanics and geophysical fluid dynamics. In this study, we apply the POD technique to identify dominant spatially distributed features or POD modes of heat transfer from staggered cylinders at $Re = 500$ and $Re = 1000$. The results of analyzing POD modes will allow us to elucidate the heat transfer mechanism in the problem.

The paper is organized as follows. In next section, we describe computational details for the direct numerical simulation used to obtain local heat transfer. Later, we present the results and some discussion. Finally, we conclude the paper with a short summary.

2 Computational Details

Non-dimensional unsteady, incompressible, momentum and energy equations without external forcing or buoyancy effects are:

$$\begin{aligned} \nabla \cdot \mathbf{u} &= 0 \\ \frac{\partial \mathbf{u}}{\partial t} + \mathbf{u} \cdot \nabla \mathbf{u} &= -\nabla p + \frac{1}{Re} \nabla^2 \mathbf{u} \\ \frac{\partial T}{\partial t} + \mathbf{u} \cdot \nabla T &= \frac{1}{RePr} \nabla^2 T \end{aligned}$$

Where, Re is the Reynolds number, Pr is the Prandtl number. Here Re is defined through: $\frac{DU}{\nu}$ and D is the cylinder diameter.

A computational domain with dimension of $40D \times 9D \times 1D$ (streamwise-crossflow-spanwise) was employed for this investigation. A pair of cylinders both with diameter of $D = 1$ are placed in various staggered arrangements with longitudinal separation (L) to cylinder diameter (D) ratio (L/D) and transverse separation (T) to cylinder diameter (D) ratio (T/D) of 2.5-5.0 and 0.5-1.0, respectively. In each case, the computational domain is decomposed into approximately 13000 tetrahedral elements.

Uniform steady inflow is imposed on inflow boundary and zero Neumann condition is imposed on outflow boundary while no-slip condition is imposed to cylinder walls and symmetry condition is prescribed for crossflow and spanwise directions. Temperature is set to be unity only for the upstream cylinder and zero for the downstream cylinder as well as the inflow boundary while zero

Neumann condition on temperature is imposed on the outflow boundary and symmetry condition is prescribed for crossflow and spanwise directions.

The flow parameters used in this study are $Re = 500$ and $Re = 1000$ with $Pr = 0.71$. Converged solutions were obtained by solving the governing equations using the spectral/hp element library, [KS05]. The Characteristic Galerkin method is chosen to be a stabilizer for the solver. In the resolution dependency study, we conclude that the Jacobi polynomial basis of order seven is sufficient for this investigation. Characteristic of local heat transfer is obtained by measuring the local Nusselt number on the cylinders' wall. The proper orthogonal decomposition method is applied to extract dominant features or POD modes from ensembles of simulation solutions. In order to reduce the computational cost, the method of snapshots by Sirovich, [Sir87], is employed in the POD mode extraction process.

3 Results and Discussion

3.1 Flow and Heat Transfer Characteristics

From the aforementioned flow configurations, the results from simulations suggest that flow characteristics can be divided into three regimes, [JK03], as follows:

Reattachment Regime

The reattachment regime is found for the case of $L/D = 2.5$ with $T/D = 0.5$. The inner shear layers separating from the upstream cylinder reattach onto the outer surface of the downstream cylinder then sweep along the inner surface of the downstream cylinder. These shear layers directly influence characteristic of heat transfer near the front surface of downstream cylinder. The

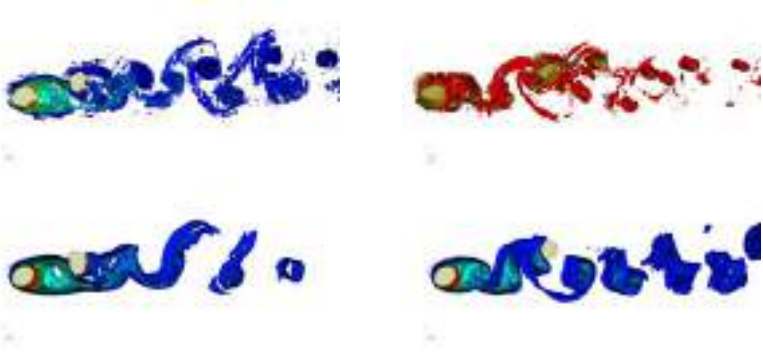

Fig. 1. Instantaneous iso-surface plots for the case of Re=500, from top to bottom: vorticity core, temperature field. From left to right: (L/D=2.5, T/D=0.5),(L/D=5.0, T/D=1.0). Each column presents the plots at the same instant.

wake of the upstream cylinder is stabilized by the downstream cylinder yielding a steady state flow circulation region. The releasing of trapped thermal energy from upstream cylinder in the outer shear layers slightly affect heat transfer characteristic in the surface of downstream cylinder. The 2S vortex shedding pattern has been observed behind the downstream cylinder, see figure 1.

Biased Gap Regime

This regime is observed for the case of $L/D = 2.5$ with $T/D = 1.0$. The flow in the gap between the cylinders is deflected down toward the upstream cylinder resulting in the deflection of thermal energy along the gap toward the upstream cylinder. The wake behind the upstream cylinder becomes unsteady while irregular vortex street is formed behind the downstream cylinder. Two distinctive near wakes are formed: one wide (downstream cylinder) and one narrow (upstream cylinder). The thermal energy is also trapped in viscous layer which is shed and convected slightly upward. Only small effects on heat transfer characteristic on the surface of the downstream cylinder are found.

Two Vortex Streets Regime

The two vortex streets regime is found for the case of $L/D = 5.0$ with both $T/D = 0.5$ and $T/D = 1.0$. Here, vortices are shed continuously from both cylinders forming two three-dimensional vortex streets. The thermal energy is trapped in unsteady viscous layers which later are shed and convected downstream. The heat transfer characteristics near the front surface of the downstream cylinder are mostly affected by the interference of primary vortex, see figure 1. In this case, large interference effects on local heat transfer characteristic of the front surface of the downstream cylinder are observed. The effects expand downstream along the cylinder surface and heighten at higher Reynolds number, however, the characteristic of vortex shedding pattern is still similar.

3.2 Proper Orthogonal Decomposition

First, we focus on the energy distribution of the POD modes for each case. In all cases, the first POD mode (the mean mode) of both velocity and temperature fields dominates all the other modes by capturing more than 60% of the total energy captured by all of the modes, see figure 2. The pairing of higher POD modes (greater than one) of the temperature field is clearly observed only for the case of L/D=5.0 with T/D=1.0 and $Re = 500$.

The spatial distribution of the modes in each flow regime is described as follows.

Reattachment Regime

The reattachment to the downstream cylinder of the flow and temperature field is fully captured by the first mode. The higher POD modes of the temperature indicates that the main activity region in this case includes the wake region of the downstream cylinder. The 2S vortex shedding pattern is confirmed by the spatial distribution of the velocity modes from the upstream and downstream cylinders.

Biased Gap Regime

In the regime, we clearly see the deflection in the first POD mode from the center of the upstream cylinder. The main activity region of the temperature field includes only in some region below and behind the downstream cylinder (only some part of the wake region of the downstream cylinder). More complicated flow structures are observed in the POD modes of the temperature field as well. POD modes of velocity show more distinctive wake regions of each cylinder which clearly observed from the distribution of the velocity modes, especially the crossflow velocity component, from the upstream and downstream cylinders.

Two Vortex Streets Regime

In the regime, the main activity region of the temperature field covered entire wake regions from both cylinders which confirms the flow and heat characteristics in section 3.1. The patterns of the POD modes becomes more distinctive for each cylinder and are clearly observable in the case of L/D=5.0 with T/D=1.0 and $Re = 500$. This fact together with the distribution of the energy distribution of the eigenvalues in figure 2 indicates that the existence of the downstream cylinder provides only slightly affects to the pattern of the temperature field compared to the case of single cylinder. However, it is not the case for higher Re. We also find that the lower T/D ratio, the more complicated structures in the wake region are formed.

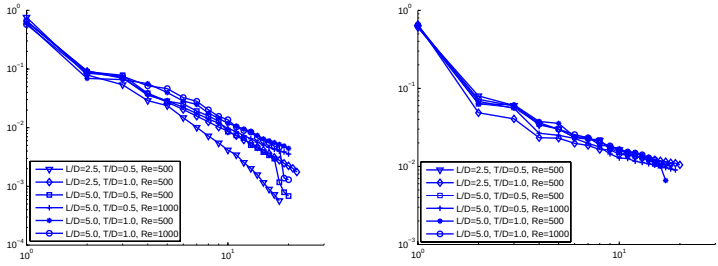

Fig. 2. Energy distribution of POD modes for all cases. Left: Velocity fields. Right: Temperature fields

Fig. 3. Proper orthogonal decomposition modes. Left to right: (L/D=2.5, T/D=0.5), (L/D=5.0, T/D=1.0). Top to bottom: streamwise velocity first mode and second mode, temperature first mode and second mode.

4 Summary

Incompressible flow around a pair of circular cylinders in staggered arrangements with heated upstream cylinder is investigated in this paper. We have found that: flow configuration in the two vortex streets regime leads to large interference effects on local heat transfer characteristic of the front surface of the downstream cylinder compared to the other two regimes. And, in the same regime, the wake of the upstream cylinder exhibits stronger unsteadiness for longer transverse pitch ratio. From the proper orthogonal decomposition analysis, we found that the spatial distribution of the modes in each flow regime directly relates to the flow characteristic in that particular regime besides the analysis indicates that for a larger L/D and T/D ratio in the lower Reynolds number cases, the existence of the downstream cylinder slightly affects the pattern of the temperature field.

Acknowledgments

The authors gratefully acknowledge high performance computing service from both Large Scale Simulation Research Laboratory, NECTEC and Thai National Grid Center.

References

[Wil96] Williamson, C.H.K.: Vortex dynamics in the cylinder wake. Ann. Rev. Fluid Mech. 28, 477–539 (1996)

[PS06] Praisner, T.J., Smith, C.R.: The Dynamics of the Horseshoe Vortex and Associated Endwall Heat Transfer–Part I: Temporal Behavior. J. Turbomach 128(4), 747–754 (2006)

[BC06] Bouhairie, S., Chu, V.: Two-dimensional simulation of unsteady heat transfer from a circular cylinder in crossflow. J. Fluid Mech. 570, 177–215 (2006)
[Fie98] Fiebig, M.: Vortices, Generators and Heat Transfer. Chemical Engineering Research and Design 76, 108–123 (1998)
[ZY06] Zhou, Y., Yiu, M.W.: Flow structure, momentum and heat transport in a two-tandem-cylinder wake. J. Fluid Mech. 548, 17–48 (2006)
[KS05] Karniadakis, G.E., Sherwin, S.A.: Spectral/hp element methods for computational fluid dynamics. Cambridge University Press, UK (2005)
[Sir87] Sirovich, L.: Turbulence and the dynamics of coherent structures. Parts I, II and III., Quart. Appl. Math. XLV, 561–590 (1987)
[HLB98] Holmes, P., Lumley, J.L., Berkooz, G.: Turbulence, Coherent Structures, Dynamical Systems and Symmetry. Cambridge University Press, UK (1998)
[JK03] Jester, W., Kallinderis, Y.: Numerical study of incompressible flow about fixed cylinder pairs. J. Fluid and Structures 17, 561–577 (2003)

“*This page left intentionally blank.*”

Effect of Rotation Rates and Gap Spacing on the Structure of Low Reynolds Number Flow over Two Rotating Circular Cylinders

Surattana Sungnul[1] and N.P. Moshkin[2]

[1] Department of Mathematics, King Mongkut's University of Technology North Bangkok, Bangkok, 10800, Thailand
ssj@kmutnb.ac.th
[2] School of Mathematics, Suranaree University of Technology, Nakhon Ratchasima, 30000, Thailand
moshkin@math.sut.ac.th

Summary. A two-dimensional numerical study on the laminar flow past two circular cylinders rotating with constant angular velocity was carried out. Algorithm of solution based on the projection method. The numerical algorithm has been validated using available experimental and numerical examples. The flow structure around two rotating cylinders were found to differ substantially from the behavior of two non rotating circular cylinders placed in a uniform stream. The diagram of flow structures was constructed depending on the Reynolds number, the rate of cylinder rotation and the gap spacing. The drag and lift forces are affected by rotation. The drag force decreases with increasing rotational velocities even leading to negative values and the lift force changes direction from repulsion to attraction force.

1 Introduction

There has not been extensive research on free stream flow around two rotating circular cylinder. Most of the reported studies on two cylinder configurations were concerned with two non rotating cylinders of an identical diameter (see for example [Kang03] and literature cited there).

In the present paper, flow structures were calculated between two identical rotating circular cylinders which are held fixed side-by-side (or transverse) against a uniform stream flow directed perpendicular to the line connecting the cylinders' centers, at different Reynolds number, gap spacing and rate of cylinder rotations.

2 Governing Equations and Numerical Methods

Let us consider two infinitely long cylinders placed in a uniform flow, perpendicular with their line of centers, of an incompressible fluid having free

stream velocity U_∞. Let a system of Cartesian coordinates (x, y, z) be chosen so that the centers of the cylinders lie along the x-axis. The cylinders being considered infinitely long, the flow does not depend on z-coordinate. The most convenient coordinate system for a pair of cylinders is the orthogonal bipolar cylindrical coordinate system. The governing equation is the Navier-Stokes equations written in cylindrical bipolar coordinates. Numerical simulations of two-dimensional incompressible flow over two rotating circular cylinders in side-by-side arrangement are conducted using projection method.

The cylindrical bipolar coordinate system defined by the following equations

$$x = \frac{a \sinh \eta}{\cosh \eta - \cos \xi}, \quad y = \frac{a \sin \xi}{\cosh \eta - \cos \xi}, \tag{1}$$

where $\xi \in [0, 2\pi)$, $\eta \in (-\infty, \infty)$, a is a characteristic length in the cylindrical bipolar coordinate system which is positive. This transformation maps the (x, y) plane (from which the domain occupied by the cylinders is excluded) into the rectangle $\eta_2 \le \eta \le \eta_1$, $0 \le \xi \le 2\pi$, $\eta_2 < 0$, $\eta_1 > 0$. The surfaces of the cylinders are located at $\eta = \eta_2$ and $\eta = \eta_1$. The cylinders' radii r_1 and r_2 and the distances of their centers from the origin d_1 and d_2 are given by $r_i = a \ \mathrm{csch}|\eta_i|, \quad d_i = a \ \coth|\eta_i|, \quad i = 1, 2$. The center to center distance between the cylinders is $d = d_1 + d_2$. The boundary conditions are a no-slip requirement on cylinders

$$v_\xi = \omega_i r_i, \ v_\eta = 0, \ \eta = \eta_i, \ i = 1, 2, \tag{2}$$

where v_ξ and v_η are the physical components of velocity vector $v = (v_\xi, v_\eta)$ in the coordinate system (1), ω_i, $i = 1, 2$ are rotational velocities of the cylinder walls. Positive values of ω_i, $i = 1, 2$ correspond to counterclockwise rotation. Upstream and downstream boundary conditions at the infinity are

$$v_x = 0, \quad v_y = U_\infty, \quad r^2 = x^2 + y^2 \to \infty, \tag{3}$$

where v_x and v_y are components of the velocity vector in x and y directions, respectively. The net force exerted by fluid on an immersed body with surface Σ are $F = \int_\Sigma \tau \, dS$. The force per unit area exerted across a rigid boundary element with outward normal n in an incompressible fluid is defined by $\tau = -pn - \mu(n \times curl(v))$ where p is the pressure and μ is the coefficients of dynamic viscosity. If F_{x_i} and F_{y_i}, $i = 1, 2$ are the lift and drag on the cylinders, the lift and drag coefficients are defined by $C_{L_i} = \frac{F_{x_i}}{\rho U_\infty D}$, $C_{D_i} = \frac{F_{y_i}}{\rho U_\infty D}, i = 1, 2$, and each consists of components due to the friction forces and the pressure $C_L = C_{Lf} + C_{Lp}$, $C_D = C_{Df} + C_{Dp}$,

The problem variables can be made dimensionless by using characteristic length D, the diameter of cylinders, the velocity scale U_∞, the oncoming free stream velocity and kinematic viscosity coefficient ν. For such choice of parameters the solution depends not only on the Reynolds number, Re, but also on the non-dimensional gap spacing between two cylinders, g , and

Table 1. Sequence of grid; Drag and lift coefficient at $Re = 20$ and $g = 14$, $\alpha = 1.0$

grid	C_D	C_{D_p}	C_{D_f}	C_L	C_{L_p}	C_{L_f}
40×40	1.858	1.033	0.825	2.740	2.393	0.347
80×80	1.887	1.061	0.826	2.797	2.437	0.360
160×160	1.901	1.074	0.827	2.802	2.440	0.362

Table 2. Hydrodynamic parameters of flow over a rotating circular cylinder at $Re = 20$ with $g = 14$

Re	Contribution	C_D			C_L		
		$\alpha = 0.1$	$\alpha = 1.0$	$\alpha = 2.0$	$\alpha = 0.1$	$\alpha = 1.0$	$\alpha = 2.0$
20	Present (80x80)	2.119	1.887	1.363	0.291	2.797	5.866
	Badr *et al.* (1989)	1.990	2.000	—	0.276	2.740	—
	Ingham and Tang (1990)	1.995	1.925	1.627	0.254	2.617	5.719
	Chung (2006)	2.043	1.888	1.361	0.258	2.629	5.507

on parameters, α_i representing the ratios of the rotational velocities of the cylinder walls to the oncoming flow velocity

$$Re = U_\infty\, D/\nu,\ \ \alpha_i = D\omega_i/2U_\infty,\ i = 1, 2,\ \text{ and }\ g = \frac{d - r_1 - r_2}{D}.$$

It is well known that for large gap spacing between the two surfaces of the cylinders the mutual influence between cylinders disappear, leading to separate flow over single cylinders. To validate the numerical algorithm, the uniform flow past fixed and rotating circular cylinders with $0 \leq Re \leq 40$, $0 \leq \alpha_1 (= \alpha_2) \leq 2.5$ and with a large gap between cylinder surfaces $g = 14$ have been calculated and the results compared with experimental and simulation data for flow past a single cylinder. All the simulations have been performed in a large domain so as to reduce the influence of the outer boundary. A sequence of uniform grids is used. The accuracy and grid independence of the numerical results is checked by computations on various grids and shown in Table 1. The simulation was carried out on three grids with $h_{\xi 1} = 0.165, h_{\eta 1} = 0.174,\ h_{\xi 2} = 0.082, h_{\eta 2} = 0.087,\ h_{\xi 3} = 0.041, h_{\eta 3} = 0.043$. The time step size $\triangle t = 0.001$.

To the authors' knowledge, there are very few published data of drag and lift coefficients at $Re \leq 40$ and angular speed even for flow past single cylinder. Table 2 lists the calculated lift and drag coefficients and makes a comparison with [Badr89] [Ingh90] and [Chung06]. It can be seen that the differences are acceptable for C_D and C_L.

3 Results

After validating the numerical method, we have conducted numerical simulations of flow past constantly rotating circular cylinders of equal radii in a

side-by-side arrangement at Reynolds numbers $Re = 5,\ 10,\ 20$ and 40, rate of rotation $0.5 \leq \alpha \leq 5.0$ and nondimensional gap spacing $g = 0.5,\ 1,\ 1.5$. Both cylinders are placed in a stream (from down to up) of uniform velocity U_∞ at infinity. The left cylinder ($r = r_2$) is rotating with constant clockwise angular velocity and right cylinder ($r = r_1$) is rotating with constant counterclockwise angular velocity. The influence of the rotation rate $\alpha = \alpha_1 = \alpha_2 = |\omega_i|D/2U_\infty$ is demonstrated in Figures 1 and 2.

Figure 1 gives the values of drag and lift coefficients in cases $Re = 10,\ 20,\ 40$ and $g = 1$ for $0.5 \leq \alpha \leq 3.0$. Indexes 1 and 2 correspond to the right and left cylinders, respectively. The fluid forces are distributed over the two cylinders such that lift forces in $x-$direction on the combined system are in equilibrium, $C_{L_1} + C_{L_2} \equiv 0$. However, the fluid forces acting upon an individual cylinder demand that some additional external forces are applied to it in order for its position to remain fixed. Figure 2 demonstrates the vectors of total force acting on right cylinder as a function of the rotation rate α at $Re = 20$.

The absolute values of lift coefficients increase with increasing α up to $\alpha = 2.0$ for the $Re = 10$ and up to $\alpha = 2.5$ for the $Re = 20,\ 40$. The lift forces acting on cylinders mostly result from the pressure force, as shown in

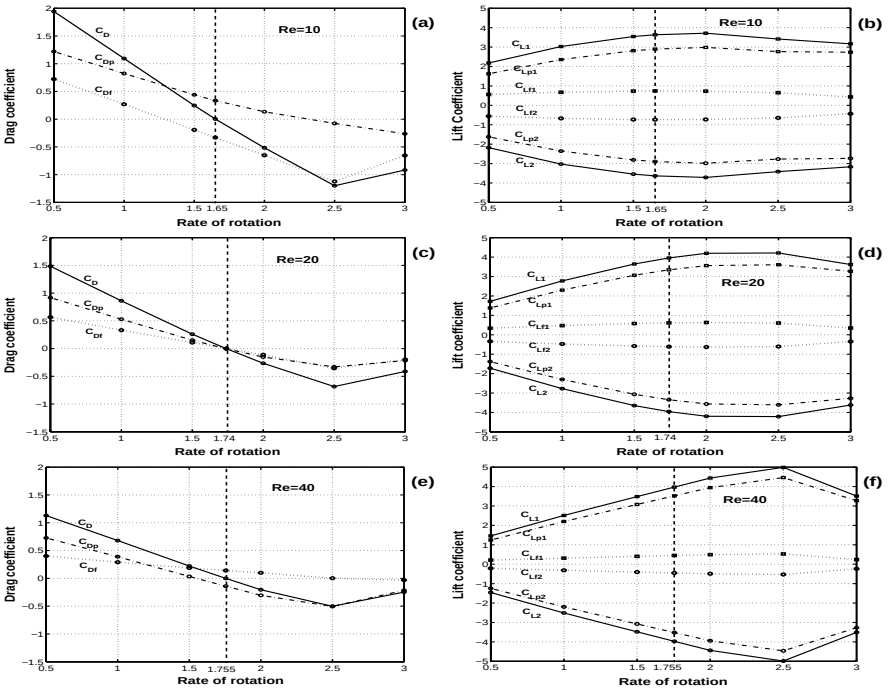

Fig. 1. Drag and lift coefficients at $Re = 10$ (a)-(b), $Re = 20$ (c)-(d), $Re = 40$ (e)-(f) and $g = 1$, $\alpha \in [0.5, 3.0]$

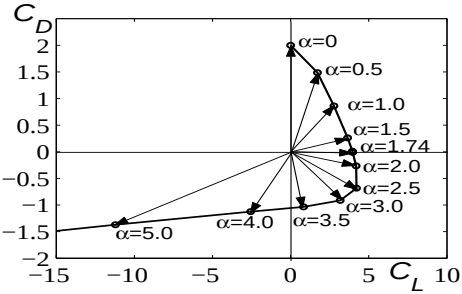

Fig. 2. Vector of force on right cylinder. $Re = 20$, $g = 1$

the Figures 1(b), 1(d) and 1(f). The pressure contribution in C_L increases with increasing Re, which is the same behavior as observed in the study of [Stoj02]Stojkovic *et. al.* (2002) for the case of a single rotating cylinder. The drag coefficients decrease with increasing α up to $\alpha = 2.5$ (see Figures 1(a), 1(c), and 1(e)). For $\alpha = \alpha^* \approx 1.65$ ($Re = 10$), $\alpha = \alpha^* \approx 1.74$ ($Re = 20$) and $\alpha = \alpha^* \approx 1.755$ ($Re = 40$) the drag force becomes zero. This case corresponds to the self-propelled motion of cylinders as a coupled body. It is interesting that both C_{D_p} and C_{D_f} decrease with increasing α up to $\alpha = 2.5$, (see Figures 1(a), 1(c) and 1(e)), resulting in negative values of C_{D_p} and C_{D_f} for higher rotational velocities. This is opposite to the case of flow past a single rotating cylinder, where C_{D_f} increases and C_{D_p} decreases with increasing α [Stoj02](Stojkovic *et al.*, 2002). Additionally, for $Re = 10$ and $\alpha > \alpha^* \approx 1.65$ the total drag force is negative because C_{D_f} dominates over C_{D_p}. In the case of flow around a single rotating cylinder the effect is quite different. Rate of decrease C_{D_p} and C_{D_f} with increasing α depends on Reynolds number. At $Re = 10$, C_{D_f} decreases more quickly than C_{D_p}. At $Re = 20$, C_{D_p} decreases faster than C_{D_f} up to values $\alpha = \alpha^* \approx 1.74$. Further rates of decrease are approximately identical up to $\alpha = 2.5$. At $Re = 40$, rate of decrease of C_{D_p} is much faster than C_{D_f}. This behavior is visible in Figures 1(a), 1(c) and 1(e). It has to be pointed out that the self-propelled regime happened due to different reasons at $Re = 10$, $Re = 20$ and at $Re = 40$. In the case of $Re = 10$ the drag $C_D \simeq 0$ is due to $C_{D_p} \approx -C_{D_f} \approx 0.33$. In the case of $Re = 20$ the self-propelled regime corresponds to $C_D \simeq 0$ due to $C_{D_p} \approx -C_{D_f} \approx 0$. At $Re = 40$, $C_D \approx 0$ due to $C_{D_p} = C_{D_f}$ and C_{D_f} is positive.

It is interesting that C_D decreases up to $\alpha = 2.5$ and for $\alpha > 2.5$ drag coefficient increases for all $Re = 10,\ 20,\ 40$. Increasing of drag coefficient for $Re = 10$ causes by the increasing of C_{D_p}. Coefficient C_{D_f} continues to decrease for $\alpha > 2.5$. In case of $Re = 20$ both pressure and friction coefficients start to increase at $\alpha > 2.5$ consequently lead to increasing of C_D. Quite opposite behavior of C_{D_p} and C_{D_f} at $Re = 40$, compared with case $Re = 10$, observe in Figure 1(e). Increasing of C_D for $\alpha > 2.5$ is happened due to increasing C_{D_f}. Coefficient C_{D_p} continues to decrease. Fig. 2 demonstrate

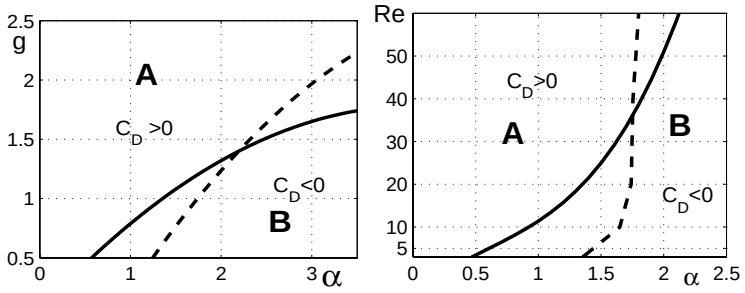

Fig. 3. Flow patterns observed behind two side-by-side circular cylinders with varying Re, g, and α

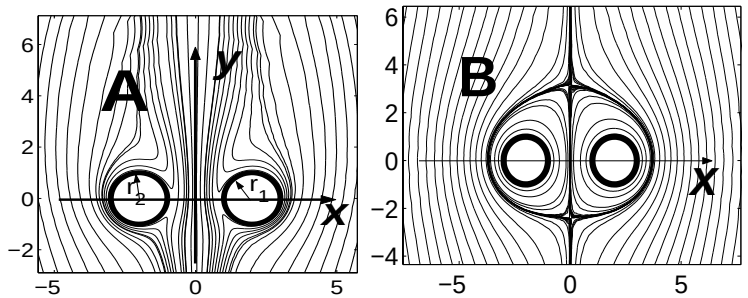

Fig. 4. Two types of flow patterns observed behind two side-by-side circular cylinders

the diagram of force vector acting on the right cylinder ($r = r_1$). There is a repulsive force acting on the cylinders, $C_{L_1} > 0, C_{L_2} < 0$ for $\alpha < 3.6$. For the higher speed of rotation a repulsing force transforms to an attraction force $C_{L_1} < 0, C_{L_2} > 0$.

It has been found that the flow pattern strongly depends both on the Reynolds number, gap spacing, and rate of rotation and, moreover, either of two flow patterns can occur at certain flow conditions, these patterns called **"A"** and **"B"** in Fig. 4. The schematic diagrams of $g-\alpha$ and $Re-\alpha$ plane are symbolized in Fig. 3. The solid lines represent the approximate boundaries between two type of flow patterns. These pattern are shown in Fig. 3. The dashed lines correspond to the self-propelled motion of two cylinders as a coupled body, $C_D = 0$.

Acknowledgments

The authors acknowledgment the financial support of the Department of Mathematics, King Mongkut's University of Technology North Bangkok.

References

[Kang03] Kang, S.: Characteristics of flow over two circular cylinders in a side-by- side arrangement at low Reynolds numbers. Phys. of Fluids 15(9), 486–498 (2003)

[Badr89] Badr, T., Dennis, S.C.R., Young, P.J.S.: Steady and unsteady flow past a rotating circular cylinder at low Reynolds numbers. Computers & Fluids 17(4), 579–609 (1989)

[Ingh90] Ingham, D.B., Tang, T.: A numerical investigation into the steady flow past a rotating circular cylinder at low and intermediate Reynolds numbers. J. Comput. Phys. 87, 91–107 (1990)

[Chung06] Chung, M.-H.: Cartesian cut cell approach for simulating incompressible flows with rigid bodies of arbitrary shape. Computers & Fluids 35(6), 607–623 (2006)

[Stoj02] Stojkovic, D., Breuer, M., Durst, F.: Effect of high rotation rates on the laminar flow around a circular cylinder. Phys. of Fluids 4(9), 3160–3178 (2002)

“*This page left intentionally blank.*”

Improvement of Reduced Order Modeling Based on POD

M. Bergmann, C.-H. Bruneau, and A. Iollo

INRIA Bordeaux Sud Ouest, Team MC2 and Université de Bordeaux, UMR 5251, Bordeaux, F-33000, France
michel.bergmann@inria.fr, charles-henri.bruneau@math.u-bordeaux1.fr, angelo.iollo@math.u-bordeaux1.fr

Summary. This study focuses on stabilizing reduced order model (ROM) based on proper orthogonal decomposition (POD) and on improving the POD functional subspace. A modified ROM that incorporates directly the pressure term is proposed. The ROM is stabilized using Navier-Stokes equations residuals and exploiting ideas similar to the variational multiscale method. The POD functional subspace is improved thanks to an hybrid method that couple DNS and POD ROM. Results are shown for a 2D confined cylinder wake flow.

1 Introduction

This paper focuses on improving reduced order modeling (ROM) based on proper orthogonal decomposition (POD). Besides the possible inherent lack of numerical stability of POD/Galerkin methods [10], the main shortcomings are the following. Firstly, since in most of the POD applications the ROM is built from a velocity database it is necessary to model the pressure term [5, 8]. To overcome this difficulty, a pressure extended ROM is introduced in §2, so that the pressure term can be directly approximated using the pressure mode. Secondly, due to the energetic optimality of the POD basis, only few modes are sufficient to give a good representation of the flow kinetic energy. However, the viscous dissipation mainly takes place in the small unresolved eddies. A ROM built with very few modes is thus not able to dissipate enough energy. It is then necessary to close the ROM by modeling the effects of the unresolved modes. In this study, we use the residuals of the Navier-Stokes (NS) equations (§3) and exploit ideas similar to the variational multiscale method (VMS) [1]. Finally, since POD basis functions are optimal to represent the main characteristics of the flow configuration used to build them, the same basis functions are not optimal to represent the main characteristics of other flow configurations [3, 7, 9]. To overcome this problem, we propose an hybrid method that couples DNS and ROM to adapt the POD basis functions at low numerical costs (§4).

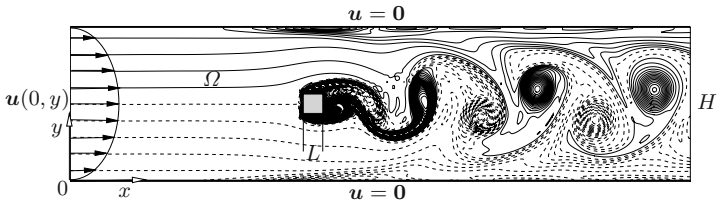

Fig. 1. Flow configuration and vorticity snapshot at $Re = 200$

Our paradigm is the confined square cylinder wake flow (figure 1) in laminar regime, *i.e.* at Reynolds number $Re = U_\infty L/\nu \leq 200$, with $U_\infty = u(0, H/2)$, L the lenght of the side of the square cylinder and ν the kinematic visosity. We use the same parameters as those introduced in [5].

2 A Pressure Extended Reduced Order Model

It has been proven [8] that neglecting the pressure term can lead to large ROM errors. One solution is to model this pressure term [5, 8]. The pressure term can also be calculated using a pressure extended ROM with $p = \widetilde{p}$. Indeed, the POD flow fields write $\widetilde{\boldsymbol{u}}(\boldsymbol{x}, t) = \sum_{i=1}^{N_r} a_i(t)\boldsymbol{\phi}_i(\boldsymbol{x})$ and $\widetilde{p}(\boldsymbol{x}, t) = \sum_{i=1}^{N_r} a_i(t)\psi_i(\boldsymbol{x})$, see [2] for more details. Moreover, it is possible to evaluate the Navier-Stokes residuals (§3). The ROM, noted $A^{[N_r]}$, is:

$$\sum_{j=1}^{N_r} L_{ij} \frac{\mathrm{d}a_j}{\mathrm{d}t} = \sum_{j=1}^{N_r} B_{ij} a_j + \sum_{j=1}^{N_r} \sum_{k=1}^{N_r}, C_{ijk} a_j a_k \tag{1}$$

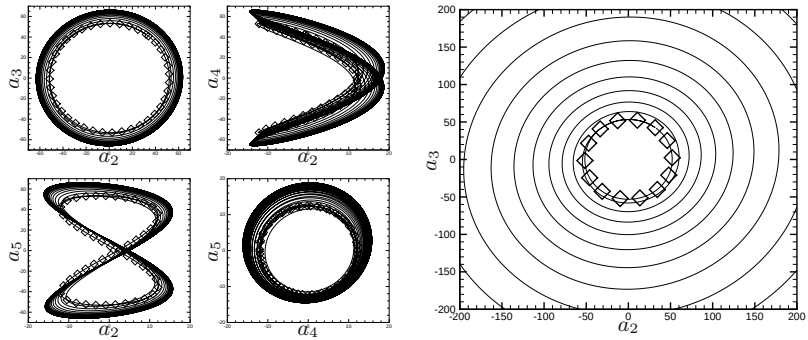

(a) $N_r = 5$ (b) $N_r = 3$

Fig. 2. Comparison of the NS $\diamondsuit$ and the ROM —— limit cycles

where the ROM coefficients are given in [2]. The $A^{[N_r]}$ model is tested at $Re = 200$. The POD snapshot method introduced by Sirovich [11] was used. Here, only the first 5 modes are sufficient to represent more than 98% of the kinetic energy. As it is shown in figure 2, the solution of model (1) built with 5 modes reaches erroneous limit cycles, and can even diverge with 3 modes.

3 Stabilization of Reduced Order Models

The aim of this section is to derive stabilization methods that involve very few empirical parameters. The two kinds of stabilization methods presented in what follows use the residual of the Navier-Stokes operator evaluated with the POD flow fields $\widetilde{\boldsymbol{u}}$ and $\widetilde{p}$. These residuals, called POD-NS residuals, are:

$$\boldsymbol{R}_M(\boldsymbol{x}, t) = \frac{\partial \widetilde{\boldsymbol{u}}}{\partial t} + (\widetilde{\boldsymbol{u}} \cdot \boldsymbol{\nabla})\widetilde{\boldsymbol{u}} + \boldsymbol{\nabla}\widetilde{p} - \frac{1}{Re}\Delta\widetilde{\boldsymbol{u}}, \tag{2a}$$

$$R_C(\boldsymbol{x}, t) = \boldsymbol{\nabla} \cdot \widetilde{\boldsymbol{u}}. \tag{2b}$$

We look for the missing scales $\boldsymbol{u}'(\boldsymbol{x}, t) = \boldsymbol{u}(\boldsymbol{x}, t) - \widetilde{\boldsymbol{u}}(\boldsymbol{x}, t)$ and $p'(\boldsymbol{x}, t) = p(\boldsymbol{x}, t) - \widetilde{p}(\boldsymbol{x}, t)$, where $\boldsymbol{u}$ and p denote the exact fields. Since the resolution of the fine scales equations requires high computational costs, the objective is to derive stabilization methods based on approximations of these fine scales.

3.1 Residuals Based Stabilization Method: Model $B^{[N_r;K]}$

The goal of this method is to approximate the fine scales u' and p' onto some adapted basis functions. The method is the following.

1. Integrate the ROM $A^{[N_r]}$ to obtain N_s coefficients $a_i(t_k)$, $k = 1, \ldots, N_s$.
2. Compute the fields $\widetilde{\boldsymbol{u}}(\boldsymbol{x}, t_k)$ and $\widetilde{p}(\boldsymbol{x}, t_k)$, and then $\boldsymbol{R}_M(\boldsymbol{x}, t_k)$ and $R_C(\boldsymbol{x}, t_k)$.
3. Compute the POD modes $\boldsymbol{\phi}'_i(\boldsymbol{x})$ and $\psi'_i(\boldsymbol{x})$ of $\boldsymbol{R}_M(\boldsymbol{x}, t_k)$ and $R_C(\boldsymbol{x}, t_k)$.
4. Add the K first residual modes $\boldsymbol{\phi}'_i$ and ψ'_i to the existing POD basis $\boldsymbol{\phi}_i$ and ψ_i (using Gram-Schmidt process) and build a new ROM, noted $B^{[N_r;K]}$.

3.2 SUPG and VMS Methods: Models $C^{[N_r]}$ and $D^{[N_r]}$

The streamline upwind Petrov-Galerkin (SUPG) method is a simplified version of the complete variational multiscale (VMS) method [1]. The main idea of both methods is to approximate the fine scales by $\boldsymbol{u}' \simeq -\tau_M \boldsymbol{R}_M$ and $p' \simeq -\tau_C R_C$. The SUPG and VMS ROMs can be formally written:

$$\sum_{j=1}^{N_r} L_{ij} \frac{\mathrm{d}a_j}{\mathrm{d}t} = \sum_{j=1}^{N_r} B_{ij} a_j + \sum_{j=1}^{N_r}\sum_{k=1}^{N_r} C_{ijk} a_j a_k + F_i(t). \tag{3}$$

- For the SUPG reduced order model, noted $C^{[N_r]}$, we have:

$$F_i^{SUPG}(t) = (\widetilde{\boldsymbol{u}} \cdot \boldsymbol{\nabla}\boldsymbol{\phi}_i + \nabla\psi_i,\, \tau_M\, \boldsymbol{R}_M(\boldsymbol{x},\, t))_\Omega + (\boldsymbol{\nabla} \cdot \boldsymbol{\phi}_i,\, \tau_C\, R_C(\boldsymbol{x},\, t))_\Omega. \tag{4}$$

- For the VMS reduced order model, noted $D^{[N_r]}$, we have:

$$\begin{aligned} F_i^{VMS}(t) = F_i^{SUPG}(t) &+ (\widetilde{\boldsymbol{u}} \cdot (\boldsymbol{\nabla}\boldsymbol{\phi}_i)^T,\, \tau_M\, \boldsymbol{R}_M(\boldsymbol{x},\, t))_\Omega \\ &- (\boldsymbol{\nabla}\boldsymbol{\phi}_i,\, \tau_M\, \boldsymbol{R}_M(\boldsymbol{x},\, t) \otimes \tau_M\, \boldsymbol{R}_M(\boldsymbol{x},\, t))_\Omega \end{aligned} \tag{5}$$

In this study parameters τ_M and τ_C are determined using optimization.

3.3 Results of Stabilization Methods

The limit cycles, over 1000 vortex shedding periods, obtained with models B, C and D are represented in figure 3 for $N_r = 5$ and $N_r = 3$ respectively and $K = 2$. These limit cycles are compared to exact ones obtained by DNS. Excellent agreements are observed, thus validating our stabilization methods.

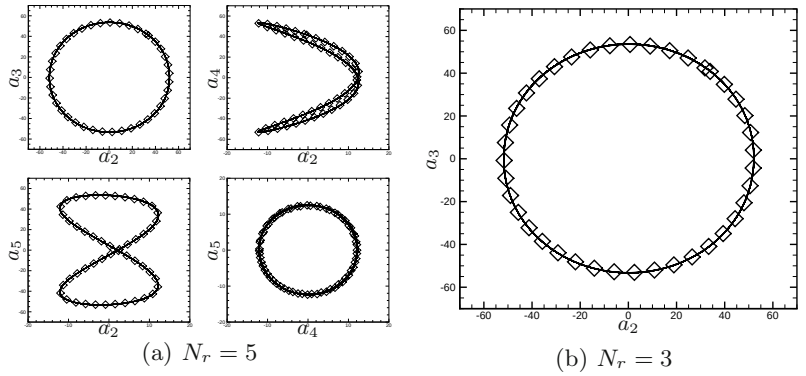

(a) $N_r = 5$ (b) $N_r = 3$

Fig. 3. Comparison of the NS $\diamondsuit$ and the stabilized ROM —— limit cycles

4 Improvement of the Functional Subspace

The main drawback of the POD basis is that it is only able to give an optimal representation of the snapshots set from which it was derived [3, 7, 9]. To overcome this drawback, a solution is to use a database composed by several dynamics [3, 4, 6], but we privilege the idea of updating the POD basis during the simulation. Since each actualization requires a large computational effort (DNS), the aim of this section is to present efficient methods to actualize the functional subspace when input system parameters change. For simplicity reasons, we only focus on Reynolds number, but the forthcoming process is transposable to other input parameters. Our goal is to obtain the target basis at $Re_2 = 200$ starting from the initial basis at $Re_1 = 100$. The idea is to actualize the snapshots database replacing older snapshot with new one. A

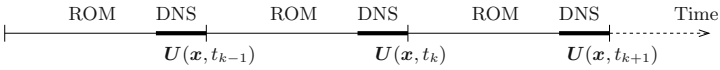

Fig. 4. Schematic representation of the hybrid DNS/ROM method

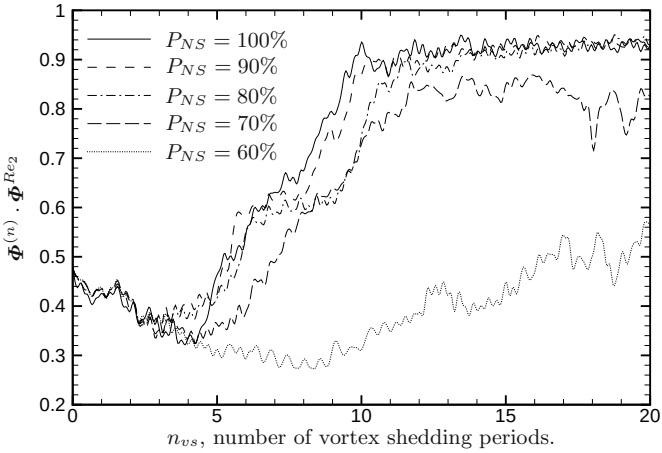

Fig. 5. Evolution of the convergence criterion for the hybrid method.

new snapshot is available after few DNS iterations. The corresponding POD basis, $\boldsymbol{\Phi}^{(n)}$, is computed using an efficient method (see [2]). All the ROM coefficients are built using $\boldsymbol{\Phi}^{(n)}$, and the integration is performed using $Re \equiv Re_2$. A schematic representation of the algorithm is presented in figure 4. Figure 5 presents the evolution of the convergence criterion $\boldsymbol{\Phi}^{(n)} \cdot \boldsymbol{\Phi}^{Re_2}$ for different percentages of DNS. Denoting T_{NS} and T_{ROM} the time intervals where we use either DNS or ROM respectively, the percentage of DNS is $P_{NS} = T_{NS}/(T_{NS} + T_{ROM})$. It can be seen that 10 vortex shedding periods are necessary to converge towards the target basis using only DNS ($P_{NS} = 100\%$). Same results can be obtained with $P_{NS} = 90\%$, $P_{NS} = 80\%$ and with 70% DNS. However, no convergence is obtained with $P_{NS} \leq 70\%$. Hence, a sufficient amount of DNS is necessary to converge toward the target basis.

5 Conclusions

The objective of this paper is to improve reduced order modeling based on POD. We have built a pressure extended ROM, so that it is not necessary to model the pressure term. Although this model gives very good results, it is still necessary to model the effects of the unresolved fines scales. In this respect, we propose stabilization methods that consist in modeling the effect of the fine scales using residuals of Navier-Stokes operator evaluated from POD fields. The first method proposed consists in enlarging the POD subspace with few residuals modes. No empiric parameter has to be estimated

in this approach. The second approach proposed relies on an approximation of the fine scale equation. Both SUPG and VMS methods give good results. In this approach, only two parameters have to be estimated. Finally, our aim is to derive an efficient method to adapt the POD basis when input parameters change. An hybrid method that couples DNS and ROMs is proposed. The idea is to update the database when dynamical evolution occurs. This method works very well if a sufficient amount of DNS is performed. Approximatively 20% of the total numerical costs can be saved using such an hybrid method.

References

[1] Bazilevs, Y., Calo, V.M., Cottrell, J.A., Hugues, T.J.R., Reali, A., Scovazzi, G.: Variational multiscale residual-based turbulence modeling for large eddy simulation of incompressible flows. Comput. Methods Appl. Mech. Engrg. 197, 173–201 (2007)

[2] Bergmann, M., Bruneau, C.-H., Iollo, A.: Improvement of reduced order modeling based on proper orthogonal decomposition. Research Report 6561, INRIA, 06 (2008)

[3] Bergmann, M., Cordier, L.: Optimal control of the cylinder wake in the laminar regime by trust-region methods and pod reduced-order models. J. Comp. Phys. 227(16), 7813–7840 (2008)

[4] Burkardt, J., Gunzburger, M.D., Lee, H.-C.: Centroidal Voronoi Tessellation-Based Reduced-Order Modeling of Complex Systems. Technical report, Florida State University (2004)

[5] Galletti, B., Bruneau, C.-H., Zannetti, L., Iollo, A.: Low-order modelling of laminar flow regimes past a confined square cylinder. J. Fluid Mech. 503, 161–170 (2004)

[6] Ma, X., Karniadakis, G.E.: A low-dimensional model for simulating three-dimensional cylinder flow. J. Fluid Mech. 458, 181–190 (2002)

[7] Noack, B.R., Afanasiev, K., Morzyński, M., Tadmor, G., Thiele, F.: A hierarchy of low-dimensional models for the transient and post-transient cylinder wake. J. Fluid Mech. 497, 335–363 (2003)

[8] Noack, B.R., Papas, P., Monkewitz, P.A.: The need for a pressure-term representation in empirical galerkin models of incompressible shear-flows. J. Fluid Mech. 523, 339–365 (2005)

[9] Prabhu, R.D., Collis, S.S., Chang, Y.: The influence of control on Proper Orthogonal Decomposition of wall-bounded turbulent flows. Phys. Fluids 13(2), 520–537 (2001)

[10] Rempfer, D.: On low-dimensional Galerkin models for fluid flow. Theor. Comput. Fluid Dyn. 14, 75–88 (2000)

[11] Sirovich, L.: Turbulence and the dynamics of coherent structures. Quarterly of Applied Mathematics XLV(3), 561–590 (1987)

Part 41
Technical Notes

“*This page left intentionally blank.*”

Modelling and Simulation of Droplet Distribution from Entrained Liquid Film in Gas-Liquid Systems

L.E. Patruno[1], C.A. Dorao[2], H.F. Svendsen[1], and H.A. Jakobsen[1]

[1] Department of Chemical Engineering, Norwegian University of Science and Technology, N-7491 Trondheim, Norway
patruno@nt.ntnu.no
[2] Department of Energy and Process Engineering, Norwegian University of Science and Technology, N-7491 Trondheim, Norway

The description of the interaction between phases in multiphase flow is of major interest for the oil and gas industry. The presence of droplets in the gas phase can produce erosion and breakdown of equipment. The use of conventional separators may not be enough since new droplets may be created from entrained liquid films at the walls. Previous work [ANSSZZ04] presented possible frameworks to describe the interaction between one sized droplets and wall films by using a two dimensional (time plus space) transport equation for the liquid film. This work presents a possible framework to model the droplet–film interaction using a population balance type of equation in which the mathematical formulation is

$$\begin{cases} \frac{\partial}{\partial z} u_f f_f(z) = \int_{\xi_{min}}^{\xi_{max}} \lambda(\hat{\xi}) f_d(\hat{\xi}, z) d\hat{\xi} - \beta f_f(z) & \text{in } \Omega_z = (z_{min}, z_{max}) \\ \frac{\partial}{\partial z} u_d f_d(\xi, z) = -\lambda(\xi) f_d(\xi, z) + \chi(\xi) \beta f_f(z) & \text{in } \Omega = (\xi_{min}, \xi_{max}) \times \Omega_z \\ f_d(\xi, z) = f_d^0(\xi) \qquad \text{on } \Gamma_\xi = [\xi_{min}, \xi_{max}] \\ f_f(z) = f_f^0 \qquad \text{on } \Gamma_z = [z = z_{min}] \end{cases} \tag{1}$$

where f_d is the droplet concentration, f_f is the film height, u_d and u_f are the corresponding velocities, λ is the deposition rate, β is the entrainment rate and χ is the entrainment spectrum. The variable ξ is the droplet mass and z is the position along the pipe.

There are many models for the entrainment rate, most of them considering an entrainment inception or critical liquid flow rate below which no entrainment occurs. These models take into account the shear velocity between the gas phase and the film surface and model the generation of droplets which can be due to role wave, wave undercut, bubble burst or liquid impingement phenomena [KI82]. The entrainment spectrum is commonly assumed to be a log-normal distribution in droplet sizes. The deposition rate takes proportionalities to the droplet concentration near the surface of the liquid film. The most frequently used correlation is the one called diffusion droplet and was presented by [PF66]. If droplet size discrimination is to be modelled,

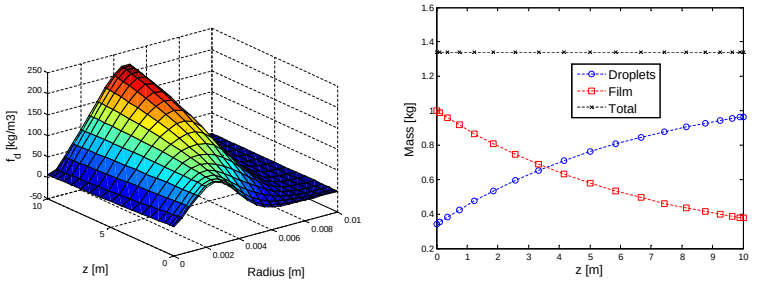

Fig. 1. Modelling results by considering entrainment and deposition

then a more complex model which accounts for the entrainment spectrum and droplet breakage [PDDSJ08] has to be considered.

Then Eq. (1) is solved by using the Least Squares Spectral Method and both the droplet size distribution and the liquid film height are approximated with Lagrangian Interpolation Polynomials through the Gauss-Lobatto quadrature rule points as proposed by [DJ06]. As an example of the results obtained, we can mention the application of this framework to an over-entrained system (where the entrainment rate is much higher than the deposition rate). We can observe in Fig. 1 the expected growth in the total mass existing in the droplet phase and a decrease in the mass of the liquid film.

References

[ANSSZZ04] Alipchenkov, V.M., Nigmatulin, R.I., Soloviev, S.L., Stonik, O.G., Zaichik, L.I., Zeigarnik, Y.A.: A three-fluid model of two-phase dispersed-annular flow. Int. J. Heat and Mass Transfer 47, 5323–5338 (2004)

[DJ06] Dorao, C.A., Jakobsen, H.A.: A least squares method for the solution of population balance problems. Computers & Chemical Engineering 30(3), 535–547 (2006)

[KI82] Kataoka, I., Ishii, M.: Mechanism and correlation of droplet entrainment and deposition in annular two-phase flow. NUREG/CR-2885, ANL-82-84 (1982)

[PDDSJ08] Patruno, L.E., Dorao, C.A., Dupuy, P.M., Svendsen, H.F., Jakobsen, H.A.: Identification of droplet breakage Kernel for population balance modelling. Chemical Engineering Science (CES) (in press) (2008) doi:10.1016/j.ces.2008.05.015

[PF66] Paleev, I.I., Filipovich, B.S.: Phenomena in liquid transfer in two-phase dispersed annular flow. Int. J. Heat Mass Transfer 9, 1089 (1966)

The Effect of the Number of Computational Grids on Calculation Results of Co-axial Jet Flows by Large Eddy Simulation Using Dynamic SGS Model

Hirotatsu Watanabe[1,2], Yohsuke Matsushita[1], Hideyuki Aoki[1], and Takatoshi Miura[1]

[1] Department of Chemical Engineering, Graduate School of Engineering, Tohoku University, 6-6-07 Aoba, Aramaki, Aoba-ku, Sendai 980-8579 Japan
hiro@tranpo.che.tohoku.ac.jp
[2] Research Fellow of the Japan Society for the Promotion of Science

1 Introduction

A properly designed co-axial jet would efficiently mix the air and the fuel, and provides the clean combustion. It is important to carry out LES by using the appropriate number of computational grids in order to apply the LES to many combustion systems. In this study, LES using the Smagorinsky model and the dynamic SGS model for co-axial jet flows is carried out, and the effect of the number of computational grids on calculation results is investigated.

2 Numerical Calculation

The configuration of the computational domain is the same as the experimental facility of Habib *et al*. [1]. Transport equations used in this study can be expressed in a three-dimensional cylindrical coordinate system. The eddy viscosity μ_{SGS} is described as follows:

$$\mu_{\mathrm{SGS}} = \rho C \bar{\Delta}^2 |\bar{S}| \tag{1}$$

where C is the dimensionless model coefficient, $\bar{\Delta}$ is the grid-filter width, and $|\bar{S}| = (2S_{ij}S_{ij})^{1/2}$ is the strain rate tensor. In this study, the model coefficient is determined using Smagorinsky model with Van Driest damping function near wall and the dynamic SGS model [2]. In the Smagorinsky model, C represents C_{s}^2 in Eq. (2). C_{s}^2 is called Smagorinsky constant. In this study, C_{s}^2 is set to 0.1. In dynamic SGS model, C is determined dynamically by applying a least-square approach [3]. The governing equations are discretized using a finite volume method. QUICK is adopted in the convective terms and second-order central difference scheme is adopted in the diffusive terms. The second-order fully implicit scheme is used for time integral and time step is

50 μsec. In this study, CVs (Control Volumes) and the division number for x, r, θ are 333,294 CVs (151 60 40), 525,840 CVs (244 60 40), 783,240 CVs (204 67 60), respectively.

3 Results

Fig. 1 shows the axial turbulence intensity profiles. When the Smagorinsky model is used, turbulent fluctuations strongly depend on the number of CVs. Although turbulent intensities are underestimated using 333,294 CVs and 525,650 CVs, those using 783,240 CVs show good agreement with experimental results. When the dynamic SGS model is used, the number of CVs is less effective on turbulent intensities, and those are good agreement with experimental results. It is shown that the dynamic SGS model does not need the number of CVs which is used in the calculation using the Smagorinsky model to provide accurate flow fields.

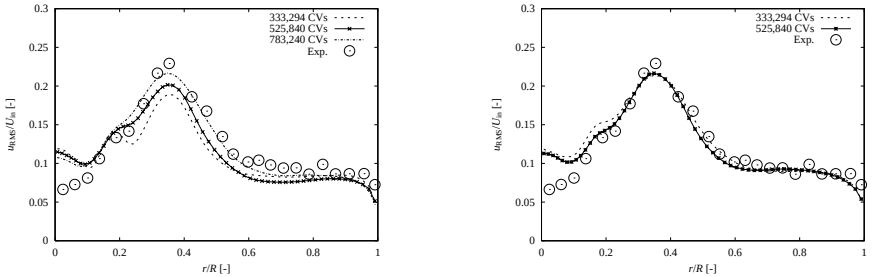

Fig. 1. The axial turbulence intensity profiles at $x/D = 0.616$ (left:standard Smagorinsky model, right:dynamic SGS model)

Acknowledgement. This study was partiallly supported by a Grant-in-Aid for Scientific Research (DC-2 19-3358) by the Japan Society for the Promotion of Science.

Nomenclature. R:radius [m], u: axial velocity component [ms^{-1}], x, r, θ: cylindrical coordinate.

References

[1] Habib, M.A., et al.: J. Fluids Eng. 102, 47–53 (1981)
[2] Germano, M., et al.: Phys. Fluids 3(7), 1760–1765 (1991)
[3] Lilly, D.K.: Phys. Fluids 4(3), 633–635 (1992)

Development and Application of the Collocations and Least Squares Method

Vadim Isaev[1] and Vasily Shapeev[2]

[1] Novosibirsk State University, Pirogova str. 2, Novosibirsk, 630090, Russia
issaev.vadim@gmail.com
[2] Khristianovich Institute of Theoretical and Applied Mechanics,
Siberian Branch of Russian Academy of Sciences,
Institutskaya str. 4/1, Novosibirsk, 630090, Russia
shapeev@itam.nsc.ru

The collocations and least squares (CLS) method is a projection method including the least squares algorithm. A computational domain is covered by a grid in the method. An approximate solution is found as a linear combination of basis functions in each cell of the grid in the CLS method. One can use different bases. Here, only polynomial basis functions are applied. Coefficients of the linear combinations for all cells are found from an overdetermined system of linear algebraic equations (SLAE). The latter consists of collocations equations, matching conditions between adjacent cells, boundary conditions. Collocations equations are obtained from requirements that the approximate solution must satisfy the equations of a considered problem at certain points in each cell.The use of overdetermined systems provides additional numerical stability in the CLS method in comparison with pure collocations method. At the same time no tricks like artificial viscosity introduction are used here.

New versions of the CLS method are proposed and implemented here. They are more general than those proposed before (Shapeev et al., 2003). Abilities of the method were extended here by a combined use of new algorithms. The first one is an orthogonal linear algebra method. It is used for a solution of overdetermined systems instead of the least squares method (LSM). The latter worsens the conditionality of a SLAE during the process of solving. The orthogonal method does not have this disadvantage and gives the same solution as LSM in case of round-off errors absence. The second enhancement of the CLS method is a good choice of method's parameters based on results obtained by Isaev and Shapeev (2007). The third one is a new version of least-squares generalization of δ^2-process proposed in the present work. An approximate solution is constructed in the CLS method with the use of an iterative process. The acceleration algorithm allows to carry out calculations on grids that are finer than applicable without the acceleration ones.

Abilities of the CLS method are demonstrated here on a test problem for Navier-Stokes equations. The latter is the 2D lid-driven cavity flow problem.

Table 1. Characteristic values of velocity components in the lid-driven cavity

Re=100			Re=1000		
v_{1min}	v_{2min}	v_{2max}	v_{1min}	v_{2min}	v_{2max}
Botella O. and Peyret R. (1998)					
−0.2140424	−0.2538030	0.1795728	−0.3885698	−0.5270771	0.3769447
Garanzha V.A., Konshin V.N. (1999)					
−0.2140423	—	—	−0.388569	—	—
present paper					
−0.2140426	−0.2538026	0.1795697	−0.3885733	−0.5270812	0.3769574

It is considered by many authors as a benchmark test for the assessment of numerical methods and validation of Navier-Stokes codes. There are Moffat's chains of eddies near bottom right and bottom left cavity corners. The eddies in such sequences become weaker and smaller with the decrease of distance between the cavity corner and a vortex center. The presence of singularities makes it difficult to properly evaluate the accuracy of the numerical results, mainly in the neighborhood of upper cavity corners. This is the reason why one may prefer to consider so-called "regularized driven cavity", where the velocity is smoothed by the subtraction of leading parts of singularities. This approach was implemented here in the CLS method. Some results of numerical experiments are shown in Table 1. A uniform grid 320×320 is used for $\mathrm{Re} = 100$. The results for $\mathrm{Re} = 1000$ are obtained by Richardson extrapolation for grids 80×80, 160×160 and 320×320. Values v_{2min} and v_{2max} are extremums of the vertical velocity component on the horizontal center line, value v_{1min} is the minimum of the horizontal component on the vertical center line. Some experiments were carried out on nonregular grid obtained from Gauss-Lobatto grid after division of prolate cells into smaller ones.

Improvements of the CLS method proposed here allow one to carry outcalculations in a wide range of Reynolds numbers (from 1 to 7500) on fine grids (up to 1280×1280). There are about $25 \cdot 10^6$ unknowns in the CLS method on the grid 1280×1280. The accuracy of the solution on this grid is not smaller that on previous one (640×640) because of a large amount of arithmetical operations in the CLS method, but grid 1280×1280 has better resolution capability then 640×640. It allows to properly specify fine-scale vortex structures in the fluid. Results of numerical experiments are in a good agreement with highly accurate results obtained by a spectral method, Botella and Peyret (1998), and those obtained by a compact finite-difference scheme, Garanzha and Konshin (1999). Eddies located near the bottom right corner of the cavity are usually called BR_1, BR_2, BR_3, etc. Vortices BR_1 and BR_2 were detected here at Re=100, BR_1, ..., BR_4 at Re=7500. This work was supported by the RFBR, Projects No. 06-01-00080-a, 08-01-08210.

Combined Experimental and Numerical Analysis of Incompressible Flow around an Airfoil

Mahmood Farzaneh Gord and Hamid Haji'alizadeh

Department of Mechanical Engineering, Shahrood University of Technology, Shahrood, Iran
mahmood.farzaneh@yahoo.co.uk

Abstract. In this paper a combined experimental and numerical analysis has been carried out to study incompressible flow around an airfoil. Numerical analysis combined vortex panel method techniques for solving potential flow around the airfoil and Von Karman boundary layer Integral equation solver. The governing equation (Laplace's equation or the linearized form in compressible flow) is recast into an integral equation. This integral equation involves quantities such as velocity, only on the surface, whereas the original equation involved the velocity potential all over the flow field. The inviscid solution then is injected into a Von Karman Integral equation solver to predict Drag coefficient. In this paper this method has been used to analysis the flow over a prototype airfoil and results were compared with experimental values achieved from wind tunnel tests. Results show that this method has a good capability to predict velocity profile and pressure and drag coefficients over the surface.

1 Introduction

The first step in airfoil design is choosing a method that has the proper balance of fidelity and speed for the given application. As such, a variety of computational analysis methods are available to the airfoil designer. These range from linear methods, concerned with solving the velocity potential equation, to more complicated methods that involve solving the Euler (inviscid) or Navier-Stokes (viscous) equations at various points on and around the airfoil to determine the nature of the flow. The linear methods are much faster but much more limiting in application while the flow solver methods, often referred to as Computational Fluid Dynamics (CFD) are less limiting but more computationally intense to solve. The airfoil to be designed over the course of this project is planned for application into a subsonic low-Reynolds number environment as described earlier. Therefore, the otherwise limited linear methods can be used to determine the airfoil characteristics. Specifically, a vortex panel method will be employed for the calculation of lift and pitching moment properties, while a boundary layer analysis will be necessary for some of the peculiarities associated with a low-Reynolds number flow. The

vortex panel method belongs to a class of more general methods known as panel methods. These methods work by stating that the governing flow equations can be solved via a superposition of elementary flows. These elementary flows can be sources, sinks, doublets, vortices, and others. The elementary flows are placed at control points along the perimeter of a body, typically at the centre of a straight segment. Lifting bodies can only be approximated with vortex flows, while non lifting (symmetrical) flow can be approximated with sources and sinks, among others. The vortex allows for the creation of circulation, an abstraction quite necessary for lifting flow fields.

2 Numerical Method

A one-way coupled inviscid - boundary layer model is used in the numerical analysis. The inviscid flow is computed with a linear vortex panel method (boundary element method), which provides the lift and moment coefficients. Firstly, the method divides the airfoil surface into a number of panels , a total of N as show in Fig. 1. Then The method begin by stating that the Laplace equation can be solved as a superposition of several simple solutions, which have physical interpretation. By superposing these solutions, flow pattern that resembles the flow over the given geometry can be computed. The boundary layer is computed using Von Karman integral formulation: the laminar part of the flow is computed with a two-equation formulation, and the turbulent part is solved with Head's model. An e9-type amplification formulation is used to locate the transition area. Finally, the drag coefficient is computed using the Squire-Young formula.

3 Experimental Apparatus

For experimental measurements a prototype coincident airfoil with a chord length of 74.9 mm was considered and its profile is given in table 1. Six pressure tapping with the whole diameter of 1.7 mm were used on the body and dynamic pressure around the airfoil could be obtained. In figure 2 the location of pressure tappings and the dimensions of model are given. The

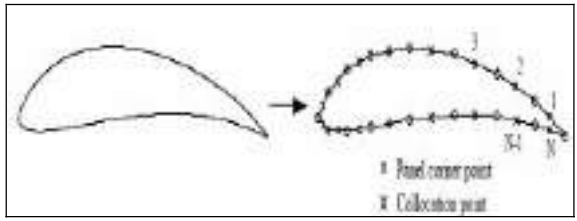

Fig. 1. Panels elements on an airfoil

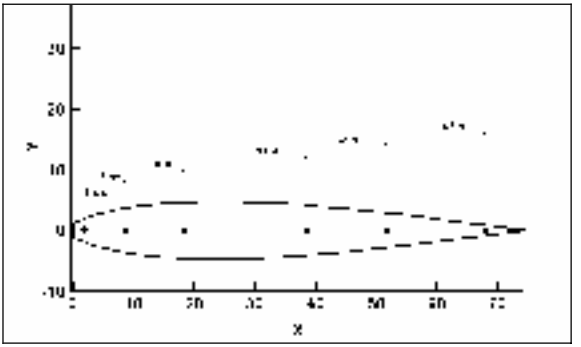

Fig. 2. Pressure tapping location of the airfoil model

tunnel, of the open circuit type, is constructed mainly in aluminum and supported by a tubular steel framework. The air enters the tunnel through a carefully shaped inlet, the entrance being covered by a protective screen. The working section is of perplex giving full visibility and the various models are supported from one of the sidewalls. At the upstream end of the working section there is a static tapping and a total head tube to get static pressure. Maximum air velocity is about 47.57 m/s and it is controlled by means of a double butterfly valve on the fan outlet.

4 Results and Discussions

The computation has been carried out for a prototype airfoil. The airfoil has been discreted to 45 elements. Figure 3 show the variation of pressure coefficient around airfoil. Results have been obtained for angle of attack 0 to 12 degree with step of 3 degree. Here only one case has been presented. As it can be seen, the good agreement has been obtained between numerical and experimental values.

Figure 4 shows the effect of angle of attack on the lift coefficient for computation and measured values. The comparison of the lift characteristics between the test cases with the experimental data yielded some interesting results. The computed values were reasonably close to the experimental data at small angles of attack, but over predicted lift as angle of attack increased. Over prediction of lift is to be expected from this type of analysis. This is because the panel method, even when combined with a boundary layer analysis, assumes that the flow is 100% attached. A thicker airfoil such as this will exhibit separation at the trailing edge as the angle of attack is increased, which will tend to decrease the lift and increase the drag. This is explained by the fact that, at large angles of attack the body ceases to be streamlined. The point of separation moves a considerable way towards the front of the body and the wake consequently becomes wider.

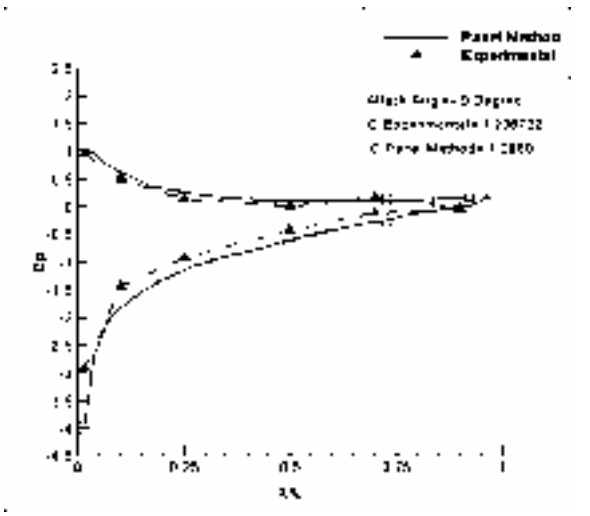

Fig. 3. Experimental and theorical pressure coefficient variation around the airfoil with angle of attack 9

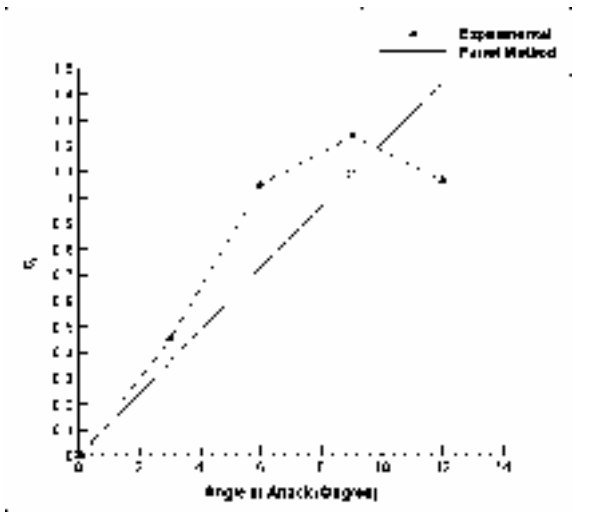

Fig. 4. Experimental and Numerical lift coefficient variation with angle of attack

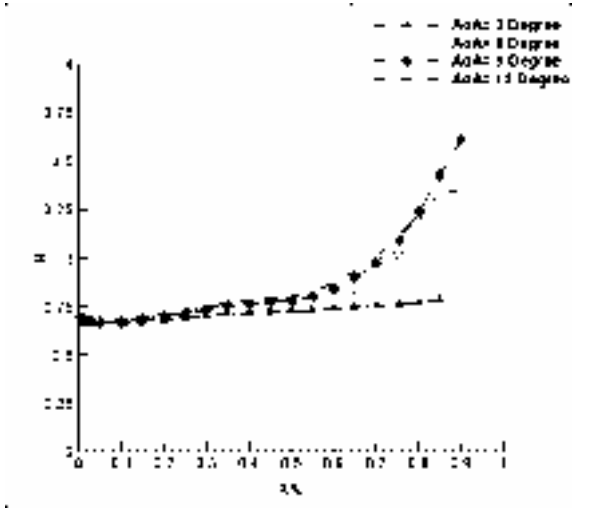

Fig. 5. Variation of shape factor on upper side of airfoil for attack angles 3 to 12 degree

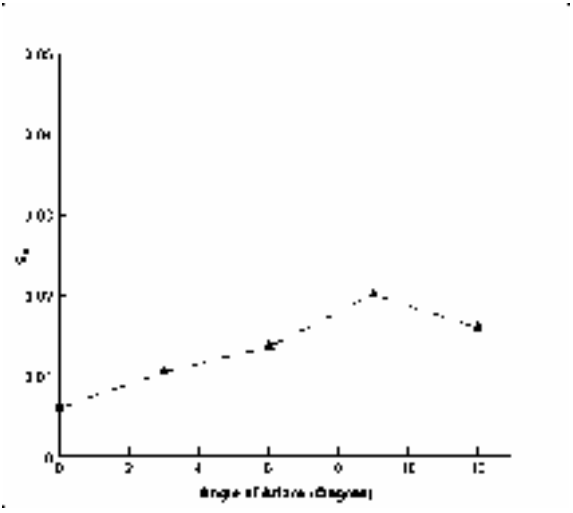

Fig. 6. Variation of drag coefficient for attack angles 3 to 12 degree

Analysis of the boundary layer can be used to predict where separation will occur. Since the adverse pressure gradient is the necessary part of separation and also shape factor increases in adverse pressure gradient, so by evaluating the variation of shape factor on upper side and lower side of the airfoil we can

predict the probability of separation. In figure 5 the variation of the shape factor for upper of the airfoil are shown for various attack angles. According to the figure it can be seen that shape factor has the maximum value at angle of attack 9 and its value is about 3.6. In laminar flows the value of shape factor from 2.6 at zero pressure gradient reaches to a value about 3.5 at separation and in turbulent flows it reaches from 1.3 to 2.5.

In figure 6 variation of drag coefficient has shown for various attack angles. According to figure 6 with increment in attack angle, the plane area of the airfoil that is in front of the flow will be increased and thus the drag force will be increased. At attack angle after 9 degree because of turbulence the drag coefficient has a significant drop. It's because of that turbulent flow has a higher momentum than laminar flow and can resist opposite separation.

5 Conclusion

In this study a combined numerical and experimental study has been carried out to analysis flow field around an airfoil. The numerical method has based on boundary element method which extremely fast comparing Euler (inviscid) or full Navier-Stokes Navior-Stukes solver. The results show good agreement with measured values for non-separated flow fields. As expected for separated flow files, the method predicts poor results and boundary layer analysis used to predict separation point on airfoil and skin friction and drag coefficients. The method would be an ideal tool for analyzing airfoils.

References

[Abb59] Abbott, I.H., von Doenhoff, A.E.: Theory of Wing Sections. Dover, New York (1959)

[CEB99] Cebeci, T., Cousteix, J.: Modeling and computation of boundary layer flows. Horizons publishing Inc., Long beach (1999)

[CHR00] Christian, W.: Shape Optimization of Low Speed Airfoils using MATLAB and Automatic Differentiation. Licentiate's Thesis Royal Institute of Technology Department of Numerical Analysis and Computing Science (2000)

[APS05] Apsley, D.: Turbulent Boundary Layers (2005)

[MOO03] Moores, J.: Potential Flow 2-Dimensional Vortex Panel Model: Applications to Wing mills, A Thesis Submitted In Partial Fulfillment Of The Requirements For The Degree Of Bachellor Of Applied Science, Faculty Of Applied Science And Engineering University Of Toronto (2003)

[SCH79] Schilichting, H.: Boundary layer theory, 7th edn. McGraw-Hill Inc., New York (1979)

[WHI74] White, F.M.: Viscous fluid flow. McGraw-Hill Inc., New York (1974)

CFD Simulation of Gas-Water Two-Phase Flow in Turbocharger

J. Yao[1], Y. Yao[1], P.J. Mason[1], T. Zhang[1], F.J.G. Heyes[2], and P.E. Roach[2]

[1] Faculty of Engineering, Kingston University, London SW15 3DW, UK
[2] Napier Turbochargers Ltd., Lincoln LN5 7FD, UK

A turbocharger is widely used by industry as an efficient thermal performance enhancement device, and its efficiency is often dependent on the conditions and properties of the working fluid. One industry problem is the use of low-grade diesel, that produces various combustion products, and thus causes blade throat blockage, blade corrosion, damage, etc. At present, one solution is to attach an *ad hoc* online water washing system that operates daily to remove in part any accumulated solid deposits. While the method works well, an in-depth understanding of the washing mechanism is still quite limited. Complementary to essential in-house rig testing, it is now feasible to carry out numerical simulation of flow thus to provide further understanding. A combined experimental and numerical study of gas-water two-phase flow in turbocharger has therefore been proposed with some results presented here.

The configuration considers a generic turbocharger, which consists of a 90-degree bent duct, three guide struts with a central cone, and a row of 24 blades downstream. It is mounted onto an in-house test bed, which runs at conditions close to engine operation conditions. Assessment of water washing performance (i.e. coverage area) is indirectly evaluated by measuring the blade surface temperature, and data are used for numeircal validation.

The same configuration including three water injectors, located evenly in the circumferential directions, is used in simulation. The Eulerian-Lagrangian model is adopted, with the gas flow treated as the continuous phase and the water droplets as the dispersed phase. The particle tracking technique in ANSYS-CFX package is used for capturing the water droplets' trajectory. The physical process of water droplet splitting is considered by a primary break-up model in the vicinity of injector exit, and a secondary break-up model in the near-field. Other sub-models are also adopted, including a liquid evaporation model. To represent continuous water flow, a total of 30,000 liquid particles (at room temperature) were injected into the flow domain from three water injectors in an un-correlated manner. The CFD prediction of water coverage on the blades is used to compare with experimental

measurements. The simulation provides further flow details, e.g. the water droplet trajectory and distribution: all are difficult to obtain in the experiment.

Figure 1 gives the comparison of percentage of water coverage by numerical prediction and experimental measurement and the distribution of particle sizes along the trajectory length between the injector exit and the blade row surface. Here we only present the results obtained under the condition of water mass flow rate of $\dot{m} = 0.15$ kg/sec, water pump pressure of 4 bars, and the turbocharger operating at a loading between 750 and 950 (N/Sqrt). It can be seen that the CFD predicted water converge on the blade surface has fairly good agreement with the measurement in general, despite slight over-predictions observed (about 8% in max). Similar results were also obtained at higher water pump pressure of 8 bars (not shown here).The possible reason is probably due to the influence of the sub-models, e.g. liquid break-up and evaporation, and thus further optimization is needed to improve the predictions. It also shows the particle size variations at 800 (N/Sqrt) loading along the trajectory path, which is difficult to measure. In agreement with the primary break-up model adopted, the initial particle size is kept as a constant of 6 mm in the vicinity of the injector exit, equivalent to injector diameter. While the water droplet breaks up, its size decreases along the trajectory path with smallest water droplets (about 0.001 mm) predicted on the blade surfaces. While the size and distribution of water droplets on the blade surface are dependent on various factors (e.g. the mainstream gas inflow and the water injection conditions), further simulation studies will focus on parameter optimization, especially the correlation of the injector number and the water coverage, the effect of injector exit shape and orientation, etc. In summary, we have presented the numerical prediction of water coverage, water droplets size and distribution on a blade row ring in a turbocharger, using the CFD modeling of two-phase flow. The results obtained agree fairly well with the test and further optimization studies are ongoing based on this work.

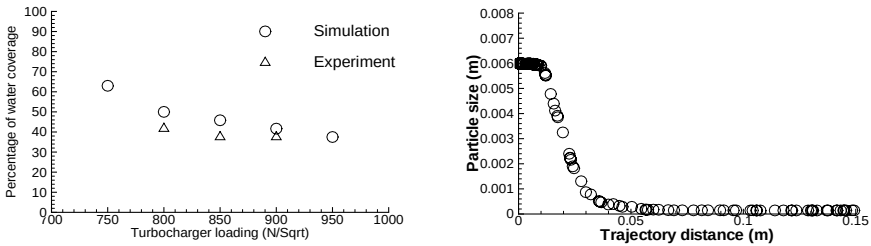

Fig. 1. Comparison of the percentage of water coverage under different loadings (left) and the distribution of particle size at 800 (N/Sqrt) loading along the trajectory path (right)

Numerical Analysis of Optical Systems for Compressible Flow Visualization

Dai Kikuchi[1] and Mingyu Sun[2]

[1] Graduate School of engineering, Tohoku University, Aramaki aza aoba 6-3, Aoba-ku, Sendai, Japan
dai@iswi.cir.tohoku.ac.jp
[2] Center for Interdisciplinary Research, Tohoku University, Aramaki aza aoba 6-3, Aoba-ku, Sendai, Japan
sun@cir.tohoku.ac.jp

Abstract. We have developed a computer-aided analysis tool for shadowgraph and schlieren optical systems by combining computational fluid dynamics (CFD) and ray-tracing method. Investigation of the effect of shape and location of optical components has been succeeded by using this technique. It opens a way to develop a computer-aided analysis tool for optimization of optical systems in laboratory.

1 Introduction

Shadowgraph method and schlieren method have been used for experimental compressible flow visualization for a long time. The quality of the image depends on various factors of the optical systems such as shape and location of the optical components [Set01]. Therefore, it is necessary to optimize an optical system for the experimental condition by taking a few tests and only an experienced person can do that efficiently, especially for experiment in large scale facilities. In order to solve this problem, we propose a technique to simulate numerical images to optimize an optical system on the computer before an experiment. In this technique, the flowfield in test section is given by computational fluid dynamics (CFD) and numerical images are obtained by tracing rays through the numerical solution given by CFD as well as the optical system (ray-tracing method).

In the previous studies, numerical shadowgraph and schlieren images were displayed by using ray-tracing method [Yat93]. But, this technique is based on a formula of density gradient that are valid under straight-ray approximation in the flowfield for very simple optical systems. Therefore, this technique is not general enough for the purpose of optimization of optical systems.

We attempt to display optical images by simulating propagation of rays in the flowfield in the test section only based on geometrical optics. For this purpose, it is necessary to simulate refraction of rays due to density variation and trace each ray in the flowfield.

2 Optical Systems

Fig.1 shows shadowgraph and schlieren optical systems using in this paper. First, rays radiate from a light source and are transformed into parallel beams by a lens in both optical systems. In the flowfield in the test section, rays are refracted due to density variation in the case of compressible flows, and finally forming bright and dark pattern at the recording plane. The pattern of light irradiance at the recording plane is due to light refraction in the flowfield in shadowgraph systems, and shadowgraph image approximately reflects second derivative of density in the test section. Schlieren systems are different from shadowgraph systems by a cutoff inserted into the focus of the lens, and only rays not intercepted by the cutoff can reach the recording plane. Therefore, schlieren image reflects density gradient in the test section.

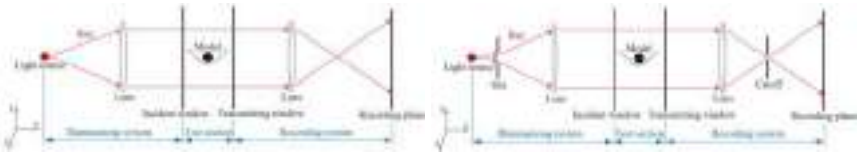

(a) Shadowgraph optical system (b) Schlieren optical system

Fig. 1. Optical systems

3 Simulation Techniques

3.1 CFD

Density distribution in the test section is simulated by VAS2D (2-D Vectorized adaptive solver) [ST99]. Computational grid of VAS2D is used as boundary planes in ray-tracing method. Fig. 2 shows density distribution and computational grid around a sphere flying at $M = 3.2$ in air simulated by VAS2D.

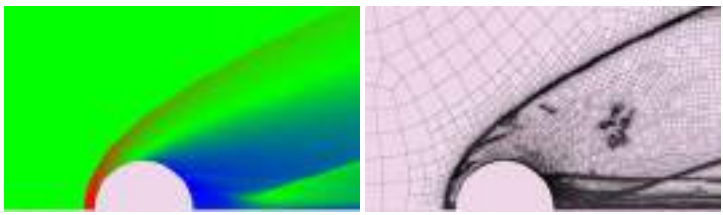

(a) Density distribution (b) Computational grid

Fig. 2. Flowfield around a sphere flying at $M = 3.2$ in air simulated by VAS2D

3.2 Ray-Tracing Method

In illuminating optical system and recording system as shown in Fig.1, rays are traced from a light source to the incident window and from the transmitting window to the recording plane based on geometrical optics. In schlieren systems, the light intensity of a ray blocked by the cutoff is set to zero. In color schlieren systems, the hue of a ray is represented in RGB format. Their intensities are reduced by a factor proportional to those of the color filter. In the test section, the distribution of refractive index is derived from density distribution based on Gladstone-Dale equation,

$$n = 1 + K\rho \tag{1}$$

where n, K, and ρ denote refractive index, Gladstone-Dale constant and density respectively. Propagation of rays through flowfield is simulated by Fermat's principle [Mer74],

$$\frac{d^2z}{dx^2} = \left[1 + \left(\frac{dz}{dx}\right)^2 + \left(\frac{dy}{dx}\right)^2\right]\left[\frac{1}{n}\frac{\partial n}{\partial z} - \frac{dz}{dx}\frac{1}{n}\frac{\partial n}{\partial x}\right] \tag{2}$$

$$\frac{d^2y}{dx^2} = \left[1 + \left(\frac{dz}{dx}\right)^2 + \left(\frac{dy}{dx}\right)^2\right]\left[\frac{1}{n}\frac{\partial n}{\partial y} - \frac{dy}{dx}\frac{1}{n}\frac{\partial n}{\partial x}\right] \tag{3}$$

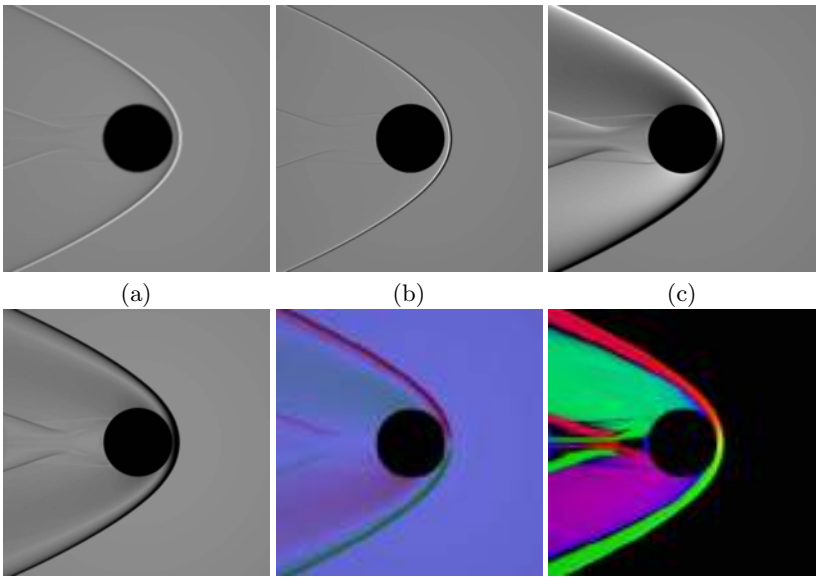

Fig. 3. Numerical images: (a) shadowgraph image focused on the left of the test section; (b) shadowgraph image focused on the right of the test section; (c) schlieren image using horizontal knife-edge; (d) schlieren image using circular cutoff; (e) color schlieren image using horizontal color filter; (f) color schlieren image using circular color filter

where x-axis and z-axis denote the direction of the light axis and that of the flow respectively as shown in Fig.1.

3.3 Adaptive Ray-Tracing Method

To reduce computing time, we propose adaptive ray-tracing method. In this method, the rays that propagate in large density variation area such as those in the neighborhood of shock waves and models are automatically increased. We succeed in reducing the computing time by more than 85% in a total by using adaptive ray-tracing method compared with the case based on uniform rays for creating a high quality image.

4 Results

Six images in Fig.3 show the examples of numerical images. They are created from the same flowfield as shown in Fig.2, but using different optical systems. These results show the influence of the shape and location of the optical components. It indicates that individual optical component can be analyzed using the present method.

5 Conclusions

We succeeded in creating realistic shadowgraph and schlieren images by combining CFD and ray-tracing method, and in analyzing the effect of the shape and location of the optical components. More than 85% computing time is successfully reduced for creating a high quality image by using adaptive ray-tracing method.

References

[Set01] Settles, G.S.: Schlieren and Shadowgraph Techniques. Springer, Heidelberg (2001)

[Yat93] Yates, L.A.: Images Constructed from Computed Flowfields. Wiley, New York (1993); AIAA 31(10), 1877–1884 (1999)

[ST99] Sun, M., Takayama, K.: Conservative smoothing on an adaptive quadrilateral grid. J. Comp. Phy. 150, 143–180 (1999)

[Mer74] Merzkirch, W.: Flow Visualization. Academic Press, New York (1974)

Application of a DRP Upwinding Scheme in Immersed Boundary Method

P.H. Chiu, Tony W.H. Sheu, and R.K. Lin

Department of Engineering Science and Ocean Engineering, National Taiwan University, No. 1, Sec. 4, Roosevelt Road, Taipei, Taiwan, Republic of China
f93525011@ntu.edu.tw, twhsheu@ntu.edu.tw, rklin@ntu.edu.tw

In this technical note we will presnet the idea of the mimic-quadric-interpolation immersed boundary (MQI-IB) method. A Dispersion-Relation-Preserving (DRP) upwinding scheme for the convective terms developed in Cartesian grids is also applied within the present analysis framework.

1 Mimic Interpolation Immersed Boundary Method

In order to satisfy the no-slip condition, the temporarily corrected velocities, $\mathbf{u}^t$ for example, at the forcing points in fictitious fine mesh are expressed as

$$\mathbf{u}^t = \begin{cases} 0 & \text{on IB} \\ f(\mathbf{u}^*) & \text{in s-f cell} \\ \mathbf{u}^* & \text{in fluid} \end{cases} \tag{1}$$

where $f(\mathbf{u}^*)$ is a function of the intermediate velocities $\mathbf{u}^*$. From the Fig. 1, the corrected velocities $\mathbf{u}^t$ in **s-f** cell are then given as follows

$$\mathbf{u}^t = \begin{cases} \mathbf{u}_5^t,\ f(\mathbf{u}_3^*, \mathbf{u}_7^*, \mathbf{u}_9^*, \mathbf{u}_b) & \text{on point 5} \\ \mathbf{u}_6^t,\ f(\mathbf{u}_1^*, \mathbf{u}_5^*, \mathbf{u}_7^*, \mathbf{u}_a) & \text{on point 6} \\ \mathbf{u}_8^t,\ f(\mathbf{u}_4^*, \mathbf{u}_5^*, \mathbf{u}_9^*, \mathbf{u}_c) & \text{on point 8} \end{cases} \tag{2}$$

With the following velocity values,

- The intermediate velocities $(\mathbf{u}_1^*, \mathbf{u}_3^*, \mathbf{u}_4^*, \mathbf{u}_7^*, \mathbf{u}_9^*)$;
- The temporarily corrected velocities $(\mathbf{u}_5^t, \mathbf{u}_6^t, \mathbf{u}_8^t)$ on the fictitious fine mesh;
- The no-slip boundary point $(\mathbf{u}_b \equiv 0)$, which is obtained from the original coarse grids,

the corrected velocity at point 2 can then take the following functional form

$$\mathbf{u}_2^{**} = f(\mathbf{u}_1^*, \mathbf{u}_3^*, \mathbf{u}_4^*, \mathbf{u}_6^*, \mathbf{u}_7^*, \mathbf{u}_9^*, \mathbf{u}_5^t, \mathbf{u}_6^t, \mathbf{u}_8^t, \mathbf{u}_b) \tag{3}$$

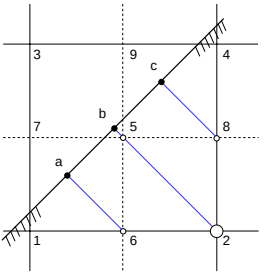

Fig. 1. Schematic of the mimic quadratic interpolation

2 Dispersion-Relation-Preserving Scheme

The twelve nodal values of ϕ shown in Fig. 2 are used to approximate the first-order derivative ϕ_x:

$$\phi_x(x,y) \simeq \frac{1}{h}\left(a_1\,\phi_{i-1,j-1} + a_2\,\phi_{i,j-1} + a_3\,\phi_{i+1,j-1} + a_4\,\phi_{i-1,j} + a_5\,\phi_{i,j} + a_6\,\phi_{i+1,j} + a_7\,\phi_{i-1,j+1} + a_8\,\phi_{i,j+1} + a_9\,\phi_{i+1,j+1} + a_{10}\,\phi_{i,j-2} + a_{11}\,\phi_{i,j-2} + a_{12}\,\phi_{i-2,j}\right) \tag{4}$$

By applying the Taylor series expansions for $\phi_{i\pm1,j}$, $\phi_{i-2,j}$, $\phi_{i,j\pm1}$, $\phi_{i,j\pm2}$, $\phi_{i\pm1,j\pm1}$, the leading eleven error terms shown in the resulting modified equation will be eliminated to yield the scheme with the spatial accuracy order of three. One more equation is needed for uniquely determining the coefficients $a_1 \sim a_{12}$ shown in (4). This is followed by conducting Fourier transform on the left and right hand sides of Eq. (4), we are led to have the following equation

$$\tilde{\alpha} = \frac{-\mathbf{i}}{h}\left(a_1\,e^{-\mathbf{i}(\alpha h+\beta h)} + a_2\,e^{-\mathbf{i}\beta h} + a_3\,e^{\mathbf{i}(\alpha h-\beta h)} + a_4\,e^{-\mathbf{i}\alpha h} + a_5 + a_6\,e^{\mathbf{i}\alpha h} + a_7\,e^{-\mathbf{i}(\alpha h-\beta h)} + a_8\,e^{\mathbf{i}\beta h} + a_9\,e^{\mathbf{i}(\alpha h+\beta h)} + a_{10}\,e^{\mathbf{i}(-\beta 2h)} + a_{11}\,e^{\mathbf{i}(\beta 2h)} + a_{12}\,e^{\mathbf{i}(-\alpha 2h)}\right) \tag{5}$$

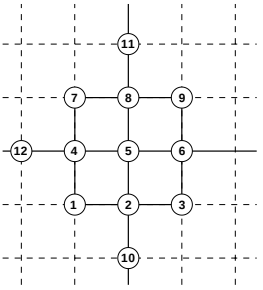

Fig. 2. Schematic of the twelve stencil points

To achieve the goal of yielding a low dispersion error, the global error E defined below should approach zero over a proper range of the modified wave number

$$E(\alpha) = \int_{-\frac{\pi}{2}}^{\frac{\pi}{2}} \int_{-\frac{\pi}{2}}^{\frac{\pi}{2}} \mid \alpha h - \tilde{\alpha} h \mid^2 \, d(\alpha h)\, d(\beta h) = \int_{-\frac{\pi}{2}}^{\frac{\pi}{2}} \int_{-\frac{\pi}{2}}^{\frac{\pi}{2}} \mid \gamma_1 - \tilde{\gamma_1} \mid^2 \, d\gamma_1\, d\gamma_2 \quad (6)$$

To make E a minimum value, the condition given by $\frac{\partial E}{\partial a_6} = 0$ is enforced for uniquely determining the coefficients $a_1 \sim a_{12}$.

“*This page left intentionally blank.*”

Convergence Acceleration Method for Linear Iterative Process

Vadim Isaev[1] and Vasily Shapeev[2]

[1] Novosibirsk State University, Pirogova str. 2, Novosibirsk, 630090, Russia
issaev.vadim@gmail.com
[2] Khristianovich Institute of Theoretical and Applied Mechanics,
Siberian Branch of Russian Academy of Sciences, Institutskaya str. 4/1,
Novosibirsk, 630090, Russia
shapeev@itam.nsc.ru

A multistep method of least squares is described in [1]. It accelerates the convergence of iterative process

$$\mathbf{x}_{n+1} = \mathrm{T}\mathbf{x}_n + \mathbf{f}, \qquad n = 0, 1, \ldots \tag{1}$$

of solving a system of linear algebraic equations (SLAE) $\mathrm{A}\mathbf{x} = \mathbf{b}$. Here, A, T are square matrices, $\mathbf{b}$ is a right-hand side parts vector, $\mathbf{x}_0$ is an initial approximation for the exact solution $\mathbf{x}$. In this method, correction ${\mathbf{y}_n}^*$ is added to a current approximation of $\mathbf{x}_n$ every k steps, i.e. $\mathbf{x}_n^* = \mathbf{x}_n + {\mathbf{y}_n}^*$. Vector $\mathbf{x}_n^*$ is an improved approximation for the n-th iteration here. The correction is a linear combination of k residual vectors $\mathbf{r}_i = \mathrm{T}\mathbf{x}_i + \mathbf{f} - \mathbf{x}_i = \mathbf{x}_{i+1} - \mathbf{x}_i$, where $i = (n-k), ..., (n-1)$, $k < n$. The error of the n-th iteration is vector

$$\mathbf{y}_n = \mathbf{x} - \mathbf{x}_n = \mathbf{x} - \mathbf{x}_{n+1} + \mathbf{r}_n = \mathbf{y}_{n+1} + \mathbf{r}_n.$$

Errors and residuals satisfy equations

$$\mathbf{r}_{n+1} = \mathrm{T}\mathbf{r}_n, \qquad \mathbf{y}_{n+1} = \mathrm{T}\mathbf{y}_n, \qquad (\mathrm{I} - T)\,\mathbf{y}_n = \mathbf{r}_n.$$

Multiplying of both sides of the latter system by T^{-1} yields SLAE

$$(T^{-1} - I)\,\mathbf{y}_n = \mathbf{r}_{n-1}. \tag{2}$$

Correction ${\mathbf{y}_n}^*$ for vector $\mathbf{x}_n$ is sought in the form ${\mathbf{y}_n}^* = \sum\limits_{i=1}^{k-1} \alpha_i\, \mathbf{r}_{n-k+i}$ here. Substitution of vector ${\mathbf{y}_n}^*$ into (2) yields overdetermined system

$$\alpha_1 \mathrm{M}_1 + \ldots + \alpha_{k-1}\mathrm{M}_{k-1} = -\mathbf{r}_{n-1}, \tag{3}$$

where columns $\mathrm{M}_i = \mathbf{r}_{n-k+i} - \mathbf{r}_{n-k+i-1},\ i = 1, \ldots, k-1$. In [1] coefficients $\alpha_1, \ldots, \alpha_{k-1}$ are found by the least squares method (LSM). Sleptsov showed that this acceleration algorithm allows one to attain a good acceleration. However, it has also a weak point. System (3) becomes ill-conditioned or degenerates with the growth of iteration number, because norms of the residuals

tend to zero when process (1) is convergent. Particularly this problem could be solved by changing of unknown variables and normalization of column-vectors M_i $(i = 1, \ldots, k-1)$. However, this trick does not eliminate all the problems arising when some of these vectors are close to linearly dependent ones. To get a working algorithm, it is necessary to decrease the number of residuals used for the correction. Otherwise, the correction $\mathbf{y}_n^*$ would be calculated with a large error and the convergence acceleration would deteriorate. Formulas of the acceleration method are derived in [1] for an arbitrary k, but a general working algorithm for specifying of the appropriate number of residuals is not proposed there. The method is implemented in [1] for $k \leq 3$ only.

A new version of Sleptsov's method is proposed and implemented here. An orthogonal method based on QR decomposition is used here for overdetermined system (3) solving. The orthogonal method is stabler to round-off errors than the LSM and yields the same solution in case of exact calculations without rounding. The number of residuals is determined here via a process of orthogonal elimination which is performed for system (3) solving. If a leading element of the elimination becomes smaller than $\varepsilon = 10^{-15}$ for a column number j $(j = 1, \ldots, k-1)$ then column-vectors M_i $(i = 1, \ldots, j)$ are close to linearly dependent. The elimination must be stopped in such a case. Only residuals $\mathbf{r}_{n-k+1}, \ldots, \mathbf{r}_{n-k+j-1}$ should be used for the correction. Values of coefficients α_i, $i = j, \ldots, k-1$ should be set to zero. Thus, as many residuals as possible are used in the new version of convergence acceleration method, and the number of residuals is automatically specified. Iterative sequence $\boldsymbol{\chi}_n = \mathbf{x}_{n \cdot s}$, $n = 1, 2, \ldots$ can be used instead of (1) in the acceleration algorithm. Here, s is a natural number, $s \geq 1$. This trick yields additional acceleration in some cases. The correction $\mathbf{y}_n^*$ for $k = 2$ completely coincides with those calculated in Eitken's δ^2-process. Therefore, Sleptsov's algorithm and its new version proposed here may by considered as generalizations of δ^2-process.

Numerical experiments show that the use of more than two residuals in the new algorithm yields essential additional acceleration. The new version of the acceleration algorithm was used in the collocations and least squares method of solving the boundary value problem for Navier–Stokes equations The use of acceleration made it possible to reduce the number of iterations needed for deriving an approximate solution by a factor of more than four. This work was supported by the RFBR, Projects No. 06-01-00080-a, 08-01-08210.

References

1. Sleptsov, A.G.: Ob uskorenii shodimosti lineinyh iteratsiy. Modelirovaniye v mehanike 3(20), 3, 132–147 (1989) (in Russian)

Heat Transfer Correlations and Pressure Drop for Cross-Cut Heat Sinks Using CFD: Technical Notes

Sun Lee[1], Gwang Hoon Rhee[1], and Seo Young Kim[2]

[1] Mechanical and information Engineering University of Seoul, Seoul, Korea
[2] Korea Institute of Science and Technology

1 Introduction

A number of analytic, numerical, and experimental research have been carried out to predict plate fin heat sinks thermal performance and pressure drop [KW03, KK98]. However, the effect of the number of cross-cut is rarely studied. The present study investigates the influence of the number of cross-cut, Reynolds number, and fin pitch on heat transfer performance and pressure drop using CFD. The simulation result was compared with the proposed model for plate-fin heat sinks with duct flow [SW02]. Figure 1 shows a schematic diagram and boundary conditions of this study

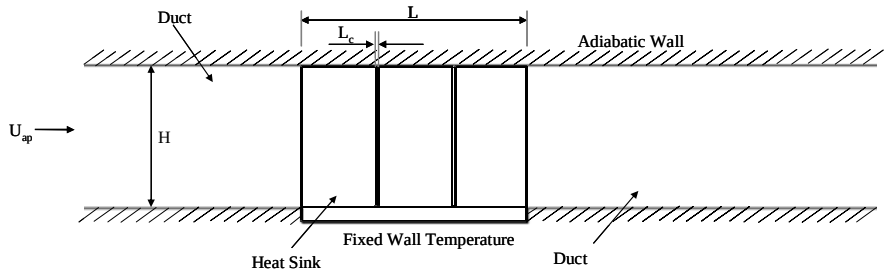

Fig. 1. Schematic diagram of Problem

2 Numerical Results and Conclusions

In this study, thermal performance and pressure drop of cross-cut heat sinks with duct-flow type arrangement has been carried out within the range of laminar flow. Here, a 3-dimensional CFD simulation of cross cut heat sink have been conducted in systematic comparison with plate fin heat sink[SW02]. Numerical results have been compared to verify the validity with the theoretical results of parallel plate channels Study from Shah and London [SW02]. By compiling the numerical data, the heat transfer and friction factor correlations with $\pm 2\%$, and $\pm 5\%$ accuracy are provided for an effective design of cross cut heat sinks. Equation (1) is the

correlation of Nusselts number (Nu), where N_l is (2). Equation (3) is the correlation of f-factor. The suggested correlations for Nu and f-factor are valid in a condition of $250 \leq \mathrm{Re} \leq 7\,50$, 4mm $\leq$ Pitch of fin(Pf), 50mm height of fin.

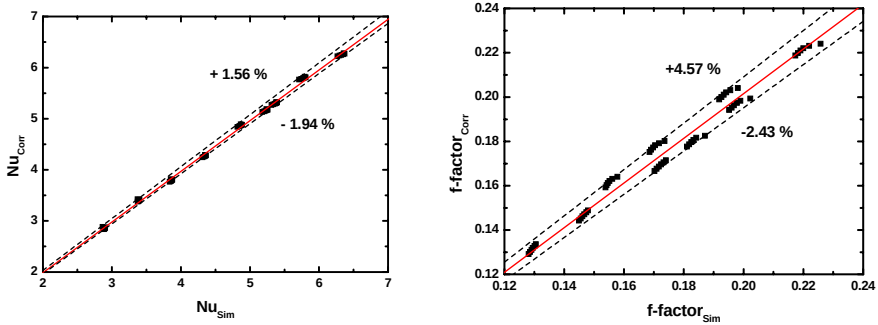

Fig. 2. Nusselts number and f-factor correlation

$$Nu = 3.53\,\mathrm{Re}^{0.146}\left(\frac{P_f}{D_h}\right)^{-1.485} N_l^{\,0.025} - 10.353 \tag{1}$$

$$N_l = \frac{L - N \times L_c}{L} \tag{2}$$

$$f = 0.584\,\mathrm{Re}^{0.085}\left(\frac{P_f}{D_h}\right)^{1.591} N_l^{\,0.064} - 0.366 \tag{3}$$

References

[SW02] Saini, M., Webb, R.L.: Validation of models for air cooled plane fin heat sinks used in computer cooling, I-THERM (2002)

[KW03] Kim, S.Y., Webb, R.L.: Thermal Performance Analysis of Fan-Heat Sinks for CPU Cooling. In: Proc. ASME IMECE 2003, Washington, DC (2003) (CD ROM)

[KK98] Kim, S.Y., Kim, J.H.: Heat Transfer Correlation of Porous in a Plate-Fin Heat Exchanger. SAREK, pp. 773–778 (1998)

CFD Study of Traveling Wave within a Piston-Less Striling Heat Engine

C.F. Cheng* and T.W. David Ngu*

*Curtin Univ. of Technology Malaysia Campus, CDT 250, 98009 Miri, Sarawak, Malaysia
chengcf@curtin.edu.my

Abstract. This paper looks into the study of a 2D traveling wave thermoacoustic heat engine using Fluent. The heat engine demonstration device by Bastyr K.J. et al [BK03] was adopted as the simulation domain. Initially, a small pressure, velocity and temperature perturbation was set in the system. Simulation result shows traveling wave formation with non-linear effects occur within the resonator.

1 Introduction

Most of the literatures available on thermoacoustic are based on linear acoustic theory. (See [BS00], [BK03]and [C97]). This posses a severe limitation to the actual system due to (1) intrinsic irreversibility of heat transfer and (2) nonlinear effects; vortex and acoustic streaming. Simulation of unsteady acoustic flow field could help to understanding better the nonlinear effects. A 2D resonator (see Fig. 1) representing the traveling wave thermoacoustic heat engine was considered. The regenerator is comprised of hot (Hot HX) and cold (Cold HX) heat exchangers with a stack placed in between.

Fig. 1. Computational domain(in cm) and mesh

All boundaries were set as wall except the resonator left end as an outflow. Temperature at hot heat exchanger was specified at $623K$ while the cold heat exchanger, stack, wall of resonator and closed end of resonator as $300K$. A small pressure perturbation ($15kPa$) is applied at all boundaries to initialize the solution. Axial velocity of $0.1m/s$ and initial temperature $300K$ were set within the resonator. The unsteady Navier- Stokes equations were solved in Fluent using the second order implicit density based solver.

2 Results and Discussions

Half wavelength axial velocity profile (Fig. 2(a)) were formed within the resonator, behaving like traveling wave. Induced temperature gradient between hot and cold heat exchangers causes the pressure different built- up near the regenerator, causing air particles to oscillate and move towards the cold heat exchanger. The pressure swing causes the formation of vortex (Fig. 2(b))at the top right corner of the cold heat exchanger which later shifted in the reverse manner. Acoustic streaming was also observed along the upper and lower wall at some distance away from the resonator outlet. We conclude that Fuent code could be employed in simulating the thermoacoustic flow field.

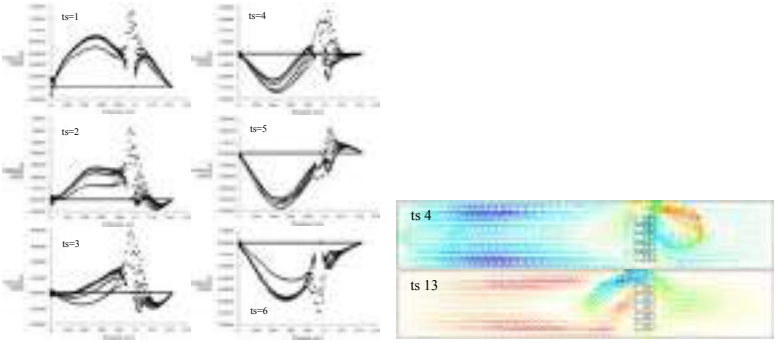

Fig. 2. (a)Axial velocity profile through timestep (*ts*) 1 to 6. (b)Velocity vector at ts=4*s* and ts=13*s*.

References

[C97] Ceperley, P.: A Pistonless Striling engine- the traveling wave heat engine. J. Acoust. Soc. Am. 66, 1508–1513 (1997)

[BS00] Backhaus, S., Swift, G.W.: A thermoacoustic- Stirling heat engine: Detailed study. J. Acoust. Soc. Am. 107, 3148–3166 (2000)

[BK03] Bastyr, K.J., Keolian, R.M.: High-frequency the moacoustic-Stirling heat engine demonstration device. ARLO 4, 2, 37–40 (2003)

[LTS05] Lycklama, J.A., Tijani, M.E.H., Spoelstra, S.: Simulation of a traveling-wave thermoacoustic engine using computational fluid dynamics. J. Acoust. Soc. Am. 118, 2265–2270 (2005)

Numerical Simulation of Acoustic Waves in Jet Flows

A.V. Fedorov[1], N.N. Fedorova[1], I.A. Fedorchenko[1], Yu.G. Korobeinikov[1], K.M. Choo[2], S.B. An[3], and H.J. Lee[2]

[1] Khrisianovich Institute of Theoretical and Applied Mechanics, Siberian Branch of RAS, 4/1, Institutskaya str., Novosibirsk, 630090, Russia
fedorov@itam.nsc.ru
[2] Dooson Corporation LTD, Korea
[3] Korea Polytechnic University, Korea

1 Introduction

A flow field resulting from supersonic gas injection into still medium possesses specific acoustical and gasdynamical characteristics and has many engineering applications. One of them is acoustic drying of materials. Numerical simulation of these kinds of problems meets certain difficulties due to non-stationary character of the phenomenon. The problem becomes even more complex if we consider amplitude-frequency characteristics of the process which depend essentially on gasdynamical and geometric parameters of the flow.

Experimental investigation of the acoustic drying mechanism has been provided at ITAM SB RAS, Novosibirsk, where the issue has being studied for a long period and a new method of acoustic convective drying of porous media has been developed [KFF06]. Numerical results have been obtained by joint effort of ITAM, Dooson Corporation LTD and Korea Polytechnic University.

2 Experimental Results

Here we describe briefly main results obtained experimentally. It has been shown that the most probable way of water extraction from the sample is a sprinkling. It concerns with both convective and acoustic regime of drying. Acoustic effect leads to an averaged drop radius decreasing. It was shown as well that the experimental data on specific humidity vs. time in the processes of convective and acoustic convective drying is described satisfactory by a linear kinetics equation. Performed investigations have shown advantage of the acoustic convective drying compare to the pure convective drying.

3 Numerical Results

In order to investigate acoustical parameters of the flow numerical simulation is applied. ITAM calculations have been carried out with the aid of an in-house code based on Navier-Stokes equations [BF96] and included laminar flow computations only. Dooson Corporation LTD results for turbulent flow have been obtained with EFD 2007 code based on URANS equations; 3D modeling has been performed in SolidWorks 2007.

First laminar flow computations of a sonic air injection into an unlimited space have been carried out for the purpose of the model validation. The obtained results have demonstrated multi-barrel structure of the flow, and comparison with an empirical relation on Mach number distribution along the jet axis has shown good agreement.

Important example for the amplitude-frequency characteristics investigation is a problem of a laminar jet interaction with an infinite rigid wall. In order to get characteristic frequency of the process obtained pressure distribution at the wall point located on the jet axis has been undergone by Fourier transformation and the power spectrum has been found. This value of 525 Hz is in a satisfactory agreement with an empirical magnitude 400 Hz [SSU75].

Performed evaluations have allowed simulating a 2D problem similar to the real drying facility. The numerical instantaneous density gradient field is presented in Fig. 1.

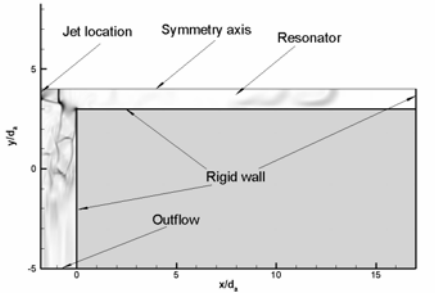

Fig. 1. Flow density gradient distribution

Turbulent parameters of the flow in 3D configuration of the drying facility have been computed as well and main flow distributions have been obtained. Optimal position of the Hartmann generator has been evaluated based on turbulent mixing characteristics of the flow. A proposal concerning the drying installation design has been made and investigations on this topic are in progress.

References

[KFF06] Korobeinikov, Y.G., Fedorov, A.V., Fomin, V.M.: Method of Material Drying and Facility for its Implementation. Russian Federation Invention Patent No. 2270966 (2006)

[BF96] Borisov, A.V., Fedorova, N.N.: Numerical simulation of turbulent flows near the forward-facing steps. Thermophysics and Aeromechanics 4(1), 69–83 (1996)

[SSU75] Semiletenko, B.G., Sobkolov, B.N., Uskov, V.N.: Approximate computation of amplitude frequency characteristics of unsteady supersonic jet interaction with a normal flat obstacle. Izv. SO AN SSSR 3(13) (1975) (in Russian)

Robust BEM Solver for Sound Scattering

Pavel Moses

Ústav technické matematiky, ČVUT v Praze - fakulta strojní, Karlovo nám. 13, 121 35 Praha 2, Czech Rep.
moses.p@seznam.cz

BEM has been extensively used for solution of sound-scattering problems. The usual approach is to transform original Helmholtz equation into boundary integral form using Green's identities or potential relations. However, numerical experiments have shown that solution to exterior problems based on the standard representation does not exist or is not unique for some wave numbers. Theoretical analysis of this issue has been carried out in [Bur73]. Several techniques have been suggested to overcome this difficulty. The Burton-Miller modification of the original integral equation seems to be the most satisfactory, being shown to have unique solution for all values of wave number. Therefore, we base our solver on this formulation rather than on the standard one. We seek solution to the equation

$$\{(M_k - \frac{1}{2}I + \mu N_k)u\}_\Gamma(x,\nu_x) = \tag{1}$$
$$= -u^i(x) - \mu w^i(x) + \{(L_k + \mu(M_k^t + \frac{1}{2}I))w\}_\Gamma(x,\nu_x)$$

for $x \in \Gamma$, which is a problem for general boundary condition. Here, Γ represents the boundary and $\mu \neq 0$ is a coupling parameter. The operators are defined as:

$$\{L_k u\}_\Gamma(x) \equiv \int_\Gamma G_k(x,y)u(x)dS,$$
$$\{M_k u\}_\Gamma(x) \equiv \int_\Gamma \frac{\partial G_k}{\partial \nu_y}(x,y)u(x)dS,$$
$$\{M_k^t u\}_\Gamma(x,s_x) \equiv \frac{\partial}{\partial s_x}\int_\Gamma G_k(x,y)u(x)dS,$$
$$\{N_k u\}_\Gamma(x,s_x) \equiv \frac{\partial}{\partial s_x}\int_\Gamma \frac{\partial G_k}{\partial \nu_y}(x,y)u(x)dS,$$

where $G_k(x,y)$ stands for an apropriate Green's function.

Discretization of the boundary integral may proceed via collocation or Galerkin methods. While collocation is often prefered due to its simplicity,

we implement Galerkin since it is hard to control the error for collocation. Hence, double integrals with weakly singular kernels must be evaluated numerically, for which we have devised effective procedure. Moreover, N_k is strongly singular and requires special treatment. So far no general procedure has been developed for integration of the strongly singular term and it is still subject of ongoing research.

Problems with plane wave as the incident boundary condition are of great practical interest (sound-scattering). Faster convergence for these problems is achieved through application of oscillatory basis functions in the form

$$\varphi = p(x)e^{-ikd\cdot x}, \tag{2}$$

where $p(x)$ is the polynomial and d the direction of the initial wave.

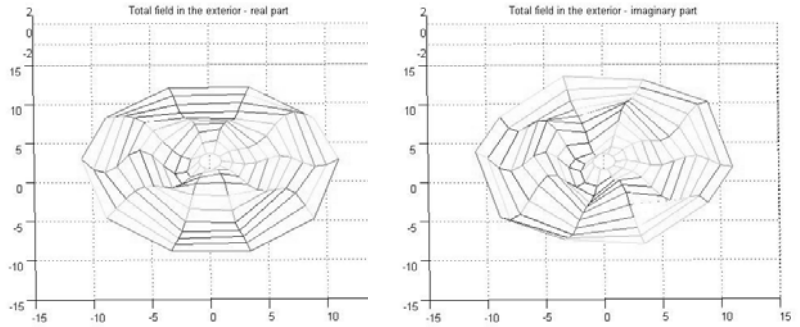

Fig. 1. Real and imaginary part of total pressure field in the vicinity of unit circle for plane wave incident condition

Acknowledgements. This work has been supported by the grant No. 106/08/0403 of Grant Agency of Czech Rep.

References

[AH90] Amini, S., Harris, P.J.: A Comparison Between Various Boundary Integral Formulations of the Exterior Acoustic Problem. Comput. Methods Appl. Mech. Eng. 84(1), 59–75 (1990)

[Bur73] Burton, A.J.: The solution of Helmholtz Equation in Exterior Domains using Integral Equations. NPL Report NAC 30 (1973)

[SR07] Steinbach, O., Rjasanow, S.: The Fast Solution of Boundary Integral Equations. Springer, New York (2007)

Author Index